

THE INTERNATIONAL ARCHIVES OF THE PHOTOGRAMMETRY, REMOTE SENSING AND SPATIAL INFORMATION SCIENCES  
ARCHIVES INTERNATIONALES DE PHOTOGRAMMÉTRIE, DE TÉLÉDÉTECTION ET DE SCIENCES DE L'INFORMATION SPATIALE  
INTERNATIONALES ARCHIV FÜR PHOTOGRAMMETRIE, FERNERKUNDUNG UND RAUMBEZOGENE INFORMATIONSWISSENSCHAFTEN

VOLUME  
VOLUME  
BAND

XXXVI

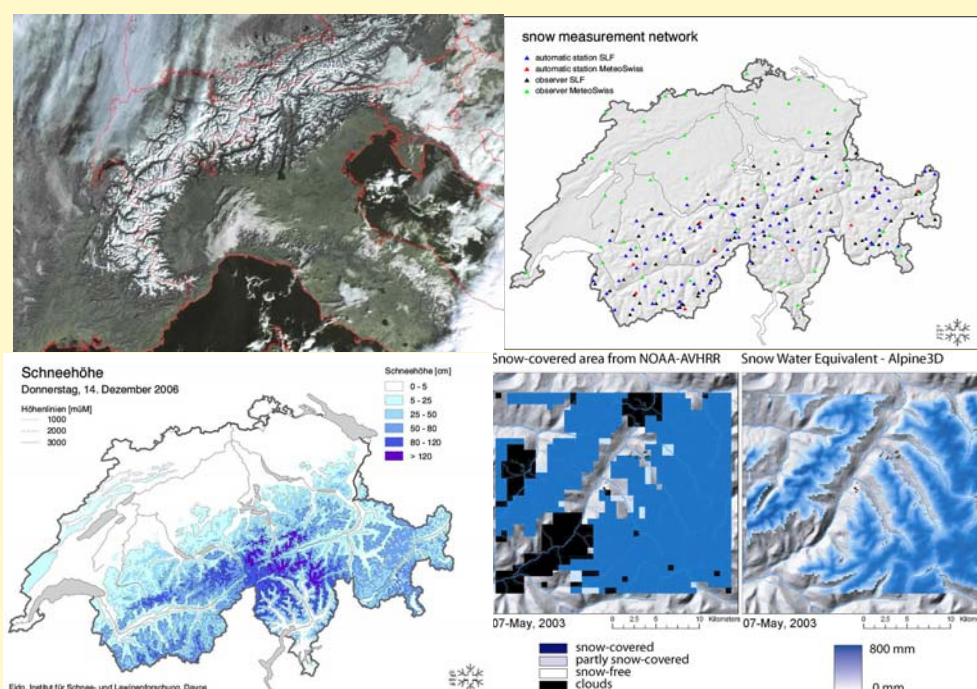
PART  
TOME  
TEIL

7 / C50

# 10<sup>th</sup> International Symposium on Physical Measurements and Signatures in Remote Sensing (ISPMSRS'07)

Davos, Switzerland

12 – 14 March 2007



## Editors

Michael Schaepman, Shunlin Liang, Nikée Groot and Mathias Kneubühler

## Organisers

ISPRS WG VII/1 "Fundamental Physics and Modelling"  
Wageningen University, The Netherlands  
Maryland University, USA  
University of Zurich, Switzerland  
PMOD/WRC, Switzerland

## Sponsors

European Space Agency (ESA)  
Swiss Academy of Sciences  
Wageningen UR / Centre for Geo-Information

HYRESSA / EU FP6  
IEEE GRSS  
University of Zurich / RSL

**PAPER SUBMISSIONS (PRESENTATIONS AND TALKS)**

<b>First Author</b>	<b>Co-Authors</b>	<b>TITLE</b>	<b>No.</b>
S. Briggs		NEW SCIENTIFIC CHALLENGES FOR ESA'S LIVING PLANET PROGRAMME	T1
G. Guyot		EVOLUTION OF RESEARCH ORIENTATION IN THE DOMAIN OF SPECTRAL SIGNATURES	T2paper, T2pres.
W. Schmutz		SPACE EXPERIMENTS OF PMOD/WRC TO MEASURE THE SOLAR CONSTANT AND THE INFLUENCE OF THE SOLAR IRRADIANCE ON THE TERRESTRIAL CLIMATE	T3
J.-L. Widlowski	M. Robustelli M. Disney J.-P. Gastellu-Etchegorry T. Lavergne P. Lewis E. Martin P. R. J. North B. Pinty M. Taberner R. Thompson M.M. Verstraete	THE RAMI ON-LINE MODEL CHECKER (ROMC)	T9
T. Quaife	P. Lewis M. Disney M. de Kauwe M. Williams B. Lawc	ASSIMILATING REFLECTANCE DATA INTO A ECOSYSTEM MODEL TO IMPROVE ESTIMATES OF TERRESTRIAL CARBON FLUX.	T11
K. Ma	F. Baret P. Barroy L. Bousquet	A LEAF OPTICAL PROPERTIES MODEL ACCOUNTING FOR DIFFERENCES BETWEEN THE TWO FACES	T13
P. Lewis	M. Disney Y. Knyazikhin T. Quaife M. Schull	MODELLING CANOPY REFLECTANCE WITH SPECTRAL INVARIANTS	T14
M.I. Disney	P. Lewis	SPECTRAL INVARIANT BEHAVIOUR OF A COMPLEX 3D FOREST CANOPY	T15
Z. Malenovský	R. Zurita-Milla L. Homolová E. Martin M.E. Schaepman J.P. Gastellu-Etchegorry R. Pokorný J.G.P.W. Clevers	RETRIEVAL OF CONIFEROUS CANOPY CHLOROPHYLL CONTENT FROM HIGH SPATIAL RESOLUTION HYPERSPECTRAL DATA	T17
N.V. Shabanov	D. Huang Y. Knyazikhin R.B. Myneni	STOCHASTIC RADIATIVE TRANSFER MODEL FOR MIXTURE OF DISCONTINUOUS VEGETATION CANOPIES	T19
M. Rast		GEO (GROUP ON EARTH OBSERVATIONS) AND ITS GLOBAL EARTH OBSERVATION SYSTEM OF SYSTEMS (GEOSS)	T22



S.L. Ustin		PLANS FOR THE U.S. NATIONAL ECOLOGICAL NETWORK:-THE CONTRIBUTION OF REMOTE SENSING	T23
R. Wolfe		PRODUCTION AND DISTRIBUTION OF NASA MODIS REMOTE SENSING PRODUCTS	T25
J. Nieke	The HYRESSA Team	USER-DRIVEN REQUIREMENTS OF THE EUROPEAN HYPERSPECTRAL REMOTE SENSING COMMUNITY	T26
W. Verhoef		A BAYESIAN OPTIMISATION APPROACH FOR MODEL INVERSION OF HYPERSPECTRAL-MULTIDIRECTIONAL OBSERVATIONS: THE BALANCE WITH <i>A PRIOR</i> INFORMATION	T27
F. M. Danson	C. Giacosa R.P. Armitage	TWO-DIMENSIONAL FOREST CANOPY ARCHITECTURE FROM TERRESTRIAL LASER SCANNING	T28
G. Sun	K.J. Ranson J. Masek A. Fu D. Wang	PREDICTING TREE HEIGHT AND BIOMASS FROM GLAS DATA	T30

## PAPER SUBMISSIONS (POSTERS)

First Author	Co-Authors	TITLE	No.
M.D. Steven	T.J. Malthus F. Baret	INTERCALIBRATION OF VEGETATION INDICES - AN UPDATE	P2
A. Riaza	C. Ong A. Müller	PYRITE MINE WASTES HYPERSPECTRAL MONITORING AS A TOOL TO DETECT CLIMATE CHANGE	P4
E. Ben-Dor	A. Chudnovski	REFLECTANCE SPECTROSCOPY IN THE 400-2400 NM TO ASSESS SETTLED DUST IN DIFFERENT URBAN ENVIRONMENTS	P5
R. Zurita-Milla	L. Gómez-Chova J.G.P.W. Clevers M.E. Schaepman G. Camps-Valls	MULTITEMPORAL UNMIXING OF MERIS FR DATA	P6
B.H. Menze	J.A. Ur	CLASSIFICATION OF MULTISPECTRAL ASTER IMAGERY IN THE ARCHAEOLOGICAL SURVEY FOR SETTLEMENT SITES OF THE NEAR EAST	P8
C.G. Marston	R.P. Armitage F.M. Danson P. Giraudoux A. Ramirez P.S. Craig	SPATIO-TEMPORAL MODELLING OF SMALL MAMMAL DISTRIBUTIONS USING MODIS NDVI TIME-SERIES	P9
A. Ramirez	R.P. Armitage F.M. Danson C.G. Marston E.Y. Ogunbadewa	WEB-BASED MODEL FOR ANALYSIS OF TIME SERIES REMOTELY SENSED DATA	P10

	M. Yebra		
A. Gidudu	H. Ruther	COMPARISON OF FEATURE SELECTION TECHNIQUES FOR SVM CLASSIFICATION	P11
J.G.P.W. Clevers	L. Kooistra M.E. Schaepman	CANOPY WATER CONTENT RETRIEVAL FROM HYPERSPECTRAL REMOTE SENSING	P12
S. Lachéradé	C. Miesch D. Boldo X. Briottet C. Valorge H. Le Men	DEVELOPMENT OF AN INVERSION CODE, ICARE, ABLE TO EXTRACT URBAN AREAS GROUND REFLECTANCES	P13
N. Sánchez	R. González J. Prado J. Martínez-Fernández C. Pérez-Gutiérrez	ESTIMATING VEGETATION PARAMETERS OF CEREALS USING AN ASTER 1A IMAGE	P16
D. Odermatt	T. Heege J. Nieke M. Kneubühler K. Itten	CONSTITUTION OF AN AUTOMIZED PROCESSING CHAIN TO ANALYSE A MERIS TIME SERIES OF SWISS LAKES	P17
O. Frey	F. Morsdorf E. Meier	TOMOGRAPHIC SAR IMAGING OF A FORESTED AREA BY TIME-DOMAIN BACK-PROJECTION	P23
L. Kooistra	L. Sanchez-Prieto H.M. Bartholomeus M.E. Schaepman	REGIONAL MAPPING OF PLANT FUNCTIONAL TYPES IN RIVER FLOODPLAIN ECOSYSTEMS USING AIRBORNE IMAGING SPECTROSCOPY DATA	P27
B. Koetz	F. Morsdorf T. Curt S. van der Linden L. Borgniet D. Odermatt S. Alleaume C. Lampin M. Jappiot B. Allgöwer	FUSION OF IMAGING SPECTROMETER AND LIDAR DATA USING SUPPORT VECTOR MACHINES FOR LAND COVER CLASSIFICATION IN THE CONTEXT OF FOREST FIRE MANAGEMENT	P29
M. Schaepman	M. Hoogerwerf J. van der Vegte F. van der Wel W. Som de Cerff R. van Hees B. Domenico S. Nativi O. Wilhelmi	THE RELEVANCE AND USE OF ATMOSPHERIC DATA ACCESS FOR THE GEOSPATIAL USER COMMUNITY (ADAGUC)	P30
Y. Zeng	M.E. Schaepman B. Wu J.G.P.W. Clevers A.K. Bregt	USING LINEAR SPECTRAL UNMIXING OF HIGH SPATIAL RESOLUTION AND HYPERSPECTRAL DATA FOR GEOMETRIC-OPTICAL MODELLING	P31
G. Schaepman-Strub	T. Painter M. Schaepman	ALBEDO ASSESSMENT AND EVALUATION OVER ARCTIC SIBERIAN TUNDRA	P35
L. Waser	M. Baltsavias H. Eisenbeiss	CHANGE DETECTION IN MIRE ECOSYSTEMS: ASSESSING	P36

	C. Ginzler A. Gruen M. Kuechler P. Thee	CHANGES OF FOREST AREA USING AIRBORNE REMOTE SENSING DATA	
Z. Kugler	T. de Groeve G.R. Brakenridge E. Anderson	TOWARDS A NEAR-REAL TIME GLOBAL FLOOD DETECTION SYSTEM (GFDS)	P37
M. Ozdogan	G. Gutman	TOWARDS GLOBAL MAPPING OF IRRIGATED AGRICULTURE	P40
A.E. Akay	I.R. Karas R. Gundogan	CLASSIFICATION OF TREE AND SHRUB SPECIES IN KSU RESEARCH AND APPLICATION FOREST IN KAHRAMANMARAS, TURKEY	P41
C. Gagliano	F. de Natale F. Incerti F. Maselli	ALTERNATIVE APPLICATION OF THE K-NN METHOD FOR MAPPING FOREST COVER TYPE	P43
B. Koetz	M. Kneubühler S. Huber J. Schopfer F. Baret	RADIATIVE TRANSFER MODEL INVERSION BASED ON MULTI- TEMPORAL CHRIS/PROBA DATA FOR LAI ESTIMATION	P45
J. Sobrino	J.C. Jiménez-Muñoz M. Gómez A. Barella-Ortiz G. Sòria Y. Julien M.M. Zaragova-Ivorra J.A. Gómez E. de Miguel M. Jiménez B. Su W. Timmermans J. Moreno L. Guanter R. Bianchi	APPLICATION OF HIGH-RESOLUTION THERMAL INFRARED REMOTE SENSING TO ASSESS LAND SURFACE TEMPERATURE AND EMISSION IN DIFFERENT NATURAL ENVIRONMENTS	P47
J. Verrelst	R. Zurita-Milla B. Koetz J.G.P.W. Clevers M.E. Schaepman	ANGULAR UNMIXING OF PHOTOSYNTHETIC AND NON- PHOTOSYNTHETIC VEGETATION WITHIN A CONIFEROUS FOREST USING CHRIS-PROBA	P49
A. Damm	P. Hostert	MODELLING REFLECTANCE OF URBAN CHESTNUT TREES: A SENSITIVITY ANALYSIS OF MODEL INVERSION FOR SINGLE TREES	P51
M. Jiménez	E. de Miguel J.A. Gómez J. A. Sobrino J.C. Jiménez-Muñoz J. Chico E. Prado C. Robles	AIRBORNE HYPERSPECTRAL SCANNER (AHS) SPECTRAL EMISSION RETRIEVAL IN 8-13 $\mu\text{M}$	P55
G. Sun	D. Liu K.J. Ranson B. Koetz	SIMULATION STUDIES OF THE EFFECT OF FOREST SPATIAL STRUCTURE ON INSAR SIGNATURE	P57
F. Daumard	Y. Goulas	ATMOSPHERIC CORRECTION OF	P58

	A. Ounis R. Pedros I. Moya	AIRBORNE PASSIVE MEASUREMENTS OF FLUORESCENCE	
V.C. Vanderbilt	C.S.T. Daughtry A. Russ S.L. Ustin J.A. Greenberg	SHOULD WE EXPECT ANOMALOUS DISPERSION IN THE POLARIZED REFLECTANCE OF LEAVES?	P59
S. Hancock	P. Lewis J.-P. Muller M. Disney	USING MONTE-CARLO RAY TRACING TO INVESTIGATE THE MEASUREMENT OF FOREST PARAMETERS WITH THE ECHIDNA™ LASER SCANNER	P60
E. Conejo	J.-P. Frangi S. Jacquemoud G. de Rosny	RAMIS: A BIOPHOTONIC PHYSIOLOGICAL PLANT SENSOR (FIELD RADIOMETER FOR CANOPY REMOTE SENSING)	P61
M. Bachmann	S. Holzwarth A. Müller	INFLUENCE OF LOCAL INCIDENCE ANGLE EFFECTS ON GROUND COVER ESTIMATES	P62
M. Pfeifer	M. Disney P. Lewis	SIMULATING CANOPY GAP FRACTION OF COMPLEX 3D FOREST SCENES OF <i>PICEA SITCHENSIS</i> (SITKA SPRUCE)	P63
M. Schlerf	W. Verhoef H. Buddenbaum J. Hill C. Atzberger A. Skidmore	COMPARING THREE CANOPY REFLECTANCE MODELS WITH HYPERSPSPECTRAL MULTI-ANGULAR SATELLITE DATA	P64
J. Keller	S. Bojinski A.S.H. Prevot	SIMULTANEOUS RETRIEVAL OF AEROSOL AND SURFACE OPTICAL PROPERTIES USING MULTI-ANGLE IMAGING SPECTRORADIOMETER (MISR) DATA	P66
J.-B. Feret	G. P. Asner C. François R. Martin S. L. Ustin S. Jacquemoud	AN ADVANCED LEAF OPTICAL PROPERTIES MODEL INCLUDING PHOTOSYNTHETIC PIGMENTS	P67
S. Zhao	L. Zhang L. Li	A METHOD FOR MEASURING THE PERMITTIVITY OF ARTIFICIAL FROZEN SOIL USING NETWORK ANALYZER	P70
T. Jackson	R. Bindlish J. Du M. Cosh L. Li P. Gaiser E. Kabala B. Hornbuckle	SOIL MOISTURE EXPERIMENTS 2005 (SMEX05): PASSIVE MICROWAVE POLARIMETRIC SIGNATURES OF SOIL MOISTURE AND VEGETATION	P72
S.G.R. Salim	N.P. Fox E.R. Woolliams R. Winkler H.M. Pegrum T. Sun K.T.V. Grattan	REFERENCE SPECTROMETRY FOR CALIBRATION OF OPTICAL EARTH OBSERVATION SYSTEMS	P73

F. Naseri	A.A. Darvishsefat H. Sobhani M. Namiranian	ESTIMATION OF FOREST STAND PARAMETERS IN DENSITY CLASSES IN ARID AND SEMI-ARID REGIONS USING LANDSAT ETM+ DATA	P75
S.K. Alavipanah	R. Amiri K. Khodaei	THE USE OF SPECTRAL SIGNATURES IN EXTRACTING INFORMATION FROM WATER QUALITY PARAMETERS IN THE LAKE URMIA, IRAN	P76
A. Bannari	A.M. Guedon A. El-Harti F.Z. Cherkaoui A. El-Ghmari A. Saquaque	SLIGHT AND MODERATE SALINE AND SODIC SOILS CHARACTERIZATION IN IRRIGATED AGRICULTURAL LAND USING MULITSPECTRAL REMOTE SENSING	P77
B. Seiler	M. Kneubühler B. Wolfgramm K.I. Itten	QUANTITATIVE ASSESSMENT OF SOIL PARAMETERS IN WESTERN TAJIKISTAN USING A SOIL SPECTRAL LIBRARY APPROACH	P78
A. Visscher von Arx	S. Huber M. Kneubühler K. Itten	LEAF AREA INDEX ESTIMATES OBTAINED FOR MIXED FOREST USING HEMISPHERICAL PHOTOGRAPHY AND HYMAP DATA	P79
S. Huber	M. Kneubühler B. Koetz J.T. Schopfer N.E. Zimmermann K.I. Itten	ESTIMATING NITROGEN CONCENTRATION FROM DIRECTIONAL CHRIS/PROBA DATA	P80
M. Jiménez	R. Díaz-Delgado P. Vaughan A. de Santis A. Fernández-Renau E. Prado O. Gutiérrez de la Cámara	AIRBORNE HYPERSPECTRAL SCANNER (AHS) A PRIORI MAPPING CAPACITY SIMULATION FOR THE <i>DOÑANA BIOLOGICAL RESERVE</i> SHRUBLANDS	P81
M. Eiden	S. van der Linden J.H. Schween C. Gerbig B. Neininger Y. Brunet N. Jarosz O. Traullé H. Geiss U. Rascher	ELUCIDATING PHYSIOLOGY OF PLANT MEDIATED EXCHANGE PROCESSES USING AIRBORNE HYPERSPECTRAL REFLECTANCE MEASUREMENTS IN SYNOPSIS WITH EDDY COVARIANCE DATA	P82
A. Psomas	M. Kneubühler K. Itten N.E. Zimmermann	HYPERSPECTRAL REMOTE SENSING FOR SEASONAL ESTIMATION OF ABOVEGROUND BIOMASS IN GRASSLAND HABITATS	P84
H.M. Pegrum	N.P. Fox E.J. Milton M. Chapman	DEVELOPMENT OF THE GONIO RADIOMETRIC SPECTROMETER SYSTEM TO CONDUCT MULTI-ANGULAR MEASUREMENTS OF TERRESTRIAL SURFACES	P90
J.T. Schopfer	S. Dangel M. Kneubühler	DUAL FIELD-OF-VIEW GONIOMETER SYSTEM FIGOS	P91



	K.I. Itten		
L. Homolová	Z. Malenovský J. Hanuš I. Tomášková M. Dvorská R. Pokorný	COMPARISON OF DIFFERENT GROUND TECHNIQUES TO MAP LEAF AREA INDEX OF NORWAY SPRUCE FOREST CANOPY	P95
A. Hüni	J. Nieke J. Schopfer M. Kneubühler K.I. Itten	2ND GENERATION OF RSL'S SPECTRUM DATABASE "SPECCHIO"	P98
B. Allgöwer		WELCOME BY SCIENCE CITY DAVOS – CUTTING EDGE RESEARCH IN A REMOTE PLACE	T0

### ABSTRACT SUBMISSIONS

First Author	Co-Authors	TITLE	No.
G. Dedieu	A. Karnieli O. Hagolle H. Jeanjean F. Cabot P. Ferrier Y. Yaniv	THE VEN $\mu$ S MISSION: EARTH OBSERVATION WITH HIGH SPATIAL AND TEMPORAL RESOLUTION CAPABILITIES	T4
A. Lyapustin	Y. Wang	A GENERIC AEROSOL-SURFACE REFLECTANCE RETRIEVAL ALGORITHM FOR MODIS	T5
C. Borel	C. Spencer	ATMOSPHERIC CORRECTION OF AIRBORNE POLARIMETRIC IMAGERY USING VECTORIZED 6S	T6
F. Baret	M. Weiss P. Bicheron R. Lacaze M. Leroy	CYCLOPES PROTOTYPE V4 LAI, FAPAR AND FCOVER PRODUCTS DERIVED FROM VEGETATION AND AVHRR SENSORS: DESCRIPTION AND VALIDATION	T7
J.-P. Muller	R. Preusker J. Fischer M. Zühlke C. Brockmann N. Fomferra P. Regner	MERIS LAND SURFACE BRDF/ALBEDO RETRIEVAL USING DATA FUSION WITH MODIS BRDF AND ITS VALIDATION USING CONTEMPORANEOUS EO AND IN SITU DATA PRODUCTS	T8
S. Liang	J. Townshend R. Dickinson	A FRAMEWORK OF A REMOTE SENSING DATA ASSIMILATION SYSTEM	T10
B. Pinty	T. Lavergne M. Vossbeck T. Kaminski O. Aussedat R. Giering N. Gobron M. Taberner M.M. Verstraete J.-L. Widlowski	PREPARING FOR THE ASSIMILATION OF REMOTE SENSING PRODUCTS BY LARGE-SCALE MODELS WITH UPDATED LAND SURFACE PROCESS SCHEMES	T12
M. Möttus	M. Rautiainen	APPROXIMATING PHOTON	T16

	P. Stenberg	RECOLLISION PROBABILITY IN VEGETATION CANOPIES	
R. Fernandes	N. Rochdi D. Beal K. Shahid S. Leblanc M. Weiss F. Baret L. Vierling X. Chen A. Conley D. Deering T. Nilson P. Stenberg	CIRCUMPOLAR ASSESSMENT OF THE RELATIONSHIP BETWEEN INFRARED VEGETATION INDICES AND LEAF AREA INDEX IN FOREST	T18
H. Löwe	T. Jonas M. Lehning	ASSIMILATION OF MODIS SNOW DATA IN A DETAILED MODEL OF ALPINE SNOW DYNAMICS AND SNOW HYDROLOGY	T20
T.H. Painter	M.P. Cassidy	INFERENCE OF IMPURITY RADIATIVE FORCING IN SNOW FROM MULTISPECTRAL TO HYPERSPECTRAL IMAGERS	T21
F. Morsdorf	O. Frey B. Koetz E. Meier	MODELING OF SMALL FOOTPRINT AIRBORNE LASER SCANNING RETURNS USING RAY-TRACING AND L-SYSTEMS	T29
A. Royer	G. Picard M. Fily	NORMALIZATION OF MICROWAVE TIME SERIES OBSERVATIONS (1979 - 2005) : APPLICATION TO SURFACE MELTING ANALYSIS OVER ANTARCTICA AND SURFACE TEMPERATURE OVER CANADA/ALASKA	P1
J. Dozier	J. Frew T. Painter	SPACE-TIME SERIES OF MODIS SNOW COVER PRODUCTS FOR HYDROLOGIC SCIENCE	P3
A. Ansari Amoli	A. Alimohammadi	A NEW MULTITEMPORAL CLASSIFICATION APPROACH FOR LAND COVER MAPPING IN IRAN, BY USING HYPERSPECTRAL MODIS DATA	P7
C.C. Borel		REFLECTANCE RETRIEVAL IN SHADE USING ADJOINT RADIOSITY	P14
O. Hagolle	G. Dedieu V. Debaecker	RETRIEVAL OF AEROSOL OPTICAL DEPTH USING MULTI-DATE AND CONSTANT VIEWING ANGLE IMAGES FROM FORMOSAT2 AND VEN $\mu$ S	P15
S.R. Soofbaf	H. Fahimnejad M.J. Valadan Zoej B. Mojaradi	ANOMALY DETECTION ALGORITHMS FOR HYPERSPECTRAL IMAGERY	P18
A. Mac Arthur	C. MacLellan T. Malthus	DETERMINING THE DIRECTIONAL RESPONSE AND FIELD OF VIEW OF TWO FIELD SPECTRORADIOMETERS	P19
E. de Miguel	R. García	THE EFFECT OF NOISE IN AHS	P20

	A. Fernández-Renau	THERMAL BANDS IN THE RETRIEVAL OF PIXEL TEMPERATURE	
L. Quental	A. Sousa S. Marsh	HYPERSPECTRAL IMAGE FILTERING AND IMPLICATIONS FOR ENVIRONMENTAL SPECTRA RELATED TO MINING CONTAMINATION: EXAMPLE FROM S.DOMINGOS MINE, SE PORTUGAL	P21
H. Fahimnejad	S.R. Soofbaf A. Alimohammadi M.J. Valadan Zoej	PREPROCESSING EO-1 HYPERION HYPERSPECTRAL DATA	P22
M. Zappa	A. Morger T. Jonas A. Stoffel N. Foppa	OPERATIONAL ASSIMILATION OF SNOW DEPTH MAPS FOR IMPROVED REAL TIME RUNOFF NOWCASTING WITH SPATIALLY DISTRIBUTED HYDROLOGICAL MODELS	P24
N. Foppa	M. Zappa M. Stähli M. Lehning D. Gustafsson	INTERCOMPARISON BETWEEN MODELLED AND SATELLITE-DERIVED SNOW COVER EXTENT WITHIN THE ALPINE AND SUBALPINE ZONE OF THE SWISS ALPS	P25
G. Picard	L. Brucker M. Fily	MODELING MICROWAVE BRIGHTNESS TEMPERATURE IN ANTARCTICA.	P26
A.J.W. de Wit	C.A. van Diepen	CROP MODEL DATA ASSIMILATION WITH THE ENSEMBLE KALMAN FILTER FOR IMPROVING REGIONAL CROP YIELD FORECASTS	P28
L. Jia	M.H. Voogt C.M.J. Jacobs B.J.J.M. van den Hurk, , A. de Wit E. Moors	SEASONAL COMPARISON OF CARBON FLUX ESTIMATES FROM C-TESSEL MODEL AND MODERATE RESOLUTION IMAGING SPECTRORADIOMETER (MODIS) OVER SEVERAL BIOMES	P32
M. Schneebeli	U. Wandinger I. Matthis E. Brocard C. Mätzler	COMBINATION OF RAMAN LIDAR AND MICROWAVE RADIOMETER SENSED WATER VAPOUR DATA	P33
A. Omani	M.R. Saradjian	ABILITIES OF DEMETER SATELLITE IN OBSERVATION OF PHYSICAL SIGNATURES PERTURBATION OF IONOSPHERE ASSOCIATED WITH SEISMIC ACTIVITIES	P34
T. Lavergne	T. Kaminski B. Pinty M. Taberner N. Gobron M. Verstraete M. Vossbeck J.-L. Widlowski R. Giering O. Aussedat	APPLICATION TO MISR LAND BRFS OF THE RPV MODEL INVERSION PACKAGE TO ASSESS ENVIRONMENTAL PATTERNS	P38
F. Fontana	C. Rixen T. Jonas S. Wunderle	VALIDATION OF REMOTE SENSING NDVI TIME SERIES WITH GROUND BASED MEASUREMENTS FROM THE	P39

		AUTOMATED CLIMATE STATION NETWORK IMIS	
A. Baraldi	D. Simonetti V. Puzzolo S. Natali	A COMPLETELY AUTOMATIC SPECTRAL RULE-BASED PRELIMINARY CLASSIFICATION OF CALIBRATED LANDSAT 5 TM AND LANDSAT 7 ETM+ IMAGES SCALABLE TO ASTER, AVHRR, MODIS, SPOT-4, SPOT-5, AND SPOT VEGETATION IMAGERY	P42
S.M. Shahrokhy		SHADOWED FEATURE CLASSIFICATION IN HYPERSPECTRAL IMAGES	P44
T. Selige	U. Schmidhalter J. Böhner	TOPSOIL MAPPING USING HYPERSPECTRAL SENSING	P46
F. Baret	G. Billard O. Marloie A. Labouret	PAR@METER: A WIRELESS SYSTEM FOR FAPAR AND LAI CONTINUOUS MONITORING	P48
J.V. Martonchik	M. Bull V.T. Dang	A STUDY OF SURFACE DIRECTIONAL SHAPES USING MISR	P50
F. Baret	M. Weiss P. Bicheron R. Lacaze M. Leroy	CYCLOPES PROTOTYPE V4 LAI, FAPAR AND FCOVER PRODUCTS DERIVED FROM VEGETATION AND AVHRR SENSORS: DESCRIPTION AND VALIDATION	P52
R.B. Myneni	W. Yang R.R. Nemani A.R. Huete R.E. Dickinson Y. Knyazikhin K. Didan R. Fu R.I. Negrón Juárez S.S. Saatchi H. Hashimoto K. Ichii N.V. Shabanov B. Tan P. Ratana J.L. Privette J.T. Morissette E.F. Vermote D.P. Roy R.E. Wolfe M.A. Friedl S.W. Running P. Votava N. El-Saleous S. Devadiga Y. Su V.V. Salomonson	LARGE SEASONAL SWINGS IN LEAF AREA OF AMAZON RAINFORESTS	P53
A. Skidmore	J. Ferwerda O. Mutanga S. van Wieren M. Peel	PLANT BIOCHEMICAL MAPS OF FORAGE QUALITY	P54

	R. Grant H. Prins		
F. Veroustraete	W.W. Verstraeten K. Hufkens B. Gielen F. Colson	PHYSICAL MODELLING OF NIKON COOLPIX CAMERA RGB RESPONSES FOR APPLICATION IN NON-DESTRUCTIVE LEAF CHLOROPHYLL IMAGING	P56
M. Rautiainen	P. Stenberg T. Manninen M. Möttöus P. Voipio	FOREST REFLECTANCE MODELING IN THE ARCTIC REGION: RESULTS FROM A CASE STUDY IN FINLAND	P65
T. Warner	A. Almutairi D. Campagna M.D. Nellis	THE ROLE OF IMAGE PROPERTIES IN DETERMINING CHANGE DETECTION ACCURACY	P68
T.H. Painter	N.P. Molotch M.P. Cassidy M. Flanner K. Steffen	CONTACT SPECTROSCOPY FOR DETERMINATION OF STRATIGRAPHY OF SNOW OPTICAL GRAIN SIZE	P69
W. Wang	S. Liang	ESTIMATING CLEAR-SKY LAND SURFACE LONGWAVE RADIATION BUDGET FROM MODIS DATA	P71
V. Lakshmi	B. Hong F. Chen E. Small	IMPLEMENTATION OF BIOPHYSICAL FACTORS INTO THE LAND SURFACE AND ATMOSPHERE INTERACTION MODEL	P74
L.O. Anderson	Y. Malhi L. Aragão Y. Shimabukuro	SPATIAL VARIABILITY OF THE SPECTRAL PROPERTIES OF FOREST STRUCTURES OVER THE AMAZON	P83
H.-Y. Kim	S. Liang	ESTIMATION OF SURFACE SHORTWAVE RADIATION BUDGET FROM MODIS DATA	P85
K. Ma	F. Baret G. Jubelin P. Burger B. Roux S. Labbé J.M. Nolot	EFFECT OF CULTIVAR SPECIFICITIES ON THE RADIOMETRIC RESPONSE: QUANTIFICATION AND CONSEQUENCES FOR BIOPHYSICAL VARIABLES ESTIMATION IN WHEAT CROPS	P86
J. Dowens	T. Malthus L. Belyea	CLASSIFICATION OF BLANKET MIRE MICROHABITATS USING FIELD AND IMAGING SPECTROSCOPY	P87
M. Leroy	P. Bicheron R. Lacaze F. Niño F. Baret J.-L. Roujean O. Hagolle G. Dedieu F. Maignan F.-M. Bréon	THE POSTEL LAND SURFACE THEMATIC CENTER	P88
I. Reusen	The HYRESSA Team	HYRESSA: TOWARDS AN IMPROVED ACCESS TO HYPERSPECTRAL DATA IN EUROPE	P89
I. Moya	F. Daumard N. Moise	SPATIAL VARIABILITY AND ALTITUDE EFFECTS OF PASSIVE CHLOROPHYLL	P93



	Y. Goulas A. Ounis	FLUORESCENCE MEASUREMENTS OVER LA MANCHA (SPAIN) FIELDS	
A.A. Mac Arthur	T.J. Malthus	THE CHARACTERISATION OF HEATHER FOLIAGE AND CANOPIES BY HYPERSPECTRAL REFLECTANCE	P94
N. Gobron	B. Pinty O. Aussedat M. Taberner F. Mélin T. Lavergne M. Robustelli J.-L. Widlowski	VALIDATION OF FAPAR PRODUCTS DERIVED FROM OPTICAL SENSORS: METHOD AND RESULTS.	P96
E.J. Milton	Colleagues from the NCAVEO Partnership	THE NCAVEO 2006 CAL/VAL EXPERIMENT	P97

### HYRESSA WORKSHOP

J.A. Gómez-Sánchez		THE ROLE OF PROTOCOLS AND STANDARDS IN HYPERSPECTRAL DATA ACQUISITION	H1
T. Malthus		OPPORTUNITIES FOR THE DEVELOPMENT OF A EUROPEAN HYPERSPECTRAL RESEARCH INFRASTRUCTURE	H2
J.-L. Brenguier		TRANS-NATIONAL ACCESS AT EQUAL TERMS TO NATIONAL RESEARCH INFRASTRUCTURES IN EUROPE: THE CASE OF RESEARCH AIRCRAFT FOR ENVIRONMENTAL STUDIES	H3
B. Weiss		EUROPEAN RESEARCH INFRASTRUCTURES FRAMEWORK PROGRAMME 7	H4



**WELCOME BY SCIENCE CITY DAVOS –  
Cutting edge research in a remote place**

*Britta Allgöwer*

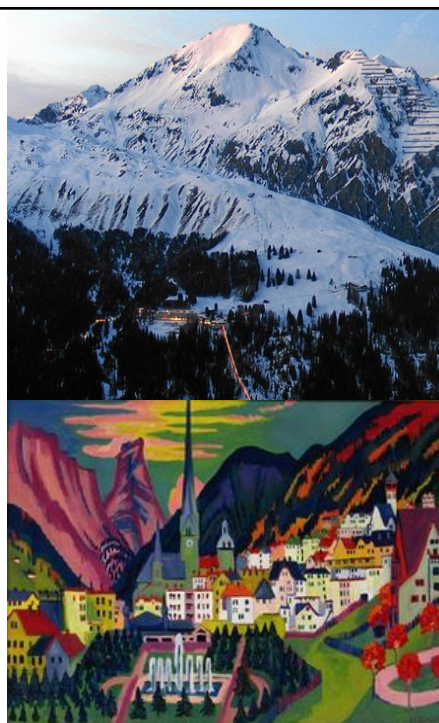
10th Intl. Symposium on Physical Measurements and Signatures in Remote Sensing  
ISPMSRS07, March 12-14, 2007, Davos, Switzerland



## Davos is more than ...

- skiing,
- the WEF,
- Hiking,
- mountain biking,
- cow bells,
- shopping,
- ...

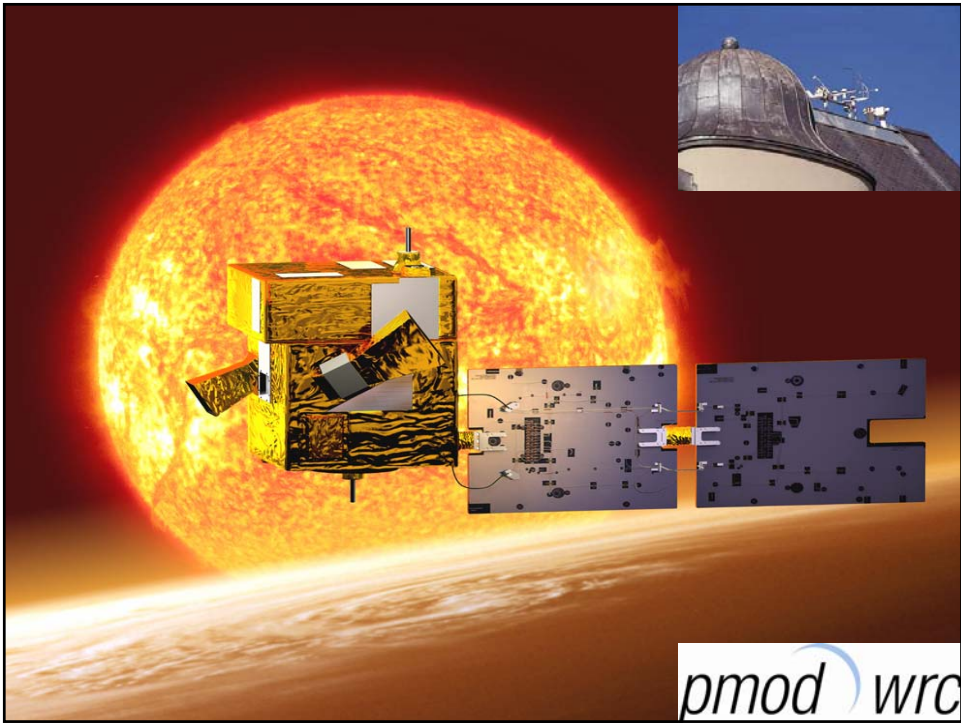
DAVOS  
WISSENSSTADT.CH



... it is home & working place to

- almost 13000 people

... and home to 4 research institutes





### Goals of SIAF

- Development of new therapies
- Innovations in allergy vaccination
- Investigation of the mechanisms of allergic infections

### Major Discoveries at SIAF

- Novel allergen-SIT vaccines
- Immunological mechanisms of asthma
- Immunological mechanisms of atopic dermatitis
- Immune tolerance pathways



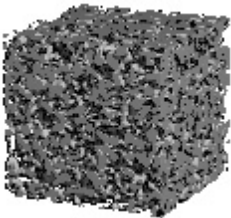
Swiss Institute of Allergy and Asthma Research  
Davos, Switzerland



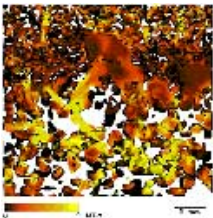




Highlights: Fundamental Snow Physics



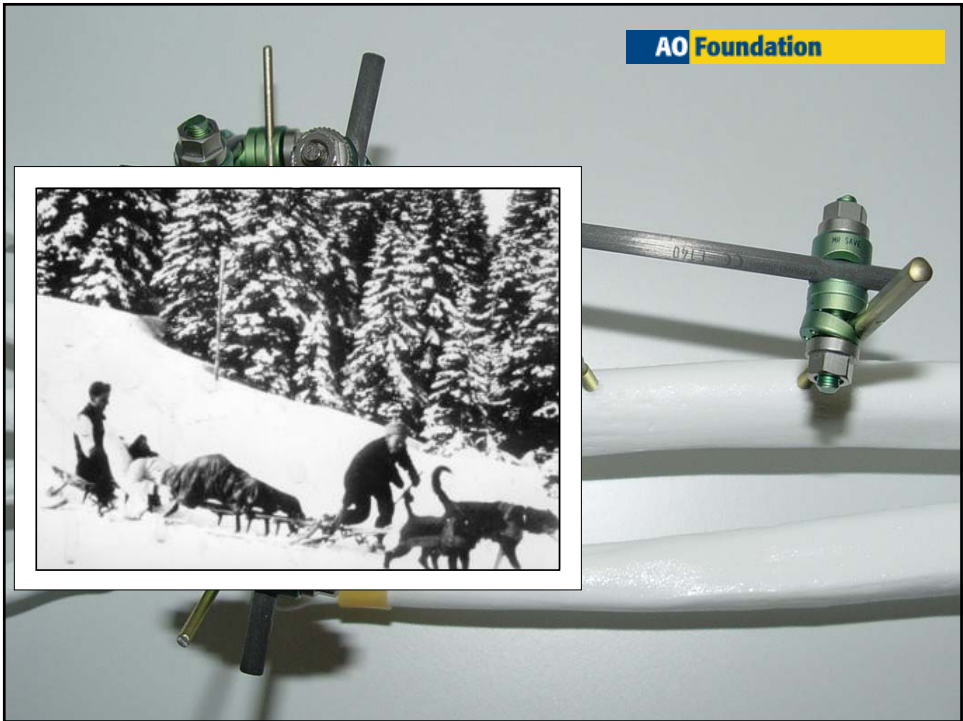
experiment...  
Worldwide first non-destructive structural analysis by X-ray tomography



and theory...  
Numerical finite element calculation of stress distribution within snow structure



- **Goals of ASSIST**
- Providing satellite information rapidly and user friendly on the platforms used by safety and rescue organisations
- preparing measures (*prevention, warning*),
- intervention measures (*closures, evacuations, rescue operations*)
- post-event measures (*event analyses*)





	PMOD/WRC 1907	SIAF 1905	SLF 1931/36 Weissfluhj.	AO Foundation/ Inst 1958
<b>Organisation SFI</b> <div><div>Stiftung Schweizerisches Forschungsinstitut für Hochgebirgsklima und Medizin, Davos (SFI)</div><div>Stiftungsrat ----- Stiftungsratausschuss</div></div>			Approx. 120, → 20 PhD students → 10 MSc students → 3 Postdoc → 10 traineeships → 5 apprenticeships 50 – 60 / year	AO Institute: 70 → 20 PhD students → 20 MSc students → 5 Postdoc AO-Foundation: 220 50 – 60 / year Awards 3 - 6
Förder	<b>Yearly budget of CHF 90 – 100 Mio</b> <b>Approximately 400 collaborators</b>			(yearly);
Aufsichtskommiss SIAF-Univ.Zürich				students vents
	<div><div>SIAF Schweizerisches Institut für Allergie- und Asthmaforschung</div><div>Univ. Zürich</div></div>	<div><div>PMOD / WRC Physikalisch- Meteorologisches Observatorium Weltstrahlungszentrum</div><div>MeteoSchiweiz</div></div>	demonstrations 2562	13952
			CHF 14 Mio., of which CHF 7 Mio. 3 <sup>rd</sup> party money	AO Inst. CHF 9.7 Mio.,(1.3 3 <sup>rd</sup> party) AO-Foundation: CHF 75 Mio

## Who is Science City Davos?

- Federal Institute for Snow and Avalanche Research (SLF/WSL)
- AO Research Institute (Association of Osteosynthesis / Arbeitsgemeinschaft für Osteosynthesefragen)
- Swiss Institute of Asthma and Allergy (SIAF)
- Physikalisch-Meteorologisches Observatorium Davos & Weltstrahlungszentrum (PMOD/WRC)
- Kirchner Museum (Museum of Ernst Ludwig Kirchner)
- Swiss Text Academy (Schweizerische Textakademie)
- Davos Tourism (DT, Davos Tourismus)
- Community of Davos (Landschaft Davos Gemeinde)



## Goals of Science City ([www.wissensstadt.ch](http://www.wissensstadt.ch))


- Interdisciplinary platform of knowledge exchange
- Innovative courses & conferences
- Own research (i.e., evolution of Alpine landscapes / land use change & disturbances)
- Welcome to **ISSW<sub>Europe</sub> 2009**: 27.9. – 2.10.2009
  - Session on Snow and Remote Sensing



## **Image courtesy / copy right**

- PMOD (Werner Schmutz)
- SIAF (Cecmi Adkis)
- SLF (Stefan Margreth)
- AO (John Wilhelm)






# New Scientific Challenges for


## ESA's *Living Planet* Programme

Stephen Briggs

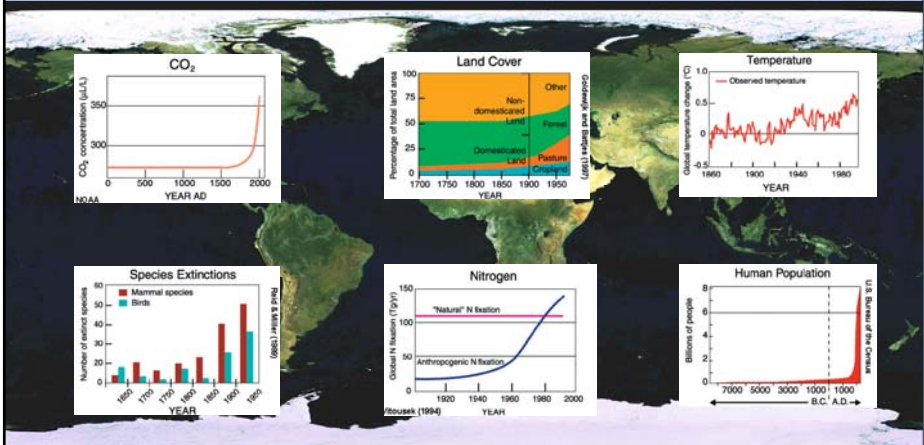
Head, ESA Earth Observation  
Science, Applications and Future Technologies Department

ISPMSRS'07, Davos, 12 March 2007





## Aspects of Global Change



**CO<sub>2</sub>**

CO<sub>2</sub> concentration (ppm)

NOAA

**Land Cover**

Percentage of total land area

Goldewijk & Battjes

**Temperature**

Global temperature change (°C)

Observed temperature

**Species Extinctions**

Number of species

Mammal species

Birds

Reid & Miller

**Nitrogen**

Global N fixation (Tg/yr)

Nature's N fixation

Anthropogenic N fixation

Vitousek (1994)


**Human Population**

Billions of people

US Bureau of the Census

**Based on information compiled by the International Geosphere-Biosphere Programme (IGBP).**


(Image: MERIS mosaic)



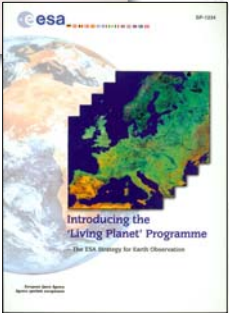
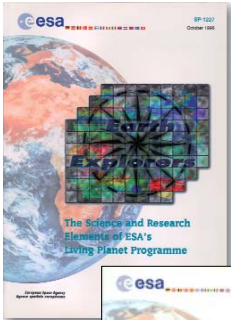
**Data Sources:**

- Carbon Dioxide: NOAA.
- Land Cover: Goldewijk & Battjes, National Institute for Public Health and the Environment (RIVM), Netherlands, 1997.
- Temperature: Source unspecified.
- Species Extinction: Reid & Miller, World Resources Institute, Washington DC, 1989.
- Nitrogen: Vitousek, 1994.
- Human Population: US Bureau of the Census






Previous strategy



- a new Earth observation strategy was introduced in the document SP-1227: **The Science and Research Elements of ESA's Living Planet Programme (1998)**
- the Earth Observation Envelope Programme containing **Earth Explorer** missions and **Development and Exploitation** components was started in 1998
- the scientific strategy was initially formulated with **nine candidate missions** that covered most fields of Earth science and through **data management and exploitation** programme elements
- implementation of the programme is based on continuous and close **interaction with the scientific community**,

  
European Space Agency  
Agence spatiale européenne

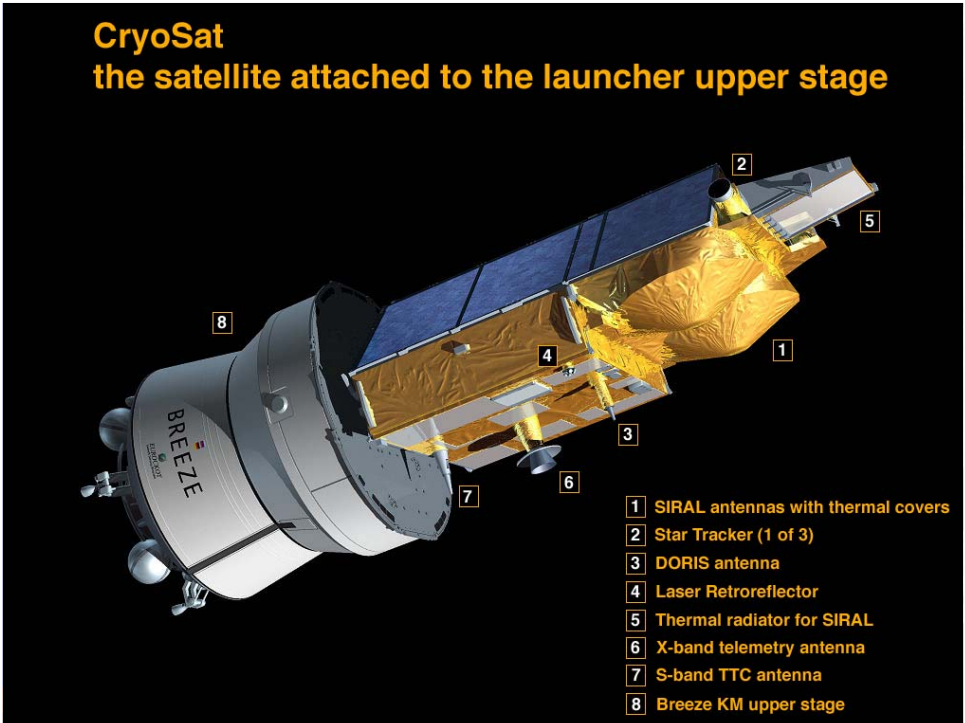
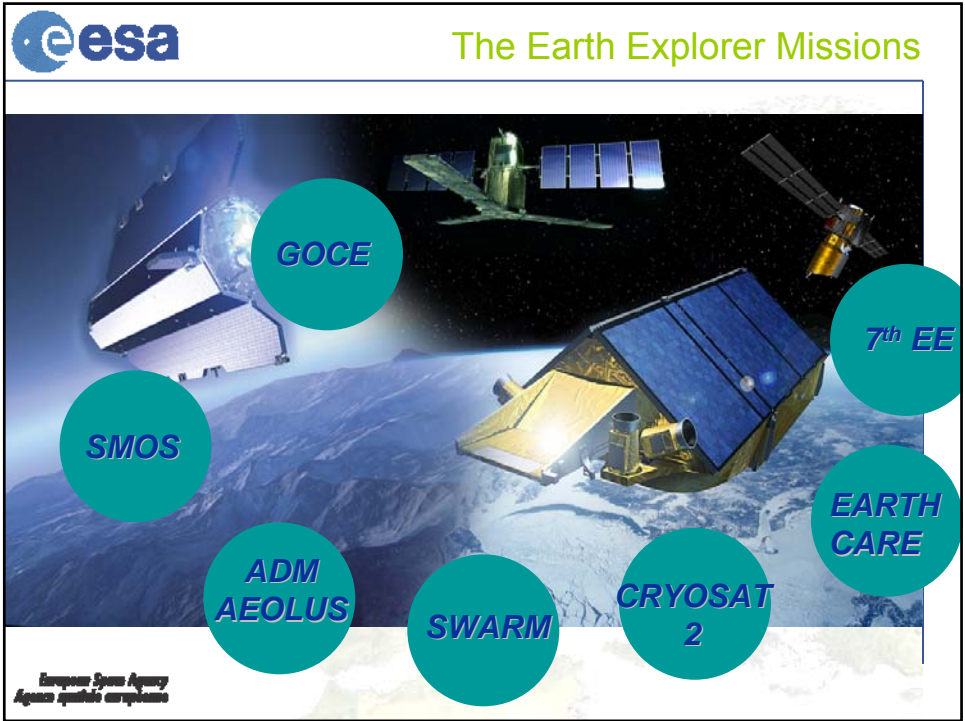



Achievements: Earth Explorers



- since then, two calls for Earth Explorer Opportunity missions and two for Core missions have been issued, with a total response of more than 80 proposals
- six missions have been selected for implementation: CryoSat, GOCE, SMOS, ADM/Aeolus, Swarm and EarthCARE. Missions implemented together with both ESA member states and international partners are among the selected ones.
- in addition a number of missions have been studied at pre Phase-A and Phase-A level
- six new mission concepts have been selected as candidates for the next EE Core mission

  
European Space Agency  
Agence spatiale européenne





### The CryoSat mission

**What are the scientific objectives?**

Improve understanding of:

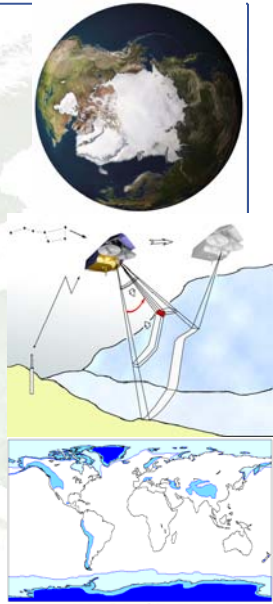
- impact of sea-ice thickness variations on climate
- mass balance of Greenland/Antarctic ice sheets

**How are they achieved?**


- SAR interferometric Radar Altimeter with *precise pointing and orbit determination*
- measurement of Arctic sea-ice thickness variations
- measurement of temporal variations in ice-sheet elevation, including dynamic margins

**What are the benefits?**

- improved parameterisation of sea-ice processes in coupled climate models
- reduced uncertainty in the ice-sheet contribution to global sea-level rise
- advances in cryosphere and climate studies

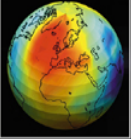


European Space Agency  
Agence spatiale européenne

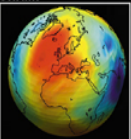


### GOCE - Gravity Field and Steady-State Ocean Circulation Explorer

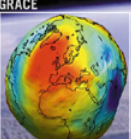
**EARLY GRAVITY MODEL**



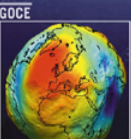
**CHAMP**




**GRACE**



**GOCE**





The GOCE Mission

**What are the scientific objectives?**

Improve understanding of

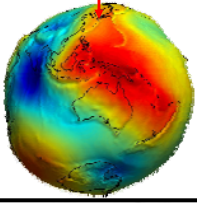
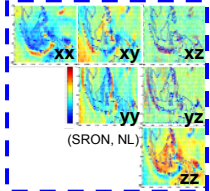
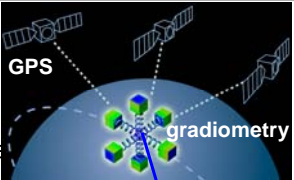
- global ocean circulation and transfer of heat
- physics of the Earth's interior (lithosphere & mantle)
- sea level records, topographic processes, evolution of ice sheets and sea level change

**How are they achieved?**

- Combination of *satellite gradiometry* and *high-low satellite-to-satellite tracking* at  $\pm 250\text{km}$  altitude
- Improved model of the static gravity field and geoid to a resolution of  $100\text{km}$  with  $1\text{mGal}$  resp.  $1\text{-}2\text{cm}$  accuracy


**What are the benefits?**

- An accurate marine geoid for absolute ocean currents
- Improved constraints for interior modelling
- Unified global height reference for land, sea, ice and surveying



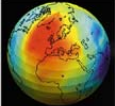
European Space Agency

Agence spatiale européenne

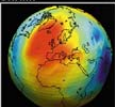


GOCE: Uniqueness and Relevance

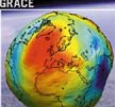
EARLY GRAVITY MODEL



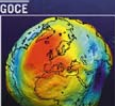
CHAMP



GRACE



GOCE

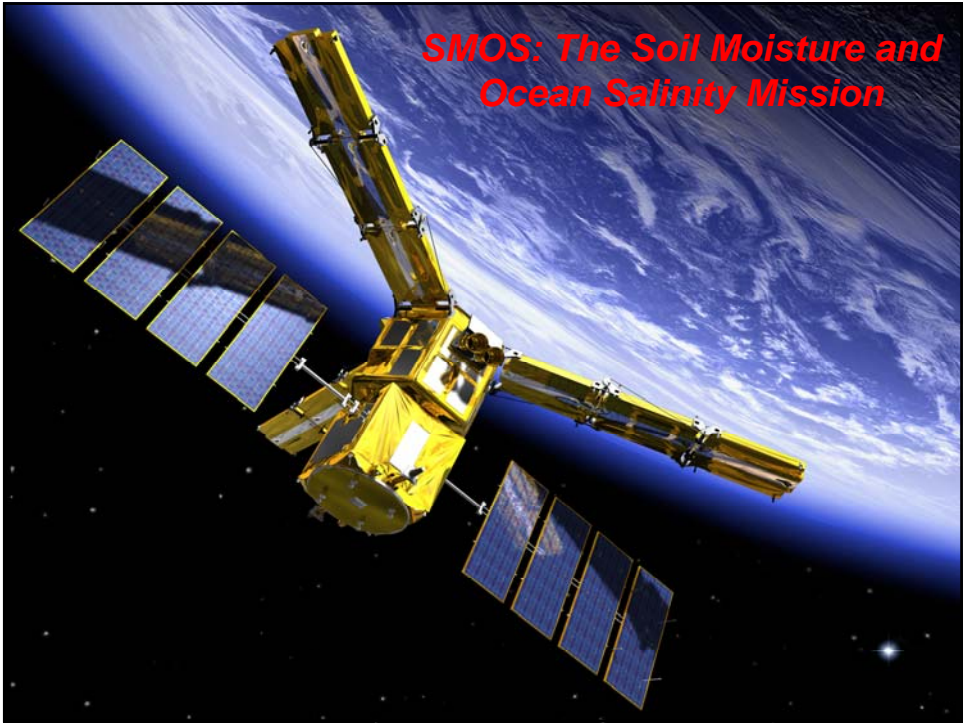



- Only mission with satellite gradiometry (3D) and drag-free control in low orbit ( $250\text{km}$ )
- GOCE will provide global static gravity field with homogeneous quality of unprecedented accuracy and resolution
- Key step in improving ocean, solid Earth and sea level modelling
- Large impact on national height systems and surveying applications on land and sea
- Essential benchmark technique for understanding mass distribution and change
- Element of IGGOS (Integrated Global Geodetic Observing System) and essential for WOCE, WCRP and CLIVAR

European Space Agency

Agence spatiale européenne







*The SMOS Mission*

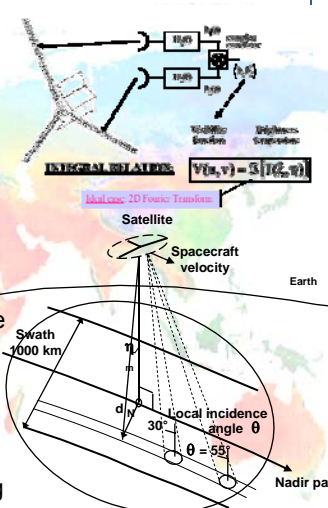
**What are the scientific objectives?:**  
To improve understanding of:

- the water cycle (and the Energy and Carbon Cycle), and
- its representation in mesoscale models (Hydrology, Oceanography and Climate).

**How are they achieved?:**  
Constraining models by global soil moisture and ocean salinity observations estimated from dual-pol., multi-angular, L-band brightness temperature measurement acquired by a 2D interferometer.

**What are the benefits?:**  
Enhancement of the model parameterisation will:

- improve the weather prediction
- improved ocean circulation/hydrology modelling
- better extreme event forecasting



**Integral Equation:**  $T_b(\nu, \theta) = \int_V T(\nu, \theta, \mathbf{r}) dV$

**Local Incidence Angle:**  $\theta = 55^\circ$

**Swath:** 1000 km

**Local Incidence angle  $\theta$**

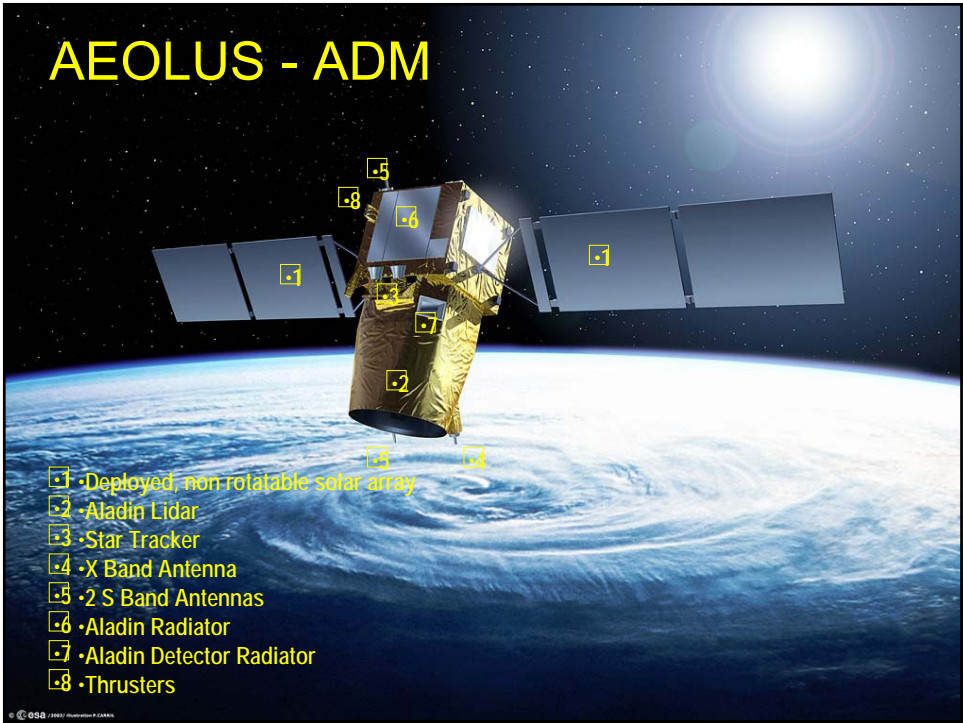
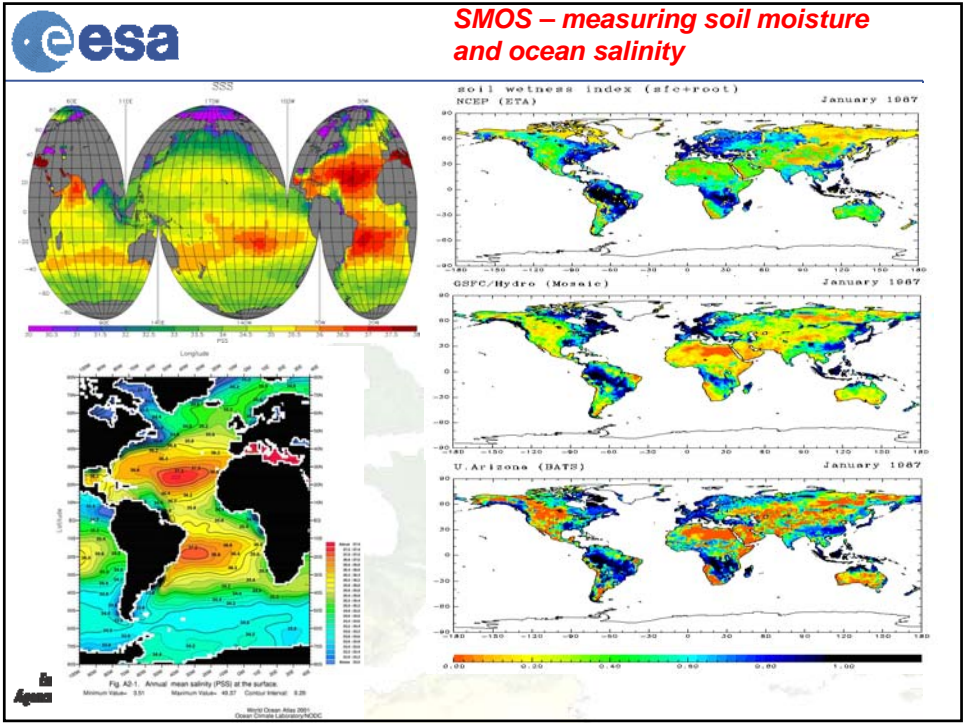
**Nadir path**


**Spacecraft velocity**

**Earth**

**Equation:**  $T_b = f(\nu, p, \theta, T, sm / s, \sigma^0, \dots)$

European Space Agency  
Agence spatiale européenne





Atmospheric dynamics mission

### Aeolus Mission

**What are the scientific objectives?**

Improve understanding of

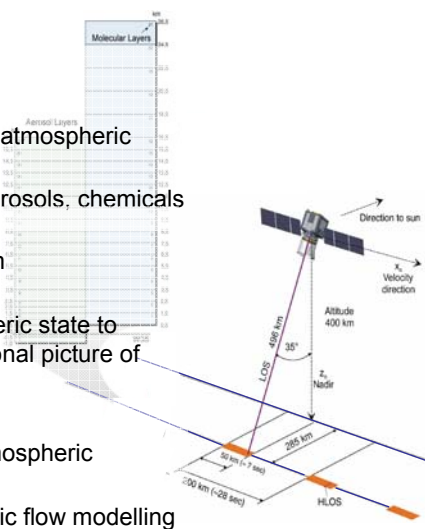
- atmospheric dynamics and global atmospheric transport
- global cycling of energy, water, aerosols, chemicals

**How are they achieved?**

- line of sight winds are derived from aerosol/molecular Doppler shifts
- Improved analysis of the atmospheric state to provide a complete three-dimensional picture of the dynamical variables


**What are the benefits?**

- Improved parameterisation of atmospheric processes in models
- Advanced climate and atmospheric flow modelling
- Better initial conditions for weather forecasting



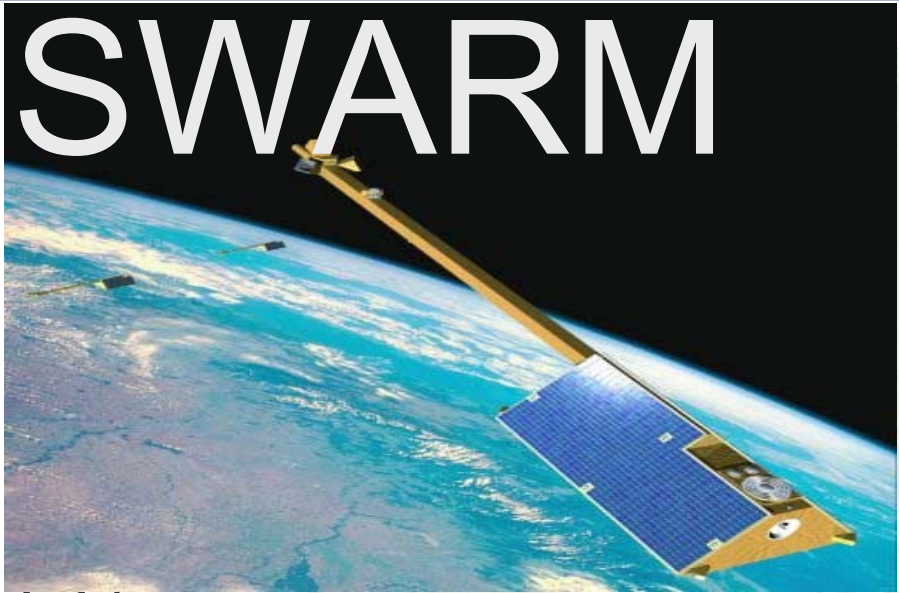
European Space Agency

Agence spatiale européenne



ESA's Magnetic Field Mission


# SWARM



European Space Agency

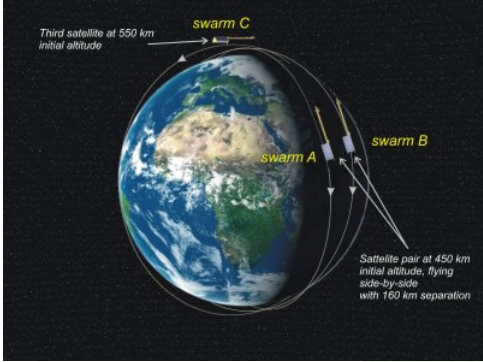
Agence spatiale européenne

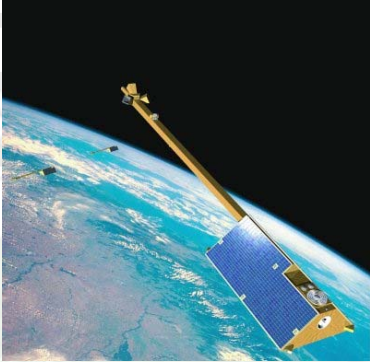




ESA's Magnetic Field Mission


The satellite constellation





- 3 satellites in three different polar orbits between 400 and 550 km altitude
- High-precision and high-resolution measurements of the magnetic field
- GPS receivers, an accelerometer and an electric field instrument provide supplementary information for studying the Earth system.

European Space Agency  
Agence spatiale européenne



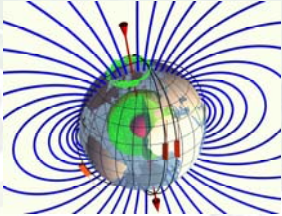
ESA's Magnetic Field Mission

The Earth's Magnetic Field  
and Environment Explorer

SWARM


Its objectives of the SWARM constellation are:

- To provide the best-ever survey of the Earth's geomagnetic field and its variation in time
- To Use of the data obtained to gain new insight into the Earth's interior and climate



European Space Agency  
Agence spatiale européenne





Swarm: Mission Requirements

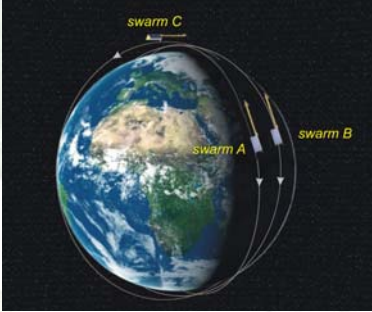
Single satellite

- Magnetic field magnitude and vector components
- Electric field vector components
- Electron density
- Air drag
- Position, attitude and time

accurate enough at satellite altitude to measure the most demanding signals at finest spatial and fastest required temporal sampling

Constellation

- 3 satellites:
  - ❑ 2 side-by-side in low orbit
  - ❑ 1 in higher orbit
- three orbital planes with two different near-polar inclinations
- Near polar orbits for global coverage



European Space Agency

Agence spatiale européenne




ESA's Cloud & Aerosol Mission

EARTHCARE



European Space Agency


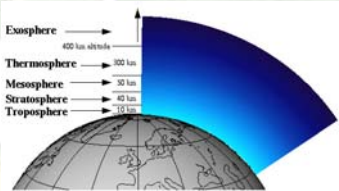
Agence spatiale européenne


ESA's **Cloud & Aerosol Mission**

### The Earth Clouds, Aerosols and Radiation Explorer

EarthCARE is a joint European (ESA) – Japanese (JAXA) mission with the objective:


- to quantify and thus improve understanding of cloud-aerosol-radiation interactions
- to include such parameters correctly and reliably in climate and weather prediction models




ESA's **Cloud & Aerosol Mission**


### Expected Scientific Output

- Vertical profiles of natural and anthropogenic aerosols on a global scale, their radiative properties and interaction with clouds
- Vertical distribution of atmospheric liquid water and ice on a global scale, their transport by clouds and radiative impact
- Cloud overlap in the vertical, cloud-precipitation interactions and the characteristics of vertical motion within clouds
- The profiles of atmospheric radiative heating and cooling through a combination of retrieved aerosol and cloud properties






Six new Earth Explorer missions (2006)




European Space Agency  
Agence spatiale européenne


1. **BIOMASS** – to take global measurements of forest biomass.
2. **TRAQ** (TRopospheric composition and Air Quality) - to monitor air quality and long-range transport of air pollutants.
3. **PREMIER** (PRocess Exploration through Measurements of Infrared and millimetre-wave Emitted Radiation) – to understand processes that link trace gases, radiation, chemistry and climate in the atmosphere.
4. **FLEX** (FLuorescence EXplorer) – to observe global photosynthesis through the measurement of fluorescence.
5. **A-SCOPE** (Advanced Space Carbon and Climate Observation of Planet Earth) – to improve our understanding of the global carbon cycle and regional carbon dioxide fluxes.
6. **CoReH2O** (Cold Regions Hydrology High-resolution Observatory) – to make detailed observations of key snow, ice and water cycle characteristics.



New Earth Explorers (1)




**BIOMASS** – the mission aims at global measurements of **forest biomass**. The measurement is accomplished by a space borne **P-band synthetic aperture polarimetric radar**. The technique is mainly based on the measurement of the cross-polar backscattering coefficient, from which forest biomass is directly retrieved. Use of **multi-polarization measurements and of interferometry** is also proposed to enhance the estimates. In line with the ESAC recommendations, the analysis for this mission will include comparative studies to measure terrestrial biomass using P- or L-band and consideration of **alternative implementations using L-band**.




**TRAQ** – the mission focuses on monitoring **air quality and long-range transport of air pollutants**. A new synergistic sensor concept allows for process studies, particularly with respect to aerosol-cloud interactions. The main issues are the rate of air quality change on regional and global scales, the strength and distribution of **sources and sinks of tropospheric trace gases and aerosols** influencing air quality, and the **role of tropospheric composition in global change**. The instrumentation consists of **imaging spectrometers in the range from ultraviolet to short-wave infrared**.






New Earth Explorers (2)

**PREMIER** – Many of the most important processes for prediction of climate change occur in the upper troposphere and lower stratosphere (UTLS). The objective is to understand the many processes that **link trace gases, radiation, chemistry and climate in the atmosphere – concentrating on the processes in the UTLS region**. By linking with MetOp/ National Polar-orbiting Operational Environmental Satellite System (NPOESS) data, the mission also aims to provide useful insights into processes occurring in the lower troposphere. The instrumentation consists of an **infrared and a microwave radiometer**.




**FLEX** – The main aim of the mission is global remote sensing of **photosynthesis through the measurement of fluorescence**. Photosynthesis by land vegetation is an important component of the global carbon cycle, and is closely linked to the hydrological cycle through transpiration. Currently there are no direct measurements available from satellites of this parameter. The main specification is for instruments to measure **high spectral resolution reflectance and temperature, and to provide a multi-angular capability**.

European Space Agency  
Agence spatiale européenne



New Earth Explorers (3)

**A-SCOPE** – The mission aims to observe **total column carbon dioxide** with a nadir-looking pulsed carbon dioxide Differential Absorption Lidar (**DIAL**) for a better understanding of the global carbon cycle and regional carbon dioxide fluxes, as well as for the validation of greenhouse gas emission inventories. It will provide a **spatially resolved global carbon budget combined with diagnostic model analysis through global and frequent observation of carbon dioxide**. Spin-off products like aerosols, clouds and surface reflectivity are important parameters of the radiation balance of the Earth. A contribution to Numerical Weather Prediction is foreseen in connection with accurate temperature profiles. Investigations on plant stress and vitality will be **supported by a fluorescence imaging spectrometer**.



**CoReH2O** – The mission focuses on spatially detailed observations of key **snow, ice, and water cycle characteristics** necessary for understanding land surface, atmosphere and ocean processes and interactions by using two **synthetic aperture radars at 9.6 and 17.2 GHz**. It aims at closing the gaps in detailed information on snow glaciers, and surface water, with the objectives of improving modelling and prediction of **water balance and streamflow for snow covered and glacierised basins**, understanding and modelling the **water and energy cycles in high latitudes**, assessing and forecasting **water supply from snow cover and glaciers**, including the relation to climate change and variability.

European Space Agency  
Agence spatiale européenne


EE-7 candidate missions - summary				
Mission	Proposers	Objective	Instrumentation and orbit	Evaluation
BIOMASS	T. Le Toan (F) and S. Quegan (UK) + 32 researchers from I, F, A, S, CDN, FIN, D, NL, US, Br, JP	Forest biomass & extent, deforested areas, flooded forests, subsurface imaging in arid areas, Antarctic ice cover, soil moisture, sea surface characteristics (salinity, low frequency surface roughness)	P-band (432-438 MHz) SAR, fully polarimetric or HH/VV polarizations Sun-synchronous, dawn-dusk orbit at 580 km	Unique long wavelength sensor Need process models for above ground biomass assimilation Concerns about ionospheric effects, biomass levels above 150 ton/ha, and radio frequency interference
TRAQ	P. Levelt (NL) and C. Camy-Peyret (F) + 125 researchers from A, B, CDN, CH, D, DK, F, FIN, GR, IE, IT, N, NL, UK, US, CHN, JP	Air quality: megacities emissions, long range transport, diurnal cycle, long-term trends, forecast Sources and sinks of trace gases and aerosols influencing air quality Climate impact of change in tropospheric composition	UV-VIS-NIR nadir grating imaging spectrometer TIR+SWIR FTS cloud imager multi-viewing polarization-resolving imaging radiometer Drifting low Earth orbit	Innovative mission concept with new orbit and new strategy for synergistic use of multiple sensors for retrieval of tropospheric gas-phase and aerosol compounds; great potential for understanding air chemistry and processes; information on air quality for users and decision makers
PREMIER	B. Kerridge (UK) + 60 researchers from D, B, UK, F, S, CH, Gr, I, CDN, Pol, US, Bul, Ind	Convective transport, thin cirrus, tropical tropopause layer, stratosphere-troposphere exchange, gravity waves and global circulation UT humidity and cirrus; radiative forcing by tropospheric O3 and CH4, stratospheric O3 and water vapour, chem-climate interaction (OH chemistry); processes linking clouds and aerosols to atmospheric chemistry and global climate	Limb imaging FTIR for trace gases and particles Push-broom mm/sub-mm wave limb-sounder Sun-synchronous orbit, loose formation flight with Metop to support tropospheric applications	The mission offers greatly improved understanding of UTLS chemistry and climate processes Synergy with MetOp/NPOESS data The timely availability of the Swedish contribution of STEAM-R is mandatory
FLEX	J. Moreno (E) + 77 researchers from B, NL, UK, D, F, E, FIN, CDN, I, CH, AUS, US, JP, Czech	Chlorophyll fluorescence for photochemical processes and terrestrial carbon sequestration, biogeochemical quantities from reflectance and thermal infrared measurements to get vegetation variables for interpretation of fluorescence measurements, and to monitor vegetation health, using fluorescence as an early indicator of stress.	Imaging Spectrometer (480-760nm), resolution 0.1nm, Multi-Angular Vegetation Imaging Spectrometer (400-2400nm), dual-view TIR spectrometer with 3 channels in the 8.8-12 $\mu$ m band Sun-synchronous orbit	Ambitious proposal on chlorophyll fluorescence, multi-spectral and thermal remote sensing Highly precise atmospheric correction together with sub-pixel cloud masking is mandatory
A-SCOPE	P. Flamant (F) + 19 researchers from NL, F, UK, D, E, I, US	Mapping sources and sinks of CO2 Global carbon cycle and regional CO2 fluxes Low bias CO2 data, aerosol and cloud information Contribution to NWP in connection with accurate T profiles Plant stress and vitality	Laser Absorption Spectroscopy (LAS) sensors for CO2 and O2 column soundings ATLID type DIAL for CO2, canopy height, aerosol/clouds layers Fluorescence imaging spectrometer for photosynthesis, plant stress and vitality. Camera for cloud and ground backgrounds Sun-synchronous orbit	Would eliminate three sources of bias for OCO and GOSAT: measure by night as well as by day (sampling time bias); will measure at high latitude; lidar will provide a clear indication of scattering material in the optical path. Potentially significant sources of bias remaining, such as surface pressure and terrain variability Programmatic assumptions of the NASA contribution need to be clarified.
CoReH2O	H. Rott (A) + 33 researchers from D, F, UK, N, I, FIN, US, CDN, A, NL, DK	Estimation of snow and ice masses and their temporal variations for climate modelling and hydrological and NWP modelling	2 SAR instruments in Ku-band (17.2 GHz) and X-band (9.6GHz) on 2 different satellites with VV + VH polarization Dawn/dusk orbit	Snow water equivalent and snowcover of unique importance Cost boundary condition may be met only by implementing the mission with a single satellite
European Space Agency Agence spatiale européenne				

Achievements: Exploitation


- more than 1,500 scientific teams are being provided with satellite data from ERS-1/2, Envisat and Third Party missions.
- users are provided with software toolboxes that ease their work
- a versatile multi-mission ground segment has been implemented, drawing on Member State facilities
- a continuous programme of workshops, summer schools and training courses has been developed
- new scientific results form the basis for implementation of new applications and services



### Achievements: Exploitation




- **develop user communities** for both institutional and commercial applications
- support European companies to develop and **demonstrate information products**
- support value adding and servicing companies in establishing **useful and cost effective services**.



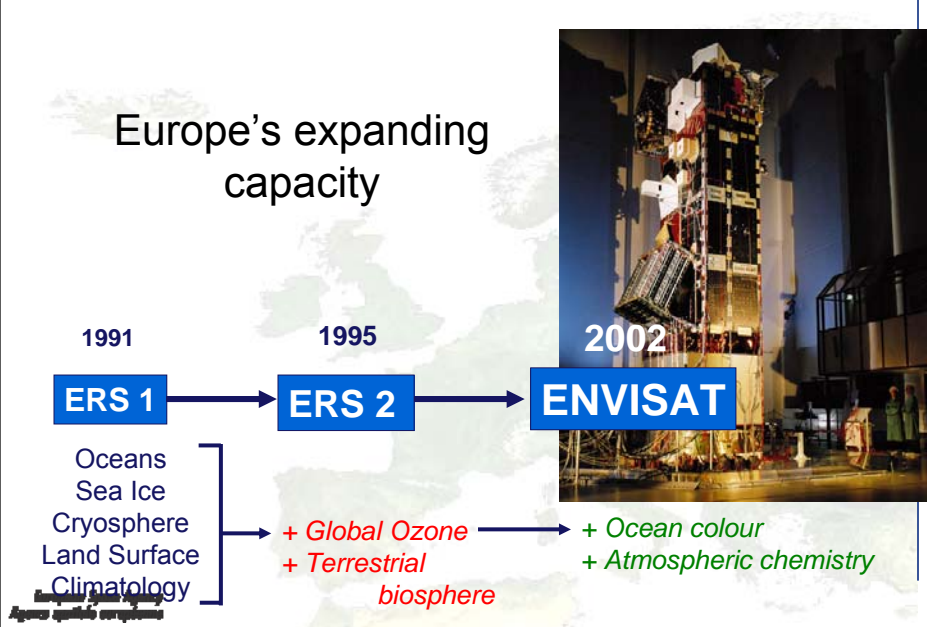
- building **industrial partnerships** to conduct pre-commercial service trials with customers
- marketable **service portfolios** developed with non-EO service suppliers engaged
- better understanding of the prospects for EO in **emerging market sectors**



- the **GMES service element** has established service partnerships
- builds largely on **scientific achievements**
- forms the **space basis for the GMES component**



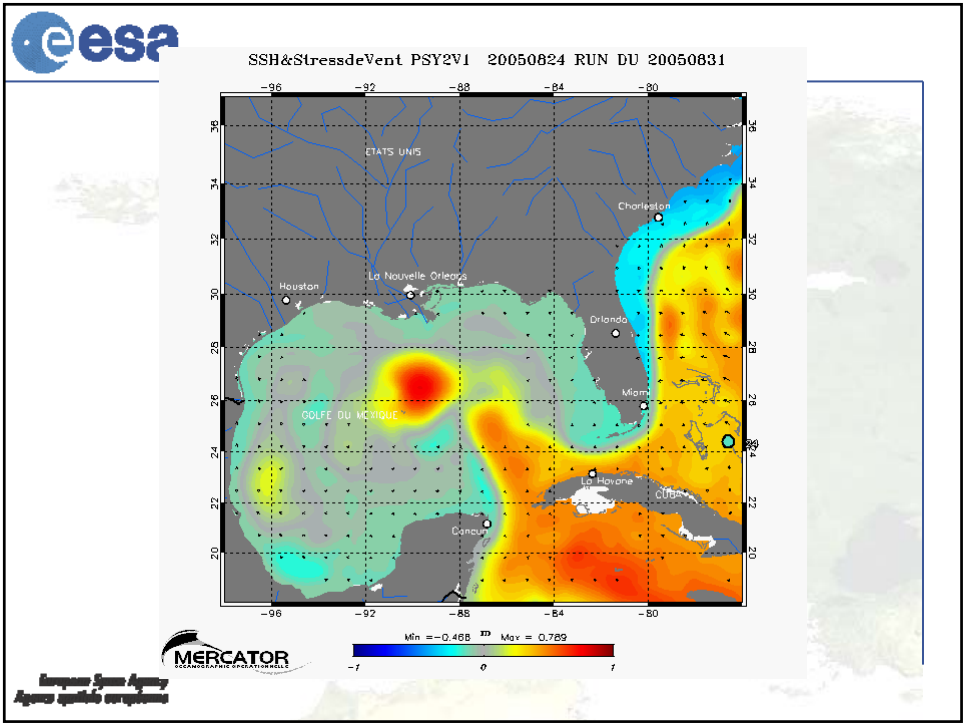
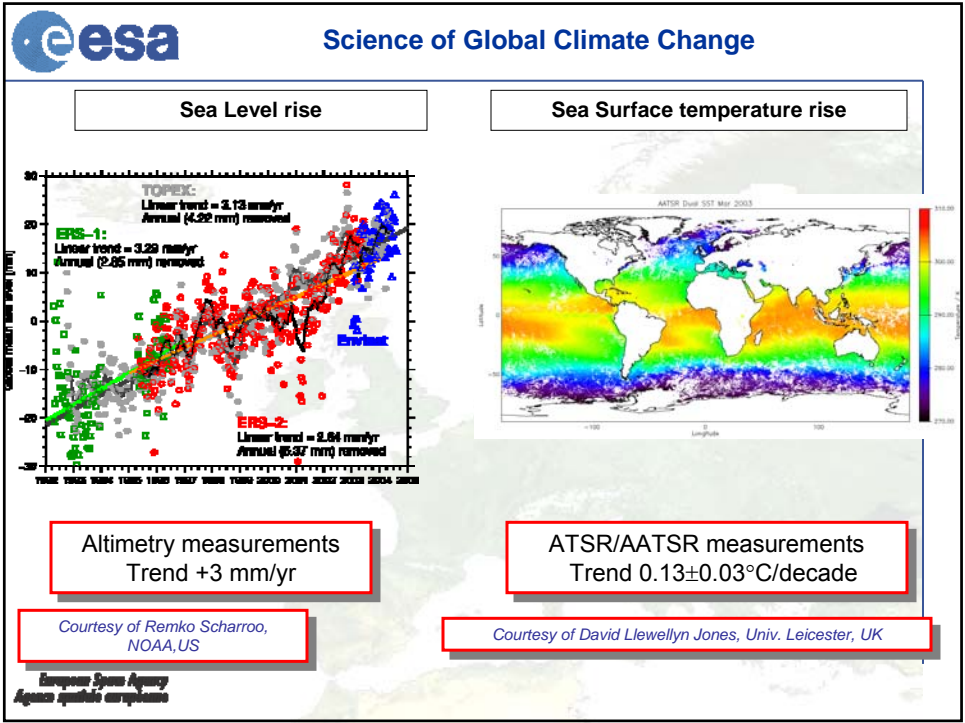
### Europe's expanding capacity

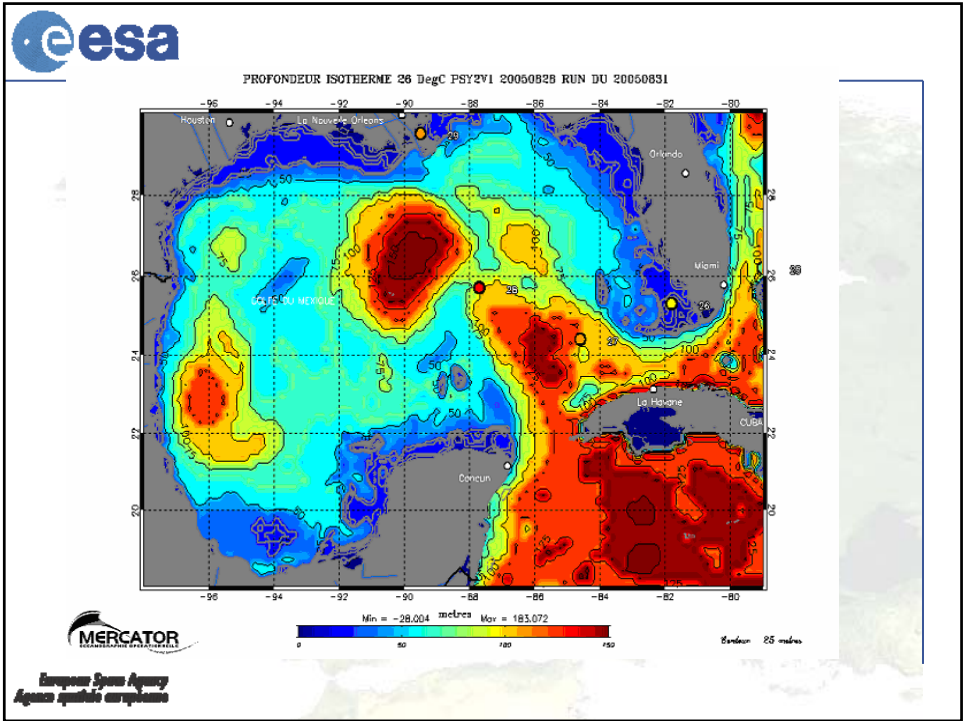


Timeline of European Earth Observation Satellites:

- 1991**: ERS 1
  - Oceans
  - Sea Ice
  - Cryosphere
  - Land Surface
  - Climatology
- 1995**: ERS 2
  - + Global Ozone
  - + Terrestrial biosphere
- 2002**: ENVISAT
  - + Ocean colour
  - + Atmospheric chemistry





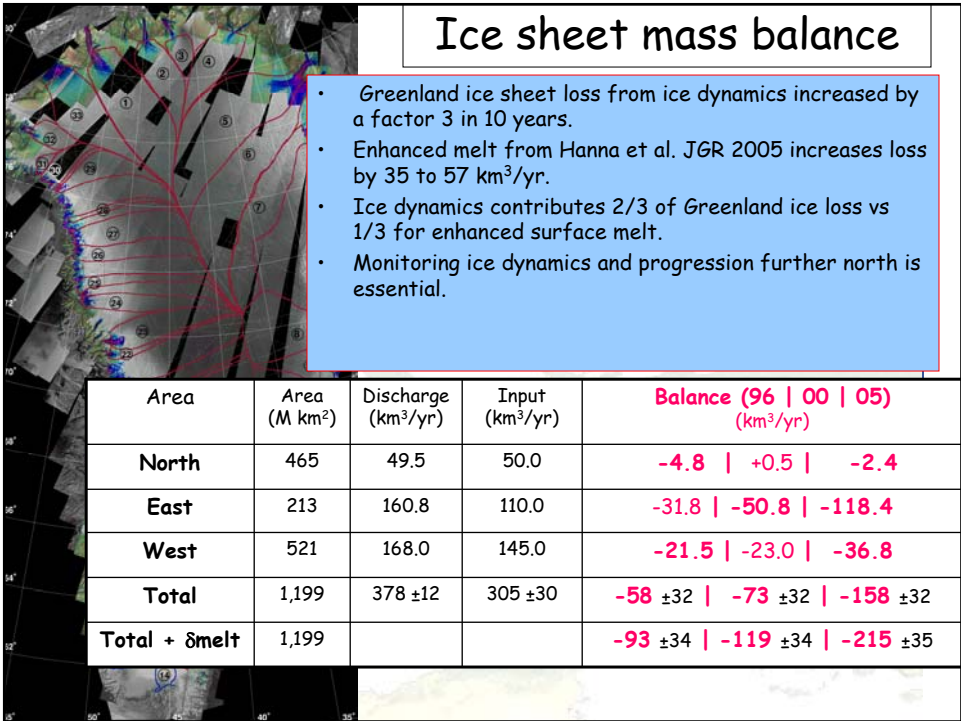
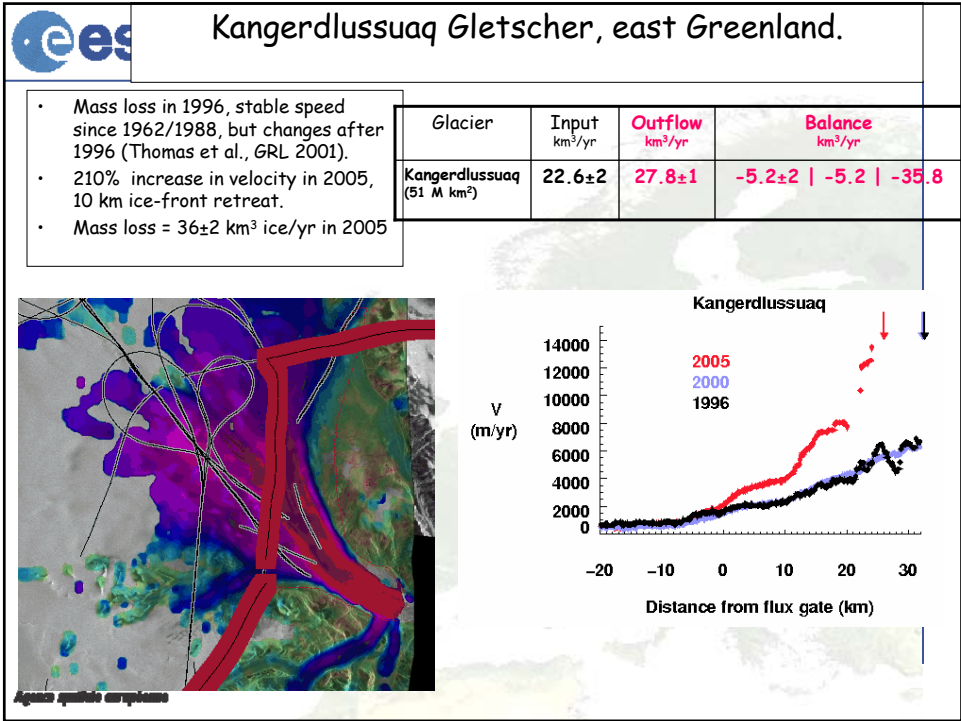


# Greenland ice velocities: Envisat vs Radarsat-1 background missions

Eric Rignot<sup>1</sup> and Pannir Kanagaratnam<sup>2</sup>

<sup>1</sup>Jet Propulsion Laboratory, Caltech  
<sup>2</sup>University of Kansas, CReSiS.



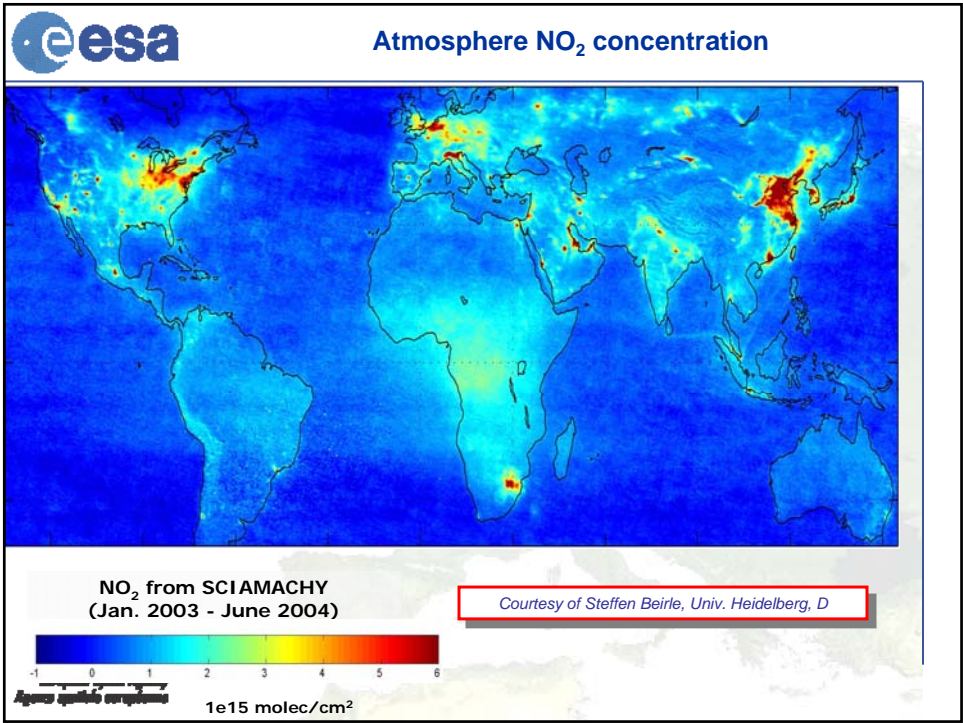
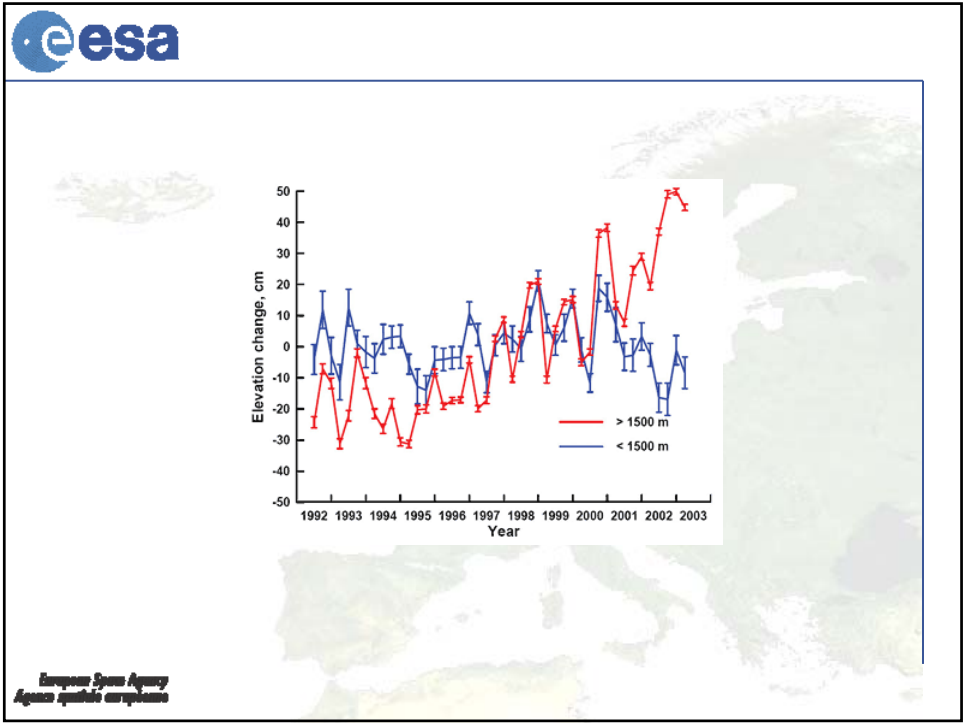


### Conclusions

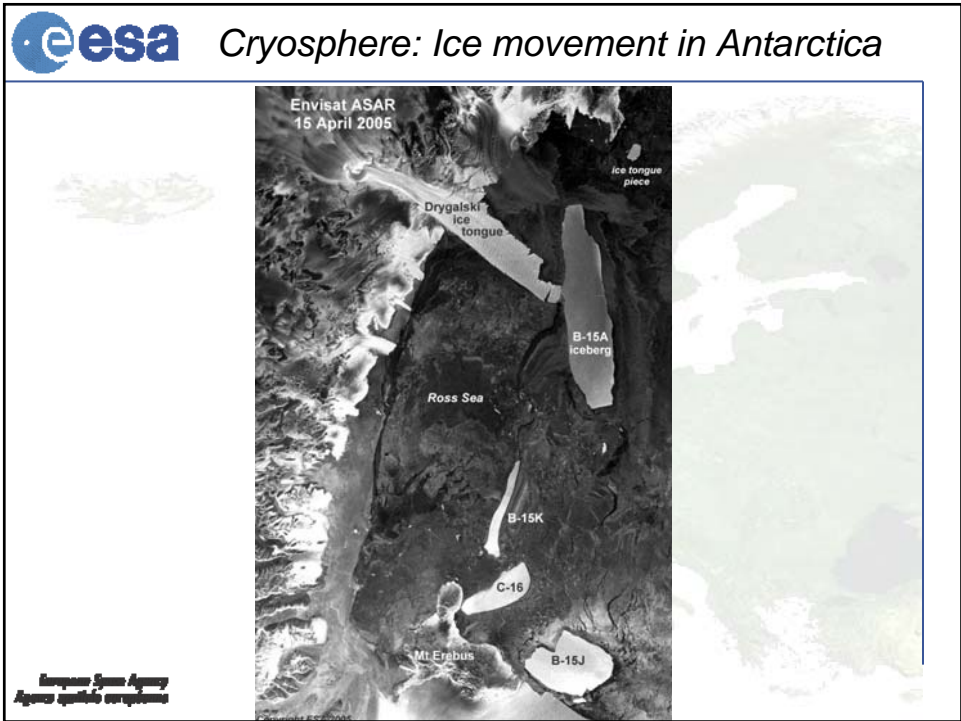
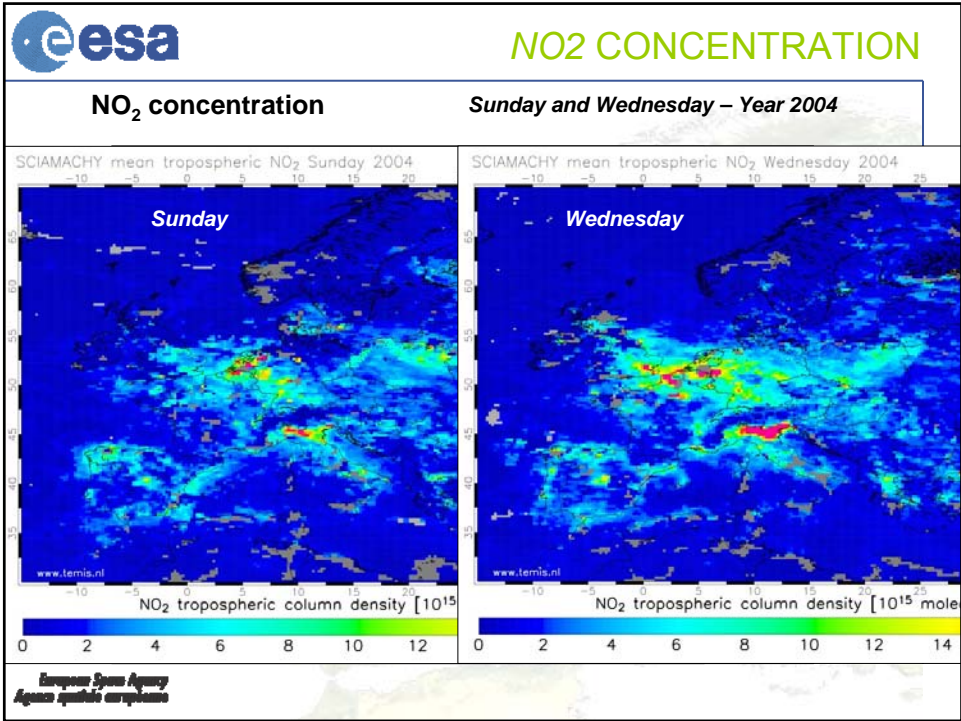
- A first mapping of Greenland ice velocities has been achieved with Radarsat-1 HH-polarization 2000 background mission.
- We can do as well with Envisat ASAR if we operate at HH-polarization, with short baselines.
- Comparison of these data with ERS-1/2 1996, Envisat ASAR 2004/2005 and Radarsat-1 2005 has been used to detect glacier speed up in Greenland and determine how the boundary of acceleration has been migrating northward.
- Mass loss from Greenland is revised upwards from these results which show dominant role of ice dynamics.
- Contribution to sea level rise of GrIS is 0.65 mm/yr in 2005, or twice that in 1995.

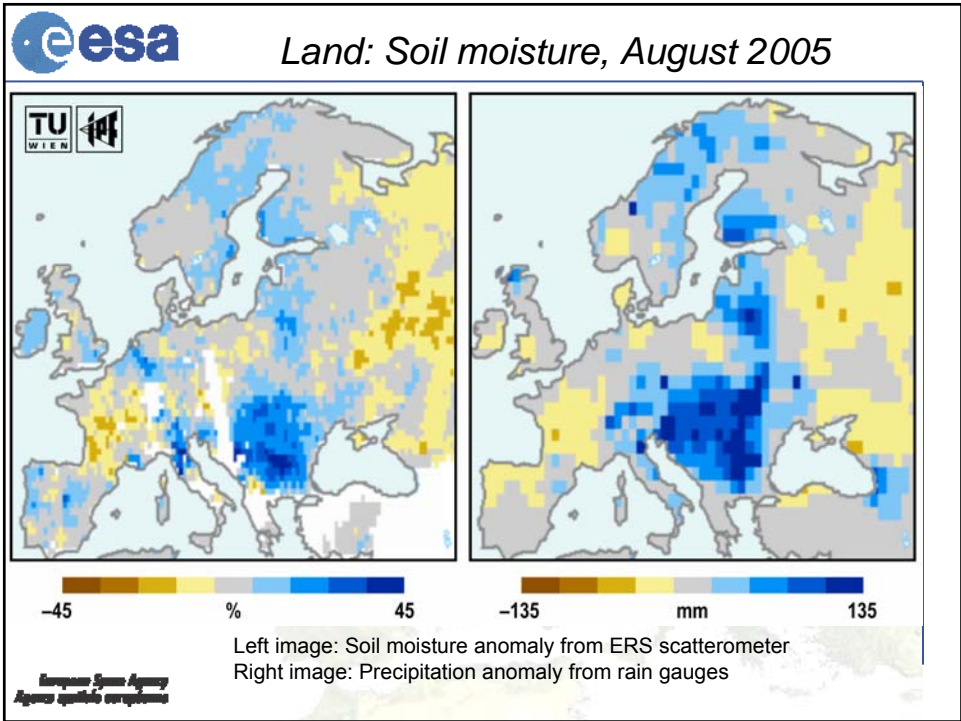
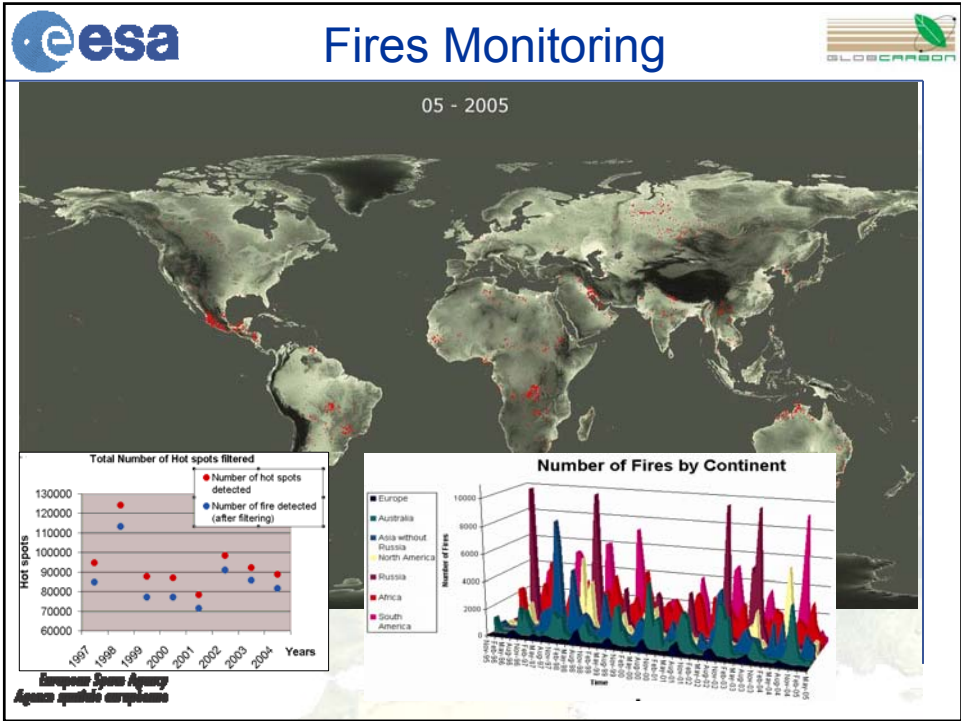
O. M. Johannessen, K. S. Khvorostovsky, M. W. Miles and L. P. Bobylev (2005): Recent ice sheet growth in the interior of Greenland. Science (In Press, and October 20, 2005 issue of Science Express).

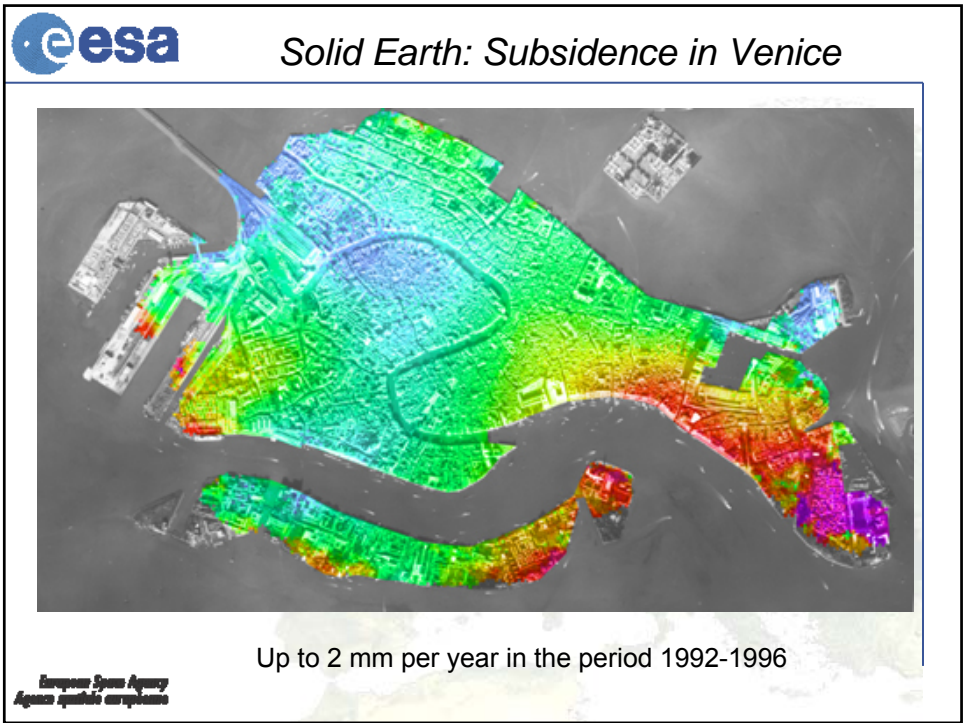
Greenland ice-sheet elevation change in cm/year (see colour scale) derived from 11 years of ERS-1/ERS-2 satellite altimeter data, 1992-2003,






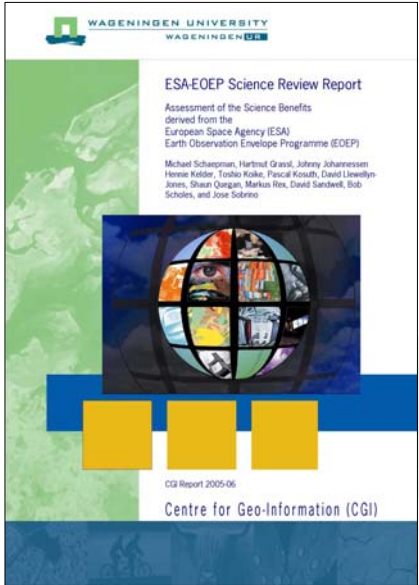










### Science review of the EOEP



- in 2005 a committee consisting of six external scientists and six ESAC members undertook a thorough review of the scientific value of the Earth Observation Envelope Programme
- the review report was extremely positive in evaluating the science output of the EOEP
- the report contained eleven recommendations to the Agency. These are all currently being implemented.

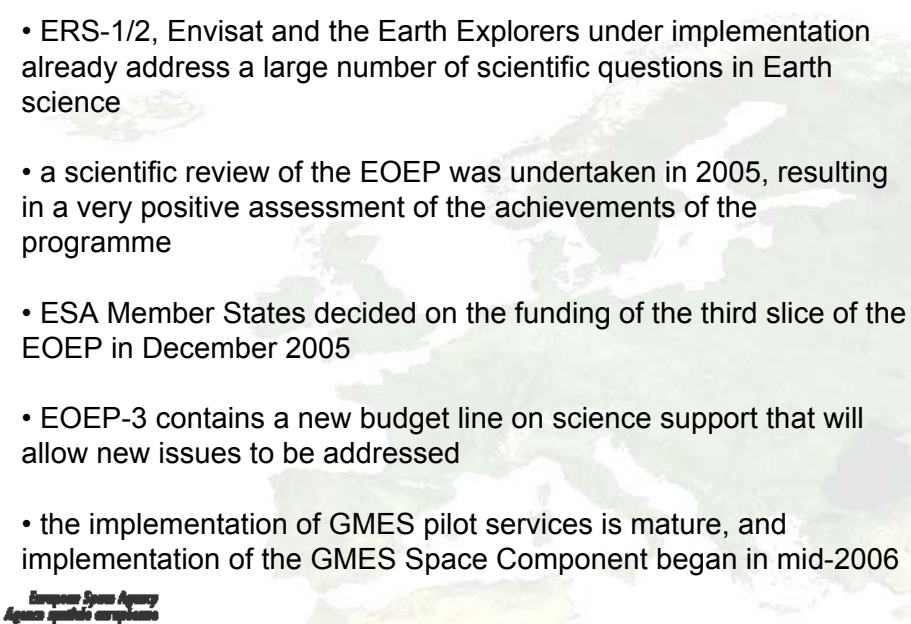







### Summary of programme to date

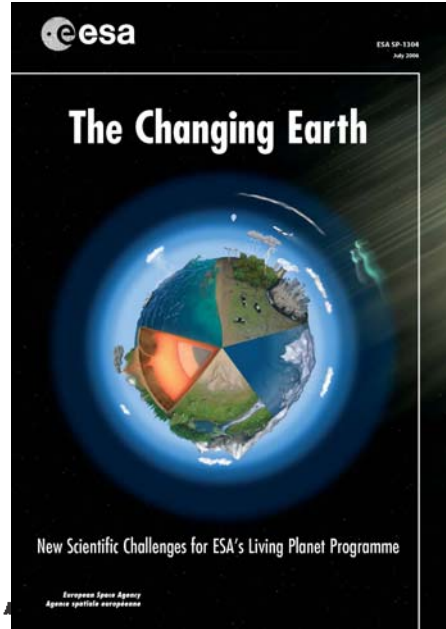
- ERS-1/2, Envisat and the Earth Explorers under implementation already address a large number of scientific questions in Earth science
- a scientific review of the EOEP was undertaken in 2005, resulting in a very positive assessment of the achievements of the programme
- ESA Member States decided on the funding of the third slice of the EOEP in December 2005
- EOEP-3 contains a new budget line on science support that will allow new issues to be addressed
- the implementation of GMES pilot services is mature, and implementation of the GMES Space Component began in mid-2006



European Space Agency  
Agence spatiale européenne



### Scientific challenges for ESA's LPP



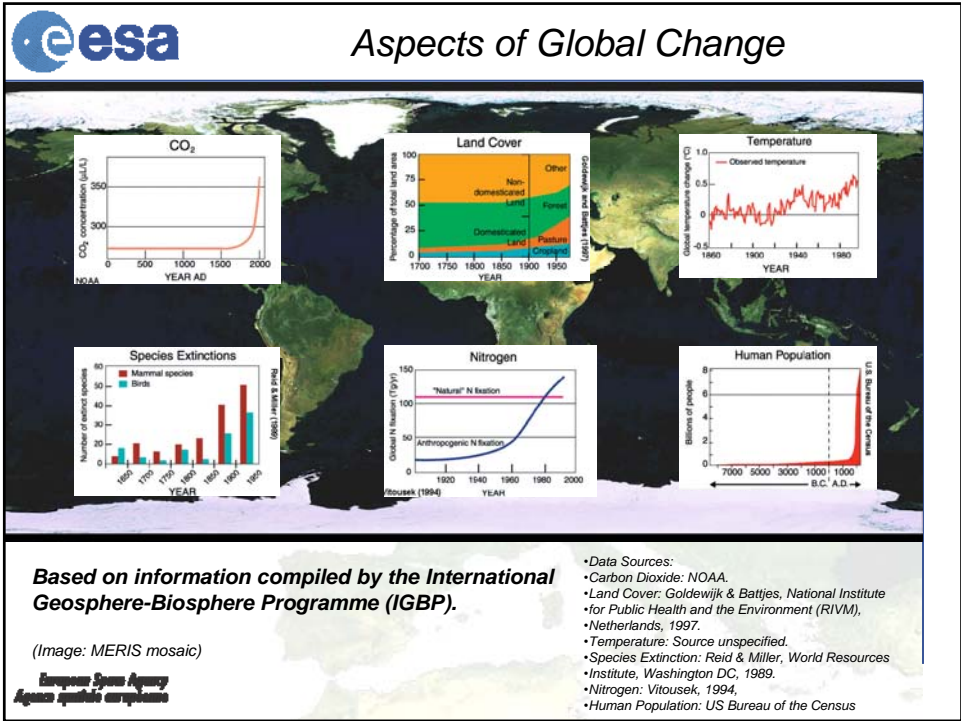
ESA SP-1306  
July 2006

**The Changing Earth**


**New Scientific Challenges for ESA's Living Planet Programme**

European Space Agency  
Agence spatiale européenne


- an updated science strategy for ESA's Living Planet Programme has been formulated under the guidance of the Earth Science Advisory Committee
- a wide consultation on the strategy with the scientific community was undertaken at a workshop in February 2006
- the document addresses Earth science through the five topics: oceans, atmosphere, cryosphere, land and solid Earth and identifies the challenges for each of these
- particular emphasis is put on the Earth system approach, and on the effect of humankind on that system









### Ocean challenges




- Quantify the interaction between variability in **ocean dynamics, thermohaline circulation, sea level, and climate**.
- Understand physical and bio-chemical **air/sea interaction processes**.
- Understand **internal waves and the mesoscale** in the ocean, its relevance for heat and energy transport and its influence on primary productivity.

- Quantify **marine-ecosystem variability**, and its natural and anthropogenic physical, biological and geochemical forcing.
- Understand **land/ocean interactions** in terms of natural and anthropogenic forcing.
- Provide reliable model- and data-based **assessments and predictions** of the past, present and future state of the ocean.







### Atmosphere challenges



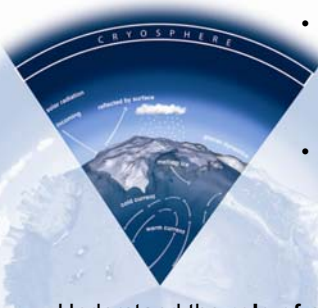
- Understand and quantify **the natural variability and the human-induced changes** in the Earth's climate system.
- Understand, model and forecast **atmospheric composition and air quality** on adequate temporal and spatial scale.

- Better quantification of the physical processes determining the **life cycle of aerosols** and their interaction with clouds.
- Observe, monitor and understand the **chemistry-dynamics coupling** of the stratospheric and upper tropospheric circulations (UTLS).
- Contribute to sustainable development through interdisciplinary research on **climate circulation patterns and extreme events**.






## Cryosphere challenges




- Quantify the **distribution of sea-ice mass and fresh-water equivalent**, assess the sensitivity of sea ice to climate change, and understand thermodynamic and dynamic feedbacks
- Quantify the **mass balance of grounded ice sheets, ice caps and glaciers**, partition their relative contributions to global eustatic sea-level change, and understand their future sensitivity to climate change through dynamic processes.

- Understand the **role of snow and glaciers** in influencing the global water cycle and regional water resources
- Quantify the influence of **ice shelves, high-latitude river run-off and land ice melt** on global thermohaline circulation, and understand their sensitivity to future climate change.
- Quantify current changes taking place in **permafrost and frozen-ground regimes**, understand their feedback to other components of the climate system, and evaluate their sensitivity to future climate forcing.

European Space Agency  
Agence spatiale européenne




## Land surface challenges



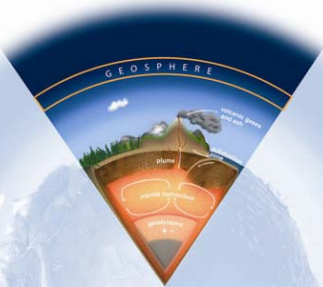
- Understand the role of terrestrial ecosystems and their interaction with other components of the Earth System for the **exchange of water, carbon and energy**, including the quantification of the ecological, atmospheric, chemical and anthropogenic processes that control these biochemical fluxes.

- Understand the interactions between **biological diversity, climate variability and key ecosystem** characteristics and processes, such as productivity, structure, nutrient cycling, water redistribution and vulnerability.
- Understand the pressure caused by **anthropogenic dynamics** on land surfaces and their impact on the functioning of terrestrial ecosystems.
- Understand the effect of land-surface status on the **terrestrial carbon cycle and its dynamics** by quantifying their control and feedback mechanisms for determining future trends.

European Space Agency  
Agence spatiale européenne




### Solid Earth challenges

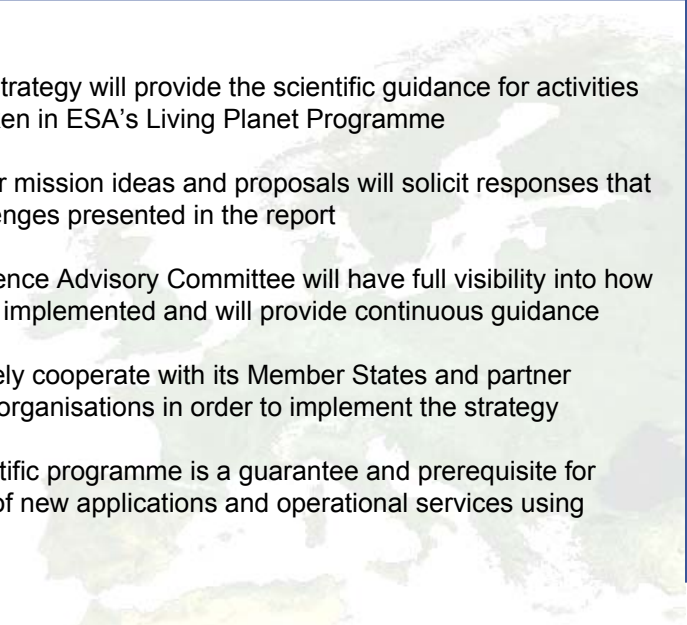


- Identification and quantification of physical signatures associated with **volcanic and earthquake processes** – from terrestrial and space-based observations.
- Improved knowledge of **physical properties and geodynamic processes in the deep interior**, and their relationship to Earth-surface changes.
- Improved understanding of **mass transport and mass distribution** in the other Earth System components, which will allow the separation of the individual contributions and a clearer picture of the signal due to solid-Earth processes.
- An **extended understanding of core processes** based on complementary sources of information and the impact of core processes on Earth System science.
- The role of **magnetic-field changes in affecting the distribution of ionised particles** in the atmosphere and their possible effects on climate.

European Space Agency  
Agence spatiale européenne



### Conclusion



- The updated strategy will provide the scientific guidance for activities to be undertaken in ESA's Living Planet Programme
- Future calls for mission ideas and proposals will solicit responses that address challenges presented in the report
- The Earth Science Advisory Committee will have full visibility into how the strategy is implemented and will provide continuous guidance
- ESA will actively cooperate with its Member States and partner agencies and organisations in order to implement the strategy
- A strong scientific programme is a guarantee and prerequisite for development of new applications and operational services using space data

European Space Agency  
Agence spatiale européenne



# Evolution of research orientation in the domain of spectral signatures

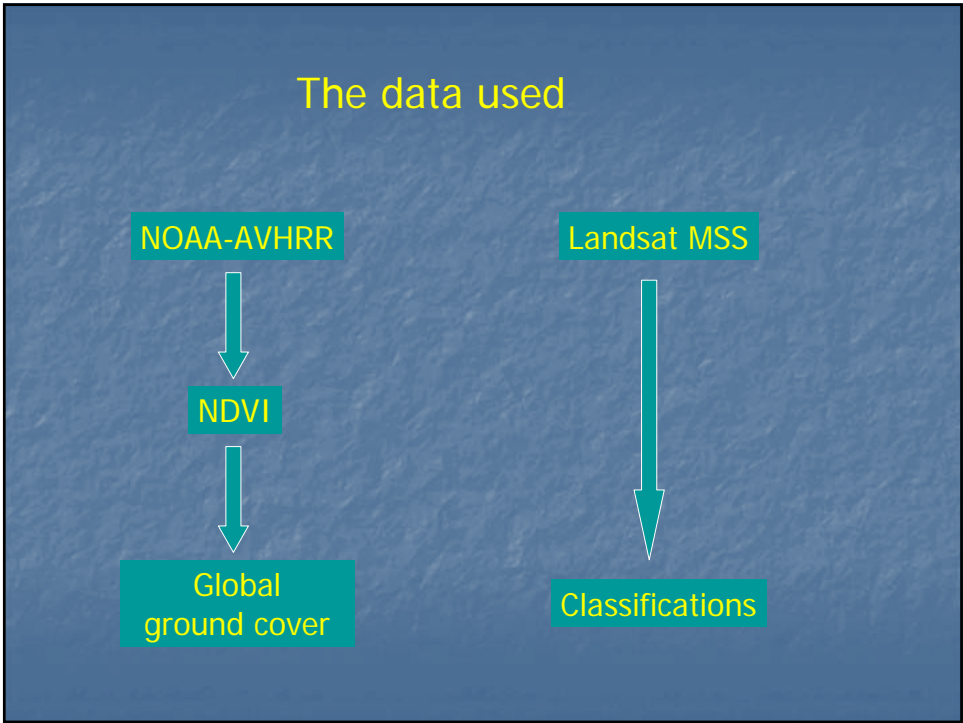
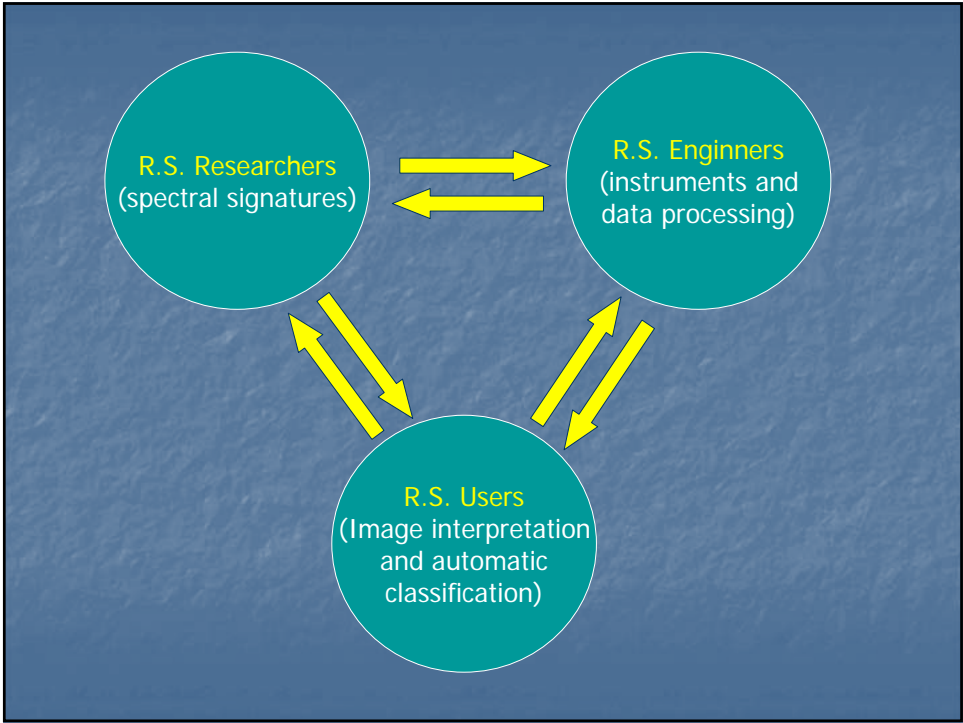
Gérard Guyot

## 1 - Position of the problem in the eighties

Avignon (1981)

Three topics:

- Determination of spectral properties of objects: material and methods
- Relationships between the characteristics of an object and its spectral properties
- Influence of the conditions of measurement



## Necessity of solving two series of problems:

- How to perform ground-level radiometric measurements
- How to extrapolate from these measurements to satellite level

## 2 - The first evolution

Bordeaux (1983), Les Arcs (1985), Aussois (1988)

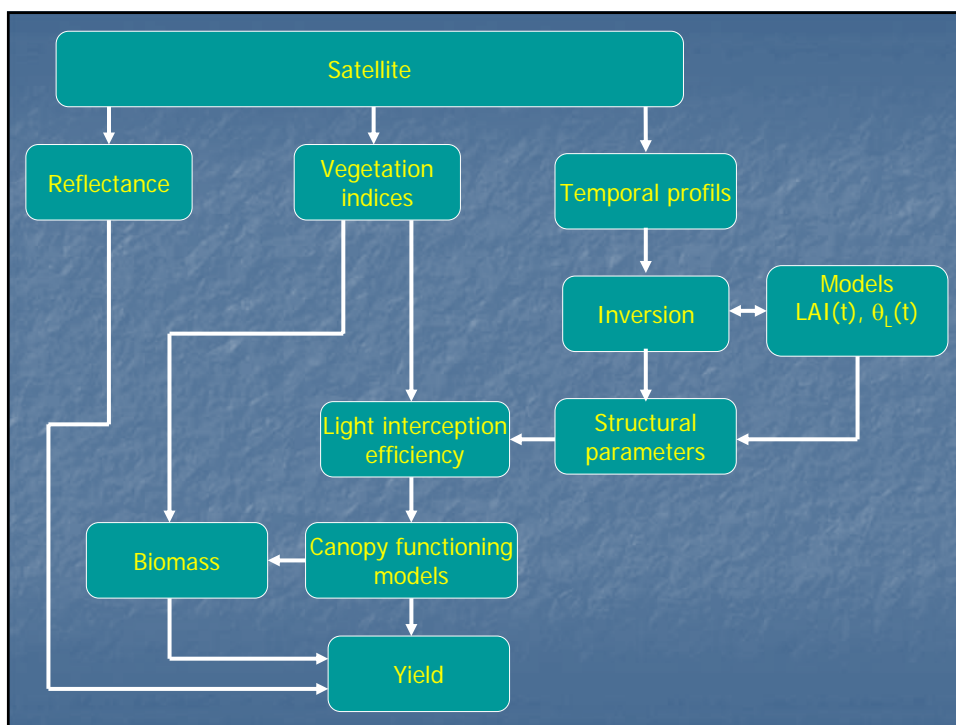
### Two main directions:

- Development of rational approaches combining ground level experiment and modelling
- Extension of the investigations to thermal infrared and microwaves

## 2 - The first evolution

Bordeaux (1983), Les Arcs (1985), Aussois (1988)

- **Modelling in the solar spectrum**
  - Search for new parameters
  - Development of simplified models
  - Assimilation of parameters
  - Combination of different approaches
  - Adjustment and calibration of models working at different levels





## 2 - The first evolution

Bordeaux (1983), Les Arcs (1985), Aussois (1988)

Topics covered:

- High spectral resolution
- Thermal infrared
- Active microwaves
- Laser active remote sensing
- Atmospheric corrections
- Calibration of data and measuring equipments

## 3 – Towards operational methods

Courchevel (1991, 1997), Val d'Isère (1994)

Four main directions:

- Development of methods based on model inversion
- First steps of assimilation methods
- Development of new techniques
- Synergistic use of measurements performed in different spectral domains



### 3 – Towards operational methods

Courchevel (1991, 1997), Val d'Isère (1994),

#### Topics covered:

- Atmospheric corrections:
- High spectral resolution
- Thermal infrared
- Active microwaves
- Passive microwaves
- Laser active remote sensing

### 3 – Towards operational methods

Courchevel (1991, 1997), Val d'Isère (1994),

- Polarisation and directional effects in the solar spectrum
- Synergy between measurements
- Remote sensing data assimilation
- Spatial and temporal signatures
- Impact assessment of environmental change

## 4 - The last evolution

Aussois (2001), Beijing (2005), Davos (2007)

- Development of application-oriented works using multi-date and multi-sensor data
- Development of advanced methods and techniques

Scientific topics	Aussois 2001	Beijing 2005	Davos 2007
Data correction and preprocessing	X	X	X
Remote sensing systems	X	X	X
Modelling			
Physical modelling	X	X	X
Model inversion	X	X	X
Data assimilation in models	X	X	X
Earth system models	—	—	X
Image classification methods	—	X	X
Land cover mapping and classification	X	X	X
Environmental change detection	—	X	X
Remote sensing applications	—	X	X
Calibration and validation RS products	—	X	X
Remote sensing data infrastructure	X	—	X

## 4 - The last evolution

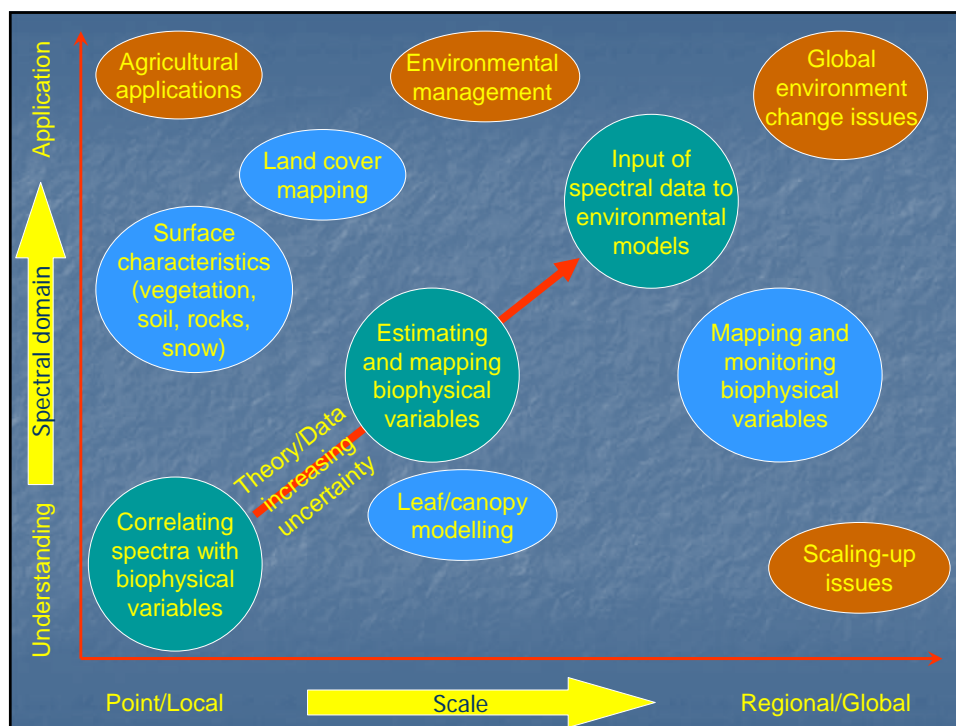
Aussois (2001), Beijing (2005), Davos (2007)

- Data preprocessing and processing
- Remote sensing systems
- Physical modelling
- Land cover mapping and classification
- Environmental change detection
- Remote sensing applications
- Calibration and validation of RS products
- Remote sensing data infrastructure

## Conclusion and perspectives







## Conclusion and perspectives

- Global environmental monitoring (decametric resolution) (CYCLOPES)
- Integration of in situ data (SensorWeb) and RS data
- Preparation of new space projects:
  - Lidar altimetry
  - Passive measurements of chlorophyll fluorescence (FLEX)
  - Combination of hyperspectral and thermal measurements with high spatial resolution
  - Analysis of surface and atmospheric anisotropy



# EVOLUTION OF RESEARCH ORIENTATION IN THE DOMAIN OF SPECTRAL SIGNATURES

Gérard Guyot

12, rue Pavilot, 84310 Morières-lès-Avignon, France – [gerard.guyot@club-internet.fr](mailto:gerard.guyot@club-internet.fr)

**KEY WORDS:** Spectral Signatures, ISPMSRS, Research orientation, Symposium

## ABSTRACT:

The series of international symposia on Physical Measurements and Signatures in Remote Sensing started in 1981 in Avignon (September 8-11) with the aim of understanding the remotely sensed spectra of surfaces at the point/local scale. Along the time, the scientific topics and spectral domains covered have progressively evolved and broaden in order to remain in the forefront of basic research in remote sensing. The aim of this paper is to briefly analyse this evolution and in conclusion to foresee the future developments.

## 1. INTRODUCTION

This series of symposia started in 1981 in Avignon (September 8-11) with the aim of understanding the remotely sensed spectra of surfaces at the point/local scale. Along the time, the objective of the symposia has broadened to encompass the application of our spectral understanding to problems of environmental understanding and environmental management from point/local and up to regional/global scales. The aim of this paper is to briefly analyse this evolution and in conclusion to foresee the future developments.

## 2. POSITION OF THE PROBLEM IN THE EIGHTIES

In the eighties, the main problem in remote sensing was the establishment of the basic knowledge for interpreting the first satellite data. The three topics selected for the sessions of the first symposium reflect this questioning:

- Determination of spectral properties of objects: equipment and methods;
- Relationships between the characteristics of an object and its spectral properties;
- Influence of the conditions of measurement.

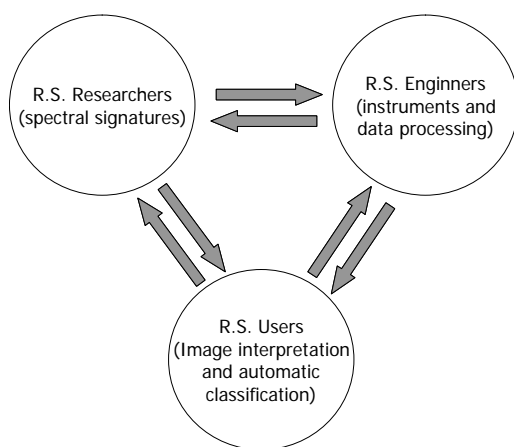


Figure 1. Relationships between remote sensing researchers, users and engineers.

In the relations between remote sensing researchers, engineers and users (Figure 1), the central question was to elucidate the role of spectral signatures research in relation to both the engineering design of satellite sensors and associated data processing and the community of users with resource management responsibility.

At that time, two series of satellite data was used: medium resolution from NOAA-AVHRR and high resolution from Landsat MSS. AVHRR data was used directly for a global characterisation of ground cover based on NDVI. MSS data was used mainly for classification of land occupation. In both cases the correction of the data was not an absolute necessity. The need of radiometric and atmospheric corrections has appeared with the preparation of the new generation of high resolution satellites: Thematic Mapper and SPOT for the comparison of data obtained at different dates and their quantitative interpretation. It was then necessary to solve two series of problems:

- How to perform ground-level radiometric measurements: The understanding of ground-based spectrometer measurements of plant canopies required a close attention to geometrical characteristics of plant and canopy. It was also necessary to take into account the effects of the field of view and polarisation of the sensors.
- How to extrapolate from these measurements to satellite level: This extrapolation showed the necessity to take into consideration the scale of spatial variability as well as the atmospheric effects in relation to view and sun angles.

## 3. THE FIRST EVOLUTION

During the period including the second, third and fourth symposium held respectively in Bordeaux (September-12-16, 1983), Les Arcs (December 16-20, 1985) and Aussois (January 18-22, 1988), we can schematically consider that the research activity has mainly evolved along two main directions:

- Development of rational approaches combining ground level experiments and modelling;
- Extension of investigations from short wavelengths to thermal infrared and microwaves.

### 3.1 Modelling in the solar spectrum

The first reflectance models were presented in Bordeaux, but it was necessary to wait for two supplementary years for having the first realistic and relatively accurate models for vegetation and snow in Les Arcs. This evolution has continued and in Aussois, modelling was the major topic of the symposium. Five orientations were defined for the research activity in this domain. They are still of interest at the present time:

- Search for new parameters accessible from space measurements for characterising in a simplified way, the different objects of interest.
- Development of simplified but realistic models delivering comparable results to those of sophisticated ones, but in a restricted domain of variation of the parameters, in order to facilitate the inversion.
- Assimilation of parameters measured by remote sensing in descriptive models in order to facilitate their inversion. This approach was discussed for the first time and will be the object of numerous studies in the nineties.
- Combination of phenomenological and basic approaches of the growth processes of plants, based on parameters measured by satellites.
- Adjustment and calibration of models working at different levels as shown on Figure 2.

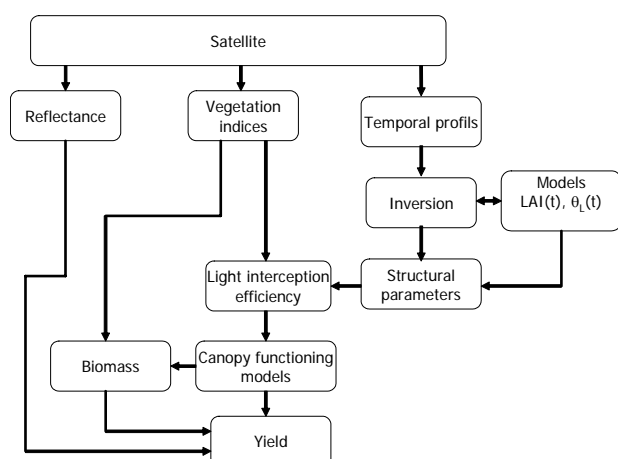


Figure 2. The different approaches used for crop yield forecasting.

### 3.2 High spectral resolution

Its interest was underlined in Bordeaux for monitoring vegetation and discriminating minerals, but the effective development of the research appeared in Les Arcs and was pursued in Aussois.

For vegetation the research was focussed on the detection of the red shift in the chlorophyll edge at  $0.68\ \mu\text{m}$  associated with various environmental stress factors. The interest of measurements in middle infrared was also shown with the use of airborne scanners over forests for mapping damages due to acid rains in Germany or determining the leaf content in starch and lignin in USA.

In geology, the utility of high spectral resolution in the  $2.0$  to  $2.5\ \mu\text{m}$  region was known from laboratory studies. Results of airborne measurements in visible and near infrared showed that complementary information was obtained for studying geomorphologic processes.

Over water, preliminary measurements were done on the chlorophyll fluorescence peak at  $685\ \text{nm}$ .

### 3.3 Thermal infrared

If the interest of these measurements was demonstrated in Bordeaux for analysing the thermal properties of natural surfaces, the decisive progress was done in Les Arcs. The significance of ground surface measurements was discussed, in particular over crop canopies for assessing their energy exchanges and a first modelling was proposed.

### 3.4 Active microwaves

The rapid development of the researches has appeared in les Arcs. One day of the symposium was jointly organised with ESA and devoted to the results of the simulation campaigns Promess and Toscane T for determining surface wind over ocean.

In 1988, the fourth symposium was jointly organised by two ISPRS working groups of commission VII: "Microwave Data" (Chairman N. Lannelongue) and "Spectral Signatures of Objects" because of the complementary scientific approaches in these two groups.

Significant progress was noted in the application of radar over ocean for determining both the wave and the wind fields. However, the models developed needed to be improved. For vegetation, soil and snow, the theoretical models presented in Les Arcs were useful for the understanding of the scattering mechanisms. In 1988 the presentation of water cloud models corresponded to a significant progress. These approaches enabled the introduction of the effects of plant geometry and canopy structure.

### 3.5 Laser active remote sensing

The new concept of active remote sensing in visible and thermal infrared was presented in Les Arcs. In short wavelengths, fluorescence and Raman scattering showed their potential for monitoring water quality (chlorophyll, organic matter, oil spills). In thermal infrared, some good results were presented on geological materials. These results were confirmed in Aussois and the research was extended towards the determination of the photosynthetic activity of plant canopies. The methods proposed were based on laser induced chlorophyll fluorescence.

### 3.6 Atmospheric corrections

The necessity of these corrections has appeared in the first symposia but not any practical method was available. The only possibility was the use of the empirical "split window" approach for correcting thermal infrared data. For the corrections in the solar spectrum the use of the atmospheric transfer codes such as 5S or Lowtran needed the measurement of atmospheric parameters and this problem was not solved in 1988.

### 3.7 Calibration of data and measuring equipment

In les Arcs, it was noted that studies involving the use of absolute radiometric calibration were rapidly developing and quantitative investigations involving energy-matter interactions have appeared.

#### 4. TOWARDS OPERATIONAL METHODS IN THE NINETIES

At the end of the fourth symposium, the Scientific Committee considered that "Spectral Signatures" was too much restrictive. It proposed to combine the two groups "Spectral Signatures" and "Microwave Data" and change the title into "Physical Measurements and Signatures in Remote Sensing". This proposal was accepted at the General Assembly of ISPRS in Kyoto in July 1988.

In the nineties three symposia were organised in Courchevel (January 14-18, 1991 and April 7-11, 1997) and Val d'Isère (January 17-21, 1994). During this period the research activity has mainly followed four directions:

- Development of methods based on model inversion in different spectral domains;
- First steps of assimilation methods;
- Exploration of new techniques such as laser active remote sensing and directional and polarisation effects in optical domain;
- Synergistic use of measurements performed in different spectral domains.

##### 4.1 Atmospheric corrections, modelling of measuring systems

A significant volume of researches has appeared in 1991 (25 papers over 163). Two atmospheric codes: Lowtran-7 and 5S were more particularly discussed. However, the application of these codes showed the necessity of atmospheric ground measurements. A decisive step has been crossed in 1994 with the presentation of a new scanning multiband sky and sun photometer which was installed in the AERONET network. In 1997 the first results of its sub-network PHOTONS in western Africa were presented. Atmospheric corrections entered thus into routine processing.

An alternative approach for atmospheric corrections presented also in 1991, was based on the use of high spectral resolution to derive atmospheric parameters. The combination of measurements under different view angles and the use of the light polarisation have induced the development of POLDER. The first results of its airborne version were presented in 1997.

In thermal infrared a few methods were proposed to overcome the emissivity problem that makes difficult to use traditional split-window techniques over land surfaces.

##### 4.2 High spectral resolution

During this period, a large emphasis was given to high spectral measurements in three domains:

**4.2.1 Vegetation:** In the nineties a large emphasis was given to the analysis of main HRS features (in particular the red edge and its shifts) through modelling and experimentation, from the leaf to the canopy level. In 1994, model inversion demonstrated some potential for the retrieval of leaf canopy biochemical composition (chlorophyll, water, nitrogen and lignin). Several studies highlighted also the possibility to obtain the total amount of HRS information with a relatively small subset of spectral bands peculiar to specific vegetation parameter or constituent, opening the way for future space instruments (MODIS...)

**4.2.2 Geology:** The development of the research was to extend the studies to complex settings, and to utilise the information gained to study the geological processes that formed or modified the areas under study.

**4.2.3 Water bodies:** HRS data were applied to the study of snow, inland waters and ocean. HRS signatures of snow were shown to be useful for estimating the depth of thin snow and the water content. Studies of inland waters were aimed at understanding water quality, especially with respect to organic content. On ocean, HRS was used to study chlorophyll blooms and red tides associated to phytoplankton density. Whether the object studied was bright snow or dark water, the signal of interest was relatively small compared to the background. Hence good calibration and the ability to correct especially for atmospheric path radiance were critical and required some more efforts.

##### 4.3 Thermal infrared

A decisive step was crossed in 1994 with the discussion of four points:

**4.3.1 Physics of the measurement:** The necessity of normalising the definitions of the temperature (surface temperature, aerodynamic temperature, brightness temperature...) and of the emissivity at the ground level has appeared.

**4.3.2 Data correction and processing:** A general agreement appeared on the necessity of decoupling temperature and emissivity (combination of day and night AVHRR data, combination of the two thermal channels of ATSR).

**4.3.3 Use of thermal data:** New promising applications appeared for estimating the energy fluxes (evapotranspiration) based on the combination of thermal and visible data into physical models.

**4.3.4 Instrumentation:** A new generation of space instruments was under preparation (ASTER, MODIS, AATSR) with better spatial, spectral and radiometric resolutions. It induced the development of new airborne equipments and also of a multi-band auto-calibrated radiometer for ground level measurements.

##### 4.4 Active microwaves

In 1991, many new results were based on progress in calibration of radar sensors. Scattering models were used to derive quantitative information on soil roughness and moisture; vegetation types, density and water content; and on ocean waves and wind. Polarisation was also developing as an important tool in soil and vegetation studies. In 1994, two significant progresses were noted:

**4.4.1 Development of practical applications:** The use of multi-parameter measurements (multi-incidence angles, frequencies and polarisations) and of some new mathematical tools for classification, offered the possibility, at least for training sites, to retrieve numerous interesting parameters: tree species, soil water content...

**4.4.2 Use of interferometry:** It was a major step. The application of this technique to ERS-1 SAR data, showed the possibility to derive topographic maps and also to detect very

small changes of the topography leading to a powerful tool for tectonic studies.

#### 4.5 Passive microwaves

The concept of Microwave Polarisation Difference Temperature (MPDT) was introduced in 1991. MPDT was sensitive to vegetation water content and it was shown that the lower frequencies were more useful for vegetation sensing. The results from SMMR demonstrated long term stability, necessary for climate change studies. The coarse resolution of this sensor did not appear to be a limiting factor. The strong correlation of SSM/I and SMMR indicated the possibility of extending the applications into the future

In 1994, results from two new instruments were presented ESTAR and PORTOS. ESTAR was an airborne system developed to test the principle of a low frequency radiometer (L band) using the antenna synthesis technique. The test of the airborne version showed the validity of this concept and its potential for space measurements.

PORTOS was a conventional radiometer (5-90 GHz) able to be used either on an airplane or at ground level. It was operationally used in numerous experiments aimed at refining the understanding/modelling of surface characteristics.

The coupling of active and passive techniques was tested in the combined use of two instruments of ERS-1 (radar altimeter, microwave sounder) and ATSR for improving derived atmospheric and surface parameters. In addition, for the first time an innovative presentation showed the coupling of a microwave emission model to a vegetation growth model.

#### 4.6 Laser active remote sensing

In 1991, the following salient points were noted:

- Development of different methodologies, for investigating the physiological status of plants by means of laser induced fluorescence. They were based on spectral and time-resolved detection. An effort was done to pass from qualitative to quantitative measurements and to develop reliable apparatus and processing techniques.
- Development of an approach using multidimensional laser induced spectral signatures for identification of oil pollutants and dissolved natural organic matter over ocean.
- Development of laboratory data bases for geological and ecological applications.
- Successful use of thermal infrared lasers for geological applications.

In 1994, significant progresses were noted on vegetation monitoring. The mechanism of plant fluorescence was better understood and it was possible to relate the physiological status of plants to three parameters: fluorescence life time, fluorescence spectrum from blue to red and photo-induced variable fluorescence. In addition, the analysis of the elastically reflected signal enabled a fast and accurate description of the architecture of a plant canopy. The comprehension of the fluorescence mechanisms offered also new perspectives for the development of passive measurements in the Fraunhofer lines or oxygen absorption band.

#### 4.7 Polarisation and directional effects in the solar spectrum

This topic was discussed for the first time in 1991. The research was mainly focussed on the non-lambertian properties of

vegetation canopies including the soil and was rapidly expanding. Progress was noted in the development of tractable models for inverting canopy reflectance properties to estimate physical parameters such as leaf area index and canopy water content. The use of both spectral and directional variables in an inversion model appeared especially promising.

The analysis of polarisation data delivered by airborne POLDER were essential for validating models and assessing the relative importance of competing light polarisation processes in the atmosphere and on the ground.

Significant progress had also appeared in both collection of calibrated, multi-spectral, multi-directional data sets supporting remote sensing research – and development of tools facilitating collection of such data (airborne simulators: POLDER, CASI, CAESAR, MODIS... and sensors for ground based measurements: PARABOLA for BRDF, sun photometer and radiometers for atmospheric properties).

#### 4.8 Synergy between measurements performed in different wavelength domains:

This topic was discussed for the first time in 1991. The use of multi-source data needed a large effort in calibration and inter-calibration with specific problems due to the non simultaneity of the measurements and the data acquisition at different scales.

In modelling it was shown how the combination of some different types of data help to model surface processes such as: monitoring of soil surface status, bio-physical and -chemical characterisation of the vegetation, synergy between temporal and spectral signatures for estimating crop yield...

The combination of visible reflectance data, surface temperature and microwave polarisation difference temperature was successfully used for inter-annual monitoring of vegetation change due to water deficit. Another original approach was the Thermal Infrared Spectral Index (TISI). This index enabling the decoupling of surface temperature and emissivity appeared as a pertinent tool for discriminating bare soils and vegetated surfaces in combination with NDVI.

#### 4.9 Remote sensing data assimilation in numerical models

The main contributions concerned crop yield prediction and determination of heat flux and evapotranspiration. A development appeared in 1994 with studies devoted to vegetation monitoring at a global scale in the framework of IGBP with a little contribution to hydrology.

In 1997, significant progresses have appeared. The most advanced techniques were shown for meteorological data, the main constraints being solved. For vegetation, the assimilation process was somewhat extended to the notion of multiple use of remotely sensed data obtained in different spectral domains and/or at different dates introducing the temporal dimension. However, in most cases, assimilation techniques were not applied to their full extent because of constraints not solved.

#### 4.10 Spatial and temporal signatures

Two interesting steps were noted in 1991: the analysis of the relationship between crop growth models and multi-source remote sensing data for improving crop yield forecasting and the combination of temporal and spatial resolutions with AVHRR and SPOT data for land cover mapping. But problems

due to both mixed pixels and heterogeneity at the scale of sub-pixels were not solved.

4.11 Impact assessment of environmental change by remote sensing

This question was discussed for the first time in 1997. Environmental change always implies a temporal dimension in data analysis, and therefore requires calibrated data sets. It must be noted that the changes are often in the same order of magnitude as instrumental drifts, calibration errors or atmospheric effects. It is therefore important to give particular attention to the quality and significance of datasets, especially if long term trends are to be deduced from them.

Some results were presented at the symposium: the evolution of global warming and the extension of the growing season in high latitudes, the TREES program for mapping and monitoring tropical forest from AVHRR imagery, and more limited studies on water cycle and quality monitoring, deforestation, forest dynamics and fires, desertification and salinity detection, soil erosion protection, air quality and aerosols, urbanisation...

5. THE LAST EVOLUTION AFTER 2000

Scientific topics	Aussois 2001	Beijing 2005	Davos 2007
Data correction and preprocessing	X	X	X
Remote sensing systems	X	X	X
Modelling			
• Physical modelling	X	X	X
• Model inversion	X	X	X
• Data assimilation in models	X	X	X
• Earth system models	–	–	X
Image classification methods	–	X	X
Land cover mapping and classification	X	X	X
Environmental change detection	–	X	X
Remote sensing applications	–	X	X
Calibration, validation RS products	–	X	X
RS data infrastructures	X	–	X

Table 1: Scientific topics covered in the three last symposia.

With the turn of the century, the volume and the quality of available data has considerably increased in the optical domain with the successful launch of VEGETATION, MODIS, MERIS, MISR and ASTER and the short lived POLDER. They were followed by AATSR, HYPERION, IKONOS Quickbird and CHRIS. In microwaves, the same phenomenon can be noted with ASAR on board ENVISAT in 2001, completing the series of data acquired by ERS 1 and 2 and RADARSAT. This data flow has induced two main orientations in the research:

- Development of application oriented works using multi-date and multi-sensor data;

- Development of advanced methods and techniques for acquiring more acute information in any spectral domain.

This period corresponds to the three last symposia organised in Aussois (January 8-12, 2001), Beijing (October 17-19, 2005) and Davos (March 12-14, 2007). The scientific topics covered are summarised in Table 1. It shows some differences and also the permanence of some problems on which research works are still in progress. The size of the symposia organised in Aussois and in Davos is similar (136 and 125 papers presented respectively) and correspond practically to the half of the Beijing Symposium (256 papers presented). This difference in the size explains the large place devoted to applications in Beijing, the volume of research papers being relatively stable in the three symposia.

5.1 Preprocessing and processing of remotely sensed data

In optical domain, the development of sophisticated correction models for instrumental transfer functions and atmospheric effects led to a continuous improvement of data preprocessing and processing techniques. The launch of POLDER and MODIS and the development of the ground level network of sun photometers AERONET, have strongly improved the accuracy of atmospheric corrections. In the context of long term trend studies the validation and intercalibration of archives of previous sensors is an absolute necessity.

In microwave domain, a similar evolution is observed. Besides the problems of calibration, the effective use of SAR data in many applications must include a strategy for coping with speckle. Different methods for speckle reduction were proposed in Aussois and in Beijing.

5.2 Remote sensing systems

A large emphasis to remote sensing systems was only given in Beijing.

In the microwave domain, the studies are mainly devoted to SAR data because of the large data set delivered by the satellites RADARSAT, ERS-1 and 2. For the passive microwaves, the development of research is slowed by technological constraints. As it has been seen in the nineties, this technique is well adapted for monitoring soil moisture, vegetation biomass and also ocean salinity. But for the moment, not any instrument is mounted aboard a satellite platform. However, three L-band sensor missions are now being prepared for launch: SMOS developed by ESA and Aquarius and Hydros developed by NASA as part of Earth System Pathfinder (ESSP). This new opportunity will probably stimulate the research.

The potential of lidar measurements was largely discussed in the nineties, but the development of this technique has also been limited by technological constraints. The application domain is limited to altimetry and structure of forest and crop canopies.

Hyperspectral studies are still expanding and are mainly oriented towards the determination of leaf nitrogen content and biochemistry using field and airborne data delivered by spectral imaging equipments. In addition, the instrument CHRIS developed by ESA delivering multi-angular and hyperspectral data has induced new studies on canopy structure and biomass.

In thermal infrared domain, the availability of data delivered by ASTER and MODIS of EOS platform and by SEVIRI on board METEOSAT-8 has stimulated research on methodologies for



retrieving accurate land surface temperatures and developing the applications (energy balance, water balance, crop growth monitoring...).

### 5.3 Physical modelling

The research activity in this domain has followed the development of remote sensing techniques. The research was oriented towards the development of invertible models representing the bidirectional properties of plant canopies. They use the multidirectional and hyperspectral data delivered by MODIS or CHRIS for retrieving information about the canopy geometry (LAI) and also on its functioning ( $fAPAR$ ). In addition the global monitoring of the environment lead to the development of models adapted to coarse resolution satellites.

### 5.4 Land cover mapping and classification

The efforts are oriented towards the standardization of land occupation classes, leading to the use of criteria having a larger definition and to the introduction of the temporal dimension. For pixel classification it is also proposed to use a continuous classification in which each pixel is affected to different classes with probabilities depending on the temporal evolution of the corresponding signal.

### 5.5 Environmental change detection

With the availability of long series of medium resolution satellite data and the development of calibration, intercalibration and atmospheric correction methods, it is still possible to monitor environmental changes. Quasi-operational methods are then proposed for monitoring vegetation phenological evolution or seasonality.

In urban planning, the extension of urban zones or changes in use of urban area are easily monitored with high resolution satellites such as Thematic Mapper or SPOT and more recently with the very high resolution satellite Quickbird.

### 5.6 Remote sensing application

The practical applications of remote sensing concern two different scales. At the global scale it is now possible to derive the information necessary for monitoring the components of the carbon cycle. At the local or regional scale, remote sensing data are entered into operational systems for driving agricultural practices and determining crop production. High spatial and temporal resolution data delivered by satellites or aircrafts are used for drawing maps of LAI, chlorophyll content, ground cover... These maps are then used for driving the cultural practices at the field level.

Thermal infrared data sometimes combined with visible and near infrared or microwaves, are used for estimating the energy fluxes exchanged at the ground surface and more particularly the evapotranspiration of plant covers.

### 5.7 Calibration and validation of remote sensing products

This essential point has been deeply investigated in the nineties. Since 2000 the studies are oriented towards the practical correction and validation of data delivered by the new satellites and of archive data. A large effort has been done for delivering remote sensing products that can be used at different scales.

## 5.8 Remote sensing data infrastructures

The utilisation of the data by the research teams is conditioned by their availability and their cost. In the last five years, the large development of research works on medium resolution satellites has been simulated by the possibility of having easily free data of MODIS, SeaWiFS and Vegetation.

## 6. CONCLUSION AND PERSPECTIVES

For concluding Figure 3 summarises the evolution in knowledge and in application domain of remote sensing data during the past 25 years. It represents schematically the evolution from the first inductive steps towards spectral understanding and environmental management. The bottom left to the top right show the increasing complexity of the problems, the extension of the scale from local to global and the development of applications. It shows also the transition of increasing uncertainty of the theory or data.

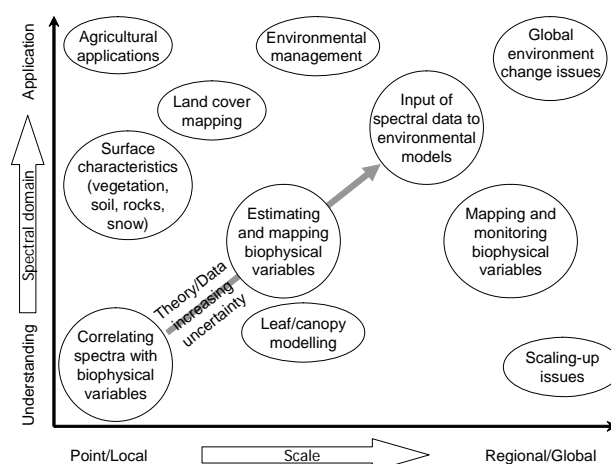


Figure 3. The relationship between the understanding to application of spectra and spatial scale.

The development of practical applications has followed the large amount of satellite data available since the years 2000. However, all the problems are not solved and new technological developments are appearing. That will induce new research activity:

- Global environmental monitoring based on medium resolution satellite data is starting to be operational. The application of models describing the functioning of plant canopies needs the use of decametric resolution data with a time interval of few days. It will then be necessary to use a constellation of satellites delivering compatible data (CYCLOPES, ESA mission project: Carbon cycle and Change in Land Observational Products from an Ensemble of Satellites)
- One way for improving radiative transfer models is the integration of *in situ* data ("SensorWeb") and remotely sensed data. This question has also to be validated.
- New spatial experiments are under study:
  - Lidar for altimetry and plant canopy geometry
  - Passive measurement of chlorophyll fluorescence in the oxygen absorption band (FLEX mission project)
  - Combination of hyperspectral measurements and thermal infrared measurements with a high spatial resolution.
  - Analysis of surface and atmospheric anisotropy.

## REFERENCES

This paper is based on the proceedings of the nine symposia published from 1981 to 2005:

Guyot G., Verbrugghe M., 1981. Spectral Signatures of Objects in Remote Sensing, Proc. 1<sup>st</sup> Int. Coll. Avignon (France), Les Colloques de l'INRA n° 5, INRA Paris France, 674 pp

Guyot G., Verbrugghe M., 1983. Spectral Signatures of Objects in Remote Sensing, Proc. 2<sup>nd</sup> Int. Coll. Bordeaux (France), Les Colloques de l'INRA n° 23, INRA Paris France, 940 pp.

Guyot G., Guyenne T.D., 1986. Spectral Signatures of Objects in Remote Sensing, Proc. 3<sup>rd</sup> Int. Coll. Les Arc (France), European Space Agency, ESA SP-247, 580 pp.

Guyot G., Guyenne T.D., Hunt J.J., 1988. Spectral Signatures of Objects in Remote Sensing, Proc. 4<sup>th</sup> Int. Coll. Aussois (France), European Space Agency, ESA SP-287, 524 pp.

Guyot G., Hunt J.J., 1991. Physical Measurements and Signatures in Remote Sensing, Proc. 5<sup>th</sup> Int. Coll. Courchevel (France), European Space Agency, ESA SP-319, 855 pp.

Guyot G., 1994. Physical Measurements and Signatures in Remote Sensing, Proc. 6<sup>th</sup> Int. Coll. Val d'Isère (France), CNES, Toulouse France, 1241 pp.

Guyot G., Phulpin T., 1997. Physical Measurements and Signatures in Remote Sensing, Proc. 7<sup>th</sup> Int. Symp. Courchevel (France), A.A. Balkema, Rotterdam, Brookfield, Vol. 1 and 2, 902 pp.

Leroy M., 2001. Physical Measurements and Signatures in Remote Sensing, Proc. 8<sup>th</sup> Int. Symp. Aussois (France), CNES Toulouse France, 758 pp.

Liang S., Liu J., Li X., Liu R., Schaepman M., 2005. Physical Measurements and Signatures in Remote Sensing, Proc. 9<sup>th</sup> Int. Symp. Beijing, China, ISPRS Vol. XXXVI, Part 7/W20, 854 pp.

Physikalisch-Meteorologisches Observatorium Davos  
World Radiation Center

*pmod* *wrc*

# Space experiments of PMOD/WRC to measure the solar constant and the influence of the solar irradiance on the terrestrial climate


Werner Schmutz  
PMOD/WRC

ISPMRS'07 12-14 March 2007 Davos, Switzerland

*pmod* *wrc*

## PMOD 1907-2007 WRC since 1971

Two activities:




12.3.2007

### Research

Energy balance and influence  
of radiation on the terrestrial  
climate

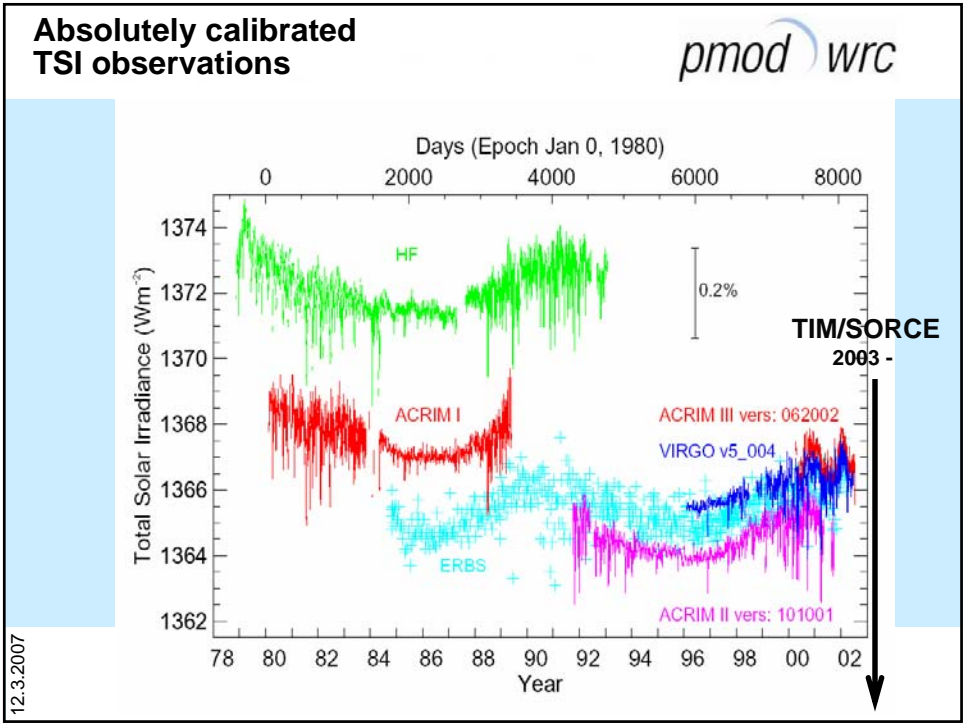
- Green house effect
- Sun-Earth connection

Overview



- Past observations of the Total Solar Irradiance (TSI) and the TSI-composite
- Why irradiance measurements
- Why continue to measure TSI
- Future irradiance observations

12.3.2007





### A side note: Need for improved Quality Assurance!

*pmod wrc*

**Difficulties:**

- Bias
- Instrument calibration in-orbit (gain and offset)

BIPM and WMO are proposing and preparing a meeting in 2008 or 2009 dedicated to calibration and traceability problems

12.3.2007

Courtesy of Nigel Fox

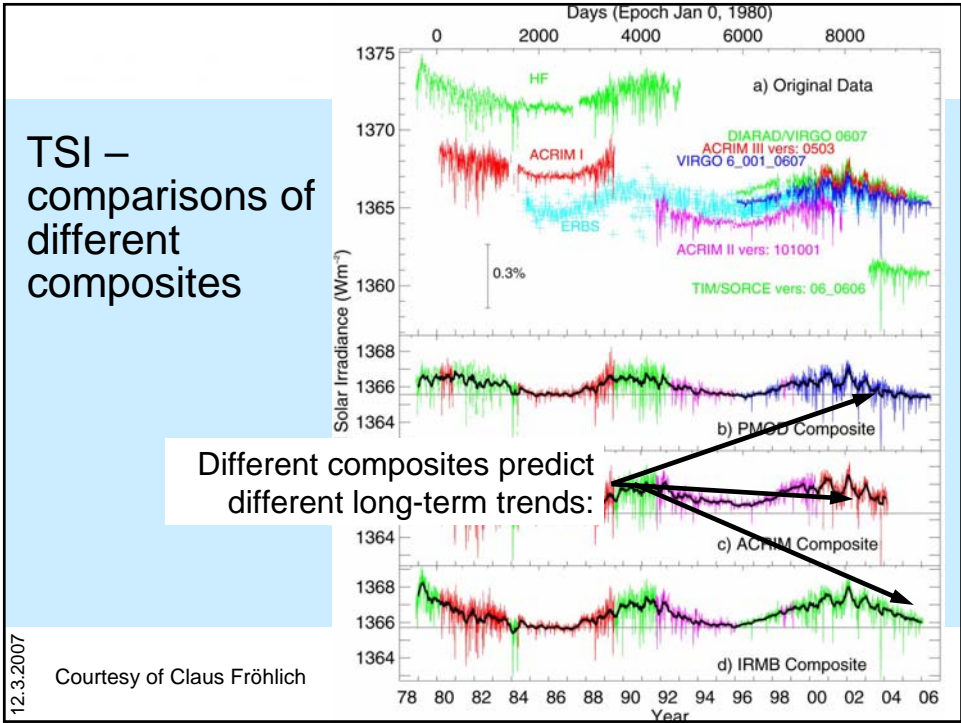
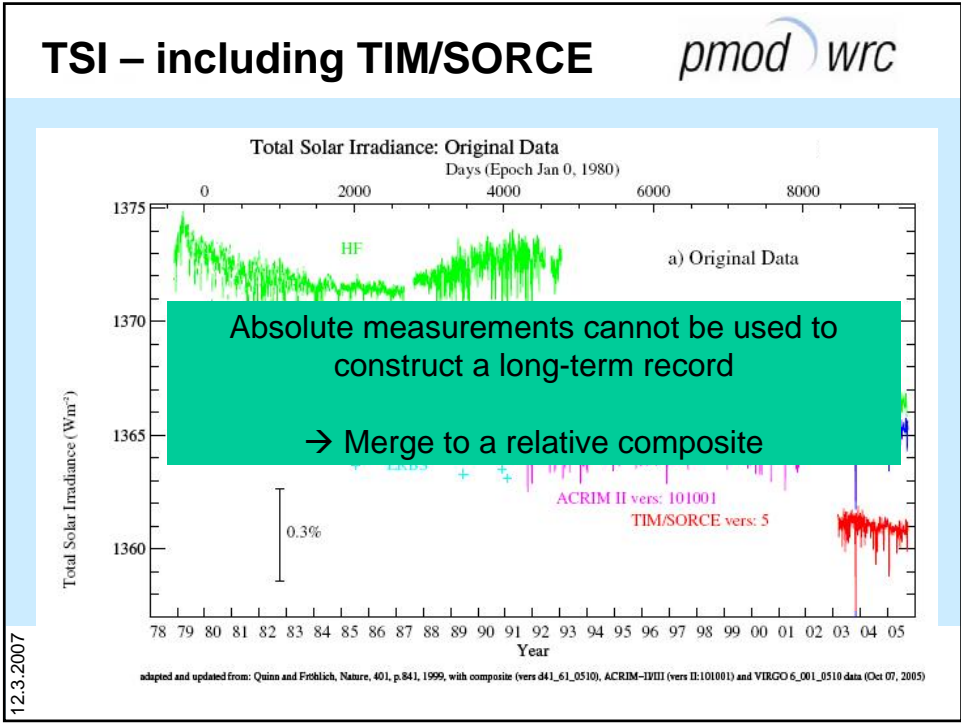
### Traceable Radiometry Underpinning Terrestrial- & Helio- Studies

*pmod wrc*

**Mission proposal: TRUTHS**

Nigel Fox	NPL	David Pollock	U of Alab.
Nigel.Fox@npl.co.uk		Mike Sandford	RAL
James Aiken	Plym Mar Lab	Michael Schaepman	U of Zur
Xavier Briottet	ONERA	Werner Schmutz	PMOD/WRC
John Barnett	Ox univ.	Keith Shine	Uni of Read
Steve Groom	Plym Mar Lab	Phil Teillet	CCRS
Claus Frohlich	PMOD/WRC	Theo Theocharous	NPL
Jo Haigh	Imp Coll	Kurtis Thome	U of Ariz
Olivier Hagolle	CNES	Terry Quinn	BIPM
Hugh Kieffer	USGS	Michel Verstraete	JRC(Italy)
Judith Lean	NRL	Emma Woolliams	NPL
John Martin	NPL	Ed Zalewski	U of Ariz

12.3.2007



### Why irradiance measurements?

*pmod wrc*

- IUGG 2007:  
Session MS020  
Solar Activity and its Influences on the Earth's Weather and Climate (IRC)
- Space Climate:**  
On long term, it is not known what dominates, secular change of Total Solar Irradiance or spectral (UV) variations  
*But:* although UV variations are much larger (up to 100%) all spectral variations are highly correlated to TSI variations

12.3.2007

### What is the influence of the Sun on the climate?

*pmod wrc*

Global and Annual Mean Radiative Forcing  
(relative to 1750 AD)

Factor	Radiative Forcing [W m⁻²]
Halocarbons	~0.2
N <sub>2</sub> O	~0.2
CH <sub>4</sub>	~0.2
CO <sub>2</sub>	~1.5
O <sub>3</sub> -trop	~0.5
O <sub>3</sub> -strat	~-0.2
Sulphate	~-0.5
BB	~-0.2
FF (BC)	~0.2
FF (OC)	~-0.2
Mineral Dust	~0.5
Aviation	~0.2 (uncertain)
Trop. aerosol	~-0.5
Land-use	~-0.2

Graphics: Dr. J. Beer EAWAG, Switzerland

IPCC 2001

12.3.2007

### Climate Anomalies versus solar influence

*pmod* *wrc*

River Thames in London 1813/1814

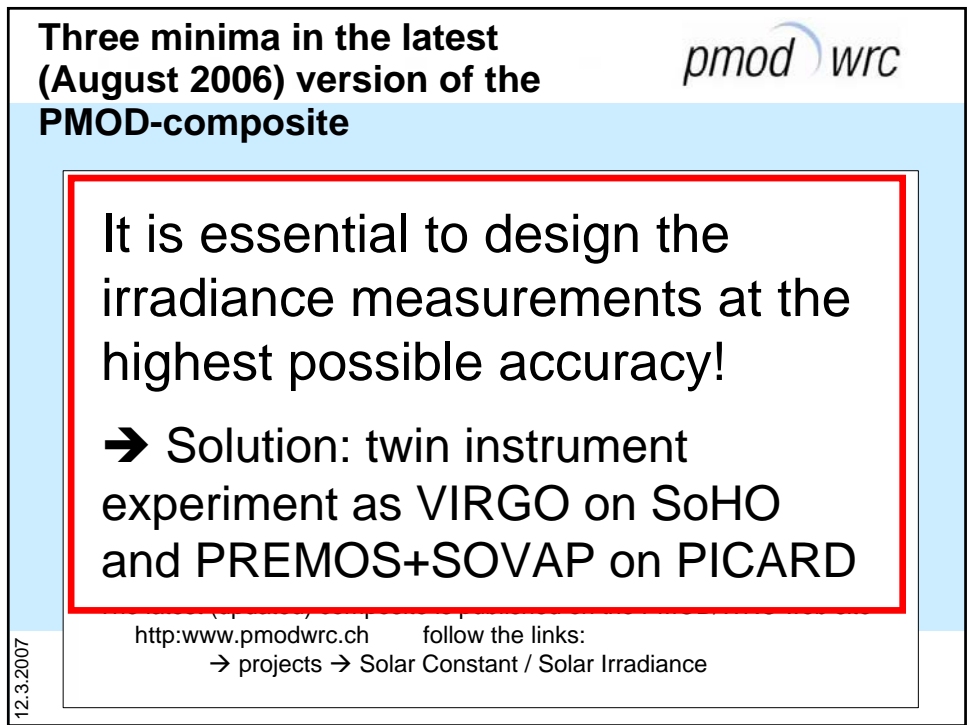
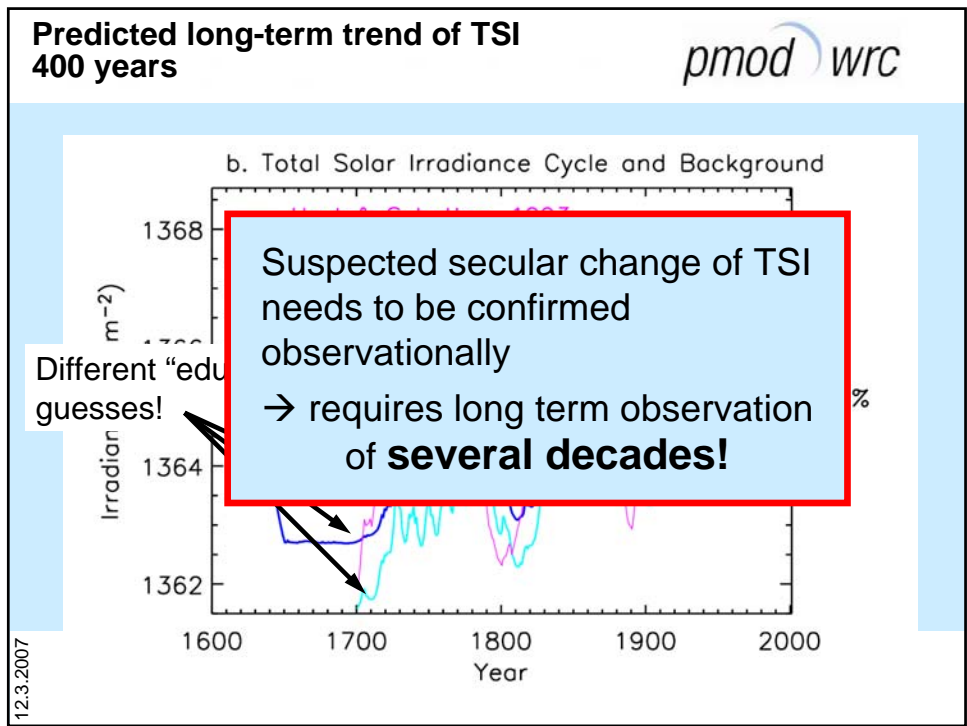
12.3.2007

### Predicted long-term trend of TSI 100 years

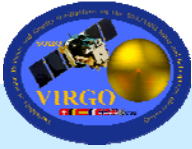
*pmod* *wrc*

Different "educated" guesses!


12.3.2007



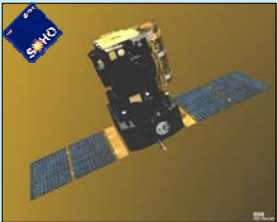





**VIRGO/SoHO:**  
operational since 1996




- Two absolute radiometers:
  - PMO6V (A & B)
  - DIARAD (L & R)
- Precision Filter Radiometer (blue, green, red)
- Image of the Sun in the green light in low resolution (12 pixels): 1 minute sampling

SoHO launch 2. December 1995

VIRGO instruments

12.3.2007

**Future TSI experiments**


- GLORY (USA: no launch date – ready to be used as gap-filler)
- SOVIM/ISS and
- PREMOS+SOVAP/PICARD  
approved TSI experiments of PMOD/WRC
- RAD/KuaFu-A only future TSI experiment presently being considered

12.3.2007

Space experiments are being built in house at PMOD/WRC

*pmod wrc*

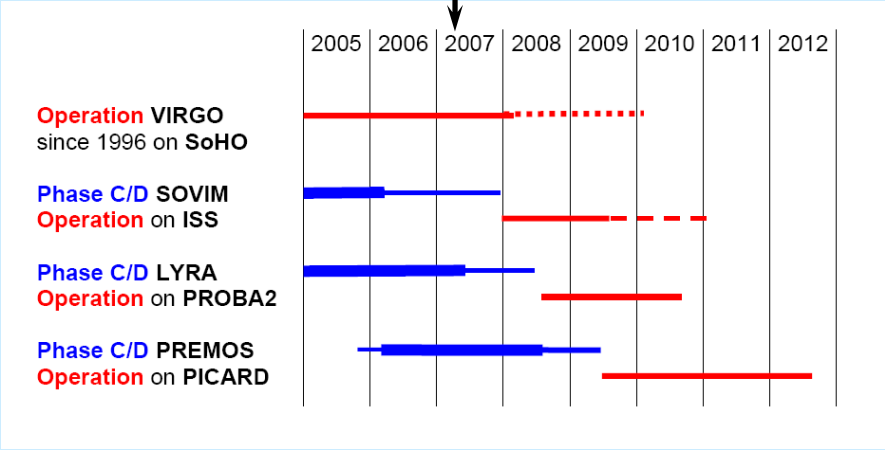


12.3.2007

Space experiments of PMOD/WRC

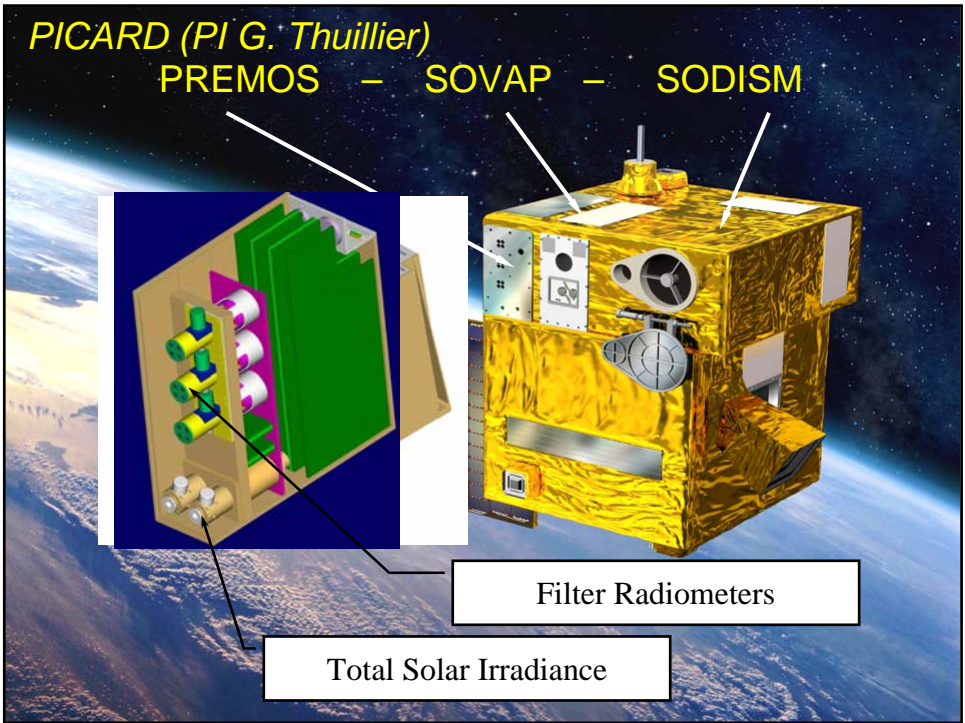
*pmod wrc*

today



Experiment	Phase	Start Year	End Year
VIRGO	Operation	1996	2010
	since 1996 on SoHO		
SOVIM	Phase C/D	2005	2007
	Operation on ISS	2008	2011
LYRA	Phase C/D	2005	2008
	Operation on PROBA2	2009	2010
PREMOS	Phase C/D	2006	2009
	Operation on PICARD	2010	2012

12.3.2007




Total Solar Irradiance observations until 2012				pmod wrc	
ACRIM III	2000 - ?				
VIRGO/SOHO	1996	-	2009 (+?)		
TIM/SORCE	2003	-	2008 - (?)		
SOVIM/ISS			2008 – 2009 ?		
PREMOS/PICARD			2009 – 2011		
SOVAP/PICARD					
(SDO 2008-2012 has no TSI instrument)					
NPOESS					2012
National Operational Environmental Satellite System may have TSI instrument but are planned to start not earlier than 2009 (?), more information as 2010					

TSI on NPOESS canceled June 2006

12.3.2007

Total Solar Irradiance  
observations until 2012



ACRIM III

2000 - ?

VIRGO/SOHO

1996 -

2007 -

2009

TIM/SORCE

2003 –

2008 -

(GLORY?)

SOVIM/ISS

2007 - 2009 ?

PREMOS-TSI/**PICARD**

2009 -

**2013**

SOVAP/PICARD

(SDO 2008-2012 has no TSI instrument)

**KuaFu-A**

2012 -


irradiance measurement experiment comprising:

→ SIM = Solar Irradiance Monitor (CN: PI Daren Lu)

→ DOR = Davos Observatory Radiometer (CH: Werner Schmutz)

12.3.2007

Conclusions



- Short-term irradiance variations (days) are closely related to variations of the chemical composition of the upper atmosphere
 

→ space weather: **operational monitoring of TSI**
- Long-term irradiance variations (tens to thousands of years) are probably (!) related to climate variations
 

→ space climate: **secular long term change of TSI**
- TSI observations are most likely continuous and overlapping until about 2012
- RAD/KuaFu-A would be a matching continuation

12.3.2007

Physikalisch-Meteorologisches Observatorium Davos  
World Radiation Center



*Thank you for your attention!*

Integration of LYRA  
on PROBA2  
5.3.2007





## THE RAMI ON-LINE MODEL CHECKER (ROMC)

J.-L. Widlowski<sup>a,\*</sup>, M. Robustelli<sup>a</sup>, M. Disney<sup>b</sup>, J.-P. Gastellu-Etchegorry<sup>c</sup>, T. Lavergne<sup>e</sup>, P. Lewis<sup>b</sup>, E. Martin<sup>c</sup>, P. R. J. North<sup>d</sup>, B. Pinty<sup>a</sup>, M. Taberner<sup>a</sup>, R. Thompson<sup>f</sup>, M. M. Verstraete<sup>a</sup>

<sup>a</sup> DG Joint Research Center, European Commission, Via E. Fermi, 1, 21020 Ispra (VA), Italy  
([Jean-Luc.Widlowski@jrc.it](mailto:Jean-Luc.Widlowski@jrc.it), [Bernard.Pinty@jrc.it](mailto:Bernard.Pinty@jrc.it), [Monica.Robustelli@ext.jrc.it](mailto:Monica.Robustelli@ext.jrc.it), [Malcolm.Taberner@jrc.it](mailto:Malcolm.Taberner@jrc.it))

<sup>b</sup> Department of Geography, University College London, 26 Bedford way, London, WC1H 0AP, UK and NERC Centre for Terrestrial Carbon Dynamics ([mdisney@geog.ucl.ac.uk](mailto:mdisney@geog.ucl.ac.uk), [plewis@geog.ucl.ac.uk](mailto:plewis@geog.ucl.ac.uk))

<sup>c</sup> Centre d'Etudes Spatiales de la Biosphère (CESBIO), 18 avenue Edouard Belin, bpi 2801, 31401 Toulouse cedex 9, France ([jean-philippe.gastellu@cesbio.cnes.fr](mailto:jean-philippe.gastellu@cesbio.cnes.fr), [emmanuel.martin@cesbio.cnes.fr](mailto:emmanuel.martin@cesbio.cnes.fr))

<sup>d</sup> Climate and Land-Surface Systems Interaction Centre, Department of Geography, University of Wales Swansea, Singleton Park, Swansea, SA2 8PP, UK ([p.r.j.north@swansea.ac.uk](mailto:p.r.j.north@swansea.ac.uk))

<sup>e</sup> Section for Remote Sensing, Research and Development Department, Norwegian Meteorological Institut, P.O.Box 43, Blindern, N-0313 Oslo, Norway ([thomasl@met.no](mailto:thomasl@met.no))

<sup>f</sup> Alachua Research Institute, Alachua, Florida, USA ([richardlthompson@cox.net](mailto:richardlthompson@cox.net)).

**KEY WORDS:** benchmarking, radiation transfer model intercomparison, RAMI, quality control, BRDF, vegetation canopy.

### ABSTRACT:

The RAMI On-line Model Checker (ROMC) is a web-based tool (<http://romc.jrc.it/>)\*\* allowing for the automated evaluation of canopy radiation transfer (RT) models. This is achieved by comparing simulation results submitted by registered ROMC users to a reference dataset established from credible 3-D Monte Carlo models during the third phase of the RADIation transfer Model Intercomparison (RAMI) exercise. Access to the ROMC is free and allows users to assess their model performance either in “debug mode” (if users want to evaluate the impact of changes in their model’s software code/parameter input with respect to some user-selected test cases identical to those in RAMI), or, in “validate mode” (if users want to evaluate the performance of their model against a random selection of test cases not included within RAMI). Upon successful submission, registered ROMC users will be presented with various results statistics and graphical displays that document the performance of their model with respect to the reference dataset. In addition to providing an indication of the overall skill of a model to correctly match the reference data, the ROMC also allows for interactive comparison/evaluation of the differences existing between various versions of the same model. Furthermore, ROMC users can download encapsulated postscript versions of these graphical results files, and – in debug mode only – may also receive ASCII files containing the ROMC reference data. ROMC graphs come with a reference number and may be used in presentations and – in validate mode – also in refereed scientific publications to underline the quality of a given model. As such the ROMC is a good example, on how a concerted, voluntary community effort (i.e., RAMI) has led to tangible results that benefit both model developers and their customers.

### 1. INTRODUCTION

Indicators as to the quality of physically-based radiation transfer (RT) models are of relevance to their developers and users, as well as the scientists, space agencies and policy makers that use or support the products and information derived on the basis of such model simulations/inversions. The radiation transfer model intercomparison (RAMI) initiative was launched in an attempt to shed light on the reliability and accuracy of existing canopy radiation transfer models. RAMI is a triennial community exercise that encourages the systematic evaluation of canopy reflectance models under well-controlled experimental conditions and on a voluntary basis (Pinty et al., 2001, 2004, Widlowski et al., 2007). Significant efforts were being made during the first (1999) and second (2002) phases of RAMI in order to document and reduce the dispersion between increasing numbers of participating models, but it was not until the completion of the third phase (2005) that a sufficiently

strong consensus emerged among RT models capable of simulating the entire palette of RAMI test cases: from simple plane-parallel turbid medium scenarios to complex heterogeneous vegetation canopies with and without underlying topography. During RAMI-3 the mutual agreement between the reflectance simulations of six state-of-the-art 3-D Monte Carlo models was estimated to lie at ~1%. This is significantly lower than anything previously achieved and well below the absolute accuracy of current space borne measurements, which prompted the usage of these model simulations in order to establish a reference dataset against which other/future radiative transfer models may now be compared.

### 2. THE ROMC REFERENCE DATA SET

The self-consistency (e.g., energy conservation) together with the absolute and relative performance of models were evaluated in great detail during RAMI-3. Substantial improvements in

\* Corresponding author; \*\* Due to a renaming of all European Commission websites this URL is likely to change in the near future to <http://romc.jrc.ec.europa.eu/>.

model agreement were observed, in particular, for the 3-D Monte Carlo (MC) models that participated. These models allow for explicit 3-D representations of complex canopy architectures and avoid unnecessary assumptions and approximations in the solving of the radiation transfer equation due to their stochastic sampling of the surface leaving radiation field (Disney et al., 2000). The average model-to-ensemble dispersion between the total BRF simulations of six 3-D MC models (e.g., dart (Gastellu-Etchegorry et al., 2004), drat (Lewis 1999), flight (North, 1996), rayspread (Widlowski et al., 2006), raytran (Govaerts and Verstraete 1998) and sprint3 (Goel and Thompson 2000)) was found to have almost halved from RAMI-2 (1.37 %) to RAMI-3 (0.72 %) for canopies with finite-sized foliage, whereas in turbid medium cases it improved by a factor of ~7 from RAMI-2 (6.36 %) to RAMI-3 (0.91 %) – see Table 1 for exact values of the dispersion in RAMI-3 (computed according to equations given in section 3.3.2 of Widlowski et al., 2007). The overall performance of these six 3D MC models in RAMI-3 thus supported their usage in the generation of a “surrogate truth” against which other RT models could then be evaluated.

model name	foliage description	
	discrete	turbid
dart	-	1.46
drat	0.55	-
flight	0.97	1.06
rayspread	0.55	0.64
raytran	0.60	0.69
sprint3	1.01	0.69

Table 1. Model-to-ensemble dispersion (in percent) for the total BRF simulations over both homogeneous and heterogeneous canopy scenes for six “credible” 3-D Monte Carlo models identified during the third phase of RAMI.

In order to obtain a “surrogate truth” estimate it was decided to simply average the BRFs that were obtained from the above set of credible MC models. Due to variable model participation (and performance) the precise number and names of the available 3-D MC models could, however, change from one experiment and measurement to the next. As a consequence, the number and names of the credible models that featured in the computation of the “surrogate truth” had to be chosen separately for every RAMI experiment and measurement. The following list of criteria was finally applied to derive the “surrogate truth” estimates from RAMI-3 simulations:

1. For every RAMI BRF (flux) measurement, identify at least two (one) 3-D Monte Carlo models that do not belong to the same RT modelling school/family,
2. If two (or more) models from the same RT modelling school/family are available, e.g., rayspread and raytran, choose the one with the least amount of apparent MC noise,
3. Remove all those 3-D Monte Carlo models from the reference set that are noticeably different from the main cluster of 3-D MC simulations,
4. If sufficient models are contained in the main cluster of 3-D MC simulations then remove those models that would introduce noticeable levels of “MC noise” into the reference set,

5. If there are two distinct clusters of 3-D Monte Carlo models, or, no obvious cluster at all, then use all available 3-D RT models to define a reference solution.

A drawback of this selection procedure lies in the fact that the ROMC reference dataset may not be fully compliant with energy conservation. This is a direct consequence of 1) not all credible models performing all test cases and measurements, and 2) the variable performance of credible models for different measurements types, as well as, structural, spectral and illumination scenarios. Nevertheless, the average absolute deviation of the ROMC reference dataset from energy conservation was found to be 0.00025 in the red, 0.00007 in the near-infrared, and  $9.5 \cdot 10^{-7}$  for conservative scattering conditions (purist corner). A synoptic table featuring the names and performances of the various 3-D Monte Carlo models that contributed toward the computation of the “surrogate truth” for all the RAMI-3 experiments and measurement types individually, can be found on the following internet page: [http://romc.jrc.it/WWW/PAGES/ROMC\\_Home/RAMIREF.php](http://romc.jrc.it/WWW/PAGES/ROMC_Home/RAMIREF.php)

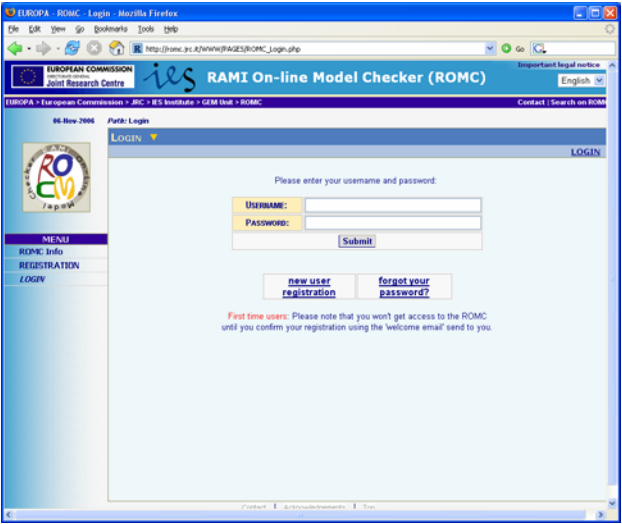


Figure 1. The RAMI On-line model checker (ROMC) website.

3. THE RAMI ON-LINE MODEL CHECKER

With this valuable reference dataset at hand, it becomes possible to allow canopy RT model owners, developers and customers to evaluate the performance of a given model even outside the frame of RAMI. To facilitate such an undertaking the RAMI On-line Model Checker (ROMC) was developed at the Joint Research Centre of the European Commission in Ispra, Italy. The ROMC is a web-based interface allowing for the on-line evaluation of RT models using as reference the “surrogate truth” derived from among the six credible 3-D Monte Carlo models identified during RAMI-3. Access to the ROMC can be obtained either via the RAMI website or directly using the URL \*\*\* <http://romc.jrc.it/>. After providing a username and valid email address, the ROMC can be utilised in two different ways: 1) in “debug mode”, which allows to repeatedly compare the output of a RT model to that of one or more experiments and/or

\*\*\* Due to a renaming of all European Commission websites this URL is likely to change to <http://romc.jrc.ec.europa.eu/>.

measurements from RAMI, i.e., the simulation results are known since they are available on the RAMI website, and 2) in “validate mode”, which enables the once-only testing of the RT model against a randomly selected set of test cases that are similar but not quite equivalent to those from RAMI, i.e., the solutions are not known *a priori* and the model runs cannot be repeated.

- In “debug mode” users may choose to execute one particular experiment and/or measurement from the set of RAMI-3 test cases *ad infinitum*, or, at least until they are satisfied with the performance of their model. Detailed descriptions of the structural, spectral, illumination and measurement conditions are available. Once the ROMC user has generated his/her model simulations, they can be up-loaded via the web-interface, and - provided that they adhere to the RAMI filenames and formatting conventions - this process will result in a series of graphical results files being made available for all test cases. In debug mode users may not only download their ROMC results but also an ASCII file containing the actual “surrogate truth” data.
- In “validate mode” ROMC users may choose between structurally homogeneous leaf canopies and/or heterogeneous “floating spheres” scenes in order to verify the performance of their model. The actual set of test cases will, however, be drawn randomly from a large list of possible ones, such that it is unlikely to obtain the same test case twice, i.e., in all likelihood one will not “know” the solution *a priori*. Again, the “surrogate truth” was derived from simulations generated by models belonging to the same set of 3-D MC models as was the case for the debug mode. In validate mode the reference data will, however, not be available for downloading. The procedure for data submission, on the other hand, is identical to that of the debug mode, and - provided that all RAMI formatting and filenames requirements are applied - leads to a results page featuring a variety of intercomparison graphics.

Registered ROMC users may download their model performance results either as jpeg formatted images directly from the ROMC website, or else, opt for receiving them via email in postscript form. Both the debug and validate mode ROMC results files feature a unique reference number. Graphs are available for individual experiments (see Figure 2) as well as for the ensemble of submitted experiments (see Figure 3). Currently the set of downloadable graphs include 1) plots of Bidirectional Reflectance Factors (BRF) from both the user’s model and the ROMC reference dataset along either the principal or the orthogonal plane, 2) 1 to 1 plots of the model and reference BRFs (or fluxes), 3) histograms of the deviations between the model and reference BRFs, 4)  $\chi^2$  graphs depicting model equivalency with the reference data set for the various submitted measurements, 5) graphs depicting the deviation of the model and reference fluxes using barcharts, and 6) Taylor diagrams (Taylor, 2001) expressing model performance in terms of correlation, standard deviation and root mean square error (see Figure 4). Statistics like the root mean square error (RMS), the signal to noise ratio (S/N) and the number of experiments included are also provided. In addition some these graphs can be received in black and white only form.

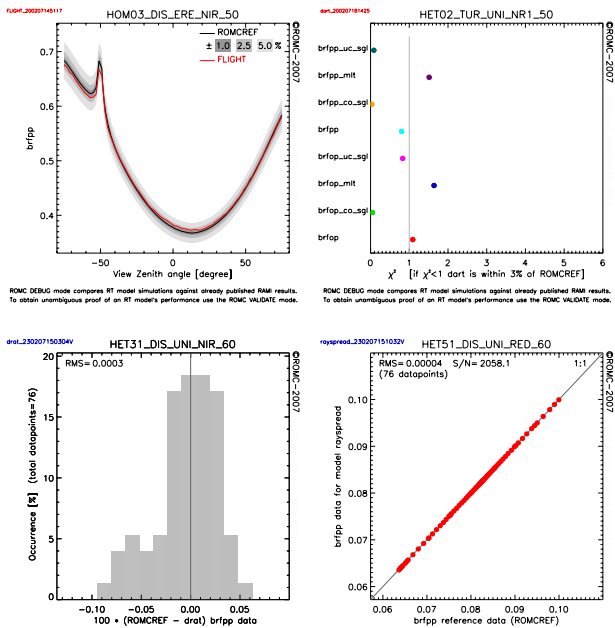


Figure 2. Examples of downloadable ROMC graphics showing model performance for individual experiments in debug mode (top) and validate mode (bottom). Shown are plots of user and reference BRFs (top left), a  $\chi^2$  graph (top right), a histogram of BRF differences (bottom left), and a 1:1 plot (bottom right).

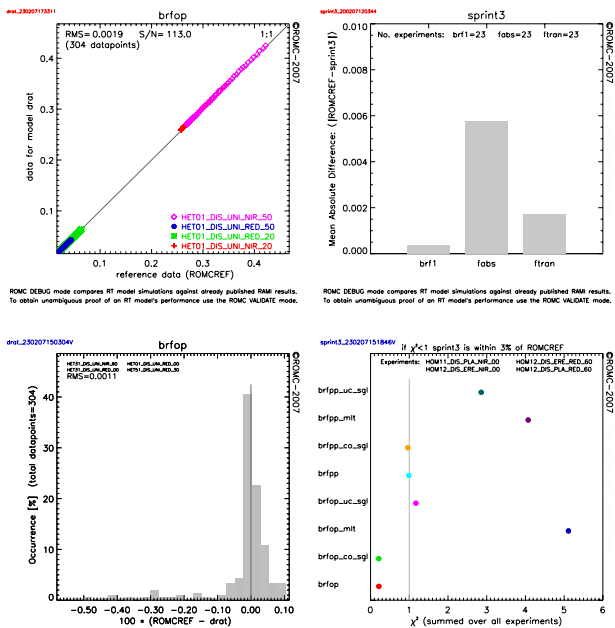


Figure 3. Examples of ROMC graphics summarising model performance for ensembles of submitted experiments carried out in debug mode (top row) and validate mode (bottom row). Shown are a 1:1 BRF plot (top left), a barchart of mean absolute flux differences (top right), a histogram of BRF differences (bottom left), and a  $\chi^2$  graph (bottom right).

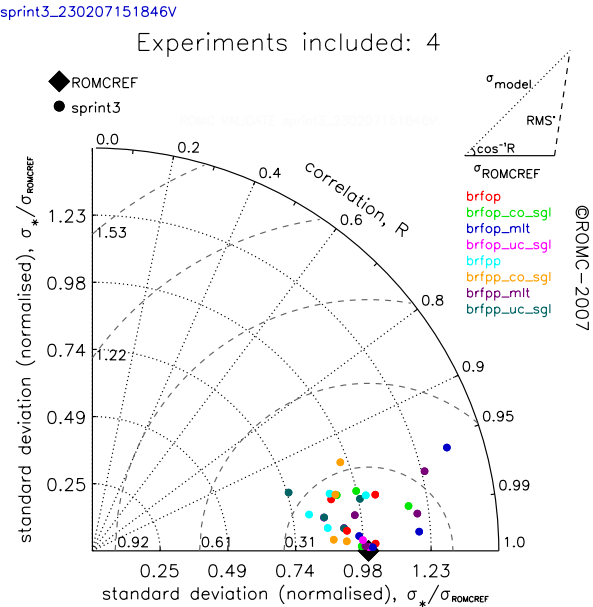


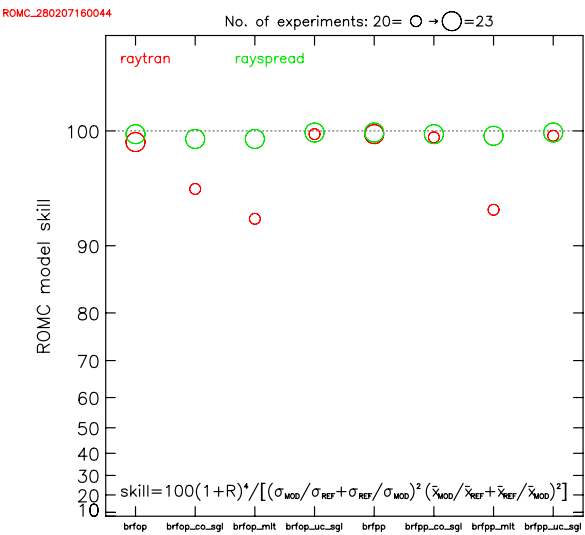
Figure 4. Examples of a Taylor graph in validate mode depicting model performance in terms of the ability to match the pattern (correlation R) and variability (normalised standard deviation) of the reference solution. The RMS difference error is also indicated (dashed isolines).

In order to provide an overall indication of a model’s capability to match the reference data set a skill metric is defined and applied to each measurement type. The ability of a skill metric should be such that 1) for any given variance the score increases monotonically with increasing correlation, and 2) for any given correlation the score increases as the modelled variance approaches the variance of the reference data set. For visualisation purposes the ROMC skill scores were defined from zero (least skillful) to 100 (most skillful). The metric that was chosen for the ROMC skill score evaluates the correlation, R between the model simulations and the reference data set, the standard deviation,  $\sigma$  of the model and reference dataset, and the mean,  $\bar{x}$  of both datasets:

$$Skill = 100 \frac{(1 + R)^4}{\left( \frac{\bar{x}_{mod}}{\bar{x}_{ref}} + \frac{\bar{x}_{ref}}{\bar{x}_{mod}} \right)^2 \left( \frac{\sigma_{mod}}{\sigma_{ref}} + \frac{\sigma_{ref}}{\sigma_{mod}} \right)^2} \quad (1)$$

Since different models may perform different numbers of experiments in debug mode the representability of the skill metric has to be related to the number of test cases on which it is based (see Figure 5).

The ROMC possesses also a series of interactive features allowing users with more than one registered model (maximum is 3), or, users that have submitted simulation results of different versions of the same model to compare these data either against the ROMC reference data or against one of their own ROMC submissions. Similar graphics as in the standard submission to the ROMC are provided both in encapsulated postscript format and as jpeg images (see Figure 6).



ROMC DEBUG mode compares RT model simulations against already published RAMI results. To obtain unambiguous proof of an RT model's performance use the ROMC VALIDATE mode.

Figure 5. The ROMC skill describing the performance of two models – belonging to the same user – over their respective sets of available simulations for the homogeneous scenes in RAMI.

Users of ROMC are encouraged to utilise only ROMC results that were obtained in validate mode for publication purposes. Those obtained in debug mode, obviously, can not qualify as unambiguous proof of model performance since all simulation results may readily be viewed on the RAMI website. It should also be noted that it is not permissible to modify, change or edit the results provided by the ROMC. This applies to ROMC graphs, statistics, as well as reference data which must all be used 'as provided' and duly referenced using either Widlowski et al., (2007) or this publication.

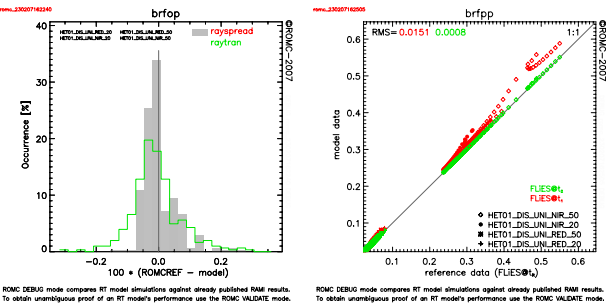


Figure 6. Examples of interactive ROMC graphics in debug mode, showing (left panel) a histogram of model-to-reference-differences for two models belonging to the same ROMC user, and (right panel) a 1:1 plot of BRFs for two different versions of the same model of a ROMC user.

Last but not least a large ensemble of FAQs are available on the ROMC website, that explain the conceptual functioning of the ROMC, the statistics and graphics provided, as well as the submission procedure and guidelines to address eventual troubleshooting. It is hoped that the ROMC will prove useful for the RT modelling community as a whole, not only by providing a convenient means to evaluate RT models outside the triennial phases of RAMI (something that was rather tedious



in the past if authors wished to rely on the experiences gained from RAMI, e.g., Gastellu-Etchegorry et al., (2004)) but also to attract participation in future RAMI activities.

In this context it is important to realize that the ROMC is primarily intended to provide rapid, indicative evaluations of the performance of RT model, in particular in validate mode. RAMI, on the other hand, approaches model evaluation in a more comprehensive manner covering many different aspects of model performance under a large variety of structural, spectral and illumination conditions. The usage of the ROMC should thus be seen as a first step toward the full participation in a next phase of RAMI. Finally it should also be noted, that it is foreseen to regularly update the reference data set of the ROMC after every new phase of RAMI, thus reflecting the improvements that are being made by the RT model community.

#### 4. CONCLUSION

The RAMI On-line Model Checker (ROMC), a web-based tool for the autonomous benchmarking of canopy radiation transfer models was presented (<http://romc.jrc.it/>). The ROMC was made possible due to substantial improvements in model agreement observed during the third phase of the RAdiation transfer Model Intercomparison (RAMI) exercise. The ROMC utilizes a reference data set established after several years of efforts of the international modeling community to identify a series of "credible" 3-D Monte Carlo models. It is expected that the ROMC will evolve into a yardstick for scientists, funding agencies, and policy makers alike when it comes to appreciating the quality of a given model and ultimately also the information that it helps retrieving from Earth Observation data.

#### 5. ACKNOWLEDGEMENTS

The RT model benchmarking activities in the frame of RAMI would not have been possible without the financial support of the European Commission, and more specifically, the Global Environment Monitoring unit of the Institute for Environment and Sustainability in the DG Joint Research Centre. The support of the RT modeling community towards RAMI should also be acknowledged. Furthermore, we would also like to thank Drs. Robert F. Cahalan, Tamás Várnai and Wout Verhoef for their valuable comments on the design of the ROMC, as well as Dr. Hideki Kobayashi for providing valuable feedback and the permission to use some of his ROMC results graphics in this publication.

#### 6. REFERENCES

- Disney, M. I., P. Lewis, and P. R. J. North (2000). Monte Carlo ray-tracing in optical canopy reflectance modeling. *Remote Sensing Reviews*, 18, 163-196.
- Gastellu-Etchegorry, J-P, E. Martin, and F. Gascon (2004). DART: a 3D model for simulating satellite images and studying surface radiation budget. *International Journal of Remote Sensing*, 25, 73-96.
- Goel, N. S. and Thompson, R. L. (2000). A snapshot of Canopy Reflectance Models and a Universal Model for the Radiation Regime. *Remote Sensing Reviews*, 18, 197-206.
- Govaerts, Y., and M. M. Verstraete (1998). Raytran: A Monte Carlo ray tracing model to compute light scattering in three-dimensional heterogeneous media. *IEEE Transactions on Geoscience and Remote Sensing*, 36, 493-505, 1998.
- Lewis, P. (1999). Three-dimensional plant modelling for remote sensing simulation studies using the botanical plant modelling system. *Agronomie - Agriculture and Environment*, 19, 185-210.
- North, P. R. J. (1996). Three-dimensional forest light interaction model using a Monte Carlo method. *IEEE Transactions on Geoscience and Remote Sensing*, 34, 946-956, 1996.
- Pinty, B., N. Gobron, J.-L. Widlowski, S. A. W. Gerstl, M. M. Verstraete, M. Antunes, C. Bacour, F. Gascon, J.-P. Gastellu, N. Goel, S. Jacquemoud, P. North, W. Qin, and R. Thompson (2001). Radiation Transfer Model Intercomparison (RAMI) Exercise. *Journal of Geophysical Research*, 106, 11,937-11,956.
- Pinty, B., J.-L. Widlowski, M. Taberner, N. Gobron, M. M. Verstraete, M. Disney, F. Gascon, J.-P. Gastellu, L. Jiang, A. Kuusk, P. Lewis, X. Li, W. Ni-Meister, T. Nilson, P. North, W. Qin, L. Su, S. Tang, R. Thompson, W. Verhoef, H. Wang, J. Wang, G. Yan, and H. Zang (2004). RAdiation transfer Model Intercomparison (RAMI) exercise: Results from the second phase. *Journal of Geophysical Research*, 109, D06210 10.1029/2003JD004252.
- Taylor, K. E. (2006). Summarizing multiple aspects of model performance in a single diagram. *Journal of Geophysical Research*, 106, D7, 7183-7192.
- Widlowski, J.-L., M. Taberner, B. Pinty, V. Bruniquel-Pinel, M. Disney, R. Fernandes, J.-P. Gastellu-Etchegorry, N. Gobron, A. Kuusk, T. Lavergne, S. Leblanc, P. Lewis, E. Martin, M. Mottus, P. J. R. North, W. Qin, M. Robustelli, N. Rochdi, R. Ruiloba, C. Soler, R. Thompson, W. Verhoef, M. M. Verstraete, and D. Xie (2007). The third RAdiation transfer Model Intercomparison (RAMI) exercise: Documenting progress in canopy reflectance modelling. *Journal of Geophysical Research*, 2007, accepted.
- Widlowski, J.-L., T. Lavergne, B. Pinty, M. M. Verstraete, and N. Gobron (2007). Rayspread: A virtual laboratory for rapid BRDF simulations over 3-D plant canopies, in *Computational Methods in Transport*, edited by Graziani, F., pp. 211-231, ISBN.10 3.540.28,122.3, Lecture Notes in Computational Science and Engineering Series, 48, Springer Verlag, Berlin.



# ASSIMILATING REFLECTANCE DATA INTO A ECOSYSTEM MODEL TO IMPROVE ESTIMATES OF TERRESTRIAL CARBON FLUX

T. Quaife<sup>a,\*</sup>, P. Lewis<sup>a</sup>, M. Disney<sup>a</sup>, M. De Kauwe<sup>a</sup>, M. Williams<sup>b</sup> and B. Law<sup>c</sup>.

<sup>a</sup> NERC Centre for Terrestrial Carbon Dynamics and Dept. of Geography, University College London, Pearson Building, Gower Street, London, WC1E 6BT UK - tquaife@geog.ucl.ac.uk

<sup>b</sup> NERC Centre for Terrestrial Carbon Dynamics and School of GeoSciences, Institute of Atmospheric and Environmental Sciences, Crew Building, Kings Buildings, University of Edinburgh, Edinburgh, EH9 3JN, UK.

<sup>c</sup> College of Forestry, Oregon State University, Corvallis, OR 97331, U.S.A.

**KEY WORDS:** Ensemble Kalman filter, MODIS, GORT, data assimilation, DALEC, GPP, NEP.

## ABSTRACT:

Ecosystem models are valuable tools for understanding the growth of vegetation, its response to climatic change and its role in the cycling of greenhouse gasses. Data Assimilation (DA) of synoptic coverage Earth Observation (EO) data into ecosystem models provides a statistically optimal mechanism for constraining the model state vector trajectory both spatially and temporally. EO “products” such as leaf area index (LAI) are attractive candidates for assimilation, but it is difficult to assign accurate uncertainty estimates to such products (a critical requirement of DA) and, more importantly, they are derived on the basis of assumptions that may be contradictory to those in the ecosystem model. An attractive alternative, therefore, is to assimilate reflectance data; the uncertainty in which is more easily understood. The assumptions made in generating the reflectance data are independent of assumptions in the ecosystem model and may consequently be treated as additional sources of uncertainty. To achieve this it is necessary to build a canopy reflectance model into the assimilation scheme. This paper describes the coupling of a canopy reflectance model to a simple ecosystem model. Reflectance data are assimilated over a boreal forest and improvements in predicted carbon fluxes are shown with comparison to field data. Previous work has highlighted problems of lost samples due to snow cover, resulting in poorly constrained flux estimates during winter months. This issue is addressed by incorporating a snow reflectance model. Results utilising the EnKF as a parameter estimator are also discussed.

## 1. INTRODUCTION

### 1.1 Background

Understanding and quantifying of the role of terrestrial vegetation in the carbon cycle is critical for climate change studies because of the feedbacks that exist with atmospheric CO<sub>2</sub> (Schimel et al., 2001). This in turn has major relevance for national and international policy (IPCC, 2001). Ecosystem models are an attractive tool for studying the terrestrial carbon cycle because they are based on process understanding. However, large uncertainties exist between models of terrestrial carbon dynamics (Churkina et al., 2005) despite advances in process based modelling (Law et al., 2001a; Rastetter, 2003) and improved networks of C flux measurements at the field scale (Valentini et al., 2000).

An issue when scaling such models up to regional or global levels is that they are not well constrained away from the field sites for which they are parameterised. An attractive option to tackle this problem is the use of Earth Observation (EO) data, which provides spatially and temporally synoptic data, to adjust model trajectories within a data assimilation scheme. Data assimilation methods have been used successfully for integrating EO data in numerical weather prediction models for some years but are only just gaining widespread attention in the terrestrial vegetation EO community. These techniques give a statistically optimal analysis of a model's state vector and/or parameters against observations and allow for explicit representation of model and data errors.

This paper follows directly on from the work of Williams et al (2005) and Quaife et al. (2007). Williams et al (2005) present a simple ecosystem model (outlined below) and assimilate field observations using data assimilation techniques. The paper shows that the model is able to reproduce observed carbon fluxes well despite its simplicity by utilising large numbers of observations. Quaife et al. (2007) take this model and assimilate MODIS surface reflectance data into it as a demonstration of the potential use of EO data in such schemes. The authors argue for the use of reflectance over “high” level EO products (such as leaf area index, LAI) on the basis that it is easier to characterise errors in reflectance data and that high level products are typically generated using assumptions that contradict those in the ecosystem model itself. This latter point may be overcome by using surface reflectance products, as assumptions in its generation will be independent of those in the ecosystem model. Furthermore the required observation operator may be built to be entirely consistent with the ecosystem model itself.

Two issues in this approach highlighted by Quaife et al. (2007) are the lack of MODIS samples in winter months owing to snow/cloud contamination (resulting in a poorly constrained model) and the need for spatialised model parameters to allow for scaling to and beyond the regional scales. These issues are addressed in this paper.

---

\* Corresponding author.

## 2. METHOD

### 2.1 Field data

The field data for this study were acquired at the Metolius forest site (44° 26' N, 121° 34' W) in Oregon that has been extensively characterised (Law, 2001a) and is part of the AmeriFlux network. It is dominated by *Pinus Ponderosa* and is regenerating since being clearfelled in 1978. The understory is mixed bitterbush (*Purshia tridentata*) and manzanita (*Arctostaphylos patula*).

Extensive ecological measurement campaigns have been carried out at this site and the collected data have been used to calibrate the DALEC model (Williams et al. 2005). These data include CO<sub>2</sub> flux measurements from an eddy covariance system (Anthoni et al., 2002), leaf area index (LAI; Law, 2001b), specific leaf area, soil respiration (Irvine et al., 2002) and above- and belowground biomass. Meteorological data (incident PAR, temperature and vapour pressure deficit) were also collected. These are used here to drive the ACM and DALEC models.

### 2.2 MODIS data

Level 2, collection 4 TERRA-MODIS 500m surface reflectance data (MOD09) were used as the observations in this study. Only bands 1 (red) and 2 (near infra red), centred at 646 nm and 848 nm were considered, although this work could easily be extended to include any number of optical wavebands. Uncertainties in the reflectance data were set as 0.004 and 0.015 for bands 1 and 2 respectively (Roy et al., 2005).

In total there were 316 acquisitions, over the 3 years (200-2002) of this study that contained no snow or cloud. Within this set there were no observations during winter months however. Extracting pixels flagged in the MODIS QA data as being snow contaminated provided an additional 18 observations spread roughly evenly over the winter months of the time period.

### 2.3 DALEC

Carbon pools and fluxes for were modelled over the three year period using the Data Assimilation Linked Ecosystem model, DALEC (Williams et al., 2005).

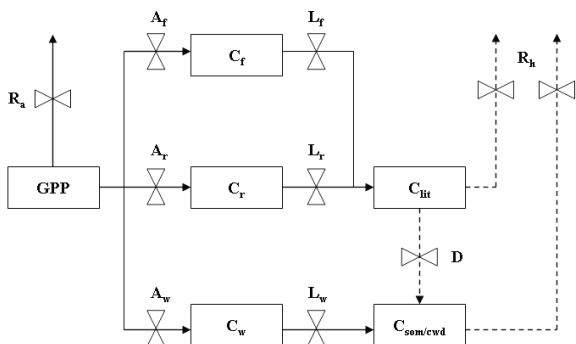


Figure 1. Schematic representation of the DALEC model.

Fig 1. Shows a diagrammatic representation of the DALEC model. The carbon pools are  $C_f$ ,  $C_r$ ,  $C_w$ ,  $C_{lit}$ , and  $C_{som/cwd}$  which represent foliar, root, woody, litter, and soil organic matter and

woody debris carbon, respectively. In addition there is a pseudo pool that represents the gross primary productivity (GPP). This is the uptake of carbon from photosynthesis. Fluxes are denoted  $R_a$  and  $R_h$  (autotrophic and heterotrophic respiration), where heterotrophic respiration is divided into  $D$  (decomposition from litter to soil organic matter), and  $L_f$ ,  $L_r$  and  $L_w$  (the rate of loss of foliar, fine root and woody carbon respectively). Dotted lines indicate a temperature dependant transform.

GPP was calculated using the Aggregated Canopy Model (ACM) of Williams et al. (1997) calibrated for a Ponderosa pine ecosystem. The net ecosystem productivity (NEP) is given by the difference of the GPP and the  $R_a$  and  $R_h$  modelled by DALEC. This provides a quantification of the strength of the ecosystem as either a source (-ve NEP) or a sink (+ve NEP) of CO<sub>2</sub>.

### 2.4 Ensemble Kalman Filter (EnKF)

The EnKF is a variant of the Kalman Filter designed to work with non-linear models due to Evensen (1994, 2003). It uses an ensemble of model states to represent error statistics in the model, as opposed to the explicit covariance matrix representation used by the Kalman Filter. It has the form:

$$\mathbf{A}^a = \mathbf{A} + \mathbf{A}' \mathbf{A}'^T \mathbf{H}^T (\mathbf{H} \mathbf{A}' \mathbf{A}'^T \mathbf{H}^T + \mathbf{R}_e)^{-1} (\mathbf{D} - \mathbf{H} \mathbf{A}) \quad (1)$$

where,  $\mathbf{A}$  is the model ensemble;  $\mathbf{A}'$  is the ensemble perturbation;  $\mathbf{R}_e$  is the covariance observation error;  $\mathbf{D}$  is the observation ensemble and  $\mathbf{H}$  is the observation operator. The superscript  $\mathbf{a}$  denotes the analysed ensemble and the superscript  $\mathbf{T}$  denotes a matrix transpose.

In this form it is not possible to assimilate canopy reflectance into an ecosystem model as top of canopy BRF is not a linear transform of a typical ecosystem model state vector (as required by the observation operator matrix  $\mathbf{H}$ ). Evensen, (2003) suggests an augmented state vector approach to handle non linear observations:

$$\mathbf{A}^a = \mathbf{A} + \mathbf{A}' \hat{\mathbf{A}}^T \hat{\mathbf{H}}^T (\hat{\mathbf{H}} \hat{\mathbf{A}}' \hat{\mathbf{A}}^T \hat{\mathbf{H}}^T + \mathbf{R}_e)^{-1} (\mathbf{D} - \hat{\mathbf{H}} \hat{\mathbf{A}}) \quad (2)$$

Where  $\hat{\mathbf{A}}$  and  $\hat{\mathbf{A}}'$  are the model ensemble and perturbation matrices augmented with predictions of BRF. In effect the BRFs become part of the model during analysis. The augmented ensemble is formed by:

$$\hat{\mathbf{A}} = \mathbf{h}(\mathbf{A}) \quad (3)$$

where  $\mathbf{h}$ , in this case, is a canopy reflectance model.

### 2.5 Canopy reflectance model

The hybrid Geometric Optic Radiative Transfer (GORT) model of Ni et al. (1999) was coupled with DALEC to provide estimates of the top-of-canopy reflectance for MODIS channels 1 and 2. The leaf area index (LAI) required to drive GORT is

provided by the DALEC model by assuming it to be a constant proportion of the foliar biomass. Leaf reflectance was determined by the PROSPECT model (Jacquemoud and Baret, 1990) and soil reflectance was modelled by the empirical spectral functions of Price (1990).

The “ancillary” parameters of the GORT model (i.e. those that are not provided by the ecosystem model) are taken from the Quaife et al. (2007) paper. These are derived by a look up table inversion of the GORT model for the field site in question.

2.6 Snow reflectance model

To enable the use of snow contaminated MODIS data in the EnKF scheme; a model of the spectral albedo of snow was used to modify the lower boundary condition of GORT. The refractive index (Kou et al., 1993) and Mie scattering coefficients (Wiscombe, 1980) of ice particles were calculated using routines available from the NASA GSFC FTP site.

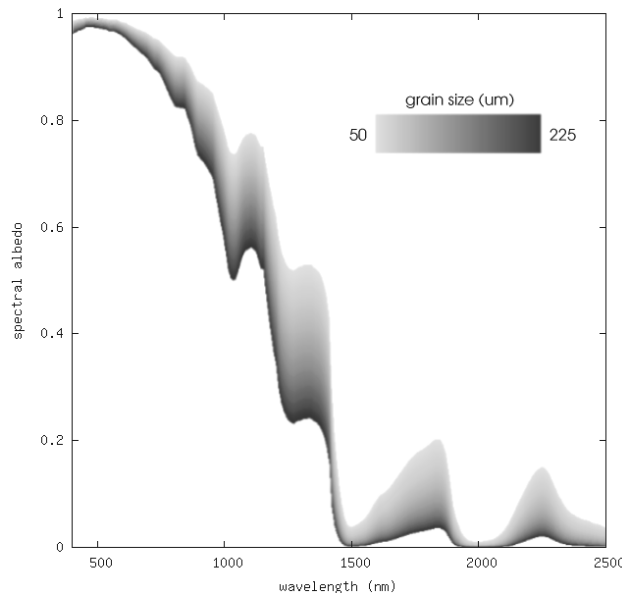


Figure 2. Snow spectral albedo as a function of wavelength and grain size (indicated by colour scale).

Integrated fluxes, taking into account multiple scattering were calculated using the DISORT code (Stamnes et al., 1988) available from the same site. This approach has been shown to provide reasonable predictions of the spectral albedo of snow by Green et al. (2002). For the purpose of extending the GORT model, the snow was assumed to be optically deep and only affect the lower boundary – no snow was taken to be resting in the tree crowns. Fig. 2 shows the spectral albedo for a range of wavelengths and grain sizes predicted by this model. Given the relative lack of sensitivity of albedo to grain size in the spectral regions of MODIS bands 1 and 2, an arbitrary grain size of 100µm was selected.

3. RESULTS

The DALEC model was run for the field site using meteorological drivers from the years 2000, 2001 and 2002. MODIS band 1 and 2 surface reflectance data were assimilated into the model using the EnKF. When the MODIS QA flags indicated snow in the retrieval the lower boundary of the GORT

model was covered with 50% snow, otherwise the GORT model was run without snow. Integrated values of GPP and NEP for the 3 years of the model run are given in Table 1 for the case where there is no assimilation, assimilation of reflectance *excluding* snow (previously reported in Quaife et al. 2007), assimilation of reflectance data *including* snow and the results of Williams et al. (2005) where large amounts of field data were assimilated.

Flux	Assimilated data	Total carbon uptake (g/m <sup>2</sup> )	Standard deviation
NEP	No data assimilation	240.2	212.2
	MODIS excluding snow	373.0	151.3
	MODIS including snow	404.8	129.6
	Williams et al. (2005)	406.0	27.8
GPP	No data assimilation	1646.4	834.5
	MODIS excluding snow	2620.3	96.8
	MODIS including snow	2525.6	42.7
	Williams et al. (2005)	2170.3	18.1

Table 1. Integrated C fluxes for 3 years.

3.1 Foliar Biomass

Fig. 3 shows the results of assimilating MODIS surface reflectance data into the DALEC model. Without the incorporation of snow contaminated pixels into the assimilation there is a clear period where the model is allowed to run without constraint and the ensemble spread increases monotonically. When the snow samples are added to the observations the model is adjusted accordingly, pulling the foliar biomass down during the winter months. The induced seasonality is quite large; in the order of 120 grams of carbon per m<sup>2</sup> over the course of a year. *Pinus Ponderosa* is evergreen and so seasonal cycles of this magnitude are unlikely. Some of the understory components are deciduous which will account, in part, for this effect but it is unlikely to explain all the variation.

3.2 Gross Primary Productivity

Without data in the winter months DALEC overestimates the GPP. The high, unconstrained, foliar biomass leads to an increase in light interception and thus greater uptake of atmospheric CO<sub>2</sub> by photosynthesis. This is rectified by the inclusion of the snow contaminated reflectance data, which pulls the foliar biomass down (Fig. 4). The integrated flux data (Table 1) only shows a slight improvement in the GPP however. This is because meteorological conditions (less incident PAR and lower temperatures) mean that GPP in the winter is low and so the correction at this time only has limited impact on the integrated quantity.

### 3.3 Net Ecosystem Productivity

The correction made to GPP is only small as a proportion of its integral. This amount of carbon as a proportion of NEP is much greater however, and so the correction to the results for NEP induced by inclusion of the winter reflectance values is significant. Fig. 5. shows that by assimilating the snow reflectance data the model predicts a stronger *source* of carbon during the winter months, which is in agreement with the observations taken at the field site. The values in Table 1. show a remarkable agreement with the values published by Williams et al (2005). Given that the GPP is overestimated this means that the total respiration from the system (autotrophic and heterotrophic) must also be overestimated to balance this out.

### 3.4 Parameter estimation

To use the techniques described above over wider areas it is important to be able to re-parameterise the DALEC model appropriately for the ecosystem in question. One option for determining the DALEC parameters is to use the EnKF itself. In this approach the parameters that are to be adjusted are placed in the model state vector and allowed to evolve with time under the influence of available observations. Fig. 7 show results of such an experiment assimilating MODIS reflectance data to adjust the rate of the carbon allocation to foliar biomass parameter.

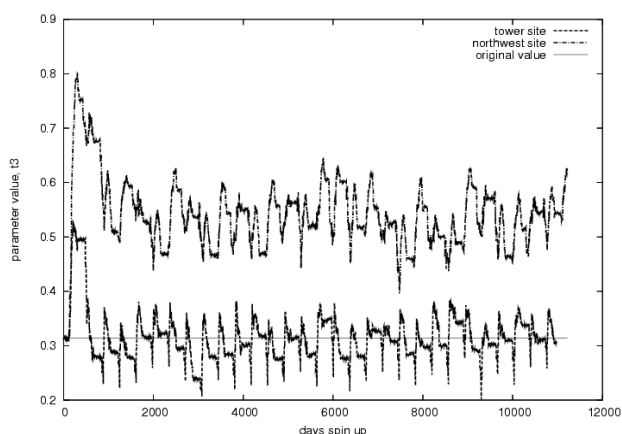


Figure 7. Parameter values derived using the EnKF and MODIS reflectance data. The “tower” site refers to the field site used elsewhere in this paper.

In these experiments a single year of meteorological data and MODIS observations were fed repeatedly into the model. When the reflectance data for the Metolius site was used the value of the parameter settles so that its mean is almost equal to that determined by Williams et al. (2005) using a quasi Newton minimisation method. When the reflectance data for a nearby site to the northwest is used the parameter takes on a higher mean value. This site has been more recently felled than the Metolius site and the younger trees are likely to be allocating more carbon to leaf material.

In these results the allocation parameter has been heavily damped by giving it a very small uncertainty and the same year of data was assimilated many times in repetition. Without damping, the parameter did not to converge toward a constant mean. This suggests that it is not possible to use such techniques at the same time as a normal assimilation run, but

instead they need to be performed off-line, much like a traditional calibration.

## 4. DISCUSSION AND CONCLUSION

This paper highlights some of the issues of using simple models in an EnKF scheme when there are long gaps between observation times. The DALEC model was designed to be used with a large number of observations, i.e. it gives reasonable, unbiased forecasts over some days or weeks, but not over several months. This is addressed here by building a modified version of an observation operator to permit assimilation of observations that had previously been disregarded (i.e. those contaminated by snow). Estimates of gross and net carbon fluxes were improved by the inclusion of these data.

Inclusion of winter observations induced a much higher variability in foliar biomass than expected. This is quite likely due to the assumption of a static 50% snow coverage for winter observations. A mechanism for determining this proportion is required to improve the observation operator for such cases. Ideally a snow hydrology model would be incorporated within the scheme and the EnKF used to adjust its parameters.

In addition, the problem of selecting an appropriate snow grain size has been ignored in these experiments. The variability of the spectral albedo as a function of grain size is small at the wavelengths being considered and so this is justified. It will certainly be a minor effect in comparison to the assumptions of a constant proportion of ground covered by snow. To bring in observations from other regions of the optical spectrum some mechanism will be required to take grain size into account.

With comparison to the field data the modelled foliar biomass is high. The GPP, in turn, is overestimated because of this. The foliar biomass field measurements are acquired using an LAI2000 probe and scaled to biomass by taking the product of the LAI and specific leaf area. The plot size for these measurements is 100×100m and so the discrepancy may be attributable to the difference in scale with the 500×500m MODIS pixels. The reference GPP data are generated from these LAI data also and so may be subject to similar scale problems. Work is currently underway to address this issue using high resolution ASTER data over the same region.

Initial results of parameter estimation exercises show the potential of EO data to provide partial model calibration for wide areas: the method appears to retrieve reasonable values for the test cases. The parameters seem unable to settle to a single value however. This may reflect inadequacies in the simple model parameterisation but will almost certainly be partly due to noise in the reflectance data. In the results shown heavy damping has been introduced to allow the parameter to settle. An implication of this is parameter estimation may need to be carried out prior to the main run of the model-EnKF scheme.

An issue that is not explored in this paper is the determination of the ancillary parameters for the observation operator. The numerical procedures currently being used are probably too slow to be used for large amounts of data. The ideal situation would be that the ecosystem model itself described as many of them as possible, but failing that an approach similar to the parameter estimation may prove useful.

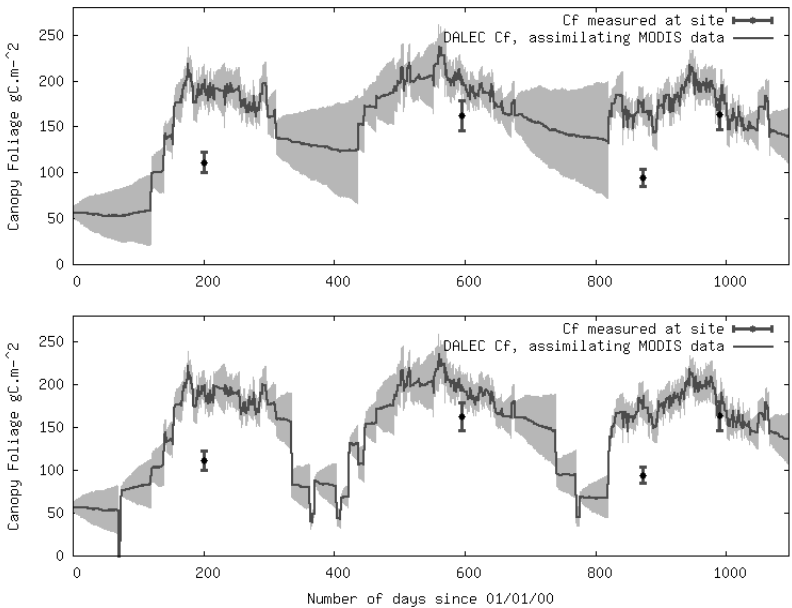


Figure 3. Foliar biomass predicted with DALEC assimilating observations of MODIS reflectance data. The top panel shows the case where snow contaminated pixels are exclude and the bottom panel show the results where snow contaminated data is used in the assimilation. The mean of the ensemble is shown with a black line and the spread about the line indicates one standard deviation of the ensemble. Field observations of canopy foliage (LAI scaled by specific leaf area) are plotted as single points with error bars.

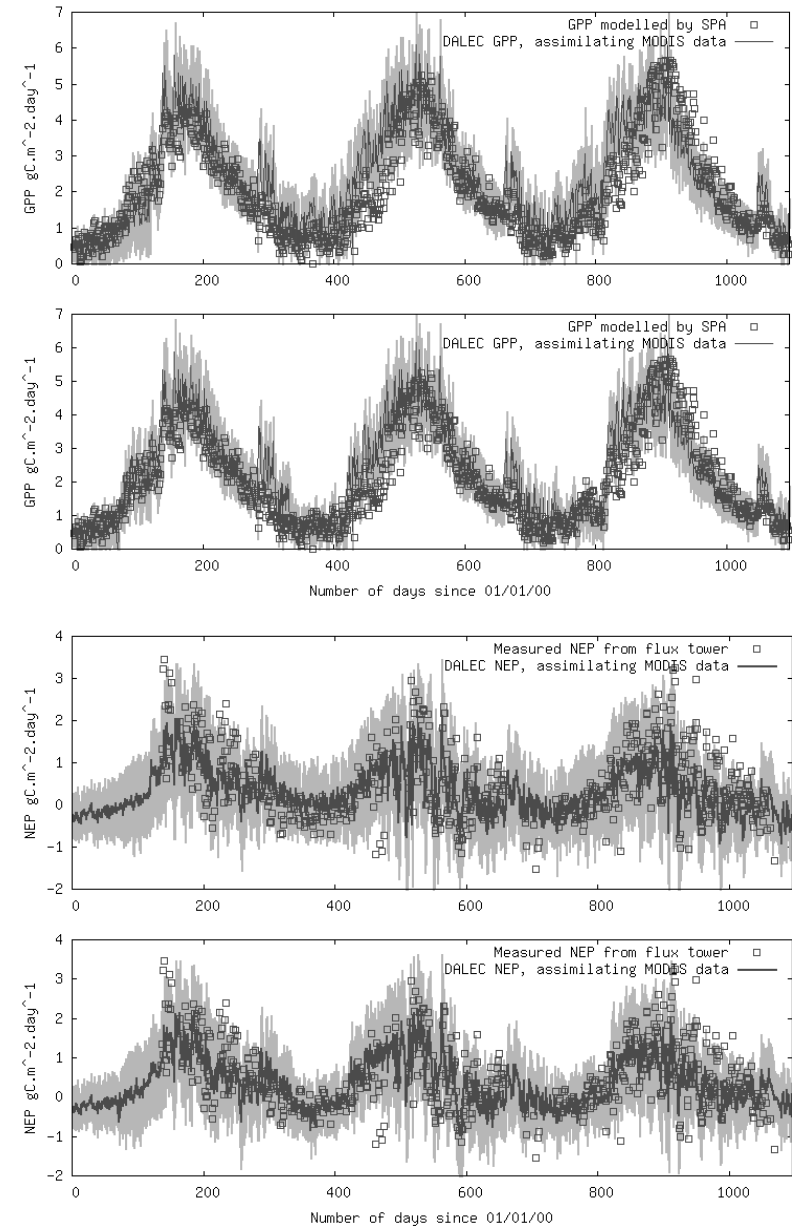


Figure 4. Gross primary productivity predicted with DALEC assimilating observations of MODIS reflectance data. The top panel shows the case where snow contaminated pixels are exclude and the bottom panel show the results where snow contaminated data is used in the assimilation. The mean of the ensemble is shown with a black line and the spread about the line indicates one standard deviation of the ensemble. Estimates of GPP modelled using the SPA model of Williams et al. (1996) are shown as small black squares.

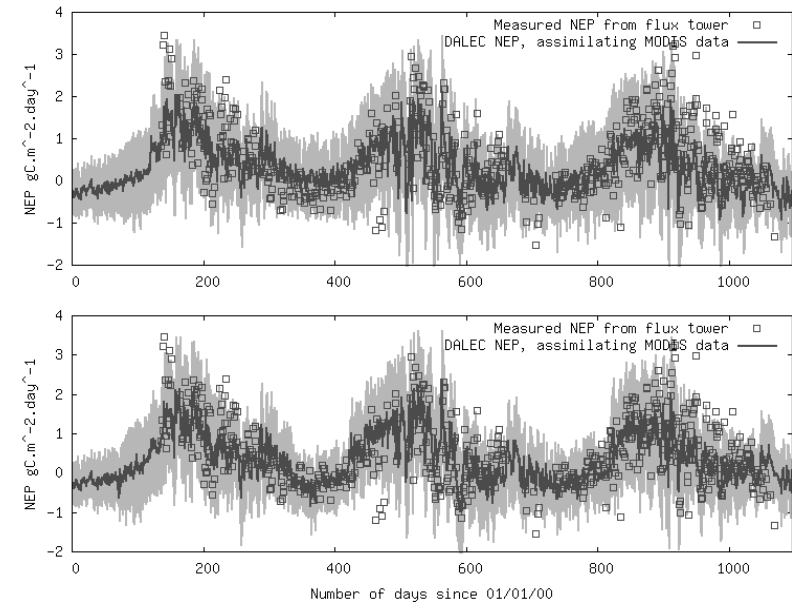


Figure 5. Net ecosystem productivity predicted with DALEC assimilating observations of MODIS reflectance data. The top panel shows the case where snow contaminated pixels are exclude and the bottom panel show the results where snow contaminated data is used in the assimilation. The mean of the ensemble is shown with a black line and the spread about the line indicates one standard deviation of the ensemble. Flux tower observations of NEP from the field site are shown as small black squares.



## REFERENCES

- Anthoni, P.M., Unsworth, M.H., Law, B.E., Irvine, J., Baldocchi, D. & Moore, D., 2002. Seasonal differences in carbon and water vapor exchange in young and old-growth ponderosa pine ecosystems. *Agricultural and Forest Meteorology*, 111, 203-222.
- Churkina, G., Schimel, D., Braswell, B.H., & Xiao, X., 2005. Spatial analysis of growing season length control over net ecosystem exchange. *Global Change Biology*, 11, 1777-1787
- Evensen, G., 1994. Sequential data assimilation with a nonlinear quasi-geostrophic model using Monte Carlo methods to forecast error statistics. *Journal of Geophysical Research*, 99(C5), 10143-10162.
- Evensen, G., 2003. The Ensemble Kalman Filter: Theoretical Formulation and Practical Implementation, *Ocean Dynamics*, 53, 343-367.
- Green, R.O., Dozier, J., Roberts, D. and Painter, T., 2002. Spectral snow-reflectance models for grain-size and liquid-water fraction in melting snow for the solar-reflected spectrum. *Annals of Glaciology*, 34, 71-73.
- IPCC, 2001, *Climate Change 2001: The Scientific Basis. Contribution of Working Group I to the Third Assessment Report of the Intergovernmental Panel on Climate Change* [Houghton, J.T., Ding, Y., Griggs, D.J., Noguer, M., van der Linden, P. J., Dai, X., Maskell, K., and Johnson, C. A. (eds.)], Cambridge University Press, Cambridge, United Kingdom and New York.
- Irvine, J. & Law, B.E. 2002. Contrasting soil respiration in young and old-growth ponderosa pine forests. *Global Change Biology*, 8, 1183-1194.
- Jacquemoud, S., and Baret, F., 1990. PROSPECT: a model of leaf optical properties spectra. *Remote Sensing of Environment*, 34, 75-91.
- Kou, L., Labrie, D. and Chylek, P., 1993. Refractive indices of water and ice in the 0.65- to 2.5- $\mu$ m spectral range. *Applied Optics*, 32 (19), 3531-3540.
- Law, B. E., Thornton, P., Irvine, J., Van Tuyl, S. & Anthoni, P., 2001a. Carbon storage and fluxes in ponderosa pine forests at different developmental stages. *Global Change Biology*, 7, 755-777.
- Law, B.E., Van Tuyl, S., Cescatti, A. & Baldocchi, D.D., 2001b. Estimation of leaf area index in open-canopy ponderosa pine forests at different successional stages and management regimes in Oregon. *Agricultural and Forest Meteorology*, 108, 1-14.
- Ni W.G., Li X.W., Woodcock C.E., Caetano M.R. and Strahler A.H., 1999. An analytical hybrid GORT model for bidirectional reflectance over discontinuous plant canopies. *IEEE Transactions on Geoscience and Remote Sensing*. 37(2), 987-999.
- Price, J., 1990. On the Information Content of Soil Reflectance Spectra, *Remote Sensing of Environment*. 33, 113-121.
- Quaife T., Lewis, P., De Kauwe, M., Williams, M., Law, B.E., Disney, M. and Bowyer, P., 2007, in press. Assimilating Canopy Reflectance data into an Ecosystem Model with an Ensemble Kalman Filter. *Remote Sensing of Environment*. In press.
- Rastetter, E.B., 2003. The collision of hypotheses: What can be learned from comparisons of ecosystem models? In Canham, C.D., Cole, J.J. & Lauenroth, W.K. (Eds.) *Models in Ecosystem Science*, (pp. 211-224). Princeton University Press: Princeton (NJ).
- Roy, D.P., Jin, Y., Lewis, P. & Justice, C.O., 2005. Prototyping a global algorithm for systematic fire-affected area mapping using MODIS time series data. *Remote Sensing of Environment*, 97, 137-162.
- Schimel, D.S. et al., 2001. Recent patterns and mechanisms of carbon exchange by terrestrial ecosystems. *Nature*, 414, 169-172.
- Stamnes, K., Tsay S-C., Wiscombe, W. and Jayaweera, K., 1988. Numerically stable algorithm for discrete-ordinate-method radiative transfer in multiple scattering and emitting layered media. *Applied Optics*. 27 (12), 2502-2509.
- Valentini, R. et al., 2000. Respiration as the main determinant of carbon balance in European forests, *Nature*, 404, 861-865.
- Williams, M., Rastetter, E.B., Fernandes, D.N., Goulden, M.L., Shaver, G.R., & Johnson, L.C., 1997. Predicting gross primary productivity in terrestrial ecosystems. *Ecological Applications*, 7, 882-894.
- Williams, M., Schwarz, P.A., Law, B.E., Irvine, J. & Kurpius, M., 2005. An improved analysis of forest carbon dynamics using data assimilation. *Global Change Biology*, 11, 89-105.
- Williams, M., Rastetter, E.B., Fernandes, D.N., Goulden, M.L., Wofsy, S.C., Shaver, G.R., Melillo, J.M., Munger, J.W., Fan, S.-M., & Nadelhoffer, K.J., 1996. Modelling the soil-plant-atmosphere continuum in a Quercus-Acer stand at Harvard Forest: the regulation of stomatal conductance by light, nitrogen and soil/plant hydraulic properties. *Plant, Cell and Environment*, 19, 911-927.
- Wiscombe, W., 1980. Improved Mie scattering algorithms. *Applied Optics*, 19 (9), 1505-1509.

## A LEAF OPTICAL PROPERTIES MODEL ACCOUNTING FOR DIFFERENCES BETWEEN THE TWO FACES

Kai MA<sup>a,\*</sup>, F. Baret<sup>a</sup>, P. Barroy<sup>b</sup>, L. Bousquet<sup>c</sup>

<sup>a</sup> INRA-CSE, UMR1114, Avignon, France

<sup>b</sup> Université d'Avignon et des Pays de Vaucluse, UMR1114, Avignon, France

<sup>c</sup> Université Paris 7 – IPGP, Paris, France

**Theme: Physical modeling in remote sensing**

**KEY WORDS:** remote sensing, vegetation, PROSPECT, radiative transfer, multilayer, QSPECT

### ABSTRACT:

Modeling radiative transfer in canopies allows efficient use of remote sensing observations to quantify vegetation state variables and functioning. Canopy radiative transfer models use requires accurate description of leaf optical properties. Although widely used, the PROSPECT leaf optical properties model is based on simplifying assumptions that limit its performances. One of these assumptions is that scattering and absorbing materials are evenly distributed in the leaf thickness, leading to the same optical properties for both faces. However, plants have developed particular adaptations resulting sometimes in strong differences in the properties of each faces, in relation to surface characteristics as well as leaf internal structure and distribution of chlorophyll and water. The objective of this paper is to develop a new model accounting for the difference between leaf upper and lower faces.

The QSPECT model is an improved version of PROSPECT where the leaf considered made of four layers corresponding to the upper and lower epidermis, the palisade and spongy mesophylls. This advanced model requires four additional parameters describing the distribution of main scattering and absorbing materials. Results acquired over few reflectance and transmittance measurements show that QSPECT is able to describe accurately the typical differences observed between upper and lower leaf faces. Of particular importance are the surface reflectivities as well as chlorophyll content distribution

### Introduction

Leaf optical properties are key input variables to understand and model radiative transfer in canopies. Radiative transfer models are very useful for exploiting remote sensing observations and transform the signal collected onboard satellite into surface characteristics such as leaf area index or chlorophyll content. Several leaf optical properties models have been proposed in the past as listed in a recent review (Jacquemoud et al., 2001). They allow to simulate leaf reflectance and transmittance from a limited set of state variables describing the content of absorbing materials such as chlorophyll, water or dry matter, and the scattering occurring at the interfaces between materials with difference in refraction index value. Most leaf optical properties models assume the leaf as an homogeneous layer with evenly distributed absorbing and scattering materials. As a consequence, reflectance and transmittance of both faces are the same. However, leaves have to ensure a number of functions under very wide environment conditions. They have therefore adapted their structure to better answer these challenges.

A typical dicotyledon leaf section shows the palisade and spongy mesophyll tissue layers, bounded by two layers of epidermal cells as illustrated in Figure 1. The epidermis is made up of a single layer of colorless cells, with few if any chloroplasts. Its main role is to protect the inner layers from

the outside environment, contributes to maintain leaf port, while controlling exchanges of gas and radiation with the cuticle (waxy, crystallized), its roughness, and the possible presence of hairs and their characteristics (length, density, shapes). Palisade cells are elongated, generally densely packed, and arranged in one to several layers. They contain the largest proportion of chloroplasts where most of photosynthesis is taking place. The spongy mesophyll is made up of highly lobed irregularly shaped cells of variable size, separated by large intercellular air-filled spaces that facilitate the circulation of gases inside the leaf. As a consequence, the small amount of absorbing material in the spongy mesophyll and the high number of discontinuities in the refraction index values, a large fraction of light incoming from the palisade mesophyll is scattered back, increasing light absorption efficiency by chloroplasts (Raven et al., 1996).

Because of the particular organization of leaves, important differences may be observed between the optical properties of upper and lower faces particularly in spectral domains where stronger absorption occurs: in the visible domain characterized by chlorophyll pigment absorption, reflectance of upper faces is generally lower than that of lower faces where more scattering occurs. Transmittance and reflectance in the near infrared domain are generally less affected. Plants will exploit these differences in leaf optical properties between faces to better suit environmental conditions. This is reported for olive trees that have leaves with more reflective lower faces. In case of

---

\* Corresponding author. This is useful to know for communication with the appropriate person in cases with more than one author.

severe water stress, olive trees orientate their leaves in a more erectophile way, exposing the lower faces towards the incoming light which reduces the amount of radiation absorbed by the canopy, hence transpiration and photosynthesis. Apart from the effect of differences between faces on canopy functioning, impact is also expected on canopy reflectance. This may induce additional uncertainties in remote sensing retrieval of some key biophysical variables such as leaf area index (LAI) or chlorophyll content.

This study will attempt to document differences between leaf optical properties faces: as a matter of fact, although differences between optical properties of the two faces are known qualitatively, very little studies documented their magnitude. More precisely, the objective of this study is to develop a leaf optical properties model that explicitly accounts for inhomogeneity in the leaf and describes the corresponding differences in leaf reflectance of both faces. The modeling will be based on the PROSPECT model proposed by Jacquemoud and Baret (1990). This model offers the advantage to be relatively simple with a limited number of variables allowing to use it in a more operational way. PROSPECT was already validated several times with relatively good performances although not describing the effects due to inhomogeneous leaf structure (Jacquemoud and Baret, 1990).

In this study, measurements of leaf optical properties are acquired to quantify the possible differences between upper and lower faces. Then, the PROSPECT model is adapted to account for the layer structure description according to Figure 1. It will be named hereafter "QSPECT". A sensitivity analysis is conducted, with emphasis on the variables that drive the differences between both faces. Finally, some validation elements are presented and discussed.

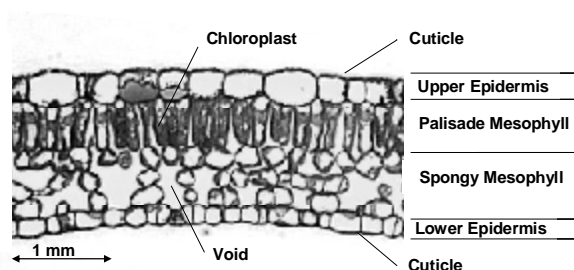


Figure 1. Structure of a typical dicotyledon leaf. Chloroplasts are drawn in one cell only of both palisade and spongy tissues.

## MATERIALS AND METHODS

Measurements were made during spring 2006. Six species of leaves were selected, describing large variability of properties between upper and lower faces: Tilia, Medlar (*Mespilus*), banana (*Musa*), Sage (*Salvia officinalis*), Ivy (*Hedera*) and Maple (*Aceraceae*).

Four leaves for each species were selected with similar visual aspects. Reflectance and transmittance of leaves were measured at three distinct locations over each of the 4 leaves, trying to avoid the larger veins when observed.

Reflectance and transmittance measurements were achieved using an ASD Fieldspec spectrophotometer (Rollin E. M. and al., 1996), with a 1 nm sampling interval from 400 to 2400 nm. Its spectral resolution varies from 1 nm in the shorter wavelengths, up to about 2 nm for the longer ones. A Li-Cor 1800-12 (Verney C. A., 2002) integrating sphere was used to get directional/hemispherical reflectance and transmittance values. The incoming light arrived almost normally to the leaf sample. The original Li-Cor lamp system was replaced by a lamp powered by a large battery ensuring steady input electric characteristics during a time period used for single measurements (few minutes) and bracketed by measurements made over reference targets. The infrared filter placed on front of the original light was removed as well. The bare fiber optic (25° field of view) was looking the integrative sphere wall. To reduce possible stray-light, the experiment was conducted in a darkroom. Reflectance (spectralon) and transmittance (Teflon sheet) target references with precisely known directional hemispherical reflectance,  $R_{ref}$  (transmittance,  $T_{ref}$ ) values were used to get absolute directional hemispherical reflectance or transmittance values of the sample.

The measurement protocol consisted in three consecutive measurement steps for each individual leaf sample:

1. Reflectance  $S_{ref}^{start}$  (transmittance,  $S_{tref}^{start}$ ) signal of the reference were first acquired.
2. Then, reflectance,  $S_{rleaf}$  (transmittance,  $S_{tleaf}$ ) of the sample were measured at three different locations on the leaf sample.
3. Finally, references were again acquired ( $S_{ref}^{end}$ ,  $S_{tref}^{end}$ ) to account for possible variation during the sample measurement.

Absolute values of reflectance ( $R^i$ ) and Transmittance ( $T^i$ ) of leaf samples  $i$  were computed as:

$$R^i = R_{ref} \frac{2 \cdot S_{rmes}^i}{(S_{rmes}^{start} + S_{rmes}^{end})}$$

$$T^i = T_{ref} \frac{2 \cdot S_{tmes}^i}{(S_{tmes}^{start} + S_{tmes}^{end})} \quad (1)$$

The sequence for reflectance and transmittance of both faces for the four leaves, took about 30 minutes in total. Absolute values of reflectance (and transmittance) were finally averaged over the four leaves and the three locations.

Uncertainties were characterized by RMSE values over the 4 replicates times 3 locations. Reflectance and transmittance on both faces have about the same uncertainties which do not vary much with wavelength except above 2000 nm where instrumental noise is dominant. For wavelengths beyond 2000nm, the mode of RMSE values is close to 0.015 (Figure 3). It is mainly explained by differences between leaves and locations, the instrumental noise being marginal (lower than 0.001) in this wavelength domain.

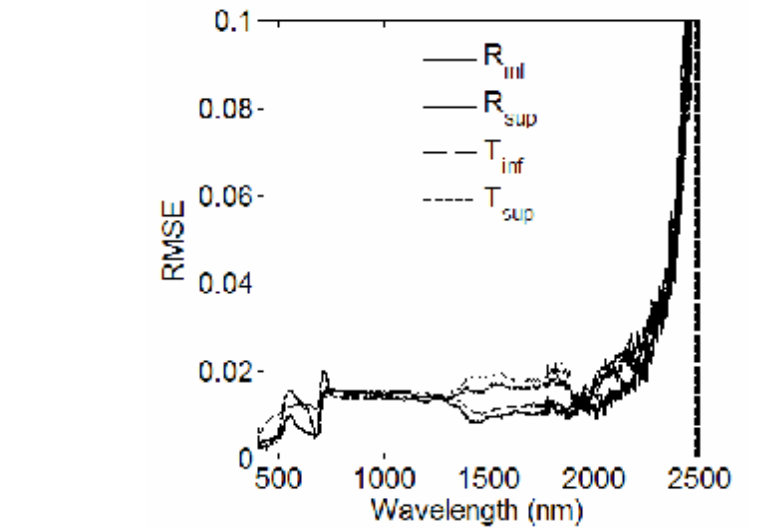


Figure 2. Inspection of the distribution of the uncertainties computed between the 12 replicates (3 locations time 4 leaves)

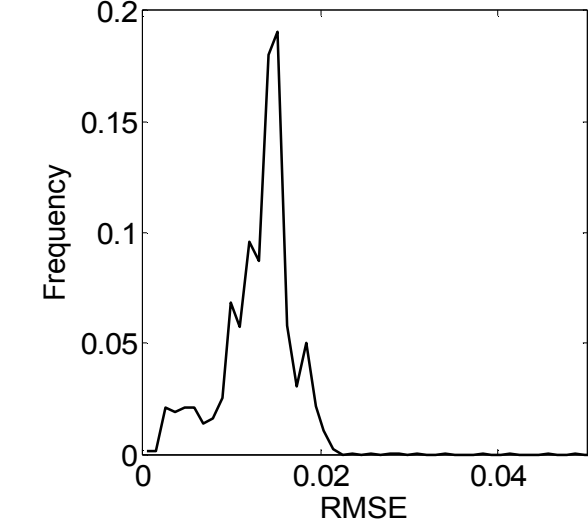


Figure 3. Histogram of the RMSE values computed for each wavelength between the 12 replicates of measurements for reflectance or transmittance of the two faces.

EXPERIMENTAL EVIDENCE OF DIFFERENCES BETWEEN FACES

Reflectance and transmittance spectra show very classical features, with low values in the visible because of chlorophyll pigment absorption, large values in the near infrared due of intense volume scattering and very low absorption, and intermediate situation in the short wave infrared dominated by water absorption features (Figure 4). Note that the absorptance (1-Reflectance-Transmittance) may be very small in the near infrared as observed for Tilia (Figure 4 right,).

Measurements show that tilia and medlar leaves exhibit large differences between both faces, while Ivy, Musa and Sage

show smaller differences and the young Maple leaves show almost similar properties on both faces.

Differences between upper and lower faces show regularities with however, variation in magnitude among leaf types and spectral domains (Figure 5). In the visible domain, upper faces reflect significantly less while transmitting about the same, therefore absorbing more light than the lower faces. Conversely, in the near infrared domain, upper faces reflect more, transmit less and absorb slightly more than lower faces. In the short wave infrared domain, upper leaves transmit less, absorb more, and generally reflect less than lower faces although two leaves are reflecting slightly more.

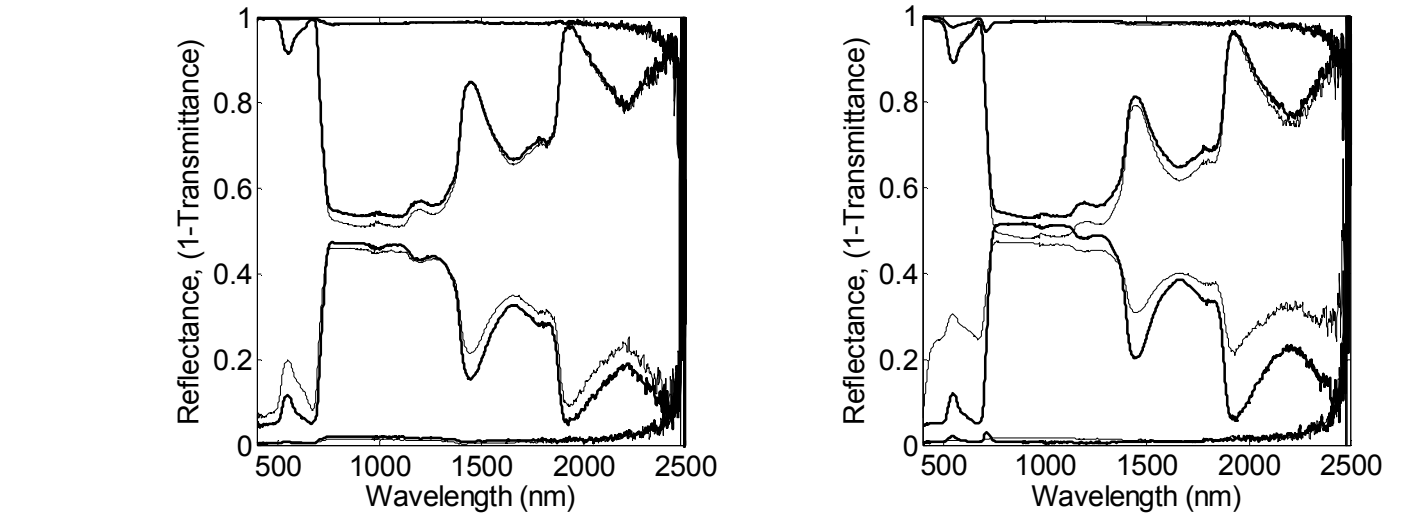


Figure 4. Sample leaf reflectance and transmittance (displayed here as 1-transmittance) measured over Ivy (left) and Tilia (right) leaves. Upper (lower) faces are represented by a thick (thin) lines. The corresponding uncertainties (RMSE values) are shown for reflectance (at the bottom) and transmittance (1-RMSE) at the top for upper (bold) and lower (thin) faces

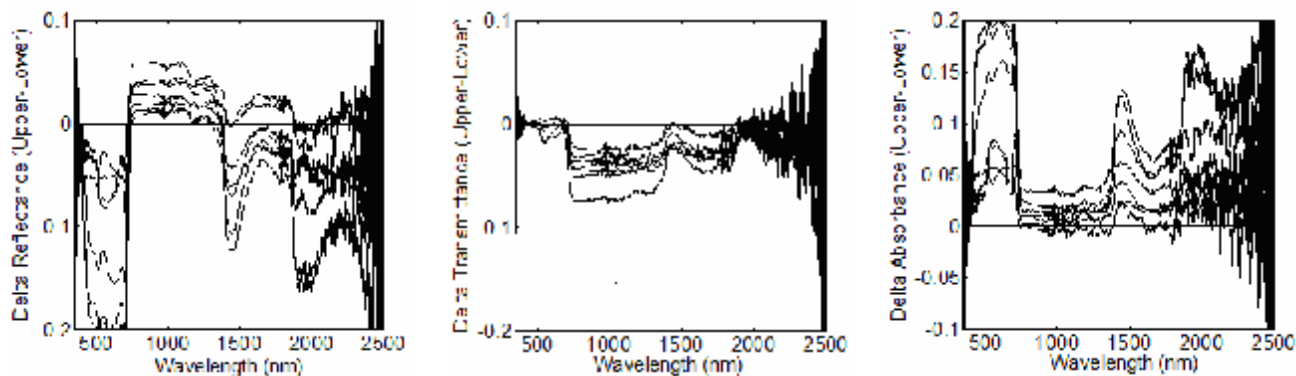


Figure 5. Differences (Delta) in Reflectance (left), Transmittance (centre), and Absorbance (right) between the Upper and Lower faces of the 7 leaves considered.

These observations could be explained qualitatively by considering the leaf as made of two layers: an upper layer made of the upper epidermis on top of the palisade mesophyll, and a lower layer made of the spongy mesophyll on top of the lower epidermis (Figure 6). Reflectance and transmittance of this system of two layers may be described simply by considering the multiple scattering between the 2 layers. For elementary fluxes, small letters are used ( $r$ ,  $t$ ) while capital letters are reserved for the net fluxes created by the 2 layers ( $R_{12}$ ,  $T_{12}$ ). Subscripts correspond to layer number (1, 2). The superscript arrows correspond to the direction of the incident flux considered ( $\uparrow$ ,  $\downarrow$ ). Reflectance of the upper (lower) face generated by a flux impinging on it,  $R_{12}^{\uparrow}$  ( $R_{12}^{\downarrow}$ ), writes:

$$\begin{aligned} R_{12}^{\downarrow} &= r_1^{\downarrow} + \frac{r_2^{\downarrow} t_1^{\downarrow} t_1^{\uparrow}}{1 - r_2^{\downarrow} r_1^{\uparrow}} \\ R_{12}^{\uparrow} &= r_2^{\uparrow} + \frac{r_1^{\uparrow} t_2^{\uparrow} t_2^{\downarrow}}{1 - r_2^{\uparrow} r_1^{\downarrow}} \end{aligned} \quad (2)$$

Similarly, transmittance of the upper (lower) face generated by a flux impinging on the face opposite to it,  $T^{\uparrow}$  ( $T^{\downarrow}$ ), writes:

$$\begin{aligned} T_{12}^{\uparrow} &= \frac{t_2^{\uparrow} t_1^{\uparrow}}{1 - r_2^{\downarrow} r_1^{\uparrow}} \\ T_{12}^{\downarrow} &= \frac{t_1^{\downarrow} t_2^{\downarrow}}{1 - r_2^{\uparrow} r_1^{\downarrow}} \end{aligned} \quad (3)$$

The first layer contains most of the chlorophyll with very strong radiation absorption. Transmittance of this layer are very small ( $t_1^{\downarrow} \approx t_1^{\uparrow} \approx 0$ ) and leaf reflectance can be approximated as the reflectance value of the first layer ( $R_{12}^{\downarrow} \approx r_1^{\downarrow}$ ). In addition, the stronger chlorophyll content in the first layer corresponds to a lower layer reflectance than that of layer 2 ( $r_1^{\downarrow} \ll r_2^{\downarrow}$ ). This proves that the upper face leaf reflectance is expected to be smaller than that of the lower face ( $R_{12}^{\downarrow} < R_{12}^{\uparrow}$ ).

In the near infrared, the smaller transmittance and the larger reflectance values of the upper as compared to those of the lower face may be explained by the is more surprising and was not expected if the reciprocity of light traveling is verified. However, the observed differences in transmittance between the two faces may probably be explained by the directionality of the incident radiation (directional flux normal to the leaf) and the hemispherical nature of the transmitted flux measured. This will be investigated more deeply later.

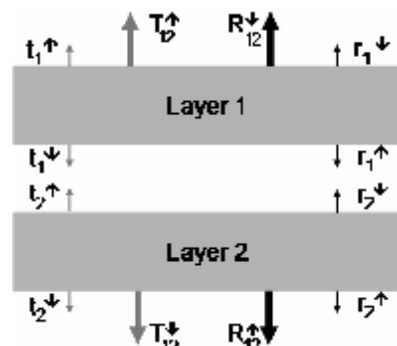


Figure 6. Schema describing the fluxes considered for a 2 layer system.

Resulting from these observations, it appears that leaf absorbance is higher over the whole spectral domain when incident light penetrates from leaf upper face as compared to leaf lower face.

## MODELING DIFFERENCES BETWEEN FACES

PROSPECT model (Jacquemoud and Baret, 1990) describes the scattering by the refractive index ( $n$ ) of bulk leaf material and by a parameter characterizing leaf mesophyll structure ( $N$ ). Absorption was modeled using a uniform distribution of absorbing materials such as chlorophyll, water and dry matter. Total absorption is the sum of the contribution of each absorbing material, itself computed as the product between the content in expressed in mass per unit leaf area ( $Cab$ ,  $Cw$  and  $Cm$  respectively for chlorophyll, water and dry matter) and the corresponding specific absorption coefficients (respectively



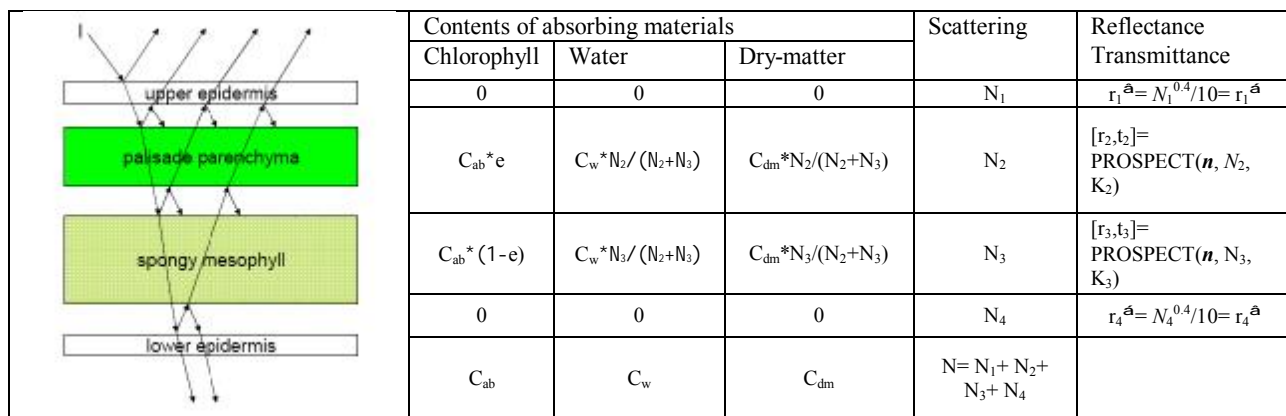


Figure 7. Scheme describing how the radiative transfer is computed within the four layers used in QSPECT model.

$K_{ab}$ ,  $K_w$  and  $K_m$ ). The interaction with leaf surface is very simply described by computing the transmissivity and reflectivity of the first interface characterized by a refraction index  $n$  and an impinging radiation coming from a solid angle  $\alpha$ .

The main adaptations of PROSPECT proposed within QSPECT consider the leaf as organized into four layers: two epidermis, palisade parenchyma and spongy mesophyll. Reflectance and transmittance values of each of the four layers are calculated using the PROSPECT model according to the scheme described in Figure 7. In the following, indices (1), (2), (3) and (4) refer to each layer according to Figure 7.

Epidermis layers are very thin with a small structure index  $N < 0.01$  and assumed having no absorption. Therefore  $r_1^a = r_1^a$  and  $t_1^a = t_1^a = 1 - r_1^a$ . Similarly,  $r_4^a = r_4^a$  and  $t_4^a = t_4^a = 1 - r_4^a$ . Since the PROSPECT model isn't applicable for such small values of  $N$ , an approximation was proposed offering a solution of continuity between reflectances computed between  $N=0$  and  $N=0.01$ :  $r = aN^b$  where  $a=1/10$ ,  $b=0.4$ , for all wavelengths since the refractive index does not vary much with wavelength, hence layer reflectance and transmittance.

Palisade and spongy mesophyll are characterized respectively with  $N_2$  and  $N_3$  structure parameters. However, parameter  $p = N_2/(N_2 + N_3)$  was preferred to better denote the gradient in scattering properties. Total chlorophyll content,  $C_{ab}$ , is distributed in the two mesophyll layers using parameter  $e$  computed as the ratio between chlorophyll concentration of the palisade mesophyll and the total chlorophyll content. Water and dry matter are assumed distributed proportionally to the  $N$  parameter in the palisade and spongy mesophyll layers.

The radiative transfer between each of these layers may be described by the following set of equations, where reflectances and transmittances of upper and lower faces of each layer  $i=1, 2, 3, 4$  are represented by  $r_i^a$ ,  $t_i^a$ ,  $r_i^b$  and  $t_i^b$ . Reflectance and transmittance made of layers 1 and 2 are noted  $R_{12}^a$ ,  $T_{12}^a$ ,  $R_{12}^b$  and  $T_{12}^b$  and computed from equations (2) and (3). For 3 layers:  $R_{123}^a$ ,  $T_{123}^a$ ,  $R_{123}^b$  and  $T_{123}^b$  are computed according to:

$$R_{123}^b = R_{12}^b + \frac{T_{12}^b r_3^b T_{12}^a}{1 - r_3^b R_{12}^a}; \quad T_{123}^b = \frac{T_{12}^b t_3^b}{1 - r_3^b R_{12}^a} \quad (4)$$

$$R_{123}^a = r_3^a + \frac{t_3^a R_{12}^a t_3^b}{1 - r_3^a R_{12}^b}; \quad T_{123}^a = \frac{t_3^a T_{12}^a}{1 - r_3^a R_{12}^b} \quad (5)$$

Finally, leaf total reflectance and transmittance noted  $R^a$ ,  $T^a$ ,  $R^b$  and  $T^b$  of upper face and lower faces for four layer system are given by:

$$R^b = R_{123}^b + \frac{T_{123}^b r_4^b T_{123}^a}{1 - r_4^b R_{123}^a}; \quad T^b = \frac{T_{123}^b t_4^b}{1 - r_4^b R_{123}^a} \quad (6)$$

$$R^a = r_4^a + \frac{t_4^a R_{123}^a t_4^b}{1 - r_4^a R_{123}^b}; \quad T^a = \frac{t_4^a T_{123}^a}{1 - r_4^a R_{123}^b} \quad (7)$$

Consistency of the computation of reflectance and transmittance for the two faces was checked in the case of homogeneous chlorophyll distribution and reflectivity of the first interface computed according to the original PROSPECT model. As expected, QSPECT simulations are equal to those of PROSPECT in this very particular case. When using typical values for the parameters, QSPECT model simulations show differences of leaf reflectances between the two faces in the visible domain. In the near infrared and short wave infrared domains, no differences are observed both in reflectance and transmittance values as expected according to QSPECT model assumptions (Figure 8).

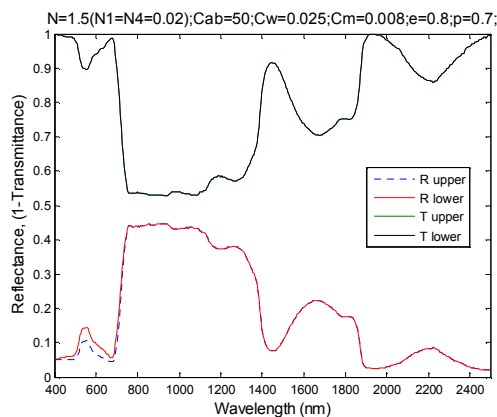


Figure 8. Reflectance and transmittance spectra of upper and lower face calculated with model QSPECT

leaf	N	$C_{ab}+C_b$ ( $\mu\text{g}/\text{cm}^2$ )	$C_m$ ( $\text{g}/\text{cm}^2$ )	$e$	$p$	$N_1$	$N_4$
Ivy	1.5	49 (51)*	0.0047	0.88	0.70	0.001	0.005
Maple(young)	1.01	18 (18)	0.0006	0.64	0.52	0.001	0.001
Tilia	1.56	44 (48)	0.0008	0.96	0.58	0.001	0.004
Medlar	1.39	34 (37)	0.0006	0.95	0.66	0.001	0.006
Musa	1.10	49 (50)	0.0007	0.96	0.79	0.001	0.003
Sage	1.19	42 (40)	0.0013	0.97	0.85	0.001	0.001

Table 1. Coefficient of Determination Obtained for the Estimation of chlorophyll, dry matter, parameter  $e$ ,  $p$  and  $N_1$ ,  $N_4$  calculated with QSPECT.

Note:\* the numbers within brackets are estimated by PROSPECT Model.

As compared to the initial PROSPECT model, description of differences between faces is achieved at the expense of 4 additional parameters that do not vary with wavelength:  $N_1$ ,  $N_4$ ,  $e$  and  $p$ . In the following section we will investigate the effect of these parameters on leaf optical properties.

SENSITIVITY ANALYSIS

Simulations will be restricted to the visible up to the beginning of near infrared domain since no differences are expected in the near and shortwave infrared domains accordingly to QSPECT model assumptions. The sensitivity analysis will be achieved over a typical leaf with  $C_{ab}=50$ ,  $C_w=0.025$ ,  $C_{dm}=0.008$ ,  $N=1.5$ ,  $N_1=0.01$ ,  $N_4=0.02$ ,  $e=0.8$ ,  $p=0.7$ . Reflectance of the upper leaf will be shown.

Figure 9 illustrates several new parameters affect the reflectance. The parameter  $e$  has greater influence in VIS, others parameters have also enough influence toward the reflectance.

VALIDATION

Validation of QSPECT was carried out over the data sets measured previously and including six types of leaves. It consisted in estimating the model parameters symbolized by the vector  $X$  by minimizing the following merit function:

$$F(X) = \sum_2 \sum_I \left( \frac{(r_{mod}(I) - r_{mes}(I))^2}{S_r} + \frac{(t_{mod}(I) - t_{mes}(I))^2}{S_t} \right)$$

Where 2 represent the upper face and lower face,  $I$  is the wavelength,  $r_{mes}$  and  $r_{mod}$  are respectively the measured and modeled reflectances,  $t_{mes}$  and  $t_{mod}$  are respectively the measured and modeled transmittances,  $S_r$  and  $S_t$  are the variances of the measured reflectances et transmittances. Inversions were performed using a routine fminsearch.M in Matlab. In Table 1 we show the coefficients of determination for each biochemical.

We notice that the parameter  $e$  and  $p$  are greater than 0.5, this result verifies that the chlorophyll is more concentrated in the upper part or in the palisade parenchyma, and the palisade parenchyma has more complex structure and more cellular component.

Figures 11 and 12 do not show any significant difference between measured and calculated ones. It exhibits root mean squares lower than 0.02, indicating good spectrum reconstruction.

These results indicate that QSPECT model is capable of being applied to different type leaves. It can describe the chlorophyll gradient and the distribution of cellular component inside leaf. Relative to model PROSPECT (Figure 13), it can accurately simulate the spectral of two faces.

CONCLUSION

This paper concerns leaf optical properties and their modeling, and provides a new model which are used to accurately simulate the different spectral of upper and lower leaf faces and estimate biochemical contents. There are still many improved aspect and further work should ulteriorly consider the effect of leaf surface which has an important role in optical properties of plant canopy.

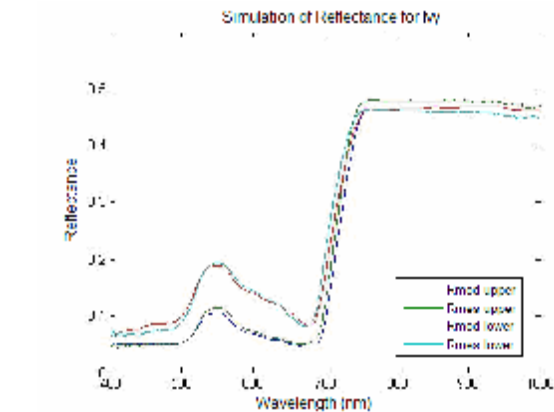


Figure 10. Comparison of the spectral reflectance and transmittance modeled and measured for Ivy By Model QSPECT.

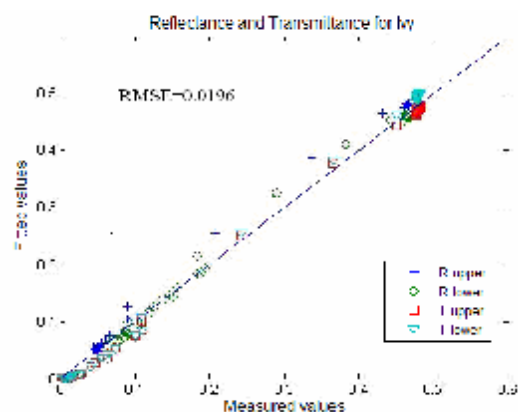


Figure 12. Comparison between simulated and measured reflectance and transmittance for Ivy.

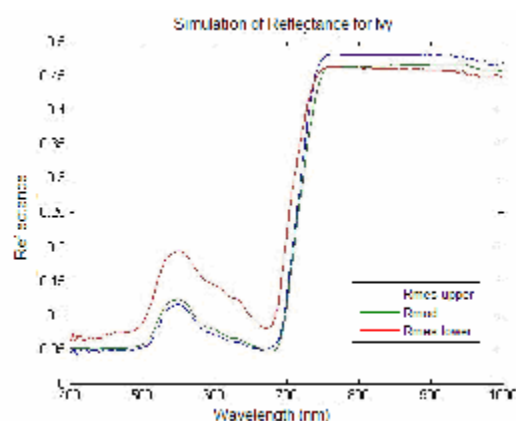


Figure 13. Comparison of the spectral reflectance and transmittance modeled and measured for Ivy by Model PROSPECT.

## REFERENCES

- Jacquemoud S, 1992. Utilisation de la haute résolution spectrale pour l'étude des couverts végétaux: développement d'un modèle de reflectance spectrale. *Université Paris 7*, Thèse de Doctorat.
- Jacquemoud S & F Baret, 1990. PROSPECT : a model of leaf optical properties spectra. *Remote Sensing of Environment*, 34, pp. 75-91.
- Jacquemoud S., Ustin S.L., 2001. Leaf optical properties: a state of the art. *8th Int. Symp Physical Measurements & Signatures in Remote Sensing, France: Aussois*, pp. 223-232.
- Nilson,T., and Kuusk, A., 1989. A reflectance model for the homogeneous plant canopy and its inversion. *Remote Sensing of Environment*, 27, pp. 157-167.
- Raven, Peter H. Evert, Ray F. And Eichhorn Susan E., 1996. *Biology of plants (fifth ed.)*. worth Publishers, New York.
- Rolilin E. M., Emery D. R., and Kerr C. H., 1996. Analytical spectral Devices(ASD) Field FR spectroradiometer User Handbook version 1.0.
- Verney C. A., 2002. Etalonnage de la sphère d'intégration externe LI-1800-12 en transmittance. *Université de Paris 7 Denis DIDEROT*, IUP Génie de l'Environnement
- Veyrat S., 1999. Modélisation des propriétés optiques des feuilles. *Université de Clermont Ferrand/INRA*, Mémoire de DEA, pp. 35-37
- William A.Allen, 1973, Transmission of isotropic light across a dielectric surface in two and three dimensions. *J. Opt. Soc. Am.* 63(6), pp. 664-666
- Yamada N & S Fujimura, 1991. Nondestructive measurement of chlorophyll pigment content in plant leaves from three-color reflectance and transmittance. *Applied Optics*, 30, pp. 3964-3973.

# MODELLING CANOPY REFLECTANCE WITH SPECTRAL INVARIANTS

P. Lewis<sup>a,\*</sup>, M. Disney<sup>a</sup>, Y. Knyazikhin<sup>b</sup>, T. Quaife<sup>a</sup> and M. Schull<sup>b</sup>

<sup>a</sup> Department of Geography, University College London, Gower Street, London, WC1E 6BT, U.K. and NERC Centre for Terrestrial Carbon Dynamics (CTCD) - plewis@geog.ucl.ac.uk

<sup>b</sup> Department of Geography, Boston University, Boston, Massachusetts, U.S.A.

Commission VI, WG VI/4

**KEY WORDS:** Spectral invariant; 3D canopy structure; Monte Carlo ray tracing; recollision probability.

## ABSTRACT:

The concept of using spectral invariants to describe the scattering and absorption processes in a vegetation canopy has been developed for application to remote sensing studies in recent years. It has been shown that an average ‘recollision probability’ can describe the main impacts of structure on directional-hemispherical scattering and transmission, and there has been some indication that this might provide a useful route to modelling canopy reflectance. In this paper, we examine how an existing formulation of canopy reflectance and transmittance describes radiometric behaviour as a function of scattering order. We note that the assumptions underlying the model break down for moderate to high leaf area index (LAI), and show that this leads to a poor description of scattering as a function of interaction order. This leads to the model parameters losing any direct biophysical meaning, becoming ‘effective’ terms. It is shown that it is useful to maintain the direct meaning of the parameters, as this potentially simplifies the modelling of bi-directional fluxes and the dependence of parameters on zenith angle and leaf scattering asymmetry. We propose a new formulation that maintains the small number of parameters in the original model but better describes the scattering behaviour.

## 1. INTRODUCTION

### 1.1 Canopy spectral invariants

The total scattering from a vegetation canopy at optical wavelengths,  $S_\lambda$ , can be expressed as a function of wavelength  $\lambda$  by:

$$S_\lambda = t_0 + (1 - t_0) \sum_{i=1}^{1=\infty} s_i \omega_\lambda^i \quad (1)$$

where  $t_0$  is the probability of radiation being transmitted through the canopy without interacting with canopy elements (the zero-order transmittance),  $\omega$  is the canopy element single scattering albedo and the terms  $s_i$  are spectrally-invariant terms dependent on the incident radiation distribution, the arrangement and angular distribution of canopy elements, and the ratio  $\xi_\lambda$  of leaf reflectance  $R_{leaf,\lambda}$  to total leaf scattering ( $\omega_\lambda = R_{leaf,\lambda} + T_{leaf,\lambda}$ ):

$$\xi_\lambda = R_{leaf,\lambda} / (R_{leaf,\lambda} + T_{leaf,\lambda}) \quad (2)$$

The canopy spectral transmittance  $T_{bs,\lambda}$  and reflectance  $R_{bs,\lambda}$  for a canopy with a totally absorbing lower boundary (‘black soil’) can be expressed in similar forms to (1):

$$T_{bs,\lambda} = t_0 + (1 - t_0) \sum_{i=1}^{1=\infty} t_{bs,i} \omega_\lambda^i \quad (3a)$$

$$R_{bs,\lambda} = (1 - t_0) \sum_{i=1}^{1=\infty} r_{bs,i} \omega_\lambda^i \quad (3b)$$

where  $t_{bs,i}$ ,  $r_{bs,i}$  are spectrally-invariant terms expressing the proportion of radiation scattered through the lower and upper canopy boundaries relative to the radiation initially intercepted by canopy foliage. Absorptance is found from energy conservation.

This is a convenient statement of canopy reflectance and transmittance because it separates the ‘geometric’ aspects of scattering (the spectral invariants) from those dependent on wavelength (leaf single scattering albedo). We can express

$T_{total,\lambda}$ ,  $R_{total,\lambda}$ , the transmittance and reflectance of a canopy with an underlying Lambertian lower boundary of reflectance  $R_{s,\lambda}$  following Knyazikhin and Marshak (2000) and Wang et al. (2003), but in this paper, we only consider the black soil ‘component’ of the canopy.

Various authors, summarised by Huang et al. (2007), have built models of canopy radiation interactions through assumptions regarding photon recollision and escape probabilities in a canopy. The recollision probability at scattering order  $i$ ,  $p_i$  is the probability that photons that have interacted with canopy elements at scattering order  $i-1$  will recollide with canopy elements. The escape probability can be partitioned into the upward escape probability,  $\rho_i$  and the downward probability,  $\tau_i$ . Then:

$$p_i + \rho_i + \tau_i = 1 \quad (4)$$

from consideration of energy conservation. The spectrally-invariant terms in equation (3) can be expressed using recollision and escape probabilities:

$$r_i = \rho_i \prod_{j=1}^{i-1} p_j \quad (5a)$$

$$t_i = \tau_i \prod_{j=1}^{i-1} p_j \quad (5b)$$

The total scattering spectral invariants  $s_i$  in equation (1) are:

$$s_i = t_i + r_i \quad (5c)$$

Under conditions of zero absorptance ( $\omega = 1$ ), the radiance on the leaves at interaction order  $i$  must be entirely scattered out of the canopy over all orders greater than  $i$ . Thus:

$$\sum_{j=i+1}^{j=\infty} s_j = s_i \quad (5d)$$

where  $s_0$  is defined as unity.

\* Corresponding author.

## 1.2 Monte Carlo simulations

We performed simulations of canopy directional-hemispherical reflectance and transmittance using a reverse Monte Carlo Ray Tracer (MCRT) drat (Lewis, 1999, modified as described in Saich et al., 2001; Disney et al., 2006), for a range of zenith angles. We did further simulations of bidirectional reflectance and transmittance, although they are not analysed in this paper. The MCRT tool drat can output results as a function of scattering order, from which we can directly simulate  $r_i$  and  $t_i$ . This allows the reflectance and transmittance to be calculated for arbitrary leaf albedo. Ray interactions are followed up to scattering order 100 in the simulations and an analytical approximation applied for further interactions (Appendix 1).

We simulated a range of canopy structures. Here we present results for homogeneous (LAI 1-20) and spherically-clumped canopies (LAI 5). The homogeneous canopies are composed of explicit representations of non-overlapping disks with a uniform angular distribution and radius 0.02 units and canopy vertical extent  $5 \times \text{LAI}$ .  $\zeta$  varies between 0.2 and 0.6 for these simulations. The spherically-clumped canopy is that of RAMI scene HET01<sup>1</sup>. It has disc leaves with a radius of 0.1 units contained in spheres of 15 unit radius distributed over a 100 unit  $\times$  100 unit area (infinitely repeated in horizontal extent) (see<sup>1</sup> for further details)

## 1.3 Some initial observations on recollision and escape probabilities

Figure 1 shows recollision probabilities for homogeneous canopies as a function of scattering order at varying values of LAI with equal leaf reflectance and transmittance, for directional-hemispherical fluxes at a zenith angle of  $0^\circ$ .

The recollision probability tends to converge to a final value after relatively few iterations, at least for low to moderate LAI. Lewis and Disney (2007) note that the number of iterations until convergence is approximately equal to the LAI. This final value,  $p_\infty$ , can be considered the recollision probability of the radiation in the canopy when it is 'well mixed' (i.e. the radiation distribution in the canopy has settled down to some final function and does not change much with each iteration). Alternatively, Panferov et al. (2001) note this as the principal eigenvalue of the radiative transfer operator.

Figure 2 shows the escape probabilities corresponding to the recollision probabilities in Figure 1. These again converge to some 'well-mixed' values,  $\rho_\infty$  and  $\tau_\infty$  in the upward and downward directions respectively, but convergence does not occur until around  $2 \times \text{LAI}$  interactions. Further, there is an approximate symmetry (in log space) between the two escape probabilities. At and after the point of convergence, the probabilities become equal, so from (4):

$$\rho_\infty = \tau_\infty = \frac{1}{2}(1 - p_\infty) \quad (6)$$

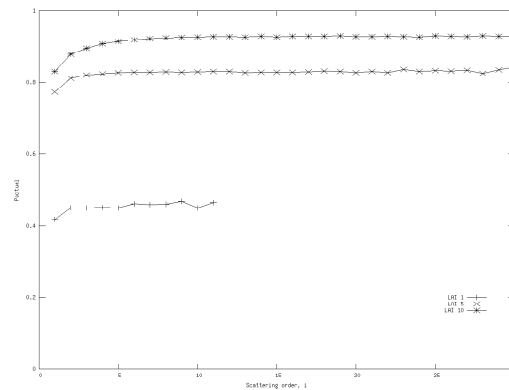


Figure 1. Recollision probability as a function of scattering order for LAI 1, 5 and 10,  $\zeta = 0.5$ , zenith  $0^\circ$ .

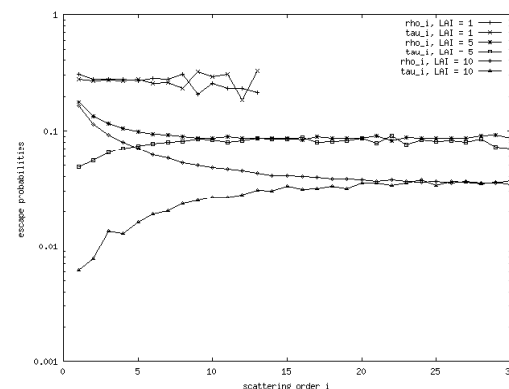


Figure 2. Upward and downward escape probabilities as a function of scattering order for homogeneous canopies at LAI 1, 5 and 10,  $\zeta = 0.5$ , zenith angle  $0^\circ$ .

## 1.4 Previous models using spectral invariants

Previous models assume that the recollision probability  $p_i$  is constant with scattering order (Huang et al., 2007). We denote this constant value  $p_{eff}$ . Under this assumption and with the energy conservation constraint (5d), we can write the total scattering through:

$$S_{R,\lambda} = \frac{S_{R,\lambda} - t_0}{1 - t_0} = \frac{(1 - p_{eff})\omega_\lambda}{1 - p_{eff}\omega_\lambda} \quad (7a)$$

where  $S_{R,\lambda}$  is the relative total scattering. The effective recollision probability  $p_{eff}$  is less than  $p_\infty$ . Canopy relative transmittance  $T_{R,\lambda}$  can be stated as:

$$T_{R,\lambda} = \frac{T_{\lambda,\theta} - t_{0,\theta}}{(1 - t_{0,\theta})} = \frac{t_{0,equiv}}{(1 - t_{0,equiv})} \frac{p_i \omega_\lambda}{(1 - p_i \omega_\lambda)} \quad (7b)$$

(Shabanov et al., 2003; Huang et al., 2007) where  $t_{0,equiv}$  is an effective value for zero-order transmittance.  $p_i$  is understood to be an equivalent recollision probability for radiation escaping through the canopy lower boundary. Shabanov et al. (2003) define  $p_i$  as the eigenvalue normalised by leaf albedo of the linear operator that assigns downward radiances at the canopy bottom to incoming radiation, but other than that it has no direct physical meaning. We see  $t_{0,\theta} p_i / (1 - t_{0,\theta})$  as the assumed model for escape probability in the downward direction,  $\tau_i$ , so:

<sup>1</sup>[http://rami-benchmark.jrc.it/HTML/RAMI3/EXPERIMENTS3/HETEROGENEOUS/FLOATING\\_SPHERES/SOLAR\\_DOMAIN/DISCRETE/DISCRETE.php](http://rami-benchmark.jrc.it/HTML/RAMI3/EXPERIMENTS3/HETEROGENEOUS/FLOATING_SPHERES/SOLAR_DOMAIN/DISCRETE/DISCRETE.php)



$$T_{R,\lambda} = \frac{\tau_t \omega_\lambda}{(1 - p_t \omega_\lambda)} \quad (7c)$$

From equations (7a) and (7c) and consideration of energy conservation, we can infer the relative reflectance  $R_{R,\lambda}$  to be:

$$R_{R,\lambda} = S_{R,\lambda} - T_{R,\lambda} = \frac{(1 - p_{equiv}) \omega_\lambda}{(1 - p_{equiv} \omega_\lambda)} - \frac{\tau_t \omega_\lambda}{(1 - p_t \omega_\lambda)} \quad (7d)$$

Equations (7a,c,d) describe canopy directional-hemispherical reflectance and transmittance. They have only five parameters  $(t_{0,\theta}, p_{equiv}, \tau_t, p_t, \omega_\lambda)$ —four of these are independent of wavelength. The spectral invariants  $p_{equiv}, \tau_t, p_t$  can be inferred from measurements of  $T_{\lambda,\theta}$  and  $R_{\lambda,\theta}$ , given additional measurements of direct transmittance  $t_{0,\theta}$  (gap probability) and leaf single scattering albedo  $\omega_\lambda$ . Alternatively,  $t_{0,\theta}$  can be calculated from analytical or numerical radiative transfer models and  $p_{equiv}, \tau_t$  and  $p_t$  inferred from simulations of the behaviour of  $T_{\lambda,\theta}$  and  $R_{\lambda,\theta}$  as a function of  $\omega_\lambda$ .

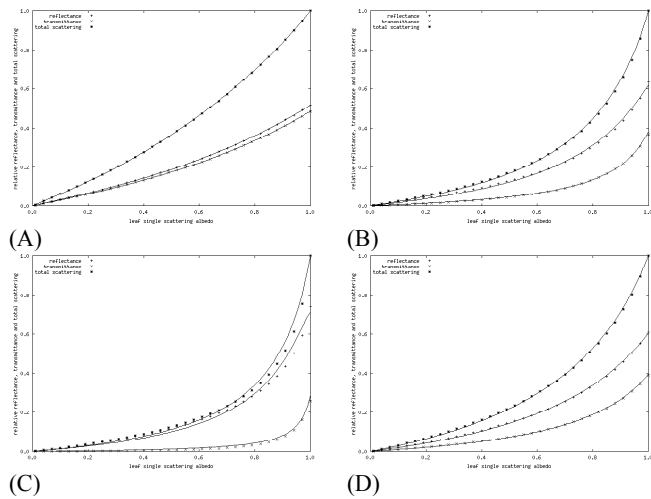


Figure 3a. Relative reflectance, transmittance and total scattering as a function of leaf single scattering albedo, for the canopies (A,B,C,D) for  $\xi=0.5$ , zenith  $0^\circ$  (symbols), with lines showing fitting of the original model.

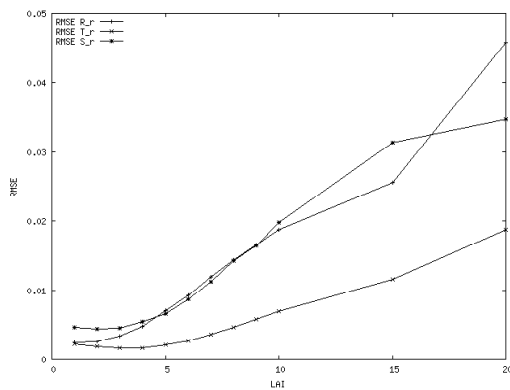


Figure 3b. Root mean square error (RMSE) for relative reflectance, transmittance and total scattering for the homogeneous canopies as a function of LAI.

Figure 3 shows the results of fitting the model presented above (the ‘original model’) to MCRT simulations of the relative reflectance, transmittance and total scattering for four canopies. Canopies A, B and C are homogeneous with LAI 1, 5 and 10 respectively. Canopy D is the RAMI heterogeneous canopy. The model fits the ‘observed’ (i.e. MCRT results) well in both cases (Figure 3b). Figure 3c shows that, except for very low LAI, the form of spectrally-invariant terms as a function of interaction order implied by the original model is inappropriate. Indeed, for moderate or high LAI (Figure 3cB,C) the assumed form for both reflectance and transmittance depart dramatically from the observed behaviour.

One could argue that this is unimportant: the models fit the observations and the departures noted are for relatively high scattering orders where the contributions are low. But the contribution of high order scattering terms is proportional to  $[\omega p_\infty]^i$ , so for example,  $\omega p_\infty=0.99$ , contributions of photons scattered 100 times are still as high as  $[0.99]^{100}=37\%$ . Clearly for low  $\omega p_\infty$  the model works well, but using inappropriate functions means that all model parameters lose any physical meaning (they all become effective terms) and any interpretation of first order scattering terms, bidirectional terms or parameter behaviour with varying  $\xi$  or zenith angle lose clarity as well.

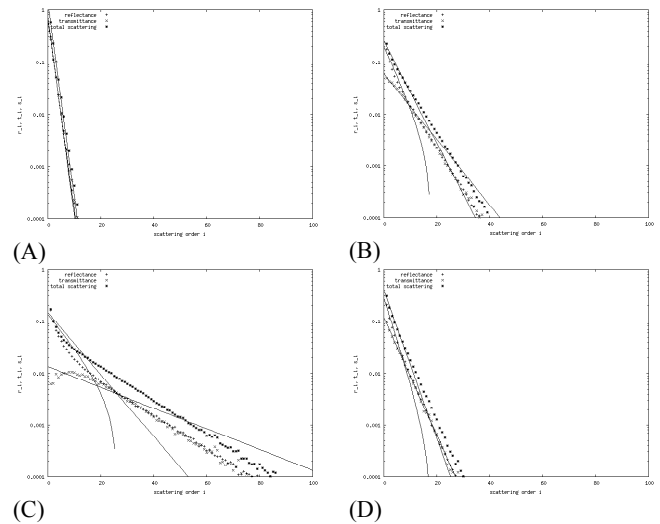


Figure 3c. Spectrally-invariant terms as a function of scattering order for canopies A, B, C and D for  $\xi=0.5$ , zenith  $0^\circ$  (symbols), with lines showing the original model.

For these reasons, we seek in this paper to establish an improved set of descriptors based around the concepts of spectral invariance. This will be achieved by more careful consideration of the modelling of escape probabilities. The next section examines scattering behaviour as a function of  $\xi$  and zenith angle.

## 2. FURTHER INVESTIGATION OF SCATTERING AS A FUNCTION OF INTERACTION ORDER

### 2.1 Behaviour as a function of $\xi$

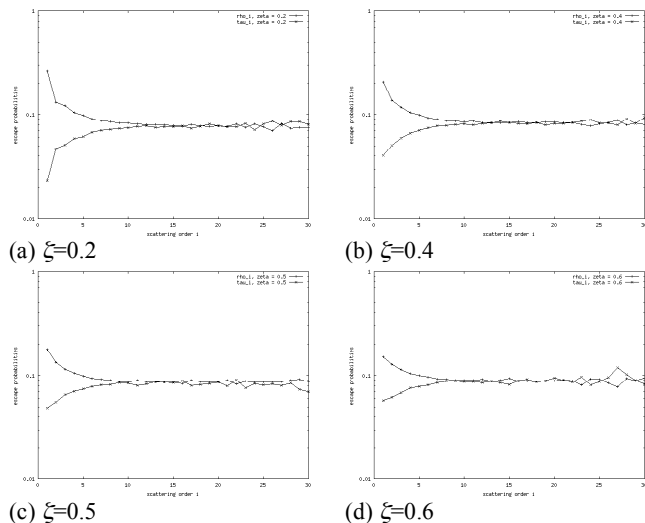


Figure 4. (a-d) Escape probabilities for varying  $\xi$ , LAI=5, zenith angle  $0^\circ$ .

Figure 4 shows the variation in escape probability with  $\xi$  for the canopy with LAI 5. We note that the interaction order of convergence appears to remain constant and that the initial escape probabilities  $\rho_1, \tau_1$  decrease with increasing  $\xi$ . If we represent the first order escape probabilities  $\tau_{1\xi}$  and  $\rho_{1\xi}$  by:

$$\tau_{1\xi} = A_1(1-\xi) + A_3\xi \quad (8a)$$

$$\rho_{1\xi} = (A_2(1-\xi) + A_4\xi) / (1 - t_{0,0}) \quad (8b)$$

then:

$$\tau_{1\xi} = A_1 + \frac{\xi}{0.5}(\tau_{1\xi=0.5} - A_1) \quad (8c)$$

$$\rho_{1\xi} = A_2 + \frac{\xi}{0.5}(\rho_{1\xi=0.5} - A_2) \quad (8d)$$

Escape (and therefore recollision) probabilities show a much weaker dependence on  $\xi$  for  $i \geq 2$ .

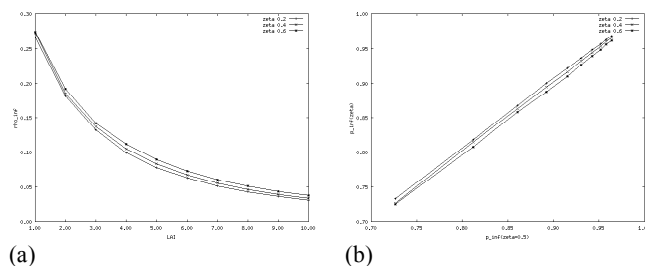


Figure 5. (a)  $\rho_\infty$  as a function of LAI for varying  $\xi$ ; (b)  $p_\infty$  for varying values of  $\xi$  as a function of  $p_\infty(\xi = 0.5)$ .

Figure 5a shows the variation in infinite scattering order escape probability  $\rho_\infty$  with LAI and  $\xi$ . The variation with  $\xi$  is relatively small compared to that with LAI or the variation in first order escape probabilities, but shows a linear dependency. This is further emphasised in Figure 5b where we see that:

$$p_\infty(\xi) = p_\infty(\xi = 0.5) - A_5 p_\infty(\xi - 0.5) \quad (8e)$$

Here,  $A_5$  is calibrated to be 0.22.

### 2.2 Behaviour as a function of zenith angle

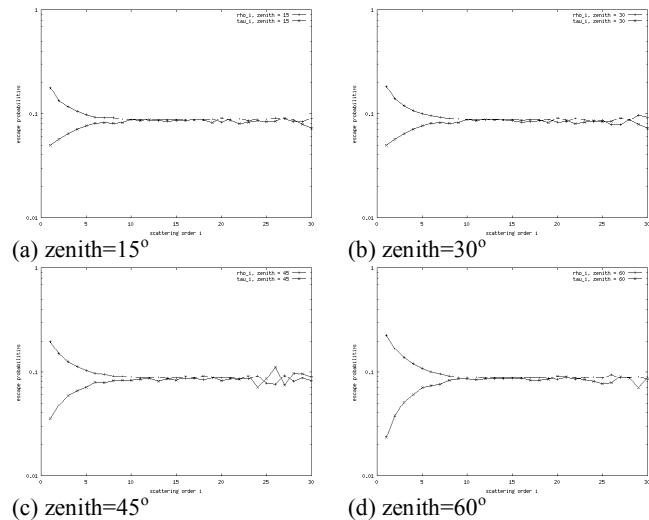


Figure 6. Escape probabilities for varying zenith, LAI=5,  $\xi=0.5$ .

Figure 6 shows escape probabilities for LAI 5 for varying zenith angles.  $\rho_\infty$  appears to be invariant with zenith angle (this is not quite true for  $\rho_{equiv}$  which varies with zenith angles greater than around  $60^\circ$  (Smolander and Stenberg, 2005)). There is generally small variation in the initial escape probabilities with zenith angle, although a small increase is seen at high angles (zenith greater than  $60^\circ$ ).

## 3. BUILDING A NEW MODEL

### 3.1 A model based on escape probabilities

Given the observations above, we propose a model relating escape probabilities:

$$\sqrt{\tau_i \rho_i} = a_i \quad (9a)$$

$$\sqrt{\frac{\tau_i}{\rho_i}} = \sqrt{\frac{r_i}{t_i}} = 1 - a_2^{i+1} \quad (9b)$$

Equation (9a) arises from the observation of near symmetry in log space of the escape probabilities. Equation (9b) is an empirical model that describes the square root of the escape ratios as shown in Figure 7.

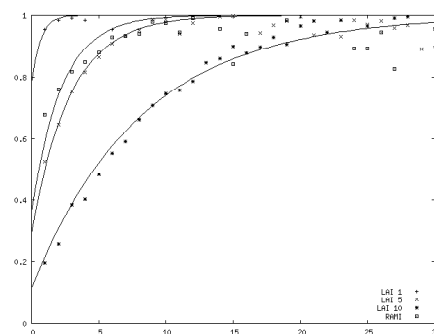


Figure 7. MCRT simulations of the square root of the ratio of downward to upward escape probabilities for canopies A, B, C and D.

From equation (9), we can formulate for the escape probabilities:

$$\rho_i = \frac{a_1}{(1 - a_2^{i+1})} \quad (10a)$$

$$\tau_i = a_1(1 - a_2^{i+1}) \quad (10b)$$

The recollision probability is found from equation (4). This fully specifies the reflectance model by calculating the terms  $r_i$  and  $t_i$  from equation (5) and the black soil reflectance and transmittance through equation (3). The model effectively has 3 parameters,  $a_2$ ,  $t_0$  and  $p_\infty$ —since  $a_1$  can be eliminated through energy conservation.

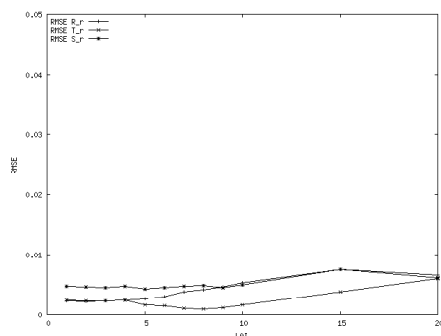


Figure 8. RMSE in model fit for the new model as a function of LAI for  $\zeta$  0.5, zenith angle  $0^\circ$ .

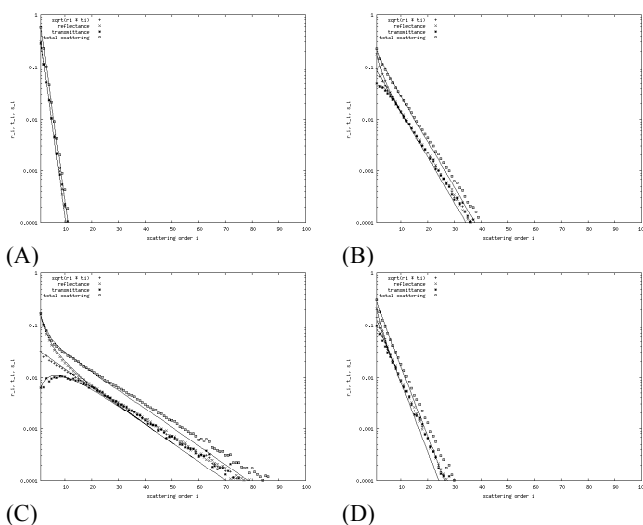


Figure 9. Spectrally-invariant terms as a function of scattering order for canopies A, B, C and D for  $\zeta=0.5$ , zenith  $0^\circ$  (symbols), with lines showing fitting of the new model

Figure 8 shows the RMSE in model fit as a function of LAI for the homogeneous canopies. Clearly this fits the MCRT simulation much better than the original model, with RMSE being mostly less than 0.05. Figure 9 shows the reflectance and transmittance terms reconstructed by fitting this model to data for canopies A, B, C and D. Comparing this with Figure 3 we can see that the fidelity of the spectral invariants is much greater. We can recognise in particular that  $p_\infty$  mostly maintains its original meaning (it still tends to be very slightly underestimated). We can consider this a successful model, in that the considerations of varying  $\zeta$ , zenith angle etc. considered above can be easily incorporated into the model. The single

main drawback is that the spectral invariants have to be calculated as products and sums of infinite series. In practice, we can resort to simpler analytical formulations for scattering orders greater than around twice the LAI, but the fact that the model cannot be simply stated in analytical form may limit its application.

### 3.2 A simpler analytical model

With this in mind, we develop a simpler analytical model that will achieve much the same ends as the new model presented above. We make the approximation:

$$\sqrt{t_i r_i} = a_3 p_\infty^{i-1} \quad (11)$$

so that:

$$r_i = \frac{a_3 p_\infty^{i-1}}{(1 - a_2^{i+1})} \quad (12a)$$

$$t_i = a_3 p_\infty^{i-1} (1 - a_2^{i+1}) \quad (12b)$$

Equation 12b leads to a pair of Neumann series for relative transmittance:

$$T_{R,\lambda} = \frac{a_3 \omega}{1 - p_\infty \omega} - \frac{a_3 a_2^2 \omega}{1 - p_\infty a_2 \omega} \quad (12c)$$

but no such series directly exists for relative reflectance. Instead, we must apply approximations to the reciprocal of  $1 - a_2^{i+1}$ . One potential function for this is:

$$\frac{1}{1 - a_2^{i+1}} \approx 1 + a_4 a_5^{i-1} \quad (12d)$$

with

$$a_4 = \frac{1}{1 - a_2^2} - 1 \quad (12e)$$

so:

$$R_{R,\lambda} = \frac{a_3 \omega}{1 - p_\infty \omega} + \frac{a_3 a_4 \omega}{1 - p_\infty a_5 \omega} \quad (12f)$$

As in the previous model,  $a_3$  can be eliminated through consideration of energy conservation. The model technically now has one additional parameter, namely  $a_5$ , although this too could be eliminated through further consideration of equation (12d).

The errors in model fitting are very similar to those shown in Figure 8, being slightly lower for higher LAI (at the cost of an additional model parameter). The fidelity in fitting the behaviour of the spectral invariants as a function of scattering order is also very similar.

## 4. DISCUSSION AND CONCLUSIONS

In this paper, we have examined a previous spectral invariant model of canopy directional-hemispherical reflectance and transmittance. We show that the model, based on assuming recollision probability to be constant with scattering order, is able to describe the required radiometric terms well for low to moderate LAI, but less well for higher LAI. The reason for this is seen to be that the model assumptions break down, and we see that the scattering behaviour as a function of interaction order is described by inappropriate functions.

We proceed to examine the scattering terms in some detail as a function of  $\xi$  and other factors and see that the spectral invariants are generally well-behaved. If a better description of the spectral invariant functions could be formulated, such factors could be quite easily incorporated into the model. We do not explicitly examine bidirectional reflectance and transmittance terms here, but it is likely that these too could be easily modelled with similar concepts, most likely as a departure from the directional-hemispherical case.

From an examination of the square root of the ratio of escape probabilities, we propose a new formulation that, when combined with an assumption regarding the log-symmetry of the escape probabilities, leads to a numerical model of relative reflectance and transmittance. Whilst the operation of this model is good in regard to its ability to reconstruct scattering behaviour as a function of interaction order, the formulation does not directly lead to an analytical solution for reflectance and transmittance. We therefore apply a further approximation that permits this. The resulting model, expressed mainly through equations (12c) and (12f), performs as well or better than the full model, although as currently implemented this is at the cost of an additional model parameter.

The final analytical model is rather similar in form to the original model, in that it contains Neumann series. In place of the single series for total relative scattering however, we have three series, one of which governs scattering at high interaction orders and the other two, which contain functional equivalences, control the variation in escape and recollision probabilities at low orders of scattering.

The next directions for model development include using equation (12d) to eliminate the parameter  $a_s$ , fully formulating for variations in zenith angle and  $\xi$ , and incorporating a treatment of bidirectional reflectance and transmittance. The model must also be nested within a fuller formulation incorporating interactions with the lower boundary. It is likely that for the black soil case the model parameters can be directly related to first-order reflectance and transmittance terms which can be analytically formulated for many cases. We can then consider the model to be essentially an improved description of multiple scattering in a canopy that is constrained by energy conservation, unlike many other formulations. The formulation appears to work reasonably well for the single heterogeneous canopy considered here, so it holds much promise as a general formulation. This should, however, be tested against a further range of conditions. Lewis and Disney (2007) showed that the original model could be applied to a description of leaf scattering, allowing for a convenient analytical nesting of this term as a function of pigment and other absorptances. Smolander and Stenberg (2005) showed that the original formulation allows for a nesting of multiple scales of clumping within a canopy. These concepts should also be further explored with the new formulation.

## APPENDIX 1

MCRT simulations here are truncated at scattering order  $i=100$ .

The sum of the scattering contributions  $z = \sum_{i=1}^{i=100} s_i$  would equal unity if this could be continued to infinity, from consideration of energy conservation. The term  $1-z$  is due to scattering at interaction orders of greater than 100. Here, if  $1-z$  is above a tolerance, further scattering orders are inferred, using the concept of recollision probability. Assuming  $p_\infty$  to be constant after 100 interactions:

$$1-z = s_{100} \sum_{i=1}^{i=\infty} p_\infty^i = s_{100} \frac{p_\infty}{(1-p_\infty)} \quad (\text{A1})$$

so

$$p_\infty \approx (1-z) / (s_{100} + (1-z)) \quad (\text{A2})$$

and further interactions estimated from  $r_{i+1} = r_i p_\infty$  and  $t_{i+1} = t_i p_\infty$ . The maximum value of  $(1-z)$  is around 0.05 for LAI 20. It is clearly insignificant for low to moderate LAI.

## ACKNOWLEDGEMENTS

We gratefully acknowledge support from the UCL Research Computing Facilities C<sup>3</sup> for much of the computing for this work. Some of this work was funded by NERC through the Centre for Terrestrial Carbon Dynamics (CTCD). Thanks to Sampo Smolander and Sian Lewis for editing.

## REFERENCES

- Disney, M. I., Lewis, P. and Saich, P. (2006) 3D modelling of forest canopy structure for remote sensing simulations in the optical and microwave domains. *Rem. Sens. Environ.* **100**(1) 114–132.
- Huang, D., Knyazikhin, Y., Dickinson, R., Rautiainen, M., Stenberg, P., Disney, M., Lewis, P., Cescatti, A., Tian, Y., Verhoef, W. and Myneni, R.B. (2007) Canopy spectral invariants for remote sensing and model applications. *Rem. Sens. Environ.* **106** 106–122.
- Knyazikhin, Y., Kranigk, J. V., Myneni, R. B., Panferov, O. and Gravenhorst, G. (1998) Influence of small-scale structure on radiative transfer and photosynthesis in vegetation cover. *Journal of Geophysical Research* **103** 6133–6144.
- Knyazikhin Y. and Marshak, A. (2000) Mathematical aspects of BRDF modeling: Adjoint problem and Green's function. *Remote Sens. Rev.* **18** 263–280.
- Lewis, P. (1999) The Botanical Plant Modelling System. *Agronomie: Agriculture and Environment* **19**(3–4) 185–210.
- Lewis, P. and Disney, M. I. (2007) Spectral invariants and scattering across multiple scales from within-leaf to canopy. *Rem. Sens. Environ.* doi:10.1016/j.rse.2006.12.015.
- Panferov, O., Knyazikhin, Y., Myneni, R. B., Szarzynski, J., Engwald, S., Schnitzler, K. G. and Gravenhorst, G. (2001) The role of canopy structure in the spectral variation of transmission and absorption of solar radiation in vegetation canopies. *IEEE Trans. Geosci. Rem. Sens.* **39**(2) 241–253.
- Saich, P., Lewis, P., Disney, M. and Thackrah, G. (2001) Comparison of Hymap/E-SAR data with models for optical reflectance and microwave scattering from vegetation canopies in *Proceedings of Third International Workshop on Retrieval of Bio- and Geo-Physical Parameters from SAR data for Land Applications*.
- Shabanov N.V., Wang Y., Buermann W., Dong J., Hoffman S., Smith G.R., Tian Y., Knyazikhin Y., Myneni R.B. (2003) Effect of foliage spatial heterogeneity in the MODIS LAI and FPAR algorithm over broadleaf forests. *Rem. Sens. Environ.* **85**(4) 410–423.
- Smolander, S. and Stenberg, P. (2005) Simple parameterizations of the radiation budget of uniform broadleaved and coniferous canopies. *Rem. Sens. Environ.* **94** 355–363.
- Wang, Y., Woodcock, C., Buermann W., Stenberg, P., Voipio, P., Smolander, H., Hame, T., Tian, Y., Hu, J., Knyazikhin, Y., Myneni, R. (2003) Evaluation of the MODIS LAI algorithm at a coniferous forest site in Finland. *Rem. Sens. Environ.* **91** 114 – 127.

# SPECTRAL INVARIANT BEHAVIOUR OF A COMPLEX 3D FOREST CANOPY

M. I. Disney<sup>a,\*</sup>, P. Lewis<sup>a</sup>

<sup>a</sup> Dept. of Geography, University College London, Gower Street, London, WC1E 6BT UK and NERC Centre for Terrestrial Carbon Dynamics - mdisney@geog.ucl.ac.uk

Commission VI, WG VI/4

**KEY WORDS:** Spectral invariant; 3D canopy structure; Monte Carlo ray tracing; recollision probability; Scots pine.

## ABSTRACT:

We present an attempt to apply the spectral invariant approach to canopy scattering of a complex forest canopy. Spectral invariant theory describes a method of expressing photon scattering as a function of purely structural properties of the canopy, the so-called photon recollision probability,  $p$  – the probability of a scattered photon undergoing further collision rather than escaping the canopy – can be used to describe the main impacts of structure on total canopy scattering. We apply a new spectral invariant formulation for canopy scattering (Lewis et al., 2007) to a detailed 3D structural model of Scots pine. This description assumes energy conservation (by definition in derivation of spectral invariant terms), and that  $p$  approaches a constant value when the scattered radiation is well-mixed (when the escape probabilities in the upward and downward direction,  $r_i$  and  $t_i$  respectively, approach each other after some finite number  $i$  of scattering interactions). We explore the behaviour of the resulting scattering from the complex models and apply the spectral invariant model description to the resulting scattering. We show that the behaviour of the spectral invariant terms ( $p$ ,  $r$ ,  $t$ ) are superficially similar to cases for simple canopies consisting of reflecting and transmitting disks, particularly for lower LAI/density cases. However, the dominance of trunks in the higher density/LAI cases violates the spectral invariant model assumptions. We suggest it may be possible to consider the scattering behaviour of the trunks and vegetation separately, considering the recollision probabilities  $p_{needle}$  and  $p_{trunk}$  independently.

## 1. INTRODUCTION

### 1.1 Canopy spectral invariants

There has been increasing interest in recent years in the so-called spectral invariant representation of vegetation canopy scattering (Knyazikhin et al., 1998; Panferov et al., 2001; Huang et al., 2007). In this approach, the total scattering from a vegetation canopy at optical wavelengths  $S_\lambda$  can be expressed as a function of wavelength  $\lambda$  as follows:

$$S_\lambda = t_0 + (1 - t_0) \sum_{i=1}^{i=\infty} s_i \omega_i^i \quad (1)$$

where  $t_0$  is the probability of radiation being transmitted through the canopy without interacting with canopy elements (the zero-order transmittance),  $\omega$  is the canopy element single scattering albedo and the terms  $s_i$  are spectrally-invariant terms dependent on the incident radiation distribution, the arrangement and angular distribution of canopy elements, and the ratio  $\zeta_\lambda$  of leaf transmittance  $T_{leaf,\lambda}$  to total leaf scattering ( $\omega_{leaf,\lambda} = T_{leaf,\lambda} + R_{leaf,\lambda}$ ) where  $R_{leaf,\lambda}$  is the leaf spectral reflectance i.e.

$$\zeta_\lambda = T_{leaf,\lambda} / (R_{leaf,\lambda} + T_{leaf,\lambda}) \quad (2)$$

The canopy spectral transmittance  $T_{bs,\lambda}$ , reflectance  $R_{bs,\lambda}$  and absorptance  $A_{bs,\lambda}$  for a canopy with a totally absorbing lower boundary ('black soil') can be expressed in similar forms. Relationships between the spectral invariant terms in  $S_\lambda$ ,  $T_{bs,\lambda}$ ,  $R_{bs,\lambda}$  and  $A_{bs,\lambda}$  can be expressed using the concept of a

recollision probability  $p_i$  (the probability that radiation incident on leaves after  $i$  interactions recollide with other canopy elements rather than escaping from the canopy). This recollision probability can also be considered in terms of the corresponding 'escape' probabilities in the upward and downward directions respectively  $r_i$  and  $t_i$  i.e.  $p_i + r_i + t_i = 1$  for energy conservation.

There have been various treatments of the concept of spectral invariants, notably by Knyazikhin et al. (1998) and Panferov et al. (2001) who have shown that the recollision probability is in fact the principal eigenvalue of the radiative transfer operator. Disney and Lewis (1998) independently noted that the multiple scattered radiation from a 3D barley canopy was well-behaved after relatively few scattering interactions. In both cases, the multiple scattering can be phrased as an infinite sum of scattering terms (a Neumann series). This sum represents the multiple interactions (and attenuation) of scattered radiation. This description of canopy scattering is spectrally invariant, depending on structure alone. The spectral invariant approach has been used by Smolander and Stenberg (2005) and others to represent scattering at multiple scales including the leaf (Lewis and Disney, 2007), shoot (Smolander and Stenberg, 2005; Mottus et al., 2007).

As noted by Huang et al. (2007) and others, the recollision probability tends to converge to its final value after relatively few iterations. can be considered the recollision probability of the radiation in the canopy when it is 'well mixed' (i.e. it has settled down to a stable value). 'Well-mixed' can be considered the point at which the escape probabilities in the upward and downward direction  $r_i + t_i$  are effectively equal.

\* Corresponding author.



There are two primary reasons why the spectral invariant approach to describing canopy scattering is attractive. Firstly, such a representation can provide a rapid, structurally consistent way to model canopy scattering. This potentially makes the spectral invariant description very useful in applications where rapid, consistent models of scattering are required, such as in look-up-table (LUT) retrieval of biophysical parameters from observations of scattering, or for assimilation of observations into models of ecosystem function. Speed is a pre-requisite in both these applications; a consistent (across wavelength and canopy structure) representation of scattering is highly desirable and makes analysis much more straightforward as only a single model of scattering is required..

Secondly, the spectral invariant approach permits the separation of scattering behaviour due to structural and biochemical influences (Lewis and Disney, 2007). These properties are often coupled and so separation of their behaviour may permit retrieval of either alone. Without this separation such retrieval may not be possible.

This paper presents an exploration of the spectral invariant approach to describing scattering from a highly-detailed 3D Scots pine canopy.

## 2. MATERIALS AND METHODS

### 2.1 3D structural model

A 3D structural model of Scots pine was developed using the Treegrow/PINOGRAM model of Leersnijder (1992). The model is based on measurements of canopy structural development made in the field. Scots pine stands were simulated over a range of ages (5 to 50 years in 5 year steps) and densities. Tree spacing was varied between ~1.5m and ~6m, covering the observed range of densities for such a canopy in managed forest stands in the UK. Full details of stand development and comparison to observed data are given in Disney et al. (2006). It is shown that the resulting canopies can be used to simulate observed reflectance well.

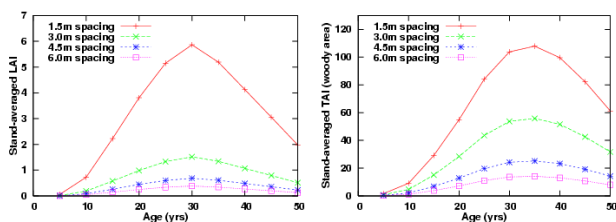


Figure 1. Stand-averaged LAI and woody area with age and density.

Figure 1 shows the variation of the stand properties with age and density. It can be seen that the stand-averaged LAI increases with age to a maximum at age 30 years. The equivalent measure of trunk area trunk, 'trunk area index', varies in the same manner, but peaks slightly later at around age 35 years due to the shift to proportionately reduced leaf area (increased trunk area) at increased age.

Figure 2 shows examples of the variation in tree spacing and crown shape (for Sitka spruce in this case) are typically observed in managed tree stands of the sort being modelled. As the trees develop in close proximity to one another, the crown size reduces and the stands become dominated internally by large quantities of trunk area.



Figure 2. Managed forest stands of 15 years (left) and 35 years (right).

### 2.2 Canopy simulation and modelling

To examine the spectral invariant behaviour of the Scots pine canopy, energy conservative (totally scattering/absorbing) simulations were carried out using the Monte Carlo ray tracing (MCRT) model, *drat* (see Pinty et al., 2004 and Widłowski et al., 2007 for model intercomparison). All 7 combinations of  $p_{\text{leaf, trunk, soil}} = 0, 1$  were simulated. In order to simulate the zero order transmission component ( $t_0$  from equation 1), reflectance and was simulated in a case with no soil i.e. illuminated from above, but with transmitted radiation passing directly through the lower boundary. In all cases, scattering was simulated to scattering order 100. This might seem excessive but when considering the scattering in energy conservative cases (no absorption), the amount of energy remaining after many scattering interactions can still be significant. The implications for this become apparent below.

Analysis of the resulting scattering behaviour is presented below, as well as results from attempting to fit the model representation of Lewis et al. (2007). This model describes R, T, S as follows:

$$R_{bs,\lambda} = \frac{1}{2}(1-t_0)(1-p_\infty) \left[ \frac{\omega_\lambda}{1-p_\infty\omega_\lambda} + \frac{c_1 d_1 \omega_\lambda}{1-p_\infty d_1 \omega_\lambda} \right] \quad (3)$$

$$T_{bs,\lambda} = t_0 + \frac{1}{2}(1-t_0)(1-p_\infty) \left[ \frac{\omega_\lambda}{1-p_\infty\omega_\lambda} - \frac{c_2 d_2 \omega_\lambda}{1-p_\infty d_2 \omega_\lambda} \right] \quad (4)$$

$$\frac{(S_{bs,\lambda} - t_0)}{(1-t_0)} = \frac{(1-p_\infty)\omega_\lambda}{1-p_\infty\omega_\lambda} + \frac{(1-p_\infty)}{2} \left[ \frac{c_1 d_1 \omega_\lambda}{1-p_\infty d_1 \omega_\lambda} - \frac{c_2 d_2 \omega_\lambda}{1-p_\infty d_2 \omega_\lambda} \right] \quad (5)$$

where, under energy conservation

$$\frac{c_1 d_1}{1-p_\infty d_1} = \frac{c_2 d_2}{1-p_\infty d_2} \quad (6)$$

The terms  $c_{1,2}$  and  $d_{1,2}$  are 'fitting' (i.e. not biophysical) parameters parameter. The derivation of the above model and assumptions underlying it are described in Lewis et al. (2007). The key for this analysis is that the behaviour of the escape probabilities  $r_i$ ,  $t_i$  in the upward and downward directions respectively are assumed well-behaved i.e. that  $\sqrt{r_i t_i}$  is approximately constant once  $p_\infty$  has been reached.

### 3. RESULTS

#### 3.1 Scattering behaviour

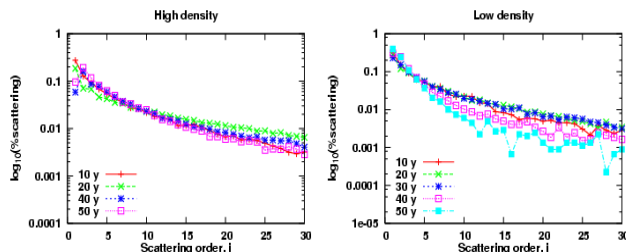


Figure 3. Canopy scattering behaviour as a function of scattering order,  $i$ .

Figure 3 shows the decay of total diffuse scattering (%) for high density (average tree spacing  $< 2\text{m}$ ) and low density (average tree spacing  $> 5\text{m}$ ) cases, as a function of scattering order,  $i$ . The terms 'high/low density' are used to imply the same spacing through the following text. In log space, the scattering in both cases decreases relatively rapidly for the first few scattering orders and then much more gradually with increasing  $i$ . In the high density case, two things become apparent: i) there is little difference between behaviour for different ages, except over the first two scattering orders; ii) the first order behaviour can be unexpected, with greater scattering at  $i=2$  than  $i=1$  in some cases. In the low density stands, there is separation of the scattering behaviour between the different stand ages. Also apparent is that simulations become quite noisy even at scattering orders  $< 20$ .

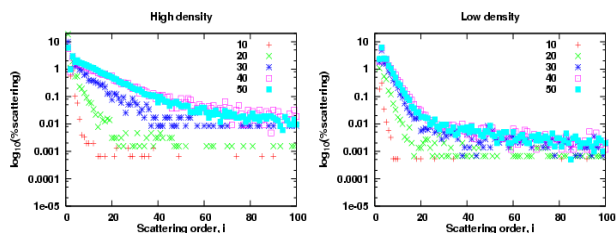


Figure 4. Canopy scattering behaviour as a function of scattering order,  $i$  density and age.

Figure 4 shows the same results as in figure 3, but over all scattering orders (i.e. to  $i=100$ ). As  $i$  exceeds 30 we see that the separation of scattering behaviour with stand age becomes more apparent even in the high density case. Most importantly, we see that the *rate of decay* of scattering is still decreasing for the older canopies and does not seem to have settled down to a constant rate, even at  $i=100$ . This is important as the model fitting described below assumes constant recollision probability  $p_\infty$  i.e. when the rate of decay of scattering from  $i$  to  $i+1$  is constant.

In the low density case, conversely, the scattering behaviour has two distinct phases. The first settles down quickly to a constant (steep) decay; the second then takes over at  $i=10-30$  (depending on stand age) and has a much more gradual decay.

#### 3.2 Escape probabilities $r_i$ , $t_i$

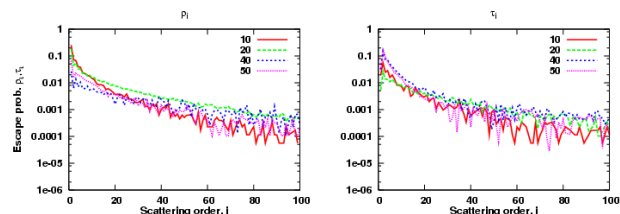


Figure 5. Upward and downward escape probabilities ( $r_i$ ,  $t_i$ ) for a high density canopy (2-3m tree spacing).

Figure 5 shows the behaviour of the escape probabilities in the upward ( $r_i$ ) and downward ( $t_i$ ) directions for the high density canopy as function of  $i$ . In both cases the behaviour follows the same path. This differs distinctly from the cases observed in idealised disk canopies seen in Lewis et al. (2007), where as  $r_i$  decreases,  $t_i$  increases. Figure 6 shows the same information for the low density canopy case.

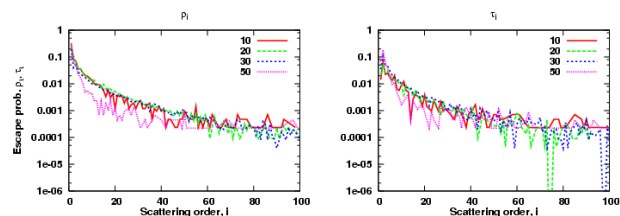


Figure 6. Upward and downward escape probabilities ( $r_i$ ,  $t_i$ ) for a low density canopy (5-6m tree spacing).

#### 3.3 Recollision probability, $p$

Figure 7 shows the variation of recollision probability  $p_i$  ( $1 - r_i - t_i$ ) as a function scattering order for high and low density stands (upper/lower panels) and for two ages, 10 and 45 years (left/right panels). In each case,  $p_i$  is shown for three view zenith angles,  $0^\circ$ ,  $30^\circ$  and  $60^\circ$  (sun zenith is  $0^\circ$  in all cases).

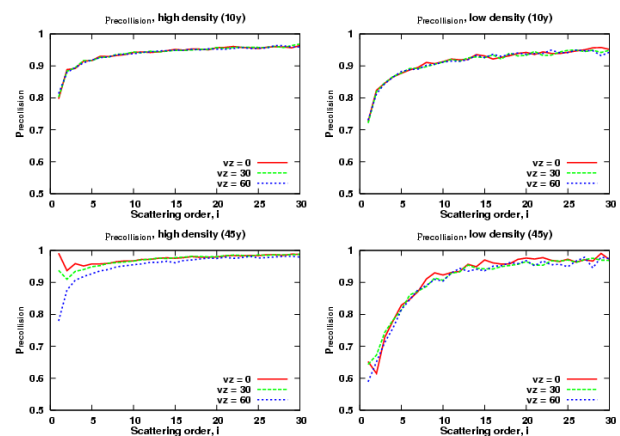


Figure 7. Recollision probability,  $p_i$ , as a function of age, scattering order and view zenith angle.

The recollision probability varies in a similar way to that seen by Lewis et al. (2007) for idealised disk canopies. Values start between 0.6 and 0.8 for  $i=1$  and progress to  $> 0.9$ . In all cases in figure 7,  $p$  does not appear have reached  $p_\infty$  even at  $i=30$ . There

is little variation with view zenith in the high density case, but this is not true for the lower density case. Other, different behaviour is seen for high density case at low  $i$ , where  $p$  can reduce before increasing again.

### 3.4 Model fitting

Figure 8 shows the results of fitting the model of spectral invariants presented by Lewis et al. (2007) (equations 3-5) to the simulated values of canopy reflectance shown above. Figure 9 shows the same information for the low density stand. In each case the solid lines are the model fits and the symbols the corresponding MCRT-simulated values.

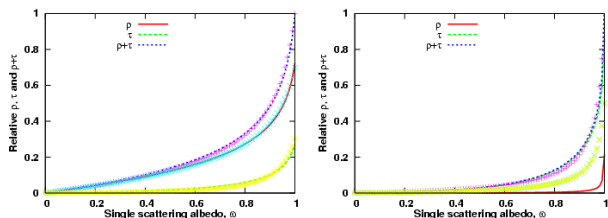


Figure 8. Model fit for high density stand, age 10yrs (left) and 45yrs (right)

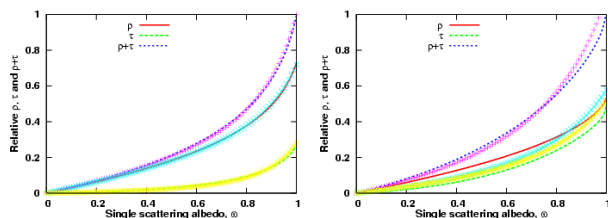


Figure 9. Model fit for low density stand, age 10yrs (left) and 45yrs (right).

The model fitting results are presented as a function of needle single scattering albedo,  $\omega$ . As a result of fitting the spectral invariant model (equations 3-5) we can express canopy scattering in this way over the whole range of possible values of  $\omega$ , rather than for some specific value. This is one of the advantages of using spectral invariants: scattering behaviour is expressed purely as a function of the structural terms contained within the model, rather than as some combined structural-biochemical scattering behaviour at specific wavelengths.

## 4. DISCUSSION

The scattering behaviour of the 3D Scots pine canopy shown in figures 3 and 4 is superficially similar to that shown by Lewis et al. (2007) for idealised disk canopies i.e. rapid reduction of scattering in the first two orders, followed by a gradual reduction until a point is reached at which further reduction of scattering is constant (in log space). This is the point at which the scattering can be considered 'well-mixed' and that  $p = p_\infty$ . Lewis et al. (2007) note that this typically occurs at  $i \approx 2LAI$ .

However, closer inspection reveals some significantly different behaviour. In particular, the first orders of scattering can increase, particularly for the very dense stands. In addition, there are large differences in behaviour with age: for the older, larger trees in figure 4 the scattering is clearly still levelling out and has not reached the plateau of  $p = p_\infty$ , even after 100

scattering interactions. This is largely due to the domination of the high density/age stands of the trunk material. Figures 1 and 2 show how much trunk material can be contained within a scene. In the energy conservation case, this trunk material is white, and so the scenes are dominated by large areas of totally reflecting solid objects (no transmission). This appears to have significant implications for the model representation and fitting.

We note that in the low density case, there appear to be two separate decay processes occurring. The first, due to the needles, dominates scattering orders  $< 20$  causing a rapid decay. Beyond this, a second decay rate takes over which is far more gradual. This is likely to be the influence of the trunks. Once a photon has penetrated through the upper crown layer, it can interact many times with the trunks before escaping through the upper (or lower) boundary. This behaviour tends to dominate for the denser/older canopies and will result in there being effectively two values of  $p$ ,  $p_{needle}$  and  $p_{trunk}$ .

The results of fitting the spectral invariant model described by Lewis et al. (2007) appear to be reasonable, particularly for the younger trees and lower density stands. However, for the high density/age the model form is clearly not appropriate. Figure 10 illustrates what is occurring during the model fitting.

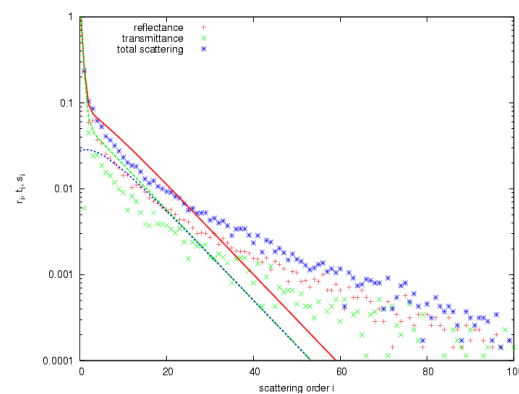


Figure 10. Model fit with scattering order,  $i$ .

Figure 10 shows the decay of the MCRT-simulated scattering terms, as well as the modelled versions of these terms resulting from fitting equations 3-5 to the simulated scattering. Although the model *can* fit to the first few scattering orders, where total energy is large, the decay of the modelled terms is far steeper than observed. As a result, the modelled value of  $p$  departs quite strongly from the 'actual' value, as a result of the two-stage behaviour described above. The result of this inappropriate fit is that although the model may seem to fit quite well, it is doing so for the wrong reasons.

A second issue that can be seen in figure 10 is the behaviour of the separate scattering components. The form of the spectral invariant model outlined above assumes energy conservation, that  $r_i$ ,  $t_i$  the upward and downward escape probabilities, approach a constant value and that  $\sqrt{r_i t_i}$  is approximately constant once  $p_\infty$  has been reached. This is clearly not the observed behaviour in figure 6. As a result, the final spectral invariant model is not appropriate for the 3D Scots pine canopies simulated here.

A further departure from the assumptions of the spectral invariant model is the issue of energy conservation. In the most extreme high density/age case, there can be energy of the order of 0.05 to 0.5% remaining even at  $i=100$ . As a result, the

assumption of energy conservation is not met. Although this might appear to be a very small amount of energy, it is the rate of decay at this stage which determines  $p_{\infty}$ .

As a result of these departures, and the lack of model fit for higher orders of scattering, we suggest that the scattering from the trunks and needles may need to be treated separately, requiring the formulation of the spectral invariant model for scattering from needles/soil (via  $p_{needle}$ ) and trunks/soil (via  $p_{trunk}$ ) as well as multiple scattering between the two components (via combination of  $p_{needle}$  and  $p_{trunk}$ ). This approach was used in Saich et al. (2004). In this case, canopy scattering,  $\rho$ , was expressed in the form

$$\rho = W + WS + T + TS + WT \quad (6)$$

Where W is the scattering from needles only; WS is scattering from needles and soil; T is scattering from trunk only; TS, scattering between trunk and soil; and WT is scattering between needles and trunk. Each of the terms in equation (6) was represented through an expression of the form

$$\rho_{W,T,S} \propto \frac{a\omega}{1-b\omega} \quad (7)$$

from the Neumann series solution for multiple scattered components. In the case of Saich et al. (2003), a and b were considered 'empirical' model fitting coefficients. However it is clear that  $a \propto (1-p)$  and  $b \propto p$  in terms of the form expressed in equations (3-5). This approach worked extremely well, and was able to describe observed scattering very closely. However the model was essentially a semi-empirical one: the various scattering terms introduced in the form of equation (6) having no direct physical equivalent.

## 5. CONCLUSIONS

A spectral invariant approach to modelling canopy scattering in a complex 3D Scots pine canopy was explored. Total canopy scattering was simulated for a range of structural scenarios spanning the range of observed canopies, using a Monte Carlo ray tracing model. A model of scattering phrased in terms of spectral invariant terms developed for an idealised disk canopy (Lewis et al., 2007) was applied to the resulting modelled scattering. The spectral invariant approach considers canopy scattering in energy conservation cases (totally scattering/absorbing canopy/soil components).

While the scattering behaviour of the Scots pine canopies superficially resembled that from the idealised disk cases, scattering decayed much more slowly. In addition, the more dense the canopy, the less the scattering behaviour resembled that of the disk canopies. Some significant radiation is

The behaviour of  $p$ , the recollision probability, was similar to that observed for the idealised disk canopies. However, the behaviour of  $r_i$  and  $t_i$ , the upward and downward escape probabilities was somewhat different. In particular, assumptions regarding the behaviour of these terms in the spectral invariant model were not met.

The spectral invariant model appears to fit quite well to the MCRT-modelled scattering behaviour. However, closer inspection shows that although the model might provide a quite

close fit in some cases (particularly for lower density/age stands), this is for the wrong reasons. The model form is not appropriate for the observed scattering behaviour.

It is proposed that the presence of large areas of trunk within the canopy dominate the scattering response, particularly at higher orders of scattering. Given the total area of trunk and branch can approach 100m<sup>2</sup> per m<sup>2</sup> of ground area in extreme cases, this is not surprising.

It is proposed that a spectral invariant model for this type of canopy requires a more complex representation to cope with: non-transmitting needles; three components as opposed to two which greatly increases the number of scattering components in the resulting signal. Specifically, observed scattering suggests the application of separate recollision probabilities for the trunk/branch and needle components,  $p_{needle}$  and  $p_{trunk}$ .

The extreme density simulations carried out here are not realistic in that intersection of scattering elements cannot be precluded for tree spacing < ~3m. In addition, the large areas of trunk and branch render the needle scattering far less significant as a proportion of total scattering.

Future work will include simulation of canopies of intermediate structural complexity i.e. somewhere between the idealised disk cases and the 3D Scots pine canopies seen here. Examples of these would be heterogeneous broadleaf-type canopies which have trunk material, but not in such large quantities as for the Scots pine canopies. The conifer-like and birch-like scenes of third RAMI experiment will provide examples for this (Widlowski et al., 2007).

## ACKNOWLEDGEMENTS

We gratefully acknowledge support from the University College London Research Computing Facilities through access to the Central Computing Cluster (C<sup>3</sup>) for much of the computing for this work. Some of this work was funded by the Natural Environment Research Council through the Centre for Terrestrial Carbon Dynamics (CTCD). The authors also gratefully acknowledge fruitful discussions with Yuri Knyazikhin and colleagues on the subject of spectral invariants.

## REFERENCES

- Disney, M. I. and Lewis, P. (1998) Multiple scattering behaviour of a 3D barley canopy, *in proc. IGARSS98*, Seattle, USA.
- Disney, M. I., Saich, P., and Lewis, P. (2003). Modelling the radiometric response of a dynamic, 3D structural model of Scots Pine in the optical and microwave domains, in *Proceedings of IEEE Geoscience and Remote Sensing Symposium IGARSS'03*, **6**, 3537–3539.
- Disney, M. I., Lewis, P., Quaife, T. and Nichol, C. (2005). A spectral invariant approach to modelling canopy and leaf scattering, in *Proceedings of ISPMSRS'05, Beijing, China, October 17-19 2005*, ISSN 1682-1750, 318–320.
- Disney, M. I., Lewis, P. and Saich, P. (2006). 3D modelling of forest canopy structure for remote sensing simulations in the optical and microwave domains, *Rem. Sens. Environ.*, **100**(1), 114–132.
- Disney, M. I., Lewis, P. and Saich, P. (2006). 3D modelling of

- forest canopy structure for remote sensing simulations in the optical and microwave domains, *Rem. Sens. Environ.*, **100**(1), 114–132.
- Knyazikhin, Y., Kranigk, J. V., Myneni, R. B., Panferov, O. and Gravenhorst, G., (1998). Influence of small-scale structure on radiative transfer and photosynthesis in vegetation cover, *Journal of Geophysical Research*, **103**, 6133–6144.
- Leersnijder, R. P. (1992) PINOGRAM: A Pine Growth Area Model, PhD thesis Wageningen University.
- Lewis, P. and Disney, M. I. (2007) Spectral invariants and scattering across multiple scales from within-leaf to canopy, *Rem. Sens. Environ.*, doi:10.1016/j.rse.2006.12.015
- Lewis, P., Disney, M. I., Knyazikhin, Y., Quaife, T. and Schull, M. (2007) Modelling canopy reflectance with spectral invariants, in *proc. ISPMRS07*, Davos, March 11-15 2007.
- Panferov, O., Knyazikhin, Y., Myneni, R. B., Szarzynski, J., Engwald, S., Schnitzler, K. G. and Gravenhorst, G. (2001). The role of canopy structure in the spectral variation of transmission and absorption of solar radiation in vegetation canopies, *IEEE Trans. Geosci. Rem. Sens.*, **39**(2), 241–253.
- Pinty, B., Widlowski, J.-L., Taberner, M., Gobron, N., Verstraete, M. M., Disney, M. I., Gascon, F., Gastellu, J.-P., Jiang, L., Kuusk, A., Lewis, P., Li, X., Ni-Meister, W., Nilson, T., North, P., Qin, W., Su, L., Tang, S., Thompson, R., Verhoef, W., Wang, H., Wang, J., Yan, G., Zang, H. (2004). Radiation Transfer Model Intercomparison (RAMI) exercise: Results from the second phase, *Journal of Geophysical Research*, **109**, D06210, doi:10.1029/2003JD004252.
- Saich, P., P. Lewis, M. Disney, P. van Oevelen, I. Woodhouse, B. Andrieu, C. Fournier, S. Ljutovac (2004) Development of vegetation architectural models for remote sensing Applications, final report of ESA Contract 14940.
- Smolander, S., and Stenberg, P. (2005). Simple parameterizations of the radiation budget of uniform broadleaved and coniferous canopies, *Rem. Sens. Environ.*, **94**, 355–363.
- Widlowski, J.-L., Taberner, M., Pinty, B., Bruniquel, V., Disney, M. I., Fernandes, R., Gastellu-Etchegorry, J. P., Gobron, N., Kuusk, N., Lavergne, T., Leblanc, S., Lewis, P., Martin, E., Mottus, M., North, P. R. J., Qin, W., Robustelli, M., Rochdi, N., Ruiloba, R., Soler, C., Thompson, R., Verhoef, W., Verstraete, M. M. and Xie, D. (in press). The third Radiation transfer Model Intercomparison (RAMI) exercise: Documenting progress in canopy reflectance models, *Journal of Geophysical Research (Atmospheres)*.



# RETRIEVAL OF CONIFEROUS CANOPY CHLOROPHYLL CONTENT FROM HIGH SPATIAL RESOLUTION HYPERSPECTRAL DATA

Z. Malenovský<sup>a,b,\*</sup>, R. Zurita-Milla<sup>b</sup>, L. Homolová<sup>a,c</sup>, E. Martin<sup>d</sup>, M. E. Schaepman<sup>b</sup>, J.P. Gastellu-Etchegorry<sup>d</sup>, R. Pokorný<sup>a</sup>, J.G.P.W. Clevers<sup>b</sup>

<sup>a</sup> Inst. of Systems Biology and Ecology, Academy of Sciences of the Czech Republic, Poříčí 3b, 60300 Brno, Czech Republic - zbynek.malenovsky@gmail.com, (lucie.homolova, eradek)@brno.cas.cz

<sup>b</sup> Centre for Geo-Information, Wageningen University, Droevendaalsesteeg 3 / PO Box 47, 6700 AA Wageningen, The Netherlands - (raul.zurita-milla, michael.schaepman, jan.clevers)@wur.nl

<sup>c</sup> Dep. of Applied Geoinformatics and Cartography, Faculty of Science, Charles University in Prague, Albertov 6, 12843 Prague 2, Czech Republic

<sup>d</sup> Centre d'Etudes Spatiales de la Biosphère, UPS-CNRS-CNRS-IRD, 18 Avenue Edouard Belin, BPI 2801, 31401 Toulouse, Cedex 9, France - (emmanuel.martin, jean-philippe.gastellu)@cesbio.cnes.fr

## Commission VI, WG VI/4

**KEY WORDS:** Remote Sensing, Hyperspectral, High Resolution, Forestry, Vegetation, Estimation, Retrieval, Neural

### ABSTRACT:

The discrete Anisotropic Radiative Transfer (DART) model, coupled with an adjusted version of the PROSPECT model, was used to retrieve total chlorophyll content ( $C_{ab}$ ) of a complex Norway spruce (*Picea abies* (L.) Karst.) canopy from airborne hyperspectral data acquired at very high spatial resolution. The radiative transfer models were parameterized by using field measurements and observations collected from a young spruce stand growing at the permanent experimental site Bílý Kříž (the Moravian-Silesian Beskydy Mts., the Czech Republic, 18.53863°E, 49.50256°N, 936 m a.s.l.). A set of the hyperspectral images with a pixel-size of 0.4 m was acquired for the test site by an airborne AISA Eagle VNIR system in September 18<sup>th</sup>, 2004. An operational canopy  $C_{ab}$  estimation was carried out by means of a PROSPECT-DART inversion employing an artificial neural network (ANN) and a vegetation index ANCB<sub>650-720</sub>. Both retrieval approaches used continuum removed reflectance values of six AISA Eagle spectral bands located between 650 and 720 nm. The  $C_{ab}$  inversion was only performed for direct sun exposed (sunlit) crown pixels in order to ensure a high quality (noiseless) reflectance signal. Results of both inversion approaches were similar, when validated against the ground measured  $C_{ab}$  of nine Norway spruce crowns. Coefficients of determination ( $R^2$ ) between ground truth and remote sensing  $C_{ab}$  estimates were 0.78 and 0.76, respectively, with root mean square errors (RMSE) of 2.95  $\mu\text{g cm}^{-2}$  for the ANN and 3.36  $\mu\text{g cm}^{-2}$  for the ANCB<sub>650-720</sub> retrieval. The spatial patterns of  $C_{ab}$  values estimated by both inversion methods were consistent with each other. About 80% of the  $C_{ab}$  estimated values had an absolute difference smaller than 2  $\mu\text{g cm}^{-2}$ .

## 1. INTRODUCTION

### 1.1 General Introduction

The total content of chlorophyll *a* and *b* ( $C_{ab}$ ) is an important biomarker of the actual plant status.  $C_{ab}$  can also be used as an indicator of vegetation gross primary productivity (Gitelson et al., 2006). A number of studies has been carried out to design an appropriate algorithm to estimate the total chlorophyll content of structurally homogeneous agriculture crops (Daughtry et al., 2000; Haboudane et al., 2002), but also for structurally complex coniferous forest canopies (Zarco-Tejada et al., 2004), using optical remote sensing data. Canopy  $C_{ab}$  content can be spatially retrieved from hyperspectral images by using chlorophyll vegetation indices (le Maire et al., 2004) or by inversion of physical radiative transfer (RT) models (Gascon et al., 2004). However, if very high spatial resolution data (pixel-size of about 1 m) is used to analyze structurally heterogeneous canopies, the complexity of the inversion increases as the scene needs to be modeled with more details. Therefore, physically based  $C_{ab}$  content retrievals for such

canopies need appropriate RT models capable to address the complexity of the scene at such a high spatial resolution.

### 1.2 Objectives

The main objective of the study was to develop a physically based approach to retrieve total chlorophyll content ( $C_{ab}$ ) of a complex Norway spruce (*Picea abies* (L.) Karst.) canopy from very high spatial resolution (0.4 m) hyperspectral data. The motivation for this work was to produce high spatial resolution maps of canopy  $C_{ab}$ , which in turn could serve as a reference to validate satellite-based chlorophyll products. Additionally, we were using this exercise to better understand the up-scaling of chlorophyll retrieval algorithms from leave to crown level.

## 2. MATERIAL AND METHODS

### 2.1 General methodology

The general methodology used in this study is schematically depicted in the flowchart of figure 1.

---

\* Corresponding author.

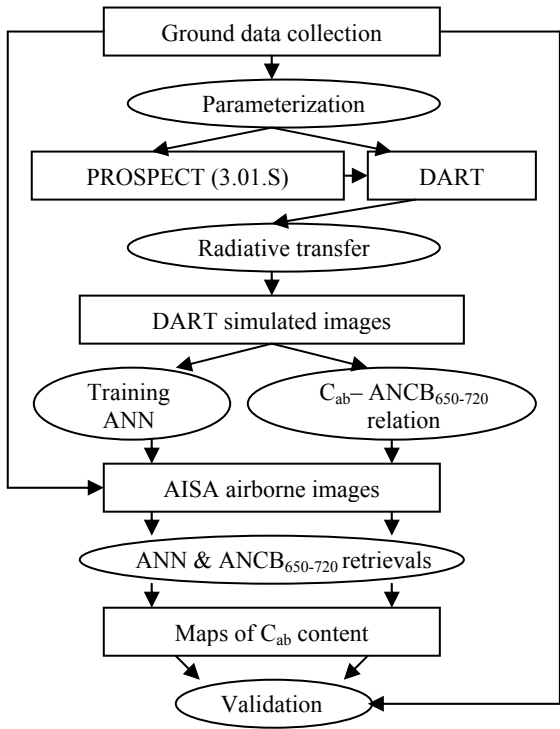


Figure 1. The methodological flowchart.

2.2 Study area and chlorophyll ground truth data

A montane forest stand of 28 years old Norway spruce trees, located at the permanent experimental research site Bily Kriz (the Moravian-Silesian Beskydy Mountains; 18.54°E, 49.50°N; altitude 936 m above sea level), was selected to conduct this study (figure 2). The average annual air temperature at this stand is about 5.5°C, the average annual precipitation amounts around 1000-1400 mm. This regularly spaced plantation was established with three years old spruce seedlings in 1981. In 2004, the spruces were about 10 m tall with an average diameter at breast height (DBH) of 12.8 cm.



Figure 2. Geographic location of the experimental research plot Bily Kriz (Europe, East border of the Czech Republic).

Needle samples collected from ten selected spruce trees were analyzed in a laboratory to obtain the canopy  $C_{ab}$  content that was later used to validate the results. Samples of last three age-classes were collected from a sunlit, transitional, and shaded branch cut off from each sampled tree. The representative  $C_{ab}$  content of each crown was computed as an average weighted by irradiation availability within the horizontal crown levels and abundance of the age-classes within the whole crown.

2.3 Hyperspectral airborne images

An airborne/field campaign was carried out at the research site in September 18<sup>th</sup>, 2004. Several multi-directional flight lines were acquired in a star pattern with an aerial VNIR hyperspectral system AISA Eagle (SPECIM Ltd., Finland). The resulting AISA Eagle images had a pixel size of 0.4m and 64 spectral bands with a Full-Width-Half-Maximum (FWHM) of about 10 nm. Data for the radiometric and atmospheric corrections and for geo-orthorectification of the AISA images were collected simultaneously with the sensor over flight. The digital numbers were transformed into radiance values using sensor calibration files with the CaliGeo software. The atmospheric correction was performed using the ATCOR-4 model (Richter and Schlapfer, 2002). The ATCOR-4 model was also used to correct the brightness reflectance gradient within the airborne images in the across-track direction (BRDF correction). The midpoint of all the flight lines was situated over the testing forest stand. Therefore, we had the opportunity to investigate the influence of the different flight directions (different geometrical set-ups of the sun-object-sensor system) on the  $C_{ab}$  estimation from AISA Eagle images. For this purpose we selected an area of 116 by 110 m that was covered by three flight lines: flight line 1 (flown from East to West), flight line 2 (flown from North to South), and flight line 5 (flown from West to East). These three AISA Eagle testing subsets were classified using a maximum likelihood rule in three classes: background, sunlit and shaded crowns (figure 3). The classification results were used to extract the signal of the sunlit crown pixels employed in  $C_{ab}$  retrieval and to compute the canopy cover (CC) of the observed Norway spruce forest stand (table 1).

2.4 Radiative transfer modelling

The leaf radiative transfer model PROSPECT (Jacquemoud and Baret, 1990) adjusted for Norway spruce needles (Malenovsky et al., 2006) was coupled with the 3D Discrete Anisotropic Radiative Transfer (DART) model (Gastellu-Etchegorry et al., 2004) to simulate hyperspectral images of the Norway spruce scene under investigation..

Parameter	Units	Values
Slope	Deg.	13.5°
Sun angles	Deg.	$\theta_s = 47.8^\circ, \varphi_s = 183.4^\circ$
Canopy cover	%	75, 85, 95
Leaf area index	m <sup>2</sup> m <sup>-2</sup>	4, 5, 6, 7, 8, 9
Chlorophyll content	µg cm <sup>-2</sup>	10, 25, 40, 55, 70, 85
Visible simulated bands	nm	652.1, 661.4, 670.7, 680.1, 689.4
NIR simulated bands	nm	698.7, 708.1, 717.4

Table 1. Basic inputs used for PROSPECT-DART modelling parameterization.

PROSPECT input parameters  $C_m$  (dry matter content;  $C_m = 0.0118\text{-}0.0233\text{ g cm}^{-2}$ ) and  $C_w$  (water content;  $C_w = 0.0365\text{-}0.0486\text{ cm}$ ) were measured on the needle samples collected for the chlorophyll analysis. The structural parameter  $N$  was retrieved from reflectance and transmittance measurements of similar needle samples ( $N = 2.02\text{-}2.08$ ). Chlorophyll content was varying between 10-85 µg cm<sup>-2</sup> according to prior measurements (see table 1).

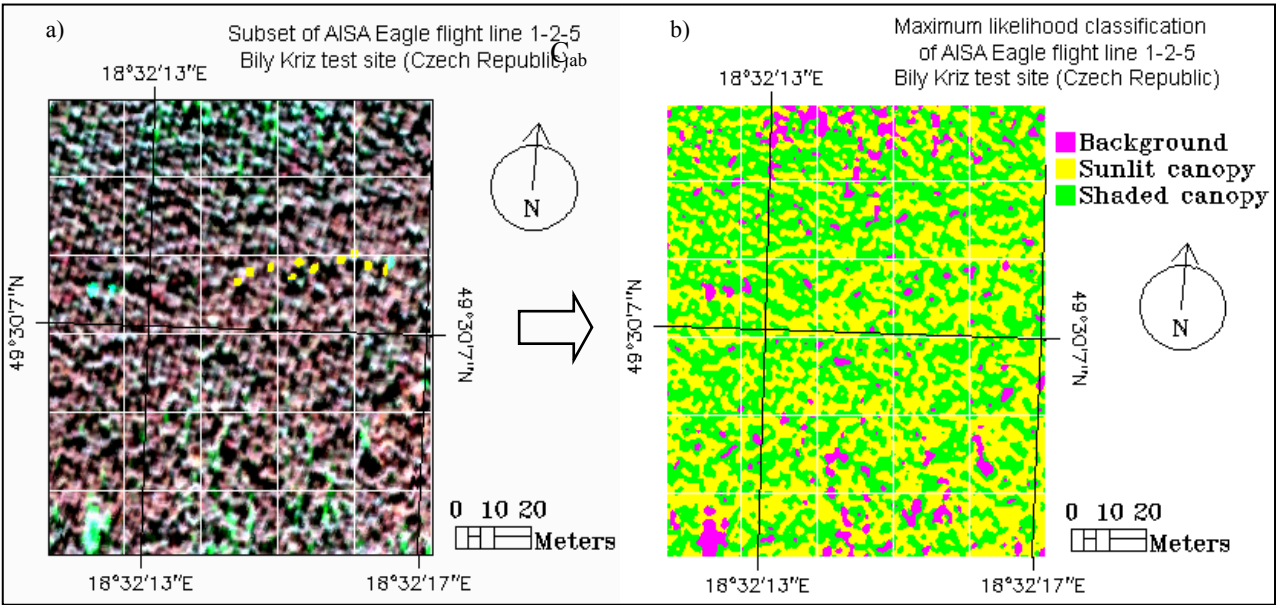


Figure 3. Testing subset of the AISA Eagle flight lines 1, 2, and 5: a) false colour RGB composition (NIR, Red, Green bands) of the Norway spruce test site with ten selected chlorophyll sampling crowns (yellow polygons), and b) thematic map of Maximum Likelihood automatic classification of the testing image subset.

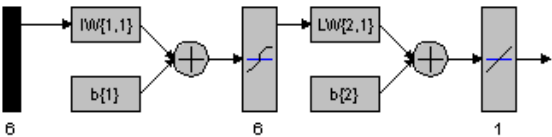


Figure 4. Design of the artificial neuron network (ANN) applied for chlorophyll content estimation ( $C_{ab}$ ).

The DART model was parameterized by means of the ground data obtained at the test site during the ground/flight campaign. Other required allometric and eco-physiological measurements of the tree crowns were obtained from previous field measurements taking place at the same research site earlier in 1997 (Pokorný and Marek, 2000). Three-dimensional representations of a Norway spruce site of an area of 6 by 6 m were constructed using four ( $CC = 75\%$ ), five ( $CC = 85\%$ ), and six ( $CC = 95\%$ ) trees in case of a regular tree distribution and five ( $CC = 75\%$ ), six ( $CC = 85\%$ ), and seven ( $CC = 95\%$ ) trees in case of an irregular (clumped) stem distribution. Each Norway spruce tree, having a total height ranging between 9 – 11 m, was created using 11 crown horizontal levels. For each level were defined specific average leaf angles (from  $25^\circ$  to  $40^\circ$ ) and specific leaf optical properties (reflectance, transmittance, and absorption). The leaf optical properties were simulated using the Norway spruce adjusted PROSPECT model and according to the proportion of the different needle age-classes that were found to be present in each of the crown levels. Destructive field measurements were used to parameterise the vertical and horizontal leaf distributions, spatially specific crown defoliation, the distribution of woody elements (DART uses superimposed parallelepipeds to represent trunks and pyramids to represent branches of first order, i.e. branches that grow directly from the trunk), and the distribution of woody tiny twigs (DART uses turbid media to represent branched smaller than 1 cm in diameter). The forest stand background, covering the continuous slope of  $13.5^\circ$ , was modelled as a mixture of bare soil and needle litter. The optical properties of the other scene surfaces (bark of trunks and branches, and forest background elements) were measured with an ASD FieldSpec Pro spectroradiometer connected to the Li-

Cor integrating sphere Li-1800-12. They were defined in DART as to be of Lambertian nature. The radiative transfer through the atmosphere above the forest stand was not included. Therefore, the spectral bands simulated by DART corresponded to the top of canopy (TOC) bidirectional reflectance function (BRF) recorded by the AISA Eagle bands (mentioned in table 1).

2.5 Chlorophyll estimating methods

The total chlorophyll content of the Norway spruce crowns was estimated from the AISA images using a database of DART simulated images by means of two methods: i) an artificial neural network (ANN) and ii) an optical vegetation index, namely Area under curve Normalized to maximal Chlorophyll absorption Band depth between 650-720 nm ( $ANCB_{650-720}$ ).

2.5.1 Artificial neural network:

The performance of several ANN architectures was tested using the neural network toolbox available in MATLAB®. A two-layer feedforward backpropagation neural network was finally selected for the analysis. A tan-sigmoidal transfer function was used in the first layer and a linear transfer function in the output layer (figure 4). The network was trained using the sunlit DART simulated pixels in the wavelength range from 650 to 720 nm, transformed by means of continuum removal (Kokaly and Clark, 1999; Curran et al., 2001). Before the training of the network, the continuum removed BRF and the  $C_{ab}$  data were pre-processed so that they have a zero mean and a standard deviation of 1. The ANN had six neurons of the first layer, because each input requires a neuron. The output layer consisted of one neuron –  $C_{ab}$  content. The Levenberg-Marquardt optimization algorithm was selected for the training of the network (it is very fast, but it requires a large amount of memory). The 216 DART simulated scenes were split into 3 groups: i) training (50%), ii) validation (25%), and iii) testing (25%) sets. To avoid the so-called overfitting of the ANN, an early stopping technique was used during the training of the network. This means that the validation dataset was presented to the network simultaneously with the training dataset and

when the error of the validation dataset was above a certain threshold then the training of the network was stopped (even though the error of the training dataset might still be declining).

**2.5.2 Chlorophyll vegetation index:** The  $ANCB_{650-720}$  is a variant of the optical index  $ANMB_{650-725}$  (Area under curve Normalized to Maximal Band depth between 650-725 nm), described in detail in Malenovsky et al. (2006). The only difference is that the  $ANCB_{650-720}$  uses a shorter wavelength range (650-720 nm) and that the normalization of the continuum removed area is done using the maximum chlorophyll absorption wavelength (in this case 670.7 nm). The  $ANCB_{650-720}$  computed from the sunlit crown pixels of the DART simulated images was statistically related to the  $C_{ab}$  used during the DART simulations. Finally, the obtained equation was applied to the sunlit pixels of the AISA Eagle images.

### 3. RESULTS AND DISCUSSION

The performance of the trained ANN was assessed using the testing dataset. Results were quite satisfactory:  $R^2$  equal 0.9988 and root-mean-square-error (RMSE) equal to  $0.40 \mu\text{g}\cdot\text{cm}^{-2}$ . The  $ANCB_{650-720}$  statistical exponential relationship established using the DART simulated images was:

$$\ln(C_{ab}) = 7.3903 - 7984.0135 / (ANCB_{650-720})^2 \quad (1)$$

with an  $R^2$  of 0.9989.

#### 3.1 Crown chlorophyll estimation

Figure 5 illustrates the validation of chlorophyll content that was estimated for each of the sampled crown used to create the validation dataset. The graphs show that both methods, applied to the three AISA flight lines, gave very similar results. The RMSE between measured and retrieved  $C_{ab}$  values was found to be about  $3 \mu\text{g}\cdot\text{cm}^{-2}$  for both methods. An outlier was identified with both methods (see graphs A, B). This point corresponds to a crown that grows next to a highly reflective metal meteorological tower. Apparently the reflectance of this tower contaminated the spectral signature of this crown and caused the  $C_{ab}$  overestimation. In general, the  $ANCB_{650-720}$  index yielded lower  $C_{ab}$  estimates for low chlorophyll concentrations, while the estimates for high  $C_{ab}$  concentrations were fitting well with the results found for the ANN approach (see graph C). Comparison with the ground truth measurements suggests that the  $ANCB_{650-720}$  approach is less accurate and probably less sensitive to retrieve lower chlorophyll content values. Finally,

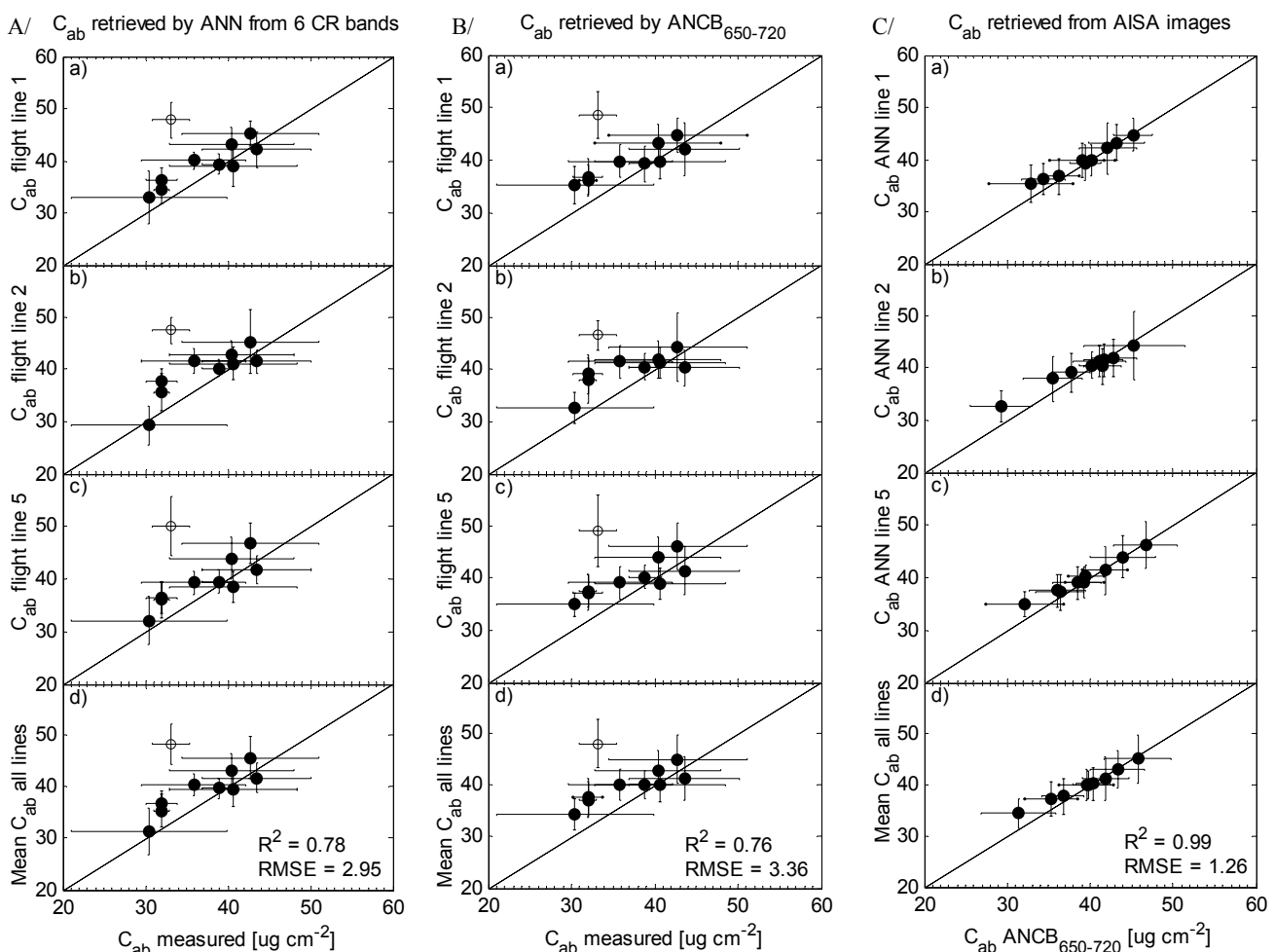


Figure 5. Validation of chlorophyll content ( $C_{ab}$ ) retrieved for ten sampled spruce crowns from the AISA Eagle flight line 1 (a), flight line 2 (b), flight line 5 (c), and mean values of all three flight lines (d) using: A/ an artificial neural network (ANN), B/ optical index  $ANCB_{650-720}$ , and C/ reciprocal comparison of both methods. (Each dot symbol represents one tree crown, empty dot means an outlier, horizontal bars represent two standard deviations of measured  $C_{ab}$  values (A,B) or retrieved by  $ANCB_{650-720}$  (C), and vertical bars represent two standard deviations of  $C_{ab}$  values estimated by ANN (A,C) and  $ANCB_{650-720}$  (B). Solid line represents a one-to-one relationship,  $R^2$  = coefficient of determination, RMSE = root mean square error).

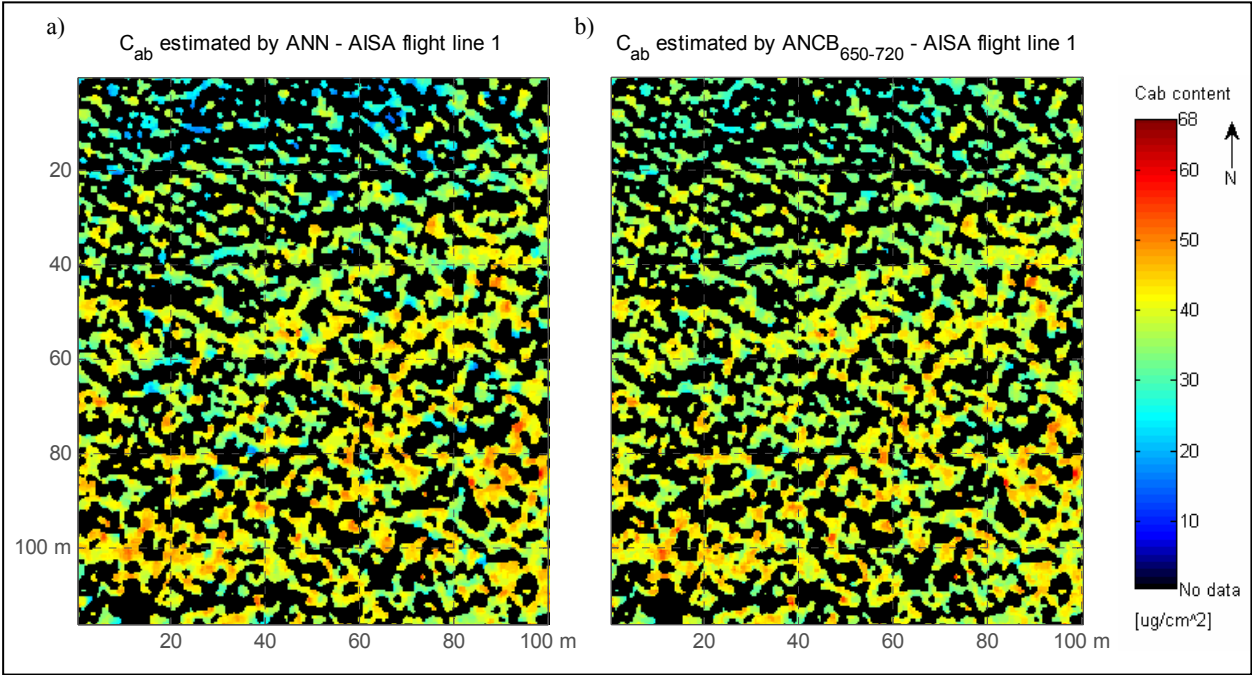


Figure 6. Maps of chlorophyll content ( $C_{ab}$ ) retrieved from sunlit Norway spruce crown pixels of the AISA Eagle testing subset (flight line 1) by means of: a) an artificial neural network (ANN), b) the optical index ANCB<sub>650-720</sub>. (Black colour indicates non-analysed shaded canopy and background).

we did not see significant differences in crown  $C_{ab}$  estimated from the different AISA flight lines. Therefore, one can conclude that both methods are most likely independent of the sun-object-sensor system set-up. Nevertheless, these methods also need to be tested for more geometrically heterogeneous ecosystems, e.g., mature Norway spruce stand with lower fractional canopy cover and significant portion of the understory, to support this conclusion.

3.2 Canopy chlorophyll estimation

The results of the chlorophyll estimation for the flight line 1 are shown in figure 6. A spatial pattern of these maps, similar for both retrieval methods, reveals lower  $C_{ab}$  values at the northern part and higher  $C_{ab}$  estimates at the southern part of the tested AISA subset. A comparable spatial pattern was found also for the flight lines 2 and 5 (maps not presented). Subtraction of the ANCB<sub>65-720</sub> chlorophyll map from the one produced using ANN resulted in an almost symmetrical Gaussian distribution (figure 7a). However, the high frequencies found for the positive differences mean that the ANCB<sub>65-720</sub> estimates are in general higher than the estimated obtained with ANN. Those positive differences mainly correspond with the lower  $C_{ab}$  content values, as already shown in the previous section of the crown level results. Looking at the absolute differences between the chlorophyll content retrieved by the ANCB<sub>65-720</sub> and the ANN, one can see that about 80% of all investigated pixels contained chlorophyll of the same concentration or plus/minus  $2 \mu\text{g}\cdot\text{cm}^{-2}$  in maximum. Next 10% of the pixels were different by means of about plus/minus  $4 \mu\text{g}\cdot\text{cm}^{-2}$  and the remaining 10% represented differences of plus/minus 6 to  $10 \mu\text{g}\cdot\text{cm}^{-2}$  (see figure 7b). The mean difference was found to be around  $1.8 \mu\text{g}\cdot\text{cm}^{-2}$ . Similar results were also obtained when analyzing the testing subsets of the AISA flight lines 2 and 5. These findings support a hypothesis that the sun-object-sensor geometrical set-up does not play an important role when retrieving green foliar

pigments from hyperspectral data of spatial resolution below 1 m.

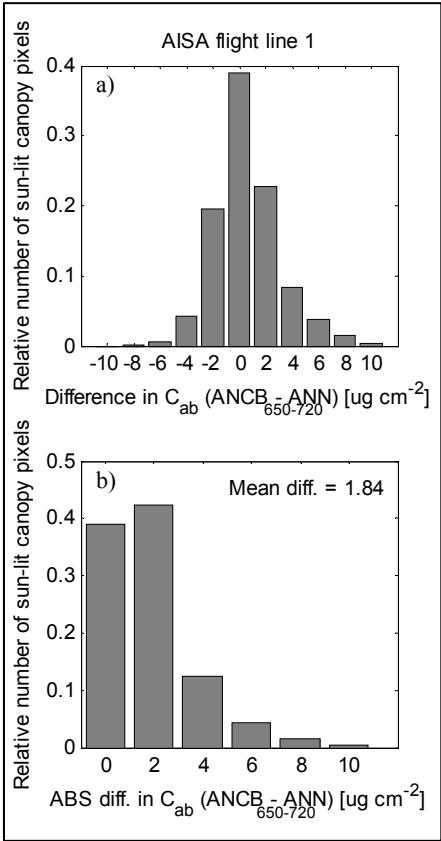


Figure 7. Histograms counting: a) differences, and b) absolute differences of the ANCB<sub>650-720</sub> and ANN chlorophyll maps produced for the testing subset of AISA flight line 1.



#### 4. CONCLUSIONS

In this paper we have tested two physically based methods to retrieve the total chlorophyll content of a complex Norway spruce canopy from hyperspectral data acquired at very high spatial resolution (pixel size of 0.4 m). The first method was based on an ANN inversion of a number of PROSPECT-DART model simulations. The second method exploited a physically inspired vegetation index trained with the radiative transfer simulations that were used for the ANN inversion. The following main conclusions can be drawn from results of this study:

- The  $C_{ab}$  content estimated by the ANN and the ANCB<sub>650-720</sub> approaches was consistent at crown and canopy level, and also comparable with the measured ground truth.
- The spatial pattern of  $C_{ab}$  estimates was similar for all tested flight directions.
- The continuum removal transformation was successfully used to minimize residual differences between the PROSPECT-DART simulated reflectance and reflectance of the real hyperspectral images.
- Pure vegetation reflectance is needed for an accurate  $C_{ab}$  estimation by means of both tested retrieving methods.
- The ANCB<sub>650-720</sub> does not seem to be sufficiently sensitive to retrieve low  $C_{ab}$  values.

#### 5. REFERENCES

- Curran, P.J., Dungan, J.L. and Peterson, D.L., 2001. Estimating the foliar biochemical concentration of leaves with reflectance spectrometry: Testing the Kokaly and Clark methodologies. *Remote Sensing of Environment*, 76(3), pp. 349-359.
- Daughtry, C.S.T., Walthall, C.L., Kim, M.S., de Colstoun, E. and Brown McMurtreyIII, J.E., 2000. Estimating corn leaf chlorophyll concentration from leaf and canopy reflectance. *Remote Sensing of Environment*, 74(2), pp. 229-239.
- Gascon, F., Gastellu-Etchegorry, J.P., Lefevre-Fonollosa, M.J. and Dufrene, E., 2004. Retrieval of forest biophysical variables by inverting a 3-D radiative transfer model and using high and very high resolution imagery. *International Journal of Remote Sensing*, 25(24), pp. 5601-5616.
- Gastellu-Etchegorry, J.P., Martin, E. and Gascon, F., 2004. DART: a 3D model for simulating satellite images and studying surface radiation budget. *International Journal of Remote Sensing*, 25(1), pp. 73-96.
- Gitelson, A.A., Vina, A., Verma, S.B., Rundquist, D.C., Arkebauer, T.J., Keydan, G., Leavitt, B., Ciganda, V., Burba, G.G. and Suyker, A.E., 2006. Relationship between gross primary production and chlorophyll content in crops: Implications for the synoptic monitoring of vegetation productivity. *Journal of Geophysical Research-Atmospheres*, 111(D8), pp. 1-13.
- Haboudane, D., Miller, J.R., Tremblay, N., Zarco-Tejada, P.J. and Dextraze, L., 2002. Integrated narrow-band vegetation indices for prediction of crop chlorophyll content for application to precision agriculture. *Remote Sensing of Environment*, 81(2-3), pp. 416-426.
- Jacquemoud, S. and Baret, F., 1990. Prospect - a Model of Leaf Optical-Properties Spectra. *Remote Sensing of Environment*, 34(2), pp. 75-91.
- Kokaly, R.F. and Clark, R.N., 1999. Spectroscopic determination of leaf biochemistry using band-depth analysis of absorption features and stepwise multiple linear regression. *Remote Sensing of Environment*, 67(3), pp. 267-287.
- le Maire, G., Francois, C. and Dufrene, E., 2004. Towards universal broad leaf chlorophyll indices using PROSPECT simulated database and hyperspectral reflectance measurements. *Remote Sensing of Environment*, 89(1), pp. 1-28.
- Malenovsky, Z., Albrechtova, J., Lhotakova, Z., Zurita-Milla, R., Clevers, J.G.P.W., Schaepman, M.E. and Cudlin, P., 2006. Applicability of the PROSPECT model for Norway spruce needles. *International Journal of Remote Sensing*, 27(23-24), pp. 5315-5340.
- Malenovsky, Z., Ufer, C.M., Lhotakova, Z., Clevers, J.G.P.W., Schaepman, M.E., Albrechtova, J. and Cudlin, P., 2006. A new hyperspectral index for chlorophyll estimation of a forest canopy: Area under curve Normalized to Maximal Band depth between 650-725 nm. *EARSeL eProceedings*, 5, pp. 161-172.
- Pokorný, R. and Marek, M.V., 2000. Test of accuracy of LAI estimation by LAI-2000 under artificially changed leaf to wood area proportions. *Biologia Plantarum*, 43(4), pp. 537-544.
- Richter, R. and Schlapfer, D., 2002. Geo-atmospheric processing of airborne imaging spectrometry data. Part 2: atmospheric/topographic correction. *International Journal of Remote Sensing*, 23(13), pp. 2631-2649.
- Zarco-Tejada, P.J., Miller, J.R., Harron, J., Hu, B., Noland, T.L., Goel, N., Mohammed, G.H. and Sampson, P., 2004. Needle chlorophyll content estimation through model inversion using hyperspectral data from boreal conifer forest canopies. *Remote Sensing of Environment*, 89(2), pp. 189-199.

#### 6. ACKNOWLEDGEMENT

This work was supported by the ESA/PECS project No. 98029 and the Research Plan AV0Z60870520 of the Institute of Systems Biology and Ecology, Academy of Sciences of the Czech Republic, v.v.i. Authors would like to acknowledge the access to the CESNET METACentrum computing cluster facilities (Brno, Czech Republic), provided under the research intent MSM6383917201.

# STOCHASTIC RADIATIVE TRANSFER MODEL FOR MIXTURE OF DISCONTINUOUS VEGETATION CANOPIES

Nikolay V. Shabanov<sup>a</sup>, D. Huang<sup>b</sup>, Y. Knjazikhin<sup>a</sup>, and Ranga B. Myneni<sup>a</sup>

<sup>a</sup>Department of Geography, Boston University, Boston, MA, 02215, USA – (shabanov, jknjazi, rmyneni)@bu.edu

<sup>b</sup>Brookhaven National Laboratory, Environmental Sciences Department, P.O. Box 5000, Upton, NY, 11973, USA – dhuang@bnl.gov

**KEY WORDS:** Radiative Transfer, Theory, Three-dimensional effects, vegetation structure, mixture modeling.

## ABSTRACT:

Modeling of the radiation regime of a mixture of vegetation species is a fundamental problem of the Earth's land remote sensing and climate applications. The major existing approaches, including the linear mixture model and the turbid medium mixture Radiative Transfer model, provide only an approximate solution to this problem. In this study we developed the Stochastic Mixture Radiative Transfer (SMRT) model, a mathematically exact tool to evaluate radiation regime in a natural canopy with spatially varying optical properties (mixture of vegetation species and gaps). The model solves for the radiation quantities, direct input to the remote sensing/climate applications: mean radiation fluxes over whole mixture and over individual species. The canopy structure is parameterized in the SMRT model in terms of two stochastic moments: the probability of finding species and the conditional pair-correlation of species. We performed analytical and numerical analysis of the radiation effects, simulated with the SMRT model for the three cases of canopy structure: a) non-ordered mixture of species and gaps (turbid medium); b) ordered mixture of species without gaps; c) ordered mixture of species with gaps. The analysis indicates that the variation of radiation fluxes between different species is proportional to the variation of species optical properties. Gaps introduce significant disturbance to the radiation regime in the canopy as their optical properties constitute major contrast to those of any vegetation species. The SMRT model resolves deficiencies of the major existing mixture models: ignorance of species radiation coupling via multiple scattering of photons (the linear mixture model) or overestimation of this coupling due to neglecting spatial clumping of species (the turbid medium approach). Overall, this study establishes an advanced theoretical basis for future mixture applications.

## 1. INTRODUCTION

Natural vegetation exhibits significant degree of spatial heterogeneity, which complicates retrieval of the Earth's land biophysical parameters from remote sensing observations. Advances in remote sensing technology, including improved geolocation, sensor optics calibration, atmospheric correction, multi-resolution, multi-spectral and multi-angular measurements, etc., provide better means to capture land surface heterogeneity. In fact, current suite of NASA's MODerate resolution Imaging Spectroradiometer (MODIS) land products already includes a product, which explicitly characterizes mixture of land cover types- vegetation continuous fields (WWW1).

The problem of mixture of vegetation species is known in remote sensing as a scaling issue, that is, given biophysical parameters and radiation field over pure species at sub-pixel scale one needs to estimate those parameters at the scale of a mixed pixel. Multiple approaches were developed to address the scaling issue, which can be grouped into two basic categories: empirical/statistical and physically-based. The approaches from the first category are widely used for sub-pixel land cover characterization: linear mixture models (DeFries et al., 1999), neural networks (Carpenter et al., 1999), Gaussian mixture discriminant analysis, decision trees and others. The key idea of the above methods is to model satellite measured radiation over a mixed pixel as a weighted sum of the radiation fields over pure classes. Linear and non-linear models were implemented to retrieve the unknown weights, corresponding to the proportion of pure land cover classes in the mixed pixel. It was noted, however, that species in a mixture may exhibit

significant degree of radiative interaction, which may bias retrievals especially in the case of linear models (Borel & Gerstl, 1994).

In contrast to the empirical methods, physically-based approaches describe in details the physical processes of interaction of radiation with canopy at the level of elementary volume of vegetation. Optical properties of a mixture in such volume are represented as weighted average of optical properties of pure species. The Radiative Transfer Equation (RTE) is used to model the radiation field with effective optical properties of mixed canopy. The above modeling principles were implemented, for instance, in a scaling scheme of the radiation block of the Common Land Model (CLM) (WWW2, Tian et al., 2003) and the MODIS Leaf Area Index (LAI) algorithm (Tian et al., 2002). The major limitation of the above schemes is that they are based on the turbid medium mixture approximation, where canopy is represented as a mixed gas of vegetation species and gaps. With the turbid medium approach, one major feature of the natural vegetation is missing- spatial structure of a mixture, which may substantially affect radiation regime.

This study is aimed to advance theoretical description of the radiation regime in vegetation canopy under condition of spatial gradient of canopy optical properties. Applications in focus include the above mentioned radiation block of CLM and the MODIS LAI algorithm. The spatial heterogeneity of a medium can be incorporated in the standard RT equation using the stochastic approach, which was originally formulated for broken clouds by Vainikko (1973a,b) and further developed by Titov (1991) and others. Additional closely related theoretical

study is the linear kinetic theory of stochastic mixture, developed by Pomraning (1991). In our former research (Shabanov et al., 2000, Huang et al., 2007) we adopted Vainikko-Titov approach for vegetation canopy and formulated the Stochastic RT (SRT) model for a single spatially discontinuous species. In the present work (Shabanov et al., 2007) we introduce a Stochastic Mixture RT (SMRT) model, an extension of the former model for the case of the structured composition of multiple vegetation species and gaps.

## 2. THE APPROACH

Consider 3D heterogeneous vegetation canopy, a mixture of  $N$  different vegetation species and gaps. The spatial structure of such canopy can be characterized by the indicator function of a canopy,  $\chi(\vec{r})$ , defined for each spatial location,  $\vec{r}$ , as follows:

$$\chi(\vec{r}) = \sum_j \chi^{(j)}(\vec{r}), \quad (1a)$$

where  $\chi^{(j)}(\vec{r})$  is an indicator function of the individual species 'j':

$$\chi^{(j)}(\vec{r}) = \begin{cases} 1, & \text{if } \vec{r} \in \text{species "j"}, j=1, N, \\ 0, & \text{otherwise.} \end{cases} \quad (1b)$$

The equations above specify overall architecture of vegetation canopy as cumulative contribution of individual species in a mixture. The indicator function is assumed to be a random variable. We further assume that a particular spatial location is occupied only by a single species, i.e.,

$$\chi^{(i)}(\vec{r}) \cdot \chi^{(j)}(\vec{r}) = 0, i \neq j.$$

Density of canopy is defined by the Leaf Area Index (LAI) – one-sided green leaf area per unit ground area [ $\text{m}^2/\text{m}^2$ ]. In the case of mixture of species,

$$\text{LAI} = \frac{1}{S} \int_V d\vec{r} d_L(\vec{r}) = \sum_j \frac{1}{S} \int_V d\vec{r} d_L^{(j)} \chi^{(j)}(\vec{r}) = \sum_j \text{LAI}^{(j)}, \quad (2)$$

where  $d_L^{(j)}$  and  $\text{LAI}^{(j)}$  are one-sided foliage area volume density [ $\text{m}^2/\text{m}^3$ ] and LAI of species 'j', respectively, and the integration is performed over a volume of canopy,  $V$ , with a footprint,  $S$ . The interaction of radiation with species leaves is characterized by spatially varying extinction coefficient  $\sigma(\vec{r}, \vec{\Omega})$  and differential scattering coefficient,  $\sigma_S(\vec{r}, \vec{\Omega}' \rightarrow \vec{\Omega})$ , (Ross, 1981),

$$\sigma(\vec{r}, \vec{\Omega}) = \sum_j \sigma^{(j)}(\vec{\Omega}) \chi^{(j)}(\vec{r}) = \sum_j d_L^{(j)} \chi^{(j)}(\vec{r}) G^{(j)}(\vec{\Omega}), \quad (3a)$$

$$\begin{aligned} \sigma_S(\vec{r}, \vec{\Omega}' \rightarrow \vec{\Omega}) &= \sum_j \sigma_S^{(j)}(\vec{\Omega}' \rightarrow \vec{\Omega}) \chi^{(j)}(\vec{r}) \\ &= \sum_j \frac{d_L^{(j)} \cdot \chi^{(j)}(\vec{r})}{\pi} \cdot \Gamma^{(j)}(\vec{\Omega}' \rightarrow \vec{\Omega}), \end{aligned} \quad (3b)$$

where  $G^{(j)}(\vec{\Omega})$  is the mean projection of leaf normals in the direction  $\vec{\Omega}$  and  $\Gamma^{(j)}(\vec{\Omega}' \rightarrow \vec{\Omega})$  is the area scattering phase function for species 'j' (Ross, 1981). The above parameters depend on the probability density of leaf normal orientation,  $g_L(\vec{r}, \vec{\Omega}_L)$ , ( $\vec{\Omega}_L$  is a leaf normal direction) and the spectral leaf

albedo,  $\omega(\vec{r}, \lambda)$  ( $\lambda$  is a wavelength) (Ross, 1981). Given the set of structural and optical parameters, the radiation regime in a vegetation canopy is described by the following 3D transport equation for radiation intensity,  $I(\vec{r}, \vec{\Omega})$ :

$$\begin{aligned} \Omega \nabla I(\vec{r}, \vec{\Omega}) + \sigma(\vec{r}, \vec{\Omega}) I(\vec{r}, \vec{\Omega}) \\ = \int_{4\pi} d\vec{\Omega}' \sigma_S(\vec{r}, \vec{\Omega}' \rightarrow \vec{\Omega}) I(\vec{r}, \vec{\Omega}'). \end{aligned} \quad (4)$$

The unique solution of the Eq. (4) is specified by the boundary conditions.

The detailed evaluation of the 3D radiation field is computationally expensive and often unnecessary for multiple applications. Namely, in application to satellite remote sensing, radiation field, averaged over a pixel is required. The stochastic approach to the radiative transfer directly addresses the above problem, by averaging the 3D RT equation (Eq. (5)) over a horizontal plane. Thus, the average 1D equation for the average radiation intensities is obtained. The mathematical formulation of the stochastic RT equation requires two types of averages:

(1)  $U^{(i)}(z, \vec{\Omega})$ , mean intensity over the portion of the horizontal plane at depth  $z$ , occupied by species 'i'; (2)  $\bar{I}(z, \vec{\Omega})$ , mean intensity over the total space of the horizontal plane at depth  $z$ ,

$$\begin{aligned} U^{(i)}(z, \vec{\Omega}) &= \lim_{R \rightarrow \infty} \frac{1}{S_R \cap T_z^{(i)}} \iint_{S_R} dx dy \chi^{(i)}(x, y, z) I(x, y, z, \vec{\Omega}), \\ \bar{I}(z, \vec{\Omega}) &= \lim_{R \rightarrow \infty} \frac{1}{S_R} \iint_{S_R} dx dy I(x, y, z, \vec{\Omega}). \end{aligned} \quad (5)$$

In the above,  $S_R$  denotes the area of a circle of radius  $R$ ;  $T_z^{(i)}$  denotes the area of the horizontal plane at depth  $z$ , occupied by species 'i'. In the framework of stochastic mixture, gaps can be treated as special type of vegetation species, optical properties of which are set to zero. Thus, in the case of  $N$  vegetation species we have  $U^{(i)}(z, \vec{\Omega})$ ,  $i=1, N$  and  $U^{(\text{gap})}(z, \vec{\Omega})$ .

The averaging procedure results in the parameterization of the resulting transfer equation in terms of two stochastic moments of a vegetation structure. The first stochastic moment is the probability,  $p$ , of finding species "i" at canopy depth  $z$ ,

$$p^{(i)}(z) = \lim_{R \rightarrow \infty} \frac{1}{S_R} \iint_{S_R \cap T_z^{(i)}} \chi^{(i)}(z, x, y) dx dy \equiv \lim_{R \rightarrow \infty} \frac{S_R \cap T_z^{(i)}}{S_R}. \quad (3)$$

The second moment is the pair-correlation function,  $q$ , between species 'i' at canopy depth  $z$  and species 'j' at depth  $\xi$  along the direction  $\vec{\Omega}$ ,

$$q^{(i,j)}(z, \xi, \vec{\Omega}) = \lim_{R \rightarrow \infty} \frac{S_R \cap T_z^{(i)} \cap T_\xi^{(j)}[\Delta \vec{r}]}{S_R}, \quad (4)$$

where

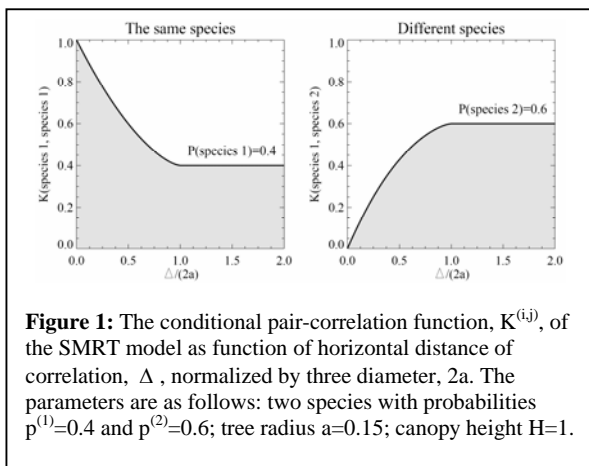
$$\Delta \vec{r} = \frac{\Omega_x}{\Omega_z} (z - \xi), \frac{\Omega_y}{\Omega_z} (z - \xi)$$

and  $\Omega_x$ ,  $\Omega_y$ , and  $\Omega_z$  are projections of a unit direction

vector,  $\vec{\Omega}$ , on the x, y, and z axes, respectively. Argument for  $T_{\xi}^{(j)}$  denotes a shift of the origin of plane  $\xi$  relative to plane z along x and y directions, required to evaluate correlation between the planes in direction  $\vec{\Omega}$ . Using the first and second moments of a vegetation structure, the conditional pair-correlation of species,  $K^{(i,j)}$ , can be evaluated as

$$K^{(i,j)}(z, \xi, \vec{\Omega}) = \frac{q^{(i,j)}(z, \xi, \vec{\Omega})}{p^{(i)}(z)}. \quad (5)$$

The two stochastic moments are key parameters of the stochastic approach, responsible for 3D radiation effects arising from non-homogeneity (3D structure) of vegetation canopy. The amount of gaps is controlled by the probability of finding species  $p^{(i)}$  (Eq. 3), while canopy structure (order/chaoticity) is controlled by the conditional pair-correlation of species,  $K^{(i,j)}$ , (Eq. 5).

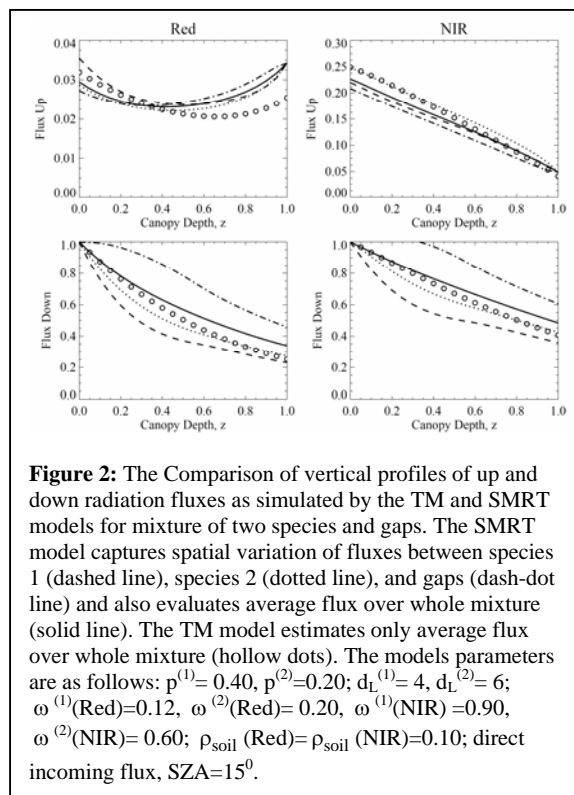


The conditional pair-correlation function can be derived according to the theory of stochastic geometry (Stoyan, Kendall, Mecke, 1995). This approach was utilized recently to derive the conditional pair-correlation function for single species (Huang et al., 2007). In this research we extended derivations to a mixture of multiple species (Shabanov et al., 2007). The derivations are based on the following assumptions about 3D stochastic canopy structure: a) tree species are modeled as identical cylinders; b) distribution of the tree centers follows stationary Poisson point process (Stoyan, Kendall, Mecke, 1995). The conditional pair-correlation function for two species is shown in Fig. 1. In the case of the same species, correlation decreases as distance increases. This corresponds to increasing probability of one of the points being out of the same crown as distance increases. In the case of different species, correlation increases as distance increases. This corresponds to increasing probability of two points to be located in different crowns of different species with increasing distance. In the case of short distances, within-species correlation is 1, while between-species correlation is 0. In the case of large distances, correlation between any species is vanishing and  $K^{(i,j)}$  converges to  $p^{(i)}$ . Both limiting cases are intuitively expected and captured by the proposed model.

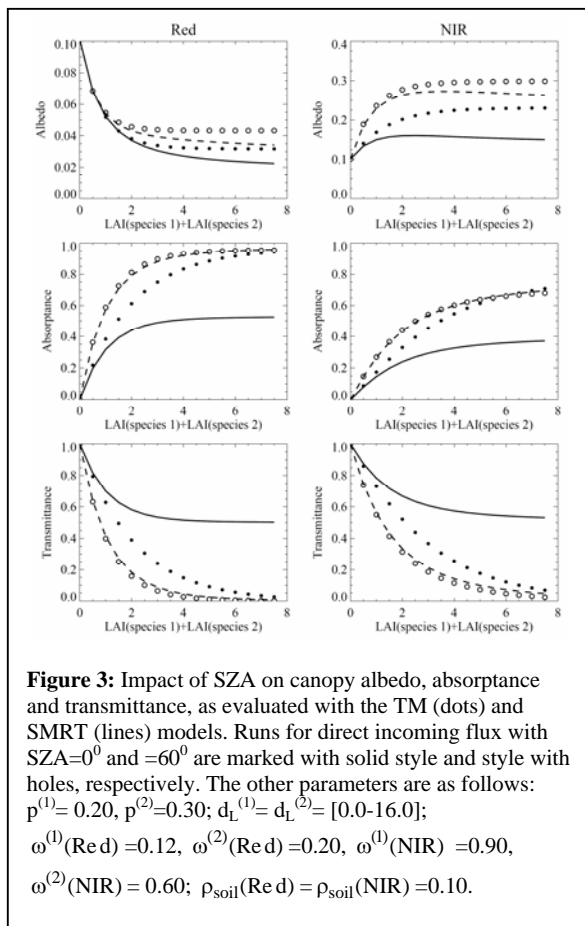
### 3. ANALYSIS

The SMRT equations were derived and implemented numerically using Successive Orders of Scattering

Approximations (SOSA) (Shabanov et al., 2007). The analytical analysis of the SMRT model is beyond the scope of this paper and details can be found in Shabanov et al., (2007). Here we review some results of numerical analysis of 3D radiation effects, resulting from 3D canopy structure. We simulated three key classes of canopy structure as captured by stochastic moments of structure: a) non-ordered/chaotic mixture of species and gaps or turbid medium ( $K^{(i,j)}=p^{(i)}$ ); b) ordered mixture of species without gaps ( $\sum_j p^{(j)}=1$ ); c) ordered mixture of species with gaps ( $K^{(i,j)} \neq p^{(i)}$ ,  $\sum_j p^{(j)} \neq 1$ ). In the analysis below, we contrast the SMRT simulations under condition of canopy structure ("SMRT", cases b and c) with turbid medium model simulations ("TM", case a). Both cases were implemented with the same set of stochastic equations and input parameters, except the conditional pair-correlation function: the analytical expression for cylindrical trees (Shabanov et al., 2007) was used to implement the SMRT model, while  $K^{(i,j)}=p^{(i)}$  was used for the TM model.



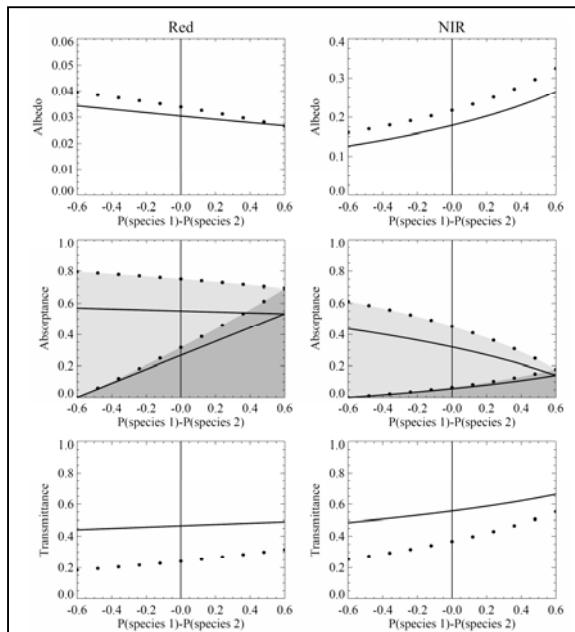
To understand the overall merits of the new model consider radiation fluxes as function of canopy depth, as shown in Fig. 2. The SMRT model differentiates between radiation fluxes over individual species, gaps, and whole mixture (corresponding to mean intensities  $U^{(i)}$ ,  $U^{(\text{gap})}$ ,  $\bar{I}$ ). The TM model provides no distinction between the above fluxes. According to the SMRT model, variation of the fluxes between individual vegetation species is relatively smaller compared to difference in fluxes between vegetation and gaps. Also note, that limitations of the TM model result in a bias (both overestimation and underestimation) in estimation of mean fluxes over whole mixture compared to the SMRT simulations (compare fluxes over whole mixture). Detailed analysis of the impact of various parameters on the SMRT and TM models simulations is presented with four case studies below (Figs. 3-6).



**Figure 3:** Impact of SZA on canopy albedo, absorbance and transmittance, as evaluated with the TM (dots) and SMRT (lines) models. Runs for direct incoming flux with  $SZA=0^\circ$  and  $=60^\circ$  are marked with solid style and style with holes, respectively. The other parameters are as follows:  $p^{(1)}=0.20$ ,  $p^{(2)}=0.30$ ;  $d_L^{(1)}=d_L^{(2)}=[0.0-16.0]$ ;  $\omega^{(1)}(\text{Red})=0.12$ ,  $\omega^{(2)}(\text{Red})=0.20$ ,  $\omega^{(1)}(\text{NIR})=0.90$ ,  $\omega^{(2)}(\text{NIR})=0.60$ ;  $\rho_{\text{soil}}(\text{Red})=\rho_{\text{soil}}(\text{NIR})=0.10$ .

First, consider impact of Solar Zenith Angle (SZA) on canopy albedo, absorbance and transmittance as function of LAI, as simulated with the SMRT and TM models at Red and NIR wavelengths (Fig. 3). The simulations were performed with SZA of  $0^\circ$  and  $60^\circ$ . Two vegetation species with gaps were used:  $p^{(1)}=0.2$ ,  $p^{(2)}=0.3$ ,  $p^{(\text{gap})}=0.5$ . The complete set of parameters is presented in the figure caption. In the case of simulations for  $SZA=0^\circ$ , the SMRT model predicts lower albedo, substantially lower absorbance and substantially higher transmittance compared to the TM model. However, at  $SZA=60^\circ$  both models demonstrate quite similar results. The key physical explanation for the difference between the SMRT and TM simulations at  $SZA=0^\circ$  is that the SMRT model accounts for radiation streaming through gaps without interaction with vegetation. This explains results for absorbance and transmittance. Albedo is lower in the case of the SMRT compared to the TM model, because in the former case a dark soil is better exposed through gaps in a relatively bright vegetation (compare  $\rho_{\text{soil}}$  and  $\omega$ ). Note the difference in models prediction for a limiting case of high LAI (cf. case for Red wavelength,  $SZA=0^\circ$ ). In the case of the SMRT model, canopy transmittance for high LAI approaches to 0.5, which corresponds to radiation streaming through gaps in the amount of  $1-(p^{(1)}+p^{(2)})$ . In contrast, in the case of the TM model, transmittance converges to 0, which is a consequence of lack of gaps in the TM model formulation. Next, we explain results for  $SZA=60^\circ$ . In this case the effect of radiation streaming is negligible: even if photon enters canopy through a gap, it will be intercepted by a lateral surface of tree foliage. Mathematically, the reasoning is as follows: as angle is

increasing, effective distance between vegetation elements,  $\Delta$ , is increasing, which results in convergence of the conditional pair-correlation function for ordered species to one for non-ordered species (cf. Fig 1).



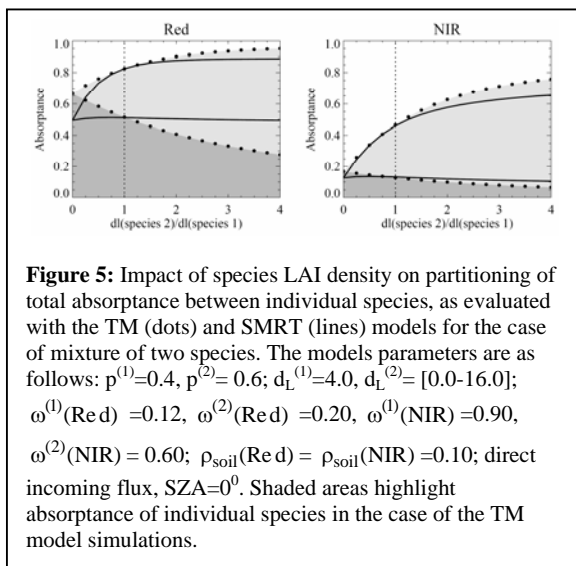
**Figure 4:** Impact of species composition on canopy albedo, absorbance and transmittance, as evaluated with the TM (dots) and SMRT (lines) models for the case of mixture of two species. The models parameters are as follows:  $p^{(1)}+p^{(2)}=0.60$ ;  $d_L^{(1)}=4.0$ ,  $d_L^{(2)}=6.0$ ;  $\omega^{(1)}(\text{Red})=0.12$ ,  $\omega^{(2)}(\text{Red})=0.20$ ,  $\omega^{(1)}(\text{NIR})=0.90$ ,  $\omega^{(2)}(\text{NIR})=0.60$ ;  $\rho_{\text{soil}}(\text{Red})=\rho_{\text{soil}}(\text{NIR})=0.10$ ; direct incoming flux,  $SZA=0^\circ$ . Shaded areas highlight absorbance of individual species in the case of the TM model simulations.

Second, consider the impact of species composition on a radiation regime (Fig. 4). Here we used two species with optical properties roughly corresponding to broadleaf (species 1) and needle leaf (species 2) forests, which have substantial contrast both at Red and NIR wavelengths. The probability of each species ( $p^{(1)}$  and  $p^{(2)}$ ) was varying from 0 up to 0.6, under restriction, that total probability of all species is constant through the simulations, i.e.,  $p^{(1)}+p^{(2)}=0.6=\text{fixed}$ . Thus, radiation regime was evaluated for all possible combinations of two species under significant amount of gaps,  $p^{(\text{gap})}=0.4=\text{fixed}$ . Our results indicate that both the TM and SMRT models simulate continuous, fairly large variation of canopy albedo, absorbance and transmittance with respect to species composition. However, the TM model introduces a significant bias in the estimation of the above parameters due to ignoring canopy structure. Finally, note that variations of canopy albedo, absorbance and transmittance with respect to species compositions are quite close to linear at Red wavelength, but demonstrate fairly large deviation from linearity at NIR wavelength.

In the third case study we probed deeper special case of mixture of species without gaps (cf. Fig. 5). Intuitively, in the case of no gaps, ordered mixture of species is quite close to non-ordered mixture (turbid medium). In this simulation we addressed two

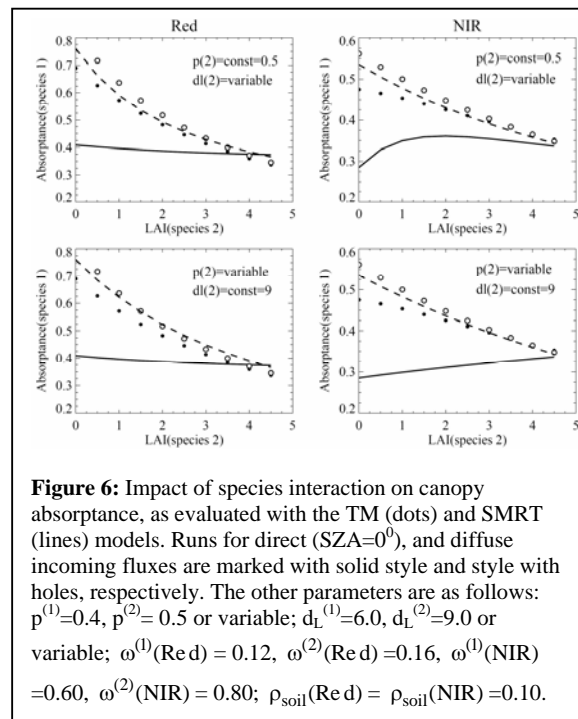


questions: a) When ordered mixture of species is important? b) Why gaps significantly perturb radiation field of ordered mixture of species? As mentioned earlier, key feature of vegetation structure, which differentiates between ordered and non-ordered cases is a presence of spatial gradient of optical properties of a medium (such as leaf albedo, density of LAI, etc). If the medium is ordered, the spatial gradient of the optical properties should be significant enough to modify the radiation regime of the SMRT simulations with respect to the TM simulations. Optical properties of gaps constitute especially large contrast to ones of any vegetation species. This explains special role of gaps in the SMRT simulations. The variation of the optical properties of vegetation species is as follows: leaf albedo may vary by factor of 2 in majority of cases, while variation in the foliage area volume density may be arbitrary large. Our test runs (not presented here) indicate no significant difference between the SMRT and TM simulations as function of variations of leaf albedo for typical vegetation canopies. Simulations for two species with varying foliage area volume density ( $d_L^{(1)}$  and  $d_L^{(2)}$ ) indicate significant bias in the estimation of absorbance by the TM model with respect to the SMRT model when  $d_L^{(2)}/d_L^{(1)}=0$ , no difference when  $d_L^{(2)}/d_L^{(1)}=1$ , and increasing bias with respect to increasing contrast in the foliage area volume density of species (Fig. 5). Note that the TM model introduces bias not only to total absorbance but also to the partitioning of total canopy absorbance between species.



Next, consider the fourth case study, demonstrating the effect of species interaction (Fig. 6). Here we evaluated the impact of LAI changes of species 2 on the absorbance of species 1. The LAI of species 2 was constructed according to two scenarios: a) keep  $p^{(2)}$  constant and vary  $d_L^{(2)}$  (top two panels for Red and NIR wavelengths); b) keep  $d_L^{(2)}$  constant and vary  $p^{(2)}$  (lower panels). We also used two illumination conditions: purely direct incoming flux,  $\text{SZA}=0^\circ$ ; and purely diffuse incoming flux. The results indicate, that absorbance of species 1 decreases by factor of two both at Red and NIR wavelengths as LAI of species 2 is changing from 0 to 4 in the case of the TM model under direct illumination. In contrast, the SMRT model predicts no significant variations in the absorbance of species 1 at Red wavelength, and increase by about 15% in the case of NIR wavelength under direct illumination. In the case of diffuse illumination the SMRT and TM models predict similar

interaction of species- decrease of the absorbance of the first species as LAI of the second is increasing. This last result of this case study match the results of the first case study: under diffuse illumination or low SZA, the simulations by both models converge. Overall, this last case study demonstrates that natural mixture of discontinuous species exhibit less radiative coupling compared to the turbid medium approximation.



The above presented analysis was focused on comparison of the SMRT and turbid medium models. Here we briefly comment on the performance of the linear mixture model. Multiple land algorithms utilized for estimation of land cover mixture from coarse resolution satellite data rely on the empirical model of linear mixture of species (cf. Section 1). Under this assumption canopy spectral reflectance of a mixed pixel is expressed as a linear combination of canopy spectral reflectances of pure species (DeFries et al., 1999). The linear mixture model ignores species radiative coupling. This coupling in a natural canopy is caused by multiple scattering, that is, after interaction with phytoelements of the first species, photon is scattered into another species. The SMRT model can be reduced to the linear mixture model, and allows analysis of empirical assumptions of the latter. According to stochastic equations (Shabanov et al., 2007), mean radiation over mixed pixel,  $\bar{I}(z, \vec{\Omega})$ , is equal to a weighted average of the radiation fields over pure species,  $U^{(i)}(z, \vec{\Omega})$ , and gaps,  $U^{(\text{gap})}(z, \vec{\Omega})$ . However,  $U^{(i)}(z, \vec{\Omega})$  are coupled through system of stochastic equations. In order to derive the linear mixture model from SMRT model one needs to break the coupling, that is, set to 0 the conditional pair-correlation function for different species,  $K^{(i,j)}=0$ , when  $i \neq j$ . This assumption apparently violates the basic geometry constraints on  $K^{(i,j)}$ , however the corresponding stochastic equations are mathematically correct and energy conservation law is preserved in this case as shown by Shabanov et al. (2007). Therefore, while radiative decoupling of vegetation species is physically meaningless, it is still a mathematically valid exercise and may describe RT processes in some other

medium. Overall, our results indicate that the linear mixture model ignores, while turbid medium overestimates species radiative coupling compared to a realistic description of the SMRT model.

#### 4. CONCLUSIONS

In this research we developed the Stochastic Mixture RT (SMRT) model for simulation of radiation regime in a natural vegetation canopy with spatially varying optical properties. The new approach provides a general solution of the problem, which includes, as special cases, the major approximate solutions, including the linear mixture and turbid medium mixture RT models. The SMRT model solves for the radiation quantities, direct input to remote sensing/climate applications: mean fluxes over mixture and over individual species. The canopy structure is parameterized in the SMRT model in terms of two stochastic moments: the probability of finding species and the conditional pair-correlation of species. The second moment is responsible for the 3D radiation effects, namely, radiation streaming through gaps without interaction with vegetation and variation of the radiation fluxes between different species. If the within- and between- species correlation is vanishing, the SMRT model reduces to the turbid medium RT model. Namely, this situation is realized in the SMRT simulations under direct illumination with low SZA or diffuse illumination. If the between- (but not within-) species correlation is set to zero, the SMRT model reduces to the linear mixture model. The analysis of the SMRT simulations indicates that the variation of radiation fluxes between different species is proportional to the variation of optical properties of species (leaf albedo, density of foliage, etc.) Gaps introduce significant disturbance to the radiation regime in the mixed canopy as their optical properties constitute a major contrast to those of any vegetation species. Set of accurate field measurements on canopy structure and radiation is required to further assess performance of the SMRT model and to improve modeling of the pair-correlation function.

#### ACKNOWLEDGMENTS

This research was supported by NASA MODIS contract NNG04HZ09C and Interdisciplinary Science (IDS) in the NASA Earth Science Enterprise grant G35C14G2.

#### REFERENCES

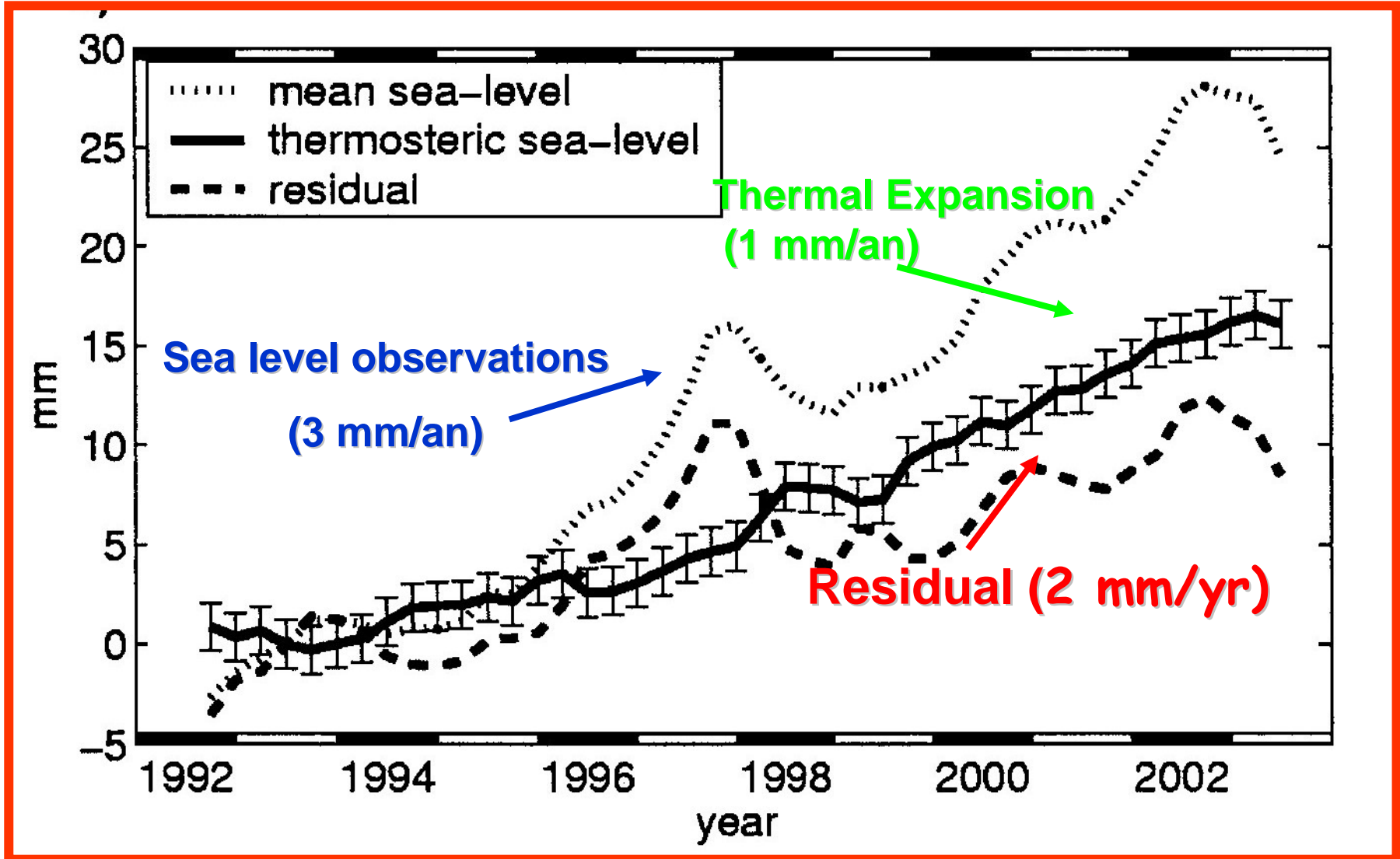
- WWW1: Vegetation continuous fields product from MODIS, <http://glcf.umiacs.umd.edu/data/modis/vcf/>
- WWW2: Common Land Model (CLM), <http://www.cgd.ucar.edu/tss/clm/distribution/clm3.0/index.html>
- Borel C., Gerstl S., 1994. Nonlinear spectral mixing models for vegetative and soil surfaces. *Remote Sensing of Environment*, 47, pp. 403-416.
- Carpenter G.A., Gopal S., Macomber S., Martens S., Woodcock C.E., 1999. A neural network method for mixture estimation for vegetation mapping. *Remote Sensing of Environment*, 70, pp. 135-152.
- DeFries R.S., Townshend J.R.G., Hansen M.C., 1999. Continuous fields of vegetation characteristics at the global scale 1-km resolution. *Journal of Geophysical Research-Atmosphere*, 104(D14), pp. 16911-16923.
- Huang D., Knyazikhin Y., Yang W., Wang W., Privette J., Deering D., Shabanov N., Myneni R.B., 2007. Stochastic transport theory for investigating the three-dimensional canopy structure from space measurements. *Remote Sensing of Environment*, accepted, June 2006.
- Pomraning G.C., 1991. *Linear kinetic theory and particle transport in stochastic mixtures*. Series on advances in mathematics for applied sciences.-Vol. 7. Singapore: World Scientific.
- Ross J., 1981. *The radiation regime and architecture of plant stands*. Hague: Dr. W. Junk Publishers.
- Shabanov N.V., Knyazikhin Y., Baret F., Myneni R.B., 2000. Stochastic modeling of radiation regime in discontinuous vegetation canopies. *Remote Sensing of Environment*, 74(1), pp. 125-144.
- Shabanov N.V., Huang, D., Knyazikhin Y., Dickinson, R.E., Myneni R.B., 2007. Stochastic Radiative Transfer Model for Mixture of Discontinuous Vegetation Canopies. *Journal of Quantitative Spectroscopy and Radiative Transfer*. In press
- Stoyan D, Kendall W.S., Mecke J., 1995. *Stochastic geometry and its applications*. Wiley Series in Probability and Statistics, Second Ed., John Wiley & Sons, pp.67-69.
- Tian Y., Wang Y., Zhang Y., Knyazikhin Y., Bogaert J., Myneni, R.B., 2002. Radiative transfer based scaling of LAI/FPAR retrievals from reflectance data of different resolutions. *Remote Sensing of Environment*, 84, pp. 143-159.
- Tian Y., Dickinson R.E., Zhou L., Zeng X., Dai Y., Myneni R.B., Knyazikhin Y., Zhang X., Friedl M., Yu H., Wu W., Shaikh M., 2004. Comparison of seasonal and spatial variations of LAI/FPAR from MODIS and Common Land Model. *Journal of Geophysical Research-Atmosphere*, 109(D1), D01103, 10.1029 /2003JD003777.
- Titov, G.A., 1990. Statistical description of radiation transfer in clouds. *Journal of the Atmospheric Sciences*, 47, pp. 24-38.
- Vainikko, G.M., 1973a. The equation of mean radiance in broken cloudiness. *Trudy MGK SSSR, Meteorological investigations*, 21, pp. 28-37, (in Russian).
- Vainikko, G.M., 1973b. Transfer approach to the mean intensity of radiation in non-continuous clouds. *Trudy MGK SSSR, Meteorological investigations*, 21, pp. 38-57, (in Russian).

# **GEO**

## **To Understand Trends, Forecast Changes, Support Informed Decisions**

**ISPMSRS, Davos 12-14 March 2007**

**Michael Rast**  
**GEO Secretariat**



1. Reduction and Prevention of Disasters
2. Human Health and Epidemiology
3. Energy Management
4. Climate Change
5. Water Management
6. Weather Forecasting
7. Ecosystems
8. Agriculture
9. Biodiversity





**Any Single Problem Requires Many  
Data Sets**

**A Single Data Set Will Serve Many  
Communities**



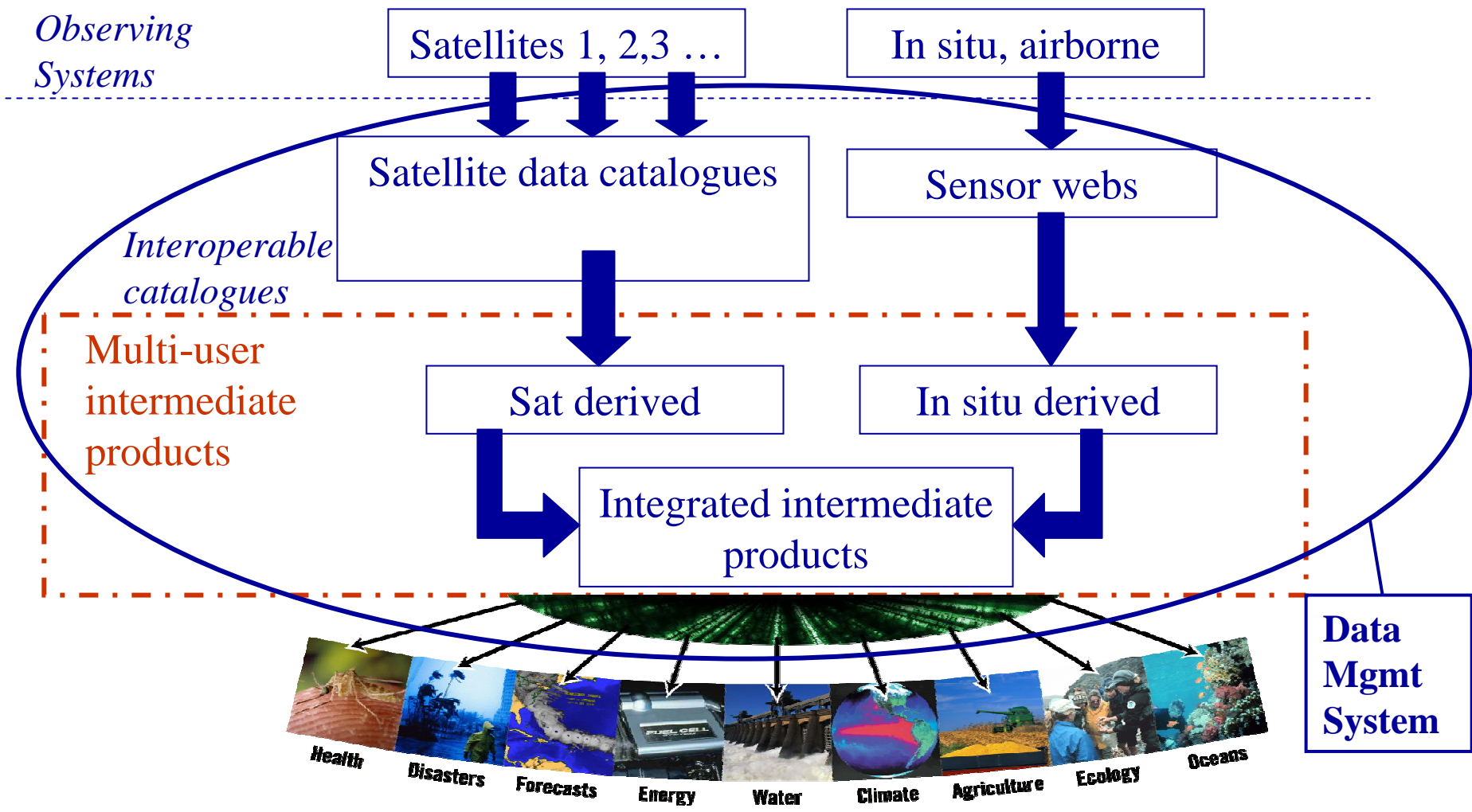
Group on  
Earth Observations

# GEOSS conceptual architecture

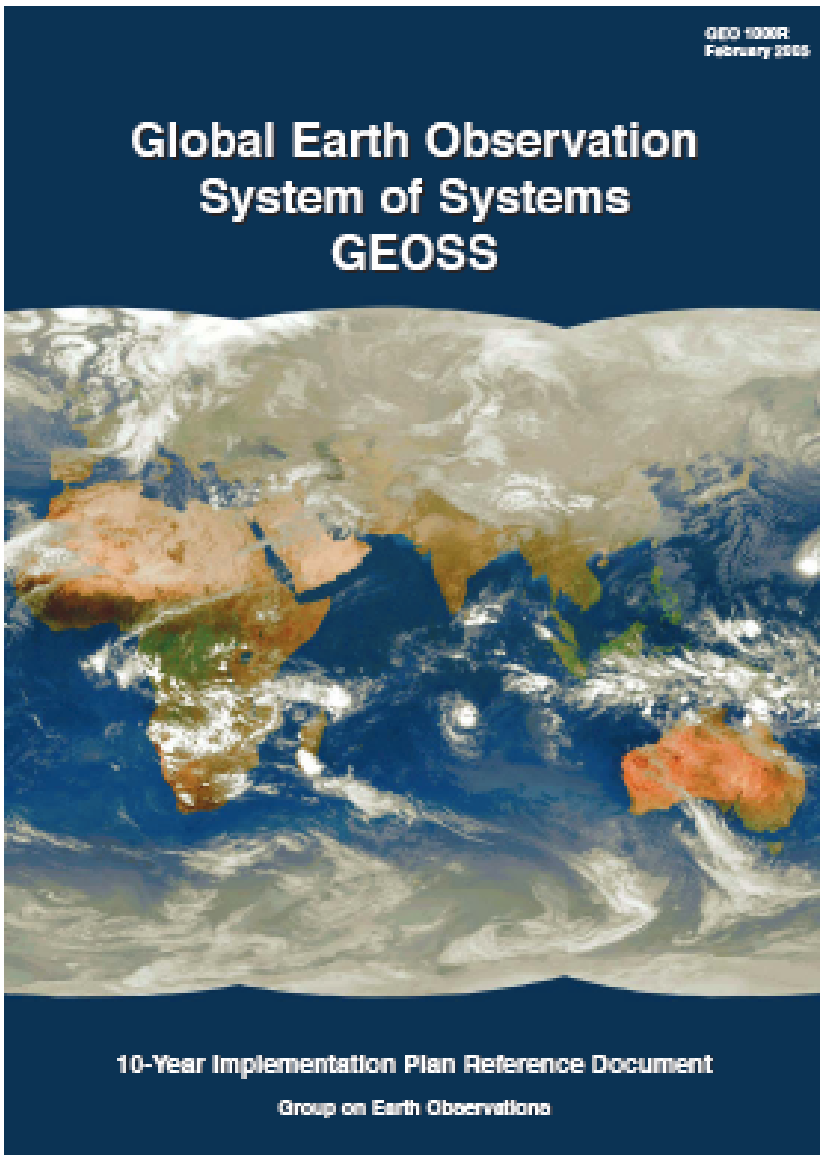
**A Global,  
Coordinated,  
Comprehensive and  
Sustained System  
of Earth Observing  
Systems**



# GEOSS conceptual architecture

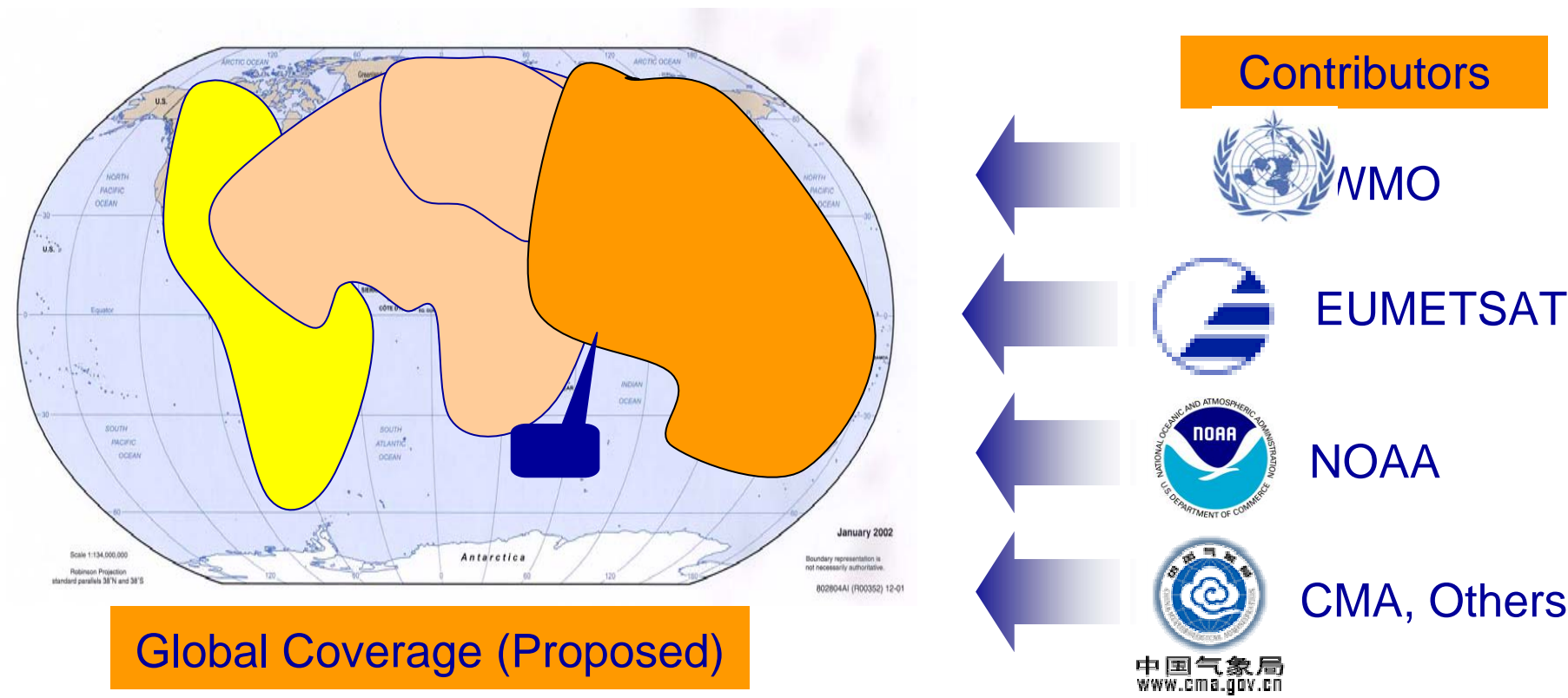


- **GEOSS 10-Year Implementation Plan Endorsed**
- **GEO Secretariat established in Geneva**





Disseminate and provide easy access to space-based, air-borne and in situ data, metadata and products to Users from all Societal Benefit Areas.





## **GEO: A User-driven Process**

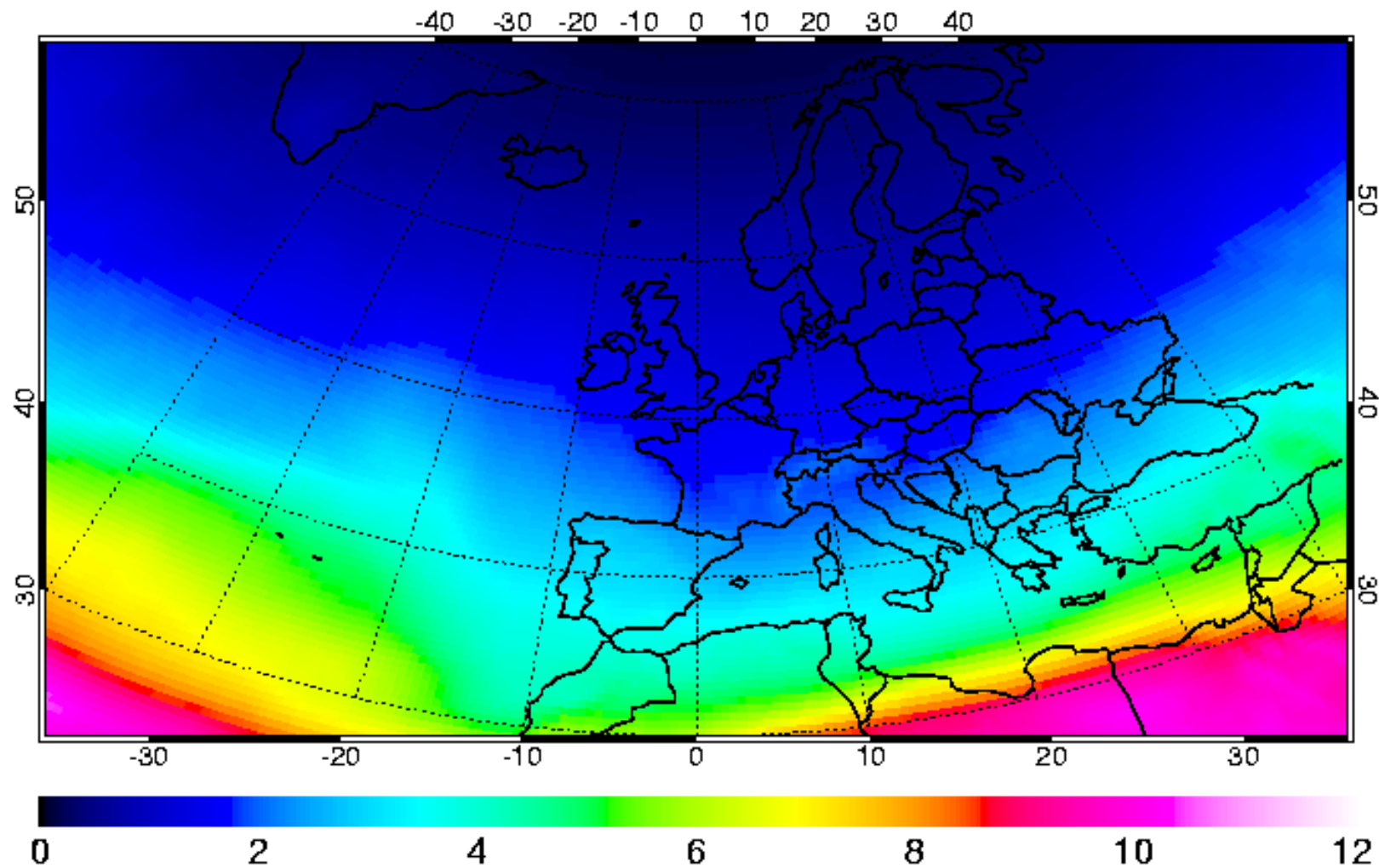
- **Improve and Coordinate Observation Systems**
- **Provide Easier & More Open Data Access**
- **Foster Use through Science and Applications**

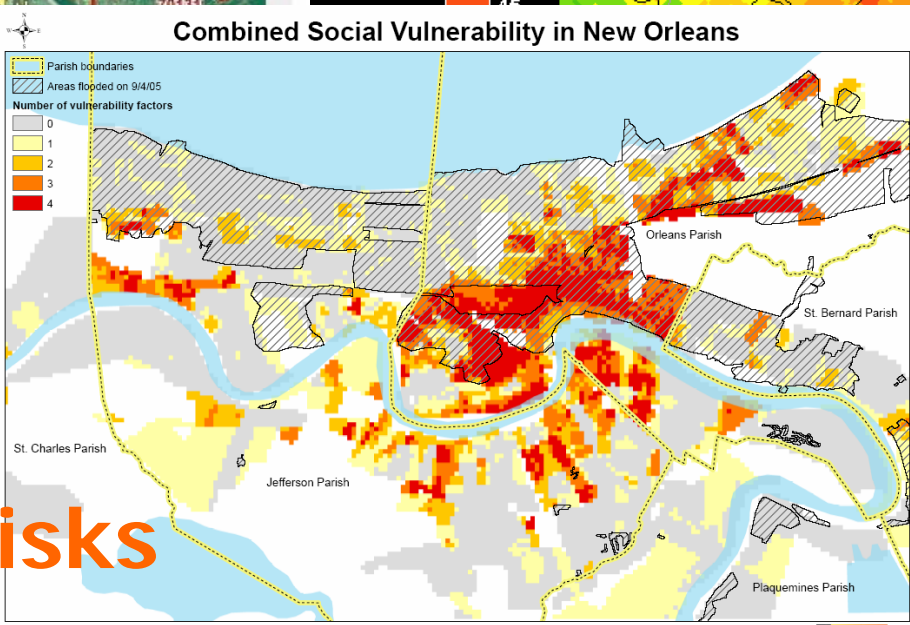
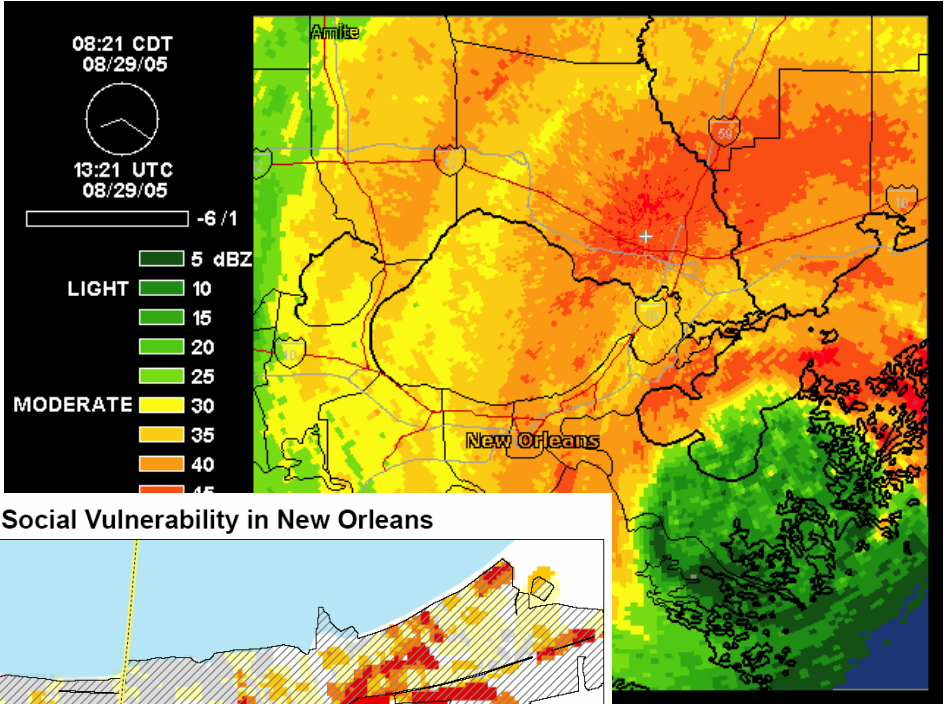
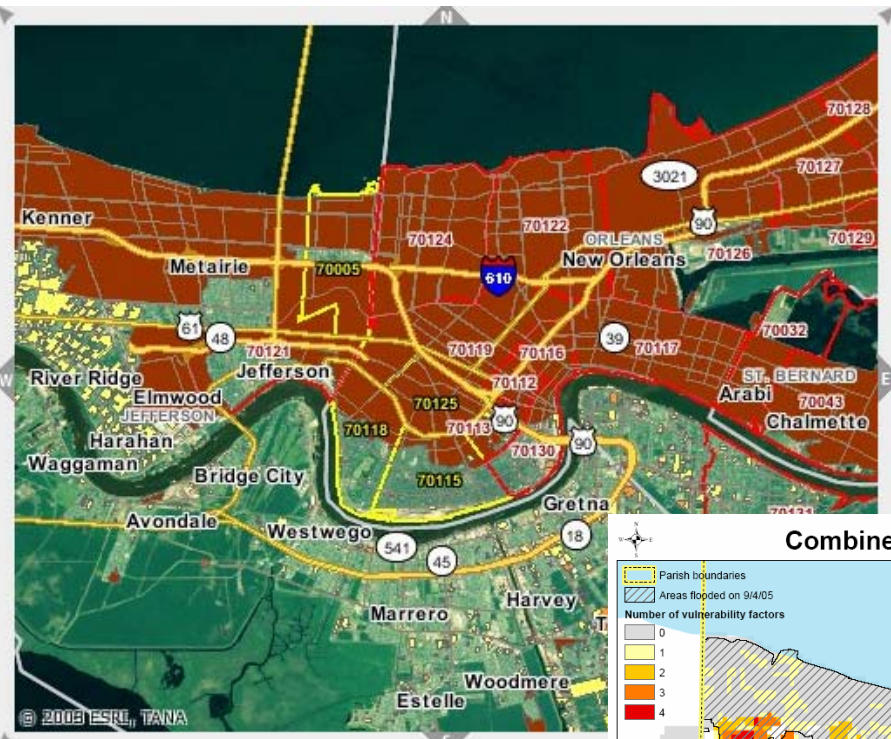
**... to answer Society's need  
for informed decision making**

# Erythemat UV index

SCIAMACHY - KNMI/ESA

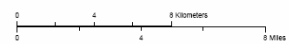
local solar noon  
29 February 2004





A grid cell is considered vulnerable if it falls in the top 3 deciles for one or more of the following measures:

- % of residents living below the poverty line
- % of residents who are African American
- % of households without a vehicle
- % of housing units occupied by renters



Powered by ArcWeb Services



Exposure

Evaluate Risks

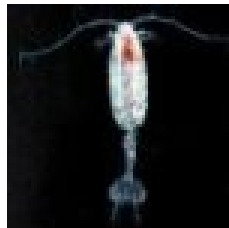
Vulnerability

Hazard

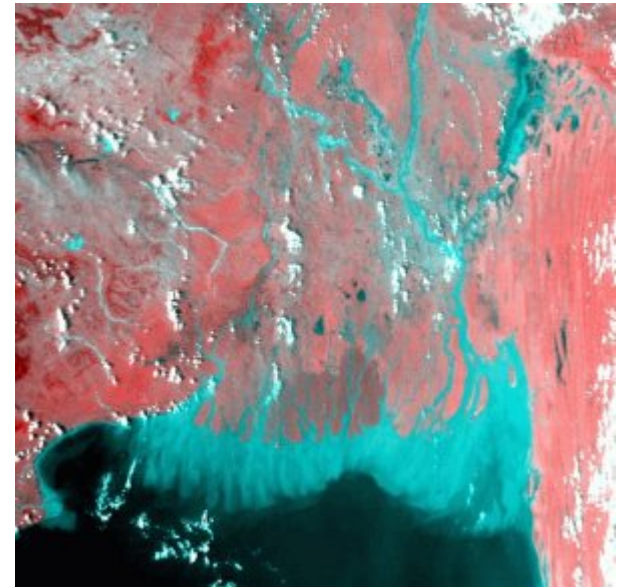


# Forecast Epidemic Outbreaks

**VIBRIO CHOLERAЕ HAS A  
MARINE ZOO NOTIC CYCLE  
ASSOCIATED WITH ALGAL  
BLOOMS**



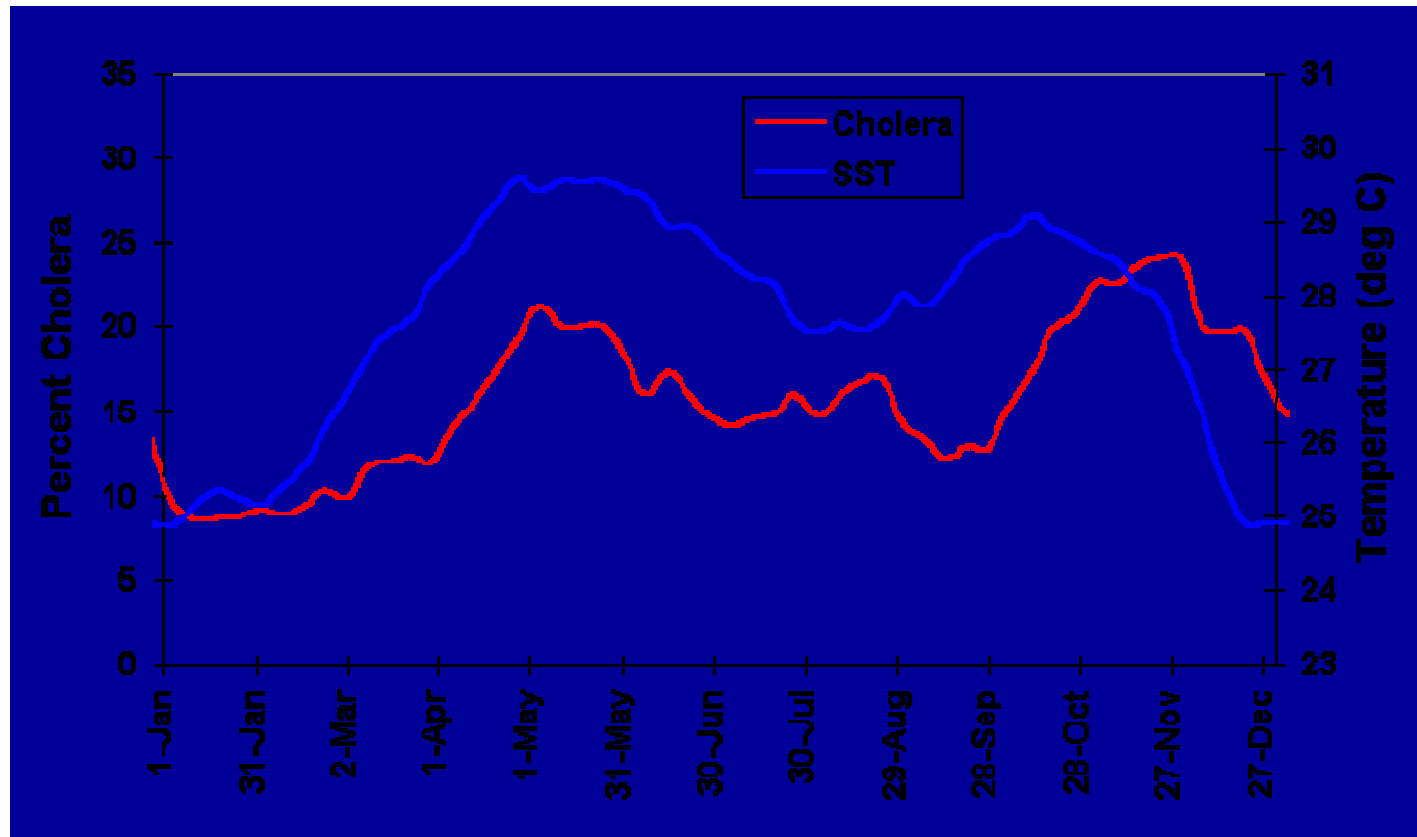
**COPEPOD**



**BAY OF BENGAL**

**AVRHH SEPT 1992  
FALSE COLOR INFRARED**

## SEA SURFACE TEMPERATURE PREDICTS CHOLERA CASES



BAY OF BENGAL



# GEOSS Architecture will Provide Systems Interoperability and Easier and More Open Data Access



# Space Systems

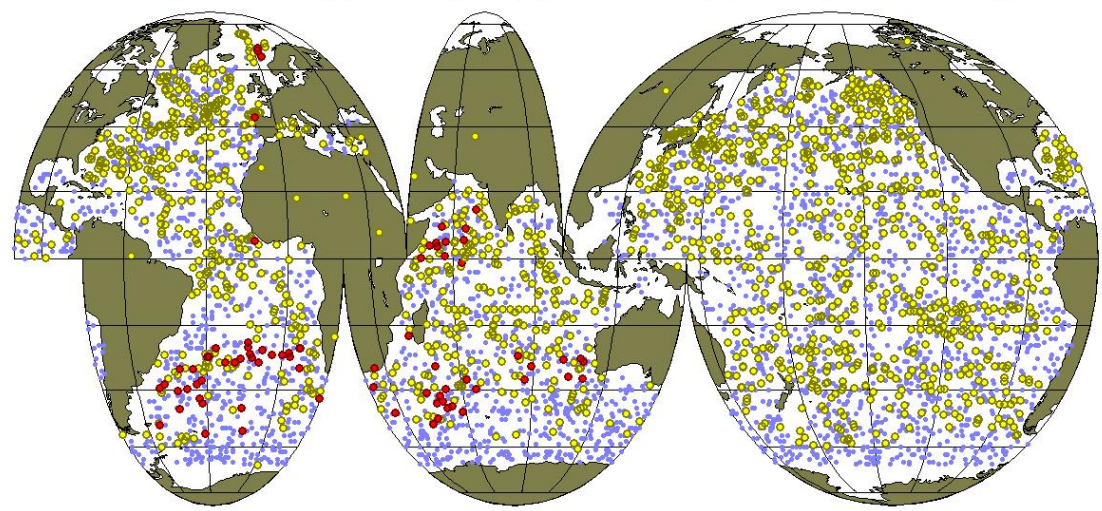




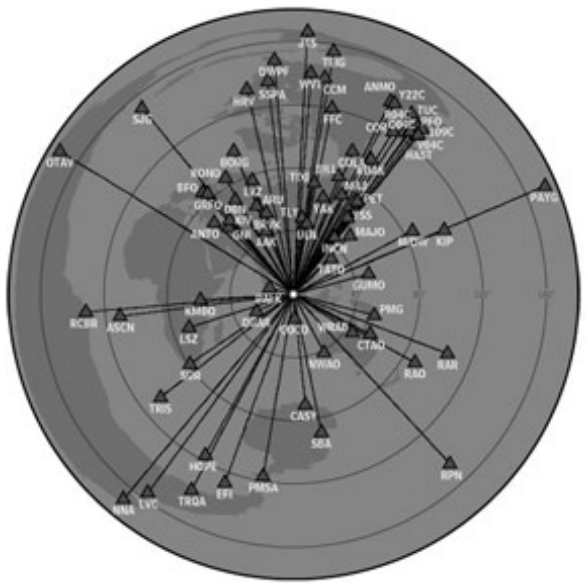
# Global In-situ Networks

## Argo Float Array

Global Argo Float Array (red – Argo UK; yellow – all Argo; blue – proposed array)



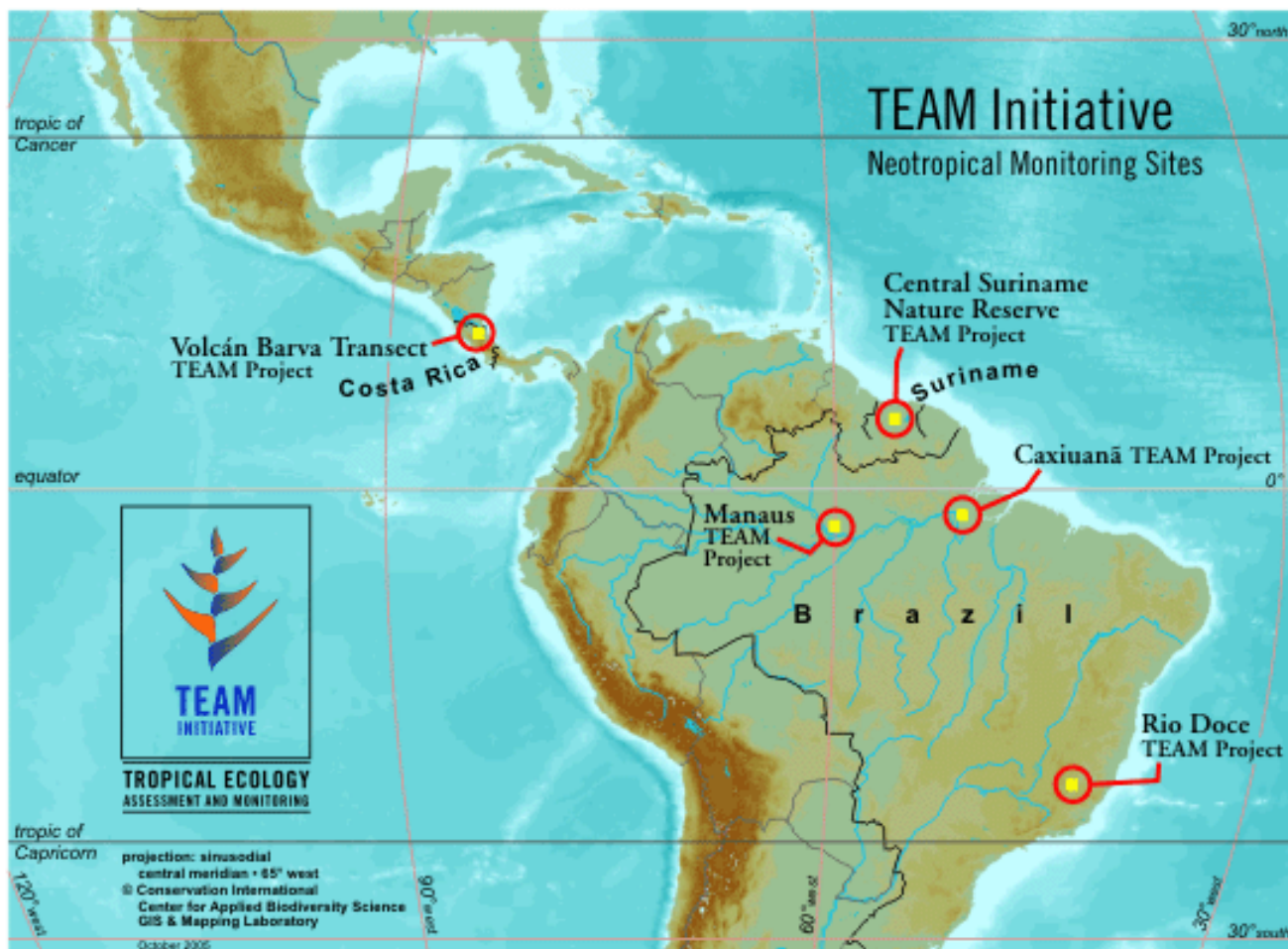
## Seismic Networks



# Regional and Local In-situ Networks

## TEAM

## Tropical Ecology Assessment & Monitoring Initiative





# The Tower of Babel

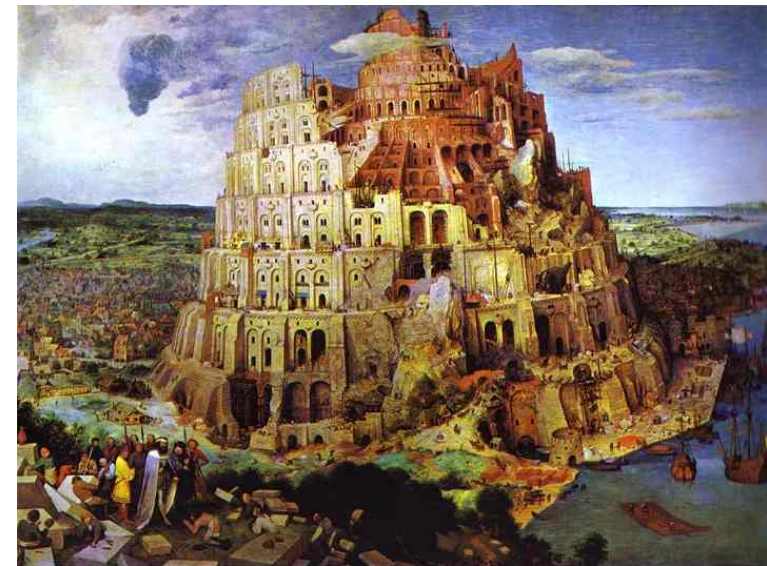
**There is a Need to Share  
all Earth Observation  
Data in Standard  
Interoperable Formats**





# Interoperability Arrangements

- **Technical Specifications for Collecting, Processing, Storing, and Disseminating Data and Products**
- **Based on Non-proprietary Standards**
- **Defining only how System Components Should Interface to be Contributed to GEOSS**

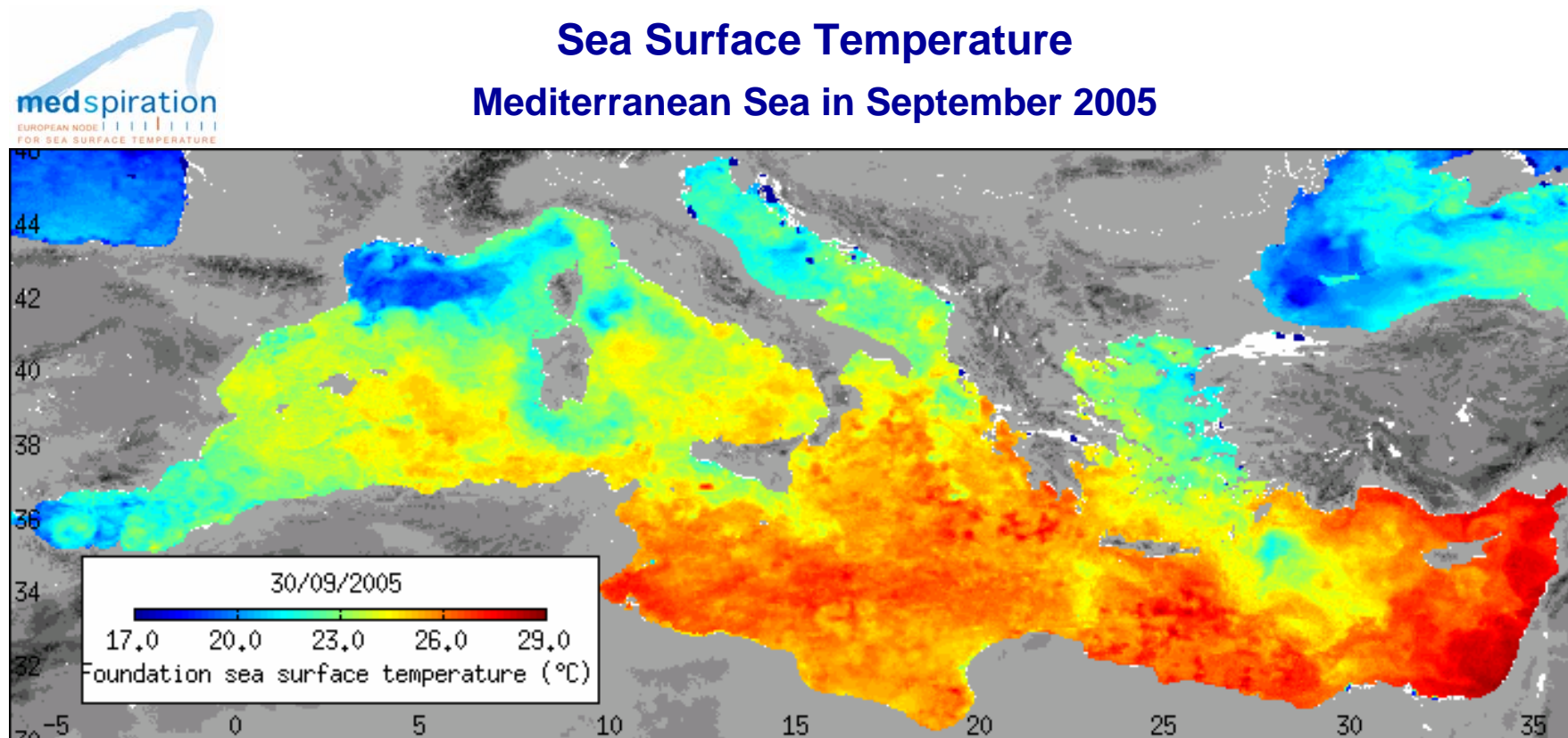


# Interoperability Arrangements

***“What few things  
must be the same  
so that everything  
else can be different”***



## Sea Surface Temperature Mediterranean Sea in September 2005



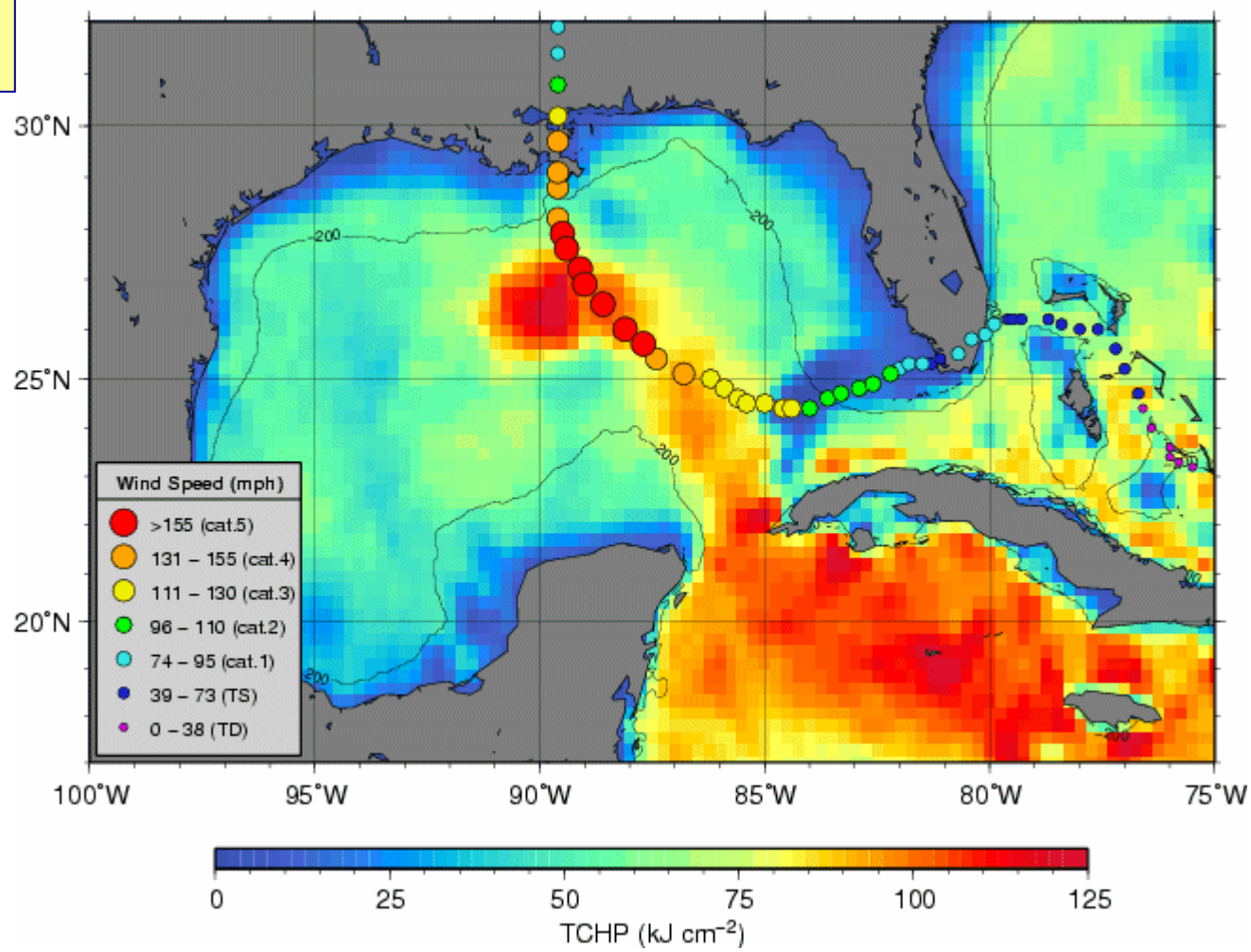
*The Medspiration project combines SST data measured independently by different satellites, including Envisat AATSR, into a set of products that represent the best measure of SST, presented in a form that can be assimilated into numerical ocean forecasting models.*

<http://www.medspiration.org>



**Hurricane Katrina**

Gulf of Mexico – Tropical cyclone heat potential (TCHP) 08/28/2005



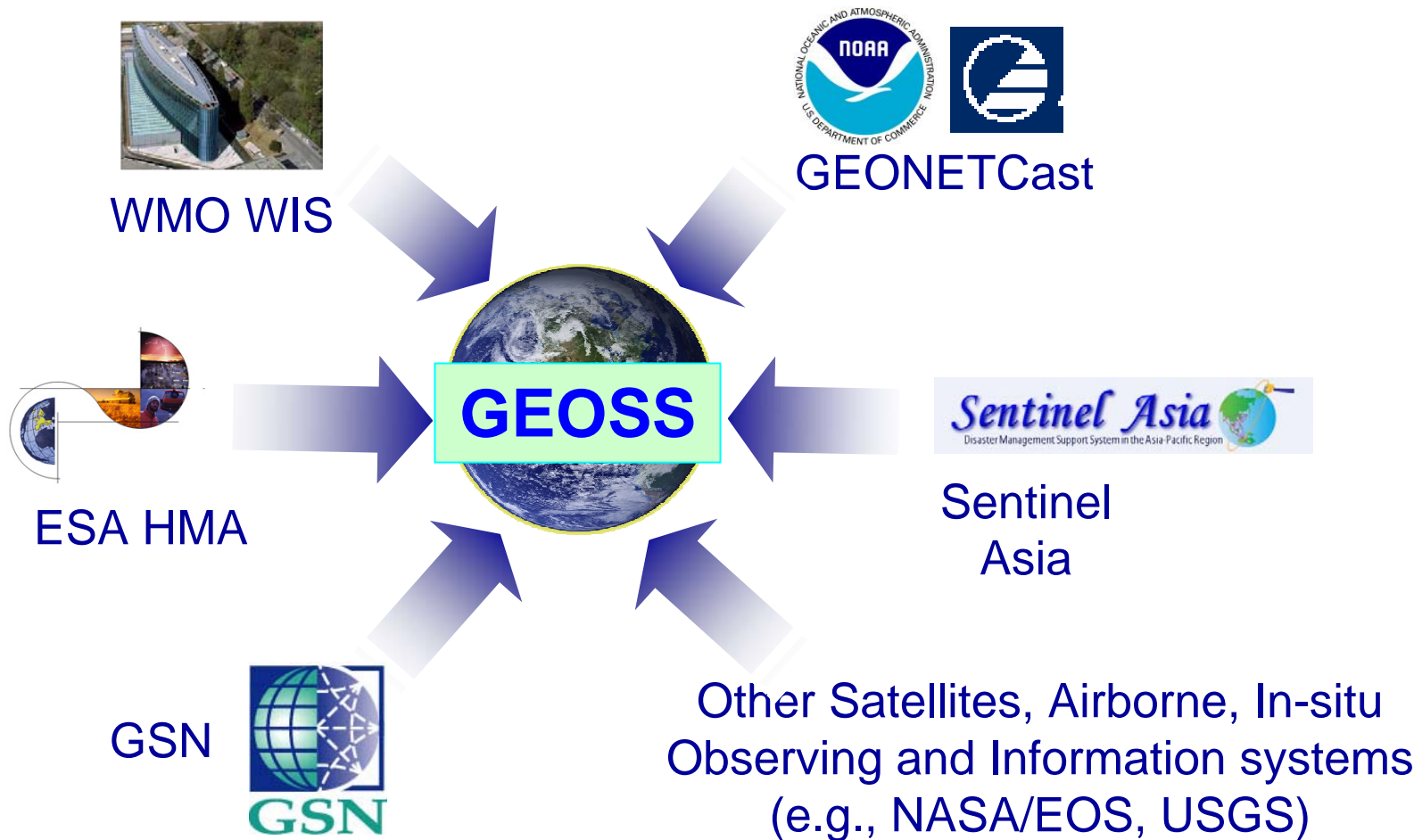
Altimetry data from ESA Envisat, NASA/CNES Topex/Poseidon & Jason-1, US Navy GFO

Figures courtesy of Gustavo Goni, NOAA/OAR/AOML



Group on  
Earth Observations

# GEOSS Components Commitments

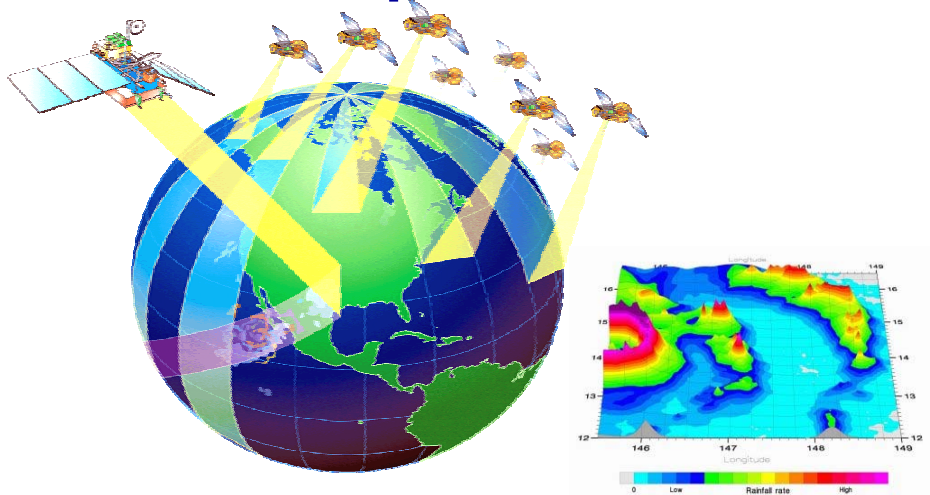


Initial Candidates of Component Contributors

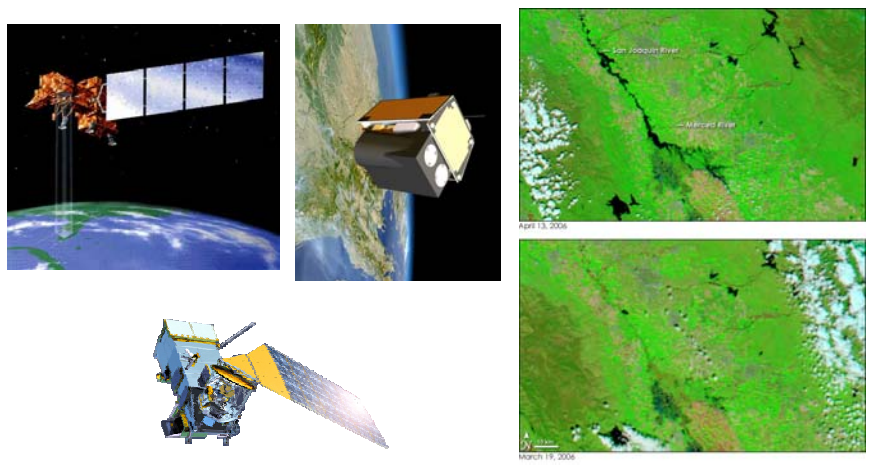


# Virtual Constellations

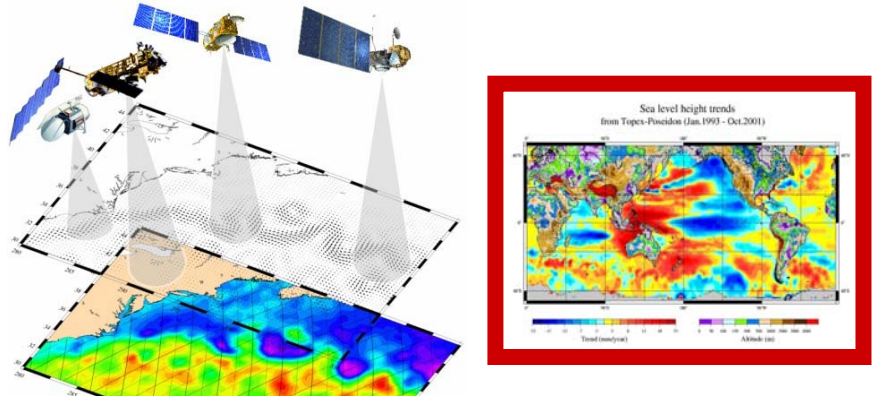
## Precipitation



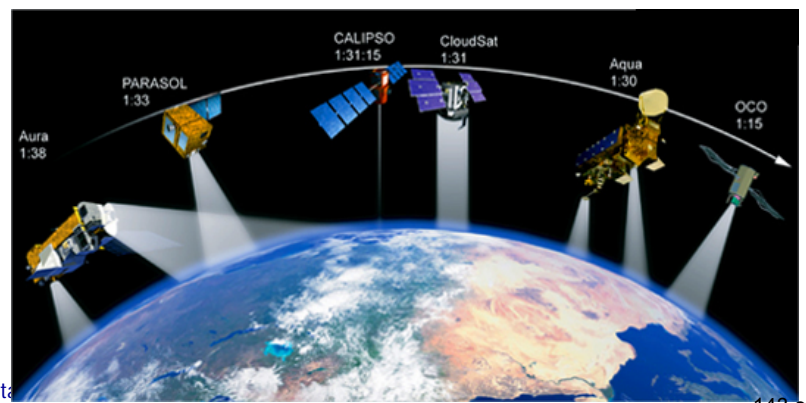
## Land-Surface Imaging



## Ocean Surface Topography



## Atmospheric Chemistry

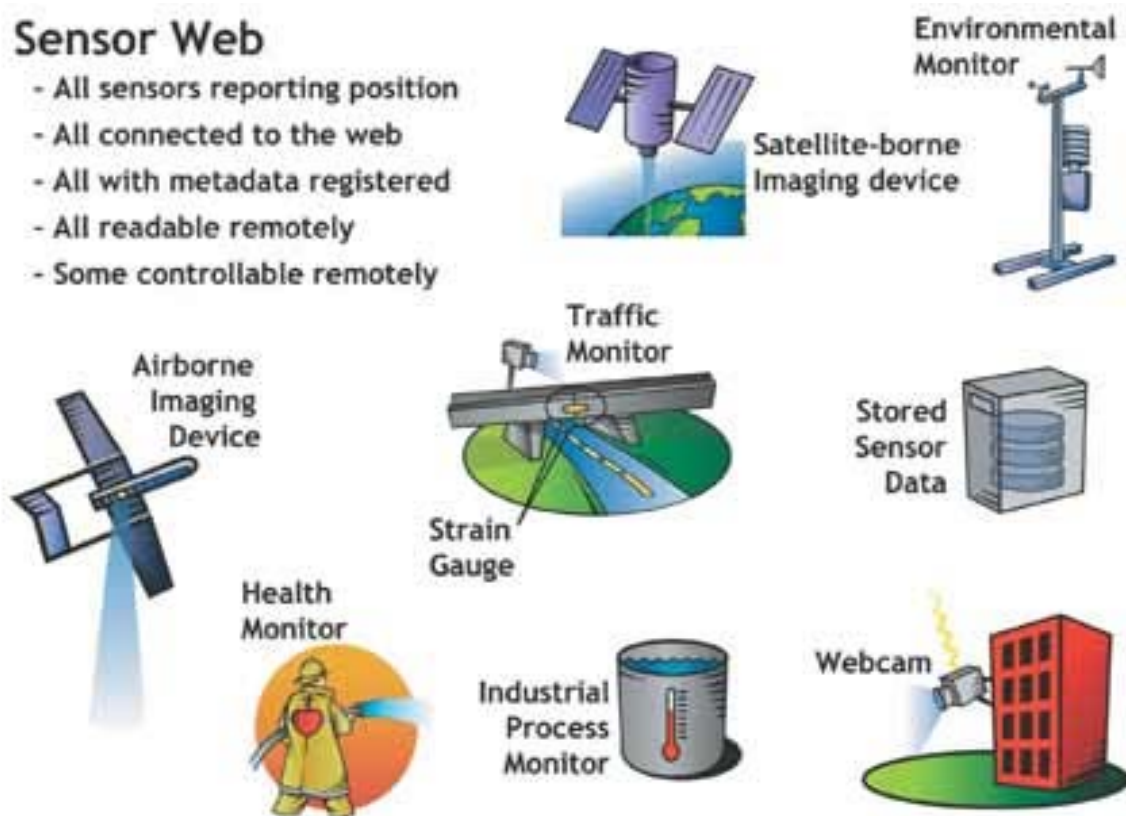




# Sensor Web For In situ Networks

## Sensor Web

- All sensors reporting position
- All connected to the web
- All with metadata registered
- All readable remotely
- Some controllable remotely



- Less development of ground based sensing network
- Develop use cases to demonstrate the value of the technology
- Target SBAs (Disaster, Health, Biodiversity, Ecosystem, Water)

**FIGURE 1** The Sensor Web will comprise diverse, location-aware environmental sensing devices that report data about their surroundings in real time.

*Image courtesy of OGC*



# GEO should Provide Easier and More Open Data Access



# GEO Web Portal and Clearinghouse

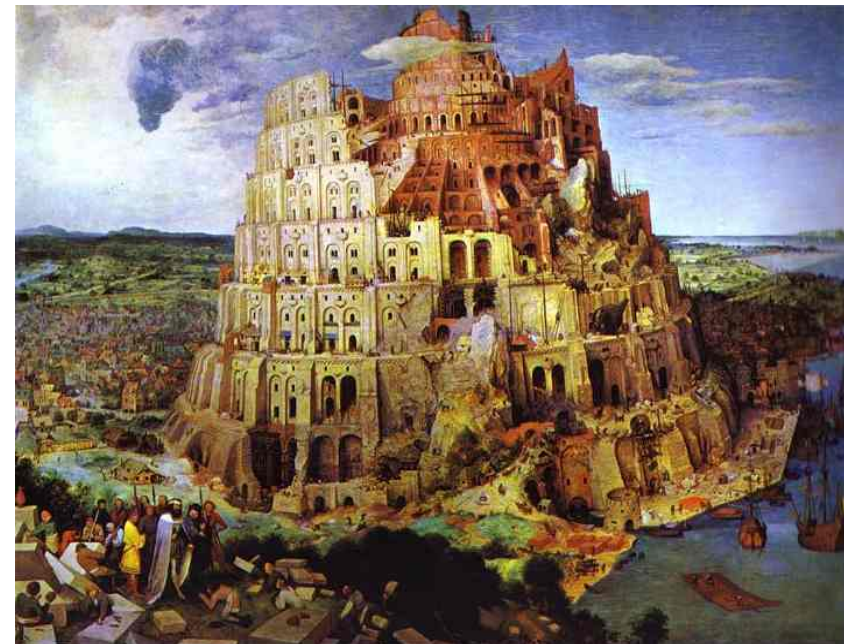
- **Defining Standards for Quality Assurance of Derived Products**
- **Providing Online Calibration and Validation**
- **Providing Tools**





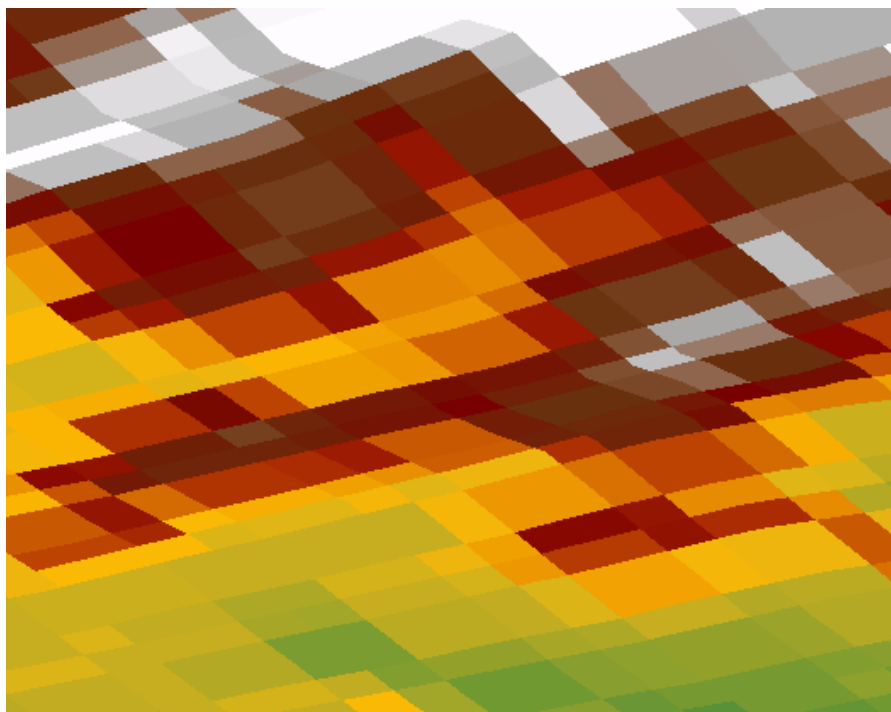
## **GEO Data Sharing Principles**

- **Full and Open Exchange of Data...Recognizing Relevant International Instruments and National Policies and Legislation**
- **Data and Products at Minimum Time delay and Minimum Cost**
- **Free of Charge or Cost of Reproduction for Research and Education**

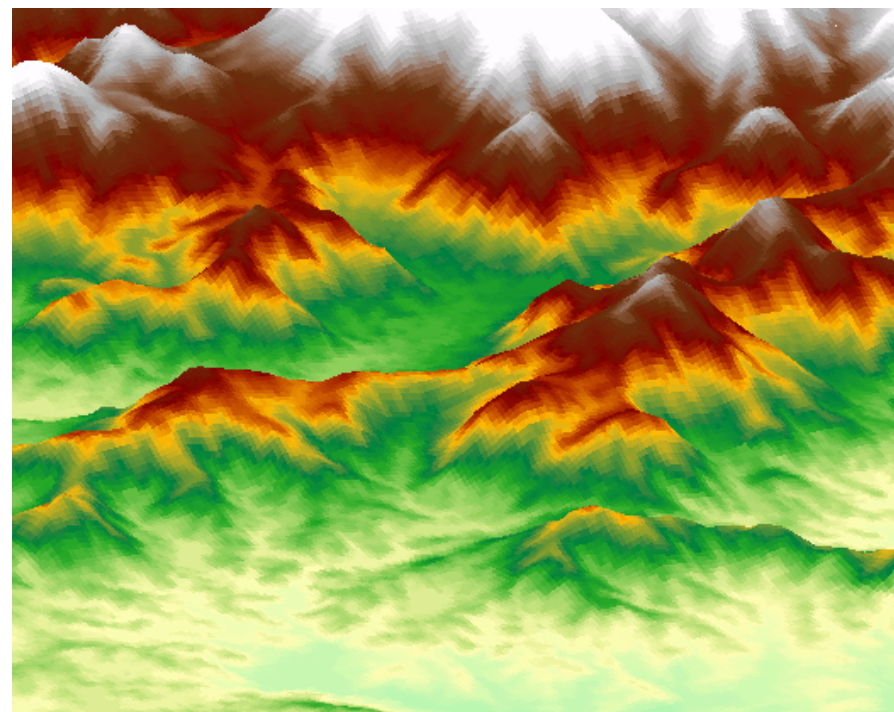




# Challenge: National Security



90 m



30 m

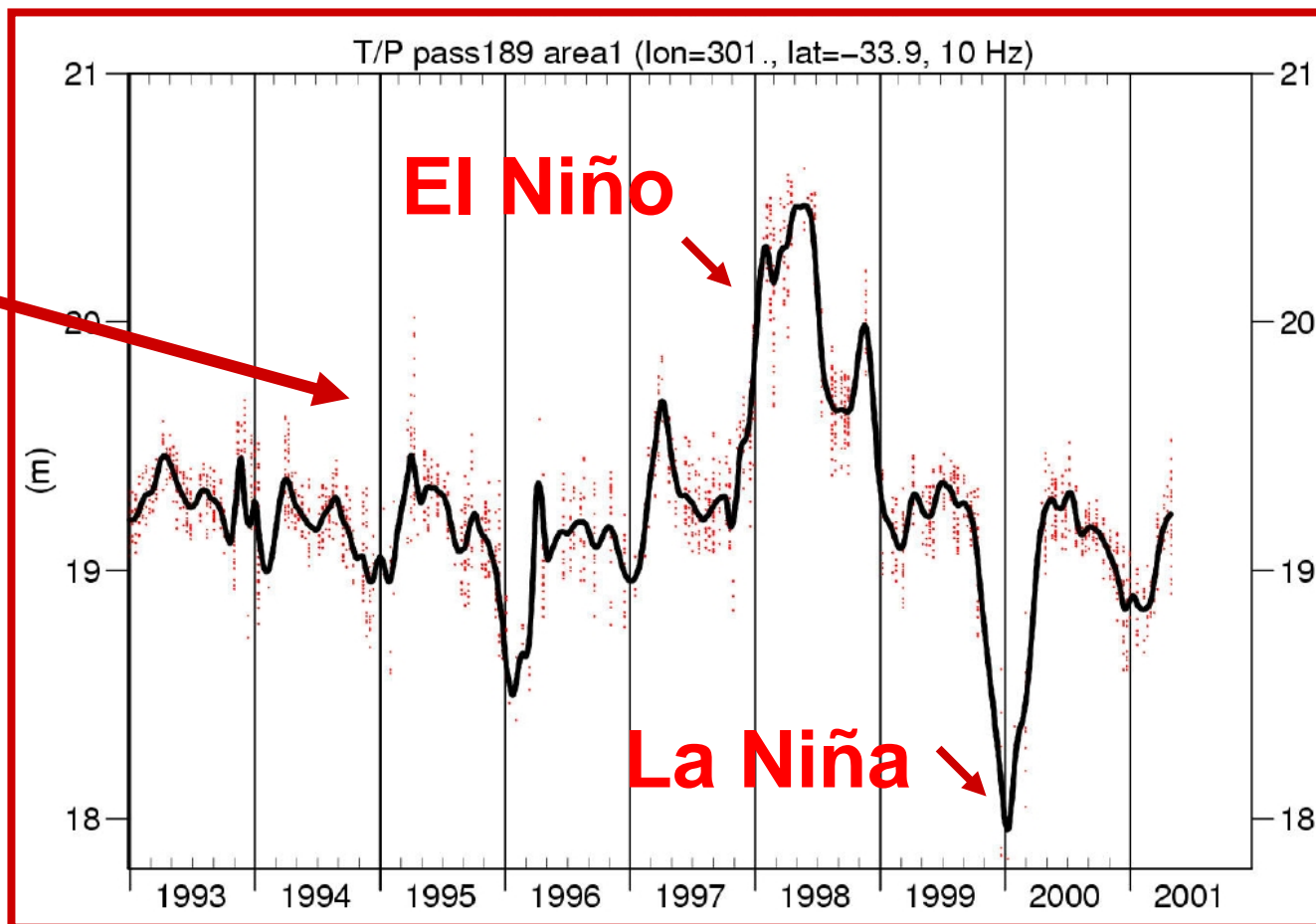
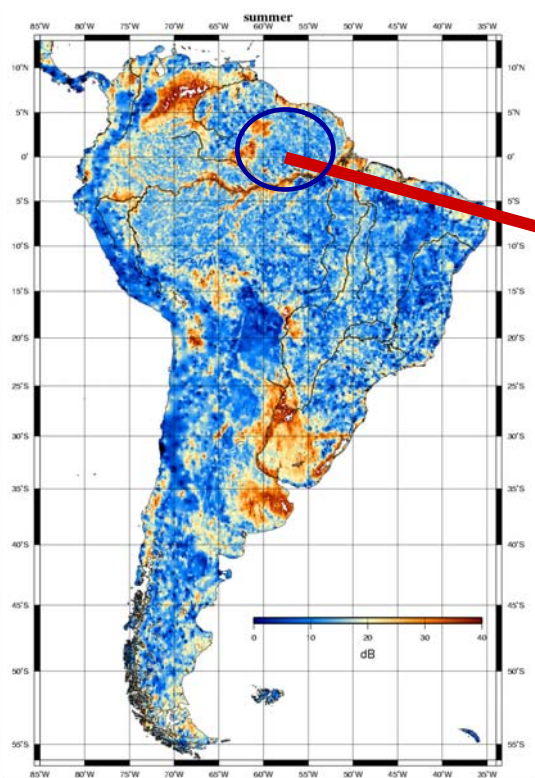
Comparison courtesy of V. Gorokhovich, CIESIN

# GEO will Foster Interdisciplinary Developments Addressing Cross-cutting Issues, Linking Local to Global



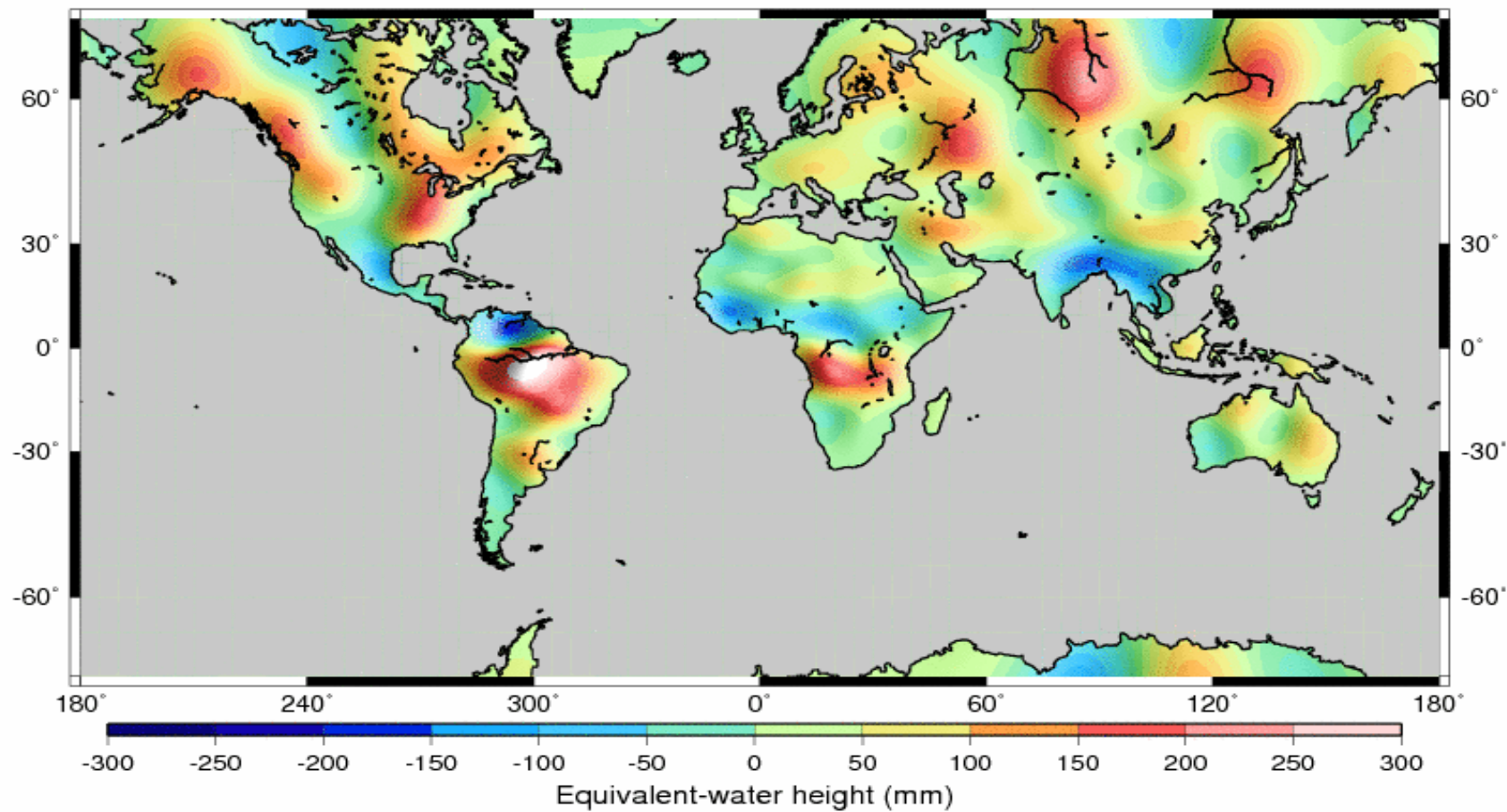
# Integrate Space and In-situ Observations

## PARANA





GRACE LW SOLUTION --- APR MAY 2002 --- DEG=25-30 --- 5 ITERATIONS



## Hydrological Applications and Run – Off Network

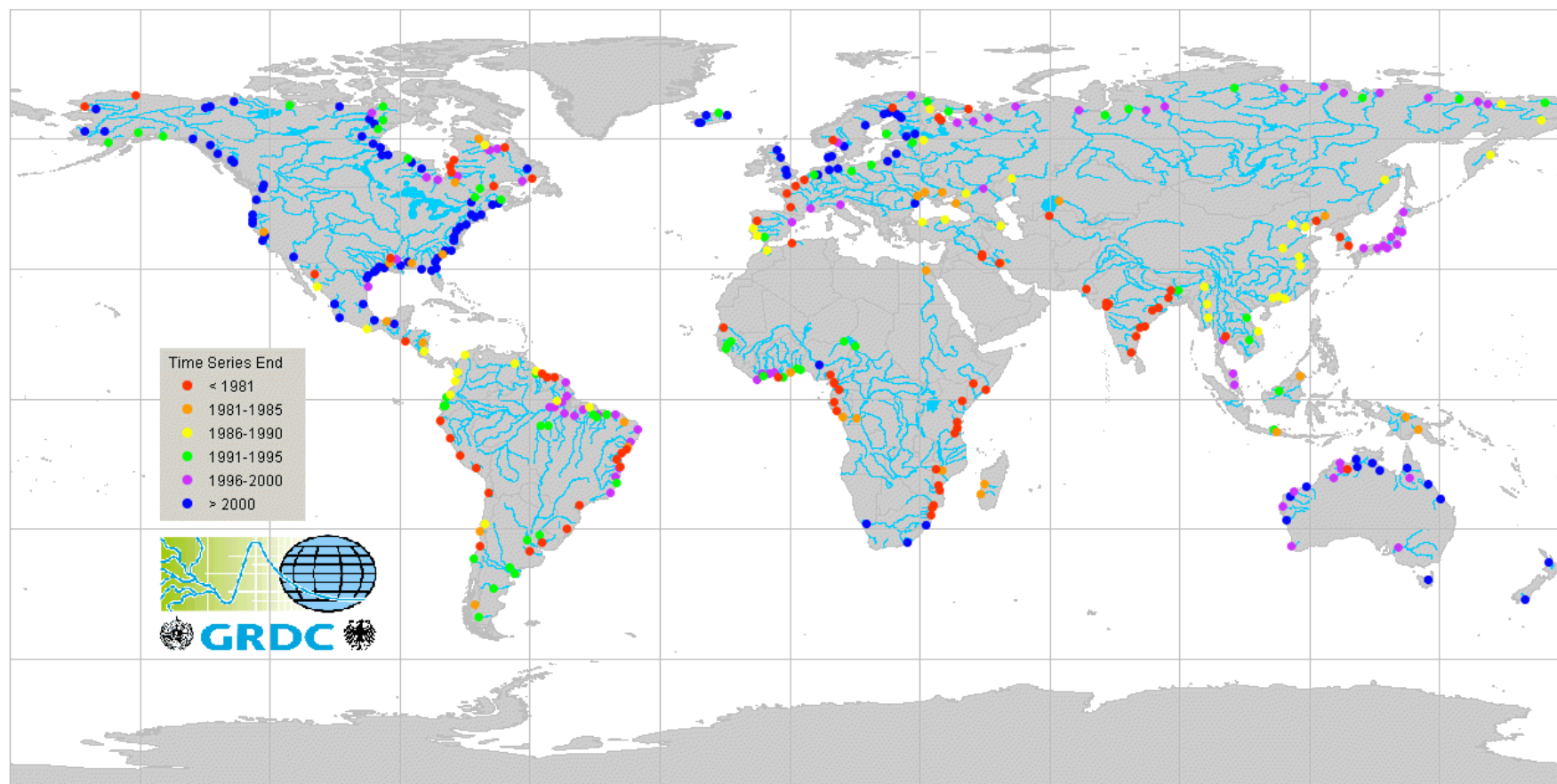
**A project is proposed aiming to restore an existing Hydrological stations network**

- **initial phase: upgrade and sustained maintenance of major global run-off stations monitoring continental freshwater fluxes into the world's oceans**
- **2<sup>nd</sup> Phase: Combining hydro-meteorological and related in-situ components with satellite observations**
- **3<sup>rd</sup> Phase: Produce an implementation plan for a broad global water cycle data integration system that combines in-situ, satellite data and model outputs**

**The main purpose of the initiative is to improve and support the closure of the global water budget in line with objectives of WMO, IGWCO, GCOS and GEWEX and to support water resources management also in the context of food security**

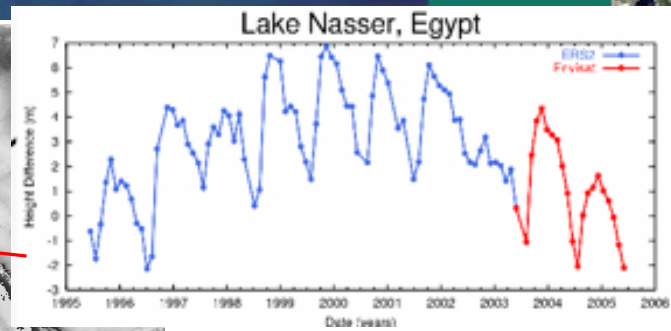
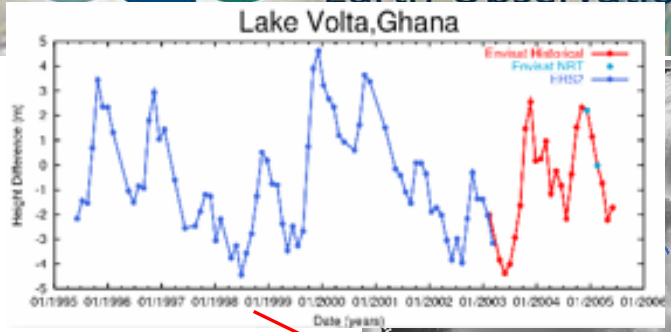


## Proposed river discharge baseline network (GTN-R; 380 stations)



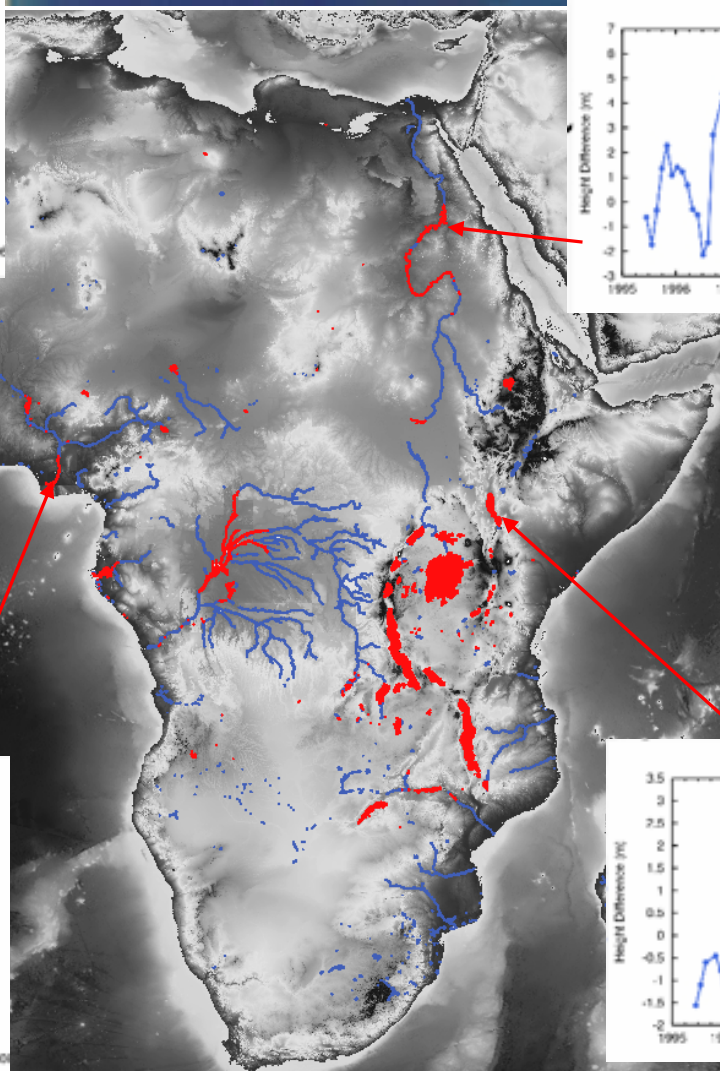
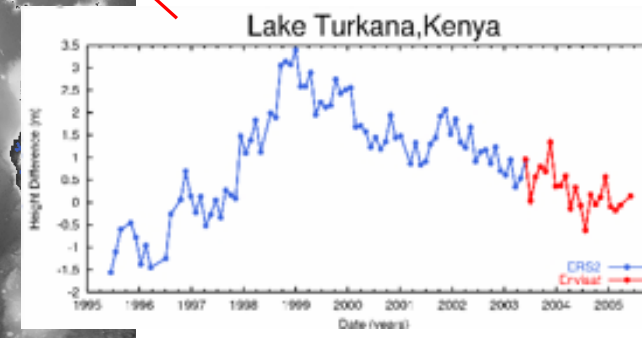
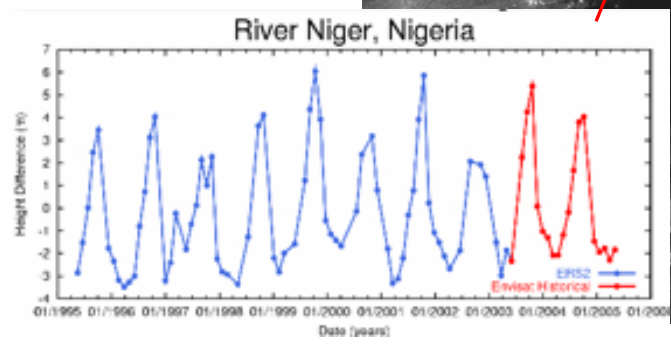
Group on  
Earth Observations

# THE RIVER AND LAKE MASK OVER AFRICA

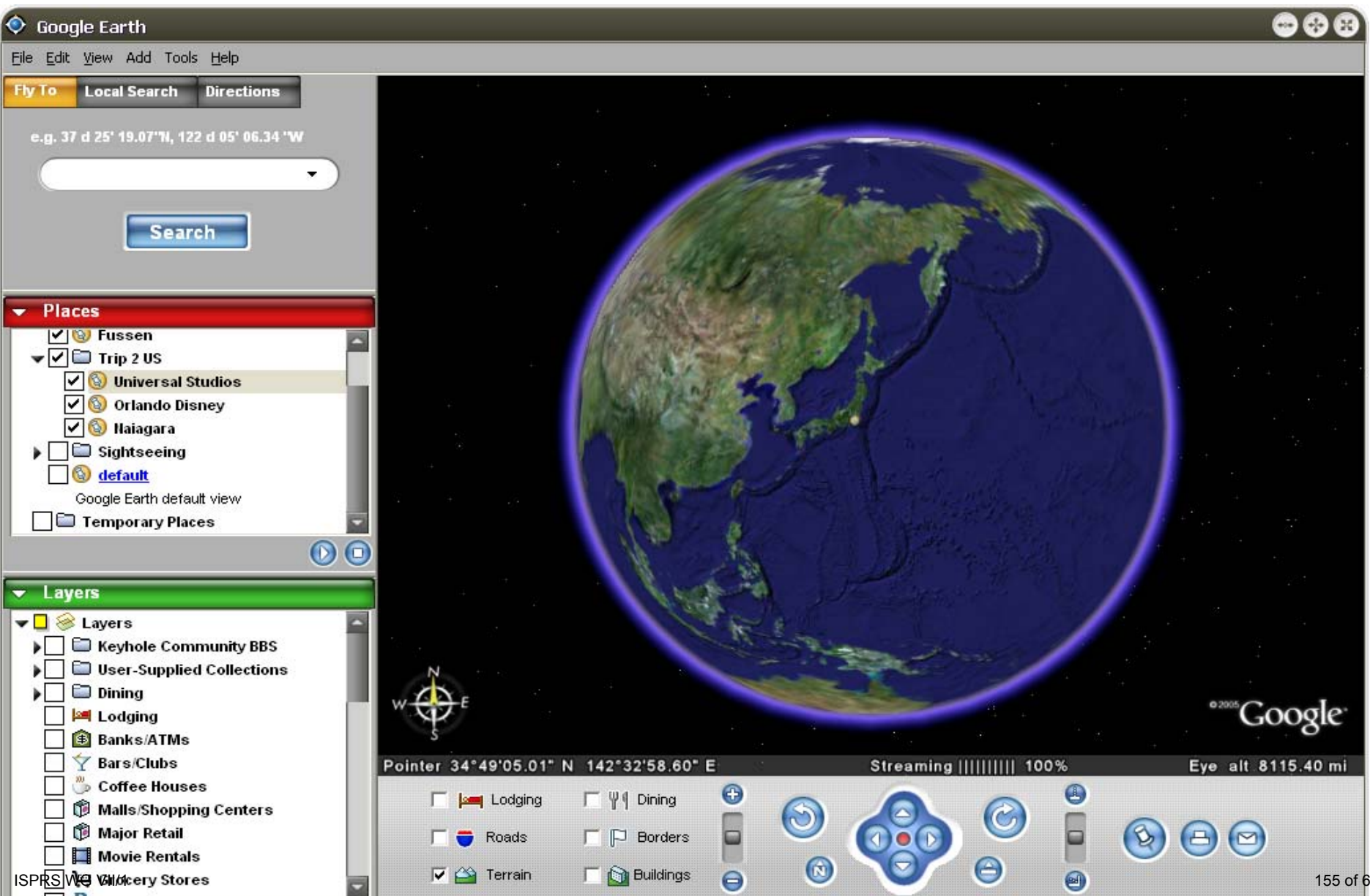


Red indicates area where NRT products are currently generated

Blue indicates area where products may be generated in the future.



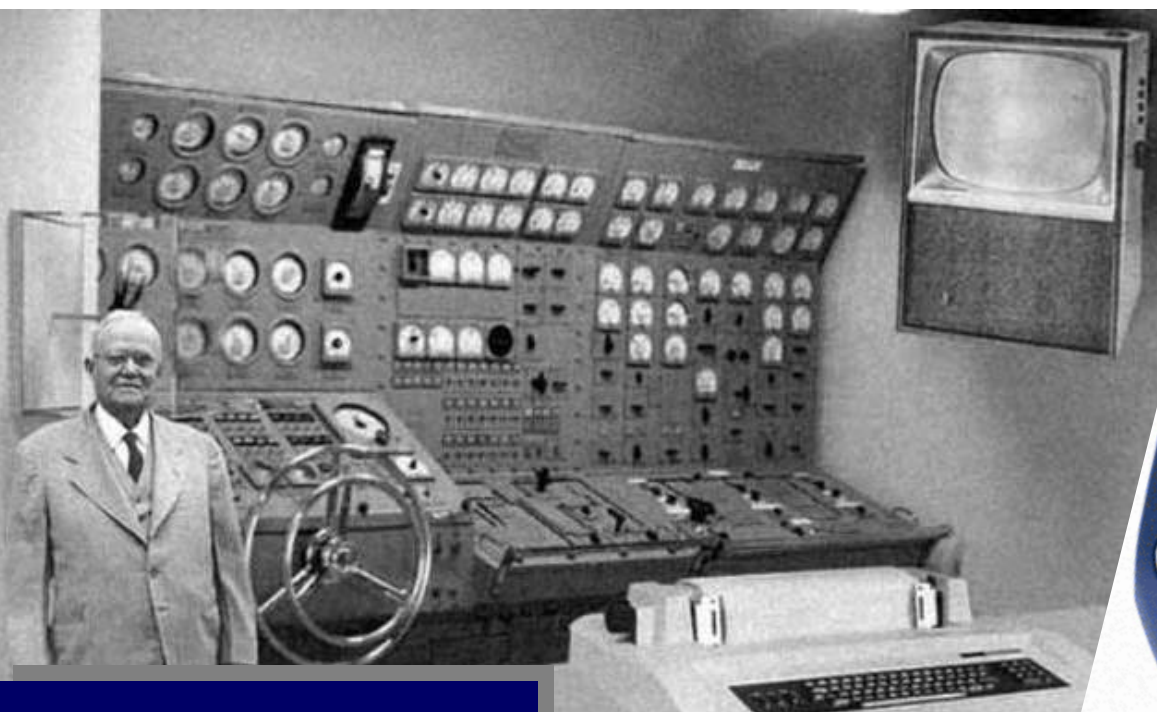








# The Future of Earth Observation?



*1964 Vision*

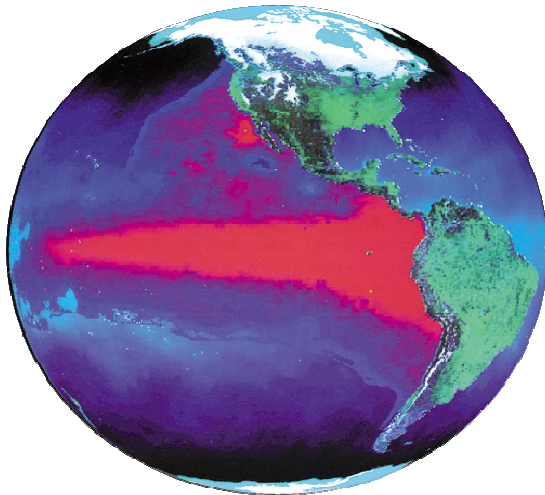


*2004 Reality*



**To Provide the Right Information, in the Right Place, at the Right Time, to the Right People**

**to Make the Right Decisions.**



**[www.earthobservations.org](http://www.earthobservations.org)**

## Plans for the U.S. National Ecological Observatory Network (NEON):

### The Contribution of Remote Sensing

**Susan L. Ustin**

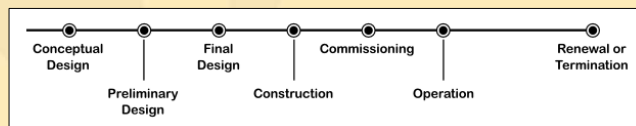
Center for Spatial Technologies and Remote Sensing  
University of California Davis



S. Ustin, ISPMSRS '07 Cutting Edge Research

### NEON Goal: Transform Ecological Sciences

- From site-based focus to Continental/Global Science
- 30 year plan to monitor environments to address “8 Grand Research Challenges”
  - NSF Major Research Equipment Facilities Center (MREFC; Infrastructure Program); expected start 2007



S. Ustin, ISPMSRS '07 Cutting Edge Research

NATIONAL ECOLOGICAL OBSERVATORY NETWORK

### Fundamental NEON Science Challenges

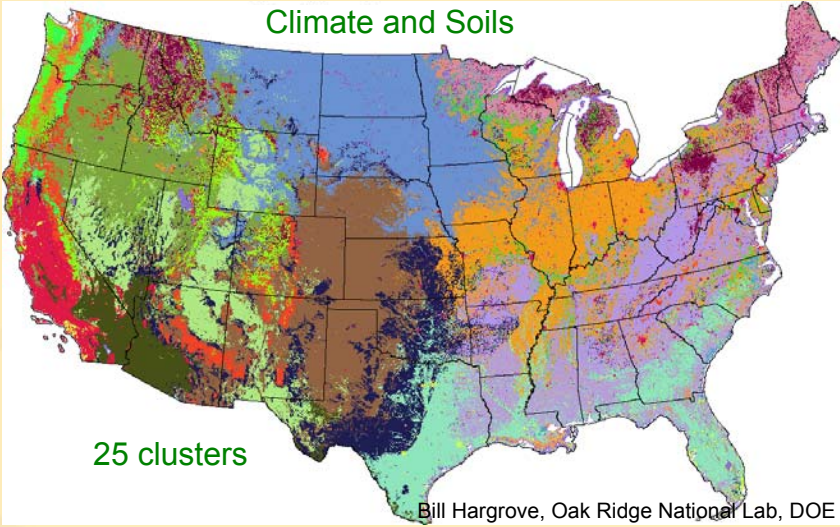
- How will ecosystems and their components respond to changes in natural- and human-induced forcings such as climate, land use, and invasive species?
  - Across a range of spatial and temporal scales?
  - What is the pace and pattern of the responses?
- How do internal responses and feedbacks to biogeochemistry, biodiversity, hydroecology and biotic structure and function interact with changes in climate, land use, and invasive species?
  - How do feedbacks vary with ecological context and spatial and temporal scales?

neon

S. Ustin, ISPMSRS '07 Cutting Edge Research

NATIONAL ECOLOGICAL OBSERVATORY NETWORK

### Site Selection: Evaluation of Environmental Variables



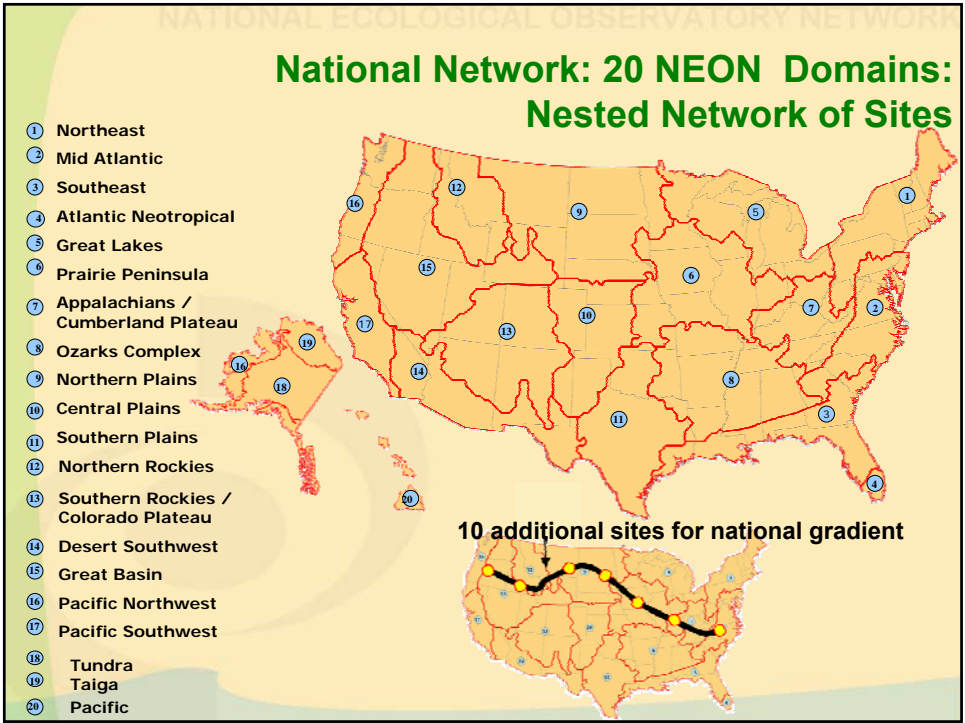
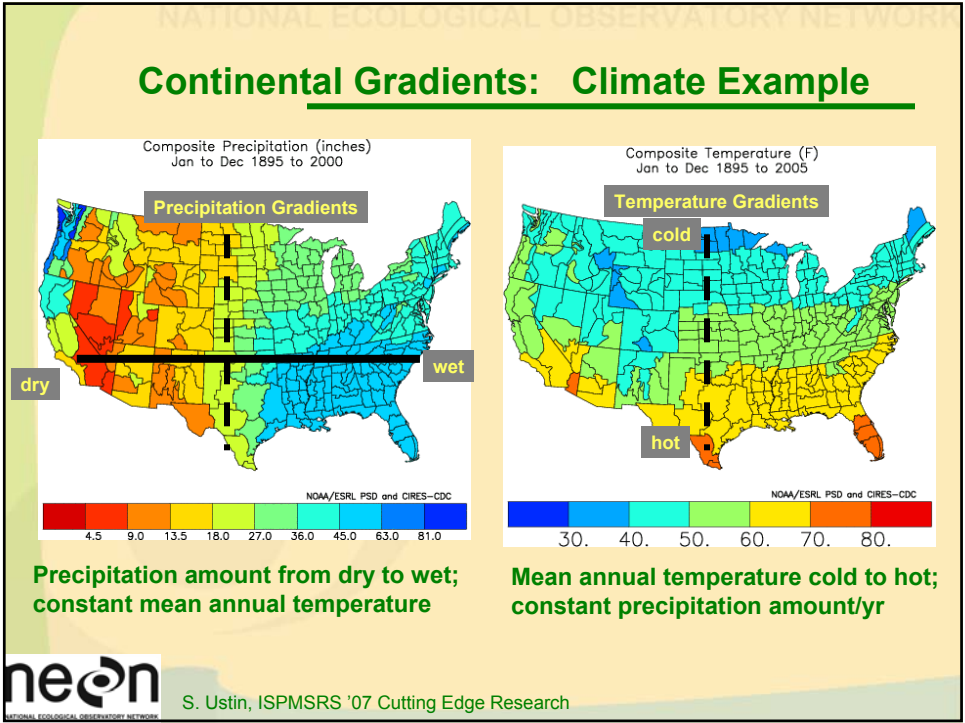
Climate and Soils

25 clusters

Bill Hargrove, Oak Ridge National Lab, DOE


neon

S. Ustin, ISPMSRS '07 Cutting Edge Research




NATIONAL ECOLOGICAL OBSERVATORY NETWORK

Concept of Fundamental Instrument Unit within a NEON Domain



Source: Image copyright CENS, illustrated by Jason C. Fisher.

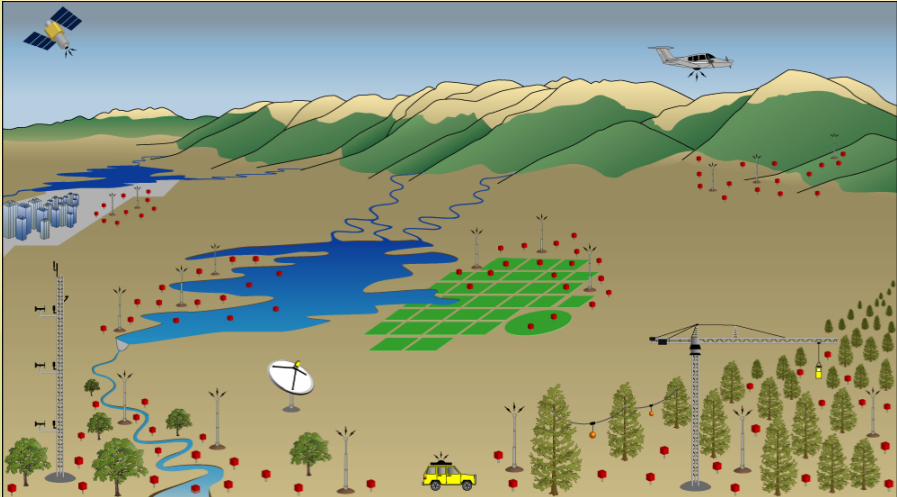



neon  
NATIONAL ECOLOGICAL OBSERVATORY NETWORK

Sensor arrays (canopy microclimate, soil, aquatic), BioMesoNet towers, and other embedded or robotically-controlled sensors are depicted.

NATIONAL ECOLOGICAL OBSERVATORY NETWORK

Nationally Distributed Observatory Network  
Deployed across wildlands and urban gradients

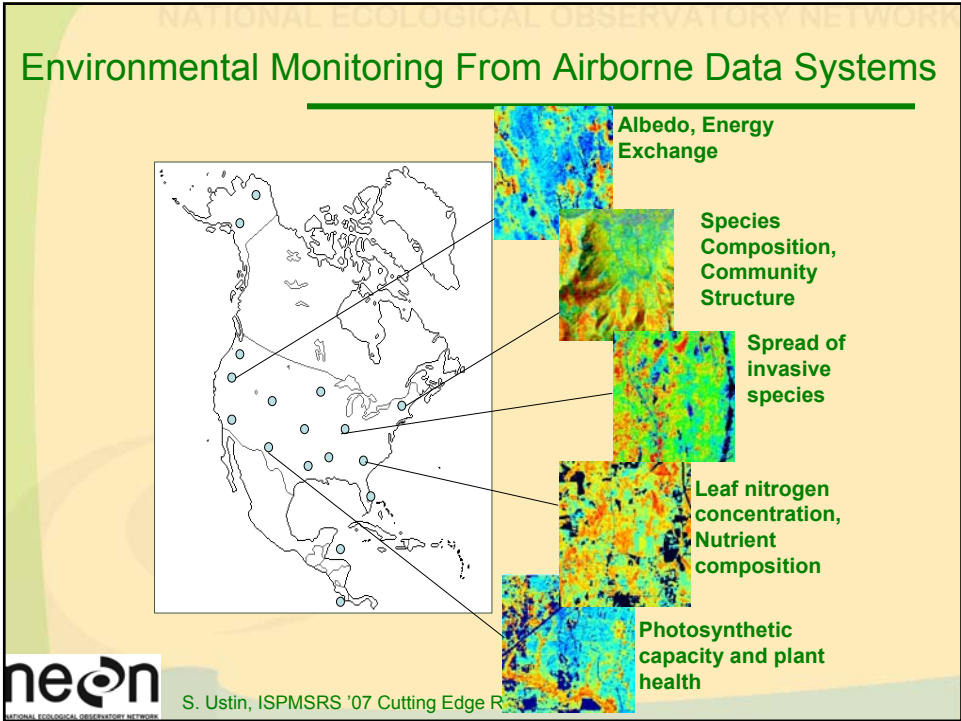




neon  
NATIONAL ECOLOGICAL OBSERVATORY NETWORK

S. Ustin, ISPMSRS '07 Cutting Edge Research





NATIONAL ECOLOGICAL OBSERVATORY NETWORK

NEON Airborne Observatory

Partnerships for Satellite Data Access

- Landsat (now operational), NPOESS, etc.
- possible hyperspectral and/or Lidar satellite imagers

NEON Airborne Plan: Flexible Responses

- 2 Continental “Large” packages (reconfigurable components)

Hyperspectral Imager and Full Waveform Lidar

- Annual/biannual mapping
- Supports continental scaling
- Satellite calibration
- Deployable to extreme events like hurricanes, wildfires, pest outbreaks

- 5 Regional “Smaller” packages
  - supports gradients & multi-domain efforts
  - provides dedicated multitemporal data

Prototype Continental Package

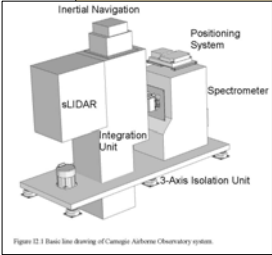


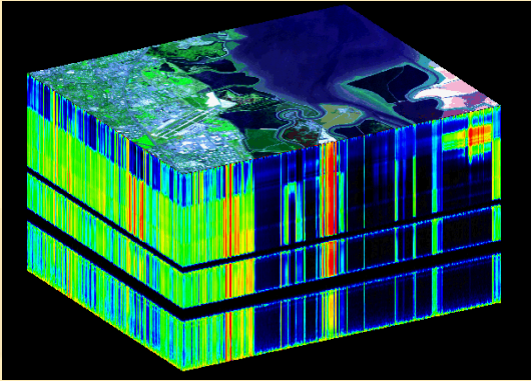
Figure 12.1 Basic line drawing of Prototype Airborne Observatory system.

NATIONAL ECOLOGICAL OBSERVATORY NETWORK


### Airborne Observation Platform

#### Airborne Hyperspectral Data

- Coupling Observations from Site Studies to Satellites
- Monitoring Climate Change Impacts



High Fidelity Imaging Spectrometers with 100s of Narrow Spectral Bands UV to Thermal Wavebands



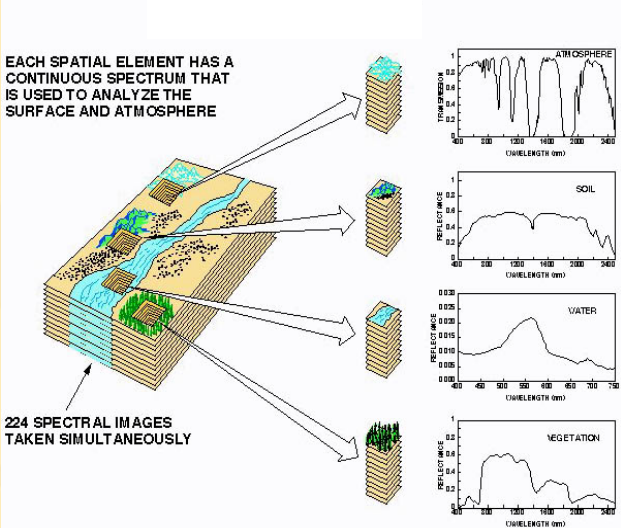
S. Ustin, ISPMSRS '07 Cutting Edge Research


NATIONAL ECOLOGICAL OBSERVATORY NETWORK

### High-Fidelity Imaging Spectroscopy

#### Standard NEON Products:

- Vegetation indexes
- Leaf Area Index
- Canopy moisture
- Canopy chemistry (terrestrial and aquatic)
- Canopy pigments (terrestrial and aquatic)
- Spectral unmixing of landscape components
- % cover, NPV, etc.
- Ecological/ Biological diversity maps

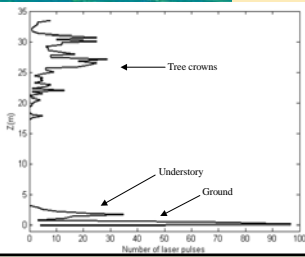

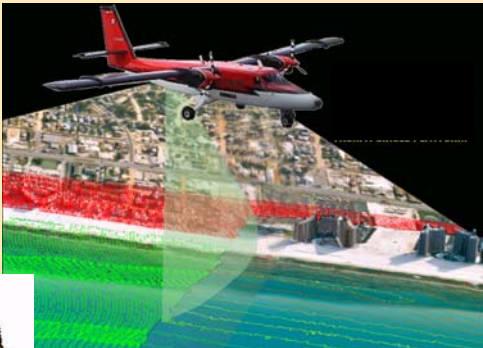




S. Ustin, ISPMSRS '07 Cutting Edge Research

### Airborne Observation Platform

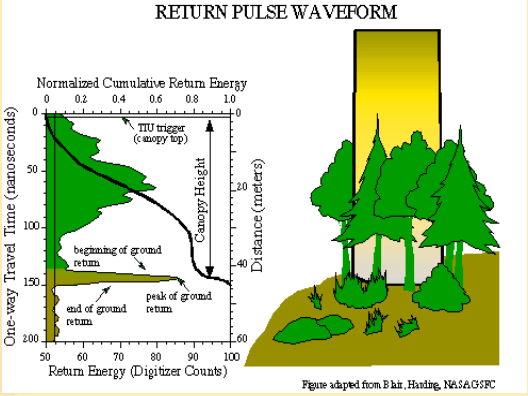
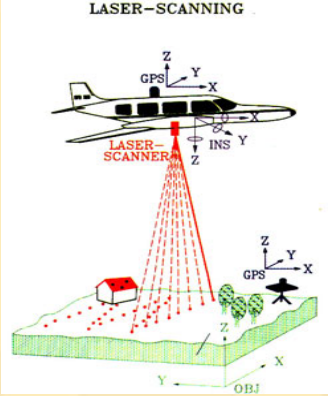
- Vegetation height & distribution of structural elements
- Canopy top topography
- Biomass
- Life form diversity



•Ground Topography & Bathymetry

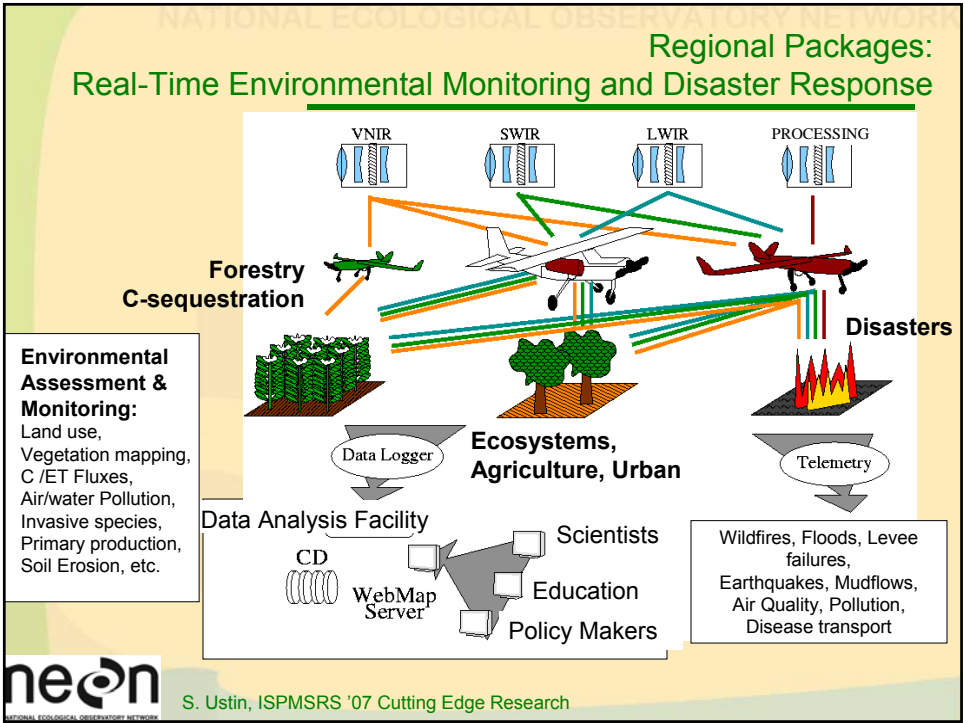
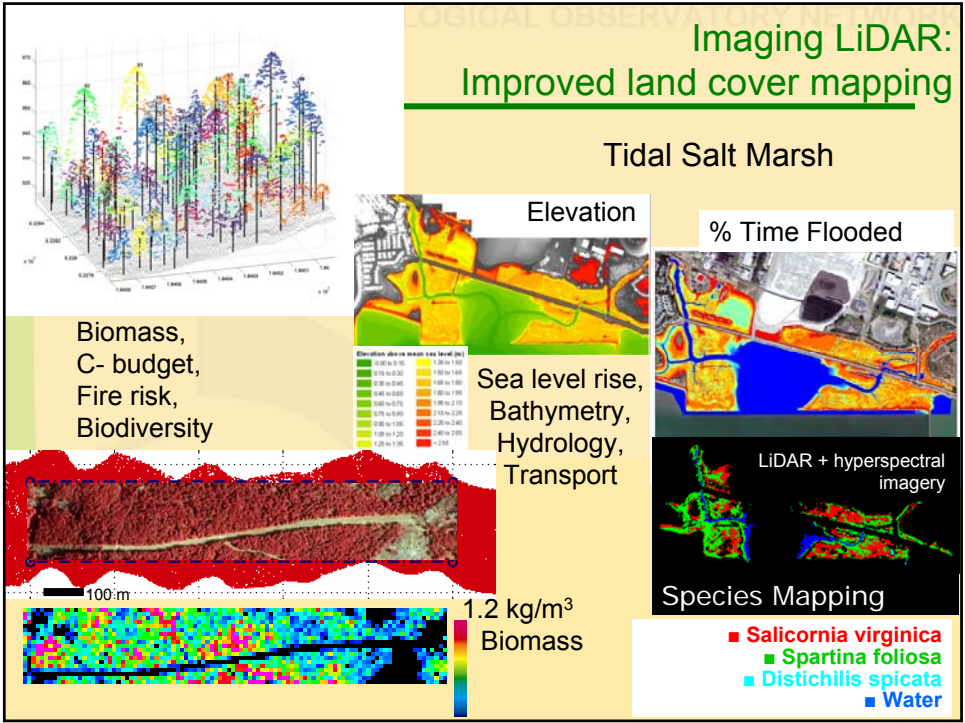
**neon** S. Ustin, ISPMSRS '07 Cutting Edge Research

### Imaging LiDAR



Differential Absorption LiDAR (multiple wavelengths)  
Imaging Full Waveform

**neon** S. Ustin, ISPMSRS '07 Cutting Edge Research







**Imaging Spectrometer:**  
400-1050 nm  
2.3 nm FWHM  
1500 pixel cross-track  
< 2.0 m GIFOV

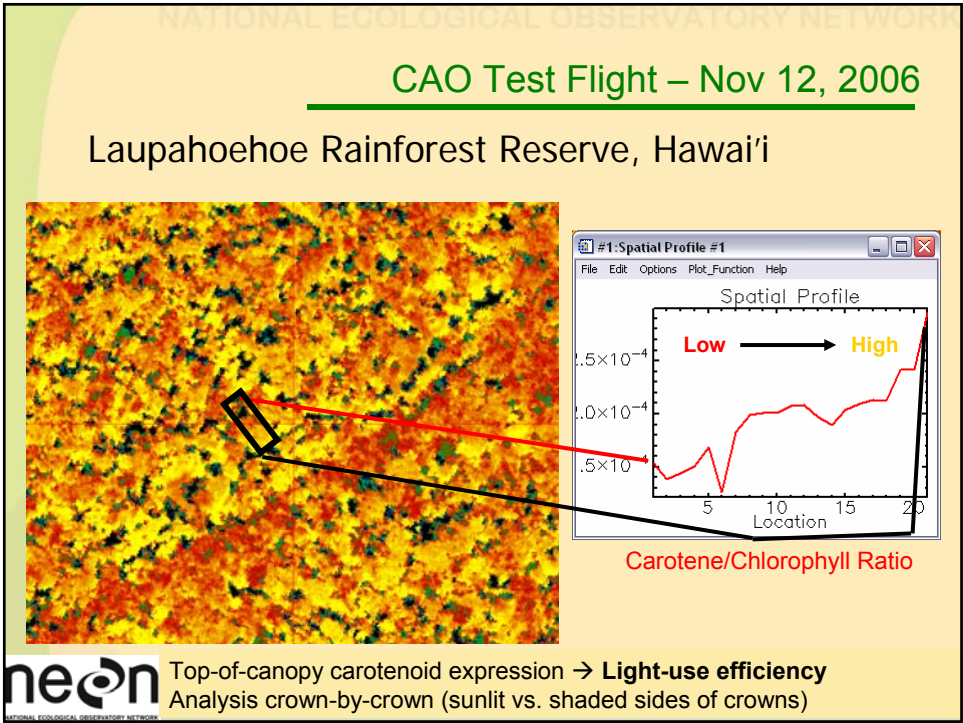
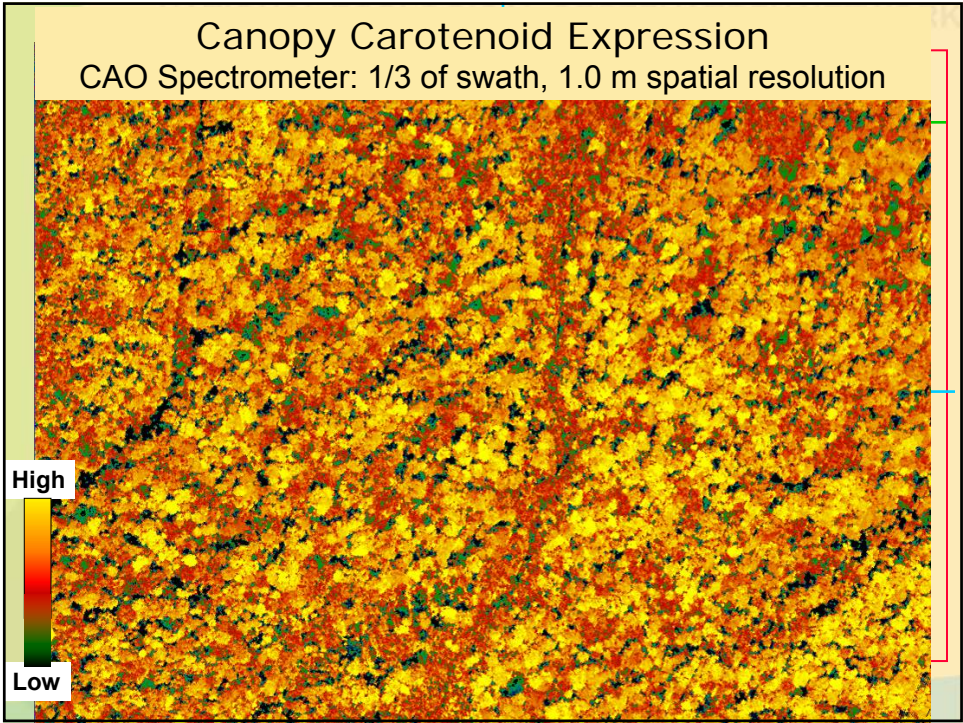
**LIDAR:**  
100 kHz  
Full waveform digitization  
< 0.5 m spot spacing

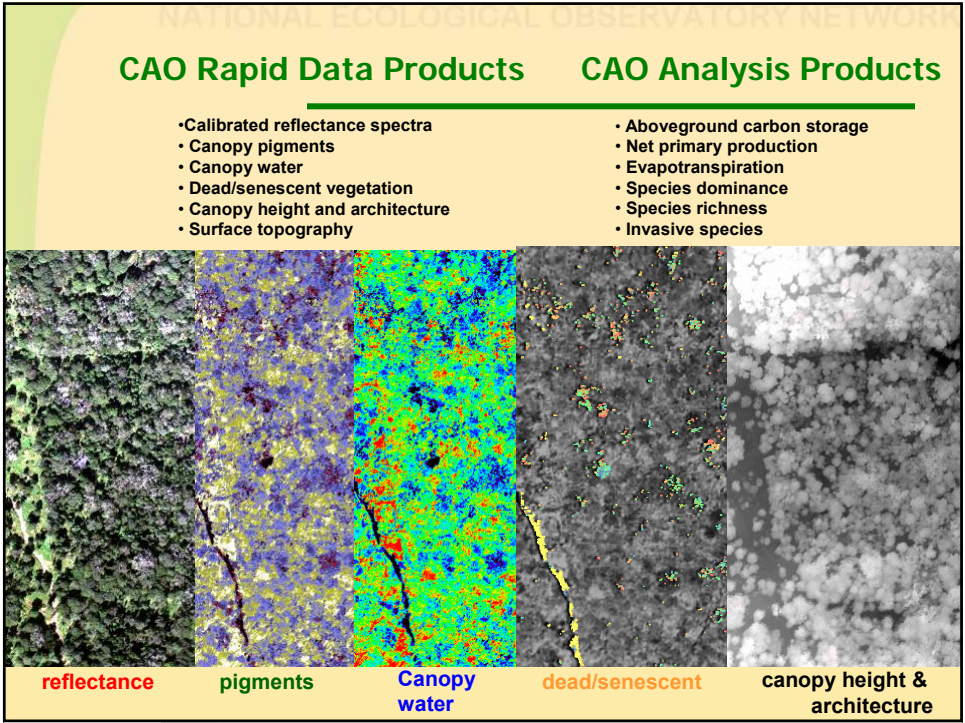
**Integration:**  
Real-time ortho-georectification  
In-flight atmospheric correction

**neon** S. Ustin, ISPMSRS '07 Cutting

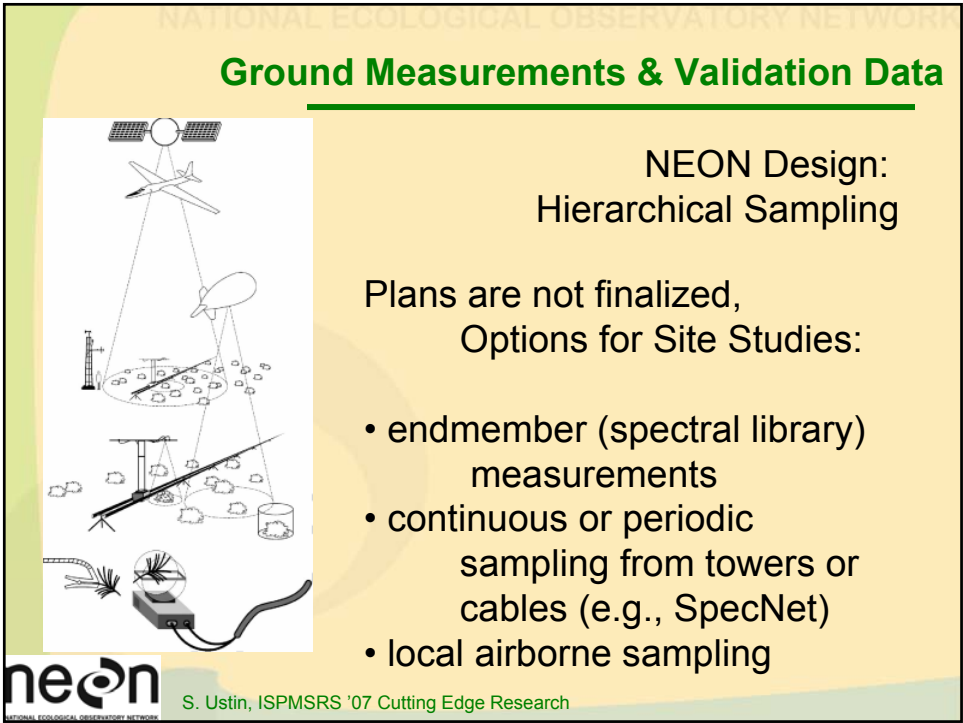
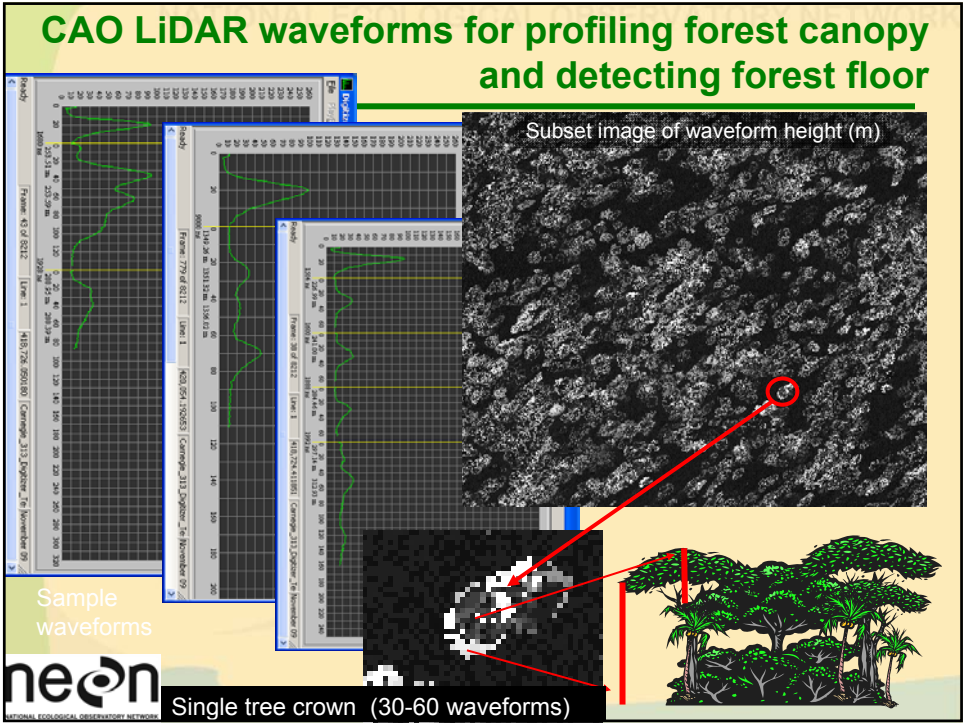
CARNEGIE AIRBORNE OBSERVATORY





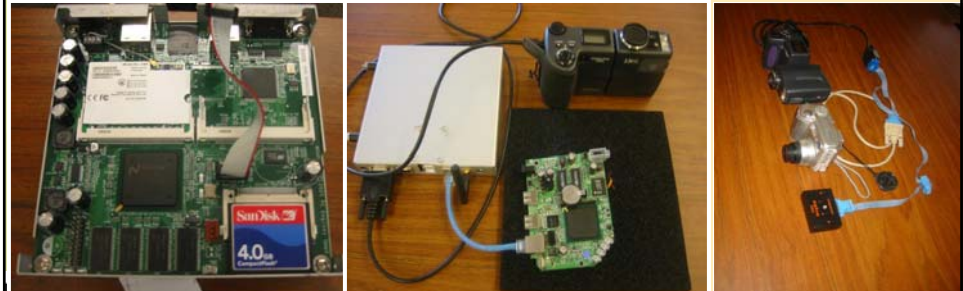
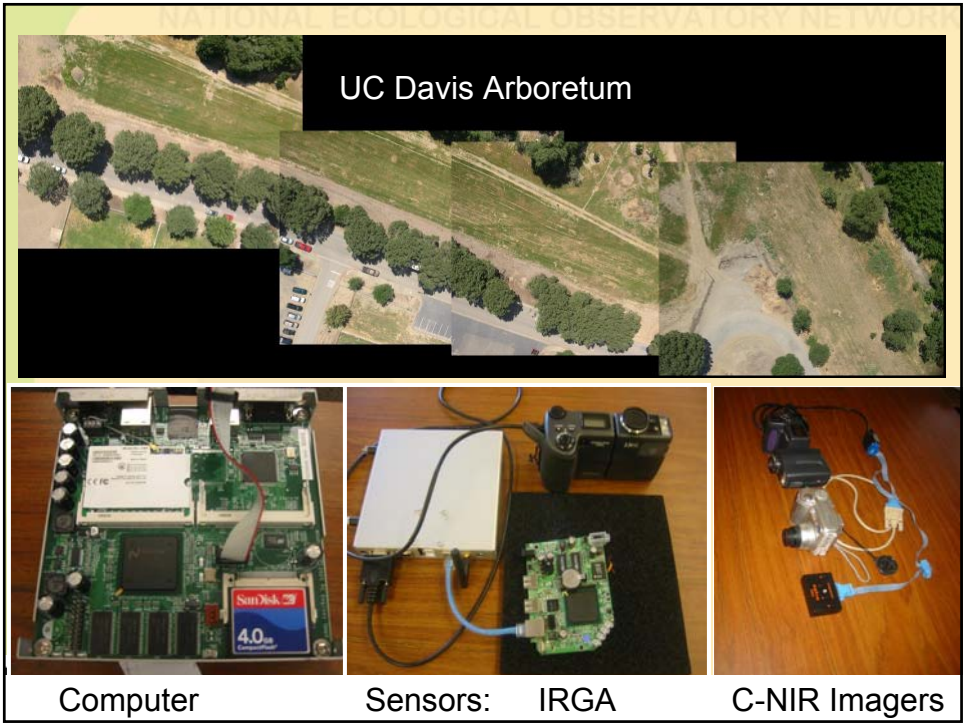












Computer      Sensors: IRGA      C-NIR Imagers

NATIONAL ECOLOGICAL OBSERVATORY NETWORK

Miniaturized Imaging Spectrometers





Imaging Spectrometers  
350-2500 nm range

Silicon 128, 256, 512 elements  
InGaAs 256 elements  
Extended InGaAs 256 elements

**Dimensions with standard detector**


Length	55 mm
Width	24 mm
Height	48 mm
Weight	~1 lb.




S. Ustin, ISPMSRS '07 Cutting Edge Research

NATIONAL ECOLOGICAL OBSERVATORY NETWORK



Thank You!



UC Davis Arboretum







S. Ustin, ISPMSRS '07 Cutting Edge Research



Production and Distribution of  
NASA MODIS Remote  
Sensing Products

ISPMSRS'07  
Mar. 14, 2007  
Robert Wolfe  
NASA GSFC Code 614.5





MODIS Land Products

Energy Balance Product Suite

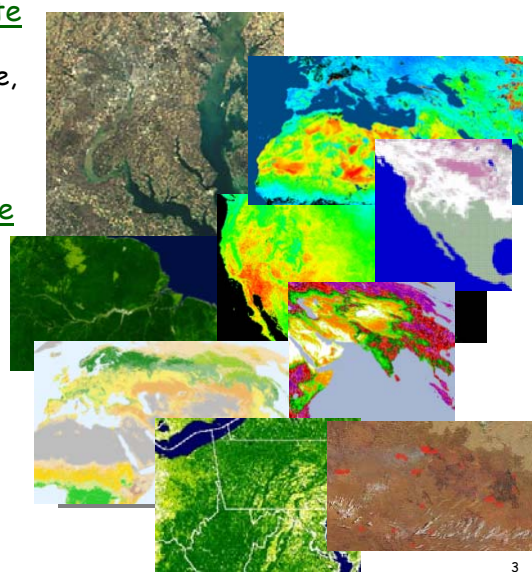
- Surface Reflectance
- Land Surface Temperature, Emmissivity
- BRDF/Albedo
- Snow/Sea-ice Cover

Vegetation Parameters Suite

- Vegetation Indices
- LAI/FPAR
- GPP/NPP

Land Cover/Land Use Suite



- Land Cover/Vegetation Dynamics
- Vegetation Continuous Fields
- Vegetation Cover Change
- Fire and Burned Area



ISPMSRS'07 - Wolfe

3





[home](#) | [products](#) | [people](#) | [news](#) | [links](#) | [tools](#)


### Mission

Global change research investigates the underlying processes of change and their manifestation, the impacts and the prediction of change. Monitoring these changes provides an important underpinning to both global change research and resource management. Monitoring of land cover and land use is an important element of the NASA Earth Science Enterprise. Moderate resolution remote sensing provides a means for quantifying land surface characteristics such as land cover type and extent, snow cover extent, surface temperature, leaf area index, fire occurrence. Satellite measurements of leaf area, leaf duration and net primary productivity provide important inputs to parameterize or validate ecosystem process models. High quality, consistent and well-calibrated satellite measurements are needed if we are to detect and monitor changes and trends in these variables. Developing the next-generation data sets for global change research is the challenge given to the MODIS Science Team.

### MODIS News...

- MODIS Reprocessing Schedule
- Collection 5 changes
- MODIS Land Collection 5 Workshop, held Jan. 17-18, 2007, at the University of Maryland
- Seeking community input on the ESDR White Papers developed by the NASA Land Measurement Team

### MODIS Web Organigram



### How to Get MODIS Data


- Land Processes (EDC) DAAC
- NSIDC DAAC (Snow/Ice Products)
- ORNL DAAC (Land Subsets)
- Level 1 and Atmosphere Distribution System (LAADS)
- MODIS Rapid Response System
- UMD Web Fire Mapper
- MODIS Direct Broadcast

### Additional MODIS Land Information

- Land Validation
- Land QA
- Land Global Browse
- Land Golden Tile Browse

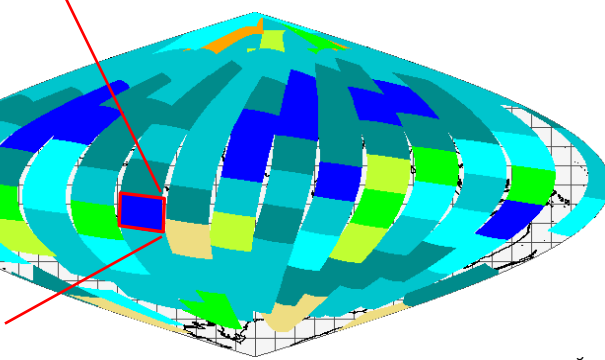

<http://modis-land.gsfc.nasa.gov/>

4



## Level 2 Products


- Retrieved geophysical parameters at the same location and in the same format as the MODIS Level 1 instrument data
  - 288 granules/day; 5 min.; approx. 2340 x 2030 km
  - 250m, 500m and 1km nadir resolutions



ISPMRSR5'07 - Wolfe

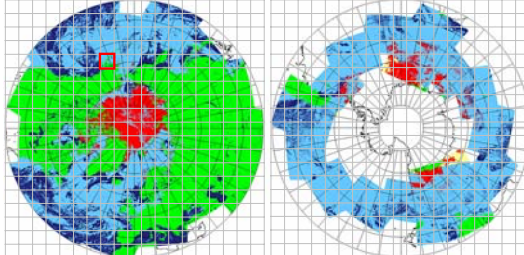
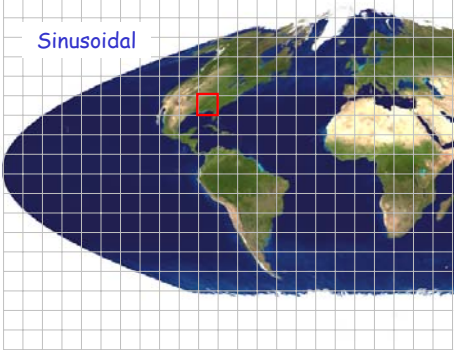
2





### Level 2G, 3 and 4 Products (fine resolution)


Sinusoidal



- Level 2G/3: earth-gridded geophysical parameters
- Level 4: earth-gridded model outputs
- Daily, 8-day, 16-day, 32-day, monthly and yearly products
- 10° x 10° Tiles (□)
- Sinusoidal (equatorial); 7.5, 15 and 30 arcsec. resolution (roughly 250m, 500m and 1 km)
- LAEA (sea-ice products, polar projection)

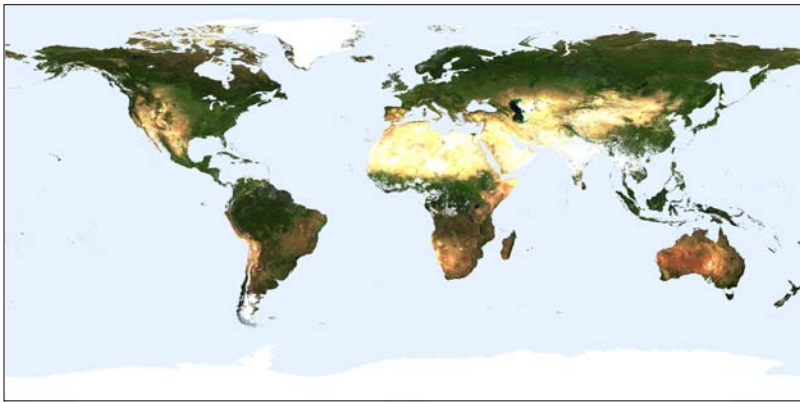
Lambert  
Azimuthal  
Equal Area  
(LAEA)

6



### Climate modeling grid products


- Resolution: 0.05° (now) and 0.25° (previous) degrees
- Almost all products are lat/long
  - sea-ice is current exception - in polar grid (snow in C5)



(from BU - NBAR CMG - days 193-208, 2001)

ISPMSRS'07 - Wolfe

7




### Product Format

- Hierarchical Data Format (HDF) - Self describing file format
- Science Data Sets (SDSs) - 2D, 3D or 4D arrays
  - Bit Fields - unsigned integers broken into groups of bits
  - Discrete values - e.g., Snow, Cloud, etc.
  - Scaled Integers - valid range, scale and offset included
- Attributes - text or other data that annotates the file (global) or arrays (SDSs)
- Metadata - ECS metadata for products (stored as attributes)
  - includes QA information, date/time products acquired/produced, etc.
- .met file also contains the ECS core metadata
  - some additional fields
  - some fields (QA, etc.) may be updated when product distributed
- HDF-EOS Metadata (SWATH or GRID) - geometric information that relates data to specific earth locations

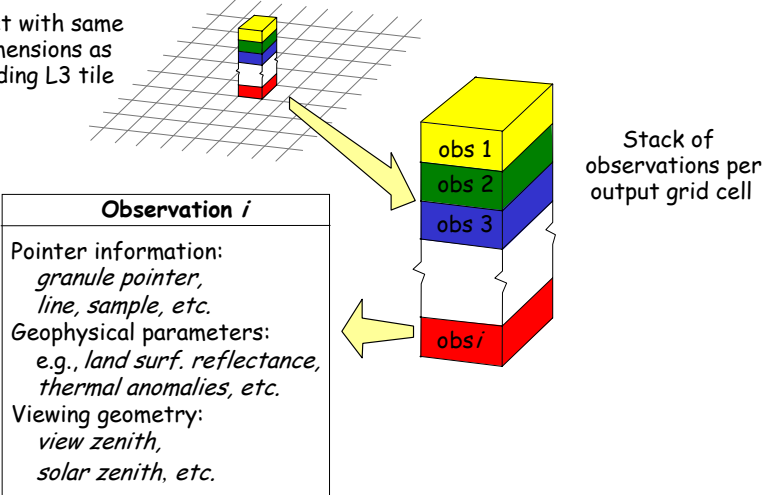
ISPMRS'07 - Wolfe

8



### L2G Format

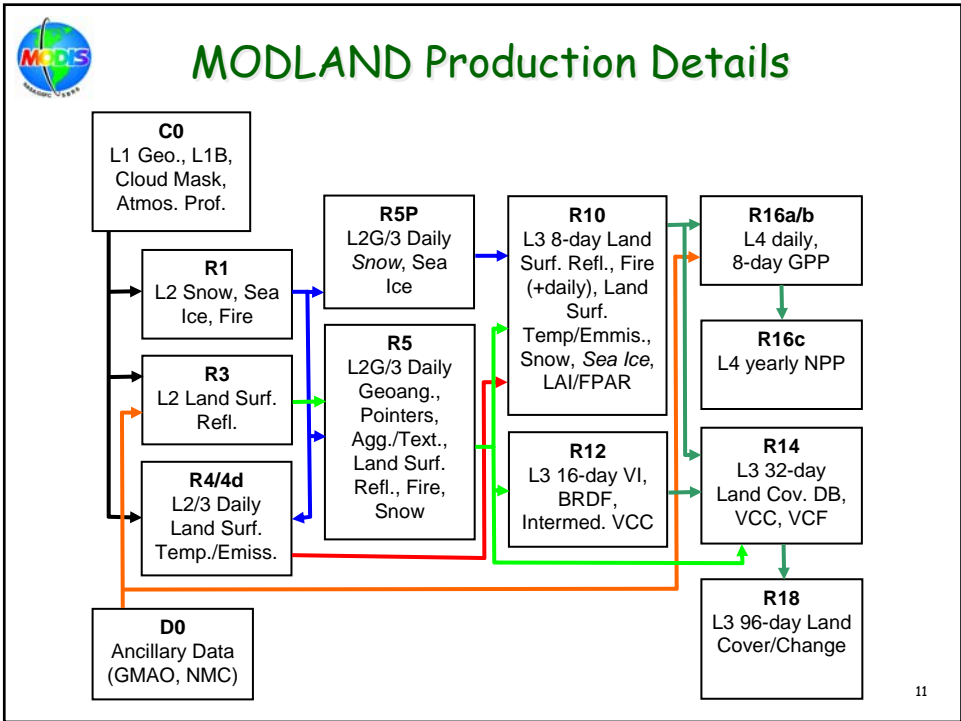
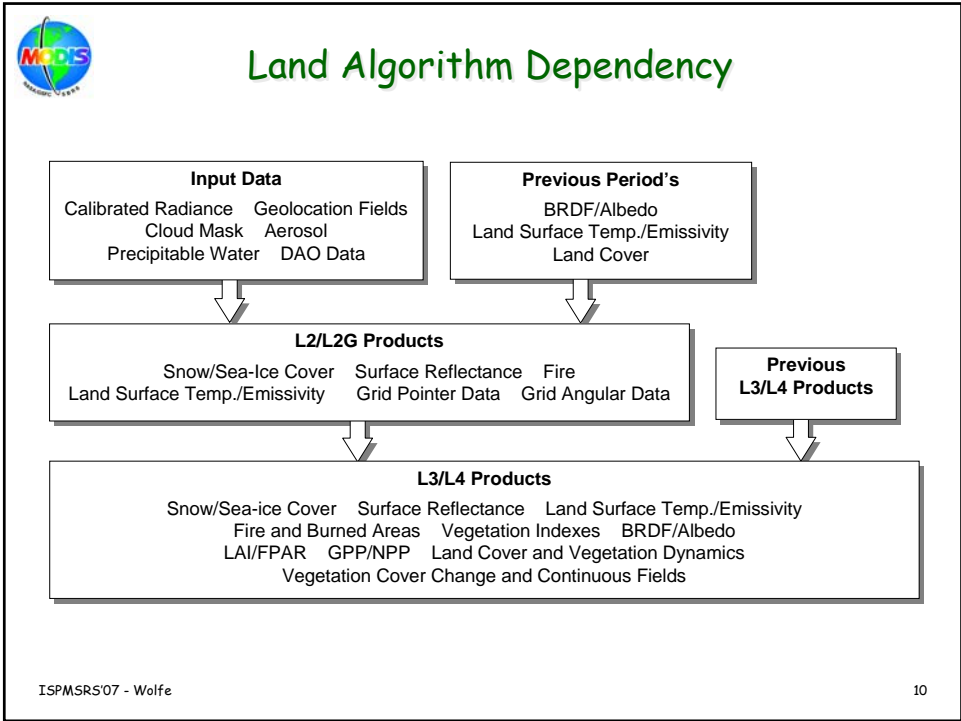
L2G product with same spatial dimensions as corresponding L3 tile

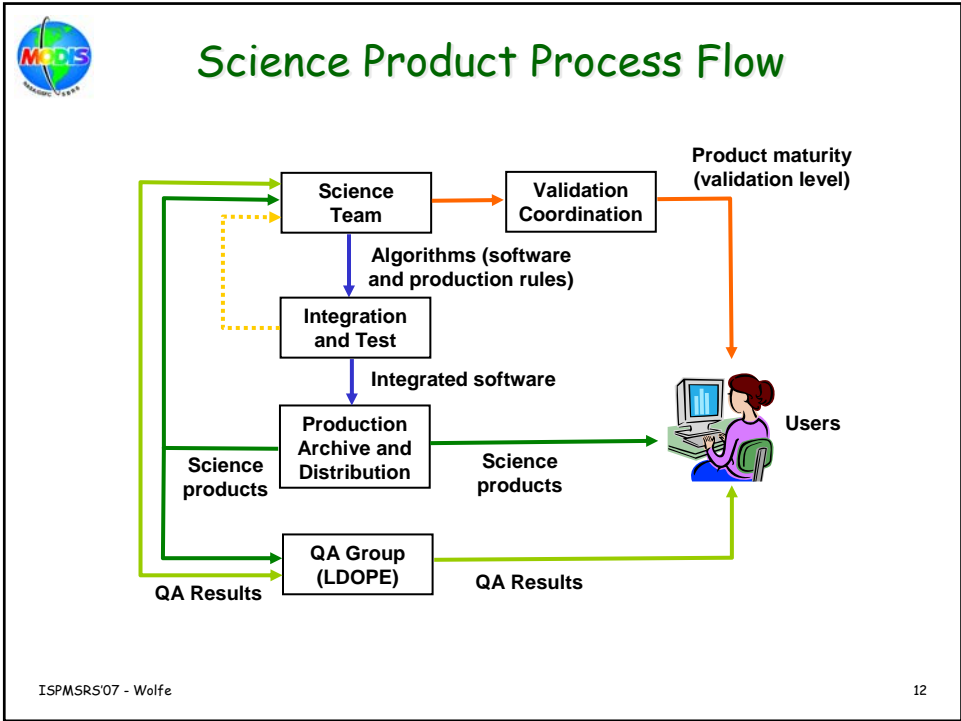


Observation <i>i</i>
Pointer information: <i>granule pointer, line, sample, etc.</i>
Geophysical parameters: <i>e.g., land surf. reflectance, thermal anomalies, etc.</i>
Viewing geometry: <i>view zenith, solar zenith, etc.</i>

ISPMRS'07 - Wolfe

9







### MODLAND QA

[http://landweb.nascom.nasa.gov/cgi-bin/QA\\_WWW/newPage.cgi](http://landweb.nascom.nasa.gov/cgi-bin/QA_WWW/newPage.cgi)

QA Summaries

Known Issues


Global Browse

Time Series



ISPMRS'07 - Wolfe





# MODLAND Validation

<http://landval.gsfc.nasa.gov/>


Val Summaries

EOS Core Sites

Major Campaigns

Val Metadata w. ORNL

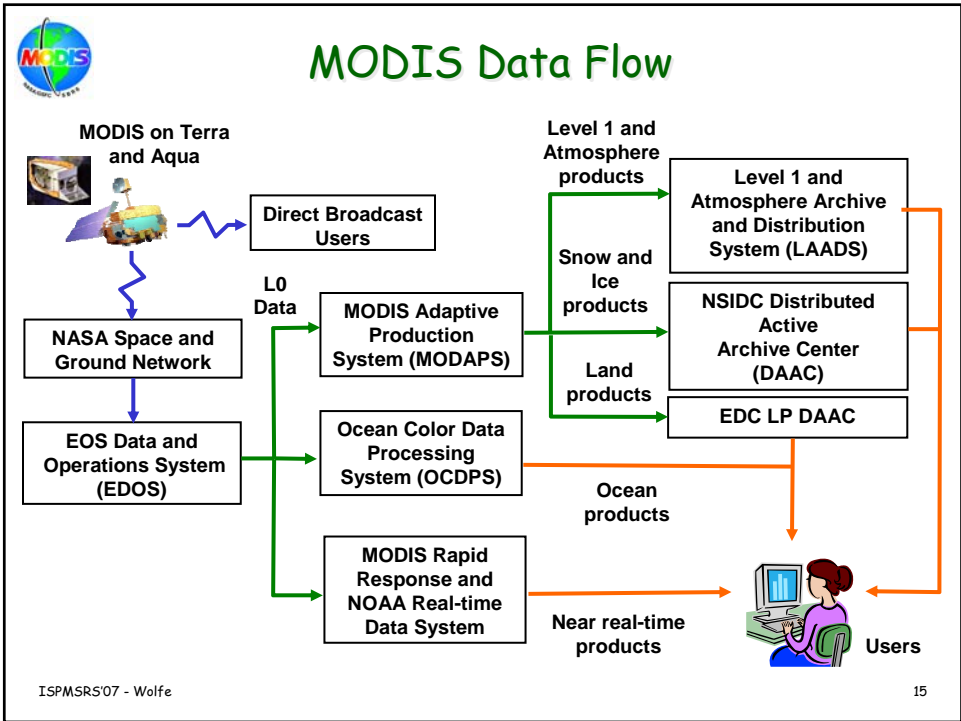
MODIS Validation Data sub sets w. EDC

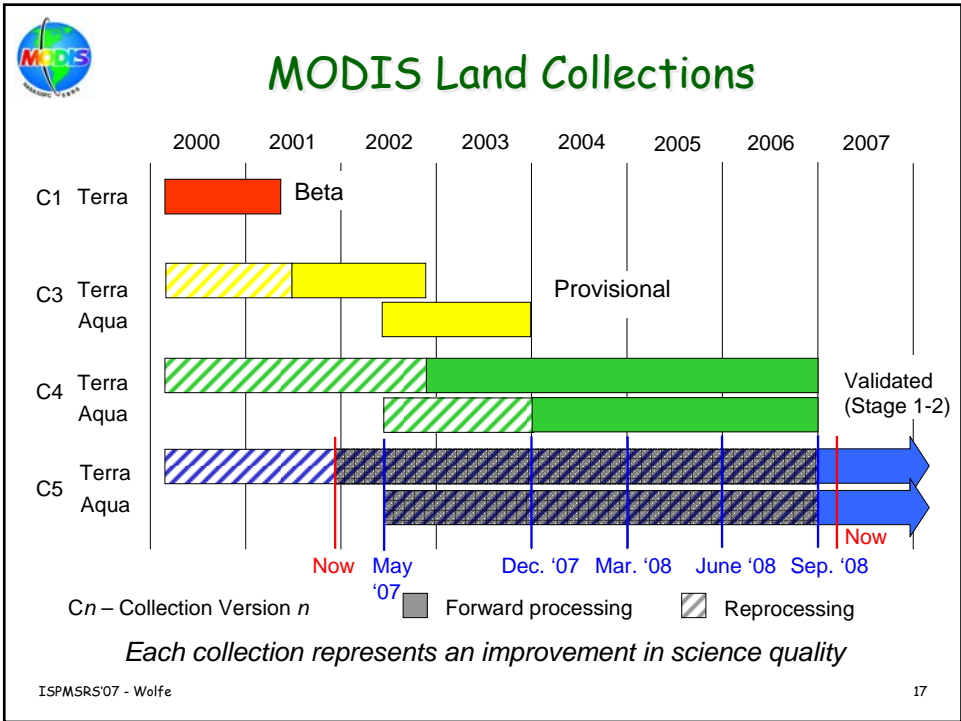
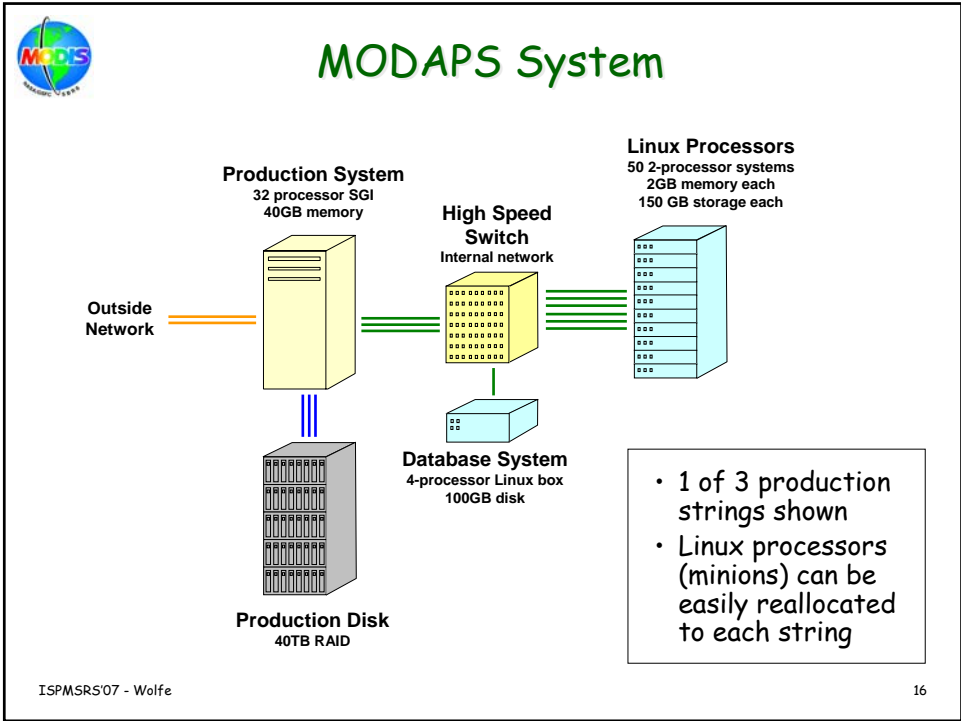



The screenshot shows the 'MODIS land team validation' website. It features a header with the NASA logo and 'GODDARD SPACE FLIGHT CENTER'. The main title is 'MODIS land team validation'. Below the title is a navigation bar with links: Home, Core Sites, Val Status, Campaigns, and Documentation. The page content includes an 'Announcements' section with several bullet points about workshops and meetings. There is also a section titled 'The MODIS Land Validation Strategy' which describes the validation process and the MODIS Land (MODLAND) product quality. At the bottom, there is a 'MODIS News' section with links to Terra and Aqua.

ISPMRSR5'07 - Wolfe

14








## MODIS Land Collection 5 Changes - Summary

- Used improved Land/Water mask and new Land Cover map based on 3 years of Collection 4 data
- Refined surface reflectance by adopting a dynamic aerosol model in atmospheric correction
- Reduced size and complexity of daily surface reflectance products
- Improved quality of the Land Surface Temperature by revising the day/night algorithm and improving the detection and filtering of cloud contaminated observations
- Increased resolution of BRDF/Albedo products to 500m; 8-day overlapped production
- Refined LAI/FPAR LUTs to improve numerical accuracy of the radiative transfer simulations; 4-day combined product
- Added fractional snow algorithm in the snow product
- Burned area product added
- Improved ancillary data interpolation to remove artifacts in the NPP product
- Reduced size of all Land products through HDF internal compression

ISPMSRS'07 - Wolfe


18




## C5 Surface Reflectance

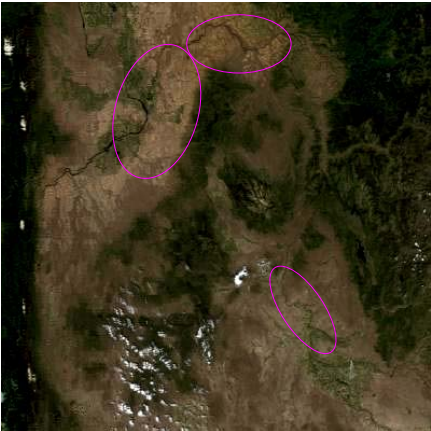
The Collection 5 surface reflectance algorithm retrieves the aerosol model along with the aerosol optical thickness.

This means less overcorrection in the surface reflectance product





C004



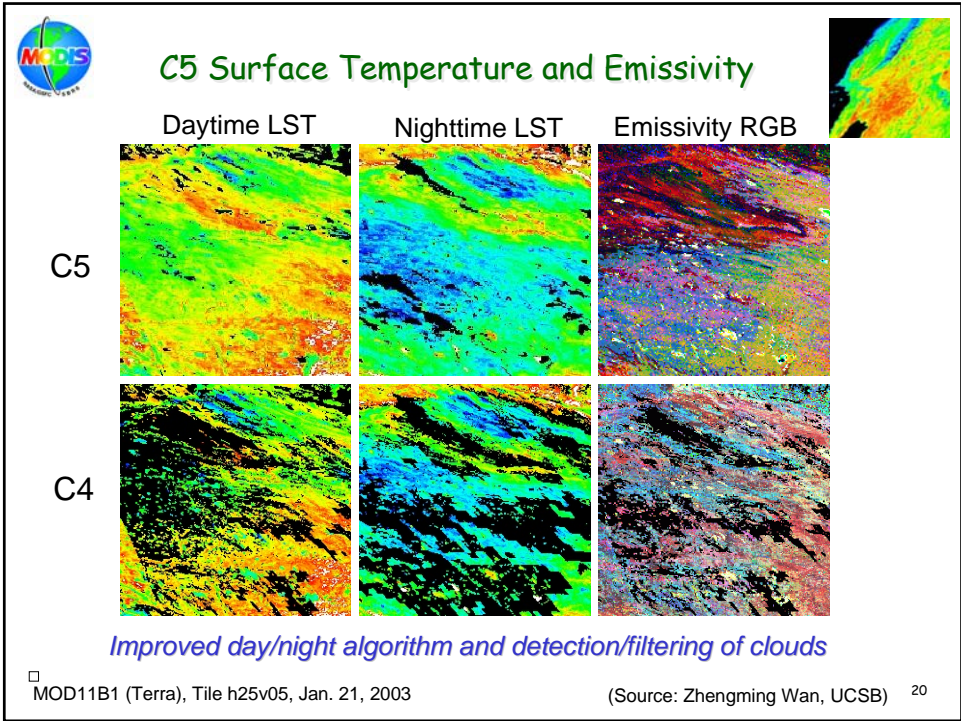
C005

ISPMSRS'07 - Wolfe

*New dynamic aerosol model*

(Source: Eric Vermote, UMD)

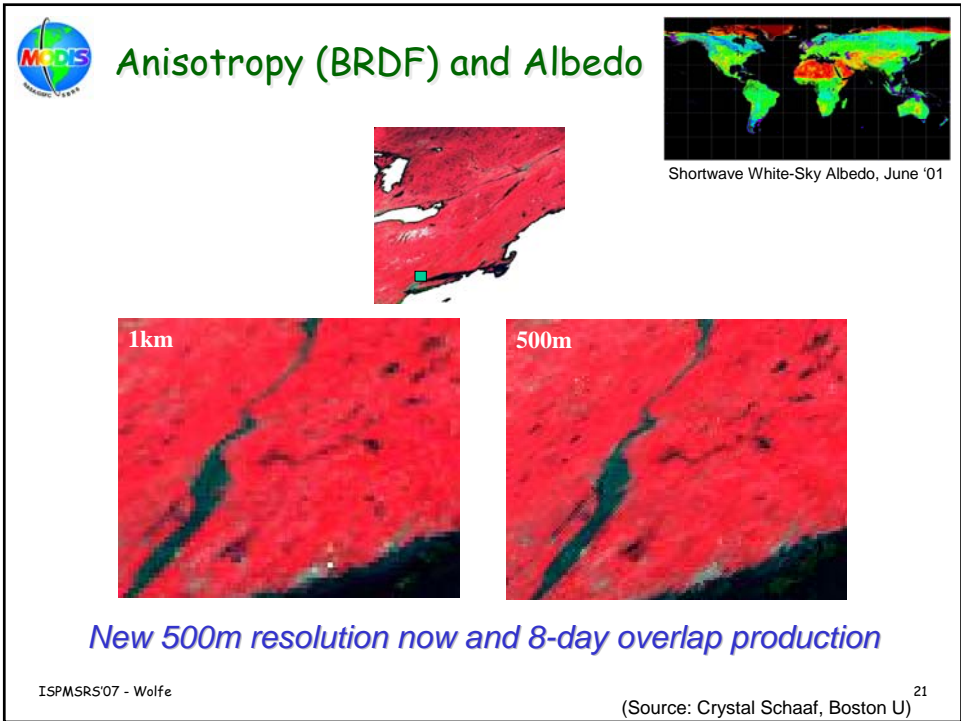
19



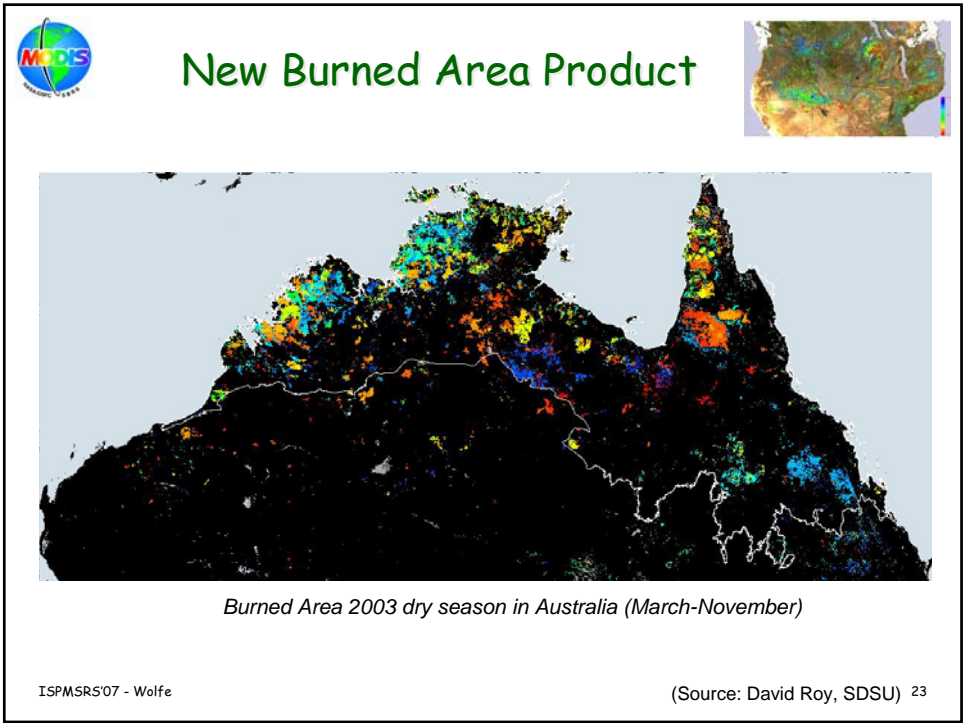
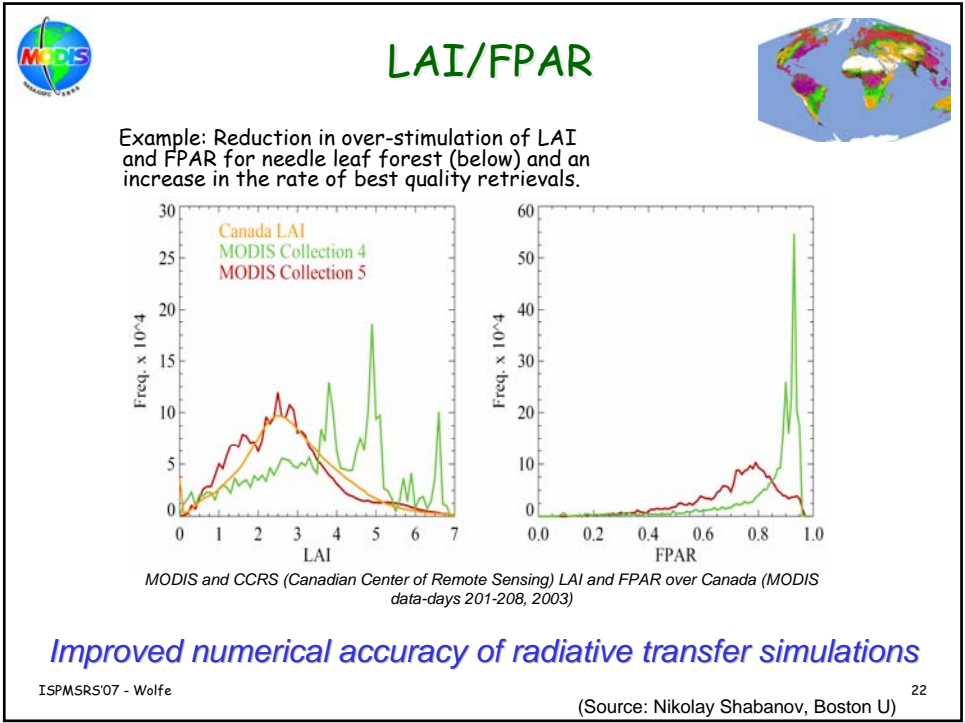
*Improved day/night algorithm and detection/filtering of clouds*


□ MOD11B1 (Terra), Tile h25v05, Jan. 21, 2003

(Source: Zhengming Wan, UCSB) <sup>20</sup>










Land C5 Reduced Product Volume

	MODAPS Production (GB/day)		Export Volume (GB/day)			
			LP DAAC		NSIDC DAAC	
	C4	C5	C4	C5	C4	C5
L2 - L3 Daily	456	140	265	31	7	<1
Level 3 8-day +	23	26	70	19	1	<1
Total	479	166	335	50	8	1

Reduced size of all Land products through HDF internal compression

ISPMSRS'07 - Wolfe

24

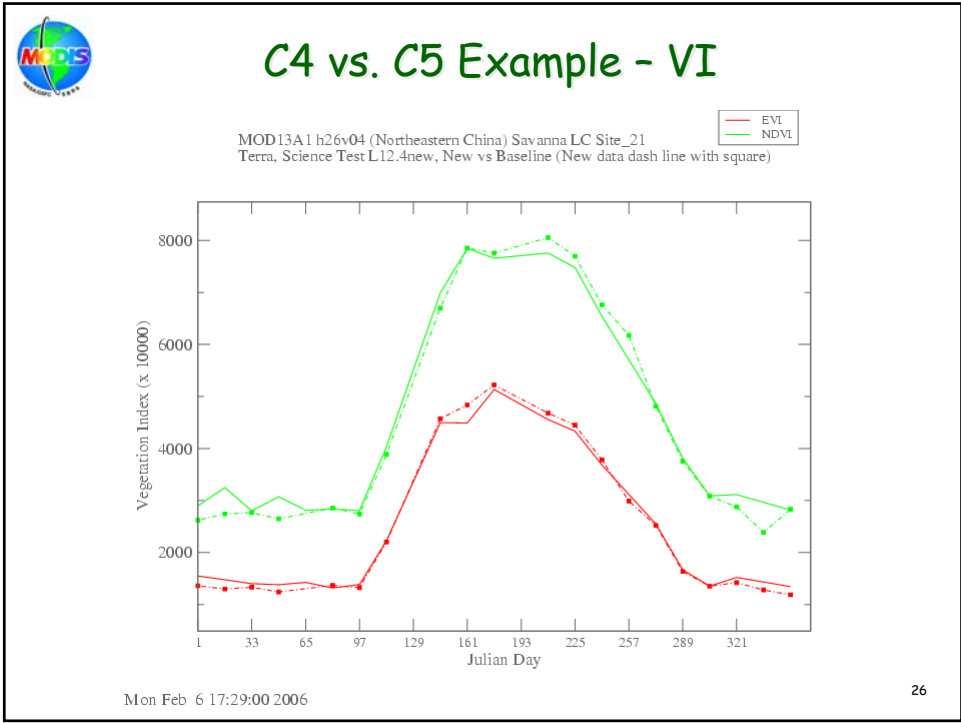



C4 to C5 Transition


- C5 data products are produced using the latest available versions of the science algorithms developed by the MODIS Land Science Team
  - changes to fix known problems
  - C5 science improvements
- C5 product format may have changed from the C4
- C5 product quality both at the pixel level and the granule level may differ from the C4
- It take  $1\frac{3}{4}$  years to complete the remaining C5 reprocessing
  - until that time, the full data record will not have been processed into either C4 or C5
- So - caution should be used if combining C5 and C4 products
  - science team members have made specific recommendations

ISPMSRS'07 - Wolfe

25









home products

MODIS News...

- MODIS Reprocessing Schedule
- Collection 5 Changes
- MODIS Land Collection 5 Workshop, held Jan. 17-18, 2007, at the University of Maryland
- Seeking community input on the ESOR White Papers developed by the NASA Land Measurement Team

MODIS Web Organigram





GODDARD SPACE FLIGHT CENTER

MODIS Land

home products people news links tools

### MODIS C5 Processing Schedule

Processing of the newest MODIS Land collection (also known as Collection 5 or C5) commenced in September of 2006 starting with the first Terra data collected in February of 2000. Collection 5 processing of current MODIS data, or forward processing, began at the beginning of 2007. The full reprocessing is expected to be completed in September of 2008.

The plan for completing each year of either Terra-only, Terra + Aqua (combined), and Aqua-only data is indicated below. Aqua launch was in May of 2002.

Expected Completion Date by Data-Year

- 2000 - completed
- 2001 - March 2007
- 2002 - August 2007
- 2003 - December 2007
- 2004 - March 2008
- 2005 - June 2008
- 2006 - September 2008

Details on the C5 reprocessing effort in relation to specific MODIS Land products can be found in presentations by individual science team members made at the January 2007 C5 Workshop.

### MODIS News...

Link to news information from the MODIS web site

MOD12G2: Global Land Cover Type - MOD12G2: Land Cover Dynamics  
Powerpoint (3.7 MB) | PDF (8.9 MB)

MODIS Active Fire Product: Collection 5 Changes  
Powerpoint (348 KB) | PDF (132 KB)

L. Oglo

browse  
• Land Golden Tile  
Browse

<http://modis-land.gsfc.nasa.gov/>

27



## Collection 6?

- We may not need to reprocess all products for C6
- A C6 reprocessing could incorporate
  - improvements in calibration and geolocation accuracy
  - essential improvements to science products
  - changes to product format
  - recent and new MODIS science products (e.g., Burned Area, MODIS water product)
  - new merged products from multiple instrument (e.g., MODIS & MISR)
- C6 would most likely not start until
  - after C5 reprocessing completes (after Sept. '08)
  - until a recompeted science team (round 3) develops and tests any improvements - C5 took more than 2 years

ISPMSRS'07 - Wolfe

28



## Getting MODIS Data

- Order from DAAC through EOS Data Gateway
  - response is a few hours
  - services (e.g. subsetting) available for some products
- Get data from DAAC data pools
  - most recently produced data are on-line and available via FTP
- Get data from other sources (LAADS, Science team sites, MODIS Rapid Response, direct broadcast, etc.)

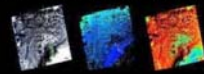


### DAAC Data Pool

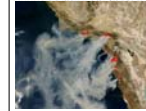


### LAADS Web

Level 1 and Atmosphere Archive and Distribution System




### MODIS Rapid Response



ISPMSRS'07 - Wolfe


29






# MODLAND Website

http://modis-land.gsfc.nasa.gov/



GODDARD SPACE FLIGHT CENTER

+ NASA Homepage




homeproductspeoplenewslinkstools

MODIS News...

- Collection 5 Change Register - MODIS 18, 2007, University Maryland, Draft Agenda
- Seeking community input on ESOR White Papers developed by the NASA Land Measurement Team

MODIS Web Organigram



Surface Reflectance

Snow Cover/Sea Ice

Land Surface Temperature

Land Cover/Dynamics

Vegetation Indices

Thermal Anomalies/Fire

LAI/FPAR

Net photosynthesis


BIO/Albedo

Vegetation Cover Conversion

Important research element means character, leaf area measurement, print inputs, process well-calibrated and tree next-generation Science

GODDARD SPACE FLIGHT CENTER


+ NASA Homepage



homeproductspeoplenewslinkstools

## Land Cover Change and Conversion

The Vegetation Continuous Fields (VCF) and its Vegetation Cover Conversion (VCC) products provide estimates of global and regional vegetation cover for the study of biogeochemical cycles, ecosystem assessment, and land management. The VCF product provides global half-year estimates of landscape components (tree cover, herbaceous cover, and bare cover) at 500m. The VCC data set provides quarterly identification of land cover change hot spots at 250m.




Product PB: John Townsend  
PL: maintained product web page

See links below to the Product Description pages posted at the EDC DNAC (product details, data access links, user guides and more...)


Product Name	Terra Product ID	Aqua Product ID
Vegetation Cover Conversion 30-Day L3 Global 250m	MOD44A	name
Vegetation Continuous Fields Yearly L4 Global 500m	MOD44B	name

ISPMRSR07 - Wolfe

30

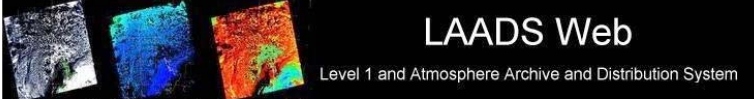


# LAADS Web



GODDARD SPACE FLIGHT CENTER

+ Visit NASA.gov



LAADS Web

Level 1 and Atmosphere Archive and Distribution System

+ HOME

- DATA

+ IMAGES

+ TOOLS

+ HELP

## Data

Search

Search for MODIS level 1 and atmosphere data products by product name, temporal window, collection, and spatial coordinates.

Shopping Cart

View, edit, and order MODIS level 1 and atmosphere data products in your shopping cart.

Data Availability

View a summary of the availability of MODIS level 1 and atmosphere data products in LAADS.

FTP Site


Access all MODIS level 1 and atmosphere data products directly through the LAADS FTP site.

Track Orders

Track previous orders for MODIS level 1 and atmosphere data products.

FIRSTGOV

+ Privacy Policy and Important Notices



Webmaster: Karen Horrocks  
NASA Official: Ed Masuoka  
+ Send Us Your Comments

http://ladsweb.nascom.nasa.gov/


ISPMRSR07 - Wolfe

31

ISPRS WG VII/1

15

188 of 620



## Browsing the Image Archive

**Level 2 Browse**

**Satellite:** Terra

**Date:** November 10, 2001

**Parameter:** RGB

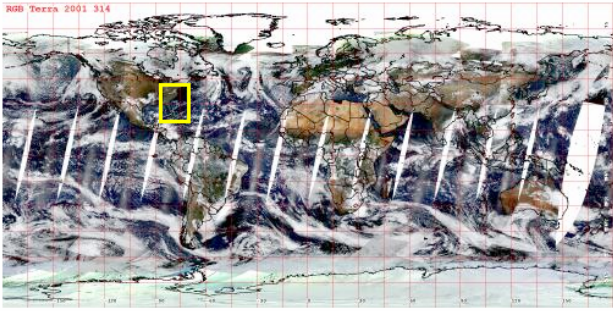
**Collection:** 5

**Satellite:**

Aqua: ☐ Terra: ☒

Month:  Day:  Year:  Parameter:

[+ Previous](#)
[+ View Help](#)




North:

West:  East:

South:

+ View high resolution image of Terra MODIS Level 2 RGB Global Composite for November 10, 2001

ISPMSRS'07 - Wolfe
32



## Summary

- MODIS production and distribution systems
  - are being continuously improved
  - enabled extensive end-to-end testing
  - achieving (relatively) fast processing rates
  - maintaining high distribution volumes and quality user services
- MODIS team has continued to carefully improve the science products
  - large reduction in product volume has been reduced
  - some product formats have been reworked to enable usability
  - C5 reprocessing is underway and will finish in Sept. 2008

ISPMSRS'07 - Wolfe
33





<http://modis-land.gsfc.nasa.gov/>



Questions?

34



# User-driven requirements of the European Hyperspectral Remote Sensing Community

Jens Nieke, the HYRESSA Team,  
and 150 European anonymous HSI researchers

HYRESSA Workshop, Davos, Switzerland, 14-15 Mar 2007  
HYRESSA - HYPerspectral REMote Sensing in Europe specific Support Actions



## Background



### What is HYRESSA?

EC project HYRESSA (FP6-2004-Infrastructures-6-SSA, Contract Number 026194); 10 partners, 9 nations:

Vito: Flemish institute for technological research, Mol, Belgium (coordination)  
DLR: German Aerospace Centre, Wessling, Germany  
RSL: University of Zurich, Remote Sensing Laboratories, Zurich, Switzerland  
GFZ: GeoForschungsZentrum, Potsdam, Germany  
WUR: Wageningen University, Centre for Geo-Information, Wageningen, The Netherlands  
INTA: Instituto Nacional de Técnica Aeroespacial, Torrejón de Ardoz-Madrid, Spain  
ILE ASCR: Academy of Sciences, Institute of Landscape Ecology, Czech Republic  
TO: Tartu Observatoorium, Toravere, Tartumaa, Estonia  
U-Helsinki: University of Helsinki, Geoinformatics Research Group (GIRG), Helsinki, Finland









# Background




## EC-INFRASTR-6: Accompanying Measures for promoting a more coordinated approach to research infrastructures in Europe

### HYRESSA Goals:


- To improve the coordination of flight campaigns and to increase the use of hyperspectral images in Europe,
- To investigate the needs of the EU hyperspectral research community,
- To evaluate needed accuracy, quality and conformity of hyperspectral images,
- To refine protocols related to calibration, acquisition, processing and in-situ measurements in compliance with standards.

HYRESSA Workshop, Davos, Switzerland, 14-15 Mar 2007

HYRESSA - HYPerspectral REMote Sensing in Europe specific Support Actions




# Background



Task	Duration	Who	1	2	3	4	5	6	7	8	9	10	11	12	13	14	15	16	17	18	19	20	21	22	23	24	
<b>HYRESSA Project</b>																											
AM1 Management of HYRESSA	24m	Vito																									
Management of HYRESSA																											
AM2 Coordination	24m	Vito	M					M																			
Coordination																											
Kick off meeting	2d			*																							
Final report	1m																										
AM3 Dissemination	2m	Vito			D1				M											M						M/D9	
Website development	21m																										
Website maintenance	12m																										
Presentations, publications																											
AM4 Contact database	2m	GFZ			M	M/D2																					
Unification of contact database	1m																										
Literature study	1m																										
Internet study	1m																										
AM5 SWOT and User Needs workshop	3m	DLR					M	D3																			
Preparation of workshop	3d						*																				
User need workshop	1m																										
Workshop report																											
AM6 Questionnaire on User Needs (QUN)	2m	RSL						D4																			
Preparation of questionnaire	2m																										
Evaluation of questionnaire	1m																										
Evaluation report																											
AM7 Exploratory workshop	3m	WUR																		M	D6						
Preparation of workshop	3d																			*							
Exploratory workshop	1m																										
Workshop report																											
AM8 Review and refinement protocols	3m	INTA																			M	D7					
Review and refinement protocols	2d																				*						
Protocol meeting	1m																										
Protocol report																											
AM9 Future collaboration plan	2m	UEDIN																						M	D8		
Future collaboration plan	2d																							*			
Future collaboration meeting																											

HYRESSA Workshop, Davos, Switzerland, 14-15 Mar 2007

HYRESSA - HYPerspectral REMote Sensing in Europe specific Support Actions



Metho

QUN: Questionnaire o

VBA: Value Benefit

Evaluation of Results

Presentation/Dissemination

**A: Best image based parameters**

**A1: Spectral parameters**

A11: No. of spectral bands	relative importance scale: 0 - 10	favoured number of spectral bands
1. Spectral bands between 380 and 450 nm		
2. Spectral bands between 450 and 700 nm		
3. Spectral bands between 700 and 1000 nm		
4. Spectral bands between 1000 and 1100 nm		
5. Spectral bands between 1100 and 1400 nm		
6. Spectral bands between 1400 and 1900 nm		
7. Spectral bands between 1900 and 2500 nm		
8. Spectral bands between 3.5 and 4.2 µm		
9. Spectral bands between 4.2 and 5.5 µm		
10. Spectral bands between 5.5 and 8 µm		
11. Spectral bands between 8 and 9 µm		
12. Spectral bands between 9 and 10 µm		
13. Spectral bands between 10 and 14.5 µm		

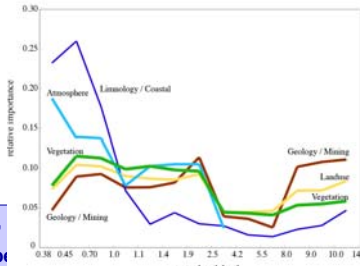
max. attractiveness of hyperspectral data  
relative value  $RV_{Hyp}$  (1/4)

A: best image  
based properties  
relative value  $RV_{ZSLA}$  (1)


B: best ergonomic  
value of user properties  
relative value  $RV_{ZSLB}$  (1)

C: lowest costs  
relative value  $RV_{ZSLC}$  (1)


D: best service  
relative value  $RV_{ZSLD}$  (1)



HYRESSA Workshop, Davos, Switzerland,  
HYRESSA - HYPerspectral REMote Sensing in Europe



Value Benefit Analysis



**Goals of a Value Benefit Analysis\*:**

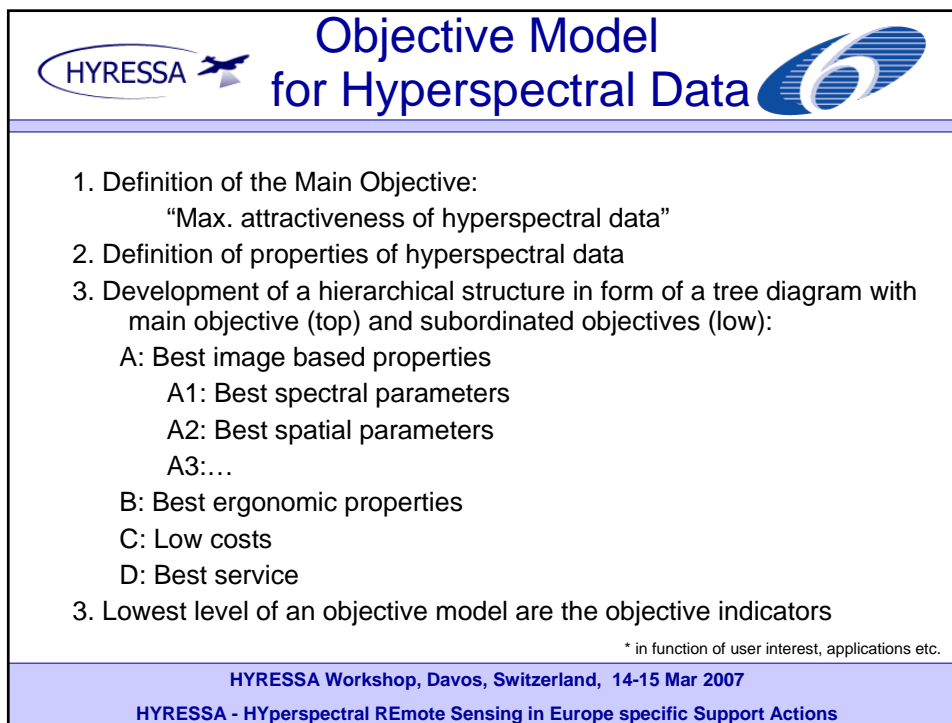
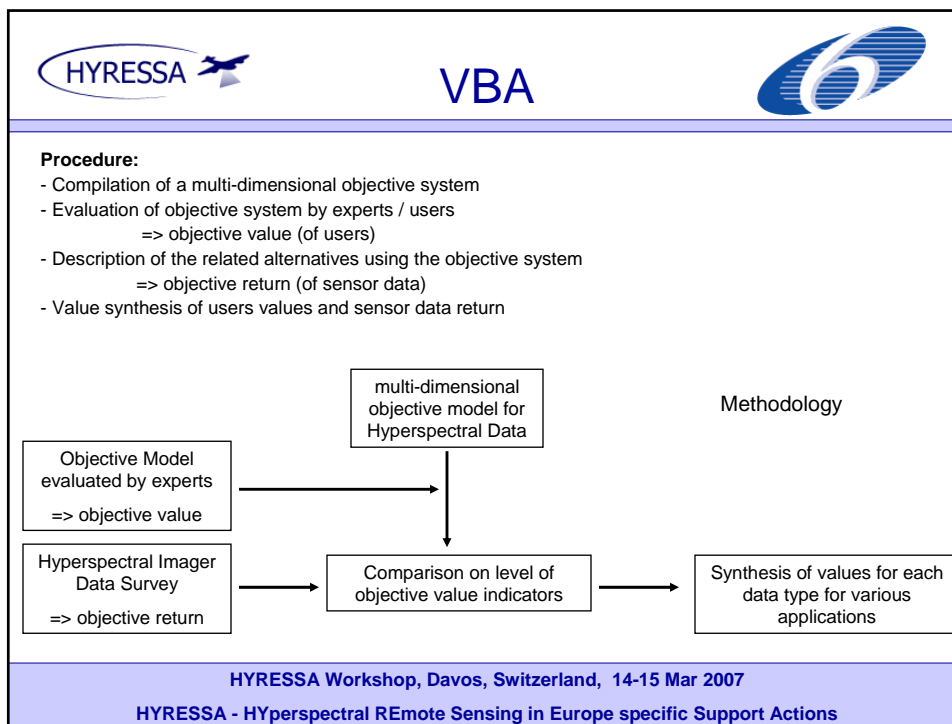
(method commonly applied in operations research and politics)


- analysis of user needs
- compare alternatives
- prepare decision-making
- unveil the decision process

\* Christof Zangemeister: Nutzwertanalyse in der Systemtechnik - Eine Methodik zur multidimensionalen Bewertung und Auswahl von Projekialternativen, 1974 (ISBN 3-923-26400-3)


HYRESSA Workshop, Davos, Switzerland, 14-15 Mar 2007

HYRESSA - HYPerspectral REMote Sensing in Europe specific Support Actions





# Mathematical Model



1. Law of Comparative Judgement

$0 \leq w_{mm} \leq 10$

2. Weights of all objective on one level = 1

$\sum_{m=1}^K g_m = 1$

3. Each alternative in evaluated using a target value

$W_n = \sum_{m=1}^K g_m \cdot w_{mn}$

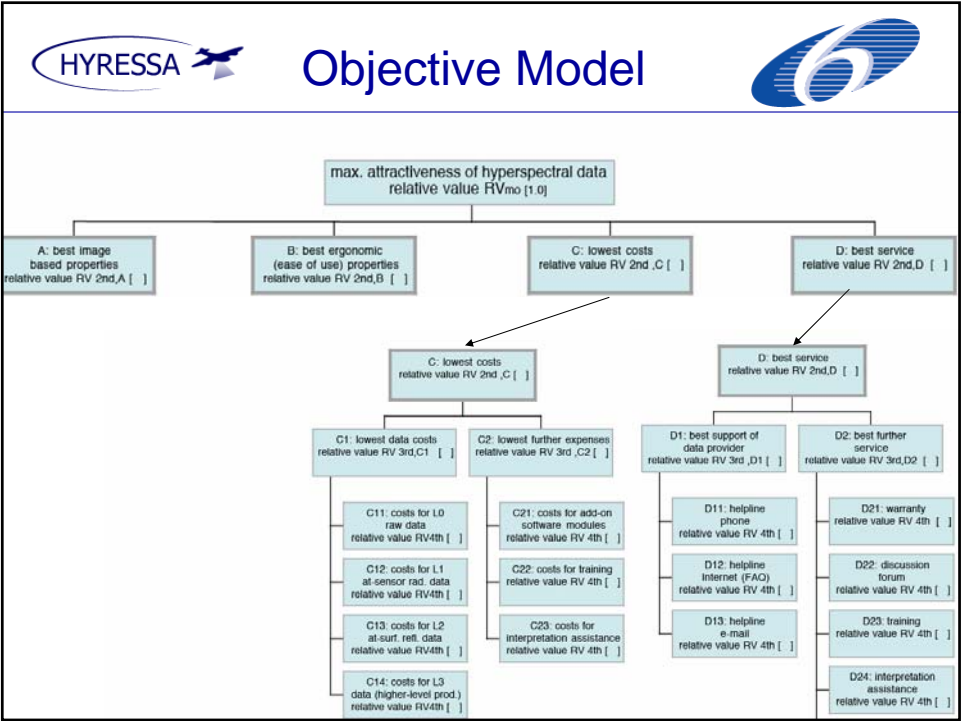
4. Completeness of the preference order

TIFF (Uncompressed) decompressor  
are needed to see this picture.

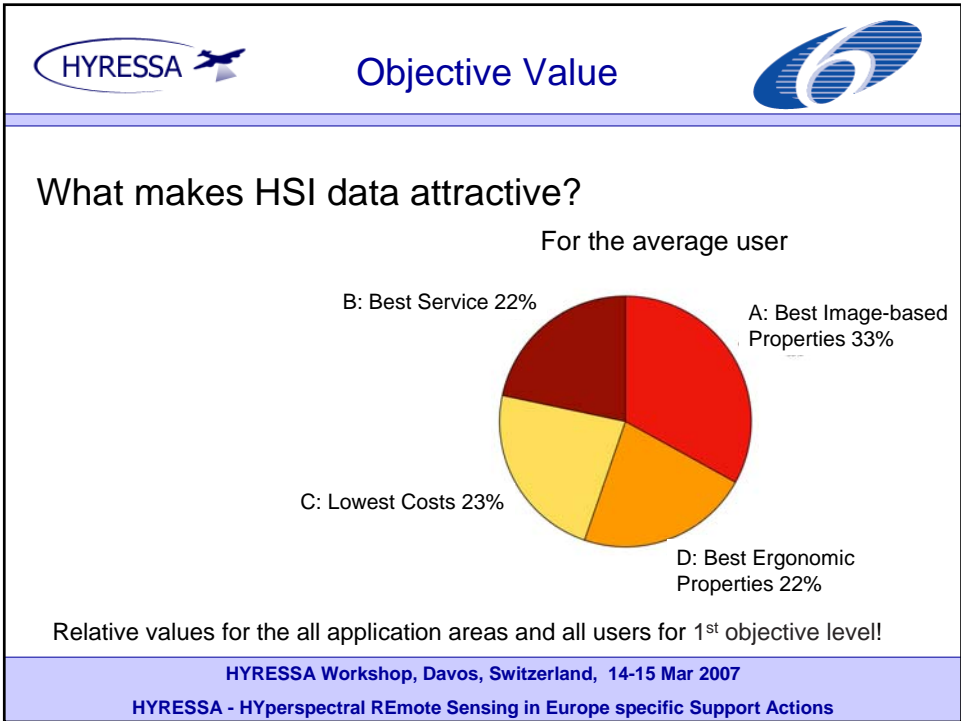
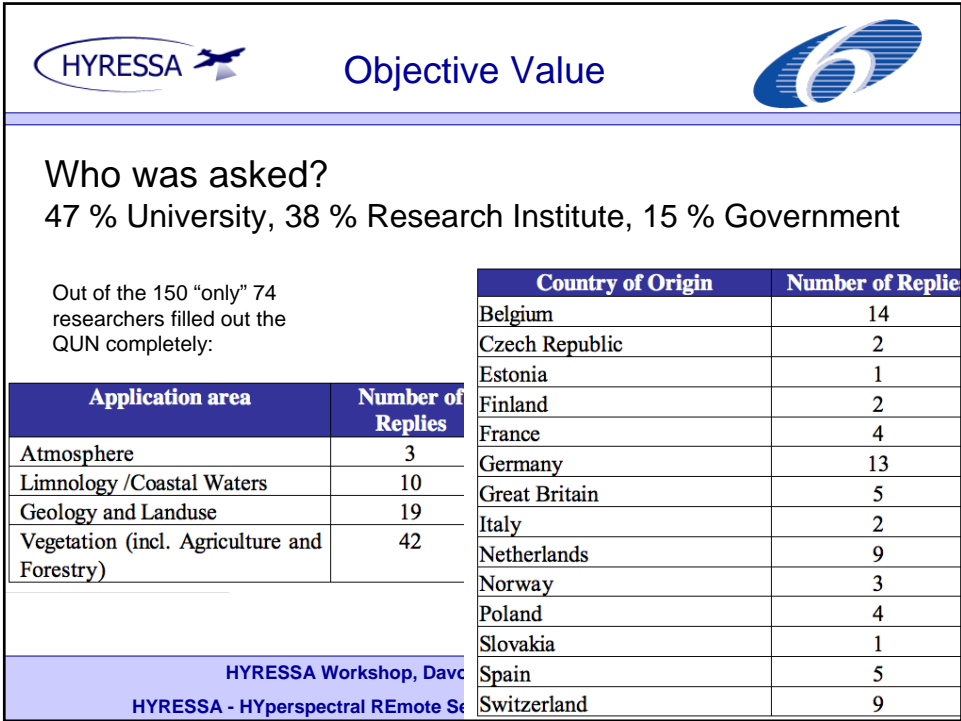
Literature:  
Torgerson; Theory of methods and scaling; Wiley & Sons (1954)  
Keeney & Raiffa; Decisions with Multiple Objectives; Preferences and Value Tradeoffs; Wiley & Sons (1976 )


HYRESSA Workshop, Davos, Switzerland, 14-15 Mar 2007

HYRESSA - HYPerspectral REMote Sensing in Europe specific Support Actions










Objective Value




What makes HSI data attractive?

Objective (2 <sup>nd</sup> level)	Vegetation	Land	Water	Atmosphere
A - Best Image based Properties	0.35	0.35	0.28	0.30
B - Best Ergonomic Properties	0.21	0.23	0.24	0.21
C - Lowest Costs	0.23	0.23	0.23	0.24
D - Best Service	0.21	0.19	0.25	0.25


Relative values for the main application areas vegetation, land, water, and atmosphere for 1<sup>st</sup> objective level!

HYRESSA Workshop, Davos, Switzerland, 14-15 Mar 2007

HYRESSA - HYPerspectral REMote Sensing in Europe specific Support Actions



Objective Value




What makes the best HSI *image*?

Objective	Vegetation	Atmosphere	Land	Water
A1 – Spectral Parameters	0.29	0.28	0.29	0.29
A2 – Geometric Parameters	0.25	0.22	0.25	0.23
A3 – Radiometric Parameters	0.27	0.24	0.28	0.27
A4 – Temporal Parameters	0.19	0.26	0.18	0.21


Relative values for the main application areas vegetation, land, water, and atmosphere for 2<sup>nd</sup> objective level: image-based properties

HYRESSA Workshop, Davos, Switzerland, 14-15 Mar 2007

HYRESSA - HYPerspectral REMote Sensing in Europe specific Support Actions



Objective Value




What makes the *best spectral parameters* of a HSI image?

Objective	Vegetation	Atmosphere	Land	Water
A11 – No. Of Spectral Bands	0.31	0.35	0.30	0.33
A12 – Spectral Resolution	0.32	0.35	0.32	0.33
A13 – Spec. Calibration Quality	0.37	0.30	0.38	0.33


Relative values for the main application areas vegetation, land, water, and atmosphere for 3<sup>rd</sup> objective level: spectral parameters

HYRESSA Workshop, Davos, Switzerland, 14-15 Mar 2007

HYRESSA - HYPerspectral REMote Sensing in Europe specific Support Actions

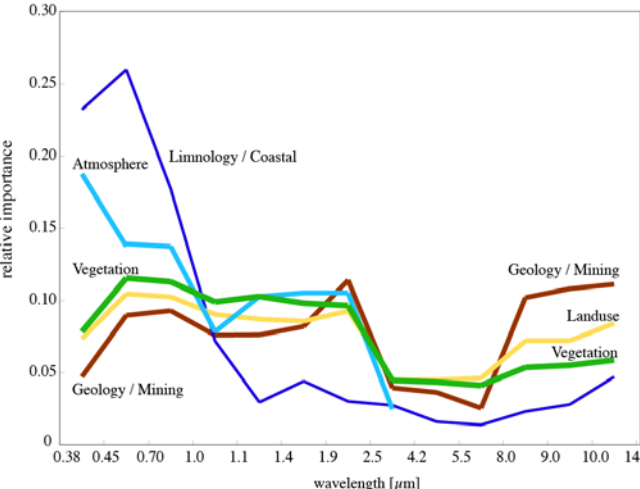


Objective Value

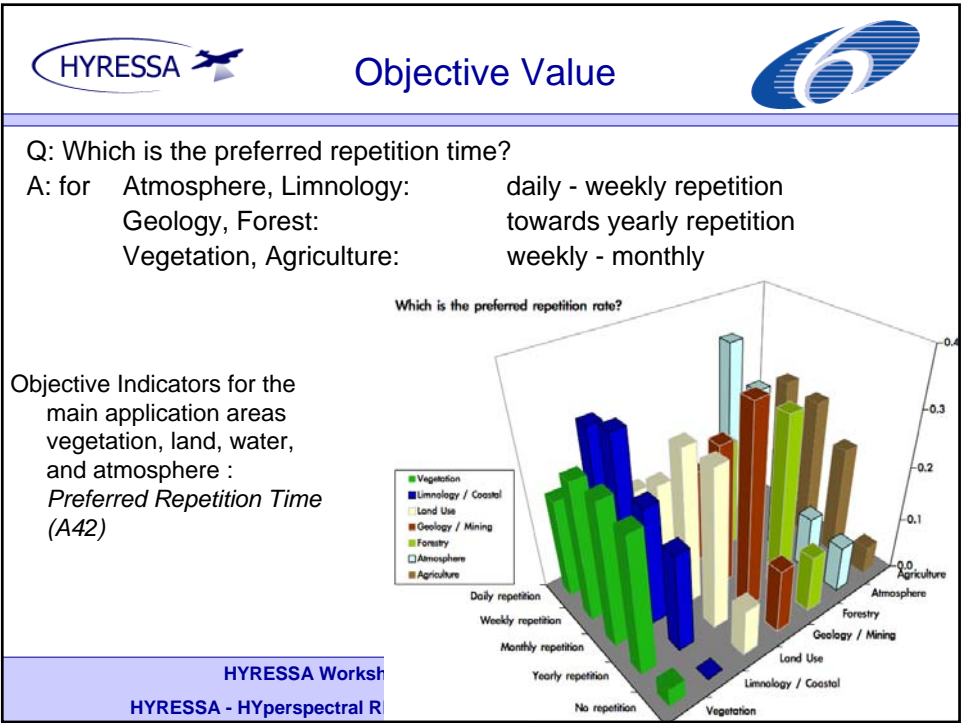
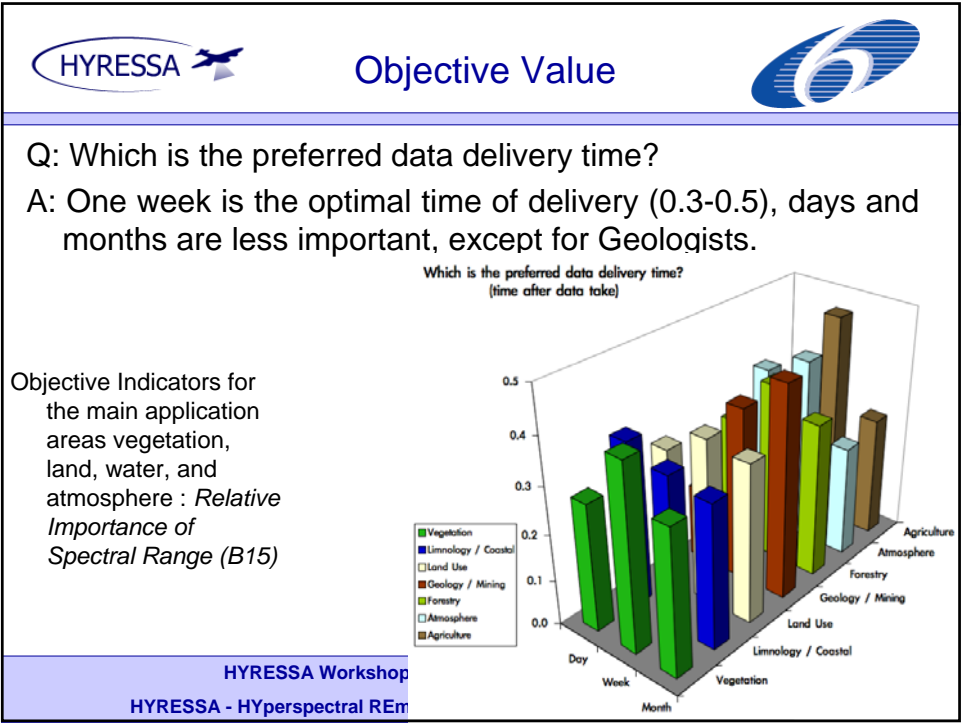


Which spectral range has the highest importance for each application?

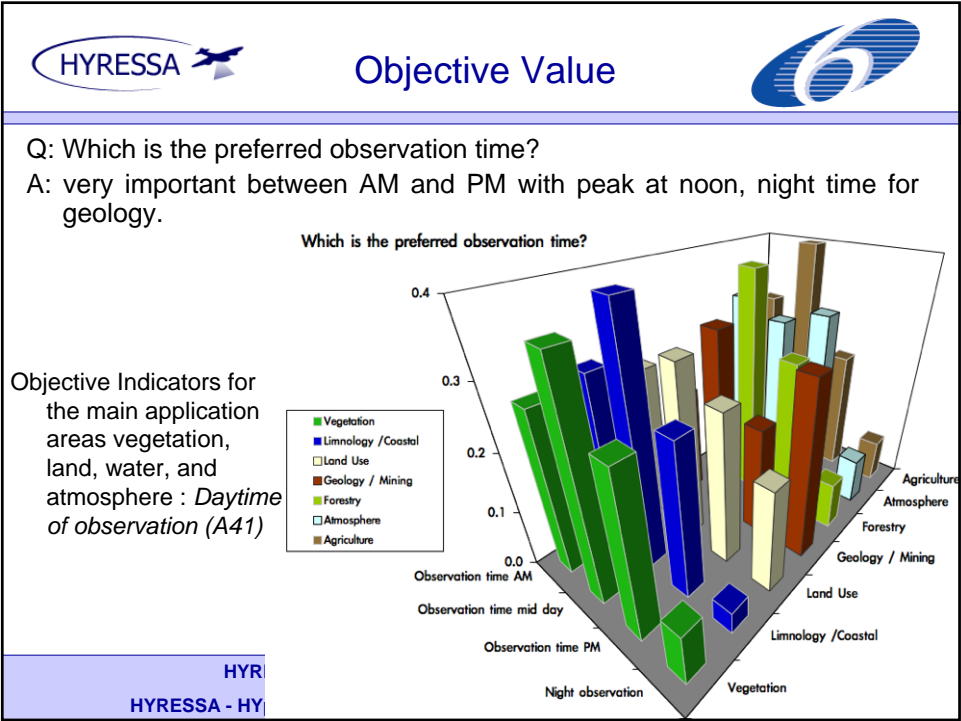
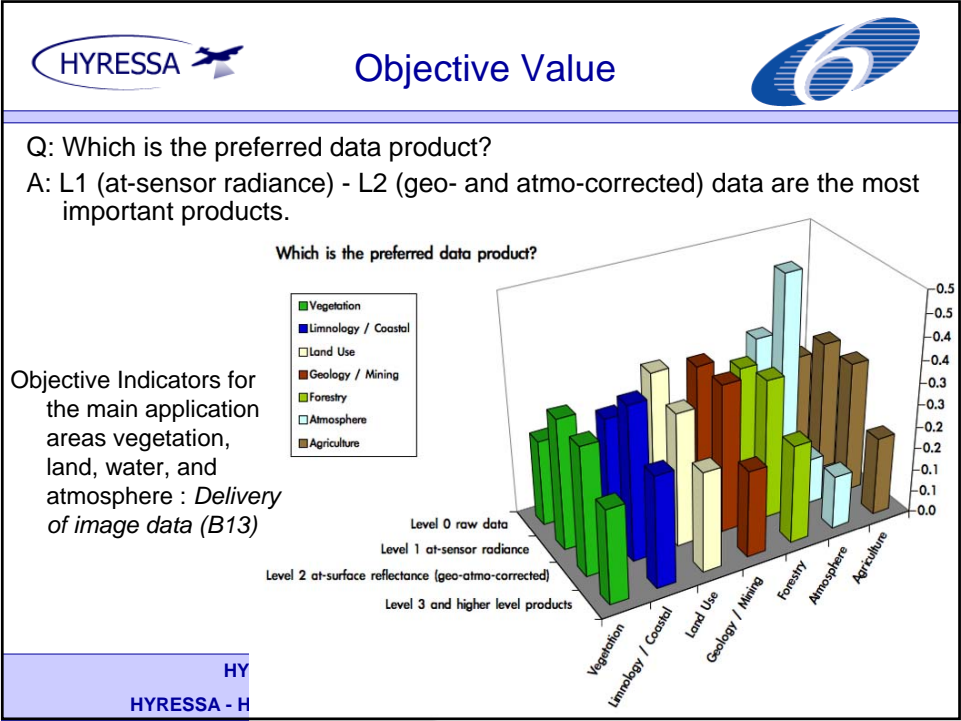
Objective Indicators for the main application areas vegetation, land, water, and atmosphere : *Relative Importance of Spectral Range (A11)*




HYRESSA  
HYRESSA - HYPersp











Objective Value




Q: How important is add-on software?  
A: Very important to all users and all applications

Objective Indicators for the main application areas vegetation, land, water, and atmosphere : *Add-on SW modules (D25)*

HYRESSA Workshop, Davos, Switzerland, 14-15 Mar 2007  
HYRESSA - HYperspectral REMote Sensing in Europe specific Support Actions



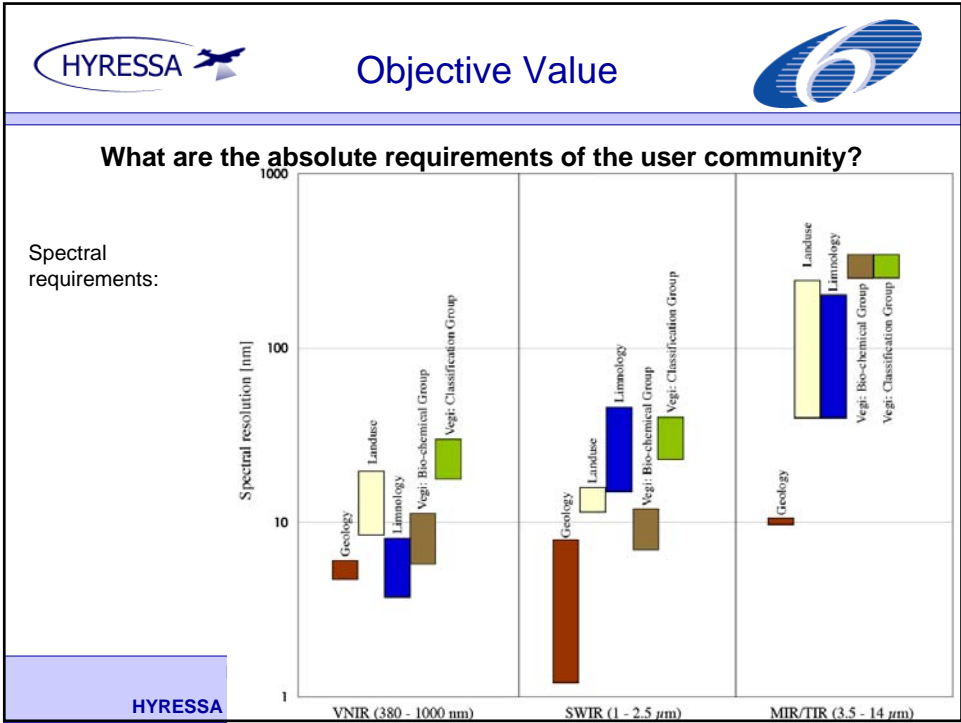
Objective Value






**What are the absolute requirements of the user community?**

Problem for the estimation of the absolute values:  
The Agriculture-Forestry-Vegetation Group was re-distributed (after re-assessment by experts) in  
Group 1) the “*bio-chemical*” group, with a main interest in high spectral and spatial resolution,  
Group 2) the “*classification*” oriented vegetation group, interested in a relatively broad spectral ( < 30 nm) and lower spatial (10-30 m) resolution.

HYRESSA Workshop, Davos, Switzerland, 14-15 Mar 2007  
HYRESSA - HYperspectral REMote Sensing in Europe specific Support Actions



	Atmos- phere <sup>14</sup>	Geology	Land-use	Limnology	Vegetation <sup>15</sup> Group-1 Group-2
No. of bands in total (VNIR-TIR)	3000	300	200	200	200 100
Spectral resolution VNIR [nm]	0.05 - 0.5	6-10	8 - 15	4 - 8	6 - 12 15 - 30
Spectral resolution SWIR [nm]	0.2 - 0.5	2 - 8	10 - 12	10 - 40	8 - 12 25 - 40
Spectral resolution MIR/TIR [nm]	NA	10	40 - 220	40 - 200	300
Spatial resolution VNIR/SWIR [m]	2500	5	4	5 - 20	4 - 5 10 - 30
Spatial resolution MIR/TIR [m]	NA	20 - 30	15	10 - 15	15 30
Swath width VNIR/SWIR [km]	1200	15 - 30	15	25 - 30	20 70
Swath width MIR/TIR [km]	0	15	15 - 20	30 - 40	20 200
SNR VNIR	1500	400	400	700	450
Preferred observation repetition rate	daily-weekly	yearly	monthly- yearly	daily- weekly	weekly- yearly
Preferred data product?	Level 1	Level 1-2	Level 1-2	Level 2	Level 1-2
Preferred observation time?	mid day	mid day or night	daytime	mid day	mid day
What implies an improved service?	add-on SW	add-on SW	add-on SW	add-on SW	add-on SW
Preferred data delivery time?	day-week	month	week	day-week	week

### Objective Return

What is the performance of the HSI data provided?

Spaceborne:




	HYPERION	CHRIS
No. of bands in total	240	18-62
Spectral resolution VNIR [nm]	10	6-33
Spectral resolution SWIR [nm]	10	NA
Spectral resolution MIR/TIR [nm]	NA	NA
Spatial resolution VNIR/SWIR [m]	30	17-33
Spatial resolution MIR/TIR [m]	NA	NA
Swath width VNIR/SWIR [km]	7.5	14
Swath width MIR/TIR [km]	NA	NA
SNR VNIR	200	200
Data Provider	USGS	ESA

Airborne:

AHS-160, AISA Dual, APEX, ARES, AVIRIS, CASI-3, HYSPEX

HYRESSA Workshop, Davos, Switzerland, 14-15 Mar 2007

HYRESSA - HYPerspectral REMote Sensing in Europe specific Support Actions


### Synthesis

What is the best data for all applications?


	Atmosphere <sup>12</sup>	Geology	Landuse	Limnology	Vegetation	Mean
AHS	0.62	0.68	0.66	0.66	0.70	0.66
AISA (DUAL)	0.56	0.55	0.54	0.55	0.56	0.55
APEX	0.70	0.74	0.72	0.78	0.76	0.74
ARES	0.67	0.75	0.72	0.74	0.75	0.73
AVIRIS	0.57	0.62	0.59	0.61	0.62	0.60
CASI	0.58	0.60	0.57	0.59	0.60	0.59
CHRIS	0.70	0.71	0.72	0.74	0.72	0.72
<b>HYPERION</b>	<b>0.75</b>	<b>0.77</b>	<b>0.78</b>	<b>0.78</b>	<b>0.78</b>	<b>0.77</b>
HYSPEX	0.69	0.72	0.68	0.72	0.72	0.71

HYRESSA Workshop, Davos, Switzerland, 14-15 Mar 2007

HYRESSA - HYPerspectral REMote Sensing in Europe specific Support Actions



## Synthesis




What is the best data for vegetation research?

	A	B	C	D	Total
AHS	0.23	0.19	0.15	0.13	0.70
AISA - DUAL	0.19	0.10	0.15	0.13	0.56
APEX	0.22	0.21	0.15	0.18	0.76
ARES	0.23	0.20	0.15	0.17	0.75
AVIRIS	0.22	0.17	0.15	0.09	0.62
CASI	0.17	0.16	0.15	0.13	0.60
CHRIS	0.17	0.16	0.23	0.16	0.72
HYPERION	0.20	0.19	0.23	0.16	0.78
HYSPEX	0.22	0.21	0.15	0.15	0.72


Image-based Properties (A), Best ergonomic Properties (B), Lowest Costs (C) and Best Service (D)

HYRESSA Workshop, Davos, Switzerland, 14-15 Mar 2007

HYRESSA - HYPerspectral REMote Sensing in Europe specific Support Actions



## Main Conclusion




- Reduce costs for HSI end-users!
- Better service (helplines, workshops, courses etc.) is recommended.
- Reasonable pricing policies of HSI data must be elaborated within a future European HSI infrastructure, e.g., trans-national group-shoots,
- Standardized and coordinated action to provide the requested HSI data with good service at reasonable price,
- HSI users have very individual preferences, leading to
  - very specific sensors requirements for a specific application group (e.g., atmospheric research), or
  - Super-sensors, which are accounting for all application groups equally.


HYRESSA Workshop, Davos, Switzerland, 14-15 Mar 2007

HYRESSA - HYPerspectral REMote Sensing in Europe specific Support Actions






## Next Steps




- Results are currently discussed within the HYRESSA Team,
- QUN and VBA shall be further evaluated at RSL to squeeze out the utmost,
- Peer-review paper on VBA results is in preparation.

HYRESSA Workshop, Davos, Switzerland, 14-15 Mar 2007  
HYRESSA - HYperspectral REMote Sensing in Europe specific Support Actions



## Conclusion on Methodology



The study showed, that a VBA is a very good method

- to analyse needs of hyperspectral data
- to support sensor/data specification-building process

Advantage:

- Easy and clear handling
- Comprehensive evaluation

Disadvantage:

- Efforts

HYRESSA Workshop, Davos, Switzerland, 14-15 Mar 2007  
HYRESSA - HYperspectral REMote Sensing in Europe specific Support Actions

## USER NEEDS OF THE EUROPEAN HYPERSPECTRAL REMOTE SENSING COMMUNITY

*Jens Nieke<sup>1</sup> and Klaus I. Itten<sup>1</sup>*

*Ils Reuser<sup>2</sup> and Stefan Adriaensen<sup>2</sup>*

*and the HYRESSA team: [www.hyressa.net](http://www.hyressa.net)*

- 1) University of Zürich, Department of Geography, RSL, Zurich, Switzerland;  
[nieke@geo.unizh.ch](mailto:nieke@geo.unizh.ch)
- 2) VITO – TAP, Boeretang 200, B-2400 Mol, Belgium

### ABSTRACT

While there is a strong need for hyperspectral imagery, the user-driven requirements are not well defined in view of protocols for calibration, acquisition, processing and in-situ measurements in compliance with existing standards. Therefore an analysis was performed in the frame of the EC project HYRESSA, regarding the question “What are the individual user requirements on hyperspectral imagery and the related data products?”. For this analysis a questionnaire and a subsequent benefit-value analysis helped to retrieve users needs and evaluate open items accordingly.

The EC funded HYRESSA project /1/ aims at investigating the user needs of the European hyperspectral research community with respect to access to and accuracy, quality and conformity of hyperspectral images - especially with the advent of next-generation European hyperspectral sensors - in order to refine protocols related to calibration, acquisition, processing and in-situ measurements in compliance with standards. This knowledge was gathered through a SWOT and User Needs workshop (at DLR in July 2006) and an on-line questionnaire (released in Nov. 2006).

The purpose of the paper is to answer the question “What makes hyperspectral data attractive?”. Following the methodology of the benefit-value analysis (BVA) /2/, the answer can be described in hierarchical ordered multidimensional objective model.

The BVA serves as well-known tool for systematic problem solving process as a possibility of comparing projects or solutions. It enables the evaluation on the basis of a multidimensional objective model and can be extended by expert's preferences. Therefore the scaling method (Law of Comparative Judgment) was applied for receiving the desired ranking judgments. The result, which is the relative value of projects concerning a well-defined main objective can now be produced analytically.

Accordingly, BVA is utilized for the determination of the rank of existing or planned hyperspectral data products and is subdivided in 6 main tasks: (1) Defining an Objective Model for hyperspectral data, (2) Objective model weighting procedure of experts, (3) Compilation of an Earth observation hyperspectral data survey, (4) Comparison on the level of the objective value indicators, (5) Synthesis of values for each sensor data and (6) Evaluation of the results.

The investigation showed, that a BVA is a suitable method to analyse needs of hyperspectral data and to support sensor/data specification-building process. The BVA has the advantage, to be easy and clear to handle, resulting in a comprehensive evaluation. The disadvantage are the necessary efforts and the partly non-availability of all sensor data parameters. The paper summarizes all results of the analysis and gives insight to BVA methodology, statistics and others more.

**Keywords:** HYRESSA, Benefit-Value-Analysis, data products, quality assessment, User Needs in Europe

## ISPMSRS Workshop in Davos

---

**References:**

1/ FP6-2004-Infrastructures-6, Contract Number 026194; URL: [www.hyressa.net](http://www.hyressa.net)

2/ Zangemeister, C. (1970): Nutzwertanalyse in der Systemtechnik. Eine Methodik zur multidimensionalen Bewertung und Auswahl von Projektalternativen. München, 370 S.

A BAYESIAN OPTIMISATION APPROACH FOR MODEL INVERSION OF  
HYPERSPECTRAL-MULTIDIRECTIONAL OBSERVATIONS: THE BALANCE WITH  
A *PRIORI* INFORMATION

Wout Verhoef<sup>a,b</sup>

<sup>a</sup> National Aerospace Laboratory NLR, P.O. Box 153, 8300 AD Emmeloord, The Netherlands  
<sup>b</sup> International Institute for Geo-Information Science and Earth Observation ITC, 7500 AA Enschede, The Netherlands  
verhoef@nlr.nl, verhoef@itc.nl

**KEY WORDS:** model inversion, hyperspectral, multidirectional, SAIL, MODTRAN, PROSPECT, Bayesian optimisation

**ABSTRACT:**

Hyperspectral-multidirectional radiance observations of the land surface from space potentially form one of the richest sources of geobiophysical information possible. For soil-vegetation objects, the retrieval of this information can be simulated by radiative transfer modelling. In combination with a couple of atmospheric parameters, the surface reflectance model SLC (soil-leaf-canopy) has more than twenty degrees of freedom, which all have a potential impact on top-of-atmosphere radiance data in hyperspectral-multidirectional feature space. With such a high dimensionality, model inversion methods like look-up table techniques and neural networks tend to become less practicable, and cost-function optimisation re-emerges as a viable alternative. However, model inversion by optimisation techniques is often plagued by numerical instability due to the so-called ill-posedness of the model inversion problem. In the present paper, this ill-posedness of the problem is investigated and diagnosed by means of a singular value decomposition (SVD) of the Jacobian matrix, which contains the partial derivatives of all observations with respect to the model variables. In addition, it is demonstrated how in a Bayesian approach the incorporation of *a priori* information can increase the numerical stability of the model inversion. This leads to an extremely efficient optimisation algorithm, which for randomly selected model variable data reaches an adequate solution in about 99% of the cases, in less than twenty iteration steps. The paper will introduce the model SLC, its coupling with the atmosphere, for which MODTRAN4 is used, and for some selected cases it will analyse the SVD results in order to explain the causes of ill-posedness. A few model inversion sequences will be presented in order to illustrate the numerical stability of the algorithm and its ability to reach a plausible solution under various circumstances. The speed of this method is still limited, but it might be applied selectively to representative pixels in a field, or to “calibrate” the fixed model parameters in a low-dimensional look-up table or neural network model inversion solution.

**1. INTRODUCTION**

Traditionally, remote sensing satellite missions for earth observation over land have often been designed to provide a range of geobiophysical products to a wide and globally distributed community of users. Operational products based on this philosophy are for instance MODIS LAI and MODIS fAPAR (Knyazikhin et al., 1998), which employ knowledge obtained from vegetation-soil radiative transfer modelling and global maps of ecotypes, but nevertheless are still basically rather sensor-specific. However, there is a growing awareness that algorithms designed for the massive processing of earth observation data into single products from single satellite missions might interfere with the consistent use of several land surface variables in dynamic process models. Also, different providers might disseminate basically the same product (e.g. LAI) derived from different sensors and based on different algorithms, making it hard for a user to decide which LAI is the most suitable for the intended application. Therefore, it becomes more and more obvious that a multisensor / multimission approach might be more successful in providing the user community with a range of products that can be assimilated in local process models in a more natural and self-consistent manner. In this way also the quality of products could be improved, since more information from various sources, including local information stored in GIS, could be integrated, thus reducing the chance of inconsistencies. In Figure 1 it is illustrated how such an approach could be applied to assimilate data from one satellite sensor. The surface object properties are stored in a GIS and by means of a generic remote sensing (RS) earth observation

model which includes the atmosphere, top-of-atmosphere (TOA) radiance image data are simulated that have been adapted to the spatial, spectral and geometric properties of the sensor that produced the actual image. Comparison of both images leads to conclusions on the adjustment of object properties and these are then fed back until actual and simulated images sufficiently match. This feedback loop establishes model inversion on the level of complete (series of) images by forward simulation, with the great advantage that the impact of the complexity of the heterogeneous landscape and the atmosphere on image formation, including topography, can be captured fairly

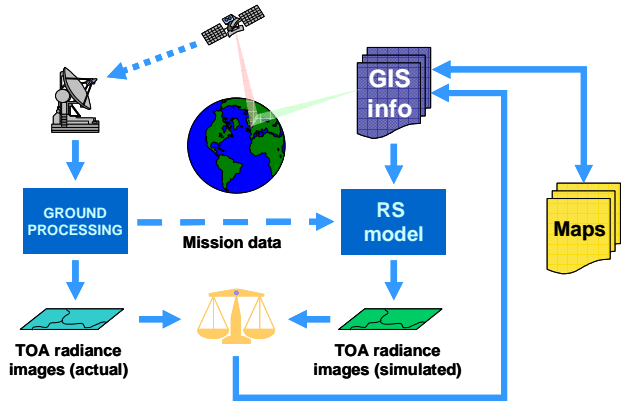


Fig. 1 Updating geographic information by balancing new earth observation data with existing forward-modelled *a priori* information.

well by forward modelling, making various atmospheric and topographic corrections unnecessary. Besides, since complete images are compared, the correct values of atmospheric parameters will be found in an early stage, as these have an effect on all pixels in the image, and thus the overall cost function for the whole image, which is to be minimised during the optimisation process, will rapidly decrease if a better characterisation of the atmosphere is found. This concept of parameter retrieval by forward modelling can be characterised by the following features:

- Simultaneous retrieval of all object properties
- Self-consistent set of object properties is obtained
- High degree of sensor-independence
- User-oriented because of local *a priori* GIS info

If current surface properties stored in the GIS are to be updated using a new satellite image, of course the question arises what should be the resistance against modifying data. Here the balance between new earth observation data and existing GIS info comes into play, and a key element one could use to base decisions on is uncertainty. If there is little uncertainty about the correctness of the current GIS info, then the resistance against changing it must be high, even if satellite earth observation data seem to indicate that there are discrepancies. On the other hand, if one actually does not know whether the current info is correct, one will be inclined to readily accept anything that can be derived from a new satellite observation. The question addressed in this paper is how one can balance both sources of information in an optimum way. For this, the model inversion of hyperspectral multidirectional radiance observations from space was taken as a prototype, since this is an ultimate example of the richness of earth observation data, for which the inversion is a challenge because of the complexity of the data, the high dimensionality and the chance of numerical problems due to ill-posedness of the model inversion problem. In what follows, first the set of coupled models used is introduced in section 2. Next the theory of Bayesian model inversion is discussed, and in section 4 some results of model inversion are presented.

2. MODELLING SET-UP

The set of models used was meant to represent the generation of TOA hyperspectral radiance data for generic soil-vegetation objects. The integrated soil-leaf-canopy model SLC (Verhoef & Bach, 2007) was used to generate surface reflectances for the former candidate mission SPECTRA over the wavelength range 400-2400 nm at 10 nm resolution and under 7 directions, as representative of data-rich inputs. The SLC model consists of the following submodels:

- 4-stream modified Hapke (1981) BRDF model
- Soil moisture effect after Bach & Mauser (1994)
- PROSPECT (Jacquemoud & Baret, 1990) leaf model
- 4SAIL2 canopy RT model (including canopy - soil interaction)

Compared to previous versions of SAIL, advancements in the 4SAIL2 model (Verhoef & Bach, 2007) can be summarized as follows:

- leaf colours different in two layers
- crown clumping effect included

- output of spectral canopy absorption (support for fAPAR) and observed fractional vegetation cover (FVC)
- numerically robust (singularities intercepted)
- speed-optimised

A complete list of object properties of the SLC model is presented in Fig. 2

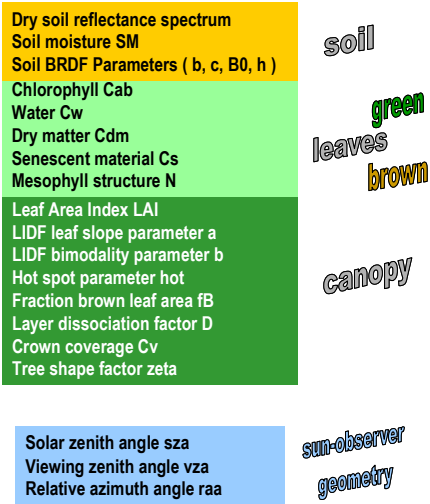


Fig. 2 Object properties of SLC model

For a given dry soil reflectance spectrum the number of free parameters is 5 for the soil, 5 for green leaves, 5 for brown leaves, and 8 for canopy structure, so 23 in total. In order to simulate observations from space of top-of-atmosphere radiances, MODTRAN4 was coupled to SLC as illustrated in Fig. 3. This coupling allows also to simulate products like fAPAR and surface albedo, but this falls outside the scope of the present paper. As an illustration, Fig. 4 shows a sample of simulated TOA observations of hyperspectral radiances under 7 directions for a soil-vegetation object with an LAI of one under standard conditions in April at mid-latitudes for an atmospheric visibility of 23 km. For model inversion, the sensitivity of TOA radiance observations to changes in surface variables is particularly important. However, for successful inversions this is not sufficient. If two variables induce similar changes in TOA radiance spectra, it will be hard to identify which variable caused the change, so changes caused by one variable should also be linearly independent from changes caused by other variables.

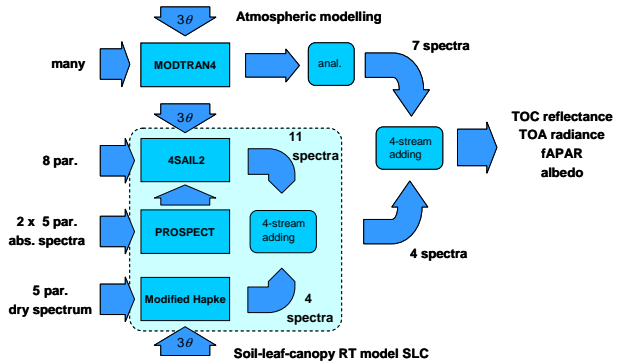


Fig. 3 Coupling of SLC outputs to MODTRAN4 for simulation of TOA radiance spectra.



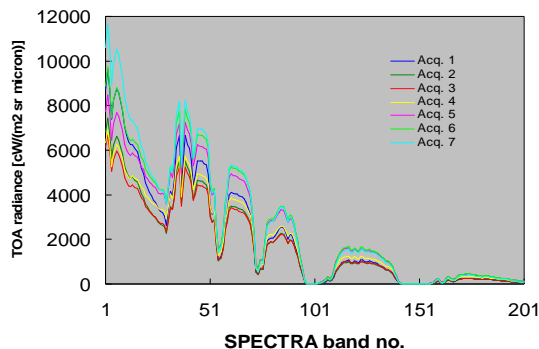


Fig. 4 Sample of simulated hyperspectral-multidirectional TOA radiance observations for a soil-vegetation object

Figures 5 and 6 show examples of the sensitivity of spectral and directional TOA radiances to a selection of surface variables. These illustrate that the sensitivities to the various parameters are spectrally and angularly quite diverse, although one can also notice similarities. Especially for the canopy structure the shapes of spectral sensitivities are often similar. Here, different parameters often give different angular responses, so that multiangular information provides quite some discriminative power. The amount of linear independence in the sensitivity to surface variables can be established by investigating the Jacobian matrix, which contains the partial derivatives of all observables (spectral bands and viewing directions) with respect to all surface variables. A very useful tool for this is singular value decomposition (SVD). Any matrix can be decomposed by SVD, and for a Jacobian matrix  $J$  one obtains

$$J = USV^T, \quad (1)$$

with  $U^T U = I$ ;  $V^T V = VV^T = I$ ;  $S$  diagonal.

The sensitivity of model observables to surface parameters is thus described by

$$\Delta r = J \Delta p = USV^T \Delta p,$$

which after pre-multiplication by the transposed of  $U$  gives

$$U^T \Delta r = S V^T \Delta p. \quad (2)$$

This result expresses that it is possible to obtain a vector of linearly transformed changes of surface variables, which are one-to-one related to the elements of a vector of linearly transformed changes of observables. The relation connecting both transformed vectors is given by the diagonal matrix of singular values  $S$ . One may state that the singular values express the local sensitivities of a set of linearly transformed observables to a set of linearly transformed surface variables. Linear dependence will be expressed by one or more singular values being equal to zero, indicating that there are certain linear combinations of observables which have no sensitivity to a space of surface variables (the so-called null-space). This is exactly the situation encountered when model inversion becomes an ill-posed problem. In that case the Jacobian matrix is singular, so that the model inversion problem has no solution, or rather has multiple solutions. Thus, singular value decomposition is a useful tool to diagnose ill-posedness. In the next section it will be shown how the ill-posedness can be reduced by using *a priori* information.

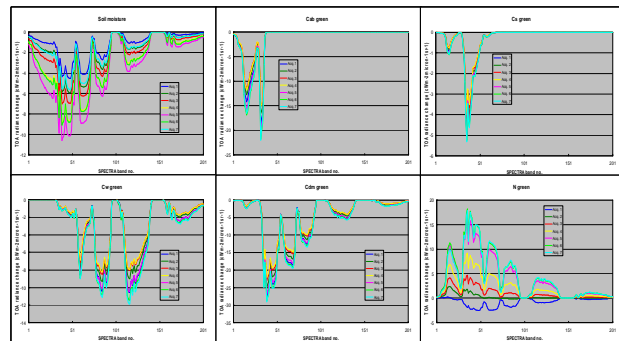


Fig. 5 Sensitivities of hyperspectral-multidirectional TOA radiance observations to soil moisture and leaf optical properties. Top row: soil moisture, leaf chlorophyll, brown pigment; bottom row: leaf water, dry matter,  $N$  parameter.

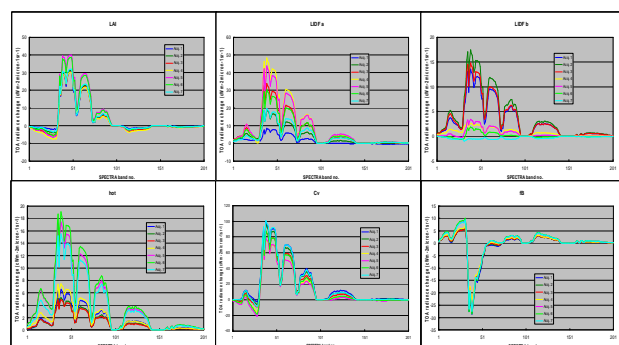


Fig. 6 Sensitivities of hyperspectral-multidirectional TOA radiance observations to canopy structure. Top row: LAI, LIDF a parameter, LIDF b parameter; bottom row: hot spot parameter, crown cover, fraction brown leaves.

### 3. BAYESIAN MODEL INVERSION

If Newton's optimisation method is applied without any regularisation by means of *a priori* information, in the neighbourhood of the final solution one can write

$$\Delta r = J \Delta p,$$

where  $\Delta p$  is the change in the surface parameters required to remove the discrepancy  $\Delta r$  between measured and modelled observables. Formally, the solution in terms of a change of parameters which removes the discrepancy in the observables is found by pre-multiplication with the transposed of  $J$ , giving

$$J^T \Delta r = J^T J \Delta p, \text{ or } \Delta p = (J^T J)^{-1} J^T \Delta r$$

However, this solution fails if the Jacobian matrix is singular, since one can show that the matrix

$$(J^T J)^{-1} J^T = VS^{-1}U^T,$$

which obviously leads to infinite changes in parameters if any of the singular values equals zero.

Regularisation of Newton's iteration method can be accomplished by mixing it with the solution which goes into the direction of the *a priori* parameter vector, and using proper weights.

For the optimisation of a single parameter  $p$ , for which a model provides the solution  $p_m$ , and the *a priori* value is  $p_a$ , the weights are related to the uncertainties attached to the model result and the *a priori* value. If these are expressed by their variances  $\sigma_m^2$  and  $\sigma_a^2$ , the Bayesian final solution is given by

$$p = \frac{\sigma_a^2 p_m + \sigma_m^2 p_a}{\sigma_a^2 + \sigma_m^2}.$$

This can also be written as an equivalent expression which balances the differences with the model solution and the *a priori* solution, where the inverse variances are used as the weights:

$$\frac{p - p_m}{\sigma_m^2} = -\frac{p - p_a}{\sigma_a^2}.$$

For normalised parameters having unit *a priori* variance, one can write

$$S^2(p - p_m) = -(p - p_a),$$

where  $S$  is the relative sensitivity of the model to changes in normalised parameters. In this relative sensitivity the noise level of the sensor should be taken into account: the higher the noise level, the lower the relative sensitivity should be. For a multivariate system one can write similarly for a transformed variable space in the equilibrium situation

$$S^2 V^T (p - p_m) = -V^T (p - p_a).$$

The goal of an iteration step in the regularised Newton optimisation method is trying to minimise the difference with the equilibrium solution, which is given by

$$p_s = V(S^2 + I)^{-1}(S^2 V^T p_m + V^T p_a), \quad (3)$$

and which clearly illustrates that more weight is given to the model solution if relative sensitivity is high, whereas in the case of no sensitivity at all the *a priori* solution is taken.

For the current vector of parameters one can write

$$p = V(S^2 + I)^{-1}(S^2 V^T p + V^T p),$$

and by subtracting this from Eq. (3) one obtains an updating rule which can be used in a regularised Newton optimisation algorithm, and reads

$$\Delta p = V(S^2 + I)^{-1}[S^2 V^T (p_m - p) + V^T (p_a - p)]$$

Since in the neighbourhood of the solution the model can be linearised as given by Eq. (2), one can write

$$V^T (p_m - p) = S^{-1} U^T (r_o - r),$$

where  $r$  is the vector of modelled observables for the current vector of parameters, and  $r_o$  is the vector of measured observables, so an iteration step should perform a change of model parameters equal to

$$\Delta p = V(S^2 + I)^{-1}[S U^T (r_o - r) + V^T (p_a - p)]. \quad (4)$$

This updating rule forms an effective cure for the ill-posedness problem, since also for singular values equal to zero a stable solution is found. In that case the corresponding linear transformations of surface variables will automatically be equated to the *a priori* ones.

## 4. RESULTS

Before showing some examples of successful retrievals of many parameters by the Bayesian model inversion algorithm from simulated hyperspectral-multidirectional TOA radiance data, the dimensionality of this kind of rich data (201 bands  $\times$  7 directions) is investigated by analysing the Jacobian matrix of model sensitivities for a single benchmark case. This case represents a clumped (less than 100% crown cover) and mixed vegetation canopy (green and brown leaves both present) with a crown LAI of one. This kind of object was chosen in order to give all parameters some sensitivity on remote sensing observables, so that a maximum potential dimensionality would be reached. For some settings of model variables the sensitivities to a subset of variables may go to zero. A trivial example is a canopy which only has green leaves (fraction brown leaf area zero). This gives zero sensitivity to the brown leaf optical properties. Another is the case of no clumping (homogeneous canopy with 100% crown cover). In this case the tree shape factor becomes irrelevant.

For the case of a hyperspectral-multidirectional mission the results are given by the red line (box symbol) in Fig. 7, which shows the retrieval error variances of the linearly transformed surface variables obtained from the SVD of the Jacobian matrix, relative to those valid for the case of guessing them from the *a priori* information. Here the *a priori* information was assumed to consist of the assumption that each variable was equal to its

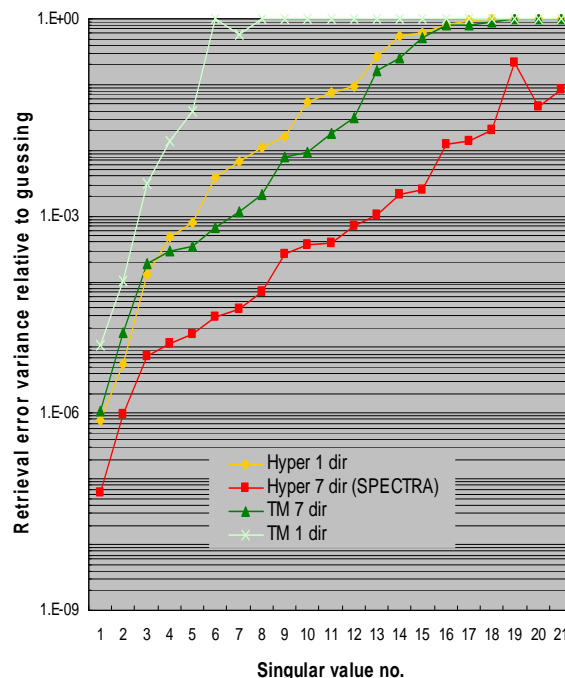


Fig. 7 Dimensionality plot for four different mission concepts.

value at the centre of its interval. The *a priori* variances (uncertainties) were expressed by assuming for each variable a uniform distribution over their entire plausible range. Dimensionality may be expressed by counting the number of linearly inde-

pendent transformed variables which can be retrieved with an error variance clearly less than the error variance corresponding to guessing. For double-normalised data, i.e. the variables are normalised by their standard deviations and the observables by their noise levels (also expressed as standard deviations), the relative error variance of a linearly independent transformed variable becomes equal to  $1/(S^2 + 1)$ , where  $S$  is the associate singular value. Calling a transformed variable retrievable if its error variance is more than ten times smaller than the one corresponding to randomly guessing, in Fig. 7 one may observe that for the hyperspectral-multidirectional mission only one singular value is found that is associated with a transformed variable that should be considered non-retrievable. The total number of singular values is 21 here, since the four Hapke soil BRDF parameters were not varied, and in this case two parameters were added to include some uncertainty due to the atmospheric adjacency effect, the fractions of dense vegetation and bare soil in the neighbourhood of the target pixel. So one may conclude that the dimensionality of the data retrievable from hyperspectral-multidirectional observations in this case is 20. For a multispectral mission (6 Landsat bands) with 7 directions the dimensionality is 12, and the same number is found for a single view nadir-looking hyperspectral mission. For a nadir-looking multispectral (Landsat bands) mission the dimensionality defined in this way is 5. Note that for this simulation the noise level was assumed to be given by  $0.1 \text{ Wm}^{-2}\mu\text{m}^{-1}\text{sr}^{-1}$ , uniformly distributed over the spectrum. For a tenfold higher noise level ( $1 \text{ Wm}^{-2}\mu\text{m}^{-1}\text{sr}^{-1}$ ) the dimensionalities obtained for the same mission types are 13, 7, 5 and 2, respectively. Here the multispectral multidirectional mission scores higher than a single-view hyperspectral mission. One may also conclude that a good signal-to-noise ratio is essential for the successful retrieval of many geobiophysical surface variables, as well as an advanced hyperspectral-multidirectional mission concept.

In order to test the performance of a Bayesian model inversion algorithm based on the regularised Newton optimisation method as outlined in section 3, 10000 combinations of randomly selected surface variables were generated, the corresponding TOA hyperspectral-multidirectional radiance data were computed by forward modelling, and next these were provided to the retrieval algorithm. In this numerical experiment all 23 variables of the SLC model were allowed to vary and these should all be retrieved as well. However, the dry soil reflectance spectrum and the atmospheric properties were assumed to be known in this case. The result was that in 99% of the cases the correct solution was found, and that the number of Newton iterations was mostly less than twenty. Computation time on a common PC is quite considerable, since one iteration requires the computation of the Jacobian matrix, which involves  $201 \times 7 \times 24$  model simulations, so that a complete sequence of iterations for a single optimisation may well take 5 to 10 seconds. However, one could imagine that the full optimisation would be applied only to field-averaged data or certain representative pixels, while look-up table methods might be applied elsewhere to capture intra-field variations (Verhoef & Bach, 2003). In that case most variables are set to fixed values, and only a few (up to four) are allowed to vary.

An example illustrating the functioning of the algorithm for the retrieval of the brown leaf optical properties is shown in Fig. 8. This example was chosen to illustrate in particular that for some parameters the final solution deviates from the correct one because of the bias created by the *a priori* solution. The modelled TOA radiances are only weakly sensitive to some object parameters, and for parameters for which this is the case the final solution will give relatively much weight to the *a priori* values.

This is illustrated in Fig. 8, where for brown leaves after 11 iterations still considerable deviations are found for the biochemical components chlorophyll, water, and brown pigment.

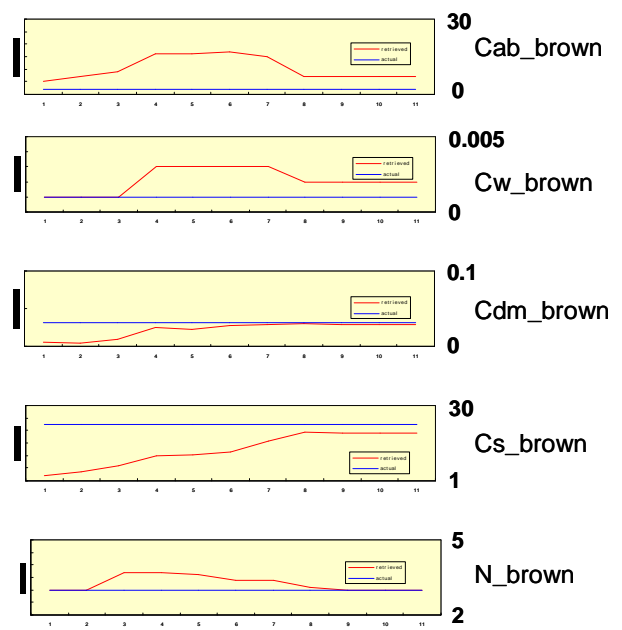


Fig. 8 Retrieval of brown leaf optical properties. Flat blue lines show the correct values to be retrieved, red lines the successive trials during 11 iteration steps. The right axis shows the names and plausible ranges of the respective parameters.

How, for the same Bayesian model inversion experiment, the most important canopy structural parameters were retrieved is shown in Fig. 9. Especially the LAI and the average leaf slope (LIDFa) are found soon. The more or less correct hot spot parameter is found only after several iterations. This is caused by the fact that the simulated observations were not in the principal plane (minimum relative azimuth about 25 deg), so sensitivity to the hot spot parameter is only small.

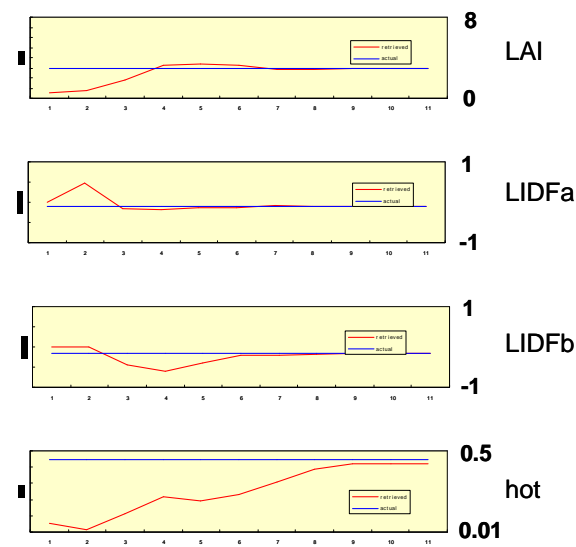


Fig. 9 Retrieval of some canopy structure parameters.

Although it was found that Bayesian retrieval of parameters by regularising Newton's method with *a priori* information, it

should be noted that some extra measures were still necessary to improve the stability of the algorithm, the most important one being the initial search for a suitable starting LAI. For this, a small look-up table is constructed which contains the model results for eight LAI values and default values for the other parameters. This look-up table is used to find the best starting LAI.

Another refinement was introduced to compensate for the non-linearity of the model's response to LAI. An exponentially transformed LAI was used to improve linearity, which has a favourable effect on convergence speed.

## 5. CONCLUSIONS

A concept of remote sensing data assimilation has been presented which retrieves land surface information from new earth observation data by comparing this to forward-modelled existing *a priori* information, and applying a feedback loop on the level of complete (series of) images. In this mechanism the balancing of old and new information plays a key role, and for this a Bayesian approach based on the uncertainties of remote sensing observables and the *a priori* surface variables appears very attractive. The concept can be used for updating of surface variables from several sensors on board of several earth observation missions, thus bridging the gaps between sensor properties and improving the continuity and consistency of land surface products. This concept has been prototyped on the information-rich simulated data that one might expect from a hypothetical hyperspectral-multidirectional earth observation mission.

The information content of hyperspectral multidirectional radiance observations from space has been investigated by means of singular value decomposition (SVD) of the Jacobian matrix, which expresses the coupled model's sensitivity to changes in surface variables. In a Bayesian context, information content can be defined by the ability to retrieve surface variables relative to the *a priori* uncertainty of these variables. This approach allows to establish the dimensionality of the data as a function of instrument performances (noise levels) for several earth observation mission concepts. Furthermore, it can be used as the basis for an efficient and stable parameter retrieval algorithm, employing Newton's method with incorporation of the *a priori* uncertainties.

Hyperspectral multidirectional earth observation data are a very rich source of information about soil-vegetation objects. In spite of the huge number of observables ( $7 \times 201 = 1407$  in our example), dimensionality appears to remain limited to 13 respectively 20, depending on the assumed noise levels. This seems to indicate that a considerable data compression by a factor of 70 should be possible. It was also found that the dimensionalities of single-view hyperspectral data and multiple view multispectral data (6 bands) are comparable and amount to about 6 and 12 for high and low noise levels, respectively. A single-view multispectral mission produces dimensionalities of 2 and 5 at the same noise levels.

*A priori* information was incorporated successfully to remove ill-posedness and to retrieve all 23 parameters of the SLC model by a Bayesian model inversion approach.

For randomly generated model cases, in 99% of the cases a correct solution was found in less than 20 iteration steps. In the remaining cases no convergence was achieved.

## 6. REFERENCES

Bach, H., Mauser, W. (1994). Modeling and model verification of the spectral reflectance of soils under varying moisture con-

ditions. *Proc. IGARSS'94*. Vol. 4. pp. 2354-2356, Pasadena: IEEE.

Berk, A., Anderson, G.P., Acharya, P.K., Chetwynd, J.H., Bernstein, L.S., Shettle, E.P., Matthew, M.W., Adler-Golden, S.M. (2000). MODTRAN4 Version 2 USER'S MANUAL, Air Force Research Laboratory. Space Vehicles Directorate, Air Force Materiel Command, Hanscom AFB, MA 01731-3010, 97 pp.

Hapke, B.W. (1981). Bi-directional reflectance spectroscopy 1. Theory, *J. Geophys. Res.* 86: 3039-3054.

Jacquemoud, S., Baret, F. (1990). PROSPECT: A model of leaf optical properties spectra. *Rem. Sens. of Env.* 34: 75-91.

Knyazikhin, Y., Martonchik, J.V., Myneni, R.B., Diner, D.J., Running, S.W. (1998). Synergistic algorithm for estimating vegetation canopy leaf area index and fraction of absorbed photosynthetically active radiation from MODIS and MISR data, *Journal of Geophysical Research*, Vol. 103, No. D24, pp. 32,257-32,276.

Verhoef, W., Bach, H. (2003). Simulation of hyperspectral and directional radiance images using coupled biophysical and atmospheric radiative transfer models. *Rem. Sens. of Env.* 87: 23-41.

Verhoef, W., Bach, H. (2007). Coupled soil-leaf-canopy and atmosphere radiative transfer modeling to simulate hyperspectral multi-angular surface reflectance and TOA radiance data. *Rem. Sens. of Env.*, 17 pp., in press.

## 7. ACKNOWLEDGEMENTS

The work reported here was supported by NLR's own research programme, as well as by the European Space Agency (ESTEC Contract No. 17169/03/NL/GS, "Impact of the Accuracy of Variables Retrievable from Multi-angular, Hyperspectral Observations on Ecosystem Model Performance", led by Massimo Menenti, with Michael Rast as the ESA study manager).

# TWO-DIMENSIONAL FOREST CANOPY ARCHITECTURE FROM TERRESTRIAL LASER SCANNING

F.M. Danson<sup>a</sup>, C. Giacosa<sup>b</sup>, R.P. Armitage<sup>a</sup>,

<sup>a</sup> Centre for Environmental Systems Research, Research Institute for the Built and Human Environment,  
School of Environment and Life Sciences, University of Salford, Manchester M5 4WT, UK -  
f.m.danson@salford.ac.uk

<sup>b</sup> School of Engineering, Geoecology and the Environment, Catholic University of Santa Fe, Santa Fe, Argentina

**KEY WORDS:** Terrestrial laser scanning, forest, gap fraction

## ABSTRACT:

Terrestrial laser scanners (TLS) are now capable of collecting 3d data clouds consisting of the x,y,z coordinates of several million laser hits, plus information on return intensity and, in some cases, target colour. TLS collect data at sub-centimetre resolution at a range of zenith view angles. This paper describes the results of a series of experiments in which a TLS was used to measure the two-dimensional structure of a broadleaf deciduous woodland canopy at a range of dates with different leaf cover. The TLS was mounted on a tripod and oriented to measure canopy gap fraction over a near-complete hemisphere. The laser data were compared with near-simultaneous hemispherical photographs of the canopy taken at the same location. Comparison of the hemispherical photography and TLS data showed that, in contrast to our earlier work in needle-leaf canopies, the TLS underestimated canopy directional gap fraction. The explanation of this difference is explored and alternative approaches to measure gap fraction from laser scanner data are suggested.

## 1. INTRODUCTION

Data on the three-dimensional structure of vegetation canopies are required to validate and test models of vegetation canopy reflectance and to better understand the role of multiple scattering at various scales (leaf/needle, shoot, branch, and crown) in determining canopy spectral signatures. Direct methods to measure canopy structure normally involve destructive sampling of canopy elements but in complex forest or woodland canopies it may be impossible to collect sufficient samples to accurately characterize canopy architecture. Indirect methods of measuring canopy structure (light interception instruments and hemispherical photography) are faster but require assumptions to be made about the clumping of foliage and the proportions of woody and non-woody material (Weiss *et al.*, 2004). Hemispherical photographs may be used to capture images of the two dimensional hemispherical projection of a forest or woodland canopy, but they do not contain information about the three-dimensional structure (Jonckheere *et al.*, 2004). This paper describes the results of an experiment to the application of Terrestrial Laser Scanners (TLS) and hemispherical photographs to measure gap fraction in woodland canopies.

Although there is now a large body of research on the interaction of airborne LIDAR pulses with forest canopies, there are only a few studies that have used TLS to examine forest structure. Most of these have been concerned with the measurement of stand variables, including tree height, stem taper, diameter at breast height and planting density (e.g., Hopkinson *et al.*, 2004; Thies *et al.*, 2004; Watt and Donghue, 2005). However, recent research has tested the potential of TLS to measure forest canopy directional gap fraction, defined as one minus the probability of a beam of light intercepting a canopy element in a given direction. Lovell *et al.* (2003) used a laser scanner to determine directional gap fraction in stands of different species and found close correlation with data from

hemispherical photography. Danson *et al.* (2007) measured gap fraction in conifer forest stands and found a maximum difference of 11% compared with gap fraction measured using hemispherical photography. This paper extends this earlier work and tests the potential of TLS for measuring directional gap fraction in broadleaf canopies with very different structure to the conifers in our earlier experiments. This work is the first stage of an exploration of TLS to measure the three dimensional structure of forest canopies noting here that forest canopy directional gap fraction is in fact a two dimensional parameter.

## 2. METHODS

TLS data were collected in a small stand of deciduous trees composed of birch and sycamore, located on the campus of the University of Salford, UK. The trees had an average height of approximately 15m. A Riegl LMZ 210i laser scanner was used to measure two orthogonal scans each covering a zenith range of 180 x 80 degrees. A scanner step resolution of 0.108 deg was used resulting in 1.2 million points in each scan. The scanner had a fixed beam divergence of 3mrad so that the beam had a diameter of 15mm at 5m, 30mm at 10m and 45mm at 15m. Data were collected on three dates 30th October, 17th November 2006 and 23rd February 2007. On the first date leaf cover was high, in November there were leaves still present in parts of the canopy and in February there were no leaves on the trees. At each date a hemispherical photograph of the canopy was taken with a six mega pixel Canon digital SLR camera equipped with a full frame hemispherical lens. Directional gap fraction was computed from the photographs using the Gap Light Analyzer software (Frazer *et al.*, 2000). To determine directional gap fraction from the TLS data the coordinates of the laser hits were converted to spherical coordinates and the number of hits in 5 degree zenith angle bands, from 0-80 degrees, compared with the total number of shots in that direction, computed from the model of Danson *et al.* (2007).



The ratio of ‘hits’ to ‘shots’ gives an estimate of the gap fraction in a given direction.



Figure 1. Hemispherical photographs of canopy in October (top), November (middle) and February (bottom)

3. RESULTS

Comparison between the directional gap fraction derived from the TLS and photography showed that the TLS estimates of gap fraction were significantly lower at all zenith angles up to 65 degrees (Figure 2). Visual inspection of the hemispherical photography and comparison with the TLS data suggested that the laser scanner was not able to detect small gaps in the canopy, even in regions where there was sparse cover of leaf or woody material.

This hypothesis was confirmed by visual inspection of the TLS intensity data displayed in a cylindrical projection (Figure 3). The intensity data showed that there were laser hits, often with intermediate to high intensity values, in regions of the canopy where leaf or woody cover was low. It also appeared that the laser data at far range values (15-20m) showed the largest discrepancy between the TLS and hemispherical photographs. It was observed that there was an increase in laser return intensity with range caused by the bi-axial configuration of the laser scanner which meant that at close range the transmitted beam and the field of view of the detector did not completely overlap and return intensity was lower than expected (Figure 3). This measurement-related characteristic of the data prevented correction of the range-intensity relationship using the radar equation described in Wagner et al. (2004) which shows that laser intensity should decrease by a factor related to range to the power four.

In an attempt to filter the TLS data to eliminate hits in directions where the canopy gap fraction was low, a rule-based algorithm was applied to the data which retained only points with intensity values less than a given threshold value. Empirically adjusting this threshold and re-computing the TLS gap fraction allowed identification of the best-fit gap fraction distribution. A filter with the threshold set to an intensity value of 0.45 produced the closest fit to the gap fraction derived for the November data (Figure 4).

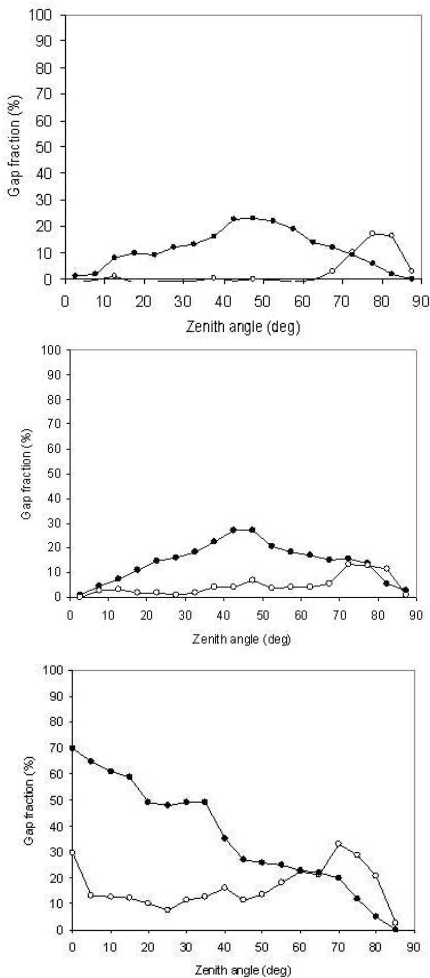


Figure 2. Comparison between gap fraction derived from TLS (open circles) and hemispherical photography (closed circles). Top: 30th October, Middle: 17th November, Bottom: 23rd February

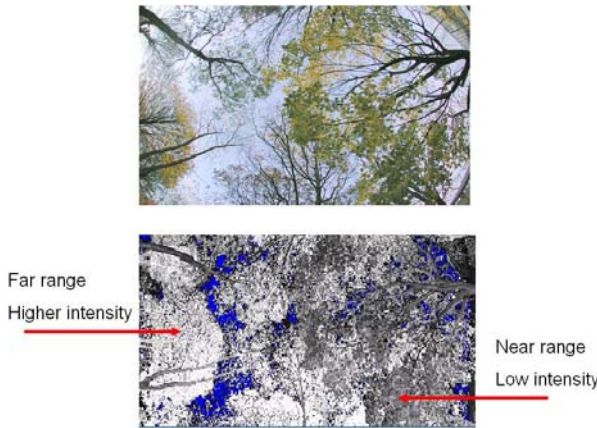


Figure 3. November hemispherical photograph and corresponding laser scanner data in cylindrical projection showing variation intensity of laser returns.

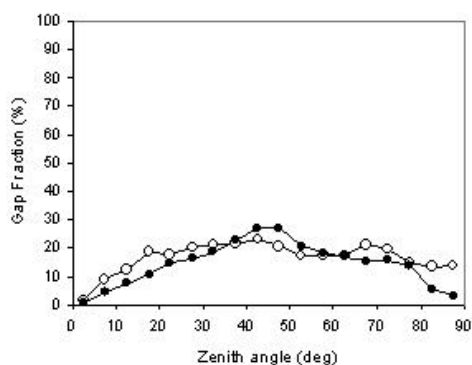


Figure 4. Directional gap fraction derived from TLS data with intensity <0.45 (open circles) and hemispherical photography 17th November.

#### 4. DISCUSSION AND CONCLUSIONS

Terrestrial laser scanners have the potential to revolutionise the measurement of vegetation canopy structure with their rapid measurement time, repeatability and accuracy. For highly clumped conifer forest canopies it appears that TLS can accurately measure canopy directional gap fraction as gaps tend to be large. In the deciduous woodland canopy chosen for this study gaps were smaller a more evenly distributed across the hemisphere and this, coupled with the relatively wide laser beam, meant that only the largest gaps were detected by the scanner, resulting in underestimation of gap fraction compared with hemispherical photography. In effect the TLS was too sensitive to canopy elements within the laser beam so that even if the fractional cover within the beam was, say, 10%, a laser return was recorded. It would be ideal if the sensitivity of the instrument could be modified so that a laser return was only triggered if the gap was greater than fifty percent. However most commercially available systems do not have such a capability. Another alternative would be to record and interpret the complete 'wave-form' of the returned energy, but this technology has only very recently been developed in a ground based instruments and this requires further testing. Finally it may be possible to use the laser return intensity data to capture additional information about the objects within the laser beam. However return intensity depends not only on the objects within the beam, but also their reflectivity, scattering characteristics and their range distribution and so that such an interpretation will not be straightforward.

This paper has shown the strengths and weaknesses of terrestrial laser scanner data for measuring directional gap fraction in deciduous woodland canopies. Further work will explore the issues of gap detection outlined above and will go to explore the application of TLS to measure the size shape and three-dimensional distribution of canopy gaps.

#### REFERENCES

Danson, F.M., Hetherington, D., Morsdorf, F., Allgöwer, B., 2007. Forest canopy gap fraction from terrestrial laser scanning. *IEEE Geoscience and Remote Sensing Letters*, 4(1), pp. 157-160.

Frazer, G. W., Canham, C. D., Lertzman, K. P., 2000. Gap light analyzer (GLA), Version 2.0: Image-processing software to analyze true-color, hemispherical canopy photographs. *Bull. Ecol. Soc. Amer.*, 81(3), pp. 191-197.

Hopkinson, C., Chasmer, L., Young-Pow, C., Treitz, P., 2004. Assessing forest metrics with a ground-based scanning lidar. *Can. J. For. Res.*, 4(3), pp. 573-583.

Jonckheere, I., Fleck, S., Nackaerts, K., Muys, B., Coppin, P., Weiss, M., Baret, F., 2004. Review of methods for in situ leaf area index determination—Part I: Theories, sensors and hemispherical photography. *Agric. For. Meteorol.*, 121(1), pp. 19-35.

Lovell, J. L., Jupp, D. L. B., Culvenor, D. S., Coops, N. C., 2003. Using airborne and ground-based ranging lidar to measure canopy structure in Australian forests. *Can. J. Remote Sens.*, 29(5), pp. 607-622.

Thies, M., Pfeifer, N., Winterhalder, D., Gorte, B. G. H., 2004. Three dimensional reconstruction of stems for assessment of taper, sweep and lean based on laser scanning of standing trees. *Scand. J. For. Res.*, 19(6), pp. 571-581.

Wagner, W., Ullrich, A., Ducic, V., Melzer, T., Studnicka, N., 2006. Gaussian decomposition and calibration of a novel small-footprint full-waveform digitising airborne laser scanner. *ISPRS Journal of Photogrammetry and Remote Sensing* 60(2), pp. 100-112.

Watt P. J., Donoghue, D. N. M., 2005. Measuring forest structure with terrestrial laser scanning," *Int. J. Remote Sens.*, 26(7), pp. 1437- 1446.

Weiss, M., Baret, F., Smith, G. J., Jonckheere, I., Coppin, P., 2004. Review of methods for in situ leaf area index (LAI) determination—Part II: Estimation of LAI, errors and sampling. *Agric. For. Meteorol.*, 121 (1/2), pp. 37-53.

#### ACKNOWLEDGEMENT

This research was funded by the EU Alfa programme ICONE under grant AML/19.0902/97/0666/II-0380-FA-FI.

# PREDICTING TREE HEIGHT AND BIOMASS FROM GLAS DATA

G. Sun<sup>1,2</sup>, K.J. Ranson<sup>3</sup>, J. Masek<sup>3</sup>, A. Fu<sup>2</sup>, and D. Wang<sup>2</sup>

<sup>1</sup> Department of Geography University of Maryland, College Park, MD 20742 USA, e-mail: Guoqing.sun@gmail.com

<sup>2</sup> State Key Laboratory of Remote Sensing, Institute of Remote Sensing Applications, Chinese Academy of Sciences, P. O. Box 9718, Beijing, 100101, China

<sup>3</sup> NASA's Goddard Space Flight Center, Greenbelt, MD, 20771 USA

**KEY WORDS:** GLAS, lidar, forest structure, biomass

## ABSTRACT:

Our previous studies using airborne lidar data have shown that the tree height indices derived from the GLAS and LVIS waveforms were highly correlated. The quartile waveform energy heights derived from GLAS and LVIS data showed significant correlations too. Because of these correlations and the fact that airborne lidar data has been shown to be an accurate index of forest biomass, we believe that the GLAS data will be useful for biomass sampling in regional to global scales. In this study, field measurements at GLAS footprints were used to further understand the physical meaning of the height indices derived from GLAS data, and to investigate the prediction capability of GLAS data. The near-repeat-pass GLAS data acquired in Fall and early Summer were compared to investigate the data stability, seasonal effects, potential for change monitoring, and provide insight in sampling strategy of the heterogeneous forest structures.

## 1. INTRODUCTION

The Geoscience Laser Altimeter System (GLAS) instrument aboard the Ice, Cloud, and land Elevation (ICESat) satellite, launched on 12 January 2003. GLAS is the first lidar instrument designed for continuous global observation of the Earth (Zwally et al., 2002). Researchers have started using GLAS data for forest studies (Ranson et al., 2004a, b; Carabajal and Harding, 2005; Lefsky et al., 2005). Measurements derived from lidar waveforms were used to characterize the canopy vertical structure. These measurements include the lowest and highest detectable returns (above a threshold noise level), and the heights within the canopy where 25, 50, 75 and 100% waveform energy were received (Blair et al., 1999). The vertical distribution of plant materials, along with the gap distribution, determines the proportion of energy scattered at a given height. The use of GLAS data for deriving accurate forest parameters for regional studies requires full understanding of their characteristics. The tree height and biomass within GLAS footprints measured in the field were used to test the prediction capability of the GLAS data. The results show some of the potentials and problems of the GLAS data for vegetation structure studies.

## 2. STUDY AREA AND DATA

### 2.1. Study site

The study sites include forests around Tahe (52.5° N, 125° E) and Changbai Mountain (42.5° N, 128° E) areas in Northern China.

More than 80 GLAS footprints were measured in Northern China. After the center of GLAS footprint was located using GPS, four sampling plots with a radius of 7.5 meters (center, 22.5m to north, south-east, and south-west from center, see Fig. 1) were located within the footprint. Diameter at breast height (DBH) and tree height of all trees with DBH > 5cm were measured. Dominant trees within a ~100m circle but not inside these sampling plots were also measured. These measurements were later used to estimate the height of dominant trees and above-ground biomass in the GLAS footprints.

### 2.2. GLAS data

GLAS carries three lasers. Laser 1 started firing on February 20, 2003 and failed only 37 days later. Anomaly studies revealed systematic problems that reduced the lifetime of the laser system. Consequently, the GLAS mission started to operate with a 91-day repeat orbit (with a 33 day sub-cycle) over selected times of the year to maximize coverage of ice-covered areas. From early October to November 19, 2003, GLAS completed the first 33-day sub-cycle using laser 2 (L2A). Since then, more 33-day sub-cycle data sets have

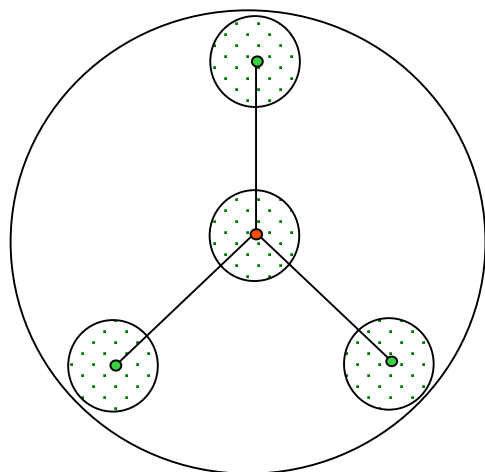


Fig. 1. Sampling plots within a GLAS footprint: Radius of sampling plots (small circle) is 7.5m. The distance between sampling plots is 22.5m.

been acquired in Feb-March, May-June and October-November periods each year. The use of laser 3 was initiated in October, 2004 (L3A), and continued in February-March (L3B), May-June (L3C), October-November (L3D) in 2005, and Feb-March (L3E), May-June (L3F) in 2006. These 33-day sub-cycles are nearly repeat-passes of the October-November 2003 data (L2A), providing a capability for seasonal and inter-annual change monitoring. GLAS data from L2A, L3A, L3C, L3D and L3F were used in this study.

GLAS uses 1064-nm laser pulses and records the returned laser energy from an ellipsoidal footprint. The footprint diameter is about 65m, but its size and ellipticity have varied through the course of the mission (Schutz et al., 2005; Abshire et al., 2005). GLA01 products provide the waveforms for each laser shot, but only an estimated geolocation for all 40 shots acquired within 1 second. For the land surfaces, the waveform has 544 bins with a bin size of 1-nsec or 15cm. The bin size from bin 1 to 151 has been changed to 60cm starting from acquisition L3A, so the total waveform length increased from 81.6m to about 150m. The product GLA14 (Land/Canopy Elevation) doesn't contain the waveform, but various parameters derived from the waveform. The GLAS waveforms were smoothed using filters, and the signal beginning and end were identified by a noise threshold. The smoothed waveform was initially fitted using many Gaussian peaks at different heights, and then the peaks were reduced to six by an iterative process (Zwally et al., 2002; Harding and Carabajal. 2005). GLAS14 data provides the surface elevation and the laser range offsets for the signal beginning and end, the location, amplitude, and width of the six Gaussian peaks. Fig. 2 shows a GLAS waveform from our study area with the Gaussian peaks (Hofton et al., 2000) and other parameters extracted from GLA14 data products. Assuming that the last peak near the

ground is from surface reflection, the distance from the signal beginning and this ground peak is the top canopy height (referred to as H14). This works only for flat area, and requires significant energy return from ground surface. For cases with dense canopies, rough surfaces with slopes, the elevation of the ground peak becomes questionable.

### 3. GLAS DATA PROCESSING

The GLA14 data were first retrieved along with the record index, the serial number of the shot within the index (from 1 to 40), acquisition time, latitude, longitude, elevation, range offsets of signal beginning, signal ending, waveform centroid, and fitted Gaussian peaks. In the GLA01 data file, the 40 shots received in one-second are assigned only one estimated latitude and longitude. Using the record index and shot number found in GLA14 data, the individual waveform was extracted from GLA01 data along with other parameters such as estimated noise level, noise standard deviation, and transmitted pulse waveform, which were used later in waveform processing.

A method for calculating the heights of quartile waveform energy from GLAS waveform was implemented. A Gaussian filter with a width similar to the transmitted laser pulse was used to smooth the waveform. For many cases, the noise level before the signal beginning was lower than the noise after the signal ending. Consequently, we estimated the noise levels before the signal beginning and after the signal ending from the original waveform separately using a method based on the histogram. Using three standard deviations as a threshold above the noise level, the signal beginning and ending were located. The total waveform energy was calculated by summing all the return energy from signal beginning to ending. Starting from the signal ending, the position of the 25%, 50%, and 75% of energy were located by comparing the accumulated energy with total energy. Since the heights of these quartiles refer to the ground surface, not the signal ending, the ground peak in the waveform needs to be located. Searching backward from the signal ending, the peaks can be found by comparing a bin's value with those of the two neighboring bins. If the first peak is too close to the signal ending, i.e. the distance from signal ending to the peak is less than the half width of the transmitted laser pulse, this peak was discarded. The first significant peak found is the ground peak. As terrain slope and surface roughness increase, the ground peak of the waveform becomes wider and the signal beginning moves upwards in a proportional manner. The distance between the signal ending and the assumed signal ending when the surface is flat was used as an adjustment to the signal beginning.

### 4. PREDICTION OF TREE HEIGHT AND BIOMASS FROM GLAS DATA

The field measurements and the processed GLAS data were used to train a neural network for prediction of tree height and stand biomass. Fig. 2 shows the correlation between field biomass measurements and the biomass predicted by a trained neural network model from GLAS indices. The model used six input variables derived from total length of waveform, top canopy height, 25% and 75% waveform quartiles, with 10 nodes in a hidden layer. Fig. 3. shows the correlation between field maximum tree height measurements and the height predicted by a trained neural network model from GLAS indices. The model used 5 input variables derived from total length of waveform, quadratic mean canopy height, 25% and 50% waveform quartiles, with 3 nodes in a hidden layer.

These neural models then were applied to all GLAS footprints acquired in Fall, 2003. The statistics of tree height and stand biomass within an area of 38° to 50° N, 120° to 130° E were calculated for major forest classes, and disturbed areas. Fig. 4 and 5 show the histograms f tree height and biomass in this region. Table 1 is a list of average tree height and biomass for various forest classes in the region.

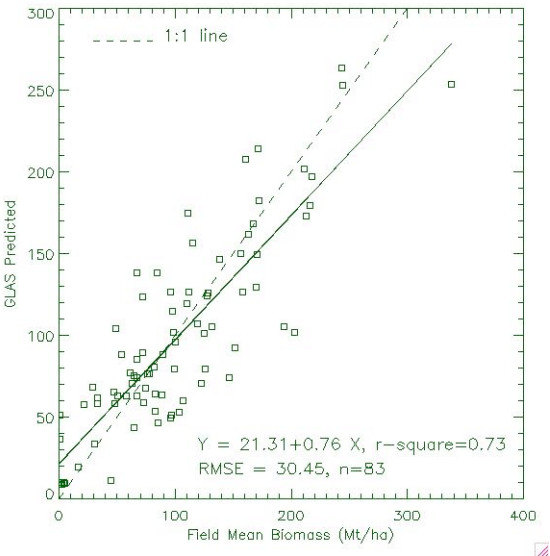


Fig. 2. Prediction of stand biomass from GLAS data.

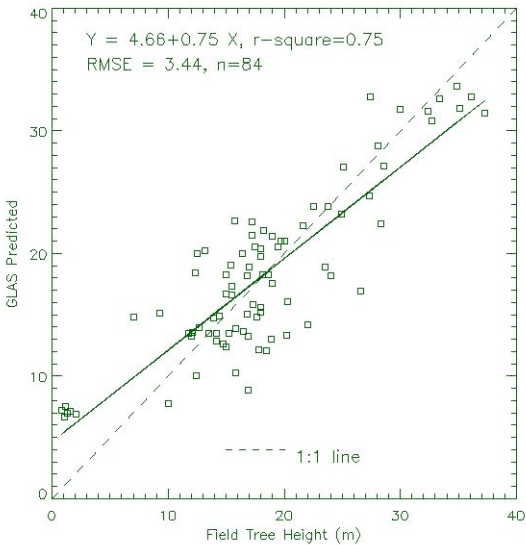


Fig. 3. Prediction of top tree height from GLAS data.

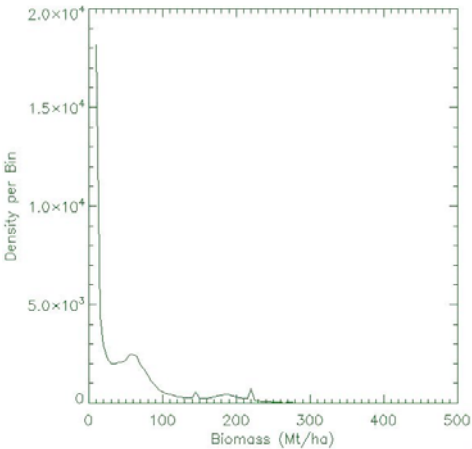


Fig. 4. Histogram of biomass in the region (min. = 6.42, max. = 427.41). Peak at < 20Mt/ha is non-forest area.

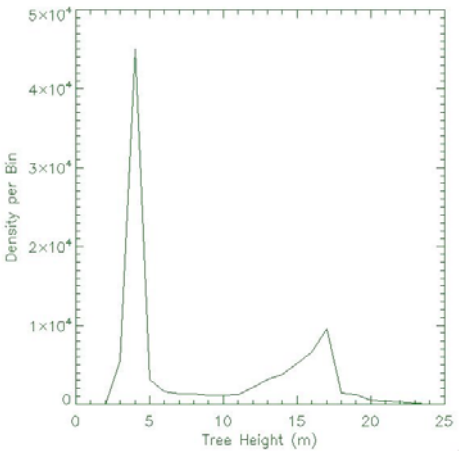


Fig. 5. Histogram of tree height in the region (min. = 2.5m, max. = 24.14m). The peak at ~4m is non-forest area.



Table 1. Average tree height and biomass for different forest types in a region of 38° – 50° N, 120° – 130° E, estimated from GLAS data. ENC – Evergreen Needle Conifer, DNC – Deciduous Needle Conifer, DB1-3 – Deciduous Broadleaf, Mix1-3 – Mixed Forests, Bn1-2 – disturbed (burned) forests.

	ENC	DNC	DB1	DB2	DB3	Mix1	Mix2	Mix3	Bn1	Bn2
Height (m)	13.33	13.96	14.12	13.79	12.02	14.53	14.45	14.27	8.85	8.88
Biomass (kg/m <sup>2</sup> )	14.93	10.72	10.18	8.67	6.44	13.75	10.96	11.77	3.75	4.17

There were total 174,553 GLAS footprints in this 12° by 10° area. 63,906 samples were in forested area (36.6% forest cover). Both the tree height and biomass values are reasonable. In the disturbed area (mainly by fire), tree height is shorter, ad biomass is lower. These results will be compared with data from other resources in future studies.

5. CONCLUSIONS

The Geoscience Laser Altimeter System (GLAS) is the first lidar instrument for continuous global observation of the Earth. Field measurements were mainly conducted at flat areas or with small slopes. The study showed that for these cases GLAS waveform data provides reasonable prediction for the heights of dominant trees and above-ground biomass. The study also shows that GLAS samples provides a reasonable statistics on biomass level, forest coverage but further studies area needed to evaluate the terrain effects, seasonal variation of GLAS samples, etc.

6. ACKNOWLEDGEMENT

This study and field work was funded by National Science Foundation of China (40571112), the 863 program (2006AA12Z114) of China, and NASA’s Science Mission Directorate.

7. REFERENCES

Abshire, J. B., X. Sun, H. Riris, J. M. Sirota, J. F. McGarry, S. Palm, D. Yi, and P. Liiva, (2005): Geoscience Laser Altimeter System (GLAS) on the ICESat Mission: On-orbit measurement performance, *Geophysical Research Letters* 32 (22).

Blair, J. B., D. L. Rabine, M. A.and Hofton, (1999): The laser vegetation imaging sensor (LVIS): a medium-altitude, digitations-only, airborne laser altimeter for mapping vegetation and topography, *ISPRS Journal of Photogrammetry and Remote Sensing* 54: 115-122.

Carabajal, C. C., and D. J. Harding, (2005): ICESat Validation of SRTM C-Band Digital Elevation Models, *Geophys. Res. Lett.*, 33, L22S01.

Hofton, MA; Minster, JB; Blair, JB., (2000): Decomposition of laser altimeter waveforms. *Ieee Transactions On Geoscience And Remote Sensing* 38 (4): 1989-1996, Part 2.

Lefsky, MA, David J. Harding, Michael Keller, Warren B. Cohen, Claudia C. Carabajal, Fernando Del Bom Espirito-Santo, Maria O. Hunter, and Raimundo de Oliveira Jr.(2005): Estimates of forest canopy height and aboveground biomass using ICESat, *Geophysical Research Letters*, VOL. 32, L22S02, doi:10.1029/2005GL023971, 2005.

Ranson, K. J., G. Sun, K. Kovacs, and V. I. Kharuk, (2004a): Landcover attributes from ICESat GLAs data in central Siberia, *IGARSS 2004 Proceedings*, 20-24 September 2004, Anchorage, Alaska, USA.

Ranson, K. J., G. Sun, K. Kovacs, and V. I. Kharuk, (2004b): Use of ICESat GLAS data for forest disturbance studies in central Siberia, *IGARSS 2004 Proceedings*, 20-24 September 2004, Anchorage, Alaska, USA.

Schutz, B. E., H. J. Zwally, C. A. shuman, D. Hancock, and J. P. DiMarzio, (2005): Overview of the ICESat Mission, *Geophysical Research Letters* 32 (22).

Zwally H.J., B. Schutz, W. Abdalati, , J. Abshire, C. Bentley, A. Brenner, J. Bufton, J. Dezio, D. Hancock, D. Harding, T. Herring, B. Minster, K. Quinn, S. Palm, J. Spinhirne, R. Thomas, (2002): ICESat's laser measurements of polar ice, atmosphere, ocean, and land. *Journal of Geodynamics* 34 (3-4): 405-445.

# INTERCALIBRATION OF VEGETATION INDICES – AN UPDATE

Michael D. Steven<sup>a\*</sup>, Timothy J. Malthus<sup>b</sup> and Frédéric Baret<sup>c</sup>

<sup>a</sup> School of Geography, University of Nottingham, Nottingham NG7 2RD, UK. - Michael.Steven@nottingham.ac.uk

<sup>b</sup> School of GeoSciences, University of Edinburgh, Kings Buildings, West Mains Road, Edinburgh EH9 3JW, UK. - tjm@geo.ed.ac.uk

<sup>c</sup> INRA-CSE, Agroparc, 84914 Avignon Cedex 09, France. - baret@avignon.inra.fr

**KEY WORDS:** Vegetation index; sensor systems; spectroradiometric measurements; validation, NDVI, SAVI, OSAVI

## ABSTRACT:

In 2003 we addressed the issue of intercalibration of vegetation indices from different satellite-based optical sensor systems with differing spectral response functions in the visible and near-infrared bands (Steven *et al.*, 2003). We used a database of spectroradiometric measurements made over a range of canopy densities, soils and foliage colours to simulate vegetation indices (NDVI, SAVI and OSAVI) to produce a table of intercalibration factors for the specific spectral response functions for 15 satellite instruments. We found that the indices are not identical, but are linearly related, allowing conversion from one system to another to a precision of 1–2%. Our results allow vegetation index data from different systems to be combined reliably. The present study extends the intercalibration of vegetation indices to include systems launched since our previous paper. We propose a standard pair of bands for the definition of vegetation indices and suggest that users apply our conversion coefficients to adjust vegetation index measurements to this standard. The margin of error in applying a two step conversion via the standard is at most 1% compared with a direct conversion from one system to the other. Independent validations of our conversion coefficients from a number of studies in the literature are discussed.

## RÉSUMÉ:

Nous avons proposé en 2003 des relations statistiques permettant de passer de valeurs d'indice de végétation d'un capteur donné, à celles d'un autre capteur ayant une réponse spectrale différente dans les bandes rouge et infra-rouge (Steven *et al.*, 2003). Une base de données expérimentale de réflectance spectrale couvrant une gamme de densité, de sols, et de couleur de feuillage avait permis de simuler les indices de végétation (NDVI, SAVI, OSAVI) pour une quinzaine de capteurs couramment utilisés. Les résultats montraient des différences marquées entre capteurs pour un même indice, mais qu'ils étaient toujours reliés de manière très forte et linéaire. Il est donc possible de passer d'un capteur à un autre avec une très bonne précision (1-2%). L'étude présente étend les résultats précédents aux nouveaux systèmes lancés ou qui vont être lancés dans un futur proche. Nous proposons un couple de bandes standard pour la définition des indices de végétation, et suggérons aux utilisateurs d'appliquer nos coefficients de conversion pour obtenir un indice de végétation 'standard'. Les incertitudes induites par le passage à l'indice de végétation 'standard' pour obtenir les valeurs de l'indice de végétation d'un autre capteur sont inférieures à 1% en comparaison d'une conversion directe. Les coefficients de conversion proposés ici sont validés et discutés à partir de différentes études publiées.

## 1. INTRODUCTION

### 1.1 Vegetation indices

Vegetation indices, based on the contrast between reflectance in the visible and near-infrared bands, have been a standard tool of earth observation since the 1970s. They have been applied in a variety of ways as measures of the vigour and productivity of vegetation; and at all scales, from continental scale vegetation dynamics, (e.g. Townshend and Justice, 1986) to regional crop predictions (de Koeijer *et al.*, 2000) and pixel-scale application in precision agriculture (Steven and Millar, 1997).

A persistent issue in vegetation monitoring is the acquisition of sufficient data to capture the dynamics of plant growth. Plant growth requires water, usually supplied by rainfall, so the more productive vegetated regions are frequently cloudy (Heller, 1961). The data acquisition problem has broadly been resolved in two ways: at higher resolutions by the development of systems with pointable cameras that can target particular sites several times within the satellite repeat cycle; and at lower

resolutions by data compositing over periods of 10 days or more. These solutions introduce their own problems. In particular, both pointing and compositing tend to increase the range of viewing angles, and to a lesser extent solar angles, used in the vegetation index product. Corrections can be made for these effects using a model of the bidirectional reflectance distribution function (BRDF), but this requires *a priori* knowledge of the vegetation type (Steven, 1998; Bacour, Bréon, and Maignan, 2006).

### 1.2 Standardisation

A complementary approach is to combine data from more than one system, sometimes referred to as the use of a virtual constellation (CEOS, 2006). Key to this approach is the adoption of a set of operating standards for the systems to be combined. Increasingly, there is a focus on ensuring the long-term continuity of vegetation observations, particularly at the larger scales, to establish a basis for monitoring the effects of climate change. There is also considerable interest in back-calibrating data from earlier systems, as near as possible to

\* Corresponding author

current standards, to establish the long-term baseline. Precise calibration of instruments is required and attention to variations in BRDF associated with different orbital characteristics (Teillet, Markham and Irish, 2006; Röder, Kuemmerle and Hill 2005; Martinez-Beltrán *et al.*, 2003).

However, as noted in our earlier paper (Steven *et al.*, 2003) there is no accepted standard for vegetation indices. Even when instruments are precisely calibrated and all the proper corrections are applied for BRDF and atmospheric effects, indices from the various measurement systems differ systematically due to differences in the position, width and shape of the wavebands used (Gallo and Daughtry, 1987; Guyot and Gu, 1994). Steven *et al.* (2003) used a database of high resolution spectra of vegetation canopies to simulate the particular near-infrared and visible band responses and thence the vegetation index as measured by different orbiting systems. Differences between NDVIs on the same target could be as high as 14%, but the indices recorded by different observation systems were highly correlated so that different systems could be intercalibrated to a degree of precision of about  $\pm 1\%$ . In the present paper we extend the intercalibration of vegetation indices forwards to include orbiting sensor systems launched since our previous report; and backwards to include historical variations in the NOAA AVHRR system. In addition, to simplify the issue of standardisation, we propose a standard pair of bands as the reference for all vegetation indices and provide conversion coefficients for operational systems (Table 1).

2. METHODOLOGY

2.1 Spectral response functions

Our solution to the differences between sensors is to simulate near-infrared and red measurements by the range of instruments available using the spectral response functions of each detector. The spectral response functions of 15 systems were reported in Steven *et al.* (2003). In the present study we extend the analysis to a total of 41 systems including some variants where more than one band combination can be used in the same system, and provide separate AVHRR simulations for NOAA6 to NOAA18 inclusive. Where possible the spectral response functions were found in the literature; others were obtained from the web or by personal communication. The spectral responses were digitised every 1nm to match the spectral data. The operators of the OrbView-2 and OrbView-3 systems were unwilling to release data on the spectral response functions of their instruments, so we tested two alternative models: a box function across the nominal wavelength range and a Gaussian fitted so that the nominal waveband limits were the half-power points. The wavebands for Venus, which are relatively narrow but not as yet precisely defined, were similarly modelled with a Gaussian on the basis of the developer's advice.

2.2 Canopy database

The simulations were performed on a database of calibrated spectral reflectance measurements of plant canopies in the field made with a GER IRIS MkIV spectroradiometer. The database consists of 166 measured reflectance spectra of crops of sugar beet and maize in the UK and France in 1989/90. The spectra were recorded in 975 channels spanning the 350–2500 nm range and were resampled to 1nm. Experimental treatments on the crops were designed to provide contrasting canopy structures from the different crop types and by thinning treatments, contrasting canopy greenness by treatments of disease or dilute

herbicide to induce chlorosis in selected canopies, and a wide range of cover densities and backgrounds including black cloth, white cloth and various soils. The database thus provides a very wide range of canopy conditions, although as noted by Steven *et al.* (2003) it does not include the effects of senescent plant material.

2.2 Spectral band simulations

Spectral band responses were simulated by convolving the spectral top-of canopy radiance data with the spectral response function and normalising to reflectance with the corresponding convolved data for the reference panel, adjusted for its true reflectance. The simulated band reflectances were then applied to compute vegetation indices. Simulations were performed for NDVI, SAVI and OSAVI. Vegetation indices from the different simulated systems were then compared. In the 2003 study we compared all possible pairs of systems. With the larger number of systems considered here, this would be prohibitive. Instead, we relate indices from different systems to a standard vegetation index based on narrow bands at 670 and 815nm. Vegetation indices based on these wavelengths are close to the optimum; only one of the operational indices studied has a greater dynamic range.

3. RESULTS

3.1 Comparison of simulated vegetation indices

The simulations for NDVI, SAVI and OSAVI show that vegetation indices from different detector systems are not identical but are very highly correlated (minimum  $r^2 = 0.984$ ). Plots of selected systems against the standard are shown in Figures 1 and 2, these examples representing the minimum and maximum slopes of the systems considered. In all cases the correlations are strong enough to allow precise linear conversion from one system to another.

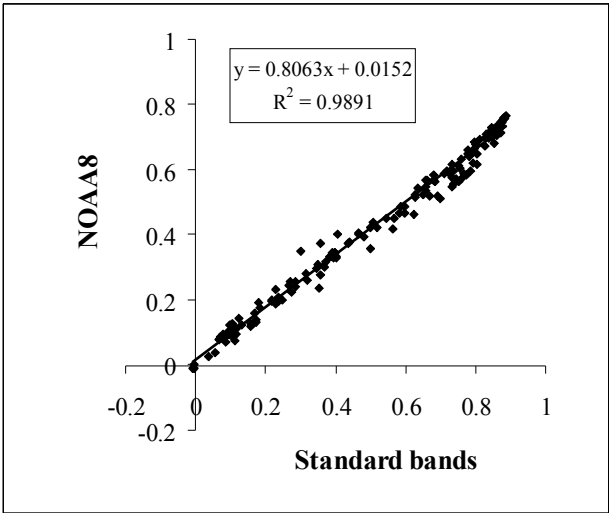


Figure 1. Regression of NDVI based on NOAA8 bands against the standard bands.

Table 1 presents the conversion coefficients to and from the standard pair of bands adopted in this study. Linear regressions for SAVI, OSAVI and NDVI differ in slope and intercept by no more than about 0.001 and 0.1 respectively. As these differences are considerably less than typical errors of

measurement, a single conversion table is adequate for the range of vegetation index formulations considered. It is likely, although untested, that the same conversion factors will apply to most other formulations of ratio-type vegetation indices in common use.

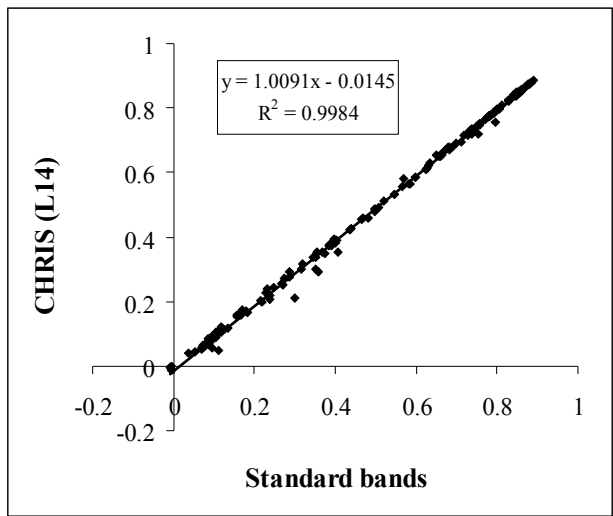


Figure 2. Regression of NDVI based on the CHRIS near-infrared (L14) and red bands against the standard bands.

Satellite sensor	A		B	
	Intercept	Slope	Intercept	Slope
ALI	-0.005	0.965	0.006	1.034
ASTER, using band 3B	-0.001	0.933	0.003	1.068
ASTER, using band 3N	0.000	0.933	0.002	1.068
ATSR2/ AATSR	0.008	0.968	-0.006	1.030
CHRIS, using band L14	-0.015	1.009	0.016	0.989
CHRIS, using band L15	0.005	0.991	-0.004	1.007
DMC	0.006	0.954	-0.005	1.046
Formosat	0.002	0.936	0.000	1.065
Ikonos	-0.010	0.870	0.015	1.144
IRS	0.005	0.950	-0.004	1.050
Kompsat	0.004	0.942	-0.003	1.058
Landsat 5 TM	0.005	0.938	-0.003	1.063
Landsat 7 ETM+	0.003	0.957	-0.002	1.041
Landsat MSS	0.029	0.883	-0.024	1.115
MERIS	0.008	0.983	-0.008	1.016
MISR	0.005	0.985	-0.005	1.014

	A		B	
MODIS	0.017	0.935	-0.015	1.065
NOAA10	0.003	0.854	0.001	1.160
NOAA11	0.015	0.831	-0.011	1.188
NOAA12	0.015	0.844	-0.012	1.173
NOAA13	0.017	0.835	-0.014	1.184
NOAA14	0.016	0.837	-0.013	1.180
NOAA15	0.016	0.902	-0.014	1.100
NOAA16	0.017	0.897	-0.015	1.107
NOAA17	0.016	0.904	-0.014	1.098
NOAA18	0.017	0.905	-0.014	1.097
NOAA6	0.021	0.850	-0.018	1.163
NOAA7	0.015	0.857	-0.012	1.155
NOAA8	0.015	0.807	-0.012	1.226
NOAA9	0.015	0.839	-0.012	1.179
OrbView-2, using block fcn	0.005	0.989	-0.004	1.009
OrbView-2, using Gaussian	0.005	0.982	-0.005	1.016
OrbView-3, using block fcn	0.002	0.937	0.000	1.063
OrbView-3, using Gaussian	0.002	0.857	0.001	1.159
POLDER	0.005	0.985	-0.005	1.014
QuickBird	0.000	0.909	0.002	1.096
Seawifs	0.005	0.982	-0.004	1.016
Severi MSG	0.012	0.926	-0.010	1.076
Spot2 Hrv2	0.012	0.921	-0.011	1.081
Spot4 Hrv2	0.010	0.917	-0.008	1.085
SPOT5	0.010	0.928	-0.008	1.073
Venus, using band B10 with Gaussian	-0.012	0.984	0.013	1.015
Venus, using band B11 with Gaussian	0.007	0.967	-0.006	1.032

Table 1. Conversion coefficients for vegetation indices for the different systems considered.

To convert a vegetation index from an operational system  $VI_{op}$  to the standard,  $VI_{std}$ , equation 1 is applied, using the slope and intercept values from column B. To convert from the standard to the operational system, equation 2 is applied, using the slope and intercept values from column A.

$$VI_{std} = VI_{op} \times [slope]_B + [intercept]_B \tag{1}$$

$$VI_{op} = VI_{std} \times [slope]_A + [intercept]_A \tag{2}$$

Spectral response data for the simulations were acquired from published sources or by direct communication from instrument manufacturers; where these data were not forthcoming, we have modelled the sensor firstly using a block function and secondly by fitting a Gaussian to the nominal bandwidth. For OrbView-2 both methods give comparable results so that adjustment to the standard can be made to better than 1% precision. For OrbView-3 however, the difference is about 8%; this uncertainty indicates that this system is unsuitable for applications requiring intercalibration with others.

Although we recommend that all vegetation indices should be converted to the standard bands, it is possible to convert from one operational system to another using Table 1 to convert first to the standard as an intermediate stage and then from the standard to the second system. On examples tested, the error in this two-stage process, as compared with direct conversion between the systems, was up to 0.01 in slope and 0.007 in intercept.

### 3.2 Validation

In our earlier study, we reported on a small number of direct comparisons of near-simultaneous vegetation index measurements by different sensors (Steven *et al.*, 2003) which broadly supported the correction coefficients established in that study. A number of more recent studies provide further supporting evidence, either by direct comparisons of image data or different forms of simulation.

Martínez-Beltrán *et al.* (2003) compared ETM+, TM, LISS and AVHRR data on selected sites in south eastern Spain. Their study was mainly concerned with the effects of spatial data aggregation on the comparisons and atmospheric effects were not considered. Their best results were with high levels of aggregation. Compared with our study, they found similar linear relationships but with substantially greater slopes of the regression for ETM+ regressed on TM or LISS and a smaller slope for TM regressed on AVHRR. When they made comparisons between ETM+ and AVHRR on different dates, the slopes differed by 0.03.

Gallo *et al.* (2005) compared NDVI values for MODIS and AVHRR over the United States for identical 16 day compositing periods. Although the compositing process can introduce a systematic upward bias in NDVI (Goward *et al.*, 1993), this would probably be similar for both systems. Gallo *et al.* found linear relationships between NDVI values from different sensors. Their regression slopes differ from ours by no more than 0.02 indicating good agreement within the limits of the data. They found a similar degree of variation when the same systems were compared over different time periods.

Fensholt, Sandholt, and Stisen (2006) compared MERIS, MODIS and VEGETATION products on grass savannah in Senegal using wide angle *in situ* measurements with band radiometers designed to approximate the relevant bands. They report generally good agreement with Steven *et al.* (2003) but with higher MERIS sensitivity to vegetation than predicted by our results. However, the accuracy of their comparisons depends on the degree to which the *in situ* sensor bands match those of the satellite instruments. In addition, wide angle measurements would exaggerate vegetation indices, particularly in the middle of the range, as they noted in their study. It is possible to make a systematic correction for the wide angle effect (Steven, 2004). However, given the degree of overlap of

the spectral bands, the angular response effect is likely to be very similar for the different systems compared.

Miura, Huete and Yoshioka (2006) compared NDVI values for a number of systems on Hyperion hyperspectral image data over tropical forest and savannah in Brazil. They applied a similar approach to our own, combining the atmospherically corrected data with spectral response functions to simulate surface measured radiance in various bands. Although relationships between simulated radiances in paired bands were found to be land cover dependent, the relationships for NDVI were independent of land cover. However, they were non-linear, requiring a quadratic function to provide an adequate conversion between systems.

Van Leeuwen *et al.* (2006) simulated NDVI from AVHRR, MODIS and VIIRS using the SAIL model with a wide range of LAI. The model was parameterised with inputs from spectral libraries of vegetation, soil and snow data. Their result for NOAA16 versus MODIS is within 0.01 of values predicted from Table 1, but their prediction for NOAA14 has a slope 0.03 higher.

## 4. CONCLUSIONS AND DISCUSSION

It is now widely recognised that vegetation indices from different systems cannot be regarded as directly equivalent, being dependent on the particular band responses of the instruments concerned. The magnitude of the correction required is significant: considering just the slopes in Table 1, the values of the correction required to match our standard bands range from -1% (CHRIS using the L14 infrared band) to +23% (NOAA8 AVHRR). The present paper and a few other studies have found that vegetation indices can be linearly intercalibrated to a degree of precision of about  $\pm 2\%$ . However, the study by Miura, Huete and Yoshioka (2006), in which a quadratic correction was required, may indicate that these relations are not quite universal. Further investigation would help to resolve these differences. Nevertheless, the intercalibration coefficients presented in Table 1 allow progress to be made in standardising systems, but with caution, for as Miura, Huete and Yoshioka point out, observations with different spectral bands are inherently different and may introduce bias into downstream products.

A number of the studies, cited above or in Steven *et al.* (2003), have attempted intercalibration by direct comparison of vegetation indices from different systems. In addition to the spectral band effects discussed here, these comparisons of necessity include errors associated with instrument calibrations and atmospheric effects as well as bidirectional effects associated with time differences between data capture by the systems compared. In addition, direct comparisons are usually confined to two or three individual systems. Similarly, studies by Röder, Kuemmerle and Hill (2005), Turner *et al.* (2006) and Zhao *et al.* (2005) have applied the direct approach to address the intercomparison of various downstream vegetation products. While these studies are important in validating such products, direct intercomparisons do not of themselves indicate the sources of errors that arise, which must ultimately be traced through the various components of the algorithms applied. Conversely, there are advantages in developing the intercalibration of systems by a component-wise approach, treating calibration, bidirectional, atmospheric and spectral band effects separately. In the present study, simultaneous measurements by a single instrument were used to simulate the



different sensors on a common set of observations. Our approach has the advantage over direct studies of being relatively free of calibration errors; such calibration errors as exist are associated with the spectral flatness of the reference panel used in the field and are expected to be very small. Moreover, our approach is able to deal with the complete range of sensors on a common basis, including sensors on systems that no longer exist or that are still in development.

Standardisation of vegetation indices and related earth observation products is important to ensure long-term data continuity as well as in addressing shorter-term monitoring issues that are not adequately provided for by single observation systems. Our results, taken together with advances in instrument calibration, characterisation of angular responses and correction of atmospheric effects indicate that standardisation is now possible for most systems, within margins of error that are reasonable for a wide range of applications. To account for differences in spectral band responses, we propose here the adoption of a pair of standard reference bands at 670 and 815nm. To standardise for bidirectional effects it is also necessary to adopt standard solar and viewing angles. Bacour, Bréon and Maignan (2006) proposed standardising on viewing at nadir with a solar zenith angle of 40°. Conveniently, these angles correspond approximately to the average measurement conditions that apply to the canopy spectral database used in the present study; the solar angle proposed is also a reasonable mid-value for summer viewing conditions at mid latitudes. A more intractable problem may be the adoption of a standard form of the vegetation index. While NDVI is one of the simplest and most widely used indices, it has well documented problems particularly with variation in soil background. Some of these problems could be resolved with little additional complexity by adoption of one of the SAVI family of indices (Huete, 1988; Rondeaux, Steven and Baret, 1996). The conversion factors in Table 1 are valid, to the precision given, for the full range of the SAVI family as well as for NDVI.

## References.

- Bacour, C. Bréon, F.M. and Maignan, F., 2006. Normalization of the directional effects in NOAA-AVHRR reflectance measurements for an improved monitoring of vegetation cycles. *Remote Sensing of Environment*, 102, pp. 402–413.
- CEOS (2006) The CEOS Virtual Constellation Concept V0.4, Committee on Earth Observation Satellites [http://stratus.ssec.wisc.edu/cryos/docs/CEOS\\_constellations.doc](http://stratus.ssec.wisc.edu/cryos/docs/CEOS_constellations.doc) (accessed 31 Mar. 2007).
- de Koeijer, K.J., Steven, M.D., Colls, J.J. and Williams, J., 2000. Integration of earth observation data with a crop model for yield forecasting. *Aspects of Applied Biology*, 60, pp. 91–98.
- Fensholt, R., Sandholt, I. and Stisen, S., 2006. Evaluating MODIS, MERIS, and VEGETATION vegetation indices using in situ measurements in a semiarid environment *IEEE Transactions on Geoscience and Remote Sensing*, 44, pp. 1774–1786.
- Gallo, K.P. and Daughtry, C.S.T., 1987. Differences in vegetation indices for simulated Landsat-5 MSS and TM, NOAA-9 AVHRR and SPOT-1 sensor systems. *Remote Sensing of Environment*, 23, pp. 439–452.
- Gallo, K., Ji, L., Reed, B., Eidenshink J. and Dwyer, J., 2005. Multi-platform comparisons of MODIS and AVHRR normalized difference vegetation index data. *Remote Sensing of Environment*, 99, pp. 221–231.
- Goward, S.N., Dye, D.G., Turner, S., Yang, J., 1993. Objective assessment of the NOAA global vegetation index data product. *International Journal of Remote Sensing*, 14, pp. 3365–3394.
- Guyot, G. and Gu, X.F., 1994. Effect of radiometric corrections on NDVI- determined from SPOT HRV and Landsat TM data. *Remote Sensing of Environment*, 49, pp. 169–180.
- Heller, J. (1961). *Catch 22*. Simon and Schuster, New York.
- Huete, A.R., 1988. A soil adjusted vegetation index (SAVI). *International Journal of remote Sensing*, 9, pp. 295–309.
- Martínez-Beltrán, C., Calera Belmonte, A. and Jochum A., 2003. Inter-satellite cross-calibration: Integration of reflectance and NDVI from different satellites by means of a linear model. In Owe, M., d'Urso, G., Moreno, J.F. and Calera, A. (Eds) *Remote Sensing for Agriculture, Ecosystems and Hydrology, SPIE*, 5232, pp. 128–139.
- Miura, T., Huete, A., and Yoshioka, H., 2006. An empirical investigation of cross-sensor relationships of NDVI and red/near-infrared reflectance using EO-1 Hyperion data. *Remote Sensing of Environment*, 100, pp. 223–236.
- Röder, A., Kuemmerle, T. and Hill, J., 2005. Extension of retrospective datasets using multiple sensors. An approach to radiometric intercalibration of Landsat TM and MSS data. *Remote Sensing of Environment* 95, pp. 195–210.
- Rondeaux, G., Steven, M.D. and Baret, F., 1996. Optimization of Soil Adjusted Vegetation Indices. *Remote Sensing of Environment*, 55, pp. 95–107.
- Steven, M.D., 1998. The sensitivity of the OSAVI vegetation index to observational parameters. *Remote Sensing of Environment*, 63, pp. 49–60.
- Steven, M.D., 2004. Correcting the effects of field of view and varying illumination in spectral measurements of crops. *Precision Agriculture*, 5, pp. 51–68.
- Steven, M.D., Malthus, T.J., Baret, F., Xu, H. and Chopping, M., 2003. Intercalibration of vegetation indices from different sensor systems. *Remote Sensing of Environment*, 88, pp. 412–422.
- Steven, M.D. and Millar, C., 1997. Satellite Monitoring for Precision Farm Decision Support. In Stafford J.V. (Ed.) "*Precision Agriculture*" *Proceedings 1st European Conference on Precision Agriculture*, Warwick, 8-10 September 1997, Bios Scientific Publishers, Oxford. pp 697–704.
- Teillet, P.M., Markham, B.L. and Irish, R.R., 2006. Landsat cross-calibration based on near simultaneous imaging of common ground targets. *Remote Sensing of Environment*, 102, pp. 264–270.
- Townshend, J.R.G. and Justice, C.O., 1986. Analysis of the dynamics of African vegetation using the normalized difference vegetation index. *International Journal of Remote Sensing*, 7, pp. 1435–1446.

Turner, D.P., Ritt, W.D., Cohen, W.B., Gower, S.T., Running S.W., Zhao M., Costa M.H., Kirschbaum A.A, Ham J.M., Saleska, S.R. and Ahl, D.E., 2006. Evaluation of MODIS NPP and GPP products across multiple biomes. *Remote Sensing of Environment*, 102, pp. 282–292.

Van Leeuwen, W.J.D., Orr, B.J., Marsh, S.E. and Herrmann, S.M., 2006. Multi-sensor NDVI data continuity: Uncertainties and implications for vegetation monitoring applications. *Remote Sensing of Environment*, 100, pp. 67–81.

Zhao, M., Heinsch, F.A., Nemani, R.R. and Running, S.W., 2005. Improvements of the MODIS terrestrial gross and net primary production global data set. *Remote Sensing of Environment*, 95, pp. 164–176.

### Acknowledgements

The authors acknowledge financial assistance at various stages of this work from NERC, AFRC, SBREC and INRA. We are particularly indebted to numerous colleagues who assisted with fieldwork in the UK and France and to the NERC Equipment Pool for Field Spectroscopy who provide instrumentation and much valued advice.

# PYRITE MINE WASTES HYPERSPECTRAL MONITORING AS A TOOL TO DETECT CLIMATE CHANGE

A. Riaza<sup>a</sup>, C. Ong<sup>b</sup>, A. Müller<sup>c</sup>

<sup>a</sup> Geological Survey of Spain (IGME), Tres Cantos (Madrid, Spain)

<sup>b</sup> CSIRO Exploration and Mining, Kensington, Australia

<sup>c</sup> DLR\_ German Aerospace Research Establishment, Remote Sensing Data Centre, Oberpfaffenhofen, Deutschland  
a.riaza @igme.es

Commission VII, WG VII/1

**KEY WORDS:** hyperspectral sensors, geoindicators, climate change, mine waste, water quality.

## ABSTRACT:

Monitoring of mine waste on sulphide deposits through remote sensing hyperspectral data contributes to predict surface water quality estimating quantitatively acid drainage and metal contamination on a yearly basis. The mineralogy of the surface crusts loaded with highly soluble salts is a record of available humidity and temperature along the year. A temporal monitoring of salt efflorescence on mine wastes at a mine site in the Iberian Pyrite Belt (Spain) has been mapped in this work using hyperspectral airborne Hymap data. Climate change estimations are made based on oxidation stages derived from well-known sequences of minerals tracing sulphide oxidation intensity, using archive spectral libraries. Therefore, mine waste weathering products of sulphide mapped from remote sensing airborne hyperspectral data can be used as a short-term record of climate change, providing a useful tool to assess environmental Geoindicators in semi-arid areas.

## 1. 1. INTRODUCTION

Rapid oxidation and evaporation of sulphides on mine waste produces iron-bearing sulphate and other metals as secondary minerals. Temperature and humidity control evaporation. On regions with a semi-arid climate where the water table is low and there is a yearly rainy and dry season, sulphate salts growth reaches a maximum at the end of the dry season. Then, the mineralogy of the precipitated salts is a record of available humidity and temperature along the year.

Climate is the controlling factor on the growth and solution of salts from pyrite and other metallic sulphide on mine waste. Most of the previous work mine waste mapping with hyperspectral data is addressed to produce environmental evidence predicting metal contamination concentration and acid drainage both on surface water and groundwater. With this study, we are using the same method and principles to estimate changes on environmental moisture availability and evaporation rate.

Geoindicators are high-resolution measures of short-term changes in the geological environment, which are significant for environmental monitoring and assessment (Berger and Iams, 1996). Most use of remote sensing as an environmental monitoring method emphasizes on broad scale imagery (Laval, 1986). The work that is described below summarizes on a single tracing technique, the surface processes typical of semi-arid environment on mine waste witnessing climate, assessing both surface water and groundwater quality in an annual time frame. It also provides traceable records of climate change using small scale targets and high spatial and spectral resolution imagery, able to provide records of climate effects.

### 1.1 Hyperspectral studies on Mine Waste

High spectral resolution on airborne and satellite spectrophotometers has enlarged the mapping capabilities of

remote sensing data, developing widely with the use of AVIRIS data operating since 1988. Advances on data calibration and the development of algorithms able to extract information from a large number of spatial spectral data based on field spectra, encouraged applications on environmental issues. Early focus on mine wastes through the study of secondary minerals began concentrating initially on iron-bearing oxides and hydroxides (Farrand and Harsanyi, 1995). It expanded soon to secondary minerals related to mine waste weathering (Clark et al, 1998; Swayze et al, 1996; Levesque, 1997). Minerals generating acid environments attracted the attention of the geological scientific community since they are highly mobile on the environment through solution on drainage water. The spectral behaviour of pyrite and sulphate derived by oxidation, and their solution properties was explored, and patterns of precipitation established and traced using remote sensing hyperspectral data (Swayze et al, 1998; 2000). The development of spectral libraries from field sites has favoured the nearly automatic mapping of ephemeral mineral features related to acid mine drainage (Ong et al, 2002; Montero et al, 2002; Ong et al, 2003; Mars and Crowley, 2003; Sares et al, 2003).

### 1.2 Regional Geology and Climate

Pyrite mining on the Iberian Pyrite Belt (Southwest Spain and Portugal) extends through history along 5000 years at least (Leblanc et al, 2000). Massive sulphide deposits hosted on a Volcano-sedimentary Complex, a thick stratigraphical series of volcanic detrital origin, are widespread throughout the region (Almodovar, 1998). This geological frame provides high geoavailability for pyrite oxidation. The water quality on the rivers flowing through the area is subject to seasonal variations related to rainfall rate (Olias, 2004).

The mine site of study is located on the inner mountain chain with low altitude near the Atlantic coast (fig. 1). The regional climate follows a Mediterranean climate trend smoothed by the

influence of the atlantic ocean (Font Tullot, 1983). The Mediterranean climate is characterized by a wet season from October through May, and a dry season from late May through the summer. The insulation rate is extremely high throughout the year. Low precipitation rate defines a semi-arid climate with permanently low water table. Industrial operation on most metallic mine sites in the Iberian Pyrite Belt is stopped today. Most mine facilities are abandoned and under environmental control of the authorities. They are numerous and the wide regional exposure of abandoned mine waste makes the Iberian Pyrite Belt a training field to test environmental monitoring methods.

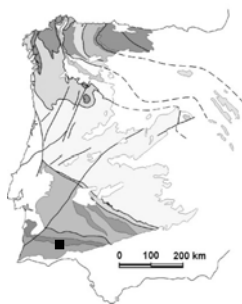


Figure 1. Location of the area of study in the Iberian Massif (Spain and Portugal).

### 1.3 Pyrite Mine Waste Weathering

Mine sites of metallic sulphide ore deposits are nowadays in many countries undisturbed by industrial activity, exposed to the atmospheric agents. Pyrite, the iron disulphide mineral, is then prone to oxidation under rates only controlled by atmospheric conditions. Pyrite oxidation is a complex process that proceeds rapidly when this mineral and other sulphides are exposed to air, releasing sulphate into water and lowering water Ph values (Nordstrom and Alpers, 1999).

Soluble secondary salts are formed from the evaporation of acid-drainage waters. Efflorescent crusts are common on the surfaces and on the edges of natural and mine-drainage streams and ponds. The mineralogy of the product salt can change with progressive evaporation of acid water (Nordstrom and Alpers, 1999). The greatest salt growth occurs when the growing crusts are replenished by acid water, such as a flowing drainage stream or waters wicked to the surface of mine waste dumps by capillary action (Plumlee, 1999). The soluble secondary salts can also form as weathering products of sulphide that are in contact with atmospheric moisture.

Due to their high solubilities, secondary salts form where sulphides have been exposed to weathering by oxygenated waters. Mine waste piles, mine workings and mill tailings are hosts for these minerals.

Particles in finely milled ore and tailings have very high surface areas and abundant broken crystal edges. This enhances mineral reactivity relative to those of mined rock and waste rock (Plumlee, 1999). Oxidation rates on sulphide mine-waste dumps are six orders of magnitude high than granite piles. The reaction of pyrite oxidation is highly exothermic, increasing the environmental temperature around mine waste significantly.

Climate plays an important role in the development of salt crusts on mine waste dumps of abandoned ore bodies to oxidation (Seals and Hammarstrom, 2003). Temperature and humidity are the prime variables that control evaporation. Arid environments are prone to concentrate metals and acidity potential because of the concentrating effects of the evaporation

of mine effluent and the resulting storage in highly soluble metal-sulphate salt minerals. Low water tables in semi-arid climate increase the exposure of waste to air, favouring deep weathering and sulphide oxidation profiles (Plumlee, 1999).

At the end of the rainy season, mine dumps and mud tailings are relatively saturated with water and afterwards begin to dry progressively. As they dry up and ventilate, sulphide oxides to sulphate, the pH falls and the pollutants solubilize. The concentration of water-soluble sulphate and heavy metals increases with declining moisture. These solubilized elements, with evaporation, rise by capillary action to the surface, forming a white salty crust composed of  $\text{Fe}^{2+}$  and other metals hydrated sulphates.

A sequence of salts from early to later formed is established from a solution of pyrite (Buurman, 1975; Alpers et al, 2003). Ferrous sulphate salts are found close to pyrite sources (melanterite  $\text{Fe}^{2+}(\text{SO}_4) \cdot 7(\text{H}_2\text{O})$ , rozenite  $\text{Fe}^{2+}(\text{SO}_4) \cdot 4(\text{H}_2\text{O})$ , szomolnokite  $\text{Fe}(\text{SO}_4) \cdot \text{H}_2\text{O}$ ), whereas Ferric-bearing minerals (rhomboclase  $\text{HFe}^{3+}(\text{SO}_4) \cdot 2 \cdot 4(\text{H}_2\text{O})$ , voltaite, halotrichite  $\text{Fe}^{2+}\text{Al}_2(\text{SO}_4)_4 \cdot 22(\text{H}_2\text{O})$ ) can be considered hydrologic dead-ends, where most of the  $\text{Fe}^{2+}$  has had time to oxidize to  $\text{Fe}^{3+}$ .

Further oxidation leads to the formation of schwertmannite ( $\text{Fe}_3 + 16\text{O} + 16(\text{OH}) + 12(\text{SO}_4) + 2$ ) and the group of jarosite-alunite ( $(\text{SO}_4)_2\text{KFe}_3(\text{OH})_6$ ,  $\text{KAl}_3(\text{SO}_4)_2(\text{OH})_6$ ). The mineralogy of oxidized zones on gossans is dominated by hematite ( $\text{Fe}_2\text{O}_3$ ), goethite ( $\text{FeO}(\text{OH})$ ) and jarosite ( $(\text{SO}_4)_2\text{KFe}_3(\text{OH})_6$ ).

Preliminary work mapping the Sotiel mine site in the Iberian Pyrite Belt using Hymap data orientated to contamination estimations precedes this work (Zabcic et al, 2005).

## 2. METHOD

### 2.1 Dataset

Hymap airborne hyperspectral data were collected on 6<sup>th</sup> May 1999, and 19<sup>th</sup> May 2004, and on 14<sup>th</sup> August 2004, and 17<sup>th</sup> June 2005 over the Sotiel minesite in the Iberian Pyrite Belt (Spain). The spatial resolution fluctuates from 5 m in 1999 to 4 m in 2004 and 2005. Pre-processing was performed with routines developed by Hyvista (Cocks et al, 1998) and the German Space Establishment DLR (Richter and Schlöpfer, 2002; Schlöpfer and Richter, 2002).

Five years lapse from the first flight (May 1999) to the second flight (May 2004). Both flights record the state of pyrite weathering at the end of the wet season, before the intense evaporation process starts, which should progress during the dry season. The three flights from May 2004 to June 2005 cover one year. The first flight took place at the end of the humid season (May 2004). The state of oxidation at the peak of the dry season the same year is traced by the August 2004 flight. The last flight takes place one year later in the middle of an extremely dry and warm summer (June 2005).

Rainfall and temperature records from the weather station of Ronda (Instituto Meteorológico Nacional, Huelva), are considered from 1998 to 2005 (fig.2). The hydrological year begins typically with an intense rain event in October, and minor rainfall along autumn and spring. The very dry and warm season starts in May and reaches minimum rainfall in August. The temperature estimations respond to a complex evaluation of weather and climate parameters (Instituto Meteorológico Nacional, [www.inm.es](http://www.inm.es)).

The autumn 1998 was normal temperature and very dry, followed by a normal temperature and very dry winter 1999. The spring 1999 was dry and warm. Water availability was scarce in May 1999, and relatively mild temperatures would

indicate low evaporation and possible preservation of soluble salts from the previous year.

Autumn, winter and spring before May 2004 were very humid and warm. The following summer was extremely warm and dry, suggesting high evaporation rates. Intense pyrite oxidation products would grow, which should be present in August 2004. The following year was very dry and warm. Water availability was scarce, and further evaporation would strengthen oxidation. The June 2005 flight should summarize the results through mine waste weathering products.

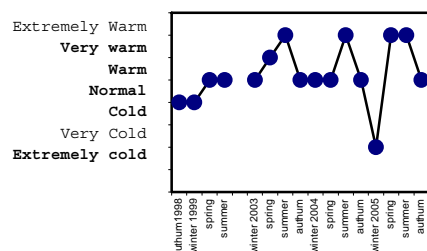


Figure 2. Temperature records during the time span previous to the analysed imagery (Ronda station, Instituto Meteorológico Nacional, Spain, [www.inm.es](http://www.inm.es)).

Fieldwork was conducted in summer 2005 and 2006. Samples were collected over the mine waste dumps and the Odiel river flow path and sides. Field spectra were collected using an ASD Fieldspec-pro Spectrophotometer both for calibration and interpretation purposes. Laboratory spectral measurements on those samples were taken with a Perkin Elmer Lambda 9 Spectrophotometer provided with an integrating sphere, in the visible and near infrared wavelength range (0.4  $\mu\text{m}$ -2.4  $\mu\text{m}$ ) with a spectral resolution of 0.001  $\mu\text{m}$ . Samples both from loose material and crusts formed over the ground on mine dumps and river sediments, were measured to ascertain spectral differences related to dehydration, oxidation and subsequent compaction from solutions after rainy events. Selected samples of crusts and loose material from the mine dump were analysed by X-ray diffraction.

## 2.2 Image processing

Hyperspectral imagery provides wide possibilities to map complex features of the surface of the earth, offering a high dimensionality of data, if careful signal to noise ratio and good spatial resolution are ensured. The procedure for feature extraction for thematic purposes used on this work is an interpreter oriented sequential spectral unmixing using standard algorithms, leading to a spatial pattern and spectral identification on the scene (Hubbard and Crowley, 2005) summarized on a map. The dimension of the data is reduced along various image processing steps tailored to the scene, ending on a map of pyrite oxidation products on the abandoned mine site.

The first step uses a false colour composite with Hymap channels 10, 39 and 125 to build a spectral library with basic land use end-members on the scene. Spectral Angle Mapper produces a first estimation of the spectral diversity of open land, which is digitally used as a mask on subsequent image processing steps. Areas mainly covered by vegetation, clear water and urban areas are excluded for analysis from this step on.

The areas mapped as open land on the first step are explored by Minimum Noise Fraction transforms, subsequent Pixel Purity

Index (Boardman, 1993) and n-dimensional analysis. Mine sites and the main areas covered by sulphate salts are commonly identified from bare open and cultivated land at this stage. The data dimensions are reduced further, repeating the procedure to qualify areas within early-formed salts and among the more oxidized zones, which are isolated on corresponding masks. A final map is compiled gathering all endmembers corresponding to pyrite oxidation products on the scene. A spectral library is finally built with such endmembers, which are then mineralogically identified using a selection from archive spectral libraries.

Spectral Angle Mapper (Kruse, 1993) is used to test scene similarity from the second step, helping to identify endmembers more representative of sulphate salt coverage according to field experience and comparison with the shape of the corresponding spectra with archive spectral libraries. Spectral shape information is so derived from Hymap data.

A number of individual mineral substances precipitated from pyrite acid water were identified on public domain spectral libraries, ranging from melanterite, the first-formed sulphate, to hematite when dehydration and oxidation is completed (fig.3). Eighteen existing spectra from sulphide oxidation products in public domain spectral libraries (Clark et al, 1993; Crowley et al, 2003) were used as references with the Spectral Analyst (RSI, 2000) to get a comparative score of similarity for spectra from every map unit. Spectral Angle Mapper, Spectral Feature Fitting and Binary Encoding were taken into account on equal weights on the final similarity score. The dominant mineral was assigned to the map units (fig.3).

Comparison with the selected sulphate and iron oxides and hydroxides spectral library through the Spectral Analyst (RSI, 2000) confirms field expectations and prior mineralogical studies. Spectra with dominant hematite, jarosite or alunite can be identified on well-developed areas.

## 3. SPATIAL PATTERN ON PYRITE OXIDATION PRODUCTS: A CLIMATE CHANGE RECORD

The mine works in Sotiel spread along the river Odiel. The mines on the Iberian Pyrite Belt were already operated by Tartesians and Phoenicians before Roman times. Mining was continuous along the Middle Ages using handcraft methods, up to the intensive operation during the Industrial Revolution in the 19<sup>th</sup> Century. Today, massive sulphide deposits hosted on basalts were mined until the eighties, when mining stopped. From 1991 to 2001, the ore processing plant of the Sotiel minesite toasted industrial sulphide waste to produce sulphuric acid delivered to the nearby coastal industrial facilities.

The operating underground mine works are displayed along the river Odiel (fig.3). A tape transported the ore from the mine uphill to the ore processing plant. Mill tailings from the ore processing plant are stored on an adjacent dam, which drains to a southerner dam flowing to the river Odiel, upstream from the mine works. The sides of the river show products from precipitations from acid water along the whole length of the flow path.

The observed oxidation patterns shown by hyperspectral image processing on the four Hymap flights are diverse within the mine site. They would be described separately for different domains: the area around the ore processing plant including the two mill tailings dams, the mine works by the river, and the flow path of the river.



3.1 The mine dumps by the river

The mine waste piles at the mine operating works by the river and the riversides are more reliably translating climate effects. In May 1999, copiapite, halotrichite, and partly rozenite are restricted to pools of standing water left by poor water flow (fig. 3). Alunite and jarosite cover the slopes of waste piles, whereas schwertmannite and minor hematite patches occur on the flat top of piles.

The mine waste piles and works by the river, show in May 2004 the schwertmannite flat tops of piles in 1999 oxidized partially to hematite or jarosite; copiapite and halotrichite from ponds oxidize to alunite and jarosite; jarosite slopes oxidize to goethite. The general trend from May 1999 to May 2004 is clearly increasing oxidation.

The dry period from May to August 2004 increases dehydration and oxidation. The waste flat tops are homogeneously covered by hematite; goethite is generalized on slopes, and the extent of schwertmannite is reduced.

The same emphasized oxidation trend is displayed in June 2005 on the waste at the riverside mine works in comparison with August 2004, after an extremely dry and warm year. Hematite is homogeneously consistent on flat tops of piles, goethite, jarosite and alunite grow on the slopes, and halotrichite spreads on shallow ponds among the waste piles.

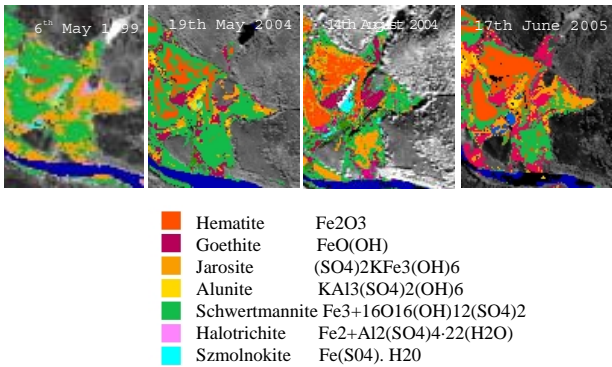


Figure 3. Maps compiled from Hymap data on the minerals product of oxidation and dehydration of sulphide waste, arranged on a precipitation and oxidation sequence. Detail of the mine dump by the river.

3.2 The river flow path

Sulphate salts and pyrite oxidation products border the bottom, banks and sides of the river Odiel, of varying mineralogy and height depending on flow rate and climate. The oxidation products grow over river sediments or underlying rock, and their occurrence is independent from industrial operation or mine works. Jarosite and schwertmannite are the most frequent salts. Jarosite tends to develop over the boulders and sands of the riverbanks (fig. 4). Schwertmannite grows on a ribbon along the steeper sides of the flow path. Melanterite may appear on isolated pools, preferably on severe drought times, when flow rate lessens.

The extent of jarosite shrinks from May 1999 to May 2004. The very humid time up to the spring 2004 is responsible for the reduction on oxidation products. The surface covered by jarosite expands during the summer, and spots of goethite point up on steeper sides in August 2004.

The picture of the river in June 2005, after a whole year of drought and warm temperature, is dramatically oxidized. Most schwertmannite has oxidized to goethite and alunite. Melanterite and rozenite are occasionally present on small pools of standing water on the bottom of the river. Jarosite remains only on the upper sandbanks. Schwertmannite shows a preference for gentle slopes, whereas goethite occurs on steep surfaces which are quickly abandoned by water for the season. Complete absence of flooding water on the flow path permits a deeper oxidation within the period of drought.

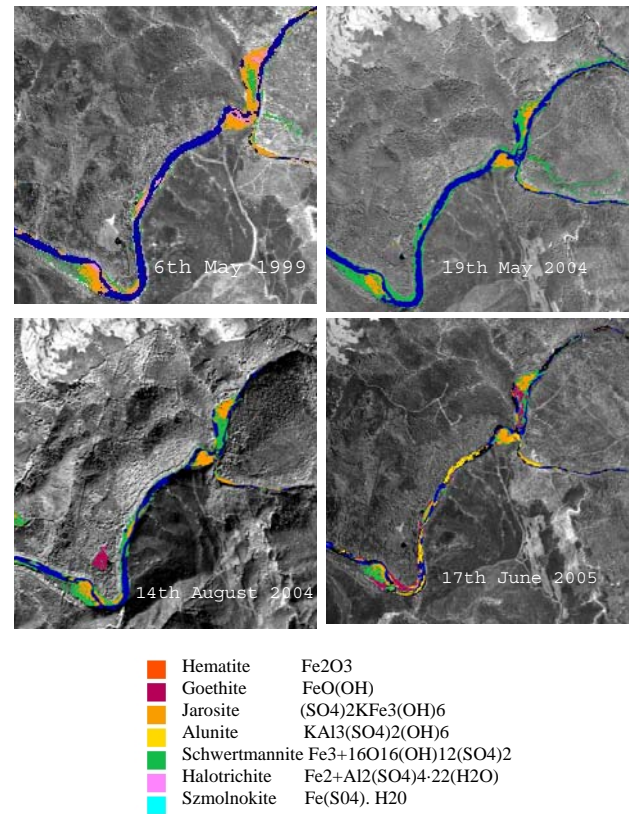


Figure 4. Maps compiled from Hymap data on the minerals product of oxidation and dehydration of sulphide waste, arranged on a precipitation and oxidation sequence. Detail of the river flow path.

3.3 Field and laboratory spectra

Spectral measurements were made in the field with an ASD Spectrometer. Also, samples were collected in the field from representative geological targets and measurements were made in the laboratory with a Perkin Elmer Lambda Spectrometer (fig.5). Mineral growth during pyrite oxidation results on a heterogeneous spatial pattern. However, mineralogically homogeneous areas can be recognized on the imagery with a strong geomorphological control. Flat areas, and slopes, host the areas where the mineralogical evolution can be traced. Hymap spectral responses from the mapped regions of interest are particularly reliable on both oxidation or hydrated ends on the mineral sequence (hematite and halotrichite or szmolnokite on our test site). Both mine dumps and river sediments or flow path display less mineralogical variability than pyrite mud.

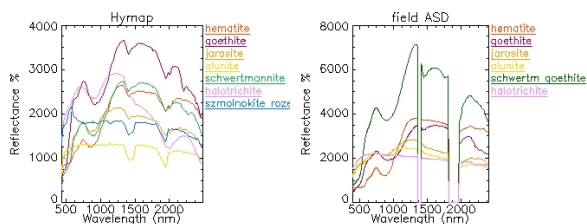


Figure 5. Spectra from Hymap mapped areas and field taken with an ASD spectrometer

#### 4. DISCUSSION

Iron sulphide weathers rapidly producing a sequence of sulphate salts, which are also highly soluble. The ore processing plant of the mine facility was still operating at the beginning of the study. Tailings would be released to the dams, changing the composition and evolution of both the surrounding areas and the previously stored mud tailings. Even after the ore processing plant stopped its activity, the site was environmentally controlled, and a water cleaning plant at the foot of the southern tailings dam was active. The interpretation of the mineral composition of crusts growing in the area in terms of climate change has to take into account the active industrial influence.

The oxidation pattern on the mine site is clearly established using archive spectral library references to map airborne hyperspectral Hymap data. A progressive oxidation is observed with increasing temperatures from spring 2004 to summer 2005. The path of growth of individual minerals on a certain surface can be followed confirming or discrediting the general trend. This is also true for weathering products growing on riversides along river courses with acid drainage water.

The oxidation patterns follow different trends on mud tailings than on waste piles. Fine particles in mud tailings favour mineral reactivity (Plumlee, 1999). In addition, mud tailings is a homogeneous viscous mass with a smooth outer surface sheltering rainwater, which dissolves the upper weathering products rapidly. Mud tailings are witnesses of short weather events. Mine waste piles are more resistant to weathering because of their coarse particles. They respond to weather events slower than mud tailings, acting as more reliable traces of seasonal or longer periods of climate change.

The maps compiled using hyperspectral analysis of Hymap data describe faithfully the diverse weathering trend of mud tailings and mine waste piles. Mine waste piles on completely abandoned mine sites and riversides of acid mine drainage flowing water are preferred to record effects of climate change on a long term basis. For that purpose, hyperspectral remote sensing data must be taken at chosen dates related to the weathering seasonal evolution dependent on humidity and temperature.

To produce maps that can describe this very detailed evolution, hyperspectral image processing has to be applied sequentially identifying the areas critical on the mine site, and related to mine site weathering products, such as riversides. The image processing procedure must be applied to subscenes isolating the target areas. Different image processing procedures can be necessary per subscene to reach a map responding to the maximum spectral complexity of the target, in terms of weathering products.

#### 5. CONCLUSIONS

Sulphide mine waste in semi-arid environment can be used as a small scale target to provide information of short-term climate changes. Therefore, it may be included among Geoindicators, when hyperspectral remote sensing is used as a monitoring tool. Hyperspectral data have been able to distinguish different degrees of oxidation and dehydration on pyrite mud tailings and waste piles on an abandoned mine facility. Mineral indicators of such stages are suggested using the spectral analysis techniques comparing with spectral libraries collected from foreign samples to the study site.

The salt sequence on the oxidation process is confirmed on the most stable areas on the mine facility. The annual monitoring of weathering products at the end of the wet season and the climax of the dry season, can be used as a climate record. Changes on evaporation, humidity and temperature can be inferred from the mine waste weathering product maps.

Effect of particle size on the evaporation mineralogical pattern is critical on mineral reactivity. Mill tailings both around the ore processing plant and both dams display fresh weathered products of pyrite more easily. Mine waste dump piles and salts precipitated along the flow path of flowing acid water are more reliable to display seasonal climate effects, independent of sparse rain events or water transfer during mine waste operation actions.

Image processing must be tailored per scene and per domain within the mine site. Otherwise, the spatial mineralogical pattern is lost, as well as the interpretation ability in terms of climate change, and metal contamination estimations or acid drainage prediction. The resulting maps agree on their conclusions when applying separately image processing to subscenes, but they would never be shown through a unique image processing sequence applied to the whole scene.

#### 6. REFERENCES

- Almodovar, R., Saez, R., Pons, J.M. and Maestre, A., 1998. Geology and genesis of the Aznalcollar massive sulphide deposits, Iberian Pyrite Belt, Spain. *Mineralium Deposita* ,33, pp.111–136.
- Alpers, C.N., Nordstrom, D.K., and Spitzley, J., 2003, Extreme acid mine drainage from a pyritic massive sulfide deposit: the Iron Mountain endmember. In Jambor J.L. and Blowes D.W. and Ritchie, A.I.M. (Eds.), *Environmental Aspects of Mine-Wastes*, pp. 407-430. Ottawa: Mineralogical Association of Canada.
- Berger, A.R. and Iams W.J., 1996. *Geoindicators: Assessing rapid environmental changes in earth systems*. Rotterdam: A.A. Balkema.
- Boardman, J. W., 1993. Automated spectral unmixing of AVIRIS data using convex geometry concepts. In *Summaries Fourth JPL Airborne Geoscience Workshop*, (Washington, D.C.), JPL Publication pp. 93-26, 1, 11 - 14.
- Buurman, P., 1975. In vitro weathering products of pyrite. *Geologie Mijnbouw*, 54, pp. 101-105.
- Clark, R.N., Swayze, G.A., Gallagher, A., King, T.V.V. and Calvin, W.M., 1993), The U.S. Geological Survey Digital Spectral Library: Version 1: 0.2 to 3.0  $\mu$ m. *U.S. Geological Survey, Open File Report* pp. 93-5 92.
- Clark, R.N., Vance, J.S. and Livo, K.E., 1998. Mineral Mapping With Imaging Spectroscopy: The Ray Mine, Az. From: Mineral Mapping with Imaging Spectroscopy: the Ray Mine, AZ. Roger N. Clark, Sam Vance, Rob Green, *Summaries of the 7th Annual JPL Airborne Earth Science Workshop*, R.O. Green, Ed., JPL Publication 97-21. Jan 12-14, pp. 67-75.

- Cocks, T., Janssen, R., Stewart, A., Wilson, I. and Shields, T., 1998. The Hymap<sup>TM</sup> Airborne Hyperspectral Sensor: The system, calibration and performance. *Proceedings 1st EARSEL Workshop on Imaging Spectroscopy*, Zurich, October 1998, pp. 37-42.
- Crowley, J.K., Williams, D.E., Hammarstrom, J.M., Piatak, N., Chou, I-M. and Mars, J.C., 2003. Spectral reflectance properties (0.4–2.5  $\mu\text{m}$ ) of secondary Fe-oxide, Fe-hydroxide, and Fe-sulphate-hydrate minerals associated with sulphide-bearing mine wastes. *Geochemistry: Exploration, Environment, Analysis*, 3- 3, pp. 219-228(10).
- Farrand, W.H. and Harsanyi, J.C. 1995. Mineralogic Variations in Fluvial Sediments Contaminated by Mine Tailings as Determined From AVIRIS Data, Coeur d'Aldene River, Idaho. *AVIRIS Workshop*, pp. 47-50, JPL Publication.
- Font Tullot, I., 1983): *Climatología de España y Portugal*. Madrid, 296 p. Madrid: Instituto Nacional de Meteorología Publications.
- Hubbard, B.E. and Crowley, J.K., 2005. Mineral mapping on the Chilean-Bolivian Altiplano using co-orbital ALI, ASTER and Hyperion imagery, Data dimensionality issues and solutions. *Remote Sensing of Environment*, 99, pp. 173-186.
- Instituto Nacional de Meteorología, Spain, *Resumen Anual Climatológico de los años 2003, 2004 y 2005*. www.inm.es
- Kruse, F.A., Lefkoff, A.B., Boardman, J.B., Heidebrecht, K.B., Shapiro, A.T., Barloon, P.J., and Goetz, A.F.H., 1993). The Spectral Imaging Processing System (SIPS) – Interactive Visualization and Analysis of Imaging Spectrometer Data. *Remote Sensing of Environment*, 44, pp. 145-163.
- Laval, K. 1986. General circulation model experiments with surface albedo changes. *Climatic Change*, 9, 1-2, pp. 91-102.
- Leblanc, M., Morales, J.A., Borrego, J. and Elbaz-Poulichet, 2000. A 4500 years old mining pollution in Southwestern Spain: Long-Term concerns for modern mining. *Economic Geology*, 95, pp. 655-672.
- Lévesque, J., Szeredi, T., Staenz, K., Singhroy, V. and Bolton, D., 1997. Spectral Unmixing for Monitoring Mine Tailings Site Rehabilitation, Copper Cliff Mine, Sudbury, Ontario. *Twelfth International Conference and Workshops on Applied Geologic Remote Sensing*, Denver, Colorado, 17-19 November 1997, pp. 340-347.
- Mars, J.C. and Crowley, J.K., 2003. Mapping mine wastes and analyzing areas affected by selenium-rich water runoff in southeast Idaho using AVIRIS imagery and digital elevation data. *Remote Sensing of Environment*, 84, 3, pp. 422-436.
- Montero, I. and Brimhall, G., 2002. Multiplatform VIS/SWIR Hyperspectral Approach to the Study of Acid Mine Drainage from Abandoned Mines. *Denver Annual Meeting Geological Society of America* 2002, 43507.
- Nordstrom, D.K. and Alpers, C.N., 1999. Geochemistry of acid mine waters. In Plumlee G.S. and Logsdon M.J.: The Environmental Geochemistry of Mineral Deposits. Part A: Processes, Techniques, and Health Issues. *Reviews in Economic Geology*, 6A, pp. 133-160.
- Ong, C. and Cudahy, T., 2002. Deriving Quantitative Monitoring Data Related to Acid Drainage Using Multi-temporal Hyperspectral Data. *AVIRIS Workshop*, 5pp.
- Ong, C., Cudahy, T.J. and Swayze, G., 2003. Predicting Acid Drainage Related Physicochemical Measurements Using Hyperspectral Data. *Proc. 3<sup>rd</sup> EARSEL Workshop on Imaging Spectroscopy*, Herrsching, 13<sup>th</sup>-16<sup>th</sup> May 2003, pp. 363-369.
- Olias, M., Nieto, J.M., Sarmiento, A.M., Cerón, J.C. and Canovas, C.R., 2004. Seasonal water quality variations in a river affected by acid mine drainage: the Odiel River (South West Spain). *Science of The Total Environment*, 333, 1-3, pp. 267-281.
- Plumlee, G.S., 1999. The environmental geology of mineral deposits. Part A: Processes, Techniques, and Health Issues. *Reviews in Economic Geology*, 6A, pp. 71-116.
- Richter, R. and Schlöpfer, D., 2002. Geo-atmospheric processing of airborne imaging spectrometry data. Part 2: atmospheric/topographic correction, *International Journal of Remote Sensing*, 23, pp. 2631-2649.
- RSI, 2000. ENVI User's Guide, Research Systems Inc. Publications.
- Sares, A., Hauff, Ph.L., Peters, D.C., Coulter, D.W., Bird, D.A., Henderson III, F.B. and Prosh, E.C., 2003. Characterizing Sources of Acid Rock Drainage and Resulting Water Quality Impacts Using Hyperspectral Remote Sensing – Examples from the Upper Arkansas River Basin, Colorado. *Proceedings Geospatial Conference*, December 7<sup>th</sup>-9<sup>th</sup> 2004, Atlanta (GA, USA), pp 20.
- Schlöpfer, D. and Richter, R., 2002. Geo-atmospheric processing of airborne imaging spectrometry data. Part 1: parametric orthorectification. *International Journal of Remote Sensing* 23, pp. 2609-2630.
- Seals II, R.R. and Hammarstrom, J.M., 2003. Geoenvironmental models of mineral deposits: examples from massive sulfide and gold deposits. In Jambor, J.L. Blowes, D.W. and Ritchie, A.I.M. (2003), *Environmental Aspects of Mine-Wastes*, pp. 11-51. Ottawa: Mineralogical Association of Canada.
- Swayze, G.A., Smith, K.S., Clark, R.N., Sutley, S.J., Pearson, R.M., Vance, J.S., Hageman, Ph.L., Briggs, P.H., Meier, A.L., Singleton, M.J., and Roth, S., 2000,. Using imaging spectroscopy to map acidic mine waste. *Environmental Science and Technology*, 34, pp. 47-54.
- Swayze, G.A., Clark, R.N., Smith, K.S., Hageman, P.L., Sutley, S.J., Pearson, R.M., Rust, G.S., Briggs, P.H., Meier, A.L., Singleton, M.J. and Roth, S., 1998. Using Imaging Spectroscopy To Cost-Effectively Locate Acid-Generating Minerals At Mine Sites: An Example From The California Gulch Superfund Site Airborne Visible/Infrared Imaging Spectrometer (AVIRIS): 1998 *JPL Airborne Geoscience Workshop Proceedings*, Leadville, Colorado, 1998, pp. 49-53.
- Swayze, G.A., Clark, R.N., Pearson, R.M. and Livo, K.E., 1996. Mapping Acid-Generating Minerals at the California Gulch Superfund Site in Leadville, Colorado using Imaging Spectroscopy. *Summaries of the Sixth annual JPL Airborne Earth Sciences Workshop*, R.O: Green (ed.), JPL Publication 96-4, March pp. 4-8.
- Zabcic, N., Ong, C., Müller, A., Rivard, B., 2005. Mapping pH from airborne hyperspectral data at the Sotiel-Migollas mine; Calanas, Spain. *Proceedings 4th EARSEL Workshop on Imaging Spectroscopy*, 27th-29th April 2005, Warsaw (Poland), pp. 467-472.

## 7. ACKNOWLEDGEMENT

Thanks are due to J.M. Moreira and A.Gil for information on mine site inventories belonging to the Servicio de Información y Evaluación Ambiental de Andalucía (Spain). The Instituto Meteorológico Nacional provided historic climate data on the area. The Junta de Andalucía granted entrance to restricted areas of the Sotiel mine site. J.M. Nieto and R. Sáez pointed to critical knowledge on the evolution of weathering minerals of local mine sites. The Science Council of Spain funded part of this work (CGL2005-02462/BTE; CGL2006-01544/CLI).



# REFLECTANCE SPECTROSCOPY IN THE 400-2400 nm TO ASSESS SETTLED DUST IN DIFFERENT URBAN ENVIRONMENTS

E. Ben-Dor and A. Chudnovsky

Department of Geography and Human Environment, Tel-Aviv University,  
Ramat Aviv, P.O.B. 39040, 69978, Israel  
e-mail: [chudnovs@post.tau.ac.il](mailto:chudnovs@post.tau.ac.il)

Commission VI, WG VI/4

**KEY WORDS:** Indoor dust loadings, Reflectance Spectroscopy, Geographical Information System, Indoor Dust Mapping

## ABSTRACT:

The aim of this study was to apply a spectral reflectance approach to account for small amounts of sediment dust in occupied homes. We examined the method's ability to predict the gravimetric weight of sediment dust particles solely from the reflectance data (400-2400 nm). Multivariate data analysis based on Partial Least Squares (PLS) regression was run to predict the dust loads solely from reflectance data. For both experiments use of difference index (when the dust trap background spectra was subtracted from the total measured reflectance) in the PLS analyses was found to demonstrate the best pre-treatment in PLS modeling. Maps of dust distribution, based both, on the reference gravimetric and spectrally predicted weight values was generated. Reasonable explanation was provided to the calculated distribution that can be further used by decision makers to improve the indoor life quality. We conclude that this methodology (simple and rapid in-situ spectral measurements with appropriate analyses), can be employed to assess dust in both indoor and outdoor environments (in small and high dust content). This information can be used for initial decision making, improving indoor conditions, and tracking dust contamination following environmental change.

## 1 Introduction

Today, the basic academic training related to indoor and outdoor air quality is within a single discipline and a new multidisciplinary paradigm is needed [1]. The synergy of reflectance spectroscopy and multivariate statistical methods to quantitatively measure dust loadings could eventually become the preferred method for accurate, comprehensive, and almost real-time assessment of indoor-environment dust information.

Reflectance spectroscopy of solid particles in the Visible-, Near Infrared-, and Short Wave Infrared (VIS-NIR-SWIR) region is a well-known technique by which the chemical composition of many materials can be rapidly and quantitatively assessed [2, 3]. This method is known for its simplicity, accuracy, and ability to analyze many constituent components simultaneously. The constraints inhibiting the adoption of this method are 1) the relatively low sediment dust load that mask out the dust signals; and 2) the strong spectral responses of the target's background, that may be beyond the detection limit.

The total mass of dust particles settling in an indoor environment is an important parameter for estimating people's exposure to dust in both their residences and workplaces. Previously, we have developed a new and sensitive method aimed to assess the small amounts of artificial dust under laboratory conditions, using reflectance spectroscopy [4,5]. In this study we wish to (1) examine the potential of our method over an actual indoor dwelling environment; and (2) map the results of the gravimetrically measured and spectrally predicted samples in order to generate a pattern of settled dust distribution encompassing the study area.

## 2 Study Area

Two field experiments of one month length were conducted, one during the spring season (April 2005) and the second during the summer season (August 2005). Similar locations were used for the dust traps during the spring and the summer seasons, but, the summer experiment was expanded to a higher sample set. Forty-five dwellings from the northern and central parts of Tel Aviv city were sampled during April 2005, and one-hundred thirty five dwellings were sampled during August 2005. The traps (2-4 in each dwelling) were placed on flat surfaces (tables, shelves, and boxes) at a height of 1.3 m above the floor and positioned on surfaces where the column of air above the sampling surface was not obstructed, at least 0.5 m away from large electrical appliances (Edwards et al. 1998). Additionally, several traps were placed outdoors to identify the differences between the indoor and outdoor amounts of dust settled during both seasons.

## 3 Method

### 3.1 Dust Traps

We have found that the optimal configuration of a dust trap for spectral analysis is a glass disk (2 mm thick), with a black carbon background placed underneath. Measuring the reflectance of the dusty glass trap maximizes any meaningful spectral response of the dust mixture. Each glass trap was measured spectrally before and after exposing it to the dust in the indoor environment to enable precise identification of the spectral changes.

### 3.1 Gravimetric Weight Measurements

The traps were cleaned, numbered, and gravimetrically measured before and after they were exposed to the dust during the field study experiment, using a sensitive gravimetric weight with a precision of  $\pm 0.01$  mg, and a maximal weighing capability of 60 g. The difference between the dusted and cleaned glass traps was calculated and used as reference values for the PLS modeling (Y-variable).

### 3.2 Spectral Measurements

Dust samples were scanned by the Analytical Spectral Devices FieldSpec Pro (ASD 2001) spectrometer with a total of 2100 spectral bands (350-2500 nm) by attaching the contact probe ('potato') device to the dust sample. The 'potato' was set on a stable tripod base and maintained in a constant position at a nadir-looking angle. BaSO<sub>4</sub> was used as a white reference to calibrate the measurement data to reflectance values at the same angle. Additionally, each dust trap was measured gravimetrically using a sensitive analytical scale model Mettler AE163, with a precision of 0.01 mg, to enable us to compare the total amounts of dust that settled during each season.

Similarly to the reference gravimetric measurements, each dust trap was spectrally measured before and after the exposure to the dust.

### 3.3 Multivariate Modeling

The multivariate calibration models were calculated by Partial Least Squares (PLS) regression, with total dust loadings and NIR-SWIR spectra correlated. All data management, calculations and PLS analyses were performed using the Unscrambler software, Version 9.1<sup>33</sup>.

The difference between the predicted and measured gravimetric weights was expressed as a root mean square error of prediction. Root Mean Square Error of Prediction (RMSEP), and Root Mean Square Error of Calibration (RMSEC) are direct estimates of the prediction and modeling errors, expressed in original units. RMSEP is defined as the square root of the average of the squared differences between predicted and measured values of the validation objects:

$$RMSEP = \left[ \frac{\sum (X_m - X_p)^2}{n_v} \right]^{1/2} \quad (1)$$

where  $X_m$  is the gravimetrically measured weight of a sample,  $X_p$  is the predicted value of the sample on the basis of spectral analysis, and  $n_v$  is the number of samples in the calibration stage [6].

The predictive capability of all models was compared in terms of the relative standard error for both calibration and validation sets (denoted as RMSEC (%) and RMSEP (%), respectively; see Table 3):

$$\% RMSE = \left[ \frac{\sum (X_m - X_p)^2}{\sum X_m^2} \right]^{1/2} \times 100 \quad (2)$$

The results of all spectral measurements were divided into three subsets: 1) A calibration set (training set) to establish the model; 2) a validation (test) set, to validate the model; and 3) the external test set (the second validation set), to examine the model's predictive ability. A calibration set contained of 55 and 85 samples during spring and summer experiments consequently, validation sets comprised of 18 and 25 samples, and finally test sets comprised of 17 and 25 samples. In this way we were able to assess the predictive

capability of the final model, and the ability of spectroscopy to quantify the small amounts of settled particulate matter.

In real world environments, reflectance spectra of dust particles may contain materials displaying various particle size distributions and mixtures of materials that may cause baseline shifts due to their reflectance properties. Different pretreatments are used to simplify the spectral signals in order to ensure stable calibration and improve the predictive ability of the final model. To eliminate undesirable variation in the spectral data, two types of pretreatments are commonly reported: differentiation and signal correction. Various orders of spectra derivatives are used to correct baseline variations. In the present case, first and second derivatives were used as pretreatments.

To minimize the effect of the glass background we calculated spectral ratio (RI) ( $B_{ratio(\lambda)}$ , Eq. 3) and spectral difference (DI) ( $B_{diff(\lambda)}$ , Eq. 4) indexes by calculating the apparent ratio or difference values for each waveband, taking the single-beam spectrum against that of the glass background, as follows:

$$RI = B_{ratio(\lambda)} = B_{rad(\lambda)} / B_{background(\lambda)} \quad (3)$$

$$DI = B_{diff(\lambda)} = B_{rad(\lambda)} - B_{background(\lambda)} \quad (4)$$

where:

$B_{rad(\lambda)}$  - reflectance of the mixture on the glass trap

$B_{background(\lambda)}$  - reflectance of the glass trap

The same pre-treatments that were applied on the raw spectra were tested also on the DI and RI indexes [6].

## 4 Results

During the spring, the gravimetric weight (90 samples) ranged from 0.01 to 3.5 mg, with an average of 1.7 mg. During the summer, the gravimetric weight (135 samples) was lower and ranged from 0.01 mg 2.5 mg, with an average of 1.1 mg. This difference may be explained by the large difference in the outdoor dust concentrations resulting from the spring dust storm events that are also partially expressed in the indoor environment. This suggests that outdoor dust has a significant effect on the indoor dust environment. An additional factor influencing the dust deposition loads is the influence of anthropogenic activity as well as the effect of crowding. Owing to the incomparable environmental conditions between the dwellings (open and closed windows, different indoor activities, etc.), it is impossible to make an unequivocal conclusion regarding the quantitative differences between settled dust among dwellings in similar locations.

### 4.1 Prediction of Gravimetric Weight for Field Survey

For both experiments the best-fit model for the calibration set is achieved when the difference manipulation is used. Applying this model to the external test set gave favorable predicted values, with a RMSEP of 7.2%, confirming the model's relatively good predictive ability (Table 1):



Model	Prediction on external test set	
Spring	RMSEP (%)	$r^2$
DI	7.2	0.93
(DI)'	10.3	0.90
DI on 50 wavelengths	10.8	0.90
Summer		
DI	7.5	0.94
(DI)'	8.3	0.93

Table 1: Best results obtained for external test set prediction statistics resulted from different PLS models

The high predictive ability of the external test set, at the validation test set level, enabled us to conclude that the constructed PLS models can be used to precisely predict the gravimetric weight of loaded dust. Generally, the best model was obtained when DI was calculated and PLS calibration models were run on the full spectral range. Applying this model to the external test set gave favorable prediction values, with a RMSEP of 7.2% for spring and 7.5% for summer, confirming the model’s confidence with only four PLS components (data not shown). The first four components in the PLS DI model explained 99% of the X variance (spectra), and 94% of the Y variance (weight). The score plot of the samples from the PLS modeling (figure not shown) was perfectly arranged along its axis according to their gravimetric weights, with a positive increasing. This indicates that most of the spectral variation is related to the settled dust that was modeled by PLS.

Figures 2-3 show the predicted versus the measured gravimetric values of the indoor dust for spring and summer consequently:

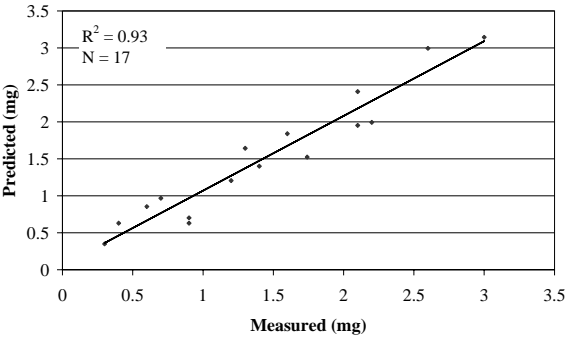


Fig. 2 Measured versus predicted gravimetric weights (run on the external 17 samples test set) accepted for spring.

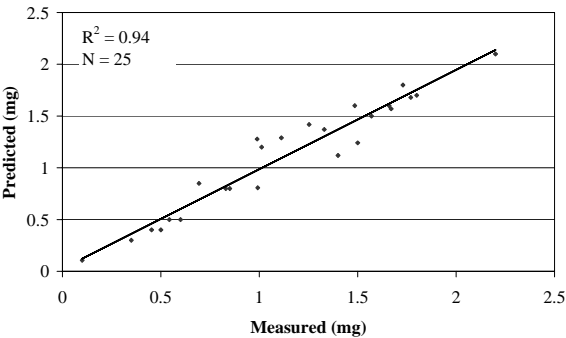


Fig. 3 Measured versus predicted gravimetric weights (run on the external 25 samples test set) accepted for summer.

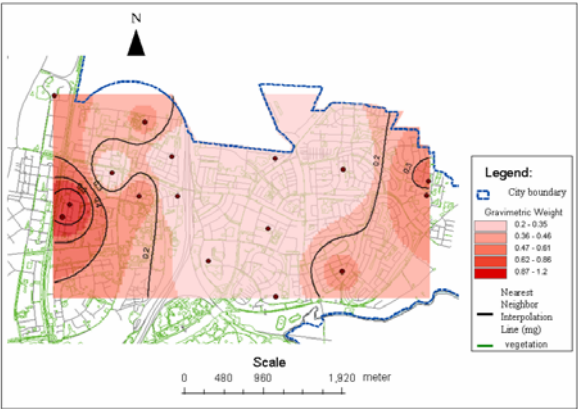
The results indicate that gravimetric weight can be predicted with a high confidence level solely on the basis of spectral measurements. Hence, many samples can be measured along large scale and in a very short time domain. RMSEP values for both experiments are quite impressive when taking into account the relatively small amount of settled dust with a narrow gravimetric weight of  $\pm 0.01$  mg (min and max values are 0.12-3.5 mg for spring and 0.11-2.5 mg for summer).

4.2 Spatial Mapping of the Indoor Settled Dust Distribution

The maps were generated in order to demonstrate the powerful application of the multivariate spectral data modeling, facilitating the interpretation of the spectral measurements results. We used the IDW (Inverse Distant Weighted) Interpolation method within the Geographic Information System (GIS) (ArcGIS Geostatistical Analyses), the technique that calculates a grid value with the nearest real value, then produces specific, stepped contours [7].

For both experiments, Iso-Dust maps demonstrated that physical and anthropogenic factors plays an important role in total amounts of settled dust. Physical factors are the outside climate conditions, micro topography, wind regime and the distance from the Mediterranean Sea. Anthropogenic factors are the orientation of a building, the floor height, the inner structure of a dwelling unit, the density of the of the sampling location area, the “opening” of the dwelling to the outdoor environment, indoor antropogenic activity, and the existance of local sources of pollutants such as traffic and industry.

Figure 4 presents the settled dust distribution map, the “iso-dust” maps for Northern and Central Tel-Aviv Area during spring season:



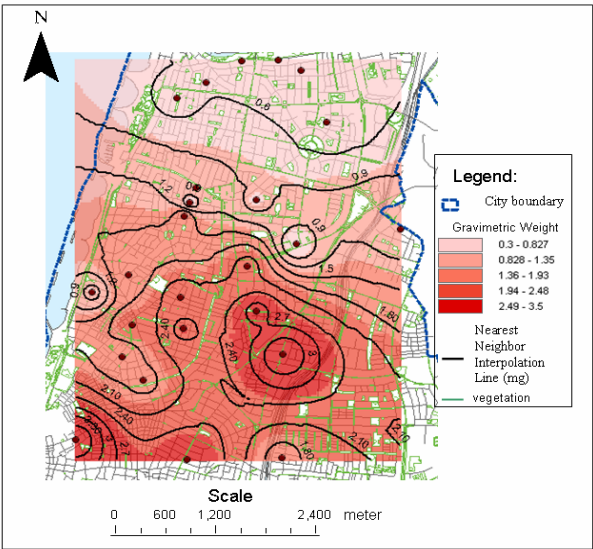


Figure 4: General spatial pattern of settled dust distribution based on the indoor environment measurements as obtained in Experiment 1: Northern (upper) and Central parts of Tel-Aviv (lower). Gravimetric weight of dust samples as a GIS layer was calculated based on the Nearest Neighbor Interpolation.

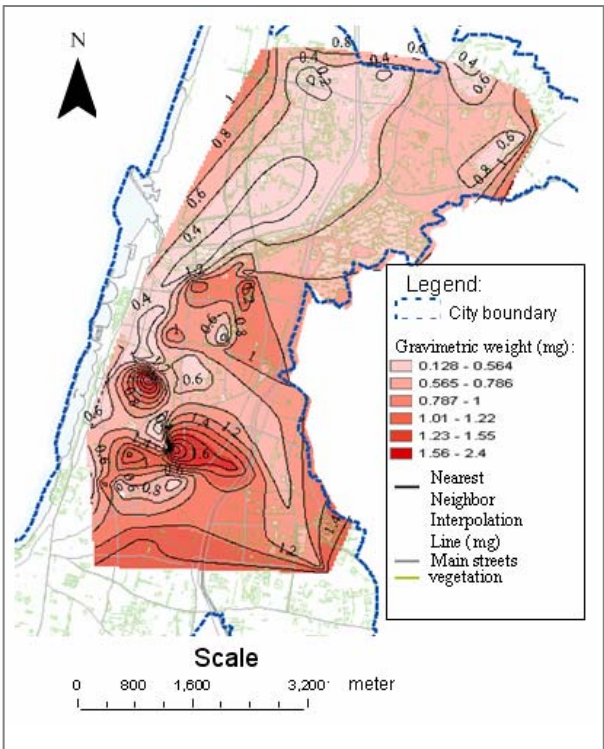


Fig. 5 Spatial Distribution of Indoor Settled Dust in Tel-Aviv during summer

As can be seen from Fig. 4, the map shows the existence of dusty areas in the urban environment. A careful examination of the iso-dust pattern reveals the following findings:

- 1) High amounts of dust were measured in high densely populated area, orientated to the road where at least half of a window was constantly opened allowing the fresh and

polluted air penetrate the dwelling. On the contrary, sampling locations where the vegetation areas are prevealed, houses oriented to the vegetated inner side of a building characterized by low amounts of dust (under the same indoor conditions).

- 2) There is distinct quantitative difference between northern vegetated and central dense populated parts of the city. Higher amounts of dust were measured in central Tel-Aviv whereas northern part was characterized by lower amounts of dust.
- 3) Orientation of a dwelling has an influence on the total amounts of settled dust. Among the dust samples from the central part Tel-Aviv area, samples that were located at areas oriented to vegetation or to inner side of a building (yard of a building) were characterized by lower amounts of dust (under the same indoor conditions, open, closed windows) than those oriented to the roads.

During summer experiment (Figure 5) different spacial pattern is readily observed:

- 1) It is clearly seen that higher amounts of dust are settled in the inner part of the city than in the vicinity of the sea shore. We may suppose that wind breeze that have mostly western direction transports dust in the urban area. In the central part of the city the wind is weakened by the densely populated buildings. Future study should explore the spatial pattern of the indoor settled dust distribution as a function of wind regime in the city.

During both experiments anthropogenic factors were found to be important. The most significant in our study area are the “opening” of the dwelling to the outdoor environment (open- closed windows), and the existence of local sources of pollutants such as traffic.

Several applicative conclusions may be proposed on the basis of the results of our study. For example: positive vegetative climate effects can be achieved by combining vegetation on walls, and around the buildings, better management of the indoor ventilation can improve the life quality.

5 Conclusion

It can be concluded that reflectance spectroscopy is sufficiently sensitive to detect very small amounts of dust in the real indoor environment. Since a low dust load is a much more interesting phenomenon than a high dust load (which is visible using many methods), we concluded that the presented method has high scientific merit as well as industrial applications. The method we have proposed can be utilized in a simple and low-cost mode and work under high power. Thus it can be made available to individuals, commercial organizations or governmental authorities to monitor different indoor environments. The extracted information can be used for initial decision making, improving indoor conditions, and tracking dust contamination following environmental change. We believe that the possibility of building a model or models (perhaps different for different seasons) that will give an immediate qualitative and quantitative answer regarding indoor dust conditions opens up new opportunities for more professional indoor environmental monitoring. With minor modifications, the method can be adapted for outdoor use, such as assessment of dust contamination in large areas during a short sampling time period.

## References

- [1] Sundell, J. (2004). On the History of Indoor Air Quality and Health. *Indoor Air*, 14(7), 51-58.
- [2] Ben-Dor E. and Banin, A. (1995). Near Infrared Analysis (NIRA) as a Rapid Method to Simultaneously Evaluate Several Soil Properties. *Soil Science Society of American Journal*, 59, 364-372.
- [3] Coscione, A., de Andrade, J., Poppi, R., Mello, C., van Raij, B. and de Abreu, M. (2000). Multivariate Calibration Applied to a Highly Interfering Chemical System: The Simultaneous Spectrophotometric Determination of Aluminium and Iron in Plants Using Xylenol Orange and Partial Least-Squares Regression. *Analytica Chimica Acta*, 423(1), 31-40.
- [4] Chudnovsky, A. Ben-Dor, E. and Paz, E. Indoor Sediment Dust Load as Monitored by Reflectance Spectroscopy in the NIR-SWIR Region (1.2-2.4  $\mu\text{m}$ ). Proceedings of the 11th SPIE International Symposium on Remote Sensing, 2004, Maspalomas, Gran Canaria, Spain.
- [5] Chudnovsky, A., Ben-Dor, E. and Paz, E. (2007). Using NIRS for Rapid Assessment of Low Content of Sediment Dust in the Indoor Environment, *Journal of Near Infrared Analyses*, 15(1): 59-70.
- [6] Esbensen, K. (2002). Multivariate Data Analyses, an Introduction to Multivariate Data Analyses and Experimental Design. 5th Edition, Alborg University, CAMO.
- [7] Maguire, D., Batty, T. and Goodchild, M. (Eds.) (2005). GIS, Spatial Analysis, and Modeling. ESRI Press.

MULTITEMPORAL UNMIXING OF MERIS FR DATA

Raúl Zurita-Milla <sup>a,\*</sup>, Luis Gómez-Chova<sup>b</sup>, Jan G.P.W. Clevers<sup>a</sup>, Michael E. Schaepman<sup>a</sup>, Gustavo Camps-Valls<sup>b</sup>

<sup>a</sup> Centre for Geo-Information, Wageningen University and Research Centre, Wageningen, The Netherlands  
<sup>b</sup> GPDS, Dept. Ingeniería Electrónica, Universidad de Valencia, Dr. Moliner 50, 46100, Burjasot, Spain

Commission VII, WG VII/1

**KEY WORDS:** time series, linear spectral unmixing, spectral purity index, LGN, sub-pixel accuracy

ABSTRACT:

The possibilities of using MERIS full resolution (FR) data to extract sub-pixel land cover composition over The Netherlands are explored in this paper. More precisely, the use of MERIS FR time series is explored in this paper since it should facilitate the discrimination of spectrally similar land cover types because of their seasonal variations. The main steps of the methodology used to extract sub-pixel information can be summarized as follows. First, a set of seven MERIS FR Level 1b images that covered the period February to December 2003 were selected. Second, the images were projected into the Dutch national coordinate system. Special attention was paid to this process in order to account for the orbital differences of each MERIS acquisition. Third, a cloud screening algorithm was applied to all MERIS images. Next, the MERIS level 1b TOA radiances were converted into surface reflectance. After that, the latest version of the Dutch land use database (LGN5) was used to support the selection of the endmembers from the MERIS images. Finally, a constrained linear unmixing algorithm was applied to each of the MERIS scenes and to the multi-temporal dataset. The results were validated both at sub-pixel and per-pixel scales using the LGN5 as a reference. The paper concludes by describing the potential and limitations of the selected approach to extract sub-pixel land cover information over heterogeneous and frequently clouded areas.

1. INTRODUCTION

Obtaining reliable and up-to-date land cover information is essential to better understand the Earth’s system. In this respect, the ME<sup>DI</sup>um Resolution Imaging Spectrometer (MERIS) that flies on board the ESA/ENVISAT satellite provides hyperspectral data at unprecedented spatial, spectral and temporal resolutions (Rast and Bezy, 1999). Indeed, MERIS delivers data at 300m (full resolution mode) and at a very high spectral (15 narrow bands) and temporal resolution (revisit time 2-3 days). Because of these characteristics, MERIS has found a number of applications in land remote sensing. For instance, due to its high spectral and temporal resolutions MERIS has been selected to produce a new global land cover map (Arino et al., 2005). However, the use of MERIS for land cover mapping over highly heterogeneous landscapes might not be very appropriate because a number of land cover types will be present in each MERIS pixel. This will lead to the so-called *mixed pixel problem*. In this kind of landscapes, the use of high spatial resolution sensors, like Landsat TM, would be more appropriate. Nevertheless, the temporal and spectral resolutions provided by high spatial resolution sensors are usually not sufficient to accurately map/monitor vegetation dynamics in heterogeneous landscapes. This problem is especially important for areas having persistent cloud coverage throughout the year and/or for areas that have spectrally similar land cover types. Linear spectral mixture analysis is a relatively straightforward method that can be used to deal with the mixed pixel problem (Settle and Drake, 1993; Ichoku and Karnieli, 1996). In this analysis each pixel is modelled as a linear combination of the pure spectral response of each of the classes that are present in the pixel. Several studies (e.g. Lobell and Asner, 2004) have shown that linear mixture analysis can benefit from a high temporal resolution because, in this case, the classes are not

only defined by their spectral signature but also by its evolution over time. In this paper we are thus concerned with exploring the use of MERIS full resolution (FR) time series to extract sub-pixel land cover information from highly heterogeneous and cloudy areas.

2. STUDY AREA AND DATASETS

2.1 MERIS Full resolution data

A temporal series of MERIS FR level 1b images (geo-located TOA radiances) acquired over The Netherlands in 2003 was selected to illustrate this work. The Netherlands was selected as study area because of the heterogeneity of its landscapes, cloud coverage and the availability of an up-to-date high spatial resolution land use database that can be used to validate the results. The acquisition dates were chosen according to two criteria: (i) to maximize the number of cloud free pixels in each scene and (ii) to get, at least, one image per month so that the phenological cycle is fully captured. Unfortunately, no suitable MERIS FR scene was found for the months of January, March, June, September and November. Therefore, an uneven temporal series of seven images is considered (Table 1).

Table 1. MERIS acquisition dates

18 February	6 August
16 April	15 October
31 May	8 December
14 July	

The MERIS FR images were first projected into the Dutch national system (RD) using the geo-location information provided with the data and a nearest neighbour resampling method. After that, a cloud screening algorithm (Gomez-Chova

\* Corresponding author. Raul.Zurita-Milla@wur.nl.

et al., 2006) was applied to all the images to identify and mask out cloud contaminated pixels. Then, the TOA radiances were transformed into surface reflectance using an algorithm specifically designed for the MERIS sensor (Guanter et al., 2007). This algorithm is intended for correction of land targets because the low accuracy of aerosol optical thickness retrievals over water. However, in this study, the algorithm was modified to include the first 10km of water from the shoreline in order to obtain surface reflectance over coastal and inland waters, which represent a high percentage of the total area of The Netherlands.

## 2.2 Reference dataset

The latest version of the Dutch land use database, the LGN5, was used as a reference in this study. This geographical database is based on a multi-temporal classification of high resolution satellite data acquired in 2002 and 2003; several types of ancillary data were also used to produce the land use database – see (Hazeu, 2005) for more details. The LGN5 has a pixel size of 25m and maps 39 classes. The unmixing of all these classes would be unrealistic, since some of the classes are rather small and/or sparsely distributed and/or heavily based on available ancillary data, which mainly describes land uses rather than land covers types. Consequently, the LGN5 was thematically aggregated into the main 12 and 4 land cover types of The Netherlands. The aggregation to 12 classes is meant to offer a detailed distribution of the following classes: grassland, summer crops, winter crops, orchards, deciduous forest, coniferous forest, water, built-up, greenhouses, bare soil (including sand dunes), heathlands, and swamps. The aggregation to 4 classes considers the following main land cover classes: vegetation, bare soil, water and built-up. Despite its simplified legend, the aggregation to 4 classes is of great interest because it can be used as a proxy of fractional vegetation cover and because it might be of help during the inversion of biophysical and biochemical parameters. For example, the presence of sub-pixel water in a pixel might bias the LAI estimate.

## 3. SPECTRAL UNMIXING

A fully constrained linear spectral unmixing (FCLSU) was applied to each MERIS image (mono-temporal case) as well as to a multitemporal composite (layerstack) of all the MERIS images. The FCLSU (Heinz and Chang, 2001), which guarantees a physical interpretation of the results, can be formalized as follows:

$$p_i = \sum_{c=1}^{c=nc} (f_c \cdot \mu_{ci}) + \varepsilon_i \quad (1)$$

Subject to:

$$0 \leq f_c \leq 1 \quad \text{and} \quad \sum_{c=1}^{c=nc} f_c = 1 \quad (2)$$

where  $p_i$  is the pixel value for the band- $i$ ,  $nc$  represents the number of classes that are being unmixed,  $f_c$  is the fraction of class- $c$  present in the pixel, and  $\mu_{ci}$  is the pure signal of the class- $c$  in the band- $i$  (this signal is commonly known as “class endmember”). Finally, the term  $\varepsilon_i$  represents the per band residual error.

Notice that the number of dates used in multitemporal unmixing is pixel dependent (each pixel was unmixed with the maximum number of cloud free dates). This means that the quality of the unmixing might also be pixel-dependent and that, if critical (phenological) dates are missing for a number of pixels (areas), the accuracy of the results on those pixels (areas) might be lower.

### 3.1 Selection of endmembers

A fully automatic class endmember selection method was used in this study. The method only needs the land cover fractions computed for each MERIS date using the LGN5 as a reference and the cloud mask that belongs to each MERIS image. First, the fractions of each land cover class were summed up for all the acquisition dates. Next, these “multitemporal fractions” were used to compute a multitemporal version of the standard purity index, SPI (Zurita-Milla, 2007):

$$SPI = \sqrt{\sum_{c=1}^{c=nc} (f_c - f_{maxclass})^2 / (nc - 1)} \quad (3)$$

where  $f_c$  represents the multitemporal fraction of class- $c$  in a given pixel and  $f_{maxclass}$  is the maximum multitemporal fraction. Therefore, the multitemporal SPI equals one when the pixel has only one class for all the dates under study, and it equals zero when the sum of the fractions is the same for all the classes ( $f_c = f_{maxclass} = 1/nc$ ).

Pure pixels were identified for each date by first applying the corresponding cloud mask to the multitemporal SPI image and then applying a SPI threshold to the remaining (cloud free) pixels. The SPI threshold was adaptively tuned until at least 20 pixels were found for all classes. After that, a neighbourhood constraint is applied to these SPI pure pixels: only the pure pixels surrounded by pure pixels of the same land cover class are selected to compute the endmembers (erosion filter of 3 by 3 pixels). If after applying the neighbourhood constraint a class has less than 5 pixels left, then the constraint is relaxed and all the pixels identified in the previous step are selected as pure pixels to compute the endmember of that class. Finally, the endmembers of each class were created by averaging the pure pixels identified in the previous step.

### 3.2 Validation datasets

Although the MERIS sensor has a large swath that allows a revisit time of 2-3 days, the ENVISAT platform only repeats orbit every 35 days. This means that each of the MERIS images that were selected for the analysis might have been acquired from a slightly different orbit. This, in turn, implies that each of the MERIS images might have a slightly different observation geometry. Therefore some (sub-pixel) differences in the instantaneous field of view of each “pixel” are to be expected when using images acquired from different orbits.

In order to account for this effect, each MERIS pixel was reprojected into the original LGN5 25m grid so that the “actual land cover fractions” seen by MERIS at each acquisition date could be computed. After this, the sub-pixel land cover fractions were assigned to the corresponding 300 by 300m MERIS pixel. The class having the highest fractional coverage was used to produce a hard land cover classification for each MERIS acquisition date. This processing step allows both a



sub-pixel and a per-pixel validation of the unmixing results for each of the MERIS FR images.

In order to create a validation dataset for the multitemporal results, the LGN5 was spatially aggregated to match the nominal MERIS FR pixel size. A majority filter with a kernel of 12 by 12 LGN5 pixels was used to obtain a land cover classification map at 300m. During this spatial aggregation, the fractions of the different land cover types present in each 300 by 300m pixel were recorded.

### 3.3 Accuracy assessment

The fractional maps computed in the previous section were used as ground truth for the validation of the monotemporal and multitemporal unmixing. Assuming that the unmixed fractions are correctly positioned within each pixel, a kind of overall sub-pixel accuracy (OSA) can be computed as follows:

$$OSA = \sum_{c=1}^{c=nc} d_c / \sum_{c=1}^{c=nc} f_c = \sum_{c=1}^{c=nc} d_c \quad (4)$$

$$d_c = \min\{f_c^{LGN5}, f_c\}$$

where  $d_c$  are the correctly classified abundances for each pixel. These abundances can be computed as the minimum of  $f_c^{LGN5}$  and  $f_c$ , which respectively are the LGN-based and the unmixed abundances. Notice that the sum of  $f_c$  for all classes adds to unity (Eq. 2).

After the sub-pixel accuracy assessment, the unmixed fractions were used to produce land cover classification maps for each date. The class having the maximum fractional coverage was used to label each pixel. Subsequently, a classical classification accuracy assessment was done by comparing these images with the land cover maps that were computed for each date. Similarly, the hard classified multitemporal image was validated using the aggregated LGN5 as a reference. The confusion matrix and the kappa index were used for the per-pixel accuracy assessment.

## 4. RESULTS AND DISCUSSION

### 4.1 MERIS pre-processing

A visual inspection of the reprojected MERIS images did not show any major shift between them (besides the expected

differences due to different acquisition orbits). Images also overlapped quite well the reference dataset. This can be considered as a preliminary quality proof of the ground control points provided with the images. Although a quantitative assessment of the geolocation accuracy might have been more appropriate, here we decided to keep it simple in order to also test the operability of the unmixing of MERIS FR time series. Therefore, in this study, the pre-processing steps were reduced as much as possible.

With respect to the cloud screening method, all the clouds and cloud borders were masked out. The validation of the cloud mask revealed that a small amount of pixels belonging to the classes greenhouses (sun glint on glass roofs) and bare soil (sand dunes) were identified as clouds because these classes have similar reflectance behaviour as clouds. However, the classes that were misclassified represent less than 0.5% of The Netherlands and, therefore, they are not statistically representative in the clustering process used by the cloud screening algorithm.

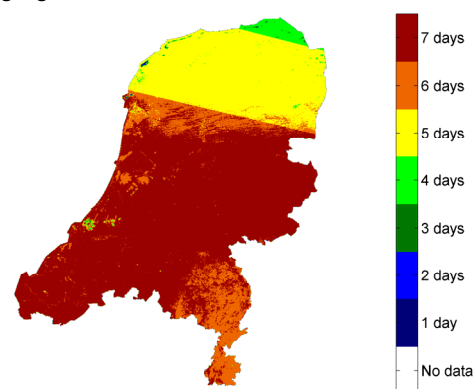


Figure 1. Total number of usable dates

Figure 1 shows the number of usable dates for each MERIS FR pixel. It should be noted that the northern and south-eastern parts of the Netherlands have less usable pixels than the rest of the country. This is not only because of the cloud coverage but also because some of the MERIS FR images did not cover the whole of The Netherlands.

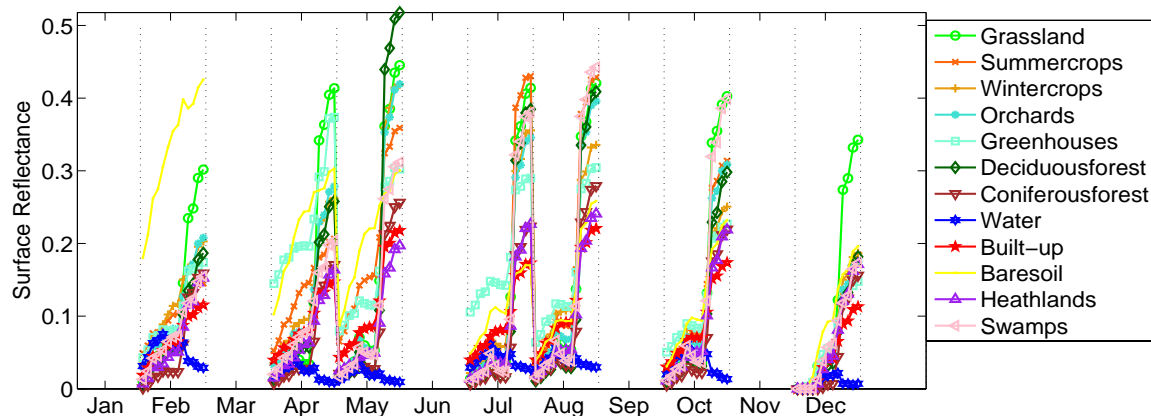


Figure 2. Spectral signature of the endmembers extracted from the MERIS FR time series.

Table 2. Summary of the accuracy assessment for the 12 classes case

Date	18-2-2003	16-4-2003	31-5-2003	14-7-2003	6-8-2003	15-10-2003	8-12-2003	Multitemp
mean OSA	43.54	52.70	42.35	45.46	36.88	41.56	44.78	52.72
Kappa	0.33	0.44	0.33	0.36	0.27	0.30	0.32	0.45
OA	44.29	54.17	43.88	46.06	35.29	41.87	45.68	55.17

Table 3. Summary of the accuracy assessment for the 4 classes case

Date	18-2-2003	16-4-2003	31-5-2003	14-7-2003	6-8-2003	15-10-2003	8-12-2003	Multitemp
mean OSA	77.20	82.84	78.21	83.07	80.01	74.52	74.28	82.51
Kappa	0.52	0.73	0.60	0.69	0.58	0.50	0.50	0.71
OA	80.83	88.27	83.09	87.28	82.54	76.66	77.56	87.81

Table 4. User’s and producer’s accuracies (UA and PA, respectively) for the 12 classes case

Class	Grassland	Summer Crops	Winter Crops	Orchards	Greenhouses	Deciduous. Forest
UA	70.96	58.40	17.59	4.19	16.27	13.40
PA	72.90	26.29	18.58	0.97	68.66	35.79

Class	Coniferous Forest	Water	Built-up	Bare soil	Heathlands	Swamps
UA	50.09	86.95	71.67	10.79	13.72	5.05
PA	71.78	88.70	41.45	37.17	31.88	15.17

Table 5. User’s and producer’s accuracies (UA and PA, respectively) for the 4 classes case

Class	Vegetation	Bare soil	Water	Built-up
UA	87.58	36.65	92.55	78.42
PA	98.05	24.71	84.79	25.59

4.2 Endmembers

Most of the endmembers were computed as average of the pixels selected using the initial SPI threshold of 0.95. Nevertheless, for some small classes, the SPI threshold was reduced in order to get, at least, 20 pixels for those classes. For instance, the SPI threshold had to be reduced to 0.87 to extract 20 “pure pixels” of the greenhouse class on cloudy dates (31<sup>st</sup> May and 6<sup>th</sup> August). For the small and sparse classes the neighbourhood constraint was, in general, not applied because very few clusters of 3 by 3 pure pixels can be found. Figure 2 shows the spectral signature of the endmembers selected in this study. Grassland presents the highest NIR reflectance all year around. During the months of May, July and August the endmember of deciduous forest also shows high reflectance (high greening of vegetation). The rest of the vegetated classes appear to have a very similar spectral signature. Therefore, high confusion is expected among most of the vegetated classes.

4.3 Unmixing

A fully constrained linear spectral unmixing was applied to each of the seven MERIS images and to the multitemporal time series using the 12 endmembers depicted in figure 2. The fractions for the 4 classes case were computed by aggregating all the fractions of vegetated classes into a single vegetation class and by grouping the fractions of greenhouses and built-up into a single built-up class. The unmixed fractions were then compared with the reference fractions that were generated according to the viewing geometry of each date (see section 2.3). The overall sub-pixel accuracy (OSA; Eq. 4) was used to do this comparison. As an example, figure 3 illustrates the OSA for the multitemporal unmixing of 12 and 4 classes. In general, homogeneous areas tend to agree well with the reference dataset

and, as expected, the 4 classes case offers better OSA values because the spectral confusion among vegetated classes is now removed. However, in the case of 12 classes, low agreements are found in the north and south eastern part of the country. These areas do not only have more heterogeneous pixels than the rest of the country but were also unmixed using fewer dates. Subsequently, the unmixed fractions were transformed into a hard classification map and the overall classification accuracy (OA) and the kappa statistic were computed by comparing these maps with the reference land cover maps.

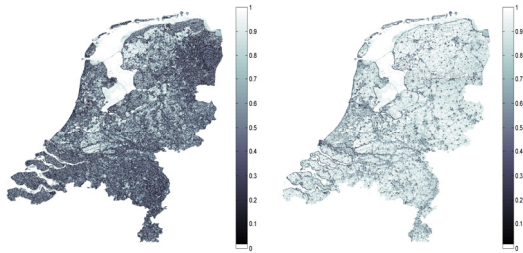


Figure 3. Overall sub-pixel accuracies (OSA) for the multitemporal unmixing of 12 (left) and 4 (right) classes.

Tables 2 and 3 summarise the results of the sub-pixel and per-pixel classification accuracy assessment for the 12 and 4 classes cases. Three main conclusions can be drawn from these tables. (i) Classification results for the 4 classes case are much higher than the results obtained for 12 classes. This is mainly because the vegetated classes are spectrally very similar. (ii) The multitemporal approach yielded the highest classification results, since adding the temporal evolution (phenology) simplifies the discrimination of spectrally similar land cover types. Nevertheless, the difference between the classification results of the best monotemporal image (April) and the

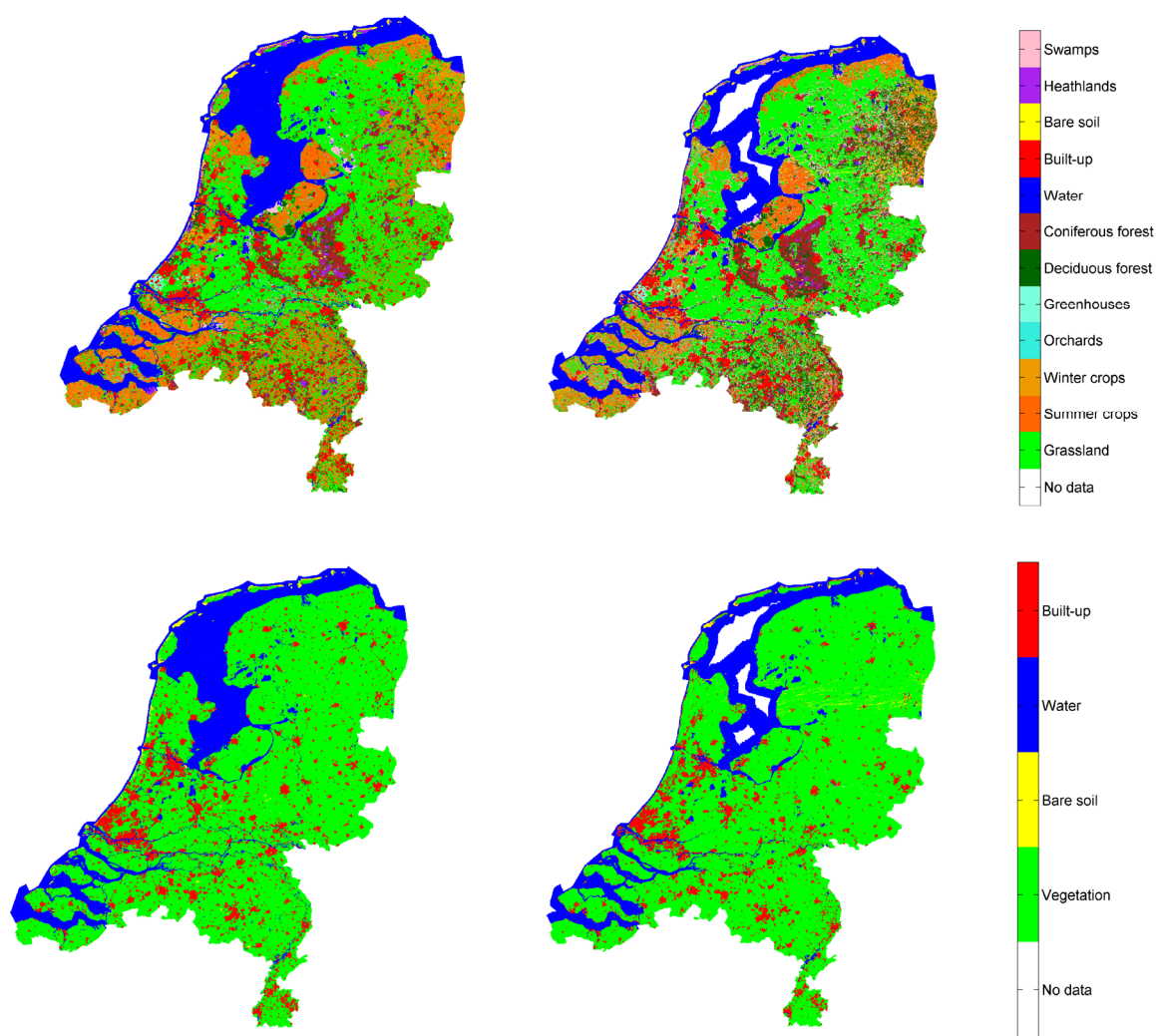


Figure 4. Reference dataset (left) and Multitemporal hard classified images (right) for 12 (top row) and 4 (bottom row) classes.

multitemporal approach is not very large. This indicates that the selection of the dates for the unmixing is critical (e.g. in spring most of the vegetated classes appear to have a large separability). (iii) The OSA and the OA values are in the same order of magnitude. However, the OSA refers to the sub-pixel abundances and therefore it inherently contains more information than the OA computed from the hard classified images.

Figure 4 shows the reference datasets and the hard classification results that were obtained for the multitemporal 12 and 4 classes cases. Notice that the gap in the inland waters of the north of Netherlands is caused by the atmospheric correction (recall that only the first 10 km of coastal water were atmospherically corrected).

Finally, Tables 4 and 5 show the user's and producer's accuracies for the multitemporal case. For the 12 classes unmixing, the classes orchards, swamps and winter crops present the three poorest producer's and user's accuracies followed by the classes heathlands, bare soil and deciduous forest. This suggests that a further simplification of the 12 classes cases is needed. With respect to the 4 classes case only the bare soil class appears to have poor user's and producer's accuracies. This could be due to fact that the class bare soil is rather small (it mainly comprises sand dunes in coastal areas).

5. CONCLUSIONS

This study has shown that the use of MERIS FR data has a great potential to extract sub-pixel land cover composition over heterogeneous and frequently clouded areas. The multitemporal unmixing of MERIS FR data yielded sub-pixel and per-pixel overall accuracies that were very similar to the ones obtained for the best monotemporal image. This indicates that the selection of dates used for the unmixing is critical. Vegetation phenophases and the spectral separability of the endmembers should be further studied in order to optimize the best combination of dates and classes to be unmixed. Nevertheless, we should keep in mind that all the unmixing results have been validated using a static dataset produced using a combination of high resolution satellite data from 2002 and 2003 and several sources of ancillary data. Thus, validation results might be slightly affected by the period in which the reference dataset was produced.

The overall classification accuracy (OA) for the multitemporal 12 classes case was moderately good (around 55%) while the aggregated 4 classes case yielded better OA (around 88%). Furthermore, the overall sub-pixel accuracies (OSA values) were in the same order of magnitude as the overall classification accuracy. Therefore, we are confident that the extracted sub-pixel information might be of great utility in remote sensing monitoring activities, such as land cover change detection or retrieval of biophysical parameters from MERIS

FR data. Additional work will be devoted to the use of the 4 classes case as a proxy of fractional vegetation cover.

calibration on regional land cover mapping and land products. *International Journal of Remote Sensing* 28(3), pp. 653-673

### ACKNOWLEDGEMENTS

The authors would like to thank Dr. Luis Guanter for providing the atmospheric correction algorithm and for fruitful discussion on cloud screening. This paper has been partially supported by the Spanish Ministry for Education and Science under project DATASAT ESP2005-07724-C05-03. The contribution of R. Zurita-Milla is granted through the Dutch SRON GO programme (EO-061).

### REFERENCES

Arino, O., Trebosson, H., Achard, F., Leroy, M., Brockman, C., Defourny, P., Witt, R., Latham, J., Schmullius, C., Plummer, S., Laur, H., Goryl, P. and Houghton, N., 2005. The globcover initiative. European Space Agency, (Special Publication) ESA SP 597, pp 171-175.

Gomez-Chova, L., Camps-Valls, G., Amoros-Lopez, J., Guanter, L., Alonso, L., Calpe, J. and Moreno, J., 2006, New Cloud Detection Algorithm for Multispectral and Hyperspectral Images: Application to ENVISAT / MERIS and PROBA / CHRIS Sensors. IEEE International Geoscience and Remote Sensing Symposium. Denver, Colorado, July 31-August 4, 2006.

Gomez-Chova, L., Camps-Valls, G., Amoros-Lopez, J., Martín, J.D., Calpe, J., Alonso, L., Guanter, L., Fortea, J. C. and Moreno, J., 2006. Cloud detection for MERIS multispectral images. Proceedings of the MERIS (A)ATSR Workshop. ESA Publications Division, ESA SP-597.

Guanter, L., González-Sampedro, M. C. and Moreno, J., 2007. A method for the atmospheric correction of ENVISAT/MERIS data over land targets. *International Journal of Remote Sensing*, vol. 28(3), pp. 709–728.

Hazeu, G., 2005. The Dutch Land Use Database LGN. <http://www.lgn.nl/> (accessed 19 Feb. 2007)

Heinz, D. and Chang, C.-I., 2001, Fully constrained least squares linear mixture analysis for material quantification in hyperspectral imagery, *IEEE Transactions on Geoscience and Remote Sensing*, vol. 39(3), pp. 529–545.

Ichoku, C. and Karnieli, A., 1996. A review of mixture modelling techniques for sub-pixel land cover estimation. *Remote Sensing Reviews*, 13, pp. 161-186.

Lobell, D.B. and Asner, G.P., 2004. Cropland distribution from temporal unmixing of MODIS data. *Remote Sensing of Environment*, 93, pp. 412-422.

Rast, M. and Bezy, J.L., 1999. The ESA Medium Resolution Imaging Spectrometer MERIS a review of the instrument and its mission, *International Journal of Remote Sensing*, 20(9), pp. 1681 – 1702.

Settle, J.J. and Drake, N.A., 1993. Linear mixing and the estimation of ground cover proportions. *International Journal of Remote Sensing* 14(6), pp. 1159-1177.

Zurita-Milla R., Clevers, J. G. P. W., Schaepman, M. E. and Kneubuchler, M., 2007. Effects of MERIS L1b radiometric

# CLASSIFICATION OF MULTISPECTRAL ASTER IMAGERY IN ARCHAEOLOGICAL SETTLEMENT SURVEY IN THE NEAR EAST

Bjoern H. Menze<sup>1</sup> and Jason A. Ur<sup>2</sup>

<sup>1</sup>Interdisciplinary Center for Scientific Computing (IWR), University of Heidelberg, Germany

<sup>2</sup>Department of Anthropology, Harvard University, USA

bjoern.menze@iwr.uni-heidelberg.de, jasonur@fas.harvard.edu

**KEY WORDS:** Archaeological remote sensing, settlement mounds, soil mark, survey techniques, spatio-temporal sampling, fusion

## ABSTRACT:

In alluvial areas of the Near East, the former locations of settlements are often represented by “tells”, small artificial mounds resulting from millennia of human settlement activity, especially the continual construction and decay of mud brick architecture. To identify such tells and other, smaller settlement sites in the modern landscape, we develop a classifier which screens wide areas for tell-specific soil-changes, based a characteristic spectral signature in ASTER imagery. Using data from sites identified from CORONA imagery and field survey on a north Syrian plain, a Random Forest classifier was trained, using the raw reflectances, vegetational features, correlation with prototype-spectra of the JPL ASTER SpecLib, and time flags as input features. A spatio-temporal sampling strategy allowed us to classify and fuse results from any ASTER images available for a certain region. The classifier was tested in an independent test area, centered around Tell Hamoukar, with close ground control from an archaeological survey. In this test area it was possible to identify 32 out of the 49 site bigger than 2ha. Overall we found that multi-spectral ASTER imagery can be used to provide highly specific information on character and composition of the ground, a tool which can be used in survey planning or the screening of wide regions for conservational issues or studies in landscape archaeology.

## 1 INTRODUCTION

Archaeologists recognize the scale and spatial distribution of settlement as critical variables in the study of the origins of urbanism and social complexity, making their location and measurement an important component of archaeological research. Tells, the arabic name for the settlement mounds of the Near East, represent places which were occupied over millennia, often since the beginning of farming in the early Neolithic. Due to a predominantly mud brick-based building technique many of them grew to considerable heights (Rosen, 1986) and some even achieved urban status (Wilkinson, 1994) during the Bronze Age. Today, thousands of these settlement sites still can be found in Near Eastern landscapes. Some of them are mounds of sizes which even allow to spot them in global elevation models (Sherratt, 2004, Menze et al., 2006), other sites are only visible from characteristic changes of the soil, changed by the debris of millennia of settlement activity (Wilkinson et al., 2006). In the present work, the use of ASTER imagery for providing means of prospecting for these remains of the earliest human settlement system will be evaluated (Altaweel, 2005). So far, most archaeological applications use (high resolution) satellite images as an replacement for standard aerial photography. In these applications, the spectral information only provides qualitative information, e.g. enabling the interpretation of a scene in a false-colour coding (Lasaponara and Masini, 2007, Masini and Lasaponara, 2006, for example), but is not used explicitly to identify spectral signatures which are of archaeological interest. In the following, we will illustrate how the spectral information of multi-spectral satellite imagery can be used for such an approach. While this machine-based search for a specific ground cover is a well established tool in agricultural or geological remote sensing, such an automated classification of spectral imagery has not been pursued in archaeological remote sensing, so far.

Operating since the year 2000, the Advanced Spaceborne Thermal Emission and Reflection Radiometer (ASTER), provides spectral imagery for any region worldwide and at many points in time. Few applications, however, use the full information of

whole multi-temporal data sets. Often, the classification of surface features is limited to the classification of one single image and to data which were acquired at the same date and under similar environmental conditions (Apan et al., 2002, for example). Among the approaches which use images and spectral signals of different points in time, most search for a characteristic change pattern along the temporal dimension, e.g. in a change detection between different scenes (Bruzzone et al., 2004, Im et al., 2007), or in the classification of vegetational features according to their trajectory along the seasonal cycle (Chattopadhyay and Dutta, 2006, Hayes and Cohen, 2007, Xiao et al., 2006). Characteristic patterns found along the temporal dimension are used to identify the different types of ground cover and then serve as input features in a subsequent classification. Unfortunately, the spectral pattern of soils does not show such a characteristic seasonal dependence. Variations of the spectral pattern are dominated by short time changes due to precipitation and other meteorological and environmental factors. Thus, approaches using the temporal dimension as in (Chattopadhyay and Dutta, 2006, Hayes and Cohen, 2007, Xiao et al., 2006) are not easily applicable to identify tell-specific soil changes. Instead of searching for characteristic trajectories along the temporal axis in an ordered set of images, we will propose a classifier in the following which can be applied individually to any single image, irrespectively of its time of acquisition. Together with an appropriate fusion strategy, this will allow all information of all ASTER scenes available for a certain region to be used. To this end, we will employ a spatio-temporal sampling strategy (sections 2 & 3), allowing to obtain a classifier which can be trained on the maximal number of different environmental situations in different ASTER scenes. We will evaluate the use of different fusion strategies available from sensor fusion when applying this classifier to a multi-temporal data set (Benediktsson and Kanellopoulos, 1999, Jeon and Landgrebe, 1999, Bruzzone et al., 1999, and references therein) and finally test the optimized classifier in a region with close archaeological ground control (sections 4 & 5).



## 2 MULTI-TEMPORAL CLASSIFICATION STRATEGY

Designing a classifier for a specific problem on a certain type of data typically follows a very standardized procedure. In a classification task on a single spectral image, for example, it is the collection of a training data set in a first step, to be followed by the definition of a feature representation and the classification algorithm. Parameters of feature selection and classification are then evaluated by an error measure which is appropriate to the learning task and are finally optimized accordingly.

To obtain a classifier in the given application which is robust against the variations of the data along the time-line, the normal sampling of the training data in the spatial dimensions is extended by an additional sampling in the temporal direction, in the combined space of coordinate-space and time. As the resulting classifier is supposed to be applied to any available ASTER image of a certain region, the standard classifier design is also extended by a subsequent fusion step, to pool the results map of all individual images. In our search for a tell-like surface or soil pattern we used the following scheme, under particular consideration of the multi-temporal extension of the classification:

**1. Sampling.** The detection task is transformed to a binary classification. In addition to the verified tell sites, a number of “non-tell” locations are chosen randomly. For all locations of both groups, spectra are sampled from all imagery available at these locations. Relying on a non-parametric classification model in the following, the sampling is of crucial importance in the design of the classifier.

**2. Features.** In addition to the “raw” spectral reflectances, secondary features transport prior knowledge on: a) Invariants – Vegetation indices represent established normalization strategies on the reflectance of specific channels. b) Subclasses – Prototypes of expected spectral patterns, i.e. rock, soil-types, water, can be compared against the observed pattern, e.g. in a correlation with the signal. c) Temporal features – Indicate the date of acquisition.

**3. Classifier.** Due to the lack of information about the presence of subgroups (such as high-, low-mounded tells, tells under modern settlement in the tell class, but also like crop fields, bare soil, rocks, modern settlements in the non-tell class) and due to the inhomogeneity of the features (categorical, nominal), the non-linear and non-parametric “Random Forest” classifier (Breiman, 2001) has been chosen. It is a tree based ensemble learner with few, easily adjustable hyper-parameters.

**4. Optimization.** A cross-validation both over the spatial box-grid (Lahiri, 2003) and the temporal dimension, i.e. the single image covering the training area, is used to evaluate and adjust the parameters of steps 1.-3., i.e. the sampling strategy, the optimal choice of features, and the hyper-parameters of the classifier.

**5. Fusion.** As the classification procedure (steps 1.-4.) can be applied to any available image of the region under study, it allows for a fifth step: Pooling the result maps of all available images.

The resulting classifier differs from hierarchical approaches in multi-sensor fusion (Briem et al., 2002, Jeon and Landgrebe, 1999, Zhu and Tateishi, 2006) as it avoids the training of a new classifier for each sensor, or, in this application, for each image. It allows for a robust, independent classification of single images, regardless of their time of acquisition, without the need to manually select the data for specific time-points or specific environmental conditions in training or in application.

## 3 METHODS

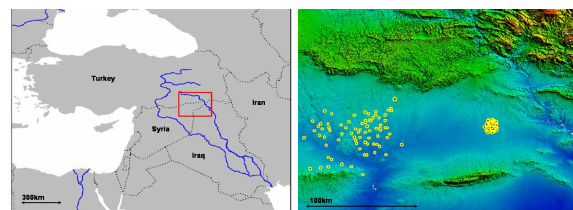


Figure 1: The Khabur plain, region under study: location, with the Upper Khabur basin indicated (left) and digital elevation model (right). Indicated yellow are training sites (west, compare Fig. 2) and test area centered around Tell Hamoukar (east, Fig. 6).

### 3.1 Satellite data and Region under study

The study is based on ground truth on a part of a north Mesopotamian plain (the Upper Khabur basin), in the province of Hasake, Syria, close to the Turkish and the Iraqi borders (Fig. 1, left). The training sites (128 sites) are situated in an area of approx.  $90\text{km} \times 60\text{km}$  in the western part of that plain (Fig. 1, right). These settlement sites were identified by analyzing declassified CORONA imagery in conjunction with several seasons of survey fieldwork (Wilkinson, 1997, Ur, 2004). The training sites include low- and high-mounded tells, as well as sites which are (partially) situated beneath modern settlements. The training area is partially covered by 16 cloud free ASTER swaths (Fig. 2), acquired during different times of the year between 2003-2006, most of them during the dry-season from May-October (Fig. 3). A second region approx.  $100\text{km}$  east to this area was subject to an intensive ground survey (Ur, 2002b, Ur, 2002a) and used for the evaluation of the ASTER classification (Fig. 1, right). It is an circular area of approx.  $125\text{km}^2$ , and with a reported number of 75 archaeologically relevant sites, ranging from low mounded areas with moderate densities of pot sherds or minor soil changes to major mounds like Tell Hamoukar in its center. This test area is covered by 9 cloud-free ASTER swaths from 2003-2007, most of them acquired during the dry-season as well. For both training and test data, the 6 SWIR and 5 TIR channels were interpolated to the maximal resolution of the 3 VNIR channels ( $15\text{m} \times 15\text{m}$ ) using a nearest-neighbor approach.

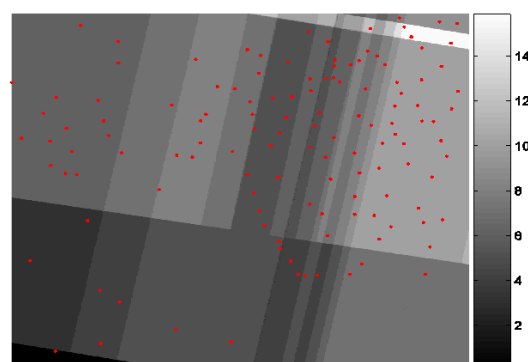


Figure 2: Number of ASTER images for a tell site (indicated red) in the training area. Tell sites are covered by 2 to 15 ASTER images (see scale bar).

### 3.2 Implementation of the classifier

The classifier was trained and optimized on the first training data set and then applied to the second test set. It was implemented and optimized on the training data according to the multi-temporal classification strategy (section 2):

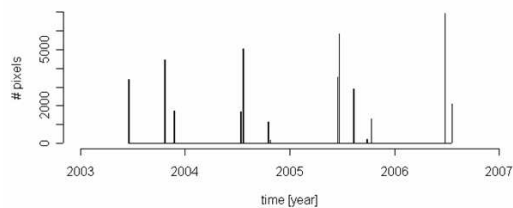


Figure 3: Pixels of tell sites in the training set, along time.

**1. Sampling.** The detection task was transformed to a binary classification, discriminating between the class of spectra from archaeologically relevant sites and a non-tell or “background” class. All spectra available from tell sites (ts) were included in the training data ( $N_{site}^{ts} = 11215$  pixels, 0.24% of the 4 702 671 pixels in the test region;  $N_{spec}^{ts} = 40306$ ). The locations of the background class (bg) were randomly sampled from the remaining regions ( $N_{site}^{bg} = 9961$ , 0.21%) and the spectra available from these pixels were subsampled to approximately match  $N_{spec}^{ts}$ , and included into the training set ( $N_{spec}^{bg} = 50000$ ).

**2. Features.** In total 25 features were included into the training set. Beside the raw reflectance of the 14 spectral channels, two time flags were included (year, day of the year). To obtain invariance against seasonal influences, three vegetation indices were included, representing differently normalized spectral channels (NIR / R; NIR - R “VIDIFF”; (NIR-R) / (NIR+R) “NDVI”). For six classes of the JPL ASTER SpecLib<sup>1</sup> (manmade, minerals, rocks, soil, vegetation, water), averaged spectra were subsampled from full resolution to the 14 ASTER channels and used for correlation with the raw spectra. The resulting correlation coefficients were also used as input features.

**3. Classifier.** To classify the rather unstructured set of spectral features, Random Forest (Breiman, 2001) was chosen, a non-parametric and non-linear ensemble learner based on decision trees, a class of classifiers allowing for scale invariant learning. Prior comparisons of Random Forest, a RBF-kernel support vector machine (SVM) and a linear SVM on the raw spectral features of a subset of the training data (approx. 7000 tell class and 8000 background class samples) had indicated the need for a non-linear classifier (linear SVM 21.4% classification error in a ten-fold cross validation), and a gave slight advantage of a Random Forest (18.2%, using default parameters) against the non-linear SVM (20.4%, optimizing the kernel-width in an internal five-fold cross-validation). In the following, Random Forest was always applied with the default parameters of (Liaw and Wiener, 2002) ( $n_{tree} = 300$  trees,  $m_{try} = 4$  variables).

**4. Optimization.** During training, feature subsets were evaluated in a random, unblocked cross-validation (“full Xval”, table 1), in a blocked cross-validation over a spatial grid (“spatial Xval”) and over both a spatial grid and a flag of the ASTER image, i.e. a temporal label (“spatial & temp Xval”). The spatial-box grid had a side-length of 6km, an extension beyond the length of most structures on the ground. For comparison, classifiers solely trained on single images were also applied to the remaining data (training on one image, classifying all others, averaging prediction accuracies at the end). Using the posterior probability of the Random Forests in prediction, the performance was measured by the average image-wise area-under-the-curve (AUC) of the receiver-operator characteristic (ROC), in order to compare binary ground truth with the predicted probability of the presence of a tell-like soil change. Thresholding the posterior probability at 0.5, the classification accuracy was evaluated as well.

**5. Fusion.** Using the optimized classifier, all cross-validated results were pooled using different fusion strategies: Averaging

<sup>1</sup>ASTER Spectral Library. <http://speclib.jpl.nasa.gov/>

thresholded probability maps using thresholds of 0.5, 0.7, and 0.9, averaging the posterior probability, and a Naive-Bayes approach on the probabilities was tested. Finally, classification accuracy and AUC of the ROC for the fused results were compared against the labels of the originally sampled training locations to find the best fusion strategy.

4 RESULTS

4.1 Training – “What do we learn from the learning algorithm?”

Evaluating the classification performance on the training set primarily aims at a better understanding of the learning problem and at an optimization of the design of the classification strategy. Three different cross-validation approaches measured or “simulated” different scenarios (table 1): The random cross-validation approximates an upper limit to the bayes error of the training data and is the most optimistic. The spatial cross-validation is an approximation to the optimal spatial generalization error, e.g. to results obtained when the same ASTER image is used in training and testing (or just imagery acquired on the same date). The spatio-temporal cross-validation is the most pessimistic of the three scenarios. It tests the performance on data which is both distant in space and in time, for example, on an ASTER image with a different date and from a different region than the training data. Assuming that training and test region have certain similarities, and that it might be possible to select images for their acquisition time –which will be given in most tests or applications– the real classification error will be somewhere in between the classification results of a spatial and a spatio-temporal resampling scheme.

Accuracy	all	w/o Spec	w/o Envir	w/o SpecLib	w/o Time
full Xval	82.	79.3	(82.0)	(83.2)	(81.8)
spatial Xval	78.1	75.6	77.1	78.2	77.2
spatial&temp Xval	69.9	(70.2)	67.7	69.5	70.4
single classifier	61.2	61.4	61.3	61.4	–
AUC ROC	all	w/o Spec	w/o Envir	w/o SpecLib	w/o Time
full Xval	90.5	87.0	(89.8)	(91.0)	(89.7)
spatial Xval	85.6	83.0	84.7	85.9	84.9
spatial&temp Xval	76.2	(76.4)	73.9	75.9	76.4
single classifier	66.7	66.6	66.3	67.4	–

Table 1: Accuracies and area under the curve (AUC) of the ROC on the differently cross-validated training data; on the full set of features (all) and with single feature groups removed (w/o). Non-significant differences to the results on the full set of features are in brackets.

We find that approx. 70-80% of the observation (table 1) are classified correctly when using the spatio-temporal sampling, as opposed to a classification accuracy of approx. 60% from classifiers trained on spectra sampled in coordinate-space only. Predicting full result maps of the training regions in a spatial cross-validation, the majority of the pixels in 124 out of the 128 tell sites were classified correctly. False negative pixels within the area of the 124 sites typically occurred at the borders of the tell sites. False positives pixels in the background region were primarily due to modern settlements. Studying false positive sites in high resolution imagery also revealed the presence of settlement mounds within the training region which were unrecorded in our training data (Fig. 7).

The contributions of the different feature classes (raw spectral channels, vegetation indices, correlation with prototype-spectra,

time-flags) were also tested in the different cross-validation scenarios. Each of the classes was removed from the feature set and the classification was repeated (table 1). These classification results were then compared against the results on the full set of features and tested for significant differences using a paired Cox-Wilcoxon test on the results of the single spatio-spectral blocks. We observe that raw reflectance spectra are relevant features in the random and the spatially blocked cross-validation, while secondary features like vegetation indices and prototype correlation are relevant in the test of spatio-temporal generalization. Time flags show an indifferent behavior. They improve the classification performance in random and a spatially blocked cross-validation, but decrease the spatio-temporal accuracy.

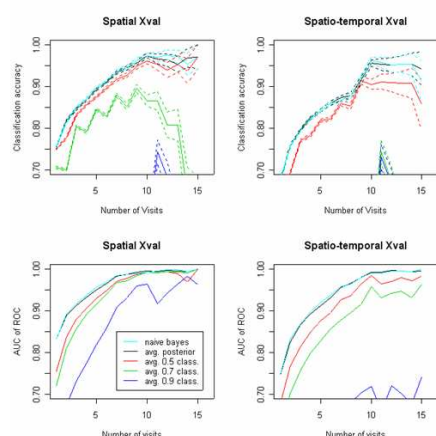


Figure 4: Fusion of single results at a location in a spatial and a spatio-temporal cross-validation. Details see text.

Optimal fusion strategies were evaluated in a second step. For each location the cross-validated observations available from the training data set were fused to a single prediction (Fig. 4), which was then compared to the label of the location. If more observations than necessary were available for a single location, e.g. when assessing the performance of three combined observations while five were available for the location, observations were subsampled accordingly. We observe that the classification accuracy increases from approx. 70% to >> 90% with a nearly complete class separation both for the spatial and the spatio-temporal cross-validation ( $\text{AUC ROC} \gg .95$ ). The direct average of the class posterior probabilities performs best, together with the application of the product rule on the probabilities (Naive-Bayes). Averaging the classification error ranks third, while averages of classification maps thresholded at other probability than 0.5 – potentially allowing to trade sensitivity and specificity– perform the worst.

#### 4.2 Testing – “What do we learn from the learning problem?”

While the evaluation of classification performances on the training data set primarily serves technical purposes, the application of the classifier to the test region allows us to assess the relevance of the classification algorithm in the application it has been designed for. Thus, all nine ASTER image covering the test area were classified using the the Random Forest classifier on the full set of features. In the fusion of the result maps, the two top performing approaches (average posterior, Naive-Bayes) were tested, but for reasons of comparison the classification performance at a 0.5 and a 0.7 threshold was determined as well. Results were compared qualitatively in a pixel-wise manner –using the precision-recall-curve– and in a quantitative approach determining the number of detected sites.

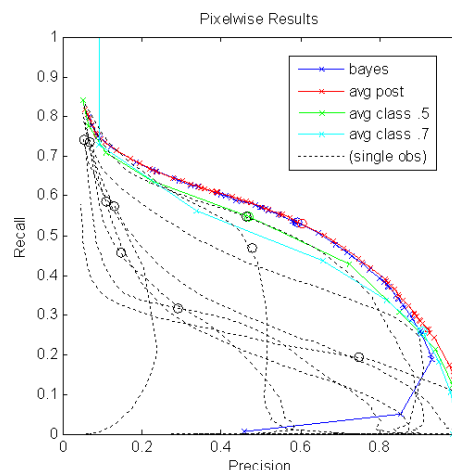


Figure 5: Pixel-wise precision and recall on the test data for the different fusion strategies and for single images. Points indicate classification results with a fixed threshold (e.g. 0.5 probability).

As the number of “background” pixels outnumber the pixels of tell sites in the given detection problem significantly, precision (true positive / (true positives + false positives)) and recall (true positives / (true positives + false negatives)) were used to concentrate the evaluation on the smaller, but more important class of tell-pixels (positives). We find that average posterior and Naive-Bayes perform best (Fig. 4), with nearly identical classification results when using the optimal threshold from the training (recall 0.54, precision 0.59). As the Naive-Bayes approach assigns high probabilities to pixels which do not belong to the tell class, its AUC is somewhat smaller than the one from the average posterior. The average classification strategy (threshold 0.5) shows acceptable results, still better than the best classification of a single image. The average 0.7 classification –representing a robust error measure on the posterior– has the highest precision among all approaches (0.91), but at a very low recall (0.26). Overall we observe again that the averaging improves the results significantly and that average posterior and Naive-Bayes perform best, although the latter has a somewhat smaller area under the convex curve of precision and recall.

To determine a “site detection rate”, the true positive site “hit” and the false positive site “miss” has to be defined. Ground truth allowed to assign each *pixel* of the survey area either to the tell or to the background class (Fig. 6 c). As slight shifts occurred frequently between the ground-truthed tell sites and regions with a tell-like spectral signature (either due to registration or projection artifacts, or to real differences between these borders) areas around tells were extended by a distance of 90m (approx. TIR pixel-size, see dark blue region in Fig. 6 d). “Positive” pixels in these regions were considered to be “true positive”. Remaining areas of the survey region (bright blue in Fig. 6 d) were considered to belong to the background class. Here, “positive” pixels were “false positives”. A *tell site* of the ground truth data set was “detected”, if more than 15 adjacent “true positive” pixels (four-neighborhood) could be found in its vicinity and the center of the connected pixels was within the confirmed tell region. Areas of 15 or more “false positive” pixels in the background region were considered to be a false positive site. Fifteen pixel correspond to a site of approx. 0.3ha, the smallest size of a tell site in the training data.

Following this definition, we were able to identify a major subgroup of 34 sites among the 75 confirmed sites of the test set, at a number of approx. 20 false positives. Among the false positive



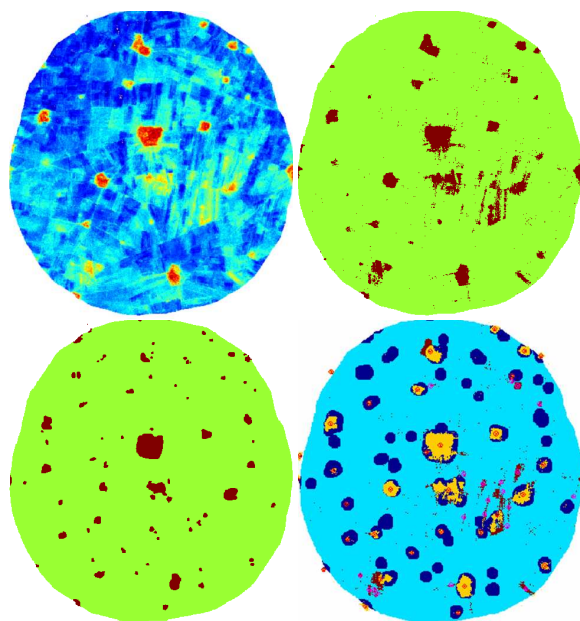


Figure 6: The test region. From top to bottom: a) average posterior (left), b) binary classification (right), c) ground truth (left), d) classification results (right). Tell Hamoukar is slightly north to the center.

“hits”, most occurred in regions of known tells and coincide with the outlines of selected modern agricultural fields. Most false negative were minor sites; among the 49 sites with a size of more than  $2ha$  (approx. two TIR pixels), 32 were detected successfully.

## 5 DISCUSSION

In most applications of archaeological remote sensing, satellite images are used primarily for visual interpretation and as a replacement for aerial imagery (Lasaponara and Masini, 2007, Masini and Lasaponara, 2006). Instead of using spectral information for a false-colouring of a scene and in a qualitative interpretation only, we explicitly used characteristic changes in the reflectance of the soil (Wilkinson et al., 2006) in a quantitative approach. Exploiting the spectral information of the satellite data directly, we were able to identify a spectral signature of archaeologically relevant soil marks and places of former settlement activity (Fig. 7). The ability to determine the locations of archaeological sites greatly enhances the efficiency of ground survey, the process by which the chronological range of occupation is determined. Ultimately, we will use these chronological patterns to build up a history of settlement in the region over some eight millennia which will allow us to investigate the spatial dimensions of the evolution of early urbanism and land use in one of the regions of the earliest cities in the Near East.

The spatio-temporal sampling strategy allowed us to obtain a classifier which is robust against temporal variations of the spectral signature of the ground. It can be applied to any ASTER image available for a region of interest without being restricted to certain periods of the year, and thus provides means to analyze and fuse all information which is available for that region. Fused result maps outperform any single observation both on training and on test data, reducing “noise” in the spectral signal due to environmental influences. Averaging the posterior probability performs better than a Naive-Bayes approach or the results from the ensemble-vote of a classification, indicating that the result maps of the ASTER images are indeed “noisy” realizations of an iid

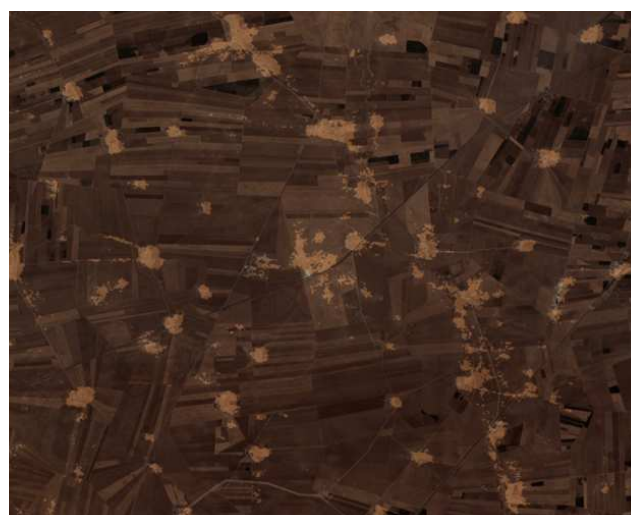
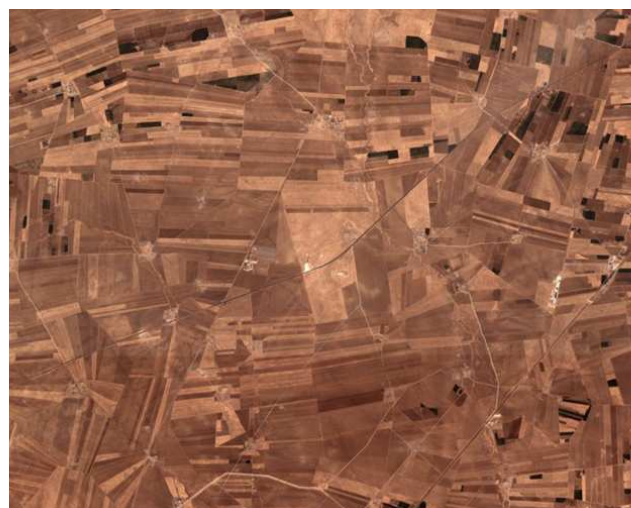


Figure 7: Survey of wide regions. Top: High resolution imagery of the Khabur plain. Bottom: Binary classification map provides adjunct information. Tell-like regions are indicated by brighter color. (Cross-validated and fused results for the western part of the training region.)

(independent and identically distributed) process, rather than independent sources of information (independent distributed), often assumed in sensor-fusion (Benediktsson and Kanellopoulos, 1999, Jeon and Landgrebe, 1999, for example). From a practical perspective, this relieves the operator from the deliberate choice of selecting the “best” available ASTER image, when relying on the standard approach of only using one single image for the classification. However, restricting the fusion process to a selection of optimal result maps might enhance the performance of the fusion step even further (either determined in a visual inspection of the results or in an automated procedure (Petrakos et al., 2001)). The fusion of all information itself has proven to be of major relevance in the detection of a characteristic soil signature of former settlement sites.

Comparing classification results in the Tell Hamoukar region with ground truth from field survey (Ur, 2002a, Ur, 2002b), we observe a high correspondence for major sites. Minor sites, a group not represented overly well in the training data, could not be identified with the same reliability. Obviously, the spatial resolution of the ASTER sensor sets lower limits to the identification of small sites from satellite imagery, but it might be argued as well that small sites do not show the same soil composition, erosion be-

havior, or response to precipitation as major ones do. Thus, using a classifier which is explicitly trained to identify subgroups like minor, low mounded sites, but also like high mounded tells or mounds in vicinity or beneath modern settlement, might alleviate this problem. In addition to reduce false negatives, such a classifier might also allow to gain more insights in the character of false positive sites. It remains open, for example, whether in regions of recent agricultural earthworks, the leveling of former sites might have been the major source of these classification errors. False positives in the area of modern settlements might result from covariates in the (current) training data, or might resemble the spectral characteristic of ancient debris indeed, eventually indicating the presence of (unrecorded) former sites at the same place. Studying false positives should be a major objective in a more “prospective” ground study.

So far the classifier generalized well over the distance of around 100km, from our training area in the southwestern region of the Upper Khabur basin to our testing area in the eastern end (Fig. 1). Regions with different soil or precipitation pattern, however, might require a “local” retraining or recalibration of the classifier. Here, a combined approach with other modalities, e.g. with results from the SRTM model (Menze et al., 2006), might be preferable. In addition to the “extrapolation” of knowledge from one region to another, as evaluated in this study, an “interpolation” of information in regions already surveyed (Fig. 7) will always be possible, providing a tool to classify the spectral signature of site already known or even to identify sites which remained undetected on the ground.

Soil changes provide relevant adjunct information in the identification of former settlement places. In the ground survey of the test region, for example, a visible soil change was one of three criteria out of which two had to be fulfilled to mark a former settlement site, the others being topographic moundedness and presence of surface artifacts above a certain density threshold (Ur, 2002a, p. 61). Being able to identify soil changes not only on the ground, but also remotely from satellite data, a combined evaluation of CORONA data –or other high resolution imagery– together with the proposed ASTER classification, might now allow to pursue a relevant part of such a survey in advance and “off-site”. Potential sites as identified via the ASTER classification could be used to guide ground control in a more efficient manner, which would allow broader geographic coverage during the limited time available for field survey.

## 6 CONCLUSIONS

In the identification of a spectral signature for ancient settlement places in ASTER satellite imagery, we developed a novel spatio-temporal sampling strategy. It yields a robust classifier which can be applied to any data available for a certain region, enables a fusion of all available images, and allows the identification of the spectral signature of ancient settlement sites in ASTER imagery. As an adjunct source of information in addition to highly resolved monochrome imagery (CORONA, QuickBird) the main potential of this approach is in a fast screening of wide regions and the mapping of whole settlement systems (Fig. 7), for survey planning and risk assessment in conservational issues. In regions which are not accessible to ground survey at present –in the Middle East, for example, wide areas of Iran, Iraq, Afghanistan (Petrie, 2007)– spectral imagery will provide the only means to access information on character and composition of the ground at all.

## REFERENCES

- Altaweel, M., 2005. The use of aster satellite imagery in archaeological contexts. *Archaeological Prospection* 12, pp. 151–166.
- Apan, A., Kelly, R., Jensen, T., Butler, D., Strong, W. and Basnet, B., 2002. Spectral discrimination and separability analysis of agricultural crops and soil attributes using aster imagery. In: *Proc 11th ARSPC (Australasian Remote Sensing and Photogrammetry Conference)*, Brisbane/Australia, pp. 396–411.
- Benediktsson, J. and Kanellopoulos, I., 1999. Classification of multi-source and hyperspectral data based on decision fusion. *IEEE Transactions on Geoscience and Remote Sensing* 37, pp. 1367–1377.
- Breiman, L., 2001. Random forests. *Machine Learning* 45, pp. 5–32.
- Briem, G., Benediktsson, J. and Sveinsson, J., 2002. Multiple classifiers applied to multisource remote sensing data. *IEEE Transactions on Geoscience and Remote Sensing* 40, pp. 2002–2291.
- Bruzzzone, L., Cossu, R. and Vernazza, G., 2004. Detection of land-cover transitions by combining multivariate classifiers. *Pattern Recognition Letters* 25, pp. 1491–1500.
- Bruzzzone, L., Prieto, D. and Serpico, S., 1999. A neural-statistical approach to multitemporal and multisource remote-sensing image classification. *IEEE Transactions on Geoscience and Remote Sensing* 37, pp. 1350–1359.
- Chattopadhyay, A. and Dutta, S., 2006. Mapping monsoonal soil wetness regions from multi-temporal vegetation dataset. *International Journal of Remote Sensing* 27, pp. 4693–4700.
- Hayes, D. and Cohen, W., 2007. Spatial, spectral and temporal patterns of tropical forest cover change as observed with multiple scales of optical satellite data. *Remote Sensing of Environment* 106, pp. 1–6.
- Im, J., Rhee, J., Jensen, J. and Hodgson, M., 2007. An automated binary change detection model using a calibration approach. *Remote Sensing of Environment* 106, pp. 89–105.
- Jeon, B. and Landgrebe, D., 1999. Decision fusion approaches for multitemporal classification. *IEEE Transactions on Geoscience and Remote Sensing* 37, pp. 1227–1233.
- Lahiri, S., 2003. *Resampling Methods for Dependent Data*. Springer-Verlag, New York and Heidelberg.
- Lasaponara, R. and Masini, N., 2007. Detection of archaeological crop marks by using satellite QuickBird multispectral imagery. *Journal of Archaeological Science* 34, pp. 214–221.
- Liaw, A. and Wiener, M., 2002. Classification and Regression by randomForest. *R News* 2, pp. 18–22.
- Masini, N. and Lasaponara, R., 2006. Satellite-based recognition of landscape archaeological features related to ancient human transformation. *Journal of Geophysical Engineering* 3, pp. 230–235.
- Menze, B., Ur, J. and Sherratt, A., 2006. Detection of ancient settlement mounds – Archaeological survey based on the SRTM terrain model. *Photogrammetric Engineering and Remote Sensing* 72, pp. 321–327.
- Petrakos, M., Benediktsson, J. and Kanellopoulos, I., 2001. The effect of classifier agreement on the accuracy of the combined classifier in decision level fusion. *IEEE Transactions on Geoscience and Remote Sensing* 39, pp. 2539–2546.
- Petrie, C., 2007. Remote sensing inaccessible Routes: Tracing Old Routes from India to Afghanistan. online. <http://www.archatlas.org/>.
- Rosen, A., 1986. *Cities of Clay: The Geoarchaeology of Tells*. University of Chicago Press, Chicago and London.
- Sherratt, A., 2004. Spotting tells from space. *Antiquity* 78, online. <http://antiquity.ac.uk/ProjGall/sherratt/>.
- Ur, J., 2002a. Settlement and Landscape in Northern Mesopotamia: The Tell Hamoukar Survey. *Akkadica* 123, pp. 57–88.
- Ur, J., 2002b. Surface Collection and Offsite Studies at Tell Hamoukar, 1999. *Iraq* 64, pp. 15–43.
- Ur, J., 2004. *Urbanism and Society in the third Millennium upper Khabur Basin*. PhD thesis, The Department of Near Eastern Languages and Civilizations, The University of Chicago.
- Wilkinson, K., Beck, A. and Philip, G., 2006. Satellite Imagery as a Resource in the Prospection for Archaeological Sites in Central Syria. *Geoarchaeology* 21, pp. 735–750.
- Wilkinson, T., 1994. The Structure and Dynamics of Dry-Farming States in Upper Mesopotamia. *Current Anthropology* 35, pp. 483–520.
- Wilkinson, T., 1997. *Archaeological Survey of the Tell Beydar Region, Syria*. Prepress, Turnhout/Belgium.
- Xiao, X., Boles, S., Frolking, S., Li, C., Babu, J., Salas, W. and Moore, B., 2006. Mapping paddy rice agriculture in South and Southeast Asia using multi-temporal MODIS images. *Remote Sensing of Environment* 100, pp. 95–113.
- Zhu, L. and Tateishi, R., 2006. Fusion of multisensor multitemporal satellite data for land cover mapping. *International Journal of Remote Sensing* 27, pp. 903–918.



# SPATIO-TEMPORAL MODELLING OF SMALL MAMMAL DISTRIBUTIONS USING MODIS NDVI TIME-SERIES DATA

C G Marston<sup>a</sup>, R P Armitage<sup>a</sup>, F M Danson<sup>a</sup>, P Giraudoux<sup>b</sup>, A Ramirez<sup>a</sup> and P S Craig<sup>a</sup>

<sup>a</sup> School of Environment and Life Sciences, University of Salford, Salford, M5 4WT, UK

<sup>b</sup> University of Franche-Comte, Besancon, France  
c.g.marston@pgr.salford.ac.uk

**KEY WORDS:** Echinococcus, Rodents, Landscape, MODIS, Time-series, Spatio-temporal

## ABSTRACT:

This work modelled the spatial distribution of the rodent species that act as hosts in the transmission cycle of the parasitic tapeworm *Echinococcus multilocularis*. The rodent distribution was modelled in relation to landscape characteristics in four ways, using (1) a Landsat ETM+ derived hard classification, (2) single-image Landsat ETM+ derived NDVI, (3) single-image MODIS 16-day composite NDVI, and (4) time-series MODIS 16-day composite NDVI imagery. The MODIS time-series imagery produced the strongest relationships and explained the highest percentage deviance of the relationships present (up to 41.4%), whereas the hard classification method only explained up to 21.2% of deviance. Single-image NDVI datasets produced poor results, with Landsat ETM+ derived NDVI explaining only up to 11.9% of deviance, and MODIS derived NDVI up to only 8.78%. These results confirm that using time-series NDVI data to model rodent distributions is a valid method, and can offer improved results over single date NDVI and hard classification methods.

## 1. INTRODUCTION AND BACKGROUND

The fox tapeworm *Echinococcus multilocularis* (*Em*) is one of the World's most dangerous human parasites causing fatalities in 95% of infected patients. The tapeworm exists in a transmission cycle between small mammals and foxes, and the parasite is increasingly infecting domestic dogs that predate infected rodents, leading to increased transmission to dog owners via dog faeces contaminated with *Em* eggs. In central China, where the parasite is endemic, there is currently an urgent need to develop spatial models to predict the location and extent of *Em* transmission foci so that limited medical resources can be effectively targeted and appropriate control programmes implemented.

This study aims to assess the relationship between small mammal distributions and spatio-temporal landscape variables, and develop a model to accurately predict the spatial distribution of locations where the parasite hosts are likely to be present. Field observations have indicated that there are spatial relationships between heavily grazed areas with low biomass that are the optimal habitat of rodent species (*Ochotona* sp.) known to be involved in the *Em* transmission cycle, and small mammal distributions in our study region in Shiqu county, western Sichuan Province, China.

Knowledge of land cover and land cover change is an important input in modelling ecological processes from the regional to the global scale (Schwarz *et al.*, 2005), and Geographical Information Systems now facilitate the incorporation of these spatio-temporal land-cover relationships into epidemiological investigations of wildlife diseases (Pfeiffer *et al.*, 2002). Several previous investigations have related satellite-derived land cover and Digital Elevation Model data to rodent populations that act as disease transmission vectors of Hantavirus, with studies by Goodin *et al.* (2006), Suzan *et al.* (2006) and Glass *et al.* (2000) showing that direct relationships exist between landscape structure and topographical variables, and the distribution of

rodents. Studies by Boone *et al.* (2000) also successfully utilised satellite-derived vegetation and topographical data to predict the infection status of Deer mice with the Sin Nombre Virus with up to 80% accuracy in the USA.

These successful studies show that modelling rodent population distributions through landscape characteristics is a viable methodology, however, previous work using remotely sensed data to assess landscape-rodent relationships have concentrated on hard classification methods using single date medium spatial resolution imagery. Limitations result from attempting to classify continuous variables such as vegetation gradients into discrete classes. This may result in information on sub-class variation being lost, when this variation may be integral in the observed relationships. Continuous measurements such as a vegetation index, for example the Normalised Difference Vegetation Index (NDVI), the most widely used vegetation index for retrieval of vegetation canopy biophysical characteristics (Jiang *et al.*, 2006), may be better suited to define, characterise and quantify landscape characteristics. This NDVI data could then be modelled with rodent presence; as rodent distribution is often related to the spatial distribution of areas of differing vegetation characteristics, this could be a viable alternative to using a hard classification method.

Furthermore, as vegetation experiences a seasonal growth and senescence cycle, resulting in seasonal landscape change, time-series NDVI data offers the potential to better quantify the spatio-temporal characteristics of this seasonal vegetation cycle rather than measuring NDVI at only one point in time. Time-series NDVI data has previously been used successfully for various applications, including quantifying vegetation cycles, assessing land cover change and to map the spatial distribution of habitats by Beck *et al.* (2006), Xiao *et al.* (2006), Lunetta *et al.* (2006) and Jin *et al.* (2005), and could offer significant advantages over single-date vegetation index data.

The research described in this paper develops a multi-temporal model of landscape change over large areas using time-series MODIS NDVI 16-day composite 250m resolution imagery. The main advantage of these datasets is that the regular repeat coverage of the MODIS NDVI data product allows assessment of temporal variability in the landscape which is expected to better describe small mammal distributions.

## 2. STUDY SITE AND DATA COLLECTION

The study area for this investigation is located near the town of Serxu, Shiqu county, Sichuan Province, China (Figure 1). This site is located on the eastern Tibetan plateau at high altitude between 4000 and 4300m above sea level. Although this area is above the tree line, variation in the herb and shrub layers of vegetation produces a variety of habitats across the study area.

Rodent transects totalling approximately 35km in total length were surveyed in summer 2001, with presence or absence of three species and groups of rodents being recorded at 10 metre intervals, giving a total of 3485 transect points. Visual sightings of rodents, presence of rodent droppings or rodent holes (both identifiable to species or group of species level) were used to determine rodent presence. These rodent groups were *Ochotona curzoniae* or black-lipped pika (Occu), *Ochotona cansus* or gansu pika (Occa), and a generically described group of rodents consisting of *Arvicola terrestris* and *Microtus arvalis* (Smallsm). Each of these has different habitat requirements, and will therefore exhibit different relationships with the spatial landscape and habitat arrangement.

Map and habitat data was not available for this area, therefore it was necessary to generate the required datasets. Shuttle Radar Topography Mission Digital Elevation Model data was acquired and used to produce a 3D topographical model of the study area, enabling topographical variables such as altitude, slope and aspect to be calculated. A Landsat ETM+ image (acquisition date 3<sup>rd</sup> July 2001) was also obtained and subjected to a supervised classification using training areas of known habitats visited during fieldwork. This Landsat ETM+ image was atmospherically corrected and used to derive a NDVI dataset for the study area. Also, multiple MODIS 16-day composite vegetation index data at 250m spatial resolution were acquired for the period between 6th April 2000 and 24th May 2006, 138 images in total, to allow the spatio-temporal modelling of vegetation change.

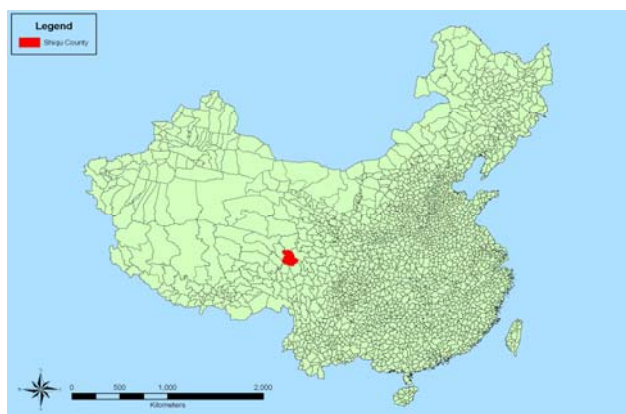


Figure 1. Study site location, Shiqu county, China.

## 3. METHODOLOGY

The rodent transect data were overlaid on the supervised classification derived from the Landsat ETM+ image using ArcView 9.1. A buffer of 500m was created around each of the 3485 rodent transect points. Within these buffers the proportion (%) of each habitat type was calculated. This proportional land cover data was combined with the rodent transect data was analysed using a Generalised Additive Model (GAM).

To explore whether a continuous NDVI dataset better characterised the landscape and its relationship with rodent distribution, a NDVI dataset was generated from the Landsat ETM+ image using Erdas Imagine 8.6. This NDVI image was then overlaid with the rodent index data, and a spatial join was performed to extract the NDVI value for the location of each rodent transect point.

Analysis of the 250m resolution MODIS 16-day composite vegetation index data imagery that had been acquired was also performed. The NDVI datasets were extracted from this data product, and were then reprojected to the UTM WGS84 projection to ensure compatibility with the other datasets utilised in this investigation, and subset to the region of the study site to reduce storage demands and reduce processing time. Initially a single NDVI image corresponding to the same period as the Landsat ETM+ image was acquired (3-11 July 2001), was overlaid with the rodent transect data, and again, a spatial join was performed extracting a MODIS NDVI value for each rodent transect point.

Next, the relationship between rodent distribution and time-series NDVI data was analysed. All 138 time-series NDVI composite images were stacked in acquisition date order which enabled the extraction of seasonal NDVI profiles over a six-year period for any location within the extent of the image. These seasonal NDVI profiles were extracted for each MODIS pixel containing rodent transect points. As MODIS 16-day composite images are produced for the same calendar periods each year (for instance the first image in each year covers the period 1-16 January), it is possible to collapse the six-year NDVI profile down into a single 'standardised' annual NDVI profile for that location. This was initially performed using the mean NDVI value for each 16-day period, and also the median and maximum NDVI values. This should have the effect of 'smoothing' the profile and removing noise. On examination, the 'standardised' profiles using the mean and maximum NDVI values were susceptible to the effects of outlying values, and were therefore disregarded.

Data quantifying the characteristics of the median standardised annual NDVI profile was then extracted, including maximum NDVI, minimum NDVI, mean NDVI, NDVI range, growing season (length of period when NDVI > 0.3), and greening period (when NDVI value rises above 0.3) allowing quantitative analysis methods to characterise spatial and temporal variation in the NDVI to be performed. This data was then combined with the rodent index data, and Landsat NDVI, MODIS single date NDVI and standardised time-series profile data were all analysed using a GAM.

4. RESULTS

The rodent index data, each landscape variable, and the topographical variables of slope, altitude and aspect were entered individually into a Generalized Additive Model. The results, showing % deviance explained, are displayed in Table 1. Although many of the land cover class and topographical variables gave poor results, the disturbed class for Occu (21.2%), Wet Grassland for Occa (18.1%) and Bog for Smallsm (18.1%) showed the highest single class degree of explanation, and indicated that relationships between the rodent presence and proportion of these land cover classes. The strongest relationship existed between Occu and the disturbed land cover class, and when plotted graphically it was obvious that the probability of Occu being present as the proportion of disturbed land increased within the buffered areas (Figure 2), which was supported by field observations.

Variable	Occu	Occa	Smallsm
Village	2.86%	2.86%	2.86%
Road	10.20%	14.00%	8.65%
Bog	3.62%	3.52%	18.10%
Water	1.54%	10.80%	6.24%
Grass	7.24%	5.64%	9.84%
Broadleaf	5.18%	11.30%	11.60%
Bare	4.79%	5.64%	8.89%
Disturbed	21.20%	14.10%	13.30%
Yellowbrush	1.34%	1.58%	4.66%
Wet Grassland	16.10%	18.10%	4.34%
Slope	4.50%	3.00%	3.82%
Altitude	2.92%	8.26%	12.70%
Aspect	6.69%	9.70%	5.09%

Table.1. Deviance explained (%) of rodent distribution related to proportion of each land cover class and topographical variables.

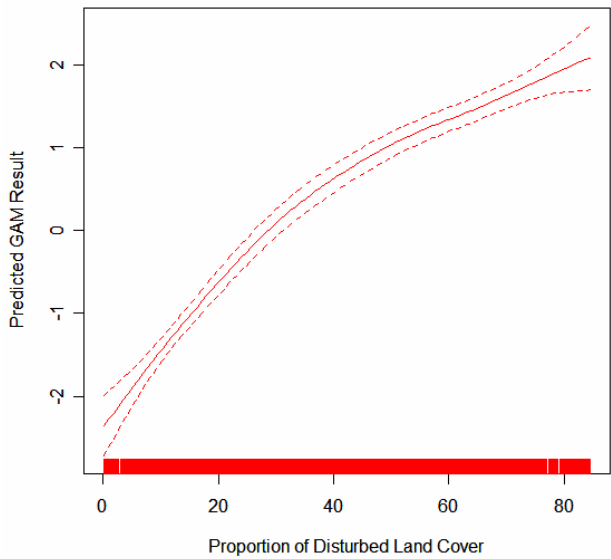


Figure 2. Occu distribution related to proportion of ‘Disturbed’ land cover class.

The characteristics of this disturbed class are very low biomass levels, and often bare soil, therefore it could be expected that a similar relationship may be observed between rodent distribution and NDVI as was observed with the ‘Disturbed’ land cover class. However, as Table 2 shows, attempts to model the relationships between rodent distribution and NDVI datasets derived from both the Landsat ETM+ and MODIS imagery did not explain as much deviance as the hard classification model.

The results of the single-date GAM analysis of rodent distribution and the Landsat ETM+ and MODIS NDVI datasets produced poor results for all three rodent groups, with the maximum deviance explained being 11.9% for Occu related to Landsat ETM+ NDVI. This was disappointing as the relationships between the disturbed (low biomass) land cover class and rodent distribution that had previously been confirmed using the hard classification were not repeated when related to a continuous vegetation dataset. The relationship between rodent distribution and MODIS NDVI was even lower, although this may be a result of the coarse 250m spatial resolution of the MODIS imagery.

Variable	Occu	Occa	Smallsm
Landsat ETM+ NDVI	11.9%	3.17%	4.86%
MODIS NDVI	5.03%	4.83%	8.78%

Table.2. Deviance explained (%) of rodent distribution related to single date Landsat ETM+ and MODIS derived NDVI data.

The results of the GAM analysis of rodent distribution and time-series MODIS NDVI data produced improved results over the single-date NDVI data. When each individual variable of the NDVI cycle was analysed in relation to the rodent distribution data the results were poor, accounting for between 3.47% and 15.6% of deviance explained. However, when a combination of all these variables were modelled with rodent distribution results improved significantly, with 41.4% deviance explained for Occu, 37.6% for Occa and 34.7% for Smallsm. Therefore, it can be assumed that modelling several variables relating to the seasonal spatio-temporal NDVI profile produces improved results, and is a more appropriate methodology than using single-date NDVI imagery. The differences in deviance explained values between Occu, Occa and Smallsm may result from Occu being present at a larger number of transect points than Occa or Smallsm, and therefore having more data items to model.

Variable	Occu	Occa	Smallsm
Maximum NDVI	13.7%	9.06%	15.6%
Minimum NDVI	7.06%	9.87%	4.55%
Mean NDVI	13.0%	6.91%	10.2%
NDVI range	3.47%	6.92%	9.04%
Greening period	12.3%	7.45%	9.84%
Growing season length	9.59%	9.54%	6.88%
All variables combined	41.4%	37.6%	34.7%

Table.3. Deviance explained (%) of rodent distribution related to quantified measurements of the standardised annual NDVI profile.

Another limitation of the MODIS time-series data is the 250m spatial resolution. It is likely that sub-pixel landscape and ecological features exist which influence rodent distributions, and cannot be identified using this coarse-resolution imagery. Higher spatial resolution time-series data could overcome this limitation, improving the rodent-landscape models. Other unidentified ecological processes could also influence the accuracy of the time-series model that were not quantified in this investigation. Also fieldwork observations identified areas of ideal rodent habitat that had no rodents present, further complicating the situation. Although the results of this study have shown the advantages and potential of using time-series NDVI datasets to model rodent distributions over single-time NDVI datasets, further research is required to better understand this relationship.

## 5. CONCLUSION

This investigation modelled rodent distribution in relation to landscape characteristics using four separate landscape-quantifying datasets, (1) a Landsat ETM+ hard classification, (2) single-image Landsat ETM+ derived NDVI, (3) single-image MODIS 16-day composite NDVI, and (4) time-series MODIS 16-day composite NDVI imagery. The success of these methods was variable, with the hard classification method displaying a relationship between Occu distribution and the 'Disturbed' land cover class, but showing poor relationships between the other landscape variables and rodent distribution. Both the Landsat ETM+ and MODIS derived NDVI single-image datasets gave poor results when modelled against rodent distribution, however the MODIS time-series NDVI data gave much improved results over the hard classification and the single-date NDVI datasets: for Occu, time series data explained 41.4% of deviance as opposed to 11.9% (single-image Landsat ETM+ NDVI) or 5.03% (single-image MODIS NDVI). For Smallsm it explained 34.7% of deviation as opposed to 4.86% and 8.78%. It is likely that these figures could be improved further should higher spatial resolution time-series imagery become available, if additional ecological data is introduced into the models, and if methods of dealing with the effects of spatial autocorrelation are developed. Even with these limitations, these results show that rodent distributions can be successfully modelled using time-series NDVI data, and that this method is a viable alternative to using both single-image NDVI and hard classification data methods. It is hoped, in turn, that this method will significantly contribute to the regional scale prediction of *Em* rodent host distribution, and therefore also to the regional scale prediction of *Em* transmission foci.

## REFERENCES

- Beck P S A., Atzberger C., Hogda K A., Johansen B. and Skidmore A K., 2006, Improved monitoring of vegetation dynamics at very high latitudes: A new method for using MODIS NDVI, *Remote Sensing of Environment*, 100(3), pp. 321-334.
- Boone J D., McGwire K C., Otteson E W., DeBaca R S., Kuhn E A., Villard P., Brussard P F. and St Jeor S C., 2000, Remote sensing and geographic information systems: charting sin nombre virus infections in deer mice. *Emerging Infectious Diseases*, 6(3), pp. 248-258.
- Glass G E., Cheek J E., Patz J A., Shields T M., Doyle T J., Thoroughman D A., Hunt D K., Ensore R E., Gage K L., Irland C., Peters C J. and Bryan R., 2000, Using remotely sensed data to identify areas at risk for hantavirus pulmonary syndrome, *Emerging Infectious Diseases*, 6(3), pp. 238-247.
- Goodin D G., Koch D E., Owen R D., Chu Y K., Hutchinson J M S. and Jonsson C B., 2006, Land cover associated with hantavirus present in Paraguay, *Global Ecology and Biogeography*, 15(5), pp. 519-527.
- Jiang Z., Huete A R., Chen J., Chen Y., Yan G. and Zhang X., 2006, Analysis of NDVI and scaled difference vegetation index retrievals of vegetation fraction, *Remote Sensing of Environment*, 101(3), pp. 366-378.
- Jin S. and Sader S A., 2005, MODIS time-series imagery for forest disturbance detection and quantification of patch size effects, *Remote Sensing of Environment*, 99(4), pp. 462-470.
- Lunetta R S., Knight J F., Ediriwickrema J., Lyon J G. and Worthy L D., 2006, Land-cover change detection using multi-temporal MODIS NDVI data, *Remote Sensing of Environment*, 105(2), pp. 142-154.
- Pfeiffer D U. and Hugh-Jones M., 2002, Geographical information systems as a tool in epidemiological assessment and wildlife disease management, *Revue Scientifique et technique De L Office International Des Epizooties*, 21(1), pp. 91-102.
- Schwarz M. and Zimmermann N E., 2005, A new GLM-based method for mapping tree cover continuous fields using regional MODIS reflectance data, *Remote Sensing of Environment*, 95(4), pp. 428-443.
- Suzan G., Giermakowski J T., Marce E., Suzan-Azpiri H., Armien B. and Yates T L., 2006, Modelling hantavirus reservoir species dominance in high seroprevalence areas on the Azuero peninsula of Panama, *American journal of Tropical Medicine and Hygiene*, 74(6), pp. 1103-1110.
- Xiao X., Boles S., Froking S., Li C., Babu J Y., Salas W. and Moore III B., 2006, Mapping paddy rice agriculture in south and southeast Asia using multi-temporal MODIS images, *Remote Sensing of Environment*, 100(1), pp. 95-113.

## ACKNOWLEDGEMENTS

Acknowledgements must also be made of the National Institute of Health, National Science Foundation, USA, through which the funding for this research was provided, and also the contribution of our Chinese co-workers during fieldwork periods who provided invaluable support and assistance.

WEB-BASED MODEL FOR ANALYSIS OF TIME SERIES REMOTELY SENSED DATA

Ramirez, A.<sup>ab</sup>, Armitage, R.P.<sup>b</sup>, Danson, F.M.<sup>b</sup>, Marston C.G.<sup>b</sup>, Ogunbadewa, E.Y.<sup>b</sup> and Yebra, M.<sup>c</sup>

<sup>a</sup>Computer Science Department, Universidad Católica Nuestra Señora de la Asunción, Asunción, Paraguay  
<sup>b</sup>Centre for Environmental Systems Research, University of Salford, Manchester, UK  
<sup>c</sup>Department of Geography, University of Alcala, Spain  
A.Ramirez@salford.ac.uk

KEY WORDS: Web-based model, Interoperability, Time-series

ABSTRACT:

Powerful computer-based tools exist to process and analyse data collected by terrestrial remote sensing scientists, but in many cases there is a lack of interoperability between the processing tools which leads to problems for application scientists. A Web-based model is introduced to address the problem of interoperability by developing a data model which allows integration of both available sources of data and analytical tools. The application is flexible in terms of functionality, allowing scientists to produce their own data sets, add user-specific tools and create customized output according to their needs. The value of the proposed tool for the research community is that it will remove the necessity for the scientist to be involved in how the data are managed or formatted, and leave them to focus on data analysis and interpretation.

1. INTRODUCTION

Scientists often need to interpret a large amount of data to draw conclusions about certain phenomena. This interpretation process requires the use of different computer based tools to address different aspects of a research problem. Addressing a particular research topic demands not only the use of existing tools, but also the production of programming solutions in order to complement what has already been done. This work introduces a framework that consists of a Web-based model, which in the first instance has been implemented for the analysis of MODIS time series data sets, but may be adapted for other applications.

2. COMPONENTS AND FUNCTIONALITIES OF THE WEB BASED MODEL

The schematic diagram shown in Figure 1 identifies the components of the Web-based model proposed in this work and the interaction between them. The scientists and programmers can interact with both the database and the web based interface in order to prepare the data and add the required functionalities according to a given research topic. The integration of external sources of data, as well as existing data processing and analysis tools is also allowed.

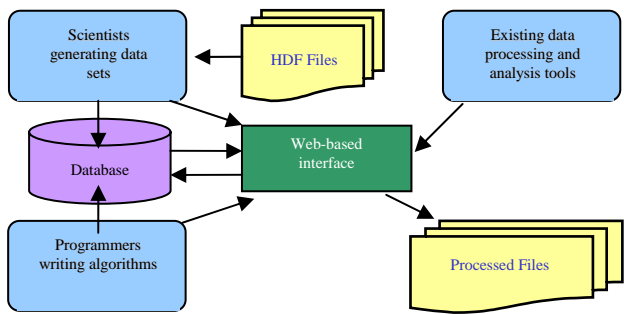


Figure 1: Schematic diagram of the Web-based model

The functionalities of the model presented in this work and their current status are depicted in Table 1.

FUNCTIONALITY	STATUS
Database creation and maintenance	The creation of data sets is already available, whereas the developing of maintenance features is still in progress.
Integration of existing data and processing tools	The automated generation of scripts for the Modis Reprojection Tool (MRT) is already implemented and the integration of other ancillary tools is still in progress.
Modis data edition	Basic edition capabilities are already implemented for the Modis Cloud Mask Product.
Modis data analysis and processing	Analysis and processing of Modis Cloud Mask Product is already implemented.
Report generation with graphs, charts and tables	The developing of report generation capabilities is still in progress.

Table 1. Functionalities of the Web based model

3. A DATABASE APPROACH

Relational Database Systems provide a method for storing data in an application-independent manner, which means that the data is held in such a way that modifications to the structure of the database will not affect any of the programs used to access the data. In a different approach, the same information may be held in several files and directories. Apart from wasting disk space, this makes the operations on the data more time consuming.



The idea behind using a Database System for storing MODIS data relies on the fact that within a database the data is stored in way that makes it easily accessible. Another key concept of this approach is flexibility, as developments can progress around a database in an incremental way.

The Relational Database System chosen for this work was Oracle 10g Express Edition (Oracle Database XE) which is free to develop, deploy and distribute. The database was tested in both Windows XP and Unix-based operating systems. Additional tests were made using MySQL and PostgreSQL which are both open source database systems.

3.1 Building Datasets

The model presented in this work allows scientists to produce their own datasets which can be processed at any time from its creation. Metadata are used to describe the information associated with these datasets. In fact, metadata describes how and where a particular set of data was acquired, and how the data is formatted. This gives relevant information not only to the scientists, but also to the programmers, who are developing the different functionalities within the model, in order to interact with the data. For example, an image is just a matrix of numbers without associated metadata to describe what is being represented.

4. WORKING EXAMPLE: CLOUD COVER DATA

As a working example, we focused on the Modis Cloud Mask Product which indicates whether a given view of the earth surface is obstructed by clouds or optically thick aerosol. All Modis Standard Products are in the Hierarchical Data Format (HDF) which is a physical file format for storing and sharing scientific data (Weaver and Singh, 2002). The Cloud Mask Product is generated at 1 kilometre and 250 metres spatial resolutions. There are two Modis Cloud Mask data product files: MOD35\_L2, containing data collected from the terra platform, and MYD35\_L2, containing data collected from the Aqua platform (Modis, 2007).

4.1 Modis Data Processing Tools

Tools for working with Modis data are freely available from the Internet. A number of these tools were integrated into the framework being developed (Table 2).

Tool	Description	Limitations
Modis Reprojection Tool (MRT)	Tool for reprojecting Modis images into standard map projections.	Not suitable for processing a large amount of images at once.
HDF View	Tool for browsing and editing HDF files.	Very basic editing capabilities.
HDF Tool	Multifunctional data processing and visualization tool for Modis data.	Not suitable for processing a large amount of images at once.

Table 2. Modis data processing tools used in this research

4.2 The Modis Cloud Mask Scientific Data Set

The Modis Cloud Mask Scientific Data Set (SDS) is part of the science parameters of the Modis Cloud Mask Product and contains the cloudiness information. Each pixel in the Cloud Mask is assigned 6 bytes (48 bit array). Individual bits or group of bits are set to denote various cloud conditions and characteristics for that pixel. Table 3 gives a description of the information stored in the first byte of the Cloud Mask SDS.

Bits	Field Description	Bit Interpretation Key
0	Cloud Mask Flag	0 = Not Determined 1 = Determined
1-2	Unobstructed FOV Quality Flag	0 = Confident Cloudy 1 = Probably Cloudy 2 = Probably Clear 3 = Confident Clear
3	Day / Night Flag	0 = Night 1 = Day
4	Sunglint Flag	0 = Yes 1 = No
5	Snow / Ice Background Flag	0 = Yes 1 = No
6-7	Land / Water Background Flag	0 = Water 1 = Coastal 2 = Desert 3 = Land

Table 3. First Byte of the Cloud Mask Scientific Data

The information encoded in the Unobstructed FOV Quality Flag has four possible combinations, as can be seen in Table 4. This information indicates the probability of clear sky for every pixel in the image.

Value of Bit 2	Value of Bit 3	Bit Interpretation Key
0	0	Cloud
1	0	66% Probability of Clear
0	1	95% Probability of Clear
1	1	99% Probability of Clear

Table 4. Possible values of the Unobstructed FOV Quality Flag

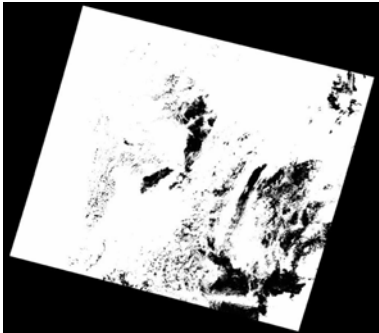
4.3 Bit Extraction Process

An algorithm was written to perform the bit extraction. It takes Modis Cloud Mask Product file as an input, while the output overwrites the value of the first byte of the Cloud Mask SDS for every pixel in the image, taking into account only the values of the second and third bit which have the relevant information.

The image in Figure 2 covers the United Kingdom and surrounding areas and shows the information stored in the first byte of the Cloud Mask SDS (Table 3) which corresponds to a Modis Cloud Mask Product HDF file. The resulting image after performing the bit extraction is shown in Figure 3.



Figure 2. Image before performing the bit extraction



Confident Clear	Probably Clear	Probably Cloudy	Confident Cloudy

Figure 3. Image after performing the bit extraction

5. DATA ANALYSIS

After processing a set of images corresponding to a given year, two stacks of binary files were produced with the intention of calculating the cloud cover probability in a given region. The pixel values of the images within the first stack indicate whether the Cloud Mask Algorithm was executed or not. Whereas the pixels values of the images within the second stack indicate cloudy areas or a high probability of clear sky. The analysis process is shown in Figure 4.

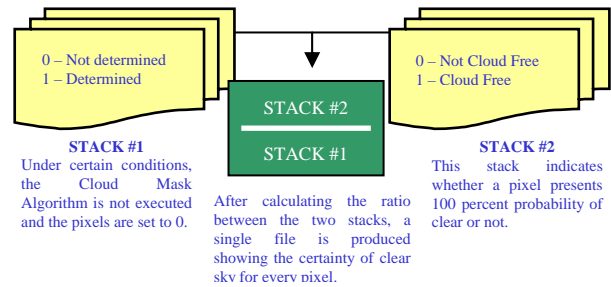


Figure 4. Data analysis process

6. RESULTS

The values of the pixels in the images (Figure 5, Figure 6) show the percentage of cloudy days across England, Scotland and Wales corresponding to January and June 2005. The darker areas suggest higher probability of clouds, while the brighter areas indicate higher probabilities of clear sky. The range for

January 2005 is 0-41% and the range for September 2005 is 0-65%.



Probability of clear sky				
Low				High

Figure 5. January 2005



Probability of clear sky				
Low				High

Figure 6. June 2005

## 7. CONCLUSIONS

After processing remotely sensed data within the framework proposed, the following advantages are noted:

- Easy creation and maintenance of large data sets.
- Faster processing of data sets.
- Flexibility for integrating existing ancillary tools.
- Easily adaptable programming solutions to existing processes.

The model proposed in this work has some limitations that are being addressed in order to improve the overall performance. The redundancy in the information stored in the database will be reduced after optimizing the data analysis process. The integration of existing data processing and analysis tools has also to be improved.

Further work will expand the model in order to perform the processing of other Modis product files. We will continue to test the bit-extraction algorithm on other years, and we will also work on speeding up the processing time of the images which will allow faster processing of data for longer periods of time.

## REFERENCES

Modis Atmosphere. [http://modis-atmos.gsfc.nasa.gov/MOD35\\_L2/index.html](http://modis-atmos.gsfc.nasa.gov/MOD35_L2/index.html) (accessed 3<sup>rd</sup> April 2007).

Weaver, R., Singh, S., 2002. Extracting and Viewing Bit-Level Metadata in EOS Files. *Earth Science Technology Conference – Pasadena, CA (USA)*.

## ACKNOWLEDGEMENT

This research was funded by the EU Alfa programme ICONE under grant AML/19.0902/97/0666/II-0380-FA-FI.

# Comparison of Feature Selection Techniques for SVM Classification

Gidudu Anthony<sup>a</sup> and Heinz Ruther<sup>b</sup>

<sup>a</sup> Dept. of Surveying, Makerere University, P. O. Box 7062, Kampala, Uganda - agidudu@tech.mak.ac.ug

<sup>b</sup> Dept. of Geomatics, University of Cape Town, 7701, Rondebosch, Cape Town, South Africa - hruther@ebe.uct.ac.za

**Key Words:** *Support Vector Machines, Feature Selection, Exhaustive Search, Population Based Incremental Learning*

## Abstract:

The use of satellite imagery in the derivation of land cover information has yielded immense dividends to numerous application fields such as environmental monitoring and modeling, map making and revision and urban studies. The extraction of this information from images is made possible by various classification algorithms each with different advantages and disadvantages. Support Vector machines (SVMs) are a new classifier with roots in statistical learning theory and their success in fields like machine vision have drawn the attention of the remote sensing community. Previous studies have focused on how SVMs compare with traditional classifiers such as maximum likelihood and minimum distance to means classifiers. They have also been compared to newer generation classifiers such as decision trees and artificial neural networks. In this research the understanding of the application of SVMs to image classification is furthered by proposing feature selection as a way in which remote sensing data can be optimized. Feature selection involves selecting a subset of features (e.g. bands) from the original set of bands that captures the relevant properties of the data to enable adequate classification. Two feature selection techniques are explored namely exhaustive search and population based incremental learning. Of critical importance to any feature selection technique is the choice of criterion function. In this research a new criterion function called Thornton's separability index has been successfully deployed for the optimization of remote sensing data for SVM classification.

## 1.0 INTRODUCTION

Feature selection is defined as "the search for a subset of the original measurement features that provide an optimal trade off between probability error and cost of classification" (Swain and Davis, 1978). It involves selecting a subset from the original set of features (e.g. bands) that captures the relevant properties of the data (Gilad-Bachrach et al, 2004) to enable adequate classification (Wu and Linders, 2000). Feature selection is, in part, motivated by Hughes phenomenon (Hughes, 1968), which postulates that in the presence of a limited training sample size, contrary to intuition, the mean accuracy doesn't always increase with additional measurements. Rather it exhibits a peaking effect i.e. the accuracy will increase until a certain point beyond which increase in additional measurement will yield no significant improvement in classification accuracy (Muasher and Landgrebe, 1982). The challenge therefore is to identify the subset of bands which will yield similar, if not better, accuracies as compared to when all the bands are used in a classification task. In effect, feature selection is an optimization task. In this research two feature selection techniques namely exhaustive search and population based incremental learning (PBIL) are investigated in as far as their ability to optimize remote sensing data for Support Vector Machine (SVM) Classification.

## 2.0 SUPPORT VECTOR MACHINES

Support Vector Machines (SVMs) are a new supervised classification technique that has its roots in Statistical Learning Theory (Vapnik, 1995). Having taken root in machine vision fields such as character, handwriting digit and text recognition (Vapnik, 1995; Joachims, 1998), there has been increased interest in their application to image classification (Huang et al, 2002; Mahesh and Mather, 2003). SVMs are non-parametric hence they

boast the robustness associated with Artificial Neural Networks (Foody and Mathur, 2004a; Foody and Mathur, 2004b) and other nonparametric classifiers.

SVMs function by nonlinearly projecting the training data in the input space to a feature space of higher (infinite) dimension by use of a kernel function. This results in a linearly separable dataset that can be separated by a linear classifier. This process enables the classification of remote sensing datasets which are usually nonlinearly separable in the input space. In many instances, classification in high dimension feature spaces results in overfitting in the input space, however, in SVMs, overfitting is controlled through the principle of structural risk minimization (Vapnik, 1995). The empirical risk of misclassification is minimised by maximizing the margin between the data points and the decision boundary (Mashao, 2004). In practice this criterion is softened to the minimisation of a cost factor involving both the complexity of the classifier and the degree to which marginal points are misclassified, and the tradeoff between these factors is managed through a margin of error parameter (usually designated  $C$ ) which is tuned through cross-validation procedures (Mashao, 2004). The functions used to project the data from input space to feature space are sometimes called kernels (or kernel machines), examples of which include polynomial, Gaussian (more commonly referred to as radial basis functions) and sigmoid functions. Each function has parameters which have to be determined prior to classification and they are usually determined through a cross validation process. A deeper mathematical treatise of SVMs can be found in Christianini (2002), Campbell (2000) and Vapnik (1995).

### 3.0 FEATURE SELECTION

Feature selection may be categorized into wrapper and filter models (Kohavi and John, 1991). The wrapper model selects features by directly optimizing the performance of the classifier i.e. this model seeks the subset of features yielding the best classification accuracy result. Since many subsets may have to be tried out, this approach is computationally inefficient (Kavzoglu and Mather, 2002).

Filter models are described as feature selection algorithms which use a performance metric (i.e. evaluation function) based entirely on the training data without reference to the classifier for which the features are to be selected (Kavzoglu and Mather, 2002). Examples of criterion functions encountered in remote sensing literature include statistical separability measures such as Wilk's  $\Lambda$ , Hotelling's  $T^2$  and more commonly separability indices. Separability indices give a measure of how separable training data classes are hence giving an indication of how easily the dataset may be correctly classified.

Pudil and Somol (2005) further categorizes feature selection methods into optimal and suboptimal methods. Optimal methods search for the optimal subset out of all possible subsets e.g. exhaustive search methods. Suboptimal methods on the other hand make a trade off between the optimality of a selected subset and computational efficiency. Some of the search methods in this regard include greedy eliminative search, random search and guided random search methods. In this paper we consider a guided random search method called Population Based Incremental Learning (PBIL).

#### 3.1 Exhaustive Search Method

The exhaustive search method (also called enumerative search method) works by considering all possible band combinations by way of calculating their separability indices. Although this search method guarantees the optimality of solution, it poses the problem of being computationally prohibitive (Pudil and Somol, 2005). For a dataset with  $d$  features (i.e. bands),  $2^d - 1$  combinations are possible. This method is practicable if the number of bands is less than 10. The use of 10 or more bands would be costly in terms of computational speed. Dutra and Huber (1999) however are of the opinion that advancements in computer technology should eventually render exhaustive search an operational reality. This, including the fact that the datasets considered in this research had less than ten bands, influenced the authors decision to consider this method.

#### 3.2 PBIL

In the random search method, a subset of features (bands) is taken at random and their separability index calculated. If many bands are being considered, the chances of hitting on the optimum subset in a limited random search will be small. However if good separability indices are possible from a variety of band combinations, there is a higher probability of encountering one of the optima quickly. The time it takes to converge to the optimum subset can be dramatically reduced by modifying the random search to a guided random search. The guided random/stochastic search method is a randomized search in which attention is adaptively increased to focus on the band combinations that return promising results. Population Based Incremental Learning is a

genetic algorithm that can be used to perform a guided random search.

Genetic algorithms are motivated by the evolutionary biology principle of natural selection and genetics. From a biological context, all living organisms are made up of cells characterized by a set of chromosomes. Chromosomes consist of genes that encode peculiar traits. During reproduction, genes from parents combine to form a new chromosome with traits from either parent. According to Darwin's theory, this breeding results in the fit traits being propagated at the expense of the weaker ones which end up being filtered away. It is on this basis that genetic algorithms are tailored.

A genetic algorithm functions by randomly generating a population of 'chromosomes'. The 'chromosomes' are of equal length and may be represented by a special coding technique e.g. binary code (Tso and Mather, 2001). The fitness level of each 'chromosome' is then calculated based upon which random pairs of 'chromosomes' are bred to generate a new pool of 'chromosomes'. Breeding is effected through two mechanisms called crossover and mutation. Crossover involves the exchange of genes between two parent 'chromosomes' whereas mutation is carried out by randomly changing binary values that are representative of genes/traits. Crossover and mutation facilitate genetic diversity without which the genetic algorithm would settle into a sub-optimal state. The process of selecting and breeding define a generation. The progression of genes from one generation to another is dependent on how well the 'chromosomes' pass a fitness test. The 'chromosomes' with high fitness levels may be programmed to have a higher probability of selection to ensure that strong traits are passed on to the next generation. The number of generations may be fixed or the breeding process allowed to continue until a satisfactory level of fitness is attained.

Population Based Incremental Learning (PBIL) is an adaptation of genetic algorithms whereby the population is replaced by a probability vector instead of storing each possible solution explicitly. It is this probability vector that is updated when one progresses from one generation to another rather than the fixed population (Gosling and Crompton, 2004).

Linking feature selection to PBIL, the elements of the probability vector define the probability of selection of each feature. The idea is to use PBIL to determine the subset of bands which when classified will give as good classification results (if not better) than when all bands are utilized. In the absence of *a priori* knowledge of the importance of the bands, the probability vector is initialized to a value for example 0.5. This would mean that in a randomized selection operation, each band has an equal chance of being chosen.

In each generation a population of trials is created by sampling the probability vector with a random vector. This ensures that the inclusion of a given feature follows the probabilities in the probability vector. The fitness of each trial is determined by calculating the separability index and the trial yielding the highest index is identified as the best (chromosome in genetic algorithm technology) in that generation. Based on these results the probability vector is adjusted to reflect the best trial. If for example bands 1, 3 and 4 ended up being the best trials out of 9 bands, the probability vector corresponding to these bands would be increased slightly (by 10% from 0.5 to 0.55) while the other values



would be reduced in the same proportion (from 0.5 to 0.45). This enables the subsequent generation to contain a greater proportion of trials that resemble to some degree the best trial of the previous generation.

Before proceeding to the next generation, mutation is applied to the probability vector to increase the search space in an attempt to avoid convergence towards a local optimum. Mutation may be implemented by a secondary adjustment to the probability vector in which the vector values are relaxed towards the neutral value (0.5 in this case) (Gosling et al, 2004).

Ultimately, after a series of generations the separability index of the best trial in each generation improves until the global optimum emerges. The final probability vector will also have converged towards 0 or 1 indicating the bands that had a higher or lower probability of being selected. The best trial at the end of the whole process would then represent the subset of bands with potential to yield classification accuracies comparable to those derived from using all the bands

The interest in PBIL over the traditional genetic algorithm stems from the fact that PBIL results have been found to be more accurate, and are attained faster than the traditional genetic algorithms, both in terms of the number of evaluations performed and the clock speed. This gain in clock speed is attributed to the simplicity of the algorithm (Baluja, 1994). In view of this documented simplicity and associated accuracy, PBIL was selected to facilitate feature selection in this research.

### 3.3 Separability Indices

The choice of adopted separability index, i.e. evaluation function, should be related to the behavior of the error made by the classifier used if the optimal subset is to be selected (Bruzzone and Serpico, 2000). Separability analysis is performed on the training data to give an indication of the expected classification error for various band combinations (Swain and Davis, 1978). However, finding an appropriate definition of interclass separability is not trivial (Schowengerdt, 1997).

In light of the fact that nonparametric classifiers are gaining prominence in remote sensing studies, there is a corresponding need for separability measures tailored around the uniqueness of these nonparametric classifiers. Whereas Kavzoglu and Mather (2002) have used the Mahalanobis distance classifier to select features for artificial neural networks (which is a nonparametric classifier like the SVMs used in this research), this research proposes a separability index tailored for the uniqueness of nonparametric classifiers. This separability measure is called Thornton's separability index.

Thornton's separability index is defined as the fraction of data points whose classification labels are the same as those of their nearest neighbors. Thus it is a measure of the degree to which inputs associated with the same output tend to cluster together (Greene, 2001). Greene (2001) expresses this concept by the following formula:

$$\text{Thornton's separability index} = \frac{\sum_{i=1}^n (f(x_i) + f(x'_i) + 1) \bmod 2}{n} \quad (1)$$

Where  $x'$  is the nearest neighbor of  $x$   
 $n$  is the number of points.

With this separability measure, well separated classes will have high separability indices equal to or tending towards unity. As the clusters move closer to each other and points from opposing classes begin to overlap the index begins to fall (Greene, 2001). A separability index of zero, therefore, denotes totally mixed up classes. The interest in this separability measure stems from its simplicity, speed and the fact that it is nonparametric which augers well with the SVM classifier which is also nonparametric.

## 4.0 STUDY AREA

To carry out this research, two study areas were considered namely: Masai Mara in Northern Tanzania and Malmesbury located in the Western Cape Province of South Africa. The Masai Mara study area was sectioned off from the Mara River Basin. Based on prior field work, six land cover classes were sought namely: wetlands, water (lakes and rivers), Bush/shrub/trees, Grasslands, "bare ground" and Roads. For the Malmesbury dataset, three land cover classes were sought for namely fields, trees and built up areas. In both cases landsat imagery was used.

## 5.0 METHODOLOGY

### 5.1 Data Processing

For each dataset, sample data corresponding to known land cover was imported into Matlab for preparation and derivation of optimum SVM parameters through cross-validation. Cross validation involves dividing the sample data into training and testing data. The training data is then used to derive kernel parameters whose measure of efficiency was determined by how well they predicted the test data classes. The kernel parameters yielding the best prediction are considered optimum and are subsequently used to classify the image. For the polynomial kernel, polynomial degree and constant C were the sought after parameters while for the radial basis function the kernel width and constant C were the required parameters which needed to be determined. The OSU\_SVM Version 3.00 toolkit (developed at Oklahoma State University) was used to give Matlab SVM functionality. This toolbox was selected for its simplicity and ease of use.

### 5.2 Classification

SVMs are essentially a binary classification technique, however they can be adopted to handle the multiclassification tasks usually encountered in remote sensing research. To effect this, two common approaches are encountered in SVM literature. The first approach is called the 'one against one' approach and involves constructing a machine for each pair of classes resulting in  $N(N-1)/2$  machines. When applied to a test point, each classification gives one vote to the winning class and the point is labeled with the class having most votes. The second approach involves the 'one against all' approach where by the N class dataset is divided

into N two-class cases. Proponents of the ‘one against one’ approach contend that it has the advantage of avoiding highly unbalanced training data (Gualtieri and Cromp, 1998). It is however acknowledged that this approach involves constructing more SVMs as compared to the ‘one against all’ approach, hence it is more computer intensive. In this research, the ‘one-against-all approach’ was adopted. By implication therefore, different classes needed different kernel parameters. IDRISI Kilimanjaro Edition image processing software was then used to integrate the resultant class images into a land cover map. This land cover map was then georeferenced and subjected to accuracy assessment. The accuracy measure used was the overall accuracy, which gives a measure of agreement between a derived map and ground truth data.

5.3 Feature Selection

The exhaustive search method was used to compare all possible band combinations with the original band set. For both study areas 63 combinations were considered. The measure of comparison was Thornton’s separability index. For each study area and each land cover type, the separability index (S.I) of each subset was compared with the S.I of the original bands. The subset with the least number of bands yielding the closest S.I to the original bands was selected for the classification process. This subset of bands was then used to derive optimum SVM parameters mentioned previously, and subsequently used to classify the study area.

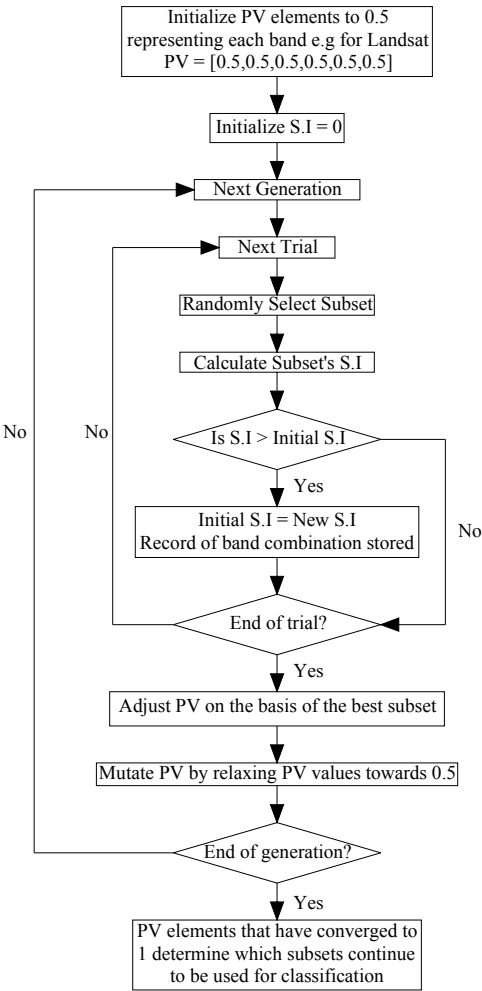
The Figure 1 shows a simplified flow chart of the algorithm used to effect PBIL classification technique.

5.4 Comparison of Feature Selection Techniques

For each study area overall accuracies were compared before and after feature selection. The significance of these differences was determined using a binomial test of significance at the 95% confidence level (critical Z value = 1.96). It is based on these comparisons that conclusions were drawn about the effectiveness and efficiency of the investigated optimization techniques.

6.0 RESULTS AND DISCUSSIONS

The Tables 1 and 2 show the selected optimum bands following the exhaustive search (ES) and PBIL for Masai Mara and Malmesbury study areas respectively. One observation from Table 1 is that ES resulted in fewer bands than PBIL. Using fewer bands for classification has the advantage of reducing the time taken to effect classification. In Table 2 on the other hand, it is only in the class ‘built up areas’ that ES has fewer bands as compared to PBIL. In the other classes i.e. ‘trees’ and ‘fields’ both ES and PBIL have resulted in identifying the same four bands.



PV – Probability Vector, SI – Separability Index

Figure 1: PBIL methodology

Table 1: Landsat Bands selected for Masai Mara

Class	E.S	PBIL
Wetlands	1, 2 & 6	3, 4, 5 & 7
Water	5	1 & 7
Bush/Shrub/Trees	3, 4 & 5	1, 3, 4, 5 & 7
Grasslands	3 & 4	3, 4 & 5
Bare ground	3 & 5	3, 4 & 5
Roads	2 & 5	3, 4 & 5

Table 2: Landsat Bands selected for Malmesbury

Class	E.S	PBIL
Built up areas	2, 4, 5 & 6	1, 3, 4, 5 & 6
Trees	3, 4, 5 & 6	3, 4, 5 and 6
Fields	1, 3, 4 and 5	1, 3, 4 & 5

Table 3 depicts the overall classification accuracies before (Pre-FS) and after feature selection (ES and PBIL). From this table it can be seen that for the Masai Mara dataset, overall accuracy has improved following the application of the polynomial SVM classifier to the results of ES and PBIL. On the other hand, the

application of the RBF SVM classifier to both feature selection techniques has resulted in reduced overall accuracy. For the Malmesbury dataset, the polynomial SVM classifier has yielded reduced overall accuracies when applied to ES and PBIL results while the RBF SVM classifier has yielded improved overall accuracies.

Table 3: Overall accuracies for both datasets

	Masai Mara			Malmesbury		
	Pre-FS	ES	PBIL	Pre-FS	ES	PBIL
SVM						
Polynomial	0.67	0.71	0.75	0.69	0.65	0.66
RBF	0.83	0.64	0.79	0.65	0.66	0.66

Tables 4 and 5 give further analysis of these results by giving a summary of the significance of the differences between the overall accuracies before and after feature selection. For the Masai Mara dataset, feature selection has resulted in significantly better overall accuracies when the polynomial SVM is used, while yielding significantly worse overall accuracies when the RBF classifier is applied. In the case of the Malmesbury dataset, the differences in the overall accuracy using the results of feature selection are insignificant.

Table 4: Assessment of overall accuracies for Masai Mara

SVM	ES		PBIL	
	Significance	Comment	Significance	Comment
Polynomial	4.65	Significantly Better	11.07	Significantly Better
RBF	-23.74	Significantly Worse	-5	Significantly Worse

Table 5: Assessment of overall accuracies for Malmesbury

SVM	ES		PBIL	
	Significance	Comment	Significance	Comment
Polynomial	- 0.55	Insignificant	- 0.37	Insignificant
RBF	0.18	Insignificant	0.18	Insignificant

Of the two feature selection methods, ES is more computer intensive and hence more time consuming given that the S.Is of all possible combinations have to be evaluated before a ranking process enables the identification of the optimal subset. The efficiency of the ES technique can be improved by restricting the search to the subset of bands that is greater than the datasets intrinsic dimensionality (Dean and Hoffer, 1983). For landsat, the intrinsic dimensionality is two or three. This implies that to make ES more competitive, the search for optimal subset, only band combinations with three or more features need be considered.

On trial as well in this search was Thornton’s separability index and on the balance of the results posted, it has performed well.

7.0 CONCLUSIONS

From the results, both Exhaustive Search and Population Based Incremental Learning are appropriate feature selection techniques for Support Vector Machine classification and so is Thornton’s separability index an appropriate criterion function. The authors would like to recommend that a logical progression of this

research would be to investigate appropriate feature selection techniques for emerging multi-classifier SVMs.

ACKNOWLEDGEMENTS

The authors would like to acknowledge the financial support of the German Academic Services (DAAD) and Makerere University – Uganda. They would also like to extend an arm of gratitude to the Council for Geoscience, Geological Survey South Africa who availed the images for this research.

REFERENCES

Baluja, S. 1994. *Population Based Incremental Learning – A Method for integrating Genetic Search Based Function Optimization and Competitive Learning*. Technical Report No. CMU-CS-94-163. (Pittsburgh, Pennsylvania: Carnigie Mellon University).

Bruzzone, L., and Serpico, S. B. 2000. A technique for feature selection in multiclass problems. *International Journal of Remote Sensing*, **21**, 549–563.

Campbell, C. 2000. *An Introduction to kernel Methods, Radial Basis Function Networks: Design and Applications*. (Berlin: Springer Verlag).

Christianini, N., and Shawe-Taylor, J. 2000. *An introduction to support vector machines: and other kernel-based learning methods*. (Cambridge and New York: Cambridge University Press).

Dean, M. E., and Hoffer, R. M. 1983. Feature Selection Methodologies Using Simulated Thematic Mapper Data. In *Proceedings of the 9<sup>th</sup> International Symposium of Machine Processing of Remotely Sensed Data*. Pp: 347 – 356, Purdue University, West Lafayette, Indiana. 21<sup>st</sup> – 23<sup>rd</sup> June 1983.

Dutra, L., and Huber, R. 1999. Feature Extraction and selection for ERS-1/2 InSAR Classification. *International Journal of Remote Sensing*, **20**, 993 – 1016.

Foody, M. G. 2002a. Hard and soft classifications by a neural network with a non-exhaustively defined set of classes. *International Journal of Remote Sensing*, **23**, 3853 – 3864.

Foody, M. G. 2002b. Status of land cover classification accuracy assessment. *Remote Sensing of Environment*, **80**, 185 – 201.

Gilad-Bachrach, R., Navot, A., and Tishby, N. 2004. Margin based Feature Selection – Theory and Algorithms. In *Proceedings of the 21<sup>st</sup> International Conference on Machine Learning*, Banff, Alberta, Canada. 4<sup>th</sup> – 8<sup>th</sup> July 2004.

Gosling, T., Nanlin, J., and Tsang, E. 2004. *Population Based Incremental Learning Versus Genetic Algorithms: Iterated Prisoners Dilemma*. Technical Report No. CSM-401. (Essex: University of Essex, England).

Greene, J. 2001. Feature subset selection using Thornton’s separability index and its applicability to a number of sparse proximity-based classifiers. In *Proceedings of the 12<sup>th</sup> Annual Symposium of the Pattern Recognition Association of South Africa*. November 2001

Huang, C., Davis, L. S., and Townshed, J. R. G. 2002. An assessment of support vector machines for land cover

classification. *International Journal of Remote Sensing*, **23**, 725–749.

Hughes, G. F. 1968. On the mean accuracy of statistical pattern recognizers. *IEEE Transactions on Information Theory*, **14**, 55–63.

Joachims, T. 1998. Text categorization with support vector machines—learning with many relevant features. In *Proceedings of the 10<sup>th</sup> European Conference on Machine Learning, Chemnitz, Germany*. (Berlin: Springer), pp. 137–142.

Kavzoglu, T. and Mather, P. M. 2002. The role of feature selection in artificial neural network applications. *International Journal of Remote Sensing*, **15**, 2919–2937.

Kohavi, R., and John, G. 1997. Wrapper for feature subset selection. *Artificial Intelligence*, **97**, 273 – 324.

Mahesh P., and Mather, P. M. 2003. Support Vector classifiers for Land Cover Classification. In *Proceedings of the 6<sup>th</sup> Annual International Conference, Map India 2003, New Delhi, India*. 28<sup>th</sup> – 31<sup>st</sup> January 2003.

Mashao D. 2004. Comparing SVM and GMM on parametric feature-sets. In *Proceedings of the 15<sup>th</sup> Annual Symposium of the Pattern Recognition Association of South Africa*, Cape Town, South Africa. 27<sup>th</sup> – 29<sup>th</sup> November 2004.

Muasher, M. J., and Landgrebe, D. A. 1982. A binary tree feature selection technique for limited training sample size. In *Proceedings of the 8<sup>th</sup> International Symposium of Machine Processing of Remotely Sensed Data*. Purdue University, West Lafayette, Indiana. 7<sup>th</sup> – 9<sup>th</sup> July 1982. Pp. 130 – 137

Pudil, P., and Somol, P. 2005. An Overview of Feature Selection Techniques in Statistical Pattern Recognition. In *Proceedings of the 16<sup>th</sup> Annual Symposium of the Pattern Recognition Association of South Africa* Nov 2005.

Schowengerdt, R. 1997. *Remote Sensing: Models and Methods for Image Analysis* (2<sup>nd</sup> Edition). (San Diego: Academic Press).

Swain, and P.H., and Davis, S. M. 1978. *Remote Sensing: The Quantitative Approach*. (New York : McGraw-Hill ).

Tso, B., and Mather, P. 2001. *Classification Methods for Remotely Sensed Data*. (London and New York: Taylor and Francis).

Vapnik, V. N. 1995. *The Nature of Statistical Learning Theory*. (New York: Springer-Verlag).

Wu, D., and Linders, J. 2000. Comparison of three different methods to select features for discriminating forest cover types using SAR imagery. *International Journal of Remote Sensing*, **21**, 2089 – 2099.

# CANOPY WATER CONTENT RETRIEVAL FROM HYPERSPECTRAL REMOTE SENSING

J.G.P.W. Clevers, L. Kooistra & M.E. Schaepman

Wageningen University, Centre for Geo-Information, P.O. Box 47,  
6700 AA Wageningen, The Netherlands  
jan.clevers@wur.nl

Commission VII, WG VII/1

**KEY WORDS:** Remote Sensing, Hyperspectral, Canopy Water Content, First Derivative, PROSPECT, SAILH, Fieldspectrometer

## ABSTRACT:

Biogeochemical processes in plants, such as photosynthesis, evaporation and net primary production, are directly related to foliar water. Therefore, canopy water content is important for the understanding of the terrestrial ecosystem functioning. Spectral information related to the water absorption features at 970 nm and 1200 nm offers possibilities for deriving information on leaf and canopy water content.

Hyperspectral reflectance data representing a range of canopies were simulated at the leaf level using the PROSPECT model and at the canopy level using the combined PROSPECT+SAILH model. The simulations were in particular used to study the spectral information related to the water absorption features at about 970 nm and 1200 nm. At the leaf level this information was related to the leaf water content. At the canopy level this information was related to the leaf area index (LAI) and the canopy water content (CWC). In particular derivative spectra close to these absorption features showed a strong predictive power for the leaf and canopy water content. Ratio indices defining the absorption features had a smaller predictive power.

The feasibility of using information from the water absorption features in the near-infrared (NIR) region of the spectrum was tested by estimating canopy water content for two test sites with different canopy structure. The first site was a homogeneously managed agricultural field with a grass/clover mixture and with very little variation within the field, being part of the Droevendaal experimental farm at Wageningen, the Netherlands. The other site was a heterogeneous natural area in the floodplain Millingerwaard along the river Waal in the Netherlands. Spectral information at both test sites was obtained with an ASD FieldSpec spectrometer during the summer of 2004 and 2005, respectively.

Individual spectral bands and traditional vegetation indices based on red and NIR spectral bands yielded moderate estimates for CWC. Ratio indices describing the absorption features clearly yielded better results. Best results were obtained for the derivative spectra. Highest correlation with CWC was obtained for the derivative spectrum at the slopes of the first water absorption feature. However, here absorption by atmospheric water vapour also should be taken into account, yielding a preference for the right shoulder at about 1040 nm.

## 1. INTRODUCTION

The canopy water content, being the difference between fresh and dry matter weight, is of interest in many applications. Biogeochemical processes, such as photosynthesis, evaporation and net primary production, are directly related to foliar water and are moreover commonly limited by water stress. Thus, canopy water content is important for the understanding of the terrestrial ecosystem functioning (Running and Coughlan, 1988).

Water absorption features for liquid water can be found at approximately 970, 1200, 1450 and 1950 nm (Curran, 1989). The features at 1450 and 1950 nm are most pronounced. However, at about 1400 and 1900 nm also broad absorption features occur due to water vapour in the atmosphere. As a result, hardly any radiation is reaching the Earth's surface and, thus, the liquid water bands at 1450 and 1950 nm cannot be used. The features at 970 and 1200 nm are not that pronounced, but still clearly observable (Danson *et al.*, 1992; Sims and Gamon, 2003). Therefore, these offer interesting possibilities for deriving information on leaf and canopy water content. However, in these regions also minor absorption features due to atmospheric water vapour occur at 940 and 1140 nm (Iqbal,

1983). These are shifted somewhat to shorter wavelengths in comparison to the liquid water bands caused by water in the canopy. Figure 1 illustrates the position of the liquid water absorption features in the near-infrared (NIR) region for some spectral measurements on grassland plots.

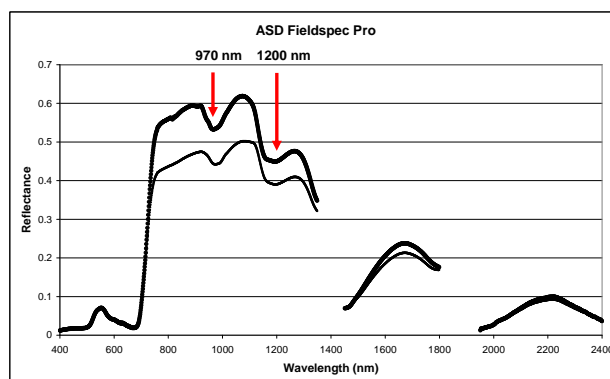


Figure 1. Example of two spectral signatures of grassland plots measured with the ASD FieldSpec Pro. The position of the water absorption features at 970 nm and 1200 nm are indicated.



At the leaf level use is often made of the leaf water content in terms of the so-called equivalent water thickness (EWT), defined as the quantity of water per unit leaf area in  $\text{g}\cdot\text{cm}^{-2}$ . At the canopy level the canopy water content (CWC) can be defined as the quantity of water per unit area of ground surface and thus is given in  $\text{g}\cdot\text{m}^{-2}$ :

$$CWC = LAI \times EWT \quad (1)$$

Thus far, a limited number of studies have developed spectral indices using the water absorption bands at 970 and 1200 nm for estimation of canopy water content. Danson *et al.* (1992) showed that the first derivative of the reflectance spectrum corresponding to the slopes of the absorption feature provides better correlations with leaf water content than those obtained from the direct correlation with reflectance. This was confirmed by Clevers and Kooistra (2006).

Peñuelas *et al.* (1993) focused on the 950-970 nm region and defined the so-called water band index (WI):

$$WI = \frac{R_{900}}{R_{970}}, \quad (2)$$

where  $R_{900}$  and  $R_{970}$  are the spectral reflectances at 900 and 970 nm, respectively.

Gao (1996) defined the normalised difference water index (NDWI) as:

$$NDWI = \frac{(R_{860} - R_{1240})}{(R_{860} + R_{1240})}, \quad (3)$$

where  $R_{860}$  and  $R_{1240}$  are the spectral reflectances at 860 and 1240 nm, respectively.

Finally, a continuum removal approach can be applied to the two absorption features at about 970 and 1200 nm. This is a way of normalizing the reflectance spectra (Kokaly and Clark, 1999). Subsequently, the band depth is calculated for each wavelength by calculating one minus the continuum removed spectra. From this spectral band depth, Curran *et al.* (2001) defined the maximum band depth, the area under the curve, and the maximum band depth normalised to the area of the absorption feature. Malenovsky *et al.* (2006) used the area under the curve normalised by the maximum band depth (ANMB) as an alternative index.

The objective of the present study is to compare different vegetation indices based on the water absorption features at 970 and 1200 nm in estimating the canopy water content. First, model simulations using the PROSPECT and SAILH radiative transfer models were used for studying the relationship between indices and leaf and canopy water content. Subsequently, field spectro-radiometer measurements obtained from two study sites (a cultivated grassland area and a natural area) were analysed.

## 2. MATERIAL AND METHODS

### 2.1 Study Sites and Field Data

The first study site concerns a grassland field with a mixture of grass and white clover at the 'Droevendaal' experimental farm

in Wageningen, the Netherlands. A total of 20 plots were defined within a 2.2 ha field. Plots were each 15 m long and 3 m wide and they were harvested using a plot-harvester on July 30<sup>th</sup>, 2004. Biomass (fresh weight) was determined with a built-in weighing unit on the harvester. Samples of the harvested material were oven dried for 72 hours at 70°C and dry matter weight as well as canopy water content was determined.

The second study site is a very heterogeneous natural area in the floodplain Millingerwaard along the river Waal in the Netherlands. This is a nature rehabilitation area, meaning that individual floodplains are taken out of agricultural production and are allowed to undergo natural succession. This has resulted in a heterogeneous landscape with river dunes along the river, a large softwood forest in the eastern part along the winter dike and in the intermediate area a mosaic pattern of different succession stages (pioneer, grassland, shrubs). Nature management (e.g., grazing) within the floodplain is aiming at improvement of biodiversity. Based on the available vegetation map of the area, 12 locations with specific vegetation structure types were selected. For each location a plot of 20 x 20 m was selected with a relatively homogeneous vegetation cover. End of June 2005 vegetation fresh biomass was sampled in three subplots per plot measuring 0.5 x 0.5 m. After drying for 24 hours at 70°C, vegetation dry matter weight and canopy water content were determined. Subsequently, the average canopy water content per plot was calculated.

### 2.2 Field Spectroradiometer Measurements

July 29<sup>th</sup>, 2004, a field campaign with an ASD FieldSpec Pro FR spectroradiometer was performed at site 1 (Wageningen). The spectroradiometer was deployed using a fiber optic cable with a 25° field of view. Measurement height above the plot was about 1 – 1.5 m. As a result, the field of view at the plot level was circular with a radius ranging from 0.22 – 0.33 m. About 10 measurements per plot were performed, whereby each measurement represents the average of 50 readings at the same spot. The sampling interval was 1 nm. Calibration was done by using a Spectralon white reference panel.

June 19<sup>th</sup>, 2005, a field campaign with an ASD FieldSpec Pro FR spectroradiometer was performed at site 2 (Millingerwaard). For every plot 12 measurements were performed according to the VALERI (Validation of Land European Remote sensing Instruments) sampling scheme (Morissette *et al.*, 2006), whereby each measurement was the average of 15 readings at the same spot. Measurement height was about 1 m above the vegetation. A Spectralon white reference panel was used for calibration.

After calculating average spectra per plot, the resulting spectra were smoothed using a 15 nm wide moving Savitsky-Golay filter (applying a second order polynomial fit within the window) to reduce instrument noise.

### 2.3 Reflectance Models

The PROSPECT model is a radiative transfer model for individual leaves (Jacquemoud and Baret, 1990). It simulates leaf spectral reflectance and leaf spectral transmittance as a function of leaf chlorophyll content ( $C_{ab}$ ), equivalent leaf water thickness (EWT) and a leaf structure parameter ( $N$ ). The most recent version of PROSPECT was used including leaf dry matter ( $C_m$ ) as a simplification for the leaf biochemistry (protein, cellulose, lignin).

The one-layer SAILH radiative transfer model (Verhoef, 1984) simulates canopy reflectance as a function of canopy parameters (leaf reflectance and transmittance, leaf area index and leaf inclination angle distribution), soil reflectance, ratio diffuse/direct irradiation and solar/view geometry (solar zenith angle, zenith view angle and sun-view azimuth angle). It was modified by taking the hot spot effect into account (Kuusk, 1991).

The output of the PROSPECT model can be used directly as input into the SAIL model. As a result, these models can be used as a combined PROSPECT-SAILH model. Simulations were performed at a 5 nm spectral sampling interval. Since the absorption features of leaf constituents are implemented in the PROSPECT model by means of look-up tables and not as continuous functions, simulated spectra have to be smoothed for calculating useful derivatives. Therefore, the simulated spectra were smoothed using a 15 nm wide moving Savitsky-Golay filter (applying a second order polynomial fit within the window).

The inputs for the PROSPECT simulations are shown in Table 1 and those for the combined PROSPECT-SAILH simulations are shown in Table 2.

PROSPECT parameters	Nominal values and range
Equivalent water thickness (EWT)	0.01 – 0.10 g.cm <sup>-2</sup> (step of 0.01)
Dry matter (C <sub>m</sub> )	0.005 / 0.010 / 0.015 g.cm <sup>-2</sup>
Structural parameter (N)	1.0 – 2.0 (steps of 0.25)
Chlorophyll a+b (C <sub>ab</sub> )	40 µg.cm <sup>-2</sup>

Table 1. Nominal values and range of parameters used for the leaf simulations with PROSPECT

SAILH parameters	Nominal values and range
Equivalent water thickness (EWT)	0.01 – 0.10 g.cm <sup>-2</sup> (step of 0.01)
Dry matter (C <sub>m</sub> )	0.005 g.cm <sup>-2</sup>
Structural parameter (N)	1.0 / 1.8 / 2.5
Chlorophyll a+b (C <sub>ab</sub> )	40 µg.cm <sup>-2</sup>
Leaf area index	0.5/ 1.0 / 1.5 / 2 / 3 / 4 / 5 / 6
Leaf angle distribution	Spherical / Planophile / Erectophile
Hot-spot parameter	0 / 0.1
Soil reflectance	0.0 / 0.1 / 0.2
Diffuse/direct radiation	0
Solar zenith angle	15° / 30° / 45°
Viewing angle	-30° / 0° / 30°
Sun-view azimuth angle	0°

Table 2. Nominal values and range of parameters used for the canopy simulations with the combined PROSPECT-SAILH model

3. RESULTS AND DISCUSSION

3.1 Simulations PROSPECT Leaf Reflectance Model

Clevers and Kooistra (2006) showed before with PROSPECT model simulations that the leaf dry matter content and particularly the leaf structural parameter have a huge effect on

the relationship between the spectral reflectance in the 900 – 1300 nm range and the equivalent water thickness (EWT). Due to this, individual spectral bands are not well correlated with EWT. However, when calculating the first derivative spectra correlations increase significantly. The derivatives at spectral regions close to the water absorption features at 970 and 1200 nm are mainly depending on the EWT and are hardly affected by the leaf structural parameter and the leaf dry matter content. As an example, Figure 2 shows the relationship between the derivative at 942.5 nm and EWT. The wavelength 942.5 nm is at the left shoulder of the 970 nm absorption feature. Good results were also obtained using derivatives at the right shoulder of this feature and at the left shoulder of the 1200 nm absorption feature. Figure 3 illustrates the relationship between the water band index (WI) and EWT. Results for the WI were better than those for the NDWI or for the indices based on the continuum removal method (results not shown). Best results were obtained for the first derivative (R<sup>2</sup> of 0.96 at 942.5 nm).

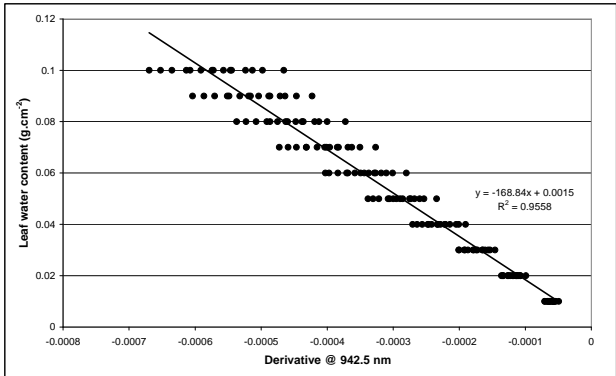


Figure 2. Relationship between first derivative of leaf reflectance at 942.5 nm and equivalent water thickness (PROSPECT simulations with various C<sub>m</sub> and N values, cf. Table 1)

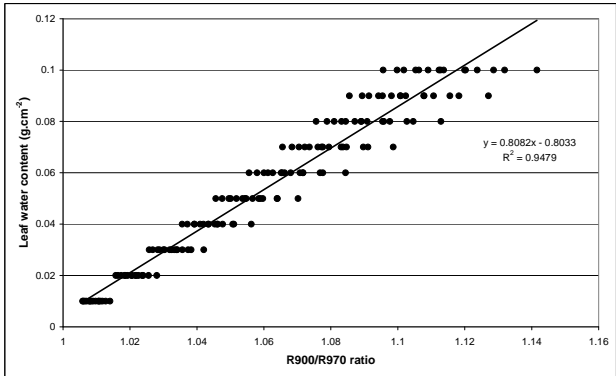


Figure 3. Relationship between the water band index and equivalent water thickness (PROSPECT simulations with various C<sub>m</sub> and N values, cf. Table 1)

3.2 Simulations SAILH Canopy Reflectance Model

At the canopy level Clevers and Kooistra (2006) showed before that individual spectral bands in the 900 – 1300 nm range are not well correlated with the canopy water content (CWC) using simulations with the combined PROSPECT-SAILH model. However, the first derivative is much better correlated with CWC. High correlations are obtained at the shoulders of the water absorption features. The same regions with high coefficients of determination can be observed as at the leaf

level. The effect of variables other than the leaf water content and the LAI are minimised by using the derivative spectra. As an example, Figure 4 shows the relationship between the first derivative at 942.5 nm and CWC for varying leaf angle distribution functions. Again the first derivative showed better results than the afore mentioned indices from literature. The best one of these again is the WI, which is illustrated in Figure 5. The first derivative also yielded stable results for various illumination-viewing combinations. As an example, Figure 6

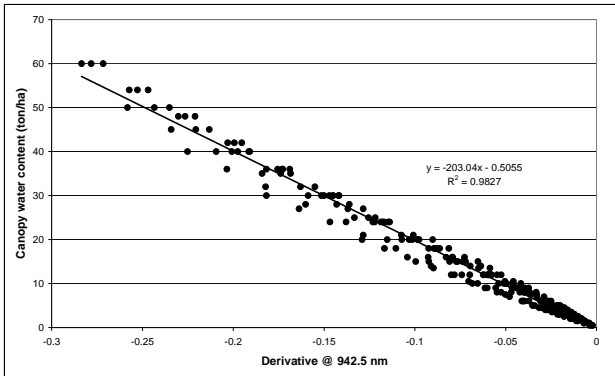


Figure 4. Relationship between first derivative of leaf reflectance at 942.5 nm and canopy water content (PROSPECT-SAILH simulations with various leaf angle distributions, cf. Table 2)

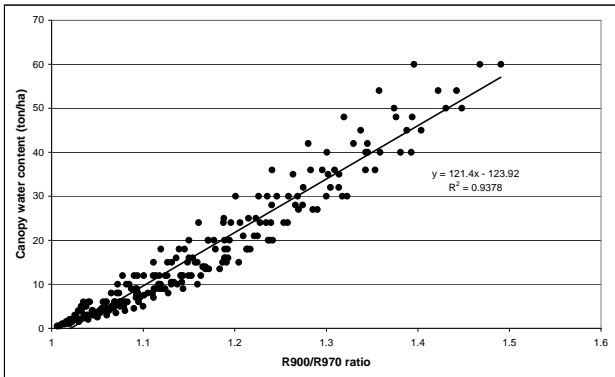


Figure 5. Relationship between the water band index and canopy water content (PROSPECT-SAILH simulations with various leaf angle distributions, cf. Table 2)

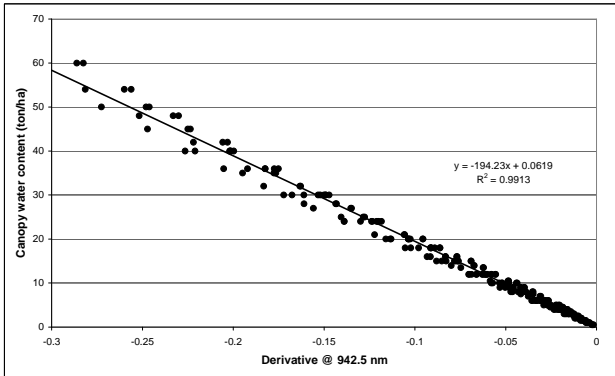


Figure 6. Relationship between first derivative of leaf reflectance at 942.5 nm and canopy water content (PROSPECT-SAILH simulations in nadir, hotspot and coldspot, cf. Table 2)

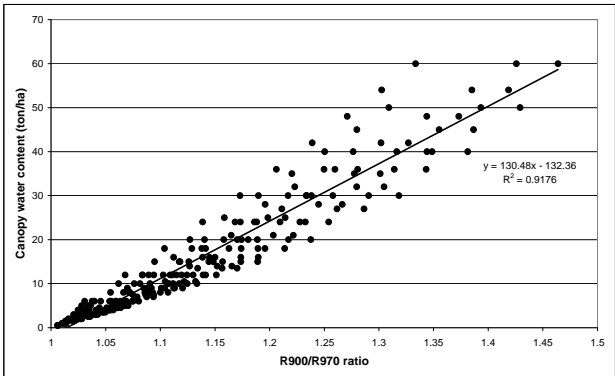


Figure 7. Relationship between the water band index and canopy water content (PROSPECT-SAILH simulations in nadir, hotspot and coldspot, cf. Table 2)

shows the relationship between the first derivative at 942.5 nm and CWC for nadir viewing, viewing into the hotspot and, opposite to this, viewing into the coldspot. The same relationship is obtained as for the varying leaf angle distributions in Figure 4. For comparison the result for the WI is illustrated in Figure 7, which again shows more scattering due to the varying observation geometry.

3.3 Test site 1: Wageningen

Using the field spectroradiometer measurements obtained in 2004 at the Wageningen test site, we also found a better relationship between the first derivative at the shoulders of the water absorption features and the canopy water content than between individual spectral bands in the 900 – 1300 nm region and the CWC. For consistency, Figure 8 shows the relationship between the first derivative at 942.5 nm and CWC, although some other derivatives near to 942.5 nm gave slightly better R<sup>2</sup> values. At 942.5 nm an R<sup>2</sup> value of 0.71 was found, whereas at 950.5 nm we found the maximum R<sup>2</sup> value of 0.80. So, we see that the R<sup>2</sup> varies strongly with wavelength for this data set. When Figure 8 is scaled in the same way as Figure 4, we see that the simulated relationship fits very well with the one given in Figure 8. The ratio-based water band indices and the indices based on the continuum-removal method perform worse than the first derivative, but better than the individual spectral bands. Figure 9 illustrates the results for the WI, yielding an R<sup>2</sup> value of 0.26.

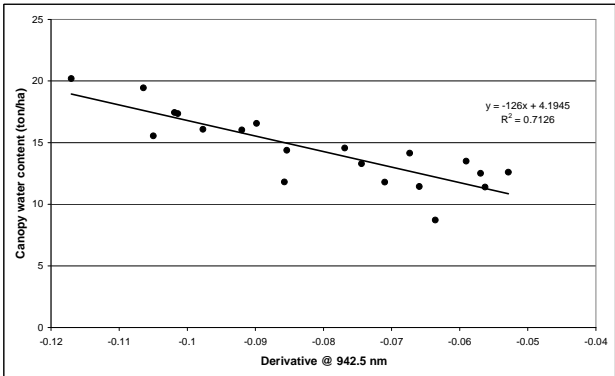


Figure 8. Relationship between first derivative of canopy reflectance at 942.5 nm and canopy water content at the Wageningen test site

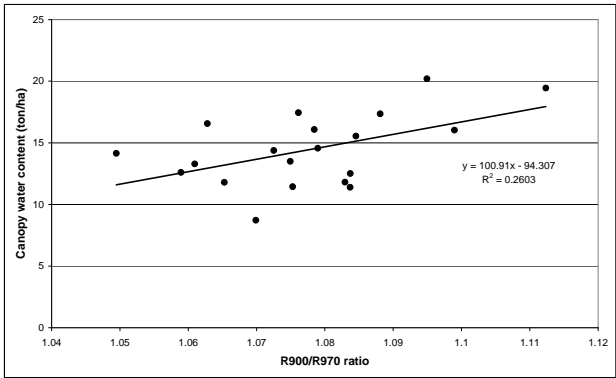


Figure 9. Relationship between the water band index and canopy water content at the Wageningen test site

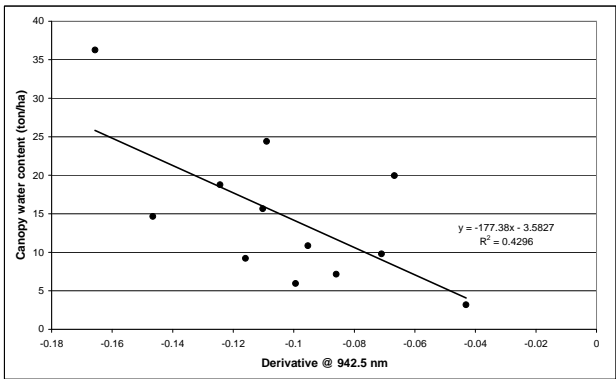


Figure 10. Relationship between first derivative of canopy reflectance at 942.5 nm and canopy water content at the Millingerwaard test site

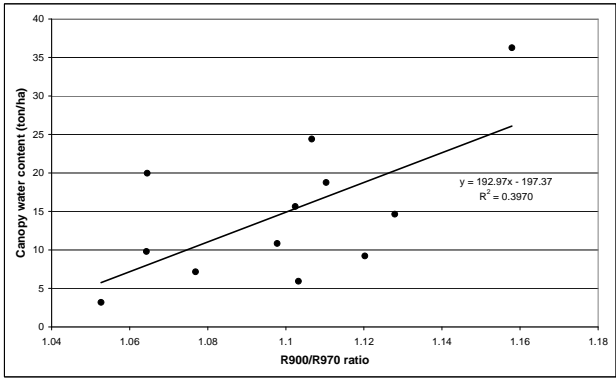


Figure 11. Relationship between the water band index and canopy water content at the Millingerwaard test site

3.4 Test site 2: Millingerwaard

For the Millingerwaard test site in 2005 both field spectroradiometer measurements and canopy water content were obtained. Direct regressions of CWC on individual spectral bands obtained from the field spectroradiometer yielded poor results.  $R^2$  values for the first derivative spectra yielded better results, although  $R^2$  values were not really high for this heterogeneous vegetation site. Figure 10 illustrates the relationship between the first derivative at 942.5 nm and CWC, whereas Figure 11 shows the result for the WI, again being the best water band index. For this data set the first derivative at 1266.5 nm yielded the highest correlation with CWC ( $R^2$  of

0.60). This lies at the right shoulder of the 1200 nm absorption feature. Due to the heterogeneous nature of the vegetation in the Millingerwaard, results are worse than for a homogeneous grassland parcel at the Wageningen site.

4. CONCLUSIONS

Results presented in this paper show that the spectral derivative for wavelengths on the slopes of the water absorption features at 970 nm and 1200 nm can be used for estimating canopy water content (CWC). Model simulations show a good relationship between the derivative at 942.5 nm and CWC, which is not very sensitive for leaf and canopy structure. In addition the influence of sun-viewing geometry seems to be minimal. Field spectroscopic measurements on plots in a homogeneous grassland parcel confirm these results. For a nature area with many different plant species, results were less good, but still results show the potential of the derivative of the spectral reflectance at the shoulders of the mentioned water absorption features. The relationship between derivative and CWC based on the real spectral measurements obtained in the field appears to match the simulated relationship at the same spectral position obtained from a combined PROSPECT-SAILH model. This shows that we may transfer simulated results to real measurements obtained in the field for various vegetation types. Of course, more research is required on this subject. This study clearly indicates that derivatives provide better results in estimating canopy water content than reflectances or indices as used in literature (Sims and Gamon, 2003). Moreover, this paper shows that results obtained at the leaf level can be upscaled to the canopy level using field spectroradiometers. Next step should be the upscaling to the regional level using airborne hyperspectral data.

In this paper we used the derivative at 942.5 nm for illustrating the potential of the derivative in estimating CWC. However, in this region of the electromagnetic spectrum one also has to take the influence of the atmosphere into account. Significant absorption due to water vapour in the atmosphere occurs at 940 nm and 1140 nm (Gao and Goetz, 1990; Iqbal, 1983). These atmospheric absorption features are at shorter wavelengths as compared to the liquid water absorption features in the plant material, meaning they are at the left shoulders of the plant water absorption features. Therefore, the derivative at the right shoulders of the absorption features will be more useful for practical applications because they are not influenced by atmospheric water vapour. Figure 12 shows results for the  $R^2$

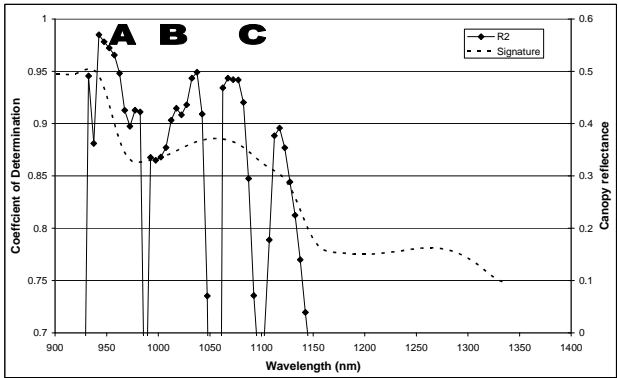


Figure 12. Coefficients of determination between canopy water content and first derivative of canopy reflectance. The dotted line provides an example of a canopy reflectance signature (PROSPECT-SAILH)

values of the derivatives over the 900 – 1300 nm region and the CWC for model simulations with the combined PROSPECT-SAILH radiative transfer model. Although  $R^2$  values are highest at the left shoulder of the 970 nm absorption feature, derivatives at the right shoulder also provide high  $R^2$  values. Therefore, for practical applications a derivative at about 1040 nm also seems to be feasible.

## REFERENCES

- Clevers, J.G.P.W. and L. Kooistra, 2006. Using spectral information at the NIR water absorption features to estimate canopy water content and biomass. *ISPRS mid-term symposium 2006 remote sensing: from pixels to processes*, 8-11 May 2006, Enschede, The Netherlands, pp. 6.
- Curran, P.J., 1989. Remote sensing of foliar chemistry. *Remote Sensing of Environment*, 30(3), pp. 271-278.
- Curran, P.J., J.L. Dungan and D.L. Peterson, 2001. Estimating the foliar biochemical concentration of leaves with reflectance spectrometry testing the Kokaly and Clark methodologies. *Remote Sensing of Environment*, 76(3), pp. 349-359.
- Danson, F.M., M.D. Steven, T.J. Malthus and J.A. Clark, 1992. High-spectral resolution data for determining leaf water content. *International Journal of Remote Sensing*, 13(3), pp. 461-470.
- Gao, B.C., 1996. NDWI - A normalized difference water index for remote sensing of vegetation liquid water from space. *Remote Sensing of Environment*, 58(3), pp. 257-266.
- Gao, B.C. and A.F.H. Goetz, 1990. Column atmospheric water vapor and vegetation liquid water retrievals from airborne imaging spectrometer data. *Journal of Geophysical Research*, 95(D4), pp. 3549-3564.
- Iqbal, M., 1983. *An introduction to solar radiation*. Academic Press, Ontario, 390 pp.
- Jacquemoud, S. and F. Baret, 1990. Prospect - a model of leaf optical properties spectra. *Remote Sensing of Environment*, 34(2), pp. 75-91.
- Kokaly, R.F. and R.N. Clark, 1999. Spectroscopic determination of leaf biochemistry using band-depth analysis of absorption features and stepwise multiple linear regression. *Remote Sensing of Environment*, 67(3), pp. 267-287.
- Kuusk, A., 1991. The angular-distribution of reflectance and vegetation indexes in barley and clover canopies. *Remote Sensing of Environment*, 37(2), pp. 143-151.
- Malenovský, Z., C. Ufer, Z. Lhotáková, J.G.P.W. Clevers, M.E. Schaepman, J. Albrechtová and P. Cudlín, 2006. A new hyperspectral index for chlorophyll estimation of a forest canopy: Area under curve normalised to maximal band depth between 650-725 nm. *EARSeL eProceedings*, 5(2), pp. 161-172.
- Morisette, J.T., F. Baret, J.L. Privette, R.B. Myneni, J.E. Nickeson, S. Garrigues, N.V. Shabanov, M. Weiss, R.A. Fernandes, S.G. Leblanc, M. Kalacska, G.A. Sanchez-Azofeifa, M. Chubey, B. Rivard, P. Stenberg, M. Rautiainen, P. Voipio, T. Manninen, A.N. Pilant, T.E. Lewis, J.S. Iames, R. Colombo, M. Meroni, L. Busetto, W.B. Cohen, D.P. Turner, E.D. Warner, G.W. Petersen, G. Seufert and R. Cook, 2006. Validation of global moderate-resolution LAI products: A framework proposed within the CEOS Land Product Validation subgroup. *Ieee Transactions on Geoscience and Remote Sensing*, 44(7), pp. 1804-1817.
- Penuelas, J., I. Filella, C. Biel, L. Serrano and R. Save, 1993. The reflectance at the 950-970 nm region as an indicator of plant water status. *International Journal of Remote Sensing*, 14(10), pp. 1887-1905.
- Running, S.W. and J.C. Coughlan, 1988. A general-model of forest ecosystem processes for regional applications .1. Hydrologic balance, canopy gas-exchange and primary production Processes. *Ecological Modelling*, 42(2), pp. 125-154.
- Sims, D.A. and J.A. Gamon, 2003. Estimation of vegetation water content and photosynthetic tissue area from spectral reflectance: a comparison of indices based on liquid water and chlorophyll absorption features. *Remote Sensing of Environment*, 84(4), pp. 526-537.
- Verhoef, W., 1984. Light scattering by leaf layers with application to canopy reflectance modeling: the SAIL model. *Remote Sensing of Environment*, 16(2), pp. 125-141.



## DEVELOPMENT OF AN INVERSION CODE, ICARE, ABLE TO EXTRACT URBAN AREAS GROUND REFLECTANCES

S. Lachérade<sup>a,\*</sup>, C. Miesch<sup>a</sup>, D. Boldo<sup>b</sup>, X. Briottet<sup>a</sup>, C. Valorge<sup>c</sup>, H. Le Men<sup>b</sup>

<sup>a</sup> ONERA, Optical Dept., 2 avenue Edouard Belin, 31000 Toulouse, France - (lacherad, miesch, briottet)[@onecert.fr](mailto:@onecert.fr)

<sup>b</sup> IGN, Saint Mandé, France – (boldo, le-men)[@ign.fr](mailto:@ign.fr)

<sup>c</sup> CNES, avenue edouard Belin, 31000 Toulouse, France, christophe.valorge[@cnes.fr](mailto:@cnes.fr)

**KEY WORDS:** Urban area, hyperspectral, reflectance, environment effects, shadows, atmospheric correction, radiative transfer

### ABSTRACT:

Automatic mapping of urban materials from remotely sensed radiance images remains difficult because of the complex physical phenomena induced by relief. Indeed, shadows and environment effects disrupt the radiance incoming the sensor. Moreover, the measured radiance depends on the illumination conditions of the observed area. This is quite problematic for multi-temporal analysis. Images are often taken in different illumination conditions thus shadows are not located in the same place.

This paper describes a new physical model, ICARE, able to solve the radiative transfer inversion problem over urban areas, in the reflective domain ( $0.4\ \mu\text{m} - 2.5\ \mu\text{m}$ ), from high spatial and spectral resolution images. This new approach takes into account the complex relief of 3D structures, the spatial heterogeneity of the scene and atmospheric effects, in order to extract rigorously the ground surface reflectance, even in shadows areas. The resolution method consists in modelling separately the irradiance and radiance components at ground and sensor levels.

The validation of ICARE is checked through the CAPITOUL trial, carried out in Toulouse (France, 2004). Measurements were performed using two airborne Pelican image systems consisting in 8 high spatial (20 cm) and spectral (30 nm) resolution cameras. Results are presented over typical urban structures in Toulouse center completed by an error budget. They demonstrate that extracted reflectances correspond very well to ground reflectance measurements. Moreover, there is a good continuity between reflectance obtained over sunny and shadowed materials. That proves that shadows areas and environment effects are well corrected.

To quantify the gain brought by ICARE, a comparison between classification based on radiance and reflectance images, obtained by inversion, is introduced.

### 1. INTRODUCTION

Recent studies estimate that more than 75% of the world's population are living in urban areas. A better understanding of this environment is required in many applications, to study its spatial evolution, impact on the environment, or problems of town planning and organization. With the advent of high spatial resolution sensors from the visible to the short wave infrared domain [ $0.4\ \mu\text{m} - 2.5\ \mu\text{m}$ ], it is now possible to get accurate information from airborne and satellite images.

Due to their highly structured geometry, an important part of urban areas exhibits shadows. Therefore, airborne or satellite acquisitions over urban areas will depend on the illuminations conditions. This drawback must be overcome to improve applications as mapping or urban change detection, which often use images from different time or different sensors. Moreover, there are important coupling effects at the interface of the 3D ground and the low atmosphere layer like multiple reflexions on wall. All of these phenomena make it difficult to classify automatically urban materials from airborne radiance measurements. Preprocessing algorithms are usually required to retrieve ground surface intrinsic properties like reflectance that is independent of the irradiance conditions and thus improve classification performance.

Currently, different methods are used to solve the inverse transfer radiative problems (i.e. retrieving ground reflectance from radiance images) but most of them do not account for ground heterogeneity. These codes often consider a flat and homogeneous landscape with a lambertian assumption, e.g., ATREM (Goetz, 1997), ACORN (Miller, 2002). Improvements

have been carried out in FLAASH (Anderson, 2002) and COCHISE (Miesch, 2005) as they consider a heterogeneous background. Nevertheless, these codes are not able to deal with urban areas where the relief plays very important part in the remotely sensed features. At present, two models currently take into account the ground topography in mountainous region: ATCOR4 (Richter, 2002) and SIERRA (Lenot, 2003). They consider a heterogeneous background and the ground topography is modelled by a digital elevation model (DEM). But these codes are not adapted to the very uneven structure of urban areas for two main reasons. First, the earth-atmosphere coupling term and the multiple reflexions are still roughly modelled which causes important errors notably in shadows where environment effects are preponderant. Secondly, the use of DEM images prevents wall modelling or all vertical objects present in an urban area whereas walls have a large contribution in the urban radiative transfer.

The need for a retrieval model that is able to understand and model the signal over urban areas led us to develop the method we report here. This method, named ICARE (Inversion Code for urban Areas Reflectance Extraction), consists in modelling separately the irradiance and radiance components at ground and sensor level by use of models derived principally from improved versions of the usual spatially resolved approaches. Each component takes into account the relief, ground heterogeneity and atmospheric corrections.

In order to check the validity of the different assumptions made, a field campaign is carried out to validate our model on real images and first results are presented. Then, usual classification algorithms are applied on the reflectance and radiance images

to quantify the gain brought by ICARE. The paper will insist particularly on the experimental validation of this model.

## 2. RADIATIVE TRANSFER MODELLING OVER URBAN AREAS

### 2.1 Physical modeling

This part describes the main characteristics of the physical model implemented in ICARE. This approach consists in determining an analytical expression for each of the component involved in the total radiance reaching a given sensor observing an urban scene. We use here a complete separation of the atmospheric and ground optical properties to lead to an easily tractable inversion. The full spectral domain of ICARE ranges from the visible to the near infrared domain  $[0.4\mu\text{m} - 2.5\mu\text{m}]$ . In this domain, optical properties of the ground correspond to its spatial and spectral bidirectional reflectance:

$$\rho^{dd}(\theta_i, \varphi_i, \theta_r, \varphi_r, \lambda) = \frac{\pi R(\theta_i, \varphi_i, \theta_r, \varphi_r, \lambda)}{I(\theta_i, \varphi_i) \cos(\theta_i)} \quad (1)$$

Where  $I(\theta_i, \varphi_i)$  is the irradiance incident on the surface in the direction  $(\theta_i, \varphi_i)$  and  $R(\theta_i, \varphi_i, \theta_r, \varphi_r)$  the corresponding reflected radiance in the direction  $(\theta_r, \varphi_r)$  at the wavelength  $\lambda$ ,  $\theta$  is the zenithal angle et  $\varphi$  the azimuthal angle.

In this paper, a lambertian assumption is made on the ground reflectance. Only spatial and spectral heterogeneity is taken into account. Thus the spectral bidirectional reflectance  $\rho(\theta_i, \varphi_i, \theta_r, \varphi_r, \lambda)$  is simply noted  $\rho(\lambda)$ .

Considering an airborne or satellite sensor observing an urban scene and  $i$  a pixel of the sensor image, the total radiance received by this sensor can be written as the sum of three main contributors (Figure 1) :

$$R_{\text{sensor}}(i) = R_{\text{diffuse}}(i) + R_{\text{atmospheric}}(i) + R_{\text{direct}}(i) \quad (2)$$

The first component corresponds to scattered photons coming from the target neighbouring ( $R_{\text{diffuse}}$ ).  $R_{\text{atmospheric}}$  refers to photons coming to the sensor without reaching the surface.

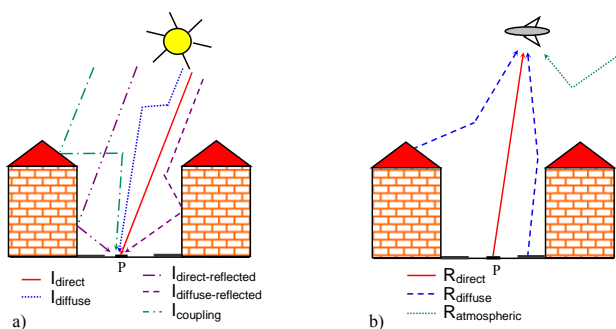


Figure 1: Irradiance components at ground level (a) and radiance components at sensor level (b).

$R_{\text{direct}}$  is the upwelling radiance directly transmitted from the ground to the sensor. This component plays an important role as it brings the searched reflectance:

$$R_{\text{direct}}(i) = (I_{\text{direct}}(P) + I_{\text{diffuse}}(P) + I_{\text{reflected}}(P) + I_{\text{coupling}}(P)) \frac{\rho}{\pi} T_{\text{dir}}^{\uparrow} \quad (3)$$

Where  $P$  is a considered point of the ground and  $\rho$  its reflectance.  $I_{\text{direct}}$ ,  $I_{\text{diffuse}}$ ,  $I_{\text{reflected}}$  and  $I_{\text{coupling}}$  are the different irradiance components incident to the ground according to their type of path (Figure 1).  $T_{\text{dir}}^{\uparrow}$  is the upward total transmission of the atmosphere on the path ground-sensor.

Using equations 1 and 2, we can extract an analytical expression of the reflectance using a lambertian hypothesis:

$$\rho = \frac{\pi(R_{\text{sensor}} - R_{\text{diffuse}} - R_{\text{atmospheric}})}{T_{\text{dir}}^{\uparrow} (I_{\text{direct}} + I_{\text{diffuse}} + I_{\text{reflected}} + I_{\text{coupling}})} \quad (4)$$

To solve this equation, our method consists in estimate each component of equation (4).

### 2.2 Model implementation

The ICARE implementation is based on the radiative transfer code 6S which is used to compute the atmospheric components. ICARE needs three entry data: a digital vector model of the relief of the scene, atmospheric conditions during the acquisition and a calibrated radiance image of the scene. Three radiative components could be directly computed from these data: the direct and diffuse irradiances at the ground level and the atmospheric intrinsic radiance at sensor level. Indeed, these three components only depend on the illumination conditions of the scene. The other components of the radiative transfer equation need neighbourhood notions that mean reflectance values of the environment. To solve this problem, an iterative algorithm is carried out.

To initialise the iterative method, an average reflectance of the entire scene is computed using a flat homogenous assumption of the scene. This hypothesis implies that some environments effects like reflected irradiances are not considered in this first step. Only a basis approach of the coupling earth-atmosphere irradiance is computed. This averaged reflectance is applied on all viewed surfaces by the sensor. According to its zenithal angle, different parts of the scene are hidden. The iterative process will not be able to evaluate their reflectance. For example, walls will not be seen by a nadir acquisition. However, the optical properties of these hidden surfaces are necessary in particular to compute environment effects. Thus, spectral default values are attributed to all not viewed surfaces of the scene.

The next step of the implementation consists in computing all the different irradiance component on the ground and radiance components at sensor level. Knowing all the unknown components of Equation 4, it is possible to evaluate a first value of the ground reflectance for each pixel of the sensor. Then an iterative approach is processed until the reflectance map obtained focused on constant values. The numbers of iteration

needed for these computations depends on the scene but 6 iterations are often sufficient.

3. DESCRIPTION OF THE EXPERIMENT CAMPAIGN

An experimental validation campaign of this model took place in Toulouse in April 2004, including airborne acquisitions at high spatial and spectral resolutions and ground truth measurements within the same resolution. The airborne acquisitions were performed using simultaneously two high spatial resolution systems (PELICAN) (Duffaut, 2005) composed of four cameras each (Figure 2). Thus, eight registered images were acquired simultaneously in eight spectral bands over our test area.

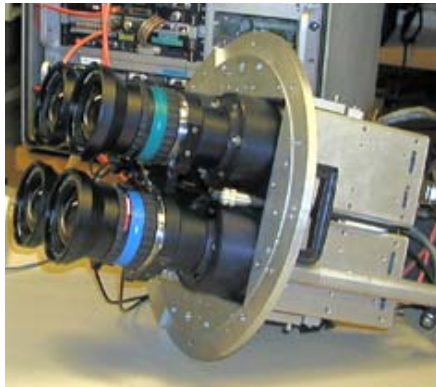


Figure 2: The PELICAN system.

The flight altitude was 2250 m and the spatial resolution at ground level 20 cm. All acquisitions were realised at nadir viewing angle. Indeed, it is the viewing angle where the largest number of urban surfaces could be viewed by the sensor. Only walls are hidden. The eight narrow filters associated to the cameras were located in the visible and near infrared spectral domain from 420 nm to 917 nm.

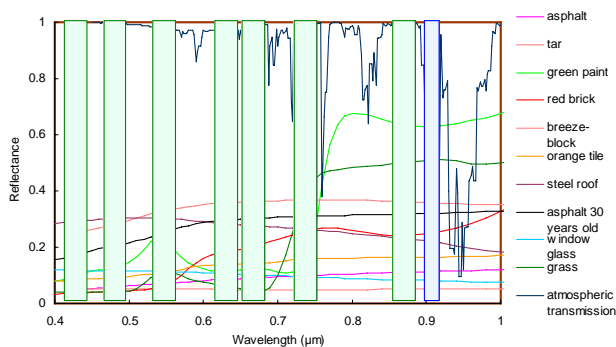


Figure 3: Location of the eight narrow filters.

The spectral location of these bands was chosen corresponding to two criteria. First, the goal of these bands was to allow a spectral discrimination of most of urban manmade materials. Figure 3 shows spectral reflectances of different urban materials coming from ASTER database (ASTER). Secondly, the different filters have to be well distributed over the spectral domain in order to validate ICARE while avoiding main gaseous absorption bands. Only the eighth band doesn't respect these rules. Unlike the others, it has been chosen to determine the water vapour content for others applications. Subsequently, only the first seven filters will be used in this paper.

The test site chosen for the experimental validation of ICARE is the préfecture area in the centre of Toulouse (Figure 4). It is composed of a closed courtyard surrounded by typical Toulouse buildings. This site corresponds to a typical urban area. The main advantage is that the courtyard has restricted access for people and cars which made easier ground truth measurements.



Figure 4: Airborne image of the Préfecture of Toulouse.

The digital vector model associated to this scene was provided by the Institut Géographique National (IGN) from stereoscopic images of Toulouse acquired in December 2003. It contains a precise geometry of the different buildings on the scene. To link this 3D vector model to airborne images, a triangulation of the model was performed to obtain triangles with a spatial resolution of 20 cm. The geometrical accuracy of the urban structure is very important as shadows areas are directly calculated from it. Airborne acquisitions were registered in the eight bands and georeferenced by IGN for the treatments.

Airborne measurements took place in April 2004 for two days running with two acquisitions per day at 14hUT and 16hUT. Ground measurements consist in irradiance, radiance and reflectance measurements on the courtyard's ground. These measurements have been done along four defined profiles in order to be able to compare measurements between two series. These series have been planned just before and after each airborne acquisition. The goal of these combined measurements was first to validate the reflectance estimated by ICARE and also to validate intermediate steps of the processing like irradiance computations. Ground measurements have been performed with an ASD FieldSpec PRO spectroradiometer.

The trial was achieved with clear sky conditions and aerosols were supposed to be urban type. A sun photometer located in the centre of Toulouse gave us information about their optical thickness. Measurements done during the experiment showed that the classical Bouguer-Lambert law could not be applied here because of the important variation of the optical depth during the day. Therefore, the aerosols' spectral optical depth was derived directly from irradiance measurements on the ground done with a sun photometer and then adjusted with Junge's law.

4. ICARE VALIDATION

4.1 Experimental validation

The goal of this experimental validation is to evaluate if the different assumptions done in ICARE are sufficient to retrieve ground reflectances from high resolution airborne images even

in shadowed areas. The results exhibit in this article corresponds to the first acquisition of the second day of the campaign, acquired at 14hUT. The four profiles present on the airborne image of the préfecture's courtyard (Figure 5) correspond to the different ground measurements profiles.

Figure 5 illustrates the results produced by the retrieval method ICARE on the préfecture area in Toulouse in the spectral band centred at 485 nm. We can see that shadows are well removed after ICARE processing. Details which were hidden in shadowed areas like cars appear in the reflectance image. Another important point is that we can see on the radiance image that roof's tiles exhibit different colours depending on their relative orientation to the incidence solar angle. Meister (Meister, 2000) shows that this phenomenon is mainly due to the variation of the direct irradiance component with the slope of the roofs. Bidirectional effects of the reflectance of tiles play also a role in the signal received by the sensor but only in a second order. This variation in the appearance of the roofs is quite a problem in classification processing. These phenomenons are no longer present in the reflectance image. ICARE takes into account the slope of the roofs in its physical modelling and the resulting reflectance obtained after processing are then independent of the illumination conditions.

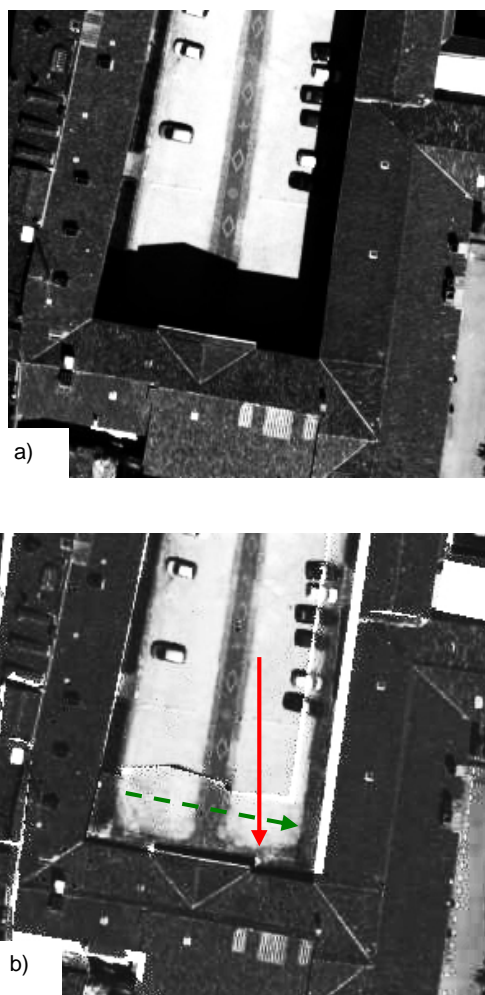


Figure 5: a) Radiance image at 485 nm, b) Reflectance image obtained after inversion at 485 nm.

The main artefact which appears in the reflectance image is the white and black areas located at the border of the shadowed areas and also at the place of a change of slope. It corresponds

to a geometric error of the 3D vector model. Indeed, the shadows map is computed from the geometric information provided by the vector model. If a side of a building is not well located, the end of the generated shadows will not be coherent with the real scene viewed by a sensor. It creates an error in the calculation of the direct irradiance component. If a pixel located normally in a sunny areas is modelling by the vector model in shadows, it will be characterised by an important radiance at the entry of the sensor (corresponding to a sunny area) and by a low irradiance level on the ground. The reflectance extracted by ICARE will be therefore very high to find coherence between irradiance and radiance levels. That explained the white areas observed in the reflectance image. Black areas are generated by the same phenomenon: a pixel really located in shadowed areas and a corresponding surface on the ground located in a sunny area. Thus, the most important errors in the reflectance image obtained by ICARE are caused by geometric errors in the 3D model of the relief. The quality of the reflectance image depends entirely of the quality of the vector model of the scene. Another important result to highlight is that the reflectance level retrieved by ICARE in shadowed areas is the same that the one obtained in sunny areas (Figure 6). There is no gap, no discontinuity in the reflectance image depending on the illumination conditions (apart from geometric errors). It means that the environment effects, preponderant in shadowed areas, are correctly modelled. This important result allows us to validate the approaches used to model the different environment components: the diffuse upwelling radiance and also the reflected irradiance components.

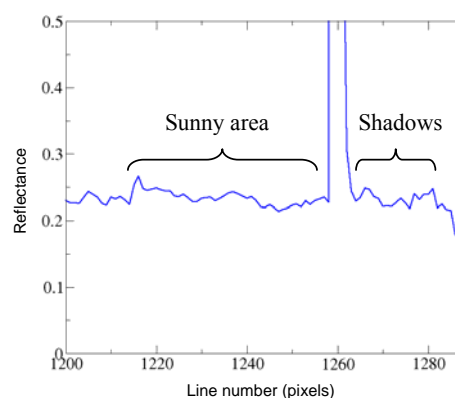


Figure 6: Reflectance values obtained along the red arrow Figure 6b) at 485 nm.

Finally, another point to be discussed in the validation experimental, and perhaps the most important point for our experimental validation, is the comparison between the retrieved reflectances and the one measured at the ground. Previous results show that the model used to evaluate environment effects allow us to obtain a good continuity between sunny and shadowed areas but it is very important to determine if the reflectance values retrieved after inversion corresponds to ground measurements. An absolute error would not be important for classification analysis where the most important thing is the relative difference observed between different materials. But it could be very important to determine the material's name directly from the reflectance image. Many urban materials are characterised by a relative flat reflectance over the visible and near infrared region (Lachérade, 2005) and thus, the level of these reflectance is sometimes the only clue to determine the analysed material. The goal of ICARE is not only to allow an improvement in classification results but also to



give to the scientific community a tool to analyse the absolute optical properties of manmade materials directly from remote sensing images. Thus, the absolute accuracy of the retrieved reflectance is very important.

Figure 7 shows the comparison of the reflectance retrieved by ICARE at 485 nm and the reflectances measured on the ground.

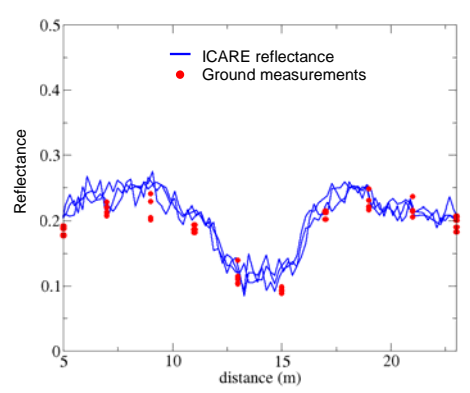


Figure 7: Comparison at 485 nm of reflectances retrieved by ICARE (blue lines) and ground measurements (red points) along the red line Figure 6b).

Red points correspond to the ground measurements before and after each airborne acquisition along a determined profile at the same points in the courtyard. Variations observed in their reflectance level are due to the spatial variability of the ground. Courtyard is composed of gravel. As the spatial resolution of the ground measurements is 20 cm, reflectance measurements include the spatial heterogeneity of the ground which explains the observed variability. In order to take into account the spatial variability also present in the retrieval image of reflectance, three close profiles to ground measurements profile were extracted. They are represented by the blue lines.

This graph shows that at 485 nm, the accuracy of the retrieved reflectance after inversion is very good. The spatial variation of the reflectance along the profile corresponds to that which was measured during ground measurements. The absolute reflectances obtained from the airborne image after the inversion method show a good agreement with the "real" reflectance of the materials at the studied spatial resolution.

As the spatial comparison between modelled and measured reflectances seems to be valid, the Figure 8 shows the spectral comparison in one point of the previous profile.

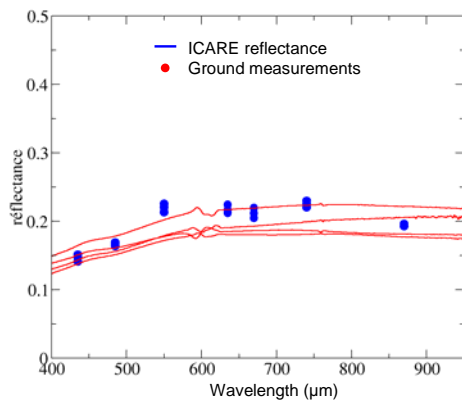


Figure 8: Spectral comparison of reflectances retrieved by ICARE in the 7 spectral bands and ground spectral reflectance measured with the ASD spectrometer.

Blue points correspond to the seven reflectance values extracted from the seven bands used during the airborne acquisition. The red lines are the corresponding spectral reflectances measured in the courtyard with the ASD spectrometer. These results are satisfactory insofar as the retrieved reflectance values show a maximum absolute error less than 0.04 whatever the spectral band. The little variation observed on the extracted reflectance between the different spectral bands is probably due to the absolute calibration of the camera. Indeed, each spectral band of the airborne instrument was separately calibrated during a vicarious calibration. This calibration has direct consequences on the radiance level in images and thus on the reflectance extracted by ICARE.

To confirm these results, similar comparisons were performed over another test site located in the surroundings of Toulouse. Analyses show that the accuracy of ICARE allows us to determine the absolute reflectance of urban materials with a performance better than 0.04 peak-to-peaks.

4.2 Classification results

This study carries out that ICARE is able to retrieve the spectral materials of urban materials directly from airborne images. The main application using these images is classification. The goal of this section is not to develop classification methods on the reflectance images but just to quantify the gain brought by ICARE with a typical classification algorithm. The classification tool used here is the unsupervised classification algorithm of the K-Means which is implemented in the software ENVI Version 4.2. The evaluation of the accuracy of the classification results was determined by comparison with the classification results realised by a photo-interpreter.

Figure 9 emphasizes the classification results obtained from the radiance and reflectance images. We find again the different problems of the radiance image, touched on previously. The shadowed areas are put in a "shadows class" and the materials in the shadows could not be identified. Moreover, the classification algorithm determines two different materials on the roof whereas it is the same. It is due to the variation of the slope of the roofs. Thus, the number of good classified pixels is only about 54%. On the reflectance image, some of the problems have been corrected because the retrieved reflectance is independent of the illumination conditions. The shadowed areas are corrected and the materials located in these areas are well identified. There are no longer problems for roofs. One material (tiles here) is identified for the roofs. Therefore the reflectance image gives us a number of good classified pixels of about 74%. The use of ICARE largely improves the results of classification.

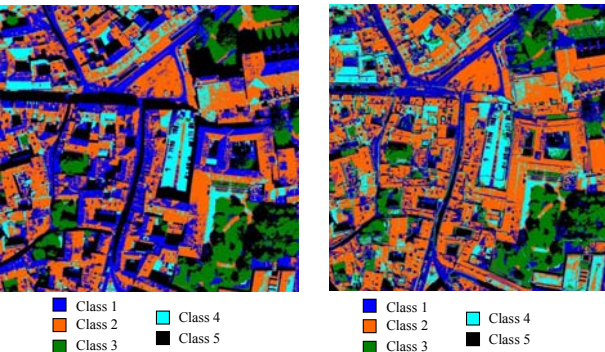


Figure 9: Classification results obtained on the radiance image (on the left) and on the reflectance image (on the right).



Nevertheless, classification results obtained with ICARE could still be improved. For example, trees are not yet modelled in the digital vector model of the relief. Therefore, the shadows generated by the tree are not computed and thus not corrected. The accuracy of the inversion and thus on the classification, will depend mainly on the accuracy and level of details of the geometric vector model used for the reflectance retrieval.

## 5. CONCLUSIONS AND PERSPECTIVES

In this work, an inverse radiative transfer model operating in the visible and short wave infrared is presented. The objective of the study was to develop a code able to deal with urban areas. It takes into account atmospheric corrections and environment effects in order to retrieve ground reflectance from radiance images. To solve the inverse problem, irradiance and radiance components are modelled separately. The effects of the various assumptions made were checked through an experimental campaign. This field campaign was carried out in Toulouse using two PELICAN systems. Results demonstrate that the physical modelling is well adapted to urban areas. Shadows are well corrected and there is no bias between reflectances in shadowed and sunny areas for the same materials. Moreover, the absolute reflectance of the urban materials is retrieved with an absolute accuracy better than 0.04 peak-to-peaks over the whole studied spectral region (visible and near infrared). To quantify the improvement provided by ICARE, a usual classification algorithm was applied on the radiance and reflectance images. A comparison realized between results obtained after the classification shows that the use of ICARE have the outcome to largely improve the number of good classified pixels from 54% with the radiance image to 74% with the reflectance image.

The next step of this work will be to confirm experimental results over different site tests, characterised with different architecture, with different viewing angles, and also to enlarge the experimental validation (actually limited by the camera to the silicium domain) to the whole near infrared. Moreover, two approaches are considered to improve ICARE: the improvement of the physical algorithm and the improvement or post-correction of the entry data. First, ICARE's processing actually uses a lambertian assumption. It will be necessary to take account of these directional effects in the direct-direct component. Secondly, we have seen on the validation results that the most important error comes from the digital vector model. It would be important to find methods to improve model vectors accuracy by two ways: by correcting the geometric location of different objects and also by improving the level of details included in the vector model. For example, it would be useful to model vegetation like trees. All these perspectives represent a lot of future work but the first encouraging results obtained with ICARE allow us to think that this model could be an important improvement for the study of urban areas from remote sensing images.

## 6. REFERENCES

G.P. Anderson, G.W. Felde, M.L. Hoke, A.J. Ratkowski, T. Cooley, J.H. Chetwind, J.A. Gardner, S.M. Adler-Golden, M.W. Matthew, A. Berk, L.S. Bernstein, P.K. Acharya, D. Miller, P. Lewis, 2002, MODTRAN4-based atmospheric correction algorithm : FLAASH (Fast Line-of-sight

Atmospheric Analysis of Spectral Hypercubes), *SPIE Proceedings*, Vol. 4725, p. 65-71.

ASTER, NASA/JHU, <http://speclib.jpl.nasa.gov/>, visited in 2006.

J. Duffaut, P. Déliot, 2005, Characterization and calibration of a high-resolution multi-spectral airborne digital camera. *Optical Complex Systems 2005*, Marseille (France), October 24<sup>th</sup>.

A.F.H. Goetz, J.W. Boardman, B. Kindel, K.B. Heidebrecht, 1997, Atmospheric corrections : on deriving surface reflectance from hyperspectral imagers, *Proceedings of SPIE*, Vol. 3118, pp. 14-22.

S. Lachérade, C. Miesch, X. Briottet, H. Le Men, 2005, Spectral variability and bidirectional reflectance behaviour of urban materials at a 20 cm spatial resolution in the visible and near infrared wavelengths. A case study over Toulouse (France). *International Journal of Remote Sensing*, Vol. 26, No. 17, pp. 3859-3866.

X. Lenot, V. Achard, C. Miesch, L. Poutier, P. Pinet, 2003, Irradiance calculation over mountainous areas in the reflective domain – Comparison with an accurate radiative transfer model, *Geoscience and Remote Sensing Symposium*, Vol. 7, pp. 4298-4300.

G. Meister, A. Rothkirch, H. Spitzer and J. Bienlein, 2000, BRDF field studies for remote sensing of urban areas. *Remote Sensing Reviews*, 19, pp. 37-57.

C. Miesch, L. Poutier, X. Briottet, X. Lenot, V. Achard, Y. Boucher, 2005, Direct and inverse radiative transfer solutions for visible and near-infrared hyperspectral imagery, *Geoscience and Remote Sensing, IEEE Transactions on Remote Sensing*, Vol. 43, No. 7, pp. 1552 – 1562.

C.J. Miller, 2002, Performance assessment of ACORN atmospheric correction algorithm, *Proc. SPIE Conf. Algorithms and Technologies Multispectral, Hyperspectral and Ultraspectral Imagery* Orlando, FL, Vol. 4725.

R. Richter, D. Schlöpfer, 2002, Geo-atmospheric processing of airborne imaging spectrometry data. Part 2: atmospheric/topographic correction, *International Journal of Remote Sensing*, Vol. 23, No 13, pp. 2631-2649.

# ESTIMATING VEGETATION PARAMETERS OF CEREALS USING AN ASTER 1A IMAGE

N. Sánchez<sup>a\*</sup>, R. González<sup>a</sup>, J. Prado<sup>b</sup>, J. Martínez-Fernández<sup>c</sup>, C. Pérez-Gutiérrez<sup>d</sup>

<sup>a</sup> Faculty of Agrarian and Environmental Sciences, University of Salamanca, Filiberto Villalobos 119, 37007 Salamanca, Spain - nilda@usal.es, raulgonzalezbarrio@hotmail.com

<sup>b</sup> Foundation of Locals Initiatives in Castilla y León. Bordadores 14. 37002 Salamanca, Spain - jepradogo@hotmail.com

<sup>c</sup> Department of Geography. University of Salamanca. Cervantes 3, 37002, Salamanca, Spain. Centro Hispano Luso de Investigaciones Agrarias. University of Salamanca. Curueño, s/n. 37185. Villamayor, Salamanca, Spain - jmf@usal.es

<sup>d</sup> Polytechnic School of Ávila. University of Salamanca. Hornos Caleros, 50. 05003, Ávila, Spain - carpegu@usal.es

## Commission VII, WGVII/1

**KEY WORDS:** ASTER, radiometric correction, vegetation indices, radiance, reflectance, biomass.

### ABSTRACT:

The purpose of the present study is the validation of the ASTER images through the indirect estimation of several parameters of dry crops cover. Since 1999 the Department of Geography of the University of Salamanca (Spain) has established a network named REMEDHUS in this area consisting of twenty three stations for the measurement of soil moisture over a large area of 1,300 km<sup>2</sup> characterized by different soil and land use types. The objective of this project is to develop an efficient monitoring system of climatic, edaphologic and biophysical parameters. Moreover, the climatic monitoring is carried out by a meteorological station that provides a daily dataset.

In 2005, this database was completed with a field campaign to estimate biophysical parameters such as plant biomass, water content and height. The direct field measurement was done around the REMEDHUS stations in two campaigns in April 2005, the same date of the acquisition of an ASTER 1A image in the same area. The vegetation cover present in these plots is a dry crops shape (cereals), in the growing stage of its phenologic cycle. The image was orthorectified by a rigorous model. The radiometric treatment consisted of two-level calibrations based on: 1) the ERSDAC (Earth Remote Sensing Data Analysis Center, provider of ASTER) algorithm implemented by a specific application with the coefficients, gain and offset, provided in the image file, and 2) conversion of these at-satellite radiance values in at-surface reflectance by means of a method developed by Pons and Solé-Sugrañés (1994) for VNIR Landsat TM images, here adapted for ASTER. RVI (Ratio Vegetation Index) and NDVI (Normalized Difference Vegetation Index) were tested with the obtained reflectance values. Good correlations were obtained with both indices and the biophysical on-the-ground parameters (aerial biomass, water content and plant heights), in all cases correlation coefficient higher than 0.7. The results show that it is possible to infer a direct relationship between the plant parameters and the indices, taking into consideration two prior constrictions: the radiometric performance of the images into physical values and the use of the vegetation indices at the growing stage of the crops cycle, related to vegetative activity.

### 1. AREA

The study site is located in the semi-arid sector of the Duero Basin, Spain, (41,1°–41,5° N; 5,1°–5,7° W), covering a plain area of about 1300 km<sup>2</sup> (Figure 1). The REMEDHUS network has been operating in this area since June 1999. The total number of stations of soil moisture measurement used in this study is 23 and all are over agricultural fields (Ceballos et al., 2005).

The most frequent land-uses in this area are: rainfed crops (winter cereals and pastures), irrigated crops, vineyards and small forest covers. The vegetation ground measurement coincides with dry lands (stations of soil moisture measurements of REMEDHUS).

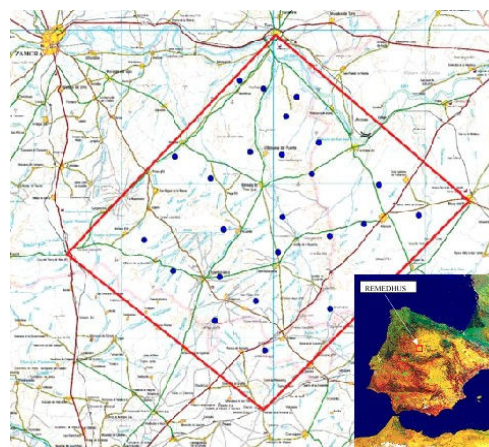


Figure 1. Location map of the study area: Soil Moisture Measuring Station Network (REMEDHUS) in Spain.

## 2. DATA

### 2.1 Basics on ASTER imagery

ASTER level 1A products are generated from the raw level 0 instrument data by adding metadata, including the geometric and radiometric correction coefficients, and reformatting into Earth Observing System (EOS) hierarchical data format (HDF) files; the imagery data remain identical (Arai and Tonooka, 2005). The level-1B data is generated by applying these coefficients for radiometric calibration and geometric re-sampling. Using level 1B, it is necessary to convert the digital levels into radiance values applying the unit conversion coefficients for each band. Level 2B are products of physical parameters generated on the basis of user request (Ninomiya et al., 2005): level 2B01 is at-surface radiance and level 2B05 is at-surface reflectance. The necessary atmospheric correction is based upon a look-up table approach using results from a Gauss-Seidel iteration radiative transfer code. The complete algorithm is detailed in the ERSDAC documentation (<http://www.science.aster.ersdac.or.jp/en/documnts/pdf/2b0105.pdf>).

### 2.2 Field data

The field measurement consists of direct (destructive) estimation of water content (g), aerial biomass expressed in damp weight ( $\text{g m}^{-2}$ ) and plants height (cm). The agricultural use of the selected plots is rainfed cereals, mainly barley and wheat. The field measurement took place at the same date of the satellite image (April, 28), in the growing season.

## 3. METHODS

### 3.1 Geometric correction

Firstly, a process of geometric treatment is needed to correlate the field measurement and the digital operations on the image. Orthorectification by rigorous model (Toutin, 2004) is applied by means a 30 ground control points and a DEM proceeding of the official cartography of the Castilla-León Region government (performed at 15 m pixel size, as ASTER spatial resolution, and 1 m high-resolution). The geo-location resulting from this process has a sub-pixel accuracy. The resample from raw scene to warped scene was made using nearest neighbour method trying not to change the original value of digital levels of every pixel.

### 3.2 Radiometric correction

#### 3.2.1 Digital levels from 1A to at-satellite radiances

At-satellite radiance can be obtained from level 1A applying the coefficients gain and offset for every pixel:

$$L = \frac{[A]DN}{[G]} + [D] \quad (1)$$

Where:

L: radiance,  $\text{W/m}^2/\text{sr}/\mu\text{m}$

A: linear coefficient

G: gain (constant values in each band)

D: offset

DN: digital levels of band n

The application of this formula has two approaches: using mean values of A and D in [1] or using array values of A and D in [1] for each pixel, included in the image header file. Here the radiance has been calculated with the complete array

#### 3.2.2 At-satellite radiance to at-surface reflectance

The method proposed is based on a simplified model for radiometric corrections proposed by Pons and Solé-Sugrañés (1994) and refined in Salvador et al. (1996) for Landsat TM. Since we use only the red and infrared bands of ASTER, coinciding closely with those of Landsat, the model can be adapted. This radiometric correction includes atmospheric and illumination corrections. The inputs required are: DEM, standard astronomic parameters such as exoatmospheric solar irradiance and atmospheric optical depth, date and time of the satellite pass and sensor viewing angle. The model assumes that all surface are Lambertian reflectors, which is reasonable for the green cereals cover at this phenologic state (midgrowth) and can not be used over self-shadowed pixels.

The adapted equation for the present work is:

$$R = \frac{\pi L d^2}{(\mu_s S_0 e^{(-\tau_0/\mu_0)} e^{(-\tau_0/\mu_v)})} \quad (2)$$

Where:

R is at-surface reflectance.

L is at-satellite radiance (obtained in the previous step).

d is the Sun-Earth distance at the acquisition date. d can be calculated (Yang and Vidal, 1991) as

$$d = 1 / \{ [1 + e \cos(\{D-4\} 2\pi/365.25)] / (1-e^2) \} \quad (3)$$

D is the day number of the year and e the orbit eccentricity.

$\mu_s$  is the cosine of the angle between incident beam and the normal at the surface, depending of the DEM (slope and aspect for each pixel of DEM).

$S_0$  is the exoatmospheric solar irradiance for the two bands; the reference values (Dozier, 1989) are:  $1557 \text{ Wm}^{-2}\mu\text{m}^{-1}$  for the red band and  $1047 \text{ Wm}^{-2}\mu\text{m}^{-1}$  in the infrared.

$\tau_0$  is the optical depth of the atmosphere for the two bands, extracted of the U.S. standard values or by means of an empiric estimation with the radiation value (provided by the climatologic station in the area). Standard values were chosen ( $\tau_0 \text{ red}=0.25$ ;  $\tau_0 \text{ NIR}=0.20$ ).

$\mu_0$  is the cosine of the angle between the solar vector and the normal to a horizontal surface. This angle is provided as metadata in the header file.

$\mu_v$  is the cosine of the zenithal viewing angle (cosine of the off-nadir angle, supplied in the header file).

### 3.3 Vegetation indices

Vegetation indices typically correlate well with the plant biomass and the leaf area index on agricultural covers, since

they often reflect the vigour and health of the plants (Pinter Jr. et al., 2003) and offer a good basis for calculating plant biophysical parameters. The NDVI is the most commonly used index for extracting the biophysical properties of the vegetation. There is the problem of NDVI saturation at high LAI values (Smith et al., 2005) which can mean that the NDVI is not appropriate in the discrimination of high-density covers (Srinivas et al., 2004). In particular, the NDVI can only be related directly to the biomass in the plant growth stage, when photosynthetic activity is very high and the NDVI expresses the plant mass potential, which is the case of the present work.

The reflectance values derived from the radiometric correction were used to calculate the vegetation indices: RVI (Pearson and Miller,1972) and NDVI (Rouse et al., 1974). Finally, the results were overlaid with the measured stations and correlated with the parameters of the vegetation.

4. RESULTS AND DISCUSSION

The Table 1 shows the correlation between biophysical parameters and the two indices resulting from the reflectance levels:

Coefficient of Correlation, <i>r</i>		
	RVI	NDVI
Water content(g)	0,7757	0,7605
Biomass (g/m2)	0,7976	0,7734
Height (cm)	0,8196	0,8015

Table 1. Correlation between biophysical parameters and the RVI and the NDVI indices.

Observing the correlations obtained, it can be suggested that:

- Values of correlation greater than 0.7 should explain the dependency between the dependent and the independent variables, or, in other words, it is possible to predict the ground values from vegetation indices values extracted from the image.
- The variables best correlated are RVI and height. Biomass is also well correlated.

Taking advantage of the ASTER Research of Opportunity, this paper presents the results of comparing some vegetation parameters with the ASTER images provided by ERSDAC. The methodology used is based on Vegetation Indices that are correlated with the direct ground measurements. On the other hand, the use of recent remote sensing imagery presents the difficulty of obtaining physical values prior to digital treatment. For a common user, this step might not be not very familiar, especially when working with recent sensors. Thus, this work presents a simple method to perform easily the radiometric correction of digital values and the possibility to compare results with ground measurements.

A likely correlation has been found between the ground parameters (biomass, height, water content) measured in the cereals cover in this area and digital measurements made by ASTER images. Biomass and height are in particular directly proportional to the values of vegetation indices.

The best correlation was obtained with RVI and NDVI related with biomass and plant height, coinciding with a maximum of photosynthetic activity in the month of study (April). Nevertheless, the vegetation indices illustrate growing activity rather than plant biomass. If the biomass is well correlated with the vegetation indices, it might be because in April biomass is strictly related to the vegetation activity for rainfed crops.

This correlation might encourage the progress of this study issue, however it is advisable to establish in future experiments new ground vegetation areas and also to improve some aspects of the measurements, i.e. Leaf Area Index, radiometric direct measurements, green cover percentage, etc. Besides, it would be necessary to establish permanent stations and monitor them throughout the whole year with a larger number of images.

5. REFERENCES

Arai, K. and Tonooka, H., 2005. Radiometric Performance Evaluation of ASTER VNIR, SWIR, and TIR. *IEEE Transactions on Geoscience and Remote Sensing*, 43 (12), pp. 2725-2732.

Ceballos, A., Scipal, K., Wagner, W. and Martínez-Fernández, J., 2005. Validation of ERS scatterometer-derived soil moisture data in the central part of the Duero Basin, Spain. *Hydrological Processes*, 19, pp. 1549–1566.

Dozier, J., 1989. Spectral Signature of Alpine Snow Cover from the Landsat Thematic Mapper. *Remote Sensing of Environment*, 28, pp. 9-22.

Ninomiya, Y., Fu, B. and Cudahy, T. J., 2005. Detecting lithology with Advanced Spaceborne Thermal Emission and Reflection Radiometer (ASTER) multispectral thermal infrared “radiance-at-sensor” data. *Remote Sensing of Environment*, 99, pp. 127-139.

Pearson, R.L., and Miller, L.D., 1972. Remote mapping of standing crop biomass for estimation of the productivity of the short-grass Prairie, Pawnee National Grasslands, Colorado. Proc. of the 8th International Symposium on Remote Sensing of Environment, ERIM, Ann Arbor, MI, pp. 1357-1381.

Pinter Jr., P. J., Hatfield, J. L., Schepers, J. S., Barnes, E. M., Moran, M. S., Daughtry, C. S. T. and Upchurch, D. R., 2003. Remote Sensing for crop management. *Photogrammetric Engineering & Remote Sensing*, 69(6), pp. 647-664.

Pons, X. and Solé-Sugrañés, L., 1994. A Simple Radiometric Correction Model to Improve Automatic Mapping of Vegetation from Multispectral Satellite Data. *Remote Sensing of Environment*, 48, pp. 191-204.

Rouse, J. W., Haas, R. H., Shell, J. A., Deering D.W., and Harlan, J.C., 1974. Monitoring the vernal advancement of retrogradation of natural vegetation. Final Report, Type III, NASA/GSFC, Greenbelt, MD, 371 pp.

Salvador, R., Pons, X. and Diego, F., 1996. Validación de un método de corrección radiométrica sobre diferentes áreas montañosas. *Revista de la Asociación Española de Teledetección*, 7 pp. 1-5.

Smith, A. M., Nadeau, C., Freemantle, J., Wehn, H., Teillet, P. M., Kehler, I., Daub, N., Bourgeois, G. and de Jong, R., 2005. Leaf area index from CHRIS satellite data and applications in plant yield estimation. 26th Canadian Symposium on Remote Sensing Wolfville, Nova Scotia.

Srinivas, P., Das, B. K., Saibaba, J. and Krishnan, R., 2004. Application of Distance Based Vegetation index for agricultural crops discrimination. XXth ISPRS Congress. Commission 7, Istanbul, Turkey.

Toutin, Th., 2004. Geometric Processing of Remote Sensing Images: Models, Algorithms and Methods (review paper). *International Journal of Remote Sensing*, 25 (10), pp. 1893-1924.

Yang, C. and Vidal, A., 1990. Combination of Digital Elevation Models with SPOT-1 HRV Multispectral Imagery for Reflectance Factor Mapping. *Remote Sensing of Environment*, 32, pp. 35-45.

## 6. ACKNOWLEDGEMENTS

This study was fully supported by the Spanish Ministry of Science and Technology (ESP2006-00643 Project) and the Spanish Ministry of Environment (RESEL Project). The image was supplied by an ASTER Announcement of Research Opportunity of ERSDAC (Japan).



# CONSTITUTION OF AN AUTOMIZED PROCESSING CHAIN TO ANALYSE A MERIS TIME SERIES OF SWISS LAKES

Daniel Odermatt<sup>a,\*</sup>, Thomas Heege<sup>b</sup>, Jens Nieke<sup>a</sup>, Mathias Kneubühler<sup>a</sup> and Klaus Itten<sup>a</sup>

<sup>a</sup> Remote Sensing Laboratories (RSL), Dept. of Geography, University of Zurich, Winterthurerstrasse 190,  
CH-8050 Zurich, Switzerland - (dodermat, nieke, kneub, itten)@geo.unizh.ch

<sup>b</sup> EOMAP GmbH & Co. KG, Sonderflughafen Oberpfaffenhofen,  
D-82205 Gilching, Germany - heege@eomap.de

**KEY WORDS:** Inland water, Case II water, lakes, MERIS, water constituents

## ABSTRACT:

The physically based Modular Inversion & Processing System (MIP) is used in an automated processing chain for inland water constituent retrieval from MERIS level 1B data. Preprocessing routines are used to automatically convert the ESA generic data products into MIP input data format. Water/land masking, atmospheric correction and water constituent retrieval are accomplished by simple batch executables from MIP. The accuracy of the constituent retrieval mainly depends on the spectral fit between the image input data and the radiative transfer model results extracted from a database. Therefore, thresholds and initial values for model fitting have to account for all occurring lake specific temporal variations and need careful adjustment.

## 1. INTRODUCTION

Monitoring of water quality in lakes is required as an integral part of water resource management, in order to guarantee the sustainable use of water and to track the effects of anthropogenic influences. Simultaneously, adequate monitoring is required to report the effects achieved by management programs.

For most of the large glacial and fluviglacial lakes in the Swiss midland and south of the Alps, in situ water quality monitoring was established in the 1950s or 1960s. The data gathered since then reveals a period of over-fertilisation, with pronounced lake specific phosphorus concentration maxima between 1970 and 1985, followed by an ongoing decrease (Liechti, 1994). These monitoring programs are directed by cantonal, interregional and international authorities, and carried out by either the authorities themselves or respective research institutes.

Within ESA's APEX airborne imaging spectrometer experiment project (Nieke et al., 2005), it is planned to monitor the water quality of lakes and coastal areas using high spectral and spatial resolution data. First flights of APEX are planned 2008. An APEX level 2/3 processor chain is currently implemented and a limnology and coastal processor is under development (Schlöpfer, 2007). In order to test the approach and algorithms, MERIS and other sensor data is applied to provide a sound validation tool for future semi-automatical data retrieval and processing.

The MERIS instrument onboard ENVISAT offers increased potential to support established monitoring programs by means of remote sensing. MERIS level 2 water constituent products were found not to be accurate for inland waters (Gege and Plattner, 2004). However, remarkably improved results were achieved by customizing retrieval algorithms to lake specific properties (Giardino and Gomasasca, 2006). Moreover, methods were found that allow the integration of MERIS derived concentrations with in situ measurements (Miksa et al., 2006;

Heege, 2000), using the Modular Inversion & Processing System (MIP) (Heege and Fischer, 2004).

In this work, a processing chain to automatically derive water constituents from MERIS level 1B data for Swiss lakes is built around MIP. MIP is well automatable as it performs image based aerosol retrieval and atmospheric correction in advance of the water constituent retrieval. Still, the large number of input variables for atmospheric correction and constituent retrieval require accurate adjustment in terms of the high regional and temporal variability of inland water.

## 2. DATA

### 2.1 Satellite imagery

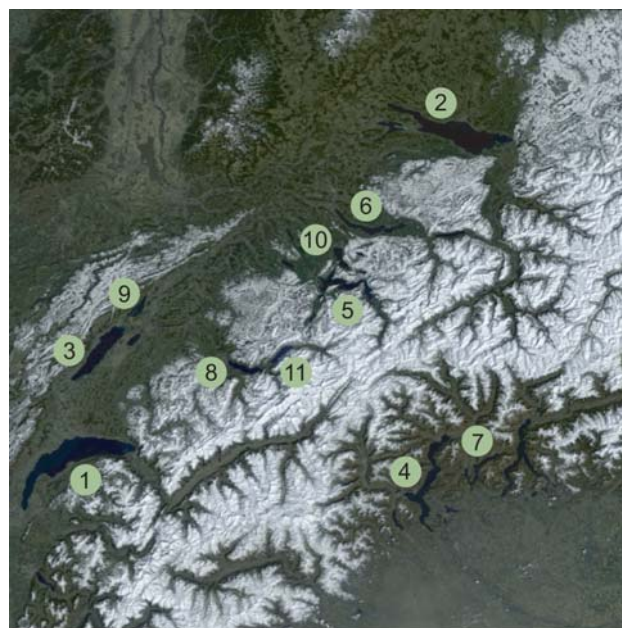


Figure 1. RGB composite of MERIS channels 8/6/3 (681/620/490 nm), acquired 29 March 04.

Lake numbers refer to Table 1.

57 MERIS datasets covering the years 2003 to 2006 in approximately fortnightly temporal resolution are analysed. The data was delivered as level 1B full resolution quarter scenes (“imagettes”), measuring 1153 square pixels at a nominal ground resolution of 260x290 m. The ground area represented by each imagette has almost the size of Switzerland, covering all lakes that are large enough for analysis (Fig. 1).

The data are geolocated but not geometrically corrected. It comes as at-sensor radiances, without atmospheric correction applied, but a large set of metadata is provided within the files delivered in the proprietary PDS format (ESA, 2006). For further processing, the PDS files were converted to HDF, making use of the batch executable “pds2hdf” contained in ESA’s free EnviView application (Brooker et al., 2002).

2.2 Water quality reference data

In situ data from governmental water quality monitoring programs is used to compare the results from MIP processing where they coincide with ENVISAT overflights. Furthermore, knowledge of the methods currently used in water quality monitoring and the physical connectivity of measurements taken by either method is crucial in order to integrate results from satellite remote sensing in common ongoing monitoring programs.

The monitoring programs for the 11 largest Swiss lakes are administrated by 9 different cantonal departments or regional authorities (Tab. 1). Continuous chlorophyll-a (chl-a) and biomass measurements are collected in 10 of these lakes by 8 different departments and research institutes (see Acknowledgements). The methods used for chl-a determination are based on 20 m composite samples (Utermöhl, 1958), on sample profiles (DEV, 1986) or on fluorescence probe profile measuring (Turner Designs, 2004).

	Lake Name	Area (km <sup>2</sup> )	Freq. (d)	Chl-a method	Depth (m)
1	Geneva	580	14	Probe profile	0-10
2	Constance	536	14	Probe profile	0-10
3	Neuchâtel	215	30	Composite sample	20
4	Maggiore	210	14	Composite sample (Chemistry only)	20
5	Lucerne	114	30	-	-
6	Zurich	88	30	Probe profile	0-10
7	Lugano	49	14	Sample profile	0-10
8	Thun	48	30	Composite sample	20
9	Biel	40	30	Composite sample	15
10	Zug	38	30	Probe profile	0-10
11	Brien	30	30	Composite sample	20

Table 1. Water monitoring data routinely collected in the 11 largest Swiss lakes (Fig. 1).

Empirical methods to correlate 20 m chl-a depth composite sample results to remote sensing data exist (Heege, 2000) and in an analysis of MERIS data of Lake Constance, they were found to be quite accurate (Miksa et al., 2006). But varying depth distribution of chl-a concentrations is thereby not considered and may cause large deviations. The remotely sensed chl-a values can only be considered accurate, if the maximum concentration is located near the surface. In the probe profile data for chl-a in Lake Geneva in 2003 for example, 5 out of the

total 18 profiles show significantly higher values in positions below 2 m than above.

Fluorescence probe profile data resolves depth in intervals of 0.5 to 1 m, but the brightness of the underwater light field in the top layer leads to inaccurate results just below the surface. For Lake Constance for example, values from surface to 2 m depth are extrapolated from deeper layers. This implies the assumption of small chl-a concentration variation with depth, similar to composite sample data. Additionally, the results from an instrument intercomparison campaign showed that the chl-a concentration results from 8 different fluorescence sondes diverge by more than 20% in average (GBL, 2006). Thus, the question how in situ data from both methods are best compared to chl-a values retrieved from MERIS data has to be addressed in future work.

3. METHODS

3.1 Image preprocessing

After conversion of the MERRIS datasets to HDF format, specific IDL routines are used to extract single image clippings for each lake (Fig. 2). The output is saved in MIP-readable BIL-files and respective input file structures for MIP retrieval modules (Fig. 3, *Image Preprocessing*).

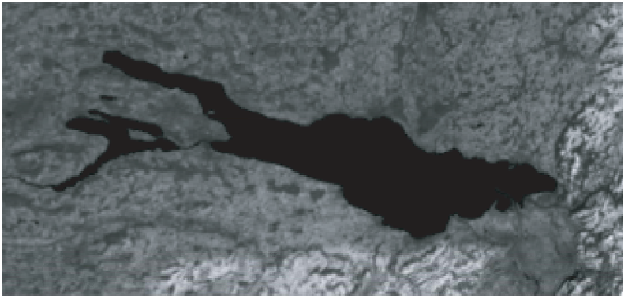


Figure 2. Mission input data: Lake Constance clipping from MERIS scene 29.3.04, depicted as channel 14 (885 nm) greyscale.

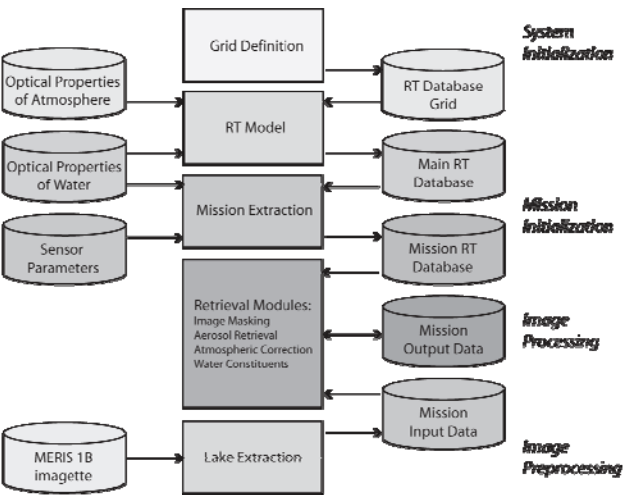


Figure 3. Flow chart of input imagery preprocessing (lower workflow) and MIP processing (upper workflow).

Darker shading indicates direction of work  
(modified from Miksa et al., 2006).

The clipping areas are set according to the longitude and latitude grid values contained in the image metadata. The grid point positioning values in MERIS metadata were found to deviate in an order of tenths of degrees from map values. Thus, reliable extraction of single lakes is possible for large, detached lakes such as Lake Geneva and Constance. Smaller, adjacent lakes could be extracted as clusters where they are found to be qualitatively similar. In cases where they have to be separated (i.e. Lake Thun and Lake Brienz), the shorelines contained in the metadata must be used with simple geometric positioning routines. Such routines identify a lake's relative position within the grid, making use of its size and the shape of surrounding shoreline patterns in its neighbourhood. Other parameters taken from metadata for further use in MIP processing are time and date of acquisition and observation angles. The elevation metadata differs by hundreds of meters for some lakes, obviously due to coarse resolution (i.e. in mountain valleys). A constant value for each lake is used instead. The metadata of the original images contain two different sets of calibration gain factors, which do not occur periodically but are indicated in the file names. The files labelled "PNIPA" and "PNUPA" contain calibration gain factors somewhat higher than those in files labelled "PNEPA". The application to the respective scenes was implemented in the preprocessing routines.

### 3.2 MIP processing

MIP uses a main radiative transfer database, built from simulation results of a coupled, plane-parallel atmosphere-water model, currently by use of the FEM-method (Kisselev and Bulgarelli, 2004). The main database contains optical properties for atmosphere, water surface and constituents, that allow optimization of fit between modelled and measured spectra in a later step. In order to process input data from different lakes, the database had to be supplemented with atmospheric optical properties accounting for different elevation levels (Fig. 3, *System Initialization*). For MIP batch processing, specific mission radiative transfer databases are extracted for each lake clipping, accounting for its specific flight geometry (Fig. 3, *Mission Initialization*). EOMAP provided batch executable modules from MIP, which perform simple (meaning non-iterative) unsupervised land/water masking, atmospheric correction and chl-a, yellow substance (y) and suspended matter (sm) retrieval. We optimise a single set of input variables for each lake. This set is supposed to be as representative as possible for the total 57 acquisition dates. The optimisation of input variables was started with Lake Constance, where most previous knowledge exists.

For land/water masking, estimates of aerosol type (continental, maritime, rural), aerosol optical thickness (AOT, at 550 nm) and water constituents are used. Thresholds for land/water discrimination are derived from simulated, Q-factor corrected underwater reflectances in channels close to 730 and 800nm and applied to the image croppings. The output files contain unchanged at-sensor radiances above water surfaces and zero values above land surfaces (Fig. 4) (Heege, 2000).

Channels 13 (865 nm) or 14 were found to be most suitable for atmospheric correction. The masked radiances (Fig. 4) serve as input files, and the same aerosol type estimate as for land/water masking is used. Again, underwater reflectance in the selected channel is calculated and Q-factor corrected, using estimated

initial values of water constituent concentrations. The concentration of the estimated aerosol type is then retrieved for each pixel, connecting the calculated underwater reflectance to the measured at-sensor radiance in the respective channel. The output is written in Q-corrected subsurface reflectance. The channel used for aerosol retrieval results in constant, low values. Channels at shorter wavelengths however can now be used for water constituent retrieval. (Fig. 5).

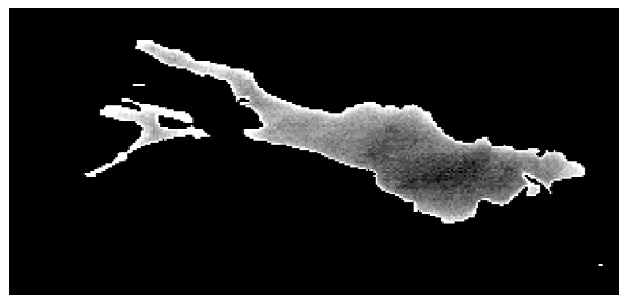


Figure 4. Scene from Figure 2 after land/water masking, depicted as channel 14 contrast enhanced greyscale. Brightness indicates atmospheric influence.

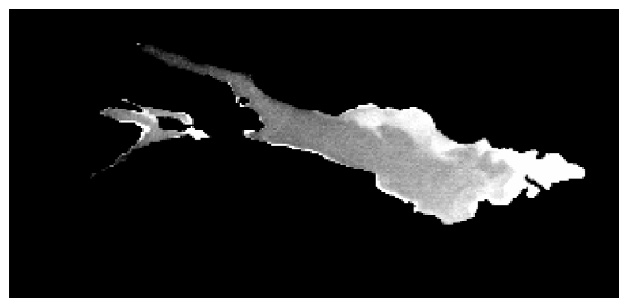


Figure 5. Scene from Figure 2 after atmospheric correction, depicted as channel 4 (510 nm) contrast enhanced greyscale. Brightness indicates high subsurface reflectance.

The subsurface reflectances in channel 1-9 (412-735 nm) are finally used for the retrieval of the water constituents chl-a, y and sm. Therefore, initial values and maximum, minimum and tolerance thresholds for each parameter are estimated. Weighting factors can be set for each channel in use. By means of a Simplex algorithm, the simulated subsurface reflectance for varying constituent concentrations is then fitted with the subsurface reflectance from atmospherically corrected image pixels (Heege, 2000).

## 4. DISCUSSION

The land/water masking functionality of MIP is much more sensitive to aerosol concentration estimates than to aerosol type. When continental AOT is changed from 0.05 to 0.1, the number of pixels masked as water for Lake Constance drops by more than 5% in 15 of the 57 clippings. However, most land/water masks change only marginally. When changing aerosol type from continental to maritime, the number of pixels masked as water increases on two dates (25.5.04 and 28.7.05) by more than 5%. In order to keep as many pixels as possible for subsequent processing steps, higher aerosol concentrations were not examined in detail and maritime aerosol type was preferred.



The effect of sun glitter was neglected in the beginning, but it was soon found to be a major source of errors. It will have to be taken into account for improvement of the processing chain. Images acquired at large eastward observation zenith angles, high illumination zenith angles and high wind speed above water surface are often contaminated by specular surface reflectance. This leads to increased at-sensor radiances and therefore to erroneous processing results, affecting for example almost a third of the data for Lake Constance. The sun glitter contamination can not be corrected, thus it leads to a reduction of the temporal resolution of satellite based observation.

In first tests on Lake Constance, the processing chain worked smoothly, but most of the processing outputs for the 57 MERIS datasets did not resist closer examination. In about a third of the cases, resulting chl-a concentrations are clearly out of the expected range from 0.5-15  $\mu\text{g/l}$ . In most other cases, a comparison between modelled and measured spectra suggests that further optimisation of the input values used in the processing chain would lead to a significant increase in accuracy. To support such input estimates, extensive reference data is available for Lake Constance (Heege, 2000; Gege, 1994). However, the assumptions considered appropriate in precedent research on Lake Constance have changed over time. If this is due to an actual change in water constituent mixture, this rises the question, if and to what extent occasional updates of input variables through reference measurements are required in order to ensure persistent data quality from remote sensing methods in the future.

The automatic extraction of chl-a concentrations from single image pixels corresponding to certain in situ sampling sites on the lake was found complicated due to the error of the positioning information in the MERIS metadata. An attempt to approximate the sampling location from its position relative to the southern, northern and eastern shore of the lake failed, because in many datasets, not the entire lake is visible. A test for the fraction of the lake represented in the clipping was implemented. More sophisticated positioning and possibly interpolation procedures have to be introduced to avoid further decrease of temporal resolution due to fractional cloud coverage and scenes only partly affected by sunglitter.

The influence of adjacency effects causes an increase in accuracy with increasing distance from the shorelines. This is visible in AOT calculations from the atmospheric correction module. It was also found in previous work, that satellite measurements matched best with reference data from the sampling site Fischbach-Uttwil in the lake's center, compared to sites closer to the shore like in the Bay of Bregenz or Lake Überlingen (Miksa et al., 2006). Therefore, correction of adjacency effects has to be taken into account, not only to improve the accordance with water quality monitoring measurements, but also to enable the derivation of accurate results in cases where not the entire lake can be analysed, as described above.

## 5. OUTLOOK

Currently, the scenes where the water constituent retrieval for Lake Constance failed are evaluated individually. In most cases, changing the initial values of system variables will lead to sound results. Proper analysis of the values found in this way should then allow a synthesis towards an automatable set of input values, that accounts for the temporal variation. This

procedure will be repeated for the other lakes presented in this work, in order to find out how atmosphere and water constituents vary in time and space, and how such effects can best be accounted for. Only if these problems are approached, remote sensing can reliably contribute to inland water quality monitoring programs.

The 57 datasets were chosen in order to achieve measurement intervals of about two weeks. More datasets with little cloud coverage are available, but were not taken into account because the temporal coverage seemed satisfactory. Regarding the reduction in temporal resolution caused by sun glitter, it remains to be seen if additional MERIS data could sufficiently compensate for data gaps, or if the integration of other sensors such as MODIS would be necessary to achieve a fortnightly coverage, which seems desirable according to current in situ monitoring.

Apart from the simple retrieval presented here, MIP also offers a module for processing iteratively. In this coupled mode, the results of precedent module iterations are used as initial values in subsequent calculations. This might possibly reduce some of the errors introduced by variable estimations, but it also leads to additional complexity and increased processing time. Therefore, its implementation might be an option at a later date, but is not decided yet.

To facilitate the integration of results from remotely sensed data into current in situ monitoring, further work on the comparability to in situ data is necessary. It has to be examined, if data measured by submerged fluorescence probes correlates with satellite image derived measurements in a similar way like 20 m composite samples do. As the remote sensing signal originates from the top layer, where fluorescence probe data is known to be erroneous, there might even be potential for a reasonable combination of both methods by establishing a transfer function. In any case, combined in situ and satellite data acquisition would be necessary to address this issue.

## REFERENCES

- Brooker, G., Ferguson, C., Goldsmith, P., de Deus Silva, M., Jalota, L., 2002. *EnviView User Guide*. Issue 2.0.7, 21 Aug. 2002, VEGA Group PLC/ESTEC, [http://earth.esa.int/services/download/EnviViewUserGuide\\_v2.07.pdf](http://earth.esa.int/services/download/EnviViewUserGuide_v2.07.pdf), (accessed 27 Mar. 2007).
- DEV, 1986. Bestimmung des Chlorophyll-a-Gehaltes von Oberflächenwasser (L 16). In: *Deutsche Einheitsverfahren zur Wasser-, Abwasser- und Schlammuntersuchung*. Losblattsammlung. VCH Verlagsgesellschaft, Weinheim (in German).
- ESA, 2006. *MERIS Product Handbook*. Issue 2.0, 14 Apr. 2006, <http://www.envisat.esa.int/handbooks/meris/>, (accessed 27 Mar. 2007).
- GBL, 2006: Seesonden Ringversuch Bodensee, 31. August 2006. Datenzusammenstellung und Auswertung. Gewässer- und Bodenschutzlabor (GBL) des Kantons Bern (in German).
- Gege, P., Plattner, S., 2004. MERIS validation activities at Lake Constance in 2003. In: *Proc. of the MERIS User Workshop*, Frascati (Italy), 10-13 November 2003.

- Gege, P. 1994. Gewässeranalyse mit passiver Fernerkundung: Ein Modell zur Interpretation optischer Spektralmessungen. Ph.D. thesis. In: *DLR-Forschungsbericht 94-15*, 171 p (in German).
- Giardino, C., Gomasasca, M., 2006. Derivation of chlorophyll-a concentrations and bottom properties of Lake Garda from remote sensing. In: *EARSeL Newsletter*, No. 66, pp. 17-19.
- Heege, T., Fischer, J., 2004. Mapping of water constituents in Lake Constance using multispectral airborne scanner data and a physically based processing scheme. In: *Can. J. Remote Sensing*, Vol. 30, No. 1, pp. 77-86.
- Heege, T., 2000. Flugzeuggestützte Fernerkundung von Wasserinhaltsstoffen am Bodensee. Ph.D. thesis. In: *DLR-Forschungsbericht 2000-40*. 141 p (in German).
- Kisselev, V., Bulgarelli, B., 2004. Reflection of light from a rough water surface in numerical methods for solving the radiative transfer equation. In: *Journal of Quantitative Spectroscopy and Radiative Transfer*, Vol. 85, 419-435.
- Liechti, P., 1994. Der Zustand der Seen in der Schweiz. In: *Schriftenreihe Umwelt*, Bundesamt für Umwelt, Berne, Switzerland, Vol. 237, 159 p. (in German).
- Miksa, S., Haese, C., Heege, T., 2006. Time series of water constituents and primary production in Lake Constance using satellite data and a physically based modular inversion and processing system. In: *Proc. Ocean Optics Conf. XVIII*, Oct.9-13, 10 p.
- Nieke, J., Itten, K. I., Debryun, W., 2005. The Airborne Imaging Spectrometer APEX: From Concept to Realisation. In: *Proc. 4th EARSeL Workshop on Imaging Spectroscopy*, Warsaw, 27-29 April 2005, CD-ROM.
- Schläpfer, D., Nieke, J., Dell'Endice, F., Hueni, A., Biesemans, J., Meuleman, K., Itten, K. I., 2007. Optimizing the workflow for APEX Level2/3 processing. In: *5th EARSeL Workshop on Imaging Spectroscopy*, Bruges.
- Turner Designs, 2004: SCUFA User's Manual. Issue 2.3, 27 Sep. 2004, Turner Designs, Sunnyvale (CA), [http://www.turnerdesigns.com/t2/doc/manuals/scufa\\_manual.pdf](http://www.turnerdesigns.com/t2/doc/manuals/scufa_manual.pdf), (accessed 2 Apr. 2007).
- Utermöhl, H., 1958. Zur Vervollkommnung der quantitativen Phytoplankton-Methodik. In: *Mitt. Int. Ver. Theor. Angew. Limnol.* Vol. 9. 38 p (in German)
- Bellinzona, Commission Internationale pour la Protection des Eaux du Lac Léman (CIPEL), UMR CARRTEL in Thonon-les-Bains, Service de la Protection de l'Environnement de Neuchâtel, Amt für Lebensmittelkontrolle Kanton Zug, Amt für Umweltschutz Kanton Zug, Amt für Abfall, Wasser, Energie und Luft Kanton Zürich, Wasserversorgung Zürich.

## ACKNOWLEDGEMENTS

The authors would like to thank David Finger from EAWAG Kastanienbaum, the Swiss National Science Foundation and the following institutions: Aufsichtskommission Vierwaldstättersee (AKV), Amt für Umwelt und Energie Kanton Luzern, Amt für Umwelt Kanton Nidwalden, Amt für Landwirtschaft und Umwelt Kanton Obwalden, Gewässer- und Bodenschutzlabor des Kantons Bern, Amt für Umweltschutz Kanton Bern, Internationale Gewässerschutzkommission für den Bodensee (IGKB), Institut für Seenforschung Langenargen, Commissione Internazionale per la Protezione delle Acque Italo-Svizzere (CIPAIS), Istituto per lo Studio degli Ecosistemi in Verbania Pallanza, Ufficio Protezione e Depurazione Acque in



# TOMOGRAPHIC SAR IMAGING OF A FORESTED AREA BY TIME-DOMAIN BACK-PROJECTION

Othmar Frey, Felix Morsdorf, Erich Meier

Remote Sensing Laboratories RSL, University of Zurich  
Winterthurerstrasse 190, CH-8057 Zurich, Switzerland  
ofrey@geo.unizh.ch

**KEY WORDS:** SAR, multi-baseline SAR, tomography, time-domain, back-projection, forest, vegetation

## ABSTRACT:

Recently, various attempts have been undertaken to retrieve information about the three-dimensional structure of vegetation from multi-baseline synthetic aperture radar data. Although tomographic processing of such data has been demonstrated, yet, there are still several problems that limit the focusing quality. In particular, the frequency-domain based focusing methods are susceptible to irregular and sparse sampling, two problems, which are unavoidable in case of multi-pass, multi-baseline radar data acquired by an airborne system. We propose a time-domain back-projection algorithm, which maintains the original geometric relationship between the original sensor positions and the imaged target and is therefore able to cope with irregular and sparse sampling without introducing any geometric approximations. Preliminary results obtained with a newly acquired P-band tomographic data set consisting of eleven flight tracks are shown and discussed.

## 1 INTRODUCTION

In a conventional synthetic aperture radar (SAR) image multiple back-scattering elements distributed along the elevation component are projected to the two-dimensional slant-range plane. With Pol-InSAR techniques only a very limited number of different scattering elements can be localized within a resolution cell. Tomographic processing of SAR data, however, allows resolving the ambiguity in the elevation component and is therefore suitable to produce true three-dimensional images. Hence, different back-scattering elements within a volume can directly be localized. This property can be exploited for the reconstruction of volumetric structures, such as forested areas, as well as for a more detailed imaging of built-up areas and mountainous regions, which exhibit a high percentage of layover regions. Tomographic processing of SAR data requires that the synthetic aperture in azimuth be extended by a second dimension in direction orthogonal to the plane spanned by the vectors in azimuth and the line of sight. The sampling in this direction, called the normal direction, is realized by coherently combining a sufficient number of adequately separated flight paths.

A critical issue with respect to processing SAR data tomographically is that the common Fourier-based SAR processing algorithm, the SPECAN (SPECtral ANALysis) approach, which has been used by (Reigber and Moreira, 2000), requires a regular sampling spacing as well as a densely sampled synthetic aperture. In reality, the sampling spacing is not uniform at all when dealing with airborne SAR data of multiple acquisition paths, and, in addition, the synthetic aperture in the normal direction is sampled sparsely. Therefore these reconstruction approaches are prone to artifacts and defocusing in the final tomographic image. In order to overcome these problems modern spectral estimation methods have been proposed including spectral estimation by the Capon method (Lombardini and Reigber, 2003) and subspace-based spectral estimation such as MUSIC (Guillaso and Reigber, 2005), (Gini and Lombardini, 2005). But, since these methods only replace the last step, the spectral estimation, they still involve the geometric approximations made beforehand.

We adopt a time-domain back-projection (TDBP) processing technique, which maintains the entire three-dimensional geometric

relationship between the exact sensor positions and the illuminated area while focusing the data. The key feature of the TDBP approach is an accurate handling of the complex geometry of irregularly spaced and sparsely sampled airborne SAR data.

In the next section, the Fourier-based SPECAN approach is revised in order to highlight the approximations that are involved. The same framework is also used to derive the sampling constraints and the spatial resolution for data processing in the normal direction. Then, the formulation of the TDBP algorithm for tomographic processing is presented. Further, we describe the measurement set-up of a tomographic SAR experiment and present preliminary results obtained from the TDBP-based tomographic reconstruction of a forested area from E-SAR P-band data.

## 2 THE SPECAN ALGORITHM, SPATIAL RESOLUTION AND SAMPLING SPACING IN THE NORMAL DIRECTION

For the first demonstration of airborne SAR tomography (Reigber and Moreira, 2000) the three-dimensional focusing of the data was accomplished by a combination of the extended chirp scaling algorithm (Moreira and Huang, 1994), which was used to focus each data track in range and azimuth direction, and the SPECAN algorithm, which was applied to focus the data in the normal direction. The SPECAN approach was originally designed for azimuth compression of ScanSAR data. The peculiarity of this algorithm lies in the fact that the focused data is obtained by a Fourier transform after a deramping operation.

We want to look again in some detail at the derivation of the SPECAN algorithm for focusing in the normal direction for two reasons: first, to highlight the approximations that are involved in the SPECAN approach, and second, because it provides a good framework to derive two important parameters, the *spatial resolution*  $\delta_n$  and the *Nyquist sampling spacing*  $d_n$  in the normal direction.

The model that is used to derive these parameters follows to a large extent the derivation presented in (Reigber and Moreira,

2000). However, the signal model is loosely based on the derivation of the SPECAN algorithm for azimuth focusing as it is presented in (Cumming and Wong, 2005).

The simplified tomographic acquisition geometry that forms the basis for the derivation of the spatial resolution and the sampling constraints in normal direction  $n$  – i.e. orthogonal to the plane spanned by the slant-range direction and the azimuth direction – is depicted in Fig. 1.  $r_0$  is the range distance at the point of closest approach along the synthetic aperture in normal direction  $n$ . Equally spaced baselines  $d_n$  are assumed and the variation of the off-nadir angle is neglected, so, the vector  $\vec{n}$  in normal direction is assumed to be invariant for all acquisition paths. Target coordinates are identified by a bar above the symbol. Assuming

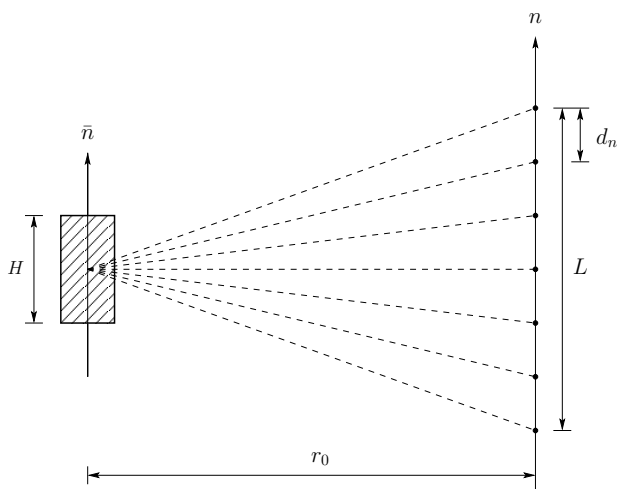


Figure 1: Simplified tomographic imaging geometry after (Reigber and Moreira, 2000). A volume is illuminated from different positions along a synthetic aperture in normal direction  $n$ . Each position in normal direction corresponds to a sensor path in azimuth direction. The sensor paths are separated by a constant sampling spacing  $d_n$ . The maximal height of the volume is  $H$ .  $L$  is the length of the synthetic aperture in normal direction.

that the synthetic aperture in the normal direction  $n$  is continuous – imagine an infinite number of single look complex images, represented by  $s_r$ , acquired from an infinite number of different, parallel flight tracks along  $n$  – the focused signal in normal direction  $v(\bar{n}_0)$  at position  $\bar{n}_0$  in the object space can be written as the following convolution in the time domain:

$$v(\bar{n}_0) = \int_{-L/2}^{L/2} s_r(\bar{n}_0 - n) h(n) dn \quad (1)$$

This is equivalent to:

$$v(\bar{n}_0) = \int_{\bar{n}_0 - L/2}^{\bar{n}_0 + L/2} s_r(n) h(\bar{n}_0 - n) dn \quad (2)$$

$L$  is the length of the synthetic aperture in normal direction  $n$ .  $s_r$  is the demodulated, received signal.  $h$  is the matched filter, i.e. the time-reversed reference function, which can be written as:

$$h(\bar{n}_0 - n) = \exp\left(\frac{ik}{r_0}(\bar{n}_0 - n)^2\right) \quad (3)$$

This formulation implements a quadratic phase history, which is obtained by approximating the hyperbolic range history by a sec-

ond order Taylor series expansion about the point  $n = \bar{n}_0$ :

$$r(n, \bar{n}_0) = 2\sqrt{r_0^2 + (\bar{n}_0 - n)^2} \simeq 2r_0 + \frac{(\bar{n}_0 - n)^2}{r_0} \quad (4)$$

$r(n, \bar{n}_0)$  is the two-way path length between the sensor at position  $n$  and a back-scatterer within the observed volume at height  $\bar{n}_0$ , with a range distance  $r_0$  at the point of closest approach. Inserting eq. (3) into eq. (2) and expanding the quadratic phase term yields:

$$v(\bar{n}_0) = \exp\left(\frac{ik}{r_0}\bar{n}_0^2\right) \cdot \int_{\bar{n}_0 - L/2}^{\bar{n}_0 + L/2} \underbrace{s_r(n) \exp\left(\frac{ik}{r_0}n^2\right)}_{s_d(n)} \exp\left(-\frac{i2k}{r_0}\bar{n}_0 n\right) dn \quad (5)$$

The exponential within the underbraced term in eq. (5) can be interpreted as a deramping operation which leads to the deramped signal  $s_d$ . Then, the whole integral is equivalent to a Fourier transform of the deramped signal  $s_d$ :

$$v(\bar{n}_0) = \exp\left(\frac{ik}{r_0}\bar{n}_0^2\right) \int_{\bar{n}_0 - L/2}^{\bar{n}_0 + L/2} s_d(n) \exp\left(-\frac{i2k}{r_0}\bar{n}_0 n\right) dn \quad (6)$$

So, in practise, the focused image  $v(\bar{n}_0)$  can be obtained by applying a FFT to the deramped signal  $s_d$ .

The phase term in the exponent of eq. (6) can be written as:

$$-\frac{2k}{r_0}\bar{n}_0 n = -K_{nr}\bar{n}_0 n \quad (7)$$

where  $K_{nr} = \frac{2k}{r_0}$  is interpreted as the spatial frequency modulation rate of the signal in normal direction. As it is well known from pulse compression of linear FM signals in range direction, the resolution in the time domain after compression is given by the reciprocal of the processed bandwidth, which is the product of the FM rate and the integration time. Translated to the normal direction and expressed in the spatial domain, the spatial resolution  $\delta_n$  is the inverse of the product of the spatial frequency modulation rate  $K_{nr}$  and the integration path  $L$  times  $2\pi$ :

$$\delta_n = \frac{2\pi}{K_{nr} \cdot L} = \frac{2\pi}{\frac{2 \cdot 2\pi}{r_0 \lambda} \cdot L} = \frac{\lambda r_0}{2L} \quad (8)$$

The Nyquist sampling spacing  $d_n$  in normal direction is equivalent to the inverse of the spatial bandwidth  $k_n$  times  $2\pi$ , where  $k_n(\bar{n}_0) = K_{nr} \cdot \bar{n}_0 = \frac{2k}{r_0}\bar{n}_0$ :

$$d_n(\bar{n}_0) \leq \left| \frac{2\pi}{k_n(\bar{n}_0)} \right| = \frac{2\pi}{K_{nr} \cdot \bar{n}_0} = \frac{\lambda r_0}{2\bar{n}_0} \quad (9)$$

Eq. (9) describes the relationship between sampling spacing and the maximal height  $\bar{n}_0 = H$  of the imaged volume that can be reconstructed unambiguously:

$$d_n(\bar{n}_0 = H) \leq \frac{\lambda r_0}{2H} \quad (10)$$

### 3 3D FOCUSING IN THE TIME-DOMAIN

In (Nannini and Scheiber, 2006) an algorithm has been proposed which is also based on single look complex images processed by the extended chirp scaling algorithm including aircraft motion compensation to a straight line. However, instead of focusing the data by deramping and spectral estimation, which would

previously involve generating synthetic tracks followed by a regularization of the samples in the normal direction, a time-domain beamformer (TDB) was applied to focus the data in the third dimension. Every voxel within the volume is focused by a so-called *ad hoc* reference function as it is also known from time-domain back-projection processing. The focusing quality of the TDB approach was found to be superior to the SPECAN based algorithm presented in (Reigber and Moreira, 2000) for unevenly spaced baselines. But in spite of the fact that the TDB directly accounts for the irregular track distribution in normal direction it is still based on artificial, linearized flight tracks, which lie in parallel to each other and which do not represent the true geometry of the flight tracks.

We aim at a complete processing in the time domain – after range compression – and focus the data by using the true geometry of the irregularly sampled tomographic acquisition pattern. Our TDBP processor, which has been tested with airborne (Frey et al., 2006) and spaceborne SAR data (Frey et al., 2005), is extended in order to work with an irregularly sampled, two-dimensional synthetic aperture. Actually, the extension is a very natural one in the way that the signal contributions are not only combined along the flight path but are also coherently added along the normal direction. The main point is that the geometric relationship between every sensor position and the illuminated volume is maintained during focusing without introducing any geometric approximations.

Following the derivations presented in (Frey et al., 2005) the back-projected signal  $s_k$  corresponding to the flight track  $k$  can be expressed as a function of the grid point  $\vec{r}_i$ :

$$s_k(\vec{r}_i) = \sum_{j=a_k(\vec{r}_i)}^{b_k(\vec{r}_i)} g_k(R_k, \vec{r}_{S_{jk}}) \cdot R_k \cdot \exp(i2k_c R_k) . \quad (11)$$

- $\vec{r}_i$  : position vector of the target
- $a_k, b_k$  : indices of first, last azimuth position of the sensor within the synthetic aperture of the target position  $\vec{r}_i$
- $\vec{r}_{S_{jk}}$  : position vector of the sensor,  $j \in [a_k, b_k]$
- $R_k = |\vec{r}_i - \vec{r}_{S_{jk}}|$  : range distance
- $g_k(\cdot)$  : range-compressed signal of data track  $k$
- $k_c = 2\pi f_c / c$  : central wavenumber
- $f_c$  : carrier frequency
- $c$  : speed of light

By extending the coherent addition of the signal contributions to the normal direction the back-projected signal  $v$  is obtained, which maps the volume at the position  $\vec{r}_i$ :

$$v(\vec{r}_i) = \sum_{k=1}^m \sum_{j=a_k(\vec{r}_i)}^{b_k(\vec{r}_i)} g_k(R_k, \vec{r}_{S_{jk}}) \cdot R_k \cdot \exp(i2k_c R_k) , \quad (12)$$

where  $m$  is the number of flight tracks that build the tomographic pattern. The boundaries of the synthetic aperture in azimuth direction,  $a_k$  and  $b_k$ , vary as a function of the grid position  $\vec{r}_i$ . This means that we sum up the contributions from those sensor positions  $\vec{r}_{S_{jk}}$  which actually build the synthetic aperture for the grid position  $\vec{r}_i$ . Note that an appropriate interpolation procedure is required in order to retrieve the data values at the correct range distances because of the discrete representation of the range-compressed data.

#### 4 EXPERIMENTAL SET-UP

An extensive airborne SAR campaign has been carried out in September 2006. Two fully polarimetric tomographic data sets

- an L-band and a P-band data set - of a partially forested area have been acquired by the German Aerospace Center's E-SAR system. Eight corner reflectors were deployed for geometric and radiometric calibration purposes. The positions of the corner reflectors were measured by carrier-phase differential GPS. Several ground truth data are available: Four plots each of which consisting of nine accurately positioned hemispherical photographs have been sampled. The camera positions were measured with the help of a Leica total station to an absolute positioning accuracy lower than 10 cm. A digital elevation model (DEM) derived from airborne laser scanning (Falcon II, Toposys GmbH) is available for comparison of the ground level and a digital surface model (DSM) acquired by the same sensor is also at hand. However, the DSM is of limited value in terms of indicating forested areas because it stems from an campaign in early spring of 2003. So, besides the long time span as a limiting factor, it must also be assumed that the deciduous trees were mostly transparent to the laser signal and therefore do not appear in the DSM.

In Table 1 the system parameters of the E-SAR system are summarized. Note that the reduced chirp bandwidth of only 70 MHz in the P-band is due to restrictions imposed by the Swiss Federal Office of Communications to prevent interference of the radar signal with existing RF communication services within the band 390-395 MHz. The nominal chirp bandwidth is 94 MHz for both L- and P-band. The 12 P-band data sets were acquired within

	P-band	L-band
<b>Carrier frequency</b>	350 MHz	1.3 GHz
<b>Chirp bandwidth</b>	70 MHz	94 MHz
<b>Sampling rate</b>	100 MHz	100 MHz
<b>Polarizations</b>	HH-HV-VV-VH	HH-HV-VV-VH
<b>PRF</b>	500 Hz	400 Hz
<b>Ground speed</b>	90 m/s	90 m/s

Table 1: E-SAR system parameters.

one air mission. The maximal time span between the first and the last track is approx. 2 h. Due to mission duration constraints the 17 L-band tracks had to be shared among 2 missions resulting in a longer maximal time span of approximately 4.5 h between the first track of the first mission and the ultimate track of the second mission. The tracks of each tomographic pattern were flown in an interleaved manner in case that an unexpected incidence would have caused an untimely abortion of the data acquisition. In Fig. 2 and Fig. 3, respectively, the geometric configurations of the actual flight tracks for both tomographic data sets, P- as well as L-band, are shown. The flight direction is from east to west and the sensor is left-looking. In addition to the actual flight tracks, their projections to the horizontal plane and to the northing-height plane are also depicted. Each of the missions was completed by a control track which has the same nominal flight geometry as the first track. This allows assessing the amount of temporal decorrelation between the first and the last track. Table 2 contains a summary of the parameters which characterize the tomographic data sets.

#### 5 PRELIMINARY RESULTS

A partially forested area of 400 m x 1000 m has been selected for tomographic processing using the HH channel of the P-band tomographic SAR data set. For simplicity, and since the selected area is relatively flat, a 3D reconstruction grid consisting of a set of horizontal layers has been chosen. The voxel spacing is 1 m for both, easting and northing direction, and 1.5 m in vertical direction.

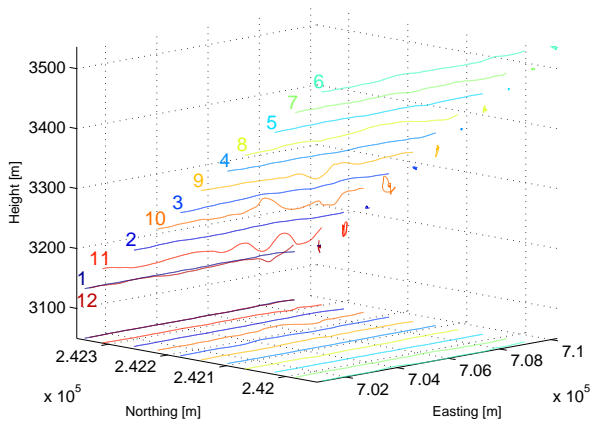


Figure 2: P-band tomographic acquisition pattern consisting of 11 flight tracks + 1 control track. The flight direction is from east to west and the sensor is left-looking. In addition to the actual flight tracks, their projections to the horizontal plane and to the northing-height plane are depicted.

	P-band	L-band
Number of flight tracks	11+1	16+1
Nominal track spacing $d_n$	56.6 m	14.14 m
Horizontal baselines	40 m	10 m
Vertical baselines	40 m	10 m
Synthetic aperture in normal direction $L$	566 m	212 m
Nominal resolution in normal direction $\delta_n$	3 m	2 m
Approx. unambiguous height $H$	30 m	30 m

Table 2: Nominal parameters for tomographic processing of the P- and L-band SAR data sets.

In Fig. 4 seven tomographic slices of the imaged volume are depicted. Three of them run in south-northern direction and the other four run in west-eastern direction. For smoother visualization the data have been upsampled in the vertical direction by a factor of 2 after focusing. The tomographic slices represent the measured radar intensity values in dB. The dotted and the dashed lines indicate the height information taken from the laser DEM or DSM, respectively. In addition, the topmost horizontal layer of the volume is shown as well as an orthorectified RGB image of the same area. The RGB image was taken from the same platform during the airborne laser scanning campaign in 2003.

6 DISCUSSION AND CONCLUSIONS

High intensity values are predominantly located at the ground level within forested areas as can be seen by comparing the tomographic slices with the laser DEM/DSM. This outcome conforms with what can be expected from horizontally polarized P-band radar back-scattering of a forested area, where double-bounce scattering from the ground surface and tree trunks is a dominant scattering mechanism. However, the high intensity values are accompanied by high side lobes in the normal direction. Besides the above-mentioned limitations dictated by sparse sampling, a very probable source of these side lobes are range timing uncertainties, which still have to be eliminated by a refined geometric calibration. A system inherent problem is still given by the limited unambiguous height in the normal direction. But, it is expected that the side lobes can be much reduced by a refined phase

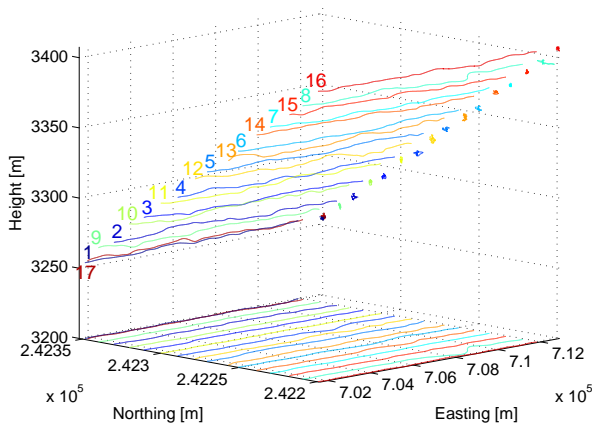


Figure 3: L-band tomographic acquisition pattern consisting of 16 flight tracks + 1 control track. The flight direction is from east to west and the sensor is left-looking. In addition to the actual flight tracks, their projections to the horizontal plane as well as to the northing-height plane are depicted.

calibration with the help of the corner reflectors.

After reprocessing of the calibrated data we intend to evaluate the quality of the TDBP-based tomographic processing (PSLR, ISLR, etc.) for all polarimetric channels. We will also quantitatively analyse whether the locations where high intensity values are detected actually conform with the occurrence of trees as indicated by the laser DEM and DSM and whether the intensity and the localization of the imaged scattering mechanisms are meaningful. The combination of all polarimetric channels of both the P-band and the L-band multi-baseline data sets is expected to give interesting insights with respect to mapping the structure of forested area by multi-baseline SAR data.

ACKNOWLEDGEMENTS

The authors would like to thank Ralf Horn, Rolf Scheiber and Martin Keller at the German Aerospace Center (DLR) for their ongoing cooperation and technical support. They would also like to thank the procurement and technology center of the Swiss Federal Department of Defense (armasuisse) for funding and supporting this work.

REFERENCES

Cumming, I. G. and Wong, F. H., 2005. Digital Processing of Synthetic Aperture Radar Data: Algorithms and Implementation. Artech House Inc., Boston, London.

Frey, O., Meier, E. and Nüesch, D., 2005. A Study on Integrated SAR Processing and Geocoding by Means of Time-Domain Backprojection. In: Proceedings of the Int. Radar Symposium, Berlin.

Frey, O., Meier, E. and Nüesch, D., 2006. An integrated focusing and calibration procedure for airborne sar data. In: Proc. of EUSAR 2006 - 6th European Conference on Synthetic Aperture Radar.

Gini, F. and Lombardini, F., 2005. Multibaseline cross-track SAR interferometry: a signal processing perspective. Aerospace and Electronic Systems Magazine, IEEE 20(8), pp. 71–93.

Guillaso, S. and Reigber, A., 2005. Polarimetric SAR Tomography (POLTOMSAR). In: Proceedings of POLINSAR'05, Frascati, Italy.

Lombardini, F. and Reigber, A., 2003. Adaptive spectral estimation for multibaseline SAR tomography with airborne L-band data. In: Geoscience and Remote Sensing Symposium, 2003. IGARSS '03. Proceedings. 2003 IEEE International, Vol. 3, pp. 2014–2016.

Moreira, A. and Huang, Y., 1994. Airborne SAR Processing of Highly Squinted Data Using a Chirp Scaling Approach with Integrated Motion Compensation. IEEE Transactions on Geoscience and Remote Sensing 32(5), pp. 1029–1040.

Nannini, M. and Scheiber, R., 2006. A Time Domain Beamforming Algorithm for SAR Tomography. In: Proc. of EUSAR 2006 - 6th European Conference on Synthetic Aperture Radar.

Reigber, A. and Moreira, A., 2000. First Demonstration of Airborne SAR Tomography Using Multibaseline L-Band Data. Geoscience and Remote Sensing, IEEE Transactions on 38(5), pp. 2142–2152.



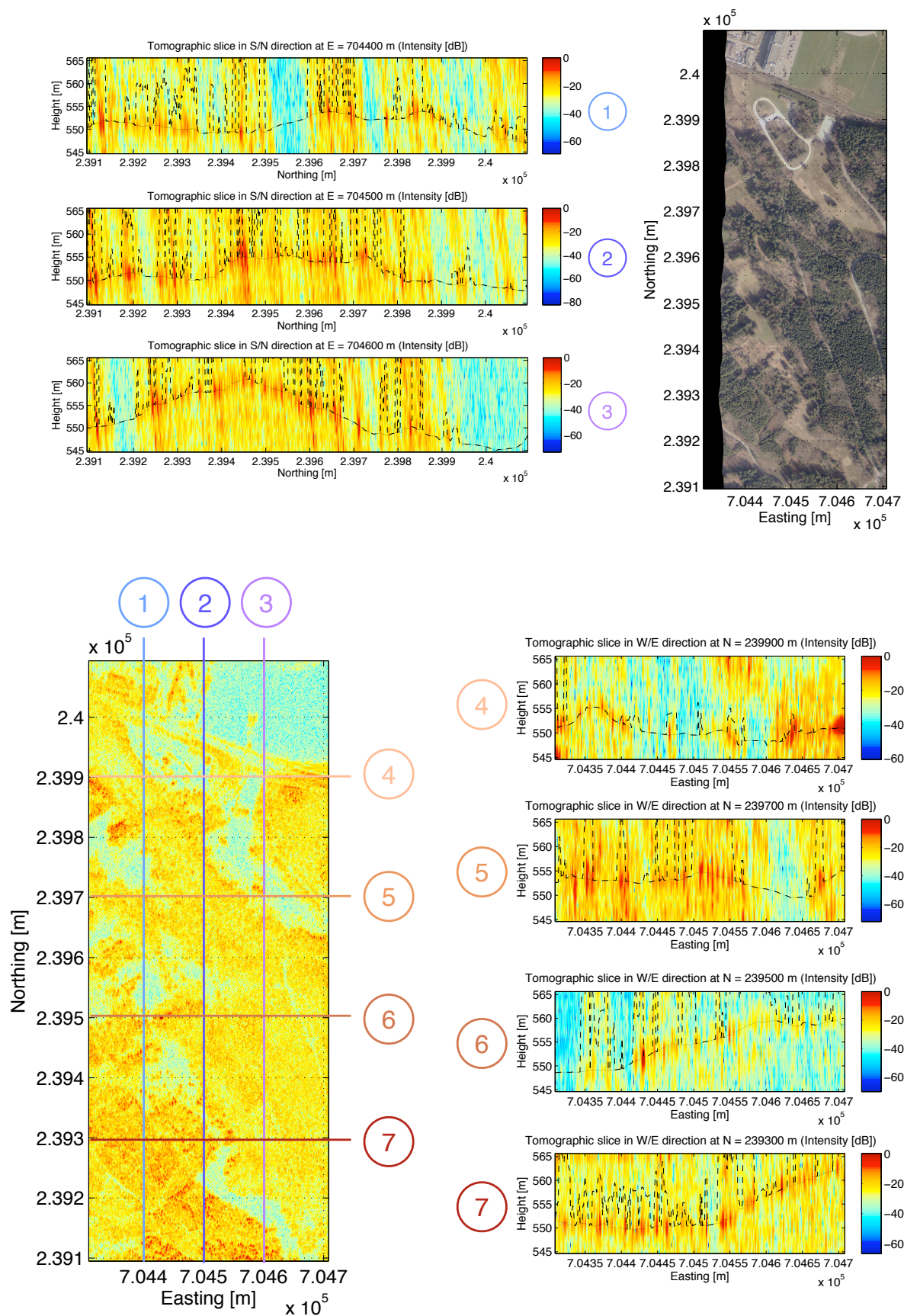


Figure 4: Tomographic slices of a forested area derived from P-band HH E-SAR data. Upper left: tomographic slices in south-northern direction. Lower left: topmost horizontal layer of the reconstruction grid. Lower right: tomographic slices in west-eastern direction. Upper right: RGB ortho-image of the same area. Dotted/dashed lines in the tomographic slices: DEM/DSM from airborne laser scanning (Falcon II, TopoSys GmbH).

# REGIONAL MAPPING OF PLANT FUNCTIONAL TYPES IN RIVER FLOODPLAIN ECOSYSTEMS USING AIRBORNE IMAGING SPECTROSCOPY DATA

L. Kooistra \*, L. Sanchez-Prieto, H.M. Bartholomeus, M.E. Schaepman

Wageningen University, Centre for Geo-Information, Droevendaalsesteeg 3, NL-6708 PB Wageningen, The Netherlands

Commission VII, WG VII/1

**KEY WORDS:** imaging spectroscopy, spectral mixture analysis, plant functional types, plant traits, dynamic vegetation model

## ABSTRACT:

Monitoring and forecasting of natural vegetation succession is essential for optimal management of river floodplain ecosystems in Western Europe. For example the development of woody vegetation types (e.g., softwood forest) increases the hydraulic resistance of the floodplain and can have negative effects on the discharge capacity of the river. However, from a biodiversity point-of-view this development results in higher valued nature reserves. The current challenge for river managers is therefore how to combine sustainable flood protection and floodplain rehabilitation in the best possible way. Natural vegetation in these floodplain ecosystems consists of a continuum between grassland and forest. Ground coverage by woody plants (trees and shrubs) ranges from non-existent to complete and forms a mosaic pattern within the ecosystem.

Dynamic vegetation modeling becomes an increasingly important tool to assess the current and future state of these complex ecosystems. In this approach, remote sensing is used to derive spatial continuous input data of the state of the ecosystem to initialize these models at simulation start. Also site-specific remote sensing derived variables (e.g., LAI, biomass, canopy N) are assimilated in these models resulting in more reliable and accurate predictions. Interfacing between remote sensing and dynamic vegetation models requires a proper representation of the grassland-forest continuum. For global scale modeling, plant functional types (PFT), i.e., groups of plant species that share similar functioning are adopted to represent vegetation distribution and derived using remote sensing based methods. Also on a regional scale the use of PFTs could be of interest to map vegetation heterogeneity through separately specifying the composition and structure of PFTs within a grid cell.

In this study we investigate the possibilities to derive the spatial distribution of PFTs for floodplain ecosystems from imaging spectroscopy data at the regional level. Field and airborne data (HyMap) were acquired for a floodplain along the river Rhine in the Netherlands and used to derive spatial continuous PFT maps. Spectra of main PFTs (grass, herbs, shrub, and trees) were selected from the image data and identified as endmembers using a site-specific library. The results show that spectral unmixing analysis can be used for mapping plant functional types to characterize the complex structure and composition of a natural floodplain ecosystem. Spatial distributions of herbaceous and tree PFTs are well in agreement with actual situation as observed in the field. Modelled fractional coverage of the herbaceous PFTs agreed reasonable well with field observed abundances ( $R^2$  between 0.35 and 0.56). Further work is required to upscale the approach from the floodplain level to the river catchment scale using medium-resolution sensors like MODIS and MERIS.

## 1. INTRODUCTION

Monitoring and forecasting of natural vegetation succession is essential for optimal management of river floodplain ecosystems in Western Europe. For example the development of woody vegetation types (e.g., softwood forest) increases the hydraulic resistance of the floodplain and can have negative effects on the discharge capacity of the river. Natural vegetation in these floodplain ecosystems consists of a continuum between grassland and forest. Ground coverage by woody plants (trees and shrubs) ranges from non-existent to complete and forms a mosaic pattern within the ecosystem (Ward *et al.*, 2002).

Increasingly, dynamic vegetation models (DVM) are being used to model the influence of natural vegetation succession on river discharge and flooding patterns (Baptist *et al.*, 2004). Traditional characterisation of vegetation dynamics by using aerial photograph derived vegetation or ecotope maps do not fulfil modelling requirements. The derived vegetation polygons consist of mixed units with a complex structure which cannot directly be linked to hydrodynamic processes.

For global scale climate modelling, plant functional types (PFT), i.e., groups of plant species that share similar functioning are adopted to represent vegetation distribution and derived using remote sensing based methods (Bonan *et al.*, 2003). Also on a regional level, several dynamic vegetation models use a PFT based approach which defines it as a group of species that share traits (morphological and physiological attributes) and play a similar role in an ecosystem (Paruelo and Lauenroth, 1996). Plant traits which influence water flow in floodplain systems (e.g., height, flexibility, density) have been identified in earlier studies (Anderson *et al.*, 2006) and could be used as a basis for the definition of PFTs.

Also on a regional scale, remote sensing based techniques would be the most appropriate method to survey the heterogeneous vegetation composition of a natural floodplain. This paper explores the possibilities to derive the spatial distribution of PFTs for floodplain ecosystems from imaging spectroscopy data. We are especially interested in the opportunities of imaging spectroscopy data to separately specify the composition and structure of PFTs within a grid

---

\* Corresponding author: e-mail Lammert.Kooistra@wur.nl

cell. Spectral mixture analysis (SMA) (Smith *et al.*, 1985) is examined as a possible tool that takes advantage of the high-dimensional spectral information content of imaging spectroscopy data to discriminate PFTs at the sub-pixel level, thus overcoming possible limitations in spatial resolution.

2. MATERIAL AND METHODS

2.1 Study area

The Millingerwaard floodplain (51°84'N, 5°99' E) along the river Waal in the Netherlands was chosen for this study. The floodplain is part of the Gelderse Poort nature reserve and considered a nature rehabilitation area, meaning that for some time now areas have been taken out of agricultural production and are allowed to undergo natural succession. This has resulted in a heterogeneous landscape (Figure 1) with river dunes covered by pioneer vegetation (MNV) along the river, a large softwood forest in the eastern part along the winterdike (MWT) and in the intermediate area a mosaic pattern of different succession stages ranging from herbaceous (RNV) to shrubs (SWS, MWS) and areas influenced by grazing (SNV). Nature management (e.g., grazing) within the floodplain is aiming at improvement of biodiversity. In addition, measures for reduction of the hydraulic resistance of the vegetation (e.g., harvesting of softwood forest) have been carried out. Plant functional types were defined as vegetation clusters with similar impact to water flow impact and were identified based on three plant traits (Anderson *et al.*, 2006): height, flexibility and density (Table 1).

Plant Functional Type	Height (m)	Flexibility <sup>1</sup> (cm)	Density <sup>2</sup>
Soft Non-woody Vegetation (SNV)	0 - 0.5	<1	Herbaceous
Medium Non-woody Vegetation (MNV)	0.5 - 1	<1	Herbaceous
Robust Non-woody Vegetation (RNV)	1 - 2	<1	Herbaceous
Soft Woody vegetation with Shrub structure (SWS)	0.5 - 4	0 - 5	Shrub
Medium Woody vegetation with Shrub structure (MWS)	0.5 - 10	5 - 15	Shrub
Medium Woody Vegetation with Tree structure (MWT)	0.5 - 35	5 - 15	Tree

1: based on stem thickness; 2: based on species composition

Table 1. Main plant functional types for vegetation in floodplain Millingerwaard along the river Waal in the Netherlands

2.2 Data

Imaging spectrometer data for the Millingerwaard were acquired on July 28, 2004 using the HyMap sensor in 126 spectral bands ranging from 400 to 2500 nm (bandwidth 15 - 20 nm). The data were processed to surface reflectance by partially compensating for adjacency effects and directional effects using the model combination PARGE/ATCOR-4 (Richter and Schläpfer, 2002). The spatial resolution of the images is 5 m. Ground measurements include top-of-canopy reflectance measurements as well as leaf optical properties measurements at all ground plots as well as several reflectance measurements of calibration surfaces using an ASD FieldSpec instrument. A mask was applied to select the Millingerwaard floodplain and to remove all areas covered with water (river and lakes).

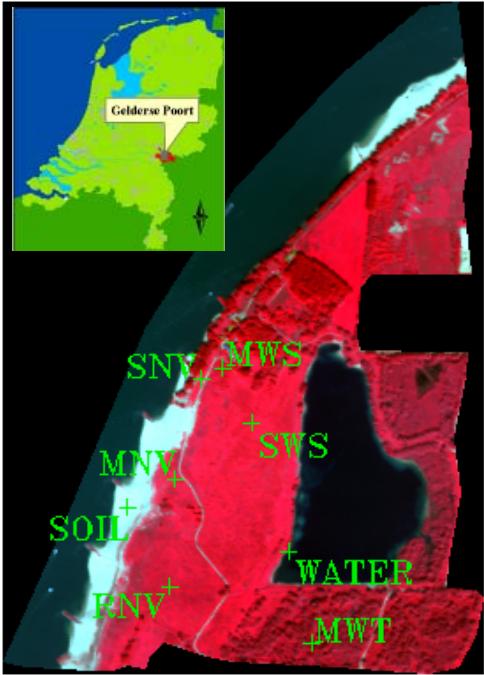


Figure 1. HyMap image for the Millingerwaard floodplain along the river Waal. The indicated points show the location of ‘pure’ PFTs from the field polygons for which spectral endmembers were derived from the image. Inset shows the location of the floodplain within the Gelderse Poort nature reserve.

Three field datasets describing species composition and vegetation structure were available for the floodplain. In 2004 and 2005, vegetation relevees were made according to the method of Braun-Blanquet in 2x2 m plots for 21 and 14 locations, respectively. Abundance per species was estimated optically as percentage soil covered by living biomass in vertical projection, and scored in a nine-point scale. The coordinates of the central location of each ground plot was determined using a differential global positioning system. Part of the 2004 and 2005 datasets were used for endmember selection while the rest of locations was used to assess the accuracy of the spatial distributions for the PFTs SNV, MNV and RNV. A third dataset consisted of a database provided by the Ark Nature Foundation with GPS measured field locations of all individual shrub and tree species in the central part of the floodplain. For every shrub and tree, parameters like stem diameter, height, volume and species type were recorded. This database was used to assess the accuracy of the spatial distribution for the PFTs SWS and MWS which both consist of vegetation with a shrub structure.

2.3 Endmember selection and spectral unmixing

As the vegetation structure within the floodplain is highly heterogeneous, we expect that the measured spectral signal for every pixel is the result of fractions in which different PFTs and also the soil background occur. Since we are interested in these fractions, spectral mixture analysis (SMA) was applied. This method assumes that a value at a given pixel is the result of a linear combination of one or more components, or endmembers (Tompkins *et al.*, 1997). The application of SMA to an image to identify PFTs requires a careful selection of endmembers related to two aspects: a) an actual list of endmembers to



include and b) identification of potential endmembers (Rosso *et al.*, 2005). For image-based extraction of endmembers, several algorithms are available (Plaza *et al.*, 2004) and have been applied in earlier vegetation studies: e.g., PPI (Schmid *et al.*, 2005; Rosso *et al.*, 2005) or SSA (Bateson *et al.*, 2000).

In our study, we used a manual approach based on field data for endmember selection. Based on the available field information, candidate pixels were selected from locations where the PFTs appeared pure or had a relative homogeneous species composition. Candidate pixels for endmember extraction of the PFTs SNV, MNV and RNV were selected using the vegetation relevés acquired in 2004 and 2005. Selection of endmember spectra for the PFTs SWS, MWS and MWT was based on the Ark database. The database was used to derive point density grid of the number of individual shrub and trees species within a 5 m pixel according to the HyMap pixel size. Pixels with the highest number of shrub and tree locations were used to derive endmember spectra for the PFTs SWS, MWS and MWT. Final locations for the selected endmembers are presented in Figure 1.

A forward minimum noise fraction (MNF) (Green *et al.*, 1988) transformation was applied to the HyMap image to reduce interband correlation and data redundancy. The MNF analysis showed that the first eigenimage had an eigenvalue of 105.1; by the 10<sup>th</sup> eigenimage the eigenvalue dropped to 6.8, and after the 30<sup>th</sup>, eigenvalues became asymptotic between around 1.3. By the 25<sup>th</sup> eigenimage most of the structural features of the floodplain disappeared, indicating increasing noise content. As a result, the first 30 bands with an eigenvalue were used for SMA. The SMA algorithm implemented in ENVI was used for this study. This algorithm provides no fully constrained option. However, for the constraint that fractions should sum up to one, a weight of 1000 was assigned.

## 2.4 Accuracy assessment

To assess the accuracy of SMA for mapping the abundance of PFTs in the Millingerwaard, three methods were used. First, the fit of the SMA model was assessed based on the spatial continuous map for the root mean square error (RMSE). Higher values of RMSE indicate regions that could contain lacking endmembers. Secondly, the dataset with actual PFTs abundances from the field in 2004 and 2005 was compared to SMA modelled abundances for these observations. As a third method, the locations of the two main shrub species available in the database of the Ark Foundation was overlaid with the abundance maps of SWS and MWS.

## 3. RESULTS AND DISCUSSION

### 3.1 Endmember selection

Six endmembers indicating different PFTs (Table 1) and a soil endmember were used as input to SMA for the Millingerwaard (Figure 2). Main differences between the PFT endmembers can be observed in the reflectance around the green (550 nm) and red (650 nm) band, around the liquid water absorption features at 970 nm and 1200 nm and large difference in intensity over the NIR and SWIR wavelength region. The soil endmember exhibits high reflectance across the entire spectral range. Small absorption features around 2250 nm and 2350 nm indicate low clay and carbonate mineral concentrations in the soil.

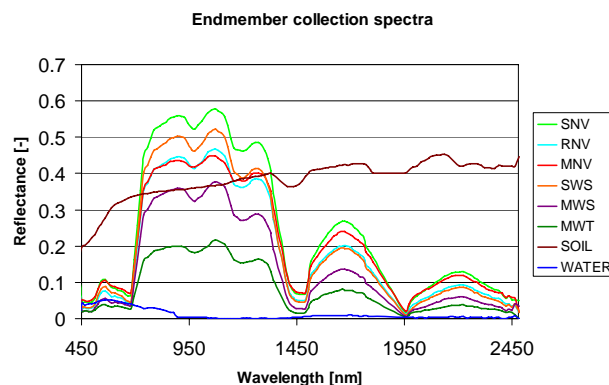


Figure 2. Spectral plot of seven endmembers used with SMA

### 3.2 Fraction images

SMA generated seven fraction images (six PFTs and soil) and a RMSE image. The spatial distribution of the PFTs in the fraction images (Figure 3) show clear patterns which agree with the observed situation in the field. The coverage of SNV is characterized by dense short (grazed) grassland vegetation and occurs in several areas of the floodplain (Figure 3). A clear hotspot can be observed in a triangular area in the north of the floodplain which is a former agricultural field under grazing management. In the central area of the floodplain, smaller grazing areas and paths which are used by cattle can be identified. Abundance of MNV is mainly located on the sandy levee along the river. This PFT is characterized by a relatively open structure and influence of the soil background in the reflectance signal (Figure 4). Apart from the levee, the PFT MNV is also abundant in the Northern part of the floodplain where the upper clay layer has been removed until the sandy subsoil. The resulting vegetation is dominated by pioneer species and has a relatively open structure.

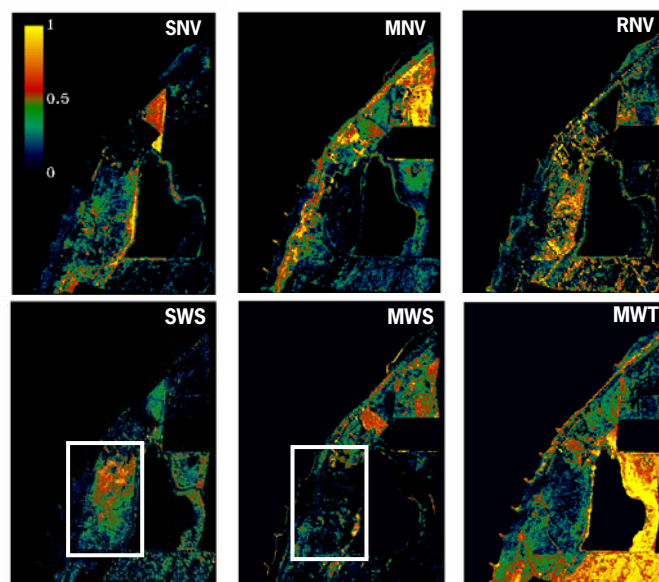


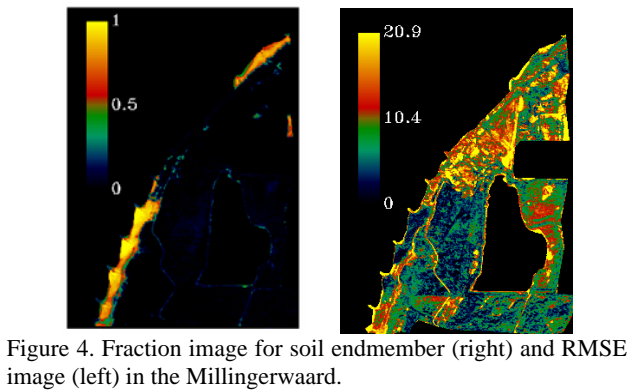
Figure 3. Fraction images per plant functional type in the Millingerwaard. The rectangles for SWS and MWS show the areas which were compared with the database of the Ark Foundation (Figure 6).

The coverage of RNV, which is dominated by *Rubus caesius* and *Urtica dioica*, is mainly concentrated in the central area of the floodplain. This area was formerly used as arable land with a relatively high nutrient input. This has resulted in natural vegetation with a dense structure and a high productivity. In addition, this PFT is also found as main understory of the softwood forest (MWT), indicated by the patchy abundance in the south-eastern part of the floodplain where the softwood forest is located. The process of shrub encroachment can be clearly observed from the spatial distribution of SWS (Figure 3) which is dominated by *Crataegus monogyna*. The direction of this process is from the North-eastern part within the indicated rectangle to the South-west. The vegetation of MWS is characterized by the presence of *Samubucus Nigra* and the fraction map shows that this PFT is abundant in some concentrated areas of the floodplain.

Comparison of the spatial pattern of MWS with the actual situation shows that not only vegetation with a shrub structure is classified as having a high abundance but also a part of the tree dominated areas. Some areas with increased coverage of the tree species *Populus* are confused with the shrub based PFT MWS. This confusion between MWS and MWT could be explained by the overlap in these two classes where main differences are related to height and species composition. Forested areas dominated by willow trees (*Salix fragilis* and *Salix Alba*) are mainly classified as MWT. The high abundance of MWT in the South-eastern part of the floodplain is explained by the relatively lower and wet position of this area resulting in a high abundance of willow trees. Areas with a MWT abundance below 0.5 depicted as green in the fraction image (Figure 3) do not agree with the actual situation. These areas are mainly covered by vegetation with a herbaceous structure (SNV, MNV). Possibly, the SMA algorithm uses the MWT endmember to compensate for the lower spectral reflectance in these areas due to lower vegetation coverage. Going from the sandy beaches along the river a small transitional area with decreasing abundance of soil can be observed (Figure 4). However, in the central part of the floodplain the abundance of open soil as modelled by SMA is relatively low.

3.3 Accuracy assessment

The RMSE map was used for a first assessment of the accuracy of the PFT fraction images generated for the Millingerwaard. Higher values of RMSE indicate regions that could contain lacking endmembers. High RMSE values for the forested area in the centre of the image can be explained by the choice of the MWT endmember (Figure 1). The vegetation structure of the



latter endmember was characterized by a dense coverage of willow trees, while for the central forest area the structure has a more open character while also species coverage is more divers (including *Populus*). High RMSE values in the willow forest in the Eastern part of the floodplain can be explained by presence of small lakes which are covered by willow trees. As a result mixed pixels are present with both influence of water and vegetation. However, an endmember for water was not included in our analysis, resulting in increased values for RMSE. High RMSE values along the river are explained by the heterogeneous coverage of the groins (e.g., vegetation, stones of basalt rock) and the influence of wet soils along the shores of the river. Finally, in our endmember set we have not accounted for a shadow component (Li *et al.*, 2005). This could be especially relevant for forest edges, hedges with a composition of both shrub and trees and for locations with individual large trees. Removal of the errors related to non-vegetated areas (e.g., rock, soil, water, dust road etc.) could be achieved by using an effective VI-based masking procedure (e.g., NDVI). However, as vegetation coverage is abundant related to the spatial resolution of the HyMap image (5 m) complete removal of all non-vegetated components is difficult.

Comparison of the predicted vs. observed coverage for the herbaceous PFTs SNV, MNV and RNV shows a reasonable agreement as indicated by  $R^2$  values of 0.56, 0.35 and 0.43, respectively. Negative fractions for some of the plots are explained by the fact that for this study we used an unconstrained implementation of the SMA algorithm. However, no large negative values were derived using SMA. In general fractions for all three herbaceous PFTs are underestimated. Comparison of the individual plots with the expected one-to-one line shows that this is especially the case for SNV and to a lesser extent for MNV and RNV. This can

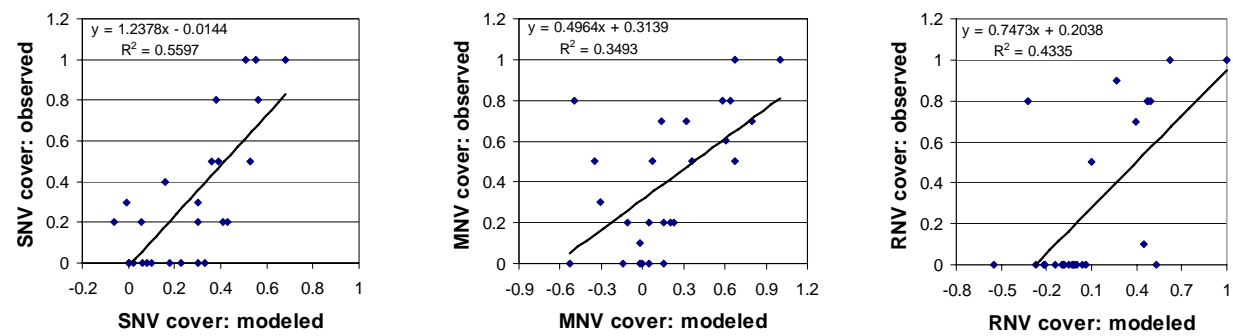


Figure 5. Comparison of results from predicted fractions using SMA and fractions observed in field plots in 2004 and 2005 (n = 26) for PFTs SNV, MNV and RNV, respectively.



partly be explained by the difference in the sample units of the vegetation relevée (2x2 m) and the spatial resolution of the HyMap image (5x5 m). For this study we assumed that the PFT abundances in the plot of the vegetation relevée are representative for the co-located HyMap pixel. However, especially the spatial structure for SNV is relatively narrow (e.g., grazing paths) with small areas with a homogeneous coverage. This means that translation of the field relevée abundances to the HyMap pixel resolution, results in an overestimation of the SNV abundance for the field observed value in Figure 5.

Plots which are located on the x-axis in Figure 5 indicate that the SMA model calculates the presence of a certain PFT while in the field situation this PFT is not abundant. Overestimation for these fractions shows maximum values up to 0.3, 0.2 and 0.48 for SNV, MNV and RNV respectively.

The accuracy of the estimated fractions for the PFTs SWS and MWS was assessed through a comparison of the fraction images with the locations of individual shrub stands (database Ark Foundation) for the central part of the Millingerwaard (Figure 6). Differences between SWS and MWS are related to height of the vegetation and the thickness of the stem (or 'flexibility') as indicated in Table 1. Based on this difference we related the location of the *Crataegus monogyna* (n=2100) to the SWS fraction image and the location of *Samubucus Nigra* (n=1254) to the MWS fraction image. The comparison shows (Figure 6) that there is a reasonable agreement between individual shrub locations and areas with a relatively high abundance of SWS and MWS. However, high abundance of SWS is not only related to *Crataegus monogyna* but also to *Samubucus Nigra*, while certain patterns for MWS are also related to the presence of *Crataegus monogyna*. This agrees with the concept of PFTs where differences between vegetation units are related to their plant traits instead of their species composition. In addition, the comparison shows that younger shrub plants which are mainly located in the southern part of the floodplain are not always recognized. This could be explained by their spectral resemblance to the rough herbaceous PFTs. In this analysis we did not include available information on species height and

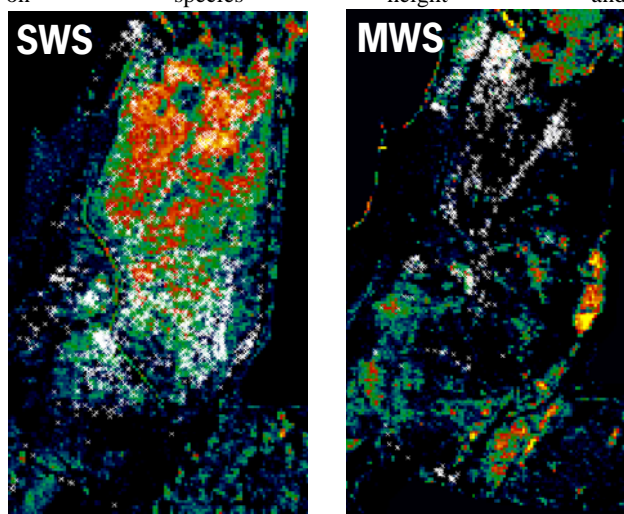


Figure 6: Comparison of fraction images for SWS and MWS with the locations for individual species of *Crataegus monogyna* (n=2100) and *Samubucus Nigra* (n=1254), respectively. Locations were taken from the database of the Ark Foundation

volume which could be used to get a better explanation of the spatial structures in the fraction images of SWS and MWS.

Experience of nature managers within the floodplain Millingerwaard indicates that vegetation succession in the floodplain has resulted in a gradual increase of shrub coverage at the expense of grass and herbaceous vegetation types. In this study we focussed on mapping of PFTs. However, based on available hyperspectral data for 2001 and 2005 for this floodplain, we will investigate the possibilities of these data in combination with SMA to monitor these shrub encroachment processes.

In a next step, these imaging spectroscopy derived vegetation variables (e.g., PFT, LAI, biomass, vegetation structure) can be used for initialization and calibration of dynamic vegetation models with the objective to test ecological hypotheses or to assess and forecast the state of future landscapes (Kooistra *et al.*, 2007). In addition, further work is required to upscale the approach from the floodplain level to the river catchment scale using medium-resolution sensors like MODIS and MERIS.

#### 4. CONCLUSIONS

This paper shows that SMA can be used for mapping plant functional types to characterize the complex structure and composition of a natural floodplain ecosystem. The results show that spatial distributions of herbaceous and tree PFTs are well in agreement with actual situation as observed in the field. For older plants, the spatial distribution of shrub PFTs is well in agreement with the field situation. Younger shrub plants are not always recognized which could be explained by their spectral resemblance to the rough herbaceous PFTs. The modelled fractional coverage of the herbaceous PFTs agreed reasonable well with field observed abundances with  $R^2$  values ranging between 0.35 and 0.56. In this study we used a manual approach for endmember selection. Although the use of image based endmember extraction techniques would be of interest to investigate, our experience is that the use of field information is an important requirement for proper selection in complex vegetated areas.

#### ACKNOWLEDGMENTS

The authors wish to acknowledge the Belgian Science Policy Office for providing the HyMap data-set and Staatsbosbeheer for their permission to access the Millingerwaard test area. We would like to thank Bart Beekers and Johan Bekhuis of the Ark Nature Foundation for provision of the woody species database.

#### REFERENCES

- Anderson, B.G., Rutherford, I.D., and Western, A.W., 2006. An analysis of the influence of riparian vegetation on the propagation of flood waves. *Environmental Modelling and Software*, 21, pp. 1290-1296.
- Baptist, J.P., Ellis Penning, W., Duel, H., Smits, A.J.M., Geerling, G.W., Van der Lee, G.E.M., and Van Alphen, J.S.L., 2004. Assessment of the effects of cyclic rejuvenation on flood levels and biodiversity along the Rhine river. *River Research and Applications*, 20, pp. 285-297.
- Bonan, G.B., Levis S., Sitch S., Vertenstein, M., Olson K.W., 2003. A dynamic global vegetation model for use with climate

models; concepts and description of simulated vegetation dynamics. *Global Change Biology*, 9, pp. 1543-1566.

Green, A.A., Berman, M., Switzer, P., Craig, M.D., 1988. A transformation for ordering multispectral data in terms of image quality with implications for noise removal. *IEEE Trans. Geosci. Remote Sens.*, 26, pp. 65-74.

Kooistra, L., Wamelink, G.W.W., Schaepman-Strub, G., Schaepman, M., van Dobben, H., Aduaka, U., and Batelaan, O., 2007. Assessing and predicting biodiversity in a floodplain ecosystem: assimilation of Net Primary Production derived from imaging spectrometer data into a dynamic vegetation model. *Remote Sensing of Environment*, (submitted).

Li, L., Ustin, S.L., and Lay, M., 2005. Application of multiple endmember spectral mixture analysis (MESMA) to AVIRIS for coastal salt marsh mapping: a case study in China Camp, CA, USA. *International Journal of Remote Sensing*, 26, pp. 5193-5207.

Paruelo, J.M., Lauenroth, W.K., 1996. Relative abundance of plant functional types in grasslands and shrublands of North America. *Ecological Applications*, 6(4), pp. 1212-1224.

Plaza, A., Martinez, P., Perz, R., and Plaza, J., 2004. A quantitative and comparative analysis of endmember extraction algorithms from hyperspectral data. *IEEE Transactions on Geoscience and Remote Sensing*, 42, pp. 650-663.

Richter, R., and Schläpfer, D., 2002. Geo-atmospheric processing of wide FOV airborne imaging spectrometry data. In *Proceedings of SPIE - The International Society for Optical Engineering*, Vol. 4545, pp. 264.

Rosso, P.H., Ustin, S.L., and Hastings, A., 2005. Mapping marshland vegetation of San Francisco Bay, California, using hyperspectral data. *International Journal of Remote Sensing*, 26, pp. 5169-5191.

Schmid, T., Koch, M., and Gumuzzio, J., 2005. Multisensor approach to determine changes in wetland characteristics in semiarid environments (Central Spain). *IEEE Transactions on Geoscience and Remote Sensing*, 43, pp. 2516-2525.

Smith, M.O., Johnstonn, P.E., and Adams, J.B., 1985. Quantitative determination of mineral types and abundances from reflectance spectra using principal component analysis. *J. Geophys. Res.*, 90, pp. 797-804.

Tompkins, S., Mustard, J.F., Pieters, C.M., and Forsyth, D.W., 1997. Optimization of endmembers for spectral mixture analysis. *Remote Sensing of Environment*, 59, pp. 472-489.

Ward, J.V., Tockner, K., Arscott, D.B., and Claret, C., 2002. Riverine landscape diversity. *Freshwater Biology*, 47, pp. 517-539.

# FUSION OF IMAGING SPECTROMETER AND LIDAR DATA USING SUPPORT VECTOR MACHINES FOR LAND COVER CLASSIFICATION IN THE CONTEXT OF FOREST FIRE MANAGEMENT

B. Koetz<sup>a,\*</sup>, F. Morsdorf<sup>a</sup>, T. Curt<sup>b</sup>, S. van der Linden<sup>c</sup>, L. Borgniet<sup>b</sup>, D. Odermatt<sup>a</sup>, S. Alleaume<sup>b</sup>, C. Lampin<sup>b</sup>, M. Jappiot<sup>b</sup> and B. Allgöwer<sup>d</sup>

<sup>a</sup> Remote Sensing Laboratories (RSL), Dept. of Geography, University of Zurich, Winterthurerstrasse 190, CH-8057 Zurich, Switzerland, Email: bkoetz@geo.unizh.ch

<sup>b</sup> Cemagref, Aix-en-Provence, Mediterranean ecosystems and associated risks research unit, 3275 route de Cézanne-CS 40061-13182 Aix en Provence cedex 5, France

<sup>c</sup> Geomatics Department, Humboldt-Universität zu Berlin, Unter den Linden 6, D-10099 Berlin, Germany

<sup>d</sup> Geographic Information Systems, Dept. of Geography, University of Zurich, Winterthurerstrasse 190, CH-8057 Zurich, Switzerland

## Commission VII, WG 1

**KEY WORDS:** Support Vector Machines, land cover classification, hyperspectral, LiDAR, multi-sensor fusion

### ABSTRACT:

A combination of the two remote sensing systems, imaging spectrometry (IS) and Light Detection And Ranging (LiDAR), is well suited to map fuel types, especially within the complex wildland urban interface. LiDAR observations sample the spatial information dimension describing geometric surface properties. Imaging spectrometry on the other hand samples the spectral dimension, which is sensitive for discrimination of species and surface types. As a non-parametric classifier Support Vector Machines (SVM) are particularly well adapted to classify data of high dimensionality and from multiple-sources as proposed in this work. The presented approach achieves an improved land cover mapping based on a single SVM classifier combining the spectral and spatial information dimensions provided by imaging spectrometry and LiDAR.

### 1. INTRODUCTION

Accurate description of wildland fuel types and fuel properties is vital for understanding the processes involved in initiation and propagation of forest fires (Carlson and Burgan 2003). Remote sensing offers the potential to provide spatially distributed information on fuel types important for the assessment of fire risk and to mitigate the impact of wildland fires (Chuvieco 2003; Justice et al. 2003). Data of the two remote sensing systems, imaging spectrometry and LiDAR, are well suited to map the diverse and heterogeneous fuel types, especially within the complex Mediterranean environment and the wildland urban interface (WUI).

Land cover monitoring in the context of forest fire management enables the assessment of the spatial distribution for different fuel types. The classification of fuel types is specifically dependant on the height, density and the surface type of the fuel. LiDAR observations sample the spatial information dimension describing the geometric properties of natural and artificial surfaces (Andersen et al. 2005; Morsdorf et al. 2004). Imaging spectrometry on the other hand samples the spectral dimension, which is sensitive for discrimination of species, surface types and fuel moisture (Jia et al. 2006; Kötz et al. 2004). The observations of these two remote sensing systems can mutually complement each other and are thus indispensable for comprehensive and specific fuel type mapping. Spatial distribution of land cover together with additional properties on the fuel structure and condition can be further translated into fuel models important for the parameterization of forest fire behaviour models.

The synergistic use of LiDAR and spectral data has already been exploited for land cover mapping purposes (Hill and Thomson 2005; Hodgson et al. 2003; Packalen and Maltamo 2007). Nevertheless commonly used statistical classification

methods, such as maximum likelihood classification, are limited to classify high dimensional data typically provided by multiple sources (Benediktsson et al. 1990). With increasing numbers of input dimensions and complexity of the data the description of an appropriate multivariate model required by statistical approaches becomes impractical. Several non-parametric classifiers have been introduced which do not require such prior knowledge on the statistical distribution of the data to be classified.

Being such a non-parametric classifier Support Vector Machines (SVM) are particularly well suited to classify data of high dimensionality and from multiple sources (Waske and Benediktsson 2007 (in review)). SVM delineate two classes by fitting an optimal separating hyperplane to those training samples that describe the edges of the class distribution. As a consequence they generalize well, even when only small training sets are available for the classification of high dimensional data (Pal and Mather 2006).

Within the presented study we focus on mapping fuel types at landscape level based on airborne LiDAR and imaging spectrometer data over a Mediterranean site south of Aix-en-Provence.

The final performance of the data fusion approach is assessed by the accuracy of the classification based on the combined imaging spectrometry and LiDAR data compared to a pure spectral classification input.

### 2. DATA

An airborne survey was conducted early October 2006 over a Mediterranean site south of Aix-en-Provence, France. The covered site comprised typical Mediterranean vegetation intermixed with urban structures. Vegetation covered a typical range of French Mediterranean wildland fuels: (i) fire-resistant

matorrals (so-called garrigue) dominated by species such as the sclerophyllous *Quercus coccifera* and *Ulex* spp.; (ii) fire-prone *Pinus halepensis* woodlands; and (iii) fire-resistant *Quercus* woodlands (*Q. ilex*, *Q. pubescens*). These three predominant vegetation types are mixed as a function of fire history and vegetation dynamics (Quézel and Médail 2003). These vegetation types are intermingled with human settlements and buildings forming a wildland-urban interface. This entails frequent management practices of vegetation in the region such as shrub-clearing of the understorey, and thinning of the overstorey.

The employed remote sensing systems the LiDAR (Optech, ALTM3100) and the imaging spectrometer (AISA-Eagle) were mounted together with a very high-resolution photogrammetric camera (40 cm spatial resolution) on a helicopter and operated by the company HELIOGS. The airborne survey was organized to cover a region of about 13.6 x 3.6 km in a spatial resolution of 1 meter. In the presented study only subset is presented (Fig. 1-2).

After pre-processing, LiDAR derivatives and spectral bands of the imaging spectrometer were co-registered and as layer stack jointly considered for the classification. Parallel to the airborne survey a comprehensive field campaign was conducted for the validation of the fuel types derived from the observations of the two remote sensing systems. The field measurements collected describe the relevant fuel types, including a specific characterization of the WUI interface and species composition. Fuel properties such as biomass and fuel moisture content were also sampled.

2.1 Imaging Spectrometer

The imaging spectrometer data employed in this study has been recorded by the AISA/Eagle imaging spectrometer (Tab. 1). The proposed thematic analysis required a dedicated geometric and radiometric pre-processing of the imaging spectrometer data. The image data was geometrically corrected by the parametric geocoding approach PARGE. Topography and illumination effects were taken into account based on the digital surface model provided by the LiDAR. Remaining geometric inaccuracies caused by erroneous synchronization with the inertial navigation system had to be corrected by a direct co-registration to the LiDAR data. Subsequently the physically based atmospheric correction software ATCOR4 was employed to obtain top-of-canopy reflectance (Richter and Schlöpfer 2002; Schlöpfer and Richter 2002) (Fig. 1). The original spectral range and resolution have been reduced due to data quality issues to 454-923 nm and 4.6 nm respectively.

Image area	Ground resolution	Spectral bands
2000 x 370m FOV: 36.7°	1 m IFOV: 0.036°	244 bands with 2.3 nm width 400-970 nm

Table 1. Specifications of the AISA/Eagle imaging spectrometer data

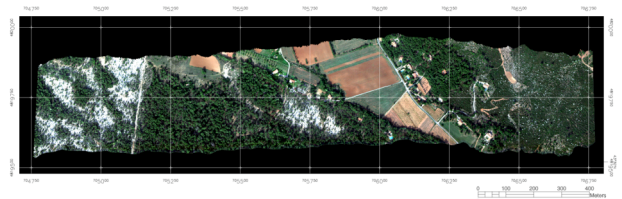


Figure 1. Geometrically and radiometrically corrected AISA/Eagle data of the study site (true colour composite)

2.2 LiDAR

The LiDAR system used was the Airborne Laser Terrain Mapper ALTM3100 laser scanner developed by the Canadian company Optech (Tab. 2). The ALTM3100 system is a laser rangefinder recording up to four returns of the laser signal from the ground surface. For a small subset of 2 x 1.5 km the full waveform of the laser return signal was also recorded with the Optech waveform digitizer. The survey was conducted with a nominal height above ground of 1000 m. This leads to average point density of 3.7 points per square meter (p/m<sup>2</sup>) enabling the processing of elevation models of the surface and terrain in the spatial resolution of one meter (Fig. 2).

Several simple derivatives describing the vertical and horizontal geometric surface properties are retrieved from the original LIDAR return distribution similar to (Naesset 2002; Naesset and Gobakken 2005). The vertical height distribution of laser returns within gridded 3 x 3 meter boxes was described by six height percentiles. Furthermore point density for six equidistant layers was derived based on the same vertical return distribution for an assessment of the vertical density distribution. Finally the difference between the digital surface and the terrain model provided an estimate of the canopy height model, which also included heights of artificial structures. All LiDAR derivatives were normalized to their respective maximal values facilitating the optimization of the SVM classification parameters.

Scan angle	Ground resolution	Point density	Laser wavelength
FOV: ±25°	1 m pixel size (DTM & DSM)	3.7 points/m <sup>2</sup>	1064 nm

Table 2. Specifications of the ALTM3100 LiDAR (Optech)

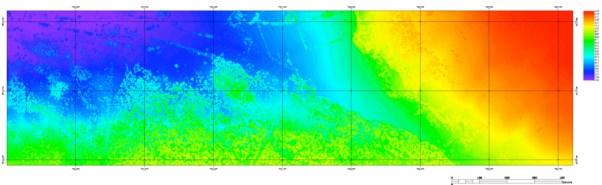


Figure 2. Digital surface model (DSM) obtained by the Optech laser scanner ALTM3100 of the study site

3. METHODS

The land cover classification was performed by the non-parametric Support Vector Machines (SVM). The SVM classification was trained and applied to three different data sets representing different input sources and information dimensionality (Fig. 3).

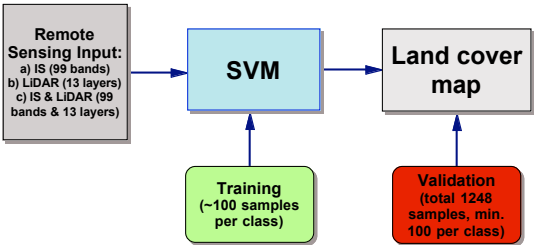


Figure 3. Processing flow of SVM classification setups a-b) single sources and c) multiple remote sensing sources

3.1 Support Vector Machines

SVM split two classes by constructing an optimal separating hyperplane, which maximizes the distance between the two

classes (Fig. 4) (Burges 1998). This hyperplane is fitted only to the training samples that describe the margins of the corresponding classes. For linear non-separable cases the data is mapped into a higher dimensional feature space that allows a linear hyperplane to split the classes newly distributed data. Separate SVM were trained for different remote sensing inputs (Fig. 3): single sources: Imaging spectrometer (IS, 99 bands), LiDAR (13 layers) and as multiple source: IS and LiDAR combined in a layer stack (99 bands + 13 layers).

To solve the multi-class problem with the originally binary SVM a one-against-all (OAA) strategy was applied (Foody and Mathur 2004): a set of binary classifiers is trained to individually separate each class from the rest. The final class label is then determined by selecting the maximum decision value, i.e. the distance of a pixel to the separating hyperplane, from the set of OAA outputs.

The training of the SVM was performed using the v-SVM approach in LIBSVM (Chen and Lin 2001). A Gaussian kernel was used to transform the data (Vapnik 1998). In this case, two parameters needed to be set for the training: the parameter  $\gamma$  that controls the width of the Gaussian kernel and  $\nu$ , an upper bound on the fraction of training errors and a lower bound of the fraction of support vectors (Schoelkopf et al. 2000). The more common C-SVM and the applied v-SVM lead to similar results, but v-SVM were chosen as they require less processing time. An IDL-implementation of LIBSVM for remote sensing data was used to train wide ranges of values for  $\gamma$  [0.001-1000] and  $\nu$  [0.001-0.2]. Subsequently the quality of the resulting classification was evaluated based on a 16-fold cross validation (Janz et al. 2007). This way, optimal parameters could be found for each binary OAA classifier and an overfitting to the reference data was avoided.

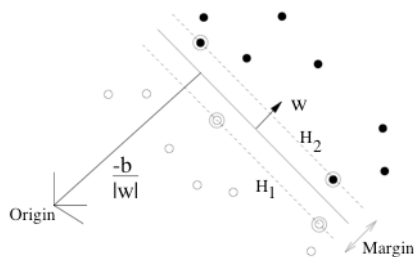


Figure 4. Fitting of a hyperplane (Burges 1998)

3.2 Classification: training and validation

A classification scheme specifically adapted to the characteristics of the wildland urban interface was developed based on the fuel type classification of the European PROMETHEUS project and the experiences in mapping urban areas (Herold et al. 2003). The classification scheme is divided into different levels as presented in Table 3. The first and second level represent functional categories and land cover classes relevant for fuel type discrimination. The third level is thematically divided by surface properties and could be extended to include different vegetation functional types or species. Only classes present in the covered area could be considered amounting up to a number of nine land cover classes.

The accuracy of a supervised classification depends significantly on the training data set. Specifically for training of SVM it is important to include mixed pixels at the border of class boundaries, as they are most efficient to determine the hyperplane between two classes (Foody and Mathur 2006). Therefore, a clustered sampling strategy was performed. For each class seed points were randomly selected where a 5 x 5 pixel cross was sampled similar to (van der Linden et al.

submitted). This strategy helped to cover the class internal heterogeneity of the different classes as well as to include mixed pixels along with adjacent pure pixels to describe the position of the hyperplane. The samples were labeled based on very high-resolution aerial photographs acquired along with the remote sensing data. For discrimination of vertical properties for certain classes, such as shrubs, the canopy height model was consulted. For each class about 100 samples were selected. For classes with a low areal coverage, such as swimming pools and roofs, a lower number of samples had to be taken.

For the accuracy assessment of the different classification results an independent validation set was collected by unstratified randomized sampling (900 samples). Additional stratified randomized sampling was necessary for underrepresented classes (roof tiles, swimming pool, road asphalt, road gravel, bare soil, bare rock) adding up to 100 samples for each class. A total of independent 1248 samples were selected and labeled to one of the land cover classes based on the very high-resolution aerial photographs.

Level 1	Level 2	Level 3
Built up	Buildings/roof	Wood shingle roof
		Tile roof
		Metal roof
		Concrete roof
	Transportation areas	Asphalt road
		Concrete road
		Gravel road
		Parking lot
	Sport infrastructure	Tartan court
Vegetation	Ground fuels (< 30 cm)	Grass & agricultural fields
	Shrub / Garriuges (< 2 m)	* extendable for different vertical structure & species
	Tree stands	* extendable for different vertical structure & species
Non-urban bare surfaces	Bare soil	
	Bare rock	
Water bodies	Swimming pools	
	Natural water bodies	

Table 3. Landcover classification scheme adapted for fuel type mapping in the wildland urban interface

4. RESULTS AND DISCUSSION

The performance of the different SVM classifications were assessed using confusion matrices and user's accuracy (Congalton and Green 1999). Three SVM classifications based on different remote sensing inputs have been validated separately to assess the advantages for land cover mapping of each sensor system and the improvement of the multiple-source fusion.

The SVM classification of the imaging spectrometer data provided acceptable results in terms of overall accuracy and kappa coefficient (Tab. 4). Class specific results reveal significant classification confusion between spectrally similar classes such as the three vegetation classes, which lead to moderate user accuracies (Fig. 5). Also some confusion between bare rock and ground fuel is evident caused probably by mixed pixels.

The overall classification performance of the pure LiDAR data was poor, but nevertheless provided significant user accuracies for classes with properties in the vertical dimension (Fig. 5).



Especially the class roof tiles performed very well, which probably can probably be explained by the absolute height above ground with concurrent opaqueness of roofs as opposed to tree canopies, which are semi-transparent three-dimensional objects. The moderate results for the shrub class is caused by issues with the vertical separability of laser returns for low canopies. Further for shrubs with high canopy density the laser is incapable of penetrating to the ground. Both issues lead to the lack of the vertical information content in the LiDAR data for certain shrub canopies.

The joint classification of the multiple sources, imaging spectrometer and LiDAR, leads to a significant improvement in terms of overall accuracy and kappa (Tab. 4). The inclusion of classes with similar geometric but different spectral properties, such as roofs of different materials (e.g. in Tab. 3), would even increase this improvement. Most of the achieved improvement in accuracy for the multiple-source classification can be explained by the decreased confusion between the vegetation classes. The vertical information content of the LiDAR observations was especially helpful to separate the classes ground fuel and tree canopy. LiDAR provides relatively to spectral information content no additional information on the class shrub due to the issues related to vertical separability of laser returns and vegetation density. Further, spectrally similar classes such as bare soil and roof tiles made of similar material could better be separated by the vertical information provided the LiDAR. This effect was not revealed by the confusion matrix but is visible in the land cover maps (Fig. 6).

Remote sensing input	Overall Accuracy	Kappa coefficient
IS & LiDAR	75.4 %	0.716
IS	69.15 %	0.645
LiDAR	31.73 %	0.226

Table 4. Accuracy assessment of the SVM classifications

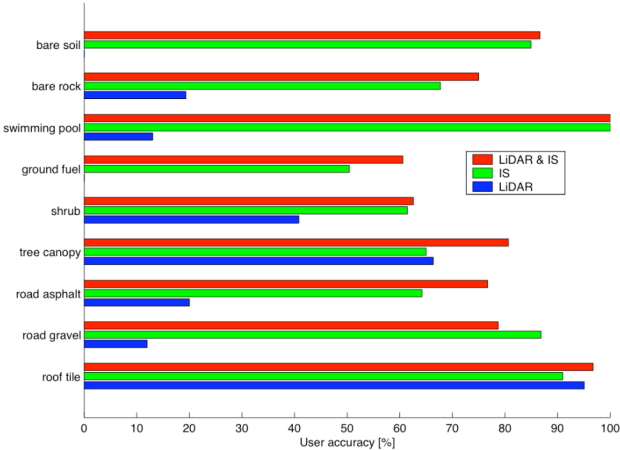


Figure 5. User accuracy of SVM classification performances based on different remote sensing data input

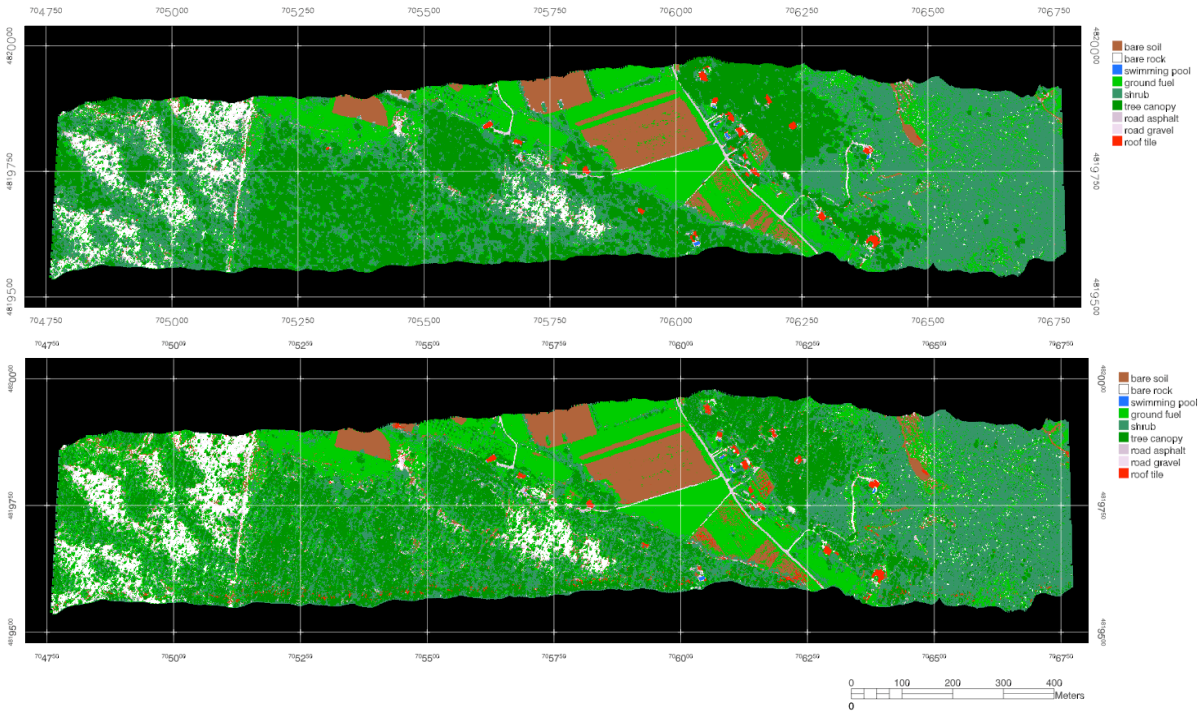


Figure 6. Land cover maps based on the different SVM classifications, upper map: product based on the multiple input sources IS & LiDAR, lower map: product based on the single input source IS

5. CONCLUSIONS

The Earth observation requirements within several scientific fields, such as urbanization, biodiversity and natural hazards, demand land cover monitoring of landscapes with increasing complexity and in ever higher levels of detail. The commonly used approach of land cover classification based on multi-spectral data is limited by the spectral similarity of certain surface types. Further, three-dimensional features of important

surface types, such as built-up urban construction or vertical vegetation structure, are not directly inferable from the spectral information content provided by passive optical sensors. Due to this underdetermined and partly indirect relationship, the interpretation of remote sensing data for land cover monitoring should rely on as many independent observations as possible. This conclusion leads to the combined exploitation of multiple information sources as provided for example by complementary sensor systems. The increased dimension and complexity of

such information also requires new classification methods to adequately interpret the data of multiple information sources. The method presented in this study is capable of a joint one-step SVM classification for the fusion of multiple-source remote sensing data provided by an imaging spectrometer and a LiDAR. The SVM classifier was able to efficiently exploit the significantly increased information content in the (hyper)spectral and the three-dimensional dimension. Specifically the SVM generalized well, even when only small training sets were available for the classification of the high dimensional data provided the multiple data sources. The three-dimensional information of the LiDAR data complemented well the spectral information leading to a significant increase in the overall land cover classification accuracy relative to the pure spectral information input. Important features of fuel types as the vertical structure vegetation and houses could be assessed with higher accuracy and reliability. This enhanced mapping of the wild land urban interface can be a significant input to forest fire behaviour models leading to improved risk assessment and mitigation of forest fires.

### ACKNOWLEDGEMENTS

This study has been funded by the EC integrated project FIRE PARADOX. The employed SVM classification tool has been developed by Andreas Janz (Humboldt-Universität) whose support is very much appreciated. The airborne survey of the imaging spectrometer and the LiDAR has been conducted by the HELIOGS.

### REFERENCES

- Andersen, H.E., McGaughey, R.J., & Reutebuch, S.E. (2005). Estimating forest canopy fuel parameters using LIDAR data. *Remote Sensing of Environment*, 94, 441-449
- Benediktsson, J.A., Swain, P.H., & Ersoy, O.K. (1990). Neural Network Approaches Versus Statistical-Methods in Classification of Multisource Remote-Sensing Data. *Ieee Transactions on Geoscience and Remote Sensing*, 28, 540-552
- Burges, C.J.C. (1998). A Tutorial on Support Vector Machines for Pattern Recognition. *Data Mining and Knowledge Discovery*, 2, 121-167
- Carlson, J.D., & Burgan, R.E. (2003). Review of users' needs in operational fire danger estimation: the Oklahoma example. *International Journal of Remote Sensing*, 24, 1601-1620
- Chen, C.-C., & Lin, C.-J. (2001). LIBSVM: a library for support vector machines. In: <http://www.csie.ntu.edu.tw/~cjlin/libsvm>
- Chuvieco, E. (Ed.) (2003). *Wildland Fire Danger Estimation and Mapping: The Role of Remote Sensing Data*. Singapore: World Scientific
- Congalton, R.G., & Green, K. (1999). *Assessing the Accuracy of Remotely Sensed Data: Principles and Practices*. Boca Raton: Lewis
- Foody, G.M., & Mathur, a. (2004). A relative evaluation of multiclass image classification by support vector machines. *Ieee Transactions on Geoscience and Remote Sensing*, 42, 1335-1343
- Foody, G.M., & Mathur, a. (2006). The use of small training sets containing mixed pixels for accurate hard image classification: Training on mixed spectral responses for classification by a SVM. *Remote Sensing of Environment*, 103, 179-189
- Herold, M., Gardner, M.E., & Roberts, D.A. (2003). Spectral resolution requirements for mapping urban areas. *Ieee Transactions on Geoscience and Remote Sensing*, 41, 1907-1919
- Hill, R.A., & Thomson, A.G. (2005). Mapping woodland species composition and structure using airborne spectral and LiDAR data. *International Journal of Remote Sensing*, 26, 3763-3779
- Hodgson, M.E., Jensen, J.R., Tullis, J.A., Riordan, K.D., & Archer, C.M. (2003). Synergistic use of lidar and color aerial photography for mapping urban parcel imperviousness. *Photogrammetric Engineering and Remote Sensing*, 69, 973-980
- Janz, A., Schiefer, S., Waske, B., & Hostert, P. (2007). A user-oriented tool for advanced classification of hyperspectral data using support vector machines. In, *EARSeL Imaging Spectroscopy workshop*. Bruegge
- Jia, G.J., Burke, I.C., Goetz, A.F.H., Kaufmann, M.R., & Kindel, B.C. (2006). Assessing spatial patterns of forest fuel using AVIRIS data. *Remote Sensing of Environment*, 102, 318-327
- Justice, C.O., Smith, R., Gill, A.M., & Csiszar, I. (2003). A review of current space-based fire monitoring in Australia and the GOF/GOLD program for international coordination. *International Journal of Wildland Fire*, 12, 247-258
- Kötz, B., Schaepman, M., Morsdorf, F., Bowyer, P., Itten, K., & Allgower, B. (2004). Radiative transfer modeling within a heterogeneous canopy for estimation of forest fire fuel properties. *Remote Sensing of Environment*, 92, 332-344
- Morsdorf, F., Meier, E., Kötz, B., Itten, K.I., Dobbertin, M., & Allgower, B. (2004). LIDAR-based geometric reconstruction of boreal type forest stands at single tree level for forest and wildland fire management. *Remote Sensing of Environment*, 92, 353-362
- Naesset, E. (2002). Predicting forest stand characteristics with airborne scanning laser using a practical two-stage procedure and field data. *Remote Sensing of Environment*, 80, 88-99
- Naesset, E., & Gobakken, T. (2005). Estimating forest growth using canopy metrics derived from airborne laser scanner data. *Remote Sensing of Environment*, 96, 453-465
- Packalen, P., & Maltamo, M. (2007). The k-MSN method for the prediction of species-specific stand attributes using airborne laser scanning and aerial photographs. *Remote Sensing of Environment*, in press
- Pal, M., & Mather, P.M. (2006). Some issues in the classification of DAIS hyperspectral data. *International Journal of Remote Sensing*, 27, 2895-2916
- Quézel, P., & Médail, F. (2003). *Ecologie et biogéographie des forêts du bassin méditerranéen*. Paris: Elsevier
- Richter, R., & Schlöpfer, D. (2002). Geo-atmospheric processing of airborne imaging spectrometry data. Part 2: atmospheric/topographic correction. *International Journal of Remote Sensing*, 23, 2631-2649
- Schlöpfer, D., & Richter, R. (2002). Geo-atmospheric processing of airborne imaging spectrometry data. Part 1: parametric orthorectification. *International Journal of Remote Sensing*, 23, 2609-2630
- Schoelkopf, B., Smola, A., Williamson, R., & Bartlett, P.L. (2000). New support vector algorithms. *Neural Computation*, 12, 1207-1245
- van der Linden, S., Janz, A., Eiden, M., & Hostert, P. (submitted). Classifying segmented hyperspectral data from urban areas using support vector machines. *Journal of Applied Remote Sensing*
- Vapnik, V.N. (1998). *Statistical Learning Theory*. New York: Wiley
- Waske, B., & Benediktsson, J.A. (2007 (in review)). Fusion of Support Vector Machines for Classification of Multisensor Data. *Ieee Transactions on Geoscience and Remote Sensing*



# The Relevance and Use of Atmospheric Data Access for the Geospatial User Community (ADAGUC)

Michael E. Schaepman, Marc Hoogerwerf; John van de Vegte; Frans van der Wel; Wim Som de Cerff; Richard van Hees; Pepijn Veeffkind; Ronald van der A; Richard de Jeu; Ben Domenico; Stefano Nativi; Olga Wilhelmi

### Introduction

Having the advent of increasing data dissemination potential through Spatial Data Infrastructures (SDI), clearinghouses, and related web-portals, the atmospheric and geospatial communities currently remain separate worlds in terms of data accessibility. We develop Open Source conversion tools for atmospheric data, selected atmospheric datasets in a exchangeable format and provide a standardized web service to demonstrate the usability of the above to the geospatial and atmospheric communities.

### Method

In a user consultancy workshop, we have defined 4 relevant user communities needing flexible and reliable access to atmospheric data:

**Policy Makers** – are interested in Level 3/4 products, maps, archived for easy access. Many national and international stakeholders provide atmospheric data to their governments that deal with social and political impact of climate change.

**Earth System Scientists and Atmospheric Scientists** – are interested in Level 2/3 data, both archived and real-time. The atmospheric users are particularly interested in fast tracers like aerosols, and trace gases like NO<sub>2</sub> and SO<sub>2</sub>.

**GIS Users** – are interested in Level 2/3 data, including archived access. GIS users are characterized as being non-experts in the field of atmospheric research, their focus is more on earthbound features and earth-atmosphere interactions.

**Risk assessment community** – is interested in mapped Level 2/3 data, preferably in (near)-real time. These users are interested in products at an urban scale that are focused on industrial calamities, like gas leakage or chemical fires. Combinations with other data sources provides input to crisis information teams.

We provide 5 exemplary use cases for these communities as follows, where two are presented here:

**Local daily monitoring of air quality** – no example given

**NO<sub>2</sub> Map for Europe** – In this use case it is described how from the OMI Level 2 NO<sub>2</sub> data a map of the yearly averaged tropospheric NO<sub>2</sub> over Europe is constructed (see Example 1).

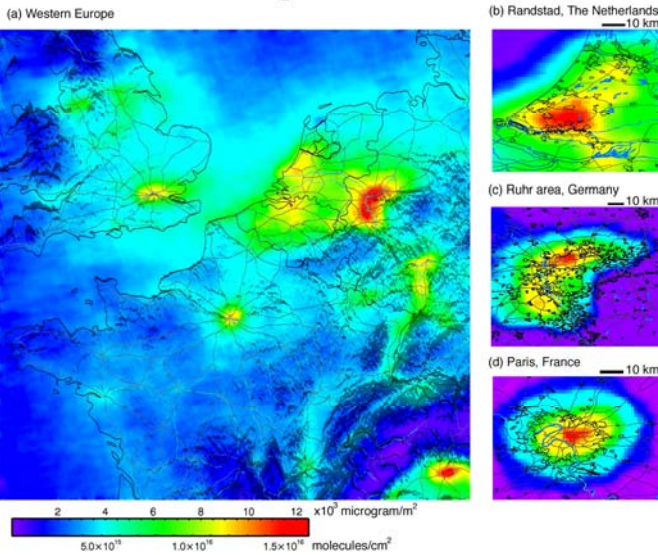
**Improved Space Estimates of NOx deposition** – Develop a methodology that integrates remote-sensing products and atmospheric chemistry models to improve quantification of reactive nitrogen deposition on ecosystems through a prototype data-assimilation system of NOx and dis-aggregation of large scale space measurements to the ecosystem scale. Validate the product against observations in two contrasting settings (see Example 2).

**Improving the Performance of River Basin Simulation Models with ADAGUC data** – no example given

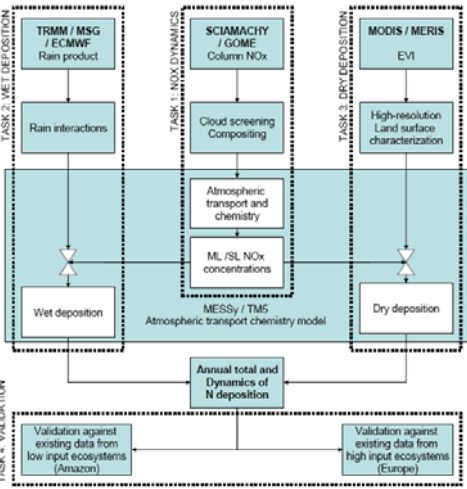
**5) Weather alert: Heavy Snow and Icy rain** – no example given

### First Results

**NO<sub>2</sub> Map for Europe**  
**OMI Tropospheric NO<sub>2</sub>, Dec 2004 until Nov 2005**



### Improved Space Estimates of NOx deposition (Scheme)



### Conclusions

First results demonstrate that structured access to atmospheric data significantly increases their use and contributes to the development of advanced applications for various stakeholders. A portal for data dissemination will be set up in a following step for user community wide access.

Centre for Geo-Information, Wageningen-UR  
P.O. Box 47, NL-6700 AA Wageningen, The Netherlands  
E-mail: michael.schaepman@wur.nl



## **Abstract for 10<sup>th</sup> Intl. Symposium on Physical Measurements and Signatures in Remote Sensing**

**Theme:** Data fusion approaches based on multi-platform or multiple sensor techniques

### **The relevance and use of Atmospheric Data Access for the Geospatial User Community (ADAGUC)**

*Michael Schaepman (Michael.Schaepman@wur.nl, WUR), Marc Hoogerwerf (Marc.Hoogerwerf@wur.nl, WUR), John van de Vegte (vegtevd@knmi.nl, KNMI), Frans van der Wel (welvdf@knmi.nl, KNMI), Wim Som de Cerff (sdecerff@knmi.nl, KNMI), Richard van Hees (R.M.van.Hees@sron.nl, SRON), Ben Domenico (ben@unidata.ucar.edu UNIDATA), Stefano Nativi (nativi@imaa.cnr.it, IMAA), Olga Wilhelmi (Olgaw@ucar.edu, NCAR)*

The atmospheric and geospatial communities are still separate worlds with their own tools and data formats. It is extremely difficult to easily share data among scientists representing these communities without performing some cumbersome conversions. ADAGUC aims to reduce the need for scientists to invent their own converter tools. Selected space borne atmospheric datasets will be made accessible to a GIS system in order to be submitted to data comparison, resampling, selection, manipulation and visualization. The user community will be intensively involved in the project to obtain a high fitness for use.

The first ADAGUC workshop (Oct 2006) was attended by a large group of users from both the atmospheric and GIS community and resulted in a better understanding of user needs that are currently translated into specifications for the user requirements document of ADAGUC.

The deliverables of this project are: Open Source conversion tools, selected atmospheric datasets in a GIS-friendly format and a web service to demonstrate the usability of the above to the geospatial and atmospheric community.



# USING LINEAR SPECTRAL UNMIXING OF HIGH SPATIAL RESOLUTION AND HYPERSPECTRAL DATA FOR GEOMETRIC-OPTICAL MODELLING

Yuan Zeng<sup>a,b,\*</sup>, Michael E. Schaepman<sup>a</sup>, Bingfang Wu<sup>b</sup>, Jan G.P.W. Clevers<sup>a</sup>, Arnold K. Bregt<sup>a</sup>

<sup>a</sup> Centre for Geo-Information, Wageningen University and Research Centre, the Netherlands - (yuan.zeng, michael.schaepman, jan.clevers, arnold.bregt)@wur.nl

<sup>b</sup> Institute of Remote Sensing Applications, Chinese Academy of Sciences, China – (yuanz, wubf)@irsa.ac.cn

**KEY WORDS:** Linear spectral mixing model, EO-1 Hyperion, QuickBird, Geometric-optical model, Forest canopy variables

## ABSTRACT:

The linear spectral mixing model is a widely used technique in remote sensing to estimate the fractions of several individual surface components present in an image pixel and the pure reflectance spectrum of a component, called endmember, is the model's necessary parameter. Different methods can be used to extract endmembers, finding out the pure pixel from hyperspectral data is the most common way, but at the regional scale, the selected single pixel can not present the typical component accurately. The objective of this paper is to estimate the feasibility of up-scaling from high spatial resolution data to medium spatial resolution hyperspectral data by linear spectral unmixing based technique for extracting the required endmembers. In this case, an inverted Li-Strahler geometric-optical model is applied to retrieve one of the forest canopy variables (crown closure) in a broadleaved forest natural reserve, located in the Three Gorges region of China. This model needs three important scene components (sunlit canopy, sunlit background and shadow). The three components' classes are firstly estimated using QuickBird fusional image with 0.6 m spatial resolution by eCognition, an object-based classification method. Then, a 50 by 50 pixels moving window calculated each component's proportion is matched to individual pixels with 30 m spatial resolution of EO-1 Hyperion data. The unmixing model is finally used for deriving the three endmembers based on the Hyperion data with surface reflectance and the per-pixel three fractions computing from QuickBird classification. From the spectral profile comparison, the scaling-based endmembers indicate the mean spectra of the components unlike the pure pixels' spectra. For validating the results, we use 32 independent sample sites collected in the study area to assess the accuracy of inverted model's outputs, and the results of scaling-based endmember extraction method ( $R^2=0.60$ ) seem better than the pixel-based method ( $R^2=0.51$ ).

## 1. INTRODUCTION

At local to regional and global scales, remote sensing has facilitated extraordinary advances in the modelling, mapping, and understanding of ecosystems and their functioning. One basic characteristic of remote sensing in the twenty-first century is the extensive use of quantitative algorithms for estimating Earth surface variables (Liang, 2004). Forests, being one of the most important natural resources worldwide, not only regulate the global atmospheric cycles, but also are increasingly being used in dynamic global vegetation models for terrestrial CO<sub>2</sub> estimations.

A lot of work in monitoring forest canopy variables using remote sensing has focussed on inverting physical based canopy reflectance models. Geometric-optical models, which treat the surface as an assemblage of discrete geometric objects with the reflectance modelled as a linear combination of viewed sunlit and shaded components, have been used successfully to estimate the forest canopy (Chopping et al., 2006; Franklin and Strahler, 1988; Gemmell, 1999; Gerard and North, 1997; Hall et al., 1995; Peddle et al., 2003; Peddle et al., 1999; Scarth and Phinn, 2000; Scarth et al., 2001; Woodcock, 1994; Woodcock et al., 1997). The accuracy of the inverted model's results is primarily related to the model inputs. In a previous study, we derived forest crown closure and crown diameter by inverting the Li-Strahler geometric-optical model (Zeng et al., 2007), one of the most important inputs is the fractional image of one scene component—sunlit background, which was calculated based on the pure reflectance spectra of viewed surface components, called endmembers. Therefore, the method and certainty of the

endmember extraction is the main factor to influence the value of the inverted Li-Strahler geometric-optical model.

Different approaches can be used to extract endmembers, like deriving the pure spectrum from the image with field training samples, directly obtaining from the observation of a field spectrometer or from an existing spectral library. For extracting the endmembers of sunlit and shaded scene components by hyperspectral remote sensing data, the most common way is selecting the pure pixels from the image. However, due to the spatial resolution of hyperspectral imagery, the "pure" pixel may still contain mixtures of components, and also, at the regional scale, the selected single pixel can not present the typical component accurately. For solving this problem, a linear spectral mixing model is addressed. Zhukov et al. (1999) unmixed low-resolution images using the information about their pixel composition from co-registered high-resolution images. Haertel and Shimabukuro (2005) estimated the components' proportions from medium spatial resolution Landsat TM data and then successfully derived the unknown components' endmembers in the low spatial resolution Terra MODIS image by the linear spectral mixing model. Zurita-Milla et al. (2006) inverted the linear spectral mixing model to obtain MERIS endmembers based on the known fractional coverages of each pixel from a Landsat TM classification. In summary, when high spatial resolution imagery is available, the linear spectral mixing model can be used to unmix low spatial resolution data and estimate the required spectral reflectance. This method can also provide an avenue to up-scale the information from local to regional studies. Accordingly, the objective of this paper is to estimate the feasibility of up-scaling

\* Corresponding author.



from high spatial resolution data to medium spatial resolution hyperspectral data by a linear spectral unmixing based technique for extracting the components' endmembers used for Li-Strahler geometric-optical modelling.

## 2. STUDY SITE

In this case, the study area, namely Longmenhe forest nature reserve, lies in the Xingshan county of Hubei province, towards the northeast of Three Gorges region in China (centred at 31°20'N, 110°29'E). The total reserve size is about 4644 ha. It is located in the temperate climate zone (Cwa-Subtropical monsoon, Koeppen (McKnight and Hess, 2000)) and is mainly dominated by natural evergreen broadleaved forest and mixed deciduous broadleaved forest. The field data were collected in June of 2003. A total of 40 sample sites (100mx100m) located in the study area were measured based on different plant strata and topographic distribution, and each of them randomly included 5 sample plots (20mx20m), which provided many field measurements about the forest canopy structure, such as crown closure, crown diameter, DBH (diameter at breast height), tree height, trunk height, tree age and visual estimations by forest experts for forest type, plant species and distribution. Those are the necessary ground truths for validating the model results.

## 3. METHOD

The overall method used in this study is shown as flowchart in Figure 1. The inverted Li-Strahler geometric-optical model is used to retrieve the forest canopy variables. The model needs three scene components: sunlit canopy (C), sunlit background (G) and shadow (T). The endmembers of these components are derived by two approaches:

- The G, C, T three components' classes are firstly estimated by a QuickBird fusional image with 0.6m spatial resolution using eCognition, an object-based classification method. Then, a 50 by 50 pixels moving window calculated each component's fraction is matched to individual pixels with 30m spatial resolution of EO-1 Hyperion image. The linear spectral mixing model is finally used for deriving the three endmembers based on the Hyperion data with surface reflectance and the per-pixel three fractions computing from QuickBird classification.
- Using the PPI algorithm to explore the pure pixel of each component directly from Hyperion hyperspectral image.

After inverting the model integrated with the components' endmembers, canopy structural parameters per forest class, and slope/aspect data, select one of the model outputs—forest crown closure to compare the two methods of endmember extraction, and make use of 32 measured field samples for validation.

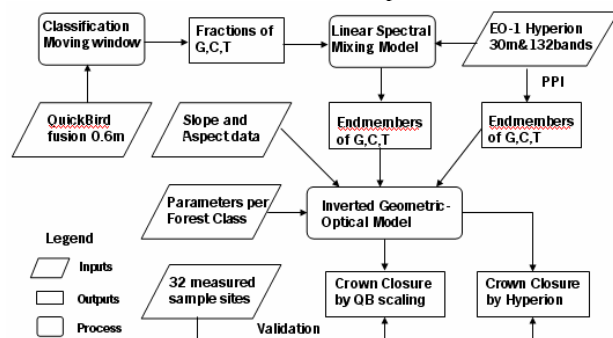


Figure 1. Flowchart of general method

## 3.1 Inverted Geometric-Optical Model

The Li-Strahler geometric-optical model (Li and Strahler, 1992; 1985) is based on the assumption that the Bidirectional Reflectance Distribution Function (BRDF) is a purely geometric phenomenon resulting from a scene of discrete three-dimensional objects being illuminated and viewed from different positions in the hemisphere. The reflectance associated with a given viewpoint is treated as an area-weighted sum of four fixed reflectance components: sunlit canopy, sunlit background, shaded canopy, and shaded background. Moreover, in most cases, these four components could be simplified to three: sunlit canopy-C, sunlit background-G and shadow-T (Li and Wang, 1995; Peddle et al., 2003; Peddle et al., 1999). This model also assumes that the resolution of the remote sensing image is much larger than the size of individual crowns but smaller than the size of forest stands, and that the individual trees are randomly (Poisson) distributed within the pixel (Woodcock et al., 1994). Based on the principle of three-dimensional geometry of a spherical crown on a flat background, each proportion of components can be expressed by a combination of the forest canopy structural parameters. For inverting the model, one of the components—sunlit background ( $K_g$ ) can be used for deriving the expected forest crown closure (CC), see equations (1) to (5) (Li and Strahler, 1992; Strahler and Jupp, 1990; Woodcock et al., 1997).

$$K_g = e^{-\pi \cdot M [\sec(\theta_i) + \sec(\theta_v) - O(\theta_i, \theta_v, \varphi)]} \quad (1)$$

$$O(\theta_i, \theta_v, \varphi) = 1/\pi (\sec \theta_i + \sec \theta_v) (t - \sin t \cos t) \quad (2)$$

$$\cos t = \frac{h |\tan \theta_i - \tan \theta_v \cos \varphi|}{r (\sec \theta_i + \sec \theta_v)} \quad (3)$$

$$M = \frac{-\ln(K_g)}{(\sec \theta_i + \sec \theta_v) (\pi - t + \cos t \sin t)} \quad (4)$$

$$CC = 1 - e^{-\pi \cdot M} \quad (5)$$

Where,  $\theta_i$ ,  $\theta_v$  are the zenith angles of illumination and viewing,  $O$  is the average of the overlap function between illumination and viewing shadows of individual crowns as projected onto the background,  $\varphi$  is the difference in azimuth angle between illumination and viewing.

Since the study area is in the mountain region and actually the crown shape of the broadleaved forest needs to be modelled as an ellipsoid, with tree height ( $h$ ) from ground to mid-crown, crown radius ( $b$ ) in vertical direction and crown radius ( $r$ ) in horizontal direction, double transformations are required to allow crowns to be treated as spheres and accommodate the sloping surface (Schaaf et al., 1994). The equations of all transformations are explained in Zeng et al. (2007).

Therefore, the required inverted model inputs for determining CC are the proportional image of  $K_g$ ; the solar zenith and azimuth angles; the view zenith and azimuth angles; the local slope and aspect image and the mean measured parameters for different kinds of forest crown shapes:  $h$ ,  $b$ ,  $r$ . Among them, deriving the component fractional image of sunlit background is the most crucial process, which needs accurately extracting the endmembers of the three scene components.

## 3.2 Endmember Extraction

### 3.2.1 Linear Spectral Unmixing based technique

Traditionally, the linear spectral mixing model has been widely used to calculate the percentages of several individual surface components contained in each pixel of a remote sensing image (Goodwin et al., 2005; Peddle et al., 1999). The model assumes that the reflectance ( $S$ ) of each pixel is a linear combination of endmembers ( $R$ ), which are the pure reflectance spectra for each component. The general equations are:

$$S_j = \sum_{i=1}^m K_i R_{i,j} + v_j \quad j = 1, 2, \dots, p \quad (6)$$

$$1 = \sum_{i=1}^m K_i \quad K_i \geq 0 \quad (7)$$

Where  $m$  is the number of components, in this case,  $m$  is the 3 components of C, G and T;  $p$  is the number of image bands;  $K$  is the fractional abundance of each component within the pixel and  $v$  is the residual for each band.

However, in this study, we use the inverted approach of this model, called linear spectral unmixing based technique. The fractions of each component within the pixel of a medium spatial resolution image are provided in advance from the overlapping high spatial resolution image, and then the endmembers of each component will be the final requirements. In practice, for deriving the endmembers, we need a test image with at least  $n$  pixels, and the number of  $n$  must be more than the number of components. Thus, equation (6) can be more conveniently expressed in matrix notation:

$$V_j = S_j - K * R_j \quad (8)$$

$V_j$ :  $n$ -dimensional vector of the residuals in band  $j$ ;

$S_j$ :  $n$ -dimensional vector of the pixels' reflectance in band  $j$ ;

$K$ :  $n \times m$  matrix of the fractions;

$R_j$ :  $m$ -dimensional vector of the components' reflectance in band  $j$ .

We seek a set of numerical values for the unknowns in  $R_j$  such that the sum of the residual squares becomes minimum (9), and then the least squares solution for  $R_j$  can be shown in (10) (Haertel and Shimabukuro, 2005):

$$\frac{\partial(V_j' V_j)}{\partial R_j} = 0 \quad (9)$$

$$R_j = (K'K)^{-1} K' S_j \quad (10)$$

The three components' endmembers can be calculated after applying equation (10) to every spectral band in the medium spatial resolution hyperspectral image, and the inputs of this method are the fractional images for each components and a corresponding overlapped image with spectral reflectance.

### 3.2.2 PPI

The PPI (Pixel Purity Index) algorithm is a common method to find the most "spectrally pure" (extreme) pixels in multi-spectral and hyperspectral images. It is computed by repeatedly projecting  $n$ -dimensional scatterplots onto a random unit vector, and then the extreme pixels in each projection (those pixels that fall onto the ends of the unit vector) are recorded and the total number of times each pixel is marked as extreme is noted. That consists of the following steps (Plaza et al., 2004): 1. A "noise-whitening" dimensionality reduction step is performed by using the MNF (Minimum Noise Fraction) transform (Green et al., 1988). 2. A pixel purity score is calculated for each point in the image cube by randomly generating lines in the  $N$ -D space

comprising the MNF transformed data. 3. All the points in that space are projected onto the lines, and the ones falling at the extremes of each line are counted. 4. After many repeated projections to different random lines, those pixels that count above a certain cut-off threshold are declared "pure". 5. These potential endmember spectra are loaded into an interactive  $N$ -D visualization tool and rotated in real time until a desired number of endmembers are visually identified as extreme pixels in the image. In this case, we use the PPI model of ENVI software to extract the components' endmembers directly from the hyperspectral data.

## 4. IMAGE DATA AND PROCESSING

For this study area, an EO-1 Hyperion image was acquired on June 10, 2004, around 11:00 a.m. local time. Hyperion, one of the three sensors on the NASA EO-1 platform, was launched on November 2000. As a push-broom imaging instrument, Hyperion provides images capable of resolving 242 spectral bands (from 0.4–2.5  $\mu\text{m}$ ) with a 10 nm spectral resolution and a 30m spatial resolution. For converting DN's to radiances, the data were scaled by 40 for VNIR and 80 for SWIR (Beck, 2003). Several stripes (data columns of poor quality) in the Hyperion data contain no information and lower radiance. Those abnormal pixels are detected and replaced by the average radiance value of their immediate left and right neighboring pixels (Han et al., 2002). In addition, an atmospheric correction is required. We use ACORN version 4.0, a commercially available atmospheric correction program based on the MODTRAN 4 radiative transfer code (AIG, 2002). Due to the low signal to noise ratio at the beginning and the end of the Hyperion spectra ( $\leq 436\text{nm}$  and  $\geq 2385\text{nm}$ ) and the heavy water absorption influences in several bands, a total of 64 bands are dropped from 196 valid bands. Geometric correction is done by 26 GCPs (Ground Control Points) relative to topographic maps and the geometric error is less than one pixel. Finally, the corrected Hyperion data with 132 bands of surface reflectance in a UTM Zone 49 N WGS-84 projection are used in this study.

The QuickBird data consisted of one panchromatic image at 0.61m resolution and one multi-spectral image with 4 spectral bands (B/G/R/NIR) at 2.44m resolution. It was collected on August 23, 2003 at 11:08 a.m. local time. This QuickBird image being the high spatial resolution data will be used together with Hyperion data to derive components' endmembers. Although the two images were acquired at different dates, the solar zenith and azimuth angles are similar ( $23.5^\circ$  and  $104.5^\circ$  for Hyperion,  $29.2^\circ$  and  $127.9^\circ$  for QuickBird) and the sensor viewing direction is also the same at nadir. Hereby, only small variation in view/illumination geometry will be expected between the two images.

For classifying the three components from the QuickBird image and matching it to Hyperion data, we firstly merge the panchromatic and multi-spectral images by principal component method and cubic convolution resampling technique of ERDAS IMAGINE software, the output image includes 0.6m spatial resolution and 4 spectral bands. Then, an object-oriented classification software eCognition is carried out for classifying the components. eCognition is designed to segment the image into units of similar spectral and spatial patterns and to classify those segments according to a pre-defined rule base (Baatz et al., 2004). Finally, the geometrically corrected QuickBird fusional image being a base image is used to spatially co-register the two images, the matched subsets of Hyperion and QuickBird data that covered the same study region are selected.

5. RESULTS

5.1 Endmembers and Model Inputs

The processed Hyperion data with surface reflectance and 30m spatial resolution is shown in Figure 2a. The dimension of this image is 208 (column) x 173 (line) x132 (band). The fusional QuickBird image with 0.6m spatial resolution and 4 spectral bands (shown in Figure 2b) is located in the centre of Hyperion image, and it includes 4300 (column) x 3400 (line) pixels.

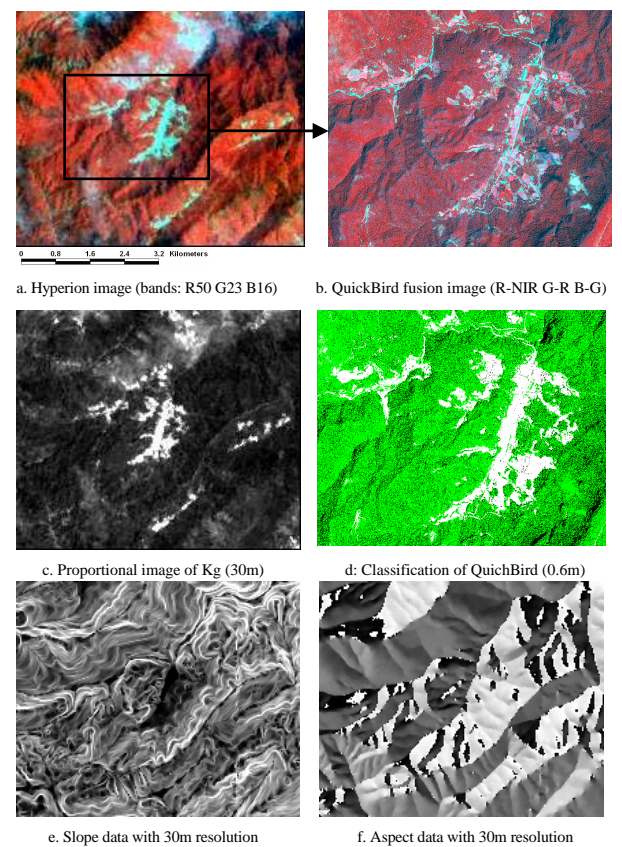


Figure 2: Processed Hyperion image, QuickBird image and the inputs of inverted Li-Strahler model

The three components classification result from the QuickBird fusional image by eCognition is shown in Figure 2d (White: G-sunlit background, Green: C-sunlit canopy and Black: T-shadow). After spatially co-registration, a subset of the Hyperion image with 86 (column) x 68 (line) is masked out for matching the QuickBird classification image. A 50x50 pixels moving window is used to calculate the fractions of each component from the QuickBird classification, and that is just matching the individual pixels of Hyperion data. Then the three components' endmembers extracted through the linear spectral unmixing based technique are shown in Figure 3. Comparing the endmembers retrieved from the pure pixels of the whole Hyperion image (G: x-104 y-89 C: x-150 y-102 T: x-127 y-117) by the PPI algorithm, the QuickBird scaling-based endmembers indicate the mean spectra of the components unlike the pure pixels' spectra.

In terms of the endmembers, the proportional images of Kg for both endmember extraction methods are derived by spectral unmixing the whole Hyperion image. Figure 2c illustrates one of the Kg images, which is from the QuickBird scaling-based

endmembers. The brighter regions express higher proportions. The other required inputs for inversion of the Li-Strahler model, slope and aspect images with 30m spatial resolution are created from DEM data using topographic analysis model of ERDAS IMAGINE, see Figure 2e-f.

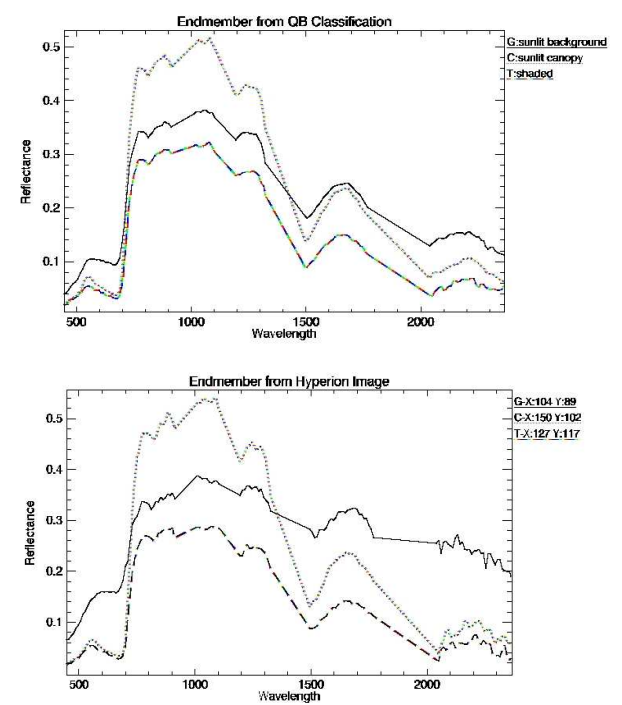


Figure 3: Components' endmembers (Up: QuickBird scaling-based method; Down: three pure pixels by PPI)

In this study area, the dominant forest communities include deciduous broadleaved forest, evergreen broadleaved forest, and conifer forest. Based on a forest classification image (Zeng et al., 2007) and the field measurements, the corresponding mean value of forest crown parameters, h, b, and r for every dominant forest class is shown in Table 1.

Dominant Forests	h (m)	b (m)	r (m)
Deciduous Broadleaved Forest	9.79	3.97	1.79
Evergreen Broadleaved Forest	8.86	3.36	1.61
Conifer Forest	8.41	4.63	1.51

Table 1. Inverted model inputs for each forest class

5.2 Model Outputs and Validation

We compiled an IDL program to implement the inversion of the Li-Strahler model integrated with the pixel-based inputs data. Figure 4 presents the final mapping results of forest crown closure distributed in the Longmenhe study area. The upper image is the model result according to the endmembers from the QuickBird scaling-based method and the other is the result for the PPI method. These two mapping images indicate the variety when one of the inverted model inputs (Kg) is different.

For validating the model outputs, we calculate the mean value of 3x3 pixels from the mapping image for comparison to one field sample site. In total 32 independent samples are included. Figure 5 illustrates the agreement between model-interpreted crown closure and ground measurements. The coefficients of determination  $R^2$  and root mean square error (RMSE) are equal



to 0.6 / 0.064 for QuickBird scaling-based method, and 0.51 / 0.048 for Hyperion PPI method respectively.

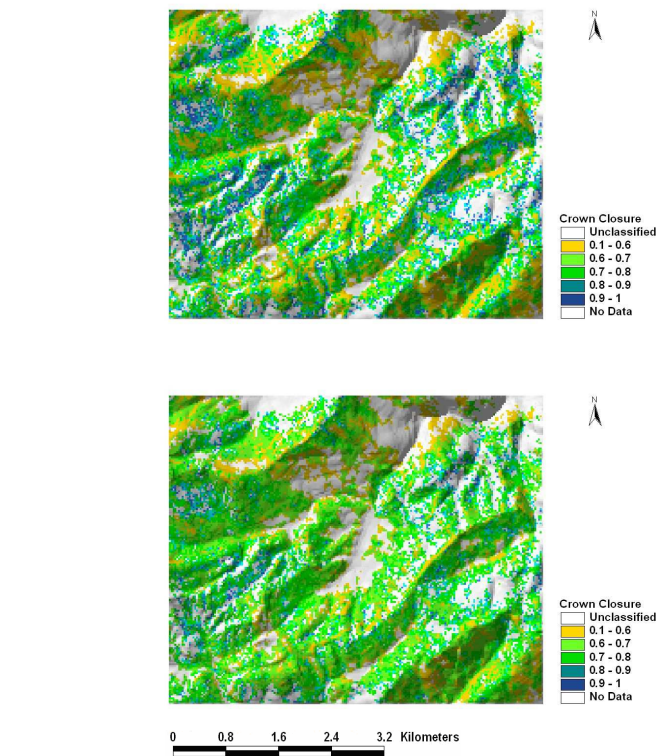


Figure 4. Mapping results of forest crown closure by the inverted geometric-optical model (Up: QuickBird scaling-based method; Down: Hyperion PPI method)

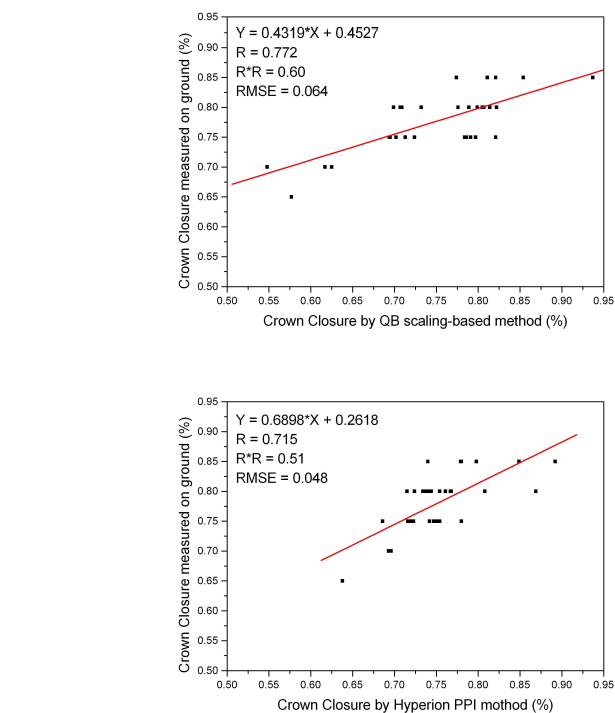


Figure 5. Linear relationship between ground measured CC and model derived CC

The validation results show that most of the model interpreted CC values are less than the ground measurements for both endmember extraction methods. But comparing the two methods, the results of QuickBird scaling-based method seem better than the pure-pixel deriving method in terms of the simulated regression lines.

### 6. CONCLUSION AND OUTLOOK

In this study, we use an inverted Li-Strahler geometric-optical model to retrieve one of the forest canopy variables (crown closure) from a hyperspectral Hyperion image collected in the Longmenhe broadleaved forest natural reserve, located in the Three Gorges region of China. For preparing the inverted model inputs, we compare two endmember extraction methods: linear spectral unmixing based technique, which requires a subset Hyperion image combined with the components' fractional images from the matched QuickBird high spatial resolution data, and another method by selecting the pure pixel directly from the Hyperion image. Depending on the comparison of derived endmember profiles and the validation of the model outputs with field measurements, we can conclude that the linear spectral unmixing based technique is an effective method to estimate the components' endmembers in a medium spatial resolution image. It can solve the mixed-pixel problem, when a matched high spatial resolution image is provided.

Since the collected QuickBird image of this case is smaller than the Hyperion image, only the overlapped region can be used for extracting the endmembers. However, if the overlapped region is including all components and it is located in a typical area of the Hyperion image, then the derived components' endmembers can be used for the whole Hyperion image. It indicates that the method of linear spectral unmixing based technique appears appropriate for up-scaling the information from high spatial resolution data, and it can also expand the consistent information from local to regional scale.

Although the endmember extraction method of linear spectral unmixing based technique is applied using QuickBird as high spatial resolution image and Hyperion as medium spatial resolution image in this study, it can be implemented for any two sets of data with different spatial and spectral resolution, such as from QuickBird to Landsat TM, from landsat TM to MODIS, and even from Hyperion to MODIS. Therefore, using this up-scaling method to explore the information from images at global scale is also feasible.

In future work, we will continue the study of quantitatively monitoring the forest canopy variables in the whole Three Gorges region of China using multi-scale and multi-spatial / spectral resolution data through the inverted Li-Strahler geometric-optical model and the up-scaling method. Even though the processes of the inverted model and the scaling method will need more careful analysis and calibrations in the future, the presented results show confidence in the approach selected.

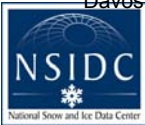
### ACKNOWLEDGMENT

We gratefully acknowledge financial support from the 'Knowledge Innovation Project' of the Chinese Academy of Sciences (No. KZCX3-SW-334). We appreciate support from Xu Wenting, Huang Jianxi and Tian Yichen for participation in the field campaign.

## REFERENCES

- AIG, 2002. ACORN 4.0 User's Guide, Boulder, CO: Analytical Imaging and Geophysics LLC.
- Baatz, M. et al., 2004. eCognition Professional User Guide 4. Definiens Imaging, Munich.
- Beck, R., 2003. EO-1 User Guide - Version 2.3, Satellite Systems Branch, USGS Earth Resources Observation Systems Data Center (EDC).
- Chopping, M., Su, L., Laliberte, A., Rango, A., Peters, D.P.C. and Kollikkathara, N., 2006. Mapping shrub abundance in desert grasslands using geometric-optical modeling and multi-angle remote sensing with CHRIS/Proba. *Remote Sensing of Environment*, 104(1): 62-73.
- Franklin, J. and Strahler, A.H., 1988. Invertible Canopy Reflectance Modeling of Vegetation Structure in Semiarid Woodland. *Ieee Transactions on Geoscience and Remote Sensing*, 26(6): 809-825.
- Gemmell, F., 1999. Estimating conifer forest cover with thematic mapper data using reflectance model inversions and two spectral indices in a site with variable background characteristics. *Remote Sensing of Environment*, 69(2): 105-121.
- Gerard, F.F. and North, P.R.J., 1997. Analyzing the effect of structural variability and canopy gaps on forest BRDF using a geometric-optical model. *Remote Sensing of Environment*, 62(1): 46-62.
- Goodwin, N., Coops, N.C. and Stone, C., 2005. Assessing plantation canopy condition from airborne imagery using spectral mixture analysis and fractional abundances. *International Journal of Applied Earth Observation and Geoinformation*, 7(1): 11-28.
- Green, A.A., Berman, M., Switzer, P. and Craig, M.D., 1988. A Transformation for Ordering Multispectral Data in Terms of Image Quality with Implications for Noise Removal. *Ieee Transactions on Geoscience and Remote Sensing*, 26(1): 65-74.
- Haertel, V.F. and Shimabukuro, Y.E., 2005. Spectral linear mixing model in low spatial resolution image data. *Ieee Transactions on Geoscience and Remote Sensing*, 43(11): 2555-2562.
- Hall, F.G., Shimabukuro, Y.E. and Huemmrich, K.F., 1995. Remote-Sensing of Forest Biophysical Structure Using Mixture Decomposition and Geometric Reflectance Models. *Ecological Applications*, 5(4): 993-1013.
- Han, T., Goodenough, D.G., Dyk, A. and Love, J., 2002. Detection and correction of abnormal pixels in hyperion images, *IGARSS*, pp. 1327-1330.
- Li, X. and Strahler, A., 1992. Geometric-optical bidirectional reflectance modeling of the discrete crown vegetation canopy: Effect of crown shape and mutual shadowing. *Ieee Transactions on Geoscience and Remote Sensing*, 30: 276-292.
- Li, X. and Strahler, A.H., 1985. Geometric-optical modeling of a conifer forest canopy. *IEEE Transactions on Geoscience and Remote Sensing*, GE-23(5): 705-721.
- Li, X. and Wang, J., 1995. *vegetation Optical Remote Sensing Models and Vegetation Structure Parameterization*. Science Press, Beijing, 118 pp.
- Liang, S., 2004. *Quantitative remote sensing of land surfaces*. Wiley series in remote sensing. Wiley-Interscience, Hoboken, NJ, XXVI, 534 pp.
- McKnight, T.L. and Hess, D., 2000. *Climate Zones and Types: Dry Humid Subtropical Climate (Cfa, Cwa)*. Physical Geography: A Landscape Appreciation. Upper Saddle River, NJ: Prentice Hall, 223-6 pp.
- Peddle, D.R., Franklin, S.E., Johnson, R.L., Lavigne, M.B. and Wulder, M.A., 2003. Structural change detection in a disturbed conifer forest using a geometric optical reflectance model in multiple-forward mode. *Ieee Transactions on Geoscience and Remote Sensing*, 41(1): 163-166.
- Peddle, D.R., Hall, F.G. and LeDrew, E.F., 1999. Spectral Mixture Analysis and Geometric-Optical Reflectance Modeling of Boreal Forest Biophysical Structure. *Remote Sensing of Environment*, 67(3): 288-297.
- Plaza, A., Martinez, P., Perez, R. and Plaza, J., 2004. A quantitative and comparative analysis of endmember extraction algorithms from hyperspectral data. *Ieee Transactions on Geoscience and Remote Sensing*, 42(3): 650-663.
- Scarth, P. and Phinn, S., 2000. Determining Forest Structural Attributes Using an Inverted Geometric-Optical Model in Mixed Eucalypt Forests, Southeast Queensland, Australia. *Remote Sensing of Environment*, 71(2): 141-157.
- Scarth, P., Phinn, S. and McAlpine, C., 2001. Integrating high and moderate spatial resolution image data to estimate forest age structure. *Canadian Journal of Remote Sensing*, 27(2): 129-142.
- Schaaf, C.B., Li, X.W. and Strahler, A.H., 1994. Topographic Effects on Bidirectional and Hemispherical Reflectances Calculated with a Geometric-Optical Canopy Model. *IEEE Transactions on Geoscience and Remote Sensing*, 32(6): 1186-1193.
- Strahler, A.H. and Jupp, D.L.B., 1990. Modeling Bidirectional Reflectance of Forests and Woodlands Using Boolean Models and Geometric Optics. *Remote Sensing of Environment*, 34(3): 153-166.
- Woodcock, C.E., 1994. Estimation of forest stand structure from Landsat TM through inversion of the Li-Strahler model, *IGARSS*, pp. 1245-1247.
- Woodcock, C.E., Collins, J.B., Gopal, S., Jakabhazy, V.D., Li, X., Macomber, S., Ryherd, S., Judson Harward, V., Levitan, J., Wu, Y. and Warbington, R., 1994. Mapping forest vegetation using Landsat TM imagery and a canopy reflectance model. *Remote Sensing of Environment*, 50(3): 240-254.
- Woodcock, C.E., Collins, J.B., Jakabhazy, V.D., Li, X., Macomber, S.A. and Wu, Y., 1997. Inversion of the Li-Strahler canopy reflectance model for mapping forest structure. *IEEE Transactions on Geoscience and Remote Sensing*, 35(2): 405-414.
- Zeng, Y., Schaepman, M.E., Wu, B., Clevers, J.G.P.W. and Bregt, A.K., 2007. Forest Structural Variables Retrieval Using EO-1 Hyperion Data in Combination with Linear Spectral Unmixing and an Inverted Geometric-Optical Model. *Journal of Remote Sensing - Special Issue of ISPMRS05*, 11(5): in press.
- Zhukov, B., Oertel, D., Lanzl, F. and Reinha?ckel, G., 1999. Unmixing-based multisensor multiresolution image fusion. *IEEE Transactions on Geoscience and Remote Sensing*, 37(3 I): 1212-1226.
- Zurita-Milla, R., Clevers, J.G.P.W. and Schaepman, M.E., 2006. Landsat TM and MERIS FR image fusion for land cover mapping over the Netherlands. *Proceedings of the 2nd Workshop of the EARSeL SIG on Land Use and Land Cover*: 34-40.





# Albedo Assessment and Evaluation over Arctic Siberian Tundra



G. Schaeppman-Strub (1) | gabriela.schaeppman@wur.nl, M. Claverie (1), T. Painter (2), M. Schaeppman (1)

(1) Wageningen University, Wageningen, The Netherlands, (2) National Snow and Ice Data Center (NSIDC), University of Colorado at Boulder, United States

## Motivation

Land surface albedo is one of the key drivers of the Earth's surface energy budget. To study the feedback of land surface albedo changes – as induced by surface changes (e.g., changing vegetation, soil moisture, thawing lake area) - to the climate in northern high latitudes, reliable albedo data fields are requested. This work aims at assessing and evaluating albedo as derived from the MODIS satellite sensor data, for the year 2000, as a first step towards a multiyear variation and sensor intercomparison analysis.

## Methodology

The statistical analysis of the quality flags indicates the reliability of the corresponding albedo products. Consequently, only albedo data based on a full BRDF inversion were analysed.

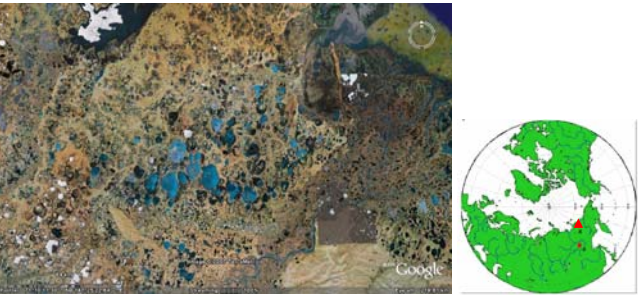
The difference of DHR and BHR<sub>iso</sub> (DHR-BHR<sub>iso</sub>) provide us with quantitative information on the importance of the distinction between the two physical properties with regard to their implementation in climate models.

Spatially averaged albedo products (DHR, BHR<sub>iso</sub>, and BRDF parameters) are used to analyse the influence of the status of the snow cover and vegetation onto the scattering regime in different spectral ranges (blue, green, red, nir, and broadband shortwave albedo).

## Data and Test Site

We analysed MOD43B1 (BRDF parameters) and MOD43B3 (DHR and BHR<sub>iso</sub>) in combination with the quality flags MOD43B2, MODIS collection 5 data, 1km spatial resolution, of the year 2000. The albedo data are produced every 8 days and rely on a 16 days composite.

The test site is located in Northeastern Siberia, with a central coordinate of 147.5deg E, 71deg N. The site is covered by MODIS tile h22v01, from which we subsetting an area of about 27'000 km² for detailed analysis.



## Results

### 1. Quality flag analysis

- Generally, a large part of the albedo data rely on a magnitude inversion rather than on a full inversion of the BRDF model. Only from March to September, the observations allow a full inversion for a significant part of the selected area.
- During the main period of the growing season (mid June to August), more than 60 percent of the data are based on a full inversion.

### 2. Differences of DHR and BHR<sub>iso</sub>

- The differences averaged over the whole area are generally small (< 0.022).
- The average of the DHR-BHR<sub>iso</sub> difference throughout the year 2000 is 0.0026, with a standard deviation of 0.0061.
- DHR is increasing with solar zenith angle. Given the high latitude of the test site (71deg), the maximum difference of DHR-BHR<sub>iso</sub> (0.0216) is reached in February, the first data point of the year, with largest solar zenith angle observations (day of year 49 +8 days).
- During winter, the DHR is generally higher than the BHR<sub>iso</sub>, whereas in summer, the albedo under direct illumination conditions (DHR) is generally lower than under diffuse illumination conditions (BHR<sub>iso</sub>).
- The above behaviour of differences is in good agreement with findings of Lyapustin, 1999, stating that at solar zenith angles of 52-57deg, the albedo is least sensitive to atmospheric influence.

Geometry/Reflection	Directional	Conical	Hemispherical
Directional			
Conical			
Hemispherical			

Albedo terminology after Schaeppman-Strub et al., RSE, 103, 27-42, 2006.

BRDF Bidirectional reflectance distribution function

BHR Bi-hemispherical reflectance

BHR<sub>iso</sub> Bi-hemispherical reflectance under isotropic diffuse illumination (white-sky albedo - WSA)

DHR Directional-hemispherical reflectance (black-sky albedo - BSA)

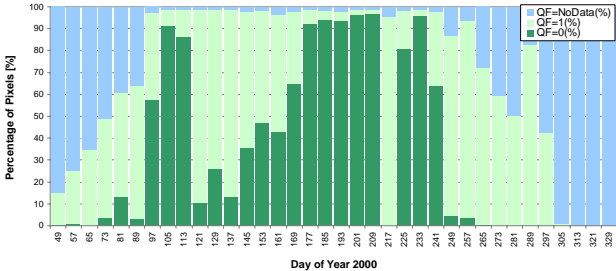


Figure 1: Analysis of quality flags (MOD43B2) of MODIS albedo data products. QF = 0 indicates that the albedo data relies on a full inversion of the BRDF model, whereas QF = 1 indicates a magnitude inversion. Quality flags of day of year 217 need further investigation.

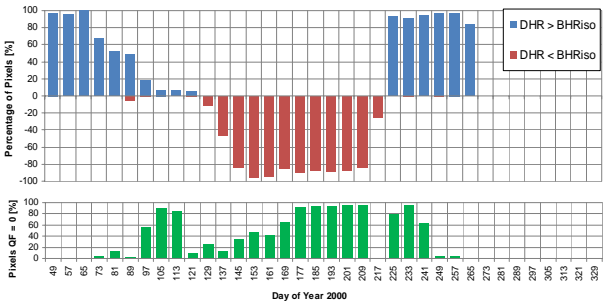


Figure 2: Analysis of the broadband (300-5000nm) DHR versus BHR<sub>iso</sub>. The percentage of pixels with zero difference is omitted (adds up to hundred percent). During the winter period, the DHR generally shows higher values than the BHR<sub>iso</sub>, whereas during summer months, the BHR<sub>iso</sub> is higher than the DHR. This mostly reflects the dependence of the difference on the solar zenith angle.

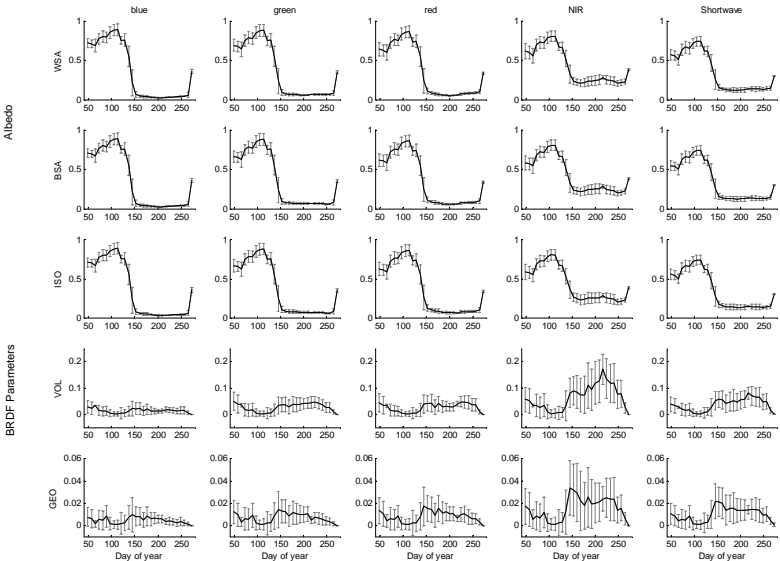


Figure 3: Variation of MODIS BHR<sub>iso</sub> (WSA), DHR (BSA), and BRDF model parameters (iso = isotropic, vol = volumetric, geo = geometric) for the year 2000.

Narrowband albedo/ albedo parameter wavelength ranges: blue 459-479nm, green 545-565nm, red 620-670nm, nir 841-876nm.

Broadband albedo /albedo parameter wavelength range: shortwave 300-5000nm.

Acknowledgment - G. Schaeppman-Strub performed her work as part of a European Space Agency (ESA) external fellowship.

## Albedo Assessment and Evaluation over Arctic Siberian Tundra

Suggested conference theme: (1) Validation of remote sensing products, (2) Remote sensing applications to carbon cycle, biochemical and –physical cycles, plant ecology, ecosystems, snow, natural ecosystems, or (3) Earth System model approaches using remote sensing

G. Schaepman-Strub (1), T. Painter (2), M. Schaepman (3)

- (1) Nature Conservation and Plant Ecology, Wageningen University, Bornsesteeg 69, 6708 PD Wageningen, The Netherlands | [Gabriela.Schaepman@wur.nl](mailto:Gabriela.Schaepman@wur.nl)
- (2) National Snow and Ice Data Center, University of Colorado at Boulder, 449 UCB, Boulder, CO USA 80309 | [tpainter@nsidc.org](mailto:tpainter@nsidc.org)
- (3) Centre for Geo-Information, Wageningen University, Droevendaalsesteeg 3, 6708 PB Wageningen, The Netherlands, [Michael.Schaepman@wur.nl](mailto:Michael.Schaepman@wur.nl)

Recent studies have shown empirical evidence that the albedo over arctic tundra is changing and that this can contribute to climate warming through potentially large positive feedbacks (e.g., Chapin, 2005). This study aims in assessing and analyzing annual albedo trends over Arctic Siberian tundra. Main factors influencing the albedo at the remote test site (70.8° N, 147.5° E) are the fractional cover and the scattering properties of snow, thawing lakes and rivers, and the vegetation (tussock-sedge, dwarf-shrub, moss tundra), as well as the sun angle (BHR, DHR) and atmospheric conditions (BHR).

This contribution is showing the annual trend (2003/2004) of satellite data derived albedo, an intercomparison of the different available products per sensor (e.g., BHR, BHR(iso), DHR), as well as an intercomparison of the corresponding physical products of different sensors (e.g., DHR MISR vs. MODIS). Further, the BRDF parameters are analyzed to assess the quantitative contribution of different scattering properties of the surface (i.e., isotropic, volumetric, and geometrical scattering component) throughout the year. It is expected that during the snow-covered period, the forward scattering is most pronounced, whereas volumetric scattering and geometric effects are increasing after the onset of the melting, driven by the greening and growing vegetation. Lakes contribute to the forward scattering through their specular reflectance or sunglint. The spectral signature in the isotropic component is analyzed to assess the fractional cover of the main surface types (snow, lakes, vegetation).

We additionally retrieve fractional snow cover, grain size and snow albedo with the multiple endmember spectral mixture model (MODSCAG), coupled with MODIS surface reflectance products. In applying this subpixel model, the albedo of the fractional snow cover is retrieved rather than a pixel composite albedo that can be contaminated by subpixel coverage of vegetation or soil in the case of incomplete snow cover. This allows the assessment of snow characteristics during e.g., the melting process, excluding the influence of the decreasing fractional snow cover.

The analysis will help to interpret albedo changes using albedo products based on semi-empirical approaches. In a further step it is important to use the results to model albedo

changes using radiative transfer models. Based on different scenarios of vegetation, snow cover, and thawing lake dynamics induced by global warming, fields of predicted albedo can be calculated. These can serve as a direct input into regional and global climate models or as a tool to validate albedo fields derived from their land surface modules.

## CHANGE DETECTION IN MIRE ECOSYSTEMS: ASSESSING CHANGES OF FOREST AREA USING AIRBORNE REMOTE SENSING DATA

L.T. Waser<sup>a,\*</sup>, E. Baltsavias<sup>b</sup>, H. Eisenbeiss<sup>b</sup>, C. Ginzler<sup>a</sup>, A. Gruen<sup>b</sup>, M. Kuechler<sup>a</sup>, P. Thee<sup>a</sup>

<sup>a</sup>Swiss Federal Research Institute WSL, Research Unit Land Resource Assessment, Zuercherstr. 111, 8903 Birmensdorf, Switzerland - (waser, ginzler, kuechler, thee)@wsl.ch

<sup>b</sup>Institute of Geodesy and Photogrammetry, ETH Zurich, Wolfgang-Paulistr. 15, 8093 Zurich, Switzerland; - (manos, ehenri, agruen) @geod.baug.ethz.ch

### ISPRS WG VII/1

**KEY WORDS:** Swiss Mire Protection Program, fractional tree/shrub cover, LIDAR, CIR-orthoimage, digital surface model (DSM)

#### ABSTRACT:

The objective of this paper is to present an approach for assessing tree growth and shrub encroachment between 1997 and 2002 in open mire land using CIR-aerial images, DSMs and LiDAR data. The study area is located in the Pre-alpine zone of Central Switzerland. The present study was carried out in the framework of the Swiss Mire Protection Program, where changes of forest area are a key issue. Automatic DSMs were generated from CIR- aerial images of 1997 and 2002. This automated DSM generation is based on high accuracy, intelligent matching methods developed at ETHZ which are able to produce very dense and detailed DSMs that allow a good 3D modelling of trees and shrubs, and a multitemporal analysis of their growth pattern. Forest masks from both years of various levels of detail were then generated combining canopy covers derived from the DSMs using multi-resolution segmentation and a fuzzy classification. On the basis of these forest masks fractional tree/shrub covers were generated using explanatory variables derived from the DSMs and logistic regression models. The models reveal a general decrease of forest area between 1997 and 2002. On the other side, the models also indicate real shrub encroachment and tree growth in open mire land.

### 1. INTRODUCTION

The present study focuses on assessing changes of tree / shrub area in a typical mire ecosystem between 1997 and 2002. The study was carried out in the framework of the Swiss Mire Protection Program which aims at conserving mire ecosystems of national importance and outstanding beauty in their present state. This implies no decrease of the mire area and no degradation of vegetation. A monitoring program based on a representative sample of 130 mires was set up in 1996 to examine the effectiveness of the conservation status (Grünig et al. 2004; Kuechler et al., 2004).

An early detection and evaluation of increase and decrease of the entire wooded area may help for preservation of these biotopes. However, several studies (e.g. St-Onge & Achaichia, 2001 and Watt & Donoghue, 2005) revealed that using traditional methods of field survey or aerial photograph interpretation to gain information on shrub encroachment and tree growth etc. is not feasible for larger monitoring programs regarding costs and time.

In contrast, increase and decrease of forest area and occurrence of shrubs can be estimated using high-resolution remotely sensed data. E.g. canopy height models can be calculated by subtracting a digital terrain model (DTM) from a digital surface model (DSM). Meanwhile, several LiDAR systems are commercially available (e.g. Baltsavias, 1999; Heurich et al., 2003; Hyypä et al., 2000), enabling the derivation of DSMs and DTMs from such data as well. Some studies suggest the use of DSM data to detect changes in the forest stands (Schardt et al., 2002; Naesset & Gobakken, 2005) and to evaluate growth estimations (including extent of forest area and shrub encroachment).

There is a growing need for sensitive tools to predict spatial and temporal patterns of plant species or communities (Kienast et al., 1996). Spatially explicit predictive modelling of vegetation is often used to construct current vegetation cover using information on the relations between current vegetation structure and various environmental attributes (Kuechler et al., 2004). E.g. Guisan & Zimmermann (2000) and Scott et al. (2002) point out that modern regression approaches have proven particularly useful for modelling spatial distribution of plant species and communities. Since old CIR-aerial images are often available and necessary variables of the DSM can be calculated, retrospective analysis of changes in forest area and shrub/tree encroachment in a mire biotope is feasible. Thus, airborne remote sensing data in combination with generalized linear models (GLM) could be useful for modelling these changes in mire ecosystems over time.

The objective of the present study is to assess changes of forest tree / shrub area in a mire ecosystem between 1997 and 2002 using logistic regression models and airborne remotely sensed data. A fractional cover approach was chosen since it is widely known that the discretization of tree covers (Mathys et al., 2006) into a limited number of categories results in a loss of information and that fractional cover has higher potential to describe accurately land cover change over time. For this modelling approach two methods have been implemented: a new image matching method (Zhang & Gruen, 2004) and a method of discrete forest masking that has already been successfully applied for 130 mire objects (Kuechler et al., 2004).

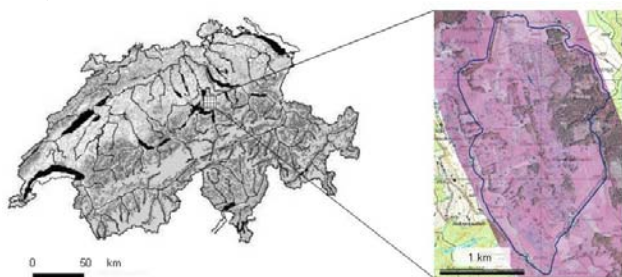
---

\* Corresponding author

## 2. MATERIAL AND METHODS

### 2.1 Study area

Models have been developed and tested for the mire "Eigenried" which is located on a small plateau in the East of Lake of Zug in the Pre-alpine zone of Central Switzerland (approx. 47°07' N and 8°32' E). The mire site covers an area of 2.61 km<sup>2</sup>. The altitude varies from 850 m to 1000 m above sea level. The landscape is highly fragmented and characterized by pastures that are crossed by shrubs and bright broad-leaved woodland (see Fig. 1 and 2). The dominant vegetation types are moist and wet meadows and pastures, low sedge poor fen, bog forest and broad-leaved woodland and willow Carr. The bordering forested area is mostly characterized by opened mixed forest (approx. 40%) and coniferous forest (approx. 60%).



**Figure 1.** Overview of the test site (CIR-orthophoto © WSL 2003 and pixelmap © 2006 Swisstopo JD052552).



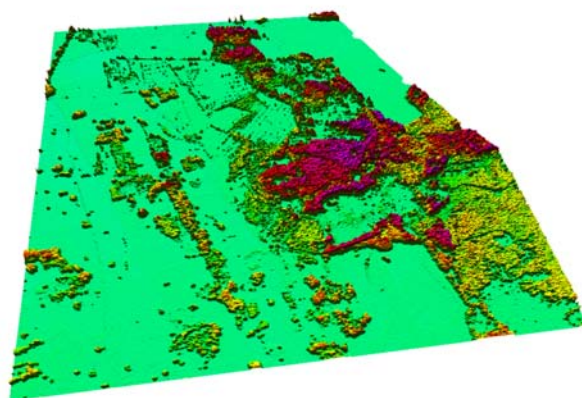
**Figure 2.** The mire is characterized by bog and fenland, bright broad-leaved woodland and shrubs.

### 2.2 Remotely sensed data

This study uses three different sets of input data: The first data set consists of CIR-aerial images: 4 (1 strip) of 1997 and 12 (2 strips) of 2002, scale 1:10000 and 1:5700, respectively. Orthoimages were produced with a spatial resolution of 0.5 m. As second data set DSMs were generated automatically from the above images of the years 1997 and 2002, respectively with a spatial resolution of 0.5 m. Third data set: national LiDAR data of the Swiss Federal Office of Topography (Swisstopo) was acquired in 2001 with leaves off. From the raw data, both a DTM and DSM are generated by Swisstopo (as raw irregularly distributed points and regular grid; the first dataset was used in this study). The average density of the DSM data was 1-2 points / m<sup>2</sup> and the height accuracy (1 sigma) 0.5 m for open areas and 1.5 m for vegetation and buildings. The DTM has an average point density of 0.8 points / m<sup>2</sup> and height accuracy (1 sigma) of 0.5 m (Artuso et al. 2003). The DTM was interpolated to a regular grid with 0.5 m grid spacing for reasons explained below.

### 2.3 Automatic generation of digital surface models

Since accurate surface information in forested and open mire land is very important for this modelling approach high-resolution DSMs of 1997 and 2002 are indispensable. Thus, a matching method which is described in detail in Zhang (2005) and Zhang and Gruen (2004) was used. This method can simultaneously use any number of images (> 2), matches very densely various primitives (grid points, feature points with good texture and edges), uses geometrical constraints to restrict the search space, combines two matching algorithms (sum of modified cross-correlation, and least squares matching) to achieve speed but also higher accuracy if needed, combines the matching results of the three primitive types with another matching approach to ensure local consistency, and performs an automatic blunder detection. The matching method is implemented in the operational, quasi-complete photogrammetric processing package Sat-PP which supports satellite and aerial sensors with frame and linear array geometry. The result was a regular grid DSM with 0.5 m spacing which was interpolated from a matching point cloud of similar density (ca. 15 million match points per stereo-pair). The matching DSMs of 1997 and 2002, and the LiDAR DSM and DTM were co-registered, using a point cloud co-registration procedure described in Akca (2005), Gruen and Akca (2005) and Akca and Gruen (2005). This co-registration uses a 7-parameter 3D similarity transformation to remove systematic differences (bias) between two datasets, e.g. due to different image orientation. For the estimation of these parameters, we used control surfaces, i.e. DSM parts that did not change in the two datasets, i.e. bare ground, and also removed large differences due to matching errors with a robust filtering. After co-registration, different products could be generated and conclusions drawn. The difference 2002-1997 matching DSM gives the changes between the two epochs, especially regarding vegetation. After co-registration, the Z-component of the Euclidian distances (sigma a posteriori) was 3.4 m, showing a clear reduction of trees and other wooded plants from 1997 to 2002. The difference matching DSMs minus LiDAR DTM gives the normalized DSMs, i.e. the 3D objects in the scene and especially the canopy models (Fig. 3). The LiDAR DSM was also subtracted from the 2002 DSM, in spite of the small time difference.



**Figure 3.** The 2002 matching DSM minus the LiDAR DTM, showing 3D objects on the terrain, especially trees and shrubs. Non-vegetation objects like buildings could be detected and eliminated by using multispectral classification, size and shape etc., thus leading to a true canopy model (see section 2.4).



2.4 Forest masks

In the present study, two forest masks serve as basis (response variable) for the fractional modelling approach. Two canopy covers were calculated by a multistage procedure using slope data of the normalized DSMs. This simple but robust algorithm incorporates a slope threshold, minimum area for tree canopy and minimum area for forest gaps in the normalized DSM data. In a second step, non-tree objects (buildings, rocks etc.) of the canopy covers were removed by an object-oriented image analysis using spectral information of the CIR-orthoimages. This implies a two stage process with a multi-resolution segmentation of the canopy cover and CIR-orthoimages and a fuzzy classification using *eCognition* (Baatz & Schäpe, 2000). The resulting forest masks of 1997 and 2002 are a product of different slope thresholds, minimum tree canopy area and minimum gap size. These thresholds for the three parameters have been set empirically but have been successfully tested for fine-scale modelling of forest area in mire ecosystems in Küchler et al. (2004). Only pixels with slope values higher than 20 degrees, a minimum tree canopy area on single tree level (5 m<sup>2</sup>) and a maximum gap size of 120 m<sup>2</sup> were considered.

2.5 Fractional tree/shrub covers

Whether a pixel belongs to a forest mask or not can be attributed to a binomial variable. Logistic regression is adapted for modelling such data (see e.g. McCullagh & Nelder, 1983). The result is a fractional tree/shrub cover, i.e. a probability for each pixel to belong to the class “tree/shrub”. The training data for the model were selected in a way to enable estimation of bias: only pixels were used which belong to the same class in both surveys i.e. that were either corresponding forest pixels or open land pixels in the 1997 and 2002 forest masks. The explanatory variables consist of five commonly used topographic parameters derived from normalized DSMs (slope, aspect, curvature, and local neighbouring functions), see table 1 and for further details see Burrough (1986). Most of these parameters have successfully been applied for ecological modelling purposes in mires (Küchler et al., 2004) or in biodiversity studies (Waser et al., 2004). Two fractional tree/shrub covers of 1997 and 2002, respectively were produced using the forest masks described in section 2.4.

Name	Derivation
curvature	curvature of the surface at each cell center (3x3 window)
plan	curvature of the surface perpendicular to the slope direction, referred to as the planform curvature (3x3 window)
prof	rate of change of slope for each cell, curvature of the surface in the direction of slope (3x3 window)
slope	rate of maximum change in z value from each cell
top	assessment of topographic position (4 classes: ridge, slope, toe slope and bottom), the resulting grid displays the most extreme deviations from a homogenous surface

**Table 1.** Overview of the five explanatory variables (derived from nDSM) used to generate the fractional shrub/tree covers.

2.6 Bias estimation

A possible bias may result from different data quality of the CIR-aerial images from the two survey times, e.g. different spatial resolution, different image scanning facilities, varying radiation etc. In the context of predictive modelling, bias denotes a systematic error in predicted values which might be misinterpreted as a change. Küchler et al. (2006) present a method of estimating bias arising from different data quality in two surveys.

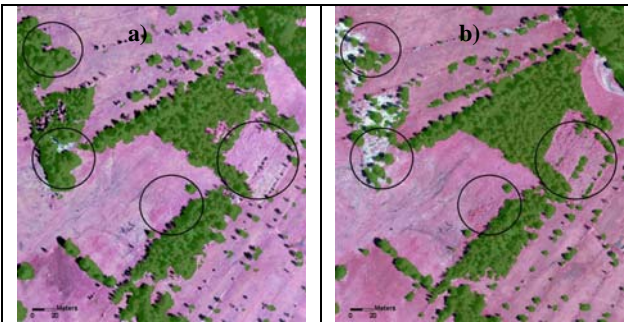
In the present study, bias was estimated by the following procedure: The probabilities of each pixel of the corresponding smoothed fractional cover (i.e. *model\_uncorr*) were added together and the sums stratified into 20 classes. Lowest class (0.0 - 0.1) of model sums corresponds to “non-tree/shrub” whereas the highest class (1.9 - 2.0) corresponds to “tree/forest”. Intermediate classes represent either partly forested areas or areas that have been deforested or areas where shrub encroachment occurred. To estimate bias, the smoothed fractional covers (2002 - 1997) were subtracted. Then distributions of the resulting differences were analysed separately within each of the 20 classes. As result, discrete bias estimations for each class were obtained. To have a continuous bias estimation the discrete values were smoothed by Loess regression with span 0.3.

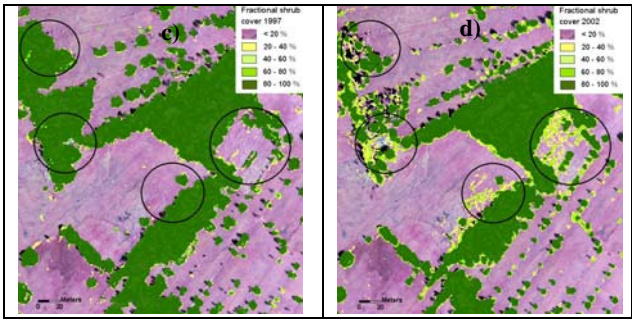
2.7 Validation data

For validation purposes ground truth data was produced using digitized samples from stereo-images. Three types of samples were distinguished and a total number of 3 x 20 samples were digitized from the aerial images: 1. Tree/shrub-less areas in 2002 that belonged to tree/shrubs in 1997 (decrease), 2. Tree/shrub-less areas in 1997 that are covered with trees/shrubs in 2002 (increase) and 3. Tree/shrub areas and tree/shrub-less areas those are unchanged between 1997 and 2002 (equal).

3. RESULTS

Fig. 4 a-d visualizes the difference between the forest masks and fractional covers of both years in a typical part of the mire where small shrubs and single trees are well present. The tree area extracted by both data sets is 0.901km<sup>2</sup> (*forest\_mask97*) and 0.832km<sup>2</sup> (*forest\_mask02*), respectively.





**Figure 4.** a) CIR-orthoimage with forest masks of 1997 and b) of 2002, c) and d) corresponding fractional tree/shrub covers. The two circles on the left side mark areas with decreased tree/shrub cover due to deforestation/loggings. The two circles on the right side mark increased tree growth / shrub encroachment.

Visual image inspection revealed that several shrubs and small single trees are still not extracted in the remaining open mire land. Therefore two fractional tree/shrub covers of 1997 and 2002 were produced using the forest masks described in section 2.4 as training data sets. A tree/shrub cover stratum of e.g. 0.1 - 1 (10-100%) means, that all pixels with a probability higher than 10% are assigned to shrub/tree etc. Fig 4c-d) shows the five predicted tree/shrub cover strata for a typical part of the mire. Tree/shrub area that is previously missed by the forest masks is extracted as well – dependent on the threshold of probability. Area of extracted trees/shrubs increases with lower probability thresholds. At the same time errors increase too. E.g. visual stereo image analysis revealed that a cover stratum of 10-100% also considers other vegetation than shrubs such as tall grass or herbs. In contrary, considering only a cover stratum of 0.5 – 1.0 (50-100%) leads to a significant underestimation of shrubs and trees in the open mire land. Decrease and increase of forest area and other wooded area (1997-2002) is given in table 2. The forest mask reveals a decrease of tree/shrub pixel portion of -0.059 between 1997 and 2002. Overall, the fractional cover approach revealed a decrease of tree/shrub probability between 1997 and 2002 of -0.029 for the uncorrected model (including bias) and -0.037 for the corrected model.

Differenececs 2002 - 1997	Description	Mean change of tree/shrub pixel portion
<i>forestmask97_02</i>	forest masks 2002 - 1997	-0.059
		Mean difference of tree probability
<i>Model_uncorr</i> (not bias corrected)	based on forest masks	-0.029
<i>Model_corr</i> (bias corrected)	based on forest masks	-0.037

**Table 2.** Variations of change estimations for tree/shrub probability (1997-2002) as obtained by different methods.

Table 3 summarizes the changes of tree/shrub pixel portion between 1997 and 2002 on the digitized sample areas between the forest masks and the changes of tree/shrub probability of the corrected fractional covers. Both the forest masks and fractional tree/shrub covers reveal no decrease/increase between 1997 and 2002 on the digitized samples where no change occurred. Forest mask and corrected model show a substantial decrease of tree/shrub probability in delineated

areas where tree/shrub area declined between 1997 and 2002. Good information on deforestation is also given by *forestmask97\_02*. However, shrub encroachment and growth of small trees in open mire land is not or only slightly detected when using the forest mask (+0.081). In contrary, the corrected model (+0.178) shows a shrub encroachment (general increase of tree/shrub probability in areas that were delineated as increase).

Differences 1997	2002- digitized as	Mean change of tree/shrub pixel portion
<i>forestmask97_02</i>	decrease	-0.602
	equal	-0.000
	increase	+0.081
		Mean difference of tree/shrub probability
<i>Model_corr.</i>	decrease	-0.518
	equal	-0.000
	increase	+0.178

**Table 3.** Mean differences in tree/shrub probability (2002-1997) on the digitized sample areas.

4. DISCUSSION AND CONCLUSION

Combining remote sensing data with regression analysis with fractional cover approaches as it is performed in many studies for land cover mapping (Guisan and Zimmermann 2000; Mathys et al. 2006) also is shown to be appropriate for fractional tree/shrub cover mapping and assessing changes of forest area in a mire biotope. The usage of standard explanatory variables as already applied in other studies (e.g. Küchler et al. 2004 and Waser et al. 2004) derived from the normalized DSM proved to be a good approach for fractional modelling. With a fractional cover approach, also subtle changes of forest area and of other wooded area can be detected before reaching a discrete threshold value. Furthermore, shrub/tree classifications based on the continuous data can be adjusted retrospectively. This may be an advantage also for mire habitat management. However, different quality of the scanned CIR-aerial images and the normalized DSMs from the two surveys 1997 and 2002 caused systematic errors in the predicted values of the models which could be misinterpreted as a change of forest area. In fact, bias proved to occur at a scale which would, without correction, make impossible e.g. a reproducible statement whether the removal of trees and shrubs or the encroachment by growing bushes was predominant in the survey time. Estimation and correction for bias is essential if any change has to be assessed by statistical modelling. Overall, the present study reveals a general decrease of forest area due to hurricane *Lothar* in 1999 and selective logging of groups of trees in the frame work of the regeneration program. These differences of the corrected fractional tree/shrub covers give us reliable indication of the magnitude of changes of tree area between 1997 and 2002. Information on shrub encroachment is essential for assessing possible impact on the mire environment. Future work will also pursue the retrieval of the type of trees/shrubs by using spectral information of ADS40 data. However, both the accuracy of the forest masks and the fractional tree/shrub covers strongly depend on the accuracy of the DSM data. Thus, DSMs derived from newly developed, high-quality matching methods are indispensable. The usage of a dense and accurate DSM and DTM are absolute prerequisites

in order to be able to derive accurate topographic parameters which in turn are used to derive the forest masks and the fractional tree/shrub covers. The fact that these topographic parameters alone almost suffice for the generation of the forest masks and the tree/shrub covers underlines the importance of DSM and DTM quality. LiDAR DSMs and DTMs as applied for this study, the latter was used in this study, have smaller point density than the DSM, and during the vegetation season, due also to partial canopy penetration or LiDAR flight with leaves off, are less accurate for modelling vegetation canopy. The present study showed that derivation of DSMs by high-quality matching, compared to LiDAR, has an additional advantage: images of 1997 and 2002 were used to derive multi-temporal DSMs, forest masks and tree/shrub covers, thus permitting a better analysis of changes of tree/shrub area. Regarding the matching DSM, a larger side overlap could reduce occlusions and lead to better modelling of small openings between trees, while increasing the number of image rays per measurement leading to higher accuracy and reliability. Use of modern digital photogrammetric sensors, would lead to avoidance of scanner and film problems, better radiometric quality, and use of the NIR for classification, all factors that would result in a more accurate mapping and change detection of trees and shrubs. Further future investigations will include the direct use of multitemporal matching DSMs and LiDAR DTMs for co-registration, therefore reducing bias errors, and estimation of forest masks and fractional covers using directly these data sets and their differences, possibly in a combination with multispectral classification.

To summarize, high-resolution 3D information as obtained by means of DSMs is indispensable for modelling changes in forest and other wooded areas. Modelling retrospective changes of these areas is feasible since old aerial images are often available and necessary variables of the normalized DSM can be calculated.

## 5. REFERENCES

- Akca, D., 2005. Registration of point clouds using range and intensity information. *International Workshop on Recording, Modeling and Visualization of Cultural Heritage*, Ascona, Switzerland, May 22-27, In E. Baltsavias, A. Gruen, L. Van Gool, M. Pateraki (eds.), Taylor & Francis/Balkema, Leiden, pp. 115-126.
- Akca, D. and Gruen, A., 2005. Recent advances in least squares 3D surface matching. In *Proceedings of Optical 3-D Measurement Techniques VII Vol. II*, Gruen, A., Kahmen, H. (eds.), October 3-5, Vienna, Austria, pp. 197-206.
- Artuso, R., Bovet, St. and Streilein, A., 2003. Practical methods for the verification of countrywide terrain and surface models. *Proceedings of the ISPRS working group III/3 workshop XXXIV-3/W13*. 3-D reconstruction from airborne laserscanner and InSAR data, 8-10 March, 2003, Dresden, Germany.
- Baltsavias, E., 1999. Airborne laser scanning: existing systems and firms and other resources. *ISPRS Journal of Photogrammetry and Remote Sensing*, 54, 164-198.
- Baatz, M. and Schäpe, A., 2000. Multiresolution Segmentation – an optimization approach for high quality multi-scale image segmentation. In J. Strobl, T. Blaschke and G. Griesebner (eds.), *Angewandte Geographische Informationsverarbeitung Vol. XII* (pp. 12-23). Heidelberg, Germany: Wichmann.
- Burrough, P.A., 1986. *Principles of Geographical Information Systems for Land Resources Assessment*. New York: Oxford University Press, 50 p.
- Gruen, A. and Akca, D., 2005. Least squares 3D surface and curve matching. *ISPRS Journal of Photogrammetry and Remote Sensing*, 59(3), 151-174.
- Grünig, A., Steiner, G.M., Ginzler, C., Graf, U. and Kuchler, M., 2004. Approaches to Swiss mire monitoring. *International Peat Journal*, 12, 55-73.
- Guisan, A. and Zimmermann, N.E., 2000. Predictive habitat distribution models in ecology. *Ecological Modeling*, 135(2-3), 147-186.
- Heurich, M., Schneider, T. and Kennel, E., 2003. Laser scanning for identification of forest structure in the Bavarian forest national park. *Proceedings of the ScandLaser Scientific Workshop on Airborne Laser Scanning of Forests* (pp. 98-107), 3-4 September 2003, Umea, Sweden, 2003, Hyypä J., Naesset H., Olssen H., Granqvist Pahlen T., Reese H. (eds) (Swedish University of Agricultural Sciences, Department of Forest Resource Management and geomatics).
- Hyypä, J., Hyypä, H., Inkinen, M., Engdahl, M., Linko, S. and Yi-Hong, Z., 2000. Accuracy comparison of various remote sensing data sources in the retrieval of forest stand attributes. *Forest Ecology and Management*, 128, 109-120.
- Kienast, F., Brzeziecki, B. and Wildi, O., 1996. Long-term adaption potential of Central European mountain forests to climate change: A GIS-assisted sensitivity assessment. *Forest Ecology and Management*, 80, 33-153.
- Kuchler, M., Ecker, K., Feldmeyer-Christe, E., Graf, U., Kuchler, H., and Waser, L.T., 2004. Combining remotely sensed spectral data and digital surface models for fine-scale modelling of mire ecosystems. *Community Ecology*, 5(1), 55-68.
- Kuchler, M., Ecker, K., Feldmeyer-Christe, E., Graf, U. and Waser, L.T., 2006. *Predictive Models of Mire Habitats: Bias in Detection of Change*. WetHydro XX. Warsaw Agricultural University Press. (in press)
- Mathys, L., Ginzler, C., Zimmermann, N.E., Brassel, P. and Wildi, O., 2006. Assessment of continuous landscape variables for extracting a discrete forest areas. *Forest Ecology and Management*, 229, 111-119.
- McCullagh, P. and Nelder, J.A., 1983. *Generalized linear models*. London: Chapman and Hall, 511p.
- Naesset, E. and Gobakken, T., 2005. Estimating forest growth using canopy metrics derived from airborne laser scanner data. *Remote Sensing of Environment*, 96(3-4), 453-465.
- Schardt, M., Ziegler, M., Wimmer, A., Wrack, R. and Hyypä, J., 2002. Assessment of forest parameters by means of laser scanning. *Proceedings from the International Society for Photogrammetry and Remote Sensing (ISPRS)*, Commission III Symposium, Vol. XXXIV, Part 3A, 9-13 September 2002, Graz, Austria, 302-309.

Scott, J.M., Heglund, P.J., Samson, F., Haufler, J., Morrison, M., Raphael, M. and Wall, B., 2002. *Predicted Species Occurrences: Issues of Accuracy and Scale*. Covelo, California: Island Press, 868 p.

St-Onge, A. and Achaichia, N., 2001. Measuring forest canopy height using a combination of LIDAR and aerial photography data. *International Archives of Photogrammetry and Remote Sensing*, XXXIV-3/W4, 131-137.

Waser, L.T., Stofer, S., Schwarz, M., Kuchler, M., Ivits, E. and Scheidegger, C., 2004. Prediction of Biodiversity - regression of lichen species richness on remote sensing data. *Community Ecology*, 5(1), 121-134.

Watt, P.J. and Donoghue, D.N.M., 2005. Measuring forest structure with terrestrial laser scanning. *International Journal of Remote Sensing*, 26(10), 1437-1446.

Zhang, L. and Gruen, A., 2004. Automatic DSM Generation from Linear Array Imagery Data. *International Archives of Photogrammetry, Remote Sensing and Spatial Information Sciences*, Vol. 35, Part B3, 128-133.

Zhang, L., 2005. Automatic Digital Surface Model (DSM) Generation from Linear Array Images, PhD Thesis, Report No. 88, Institute of Geodesy and Photogrammetry, ETH Zurich, Switzerland. URL: <http://e-collection.ethbib.ethz.ch/ecol-pool/diss/fulltext/eth16078.pdf>. (accessed: 28 January 2007)

#### ACKNOWLEDGEMENT

The study was carried out in the frame of the Swiss mire monitoring program initiated in 1996 at the Swiss Federal Research Institute WSL and funded by the Swiss Agency for the Environment, Forest and Landscape (BAFU) and WSL. We acknowledge the support of Ruedi Boesch for providing the LiDAR data (WSL) and Devrim Akca, ETH Zurich for the co-registration of the DSMs.

# TOWARDS A NEAR-REAL TIME GLOBAL FLOOD DETECTION SYSTEM (GFDS)

Zsolia Kugler<sup>a</sup>, Tom De Groeve<sup>a</sup>, G. Robert Brakenridge<sup>b</sup> and Elaine Anderson<sup>b</sup>

<sup>a</sup> Joint Research Centre, Ispra Site, European Commission, Ispra 21020, Via Fermi 1, Italy – tom.de-groove@jrc.it, zsolia.kugler@jrc.it

<sup>b</sup> Dartmouth Flood Observatory, Dartmouth College, Hanover, NH 03755, USA – G.Robert.Brakenridge@Dartmouth.EDU, Elaine.Anderson@Dartmouth.EDU

Commission VI, WG VI/4

**KEY WORDS:** Flood detection, passive microwave, AMSR-E, global monitoring, orbital gauging

## ABSTRACT:

The methodology for flood detection developed at Dartmouth Flood Observatory (DFO) (Brakenridge and others, 2007) on a global scale, was implemented at the Joint Research Centre (JRC) of the European Commission on an automatic operational basis. The technique is using AMSR-E passive microwave remote sensing data of the descending orbit, H polarization, 36 GHz band to detect flood events from space around the globe with a daily temporal resolution. DFO was formerly using the daily global composite images having 3 days of lag in time whereas JRC implemented the model on the near-real time swath data available about 24 hours after acquisition. A ratioing of the water/dry signals described in the article are considered as a tool to observe surface water area changes. Thresholding the calculated observation ratio allows the detection of riverine inundation events. Validation of the model results is ongoing. Nevertheless, preliminary results show a promising correlation of the increase in river discharge on-site and changes at the observed signal of the sensor. Thus following the technique the detection of flood events in ungauged and inaccessible remote river channels is feasible from space.

Software was developed at the JRC to automatically acquire and process the remotely sensed data in real time on an operational basis. After the validation and calibration of the satellite based near-real time Global Flood Detection System (GFDS) the remotely observed flood events are planned to be integrated into the Global Disaster Alert and Coordination System ([www.gdacs.org/floods](http://www.gdacs.org/floods)). GDACS is running at the JRC providing near real-time alerts about natural disasters around the world and tools to facilitate response coordination, including news and maps.

## 1. METHODOLOGY OF THE GLOBAL FLOOD DETECTION SYSTEM (GFDS)

### 1.1 Introduction

The Global Flood Detection System (GFDS) is part of the Global Disaster Alert and Coordination System (GDACS), which aims at providing near-real time information for rapid and effective humanitarian response to natural disasters. GDACS is a project of the European Commission and the United Nations.

Of all natural disasters, floods account for more than 70% of human fatalities and property losses around the world. The severity of flood crisis can also be expressed by the frequency of their occurrence: they constitute almost 50% of the events among other natural hazards (CRED, 2006). For this reason the systematic monitoring of this phenomenon is essential in supporting sustainable and effective mitigation efforts.

As Bjerklie et al. (2003) and Fekete et al. (1999) stated, less than 60% of the runoff from the continents is monitored at the point of inflow in the ocean, and the distribution of runoff within the continent is even less monitored. Moreover, the number of operating hydrometric gauges is decreasing since the 1980s, the delivery time is often longer than several months, and there is a great spatial disparity in the gauges (Roux et al, 2006). The Global Runoff Data Centre (GRDC) is collecting a large set of river discharge data from in situ gauging stations with near global coverage (figure 1). However, such internationally-shared runoff data are provided as monthly mean values not daily values in near-real time.

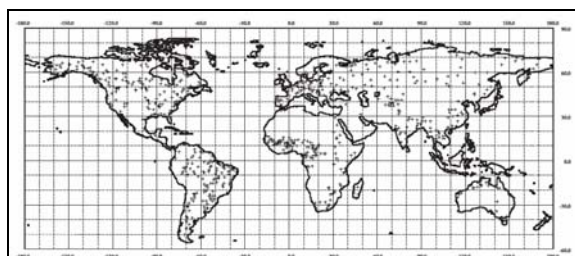


Figure 1. Best on-site gauging discharge stations around the globe collected at GRDC

Therefore, the use of remotely sensed information to derive hydrological parameters especially to monitor flood events could usefully extend or substitute for the missing measurements.

For this reason the Joint Research Centre (JRC) of the European Commission together with the Dartmouth Flood Observatory (DFO) joined forces to set up a global flood monitoring system from space. The aim of GFDS is to provide satellite based flow information around the globe substituting the missing on-site gauging in many parts of the world. The methodology discussed in the next chapters is based on Brakenridge and others (2007) and was implemented on a global operational monitoring scale at the JRC.



## 1.2 Related studies

The use of satellite based observations for river gauging measurements has the great advantage of enabling observations with a global coverage using one systematic methodology with a high repetition frequency. Moreover it has the potential to become a near-real time observation that supports rapid response to flood crisis around the globe.

Hydrographic data obtained from satellite systems and other remote sources offer the possibility of broad and potentially frequent global coverage of river discharge estimates (Barrett, 1998). Assessing river flow using remotely sensed data may then be a mean to increase the global stream flow monitoring network. Moreover, remote sensing is able to provide information over large areas, including those where ground-based data is difficult to obtain (Roux *et al.*, 2006).

The use of remote sensing tools in flood observations dates back to the early years of the first operational optical satellite systems like the Landsat Multispectral Scanner (MSS) in the 1970's and 1980's. Inundation maps were derived from satellite images in particular for flood events inside the USA (Smith, 1997). Activities of impact assessment using satellite images of the visible range is still ongoing in many scientific and also operational services (RESPOND, 2006) yet feasibility is significantly limited by cloud cover conditions.

For this reason many applications have flourished in the past using microwave remote sensing systems penetrating through the clouds for flood inundation area/stage or discharge estimations. Both passive microwave and active radar systems were studied and evaluated in their performance to support missing on-site gauging measures. However due to their different techniques results have provided different kind of information about river flow.

Besides using active systems for inundation area delineation (Hess 1995) radar altimetry was used in different studies (Briett, 1998; Koblinksky, 1993) to measure stage elevation or changes directly. The well-known scientific study of Alsdorf (2000) and his group resulted in the measurement of water level changes based on radar altimetry over the Amazon acquired from the Space Shuttle Radar Topography (SRTM) mission. Interferometric phase observations could detect water surface elevation changes in cm range. Still, the SRTM mission was providing observations only over a short period. The technology could not be implemented on an operational basis.

Other applications were using passive microwave emission of the earth's surface to estimate inundation area. The first pioneer study of using passive microwave sensor data to estimate flooded area was set up by Stippel *et al.* (1994) in the Amazon basin using the Scanning Multichannel Microwave Radiometer (SMMR). The sensor was providing measurements from 1978 to 1987 and has been used to measure time series of water levels on very large rivers, such as the Amazon. Flooded areas were derived using linear mixing models of the microwave emission from major landscape units. The measurements of the SMMR instrument were only available in weekly intervals.

All these applications do not support operational daily observations and near-real time global coverage. For this reason the JRC together with DFO has developed a technique that uses passive microwave observations of Advanced Microwave Scanning Radiometer - Earth Observing System (AMSR-E) mounted on NASA EOS Aqua satellite together with the well known MODIS sensor (Ashcroft, 2003). Acquiring data on a global scale every day unrestricted by cloud cover enables surface water measurements from space operationally in near-real time. With current fast internet technology data can be delivered to the users in about one day after the acquisition. The

U.S. National Snow and Ice Data Center (NSIDC) provides preliminary swath data available within 24 hours after the acquisition on board.

## 1.3 Methodology

The methodology aimed at setting up a routine that provides a systematic detection of flooding over river reaches around the world. The Dartmouth Flood Observatory (DFO) (Brakenridge, and others, 2007) developed a methodology to monitor river sites detecting flooding by using the difference in microwave radiation between land calibration parcels and water-including parcels along the rivers to be monitored. On global daily near-real time basis AMSR-E (Ashcroft, 2003) is providing the observations for the flood monitoring system. The methodology was implemented on a global scale at the JRC using automatic procedures from downloading to processing data and outputting of the results. Since night time radiation is more stable than day time, only descending swaths of the sensor are used. The 36GHz frequency with H polarisation appeared to be the most optimal one for monitoring aims. This frequency has a footprint size of approximately 8x12km. The selection of the H polarisation is described in detail in Brakenridge and others (2007) based on a model simulation study analysing the sensitivity of different polarizations to increases in fractional area of open water and increase of soil moisture on floodplains. Obtained Level2 swath products are associated with geolocation coordinates which makes the observed signals easy to grid into a geocoded image.

Microwave radiation over river sections and inundated swampy areas generally accounting for a lower brightness temperature (Tb) than land which is due to the different thermal inertia and emission properties of land and water. River sites to monitor were selected by having a significant empirical relationship between flow conditions and inundation area in a subpixel dimension. In case of a flood event – assuming that river flow goes over bank - land cover change can be observed along the river. With the increase of the inundation area on the floodplain Tb decreases in the wet/measurement pixel due to water's lower emission properties. Thus by monitoring the same river site over time inundations can be observed from space.

To monitor flood events, observations over selected river sites were extracted from AMSR-E data. First pixels obtained over a river site were extracted from the swath data. During historical flood events these pixels were observed to be sensitive to river flow by enlarging their water surface area in case of discharge increase. In a second step dry (calibration) pixels - observed over land - were extracted. They were selected to be close to the measurement pixel to enable the assumption of constant physical conditions nevertheless they were not affected by flood inundation.

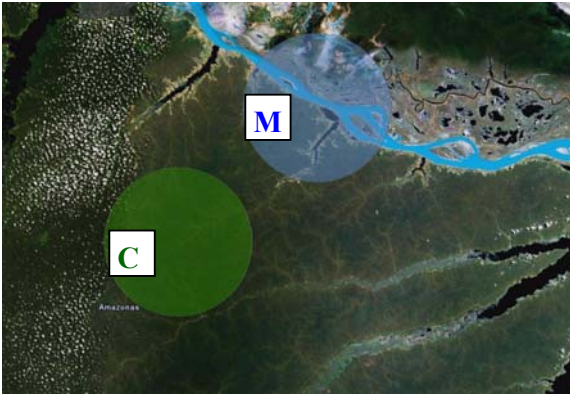


Figure 2. Observation sites over the Amazon in Brazil. Blue dot refers to the footprint of the “wet” (measurement) pixel observation, green dot to the calibration “dry” pixel. (Background: Google Earth)

Brightness temperature measures are influenced by many factors including physical temperature, permittivity, surface roughness, moisture etc. Whereas the relative contribution of these factors cannot easily be measured, they are assumed to be constant over a larger area. Therefore, by dividing the “wet signal” received over the river channel by the “dry” (calibration or comparison signal), the mentioned influences can be minimized in a consistent way. Thus, a ratio can be set up defined by the relationship:

M/C Ratio =  $Tb_m / Tb_c$  (1)

where  $Tb_m$  and  $Tb_c$  is the brightness temperature of the measurement/wet and calibration/wet pixel respectively. Resulting normalisation eliminated most of the daily and seasonal temperature variation, soil moisture effects, vegetation influences (figure 3.). Because it adapts automatically to different land surface characteristics, the methodology has the capability to be applied systematically over the globe.

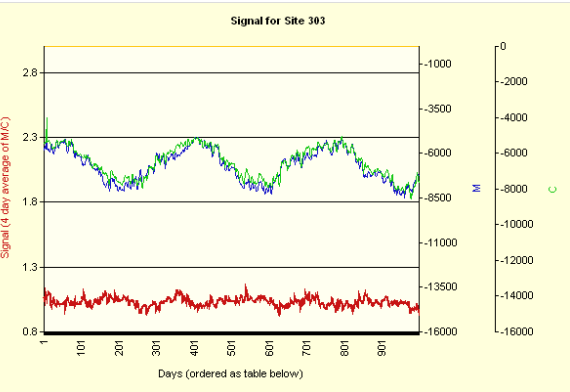


Figure 3. M/C ratio (red line) minimises radiation variation originating from seasonal variations, soil moisture, cloud cover and vegetation influences. M and C observations are blue and green lines respectively.

The time series of the M/C Ratio (1) provides the basis of river gauging measurement and flood detection from space. In normal flow conditions where water flows in-bank, dry and wet

signals have nearly the same trend over time (although unusually low flow, as well, can be detected). As soon as the river floods over-bank, the proportion of water in the wet pixel greatly increases and there is a strong response in the M/C ratio. Due to the lower emission of water the signal of the wet pixel lowers consequently, the M/C Ratio increases (figure 4.).

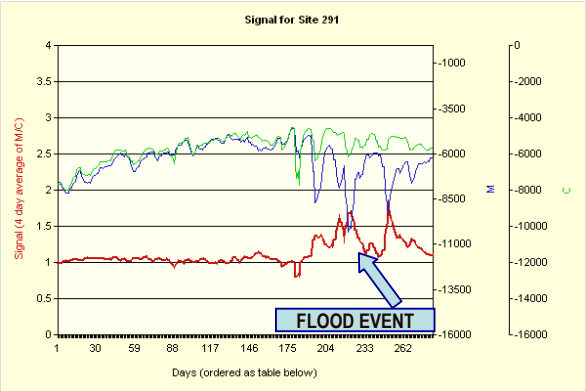


Figure 4. Flood event detected on the River Chenab in Pakistan in September 2006 from the M/C time series (red line).

Significant correlation was measured between the satellite based gauging signal and the on-site gauging measures of the selected river location (Brakenridge, and others 2007). However, the task for flood detection is simplified to the monitoring of current river status and distinguishing between normal flow and flooding. For this reason a separate process was set up to threshold the signal of riverine flooding without the need for local gauging station data. Thresholds were set by using the statistics of the time series. Signal was extracted from the complete 4 years of AMSR-E data reaching from the launch of the system June 2002 to the time of writing this paper (March 2007). The download and processing of near-real time satellite data is automatic and the signal extraction is ongoing, extending the time series of the gauging signals and updating their statistics every day.

River flooding is defined when M/C ratio is higher then 80% of it's cumulative frequency in the time series. Major flood is the 95% percentile, flood is the 80% percentile and normal flow is below the 80% percentile of its cumulative histogram. Detected flood events based on AMSR-E satellite observations are converted to disaster alerts and are implemented into the GDACS automatic disaster alerting system of natural hazards. At present, approximately 2600 river gauging sites are monitored automatically on a daily basis from AMSR-E satellite observations around the globe (figure 5.). Observations and flood alerts are summarised in database and visualised in form of maps on the GFDS web page distributing information on the internet ([www.gdacs.org/floods](http://www.gdacs.org/floods)).

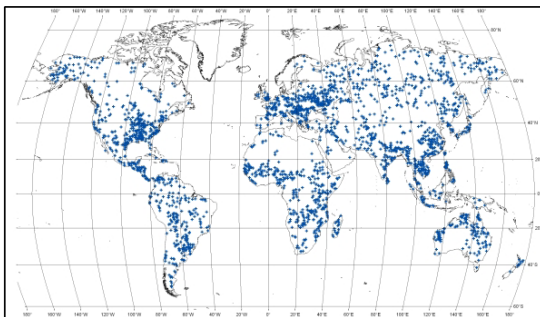


Figure 5. Space borne gauging stations around the globe monitored daily by GFDS

## 2. SIGNAL PROCESSING

### 2.1 Different sources of noise

As noted, correlation was found between the orbital gauging signals and the on site stage hydrographs at many sites (Brakenridge and others, 2006). However the signal was found to be noisy when comparing to daily discharge data provided at gauges on-site. This might be due to several influences on the received microwave radiation at the sensor.

The intensity of passive microwave radiation over an object is dependent not only on the object's temperature and incident radiation but also on the emittance, reflectance and transmittance properties of the object. Due to the variety of its possible sources and its extremely weak magnitude, the signal obtained from various ground areas is noisy (Lillesand, 1999).

A variable of great magnitude is the different radiation intensity related to the viewing geometry varying from swath to swath and from observation to observation. Nevertheless this effect should be minimised by the rationing of the two detected signals (M/C) that are separated by a short spatial distance. Secondly, the signal is influenced by many different factors besides the water surface area change. Factors like physical temperature, permittivity, surface roughness, moisture etc. not mentioning current cloud cover over the scanned area have an impact on the emitted radiation. These variations can be minimised by the proper selection of the dry/calibration pixels unaffected by river flow change but situated near to the wet pixel ensuring to have similar physical properties suitable to reduce noise after ratioing with the wet pixel.

Still different approaches were tested to reduce noise from M/C signal.

### 2.2 Spatial averaging

Spatial averaging was first tested to reduce noise from observed and calculated M/C ratios. The fractional area of the water in the wet pixel varies from swath to swath due to the different observation geometry every day. Therefore a spatial averaging was tested in order to stabilise the M/C signal.

A spatial resampling of all frequency channels is provided in the L2 data set to simplify the comparison of different channels with different footprint size. All frequency channels are available at an unsampled Level 1B resolution. The higher-resolution channels are resampled to correspond to the footprint sizes of the lower-resolution channels. The Level-2A algorithm spatially averages the multiple samples of the higher-resolution data into the coarser resolution instantaneous field of view

(IFOV) of the lower-resolution channels with the Backus-Gilbert method (Ashcroft, 2003).

The use of the spatial averaged ratio resampled at 27x16 km (resolution 3) was tested instead of using the unsmoothed original 8x12 km spatial resolution. Results are shown in figure 6.

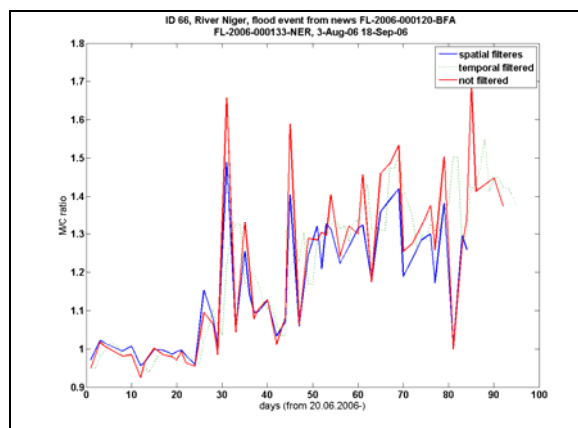


Figure 6. Spatial averaged and temporal filtered M/C signals for site along the River Niger in Mali

As visible from the figure the smoothening effect of the resampled channel did not significantly reduce the noise as expected in advance. For this reason in a second step a temporal filtering was applied to the signal.

### 2.3 Temporal filtering

Temporal filtering was introduced to reduce the swath to swath variation of the signal. The signal for one day was averaged from the last 3 days signal and the signal for the current day. This 4 days average provided a better result to stabilise the signal then the spatial resampling described in the previous section (see figure 5). A further advantage related to the temporal averaging compared to the spatial means is that on days when data are missing or near-real time data are provided with significant delay, the M/C ratio can still be calculated from the average of the observations from the previous days. Thus from the trend of the previous days an estimation for the current day can be provided. This method accords with the multi-day duration of most floods.

At the moment GFDS is applying the 4 days average to calculate M/C signal around the globe on a systematic way. Observations are provided on a daily basis and thresholds to detect flood events described in the methodology chapter are calculated based on the temporal filtered observations introduced to reduce signal noise.

## 3. VALIDATION PROCESS

### 3.1 Validation approaches

Different validation strategies could be applied for different sites. Rivers can be classified as flowing within either gauged or ungauged regions depending on if on-site measurements are taken systematically for the river. For gauged river sites, AMSR-E observations are easier to validate: hydrological measurements of either water surface elevation gauging or discharge measurements can be correlated to AMSR-E signals directly. However, care has to be taken with comparing water

elevation with space borne river gauging. The last is measuring emissivity variation in time due to flood area extent changes. The location of the river gauging sites were selected so that flood extent had a good correlation with water surface elevation changes thus also discharge changes, however in case of a flood event flood extent increase can still be observed while stage is already in the falling limb.

For ungauged river sites the validation is more difficult. Yet, known flood events help to confirm or disprove observed inundations from satellite data. Several databases exist on disaster events around the world where information was collected from news or other sources but not from physical measurements or observations. The following ones were downloaded and processed ones: CRED EM-DAT\*, GLIDE\*, ECHO project database\*, OCHA Financial Tracking System\*, DFO\*. Most databases record inundation events according to the starting and ending date, duration, and country where it did occur. Unfortunately, the detailed information on the location and the river basin is not consistently available.

3.2 Validation of ungauged river sites

The disaster event databases serve the basis for the validation for sites having no on-site gauging measurement records. Flood alerts detected from AMSR-E observations of each river site described in the methodology chapter were converted into a list of detected flood events for the given site. Detected flood events were defined as a period during which a site has continuously been facing flood or major flood alerts with no gap longer than 3 days in between. This was automatically derived from the time series of the space borne gauging measures.

Flood events detected from physical measurement can be compared with known events from the mentioned databases by matching records according to country and overlapping starting/ending date (figure 7.). From this match the correlation between remotely observed events and known events can be calculated.

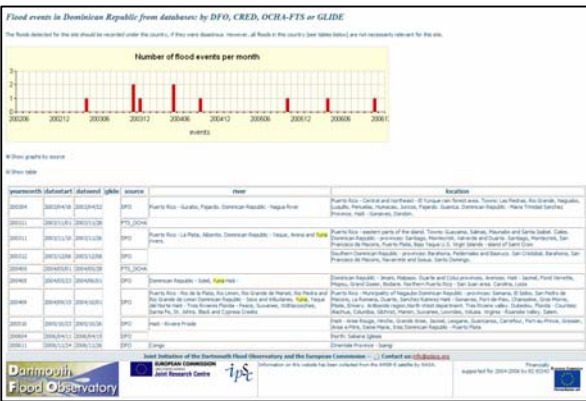


Figure 7. Validation process. Comparison of satellite based flood observations and reported flood events from news.

\* <http://www.em-dat.net/disasters/list.php>  
\* <http://www.glidenumber.net/glide/public/search/search.jsp>  
\* <https://hac.cec.eu.int/>  
\* <http://ocha.unog.ch/fts2/pageloader.aspx?page=emerg-emergencies&section=ND&year=2006>  
\* <http://www.dartmouth.edu/%7Efloods/Archives/index.html>

The first result from the ongoing validation process was not satisfactory: only about 50% of the detected events fitted the flood event databases. This was due to the fact that the flood events were matched only according to the country of their occurrence and not to river basins or regions. The matching on river name basis is ongoing. However much manual work is still to be done to extract and mach river names exactly between the two sources.

However, since non of the databases can be considered as complete, comprehensive and error free, human interpretation is necessary to confirm this match. Moreover some flood events detected from satellite imageries do not appear in the database. Thus alternative approaches can be considered like flood mapping from other satellite resources.

3.3 Quantification of accuracy

The correlation between observed and known events give a rough estimation of the accuracy of one site. The error of commission and omission could be calculated for each site following the rule table 1.:

	Known flood event	Unknown flood event
Observed flood event	Correct	Commission
Not observed flood event	Omission	Correct

Table 1. Different sources of flood detection error

In this case of course the error of comission is going to be more difficult to determine since there might be flood events that were not recorded in any of the databases however were present in field. In this case alternative approaches can be considered like comparing results with flood extent maps. Nevertheless in the first step we assume that all flood events were recorded in the databases.

The quantification of error can serve the basis for ranking sites. As a result of this validation sites could be flagged as good or bad site if a certain rate of error is achieved.

3.4 Qualitative evaluation

In case a site is flagged as a bad site not reflecting flood events from its signal peaks manual editing can be applied. For this reason a tool was set up to enhance flood detection results from signal based on several strategies:

- In a first step thresholds can be changed from the default value of 80% cumulative frequency to individual ones to fit better site specifications. Some sites can have a threshold function over time (e.g. seasonal variation) and some sites can have signal increase that is not correlated to flood events. An additional user interface has been created in the model for this purpose. This way, different analysts can manually analyse different sites and record their findings in the central database. After altering threshold values an automatic recalculation of the sites statistics and the flood events is followed.
- If threshold changes do not enhance results, the location of calibration and measurement pixel can be changed. A tool is about to be set up to automatically



- re-extract signals from AMSR-E data in case of location change.
- Sites on the same river must be compared with each other. For this reason a tool was set up to summarise flood alerts in the same country along the same river.

3.5 Validation knowledge base

A knowledge base will be added to the current flood web site. It will be possible to store extra information per site and per event. This information is necessary to see the progress of the validation and record what works for which site. JRC will propose such a knowledge base.

4. OPERATIONAL TEST DURING THE RECENT FLOODING IN BOLIVIA 2007

The first operational use of the GFDS was during the devastating flood crisis in Bolivia from the beginning of the year 2007 (glide number\*: FL-2007-000012-BOL). Harsh rainy season due to El Nino was causing flooding throughout the country, 8 provinces out of 9 were severely hit, 350 000 people were affected. Capital city Trinidad was under water; most of Beni province was inundated. Bolivian government declared a national emergency on 18<sup>th</sup> January 2007 and appealed for international help (Brakenridge, 2003). The European Commission responded to the request and the Environment Directorate-General (DG ENV) requiring spatial information about the flood disaster to support decision making processes. Besides the operational GDACS internet portal a separate home page was set up for emergency management of the crisis. Besides collecting information and maps from news and different humanitarian relief communities we tried to elaborate the severness of flood situation daily from AMSR-E observations. Inundation mapping from MODIS images was delayed by cloud cover throughout the whole month of February. Partially cloud free scenes could be acquired only at the end of the month. At this stage we can conclude that the temporal resolution of AMSR-E flood observations is one of the great advantages during the operational use of the system compared with other satellite resources like optical MODIS or active radar systems. While cloud cover or repetition time is limiting the use of the two latest satellite systems, GFDS has the advantage to provide a situation overview on a daily basis. If necessary the number of gauging locations can be extended considering the conditions set and discussed in the methodology.

To get a better overview of the disaster situation in the whole Rio Mamore river basin - where the city of Trinidad is located - we increased the number of operational orbital gauging sites (figure 8). We located one observation every 50 km along the river to ensure the spatial continuity of the observations along the channel using one calibration site over the whole reach.

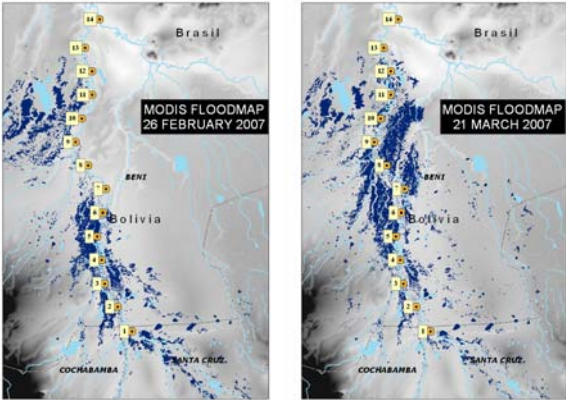


Figure 8. Location of orbital river gauging sites (yellow dots numbered sequentially) set during the flood emergency in Bolivia overlaid with the flood map derived from MODIS images (dark blue areas). Background: gtopo elevation model.

Inundation mapping was performed during the disaster event from MODIS satellite images. Comparing the flood maps obtained at the end of February and March we can observe that the flood extent decreased at the southern upstream end of the river reach while increased in the northern downstream area reflecting the flood wave propagation with time along the river. Nevertheless inundation mapping was limited by cloud cover over the region due to heavy rain fall.

Following the enlarge number of orbital gauging sites the AMSR-E observations were providing a better temporal resolution with a high spatial sampling along the Rio Mamore then compared to optical low-resolution satellite systems. A situation overview of the whole river basin could be provided every day regardless of the cloud cover conditions.

The 3D graph below (figure 9.) provides a good overview of the river gauging signal along the channel in time during the flood event. Where x axes refer to river gauging sites – numbered sequentially along to reach from upstream to downstream – y axes presents the time scale during the flooding from 01.01.2007 to 22.03.2007 and z dimension refers to the M/C gauging signal.

The propagation of the flood wave was visible on the gauging peaks highlighted with red on the graph. The signal of orbital gauging stations set along the Rio Mamore were showing a high correlation with the flood maps derived from MODIS images (figure 8.). The upstream peak at the end of February is well distinguishable from the downstream peak at the end of March in the graph. This matches perfectly with the flood maps estimated from MODIS images of the same period. Thus flood monitoring from AMSR-E observations compared with inundation mapping possibilities from MODIS images provides a higher temporal resolution thus a better situation overview in time.

\* GLobal IDentifier number (GLIDE) is a globally common unique ID code for disaster events issued by Asian Disaster Reduction Center (ADRC)



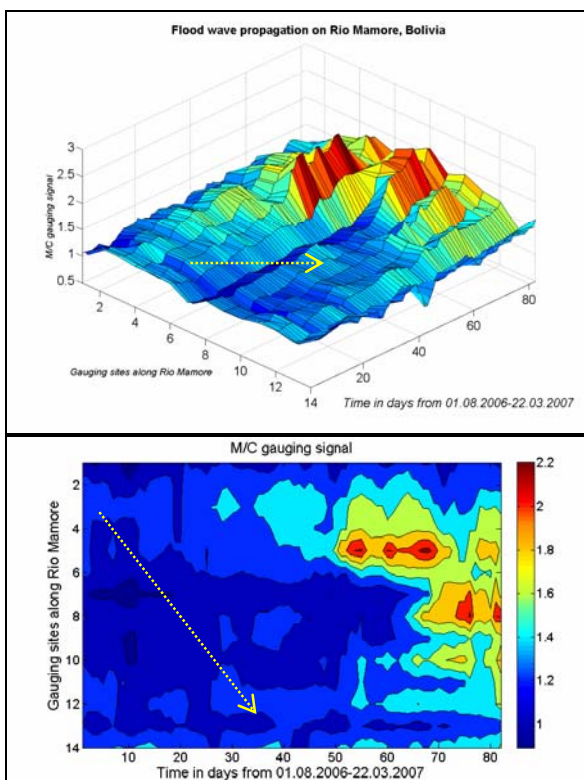


Figure 9. Three dimensional graph of the flood propagation along the Rio Mamore from AMSR-E observations. X axes: orbital gauging stations along the river; y axes: time scale; z axes: M/C values. Yellow arrow refers to the flood propagation in space and time.

## 5. CONCLUSIONS

This paper discusses the implementation of a daily flood detection technology on a global scale. The monitoring system provides a daily overview of the flow conditions of river systems in the world. Because of its general applicability, the methodology can be extended to include an arbitrary number of locations for orbital gauging. This is particularly interesting for rivers that are not monitored with on-site gauging stations.

Moreover, the use of AMSR-E observations for flood monitoring can prove to be an alternative to flood mapping in case of a persistent cloud cover over the inundated region. While the spatial resolution is low, orbital gauging observations can give a spatial overview of the disaster situation in different river sections of the same river. In addition, compared to other satellite observation systems (such as MODIS or Landsat optical images) the method provides a high temporal resolution which can be presented in a coarse but frequent map of the river flow conditions.

The use of the monitoring system during the Bolivia flood event in the first quarter of 2007 showed that the system can already provide operational results. Nevertheless, the same case study also showed that validation needs to be done taking into account local conditions.

## References from Journals:

Brakenridge, G. R., S. V. Nghiem, E. Anderson, R. Mic, 2007, Orbital Microwave Measurement of River Discharge and Ice Status, *Water Resources Research*, In press

Birkett, C.M., Contribution of the TOPEX NASA radar altimeter to the global monitoring of large rivers and wetlands, *Water Resources Research*, 34, 1223-1239, 1998.

Hess, L. L., Melack, J. M., Filoso, S. & Wang, Y. Delineation of inundated area and vegetation along the Amazon floodplain with SIR-C synthetic aperture radar. *IEEE Trans. Geosci. Remote Sensing* 33, 896-904 (1995).

Alsdorf, D.E., J. M. Melack, T. Dunne, L.A.K. Mertes, L.L. Hess, and L.C. Smith, Interferometric radar measurements of water level changes on the Amazon floodplain, *Nature*, 404, 174-177, 2000.

Barrett, E., 1998. Satellite remote sensing in hydrometry. In: Ed. H. (Ed.), *Hydrometry: Principles and Practices*. Wiley, Chichester, UK, pp. 199-224.

Roux H., and D. Dartus, 2006. Use of parameter optimization to estimate a flood wave: Potential applications to remote sensing of rivers. *Journal of Hydrology*, Volume 328, Issues 1-2, 30 August 2006, Pages 258-266

Koblinsky, C.J., R.T. Clarke, A.C. Brenner, and H. Frey, Measurement of river level variations with satellite altimetry, *Water Resources Research*, 6, 1839-1848, 1993.

Smith, L. C., 1997. Satellite remote sensing of river inundation area, stage, and discharge: A review. *Hydrol. Processes* 11, 1427-1439.

Bjerklie, D.M., S. L. Dingman, C. J. Vorosmarty, C. H. Bolster, R. G. Congalton: Evaluating the potential for measuring river discharge from space, *Journal of Hydrology* 278. (2003), pp. 17-38

Stippel, S.J., Hamilton, S.K., Melack, J.M., Choudhury, B.J., 1994. Determination of inundation area in the Amazon River floodplain using SMMR 37 GHz polarization difference. *Remote Sensing Environment* 48, 70-76.

## References from Books:

Lillesand, T.M., Kiefer, R.W.: *Remote sensing and image interpretation*, 3 ed., John Wiley & Sons, Inc., 1994

## References from Other Literature:

Fekete, B.M., C.J. Vorosmarty and W. Grabs, 1999. WMO-Global Runoff Data Center Report WMO-Global Runoff Data Center Report 22 (1999) p. 114

Ashcroft, P., and F. Wentz. 2003, updated daily. AMSR-E/Aqua L2A Global Swath Spatially-Resampled Brightness Temperatures (Tb) V001, June 2002 to recent. Boulder, CO, USA: National Snow and Ice Data Center. Digital media. (accessed 22 March 2007)

**References from websites:**

RESPOND home page, [www.respond.org](http://www.respond.org), 2006, (accessed 22 March 2007)

Ashcroft, P., and F. Wentz. 2003, updated daily. AMSR-E/Aqua L2A Global Swath Spatially-Resampled Brightness Temperatures (Tb) V001, June 2002 to recent. Boulder, CO, USA: National Snow and Ice Data Center. Digital media. (accessed 22 March 2007)

Brakenridge, G.R., Anderson, E., Caquard, S., 2003, Flood Inundation Map DFO 2003-282, Dartmouth Flood Observatory, Hanover, USA, digital media, <http://www.dartmouth.edu/~floods/2003282.html> (accessed 22 March 2007)

OFDA/CRED, 2006. "2005 disasters in numbers", OFDA/CRED, <http://www.em-dat.net> (accessed 22 March 2007)

**5.1 Appendix**

This project is a joint project between the European Commission and the Dartmouth Flood Observatory.

# TOWARDS GLOBAL MAPPING OF IRRIGATED AGRICULTURE

M. Ozdogan<sup>a,\*</sup> and G. Gutman<sup>b</sup>

<sup>a</sup> NASA/GSFC, Mail Code 614.3, Greenbelt, MD, 20771, USA - ozdogan@hsb.gsfc.nasa.gov

<sup>b</sup> NASA/HQ, 300 E Street SW, Washington D.C., 20546, USA - ggutman@nasa.gov

**KEY WORDS:** Irrigation, MODIS, Land-use/Land-cover, Agriculture, Water

## ABSTRACT:

We developed an irrigation mapping methodology that relies on remotely sensed inputs from MODerate Resolution Imaging Spectroradiometer (MODIS) instrument, globally extensive ancillary sources of gridded climate and agricultural data and on an advanced image classification algorithm. In the first step, we used climate-based indices of surface moisture status and a map of cultivated lands to provide potential, *first-cut* at global irrigation. To detect actual irrigation, in the second step, we used spatio-temporal and spectral signatures from MODIS remotely sensed data. In particular, we explored three types of irrigation-related indices: i) *Annual* – where we exploited the difference in annual greenness variability between irrigated and non-irrigated crops and related this difference to precipitation availability; ii) *Spectral* – where we exploited a vegetation index (Green Ratio Index) that is sensitive to chlorophyll content; and iii) *Inter-annual* – where we explored the differences in inter-annual changes in vegetation greenness associated with precipitation between irrigated and non-irrigated crops. In the third step, we combined our potential irrigation dataset, remotely sensed indices, and training examples within a supervised classification tool based on a non-parametric decision-tree algorithm to make a binary (i.e. irrigated vs. non-irrigated) irrigated agriculture map. A test of irrigation mapping procedure in a pilot study over the continental US produced a high spatial resolution (1 km) map of irrigated areas with better than 80 percent map accuracy and expected spatial patterns such as a strong east-west divide with most irrigated areas concentrated on the arid west along dry lowland valleys. Future improvements of the method will include estimation of sub-pixel presence of irrigation using remotely-sensed skin temperature measurements.

## 1. INTRODUCTION

### 1.1 Motivation and Objective

Accurate information on irrigation extent is fundamental to many aspects of the Earth Systems Science and global change research. These include modeling of water exchange between the land surface and atmosphere, analysis of the impact of climate change and variability on irrigation water requirements/supply, and management of water resources that affect global food security. However, the current extent of irrigated areas over continental to global scales is still uncertain and available maps are derived primarily from country level statistics and maps that are often outdated. Even in locations, such as the US, where the general extent of irrigated areas is known, irrigation-related information exists only in disparate datasets and cannot be easily synthesized into a single continental scale database.

To overcome these limitations, our objective is to develop a methodology to map irrigated agriculture globally with data from the Moderate Resolution Imaging Spectroradiometer (MODIS) instrument at 1-km spatial resolution and ancillary data on climate. Our irrigation mapping methodology is objective, it uses contemporary data, it is robust enough to handle complex forms of irrigation that occur around the globe, and can be repeated across space and time. This irrigation mapping effort is part of our larger research program to understand anthropogenic effects, specifically that of irrigation on global water and energy cycles, climate, agricultural productivity, and agricultural water sustainability. In this paper, we present the methodology and give an example from the Continental US.

### 1.2 Existing Datasets on Global Irrigation

Currently, there are three global irrigated area products with varying degrees of quality and accuracies. While such datasets have obvious limitations such as being outdated and relatively coarse resolution, they represent the state of the knowledge for the extent of irrigated areas over large geographic regions. The first one of these is the FAO Global Map of Irrigation Areas (GMIA) developed by Döll and Siebert (1999) who combined heterogeneous information on the (approximate) location of irrigated areas with information on the total irrigated area from national and international sources to generate the first global “irrigated lands” map (Figure 1a). The map is a digital raster product with 5-min. spatial resolution and for each cell contains information on the percentage of area *equipped for irrigation* over the period between 1995 and 1999. The map of Döll and Siebert (1999) has become the *de facto* present-day information source for spatial distribution of global irrigated areas although its quality is highly dependent on the national and sub-national data sources used in its making (Figure 1b).

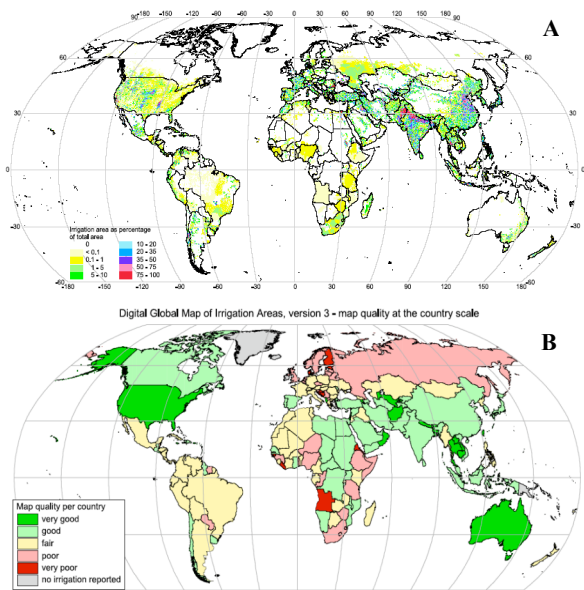
The second product was developed by the Remote Sensing and GIS group at the International Water Management Institute (IWMI) as the Global Irrigated Area Map (GIAM). This dataset has been produced using AVHRR NDVI and Land Surface Temperature data *ca.* 1999 augmented with additional information from SPOT *Vegetation*, JERS-1, and Landsat GeoCover 2000 data, mapped into 10-km grid resolution. (Thenkabail et al, 2005). The Beta release of this product has 53 irrigated classes, derived from the 628 classes in the master file.

Finally, the third product is a sub-product of the USGS Global Land Cover Map (Loveland et al., 2000). Under the auspices of the IGBP-DIS (International Geosphere Biosphere Programme-Data and Information System), a global land-cover database

---

\* Corresponding author.

was generated based on 1-km AVHRR observations received during the period April 1992 through September 1993. The USGS global land-cover data set includes several legends, all

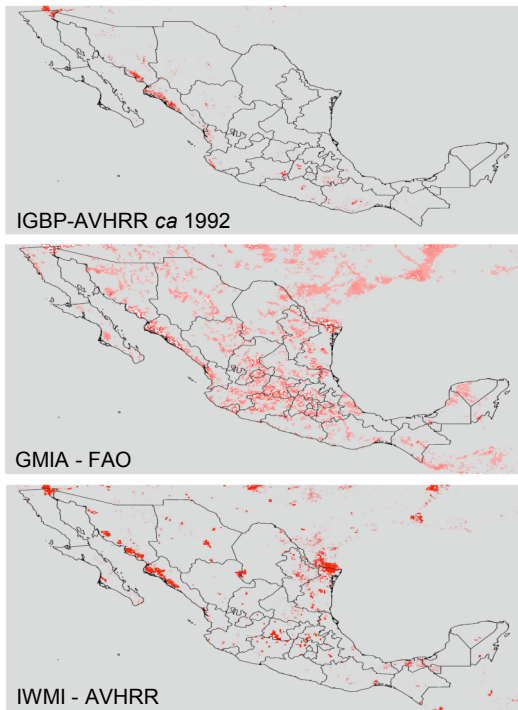


**Figure 1.** A) Global Map of Irrigation Areas (GMIA) shown as percentage of each 5min cell obtained using FAO country reports and other ancillary data; B) GMIA per country quality.

based on the same database (Loveland et al., 2000). Of these, the Global Ecosystems Legend contains four classes defined as irrigated land: *irrigated grassland, rice paddy and field, hot irrigated cropland, and cool irrigated cropland*. When combined, these classes provide one of the few sources of remotely sensed information on spatial distribution of irrigation at global scales.

While these data sources provide the best available source of information regarding the distribution of irrigation at global scales they also suffer from serious shortcomings. For example, the Doll and Siebert map (GMIA) primarily represents the areas *equipped to be irrigated circa* 1995-2000. However, the irrigated agricultural lands are extremely dynamic, driven by each year's precipitation availability, the choice of crop type, and the ability to irrigate on the farmers end. Moreover, the irrigated areas were determined from disparate data sources, primarily at the county level, the sub county information is less reliable. For example, a comparison of this product to the other mentioned products over Mexico where it is said to have low reliability (according to Figure 1b above) reveals stark differences and relative omission/commission errors (Figure 2-middle). The major shortcoming of the USGS map is that irrigated areas were determined as part of a broader classification scheme, not just irrigation. Thus the emphasis was primarily placed on other land cover types and thus irrigated classes has received less attention and decreased classification accuracy. A recent comparison by Vorosmarty (2002) of irrigated lands depicted by the USGS map to the country-level reports of irrigated area points to major uncertainties in the capacity to classify and inventory irrigated lands due to highly politicized nature of FAO data reports as well as technical limitations of the more objective geophysical datasets. This deficiency is also revealed in Figure 2-top. Likewise the major drawback of the IWMI global irrigation map product (GIAM) is that ground-truth data obtained only in India, SE Asia, Africa, and South America were used to adjust

and refine global irrigation classes. This makes the IWMI product highly parameterized per region for which extensive ground data exists. Over areas without such data and over the entire globe, the irrigation classes are rather less reliable (Figure 2-bottom).



**Figure 2.** Comparison of three global irrigation products over Mexico. As shown, the GLCC dataset (top) has large omission errors while the other two datasets have both relative omission/commission errors.

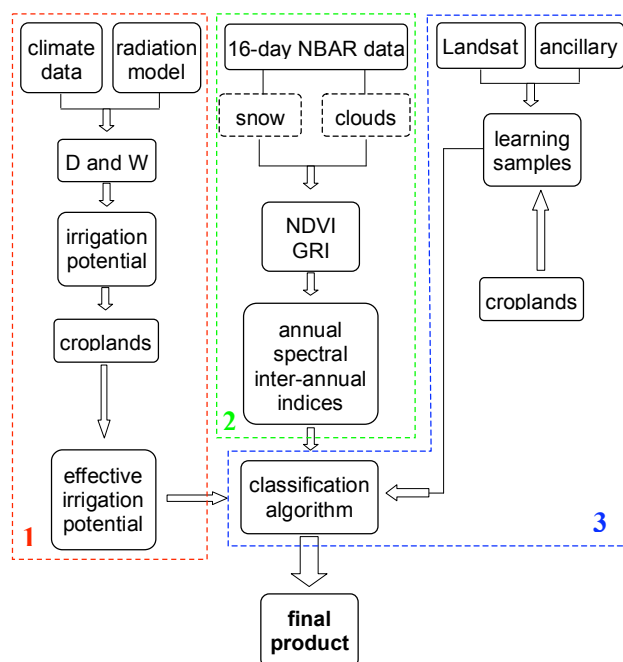
## 2. IRRIGATION MAPPING METHODOLOGY

### 2.1 Overview

As part of our objective to map irrigated lands globally, our proposed irrigation mapping procedure meets several important criteria. First, the procedure is automated and repeatable across space and time. Second, it is robust enough to capture many different forms of irrigated lands across large geographic regions. Third, it relies on high quality and objective remotely sensed observations. To meet these criteria, we take an image classification approach to irrigation mapping problem. While the intent is irrigation mapping, the fundamental process is image classification of remotely sensed, multi-temporal, multi-spectral images, guided by a climate index specifically suited for irrigation presence.

Our irrigation mapping procedure has three major parts that are schematically shown in Figure 3. In the first part, we calibrate a climatological moisture (or dryness) index along with existing agricultural maps to define irrigation potential. In the second part, we identify irrigation-related remotely sensed temporal and spectral indices. In the third and final part, we combine irrigation potential and remotely sensed indices within a supervised classification algorithm to locate irrigation at moderate spatial resolution (500m – 1000m). We initially tested our procedure in the US to map irrigated lands across the entire country. Our preliminary results from this first implementation of the procedure are extremely encouraging and warrant pursuing in other locations around globe. In the sections

that follow, we describe the steps our procedure in greater detail. In the last section, we show the first examples from the US.



**Figure 3.** Schematic representation of the proposed irrigation mapping procedure.

## 2.2 Effective Irrigation Potential

Irrigation is practiced in most countries at scales ranging from small subsistence farming to national enterprises. But the actual location is determined by a combination of factors including climate, resource availability, crop patterns, and technical expertise. Climate plays an important role in presence and distribution of irrigation as it determines natural moisture availability (precipitation), crop water demand (evaporation), and crop schedules. In this study, we developed a climate-based index for outlining potentially irrigated areas. A map of potentially irrigated areas in the form of a climate-based index provides the first approximation for areas that potentially require irrigation, which we further refine using remote sensing data.

Over large areas, presence and distribution of irrigation is primarily controlled by natural moisture availability at the surface. For example, in arid and semi-arid parts of the world, dry atmosphere and the lack of rain-supplied moisture requires exclusive use of irrigation to grow crops. In more humid locations, on the other hand, irrigation, if necessary at all, is often in the form of supplemental irrigation, meeting the excess demand of crops whose growth cycle is out of sync with natural precipitation. Thus, climatic moisture availability (or dryness) provides the first level of information on potential presence of irrigation at a given location.

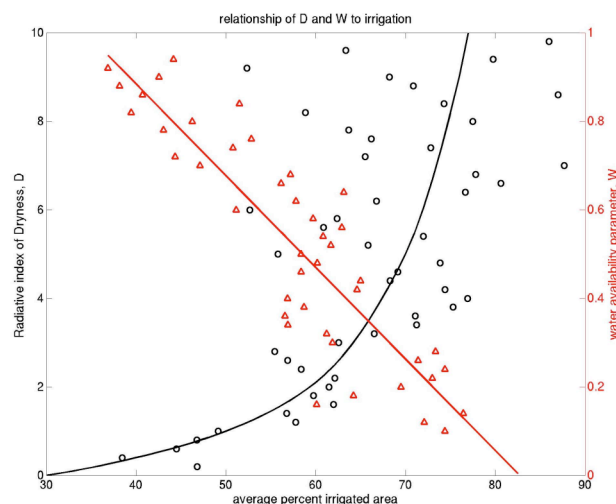
One index that provides suitable information on surface moisture status and the geobotanic state is the *Radiative Dryness Index* proposed by Budyko (1974):

$$D = \frac{R}{\lambda P} \quad (1)$$

where  $R$  is mean annual net radiation, which we estimated from Earth-Sun geometry, observed mean air temperature, and observed humidity;  $P$  is mean observed annual precipitation; and  $\lambda$  is latent heat of vaporization. The dryness ratio has been widely used to classify climate regimes and corresponding land cover in simple climate models (e.g. Gutman et al., 1984). While  $D$  provides important information on climatic moisture availability, it is not directly related to irrigation. To relate the  $D$  to irrigation, we plotted  $D$  against percent irrigation presence information from the GMIA product (Siebert et al, 2005). This relationship is shown in Figure 4 as black open circles (original aggregated data) and a black curve (fitted). While the relationship between  $D$  and fractional irrigated area show some expected patterns, the curvilinear nature of the relationship is hard to interpret. To relate dryness characterized by  $D$  to the *Water Availability Parameter*, Gutman et al (1984) used the empirical relationship suggested by Lettau (1969):

$$W = \frac{\tanh D}{D}, \quad D \geq 0 \quad (2)$$

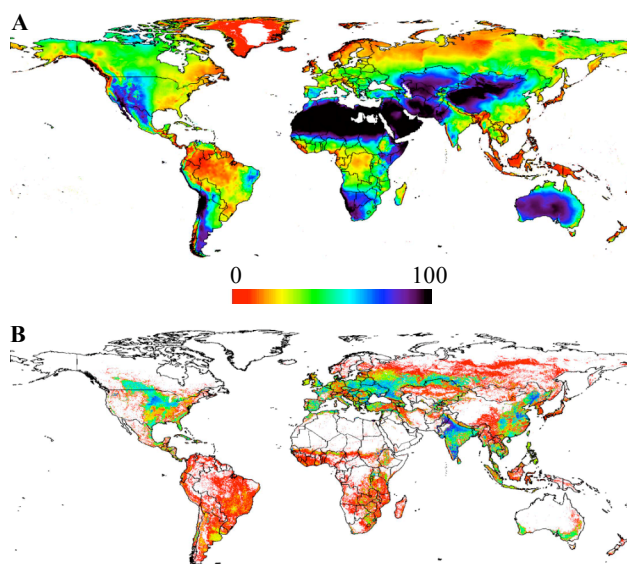
The relationship between  $W$  and fractional irrigated area is given in Figure 4 by a linear fit of the original aggregated data.



**Figure 4.** The relationship between  $D$ ,  $W$ , and global fractional irrigated area obtained from the GMIA product.  $D$  is plotted as circles and the fitted curve, while  $W$  is plotted as triangles and the straight fitted line. Note that  $W$  linearizes the relationship between  $D$  and irrigated area and thus it is used to map irrigation potential.

Using this linear relationship between  $W$  and fractional irrigated area, we mapped climate-based irrigation potential. The darkest areas in Figure 5a show highest potential for irrigation based solely on climate. Since we are ultimately interested in irrigated croplands, we further refined this map by masking out areas that are known to be not cultivated (Ramankutty and Foley, 1996) (Figure 5b). We call this final masked product the effective irrigation potential map and it shows some expected patterns. For example, while the entire Australian continent has a very high irrigation potential due to generally dry climate of the region, only cultivated lands along the southeast and southwest corners of the country have high effective irrigation potential.





**Figure 5.** Effective Irrigation Potential (B) created by crop masking the original irrigation potential map (A) developed by relating  $W$  to irrigation presence.

In our irrigation mapping procedure, we used effective irrigation potential as ancillary information in the classification process, which has generally resulted in improved classification accuracies of remotely sensed images (Strahler, 1980; McIver and Friedl, 2002).

### 2.3 Remote Sensing of Irrigation

The effective irrigation potential map shows areas that are potentially irrigated. These areas may not always coincide with areas that are actually irrigated, which is due to infrastructure and water availability. To map actual irrigation, we used remotely sensed indices based on data from the MODIS sensor.

#### MODIS Data

The MODIS sensor includes seven spectral bands that are designed exclusively for monitoring Earth's land surfaces. The MODIS instrument is located on-board both Terra and Aqua platforms, and when combined, provides at least twice-daily global coverage at 250- and 500-m spatial resolutions. Compared to the heritage AVHRR instrument, the MODIS data offers enhanced spectral, spatial, radiometric, and geometric quality for improved mapping and monitoring of vegetation activity. Hence, to date, MODIS land data has been an integral part of production of a large variety of land cover maps, including irrigation (Friedl et al., 2002; Thenkabail, et al., 2005; Xiao et al., 2006).

A large array of standard MODIS data products are operationally produced by the MODIS Land Science Team and made available to the scientific community on a timely basis. One of these products is the Nadir BRDF-adjusted Reflectance (NBAR) data (MOD34B4) (Schaaf et al., 2002). This product provides cloud-screened and atmospherically corrected surface reflectances for all MODIS land bands that have been corrected for view- and illumination-angle effects. This angular correction substantially reduces the source of noise related to surface and atmospheric anisotropy. Currently, the NBAR data is produced at aggregated 1 km spatial resolution, every 16 days with a total of 23 observations over the calendar year,

geographically organized in a MODIS tile system with the Sinusoidal Projection. In this study we used 2 calendar years (2002/2003) of NBAR data (total of 46 observations).

### 2.3.2 Irrigation-related Indices

Remote sensing of irrigated lands over large geographic regions involves significant challenges in terms of both selecting spectral bands or indices that contain maximum amount of irrigation related information and relating this information to complex forms of irrigation presence.

To determine actual irrigation presence we identified spatio-temporal patterns of vegetation greenness from remotely sensed data. In particular, we have identified three types of irrigation-related signatures. These signatures are: 1) *Annual*, we exploit the variability in timing of greenness between irrigated and non-irrigated croplands and precipitation; 2) *Spectral*, we use the Green Ratio Index (GRI) (Gitelson et al 2006) to amplify the signal; and 3) *Inter-annual*, we exploit inter-annual changes in vegetation greenness based on the hypothesis that irrigated lands would have less inter-annual variability as development of those crops does not depend on precipitation.

#### Annual Indices

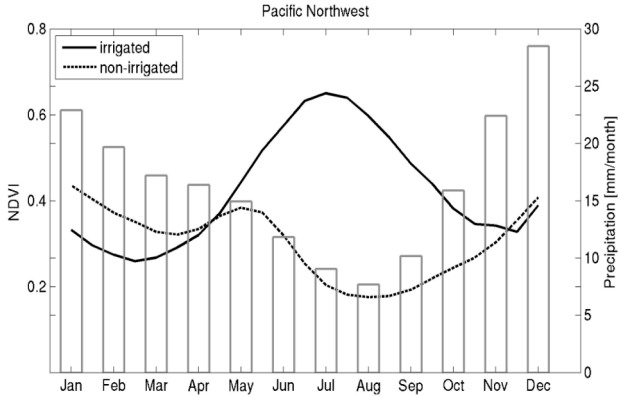
There is an overwhelming consensus that the Normalized Difference Vegetation Index (NDVI) is an important vegetation monitoring tool (Tucker, 1979; Goward et al., 1991; DeFries et al., 1998). NDVI is defined as:

$$NDVI = \frac{\rho_{nir} - \rho_{red}}{\rho_{nir} + \rho_{red}} \quad (3)$$

where  $\rho_{nir}$  and  $\rho_{red}$  respectively represent NIR and red reflectances. NDVI has been closely related to plant moisture availability (Nicholson et al. 1990), leaf area index (Xiao et al. 2002), primary production (Prince, 1991); and vegetation fraction (Gutman and Ignatov, 1998).

While NDVI has been widely used to monitor vegetation greenness in agricultural settings under a variety of climatic conditions, overwhelmingly, it is the temporal NDVI signal that has often been most related to irrigation (Tucker and Gatlin, 1984; Martinez-Beltran and Calera-Belmonte, 2001; Ozdogan et al. 2006). In particular, greenness associated with non-irrigated crops in arid/semi-arid landscapes is often a direct result of rainfall events while greenness associated with irrigated sites is generally independent of rainfall and would show a development cycle completely different than that of rain-fed crops. This differential temporal behaviour of irrigated and non-irrigated cultivations is illustrated in Figure 6 for a relatively arid location in northwestern US where year 2002 vegetation greenness for irrigated (solid) and non-irrigated (dashed) croplands are plotted in the form of mean smoothed NDVI profile (left Y-axis). Also plotted in the same figure is the monthly mean precipitation for the same year (right Y-axis). The non-irrigated crops exhibit two peaks, first following planting in the fall and second before harvest in late spring/early summer, closely following the moisture availability through precipitation. In contrast, irrigated crops peak in greenness during mid-summer when moisture availability is the smallest and greenness value of non-irrigated crops drops to its lowest value. Note that the lack of precipitation in the summer time at this location causes a large moisture deficit and makes irrigation absolutely necessary. In this particular location, the irrigated

and non-irrigated crops exhibit clearly distinct temporal greenness profiles especially when related to precipitation availability and we exploit this annual index in our irrigation mapping procedure.



**Figure 6.** An example annual index in the form of 2002 NDVI profiles for irrigated (solid line) and non-irrigated (dashed line) crops in northwestern US. Also plotted is the monthly precipitation availability. Note that irrigated crops peak in greenness when moisture availability from precipitation is the lowest suggesting irrigation presence.

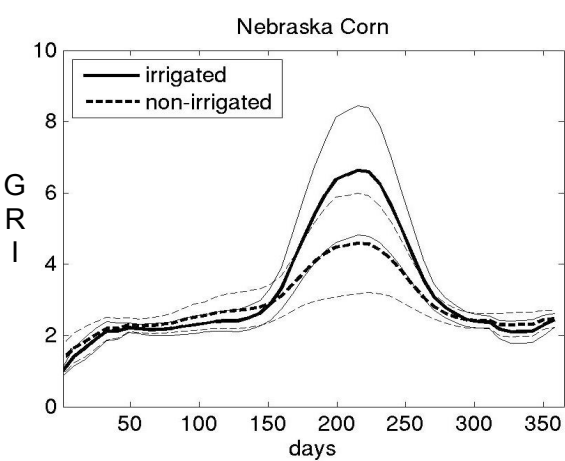
Spectral Indices

A more difficult case for distinguishing irrigated crops from non-irrigated ones occurs in locations where the same crop type is grown with and without irrigation in the same growing season. Our preliminary work with NDVI in Nebraska, USA suggests that while irrigated fields exhibit slightly larger NDVI than non-irrigated counterparts, possibly due to constant availability of moisture, the difference in NDVI is small and potentially useless in distinguishing irrigated fields. Thus, a more sensitive index is required to make this distinction.

Large body of research into spectral remote sensing of vegetation canopies indicates that moisture stress in vegetation is strongly manifested in spectral indices related to Chlorophyll content (Gitelson et al, 2003). One such index, suggested by Gitelson et al (2006) to be used with the MODIS sensor, is the Green Ratio Index (GRI) defined as:

$$GI = (\rho_{nir} / \rho_{Green}) - 1 \tag{4}$$

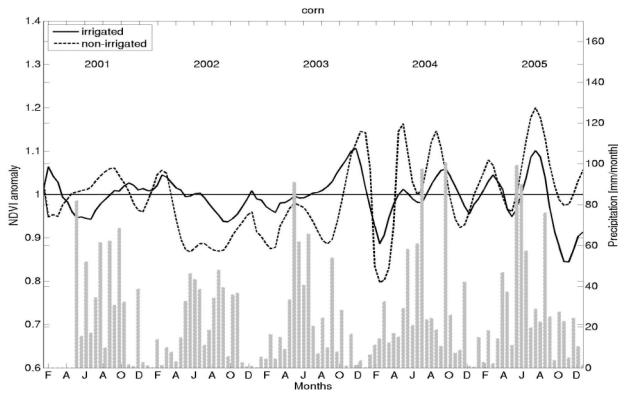
where  $\rho_{green}$  is the reflectance in green spectral region. The theoretical foundation of the *GRI* is based on the observation that in the green spectrum (centered around 510 nm) specific absorption coefficient of chlorophylls is very low while green leaves absorb more than 80 percent of incident light in this spectral range (e.g., Gitelson and Merzlyak 1994). In contrast, depth of light penetration into leaves in the blue and red spectral ranges is four- to six-fold lower (e.g., Merzlyak and Gitelson, 1994). Therefore, in the green, absorption of light is high enough to provide high sensitivity of *GRI* to Chl content but much lower than in the blue and red to avoid saturation (Gitelson et al., 2003). To demonstrate the sensitivity of *GRI* to irrigation presence, we plotted temporal *GRI* profiles of irrigated (solid line) and non-irrigated (dashed line) maize in Figure 7. While the two temporal profiles are identical in timing of greenness, the absolute values are significantly different, suggesting that soil moisture stress in maize associated with lack of moisture exhibits smaller *GRI* and thus lower Chlorophyll content than irrigated maize.



**Figure 7.** Mean temporal profiles of *GRI* associated with irrigated (solid line) and non-irrigated (dashed line) maize in Nebraska, USA. Note the difference in absolute value of *GRI*. Also plotted is one standard deviation around the mean for each.

Inter-annual Indices

Water available for agricultural crops through precipitation varies significantly across years. In addition to management practices such as fertilizer and tilling, this natural variability of moisture contributes significantly to each year's crop quality and yield that can be monitored from space through vegetation indices. In contrast, the status and quality of croplands that receive significant amounts of irrigation on a regular basis would be expected to be independent of natural precipitation availability as natural water limitation is alleviated by artificial application of water through irrigation. Thus, inter-annual variation in vegetation greenness for irrigated fields would be expected to be less than inter-annual greenness variation of non-irrigated croplands assuming the same crop type is examined across years.



**Figure 8.** Inter-annual profiles of NDVI anomaly (defined as deviation from 5-year mean) for irrigated and non-irrigated maize in Midwestern US. Also plotted is bi-monthly precipitation.

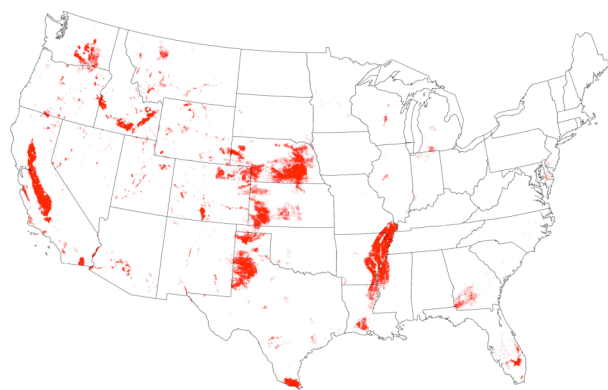
To test this hypothesis, we analyzed five years of MODIS NDVI data for maize and soybeans in Midwestern US (Figure 8). Analysis of *inter-annual* data suggests that irrigated maize indeed exhibits lower inter-annual variability (shown in Figure 8 as the solid line) than vegetation greenness associated with non-irrigated maize fields (displayed as the dashed curve) which varies significantly across years, following precipitation.

## 2.4 Classification Algorithm

As our approach to irrigation mapping is a supervised classification methodology, it requires training data that characterizes the desired output classes (irrigation in this case). We derived these training (learning) samples from several dozen high spatial resolution satellite imagery acquired by the Landsat 7 ETM+ sensor *circa* 2000. The location of the training sites were chosen to represent major irrigated land areas of the US and interpreted with the help of ancillary data sources such as county based irrigated area maps as well as based on characteristic shapes of irrigated fields. These training locations were used to extract cloud- and snow-screened high quality examples of the three irrigation related indices representing the annual, spectral, and inter-annual behaviour of irrigated and non-irrigated crops. We then used these sample data as training examples in the learning phase of the decision tree classification algorithm as shown in Figure 3.

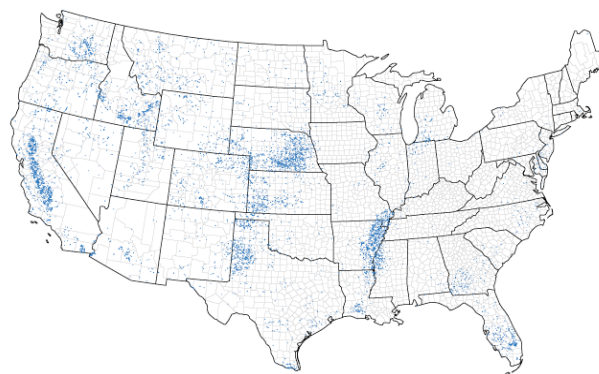
## 3. IMPLEMENTATION IN THE CONTINENTAL US

The first step in our implementation of the irrigation mapping procedure for the Continental US was to screen the MODIS time series data for clouds and snow cover. We used the quality control cloud flags that are included in the NBAR data files in the form of cloud masks for each 16-day time period for a total of 23 files per year. To minimize the potential impact of snow cover, especially in the winter months, we generated snow masks using the Normalized Difference Snow Index (Hall et al., 1995). Pixels corresponding to clouds and snow were then excluded from the analysis. The second step was to train the decision tree model with the example datasets of irrigation indices and effective irrigation potential derived from the training sites described above to automatically generate the rules and thresholds to identify irrigation. We then applied the trained decision tree to all of the individual MODIS tiles that cover the Continental US. Each tile consisted of cloud and snow screened time series of vegetation index values representing a total of 138 per-pixel observations (2 years between 2002 and 2003, 23 observations per year, and 3 vegetation indices). The end result of the classification algorithm was a two-class map showing irrigated and non-irrigated areas over the Continental US (Figure 9).



**Figure 9.** Irrigation in the Continental US *circa* 2002 obtained by implementing the procedure proposed here. The distribution of irrigated lands follows expected patterns. In the arid western portion of the US, irrigation occurs in narrow dry valleys such as the central valley of California. In more humid eastern portion of the US, irrigation occurs along major agricultural provinces.

To qualitatively assess the final irrigation map as a result of our mapping procedure, we compared it to the year 2002 USDA *dot-map* (Figure 10). The USDA *dot-map* was generated by randomly placing a dot for each 5,000 ha of irrigated area in each US county, regardless of the location of irrigation. At the continental scale, this *dot-map* is the only source of information on irrigation presence. Nevertheless, comparison of this *dot-map* to the map generated by implementing our mapping procedure reveals good agreement, suggesting that our proposed methodology is able to capture major irrigation patterns in the continental US. Moreover, it provides additional information on irrigation location, beyond the limits of the standard *dot-map* products.



**Figure 10.** County-based irrigation *dot-map* for the US for the year 2000 obtained from the USDA. The USDA *dot-map* was generated by randomly placing a dot for each 5,000 ha of irrigated area in each US county, regardless of the location of irrigation.

While our preliminary test product is at relatively high spatial resolution (500-1000 m) it may fail to capture sub-pixel presence and variability of irrigation, especially if irrigated fields are much smaller than the spatial resolution of the observing sensor. This issue may be especially important when the proposed methodology is applied to locations (for example in China) where irrigated agricultural fields are known to be small (Ozdogan and Woodcock, 2006). To improve subpixel representation of irrigation, we tested several different subpixel mapping methods and discovered that skin temperature is inversely related to irrigation presence. The future improvements of the proposed procedure will incorporate remotely-sensed skin temperature data to recover subpixel irrigation information once irrigated/non-irrigated pixels have been identified.

## References

- Budyko, M.I., 1974. *Climate and Life*. Academic Press, 508 pp.
- DeFries, R.S., Hansen, M., Townshend, J.R.G., and Sohlberg, R., 1998. Global land cover classifications at 8 km spatial resolution: The use of training data derived from Landsat imagery in decision tree classifiers, *Int. J. Remote Sensing*, 19, pp. 3141-3168.
- Döll, P. and Siebert, S., 1999. A digital global map of irrigated areas. Report A9901. Germany: *Center for Environmental systems Research, University of Kassel*.
- Friedl, M.A., McIver, D.K., Hodges, J.C.F., Zhang, X.Y., Muchoney, D., Strahler, A.H., Woodcock, C.E., Gopal, S., Schneider, A., Cooper, A., Baccini, A., Gao, A., and Schaaf, C.,

2002. Global land cover mapping from MODIS: algorithms and early results, *Remote Sensing of Environment*, 83, pp.287:302.
- Gitelson, A.A. and Merzlyak, M.N., 1994. Quantitative estimation of chlorophyll *a* using reflectance spectra: Experiments with autumn chestnut and maple leaves, *J. Photochem. Photobiol. (B)* 22, pp. 247–252.
- Gitelson, A.A., Gritz, U. and Merzlyak M.N. 2003. Relationships between leaf chlorophyll content and spectral reflectance and algorithms for non-destructive chlorophyll assessment in higher plant leaves. *J. Plant. Physiol.*, 160, pp. 271-282.
- Gitelson, A.A., Vina, A., Verma, S.B., Rundquist, D.C., Arkebauer, T.J., Keydan, G., Leavitt, B., Ciganda, V., Burba, G.G., and Suyker, A.E., 2006. Relationship between gross primary production and chlorophyll content in crops: Implications for the synoptic monitoring of vegetation productivity, *Journal of Geophysical Research*, 111, D08S11, doi:10.1029/2005JD006017.
- Goward, S.N., Markham, B., Dye, D., Dulaney, W., and Yang, J., 1991. Normalized difference vegetation index measurements from the advances very high resolution radiometer, *Remote Sensing of Environment*, 35, pp. 257-277.
- Gutman, G., Ohring, G., and Joseph, J.H., 1984. Interaction between the geobotanic state and climate: A suggested approach and test with a zonal model, *Journal of the Atmospheric Sciences*, 41, pp. 2663-2678.
- Gutman, G. and Ignatov, A., 1998. Derivation of green vegetation fraction from NOAA/AVHRR for use in weather prediction models, *Int. J. Rem. Sens.*, 19, pp. 1533-1543.
- Hall, D. K., Riggs, G. A., and Salomonson, V. V., 1995. Development of methods for mapping global snow cover using moderate resolution imaging spectroradiometer data, *Remote Sensing of Environment*, 54, pp. 127– 140.
- Lettau, H., 1969. Evapotranspiration climatology: A new approach to numerical prediction of monthly evapotranspiration, runoff and soil moisture storage, *Monthly Weather Review*, 97, pp. 691-699.
- Loveland, T.R., Reed, B.C., Brown, J.F., Ohlen, D.O., Zhu, J, Yang, L., and Merchant, J.W., 2000. Development of a Global Land Cover Characteristics Database and IGBP DISCover from 1-km AVHRR Data, *International Journal of Remote Sensing*, 21, pp.1,303-1,330.
- Martinez-Beltran, C. and Calera-Belmonte, A., 2001. Irrigated crop estimation using Landsat TM imagery in La Mancha, Spain, *Photogramm. Eng. Rem. Sen.* 67, pp. 1,177–1,184.
- Nicholson, S.E., Davenport, M.L., and Malo, A.R., 1990, A Comparison of vegetation response to rainfall in the Sahel and East Africa using normalized difference vegetation index from NOAA-AVHRR, *Climatic Change*, 17, pp. 209-241.
- Ozdogan, M., Woodcock, C.E., Salvucci, G.D., and Demir, H., 2006. Changes in summer irrigated crop area and water use in Southeastern Turkey from 1993-2002: Implications for current and future water uses, *Water Resources Management*, 20(3), pp. 467-488.
- Ozdogan, M. and Woodcock, C.E., 2006. Resolution dependent errors in remote sensing of cultivated areas, *Remote Sensing of Environment*, 103: 203-217.
- Prince, S.D., 1991. Satellite remote sensing of primary production: comparison of results for Sahelian grasslands, *International Journal of Remote Sensing*, 12, pp. 1133-1421.
- Ramankutty, N. and Foley, J.A., 1998. Characterizing patterns of global land use: an analysis of global croplands data. *Global Biogeochemical Cycles*, 12(4), pp. 667-685.
- Schaaf 2002 Schaaf, C. B., F. Gao, A. H. Strahler, W. Lucht, X. Li, T. Tsang, N. C. Strugnell, X. Zhang, Y. Jin, J.-P. Muller, P. Lewis, M. Barnsley, P. Hobson, M. Disney, G. Roberts, M. Dunderdale, C. Doll, R. d'Entremont, B. Hu, S. Liang, and J. L., 2002. Privette, First Operational BRDF, Albedo and Nadir Reflectance Products from MODIS, *Remote Sens. Environ.*, 83, pp. 135-148.
- Thenkabail, P.S., Schull, M., and Turrall, H., 2005. Ganges and Indus river basin land use/land cover (LULC) and irrigated area mapping using continuous streams of MODIS data, *Remote Sensing of Environment*, 95, pp. 317-341.
- Tucker, C., 1979. Red and photographic infrared linear combinations for monitoring vegetation, *Remote Sensing of Environment*, 8, pp. 127-150.
- Tucker, C. J. and Gatlin, T.A., 1984. Monitoring vegetation in the Nile Delta with NOAA 6 and NOAA 7 AVHRR imagery. *Photogrammetric Engineering and Remote Sensing*, 50(1), pp. 53-61.
- Vorismarty, C.J., 2002. Global water assessment and potential contributions from Earth System Science, *Aquat. Sci.*, 64, pp. 328-351.
- Xiao, X., Boles, S., Frolking, S., Salas, W., Moore, B., Li, C., et al., 2002. Observation of flooding and rice transplanting of paddy rice fields at the site to landscape scales in China using VEGETATION sensor data, *International Journal of Remote Sensing*, 23, pp. 3,009– 3,022.
- Xiao, X., Boles, S., Frolking, S., Li, C., Babu, J.Y., Salas, W., and Moore, B., 2006. Mapping paddy rice agriculture in South and Southeast Asia using multi-temporal MODIS images, *Remote Sensing of Environment*, 100, pp. 95-113.



# CLASSIFICATION OF TREE AND SHRUB SPECIES IN KSU RESEARCH AND APPLICATION FOREST IN KAHRAMANMARAS, TURKEY

A. E. Akay <sup>a,\*</sup>, I. R. Karas <sup>b</sup>, R. Gundogan <sup>c</sup>

<sup>a</sup> Department of Forest Engineering, Faculty of Forestry, KSU, 46100 Kahramanmaras, Turkey - [akay@ksu.edu.tr](mailto:akay@ksu.edu.tr)

<sup>b</sup> Department of Geodetic and Photogrammetric Engineering, GYTE, 41400 Gebze, Kocaeli, Turkey - [ragib@gyte.edu.tr](mailto:ragib@gyte.edu.tr)

<sup>c</sup> Department of Soil Science, Faculty of Agriculture, KSU, 46100 Kahramanmaras, Turkey - [rgundogan@ksu.edu.tr](mailto:rgundogan@ksu.edu.tr)

Commission VIII, WG VII/1

**KEY WORDS:** Remote Sensing, Classification, Image processing, Vegetation Identification, Forestry

## ABSTRACT

During the last few decades, remote sensing and Geographic Information Systems (GIS) technologies have become increasingly important tools for mapping, inventorying, and monitoring forest resources around the world. Using remotely sensed aerial images or digitized aerial photographs and GIS techniques to organize and analyze significant amount of spatial data, it is now becoming possible to analyze the number of variables (tree species, size and density, volume and height, growth, and etc.) for ecological and economic management of forests. Large-scale satellite images with good details are widely used in digital image processing and classification. The main purpose of this paper was using automated image processing and classification methods based on a satellite imagery to identify vegetation types in KSU Research and Application Forest in Kahramanmaras, Turkey.

## KURZFASSUNG

Während der letzten Jahre hat die Bedeutung der Technologien im Bereich der Fernerkundung und des geographischen Informationssystems (GIS) für die Kartierung, Inventarisierung, und Beobachtung von Wäldern weltweit stark zugenommen. Die Nutzung von Luftbildaufnahmen oder digital bearbeiteten Luftbildaufnahmen und GIS Technik zur Erfassung und Analyse von Daten, die sich auf große Gebiete beziehen, ermöglicht es, verschiedene Variablen (z. B. Baumarten, Größe und Dichte, Volumen und Höhe, Wachstum) zur ökologischen und wirtschaftlichen Bewirtschaftung zu analysieren. Satellitenbilder in großem Maßstab mit guter Detailwiedergabe sind weit verbreitet bei der digitalen Bildverarbeitung und Klassifikation. Das Ziel dieser Arbeit bestand darin, unter Nutzung von automatisierter Bildbearbeitung und Methoden der Klassifizierung Satellitenbilder zur Identifizierung von Vegetationstypen im Versuchsforst der Universität Kahramanmaraş, Türkei, auszuwerten.

## 1. INTRODUCTION

Classification of the objects in natural resources has been recognized as one of the important tasks by natural scientists from wide range of disciplines. In remote sensing, the classification can be defined as a process of separating features into classes or areas in remotely sensed imagery (Raffy, 1994). Even though land classification dates back to early 1990's, it has received a great interest as compute-based remote sensing and Geographic Information Systems (GIS) technologies have advanced in last few decades. Due to capabilities of these technologies to provide, organize, and analyze vast amount of spatial data, land classifications have been used for mapping, inventorying, and monitoring purposes in the field of the natural resources (Carson et al. 2001).

In the field of forestry, digital interpretation procedures have been widely used for inventorying, and monitoring forested areas based on aerial photographs and satellite digital imagery (Gougeon, 1995). There have been studies on extracting single species stands from the interpretation of remotely sensed imagery with low spatial resolution (Beaubien 1983, Jano 1984, Gillis and Leckie 1993). Large-scale satellite images with high resolution and good details have been used in pixel-based classification of individual tree crowns (Leckie 1990, Beaubien

1994, Meyer et al.1996). However, the large amount of pixels may lead to potential classification problems. For example; one conifer tree crown can contain high number of pixels (e.g. over 5000 pixels), some pixels in a tree crown can be confused with shrub species, variation in background vegetation and soil material cause high frequency of data variability, and shadow within or around the tree crown effects the classification process.

In this study, automated image classification method was applied to identify vegetation types in KSU Research and Application Forest in Kahramanmaras-Turkey, based on satellite imagery. Different image processing techniques were evaluated and various problems and limitations with these techniques were discussed.

## 2. MATERIAL AND METHODS

### 2.1. Study Area

Baskonus Research and Application Forest of Kahramanmaras Sutcu Imam University was selected as a study area due to availability and accessibility of necessary spatial data such as aerial photos, satellite image, and thematic maps. The research

---

\* Corresponding author.



forest is approximately 458 ha and located about 45 km west of Kahramanmaraş, Turkey. The research forest is dominated by conifers; *Pinus brutia*, *Pinus nigra*, *Cedrus libani*, and *Abies cilicica*. The average side-slope and ground elevation were 73% and 1165 m, respectively. Figure 1 indicates the forest boundary, topography, streams, and road network.

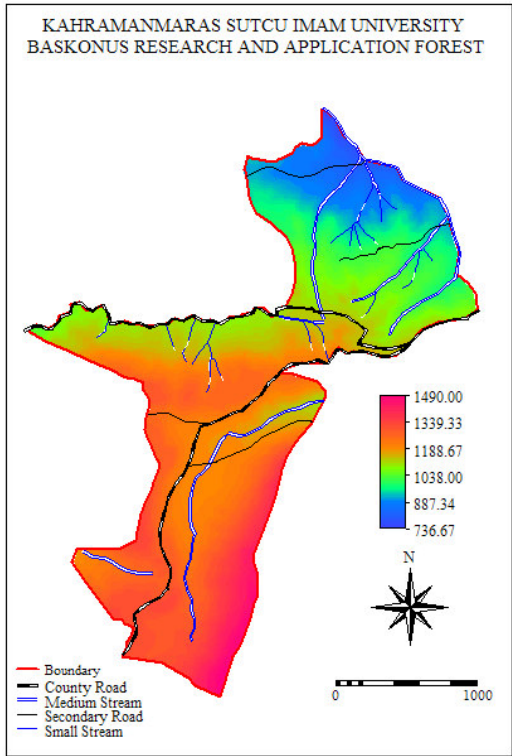


Figure 1. KSU Baskonus Research and Application Forest

2.2. Pre-Processing

In image processing, the September 2004 ASTER NIR satellite image (15 m) of Kahramanmaraş region was used (Figure 2).

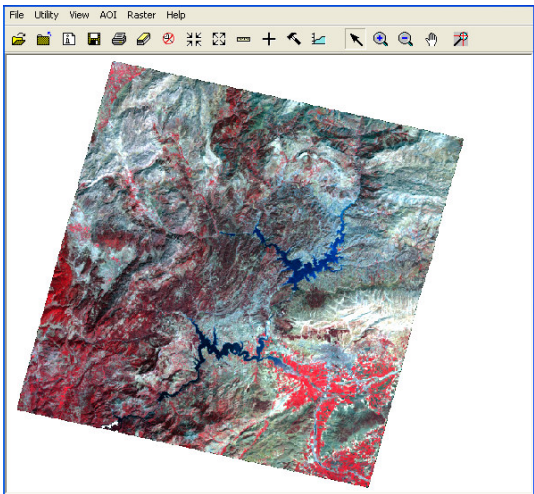


Figure 2. September 2004 ASTER NIR satellite image

The IR Aerial Photos (1:15000) taken in June 2000 and 1:25000 stand types map were used to perform accuracy assessment. The ERDAS Imagine 8.5 (Atlanta, GA, USA) was used to execute the pre-processing and classification tasks. In the first stage of pre-processing, research forest was clipped out from the satellite image by using “Mask” function in ERDAS 8.5, referencing forest boundary layer.

In subset image of the research forest, there was a high frequency of data variability due to stand density, shadow effect, background vegetation and ground materials. To reduce spatial frequency, low-pass filtering technique has been widely used (Lillesand and Kiefer, 2000). In this study, the performances of three different low-pass filtering standards (3x3, 5x5, and 7x7) were compared using “Convolution” function in ERDAS 8.5. The filtering process indicated that applying 7X7 low-pass filter maximized the filtering result and removed the data variation prior to classifications process (Figure 3).

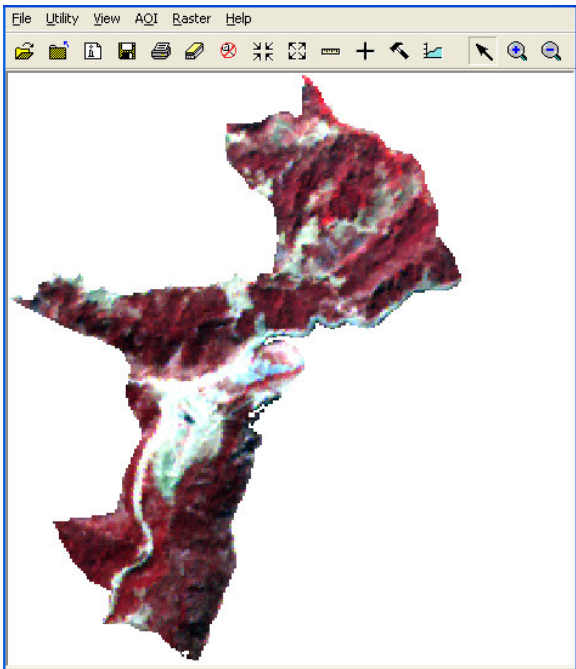


Figure 3. 7x7 low-pass filtered image of the research forest

2.3. Classifications

In classification process, firstly, Unsupervised Classification method was applied by using ten classes to identify the forest vegetation in the research forest. In ERDAS 8.5, the “Isodata” algorithm was used to perform classification repeatedly and form clusters using the minimum spectral distance formula. The result of unsupervised classification was indicated in Figure 4 (with 10 classes).

Supervised Classification method was then performed based on a set of user-defined classes, by creating the appropriate spectral signatures from the data. “User-Defined Polygon” function was employed to lower the chance of underestimating class variance since it involved a high degree of user control. To generate a signature file that accurately represents the classes to be identified, over 200 samples were repeatedly selected from the

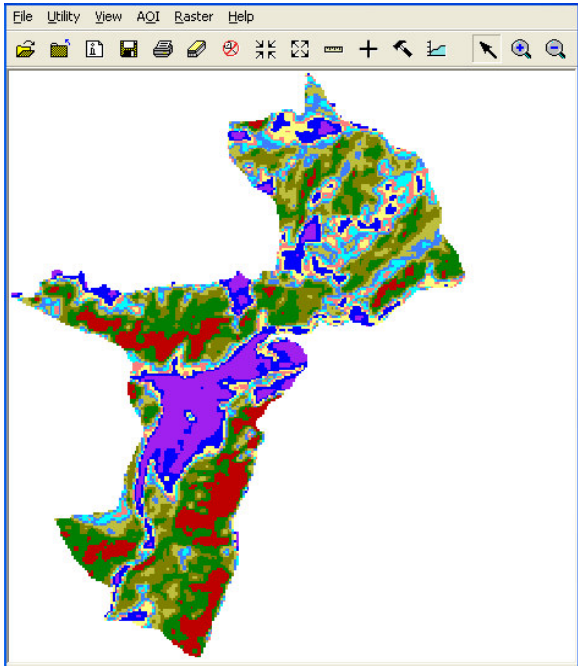


Figure 4. The image of research forest after unsupervised classification

image by drawing a polygon around training sites of interests. Once a set of reliable signatures were created, supervised classification was performed using the Maximum Likelihood (statistically-based classifier) technique provided by ERDAS 8.5 (Figure 5).

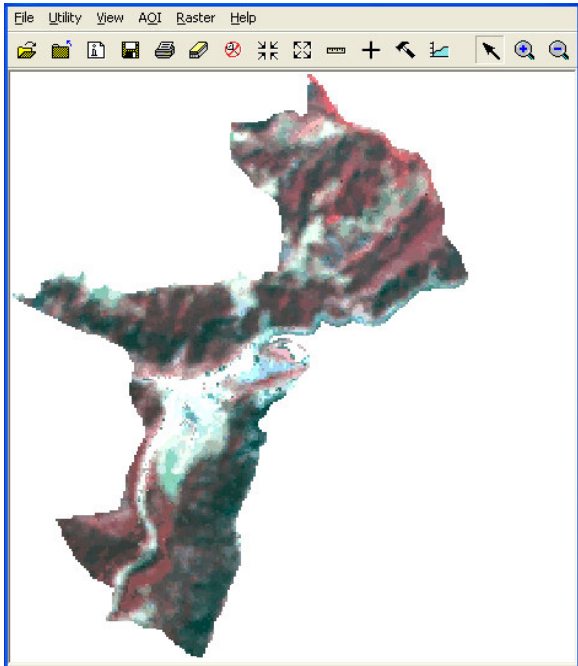


Figure 5. The image of research forest after supervised classification

After both classification methods, “Recode” function in ERDAS 8.5 was applied to combine the classes into six main classes including conifer trees, deciduous trees, shrubs, grass, agricultural vegetations, and others. In the recoding process, open grounds and roads were assigned into the same class with the name of “others”.

3. RESULTS AND DISCUSSION

In image filtering stage, spatial frequency was successfully reduced by applying 7x7 low-pass filtering. The results from classification stage indicated that unsupervised classification was not satisfactory to classify vegetation types in the research forest. Figure 6 indicated the recoded image after the unsupervised classification process.

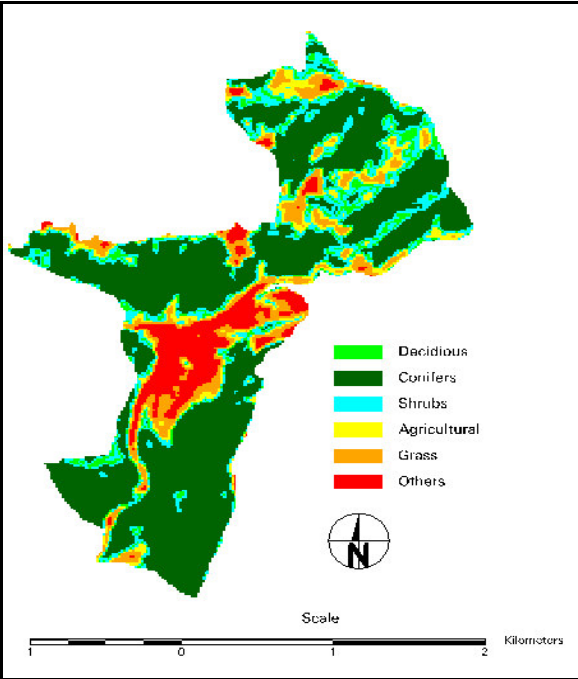


Figure 6. Recoded image after the unsupervised classification

Unsupervised classification process could not distinguishing grass from agricultural vegetation and underestimated the grass because dry grass was confused with stubble left on the agricultural fields. Conifers were generally well identified by unsupervised classification; however, deciduous trees were mixed with shrubs. In some parts of the images, open grounds and roads were also mixed with grass and agricultural vegetations.

Supervised classification, however, provided better results in terms of distinguishing forest vegetation. The recoded image after supervised classification process was indicated in Figure 7. By systematically selecting 250 sample points from the recoded image, the accuracy assessment of the supervised classification was performed by using aerial photos and stand type map as reference sources. The results indicated that, the overall classification accuracy and Kappa values were 69% and 0.55, respectively.

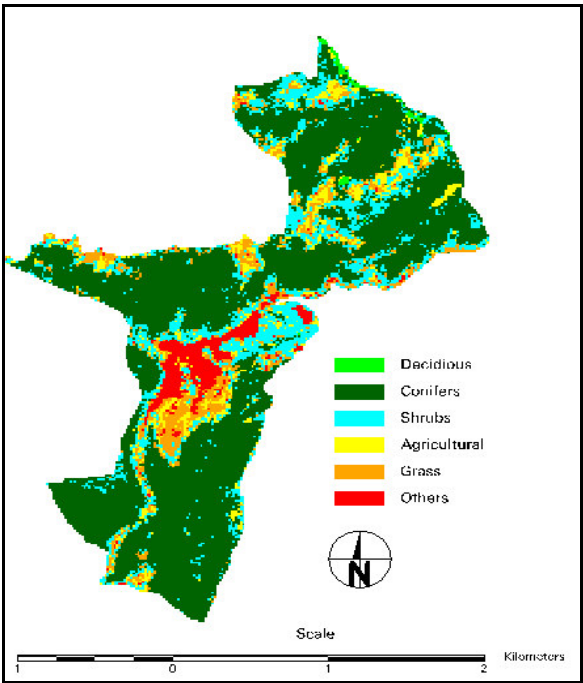


Figure 7. Recoded image after the supervised classification

Supervised classification method worked well for identifying conifers, but accuracy for deciduous trees and shrubs were relatively low due to large variation of spectral signatures. It was difficult to identify young stands due to shadow effect. The total areas for six main classes determined by both supervised and unsupervised classification methods were shown in Table 1. The results indicated that unsupervised classification overestimated three classes including deciduous, others, and grass, while underestimated conifers, shrubs, and grass.

Class Number	Class Names	Areas (%)	
		Unsupervised	Supervised
1	Decidious	6.2	0.5
2	Conifers	55.4	62.5
3	Shrubs	13.7	17.3
4	Agricultural	6.7	7.0
5	Grass	9.3	8.1
6	Others	8.7	4.7

Table 1. Total areas of six main classes after both classifications

4. CONCLUSIONS

In this study, pre-processing and classification techniques were applied and their performances were assessed in classifying vegetation types in KSU Research and Application Forest in Kahramanmaras, Turkey. For a better accurate assessment of the results, high-resolution orthophotos might be more useful to

get accurate corresponding locations to the satellite image. Conducting field verification would also be helpful to eliminate ambiguities from interpretation of reference sources. In this study, it was not intended to delineate individual trees since it was not possible using ASTER NIR image with coarse resolution of 15 m x 15 m. In future studies, satellite imagery with better spatial resolution (e.g. 1 m or less) would be used to test the results from this study and to attempt identify individual tree crowns.

REFERENCES

Beaubien, J., 1983. Une methode de rehaussement d'images Landsat pour la classification du couvert vegetal. *Proceedings, 8th Canadian Symposium on Remote Sensing*, Montreal, Quebec, pp. 559-566.

Beaubien, J., 1994. Landsat TM satellite images of forests: from enhancements to classification. *Canadian Journal of Remote Sensing*, 20(1): 17-26.

Carson, W.W., A.E. Akay, and D. Weyerman, 2001. An inventory of juniper through the automated interpretation of aerial digital imagery. *First International Precision Forestry Symposium*, University of Washington, College of Forest Resources, Seattle, Washington, USA

Gillis, M.D. and D.G. Leckie., 1993. *Forest inventory mapping procedures across Canada*, Inf. Rep. PI-X-114. Chalk River, Ontario: Petawawa National Forestry Institute. 79 p.

Gougeon, F., 1995. A crown-following approach to the automatic delineation of individual tree crowns in high spatial resolution aerial images. *Canadian Journal of Remote Sensing*, 21(3): 274-284.

Jano, A.P., 1984. Comparison of Landsat, MEIS II and Airborne MSS Data for Forest Classification in the Boreal Region of Ontario. *Proceedings, 9<sup>th</sup> Canadian Symposium on Remote Sensing*, Halifax, Nova Scotia, August 14-17, pp. 627-632.

Leckie, D.G., 1990. Advanced in remote sensing technologies for forest surveys and management. *Canadian Journal of Forestry Research*, 20: 464-483.

Lillesand, T.M. and R.W. Kiefer., 2000. *Remote sensing and image interpretation*. Fourth edition. John Wiley and Sons, Inc. New York. 724 p.

Meyer, P., K. Staenz, K.I. Itten., 1996. Semi-automated procedures for tree species identification spatial resolution data from digitized colour infrared-aerial photography. *ISPRS Journal of Photogrammetry and Remote Sensing*, 51: 5-16.

Raffy, M., 1994. The role of spatial resolution in quantification problems: spatialization method. *Int. J. Remote Sensing*, 15(12): 2381-2392.

# ALTERNATIVE APPLICATION OF THE K-NN METHOD FOR MAPPING FOREST COVER TYPE

C. Gagliano <sup>a\*</sup>, F. De Natale <sup>a</sup>, F. Incerti <sup>a</sup>, F. Maselli <sup>b</sup>

<sup>a</sup> CRA – Forest and Range Management Research Institute, ISAFa, 38050, Piazza Nicolini 6, Villazzano (Trento), Italy. Phone: +39 0461 381122; Fax: +39 0461 381131; caterina.gagliano@entecra.it

<sup>b</sup> CNR – Institute of Biometeorology, Via G. Caproni 8 – 50145 Firenze, Italy; maselli@ibimet.cnr.it

**KEY WORDS:** k Nearest Neighbour method, forest types, Landsat TM image classification

## ABSTRACT:

The present study explores the performance of a non parametric approach applied to the classification of forest types in an area of Northern Italy (Province of Trentino). The investigation has been carried out by classifying a Landsat 5 TM image on the basis of a reference data set derived from ground surveys and visual interpretation of aerial photos.

The work compares the accuracies obtained with different configurations of a k-NN classifier. In particular the paper focuses on the choice of the best band combination and of the maximum horizontal distance between training field plots and unclassified pixels. The optimal parameter set is evaluated by a leave-one-out cross-validation strategy.

As the conventional configuration of the method leads to a distortion in the estimate of the different class surfaces, a correction methodology is also considered. It consists of computing the error probability from a preliminary classification and applying appropriate prior probabilities to each forest type to influence the pixel assignment to the different classes and consequently the area estimation.

## 1. INTRODUCTION

Nowadays field works represents the main way to accurately describe the state of forests. However, new technologies can provide alternative tools useful for collecting additional data. In particular airborne and space borne sensors are currently used in forestry as an auxiliary data source, since they offer a synoptic view of large areas allowing at the same time the fast acquisition of data that can be digitally processed.

Several applications of remotely sensed data have been developed to estimate forest characteristics and to transform the results of field measurements into maps (Hame and Rauste, 1993). This is especially the case for biomass measurements (Ardö, 1992; Anderson et al., 1993), forest productivity (Ahern et al., 1991), tree cover percentage (Duncan et al., 1993), and leaf area index (Curran et al., 1992; Nemani et al., 1993). Correlations of satellite data, mainly based on Landsat 5 TM images, with forest inventory attributes have been found by several authors, e.g. for the discrimination of tree species (De Wulf et al., 1990), for the assessment of basal area (Franklin, 1986), canopy cover (Butera, 1986; Peterson et al., 1986; Oza et al., 1989), leaf area index (Spanner et al., 1990) biomass (Franklin, 1986), stand height (Horler and Ahern, 1986) and stem volume (Poso et al., 1984, 1987; Tomppo, 1990; Maselli et al., 2005; Muinonen and Tokola, 1990).

These studies have demonstrated that the operational use of digital data can be limited by the complexity of the relationships existing between spectral characteristics and forest attributes. For these reasons conventional classification methods, that assume relatively simple relationships between land surfaces and spectral characteristics, have often produced unsatisfactory results (Maselli et al., 2003).

The possibility to minimize these problems is provided by the use of more flexible classification methods as the non-parametric ones. Non-parametric methods, introduced by Fix

and Hodges (1951), are discrimination procedures that do not require any assumptions about the statistical distribution of the data unlike the common parametric approaches such as likelihood ratios (Hardin, 1994).

The most common non-parametric method applied to produce classifications and estimates of continuous forest variables is the k-Nearest Neighbour (kNN).

The kNN method is used to generalize information from field plots to pixels for map production. The decision rule assigns each pixel to a class among the closest k labelled training pixels; the k pixels correspond to the field plots where different variables have been observed. Closeness is defined in terms of a metric distance in the multi-spectral space.

Nearest neighbour techniques have been used extensively for forestry estimations in Nordic countries. Tomppo (1990), Nilson (1994) and Trotter et al. (1997) used the technique to estimate forest volume; Muinonen and Tokola (1990), Franco-Lopez et al., (2001) and Bauer (2001) applied the method for satellite images classification.

The method is highly appreciated because it allows to predict all the measured variables at the same time for each pixel or for area units of interest (Tomppo and Halme, 2004).

However there are some problems that should be taken into account when integrating satellite images and field data for mapping and monitoring purposes. Although the non-parametric methods do not require any specific distribution of the data, they assume the sample distribution of field plots to be representative of the spatial variation of the forests in the study area. Moreover, when scaling from field measurements to remotely sensed data, different kinds of error may be involved: incorrect matching between plot area and corresponding pixel area, image noises, timing difference in field data and image acquisition. Finally, to apply the kNN-estimation method, the following assumptions should be done: i. the image pixel values depend only on the forest

---

\* Corresponding author.

condition and not on the geographic location (Killki and Paivinen, 1987); ii. similar kinds of forest exist in the study area and their spectral responses depend on their characteristics. As a consequence of all factors listed above, kNN performances critically depend on a calibration process which aims to properly set the involved parameters.

The aim of this paper is to show the accuracy of kNN forest type classification when plot wise aerial photo-interpretation, combined with field data and other auxiliary information, are used as training data. In the calibration phase different configurations of a k-NN classifier were tested. In particular this study focuses on the choice of the best band combination and the setting of the maximum geographic distance between training field plots and unclassified pixels. Specific procedures to incorporate auxiliary information were also tested. The optimal setting of the parameters was defined by means of a leave-one-out cross-validation strategy. As the conventional configuration of the method leads to a distortion in the estimate of the different class surfaces, a correction methodology was also considered. This consisted of computing the error probabilities from a preliminary classification to derive prior probabilities for each forest type; these probabilities were then used to guide the pixel classification and consequently to improve the area estimates.

2. STUDY AREA

The study area is located in the Eastern Italian Alps and covers about 40.000 ha of the Trento Province corresponding to the Alta-Valsugana district. This area belongs to the Alpine mountain region and its elevation ranges between 400 and 2400m. The forest composition is therefore strongly influenced by elevation, slope and aspect. Broad-leaved deciduous forests dominate lower and warmest areas. At the highest elevation forests are dominated by mixed conifers. The dominant forest species in the area is *Picea abies*, followed by *Larix decidua* and *Pinus sylvestris*. Among broadleaved species, the more frequent is *Fagus sylvatica*, while other coniferous and broadleaved species are less common.

3. MATERIALS AND METHODS

3.1 Data set and image pre-processing

A ground reference data set, distributed all over the study area, was obtained by means of the integration of field surveys, the forest planning database of Trentino Province and the photo-interpretation of 1:10.000 black and white orthophotos from 1996. 596 plots were identified with a resulting sampling intensity of 0.015 plot/ha. The spectral signatures of all forest types found in correspondence of the training points were initially considered. Next, because of the poor separability and high spectral similarity among some original classes, some of these were aggregated and a classification scheme with six types was adopted. Table 1 shows the distribution of six different forest types in the reference data set. A mono-temporal Landsat 5TM (path 192, row 28) dated 19 June 2000 was used, georeferenced and geometrically rectified to ensure correspondence between field plots and corresponding pixels.

No topographic correction was applied to the images because previous studies carried out in the same area showed that these methods don't produce remarkable improvements in the overall classification accuracy when compared to one reached with the use of the original non-corrected images (Puzzolo et al, 2005).

Forest types	number of points	%
Forests of <i>Picea abies/Abies alba</i>	268	46.3
Forests of other broadleaves	61	10.5
Forests of other conifers	86	14.9
Forests of <i>Castanea sativa</i>	12	2.1
Forests of <i>Fagus sylvatica</i>	65	11.2
Forests of <i>Larix deciduas</i>	87	15.0

Table 1. Forest types identified in the study area

Since the relationship between forest and spectral characteristics may not be constant over a large area (mainly because of the elevation variations which can affect the vegetation structure and composition), a 10m digital elevation model was used as ancillary source of information.

3.2 kNN technique

The kNN algorithm assigns each unknown pixel to the field attributes of the most similar reference pixels for which field data exists. Similarity is expressed as the distance between the query point and the neighbouring ones. When using kNN, different types of distance metrics can be selected:

- Minkoski distance;
- Euclidean distance;
- Manhattan distance;
- Mahalanobis distance

Let  $D = \{p_1, \dots, p_n\}$  be a set of training pixels  $p_i$ . For each pixel a vector of different attributes  $m$  is known. Given the training pixel  $D = \{p_1, \dots, p_n\}$ , the spectral distance between the pixel  $p$  to be classified and each training pixel  $p_i$  is computed. To this unknown pixel an attribute vector  $m$  is assigned;  $m$  is obtained by calculating the mean or mode over all k-nearest  $p_i$  for continuous and categorical attributes respectively. Some applications assign different weights to the training pixels depending on auxiliary variables.

3.3 kNN configuration

In the current test the output variable was categorical and the nearest neighbour classifier assigned the most frequent class to each pixel  $p$ . In our kNN configuration each of the selected nearest neighbours contributes to the decision in the same way. The distances between neighbours were calculated using the Euclidean metric, which is the easiest to compute, because the use of other metrics does not generally contribute to a considerable improvement of the estimation accuracy (Maselli et al., 2005). The Euclidean distance is defined as the shortest distance between two points in the multi-spectral space. It is computed as (1):



$$d_{p(p_i)} = \sqrt{\sum_{j=1}^{nf} (x_{p,j} - x_{(p_i),j})^2} \quad (1)$$

where  $x_{p,j}$  = digital number for the feature  $j$ ;  $nf$  = number of features in the spectral space.

### 3.4 kNN calibration

Prior to any implementation, the kNN algorithm needs to be calibrated to find its best configuration. This step allows for the identification of the kNN parameters able to produce the best classification accuracy. Following a widely used approach, the current calibration was performed using a leave-one-out strategy. This technique uses the training data sample to estimate the classification accuracy by leaving out one sampling unit and classifying that unit on the basis of the rest of the sample. This omission is repeated for every unit allowing to calculate the classification error. (Gong, 1986).

In order to minimize the effects of possible positional errors, mean filters of 3x3 and 5x5 pixels were applied to the study images. The leave-one-out cross validation results derived from the filtered images were then compared with the ones obtained using the original TM bands.

As already mentioned, the relationship between forest and spectral characteristics may not be constant over a large area. Observations for adjacent pixels are in fact expected to be positively correlated while distant observations are expected to be uncorrelated (McRoberts *et al.*, 2002).

For this reason we applied a method that allowed us defining optimal geographical reference areas, in both vertical and horizontal directions (VRA and HRA), from which the nearest field plots are selected. The area has to be large enough to include all variation of forest cover types and to exclude, at the same time, more distant zones with different characteristics. Different combinations of VRA and HRA were tested and compared in terms of cross validation accuracy.

The last calibration step concerns the band combination. Since all available bands are not always needed and can even reduce the classification accuracy, a subset of bands was selected to be used in the final classification. All 63 possible combinations of the six TM bands were tested to select the subset which gave the highest classification accuracy. The thermal infrared band (TM6) was not considered due to its lower spatial resolution.

After the calibration, the optimal number of neighbours was chosen according to two different criteria: the  $k$  value had to be large enough to minimize the misclassification probability and small enough to minimize the bias. When  $k=1$ , the prediction incorporates all the variability existing in the observations, whereas the variability is reduced when  $k>1$  because the prediction is based on the mode of multiple observations (McRoberts *et al.*, 2002).

The best configuration of the kNN classification we found was then applied to the study area; the accuracy results, derived through a leave-one-out cross validation method, are presented in terms of global error matrix, overall accuracy, producer's accuracy, user's accuracy, and kappa index. The results of Chi-square ( $\chi^2$ ) tests, which allow to identify systematic errors (i.e. classification bias), are also presented; they were used to check if the true class distribution of the original sample is well represented.

The correspondence between the extent of the ground references and that of the classified areas (Maselli, 1990) was also computed by (2):

$$corr = \frac{N - \sum_{i=1}^n abs(c_i - r_i)}{N} \quad (2)$$

$corr$  = correspondence rows/columns

$N$  = total number of pixels

$C_i$  = marginal summary of column  $i$

$R_i$  = marginal summary of row  $i$

In this first trial we assumed that the prior probabilities of a given pixel were equal for all classes.

### 3.5 Alternative kNN configuration

The values found in the error matrix were used for a discrimination process based on prior probabilities. The study proposes to use the error matrix derived from the first classification as an additional information source in order to reduce the interclass confusion. The matrix, in fact, has been shown to be useful for correcting the statistical weights in discrimination processes and it can be used to improve area estimates of different cover types (Maselli *et al.*, 1990; 1992). The information deriving from the error matrix was incorporated into the classification process changing the prior probability for each class. The prior probabilities were derived from the ratios of the class frequencies in the ground reference data (marginal summary of columns in the error matrix) over those in the classification data (marginal summary of rows in the error matrix) and then used for changing the probability extraction of each class. The main difficulty in following this approach is to calculate prior probabilities appropriate to achieve optimal results.

## 4. RESULTS AND DISCUSSION

The algorithm was first used with mono-spectral data. In accordance with other studies (Lillesand *et al.*, 2004), the best single band for discriminating forest types was band 4. Other authors found the best results are achieved using visible or middle infrared bands (McRoberts *et al.*, 2002). A reason for differences could be found in the fact that the optimal band selection depends upon both the image and the application (Spanner *et al.*, 1984). In addition, the optimal band combination depends on the characteristics of the training data, forest density and considered season (McRoberts *et al.*, 2002).

The two tested filters produced results comparable with those produced without filter: the accuracy varies between 40% and 50%. On the whole, images filtered using a 5x5 mean filter provided best results in terms of overall accuracy (Figure 1) but the smoothing effect of filtering is questionable because of the masking effect on the spectral differences. The argument for using a multiple pixel window to address plot location error (Franco Lopez, 2001) remains debatable but, in our test, the classification was completed including filter.

Different HRA e VRA sizes were considered. Probably due to the characteristics of training set and of study area, the 2km HRA and the 500m VRA reached the maximum cross validation accuracy (67%).

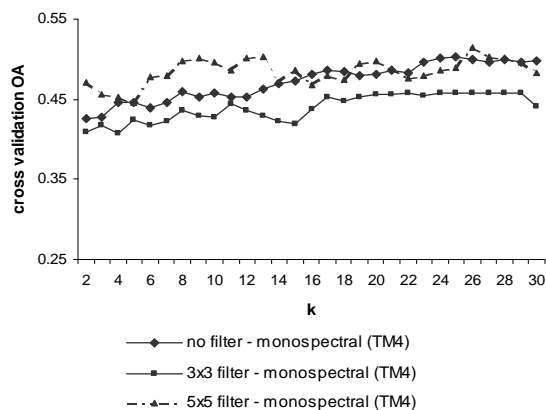


Figure 1. Overall classification accuracy for three different filters at increasing value of k

The geographical space defined by this combination allows representing the spatial variation of the field cover. The accuracy decreased to 62% when considering the maximum geographical window (5km HRA and 700m VRA), probably because a too wide selection area led to include a high number of training plots which were less representative of local conditions. Comparing the cross validation accuracies reached for the 63 band combinations we tested, we can observe that the overall accuracy did not vary too much and ranged between 0.62 and 0.67. The band combination which produced the most accurate classification was TM2, TM3 and TM7, confirming that the classification accuracy with all six bands was inferior to the accuracy obtained using a band subset. This finding can be explained by the high correlation between bands in the same spectral regions.

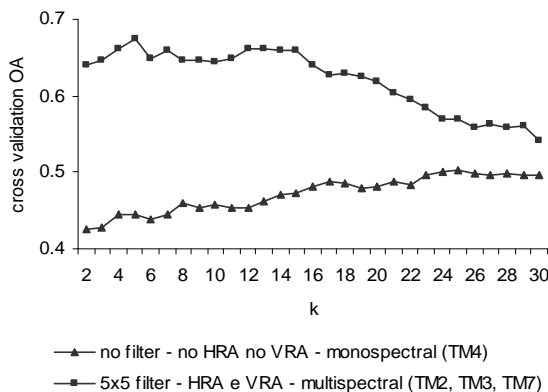


Figure 2. Overall classification accuracy before and after calibration at increasing value of k

Using the Euclidean distance, equal weighting among neighbours, a mean filter of 5x5 pixels, a HRA of 2km, a VRA of 500m and k=5 an overall accuracy of 67% was achieved (Figure 2). When the number of neighbours was varying from 5 to 1 the accuracy decreased approximately of 4% (Table 2). but the true class distribution of the original sample was preserved ( $\chi^2_{est} < \chi^2_{tab}$ ). This means that the classification accuracy can be

improved when k increases, but the estimates will be affected by bias. The most frequent class, which aggregates *Picea abies* and *Abies alba* forests, showed the higher accuracy. The *Larix decidua* class, even though represented by a high plot number, was not correctly classified (Table 3) being it was confused with other conifers.

k	OA (%)	Chi-square
1	61.66	1.4
2	63.90	67.0
3	64.59	22.1
4	66.15	33.3
5	67.36	23.8

Table 2. Overall classification accuracy and Chi-Square test ( $\chi^2_{tab}=11.07$ ;  $P=0.05$ ;  $df=5$ ) calculated for different numbers of neighbours

Forest types	PA	UA
Forests of <i>Picea abies</i> / <i>Abies alba</i>	88.06	76.87
Forests of other broadleaves	33.33	55.77
Forests of other conifers	53.49	63.89
Forests of <i>Castanea sativa</i>	52.31	53.13
Forests of <i>Fagus sylvatica</i>	58.33	53.85
Forests of <i>Larix deciduas</i>	62.30	53.52
OA	67.36%	
Kappa	0.5315	

Table 3. Confusion matrix at the end of calibration process

Applying the modified prior probabilities (Table 4) the producer's accuracy increased of 10% for larch forests while the mean producer accuracy did not change significantly. Overall accuracy and Kappa coefficient were not suited to appreciate the improvements brought by these prior probabilities but the marginal summaries of the error matrix showed a remarkable improvement. As a result, the overall accuracy and Kappa remained constant, respectively around 65% and 0.5, but the correspondence coefficient passed from 0.82 to 0.95, indicating an improved area estimation of most classes. Moreover the  $\chi^2$  statistic was not significant ( $\chi^2_{est} < \chi^2_{tab}$ ,  $P=0.05$ ), indicating that the classification was not affected by systematic errors (Table 5).

Forest types	PA	UA
Forests of <i>Picea abies</i> / <i>Abies alba</i>	85.07	81.14
Forests of other broadleaves	45.98	44.94
Forests of other conifers	53.49	57.50
Forests of <i>Castanea sativa</i>	44.62	47.54
Forests of <i>Fagus sylvatica</i>	50.00	50.00
Forests of <i>Larix deciduas</i>	55.74	60.71
OA	66.15%	
Kappa	0.5227	

Table 4. Confusion matrix with the prior probability use

5. CONCLUSIONS

Since the '80s, the kNN method is commonly used for mapping forest variables. The method requires the selection of a few estimation parameters by a calibration process. In this study, the use of filtered images, combined with setting a spatial range in which the nearest field plots are chosen and

class	True reference	Classification without priors (k=5)	Classification whit priors
Forests of <i>Picea abies/Abies alba</i>	46.29%	53.02%	48.53%
Forests of <i>Larix deciduas</i>	10.54%	12.26%	9.67%
Forests of other conifers	14.85%	12.44%	13.82%
Forests of <i>Fagus sylvatica</i>	2.07%	2.25%	2.07%
Forests of <i>Castanea sativa</i>	11.23%	11.05%	10.54%
Forests of other broadleaves	15.03%	8.98%	15.37%
		OA: 67.36%	OA: 66.15%
		corr: 0.82	corr: 0.95
		$\chi^2$ : 23.8	$\chi^2$ : 1.75

Table 5. Marginal summaries of confusion matrixes without and with prior probabilities compared to the ground references, correspondence coefficients and Chi-Square tests ( $\chi^2_{tab}=11.07$ ;  $P=0.05$ ;  $df=5$ )

the selection of an appropriate band combination made possible to improve the classification accuracy. When the calibration process was implemented the accuracy rose from 50% to 70%. One of the most important steps in kNN method is the choice of k. The results of Chi Square test showed that the selection of k=1 is appropriate to maintain the variance of observations and to preserve appropriate variability in predictions. Besides, the leave-one out cross validation showed that the selection of a higher k, equal to 5, is useful to maximize the classification accuracy. The error matrix derived from the first classification process was used as ancillary data source. The use of this information to set prior probabilities improved the discrimination of some classes but not the overall accuracy of the classification. However the use of external information preserved the class distribution of the original sample and provided better area estimation. Considering that the method was only tested using a single data set and on a single study area, further investigations are needed. The proposed configuration should be validated in areas with different forest types and topographic characteristics and with training dataset of different sizes.

6. ACKNOWLEDGMENTS

The authors would like to thank the RI.SELV.ITALIA project founded by the Italian Ministry of Agriculture and Forest Policies for data providing. The authors would like to thank also Dr. Ciaghi for the support in the photo interpretation and Marco Trombetti for the text revision.

7. REFERENCES

Ahern, F.J., Erdle, T., Maclean, D.A., Knepppek, I.D., 1991. A quantitative relationship between forest growth rates and Thematic Mapper reflectance measurements. *Int.J.Rem.Sens.*, 12, pp. 387-400.

Anderson, G.L., Hanson, J.D., Haas, R.H., 1993. Evaluating Landsat Thematic Mapper derived vegetation indices for estimating above-ground biomass on semiarid rangelands. *Rem.Sens.Env.*, 45, pp. 165-175.

Ardö, J., 1992. Volume quantification of coniferous forest compartments using spectral radiance recorded by Landsat Thematic Mapper. *Int.J.Rem.Sens.*, 13, pp. 1779-1786.

Bauer, M.E., Burk, T.E., Ek, A. R., Coppin, P.R., Lime, S.D., Walsh, T.A., Walters, D.K., Befort, W., Heinzen, D. F., 1994. Satellite inventory of Minnesota forest resources. *Photogrammetric Eng. Remote Sensing*, 60 (3), pp. 287-298.

Butera, K., 1986. A correlation and regression analysis of percent canopy closure versus TMS spectral response for selected forest sites in the San Juan national forest, Colorado. *IEEE Trans. Geosci. Remote Sens.*, GE-24(1), pp. 122-129.

Curran, P.J., Dungan, J.L., Gholz, H.L., 1992. Seasonal LAI in slash pine estimated with Landsat TM. *Rem.Sens.Env.*, 39, pp. 3-13.

De Wulf, R.R., Goossens, R.E., De Roover, B.P., Borry, F.C., 1990. Extraction of forest stand parameters from panchromatic and multispectral SPOT-1 data. *Int.J.Rem.Sens.*, 11, pp. 1571-1588.

Duncan, J., Stow, D., Fanklin, J., Hope, J., 1993. Assessing the relationship between spectral vegetation indices and shrub cover in the Jornada Basin, New Mexico. *Int.J.Rem.Sens.*,14, pp. 3395-3416.

Fix, E., Hodges, J.L., 1951. Discriminatory analysis, nonparametric discrimination consistency properties. Technical Report 4, Randolph Filed, TX: US Air Force.

Franco-Lopez, H., Ek, A.R., Baue, M.E., 2001. Estimation and mapping of forest stand density, volume, and cover type using the k-nearest neighbours method. *Rem.Sens.Env*, 77, pp. 251-274.

Franklin, J., 1986. Thematic mapper analysis of coniferous forest structure and composition. *Int.J.Rem.Sens*, 7(10), pp. 1287-1301

Gong, G., 1986. Cross-validation, the jack-knife, and the bootstrap: excess error estimation in forward logistic regression. *Journal of the American Statistical Association*, 81(393): pp.108-113.

- Hame T. and Rauste Y., 1993. Multitemporal satellite data in forest mapping and fire monitoring. Proceedings to the International Workshop. Satellite technology and GIS for Mediterranean forest mapping and fire management held in Thessaliniki, Greece 4th and 6th November.
- Hardin, P.J., 1994. Parametric and Nearest neighbour methods for hybrid classification: a comparison of pixel assignment accuracy. *Photogrammetric Eng. Remote Sensing*, 60(12), pp. 1439-1448.
- Horler, D.N.H. and Ahern, F.J., 1986. Forestry information content of Thematic Mapper data. *Int.J.Rem.Sens.*, 7(3), pp. 405-428.
- Kilkki, P. and Paivinen, R. 1987. Reference sample plots to combine field measurements and satellite data in forest inventory. In: Remote Sensing-Aided Forest Inventory. Seminars organised by SNS and Taksattoriklubi, Hyytiala, Finland, pp. 209-212.
- Lillesand, T.M., Kiefer, R.W., Jonathan, W. Chipman, 2004. *Remote sensing and image Interpretation*. 5th ed. New York, Wiley, pp 763
- Maselli, F., Conese, C., Zipoli, G., Pittau, M.A., 1990. Use of error probabilities to improve area estimates based on maximum likelihood classification. *Rem.Sens.Env*, 31, pp. 155-160.
- Maselli, F., Conese, C., Petkov, L., Resti, R., 1992. Inclusion of prior probabilities derived from a non parametric process into the maximum likelihood classifier, *Photogrammetric Eng. Remote Sensing*, 58, pp. 201-207.
- Maselli, F., Bottai, L., Chirici, G., Corona, P., Marchetti, M., Travaglino, D., 2003. Stima di attributi forestali in ambiente mediterraneo tramite integrazione di misure a terra e dati telerilevati. *Italia Forestale e Montana*, 4, pp. 251-263.
- Maselli, F., Chirici, G., Bottai, L., Corona, P. Marchetti, M., 2005. Estimation of mediterranean forest attributes by the application of k-NN procedures to multitemporal Landsat ETM+ images. *Int.J.Rem.Sens.*, 26(17), pp. 3781-3796.
- McRoberts, R., Nelson, M., Wendt, D.G., 2002. Stratified estimation of forest area using satellite imagery, inventory data, and the k-NN technique. *Rem.Sens.Env* 82, pp. 457-468.
- Muinsonen, E., & Tokola, T., 1990. An application of remote sensing for communal forest inventory. The Usability of Remote Sensing For Forest Inventory and Planning. Proceedings from SNS/IUFRO workshop in Umea 26-28 February 1990. Swedish University of Agricultural Sciences, Remote Sensing Laboratory, Report 4. 35-42. Umea, Sweden. ISBN 91-576-4208-7
- Nemani, R., Pierce, L., Running, S., 1993. Forest ecosystem processes at the watershed scale: Sensitivity to remotely sensed Leaf Area Index estimates. *Int.J.Rem.Sens.*, 14, pp. 2519-2534.
- Nilson, T., and Peterson, U., 1994. Age dependence of forest reflectance: analysis of main driving factors. *Rem.Sens.Env.*, 48, pp. 319-331.
- Oza, M.P., Srivastava, V.K., Pariswad, B.S. Setty, K.R.V., 1989. Relationship between Landsat MSS data and forest tree parameters. *Int.J.Rem.Sens.*, 10(11), pp. 1813-1819
- Peterson, D.L., Westman, W.E., Stephenson, N.L., Ambrosia, V.G., Brass, J.A., Spanner, M.A., 1986. Analysis of forest structure using thematic mapper data. *IEEE Trans. Geosci. Remote Sens.*, 24, pp. 113-121
- Poso, S., Hame, T. Paananen, R., 1984. A method of estimating the stand characteristics of a forest compartment using satellite imagery. *Silva Fennica*, 18, pp. 261-292
- Poso, S., Paananen, R. Simila, M., 1987. Forest inventory by compartments using satellite imagery. *Silva Fennica*, 21, pp. 69-94
- Puzzolo, V., Panizza, M., De Natale, F., Bruzzzone, L., 2005. Correzioni topografiche di immagini Landsat TM e SPOT HRV in aree alpine orograficamente complesse. *Rivista italiana di Telerilevamento*, 32, pp. 67-77.
- Spanner, M.A., Brass, J.A., Patterson, D.L., 1984. Feature selection and the information content of thematic mapper simulator data for forest structural assessment, *IEEE Trans. Geosci. Remote Sens.*, 22 (6), pp. 482-489.
- Spanner, M.A., Pierce, L.L., Peterson, D. Running, S., 1990. Remote Sensing of temperature coniferous forest leaf area index. The influence of canopy closure, understory vegetation and background reflectance. *Int.J.Rem.Sens.*, 11(1), pp. 95-111
- Tomppo, E., 1990. Designing a Satellite Image-Aided National Forest Survey in Finland. The Usability of Remote Sensing For Forest Inventory and Planning. Proceedings from SNS/IUFRO workshop in Umea 26-28 February 1990. Swedish University of Agricultural Sciences, Remote Sensing Laboratory, Report 4. 43- 47. Umea, Sweden. ISBN 91-576-4208-7
- Tomppo, E., Halme, M., 2004 Using coarse scale forest variables as ancillary information and weighting of variables in k-NN estimation: a genetic algorithm approach. *Rem.Sens.Env.*, 92, pp. 1-20.
- Trotter, C.M., Dymond, J R., Goulding, C.J., 1997. Estimation of timber volume in a coniferous plantation forest using Landsat TM. *Int.J.Rem.Sens.*, 18, pp. 2209-2223.

# RADIATIVE TRANSFER MODEL INVERSION BASED ON MULTI-TEMPORAL CHRIS/PROBA DATA FOR LAI ESTIMATION

B. Koetz<sup>a,\*</sup>, M. Kneubuehler<sup>a</sup>, S. Huber<sup>a</sup>, J. Schopfer<sup>a</sup>, F. Baret<sup>b</sup>

<sup>a</sup> Remote Sensing Laboratories (RSL), Dept. of Geography, University of Zurich, Winterthurerstrasse 190, CH-8057 Zurich, Switzerland, Email: bkoetz@geo.unizh.ch

<sup>b</sup> INRA CSE, Site Agroparc 84914, Avignon, France

Commission VII, WG 1

**KEY WORDS:** Leaf area index; Radiative transfer; Dynamic canopy model; Phenology; Multi-temporal; Maize; Precision farming, land surface processes

## ABSTRACT:

Leaf area index (LAI) is a key variable for the understanding and modelling of several eco-physiological processes within a vegetation canopy. The LAI could thus provide vital information for the management of the environment and agricultural practices when estimated continuously over time and space thanks to remote sensing sensors such as CHRIS/PROBA.

The spaceborne ESA-mission CHRIS/PROBA provides multi-temporal observations of the land surface in the spectral and directional information dimensions. This system represents a rich source of information for Earth observation purposes specifically adapted for monitoring the high dynamic of agricultural crops. For this purpose a radiative transfer model (RTM) is coupled to a canopy structure dynamic model (CSDM). The coupled models are used to exploit the complementary content of the spectral and temporal information dimensions for LAI estimation over a maize canopy. The resulting estimation of the temporal and spatial variation of LAI is improved by integrating multi-temporal CHRIS/PROBA data and ground meteorological observations. Further, the presented method provides the continuous LAI time course over the season, which is required by crop growth and land surface process models.

## 1. INTRODUCTION

Leaf area index (LAI) as defined by the single sided area of green leaves per unit of horizontal soil (Privette et al. 2001) is a key variable governing several processes such as photosynthesis, transpiration or rain interception. Estimates of LAI could be assimilated within vegetation process models to provide more accurate description of canopy functioning with emphasis on important environmental and economical outputs such as, carbon, water and nitrogen fluxes and stocks, canopy state and yield for crops (Chen et al. 2003; Matsushita and Tamura 2002). Remote sensing allows for detailed and frequent observations of the vegetation necessary to monitor the spatial and temporal variations of canopy characteristics (Koetz et al. 2005; Myneni et al. 1997).

At the top of the canopy, the interaction of radiation within the vegetation depends on the contribution of several components such as leaves, stems, soil background as well as the illumination and view geometries (Goel and Thompson 2000; Verhoef and Bunnik 1981). Radiative transfer models (RTM) provide an explicit connection between the canopy biophysical variables, the view and illumination geometry and the resulting canopy reflectance by exploiting our knowledge of the involved physical processes (Baret et al. 2000). The RTM have to be inverted to retrieve the biophysical variables from the measured canopy reflectance (Bacour et al. 2002; Kimes et al. 2000; Weiss et al. 2000). However measurement and model uncertainties are often leading to a large range of possible solutions, which prohibits the inversion to be properly solved (Combal et al. 2002). The regularization of such an ill-posed problem requires input of additional information to obtain more reliable and stable solutions (Combal et al. 2002; Combal et al. 2003).

Knowledge of the canopy structure dynamics is highly desirable as ancillary information to constrain the RTM inversion for the

estimation of canopy characteristics. The dynamics of the canopy structure are strongly depending on crop growth processes, which result in a relatively smooth and typical temporal profile of LAI. Simple semi-mechanistic models have been proposed to describe the LAI time course (Baret 1986; Werker and Jaggard 1997). Such models could consequently be used to exploit the information on canopy structure dynamics and get more robust and reliable estimates of LAI. The use of a canopy structure dynamics model (CSDM) allows also to derive a continuous estimation of LAI which is required in some applications, particularly those based on the forcing of agricultural growth or land surface models (Delecolle et al. 1992; Moulin et al. 1998). The coupling of radiative transfer and canopy structure dynamics models offers consequently a great potential for the interpretation of remote sensing data since it integrates several sources of information (Baret et al. 2000):

- the knowledge of radiative transfer processes within RTM
- the knowledge on some biological processes within CSDM
- the temporal and spectral dimension of radiometric information
- ancillary information such as the climatic variables partly governing the CSDM including temperature, and the prior knowledge on the canopy type.

The CHRIS instrument operated on the spaceborne platform PROBA observes the canopy reflected radiance in the spectral, directional, spatial and temporal dimensions, thus describing the canopy reflectance based on independent but complementary information sources (Barnsley et al. 2004). We propose to exploit synergistically two of these information dimensions, namely the spectral and temporal, based on multi-temporal CHRIS observations. A RTM coupled to a CSDM is used to improve the estimation of biophysical canopy characteristics relevant for dynamic land surface processes.



2. DATA

CHRIS multi-angular data sets were acquired over a test site in central Switzerland on eight different dates between 26 May 2005 and 22 September 2005 in Mode 5 (see Tab. 1). Out of this data sets, four dates that represent major steps in phenology of the selected agricultural fields were selected for further processing and data exploitation. The selected dates are 26 May 2005 (DOY 171), 20 June 2005 (DOY 196), 17 August 2005 (DOY 229) and 22 September 2005 (DOY 265). Within this study the multi-temporal aspect of nominal nadir acquisitions has been further exploited. The full directional information content of the data set is described in the a separate study (Kneubühler et al. 2006).

Spatial Sampling	Image area	View angles	Spectral bands	Spectral range
17m @ 556 km altitude	6.5x13 km (372x748 pixels)	5 nominal angles @ +55°, +36°, 0°, -36°, -55°	37 bands with 6-33 nm width	447-1035 nm

Table 1. CHRIS Specifications for Mode 5

2.1 Test Site and Field Data

The test site for this study is located in the rural border region between the two Swiss Cantons of Lucerne and Aargau in central Switzerland near the villages of Vordemwald (7°53' E, 47°16'N), St. Urban and Pfaffnau. The hilly area is dominated by agricultural fields in the lower parts (450-500 m a.s.l.) and mixed forests mainly on the hilltops (elevations up to 700 m a.s.l.). Agriculture mainly concentrates on barley, wheat, maize, sugar beet and pasture land. Ground truth data were collected in a maize field parallel to the CHRIS data takes on most dates. Ground data collection included spectroradiometric measurements using a FieldSpec Pro FR, LAI measurements using a Licor LAI-2000 Plant Canopy Analyzer (Fig. 1) and hemispherical photographs, as well as detemination of leaf water and chlorophyll content in the laboratory (Fig. 1). An operational meteorological station in the close vicinity of the study site provided basic meteorological observations such as air temperature (Fig. 2). The land use type was recorded for a large amount of agricultural fields.

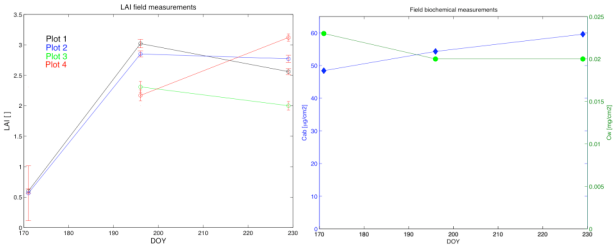


Figure 1. Biophysical (LAI) and biochemical (Cab: leaf chlorophyll content, Cw: leaf water content) field measurements

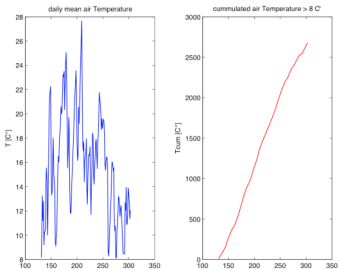


Figure 2. Daily (right: accumulated) air temperature over the maize growing season

2.2 Geometric and Atmospheric Processing

Geometric and atmospheric correction of the multi-angular CHRIS data sets under investigation was performed following an approach described in Kneubühler et al. ( 2005). Geocorrection is therefore based on a 3D physical model developed by Toutin (2004) which is implemented in the commercially available image processing software PCI/Geomatica. High locational accuracy of the respective multi-angular products after geometric correction is a prerequisite for reliable retrieval of HDRF information from the data set. The root mean square errors (RMSE) for the specific region of interest do generally not exceed one pixel. Figure 4 shows a subset of a geocorrected CHRIS nadir scene for the specific region of interest in this study. The accuracy of the geocorrection may be seen from the overlying pixelmap. Subsequent atmospheric correction of the CHRIS radiance data products is performed using ATCOR-3 (Richter 1998), which is based on MODTRAN-4. ATCOR-3 accounts for terrain effects by incorporating DEM data and their derivatives such as slope and aspect, sky view factor and cast shadow. ATCOR-3 is capable of processing data from tilted sensors by accounting for varying path lengths through the atmosphere and varying transmittance. Atmospheric correction results in the retrieval of HDRF (Hemispherical Directional Reflectance Factor) data sets for the various CHRIS view angles.

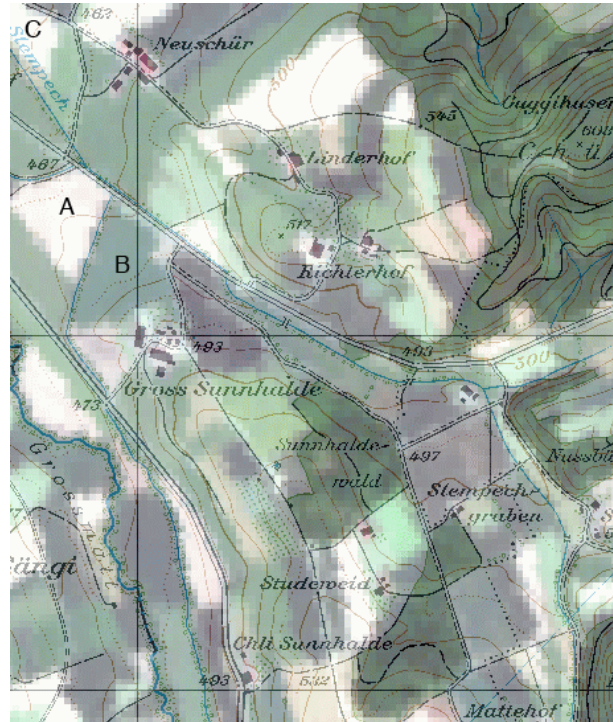


Figure 4. Geocorrected subset of the 26 May 2005 CHRIS nadir scene for the region of interest in this study with overlying pixelmap (1:25'000, © swisstopo). The investigated maize field is indicated with A , further fields with ground data B: winter barley and C: sugar beet

3. METHODS

A coupling scheme (Fig. 4) to combine two models, the RTM and CSDM, is implemented to estimate LAI based on the multi-temporal remote sensing observations (Koetz et al. 2005). The

models are first separately introduced. The coupling and LAI retrieval are subsequently presented.

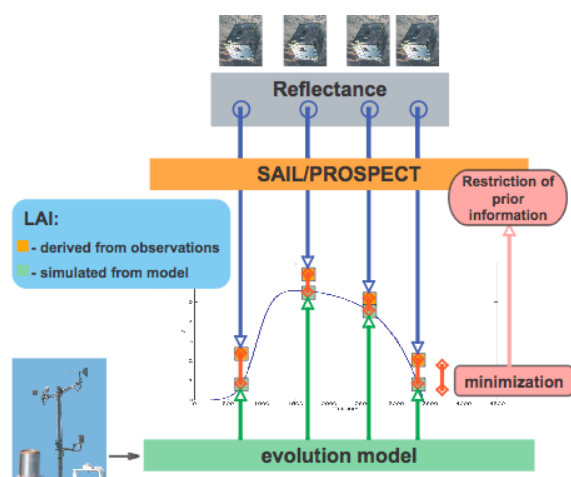


Figure 4. Concept of coupled LAI retrieval scheme (RTM & CSDM) exploiting multi-temporal CHRIS and ground meteorological observations

### 3.1 Canopy Structure Dynamics Model

The LAI temporal profile is governed by the net effect of growth and senescence, which are genetically programmed. However, the expression of this genetic potential is strongly influenced by environmental factors. The leaf area of an annual canopy typically shows first an exponential rise corresponding to dominant cell multiplication and elongation processes while the effects of competition for resources are limited. Then, this increasing absolute growth rate is rapidly modulated by senescence and competition for resources.

A simple semi-mechanistic model that describes LAI dynamics was proposed by (Baret 1986):

$$LAI = LAI_{Amp} \left[ \frac{1}{1 + e^{-b(T-T_i)}} - e^{a(T-T_s)} \right] \quad (1)$$

The independent variable  $T$  is defined as the accumulated daily mean air temperature above 8 °C starting from sowing (Durand et al. 1982). This variable was chosen since both seedling emergence and leaf area expansion are temperature dependant (Hesketh and Warrington 1989). The CSDM describes LAI in two parts, growth and senescence (Eq. 1). The growth period is defined by a logistic equation with parameter  $b$  being the relative growth rate at the inflexion point  $T_i$ . The senescence is determined by an exponential equation with parameter  $a$  being the relative growth rate and  $T_s$  the time expressed in temperature when leaves have all senesced. The parameter  $LAI_{Amp}$  describes the amplitude of maximal leaf area. The parameters  $b$ ,  $T_i$  describe the dynamics before the time of maximum LAI, while  $a$  and  $T_s$  focus on the period after the maximum LAI.

The distribution of the model parameters typical for the observed crop maize was derived from an extensive database acquired over 44 different sites spread over the world and spanning over different climatic and cultural practices conditions (Brisson et al. 2002; Duthil et al. 1999; Marloie et al. 2001).

### 3.2 Radiative Transfer Models

The turbid medium radiative transfer model SAIL (Scattering from Arbitrarily Inclined Leaves (Verhoef 1984, 1985) was used, since it describes the canopy structure in a fairly simple

way while producing nevertheless realistic results. The PROSPECT model (Jacquemoud and Baret 1990) was used to describe leaf optical properties. PROSPECT simulates leaf reflectance and transmittance spectra required by the SAIL model as a function of leaf biochemical contents and leaf structure.

The soil reflectance was assumed to keep the same spectral pattern and to exhibit predominantly variations in magnitude due to changes in soil moisture and roughness, which was described by a soil brightness factor  $s$ . A reference soil reflectance spectrum retrieved from CHRIS observations over bare soil of the same field, was considered for the cases investigated. The soil was also assumed to be a Lambertian surface.

### 3.3 LAI estimation based on Look up tables

The estimation of LAI from RTM inversion was based on a LUT (Look Up Tables) approach. It is a conceptually very simple technique, that potentially overcomes limitations of iterative optimization algorithms associated to important computation time and the risk of converging to a local minimum that is not necessary close to the actual solution (Combal et al. 2002; Kimes et al. 2000).

The generation of a look up table consists first of sampling the space of the  $p$  input variables  $V$  of the RTM ( $LUT_V$ ). A total of 100000 canopy realizations have been generated following a uniform distribution and specific ranges for the respective canopy variable. Then, the RTM was used to simulate the corresponding reflectance table ( $LUT_R$ ) with  $m$  numbers of measurement configurations, corresponding to the bands and directions considered. The range of each variable was defined according to previous experiments performed over maize crops under a range of conditions (Baghdadi and Baret 1998; Espana et al. 1998; Jacquemoud and Baret 1990). Note that the generation of the  $LUT_V$  allows already to define some prior information on the respective variable by restraining it to vary within a limited range.

The measurement configuration used represented the actual conditions of observations of CHRIS (Table 1). The view zenith angle was adapted to the actual view angle of the respective CHRIS nominal nadir scene. Because the illumination geometry was varying from date to date, four LUTs were created, each corresponding to a specific date of observation and the associated sun zenith angle. For the sake of simplicity, the fraction of diffuse irradiance was assumed to be 15% independent of the wavelength.

The selection of the solution within the LUT was achieved in two steps: the first one considered only the radiometric information. The second one used the CSDM fitted over the first estimates of LAI derived from the previous step to constrain the possible solutions based on the radiometric information. The later process could be iterated several times to reach convergence. The coupling of the RTM and CSDM models was based on the hypothesis that the remotely sensed observations of LAI (step 1) had to be consistent with the time profile of LAI generated by the CSDM. Consequently the remotely sensed LAI was recalibrated, when necessary, relative to the phenologically sound LAI provided by the CSDM (step 2). These two steps will be briefly described here after.

#### 3.3.1 Step one: exploiting the radiometric information

The LUT was sorted according to the cost function  $\chi^2_{rad}$  corresponding to the simple squared-sum of differences between the measured reflectance  $R$  and the simulated reflectance  $R_{LUT}$  found in the  $LUT_R$  (Eq. 2).

$$\chi^2_{rad} = \sum_{\lambda=1}^{11} (R_{LUT}^{\lambda} - R^{\lambda})^2 \quad (2)$$

The possible solutions considered were those that were within 20% of the best radiometric match. This ensemble of possible radiometric solutions was noted  $[S_{rad}]$ . The 20% threshold was derived after test and error trials and is consistent with what (Combal et al. 2002) proposed in an earlier study. The initial solution value,  $LAI_0$  was then set to the median value of the ensemble  $[S_{rad}]$  of best radiometric cases.

### 3.3.2 Step two: exploiting the prior information on canopy variables

The prior information was introduced here by refining the selection within the possible radiometric cases  $[S_{rad}]$  according to the following cost function,  $\chi^2_{var}$ :

$$\chi^2_{var} = \sum_{i=1}^n \left( \frac{V_i - V_i^p}{\Delta_i^p} \right)^2 \quad (3)$$

where  $n$  was the number of canopy characteristics on which prior information was exploited,  $V_i^p$  was the most probable value of the canopy variable  $i$ , and  $\Delta_i^p$  the corresponding confidence level. The LAI value of the case ensuring the minimum of  $\chi^2_{var}$  over  $[S_{rad}]$  was selected as the solution,  $LAI_1$ . Because the LUT already incorporated some prior information on the range of variation of all the canopy variables, only the LAI and soil brightness,  $s$ , were considered in equation 3. For the soil brightness, no temporal constraint was used and  $V_s^p$  and  $\Delta_s^p$  were set respectively to 0.9 and 0.2. Conversely, temporal constraints were used for LAI to get the most probable value  $V_{LAI}^p$  at a given point in time. This was achieved by exploiting the CSDM adjusted over the set of first estimates  $LAI_0(t)$ . The adjustment of the CSDM was performed using the simplex minimization algorithm (Nelder and Mead 1965). The confidence value  $\Delta_{LAI}^p$  was assumed to be within 20% of the most probable value. This value was in agreement with the magnitude of the standard deviation observed when estimating LAI from radiometric measurements without using much prior information (Combal et al. 2002). This second step was iterated a number of times up to the convergence. Experience showed that the convergence was quickly reached and only three iterations were used in the following part of the study. At last the CSDM adjusted over the most phenologically sound cases of  $[S_{rad}]$  was used to produce the final results.

## 4. RESULTS AND DISCUSSION

For the evaluation of the LAI retrieval performance estimated LAI were compared to the LAI field measurements (Fig. 5). The simple root mean square error (RMSE) was calculated to quantify the agreement between actual LAI in the field and estimated values. A linear regression was used to quantify the possible biases of the estimates. The results showed a robust performance of the LAI estimation with reasonable RMSE of 0.73. Constraining the RTM inversion with dynamic prior information on the canopy structure lead to relative low inversion uncertainties. Nevertheless, when interpreting the best linear fit a consistent underestimation of the LAI estimates is evident. The LAI underestimation is probably due to the typical row structure of the maize canopy, which is not consistent with the RTM assumption of a homogenous canopy. Simulations of a 3D-RTM comparing canopy gap fraction of heterogeneous maize canopies with turbid, homogeneous canopies support this observation. The results showed that gap fractions of a heterogeneous canopy observed from nadir were generally higher than that of a corresponding homogeneous canopy (Lopez-Lozano et al. 2007 (accepted)). Consequently

interpreting the nadir remote sensing signal of a maize canopy based on a turbid RTM would lead to an underestimation of LAI values. Forward simulation using SAIL parameterized with the field measurements lead to a significant overestimation of the near-infrared canopy reflectance relative to CHRIS observations, which further demonstrates the limitation of SAIL for the representation of maize canopy structure.

The integration of the CSDM to the retrieval algorithm allowed a continuous description of the LAI time course over the growing season. As the CSDM is capable of representing realistically the growing and senescence phases of a maize canopy the LAI values follow a phenologically sound evolution (Fig. 6). The CSDM was able to fit very well to the estimated LAI values due to the low temporal resolution of CHRIS observations.

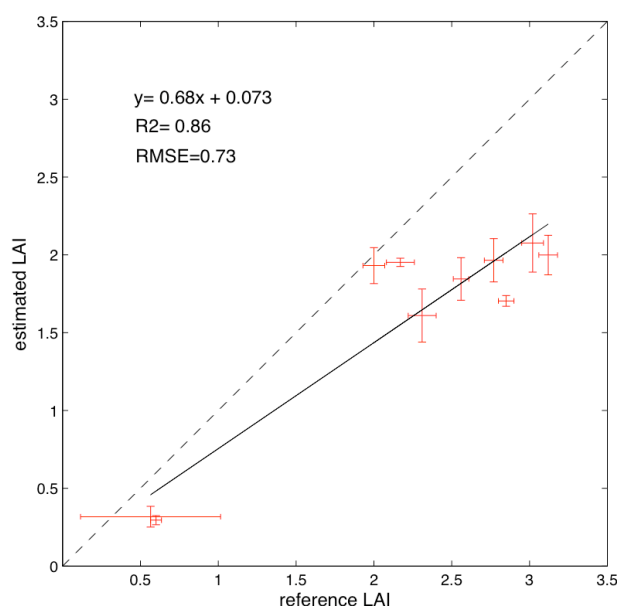


Figure 5. Estimated LAI derived from CHRIS observations validated against field data

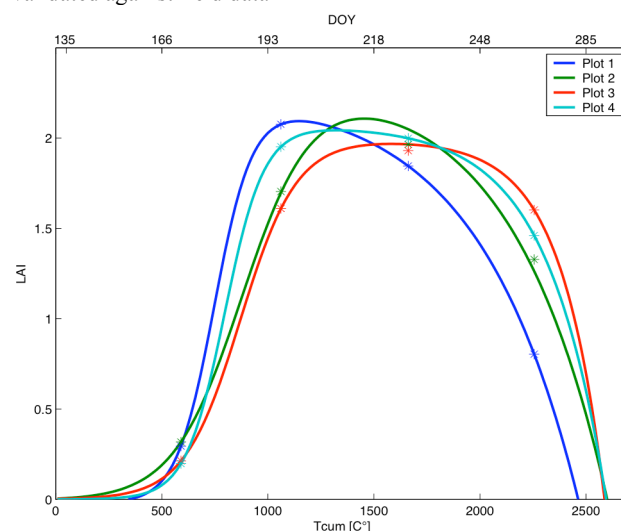


Figure 6. Continuous LAI evolution over the season described by the CSDM fitted to CHRIS observations (\*).

## 5. CONCLUSIONS

The presented analysis of the multi-temporal CHRIS data set focused on the interpretation of HDRF (Hemispherical Directional Reflectance Factor) changes contained in the

various acquisitions over time. A radiative transfer model (RTM) coupled to a canopy structure dynamic model (CSDM) was used to exploit the complementary content in the spectral and temporal information dimensions for the LAI estimation over a maize canopy. The knowledge of the canopy structure dynamic provided by the CSDM is used as ancillary information to achieve an improved robustness of the RTM inversion. Further, the presented coupled models integrate spaceborne remote sensing data with ground meteorological observations providing a continuous LAI time course over the season. Crop growth as well as surface process models require such a continuous description of the vegetation evolution. The presented methodology could also filter effects of poor cloud screening or atmospheric correction affecting operational derived biophysical products. Finally the future exploitation of the off-nadir view angles of CHRIS/PROBA could help to improve the clumping issue affecting the LAI estimation, as row clumping effects are most sensitive to nadir view angles (Lopez-Lozano et al. 2007 (accepted)). The simultaneous exploitation of spectro-directional behaviour of agricultural crops over time, sampled by the CHRIS/PROBA mission, bears thus the potential to improve the estimation of biophysical canopy characteristics relevant for applications such as precision agriculture and ecological modelling. The proposed methodology prepares for the assimilation of remote sensing observations into land surface process models. Nevertheless the effectiveness of such an approach relies on remote sensing data in relatively high temporal frequency at a pertinent spatial resolution. The planned spaceborne missions Rapideye, ESA's SENTINEL2 and Venus will hopefully provide such observations.

#### ACKNOWLEDGEMENTS

The continuous effort and support of ESA and SIRA to provide CHRIS-PROBA data to the community is gratefully acknowledged.

#### REFERENCES

- Bacour, C., Jacquemoud, S., Leroy, M., Hauteceur, O., Weiss, M., Prevot, L., Bruguier, N., & Chauki, H. (2002). Reliability of the estimation of vegetation characteristics by inversion of three canopy reflectance models on airborne POLDER data. *Agronomie*, 22, 555-565
- Baghdadi, N., & Baret, F. (1998). Amérolation du modèle de transfert radiatif SAIL à partir d'un modèle de lancer de rayons: cas du maïs. Avignon: INRA
- Baret, F. (1986). Contribution au suivi radiométrique de cultures de céréales. (p. 182). Paris: Université de Paris-Sud Orsay
- Baret, F., Weiss, M., Troufleau, D., Prevot, L., & Combal, B. (2000). Maximum information exploitation for canopy characterization by remote sensing. *Aspects of Applied Biology*, 60, 71-82
- Barnsley, M.J., Settle, J.J., Cutter, M.A., Lobb, D.R., & Teston, F. (2004). The PROBA/CHRIS mission: A low-cost smallsat for hyperspectral multiangle observations of the earth surface and atmosphere. *Ieee Transactions on Geoscience and Remote Sensing*, 42, 1512-1520
- Brisson, N., Ruget, F., Gate, P., Lorgeau, J., Nicoulaud, B., Tayot, X., Plenet, D., Jeuffroy, M.H., Bouthier, A., Ripoche, D., Mary, B., & Justes, E. (2002). STICS: a generic model for simulating crops and their water and nitrogen balances. II. Model validation for wheat and maize. *Agronomie*, 22, 69-92
- Chen, J.M., Liu, J., Leblanc, S.G., Lacaze, R., & Roujean, J.L. (2003). Multi-angular optical remote sensing for assessing vegetation structure and carbon absorption. *Remote Sensing of Environment*, 84, 516-525
- Combal, B., Baret, F., & Weiss, M. (2002). Improving canopy variables estimation from remote sensing data by exploiting ancillary information. Case study on sugar beet canopies. *Agronomie*, 22, 205-215
- Combal, B., Baret, F., Weiss, M., Trubuil, A., Mace, D., Pragnere, A., Myneni, R., Knyazikhin, Y., & Wang, L. (2003). Retrieval of canopy biophysical variables from bidirectional reflectance - Using prior information to solve the ill-posed inverse problem. *Remote Sensing of Environment*, 84, 1-15
- Delecolle, R., Maas, S.J., Guerif, M., & Baret, F. (1992). Remote-Sensing and Crop Production Models - Present Trends. *Isprs Journal of Photogrammetry and Remote Sensing*, 47, 145-161
- Durand, R., Bonhomme, R., & Derieux, M. (1982). Optimal Base Temperature for Calculating Degree-Day Sums, as Applied to Maize (*Zea-Mays-L.*). *Agronomie*, 2, 589-597
- Duthil, R., Strang, M., Norman, K., Blondlot, A., Gate, P., Baret, F., Fourty, T., Baghdadi, N., Garcia-Sanchez, P., Alarcon, S., Kerdiles, H., Gill, G., Lemoine, G., Deschaux, V., Pinet, P., Poilve, H., & Polverini, U. (1999). PAAGE: Pilot Project for Agriculture and Agri-Environment, (p. 79). Toulouse: Matra Marconi Space
- Espana, M., Baret, F., Chelle, M., Aries, F., & Andrieu, B. (1998). A dynamic model of maize 3D architecture: application to the parameterisation of the clumpiness of the canopy. *Agronomie*, 18, 609-626
- Goel, N., & Thompson, R. (2000). A snapshot of Canopy Reflectance Models and a Universal Model for the Radiation Regime. *Remote Sensing Reviews*, 18, 197-225
- Hesketh, J.D., & Warrington, I.J. (1989). Corn Growth-Response to Temperature - Rate and Duration of Leaf Emergence. *Agronomy Journal*, 81, 696-701
- Jacquemoud, S., & Baret, F. (1990). Prospect - a Model of Leaf Optical-Properties Spectra. *Remote Sensing of Environment*, 34, 75-91
- Kimes, D., Knyazikhin, Y., Privette, J.L., Abuelgasim, A.A., & Gao, F. (2000). Inversion Methods for Physically-based Models. *Remote Sensing Reviews*, 18, 381-439
- Kneubühler, M., Koetz, B., Huber, S., Schopfer, J., Richter, R., & Itten, K. (2006). Monitoring Vegetation Growth using Multitemporal CHRIS/PROBA Data. In, *IEEE IGARSS 2006*. Denver, USA
- Kneubühler, M., Koetz, B., Richter, R., Schaepman, M.E., & Itten, K. (2005). Geometric and Radiometric Pre-processing of CHRIS/Proba over Mountainous Terrain. In, *3rd CHRIS/Proba workshop*. Frascati, Italy: ESA
- Koetz, B., Baret, F., Poilve, H., & Hill, J. (2005). Use of coupled canopy structure dynamic and radiative transfer models to estimate biophysical canopy characteristics. *Remote Sensing of Environment*, 95, 115-124
- Lopez-Lozano, R., Baret, F., Chelle, M., Rochdi, N., & Espana, M. (2007 (accepted)). Sensitivity of gap fraction to maize architectural characteristics based on 4D model simulations. *Agricultural and Forest Meteorology*
- Marloie, O., Kötz, B., Bruguier, N., & Baret, F. (2001). Influence of the wind on canopy reflectance. The case of maize and wheat crops, *ISPRS Symposium on Physical Measurements & Signatures in Remote Sensing*. Aussois
- Matsushita, B., & Tamura, M. (2002). Integrating remotely sensed data with an ecosystem model to estimate net primary productivity in East Asia. *Remote Sensing of Environment*, 81, 58-66
- Moulin, S., Bondeau, A., & Delecolle, R. (1998). Combining agricultural crop models and satellite observations: from field to



regional scales. *International Journal of Remote Sensing*, 19, 1021-1036

Myneni, R.B., Keeling, C.D., Tucker, C.J., Asrar, G., & Nemani, R.R. (1997). Increased plant growth in the northern high latitudes from 1981 to 1991. *Nature*, 386, 698-702

Nelder, J.A., & Mead, R.A. (1965). A simplex method for function optimization. *Computer Journal*, 7, 308-313

Privette, J.L., Morisette, J., Baret, F., Gower, S.T., & Myneni, R.B. (2001). Summary of the International Workshop on LAI Product Validation. *Earth Observer*, 13, 18-22

Richter, R. (1998). Correction of satellite imagery over mountainous terrain. *Applied Optics*, 37, 4004-4015

Toutin, T. (2004). Review article: Geometric processing of remote sensing images: models, algorithms and methods. *International Journal of Remote Sensing*, 25, 1893-1924

Verhoef, W. (1984). Light-Scattering by Leaf Layers with Application to Canopy Reflectance Modelling - the Sail Model. *Remote Sensing of Environment*, 16, 125-141

Verhoef, W. (1985). Earth Observation Modelling Based on Layer Scattering Matrices. *Remote Sensing of Environment*, 17, 165-178

Verhoef, W., & Bunnik, N.J.J. (1981). Influence of crop geometry on multispectral reflectance determined by the use of canopy reflectance models, *Colloquium Signatures Spectrales d'Objets en Télédétection* (pp. 273-290). Les Arcs, France

Weiss, M., Baret, F., Myneni, R.B., Pragnere, A., & Knyazikhin, Y. (2000). Investigation of a model inversion technique to estimate canopy biophysical variables from spectral and directional reflectance data. *Agronomie*, 20, 3-22

Werker, A.R., & Jaggard, K.W. (1997). Modelling asymmetrical growth curves that rise and then fall: applications to foliage dynamics of sugar beet. *Annals of Botany*, 79, 657-665



APPLICATION OF HIGH-RESOLUTION THERMAL INFRARED REMOTE SENSING  
TO ASSESS LAND SURFACE TEMPERATURE AND EMISSIVITY IN DIFFERENT  
NATURAL ENVIRONMENTS

J. A. Sobrino<sup>a,\*</sup>, J. C. Jiménez-Muñoz<sup>a</sup>, M. Gómez<sup>a</sup>, A. Barella-Ortiz<sup>a</sup>, G. Sòria<sup>a</sup>, Y. Julien<sup>a</sup>, M. M. Zaragoza-Ivorra<sup>a</sup>, J. A. Gómez<sup>b</sup>,  
E. de Miguel<sup>b</sup>, M. Jiménez<sup>b</sup>, B. Su<sup>c</sup>, W. Timmermans<sup>c</sup>, J. Moreno<sup>d</sup>, L. Guanter<sup>d</sup> and R. Bianchi<sup>e</sup>

<sup>a</sup>Global Change Unit, Dpt. of Earth Physics and Thermodynamics, Faculty of Physics, University of Valencia, Dr  
Moliner 50, 46100 Burjassot, Spain – (sobrino, jcjm, monica.gomez, abaor, guillems, yves.julien,  
maria.m.zaragoza)@uv.es

<sup>b</sup>Remote Sensing Laboratory, INTA. Carretera de Ajalvir Km 4. Torrejón de Ardoz, 28850, Sapin – (gomezs,  
demiguel, jimenezmm)@inta.es

<sup>c</sup>International Institute for Geo-Information Science and Earth Observation (ITC),  
Enschede, The Netherlands – (b\_su, timmermans)@itc.nl

<sup>d</sup>Laboratory of Earth Observation, Dpt. of Earth Physics and Thermodynamics, Faculty of Physics, University of  
Valencia, Dr Moliner 50, 46100 Burjassot, Spain – (jose.moreno, luis.guanter)@uv.es

<sup>e</sup>Mission Experts Division, EO Science & Applications Department, ESA/ESRIN, Frascati  
(Rome), Italy – remo.bianchi@esa.int

**KEY WORDS:** Land surface temperature, land surface emissivity, thermal infrared, single-channel, two-channel, split-window,  
temperature and emissivity separation, Airborne Hyperspectral Scanner

ABSTRACT:

Airborne thermal infrared image data at high spatial resolution (2-4 m) acquired with the Airborne Hyperspectral Scanner (AHS) over Barrax (Spain), Görmin (Germany) and Cabauw, Loobos and Speulderbos (The Netherlands) were used to study the thermal signatures of land cover types. The processing of the airborne imagery includes atmospheric correction of the AHS thermal infrared (TIR) bands and the retrieval of different biogeophysical variables such as Land Surface Temperature (LST), Land Surface Emissivity (LSE) and Evapotranspiration (ET). The AHS instruments consists of 80 spectral bands which cover the visible and near infrared (VNIR), short wave infrared (SWIR), mid-infrared (MIR) and thermal infrared (TIR) spectral range. This paper is mainly focused on the 10 AHS TIR bands (71 – 80), located in the region between 8 and 13µm, which are used for LST, LSE and ET. The AHS imagery used in this study was acquired in the framework of three different campaigns performed in different natural environments and supported by the European Space Agency (ESA): SEN2FLEX (June and July 2005), AGRISAR (June and July 2006) and EAGLE (July 2006). LST has been retrieved from AHS TIR data using Two-Channel (TC) and TES algorithms, taking into account different band configurations. LSE has been estimated using a simplified approach with the NDVI and also with the TES algorithm. LST and LSE products have been used to retrieve the daily ET applying the simplified SEBI model. The results have been tested against measurements collected in situ, showing errors lower than 2 K for temperature and errors around 1 mm/day for evapotranspiration.

1. INTRODUCTION

Land surface temperature (LST) and land surface emissivity (LSE) are key parameters which can be retrieved from thermal infrared (TIR) data. Hence, except for solar irradiance components, most of the fluxes at the surface/atmosphere interface can only be parameterized through the use of surface temperature. LST can play either a direct role, such as when estimating long wave fluxes, or indirectly as when estimating latent and sensible heat fluxes (Kerr et al., 2004). LST can be also used as an input data in water and energy balance studies, which is an important issue in environmental studies in order to achieve a better understanding on the exchange of heat and moisture between the land surface and lower atmosphere, also leading to a better understanding on the water and carbon cycles. Moreover, many other applications rely on the knowledge of LST (geology, hydrology, vegetation monitoring,

global circulation models, evapotranspiration, etc.). Knowledge of LSE is required to obtain accurate values of LST. Surface emissivities are also indicative of composition for silicate minerals, thus being important for mineral mapping.

Different approaches have been published in the last years in order to retrieve LST and LSE from satellite data. Among these methods, we highlight the single-channel and two-channel or split-window algorithms for LST retrieval, and methods based on NDVI for LSE retrieval, specially designed to be applied to low spectral resolution data. Nowadays, different high spectral and spatial resolution sensors are available, with several thermal bands, as the Advanced Spaceborne Thermal Emission and Reflection Radiometer (ASTER) or the Moderate Resolution Imaging Spectrometer (MODIS) flying in the Terra (or also AQUA for MODIS) satellite, and also different aircraft sensors as the Digital Airborne Imaging Spectrometer (DAIS),

the Airborne Hyperspectral Scanner (AHS) or the future Airborne Reflective/Emissive Spectrometer (ARES). New methods have been developed in order to retrieve LST and LSE from multispectral data, as for example the TES method (Gillespie et al., 1998).

The goal of this paper is to analyze the feasibility of retrieving LST and LSE from AHS thermal infrared data as well as the accuracy obtained depending on the number of thermal bands used. For this purpose, single-channel, split-window and TES algorithms have been applied to AHS data and tested using field measurements collected over different plots. Regarding to the LSE retrieval, methods based on NDVI and also the TES algorithm have been employed. As an example of the application of thermal remote sensing, LST and LSE products were used as input to estimate daily evapotranspiration (ET) using a simplified model. A previous analysis of LST retrieval from AHS data acquired over the agricultural area of Barrax (Spain) in 2004 is presented in (Sobrino et al., 2006a). However, in that paper some calibration problems on the AHS instrument were found, which limited the analysis only to certain thermal bands, and discussion on the emissivity results were not presented. A complete database of AHS imagery acquired in 2005 and 2006 in different natural environments (described in Section 2) with the calibration problems solved will allow us to extract stronger conclusions on the useful of multispectral data in the LST and LSE retrieval topics.

2. DATABASE

2.1 Field Campaigns and Test Sites

The study presented in this paper has been carried out over different natural environments under the umbrella of three funded field campaigns: SEN2FLEX (Spain, 2005), AGRISAR (Germany, 2006) and EAGLE (The Netherlands, 2006). In all these three campaigns several field radiometers were used to measure LST as well as LSE. Field radiometers included single broadband ones (8-13µm) and also two multiband radiometers (model CIMEL), one of them with five TIR narrowbands in coincidence with the ASTER configuration. This instrument was used to retrieve surface emissivities with the TES algorithm applied to ground measurements (Jiménez-Muñoz and Sobrino, 2006). Detailed information of the instrumentation used and the procedure followed to measure LST and LSE can be found for example in Sobrino et al. (2006a, 2006b).

The SENTinel-2 and FLuorescence EXperiment (SEN2FLEX) is a campaign that combines different activities in support of initiatives related both to fluorescence experiments (AIRFLEX) in order to observe of solar induced fluorescence signal over multiple surface targets, and to GMES Sentinel-2 initiative for prototyping spectral bands, spectral widths, and spatial/temporal resolutions to reach mission requirements (<http://www.uv.es/~leo/sen2flex/>). SEN2FLEX was carried out during June and July, 2005, over the agricultural area of Barrax (39°3' N, 2°6' W, 700m), in Albacete (Spain). This experimental area has a flat terrain and a Mediterranean type climate. The soils of the area are *Inceptisols* in terms of soil Taxonomy. About 65% of cultivated lands at Barrax are dryland (67% winter cereals; 33% fallow) and 35% irrigated

land (75% corn; 15% barley/sunflower; 5% alfalfa; 5% onions and vegetables). Three agro-meteorological stations are located in the study area (Moreno et al., 2001).

The lack and urgent need of data for the development and validation of models and inversion algorithms for quantitative crop vegetation and surface parameter estimation under the vegetation layer, has resulted in the AGRISAR campaign. Since the understanding of bio/geo physical parameter retrieval from multi-parameter SAR as well as the direct modelling in the domain of agricultural cultivation for vegetated and non-vegetated crop fields is still unsatisfactorily, and appropriate data for their evaluation is missing, the campaign's main aim is to build up a data base for the investigation and validation of the retrieval of bio-/geo-physical parameters, obtained at different radar frequencies (X-, C- and L-Band) and at thermal as well as hyperspectral optical bands acquired over vegetated and non-vegetated agricultural fields. The Demmin test site (Görmin farm, 53°59.5' N, 13°16.5'E, 15m) is located in Mecklenburg-Vorpommern in North-East Germany, approximately 50km north of Neustrelitz and 150km north of Berlin. It is based on a group of farms, covering approximately 25,000 ha, being the main crops wheat, winter barley, winter rape, maize and sugar beet.

The EAGLE2006 campaign was carried out in order to collect data to make a profound study of bio-geophysical parameter retrieval from multi-parameter optical and SAR data as well as the direct modelling of the underlying physical processes in forests and grassland. The use of different airborne sensors, the acquisition of multi-angle and multi-sensor satellite data, as well as the procurement of a great amount of simultaneous ground measurements, lead to one of the campaign's main aim: build up a data base for the investigation and validation of the retrieval of the above mentioned parameters. It took place, from the 8th of June until the 2nd of July 2006, over central parts of the Netherlands, being these ones the grassland site at Cabauw (51°58' N, 4°54' E, 0m) and two forest sites at Loobos (52°10.03' N, 5°44.6' E, 52m) and Speulderbos (52°15.14' N, 05°41.43' E, 52m). Some characteristics are a yearly precipitation around 750 mm and a yearly average temperature about 10° Celsius.

2.2 AHS imagery

The Airborne Hyperspectral Scanner AHS (developed by SensyTech Inc., currently ArgonST, USA) is operated by the Spanish Institute of Aeronautics (INTA). It has 80 spectral bands in four ports (VNIR, SWIR, MWIR and TIR). This study is focused on the exploitation of the 10 AHS TIR bands ranging from 71 to 80.

In SEN2FLEX, AHS flights took place on June 1st, 2nd and 3rd and July 12th, 13th and 14th 2005. In AGRISAR, flights were carried out on June 6th and 10th and July 4th and 5th 2006. During EAGLE, flights took place on June 13th 2006. AHS flights were carried out at two nominal altitudes, 975m (low flight) and 2740 m (high flight) above ground level. Other altitudes were also considered due to operational reasons. The following total amount of AHS imagery is available: 24 images for SEN2FLEX-2005, 48 images for AGRISAR-2006 (6 of them not geo-referenced due to a technical problem) and 13 images for EAGLE-2006. AHS images are provided in level 1b

(at-sensor radiance) with IGM files for geometric correction. In addition, level 2b products of land surface temperatures and at-surface reflectances were provided by INTA for the AGRISAR campaign. These products were obtained using ATCOR -4 software developed by Richter (DLR).

3. LAND SURFACE TEMPERATURE AND EMISSIVITY RETRIEVAL

Three different algorithms/methods have been considered for retrieving the LST from the AHS data:

- i) Single-Channel (SCh) method, which uses only one thermal band and LST is retrieved from inversion of the radiative transfer equation,
- ii) two-channel or split-window technique (SW), in which LST is retrieved from a combination of two thermal bands,
- iii) Temperature and Emissivity Separation (TES) algorithm, developed by Gillespie et al. (1998).

The application of these algorithms to AHS data acquired in July-2004 is presented in detail in Sobrino et al. (2006a). A complete description of the application of these methods to the AHS imagery acquired during SEN2FLEX can be found in Jiménez-Muñoz et al. (2006). In that paper, the algorithms were validated against 97 values of surface temperature measured in situ over different crops (water, wheat, grass, corn, vineyard, bare soil). The results showed low bias (<0.4 K) and Root Mean Square Errors (RMSE) lower than 1.8 K.

LSE required in split-window algorithms was estimated from the NDVI, as indicated in Jiménez-Muñoz et al. (2006). LSE was also estimated with the TES algorithm.

As an example, Figure 1 shows LST maps obtained with a split-window algorithm applied to AHS bands 75 and 79 and LST maps produced with the TES algorithm for the SEN2FLEX-2005 campaign. Figure 2 shows an example of the LST product provided by INTA for AGRISAR-2006, whereas Figure 3 shows a LST map obtained with the TES algorithm for EAGLE-2006. Land surface emissivity maps obtained with the TES algorithm for different AHS bands over a sand site (EAGLE-2006) are shown in Figure 4.

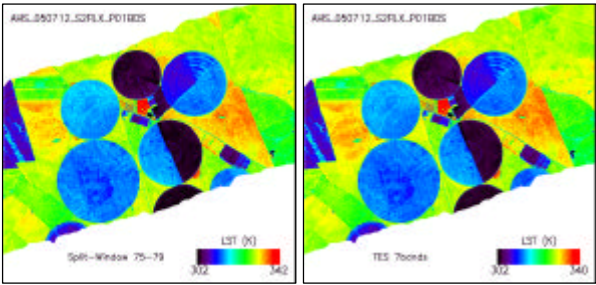
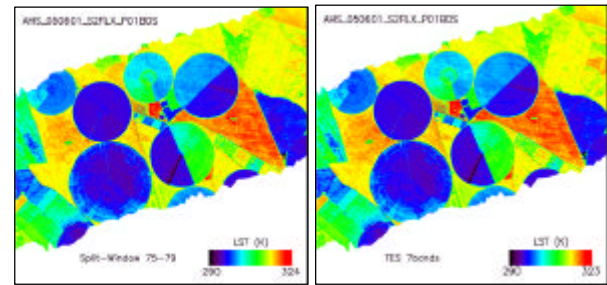


Figure 1. Land Surface Temperature maps obtained from AHS data with split-window and TES algorithms during the SEN2FLEX-2005 campaign.

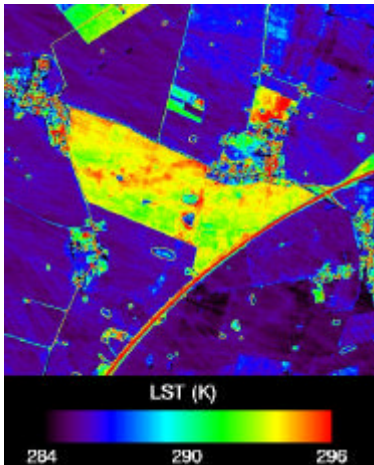


Figure 2. Land Surface Temperature product provided by INTA for the AGRISAR-2006 campaign.

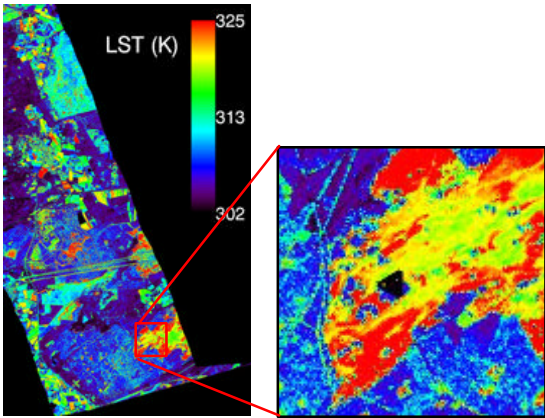


Figure 3. Land Surface Temperature map obtained from AHS data acquired during EAGLE-2006 and using the TES algorithm. The resized image corresponds to a sand site.



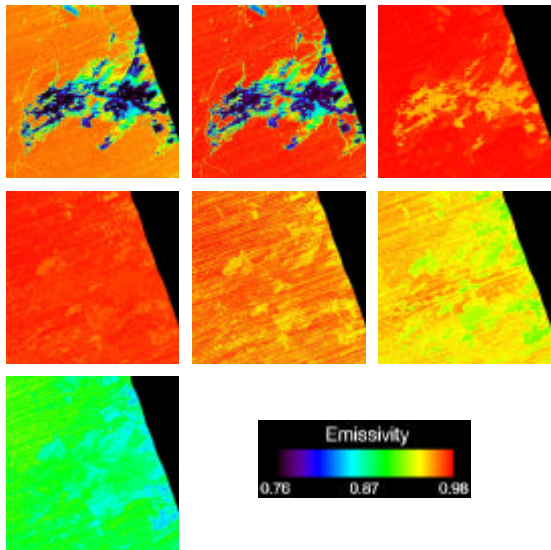


Figure 4. Land Surface Emissivity maps obtained with the TES algorithm for the sand site (see Figure 3). From left to right, images correspond to AHS bands 72, 73, 75, 76, 77, 78 and 79.

4. SIMPLIFIED METHOD FOR EVAPOTRANSPIRATION RETRIEVAL

In this paper, daily ET has been retrieved according to the methodology presented in Sobrino et al. (2005) and Gómez et al. (2005). It is based on the Simplified Surface Energy Balance Index (S-SEBI) model (Roerink et al., 2000), which solves the energy balance equation using the evaporative fraction concept.

Daily ET was retrieved from AHS data acquired during SEN2FLEX-2005 as explained in Jiménez-Muñoz et al. (2006). Values were tested against in situ measurements collected in a lysimeter station of festuca (14 test points), with a bias of 0.2 and RMSE of 1.1 mm/day. Figure 5 shows some examples of daily ET maps obtained from AHS data acquired during the SEN2FLEX-2005 campaign.

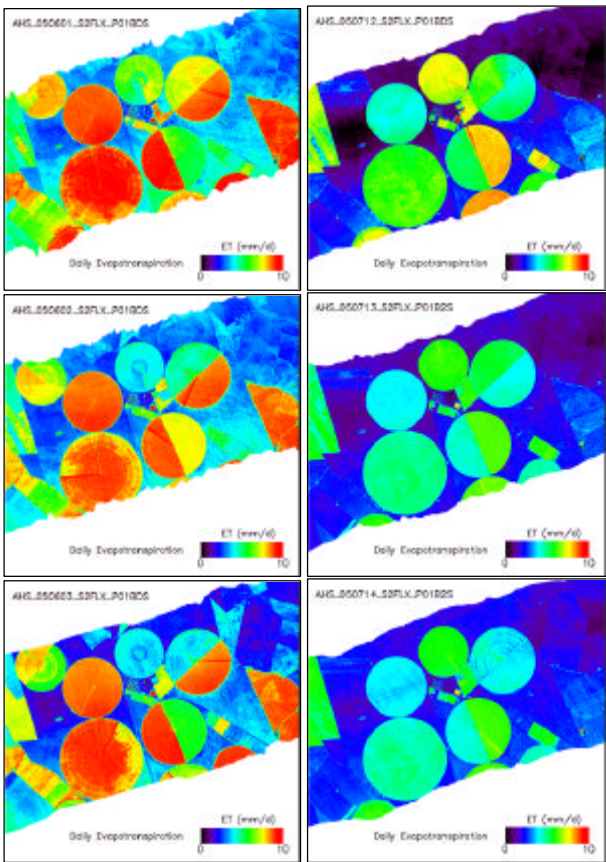


Figure 5. Daily Evapotranspiration maps obtained from AHS data acquired during the SEN2FLEX-2005 campaign.

5. CONCLUSIONS

Land Surface Temperature, Land Surface Emissivity and Daily Evapotranspiration have been retrieved from AHS data acquired in 2005 and 2006 in the framework of three different campaigns (SEN2FLEX, AGRISAR, EAGLE) carried out in different natural environments. Accuracies for LST are below 2 K (typically around 1.5 K), whereas errors for evapotranspiration are around 1 mm/day. All these variables, which are of interest in different environmental applications, have been retrieved mainly from thermal infrared data, so we claim the availability of multispectral TIR capabilities in future Earth Observation sensors.

Future work of the authors includes the processing of the complete AHS imagery, with a total amount of around 80 images, which will allow us to extract conclusions regarding the accuracy of the LST and LSE depending of the methods and number of TIR bands used.

6. ACKNOWLEDGEMENTS

We wish to thank the European Union (EAGLE project; SST3-CT-2003-502057), the Ministerio de Ciencia y Tecnología (DATASAT project; ESP2005-07724-C05-04) and the Generalitat Valenciana (Conselleria d'Empresa, Universitat i Ciència, project ACOMP06/219) for their financial support, and the European Space Agency (ESA) for the support in all the experimental field campaigns.

7. REFERENCES

Gillespie, A., Rokugawa, S., Matsunaga, T., Cothern, J. S., Hook, S., and Kahle, A. B., 1998. A temperature and emissivity separation algorithm for advanced spaceborne thermal emission and reflection radiometer (ASTER) images. *IEEE Transactions on Geoscience and Remote Sensing*, 36, pp. 1113-1126.

Gómez, M., Sobrino, J. A., Oliso, A., and Jacob, F., 2005. Retrieval of evapotranspiration over the Alpillés/ReSeDA experimental site using airborne POLDER sensor and Thermal Camera. *Remote Sensing of Environment*, 96(3-4), pp. 399-408.

Jiménez-Muñoz, J. C., and Sobrino, J. A., 2006. Emissivity spectra obtained from field and laboratory measurements using the temperature and emissivity separation algorithm. *Appl. Opt.*, 45(27), pp. 7104-7109.

Jiménez-Muñoz, J. C., Sobrino, J. A., Gómez, M., Barella-Ortiz, A., Fernández, G., Guanter, L., and Moreno, J., 2006. Processing of the AHS VNIR and TIR data for surface temperature/emissivity and evapotranspiration retrieval. In: *Proceeding of SEN2FLEX*, Holland, published on CD-ROM.

Kerr, Y. H., Lagouarde, J. P., Nerry, F., and Ottlé, C., 2004. Land surface temperature retrieval techniques and applications: case of AVHRR. In: *Thermal Remote Sensing in Land Surface Processes*, D. A. Quattrochi y J. C. Luvall (eds), CRC Press, Florida, USA, pp. 33-109.

Moreno, J., Caselles, V., Martínez-Lozano, J. A., Meliá, J., Sobrino, J. A., Calera, A., Montero, F., and Cisneros, J. M., 2001. The Measurements Programme at Barrax. In: *DAISEX Final Results Workshop*, Holland, pp. 43-51.

Roerink, G., Su, Z., and Menenti, M., 2000. S-SEBI: A Simple Remote Sensing Algorithm to Estimate the Surface Energy Balance. *Phys. Chem. Earth (B)*, 25(2), pp. 147-157.

Sobrino, J. A., Gómez, M., Jiménez-Muñoz, J. C., Oliso, A., and Chehbouni, G., 2005. A simple algorithm to estimate evapotranspiration from DAIS data: Application to the DAISEX Campaigns. *Journal of Hydrology*, 315, pp. 117-125.

Sobrino, J. A., Jiménez-Muñoz, J. C., Zarco-Tejada, P. J., Sepulcre-Cantó, G., and de Miguel, E., 2006a. Land surface temperature derived from airborne hyperspectral scanner thermal infrared data. *Remote Sensing of Environment*, 102, pp. 99-115.

Sobrino, J. A., Cuenca, J., Soria, G., Jiménez-Muñoz, J. C., Gómez, M., Zaragoza, M., Romaguera, M., Julien, Y., Shen, Q., Barella-Ortiz, A., Morales, L., Gillespie, A., Balick, L., Peres, L., Libonati, R., Nerry, F., and Fortier, M., 2006b. Thermal Remote Sensing in the Framework of the Sen2flex Project: Field Measurements, Airborne Data and Applications. In: *Second Advances in Quantitative Remote Sensing*, Valencia (Torrent), Spain, pp. 142-146.



# ANGULAR UNMIXING OF PHOTOSYNTHETIC AND NON-PHOTOSYNTHETIC VEGETATION WITHIN A CONIFEROUS FOREST USING CHRIS-PROBA

J. Verrelst<sup>a,\*</sup>, R. Zurita-Milla<sup>a</sup>, B. Koetz<sup>b</sup>, J.G.P.W. Clevers<sup>a</sup>, M.E. Schaepman<sup>a</sup>

<sup>a</sup>Centre for Geo-Information, Wageningen UR, Wageningen, The Netherlands – (Jochem.Verrelst, Raul.Zurita-Milla, Jan.Clevers, Michael.Schaepman)@wur.nl

<sup>b</sup>Remote Sensing Laboratories (RSL), Dept. of Geography, University of Zürich, Switzerland – bkoetz@geo.unizh.ch

Commission VII, WG VII/1

**KEY WORDS:** Non-Photosynthetic Vegetation, spectral unmixing, FLIGHT, multiangular, vegetation structure, PV, NPV

## ABSTRACT:

Estimating forest variables, such as photosynthetic light use efficiency, from satellite reflectance data requires understanding the contribution of photosynthetic vegetation (PV) and nonphotosynthetic vegetation (NPV). The fractions of PV and NPV present in vegetation reflectance data are typically controlled by the canopy structure and the respective viewing angle. The persistent but highly varying anisotropic behaviour of the forest canopy implies that there is canopy structural information to be exploited from multi-view angles measurements. In this work, a combination of radiative transfer modelling (FLIGHT) and linear unmixing techniques were used to isolate angular PV and NPV fractions from multi-angular CHRIS-PROBA (Compact High Resolution Imaging Spectrometer-Project for On-board Autonomy) data in order to assess their effects on a suite of vegetation indices. Angular variability in the NIR wavelengths contributed most to the angular change in PV and NPV fractions. In turn, for those pixels where the NPV fractions from near-nadir to backscatter were increasing, moderate correlations were found with the angular variability of the calculated vegetation indices. From these fractions, a Normalized Difference NPV Index (NDNPVI) was developed as a proxy for volumetric canopy composition.

## 1. INTRODUCTION

This study begins with the assumption that pixel level canopy reflectance of a terrestrial ecosystem typically consists of a proportion of Photosynthetic vegetation (PV) and a proportion of Non-Photosynthetic Vegetation (NPV: parts/ canopy components that lack chlorophyll, such as dry leaf matter, bark, wood, and stems) and eventually rock and bare soil. The fractional extent of vegetation into PV and NPV is important from biophysical and biogeochemical perspectives (Defries et al. 1999), as well as to understanding climate and land-use controls (Asner and Heidebrecht 2002). Many approaches have been developed to analyze PV, NPV and bare soil. A problem hereby is that the typical spectral regions used to detect PV – the visible and the NIR wavelengths (0.4-1.3  $\mu\text{m}$ ) - do not easily separate the individual contribution of NPV and bare soil to the measurement (van Leeuwen and Huete 1996, Roberts et al. 1998). Alternatively, spectral mixture analysis was developed to decompose image pixels into its pure constituent (Settle and Drake 1993, Adams et al. 1995). As such, pixel level reflectance can be described by a spectral mixture model in which a mixed spectrum is represented as a linear combination of pure spectra, called endmembers (EMs):

$$R(\lambda)_{\text{pixel}} = f_{\text{PV}}R(\lambda)_{\text{PV}} + f_{\text{NPV}}R(\lambda)_{\text{NPV}} + f_{\text{soil}}R(\lambda)_{\text{soil}}$$

$$\text{and } f_{\text{PV}} + f_{\text{NPV}} + f_{\text{soil}} = 1, \quad (1)$$

where  $f_{\text{PV}}$ ,  $f_{\text{NPV}}$ ,  $f_{\text{soil}}$  are the fractions of PV, NPV and soil respectively,  $R(\lambda)$  is the reflectance of each land-cover endmember at wavelength  $\lambda$ . Regarding forested surfaces, it is commonly the case that bare soil or rocks are absent in a pixel but are replaced by understory (e.g. grass or herbaceous

vegetation) or litter cover. Then, a further simplification can be made, namely,

$$R(\lambda)_{\text{pixel}} = f_{\text{PV}}R(\lambda)_{\text{PV}} + (1 - f_{\text{PV}})R(\lambda)_{\text{NPV}} \quad \text{and} \quad 0 \leq f_{\text{PV}} \leq 1. \quad (2)$$

Further, although often ignored in nadir remote sensing, sun/view geometry has a great influence on the observed reflectance of a surface, which is described by its bidirectional reflectance distribution function (BRDF). The magnitude and shape of the BRDF is governed by the composition, density, optical properties and geometric structure of the vegetation canopy. It are these BRDF effects that triggered the current advances in multi-angular remote sensing. Recently numerous studies have demonstrated that measurements from multiple view-angles (e.g. CHRIS-PROBA, MISR) can provide additional surface properties at subpixel scale (e.g. Diner et al. 1999, 2005 Widlowski et al. 2004).

Being aware of multiple viewing angles, consider, for example, the following situation where the sensor remains pointed towards a forested ecosystem but gradually overpasses from nadir to more oblique views while taking consecutive snapshots. Then not only the observed PV and NPV proportions might change per image but also, depending on forward scatter or backscatter observations, the PV and NPV spectra are equally subject to change (e.g. predominantly shaded conditions vs. predominantly sunlit conditions).

EMs are usually obtained from spectral libraries or from the images themselves (e.g. Ichoku and Karnieli 1996). Regarding the BRDF effects, extracting EMs from each angular scene would be the most adequate but it is impossible to encounter pure pixels in a forested scene (e.g. NPV). To bypass this limitation in this study, a radiative transfer model was used that

\* Corresponding author

realistically describes the physics of canopy reflectance based on abstraction of the canopy. With such a model the reflectance of a purely vegetated canopy (PV) and a purely woody canopy (NPV) can be reasonably simulated. Modelled PV and NPV reflectance trends both in the spectral and angular domain, expressed by the bidirectional reflectance factor (BRF), were proposed to act as EMs. The hybrid 3-D radiative transfer/geometric Forest Light (FLIGHT) canopy model based on Monte Carlo simulation of photon transport (North 1996) was used for this purpose.

The objective of this study is: (1) to assess how fractional coverage of PV or NPV responds to changing viewing angles by using linear unmixing, and: (2) how such effects are related to single reflectance bands and vegetation indices. In forest canopies, woody material plays a small but significant role in determining reflectance, especially those with leaf area index (LAI) <5.0 (Asner 1998). However, the author advocated that this is also dependent on the location of woody material within the canopy.

This study is focused on coniferous forests where the woody material (stem) is well separated from the vegetated crown. We hypothesize therefore that at greater viewing angles a greater proportion of NPV in the reflectance signal will become apparent due to a greater contribution of woody stems. This is especially probable in sparse coniferous stands and when observed in backscatter direction where the influence of shadowing is reduced.

2. METHODOLOGY

We address two approaches to test the above hypothesis: (1) a modelling exercise that mixes the pure BRFs into various canopy reflectances and (2), a linear unmixing exercise that uses five consecutive Compact Higher Resolution Imaging Spectrometry (CHRIS) images from five different viewing angles during a single overpass of an alpine forested ecosystem (hereafter, referred to as *angular unmixing*). In an earlier study using CHRIS (Verrelst et al. 2007) it appeared that vegetation indices shows a pronounced anisotropic behaviour, especially the light use efficiency indices. It was suggested that an eventual increased proportion of woody material could significantly affect those photosynthetic-sensitive VIs. The modelling exercise will validate this assumption by mimicking each VI with increasing NPV proportions at greater viewing angles, while the angular unmixing exercise will verify whether this assumption holds true when using the original CHRIS data.

2.1 Data and study site

CHRIS mounted onto Project for On-board Autonomy (PROBA) offers ideal opportunities to assess the effects of changing composite proportions over varying angles. Its specifications are shown in table 1. The used CHRIS image set, acquired on June 27 2004 10:41h AM local time under partly cloudy conditions (1/8<sup>th</sup> cloud cover) was geometrically and radiometrically corrected following an approach dedicated for rugged terrains (Kneubühler et al. 2005). The test site has a geometric accuracy for the five scenes of 1-2 pixels. The generated ‘surface reflectance’ represents hemispherical-directional reflectance factor (HDRF) (Schaeppman-Strub et al. 2006). Due to the cloud contamination the +55° scene was discarded in further analysis. The +21° scene is the (near-) nadir scene while the -55° scene happened to be viewing predominantly back scattering (figure 1).

Sampling	Image area	Spectral bands	Spectral range
~17 m @ 556 km altitude	13 x 13 km (744 x 748 pixels)	18 bands with 6-33nm width	447-1035 nm

Table 1. CHRIS configurations for Land Mode 3

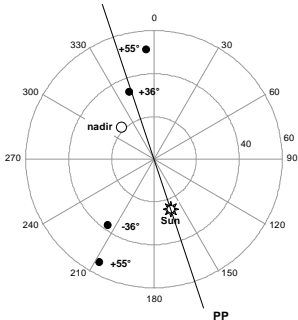


Figure 1. Polar plot of CHRIS acquisition and illumination geometry as of June 27, 2004. PP: principal plane

The study site is located in the eastern Ofenpass valley, which is part of the Swiss National Park (SNP) in South East Switzerland (10°13'48"E/46°39'45"N). The Ofenpass represents a dry inner-alpine valley with rather limited precipitation (900-1100 mm/a) on an average altitude of about 1900 m a.s.l.. The south-facing slope of the Ofenpass valley is considered as the core test site. The relatively flat part down-hill (slope < 10°), which consists of old-growth coniferous forest and an alpine meadow, were chosen as study site to assess angular PV and NPV proportions.

The evergreen coniferous forest is dominated by mountain pine (*Pinus Montana ssp. arborea*). The forest is characterized by varying density and a relatively high woody fraction (ca. 30%) due to the advanced age of the pine forest and nature management practice that stopped 70 years ago. Average LAI is 2.2 (1.0 SD). The forest ecosystem can be classified as woodland associations of *Erico-Pinetum mugo*. The understorey is characterized by low and dense vegetation composed mainly of *Vaccinium*, *Ericaceae*, and *Seslariaia* species

2.2 FLIGHT modelling

With FLIGHT, evaluation of BRF is achieved by ray tracing the photon trajectory within the discontinuous environment of a simulated forest canopy. The model allows the representation of complex vegetation structures and a correct treatment of spectral mixing resulting from multiple scattering within the scene. FLIGHT simulates a 3D forest canopy by geometric primitives with defined shapes and positions of individual stands with associated shadow effects. Within each crown envelope foliage is approximated by volume-averaged parameters with optical properties of both leaf and woody scattering elements (North 1996).

We simulated canopy reflectance of an exclusive PV and an exclusive NPV forest scene as a function of canopy variables and CHRIS acquisition geometries. The main difference between the PV and NPV simulations are that in the PV case each crown envelope (cone) represents 100% foliage, while in the NPV case each cone represents 100% bark. As input for FLIGHT averaged field measurements were used based on surveys in 4 core test sites within the forest (see table 2). The foliage optical properties were modelled by PROSPECT and coupled with FLIGHT (Kötz et al. 2004) while the spectral properties of the woody parts and background were characterized by spectrometric field measurements. Since

background is equally a mixture of PV and NPV signals (e.g. shrubs, litter) alternatively we also modelled an ‘extreme’ PV scene with background consisting of purely foliage reflectance and an ‘extreme’ NPV scene with background consisting of purely bark reflectance (see figure 2). The resultant BRF’s will act as synthetic endmembers.

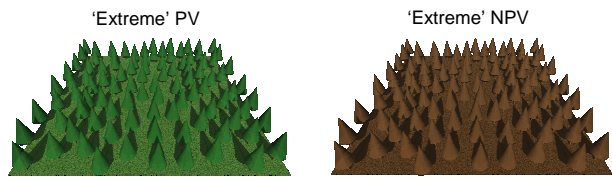


Figure 2: Visualization of a rendered purely PV canopy and a purely NPV canopy

The generated BRF’s will also be used to realize the inverse of linear unmixing. By mixing both modelled spectra in various mixtures at varying viewing angles, more natural forest canopy reflectances can be simulated. Having then PV and NPV proportions controlled, finally the angular response of vegetation indices can be assessed.

Prior to such mixing, we tested whether this straightforward approach does not conflict with the basic physical assumption of linear unmixing. This assumption states that there is not a significant amount of photon multiple scattering between macroscopic materials, in such a way that the flux received by the sensor represents a summation of the fluxes from the cover types and the fraction of each one is proportional to its covered area (Camacho-De Coca 2004). However, when photons interact with vegetation components in vertical space reflectance has the potential of becoming nonlinear (Myneni et al. 1989, Borel and Gerstl 1994). The complex FLIGHT model is specifically designed to trace these scattering trajectories depending on how each macroscopic or foliage microstructure is defined. But with the PV-NPV approach, a second problem arose due to the different nature of both constituents. A crown of 100% PV foliage propagates photons and causes further within-crown multiple scattering whereas a crown built of 100% opaque NPV foliage inhibits any further transmittance.

We compared therefore for two wavelengths ( $R_{531}$  and  $R_{570}$ ) how (post-modelling) mixed BRF signals differed with the resulted BRFs of simulated likewise mixed (pre-modelling) PV-NPV crown envelopes, while keeping the other parameters constant. As outcome of this small exercise it appeared that the BRF mixtures were conform with the BRFs of the simulated mixed PV-NPV crown envelopes (RMSE: 0.022, no significant difference found with a student’s  $t$ -test). This justifies the approach of post-modelling PV-NPV mixtures without having to rerun the radiative transfer code. Nevertheless, it has to be tested whether this apparent linearity is also valid for other wavelengths.

Name	Value/ Range	PV	NPV
Fractional cover (%)	0.64		
Leaf Area Index	2.4		
Fraction of green foliage (%)		100%	0%
Fraction of bark (%)		0%	100%
Soil		Vegetation	bark
Incident zenith (°), $\theta_i$	24.0		
Reflected zenith (°), $\theta_r$	-54.6, -37.8, +21.2 (nadir), +33.3, +51.1		

Table 2. Averaged input variables for FLIGHT based on surveys at 4 test sites. (Remaining input variables are described in Kötz et al. 2004)

3. RESULTS AND DISCUSSION

3.1 Comparison VIs: FLIGHT vs CHRIS

Figures 3a and 3c show the angular shapes of the Structure Invariant Pigment Index [SIPI:  $(R_{800} - R_{455}) / (R_{800} + R_{705})$ ] and the Anthocyanin Reflectance Index [ARI:  $(R_{550})^{-1} - (R_{700})^{-1}$ ] that were calculated from CHRIS forest HDRFs. Figure 3b and 3d show the same indices calculated from the modelled BRFs according to the sun/view geometry of CHRIS. These graphs encompass various mixtures of PV and NPV proportions (%NPV= 100-%PV) with increasing NPV values at greater angles. The outer lines are the extremes: the VI response for the exclusively simulated PV forest (blue line), and the VI response for the exclusively simulated NPV forest (pink line). To facilitate comparison each index was normalized against its nadir value, or in case of the simulations, the nadir value of 100% PV.

The modelling examples confirmed earlier observations that while some indices are extremely sensitive to viewing angles, other indices respond rather invariant (Verrelst et al. 2007). In turn, it also confirmed the hypothesis that the magnitude of NPV proportion in the signal governs the VI response. By varying the proportions of NPV at greater viewing angles, a shape was attained which is likewise to that for the VIs calculated by CHRIS. Regarding other VIs the same trend was noted (not shown here), although some VIs matched better than others (for a list of the VIs and formulas see table 3). In conclusion, these examples provided a firm basis that increased NPV at greater viewing angles exert influence on the VI response.

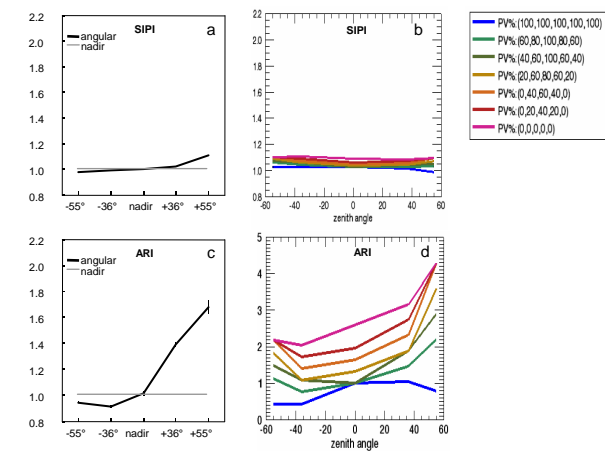


Figure 3. Averaged angular VIs (SIPI, ARI) from forest acquired by CHRIS (a, c). VIs derived from combined FLIGHT-BRFs with varying proportions of PV and NPV along the CHRIS viewing geometry (b, d). (%NPV=100-%PV)

3.2 Constrained angular unmixing of CHRIS data

The second part of the study enclosed the angular spectral unmixing. Thereby, the unmixing was forced to be fully constrained (Eq. 2). This guaranteed a physical interpretation of the results since the fractions sum up to 100% and all the fractions are positive. Linear spectral unmixing provided two main outputs: the sub-pixel fractional land cover composition itself and the spectral root mean square error (RMSE) per pixel. The RMSE was used to analyze the performance of the spectral unmixing when removing bands (Zurita-Milla et al. 2007). CHRIS bands 1 and 2 (centered around 442 and 490 nm) were

omitted, as they are very susceptible to aerosol scattering. Bands 17 and the last band (centered around 905 and 1019 nm) were also excluded because these coincide with the absorption features of oxygen and water vapour; thus not adding relevant information to forest cover interpretation. The removal of these bands resulted in a RMSE of less than 5%.

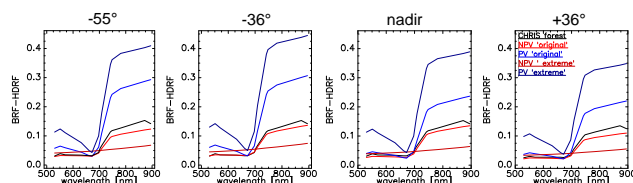


Figure 4. Angular endmembers (BRFs), plus a signature of an average forest canopy at CHRIS acquisition geometries.

Figure 4 shows a typical forest canopy reflectance of the 4 angular scenes plus the retrieved EMs. In general, CHRIS reflectance appeared to be considerably lower than the EMs. This is especially notable for the 'original' (background from spectrometric field measurements) NPV-EM that appears to be similar to an average CHRIS forest signature. Here, the rather vegetated background spectra dominated the canopy reflectance of the simulated NPV scene. Consequently the NPV fractions were overestimated. To correct for this, alternative 'extreme' scenes were simulated to ensure that the background was pure in both cases. In spite of these adjustments, however, NPV overestimation remained.

Apart from nonlinearity, the impression arose that endmember uncertainty is playing a crucial role when applying modelled EMs in satellite data unmixing. Reasons of EM uncertainty are: (1) variability in spectrometric field measurements, (2) variability in model parameters, (3) model simplifications, and (4) mismatch between BRF (FLIGHT) and HDRF (CHRIS).

Although endmember uncertainty inhibits reliable measures, yet with BRDF-adapted EMs it is assumed that the degree of error will be the same for all angular scenes. Subsequently, the *quantity of change* from one unmixed angular scene towards another unmixed scene is considered as a more reliable measure. More appealing therefore is to compare the effect of NPV change ( $\Delta$ NPV) to change in a single waveband ( $\Delta$ HDRF <sub>$\lambda$</sub> ) or a derived VI ( $\Delta$ VI). Change is defined as the normalized % difference of -55° value compared to the nadir value. E.g. for  $\Delta$ NPV:

$$\Delta\text{NPV} = \frac{\text{NPV}_{-55^\circ} - \text{NPV}_{\text{nadir}}}{\text{NPV}_{\text{nadir}}} * 100\% . \quad (4)$$

Figure 5 shows two examples of scatter plots where the normalized  $\Delta$ NPV is plotted against the normalized  $\Delta$ HDRF (of the wavebands 570 nm and 748 nm). Pixels plotted along the positive x-axis represent an increase in observed NPV, while negative values along the x-axis represent a decrease of observed NPV and thus an increase in PV. The square Pearson correlation coefficients  $r^2$  are shown in the graphs. Following, for each waveband a linear regression and correlation coefficient with  $\Delta$ NPV was calculated and then plotted (figure 6). The unmixing with the 'extreme' EMs resulted in higher correlations. Particularly in the NIR wavelengths high  $r^2$ 's were reached. In the NIR domain, scattering is very high and constitutes the main source of radiation flow with maximal interactions, such that an angular change in canopy composition will lead to a pronounced change in angular outflow.

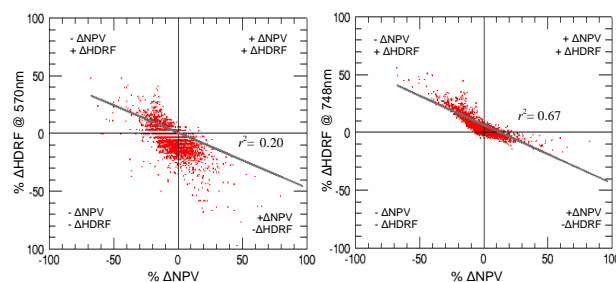


Figure 5. Scatter plots of %  $\Delta$ NPV compared to %  $\Delta$ HDFR for waveband 570 nm and 748 nm

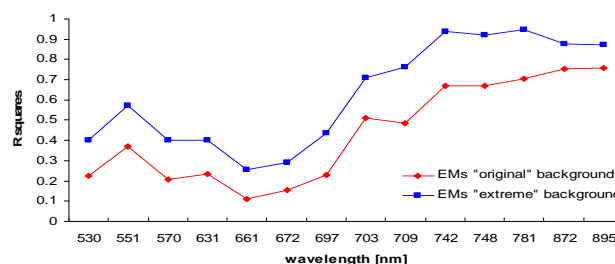


Figure 6. The  $r^2$ 's of the linear regression when correlating  $\Delta$ NPV with  $\Delta$ HDFR

Linear regression relationships were in table 3 in an analogous way calculated for scatter plots of  $\Delta$ NPV against a suite of VIs ( $\Delta$ VI). Correlations were weak when considering the complete data set ( $r^2_{\text{max}}=0.21$ ). When splitting the data set into (i) pixels where a PV increase occurred (more vegetation observed at -55°), and (ii) pixels where a NPV increase occurred (more woody parts observed at -55°), then better correlations revealed (table 3). Poor correlations were found in case of the increasing PV proportions ( $r^2_{\text{max}}=0.10$ ). Yet, in case of increasing NPV proportions remarkably higher correlations were yielded. In the latter, apart from PRI and RGRI, NPV differences captured about one third of the VI variance ( $r^2$ 's between 0.24 and 0.47).

NPV effects significantly affected the reflectance signal, though since validation data is absent, results ought to be interpreted with care. Nonlinearity and EM uncertainty are undermining the applied angular unmixing approach. Generating EMs by means of forward radiative transfer modeling is advantageous with respect to controlling BRDF variables, but it also has its limitations. For instance FLIGHT does not account for within-shoot scattering, which causes the low NIR reflectance in coniferous areas (Rautiainen & Stenberg 2005). Also, understory vegetation, which can be very abundant and variable and can considerably influence the reflected signal of the stand (Rautiainen 2005), was simply generalized in this study.

To reduce EM uncertainty, rather than relying on one generalized set of EMs, further research would be through the generation of EM sets that cover a range of spectral variability according to the satellite data (Asner & Lobell 2000). Embedding a set of PV and NPV endmembers in the unmixing procedure will lead to a set of PV and NPV fractions which can afterwards be aggregated again to single PV and NPV fractions. Another approach worthwhile to explore is to apply a so-called 'spatial unmixing'. In spatial unmixing the EMs are selected on a high resolution image while, by means of fusion, the spectral resolution is obtained from the original low resolution image (Zurita-Milla et al., 2006). This technique could solve the EM uncertainty for the image with the same geometry conditions (e.g. nadir), but does not apply to other viewing angles due to the aforementioned BRDF effects. Combining spatial unmixing

Index	Formula	$r^2$			
		+ %PV 'original'	+ %PV 'extreme'	+ %NPV 'original'	+ %NPV 'extreme'
NDVI	$(R_{NIR} - R_{RED}) / (R_{NIR} + R_{RED})$	0.00	0.00	0.42	0.45
SRI	$R_{NIR} / R_{RED}$	0.03	0.03	0.39	0.39
ARVI	$(R_{NIR} - (2R_{RED} - R_{BLUE})) / (R_{NIR} + (2R_{RED} - R_{BLUE}))$	0.02	0.02	0.39	0.45
NDVI <sub>705</sub>	$(R_{750} - R_{705}) / (R_{750} + R_{705})$	0.00	0.00	0.27	0.24
mSRI <sub>705</sub>	$(R_{750} - R_{445}) / (R_{705} + R_{445})$	0.03	0.04	0.19	0.24
mNDVI <sub>705</sub>	$(R_{750} - R_{705}) / (R_{750} + R_{705} - R_{445})$	0.03	0.04	0.20	0.25
PRI	$(R_{531} - R_{570}) / (R_{531} + R_{570})$	0.01	0.00	0.00	0.01
SIPI	$(R_{800} - R_{455}) / (R_{800} + R_{705})$	0.05	0.06	0.25	0.32
RGRI	Mean of all bands in the red range divided by the mean of all bands in the green range	0.01	0.00	0.03	0.03
ARI	$(R_{550})^{-1} - (R_{700})^{-1}$	0.10	0.08	0.43	0.47

Table 3. Definition of VIs evaluated and  $r^2$ 's of selected VIs when separating the data pool in +%PV and +%NPV

with a model-generated BRF variability to correct for the angular images will be tackled in a follow-up study.

3.3 Normalized Difference NPV Index

Finally, having recognized that canopy structural variability can be assessed when combining multiple view angles, the next step is to develop a forest structure index. Several indices that combine multiple viewing angles already exist, such as the anisotropy index (ANIX), that is defined as the ratio of the maximum and minimum BRF (Sandmeier et al. 1998), or the normalized difference angular index (NDVAI), that uses a combination of forward and backward scattered radiation (Nolin et al. 2002). These indices are proxies for surface roughness; they indicate the degree of anisotropy but do not quantify angular land cover variability. Here, we intend to go one step further by developing a forest structural proxy that makes use of derived directional fractions rather than of directional reflectance. We define the Normalized Difference NPV Index (NDNPVI) as follows:

$$NDNPVI = \frac{NPV_{back} - NPV_{nadir}}{NPV_{back} + NPV_{nadir}}, \tag{5}$$

where ‘back’ corresponds to the fractions at the -55° viewing angle. Note that using PV fractions in the equation would equally hold true, but since our interest was specifically to assess the angular variability of NPV we felt the above formulation being more appropriate. The NDNPVI is calculated for the study site (figure 7).

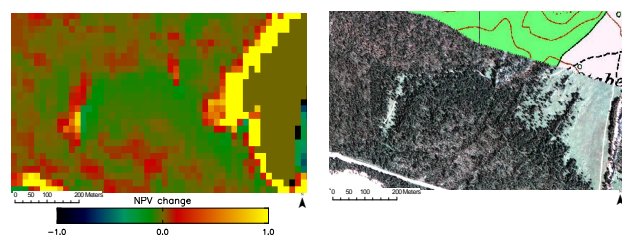


Figure 7. left: the NDNPVI; right ROSIS image (RGB) of the study site on top of the topographic map.

The green-brownish colour indicates that at those areas no angular fractional change took place, which accounts for the largest part of the study site. Areas with a more greenish colour indicate a greater fraction of observed PV at -55°, whereas areas with a more reddish colour indicate a greater angular fraction of observed NPV at -55°.

Where the boundary between forest and another land cover without NPV (e.g. meadow) occurs, however, the NDNPVI loses its sensitivity. The broad yellow strip north-west of the meadow is the result of no NPV fractions observed at nadir (exclusive meadow cover) while observing NPV fractions in backscatter direction. Having then zeros for NPV<sub>nadir</sub> in both the numerator and denominator will always result one, whatever the NPV fractions of NPV<sub>back</sub> are. Within the forest, the NDNPVI is well able to map angular fractional variability; in this way it distinguishes fully vegetated areas from woody areas. The NDNPVI can function as a suitable proxy to provide more insight in per-pixel structural canopy composition. This knowledge is crucial when attempting to interpret spectral-derived products, especially in case of photosynthesis-sensitive indices where NPV is a serious confounding factor.

4. CONCLUSION

The objective of this study was to assess how fractional coverage of PV or NPV responds to changing viewing angles and thereby how such effects are related to single reflectance bands and VIs. With FLIGHT the reflectance of an exclusively PV and an exclusively NPV forest scene were simulated as a function of coniferous forest variables and CHRIS acquisition viewing geometries. We used two approaches (1) a modeling exercise where VIs were calculated from controlled PV and NPV canopy mixtures, and (2) a linear unmixing exercise where PV and NPV proportions were extracted from angular CHRIS images and then correlated with the derived VIs. The modeling exercise showed that varying the NPV proportions at greater zenith angles did indeed govern the angular shape of VIs. The unmixing approach, however, was facing limitations in extracting reliable absolute fractions from the images themselves. Therefore the relative measure of ΔNPV rather than the absolute measure was considered being more reliable. When restricting to only those pixels where the NPV proportions increased (from nadir to backscatter) then moderate correlations were obtained with the angular variability of VIs. Alternative canopy variables that were not, or not well, mimicked by the modeled EMs in combination with limitations of the explored approach made that only a small part of the VIs’ angular variability was explained by the EMs. Finally, a volumetric canopy composition proxy was developed that capitalizes on the derived angular fractions. In the context of canopy photosynthesis studies, information about the canopy composition is crucial, though the work is still in an initial stage. Further efforts should be devoted to the robustness of this proxy and to the operability of the unmixing procedure.



## 5. ACKNOWLEDGEMENT

S. Schaminee is thanked for generating the visualisations of the PV and NPV forest. The work of J. Verrelst was supported through the Dutch SRON GO programme (Grant-No. EO-080).

## 6. REFERENCES

- Adams, J. B., Sabol, D. E., Kapos, V., Filho, R. A., Roberts, D. A., Smith, M. O., et al. 1995. Classification of multispectral images based on fractions of endmembers: Application to land-cover change in the Brazilian Amazon. *Remote Sensing of Environment*, 52(2), pp. 137-154.
- Asner, G. P. 1998. Biophysical and biochemical sources of variability in canopy reflectance. *Remote Sensing of Environment*, 64(3), pp. 234-253.
- Asner, G. P., & Heidebrecht, K. B. 2002. Spectral unmixing of vegetation, soil and dry carbon cover in arid regions: Comparing multispectral and hyperspectral observations. *International Journal of Remote Sensing*, 23(19), pp. 3939-3958.
- Asner, G. P., & Lobell, D. B. 2000. A biogeophysical approach for automated SWIR unmixing of soils and vegetation. *Remote Sensing of Environment*, 74(1), pp. 99-112.
- Borel, C. C., & Gerstl, S. A. W. 1994. Nonlinear spectral mixing models for vegetative and soil surfaces. *Remote Sensing of Environment*, 47(3), pp. 403-416.
- Camacho-De Coca, F., Garcia-Haro, F. J., Gilabert, M. A., & Melia, J. (2004). Vegetation cover seasonal changes assessment from TM imagery in a semi-arid landscape. *International Journal of Remote Sensing*, 25(17), pp. 3451-3476.
- DeFries, R. S., Field, C. B., Fung, I., Collatz, G. J., & Bounoua, L. 1999. Combining satellite data and biogeochemical models to estimate global effects of human-induced land cover change on carbon emissions and primary productivity. *Global Biogeochemical Cycles*, 13(3), pp. 803-815.
- Diner, D. J., Asner, G. P., Davies, R., Knyazikhin, Y., Muller, J. P., Nolin, A. W., et al. 1999. New Directions in Earth Observing: Scientific Applications of Multiangle Remote Sensing. *Bulletin of the American Meteorological Society*, 80(11), pp. 2209-2228.
- Diner, D. J., Braswell, B. H., Davies, R., Gobron, N., Hu, J., Jin, Y., et al. 2005. The value of multiangle measurements for retrieving structurally and radiatively consistent properties of clouds, aerosols, and surfaces. *Remote Sensing of Environment*, 97(4), pp. 495-518.
- Ichoku, C., & Karnieli, A. 1996. A Review of Mixture Modeling Techniques for Sub-Pixel Land Cover Estimation. *Remote Sensing Reviews*, 13(3-4), pp. 161-186.
- Kneubühler, M., Koetz, B., Itten, K., Richter, R., & Schaepman, M. 2005. *Geometric and radiometric pre-processing of CHRIS/PROBA data over mountainous terrain*. European Space Agency, (Special Publication) ESA
- Kötz, B., Morsdorf, F., Itten, K., Schaepman, M., Bowyer, P., & Allgöwer, B. 2004. Radiative transfer modeling within a heterogeneous canopy for estimation of forest fire fuel properties. *Remote Sensing of Environment*, 92(3), pp. 332-344.
- Myneni, R. B., Ross, J., & Asrar, G. 1989. A review of the theory of photon transport in leaf canopies. *Agricultural & Forest Meteorology*, 45(1-2), pp. 1-153.
- Nolin, A. W., Fetterer, F. M., & Scambos, T. A. 2002. Surface roughness characterizations of sea ice and ice sheets: Case studies with MISR data. *IEEE Transactions on Geoscience and Remote Sensing*, 40(7), pp. 1605-1615.
- North, P. R. J. 1996. Three-dimensional forest light interaction model using a monte carlo method. *IEEE Transactions on Geoscience and Remote Sensing*, 34(4), pp. 946-956.
- Rautiainen, M. 2005. Retrieval of leaf area index for a coniferous forest by inverting a forest reflectance model. *Remote Sensing of Environment*, 99(3), pp. 295-303.
- Rautiainen, M., & Stenberg, P. (2005). Application of photon recollision probability in coniferous canopy reflectance simulations. *Remote Sensing of Environment*, 96(1), pp. 98-107.
- Roberts, D. A., Smith, M. O., & Adams, J. B. 1999. Green vegetation, nonphotosynthetic vegetation, and soils in AVIRIS data. *Remote Sensing of Environment*, 44(2-3), pp. 255-269.
- Sandmeier, S., Muller, C., Hosgood, B., & Andreoli, G. 1998. Physical mechanisms in hyperspectral BRDF data of grass and watercress. *Remote Sensing of Environment*, 66(2), pp. 222-233.
- Schaepman-Strub, G., Schaepman, M. E., Painter, T. H., Dangel, S., & Martonchik, J. V. 2006. Reflectance quantities in optical remote sensing--definitions and case studies. *Remote Sensing of Environment*, 103(1), pp. 27-42.
- Settle, J. J., & Drake, N. A. 1993. Linear mixing and the estimation of ground cover proportions. *International Journal of Remote Sensing*, 14(6), 1159-1177.
- Van Leeuwen, W. J. D., & Huete, A. R. 1996. Effects of standing litter on the biophysical interpretation of plant canopies with spectral indices. *Remote Sensing of Environment*, 55(2), pp. 123-138.
- Verrelst, J., Schaepman, M.E., Koetz, B., & Kneubühler, M. 2007. Angular sensitivity of vegetation indices derived from CHRIS/PROBA data in two Alpine ecosystems. *Remote Sensing of Environment*. (in revision)
- Widlowski, J. L., Pinty, B., Gobron, N., Verstraete, M. M., Diner, D. J., & Davis, A. B. 2004. Canopy structure parameters derived from multi-angular remote sensing data for terrestrial carbon studies. *Climatic Change*, 67(2-3), pp. 403-415.
- Zurita-Milla, R., Clevers, J. G. P. W. & Schaepman, M. 2006. LANDSAT TM and MERIS FR image fusion for land cover mapping over the Netherlands. *2nd Workshop of the EARSeL SIG on Land Use and Land Cover*. Bonn, Germany.
- Zurita-Milla, R., Clevers, J. G. P. W., Schaepman, M. E. & Kneubühler, M. 2007. Effects of MERIS L1b radiometric calibration on regional land cover mapping and land products. *International Journal of Remote Sensing*, 28, pp. 653-673.

# MODELING REFLECTANCE OF URBAN CHESTNUT TREES: A SENSITIVITY ANALYSIS OF MODEL INVERSION FOR SINGLE TREES

A. Damm, P. Hostert

Department of Geomatics, Humboldt-Universität zu Berlin, 10099 Berlin, Germany  
(alexander.damm, patrick.hostert)@geo.hu-berlin.de

**KEY WORDS:** radiative transfer model, single trees, urban environment, HyMap

## ABSTRACT:

Trees in urban environments have important ecological functions, but often suffer from suboptimal environmental conditions. Chestnut (*Aesculus hippocastanum*) is one of the main tree species in Germany's capital Berlin, constituting 5% of all urban trees. Recently, chestnut trees are exposed to amplified stress levels due to the horse chestnut leaf miner (*Cameraria ohridella*), a parasitic insect whose larvae feed exclusively on chestnut leaves. Detecting plant damages at early stages and monitoring chestnut tree stress levels are thus important to manage urban canopies in Berlin and elsewhere. Hyperspectral data offer unique opportunities to derive detailed vegetation parameters for wide areas. Vitality parameters are commonly based on the characterization of plant physiology attributes and several studies point out the usefulness of radiative transfer modeling in this context, particularly for locally heterogeneous objects such as tree canopies. However, the selection of pixels that fully represent a single tree is not easy, because the model is highly sensitive to mixed pixels or varying illumination conditions. This is challenging, because the average chestnut crown diameter is only 15m and HyMap images offer at best a ground sampling distance of 4m, resulting in a low number of pure pixels. Tree geometry introduces further disturbance through diverse illumination constellations.

In this research, we use a combination of the radiative transfer models PROSPECT and SAIL to derive parameters of chestnut tree stress levels for the city of Berlin based on HyMap images. Our goal was to quantify the influence of pixel selection methods on the quality of the model output. Reference data was collected for 11 trees and included leaf area index, leaf chlorophyll-, water- and, dry matter content. Different methods and statistical approaches to select input pixels for the modeling were compared based on several statistical parameters. Our results clearly highlight that choosing the optimum selection method is a crucial step in the model parameterization, and different selection methods lead to significantly different model results. In our case, using an averaged signal of the illuminated crown areas results in the best agreement between the model output and reference data.

## 1. INTRODUCTION

Trees perform a series of functions in urban environments, for example in urban climate, as aesthetical components in urban planning, as a living space for urban fauna, or in the context of leisure and recreation. Only a few of these functions are financially quantifiable, but urban trees are assessed as being highly valuable (Dwyer et al., 1992; Konijnendijk et al., 2005; McPerson, 1992). At the same time, environmental conditions are far from natural, with sealed surfaces, high toxin levels, or high pressure of utilization (Konijnendijk et al., 2005). The necessary conservation of tree specific value and function is economically determined. Tree monitoring is hence an essential step to effectively manage urban trees. However, various factors hinder an efficient, spatially explicit, and objective survey. These include crown access or aspects of time and costs. Hyperspectral data offer unique opportunities to derive detailed vegetation parameters for wide areas. Vitality parameters are commonly based on the characterization of plant physiological attributes. Several studies point out the flexibility of approaches based on the inversion of radiative transfer models to predict plant physiological attributes to analyze heterogeneous broadleaved canopies (Meroni et al., 2004; Zarco-Tejada, et al., 2001; Zarco-Tejada et al., 2004). In these studies, the coupled radiative transfer models (RTMs) PROSPECT (Jacquemoud et al., 1990) and SAIL (Verhoef, 1984) were used. The applicability of these models is shown, whereas some canopy

specific effects constrained the accuracy, particularly the influence of shadow and crown geometry.

This research is focused on analyzing chestnut (*Aesculus hippocastanum*), which is one of the main tree species in Germany's capital Berlin, with hyperspectral remote sensing. Recently, chestnut trees are exposed to amplified stress levels due to the horse chestnut leaf miner (*Cameraria ohridella*), a parasitic insect whose larvae feed exclusively on chestnut leaves (Raimondo et al., 2003; Saello et al., 2003; Thalmann et al., 2003). Data from the Hyperspectral Mapper (HyMap) with a spatial resolution of 4m were used. However, the relation between sensor resolution and crown diameter leads to the question: Are the base assumptions behind the coupling of PROSPECT and SAIL also valid to derive vitality parameters of urban chestnut trees?

To provide information about the applicability, tree specific effects have to be considered. The crown geometry and sensor view led to complex crown shadow. Moreover, trees are represented by pure and mixed pixels, corresponding to a huge range of estimated parameters. Accordingly, four aspects will be analyzed in detail:

- Which parameters are relevant to simulate the reflectance of chestnut tree crowns?
- Single trees are represented by many pixels – which pixels contain the information to predict valid parameters?
- Is it possible to compensate the influence of the complex crown shadow?

- Are PROSPECT and SAIL adequate RTMs to estimate vitality parameters of single chestnut trees?

2. DATA

The choice of sample trees in urban environments is important to measure a realistic spectrum of potential canopy variations. Site specific factors, such as incoming radiance, water and nutrient availability, or pressure of use, result in a high spatial variability of canopy parameters. The phenological change within a seasonal cycle leads to additional variability and different parts of the tree crown also exhibit variations in biochemical parameters. This is mainly due to amount of light, wind pressure, or temporarily pathogenic infestations on branches. The logistic and technical constraints, such as accessible tree height, required minimum crown diameter and standardized time of data acquisition also need to be included in the tree selection process.

2.1 Canopy structure and biochemistry

With regard to the aforementioned criteria, eleven trees were selected. The trees were chosen from highly frequented street within built up areas (2 trees), areas next to water (3 trees), inside an urban forest (3 trees), and in a derelict military site (3 trees). To acquire a high temporal resolution of parameter change, the trees were sampled every 2 weeks from May 10<sup>th</sup> until September 27<sup>th</sup> in 2005. Individual trees were always sampled at a similar time of the day (Damm et al., 2006). LAI, crown geometry and the understorey were measured and described in terms of canopy structure. A LiCor-LAI2000 was used to measure LAI. The measurements were taken in four directions using a 180° cap and finally averaged for one tree. Ten leafs per tree were randomly sampled from the South-facing upper crown with the aid of a cherry-picker. The harvested leafs were photographed and prepared for laboratory analysis, and spectral measurements. For the laboratory analysis, samples of a defined area (2.83cm<sup>2</sup>) were cut from the leafs and immediately placed in liquid nitrogen. Reflectance measurements of the leafs were performed using an ASD Field Spec Pro II spectroradiometer. All measurements were taken under laboratory conditions within a van. The samples were arranged on a black background, the geometry of sensor and illumination was standardized using an ASD High Intensity Contact Probe. One measurement was performed on each leaf. The ten leaf signatures per tree were subsequently averaged for each observation date. A smooth and step filter were used to reduce remaining measurement inaccuracies and noise. The frozen leaf samples were subsequently analyzed in the laboratory. To measure the leaf chlorophyll content, samples were crushed in acetone (85%) and loaded into a High Performance Liquid Chromatography (HPLC). Samples were weighed to derive the fresh leaf mass. To measure the dry leaf mass, samples were dried in an oven at 85°C until the mass became constant and weighed again. The water content was calculated as the difference between the fresh and dry leaf mass.

parameter	unit	min – max (full veg. period)	min – max June 15 <sup>th</sup>
Chlorophyll content	µg/cm <sup>2</sup>	40 – 80	52 – 80
Water content	g/cm <sup>2</sup>	0.008 – 0.016	0.010 – 0.013
Dry matter content	g/cm <sup>2</sup>	0.004 – 0.012	0.008 – 0.012
Mesophyll structure	unitless	1.3 – 2.1	1.6 – 1.8
Leaf area index	unitless	4 – 11	4 – 11

Table 1. Field observations of canopy variables

2.2 Imaging spectrometer data

In this study, hyperspectral HyMap data were used. The imagery was acquired on June 20<sup>th</sup> in 2005, around 12 a.m. local time, i.e. five days after one of the field observation days (compare table 1). Six flight lines were acquired during a time slot of approximately one hour (solar zenith and azimuth angles between 29.8° and 35.1°; and 136.1° and 164.1°, respectively; flight headings parallel and orthogonal to the solar plane). The flight height was approximately 2000m leading to a spatial resolution of 4m. The images were geo- and radiometrically pre-processed with the modules PARGE and ATCOR4 to obtain geocoded top-of-canopy reflectance (Richter et al., 2002, Schlöpfer et al., 2002).

3. RADIATIVE TRANSFER MODELING FOR VITALITY PARAMETER ESTIMATION

It is common to combine models calculating the reflectance of green leafs and models which combine various canopy components, like subsurface, trunk, branches or leafs (Liang, 2004). PROSPECT and SAIL are well documented and often used models to simulate reflectance and transmittance for broadleaved vegetation canopies in the spectral range of 400 to 2500 nm. PROSPECT is a leaf reflectance model and based on the plate model, developed by Allen (1969). The model treats a leaf as a pile of plates with specific attributes. Reflectance and transmittance are simulated as functions of the structural parameter (N) and the combined absorption coefficients of the leaf biochemical's chlorophyll (CAB), water (CW) and dry matter (CDM) (Jacquemoud et al., 1990). SAIL is a one-dimensional, bidirectional, turbid medium radiative transfer model, that simulates the reflectance and transmittance of vegetation canopies (Verhoef, 1984). SAIL simulates the top-of-canopy-reflectance considering various parameters: sun-sensor-geometry, fraction of diffuse radiance, canopy background, LAI, and leaf angle distribution. In this study, we used a 2M-SAIL version, suitable for dealing with an unlimited number of spectral bands and multiple canopy components (Verhoef, 1985). In the direct mode, the coupled use of PROSPECT and SAIL simulates spectral reflectance and transmittance for a certain set of canopy parameters. To retrieve canopy parameters from a measured signal, it is necessary to use the coupled models in inverse mode.

3.1 Experiment setting

The influence of tree specific aspects on the model accuracy was quantified, specifically:

- parameters which significantly influence the reflectance in the near infrared (NIR) and shortwave infrared (SWIR) wavelength regions
- understorey canopy
- existence of several representative pixels
- illumination conditions

The absolute RMSE between measured and estimated parameters was hence calculated for CAB and CW.

**Parameters which significantly influence the reflectance in the NIR and SWIR:** When modeling the canopy reflectance of chestnut trees using the coupled models PROSPECT and SAIL, few parameters significantly influence the reflectance in the NIR and SWIR spectral domain. To avoid the ill-posed effect, some of these parameters have to be fixed. Previous analyses at leaf level show that the structural parameter N is rather stable for chestnut trees. Furthermore, the dry matter content is relatively high, so that the signals reach saturation. According to that, the parameters N and CDM were fixed (Damm et al., 2006).

Two experiments (termed “A” and “B”) were initiated to quantify the influence of LAI and CW. During experiment A, the LAI was fixed and the water content was set as free parameter. Both parameters were varied in experiment B.

**Understorey:** Analyzing the LAI, high values between 6 and 12 were observed. Canopy reflectance saturates, when the LAI exceeds values of 5 or 6 (Guyot, 1990). Accordingly, the negligibility of understorey is assumed. Both aforementioned experiments were subdivided again: In experiment A1 and B1, a frequently occurring grass spectrum was used as understorey spectrum. In the experiments A2 and B2, the understorey was changed using locally existing spectral signatures.

**Existence of several representative pixels:** First tests have shown a high variability of estimated parameters using all pixels representing one tree. This is mainly due to the tree inherent variability or mixed pixels along the crown edges. Two possibilities were analyzed to compensate this effect. First, a mean (μ1) and median (m1) spectrum for all pixels of one tree was calculated and subsequently used to estimate model parameters. Second, the mean (μ2) and median (m2) for parameter estimates from single pixels was calculated. The four calculation methods for 4 experiments lead to 16 test configurations, overall.

**Shadow:** The different crown shapes and viewing angles lead to complex illumination conditions. These conditions are expressed in a wide range of albedo values. Neglecting this effect results in significant inaccuracies (Zarco-Tejada et al., 2001). The brightness was categorized into 10 levels to evaluate which pixels have to be excluded for maintaining the model assumptions. These levels were tested in the 16 experiments.

3.2 Model simulation and inversion

Inversion strategies can be categorized in methods to optimize a cost function (numerical, look-up-tables (LUT)), or methods to empirically define a transfer function (e.g. artificial neuronal nets (ANN)). Different authors compared these approaches and point out advantages and constraints (Combal et al., 2002; Weiss et al., 2000). LUT-based approaches are favored to invert our model. These are simple to implement, and the results can

be considered as stable, if no more then two parameters have to be inverted.

The ranges of relevant model parameters were extracted from field observations to simulate reflectance spectra (compare tables 1 and 2). N was derived using an empirical relationship with the specific leaf area, as suggested by Jacquemoud (1990). The model was adjusted to the spectral resolution of HyMap. 100.000 spectra based on parameters from Monte Carlo simulations were used to generate the LUT (table 2).

parameter	unit	range
N structure parameter	-	1.8
CAB foliage chlorophyll content	µg/cm²	20 – 90
CW foliage water content	g/cm²	0.008 – 0.022
CDM foliage dry matter content	g/cm²	0.01
US understorey	-	vegetation/ soil/asphalt/ concrete/water
LAI leaf area index	-	2 – 8
fW fraction woody material	%	0
LAD Leaf angle distribution	-	planophil

Table 2. Ranges for Monte Carlo simulations

In order to invert PROSPECT and SAIL, we minimized the following cost function (equation 1).

$$RMSE_{rel} = \sqrt{\frac{1}{nb} * \sum_{i=1}^{nb} \left( \frac{\rho_i - \hat{\rho}_i}{\rho_i} \right)^2}$$

(1)

- where
- RMSE<sub>rel</sub>

=

relative root mean squared error
- nb

=

number of bands
- $\rho_i$

=

measured reflectance of band i
- $\hat{\rho}_i$

=

simulated reflectance of band i

4. RESULTS AND DISCUSSION

The results from the 160 experiments representing different model constellations and pixel extraction methods exhibit the high variability of model outputs (fig. 1). The absolute RMSE varied between 6.7 and 20.8 for chlorophyll and between 0.0020 and 0.0073 for water content. There are no significant differences between the three experiments A1-B1, whereas experiment B2 slightly decreases in accuracy. Accuracy seems to degrade when dark or bright pixels were used for parameter estimation, which is a violation of model assumptions. Using the mean values from estimated parameters from all pixels of one tree perform generally better as parameter estimates from averaged crown spectra. If calculating these averaged crown spectra, the conflict of dark and bright pixels with the model assumptions shifts to the mean crown spectra. Calculating the mean of the estimated parameters compensates this conflict. Similar accuracies for both mean calculation methods by moderate Albedo (40%-45%) support this conclusion. Median related estimates are less accurate.

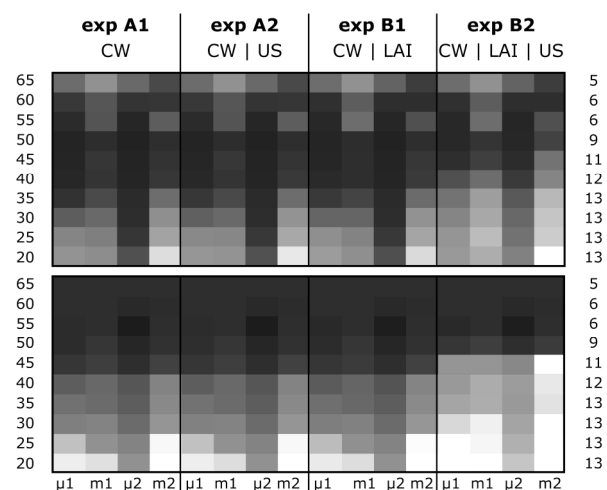


Figure 1. Accuracy matrix (RMSE absolute): chlorophyll (top) water (bottom);  $\mu 1$ ,  $m1$ : mean and median of averaged spectra;  $\mu 2$ ,  $m2$ : mean and median of estimates from single pixel inversion; left scale: NIR-plateau reflectance in %; right scale:  $n$  (unitless); dark colors correspond to low RMSE values, bright colors correspond to high RMSE values

The behavior of the absolute RMSE for experiments A1 $\mu 2$ -B2 $\mu 2$  is presented in figures 2 and 3. The accuracies for experiments A1 $\mu 2$ , A2 $\mu 2$  and B1 $\mu 2$  are nearly the same. For experiment B2 $\mu 2$  an overall decrease of accuracy occurs. The error for all experiments increased when the parameter estimation was based on dark or bright pixels. The canopy 3D structure and the related complex viewing and illumination conditions are not foreseen in the models.

To understand the meaning of the absolute RMSE, figure 4 and 5 present the best parameter estimates for chlorophyll and water content. To select the best model, the number of variable model parameters and the absolute RMSE should be minimized. Finally, the estimates from experiment A1 $\mu 2$  with a brightness level of 45% were chosen. Comparisons between estimated and measured parameters exhibit a good one-to-one relationship between ground-truth and estimates.

To evaluate the impact of tree specific effects or general canopy aspects on the model accuracy, we examined the results of experiments A1 $\mu 2$ -B2 $\mu 2$  in detail.

**Parameters influencing NIR and SWIR reflectance:** No significant differences occurred in the NIR and SWIR spectral domain for most of the model constellations. Only the model B2 $\mu 2$  which varied the leaf area index, the water content and the understorey is a negative exception. Some parameters are available to simulate the canopy reflectance in the NIR and SWIR spectral domain, but for chestnut trees only the water content is a free parameter: The structural parameter  $N$  is less variable, the values of dry mater content and LAI saturate and must be fixed.

**Understorey:** No significant improvement was achieved by integrating variable  $US$  when the  $LAI$  was fixed (difference of averaged relative RMSE for exp A1 $\mu 2$  and exp A2 $\mu 2$  for CAB 14%; for CW 0.003%). With variable  $LAI$  and fixed  $US$ , the results are similar to the both aforementioned setups (A1 $\mu 2$  and A2 $\mu 2$ ). If  $LAI$  and  $US$  were set as free parameters, a decrease of accuracy occurred, mainly resulting from the ill-posed effect.  $LAI$  was generally underestimated (values around 2), while these low values were compensated by an overestimated water content. As the  $LAI$  with measured values of 6 to 12 has no influence on the spectral response, it should be fixed.

**Existence of several representative pixels:** A high variability of results was detected for different pixels of one tree (figures 4 and 5). This is due to the model violation when introducing extremely dark or bright pixels. However, observed average values appear very reasonable. Best result was attained by calculating the mean of the estimated parameters from single pixels (averaged relative RMSE for CAB 14% vs. 16 to 20% for other methods; relative RMSE for CW 34% vs. 38 to 41% for other methods).

**Shadow:** Best results were attained by excluding very dark and bright pixels. This is mainly caused by the crown specific geometry and the sun-view conditions, which are not foreseen in the models.

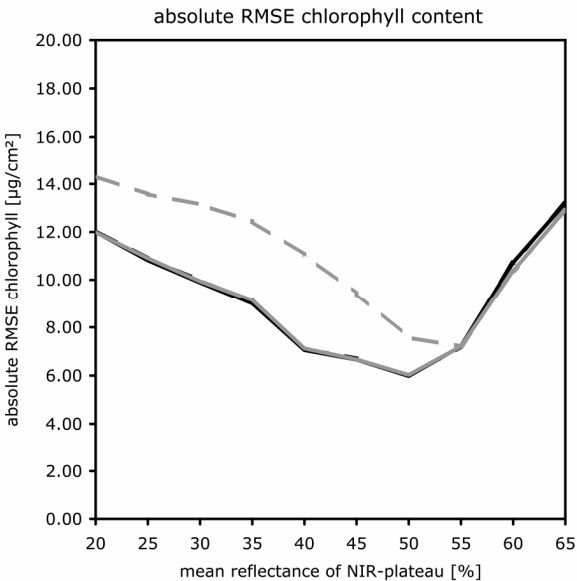


Figure 2. Absolute RMSE for chlorophyll content estimates from averaged pixel values of single trees; grey solid (exp A1); grey dashed (exp A2); black solid (exp B1), black dashed (exp B2)

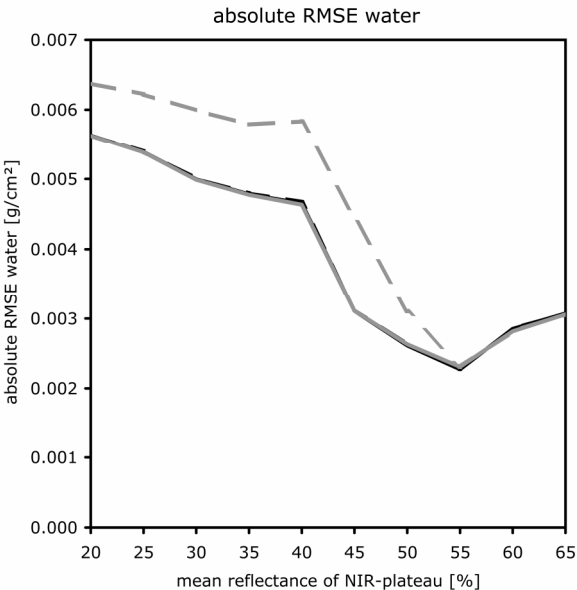


Figure 3. Absolute RMSE for water content estimates from averaged pixel values of single trees; grey solid (exp A1); grey dashed (exp A2); black solid (exp B1), black dashed (exp B2)



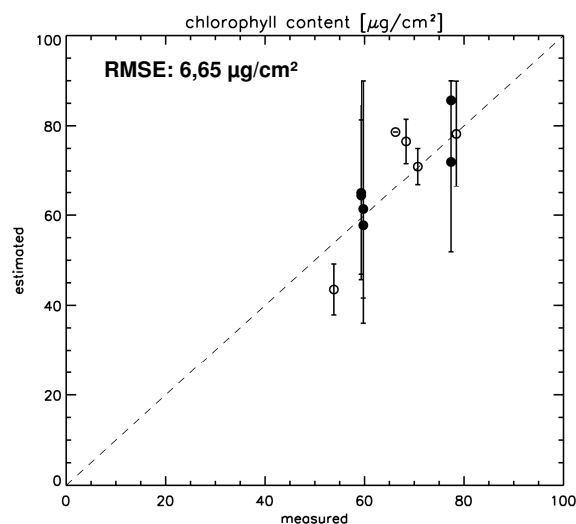


Figure 4. CAB estimates for 13 chestnut trees for best model constellation; filled circles flag trees which were mapped in two HyMap flight lines; error bars represent the range of estimated parameters

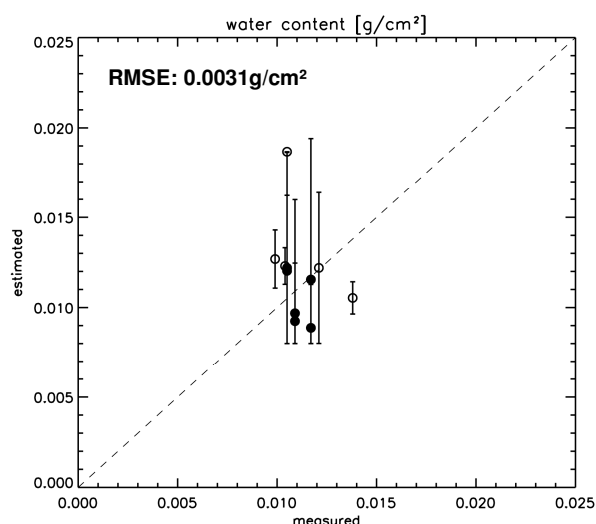


Figure 5. CW estimates for 13 chestnut trees for best model constellation; filled circles flag trees which were mapped in two HyMap flight lines; error bars represent the range of estimated parameters

## 5. CONCLUSIONS

This study aimed to determine the validity of PROSPECT and SAIL to simulate reflectance of chestnut trees. Precise and comprehensive leaf and canopy parameterization of the used models enabled a comparison of estimated and measured biochemical and structural parameters.

As anticipated, the high LAI values lead to a minor influence of understorey variations. Enhanced model accuracy is hence attainable by fixing the LAI and varying the CAB and CW parameters. For an adequate integration of several reflectance values in HyMap pixels from a single tree, calculating the mean to invert a model exhibits the best results. The influence of illumination differences induced by crown geometry can be partially compensated when excluding dark pixels. A description of the canopy's 3D structure would be essential comprehensively model this effect.

Finally, it can be stated that the combined radiative transfer models PROSPECT and SAIL offer an opportunity to estimate the vitality parameters chlorophyll and water content of chestnut trees with adequate accuracy: If pixels from the top crown are used, which are largely free of influences from the crown geometry, CAB and CW values are reliably estimated.

## ACKNOWLEDGEMENTS

The authors are grateful to Dr. B. Rank, K. Boldt and A. Voigt from the Department of Plant Physiology, Institute of Biology, Humboldt-Universität zu Berlin, for performing laboratory analyses and for helpful discussions; thanks also to Dr. B. Jäckel and S. Schmolling from the Official Bureau of Plant Protection Berlin for assistance in planning the field campaign. Alexander Damm is sponsored by a scholarship from the Berlin Graduate Support (NaFöG). This study was financed by the German Research Foundation (DFG) in the frame of the project "Urban Environmental Monitoring with hyperspectral and geometric high resolution remote sensing data" (HO 2568/2-1 and HO 2568/2-2).

## REFERENCES

### References from Journals:

- Combal, B., Baret, F., Weiss, M., Trubuli, A., Macé, D., Pragnère, A., Myeni, R., Knyazikhin, Y. & Wang, L., 2002. Retrieval of canopy biophysical variables from bidirectional reflectance using prior information to solve the ill-posed inverse problem. *Remote Sensing of Environment*, 84, pp. 1-15.
- Dwyer, J.F., McPherson, E.G., Schroeder, W.A. & Rowntree, R.A., 1992. Assessing the Benefits and Costs of the Urban Forest. *Journal of Arboriculture*, 18(5), pp. 227-234.
- Jacquemoud, S. & Baret, F., 1990. PROSPECT: A model of leaf optical properties spectra. *Remote Sensing of Environment*, 34, pp. 75-91.
- McPherson, E.G., 1992. Monitoring Urban Forest Health. *Environmental Monitoring and Assessment*, 26, pp. 165-174.
- Meroni, M., Colombo, R. & Panigada, C., 2004. Inversion of a radiative transfer model with hyperspectral observations for LAI mapping in poplar plantations. *Remote Sensing of Environment*, 92, pp. 195-206.
- Raimondo, F., Ghirardelli, S., & Nardini, A. & Saello, S, 2003. Impact of the leaf miner *Cameraria ohridella* on photosynthesis, water relations and hydraulics of *Aesculus hippocastanum* leaves. *Trees* 17, pp. 376-382
- Richter, R. & Schläpfer, D., 2002. Geo-atmospheric processing of airborne imaging spectrometry data: Part 2. Atmospheric/topographic correction. *International Journal of Remote Sensing*, 23(13), pp. 2631-2649.
- Saello, S., Nardini, A., Raimondo, F., Assunta Lo Gullo, M., Pace, F. & Giacomich, P., 2003. Effects of defoliation caused by the leaf miner *Cameraria ohridella* on wood production and efficiency in *Aesculus hippocastanum* growing in north-eastern Italy. *Trees* 17, pp. 367-375.
- Schläpfer, D. & Richter, R., 2002. Geo-atmospheric processing of airborne imaging spectrometry data: Part 1. Parametric

orthorectification. *International Journal of Remote Sensing*, 23(13), pp. 2609-2630.

Thalmann, C., Freise, J., Heitland, W. & Bacher, S., 2003. Effects of defoliation by horse chestnut leafminer ( *Cameraria ohridella*) on reproduction in *Aesculus hippocastanum*. *Trees*, 17, pp. 383-388.

Verhoef, W., 1984. Light scattering by leaf layers with application to canopy reflectance modelling: The SAIL model. *Remote Sensing of Environment*, 16, pp. 125-141.

Verhoef, W., 1985. Earth observation modelling based on layer scattering matrices. *Remote Sensing of Environment*, 17, pp. 165-178.

Weiss, M., Baret, F., Ranga, M.B., Pragnère, A. & Knazikhin, Y., 2000. Investigation of a model inversion technique to estimate canopy biophysical variables from spectral and directional reflectance data. *Agronomy*, 20, pp. 3-22.

Zarco-Tejada, P.J., Miller, J.R., Noland, T.L., Mohammed, G.H. & Sampson, P.H., 2001. Scaling-up and model inversion methods with narrowband optical indices for chlorophyll content estimation in closed forest canopies with hyperspectral data. *IEEE Transactions on Geoscience and Remote Sensing*, 39(7), pp. 1491-1507.

Zarco-Tejada, P.J., Miller, J.R., Morales, A., Berjon, A. & Agüera, J., 2004. Hyperspectral indices and model simulation for chlorophyll estimation in open-canopy tree crops. *Remote Sensing of Environment*, 90, pp. 463-476.

#### **References from Books:**

Konijnendijk C.C., Nilsson, K., Randrup, T.B. & Schipperijn, J., 2005. *Urban Forest and Trees*. Springer 520 pp.

Liang, S., 2004. *Quantitative remote sensing for land surface characterisation*. Wiley 534 pp.

#### **References from Other Literature:**

Damm, A. & Hostert, P., 2006. Deriving vitality parameters of *Aesculus hippocastanum* using radiative transfer models. *1st Workshop of the EARSeL Special Interest Group Urban Remote Sensing "Challenges and Solutions"*. Berlin, Germany.

Guyot, G., 1990. Optical properties of vegetation canopies. *Steven & Clark (Ed.): Applications of remote sensing in agriculture*. Butterworth, London, pp. 19-43.

AIRBORNE HYPERSPECTRAL SCANNER (AHS) SPECTRAL EMISSIVITY  
RETRIEVAL IN 8-13 μm.

M. Jiménez<sup>a</sup>, J. Chico<sup>a</sup>, E. de Miguel<sup>a</sup>, J. A. Gómez<sup>a</sup>, J A. Sobrino<sup>b</sup>, J. C. Jiménez-Muñoz<sup>b</sup>, E. Prado<sup>a</sup>, C. Robles<sup>a</sup>

<sup>a</sup> Remote Sensing Laboratory, INTA. Carretera de Ajalvir Km 4. Torrejón de Ardoz. 28850. Spain  
<sup>b</sup> Department of Thermodynamics, Faculty of Physics, University of Valencia. C/Dr. Moliner 50, 46100 Burjassot, Valencia, Spain  
jimenezmm@inta.es

**KEYWORDS:** AHS; Multispectral thermal imagery; Emissivity mapping; Emissivity spectral Library; ATCOR4; ISAC

ABSTRACT

Multispectral and hyperspectral thermal sensors can use spectral emissivities for mapping surface elements that show wavelength emission differences (typically minerals). The Airborne Hyperspectral Scanner (AHS) is a VIS to TIR 80 band line-scanner which collects 10 bands in the 8 to 12 μm atmospheric window, with 0.4 μm bandwidth. Multichannel temperature-emissivity separation published methods (*Reference Channel* and *Emissivity Normalization*) are evaluated here to estimate the capacity of AHS to retrieve spectral emissivity. These methods are very dependent on an accurate calibration and atmospheric correction of the at-sensor radiances, and also sensitive to the noise equivalent difference temperature (NEAT) of the channels. Emissivities obtained for some AHS 2005/2006 imagery campaigns, including day and night flights, have been tested comparing with emissivity ground truth (collected at SEN2FLEX ESA 19187/05/I-EC project) and spectral libraries available in the 8-13 μm region.

1. INTRODUCTION

In the thermal infrared (TIR) domain, the emissivity is an important parameter for mapping surface temperature and composition (Sobrino et al, 2006). In addition, inside the 8-12 μm atmospheric window mineral groups such us silicates, carbonates, sulphates exhibit measurable absorptions bands that permits mineral species identification (Vaughan et al, 2003). With this background, space missions like: Moderate Resolution Imaging Spectrometer (MODIS) and Advanced Spaceborne Thermal Emission and Reflection Radiometer (ASTER), include multispectral TIR images

Emissivity of surfaces is wavelength dependent, and is function of composition, roughness, and physical parameter e.g. moisture content (Schmugge, 2002). Multispectral airborne thermal infrared sensors such as: Thermal Infrared Multiepectral scanner (TIMS), Airborne Hyperspectral scanner (AHS), and thermal hyperspectral like: Airborne Reflective/Emissive Spectrometer (ARES) and Spatially Enhanced Broadband Array Spectrograph System (SEBASS), offer the possibility to obtain spectral emissivity maps at regional scale and improve the emissivity knowledge to develop space missions.

Considering a multichannel thermal sensor, several methods have been proposed in recent years to separate temperature and emissivity (Li et al, 1999). Table 1 shows references for some of these algorithms.

Method	Reference
Temperature-Independent Spectral Indices (TISI)	Becker and Li (1990; 1995)
Reference Channel Method (REF)	Kahle et al (1980)
Normalize Emissivity Method (NEM)	Gillespie (1985)
Alpha Emissivity Method (α)	Kealy and Gabell (1990)
Temperature and Emissivity Separation (TES)	Gillespie (1998)

Table 1: Temperature and Emissivirty separation methods references.

The Spanish National Institute for Aerospace Technology (INTA) owns and operates the Airborne Hyperspectral Scanner (AHS). AHS is an imaging spectrometer with complete spectral coverage (VIS to TIR), having multispectral in the MIR and TIR regions. INTA has the goal to offer spectral emissivi product as a deliverable for users, with this aim this work evaluate the accuracy and performances of the AHS emissivity retrieval applying, in a first approach, REF and NEM methods implemented in ATCOR4 (Dr. R. Richter, DLR and ReSe Applications Schläpfer) and ENVI (ITT Industries, Inc) software.

2. AIRBORNE HYPERSPECTRAL SCANNER (AHS)

The AHS is an airborne line-scanner imaging spectrometer manufactured by ArgonST (formerly Sensytech Inc.). Collets 80 bands form 0.45 to 12.8 microns inside atmospheric windows. It is installed in the INTA's aircraft (CASA C-212) and is integrated with INS/GPS Applanix POS-AV 414. The main characteristics of AHS are:

FOV / IFOV : 90° / 2.5 mrad Scan rates: 12.5, 18.75, 25, 35 r.p.s., (pixel 7 to 2 meters). Digitization precision: 12 bits to sample the analog signal, with gain level from x0.25 to x10. Two controllable thermal black bodies within the field of view.			
PORT	spectral coverage(μm)	n° of bands / FWHM (nm)	λ/Δλ (minimum)
Port 1	0.43 > 1.03	20 / 28 nm	16
Port 2A	1.55 > 1.75	1 / 200 nm	8
Port 2	2.0 > 2.54	42 / 13 nm	150
Port 3	3.3 > 5.4	7 / 300 nm	11
Port 4	8.2 > 12.7	10 / 400 nm	20

Table 2: AHS characteristics

3. MATERIAL

3.1 AHS data set

Two different AHS imagery were used to assess the emissivity retrieval. The imagery selected have, within the scene, surfaces with different emissivities: one group is with high and featureless emissivity spectrum like water and vegetation, and another group is with absorption presence like minerals. The images were acquired in the framework of two different projects:

Exploitation of AnGular effects in Land surface form satellites (EAGLE2006, ESA). AHS image was acquired over Ermelo (The Netherlands) on 13<sup>th</sup> June 2006, with a pixel of 6.8 meters.

At instances of Spanish National Institute for Agrarian research (INIA), INTA acquired on 10th October 2006 an AHS flight campaign over 1200 ha burned area in Guadalajara (central Spain).

3.2 Software applied

Two commercial software were used to retrieve emissivity for AHS imagery. Both applications include NEM and REF emissivity methods and were applied to AHS data set selected.

**ATCOR4:** Dr. R. Richter, DLR and ReSe Applications Schl pfer (<http://www.rese.ch/atcor/atcor4/index.html>). Specific atmospheric correction application for airborne images.

**ENVI:** ITT Industries Inc, 2006 (<http://www.RSInc.com/envi>) Remote Sensing software.

3.3 Validation data

To serve as validation for the AHS emissivity performance, field data and spectral libraries were gathered.

3.3.1 Field data

In the framework of EAGLE2006 ESA project, Global Change Unit of the University of Valencia (Spain), collects over a quartz sandy area, thermal radiometric measurements with the multiband radiance-based thermal radiometer CIMEL CE312. The measurements were carried out at the same day of an AHS flight line.

Field radiometric measurements were processed to temperature and emissivity using TES (see Table 1) (Jim nez-Mu oz, et al, 2006)

3.3.2 Spectral library

Emissivity spectra were taken from two distinct spectral libraries: John Hopkins University (Salisbury and D’Aria, 1992) available in the ENVI spectral library format. The original directional hemispherical reflectance data was converted into directional emissivity data using Kirchoff’s law  $\epsilon=1$  (Vaughan, 2003). The other spectral library was MODIS USCBS, in this case the spectrums are directly on emissivity and ascii format.

For the comparison between image emissivity and spectral library, the spectrums selected were for two groups indicated: featureless and with absorptions. Spectrums selected, as it can be seen in figure 1, were also generic (e.g for coniferous forest in the image we select pine spectrum from spectral library). In this work we only want to evaluate the AHS emissivity output

in a first approach. The original spectrums were resampled with AHS responsivity functions, which could be seen on figure 2.

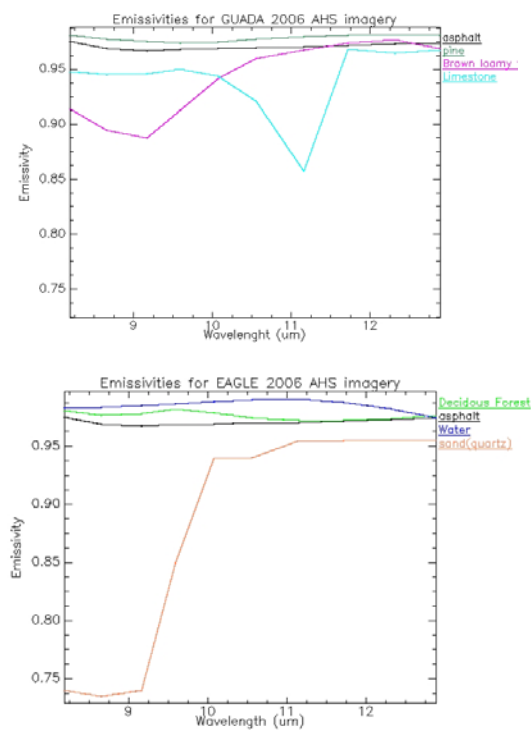


Figure 1: Resampled emissivity spectrums selected from spectral libraries for AHS imagery validation.

4. METHODS

4.1 Calibration: at-sensor radiance

AHS has two onboard calibration blackbody (BB) for thermal reference. Those BB are controllable in temperature range of -15 C (cold BB) at +25 C (hot BB) with respect to scan head heat sink temperature. The sensor measures in each scan line, in the beginning the cold BB, and at ending, the hot BB. AHS data were calibrated to at-sensor radiance using linear interpolation between cold and hot BB measured radiances and Digital Value registered. BB radiance were calculated with temperature Planck inverted, using for each channel corresponding responsivity functions of Figure 2. For EAGLE 2006 AHS flight line coldBB =21 C and hotBB=50 C, in the case of GUADA 2006 AHS flight line coldBB =16 C and hotBB=45 C.

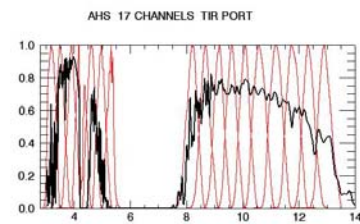


Figure 2: AHS MIR/TIR spectral responsivity functions plotted against atmospheric transmittance.

## 4.2 Atmospheric correction: at-surface radiance

In order to extract the surface temperature and emissivity from the image, it is necessary to perform an accurate atmospheric correction (Richter et al, 2005). ATCOR4 and ENVI thermal modules have different ways to correct for atmospheric effect on the observed spectral radiances:

### 4.2.1 Atmospheric correction using ENVI (ISAC)

In ENVI case, to compensate atmospheric effect, uses the In-scene Atmospheric Compensation (ISAC), developed by Aerospace corporation (SEBASS team: Johnson, 1998). ISAC is based assumption that for a given wavelength, there are measurements within the scene of a material with an emissivity nearly one (e.g vegetation or water). ISAC compensates for atmospheric transmission and upwelling radiance, assuming an atmospheric conditions homogeneous across the image but not for the effects of reflected downwelling radiance (Vaughan et al, 2003). ISAC method can be divided in following sequence steps:

- A channel with high atmospheric transmittance ( $\tau \sim 1$ ) is chose
- Compute apparent brightness temperature  $T_b$  with a constant emissivity (e.g.  $\varepsilon = 0.97$ )
- For the remaining channels a comparison in a scatter plot, between measured radiance and computed radiance, using calculated  $T_b$ , is applied.
- A straight line to the upper boundary of the points is fit. In this linear model the slope is proportional to transmittance ( $\tau$ ) and the offset is proportional to the path radiance ( $L_{pth}$ ).

Using ISAC on ENVI let you to choose two parameters for a best linear model performance: regression pixels and fitting technique. The first parameter indicate all or "MaxHit" only for pixels that have maximum brightness temperature at the channel selected as reference. For the second parameter the options are to fit over "Top of the Bins", means the pixels whose emissivity is close to 1, or reducing the pixels inside an area of 3 times a Nose equivalent sensor response (NESR) value. After an iterative analysis testing the parameters, the atmospheric correction ISAC outcome was processed with All-pixels and a fitting over an area of 0.35 NESR.

### 4.2.2 Atmospheric correction using ATCOR4

Following Richter et al 2005, the radiance equation in the thermal domain can be written as:

$$L_{sen} = L_{pth}^{\uparrow} + \tau_k (\varepsilon_k B_i(T_s)) + \tau_k (1 - \varepsilon_k) \frac{F_k^{\downarrow}}{\pi} \quad (1)$$

Where:

$L_{sen}$  at-sensor radiance

$L_{pth}$  thermal path radiance

$\tau$  transmittance

$\varepsilon$  emissivity

$T_s$  surface temperature

$B$  blackbody radiance at  $T$  temperature

$F$  thermal downwelling flux on the ground

ATCOR4 is based on the radiative transfer code MODTRAN4 (Berk et al 2000), is an specific application for atmospheric correction of airborne hyperspectral imagery. ATCOR4 estimates solar illuminations and atmospheric conditions using atmospheric look-up tables from MODTRAN4, having the

possibility to estimate atmospheric water vapor and visibility directly from the image, taking into account radiometric response in specific AHS channels. Water vapor is the main atmospheric constituent that affects the signal in the thermal domain. ATCOR4 estimates the water vapor using AHS reflective channels in the 940 nm region and the atmospheric pre-corrected differential absorptions (APDA by Schl pfer et al 1998).

## 4.3 Emissivity retrieval

For sensors with  $n$  thermal channels there are  $n$  equations with  $n+1$  uncertainties, it is an undetermined system with  $n$  emissivities plus a surface temperature (Richter et al, 2005). To address this problem the developed temperature and emissivities methods has to make some assumptions like consider a constant emissivity in one channel, but this is method depend. In this work we assess the performance of REF and NEM methods implemented in both software.

### 4.3.1 REF method

REF method was developed by Kahle et al (1980). The method assumes that emissivity in one channel has constant value for the entire image. For the channel selected the surface temperature is obtained for each pixel, the temperature calculated serves for the remaining channels emissivity calculation.

In order to test the AHS channel to be the channel reference, the imagery were process with all channels. The best channel was channel AHS 75, that also has the highest transmittance as it can be seen on Figure 2.

### 4.3.2 NEM method

NEM was developed by Gillespie (1985). The method assumes a constant emissivity in all the channels for a given pixel. All channels temperature was estimated and the maximum is considering the surface temperature. Using equation (1) all channel emissivity were derived.

In order to test the emissivity selection, the imagery was processed with interval emissivity from 0.96 to 0.99. The constant emissivity selected was 0.98 to be closer to water and vegetation and test the output for absorptions surfaces (quartz sand)

## 5. RESULTS

### 5.1 Atmospheric correction validation

The atmospheric correction is the first step to emissivity retrieval. The software proceed with different correction methods so a comparison between them for the same AHS data set is performed. Figure 3 shows this comparison for AHS EAGLE 2006 using a priori "cold" surface (e.g. water) and "hot" surface (e.g. sand). Taking into account also this comparison for AHS GUADA imagery, ISAC method outcomes a 5% less surface radiance than ATCOR4. Also it is important for emissivity retrieval to perform an accurate atmospheric correction. In order to evaluate atmospheric correction, surface temperature is compared between software output and field measurement. The field temperature measured in the EAGLE 2006 quartz sand point with CIMEL CE312, serves as validation, the average temperature at the flight time was 324° K, AHS only deviates 1° in ATCOR-4 the output and 1.5°K in ISAC outcome.



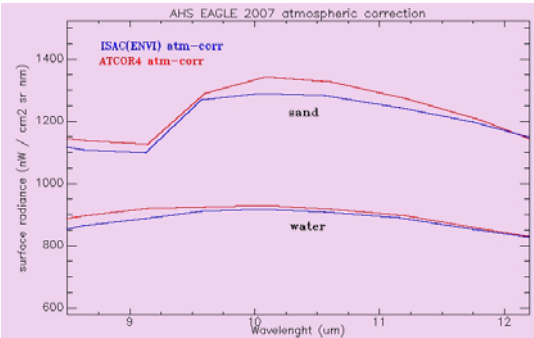


Figure 3: Surface radiance comparison between ATCOR4 and ISAC (ENVI) atmospheric correction output.

5.2 Emissivity retrieval validation

Both emissivity methods and software were used to gather emissivity from AHS data set. For each AHS flight line four emissivity imagery were obtained. Although emissivity images are very noisy, as it can be seen on Figure 4 for the example of EAGLE, surfaces are discernable using decorrelation stretch with AHS emissivity channels AHS 73,76,78. (water=blue, Deciduous forest=magenta, asphalt= cyan, and sand= green)

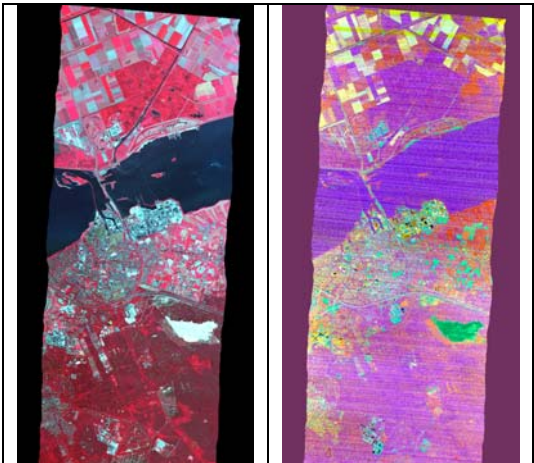


Figure 4: EAGLE 2006 imagery subset over Ermelo (The Netherlands). Left: RGB false color VNIR channels. Right: Decorrelation stretch of emissivity channels AHS 73,76,78.

For each AHS data set, four surfaces serves as evaluate the emissivity results. For each surface, comparisons between validation spectrum (see figure 1) and spectrum extract from imagery was applied. The comparison was realized for all the channels obtaining the deviation among methods along wavelength. Figure 5 shows the deviation calculated for all surfaces and methods, graphics indicates: dotted ATCOR4-NEM, dashed ATCOR4-REF, dash dot ENVI-NEM and solid ENVI-REF

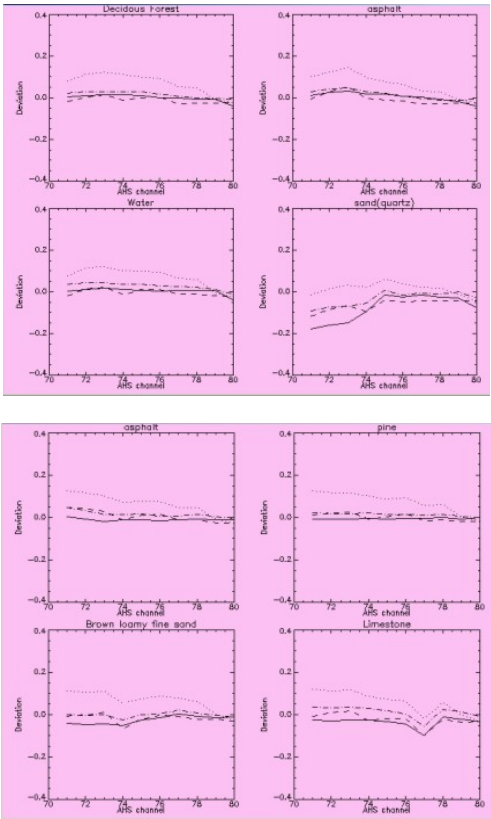


Figure 5: Emissivity deviation calculated for all surfaces and methods. Upper: EAGLE2006 and Bottom: GUADA 2006. Lines indicate: dotted ATCOR4-NEM, dashed ATCOR4-REF, dash dot ENVI-NEM and solid ENVI-REF

6. CONCLUSIONS

Both atmospheric correction methods perform very similar for gathering surface radiance, taking into account hot and cold areas, and obtained an accurate surface temperature comparing with only one field validation point.

AHS emissivity retrieval using REF and NEM had obtained encouraging results. The deviation gathered between AHS emissivity and validation data, were not higher than 0.05 except for ATCOR4 NEM method, that seems to have a bias. On the contrary this method performs better for absorptions surface like quartz sand.

A deeper evaluation for methods applied is required, in terms of image noise and parameters selection such us: reference channels and constant emissivity.

## 7. REFERENCES

- Fernandez –Renau, A. Gómez, J.A. and De Miguel, E. (2005). The INTA AHS system. Proceedings. SPIE Int. Soc. Opt. Eng. 5978, 59781L.
- Jiménez-Muñoz, J.C. and Sobrino, J.A. "Emissivity spectra obtained from field and laboratory measurements using the temperature and emissivity separation algorithm," *Appl. Opt.*, vol. 45, no. 27, 7104-7109, 2006.
- Li, Z. 1999. Evaluation of six methods for extracting relative emissivity spectra from thermal infrared images. *Remote. Sens. Env.* 69:197-214.
- Richter, R. et al 2005. Spectral and radiometric requirements for the airborne thermal imaging spectrometer ARES. *International Journal of Remote Sensing*. 26.15 3149-3162
- Schmugge et al. 2002. Temperature and emissivity separation from multispectral thermal infrared observations. *Remote. Sens. Env.* 79,189-198
- Sobrino, J.A. et al. 2006. Land surface temperature derived from airborne hyperspectral scanner thermal infrared data. *Remote. Sens. Env.* 102,99-115
- Vaughan, R.G. 2003. SEBASS hyperspectral thermal infrared data: surface emissivity measurement and mineral mapping. *Remote. Sens. Env.* 85,48-63

## 8. ACKNOWLEDGEMENTS

AHS EAGLE 2006 image was acquired in the framework of EAGLE 2006 project (ESA).

AHS GUADA 2006 image was acquired at instances of Spanish National Institute for Agrarian research (INIA).

Authors want to acknowledge Dr Rudolf Richter for guidance with ATCOR4 software.

# SIMULATION STUDIES OF THE EFFECT OF FOREST SPATIAL STRUCTURE ON InSAR MEASUREMENTS

Guoqing Sun<sup>1,2\*</sup>, Dawei Liu<sup>2,3</sup>, K. Jon Ranson<sup>4</sup>, and Benjamin Koetz<sup>5</sup>

<sup>1</sup>Department of Geography, University of Maryland, College Park, MD 20742 USA, E-mail: Guoqing@ltpmail.gsfc.nasa.gov, Phone: (301)6146655

<sup>2</sup>State Key Laboratory of Remote Sensing, Institute of Remote Sensing Applications, Chinese Academy of Sciences, P. O. Box 9718, Beijing, 100101, China, E-mail: david\_liu863@163.com,

<sup>3</sup>Graduate School of the Chinese Academy of Sciences, Beijing, 100049, China

<sup>4</sup>Biospheric Sciences Branch, NASA Goddard Space Flight Center, Greenbelt, MD 20771, USA

<sup>5</sup>Remote Sensing Laboratories (RSL), Department of Geography, University of Zurich, Winterthurerstrasse 190, CH-8057 Zurich, Switzerland

**KEY WORDS:** 3D backscatter model, Forest Spatial Structure, InSAR, Scattering Phase Center

## ABSTRACT:

The height of scattering phase center retrieved from InSAR data is considered to be correlated with tree height and the spatial structure of the forest stand. Though some researchers have used simple backscattering models to estimate tree height from the height of scattering center, the effect of forest spatial structure on InSAR data is not well understood yet. A three-dimensional coherent radar backscattering model for forest canopies based on realistic three-dimensional scenes was used to investigate the effect. A fractal tree model (L-system) was used to simulate individual 3-D tree structure of different ages or heights. Trees were positioned in a stand in specific patterns resulting in a 3-D medium of discrete scatterers. The radar coherent backscatter model used the 3-D forest scene as input and simulated the coherent radar backscattering signature. Interferometric SAR images of 3D scenes were simulated and heights of scattering phase centers were estimated from the simulated InSAR data. The effects of tree height, and the spatial distribution patterns of trees on the scattering phase center were analyzed and discussed.

## 1. INTRODUCTION

The 3D radar backscatter model developed previously at UMD/GSFC (Sun and Ranson, 1995) was an incoherence model, in which backscattering components were incoherently summed together to get the total backscattering power from a pixel or target. This model was modified into a full coherent model by considering the positions of all scatterers within a tree crown (leaves and branches) and coherently adding the backscattering components together. The phase of the scattering component was determined by its position relative to a reference point. Different from other coherent models (Lin and Sarabandi, 1999; Thirion et al., 2004), the model used here has both the tree crown components (branches and leaves) and position of each tree in a stand explicitly specified. The explicit 3D physical model of the forest stands was generated using L-system. The scattering components considered in the model are the direct backscattering from a scatterer, the double-bounce between the scatterer and ground surface, and the ground-scatterer-ground scattering. The model was used in this study for margin difference between two antennas) is different for different scattering components, so does the phase center height of these components. The position of the scattering phase center of a pixel is a result of the coherent

summation of these components. When the forest structure changes, the relative strengths of these scattering components change leading to the change of the scattering center.

## 2. COHERENT BACKSCATTER MODEL

The coherent radar backscattering model takes the 3-D forest scene as input and simulates the coherent radar backscattering signature. The model is a discrete scatterer model. Dielectric cylinders with finite length and dielectric thin disks are used to represent the trunks, branches and leaves. The radar scattering signal from trunks and branches is calculated using the infinite cylinder approximation, and that of the leaves employed the generalized Rayleigh-Gans (GRG) approximation (Karam et al., 1988). Furthermore, the attenuation of the microwave signal by the forest canopy, i.e. transmissivity matrix of the forest canopy, is estimated using Foldy's approximation. The tree crown is divided into multiple cells. Every cell is internally homogeneous. Using these approximations, the scattering matrix of every scatterer is calculated, and added together coherently. In this study, only the first order coherent scattering was taken into consideration, and the higher order scattering and the near-field coupling between adjacent scatterers were omitted.

Within a forest stand or a radar pixel there are  $N$  scatterers. The ground plane can be considered as a half-space dielectric medium with a slightly rough surface. The total scattering field from a pixel can be evaluated from

$$E^s = \frac{e^{ikr}}{r} \left( \sum_n e^{i\phi_n} F_n \right) E^i \quad (1)$$

where  $\phi_n$  is the phase compensation term which is the phase shift of the  $n$ th scatterers from local to global coordinate system.  $\phi_n$  is given by  $(\vec{k}_i - \vec{k}_s) \cdot \vec{r}_n$ , where  $\vec{k}_i$  and  $\vec{k}_s$  are the direction of incidence and scattering wave.  $\vec{r}_n$  is the coordinate vector of the  $n$ th scatterers in global coordinate system. Both  $E^s$  (scattering field) and  $E^i$  (incidence field) are vectors and can be denoted as  $\begin{bmatrix} E_{hs} \\ E_{vs} \end{bmatrix}$  and  $\begin{bmatrix} E_{hi} \\ E_{vi} \end{bmatrix}$ , respectively.  $F_n$  is the complex scattering matrix of the  $n$ th scatterer above a dielectric plane:

$$F(\theta_i, \phi_i; \theta_s, \phi_s) = \begin{bmatrix} f_{hh}(\theta_i, \phi_i; \theta_s, \phi_s) & f_{hv}(\theta_i, \phi_i; \theta_s, \phi_s) \\ f_{vh}(\theta_i, \phi_i; \theta_s, \phi_s) & f_{vv}(\theta_i, \phi_i; \theta_s, \phi_s) \end{bmatrix} \quad (2)$$

where  $f_{\alpha\beta}(\theta_i, \phi_i; \theta_s, \phi_s)$  is the scattering amplitude from direction  $(\theta_i, \phi_i)$  in  $\alpha$  polarization to direction  $(\theta_s, \phi_s)$  in  $\beta$  polarization.

$F_n$  is mainly made up of four components:

- 1)  $F_n^t$  denotes direct scattering matrix from scatterers;
- 2)  $F_n^{gt}$  denotes scattering matrix from the scatterer specular reflected from ground;
- 3)  $F_n^{tg}$  denotes scattering matrix from specular reflection of the ground by the scatterer;
- 4)  $F_n^{gtg}$  denotes ground-scatterer-ground scattering matrix.

The bistatic scattering coefficient in a pixel of area  $A$  is

$$\sigma_{\alpha\beta}(\theta_i, \phi_i; \theta_s, \phi_s) = \frac{4\pi}{A} |f_{\alpha\beta}(\theta_i, \phi_i; \theta_s, \phi_s)|^2 \quad (3)$$

### 3. SIMULATION OF 3D FOREST STAND STRUCTURE

Field measurements or a forest growth model provide information of forest species composition and tree sizes in certain growth phases. A fractal tree model (L-system) was used to simulate individual 3-D tree structure of different ages or heights. Trees were positioned in a stand in certain patterns resulting in a 3-D medium of discrete scatterers. The radar coherent backscatter model takes the 3-D forest

scene as input and simulates the coherent radar backscattering signature. Fig. 1-3 show the 3D structure of forest stands with different spatial distribution patterns of trees. These forest stands consists of 36 birch trees. Fig. 1 is a clumped distribution of trees (5 clump centers). Fig. 2 shows the random distribution of trees. Fig. 3. shows a regular 6 by 6 matrix of trees.

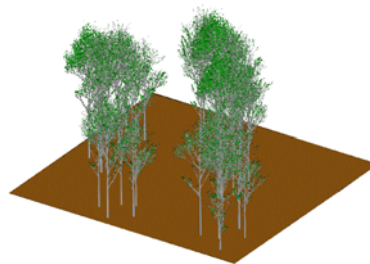


Fig.1. Clump distribution

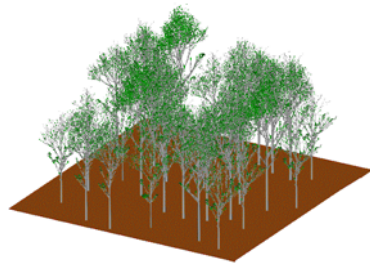


Fig.2. Random distribution

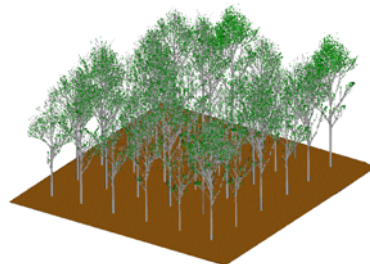


Fig.3. Regular distribution

### 4. InSAR SIMULATION

Two coherent radar images were simulated using coherent radar scattering model. The height of the scattering phase center was estimated using the following equations (Zebker et al, 1992):

$$Z(y) = h - r \cos(\theta)$$
$$\cos \theta = \cos \alpha \cos(\alpha - \theta) + \sin \alpha \sin(\alpha - \theta)$$
$$\sin(\alpha - \theta) = \frac{(r + \delta)^2 - r^2 - B^2}{2 \cdot r \cdot B} \approx \frac{\delta}{B}$$
$$\delta = \frac{\lambda \Delta \phi}{2\pi}$$

where  $\Delta \phi = \angle(E_1^* E_2)$  represents the phase difference between two simulated radar signals E1 and E2. Fig. 4 shows the height of phase center for various scattering components. The phase center of a pixel is the combined effect of the components included in the pixel. The JPL TOPSAR configuration (platform height 8500m, baseline 2.6m,  $\alpha=62.77^\circ$ ) (Zebker et al., 1992) was used in the simulation of the InSAR images.

5. RESULTS

Dependence of phase center height on stand structure

The InSAR signature from entire stands shown in Figs. 1-3 were simulated and the height of the phase center were calculated from the simulated data. The tree height changes from 6m to 15m. Table 1 shows L-HH and L-VV InSAR results, respectively.

Table 1. Height of phase center for different stands with 36 trees from simulated LVV InSAR (bottom) and LHH InSAR (top) data. Clumped – trees were clumped into 5 clusters, 6X6 – regularly planted, and random – randomly planted.

LHH		Tree Height (m)		
Stand Type	6	10	15	
Clump	3.79	6.54	9.53	
6*6	4.21	7.20	10.39	
Random	4.72	7.81	10.76	
LVV		Tree Height (m)		
Stand Type	6	10	15	
Clump	3.79	6.54	9.53	
6*6	4.21	7.20	10.39	
Random	4.72	7.81	10.76	

The height of phase center of the direct backscattering from all branches and leaves equals the height of the scatterer itself. The phase center of the total direct backscattering should be in a place within the tree crown. Since the backscattering from the ground surface was not included in this simulation, and the ground-scatterer-ground scattering was very week, the double-bounce is a major factor to lower

the phase center of a forest stand. Table 2 shows that when the tree distribution is clumped, the double-bounce scattering is strong, so the phase center in this case is lower than other distributions.

Table 2. Percentage of backscattering power (L-HH) from double-bounce scattering for three different tree distribution patterns.

	Clump	6*6	Random
Double-bounce	59%	24%	32%

Simulation of high-resolution images

Fig. 4 shows a L-HH backscattering coefficient image of the stand shown in Fig. 2. Rader incidence angle is 45°. Image pixel size is 0.5m. Fig. 5 is the corresponding power image of Fig. 4.

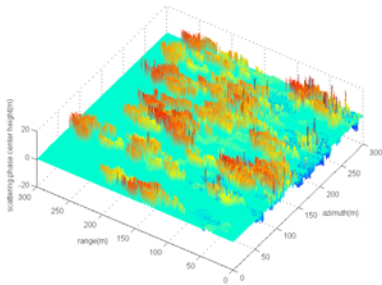


Fig. 4. The height of scattering phase of a simulated birch forest stand. L-band HH

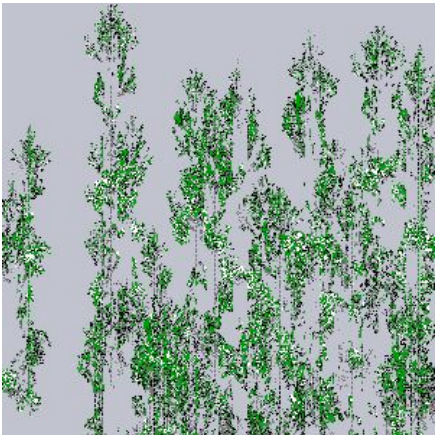


Fig. 5 is the correspondent power image of Fig. 4

6. CONCLUSION

The simulation results have shown that the location of backscattering phase center from a forest stand is influenced by the spatial structure. We will verify the results using field



measured forest structure and InSAR data in our future work.

## 7. ACKNOWLEDGEMENT

This study was funded by NASA's Science Mission Directorate, and National Science Foundation of China (40571112), the 863 program (2006AA12Z114) of China.

## REFERENCES

- Lin, Y. C. and K. Sarabandi, "A Monte Carlo coherent scattering model for forest canopies using fractal-generated trees," *IEEE Trans. Geosci. Remote Sensing*, vol. 37, pp. 440-451, Jan. 1999.
- Karam, M. A., A. K. Fung, and Y. M. M. Antar, "Electromagnetic wave scattering from some vegetation samples," *IEEE Trans. Geosci. Remote Sensing*, vol. 26, pp. 799-808, Nov. 1988.
- Sun, G. and K. J. Ranson, 1995, A three-dimensional radar backscatter model of forest canopies, *IEEE Transaction on Geoscience and Remote Sensing*, Vol. 33, No. 2, pp. 372-382.
- Thirion, L. I. Chênerie, and C. Galy, "Application of a coherent model in simulating the backscattering coefficient of a mangrove forest," *Wave in Random Media*, 2004, pp. 299-316.
- Zebker, H. A., S. N. Madsen, J. Martin, K. B. Wheeler, T. Miller, Y. Lou, G. Alberti, S. Vetrella, A. Cucci, The TOPSAR Interferometric Radar Topographic Mapping Instrument, *IEEE Transactions on Geoscience and Remote Sensing*, 1992, vol.30, No.5.

# ATMOSPHERIC CORRECTION OF AIRBORNE PASSIVE MEASUREMENTS OF FLUORESCENCE.

F. Daumard<sup>a,\*</sup>, Y. Goulas<sup>a</sup>, A. Ounis<sup>a</sup>, R. Pedros<sup>b</sup>, I. Moya<sup>a</sup>

<sup>a</sup> LMD-CNRS, Ecole Polytechnique, 91128 Palaiseau – France, (fabrice.daumard, yves.goulas, ounis, ismael.moya)@lmd.polytechnique.fr

<sup>b</sup> Universitat de Valencia, Departament de Fisica de la Terra i Termodinamica, Valencia – Spain, Roberto.Pedros@uv.es

**KEY WORDS:** Fluorescence, Airborne Measurements, Altitude Effects, MODTRAN, AirFlex

## ABSTRACT:

A new instrument for passive remote sensing of sunlight-induced fluorescence took part in a series of airborne measurements during the summer 2005 (SEN2FLEX campaign). It measured for the first time the chlorophyll fluorescence emission over a succession of cultivated fields. The sensor is based on the Fraunhofer line discrimination principle, applied to the atmospheric oxygen absorption bands at 687nm and 760nm.

Nadir viewing measurements made at various altitudes (300m-3000m) showed a continuous increase of the band depths when increasing the altitude. Among several radiative transfer models of the atmosphere, MODTRAN 4 was chosen to account for these altitude effects, because of its resolution (2cm-1) and its capability to describe multiple scattering. In order to validate the model, a data base was build up using ground measurements of the depth of the oxygen absorption band at 687 and 760 nm during a diurnal cycle.

In this paper, we compare depths measured at the ground level with the MODTRAN 4 predictions. Local aerosol contents were retrieved from spectroradiometric measurements and included in the model. It is concluded that MODTRAN 4 is able to accurately describe the variation of the atmospheric oxygen absorption bands at 760 nm. The depth variation at 687 nm are also retrieved, but with a lower accuracy, due in part to the uncertainties of the spectral characteristics of the sensor. The sensitivity to several parameters, including aerosols, water content and ozone was studied.

## 1. INTRODUCTION

The vegetation holds an important place in the cycle of carbon, in such a way that the gaseous exchange between vegetation and atmosphere is one of the key parameters of climate modeling. A way to quantify and identify these exchanges is to study the photosynthesis activity: large-scale measurement of the vegetation's photosynthesis activity may provide important information to improve the knowledge of the vegetation's role in the carbon cycle.

Fluorescence is a deexcitation mechanism in competition with photochemical conversion. Therefore, measuring the fluorescence emitted by the vegetation is one way to assess its photosynthesis activity.

The passive fluorescence measurement, which uses the sun as the light source, is a promising technique to provide large-scale data. Under natural sunlight illumination, the amount of chlorophyll fluorescence emitted by the vegetation represents less than 1% of the radiance of the vegetation: it is a very weak signal. However, at certain wavelengths where the solar spectrum is attenuated, the fluorescence signal becomes not negligible and can be quantified by the measurement of the filling of the band. This is the FLD principle (Fraunhofer Line Discriminator) (Plascyk, 1975) which was adapted to the atmospheric oxygen absorption bands (Moya et al., 1998) in order to quantify the chlorophyll fluorescence signal. The sunlight-induced fluorescence is obtained by comparing the depth of the atmospheric oxygen absorption band in the solar irradiance spectrum to the depth of the band in the radiance spectrum of the plants. In the last ten years, several passive

instruments were proposed and used (Moya et al., 1998, 2004; Louis et al., 2005) successfully to measure the fluorescence of the vegetation at short distances (<50m).

An airborne campaign lasting several days SEN2FLEX (SENtinel-2 and FLuorescence EXperiment) was carried out in summer 2005 to study the spatial variability of the fluorescence signal. The measurements were made on various crops during several days. The preliminary results showed the reproducibility of the measurements made at the same altitude and a very good correlation between depths and the calculated NDVI (Normalized Difference Vegetation Index). See accompanying paper (Moya et al., 2006). To study the air mass effect on the band depth, a flight along the same track was made at different altitudes: 327m, 640m, 1242m, and 3119m.

The aim of this paper is to present a correction model of altitude effects on the depth of A and B atmospheric oxygen absorption bands.

## 2. MATERIAL AND METHODS

The sunlight's path length varies during the day with the solar zenith angle and so does the amount of O<sub>2</sub> on the optical path crossed by the light to reach the ground. It results in a diurnal variation of depths (Moya et al., 2004).

In order to validate the model, a set of diurnal cycles of band depths have been acquired. The model is regarded as accounting for the atmospheric effects if it succeeds in predicting these diurnal cycles.

\* Corresponding author. fabrice.daumard@lmd.polytechnique.fr

2.1 Diurnal Cycle Measurements

**Sensor:** The sensor used to acquire the diurnal cycle, TerFlex, is identical to the one used for flights. It is a six channels sensor, each one constituted by a photodiode (Si PIN) and a narrow band interference filter. The set of filters used in the optical head is maintained at a constant temperature of 40°C to avoid any shifting or broadening of the transmission filters. Terflex provides a simultaneous flux measurement in the six channels ensuring time correlation. For both A and B bands, three optical measurements are performed: one in-band and two off-band, on the continuum. The use of two filters out of the band allows to interpolate the reflectance within the band. See Table 1 for filters details.

Position		FWHM	Name	Use
685.17 nm	Off band	0.5 nm	B687	Compute the B-band depth.
687.03 nm	In band	0.5 nm	F687	
757.46 nm	Off band	1 nm	B760	Compute the A-band depth.
760.55 nm	In band	1 nm	F760	
694.16 nm	Off band	5.8 nm	R695	Compute the in band reflectance.
770.55 nm	Off band	2.25 nm	R770	

Table 1. Filter Position

Terflex has been calibrated before and after the campaign. For each channel, the flux intensity and spectral transmission have been measured using a spectrally calibrated source (LiCor 1800-02). The calibration uncertainty, about 0.7% in the B-band and 1.5% in the A-band, is the standard deviation of several independent measurements.

**Experimental Setup:** The measurement campaign took place on 1, 2, 3 June 2005, at Las Tiesas-Anchor site (Barrax, Spain) (39° 03' 30'' N; 2° 05' 24'' W) under clear-sky conditions. TerFlex was installed on the ground in a vertical position: about 1.5 m height from the ground (see fig. 1).



Figure 1. TerFlex sensor in its measuring configuration.

At that height, the spot size on the target was about 20 cm. The instrument was north-to-south oriented to avoid any shading of the target. TerFlex was targeting a lambertian surface acquiring fluxes in the six channels from 10:00 to 17:00 local time. The lambertian reference (Spectralon, LabSphere) ensures that the reflexion coefficient is the same for each channel and avoids directional effects. In this manner, the band depths are simply defined by the following ratio:

$$Depth = \frac{Flux_{Off\ band}}{Flux_{In\ band}}$$

(1)

**Aerosols Measurements:** During the campaign, the aerosol properties have been monitored by the Solar Radiation Team of the University of Valencia. Using the technique described in (Martinez-Lozano et al., 2001) the aerosol optical thickness (AOT) has been retrieved from the measurements of the solar direct irradiance with a LiCor 1800 spectroradiometer. The ozone content was measured with a photometer (Microtops II) and the relative humidity was measured in a meteorological tower and with several radio soundings. By inverting the Mie theory included in the OPAC model (Optical Properties of Aerosols and Clouds) (Hess et al. 1998), the aerosol model and the particle densities that better fit the measured AOT were obtained. Several aerosol models were considered, including “continental”, “continental clean”, “maritime”, “maritime clean”, “mixture of continental and maritime”, “desert outbreak” (Saharan dust). Once identified the aerosol composition, the Mie theory was used to produce the aerosol properties (absorption spectrum, extinction spectrum, asymmetry factor, phase function) required for a more accurate description of the aerosols in MODTRAN.

2.2 Modeling :

Among several radiative transfer models of the atmosphere, MODTRAN 4 (v1r1) (MODerate Spectral Resolution Atmospheric TRANsmittance Algorithm) was chosen to correct for these altitude effects, because of its resolution, 2 cm<sup>-1</sup>, and its capability to describe multiple scattering. The MODTRAN input file is generated in order to reproduce the conditions of measurement. Table 2 shows the main parameters of the MODTRAN configuration file used.

Parameter :	Value :
Calculation Option	MODTRAN correlation-k
Type of Atmospheric Path	Slant Path to Space or Ground
Atmosphere	MidLat Summer
Mode of Execution	Radiance w/ Scattering
Scattering Algorithm	DISORT
DISORT streams	16
Temperature at First Boundary	298
Surface Albedo	1
FWHM of Slit Function	1 cm-1

Table 2. Main parameters of the MODTRAN input file.

To describe the aerosol content, MODTRAN divide the atmosphere into four vertical regions. The first one is the boundary layer. The vertical distribution of the aerosol concentration in the boundary layer is drive by the “surface meteorological range” which characterizes the visibility; this parameter is called “VIS” in MODTRAN. This parameter provides a way to increase or decrease the amount of aerosol in the boundary layer. Larger values of “VIS” reduce aerosols effects, while smaller values increase aerosol effects. For hazy conditions (“VIS” from 2 to 10 km) the boundary layer aerosol concentration is assumed to be independent of height up to 1 km with a pronounced decrease above that height. For “VIS” from 23 to 50 km (clear to very clear conditions), the vertical distribution of concentration is taken to be exponential. Above the boundary layer, the aerosol characteristics become less sensitive to weather and geography variations. At these altitudes, changes are more a result of seasonal variations. The “VIS” parameter is set using the Koschmieder formula:

$$VIS = \frac{\ln(1/\epsilon)}{Extc_{550} + 0.01159} \quad (2)$$

Where  $Extc_{550}$  is the retrieved aerosol extinction coefficient at 550 nm,  $\epsilon=0.02$  is the threshold contrast in MODTRAN and 0.01159 ( $\text{km}^{-1}$ ) is the surface Rayleigh scattering coefficient at 550 nm.

For each region, MODTRAN allows assigning aerosols properties such as extinction spectrum, absorption spectrum, asymmetry factor and phase function. This feature is used in order to have a better description of the aerosol loading.

For calculation, we used the "Correlation-k" (Slow) option of MODTRAN, which improves the accuracy of radiance calculation (Berk et al., 1999), mainly in the absorption zone. The algorithm used for the multiple scattering is DISORT (DIScrete Ordinate Radiative Transfer) (Stamnes et al, 1988), it allows a better precision than the default algorithm (Modtran 2). All the parameters driving the accuracy of the calculation are set to ensure the best precision.

The output of the computation is the radiance spectrum at the sensor level. In order to obtain fluxes, this spectrum is integrated over the measured transmission function of each TerFlex channel. Then the depths predicted by MODTRAN can be obtained.

### 3. RESULTS AND DISCUSSION

As the results are fairly the same for the entire campaign, we mainly focus on the results of the 1<sup>st</sup> of June

#### 3.1 Altitude effects

**Fluxes:** The air column between the vegetation and the sensor modify the signal coming from the vegetation: it absorbs part of the signal ( $\text{O}_2$  absorption) and contributes to it through its albedo. In order to assess these effects, flights were made along the same track at different altitudes: 327m, 640m, 1242m, and 3119m. Figures 2 show the evolution of the in-band and off-band fluxes measured on the vegetation versus the altitude.

In the A-band (Fig. 2.b) the fluxes decrease with altitude, this is the effect of the oxygen absorption.

Figure 2.a shows that in the B-band the fluxes increase with altitude. For the B-band, the signal coming from the vegetation is very weak because of the low reflectance of the vegetation in this wavelength range. Thus, the behaviour of fluxes is dominated by the contribution of the radiance of the atmosphere between the target and the sensor and not by the effect of absorption.

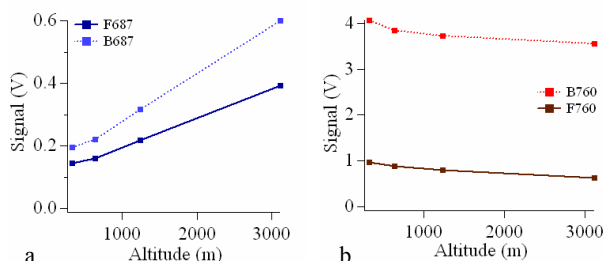


Figure 2. Radiance measured over the same field vs. altitude (3rd of June).

a. B-band.  
b. A-band.

**Depths:** Figures 3 shows that the depths increases with the altitude, this behaviour is due to the absorption of the oxygen.

This is not a negligible effect: in the A-band, measuring the depths at an altitude of 3 km instead of the ground level leads to a variation on depth bigger than the variations induced by vegetation. In the B-band, the variations induced by vegetation are of the same order of magnitude. The variation of depths due to fluorescence at ground level is about 7.6% and 2.5% in the B-band and A-Band respectively.

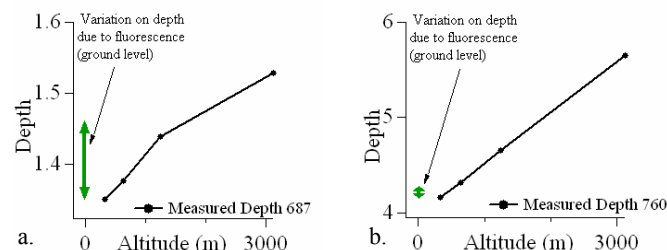


Figure 3. Depths measured over the same field vs. altitude (3<sup>rd</sup> of June).

a. B-band.  
b. A-band.

The altitude effect is so strong compared to the fluorescence signal that a model is needed to take into account this effect.

#### 3.2 Measured Diurnal Cycle

Figure 4 shows diurnal cycle records in both bands for the 1<sup>st</sup> of June from 11:00 to 17:00, local time. The depth of the A-band ranges from 4.1 (noon) to 5.26 (11:00 a.m.). Thus, the diurnal cycles imply a variation of 28% from the minimum to the maximum. In turn, the B-band values ranges from 1.32 (noon) to 1.40 (11:00 a.m.), which means a variation of 6%.

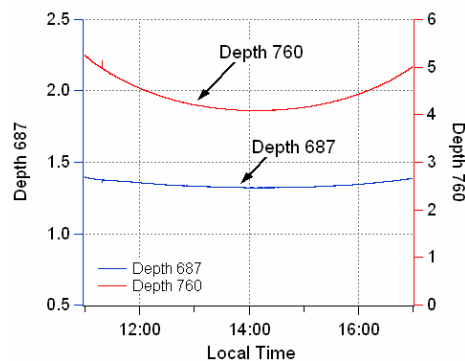


Figure 4. Diurnal cycle recorded on the 1st of June.

The uncertainty on these values, due to the calibration of the sensor, is about 0.7% in the B-band and 1.5% in the A-band.

#### 3.3 Measurement of the Channel Transmission Function

**Spectral Calibration:** Great attention has been paid to the measurement of the transmission functions because of their narrow bandwidth. A small shift of the transmission functions could dramatically change the computed flux, especially for the in-band filters. The transmission functions were measured with a HR4000 spectrometer (Ocean Optics). The spectral instrumental function of the HR4000 has been measured, using the atomic lines at 763.51 nm (Ar) and 690.67 nm (Hg) of an Hg(Ar) calibration lamp (Oriol Instruments, France). The shape of the instrumental function was found different for each atomic line with the same FWHM, of about 0.5 nm. The actual transmission functions of each channel were retrieved after

deconvolution of the measured transmission spectra by the instrumental response function of the spectrometer. The deconvolution process has reduced the FWHM of the filters of about 37% and has corrected their shape. A final accuracy of 0.1nm is estimated for the actual channel transmission.

**Radiometric Calibration:** Terflex has been calibrated against a black body (Li-Cor 1800-02, NE, USA), so that the flux obtained for each channel is comparable to the others.

3.4 Sensitivity Studies

The effect of the air mass depends on several parameters including the sensor's altitude, the sun elevation and the state of the atmosphere. The sensitive parameters of the model are the ones that could modify the scattering and absorption properties of the atmosphere. It is necessary to evaluate their influence on the computed band depths and to determine whether they need to be measured or not. The results will be compared both to the change of the depths due to fluorescence and to the accuracy of the measurement.

**Atmosphere Model Sensitivity:** MODTRAN 4 has six reference atmospheres. Table 3 present depths at solar noon the 1<sup>st</sup> of June computed with each reference atmosphere. It shows that the standard deviation for the B-band and the uncertainty on measurements are of the same order of magnitude. Attention should be paid to the choice of atmosphere model. As the campaign took place in Spain on summer, the MidLat Summer model is chosen (45N latitude, July).

Model Atmosphere	Depth B-band	Depth A-band
US Standard 1976	1.346	4.089
Tropical	1.357	4.076
MidLat Summer	1.354	4.059
MidLat Winter	1.342	4.126
SubArctic Summer	1.348	4.043
SubArctic Winter	1.333	4.104
Standard Deviation	0.64%	0.74%
Maximum Variation	1.6%	2%

Table 3. Band depths computed with MODTRAN at solar noon the 1st of June for each atmospheric model.

**Water Content :** In Table 4 the band depth at noon are calculated for various values of the water vapour column, from 0.001 g.cm<sup>-2</sup> to 6 g.cm<sup>-2</sup> (Noël et al., 2005). The measured water content value is 1.4g.cm<sup>-2</sup> giving values of the band depths of 1.354 and 4.058 for the B-band and A-band respectively. Table 4 show that the variations for the A-band are negligible. For the B-band the standard deviation of depth is not negligible compared to the uncertainty on the measurements. However, the depths computed with the default value of water content are close to the ones obtained with the actual value. One can conclude that the default value could be used without significant errors if the water content measurement is not available.

Water content (g.cm <sup>-2</sup> )	Depth B-band	Depth A-band
Default	1.3544	4.05858
0.001	1.3516	4.05844
1	1.3533	4.05854
6	1.3568	4.05851
Measured : 1.4	1.3539	4.05853
Standard Deviation	0.2%	<0.02‰

Table 4. Band depths versus the water content computed at solar noon the 1<sup>st</sup> of June.

**Ozone content:** In Table 5 the band depths are calculated for various values of the ozone content from 0.2 atm-cm to 0.5 atm-cm. The standard deviations of the band depths are small for large variation of the ozone content. Furthermore, the measured ozone content is 0.284 atm-cm at noon giving 1.3545 and 4.0584 for the B-band and A-band depths respectively. These values are close to those obtained with default setting. One can conclude that the measurement of the ozone content is optional and that the default setting can be used.

Ozone content (atm-cm)	Depth B-band	Depth A-band
Default	1.3544	4.0586
0.2	1.3547	4.0586
0.35	1.3544	4.0582
0.5	1.3541	4.0577
Measured: 0.284	1.3545	4.0584
Standard Deviation	<0.3‰	<0.2‰

Tables 5. Band depths in function of the ozone content computed at solar noon the 1<sup>st</sup> of June.

**Aerosols:** The aerosol data acquired during the campaign represent the integrated aerosol properties along the whole atmospheric column but does not give information on their vertical distribution. Consequently, they are included in MODTRAN as one single layer, discarding the others. By default, in MODTRAN, the first layer extends from 0 km to 3 km. In order to estimate the effect of aerosols vertical distribution, the variations of the band depths with the altitude of the aerosol layer have been investigated. Setting the aerosol layer at an altitude of 5 km instead of 3 km will change the average optical path length. The depth of the bands should vary consequently. It is the same issue for the layer thickness. Figure 5 presents the variation of depths when changing the altitude of the aerosol layer from 0 km to 5 km. Setting the altitude of the main aerosol layer to 5 km is not realistic physically. Calculation is made to have an increase of the effect of the aerosols distribution. The vertical scales of the graphs are defined so that the variations induced by fluorescence represent the full scale.

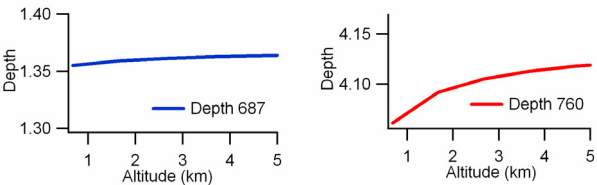


Figure 5. Band depths versus the aerosol layer altitude.

Figure 5 shows that the variation of depth induced by setting the altitude of the layer to 5 km instead of 0 km is about 0.7% for the B-band and 1.5% for the A-band. The variations are important, especially in the A-band where the maximum variation represents about the half of the effect due to



fluorescence. For the B-band the maximum variation represents less than 10% of the variation due to fluorescence. Figures 6 show that the effects are similar on the whole when one increases the aerosol layer thickness.

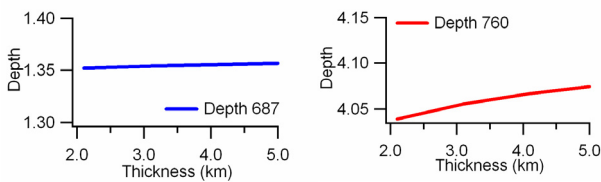


Figure 6. Band depths versus the aerosol layer thickness.

There is no measurement allowing the choice of a configuration rather than another. The LIDAR didn't function during this part of the campaign. Thus, the default configuration will be used: a layer extending from 0 to 3km. The aerosols properties used were detailed retrieved from the measurements of AOT with the OPAC model as described before. The retrieving of such detailed properties might be unnecessary. To assess the improvement induce by the use of detailed properties, the depths obtained with this description of aerosols were compared to the depths obtained with the standard aerosol models. MODTRAN has three standard aerosol models: "Rural", "Maritime" and "Urban" (Berk et al, 1999). They provide aerosol extinction characteristic of an air mass that has just moved through one of these types of areas. The parameter "VIS" is used to drive the models. Larger values of "VIS" reduce the aerosols effects, while smaller values increase the aerosol effects. In transmission mode, MODTRAN separately tabulates the transmission due to aerosols. The AOT can be deduced from this calculation by the negative of the logarithm (Conant et al.). Tables of visibility versus AOT at 700 nm were computed for each aerosol model. Then diurnal cycles were computed using the visibility matching the measured AOT. Table 6 shows, for the 1<sup>st</sup> of June, the maximum deviation of depth over a diurnal cycle computed with each standard aerosol model instead of the aerosol properties retrieved. The mean AOT was 0.1508.

Model	Rural	Maritime	Urban
VIS matching mean measured AOT (700 nm)	33.655 km	40.129 km	35.519 km
Max deviation for a diurnal cycle B-Band	0.8 %	0.8 %	0.3 %
Max deviation for a diurnal cycle A-Band	2.2 %	2.3 %	1 %

Table 6. Comparison between standard aerosol model and accurate properties of aerosols.

Although the rural model seemed to be more adapted to describe the conditions of the measurement, Table 6 shows that the model that best fits the data is the urban model. This shows that the retrieving of detailed aerosols properties is necessary because we wouldn't be able to choose a priori the built-in model that would best represent the aerosols conditions during the measurements.

3.5 Diurnal Cycle Modeling

In order to validate the model, several simulations of the diurnal cycle were computed from 9:00 to 15:00, solar time, using 30 min steps.

Figures 7 and 8 compare modeled diurnal cycles and measured ones. The two dotted curves represent the uncertainty of the measurement. The error bar represent the uncertainty due to the resolution of the spectrometer used to acquire the transmission functions estimated at 0.1 nm.

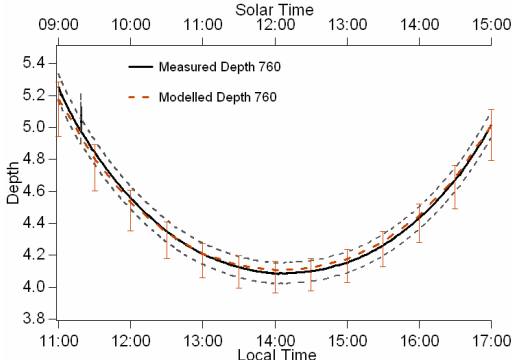


Figure 7. Comparison between measured and modeled diurnal cycle in the A-band.

Figure 7 shows that the shape of modeled curve for the A-band is in agreement with the experimental one. The model uncertainty is comparable to the measurements uncertainty.

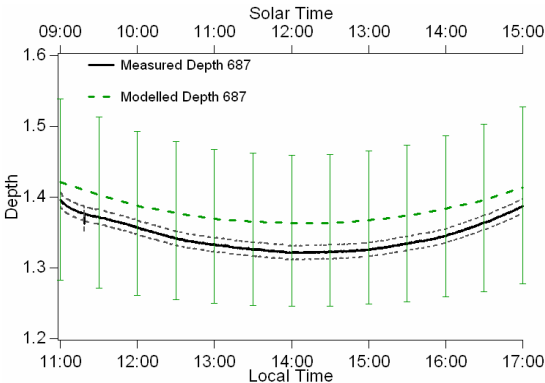


Figure 8. Comparison between measured and modeled diurnal cycle in the B-band.

Although the error bars are large, the figure 8 shows that the shape of the modeled curve is different from the measured one. That may signify that there are some unknown factors that may influence the depth of the B-band. An assumption is that MODTRAN may underestimate the radiance of the atmosphere. The undervaluation of this radiance leads to the over-estimate of the depth, as seen on Fig 8. This problem does not exist in A-band where the absorption is much stronger. Nevertheless, taking into account the error bar, the model is in agreement with the experimental values. The B-band is narrow implying that the model is highly dependent on the accuracy of the actual spectral shape of the filters. In order to have error bar of the same order of magnitude for both the model and the measurements, it would be necessary to characterize the filters with an accuracy of about 0.01 nm. In both cases, the depths obtained with MODTRAN are in agreement with the measured data within the uncertainty range. The model is able to reproduce the diurnal cycle for both bands, yet with less accuracy for the B-band. One can conclude that the model takes into account the atmospheric effects that influence the measurements so the corrections can be computed using MODTRAN 4.

### 3.6 Application to Altitude Effects

There are two types of correction: an altitude correction to correct the effect of atmospheric oxygen absorption and a time correction. This time correction allows to take into account the fact that for each altitude, as the measurements were not been made at the same time, the sun position was not the same.

**Altitude correction:** This correction allows to retrieve the fluxes at the ground level and is calculated with (3).

$$C_{alt} = \frac{Depth_{ground}}{Depth_{alt}} \quad (3)$$

Where  $Depth_{ground}$  is the depth computed at the ground level,  $Depth_{alt}$  is the depth computed at the measurement altitude of measure and  $C_{alt}$  is the correction coefficient (multiplicative) for the altitude effects.

**Time correction:** A correction computed with (4) is required because the measurements were not made at the same time.

$$C_{time} = \frac{Depth_{reference-time}}{Depth_{measure-time}} \quad (4)$$

Where  $Depth_{reference-time}$  is the depth computed at a reference time,  $Depth_{measure-time}$  is the depth computed at the measure time and  $C_{time}$  is the correction coefficient (multiplicative). All the depths in (3) and (4) are MODTRAN-computed.

Both corrections have been computed and applied to the measurements. Figures 9 shows measured and corrected depths acquired on the same bare field versus the altitude.

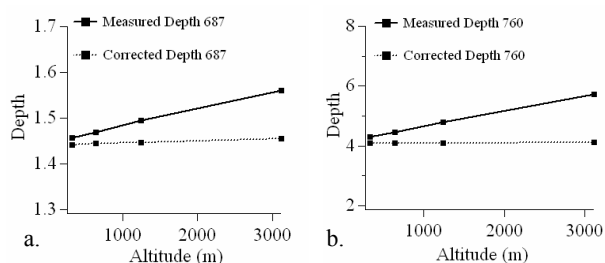


Figure 9. Depths acquired on bare field vs. altitude  
a. B-band (3rd of June).  
b. A-band (3rd of June).

Figures 9 show that the model is able to correct for the band depths: the corrected depths retrieved coincide for the four altitudes of measurements.

## 4. CONCLUSION

MODTRAN 4 can be used to account for the altitude effects on the A and B oxygen absorption bands depths. This study shows that the model does not depend critically on parameters such as water content and ozone content. Good results were obtained on both bands depths for the altitude correction up to 3km. This altitude represents about 50% of the atmospheric effects. The diurnal cycles measured with TerFlex generate a valuable set of data to validate the model for atmospheric corrections in long-range passive fluorescence measurements. The measurement of

the channels transmission function is a critical issue for the model accuracy. This point will be further improved in a forthcoming work.

## REFERENCES

- Berk, A., Anderson G.P., Acharya, P.K., Chetwynd, J.H., Bernstein, L.S., Shettle, E.P., Matthew, M.W., and Adler-Golden, S.M., 1999. MODTRAN4 user's manual.
- Conant, J., Iannarilli, F., Bacon, F., Robertson, D., and Bowers, D. PPACS – A System To Provide Measured Aerosol/Molecular Conditions To EO/IR Simulations. Aerodyne Research INC.
- Hess, M., Koepke, P., and Schult, I., 1998. Optical Properties of Aerosols and Clouds: The Software Package OPAC. *Bulletin of the American Meteorological Society*, Vol. 79, N° 5, pp. 831-844
- Louis, J., Ounis, A., Ducruet, J.M., Evain, S., Laurila, T., Thum, T., Aurela, M., Wingsle, G., Alonso, L., Pedros, R., and Moya, I., 2005. Remote sensing of sunlight-induced chlorophyll fluorescence and reflectance of Scots pine in the boreal forest during spring recovery. *Remote Sensing of Environment*, Vol. 96, pp. 37 – 48
- Martinez-Lozano, J.A., Utrillas, M. P., Tena, F., Pedros, R., Canada, J., Bosca, J.V., and Lorente, J., 2001. Aerosol optical characteristics from a summer campaign in an urbancoastal Mediterranean area. *Geosciences and Remote Sensing*, Vol. 32 No. 7, pp. 1573-1585
- Moya, I., Camenen, L., Latouche, G., Mauxion, C., Evain, S., and Cerovic, Z.G., 1998. An instrument for the measurement of sunlight excited plant fluorescence. *Photosynthesis: Mechanisms and Effects*. Dordrecht, Kluwer Acad. Pub., pp. 4265-4270
- Moya, I., Camenen, L., Evain, S., Goulas, Y., Gerovic, Z.G., Latouche, G., Flexas, J., and Ounis, A., 2004. A new instrument for passive remote sensing 1. Measurements of sunlight-induced chlorophyll fluorescence. *Remote Sensing of Environment*, Vol. 91, pp. 186-197
- Moya, I., Daumard, F., Moise, N., Ounis, A., and Goulas, Y., 2006. First airborne multiwavelength passive chlorophyll fluorescence measurements over La Mancha (Spain) fields.
- Noël, S., Buchwitz, M., Bovensmann, H., and Burrows, J. P., 2005. Validation of SCIAMACHY AMC-DOAS water vapour columns. *Atmospheric Chemistry and Physics*, Vol. 5
- Plascyk, J.A., 1975. The MKII Fraunhofer line discriminator (FLD-II) for airborne and orbital remote sensing of solar-stimulated luminescence. *Opt. Eng.*, Vol.14, pp. 113-120
- Stamnes, K., Tsay, S-C., Wiscombe, W., and Jayaweera, K., 1988. Numerically stable algorithm for discrete-ordinate-method radiative transfer in multiple scattering and emitting layered media. *Applied Optics*, Vol. 27, N° 12., pp 2502-250

## Should We Expect Anomalous Dispersion in the Polarized Reflectance of Leaves?

V.C. Vanderbilt<sup>a\*</sup>, C.S.T. Daughtry<sup>b</sup>, A. Russ<sup>b</sup>, S.L. Ustin<sup>c</sup>, J.A. Greenberg<sup>c</sup>

<sup>a</sup>NASA/ARC, Moffett Field, CA 94035, USA, [Vern.C.Vanderbilt@nasa.gov](mailto:Vern.C.Vanderbilt@nasa.gov)

<sup>b</sup>United States Department of Agriculture, Beltsville, MD 20705, USA, ([Craig.Daughtry@ars.usda.gov](mailto:Craig.Daughtry@ars.usda.gov), [Andrew.Russ@ars.usda.gov](mailto:Andrew.Russ@ars.usda.gov))

<sup>c</sup>University of California Davis, Davis, CA 95616, USA ([susan.greenberg@cstars.ucdavis.edu](mailto:susan.greenberg@cstars.ucdavis.edu))

KEY WORDS: Leaf reflectance, Polarization, Anomalous dispersion

### ABSTRACT:

The light scattered by plant canopies depends in part on the light scattering/absorbing properties of the leaves and is key to understanding the remote sensing process in the optical domain. Here we specifically looked for evidence of fine spectral detail in the polarized portion of the light reflected from the individual leaves of five species of plants. Although our initial results showed fine spectral detail in the polarized reflectance at 1350 nm wavelength, further investigation pointed to anomalous dispersion occurring not at the leaf surface but in one of the measuring instruments — in the optical fiber connecting the fore optics to the dispersion optics in the instrument. In such a situation, proper calibration should remove evidence of anomalous dispersion from the calibrated spectra, suggesting that our calibration of the data was flawed.

### 1. Introduction

The light scattered by plant canopies depends in part on the light scattering/absorbing properties of the leaves and is key to understanding the remote sensing process in the optical domain.

While this scattered light may be described by the four components of a vector, (intensity, magnitude of linear polarization, angle of plane of linear polarization, and magnitude/direction of circular polarization), significant progress has been achieved toward understanding only the first component, the intensity of the scattered light. Research shows that the magnitude of the linearly polarized light may be a significant part of the light scattered by some canopies (Vanderbilt, et al., 1985).

In this research we measured the intensity and the linear polarization of the light scattered by single leaves, testing the hypothesis that the polarized light scattered by a leaf is attributable to properties of the surfaces of the leaf and does not depend upon the characteristics of the interior of the leaf, such as its resident chlorophyll (Grant, et al., 1987a and 1993). We concentrated analysis efforts on the polarized portion of the reflected light, looking specifically for evidence of fine spectral detail, which, if found, would presumably be linked to the absorbing characteristics of the leaf cuticle. This research extends previous investigations limited to measurements in the 450 to 800 nm wavelength range of the leaves of approximately 20 species typically found in the vicinity of Lafayette, Indiana (Grant, et al., 1987a; 1987b; 1993; Vanderbilt and Grant, 1986).

### 2. Methods

We measured, Fig. 1, the detached leaves of five plant species — coffee, ficus, philodendron and spathiphyllum, all purchased at a garden store, and cannabis, grown in a greenhouse at the USDA — using two spectroradiometers, an ASD ©FieldSpec Pro (Analytical Spectral Devices, Boulder, Colorado, USA) and a GER 3700 (Spectra Vista

Corp., Poughkeepsie, New York, USA). In the experimental protocol, each leaf was observed at approximately Brewsters angle sequentially by each instrument, one instrument periodically replacing the other in the measuring setup, Fig. 1.

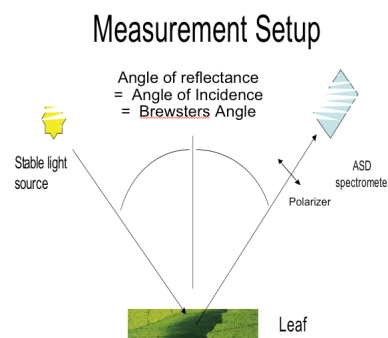


Figure 1. In the experimental protocol, after the ASD ©FieldSpec Pro collected data of a leaf, it was replaced by the GER 3700, which then collected data on the same leaf. Both spectroradiometers observed the leaf through a polarization analyzer at approximately Brewsters angle.

The bidirectional reflectance factor (BRF) and the polarized part of the BRF ( $BRF_{QU}$ ) of each target  $i$  (one of five leaf species or a ©Spectralon calibration surface) (©Spectralon is manufactured by Labsphere, North Sutton, New Hampshire, USA) were calculated from measurements by each instrument at 11 polarizer angles ( $q = -90, -70, -50, -30, -10, 0, 10, 30, 50, 70, 90$ ), first regressing the data,  $X(l, i, q)$ , recorded at each wavelength,  $l$ , and polarizer angle using eq. 1 with intercept  $C$

$$X(l, i, q) = C(l, i) + A(l, i)\sin(q) + B(l, i)\cos(q). \quad (1)$$

Rearranging provides

$$X(l,i,q) = C(l,i) + \{[A(l,i)^2 + B(l,i)^2]^{0.5}\} \sin(qq) \quad (2)$$

where  $q = \arctan[A(l,i) / B(l,i)]$ . Finally the  $BRF(l,i)$  and  $BRF_{QU}(l,i)$  for leaf  $i$  were calculated

$$BRF(l,leaf\ i) = BRF(l,spec) \frac{C(l,leaf\ i)}{C(l,spec)} \quad (3)$$

$$BRF_{QU}(l,leaf\ i) = BRF(l,spec) \frac{[A(l,leaf\ i)^2 + B(l,leaf\ i)^2]^{0.5}}{C(l,spec)} \quad (4)$$

where spec refers to ©Spectralon . We assumed the  $BRF(l,spec)=1.0$  for illumination and observation at Brewsters angle.

### 3. Results

The BRFs of individual leaves measured with each instrument, Fig. 2, appear generally comparable and display variation with wavelength typical of green leaves, revealing a green peak and the effects of chlorophyll absorption in the visible wavelength region and, in the reflective infrared spectral region between 700 and 2500 nm, an infrared plateau and the effects of water absorption.

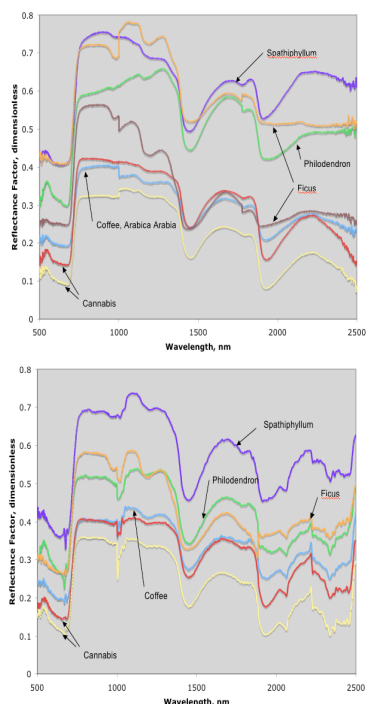


Figure 2. The relative bidirectional reflectance factor was estimated from (a) (left) ASD data and (b) (right) GER data.

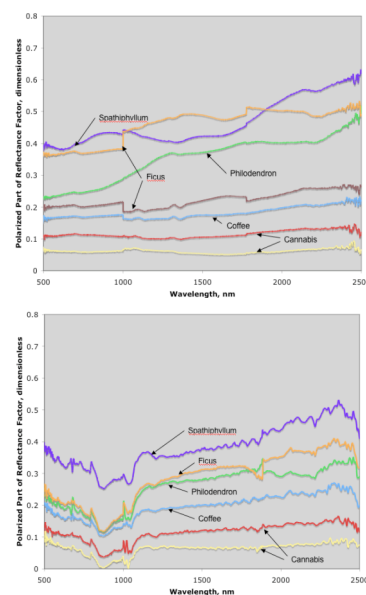


Figure 3. The polarized part of the relative bidirectional reflectance factor was estimated from (a) (left) ASD data and (b) (right) GER data of five leaf species measured as shown in Figure 1.

The  $BRF_{QU}$  of individual leaves measured with each instrument, Fig. 3, are reasonably comparable for wavelengths longer than 1000 nm, but show marked differences at shorter wavelengths where the GER spectra display much greater apparently random amplitude variation – noise - with wavelength than the ASD spectra. In the wavelength range 500 and 800 nm, the ASD results — but not the GER results — compare reasonably well with our prior research results. The general downward trend of the GER spectra with wavelength is in contrast to the generally flat character of the ASD spectra. At wavelengths longer than 1000 nm there are subtle differences near 1350 nm where the GER spectra appear relatively flat while the ASD spectra of most leaves display a miniature trigonometric sine wave atop an otherwise slowly changing response with wavelength.

### 4. Discussion

The miniature sine wave in the ASD results at 1350 nm, Fig. 3a, is characteristic of the effects of anomalous dispersion, an optical phenomenon that occurs when a light beam is specularly reflected at the surface of an absorbing material (Fowles, 1989). Typically, the magnitude of anomalous dispersion effects after just one specular reflection are small — probably too small to be consequential at present for remote sensing purposes. Thus, in general we do not expect the light singly specularly reflected by leaves to exhibit the effects of anomalous dispersion in remotely sensed data, suggesting that the evidence of anomalous dispersion displayed in Fig. 3a is due to a source other than the leaf surface. The lack of evidence of anomalous dispersion in the GER results, Fig. 3b, supports this view.

Figure 4 displays evidence of a very slight absorption in the ASD optical fiber at a wavelength of approximately 1350 nm, suggesting an explanation for the apparent anomalous dispersion effects evident in the  $BRF_{QU}$  of the leaves measured by the ASD but not the GER, an instrument with fore optics connected directly to its dispersion optics and lacking a connecting optical fiber. Based upon the evidence in Figs. 3 and 4, we believe the most reasonable explanation for the anomaly at 1350 nm in the ASD results, Fig. 3a, is that anomalous dispersion at 1350 nm occurred in the ASD optical fiber and not during the specular reflection at the leaf surface. If anomalous dispersion occurred in the ASD optical fiber, which tends to depolarize incident light, the effect should not be evident in Fig. 3a – properly calibrating the ASD data with reference to the ©Spectralon surface should have removed from the spectra, Fig. 3a, evidence of anomalous dispersion. (On the other hand, evidence of anomalous dispersion attributable to leaf surface properties, if pronounced, should appear in properly calibrated ASD and GER spectra.) Thus, in this situation we believe responsibility for the evidence of anomalous dispersion, Fig. 3a, rests with the data analyst (VCV) who most likely calibrated the leaf data using the wrong ©Spectralon data.

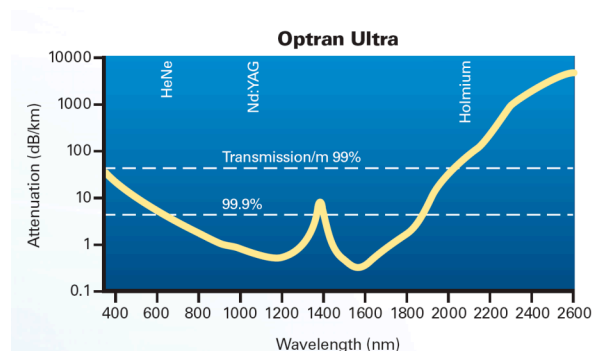


Figure 4. The attenuation of the optical fiber in the ASD instruments shows a minor absorption band at approximately 1350 nm. This figure was obtained from the optical fiber manufacturer, CeramOptec Industries Inc., East Longmeadow, Massachusetts, USA.

Assuming the  $BRF(l, \text{©Spectralon}) = 1.0$  for illumination and observation at Brewsters angle (see the Methods) is unreasonable for purposes of calculating the absolute values of the BRF and  $BRF_{QU}$  of a leaf. However, this assumption is reasonable here because the issue here concerns not the absolute magnitude but the existence of fine spectral detail in the  $BRF_{QU}$ ; thus, analysis of the relative magnitudes of

the  $BRF_{QU}$  suffices for this investigation; we incorrectly - but safely - assume the BRF of the ©Spectralon equals 1.0, because we report the relative not absolute BRF magnitudes.

One additional point to be made is that here we have not corrected these polarization results – and should have - for the polarizing effects introduced by the each of the measuring instruments.

## 5. Conclusions

We do not expect the effects of anomalous dispersion to be evident in the polarized remotely sensed reflectance spectra of leaves until the signal to noise ratio in the measuring instrumentation improves significantly. We believe the evidence of anomalous dispersion found in this research is due entirely to artifacts introduced into the results because a researcher incorrectly calibrating the data obtained from the ASD instrument.

## 6. References

- Fowles, G.R.. 1989. Introduction to Modern Optics. Dover, New York. pp. 328. ISBN 0-486-65957-7
- Grant, L., C.S.T. Daughtry and V.C. Vanderbilt. 1987a. Polarized and non-polarized components of leaf reflectance from *Coleus blumei*. *Environmental and Experimental Botany*, 27, pp. 139-145.
- Grant, L., C.S.T. Daughtry and V.C. Vanderbilt. 1987b. Variations in the polarized leaf reflectance of *Sorghum bicolor*. *Remote Sensing of Environment*, 21, pp. 333-339.
- Grant, L., C.S.T. Daughtry and V.C. Vanderbilt. 1993. Polarized and Specular Reflectance variation with Leaf Surface Features. *Physiol. Plant.*, 88, pp. 1-9.
- Vanderbilt, V.C., L. Grant and C.S.T. Daughtry. 1985. Polarization of light scattered by vegetation. (invited) *IEEE Proceedings*, 73, pp. 1012-1024.
- Vanderbilt, V.C. and L. Grant. 1986. Polarization photometer to measure bidirectional reflectance factor  $R(55,0;55,180)$  of leaves, *Optical Engineering*, 25, pp. 566-571.



# Using Monte-Carlo ray tracing to investigate the measurement of forest parameters with the Echidna™ laser scanner.

Steven Hancock<sup>1,2,3</sup>, Philip Lewis<sup>2</sup>, Jan-Peter Muller<sup>3</sup>, Mathias Disney<sup>2</sup>

<sup>1</sup>Department of Geomatic Engineering, UCL, Gower Street, London WC1E 6BT, UK

<sup>2</sup>Department of Geography, UCL, Gower Street, London WC1E 6BT, UK

<sup>3</sup>Department of Space and Climate Physics, Mullard Space Science Laboratory, UCL, Holmbury St Mary, Surrey, RH5 6NT, UK  
[shancock@geog.ucl.ac.uk](mailto:shancock@geog.ucl.ac.uk)

**KEY WORDS:** Canopy, foliage, lidar, full waveform, laser scanning, Echidna, Monte-Carlo ray tracing.

## ABSTRACT:

A Monte-Carlo ray tracer has been developed from a previous system to simulate a ground based, full waveform laser ranger, such as the Echidna™. Overlapping scans have been simulated using a geometric model of a Scots pine forest, with a sampling density far higher than would be feasible to collect in reality. An initial investigation has been carried out into the use of the simulated data to create a 3D volumetric canopy model. The algorithms needed are described and the impact of extra information, such as a second waveband on model accuracy is discussed.

## INTRODUCTION

Satellites are the only realistic way to measure forests on a global scale. Passive systems and synthetic aperture radar tend to saturate with only moderately dense woodland (Lefsky et al. 1999) and are not suitable for measuring forests for the understanding of global processes. Active systems have, so far, only measured in one view direction. Unfortunately the parameters of interest couple together within the signal and cannot be measured from a single zenith.

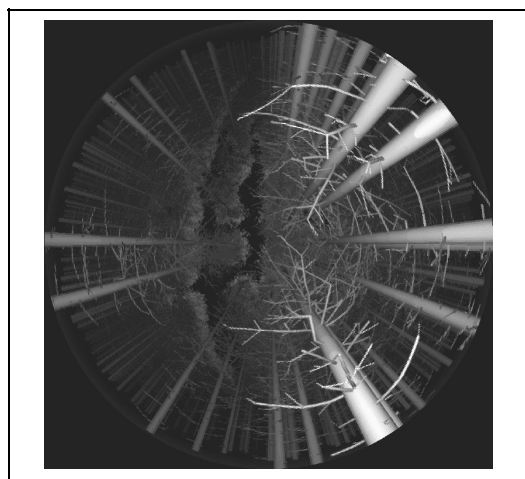


Figure 1. Hemispherical ray traced image of the Thetford model as seen by Echidna™. Brightness is scaled by range.

Lovell et al. (2003) have developed a ground based, full waveform, multi-angular laser scanner called Echidna™ which has the potential to decouple many of the contributing factors. Laser scanning can provide more accurate data than all but the most labour intensive direct methods (Danson et al. 2007) and will allow calibration of air and space borne instruments.

Through computer simulations it is hoped to gain a better understanding of how light interacts with a canopy to produce the measurements of an instrument like Echidna.

A Monte Carlo ray tracer has been developed from the earlier ray tracers of Lewis (1999) to simulate echidna. In addition to the data available to the echidna prototype, beams with additional wavelengths can be simulated and parameters that would be impossible with a real instrument, such as the contribution from multiple scattering and information about the materials visible to the beam can be recorded. Results inverted from the data available to a real instrument can be compared to this extra information to assess the accuracy of the inversion.

## Inverting lidar data

There has been considerable work put in to deriving forest information from lidar and other remotely sensed data. Some of these methods have been shown to be successful; however they tend to make estimates of just a few forest parameters (Danson et al 2007) or are not directly based upon the physical properties of the scene, relying upon species specific look up tables created from simulations (Koetz et al. 2007) or upon fitting an empirical model to the observations (Coops et al 2007). This investigation has tried to keep the assumptions physically based.

A grid of scans covering an area of forty by forty metres with a scan every twenty metres has been simulated. This is an unrealistic sampling density but it will allow the investigation of the difference such a density makes to the accuracy of the inverted parameters. Because of the density of measurements available it should be possible to create a volumetric representation of the canopy with no assumptions about homogeneity. In order to arrive at a manageable and solvable set of equations some assumptions have been made. These are;

All elements are perfect Lambertian reflectors and with known reflectances. Reflectance cannot be derived from a radiance measurement unless the structure and size of that element are known.

Layers of a canopy show no preferential alignment (either a tendency to occlude or to fill gaps) from any direction. This follows from Fisher's (1992) finding that computer generated trees are more realistic and photosynthetically efficient if

The International Archives of the Photogrammetry, Remote Sensing and Spatial Information Sciences, Vol. 34, Part  
XXX

the elements follow a random distribution than a regular pattern. From this it can be said that on average the light reflected from an area divided by the gap fraction up to that point is directly related to the objects at that region and so attenuation can be corrected for.

Some of these assumptions are valid within the simulation but do not hold in reality. Other methods for constraining the results, taking the uncertainty in the reflectances into account, will be needed.

### THEORY

For an element of material  $e$ , of area  $\delta A_e$  with a reflectance of  $\rho_e$  at an angle of incidence  $\vartheta_i$  to a laser beam of intensity  $I_0$ , at a range  $r_e$  the radiant flux from direct reflection,  $\Phi$  summed over all elements within a field of view is;

$$\Phi = I_0 \sum_e \frac{\rho_e}{r_e^2} \int \cos^2 \vartheta_i \delta A_e \quad (1)$$

This becomes easier to invert if the surface area is taken outside of the sum and the projected area weighted mean angle of incidence,  $\hat{\vartheta}_e$  used. From simulations it has been found that;

$$\Phi = I_0 \sum_e \frac{\rho_e}{r_e^2} A_e \cos^3 \hat{\vartheta}_e \quad (2)$$

The range to each element will only be known to plus or minus half the range resolution of the instrument. In the case of Echidna this is an uncertainty of 7.5cm leading to an error in the corrected radiance of up to 3% at 5m, decaying exponentially with increasing range. If elements are randomly arranged within the bins this effect should cancel out. It can be investigated with the ray tracer.

The intensity of radiation reaching the surface will be the intensity leaving the laser multiplied by the fraction of the field of view that has not been blocked up to that point. There is then an attenuated radiant flux;  $\eta$ .

The equations are much easier to deal with if a factor,  $\Psi$ , the fractional contribution of leaves to the lidar signal within a single range bin is defined.

$$\Psi = \frac{A_l \cos^3 \hat{\vartheta}_l}{A_l \cos^3 \hat{\vartheta}_l + A_b \cos^3 \hat{\vartheta}_b} \quad (3)$$

Where  $l$  and  $b$  subscripts represent leaf and bark respectively.

If, like the echidna prototype only one wavelength is available  $\Psi$  would have to be estimated with another, possibly direct measurement method. If lasers of more than one wavelength are available  $\Psi$  can be calculated using the equation;

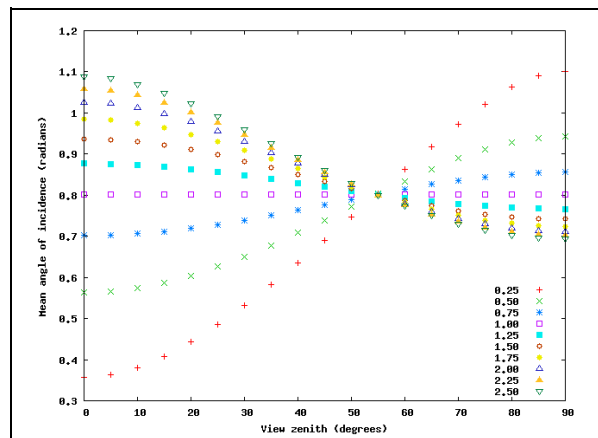
$$\Psi = \frac{\eta_\lambda \rho_{b\lambda} - \eta_\omega \rho_{b\omega}}{\eta_\lambda (\rho_{l\omega} - \rho_{b\omega}) + \eta_\omega (\rho_{l\lambda} - \rho_{b\lambda})} \quad (4)$$

Where  $\lambda$  and  $\omega$  are the two wavelengths, with radiant fluxes of  $\eta_\lambda$  and  $\eta_\omega$  and reflectance for each material,  $e$  of  $\rho_{e\lambda}$  and  $\rho_{e\omega}$ .

### Element distribution function

Campbell's ellipsoidal distribution (Campbell 1986) will be used to relate  $\hat{\vartheta}_e$  to the view zenith and azimuth angles. For simplicity in this first attempt it will be assumed that the elements are azimuthally symmetric, reducing the ellipsoids to spheroids with one vertical radius and two identical horizontal radii.

The ray tracer was used to measure  $\hat{\vartheta}_e$  at zeniths,  $\vartheta_z$  between  $0^\circ$  and  $90^\circ$  for a range of different eccentricities. The results are shown in the first graph.



Graph 1.  $\hat{\vartheta}_e$  against view zenith for spheroids of different eccentricities. The key shows the ratio of the vertical to horizontal radii.

These simulations agreed with the work of Roberts (1998), that all spheroids have a  $\hat{\vartheta}_e$  of  $\pi/4$  radians at a zenith angle of  $\mu$  (roughly equal to  $54.75^\circ$ ).  $\hat{\vartheta}_e$  can then be calculated from the equation;

$$\hat{\vartheta}_e = \left( \frac{\pi/4 + \cos 2\mu}{1 + \cos 2\mu} + \hat{\Omega}_e \right) \cos 2\vartheta_z + \frac{\pi/4 + \cos 2\mu}{1 + \cos 2\mu} \quad (5)$$

The element angular distribution can be uniquely defined by  $\hat{\Omega}_e$ , the mean angle of incidence looking along the vertical axis of a spheroid. This can be calculated by numerical integration. The above function, with  $\hat{\Omega}_e$  calculated by integration fitted to the simulated data with a root mean square error of less than 0.4%, well within the errors from stochastic ray tracing.

The International Archives of the Photogrammetry, Remote Sensing and Spatial Information Sciences, Vol. 34, Part  
XXX

All clumping at scales larger than the lidar bins has been explicitly taken into account. Clumping need only be corrected for at the scale of lidar bins. For echidna this is about the size of a pine shoot. Echidna has a constant azimuth step for all zeniths and so scans overlap for annuli near the vertical. If it is assumed that the canopy is equally clumped in all directions within a voxel (a safe assumption with pine shoots) the variation in measured surface areas between beams should be related to the clumping.

### Inverting the lidar signal

A program has been written to use the above equations to convert full waveform lidar data into a voxel representation of the canopy. It is possible to solve two separate angle distributions from multi-frequency data, but to simplify the problem for this first attempt it has been assumed that leaves and bark have the same angular distribution.  $\Psi$  is then independent of view direction. Each voxel is described by a fractional area,  $A_c$  for each material, angle distribution,  $\hat{\Omega}_e$  and the fraction of total surface area made up by leaves,  $\Psi$ . Having a separate  $\hat{\Omega}_e$  for each voxel makes no assumptions about the homogeneity above the scale of a voxel though it may prove to be an unnecessary level of detail. The voxel canopy should cover the origin of each scan to allow a correct estimate of the attenuation of the beams.

Multiple lidar bins may lie within a voxel and a lidar bin may lie within many voxels, in which case the measured flux will be due to the elements from all intersecting voxels weighted by the overlaps. In this first attempt the weighting has been ignored. It will have an effect upon the accuracy of the results, but not the overall method, which is the focus of this investigation.

Once the lidar bins have been associated with the appropriate voxels  $\Psi$  can be calculated if more than one wavelength is available. This depends only on the reflectances and uncorrected fluxes so will not alter during the iterative process. In future it may be sensible to weight the value of  $\Psi$  calculated by each beam by the gap up to that point since the signal from a beam passing through a larger gap will be more representative of the scene. In which case  $\Psi$  will alter during the iterations.

The gap is calculated by summing the projected areas of spheroids with surface areas calculated from the measured radiant flux ( $\eta$ ), the fraction of the return from leaves,  $\Psi$  and eccentricities calculated from  $\hat{\Omega}_e$  for all lidar bins up to that point. This calculation makes no assumption about the alignment of the different canopy layers. If the angular distributions, fractional contribution factor and the reflectances are known this calculated value will be the true gap up to that point.

A gap cannot close until after the last return. Gaps depend only upon  $\Psi$  and  $\hat{\Omega}_e$ . Initially the angle distributions is assumed to be spherical ( $\hat{\Omega}_e = \pi/4$ ) for all voxels.  $\hat{\Omega}_e$  is adjusted until no beams are prematurely blocked.

An initial estimate of  $A_c$  is then made, averaged over all contributing voxels and wavelengths. Once the initial values have been chosen the iterative process to refine the estimates of voxel parameters can be started.

All beams should see the same surface areas with a different orientation ( $\hat{\theta}_e$ ). If a voxel has returns from different zeniths, remembering the symmetry of a spheroid,  $\hat{\Omega}_e$  can be calculated. These factors can be used to calculate  $A_c$  for each beam and averaged together to get a value for the voxel. Every

time  $\hat{\Omega}_e$  is adjusted the gap for all voxels intersected by bins later in that beam's path will also be affected.

The process is repeated until the radiant flux predicted by the model matches that measured by the simulated lidar, within a tolerance.

## RESULTS

It has not yet been possible to compare the initial results to the original object file. A function to convert the raw object file into a volumetric representation is in development. Figure 2 shows a horizontal slice through the voxel representation, 5m above the floor. The initial results, using a set of low resolution scans, suggest that there is a large variation in both leaf area and leaf angle distribution between metre cubed volumes, justifying the high measurement density.

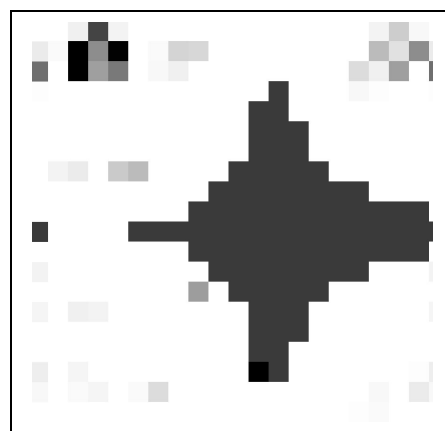


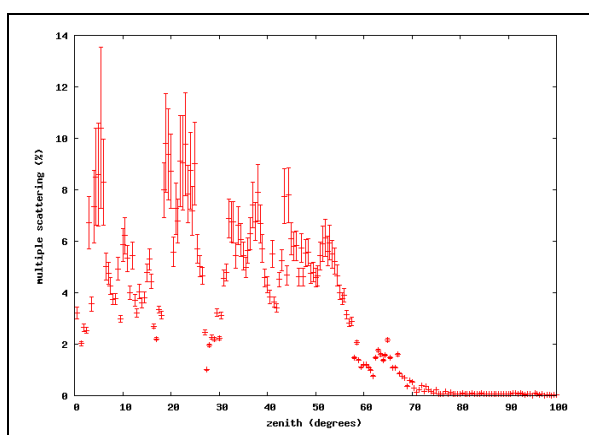
Figure 2. 10m by 10m horizontal slice through a voxel representation. The darkness indicates the area of bark projected upwards.

## DISCUSSION

This method has only taken light reflected directly from the scene into account. The second graph shows that multiple scattering makes a significant contribution to the lidar signal, even with a beam divergence of  $0.5^\circ$  and a field of view of  $0.8^\circ$ . Multiple scattering is much more significant at lower zeniths, where the beam is reflected off many small needles, than near the ground, where light is reflected from a few large, solid objects. This effect needs to be understood. A future investigation will find how this percentage changes with laser beam divergence and field of view, and how much of the scene from outside the field of view contributes to the signal.

If the inverted voxel representation is found to be a poor description of the "truth" it would be fairly simple to use a separate angular distribution for bark and leaf. Also, a single large branch passing through a voxel cannot be described by a spheroid. It would be possible to allow the spheroids to tilt to better fit reality. The effect of the detail of the angular distribution on inversion accuracy should be investigated.

At some point in a canopy a lidar beam will become so attenuated that the returned signal cannot be said to be representative of the canopy at that point. The maximum distance between scans needed to describe canopies of different element area densities will be investigated.



Graph 2. Contributions to the lidar signal from scattering for a hemispherical scan looking up from beneath a Scots Pine canopy. The results of annuli are averaged together with the bars representing variance.

This investigation has suggested a set of equations to convert full waveform lidar data collected in a forest into a volumetric representation. Algorithms for correcting for clumping are still needed. A second waveband will help a great deal with the inversion, removing the need for costly direct measurements. The accuracy of this method and the number of scans needed to describe a forest of a certain element area density will be evaluated in the near future.

## REFERENCES

- Campbell GS. 1986. Extinction coefficients for radiation in plant canopies calculated using an ellipsoidal inclination angle distribution. *Agricultural and Forest Meteorology*, v36, p317-321.
- Coops NC, Hilker T, Wulder MA, St-Onge B, Newnham G, Siggins A, Trofymow JA. 2007. Estimating canopy structure of Douglas-fir forest stands from discrete-return lidar.
- Danson FM, Hetherington D, Morsdorf F, Koetz B, Allgöwer B. 2007. Forest canopy gap fraction from terrestrial laser scanning. *IEEE Geoscience and Remote Sensing Letters*, v4, p157.
- Disney, M, Lewis, P, Saich, P, 2006. 3-D modelling of forest canopy structure for remote sensing simulations in the optical and microwave domains. *Remote Sensing of Environment*, v100 p114-132.
- Fisher JB, 1992. How predictive are computer simulations of tree architecture? *International journal of plant sciences*, v135, p137.
- Koetz B, Sun G, Morsdorf F, Ranson KJ, Kneubühler M, Itten K, Allgöwer B. 2007. Fusion of imaging spectrometer and LIDAR data over combined radiative transfer models for forest canopy characterization. *Remote Sensing of Environment*, v106, p449-459.
- Lefsky MA, Cohen WB, Acker SA, Parker GC, Spies TA, Harding D. 1999. Lidar remote sensing of the canopy structure and biophysical properties of Douglas-fir and western hemlock forests. *Remote Sensing of Environment*, v10, p339-361.
- Lewis, P. 1999. Three-dimensional plant modelling for remote sensing simulation studies using the Botanical Plant Modelling System. *Agronomie*, v19(3-4): p185-210.
- Lovell, JL, Jupp, DLB, Culvenor, DS, Coops, NC, 2003. "Using airborne and ground-based ranging lidar to measure canopy structure in Australian forests." *Canadian Journal of Remote Sensing* v29(5) p607-622.
- Roberts G. 1998. Simulating the Vegetation Canopy Lidar (VCL) over forest canopies: An investigation of the waveform information content. MSc thesis, UCL, Geography.

## RAMIS: A BIOPHOTONIC PHYSIOLOGICAL PLANT SENSOR (FIELD RADIOMETER FOR CANOPY REMOTE SENSING)

E. Conejo <sup>a</sup>, J.-P. Frangi <sup>a,\*</sup>, S. Jacquemoud <sup>b</sup>, G. de Rosny <sup>a</sup>

<sup>a</sup> Géomatériaux et environnement, Institut de Physique du Globe de Paris - Université Paris 7, Paris, France - conejo@ipgp.jussieu.fr, frangi@ipgp.jussieu.fr, derosny@ccr.jussieu.fr

<sup>b</sup> Etudes spatiales et planétologie, Institut de Physique du Globe de Paris - Université Paris 7, Paris, France - jacquemoud@ipgp.jussieu.fr

**KEY WORDS:** RAMIS, Remote Sensing, Agriculture, Vegetation, Modelling, Optical Device, Water Content, Chlorophyll Content

### ABSTRACT:

A prototype instrument called RAMIS has been designed to non-destructively measure the biochemical properties of plant leaves such as water, dry matter, and total chlorophyll content. The spectral distribution of light transmitted through the leaf is closely related to the concentration of these constituents. In consequence, their retrieval from *in situ* optical measurements is possible by selecting the appropriate wavelengths. In RAMIS, the adaxial face of the leaf is alternately illuminated by five light-emitting diodes (LED) centred at 656, 721, 843, 937 and 1550 nm and the amount of light transmitted through the leaf blade is measured by a double layer Si-Ge photodiode sensor. A measurement of the raw signal when the leaf is removed and a calibration factor allow us to derive the hemispherical leaf transmittance. The PROSPECT model which physically relates the leaf optical properties to foliage anatomical structure and biochemical composition is then inverted to estimate the water content by using a method based of neural networks. Results show a reasonable agreement between optical and gravimetric measurements.

### RESUME:

RAMIS est le prototype d'un instrument de mesure non destructive des propriétés biophysiques des feuilles comme la teneur en eau, en matière sèche et en chlorophylle. La distribution spectrale du rayonnement électromagnétique transmis à travers la feuille est fortement liée à la concentration de ces constituants. Par conséquent, il est possible de les déterminer grâce à des mesures optiques effectuées *in situ* à des longueurs d'onde convenablement choisies. Dans RAMIS, la face supérieure de la feuille est alternativement illuminée par cinq diodes électroluminescentes centrées sur 656, 721, 843, 937 et 1550 nm, la quantité de lumière qui traverse la feuille est mesurée par une photodiode bicouche Si-Ge. A partir des mesures du signal brut sans feuille et avec feuille, on déduit la transmittance hémisphérique après avoir appliqué un terme correctif. Le modèle PROSPECT qui relie les propriétés optiques d'une feuille avec sa structure anatomique et sa composition chimique est alors inversé pour déterminer la teneur en eau en utilisant une méthode basée sur des réseaux neuronaux. Les résultats montrent une concordance raisonnable entre les mesures optiques et gravimétriques.

### 1. INTRODUCTION

For various application domains such as precision agriculture, global-scale ecology, or for the validation of satellite remote sensing products, it is very important to assess the leaf biochemical composition: mainly the total chlorophyll ( $C_{ab}$ ), water ( $C_w$  also called equivalent water thickness), and dry matter ( $C_m$  also called leaf mass per area) content. The measurement of leaf chlorophyll content involves analytical chemical techniques which are time consuming and expensive. A precision balance associated with a drying oven allows one to simply determine  $C_w$  and  $C_m$  but these procedures are difficult to carry out when the experiment field is far away from the laboratory. Moreover, once detached from the plant, leaves lose water by evaporation and chlorophylls begin to degrade. These constraints limit the availability of such measurement techniques to a limited number of samples, in areas close to the analytical facilities.

In order to overcome these limits, we designed a hand-held biophotonic instrument called RAMIS (*RAdiomètre portatif de Mesure In Situ*) which is based on the interaction of electromagnetic radiation (EMR) with plant leaves (Frangi et al., 2003). It non-destructively measures the leaf transmittance at five judiciously selected wavebands sensitive to chlorophyll,

water, and dry matter. This work involves two research activities: instrumentation and modelling. Indeed we have to solve technical issues (the measurement of the fraction of light transmitted through a plant leaf at several wavelengths) and algorithmic issues (the modelling of this transmittance as a function of the leaf biochemical constituents).

This paper is organized in four sections. After describing the physical principles of the instrument, its functioning and the processing of the output signal are detailed.

### 2. PHYSICAL PRINCIPLES

The interaction of EMR with leaves can be computed from knowledge of the spectral variation of the complex refractive index: the real part explains the multiple reflections of light at the cell-air interfaces and the imaginary part the absorption of light by the leaf biochemical compounds. RAMIS is based on knowledge of these absorption properties in the solar domain from 400 nm to 2500 nm. Figure 1 presents the specific absorption coefficients of chlorophyll, water, and dry matter used in PROSPECT, a radiative transfer model which simulates the directional-hemispherical reflectance and transmittance of plant leaves (Jacquemoud and Baret, 1990) with  $C_{ab}$ ,  $C_w$ , and  $C_m$  as input parameters.

\* Corresponding author: Jean-Pierre Frangi



One can notice that the pigment absorption spectrum is distinct from the others, but that water and dry matter overlap each other, which may complicate the deconvolution of the measured signal.

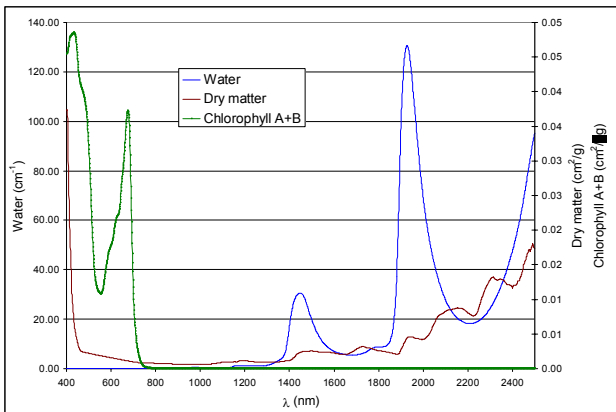


Figure 1. Specific absorption coefficients of chlorophyll, water, and dry matter

3. DESCRIPTION OF RAMIS

In RAMIS, the leaf to be measured is illuminated by five light-emitting diodes (LED) (Figure 2). Their wavebands have been selected in such a way that they correspond to the specific absorption lines of the leaf biochemical compounds. The LEDs are centred on 656, 721, 843, 937, and 1550 nm (Figure 3). Today, manufactured LEDs are available at almost any wavelength in the visible (VIS) and near-infrared (NIR), while the choice is very limited in the shortwave-infrared (SWIR).



Figure 2. Light-emitting diodes

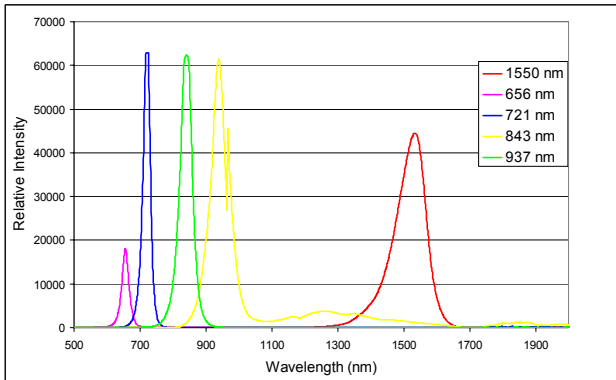


Figure 3. Spectral emission of the five LEDs

The amount of light transmitted through the blade is measured by a double layer Si-Ge photodiode also called the “sandwich” detector (Figure 4).



Figure 4. Light photodiode detector

The silicon photodiode responds to radiation from 400 nm to 1000 nm. Longer wavelengths pass through the silicon and are detected by the germanium detector underneath (Figure 5).

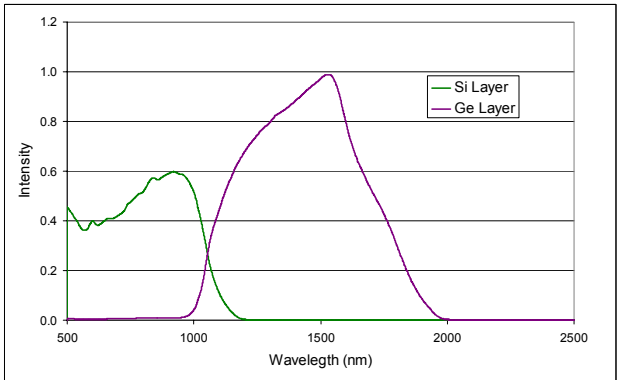


Figure 5. Spectral sensitivity of the Si-Ge sensor (Judson Technologies)

The lighting of the LEDs is controlled and the acquisitions of the output signal is achieved using a data acquisition card (Labview, National Instrument) connected to a laptop. One must emphasize that the photodiode works as a mono-channel band detector although the LEDs are sequentially powered.

The transmittance of a semi-transparent object is defined as the ratio of the transmitted flux ( $\Phi$ ) to the incident flux ( $\Phi_0$ ). To determine the transmittance of a plant leaf with RAMIS, we measure the detector output signal in the presence of the leaf and after removing it (Figure 6).

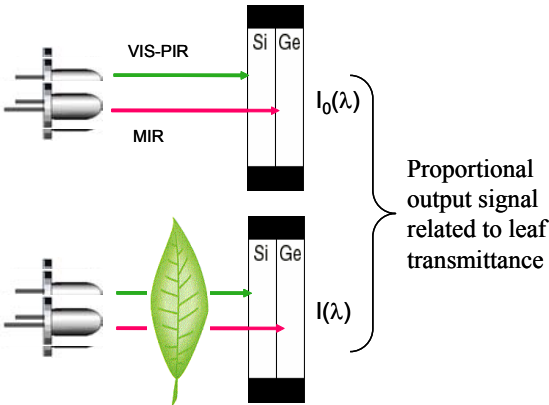


Figure 6. Principle Schematic representation of RAMIS

The diodes are successively powered, with the leaf inserted or not. The response of the photodiode is recorded as an electrical current  $I$  which is assumed to be proportional to the light flux  $\Phi$

falling on the photodiode, so long as its response to  $\Phi$  is linear :  $\Phi(\lambda) = \alpha I(\lambda)$  and  $\Phi_0(\lambda) = \alpha I_0(\lambda)$  then  $\Phi(\lambda)/\Phi_0(\lambda) = I(\lambda)/I_0(\lambda)$ . The calibration of RAMIS is performed with the help of three Lambertian diffusers (SphereOptics) of thickness 1 mm, 250  $\mu\text{m}$ , and 100  $\mu\text{m}$ , spectrally calibrated by the manufacturer and corresponding to average transmittances of 0.08, 0.25, and 0.50, respectively.

#### 4. PROCESSING OF THE RAMIS OUTPUT SIGNAL

We first tried to determine simple relationships between the RAMIS output signal and the leaf biochemical compounds. For instance, we looked at the variation of the output signal as a function of the leaf water content  $C_w$  by slowly drying a detached leaf of *Tradescantia fluminensis* in natural conditions. The leaf was periodically weighed and, at the end of the experiment, totally dried in an oven to determine the equivalent water thickness at each stage. Figure 7 shows that the ratio  $I(\lambda)/I_0(\lambda)$  calculated at 1550 nm (band 5 in Figure 3) is well related to  $C_w$ , that it decreases with  $C_w$ , and that the signal output is sensitive enough to estimate water content.

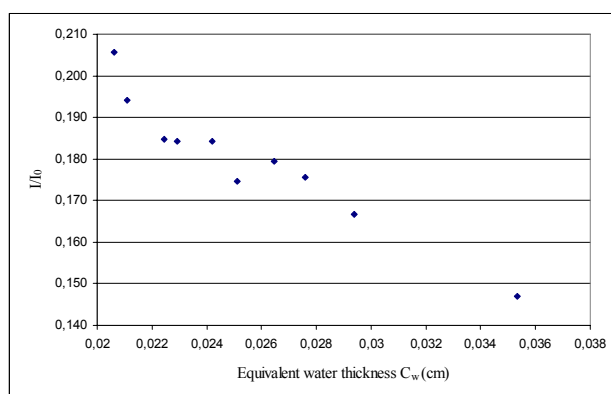


Figure 7. Relationship between the RAMIS output signal at 1550 nm and water content

Unfortunately, this relationship is not unique when trying to repeat the experiment with different leaf species showing a wide range of leaf internal structures and dry matter contents. Then we decided to calculate the ratio of the near-infrared to the short-wave infrared transmittances. The SPAD-502 (Minolta) works on the same principle: it calculates the ratio of the near-infrared to the red transmittances to retrieve  $C_{ab}$  (we actually found out that the two devices had very similar characteristics for chlorophyll estimation). However, the same kind of semi-empirical approach applied to water and dry matter was unsuccessful because of their overlapping absorption spectra, as mentioned earlier.

To overcome this problem, we introduced PROSPECT, a radiative transfer model which calculates the leaf hemispherical transmittance  $T(\lambda)$  every nanometer in the NIR and SWIR with the leaf structure, the leaf water and dry matter contents as input parameters (Jacquemoud and Baret, 1990). PROSPECT can be run in direct mode to compute the RAMIS output signal  $I(\lambda)/I_0(\lambda)$ , as long as the emission spectrum  $E(\lambda, \lambda_c)$  of each LED (Figures 3 and 8) and the responsivity spectrum  $S(\lambda)$  of the Si and Ge sensors (Figure 5) are well characterized. Equations 1 and 2 respectively give the expressions of the electrical currents  $I_0(\lambda_c)$  and  $I(\lambda_c)$  measured for each LED without a leaf and when a leaf is clamped.

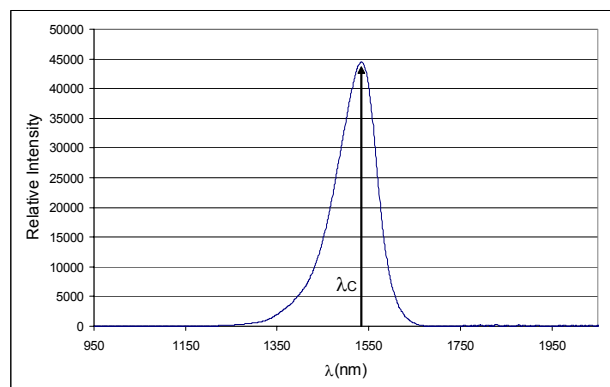


Figure 8. Spectral emission characteristics of the LED centered on 1550 nm.  $\lambda_c$  is the central wavelength,  $\lambda_i$  and  $\lambda_f$  the lower and upper bounds of the peak

$$I_0(\lambda_c) = \int_0^\infty E(\lambda, \lambda_c) S(\lambda) d\lambda \quad (1)$$

$$I(\lambda_c) = \int_0^\infty E(\lambda, \lambda_c) T(\lambda) S(\lambda) d\lambda \quad (2)$$

A « feedforward » neural network where the neurons are arranged in two layers was then implemented to relate the RAMIS output signal  $I(\lambda)/I_0(\lambda)$  to the leaf water content  $C_w$ . The training dataset was built using PROSPECT simulations. This technique has been already used to estimate the leaf biochemistry from leaf reflectance or transmittance spectra (de Rosny et al., 1995; Dawson et al., 1998; Le Maire et al., 2004). In this work, inversions were conducted on the five RAMIS transmittances measured over 130 leaf samples representing fifteen plant species collected outdoors in the spring of 2006.

Figure 9 presents the estimation of leaf water content using RAMIS compared to laboratory analytical measurements. One can see a good agreement between the two methods, specially for high values of  $C_w$ , and some difficulties to estimate low values.

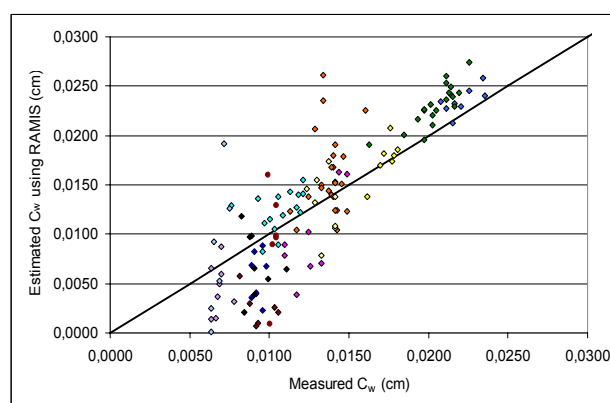


Figure 9. Validation of leaf equivalent water thickness estimation using RAMIS

## 5. CONCLUSION

In this paper, we demonstrate the ability of RAMIS to collect radiometric measurements in the field and to provide accurate and non-invasive estimates of leaf water content. The use of PROSPECT in the retrieval process implemented into RAMIS is essential to the success of this instrument. Similar studies performed by Pavan et al. (2004) to estimate chlorophyll content also led to good results.

Some improvements of the prototype are under development. For instance, the measurements of the leaf transmittance at appropriate wavelengths in the vicinity of 1600 nm should permit reliable estimates of leaf dry matter content, and therefore better estimates of water content.

## ACKNOWLEDGMENT

We thank the *Bureau de la Valorisation et des Relations Industrielles* of the University of Paris Diderot - Paris 7 for financial support. This project received the 2006 Environmental Innovative Technology Award of ADEME (French Agency for Environment and Energy Management).

## REFERENCES

Dawson, T.P., Curran, P.J., Plummer, S.E., 1998. The biochemical decomposition of slash pine needles from reflectance spectra using neural networks. *International Journal of Remote Sensing*, 19, pp. 1433-1438.

Frangi, J.-P., Jacquemoud, S., De Rosny, G., Equer, B., Roca I Cabarrocas, P., Vanderhagen, R., 2003. *Dispositif et procédé de radiométrie pour déterminer in situ le contenu biochimique de feuilles, et appareil portatif intégrant ce dispositif*, brevet INPI n°01 09334.

Jacquemoud, S., Baret, F., 1990. PROSPECT: a model of leaf optical properties spectra. *Remote Sensing of Environment*, 34, pp. 75-91.

Le Maire, G., François, C., Dufrêne, E., 2003. Towards universal broad leaf chlorophyll indices using PROSPECT simulated database and hyperspectral reflectance measurements. *Remote Sensing of Environment*, 89, pp. 1-28.

Pavan, G., Jacquemoud, S., Bidet, L., Francois, C., De Rosny, G., Frangi, J.-P., 2004. RAMIS: A new portable field radiometer to estimate leaf biochemical content. In *Proc. 7th International Conference on Precision Agriculture and Other Precision Resources Management, 25-28 July 2004, Minneapolis, USA*.

de Rosny, G., Vanderhagen, R., Baret, F., Equer, B., Frangi J.-P., 1995. A device for in situ measurements of leaf chlorophyll and carotenoid concentrations. In *Proceeding of the International Colloquium on Photosynthesis and Remote Sensing* (G. Guyot, ed), Montpellier (France), 28-30 August 1995, pp. 135-141.

INFLUENCE OF LOCAL INCIDENCE ANGLE EFFECTS  
ON GROUND COVER ESTIMATES

M. Bachmann, S. Holzwarth and A. Müller

DLR-DFD, German Remote Sensing Data Center, 82234 Wessling, Germany  
(martin.bachmann, stefanie.holzwarth, andreas.mueller)@dlr.de

**KEY WORDS:** Linear Spectral Unmixing, MESMA, Terrain Effects, Wide FOV Sensors, Accuracy Estimation

**ABSTRACT:**

An often neglected source of uncertainty on estimated cover percentage is caused by local view angle effects, where parts of bare soil patches are not visible due to vegetation blocking the sensor line-of-sight. When estimating the fractional cover of pixels far off-nadir or at slopes pointing away from the sensor, plant cover can be overestimated by more than 50%, seriously decreasing the accuracy. This problem is inherent when using wide field of view (FOV) sensors, or satellite sensors tilted off-nadir. In the following, results of a study using airborne HyMap hyperspectral data with a wide FOV of  $\pm 32^\circ$  are presented. Ground cover fractions for bare soil, green (PV) and dry (NPV) vegetation were derived using an iterative multiple endmember spectral mixture analysis (MESMA) approach. Using field measurements of geometric canopy parameters as well as terrain information, typical error margins of local incidence angle effects on unmixing results were calculated. These results are further included as a component in a per-pixel accuracy estimate to be introduced.

1. INTRODUCTION AND BACKGROUND

Natural semi-arid landscapes are characterized by a discontinuous canopy cover, resulting in a small-scaled mosaic of vegetation and bare soil patches. Ground cover fractions of bare soil, green and dry vegetation are frequently used to model soil erosion and land degradation in semi-arid environments (Puigdefábregas, 2005; Weltz et al., 1998). Especially spectral unmixing of hyperspectral data is an adequate tool in order to provide quantitative cover estimates on a subpixel scale (e.g., Okin & Roberts 2004, Ustin et al. 2005; Asner et al., 2003).

But when the terrain is rough, and when vegetation distribution is patchy, slopes pointing away from the sensor viewing direction often show an overestimation of vegetation cover (see Fig. 1).

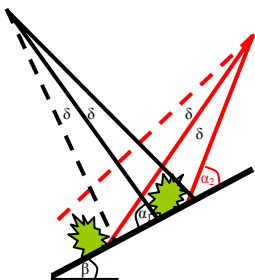


Fig. 1: Schematic sketch of local incidence geometry on cover estimates.

The degree of this overestimation is governed by the local incidence angle ( $\alpha$ ), which is a function of slope ( $\beta$ ) and view angle. Next, the typical height ( $h_{veg}$ ) and length ( $l_{veg}$ ) of the vegetation patches, as well as the size of the bare soil patches have a large influence on the effect. Assuming a landscape with

more or less equal distribution of bare soil and vegetation patches, and totally opaque vegetation, the factor of overestimation of the vegetation fraction can be approximated by

$$factor_{Overestimation\ Vegetation} \approx \frac{l_{veg} (l_{veg} + h_{veg} \tan(\alpha)^{-1})}{l_{veg}^2}$$

A graph of this function is shown in Fig. 2. Note that this effect also occurs when the sensor Instantaneous Field of View (IFOV, labelled  $\delta$  in Fig. 1) is by far larger than the patch size.

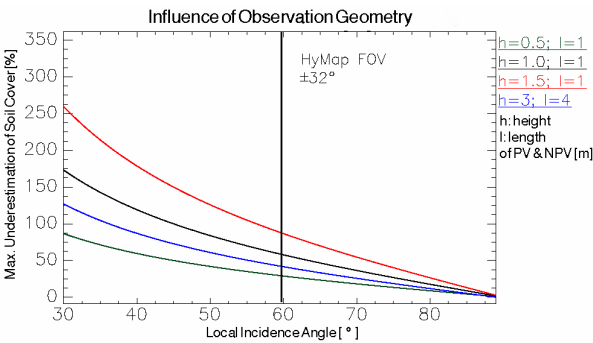


Fig. 2: Underestimation of soil cover as a function of local incidence angle and vegetation size.

## 2. DATABASE AND PRE-PROCESSING

As a test area, the Cabo de Gata natural park in south-eastern Spain is used. The terrain is rough, ranging from sea level up to 500m asl. All imagery used in this study was acquired by HyMap, an airborne whiskbroom imaging spectrometer covering the spectral range between 450 and 2500 nm with an average bandwidth of ~16nm in 128 bands (Cocks et al., 1998). The instantaneous field of view is 2.5 mrad along and 2.0 mrad across track and the total field of view is 61.3 degrees, resulting in 512 image pixels per scanline. Flight campaigns were carried out in 2003, twice in 2004, and in 2005. A total of 21 HyMap datasets was acquired, covering large areas of the natural park 'Cabo de Gata' (Bachmann et al., 2004). The subset used in this study is depicted in Fig. 3 below.

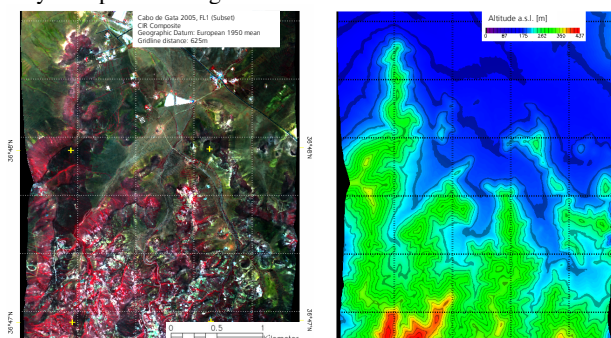


Fig. 3: Left: Subset of HyMap flightline used in this study.  
Right: corresponding DEM

Pre-processing including atmospheric and geometric correction was carried out for the selected scenes. The raw HyMap data is system corrected to at-sensor-radiance based on calibration coefficients obtained during laboratory calibration by HyVista. Afterwards geocoding and atmospheric correction are carried out as part of the standard processing chain for hyperspectral data at DLR (Habermeyer et al., 2005). The imagery was first geocoded using ORTHO (Müller et al., 2005). This automated software package is based on a parametric approach determining the viewing geometry for each pixel based on sensor-specific parameters, flight parameters such as sensor position and attitude (i.e. roll, pitch, true heading), and additional terrain information from a digital terrain model (DEM). For the atmospheric correction, ATCOR4 was used (Richter & Schläpfer, 2002). This physically based approach, using the MODTRAN radiative transfer code, corrects for atmospheric effects as well as adjacency scattering, and BRDF compensation in order to derive nadir-normalized ground reflectance. Furthermore topographic correction for different terrain illumination is applied.

To ensure a good quality of all input data, the radiometric and geometric accuracy was assessed. Based on ground control points, geocoding resulted in a data set with an RMS error in position better than 3 pixels. For the quality assessment of pre-processed HyMap data, radiometric and spectral accuracy was evaluated for the Cabo de Gata dataset. Field campaigns were carried out in 2003 and 2004 in close cooperation with GeoForschungsZentrum Potsdam (GFZ) and University of Almeria, where spectral measurements were taken in the field in order to provide ground reference data for analysis. Mean image spectra of a gravel site and other calibration targets were within one standard deviation of the corresponding ground measurements.

## 3. ESTIMATION OF GROUND COVER FRACTIONS USING LINEAR UNMIXING

### 3.1 $\mu$ MESMA – an iterative multiple endmember spectral mixture analysis approach

For the estimation of ground cover fractions, an automated iterative multiple endmember spectral mixture analysis approach (denoted  $\mu$ MESMA) is applied. The main advantage of a MESMA approach over standard unmixing is the incorporation of a large number of endmember (EM) and thus the explicit inclusion of EM spectral variability (e.g. Asner et al., 2000; Roberts et al., 1998; Garcia-Haro et al., 2005). Also the problem with linear dependencies between EM and consequently ill-conditioned models is reduced since only one EM for the classes PV, NPV and soil is used simultaneously.

While other MESMA approaches select the EM-model with the lowest unmixing RMS, the  $\mu$ MESMA approach uses a combined model selection criteria (see Bachmann et al., 2004; Bachmann et al., 2005 for a closer description). First of all, a residual analysis is conducted; therefore spectral features in the residual spectra are detected and identified using a knowledge-based approach. If the residual spectra of a mixture model shows an identifiable signal above noise level (e.g. an overestimation of clay absorbance at 2.20  $\mu$ m), it is likely that an unsuitable EM is used (i.e. a soil EM with too high clay content). Thus the calculated EM fractions are also likely to be incorrect. Consequently this mixture model is assigned a low confidential score, which will be combined with the modelling RMS error. The RMS in the SWIR2 is included with a higher weighting factor since this wavelength range is of particular interest for the separation of PV, NPV and soil due to the diagnostic absorption features of clay and lignocellulose (e.g. ASNER). Finally the mixture model with the highest confidential score is selected.

The  $\mu$ MESMA approach also includes an iterative selection of EMs based on the residual analysis in order to avoid a time-consuming 'brute-force' unmixing. Additional improvements comprise the incorporation of spatial neighbourhood information into the unmixing process, filtering and pre-processing of spectra, and the exclusion of mixture models with linear dependency and thus ill-conditioned EM models. Data products include quantitative cover estimates for PV, NPV and soil. For each pixel, a reliability estimation is computed based on residual features, unmixing RMS and on comparison with empirical regressions. Also the local incidence angle is explicitly included as one part of the reliability estimate.

### 3.2 Endmember Selection

In the framework of  $\mu$ MESMA, scene EM are automatically derived using two approaches. First, Sequential Maximum Angle Convex Cone (SMACC, see Gruninger et al., 2004) is applied in order to detect spectrally extreme pixels in the image. To improve results, erroneous spectra (saturated and / or noisy) as well as classes which are not of interest (e.g., water) are previously masked out. All proposed EM by SMACC are then classified using a feature-based approach. The final EM spectra for PV, NPV and soil are then selected using the criteria for MESMA EM by Dennison & Roberts (2003), plus the addition of spectral similarity tests.



After the first unmixing iteration, pixels with a high modelling error are automatically tested if they are potential additional EM. Thus the same steps for proposed EM as for SMACC are carried out. It has to be noted that even though the whole approach is fully automatic, a manual inspection of the proposed EM is highly recommended to ensure that only appropriate EM spectra (i.e. no mixtures, only classes of interest) are used.

3.3 Typical Accuracy

The typical accuracy of the  $\mu$ MESMA approach is listed in Table 1. The data base used for the error assessment includes spectral simulations as well as comparison with ground cover measurements taken in the field (Bachmann et al., 2005).

Table 1: Typical Error Margins of  $\mu$ MESMA

	Mean Error (*)	Minimum Error (**)	R <sup>2</sup>	Error <3% (***)
PV	9.1	6.9	0.88	50%
NPV	10.1	5.5	0.73	46%
Soil	6.1	4.6	0.80	59%

(\*) : Error margin in abundance absolute based on different test scenarios  
(\*\*) : Error margin without errors caused by EM selection  
(\*\*\*) : Percentage of models with abundance errors below 3%

The sources of error are mainly due to EM variability, and due to the high spectral similarity of classes green vegetation, dry vegetation and soil. The influence of flight orientation (and thus implicitly BRDF effects) were also addressed; in these experiments the correspondence of cover estimates in E-W & N-S orientated flightlines is typically within 4% abundance absolute in flat terrain.

4. TEST METHODOLOGY FOR LOCAL INCIDENCE ANGLE EFFECTS

4.1 Approach and Assumptions

In order to address the influence of the local incidence angle on ground cover estimates, cover fractions on both sides of north-south orientated ridges towards the sides of a north-south orientated flightline were analysed.

Ground cover is derived for PV, NPV and soil using the described  $\mu$ MESMA approach. Additional field estimates of typical canopy height and patch size are used to estimate the theoretical underestimation of soil cover.

Under the assumption that vegetation density is approximately equal on east- and west-facing slopes, systematic differences in canopy cover should be caused by the described local incidence angle effects when these slopes are located off-nadir in a north-south orientated flightline. For comparison, south- and north-facing slopes close to nadir of the flightlines were also investigated. Differences in ground cover on these slopes should be due to natural vegetation density on drier sunlit and more humid shaded slopes. Close to nadir only marginal local incidence angle effects should occur. In order to address these effects, it is highly important to reduce the influence of illumination and BRDF effects as described earlier.

4.2 Results

When comparing the typical spectra of south-oriented slopes with north-oriented, the increased soil proportion is clearly visible in the spectra of southern slopes (Fig. 4 & 5). Absorption features caused by iron are visible at 0.9  $\mu$ m, as well as clay absorption at 2.2  $\mu$ m while the holo-cellulose absorption at 2.09  $\mu$ m is reduced. The overall albedo is similar in both cases due to the terrain correction and due to the similar spectral behaviour of dry vegetation and soil. For east- and west-orientated slopes mean spectra are highly similar, showing the typical properties of mixed spectra. Thus the same type and composition of vegetation on east- and west-facing slopes can be expected also from a ‘spectral’ point of view.

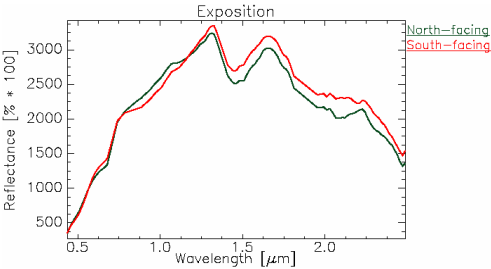


Fig. 4: Typical spectra of north- and south-facing slopes (area average).

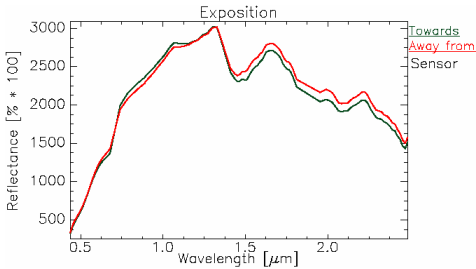


Fig. 5: Typical spectra of slopes pointing away and towards the sensor (area average).

When analysing the derived ground cover fractions, the proportion of soil on slopes pointing towards the sensor is generally higher than on slopes with a small local view angle (i.e. pointing away from the sensor).

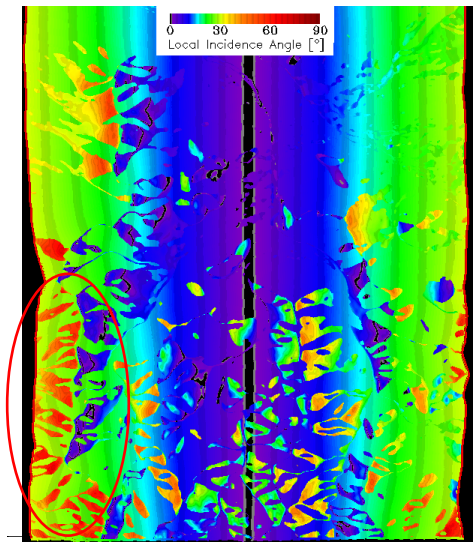


Fig. 6: Local incidence angle for test subset.

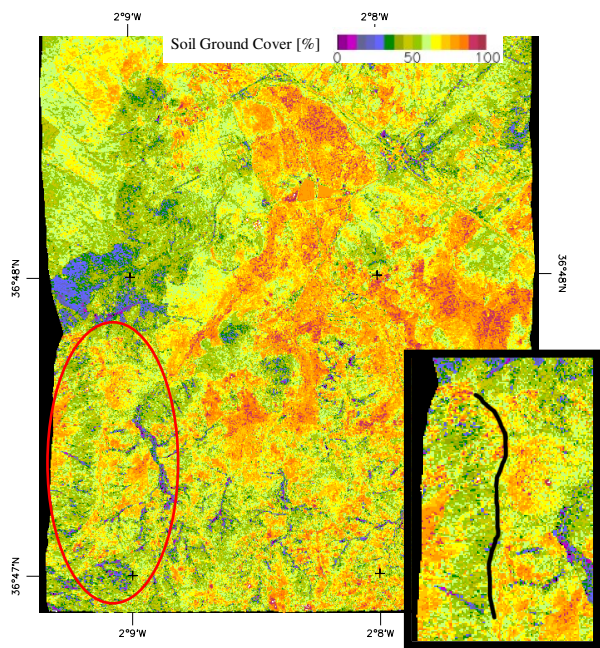


Fig. 7: Soil cover fractions derived by spectral unmixing. The black line in the inlay graph indicates the ridge location.

In the following, results for a north-south oriented ridge at the extreme side of one flightline are presented (Fig. 6 & 7). While for flat terrain measurements would be taken at a local incidence angle of 62°, angles above 80° occur at slopes pointing towards the sensor, and angles between 35-50° on slopes pointing away from the sensor.

When comparing the ground cover fractions for these slopes, the soil fraction is typically larger on slopes pointing towards the sensor by absolute ~10% cover when compared to the neighbouring slopes pointing away (Fig. 7 & 8). As also depicted, cover estimates for PV and NPV are increased by up to 8% absolute.

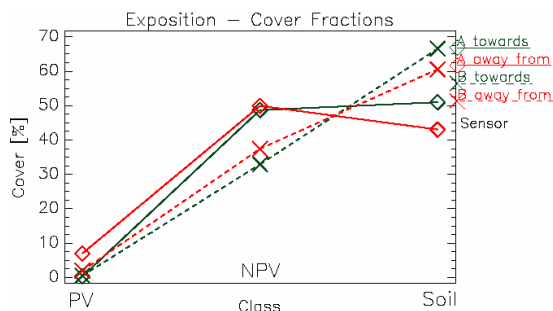


Fig. 8: Plots of typical ground cover fractions (area average) located on the sides of the ridge (see Fig. 6 & 7).

Since vegetation is not totally opaque as assumed in Fig. 2, the underestimation of soil fraction is less than predicted. But an underestimation for the whole area by approx. 20% seriously decreases the unmixing accuracy. Thus the results for such extreme slopes should be treated with care.

Consequently this additional local uncertainty is explicitly addressed in a reliability measure, depicted in Fig. 9. This measure is based on a weighted modelling RMS, features of the unmixing residuum, derivation from expectation values using empirical regression models, and the local incidence angle.

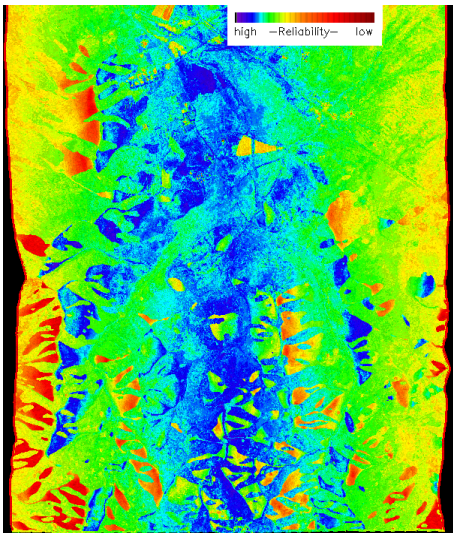


Fig. 9: Reliability index for unmixing results.

5. CONCLUSIONS

Local incidence angle effects significantly affect the accuracy of ground cover estimates for all measurements off-nadir when terrain is rough and when vegetation is patchy. When the line of sight from bare soil patches to the sensor is (partially) blocked by vegetation, the cover percentage of bare soil is underestimated while fractional cover by vegetation is overestimated.

For the presented test case in semi-arid grasslands, an overestimation of vegetation cover of up to 20% (i.e. 10% abundance absolute) in rough terrain was observed due to the described effect. For comparison, the typical error margins of the MESMA unmixing approach are better than 8.5% abundance absolute, and in about half of all cases better than 3% abundance absolute. When comparing these figures, the accuracy of retrieved vegetation and soil cover is significantly reduced by local incidence angle effects. Even though the effect is less prominent on gentle terrain and near nadir, the accuracy of all ground cover estimates by all wide FOV sensors is affected.

Since no physical correction of this effect is possible, it is reasonable to estimate the factor of overestimation based on the local relief and average vegetation height and size, and to include this in a per pixel reliability measure. By explicitly addressing this error, all following analysis methods requiring soil cover fractions (e.g. used for modelling soil erosion or land degradation) can incorporate this uncertainty.

## REFERENCES

- ASNER, G.P.; LOBELL, D.B. (2000): A Biogeophysical Approach for Automated SWIR Unmixing of Soils and Vegetation. In: *Remote Sensing of Environment* 74, pp. 99-112.
- ASNER, G.P.; BORGHI, C.E.; OJEDA, R. (2003): Desertification in Central Argentina: Changes in Ecosystem Carbon and Nitrogen from Imaging Spectroscopy. In: *Ecological Applications* 13(3), pp. 629–648.
- BACHMANN, M., MÜLLER, A., HABERMEYER, M., DECH, S. (2004): An Iterative Unmixing Approach in Support of Fractional Cover Estimation in Semi-Arid Environments. In: *Proc. of SPIE Remote Sensing Europe*, 13-16 September, Masplomas.
- BACHMANN, M., MÜLLER, A., HABERMEYER, M., SCHMIDT, M., DECH, S. (2005): Iterative Mesma Unmixing for Fractional Cover Estimates - Evaluating the Portability. In: *Proc. 4th EARSeL Workshop on Imaging Spectroscopy*, 27-29 April, Warsaw.
- COCKS, T., JENSSEN, T., STEWARD, A., WILSON, I., SCHIELDS, T. (1998): The HyMap Airborne Hyperspectral Sensor: the System, Calibration, and Performance. In: *Proceedings of the First EARSeL Workshop on Imaging Spectroscopy*, Zürich.
- DENNISON, P.E., ROBERTS, D.A. (2003): Endmember Selection for Multiple Endmember Spectral Mixture Analysis Using Endmember Average RMSE. In: *Remote Sensing of Environment* 87, pp. 123–135.
- GARCÍA-HARO, F.; SOMMER, S.; KEMPER, T. (2005): A New Tool for Variable Multiple Endmember Spectral Mixture Analysis (VMESMA). In: *International Journal of Remote Sensing* 26(10), pp. 2135-2162.
- GRUNINGER, J.; RATKOWSKI A.J.; HOKE, M. L. (2004): The Sequential Maximum Angle Convex Cone (SMACC) Endmember Model. In: *Proceedings SPIE, Algorithms for Multispectral and Hyper-spectral and Ultraspectral Imagery* Vol. 5425-1.
- HABERMEYER, M.; MUELLER, A.; HOLZWARTH, S.; RICHTER, R.; MUELLER, R.; BACHMANN, M.; SEITZ, K.-H.; SEIFERT, P.; STROBL, P. (2005): Implementation of the Automatic Processing Chain for ARES. In: *Proceedings of the 4thEARSeL Workshop on Imaging Spectroscopy*. Warsaw.
- MÜLLER, R.; HOLZWARTH, S.; HABERMEYER, M.; MÜLLER, A. (2005): Ortho Image Production within an Automatic Processing Chain for Hyperspectral Airborne Scanner ARES. In: *Proceedings of EARSeLWorkshop 3D-Remote Sensing*, Porto.
- OKIN, G.S.; ROBERTS, D.A. (2004): *Manual of Remote Sensing – Remote Sensing for Natural Resource Management and Environmental Monitoring*. Vol. 4: *Remote Sensing in Arid Regions: Challenges and Opportunities*, pp. 111-146, John Wiley and Sons, New York.
- PUIGDEFÁBREGAS, J. (2005): The Role of Vegetation Patterns in Structuring Runoff and Sediment Fluxes in Drylands. In: *Earth Surface Processes and Landforms* 30, pp. 133-147.
- RICHTER, R., SCHLÄPFER, D. (2002): Geo-Atmospheric Processing of Airborne Imaging Spectrometry Data, Part 2: Atmospheric / Topographic Correction. *International Journal of Remote Sensing* 23(13), pp. 2631-2649
- ROBERTS, D.A.; GARDNER, M.; CHURCH, R.; USTIN, S.; SCHEER, G.; GREEN, R.O. (1998): Mapping Chaparral in the Santa Monica Mountains Using Multiple Endmember Spectral Mixture Models. In: *Remote Sensing of Environment* 65, pp. 267- 279.
- USTIN, S.L.; JACQUEMOUD, S.; PALACIOS-ORUETA, A.; LI, L.; WHITING, M.L. (2005): Remote Sensing Based Assessment of Biophysical Indicators for Land Degradation and Desertification. In: *Proceedings of the 1st International Conference on Remote Sensing and Geoinformation Processing in the Assessment and Monitoring of Land Degradation and Desertification*, Trier.
- WELTZ, M.A.; KIDWELL, M.R.; FOX, H.D. (1998): Influence of Abiotic and Biotic Factors in Measuring and Modeling Soil Erosion on Rangelands: State of Knowledge. In: *J. Range Management* 51, pp. 482-495.

# SIMULATING CANOPY GAP FRACTION OF COMPLEX 3D FOREST SCENES OF *PICEA SITCHENSIS* (SITKA SPRUCE)

M. Pfeifer<sup>1,2</sup>, M. Disney<sup>2</sup>, P. Lewis<sup>2</sup>

1. Institute of Vegetation Ecology and Nature Conservation (VegNat), Potsdam University, Maulbeerallee 2, 14469 Potsdam, Germany, marion.pfeifer@googlemail.com

2. Department of Geography, University College London, Gower St., London WC1E 6BT, and NERC Centre for Terrestrial Carbon Dynamics, mdisney@geog.ucl.ac.uk, plewis@geog.ucl.ac.uk

**KEY WORDS:** Forestry; 3D canopy modelling; gap fraction; hemispherical photography.

## ABSTRACT:

We present an application of 3D canopy modelling for assessing the structural accuracy of complex 3D structural models of Sitka spruce. Such models can be used to simulate canopy reflectance at the landscape-scale with a minimum number of assumptions. Typically, however, the underlying canopy structural models require a large number of parameters, many of which are hard to measure and so must be estimated. How then can the resulting canopy structure be validated? We compare estimates of canopy gap fraction of modelled Sitka spruce from simulating hemispherical canopy reflectance from within the canopy, with those derived from upward-looking hemispherical photography from Harwood Forest, Northumberland, UK. Results show that gap fraction estimated from the 3D model canopies compares well with estimates derived from hemispherical photography. Where estimates disagree, such comparisons can be used to inform improvement of the structural models. We also use the detailed structural models to explore the sensitivity of hemispherical photography methods to error in estimating gap fraction in the field.

## 1. INTRODUCTION

Forest ecosystems and their interactions with the atmosphere, both as a sink and a source of carbon, are vital systems to study when estimating terrestrial carbon budgets (Dixon et al. 1994, Carrara et al. 2003) and ecosystem productivity (Schulze et al. 1999, Reich & Bolstad 2001). The structure of the forest canopy, especially the vertical and spatial distribution, orientation, and density of foliage and its supporting structures, plays a crucial role determining patterns of carbon exchange and nutrient cycling in the canopy, particularly via radiation interception (Ross 1981, Widowski et al. 2004).

Canopy structure i.e. the size and distribution of canopy elements (and their optical properties), is complex, spatially heterogeneous, and temporally variable (Weiss et al. 2004). This makes accurate ground-based measurements of biophysical parameters such as the leaf area index (LAI) and the fraction of absorbed photosynthetically active radiation (fAPAR) over larger areas time-consuming and expensive. Thus, research has focussed on algorithms permitting the derivation of biophysically relevant parameters from remotely sensed data (Price 1993, Sellers et al. 1994, Myneni et al. 1997), thereby providing the potential for monitoring the photosynthetic activity of terrestrial ecosystems at regional and global scales at daily time intervals (Deng et al. 2006). Such algorithms can be based on 1D and 3D radiation transfer models (Knyazikhin et al. 1998, Myneni et al. 2002, Pinty et al. 2006), which are capable of simulating radiation scattering and absorption of vegetation stands.

More recently, dynamic structural models for the growth of vegetation structure have been generated to improve the reliability of quantitative parameter estimation from satellite images (Saich et al. 2003, Disney et al. 2006). By simulating the reflectance and scattering of highly-

detailed 3D structural models of forest canopies, look-up-tables (LUTs) can be generated describing the relationship between canopy architecture and measured reflectance using a minimum number of simplifying assumptions. However, the underlying 3D structural models require a large number of parameters, many of which are often unavailable or too time-intensive to be measured in practice, which must be estimated.

Digital hemispherical photography may be a suitable tool to validate canopy structure in 3D models of vegetation structure. Hemispherical photography has been shown to be the ideal tool for studying plant canopy architecture and estimating the gap fraction in real forest stands providing information on size and density of gaps in the canopy rapidly and cheaply (reviewed in Jonckheere et al. 2004).

We simulate hemispherical reflectance from within the canopy of 3D structural forest models, and compare estimates of gap fraction derived from such simulations with estimates of gap fraction derived from upward-looking digital hemispherical photography acquired in Sitka spruce (*Picea sitchensis* (Bong.) Carr.) forest stands at Harwood Forest (Northumberland, UK). We ask the following questions:

- (1) Can we validate modelled 3D forest structure of *Sitka spruce* forest stands by comparing simulations of hemispherical reflectance of 3D models with hemispherical images required in-situ?
- (2) What is the impact on estimates of gap fraction / structure derived from hemispherical photography of: camera location (sampling frequency, proximity to trees), camera attitude, and focus. What are the implications of violating assumptions of leaf angle variability, clumping, etc on estimates of LAI derived from hemispherical photography?



2. MATERIAL AND METHODS

2.1 3D modelling of Sitka spruce canopies

We developed realistic detailed 3D structural models of Sitka spruce forest canopies in order to simulate reflectance values measured remotely (following the method of Disney et al. 2006). The mechanistic *Treegrow* model (developed from the PINOGRAM model of Leersnijder 1992, Oevelen van & Woodhouse IH 1996), an existing structural growth model of *Pinus sylvestris* L., was modified and used to generate trees for six age classes (5, 9, 12, 20, 30, and 40 years) of Sitka spruce. *Treegrow* is an empirical growth model which is parameterised by species- and site-specific empirical height and branching functions. By varying the seed for the pseudo-random number generator, five individual trees were generated per age class. These were then used for modelling forest stands permitting some tree level variability within each age class (Saich et al. 2003). Tree height was modified outside *Treegrow* to mimic observed height variation. The light extinction function implemented in *Treegrow* describes the variation with age of the percentage of light reaching the ground from the top of the canopy, and thereby determines the shape of the tree crown. The site-specific light extinction function was iteratively validated by simulating the light reduction through tree crowns, comparing resultant modelled and in-situ observed tree crown shape, and ground- to – crown heights, updating the function and when re-simulating (Disney et al. 2006). The modelled trees were validated by visual estimation (crown shape) and by comparing tree traits modelled with tree traits measured (e.g. height, diameter-at-breast height dbh, Fig. 1).

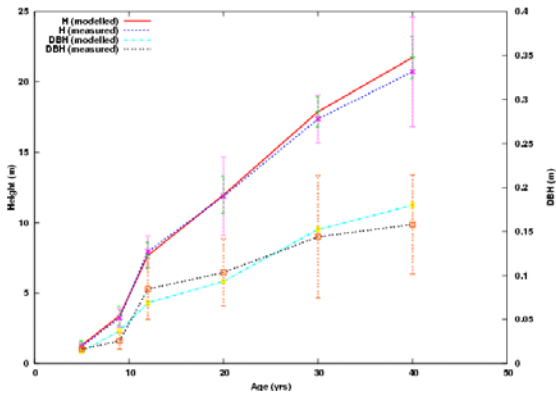


Figure 1. Tree height dbh modelled and measured at Harwood forest as a function of tree age.

Modelled trees were planted in age-specific forest stands according to measurements of tree spacing made at Harwood Forest. The observed forest stands are planted at high density and in a regular pattern causing deep shade in older forest stands and larger height-to-crown values (Fig. 2). Management at the site includes thinning to optimise growth conditions for all trees in the forest stand.

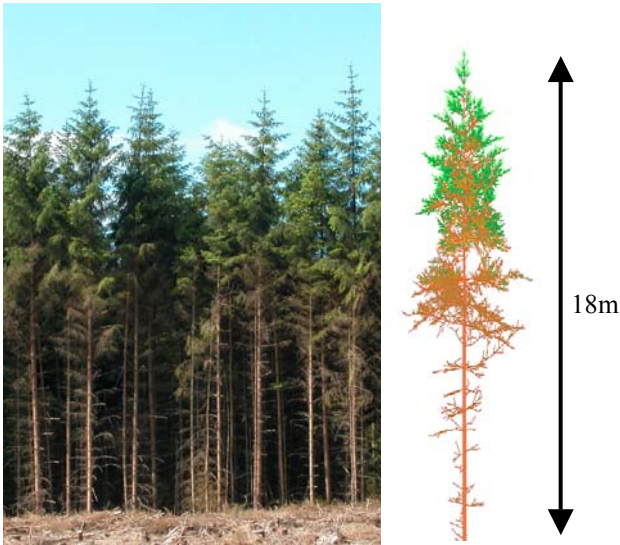


Figure 2. Left: Picture of a 30 years old forest stand of Sitka spruce taken at the Harwood Forest field site. Right: Model of a 30 years old Sitka spruce tree created with *Treegrow*.

The modelled forest stands were generated to be 300m on a side, and only the central 50 m x 50 m region was viewed in simulations to avoid edge effects (Saich et al. 2003). Because leaves are not included in the *Treegrow* model, they have been added here to the branches of the modelled trees using species- and site-specific measurements on needle size and density, and needle distribution (based on literature, Chandler & Dale 1990). The total length of green branches was obtained from the *Treegrow* derived tree model (Woodhouse & Hoekman 2000).



Figure 3. Model of a 9 yrs old Sitka spruce tree with needles. Needles were added to the “green” branches according to a Fibonacci distribution. Mean needle density and mean needle length were derived from field measurements.



## 2.2 Analysis of hemispherical images via CanEye

Hemispherical photographs were recorded in 5, 9, 12, 20, 30, and 40 years old forest stands of Sitka spruce in Harwood Forest in 2003 using a Nikon Coolpix 5000 with 180° fisheye adaptor. Hemispherical reflectance was simulated from within the forest models using a Monte Carlo ray tracing model (based on the *drat* model of Lewis, 1999) mimicking the properties of upward-looking hemispherical photography. Images were created for subsequent analysis using the CanEye software (version 4.1, Baret F. 2007: [http://www.avignon.inra.fr/can\\_eye/](http://www.avignon.inra.fr/can_eye/)). Image generation was only carried out as part of the “Transect” experiment (see below). In the other experimental cases (where gap fraction was sampled from multiple locations rather than from a single point) image generation was not appropriate.

In-situ hemispherical photographs (Fig. 4) were “thresholded” classifying pixels into vegetation / non-vegetation via an iterative algorithm that searches for the optimal threshold value (Ridler & Calvard 1978, Magid et al. 1990).

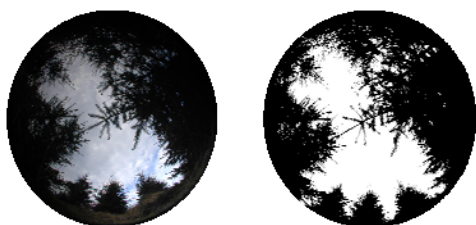


Figure 4. Hemispherical photograph of the 9 years old Sitka spruce forest stands before (left) and after (right) the “thresholding” procedure.

The leaf area index (LAI), defined as one half the total leaf area per unit ground surface area to account for irregular and non-flat forms of leaves (Chen & Black 1991, Fassnacht et al. 1994, Stenberg et al. 1994), is a critical parameter in studies of atmosphere-vegetation interaction and in models of vegetation canopy response to environmental changes (Deng et al. 2006). LAI estimates ( $LAI_{57}$ ,  $LAI_{eff}$ ,  $LAI_{true}$ ) and gap fraction probability as a function of zenith angle were automatically derived from the “thresholded” images using CanEye.  $LAI_{57}$  is derived at a view zenith angle of 57.5°, which is suggested to be almost independent of foliage inclination angle (Warren-Wilson 1963). Effective LAI ( $LAI_{eff}$ ) is directly retrieved by model inversion in CanEye based on a Poisson model (Eq. 1), where the foliage is assumed randomly distributed, and assuming an ellipsoidal distribution of the leaf inclination using look-up-table techniques (Knyazikhin et al. 1998, described in more detail in the manual of CanEye 2006).

The gap fraction  $P_0(\theta_v, \varphi_v)$  in direction  $(\theta_v, \varphi_v)$  is related to the contact frequency by

$$P_0(\theta_v, \varphi_v) = e^{-N(\theta_v, \varphi_v)} = e^{-G(\theta_v, \varphi_v)LAI/\cos(\theta_v)} \quad (1)$$

where  $N(\theta_v, \varphi_v)$  is the mean number of contacts between a light beam and a vegetation element in the direction  $(\theta_v, \varphi_v)$ , and  $G(\theta_v, \varphi_v)$  is the projection function, i.e. the mean projection of a unit foliage area in direction  $(\theta_v, \varphi_v)$ .

The “true” LAI ( $LAI_{true}$ ) is related to  $LAI_{eff}$  through the clumping index  $\lambda_0$  (Chen & Black 1992), which depends both on plant structure (foliage distribution), canopy structure, and size and shape of leaves (Eq. 2).

$$LAI_{eff} = \lambda_0 LAI_{true} \quad (2)$$

In CanEye, the clumping index is computed using the Lang & Yueqin (1986) logarithm gap fraction averaging method.

## 2.3 Simulation of the impact of camera set-up on estimates of gap fraction

5 experimental approaches were used to test the impact of observer variability during hemispherical photography on estimates of gap fraction and LAI. Images for further analysis in CanEye were created in the experiment “Transect” only.

1. “Transect”: images were simulated using at 10 camera locations along a transect through the forest canopy.

2. “Focus”: the aperture of the camera (infinitesimal pinhole) located at the image centre was enlarged to the following values (mm): 1, 5, 10, 50, 100 to simulate the impact of lack of focus in estimates of gap fraction from digital hemispherical photos.

3. “Plane”: the plane of the camera located in the image centre was tilted away from the horizontal by the following angles (degrees): 5°, 10°, 15°, 20°, 25°. This is to simulate the impact of not having a totally level camera in estimating gap fraction from digital hemispherical photos.

4. “Clone”: the “camera” was randomly located within the modelled forest stand for each ray cast and the average gap fraction was calculated. This allows calculation of the ‘forest-average’ gap fraction, which is the ‘true’ gap fraction from a photon transport point of view. That measured from hemispherical photography is a sample of the true value which will obviously be a function of the specific location from where the photograph was taken.

5. “Clone Threshold”: the same setup as in the previous case, but in this case a threshold distance away from the tree coordinates in the forest stand was specified. In reality, photographs are not taken with the camera immediately adjacent to a tree trunk, and this will act to bias the gap fraction estimates somewhat. Various thresholds distances of 100, 150 and 200 cm were used.

## 3 RESULTS

### 3.1 CanEye Analyses of hemispherical images

In the following we present results of the simulations and the hemispherical image analyses for the 5 years and 9 years old forest stands only, because the simulations for older forest stands were still processing. Results of the analyses of the simulated images are presented in figures 5 and 6. Estimates of  $LAI_{57}$ ,  $LAI_{eff}$  and  $LAI_{true}$  are presented in table 1.

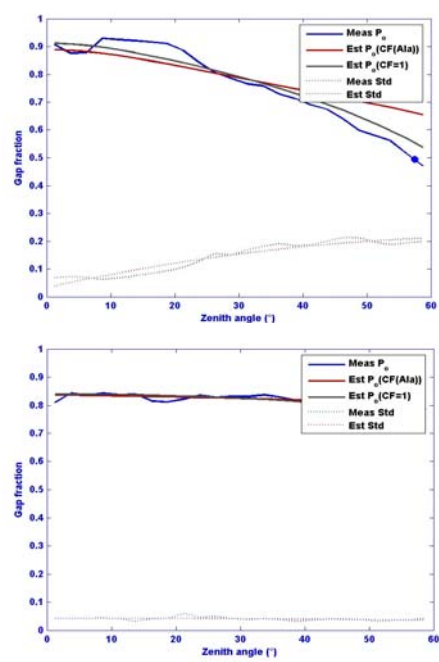


Figure 5. Gap probability as a function of view zenith angle for 9 years canopy. CanEye analyses was carried out for “thresholded” in-situ hemispherical photographs (above) and for “thresholded” simulated images (below).

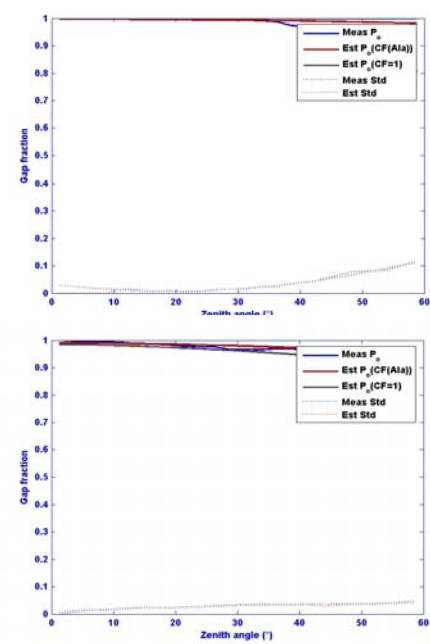


Figure 6. Gap probability as a function of view zenith angle for 5 years canopy. CanEye analyses was carried out for “thresholded” in-situ hemispherical photographs (above) and for “thresholded” simulated images (below).

Images	LAI57	LAI <sub>eff</sub>	LAI <sub>true</sub>
5yr, modelled	0.052	0.1	0.07
5y, measured	0.21	0	0.03
9yr, modelled	0.3	0.26	0.29
9yr, measured	0.76	0.6	1.4

Table 1: Estimates of LAI<sub>57</sub>, LAI<sub>eff</sub>, and LAI<sub>true</sub> derived from simulations of hemispherical reflectance within forest stands and from in-situ photographs. Results are shown for 5 years and 9 years old forest stands only.

Experiment	GP mean ± sd
“Transect” – 5 yrs	0.88 ± 0.05
“Focus” – 5 yrs	0.49 ± 0.33
“Plane” – 5 yrs	0.91 ± 0.01
“Clone_thresh” – 5 yrs	0.88 ± 0.00
“Clone” – 5 yrs	0.88
“Transect” – 9 yrs	0.39 ± 0.02
“Focus” – 9 yrs	0.09 ± 0.11
“Plane” – 9 yrs	0.28 ± 0.00
“Clone_thresh” – 9 yrs	0.39 ± 0.02
“Clone” – 9 yrs	0.35

Table 2: Impact of choice of camera location, camera attitude and camera focus on estimates of gap fraction (mean values ± 1 standard deviation) derived from hemispherical photography in five and nine years old modelled forest stands. The experiment “clone” calculates the average of randomly located measurements within the model forests.

4. DISCUSSION

Results from figures 5 and 6 show that gap fraction estimated from the 3D model canopies compares reasonably well with estimates derived from hemispherical photography in the 5 years and 9 years old modelled Sitka forest stands. However, it can be seen that gap probability did not decrease with increasing viewing angle for the simulated forest stands in the same way as seen in the real forest stands. This might be due to structural discrepancies between modelled and real forest stands. It may also be due to the fact that for angles beyond around 70° in the hemiphotos, the distortion in the projected field of view becomes large, whereas there is effectively no distortion in the simulated images.

4.1 Impact of camera set-up on estimates of gap fraction

Simulated variation in camera focus caused high variability in estimates of gap probability, while tilt angle had far less impact on estimates of gap probability (Table 2). Sampling design had an additional impact on gap probability estimates. The assignment of the camera to randomly chosen points within the forest can result in camera locations immediately beside a tree trunk, resulting in much lower (mean) estimates of gap probability than would be encountered in practice, where one would avoid taking photographs from within a metre or so of a tree trunk. However, any such avoidance will act to bias the resulting estimates of gap probability to be lower than the true values. This problem will tend to increase as forest stands are older/denser and the stem area density increases. In very dense plantation stands (see figure 1) it can be difficult in practice to find suitable spaces in which to place the camera and operator.

## 5. CONCLUSIONS

Research on techniques and algorithms for accurately and efficiently monitoring and measuring photosynthetic activity and LAI especially of forest stands has a longstanding history (Jonckheere et al. 2004, Weiss et al. 2004). While EO data have been used increasingly to derive biophysical parameters of land surfaces, dynamic structural models for forest growth have been used to improve the reliability of quantitative parameter estimation from such satellite images (Woodhouse & Hoekman 2000, Saich et al. 2003, Disney et al. 2006).

Tree growth models have been introduced to provide statistical information about dimensions and angular distributions of scattering components of forest stands that, in turn, can be used as an input to a backscatter model to predict backscatter from forest stands exploring relationships between EO data, forest structure, and biophysical parameters. 3D models are the most detailed models of this type, as they are able to proscribe the size and location of all scattering elements in the canopy. This allows them to be used for making detailed simulations of the canopy radiation regime (Widlowski et al. 2006).

Yet, a number of parameters underlying 3D structural models are unavailable or difficult to obtain. We show that digital hemispherical photography can be used to validate structural accuracy of 3D forest models generated via the tree growth model *Treegrow*. Estimates of gap probability derived from simulations of the detailed 3D structural models compared well with estimates derived from upward-looking digital hemispherical photography acquired in Sitka spruce canopies in England at least for 5 and 9 years old forest stands. However, we also found an increasing discrepancy between estimates of gap fraction (and percentage of vegetation / non-vegetation pixels in the image) for modelled and real forest stands with increasing forest age (results not shown, experiments still running). Such disagreements can be used to inform improvement of the structural models.

Age related changes in leaf structure may affect productivity of the forest, which should be manifested in the reflectance signal (see Widlowski et al. 2004, citing Caylor 2004). In upcoming experiments, we will investigate the effect of leaf structure and leaf density as well as of other structural parameters of the forest (e.g. branching traits) on the reflectance signal.

The results presented here are also relevant for generating field protocols necessary for accurate use of fisheye lens cameras to estimate LAI, as well as for testing the validity of theoretical assumptions underlying those measurements in the field. A quasi-random distribution of locations for acquiring photographs in a forest (camera locations certain distances from existing trees) is often applied in the field. This is introducing potential bias acting to reduce gap probability and LAI estimates from the resulting digital hemiphotos, especially when estimating gap probability as a function of increasing viewing zenith angle. Camera focus has the greatest impact on gap fraction probability estimates by impeding the correct classification of pixels to vegetation / non-vegetation. However, in practice this is not likely to vary as much as we have simulated here. But clearly, pixel resolution (number of pixels), and focus can have a large impact on the resulting estimates of gap fraction. Many

cameras will auto-focus on a point at infinity, but it is not clear in a dense forest canopy that this is ideal in that the lower branches of the canopy will be quite close to the camera, and as a result will be out of focus. It is these branches that will have the greatest impact on reducing gap probability, and so it is of greatest importance to get these branches into focus.

In summary, we show that it is possible to compare measured and modelled tree structure through the analysis of simulated canopy images and derived gap fraction. We also show that 3D tree models can be used very effectively to explore the impact of errors and assumptions when deriving canopy structural parameters from digital hemiphotography.

## References

- Carrara A, Kowalski AS, Neirynck J, Janssens IA, Yuste JC & Ceulemans R. (2003) Net ecosystem CO<sub>2</sub> exchange of mixed forest in Belgium over 5 years. *Agricultural and Forest Meteorology* **119**: 209-227.
- Caylor K.K., Dowty P.R., Shugart H. H. & Ringrose S. (2004) Relationship between small-scale structural variability and simulated vegetation productivity across a regional moisture gradient in southern Africa. *Global Change Biology* **10**: 374-382.
- Chandler J. W. & Dale J. E. (1990) Needle growth in Sitka spruce (*Picea sitchensis*): effects of nutrient deficiency and needle position within shoots. *Tree Physiology* **6**: 41-56.
- Chen J. M. & Black T. A. (1992) Defining leaf area index for non-flat leaves, *Plant Cell Environ.* **15**: 421-429.
- Deng F., Chen J. M., Plummer S. (2006) Algorithm for Global Leaf Area Index Retrieval Using Satellite Imagery. *IEEE Transactions on Geoscience and Remote Sensing* **44**: 2219-2229.
- Disney M, Lewis P & Saich P. (2006) 3D modelling of forest canopy structure for remote sensing simulations in the optical and microwave domains. *Remote Sensing of Environment* **100**: 114-132.
- Dixon RK, Brown S, Houghton RA, Solomon AM et al. (1994) Carbon pool and flux of global forest ecosystems. *Science* **263**: 185-190.
- Fassnacht K. S., Gower S. T., Norman J. M., et al. (1994) A comparison of optical and direct methods for estimating foliage surface-area index in forests. *Agricultural and Forest Meteorology* **71**: 183-207.
- Jonckheere I., Fleck S., Nackaerts K., et al. (2006) Review of methods for in situ leaf area index determination. Part I. theories, sensors, and hemispherical photography. *Agricultural and Forest Meteorology* **121**: 19-35.
- Knyazikhin Y., Martonchik J. V., Diner D. J., Myneni R. B. et al. (1998) Estimation of vegetation canopy leaf area index and fraction of absorbed photosynthetically active radiation from atmosphere-corrected MISR data. *Journal of Geophysical Research* **103**: 239-256.
- Leersnijder R. P. (1992) PINOGRAM: a pine growth area model. PhD thesis, Wageningen Agricultural University, The Netherlands.
- Lewis P. (1999) Three-dimensional plant modelling for remote sensing simulation studies using the botanical plant modelling system. *Agronomie - Agriculture and Environment* **19**: 185-210.
- Magid A., Rotman S. R. & Weiss A. M. (1990) Comment on "Picture Thresholding Using an Iterative Selection Method". *IEEE Transactions on Systems, Man and Cybernetics* **20**: 1238-1239.

- Myneni R. B., Ramakrishna R. N. & Running S. W. (1997) Estimation of Global Leaf Area Index and Absorbed PAR Using Radiative Transfer Models. *IEEE Transactions on Geoscience and Remote Sensing* **35**: 1380-1393.
- Myneni R. B., Hoffman S., Knyazikhin, Y., Privette J. L. et al. (2002) Global products of vegetation leaf area and fraction absorbed PAR from year one of MODIS data. *Remote Sensing of Environment* **83**: 214-231.
- Oevelen van PJ & Woodhouse I. H. (1996) NOPEX-Forest-Dynamo Ground data collection and data analysis report. Report # 70. Department of Water Resources, Wageningen Agricultural University.
- Pinty B., Lavergne T., Dickinson R. E., Widlowski J. L., et al. (2006) Simplifying the interaction of land surfaces with radiation for relating remote sensing products to climate models. *Journal of Geophysical Research* **111**: 1-20.
- Price J. C. (1993) Estimating Leaf Area Index from Satellite Data. *IEEE Transactions on Geoscience and Remote Sensing* **31**: 727-734.
- Reich P. B. & Bolstad P. (2001) Productivity of evergreen and deciduous temperate forests. In: Roy J., Saugier B., Mooney H. A. (eds) *Terrestrial Global Productivity. Physiological Ecology*. Academic Press, San Diego, pp 245-283.
- Ridler T. W. & Calvard E. S. (1978) Picture thresholding using an iterative selection method. *IEEE Transactions on Systems, Man and Cybernetics* **8**: 629-632.
- Ross J. (1981) *The radiation regime and architecture of plant stands.*, Dr. W. Junk. The Hague.
- Saich P., Disney, M. I., Lewis, P. et al. (2003) Development of architectural vegetation growth models for remote sensing applications. Final report ESA contract 14940, pp 183-187.
- Schulze E. D., Lloyd J., Kelliher F. M., Wirth, C. et al. (1999) Productivity of forests in the Eurosiberian boreal region and their potential to act as a carbon sink a synthesis. *Global Change Biology* **5**: 703-722.
- Sellers P. J., Los S. O., Tucker C. J. et al. (1994) A 1x1km NDVI dataset for global climate studies. Part 2: The generation of global fields of terrestrial biophysical parameters from the NDVI. *International Journal of Remote Sensing* **15**: 3519-3545.
- Stenberg P., Linder S., Smolander H., et al. (1994) Performance of the LAI-2000 Plant Canopy Analyzer in estimating leaf-area index of some Scots pine stands. *Tree Physiology* **14**: 981-995.
- Warren-Wilson J. (1963) Estimation of foliage denseness and foliage angle by inclined point quadrats, *Aust. J. Bot.* **11**: 95-105.
- Weiss M., Baret F., Smith G. J., Jonckheere I. & Coppin B. (2004) Review of methods for in situ leaf area index (LAI) determination Part II. Estimation of LAI, errors, and sampling. *Agricultural and Forest Meteorology* **121**: 37-53.
- Widlowski J. L., Pinty, B., Gobron, N. et al. (2004) Canopy structure parameters derived from multi-angular remote sensing data for terrestrial carbon studies. *CLIMATIC CHANGE* **67**: 403-415.
- Widlowski J. L., Pinty B., Lavergne T., et al. (2006) Horizontal radiation transport in 3-D forest canopies at multiple spatial resolutions : Simulated impact on canopy absorption. *Remote Sensing of Environment* **103**: 379-397.
- Woodhouse I. H. & Hoekman D. H. (2000) Radar modelling of coniferous forest using a treegrowth model. *International Journal of Remote Sensing* **21**: 1725-1737.

# COMPARING THREE CANOPY REFLECTANCE MODELS WITH HYPERSPECTRAL MULTI-ANGULAR SATELLITE DATA

M. Schlerf<sup>a,\*</sup>, W. Verhoef<sup>a,b</sup>, H. Buddenbaum<sup>c</sup>, J. Hill<sup>c</sup>, C. Atzberger<sup>d</sup>, A. Skidmore<sup>a</sup>

<sup>a</sup> International Institute for Geo-Information Science and Earth Observation, P.O. Box 6, 7500 AA Enschede, The Netherlands

<sup>b</sup> National Aerospace Laboratory NLR, P.O. Box 153, 8300 AD Emmeloord, The Netherlands

<sup>c</sup> Remote Sensing Department, University of Trier, Behringstrasse, D-54286 Trier, Germany

<sup>d</sup> GEOSYS, 20 Impasse René Couzinet, BP 65815, 31505 Toulouse Cedex 5, France

## Commission VI, WG VI/4

**KEY WORDS:** Canopy reflectance models, forward modelling, radiative transfer, hyperspectral, multi-angular

### ABSTRACT:

Studies that compare modelled reflectances with satellite-measured reflectances for different wavelengths and view angles are still rare. We compared model outputs from three different canopy reflectance models (SLC, FRT and INFORM) with satellite measured reflectances (Chris/PROBA). Comparison of the simulated directional reflectances reveals general agreement but also some differences among the models. In general, the radiative transfer models produce signatures comparable to measured ones for spruce and beech forest of different age and canopy structure.

## 1. INTRODUCTION

Among various methods, physically based radiative transfer models have proved to be a promising alternative to estimate biophysical vegetation attributes. However, the existence of many canopy reflectance models with different levels of complexity makes it difficult to choose the most appropriate model for a given application. Intensive research has been done on comparing different models in predicting canopy bidirectional reflectance (Jacquemoud et al., 2000; Bacour et al., 2002; Pinty et al., 2004) but studies that compare modelled reflectances with satellite-measured reflectances for different wavelengths and view angles are still rare. The objective of this study is to evaluate the performance of three canopy reflectance models SLC (Soil-Leaf-Canopy; Verhoef & Bach, 2007), FRT (Forest Reflectance and Transmittance; Kuusk & Nilson, 2000) and INFORM (Invertible Forest Reflectance Model; Schlerf & Atzberger, 2006; Atzberger, 2000) in the direct mode and to compare the model outputs with hyperspectral and multi-directional canopy reflectances from Chris/PROBA images.

## 2. METHODS

### 2.1 Canopy reflectance models

The three models SLC, FRT, and INFORM simulate the bi-directional reflectance of forest stands between 400 and 2500 nm as a function of leaf attributes, canopy attributes, and external parameters. A forested scene is divided into four components: sunlit tree crowns, sunlit ground, shaded crowns, and shaded ground.

*INFORM* is a combination of the PROSPECT leaf model (Baret and Fourty, 1997), the SAILH radiative transfer model for

homogeneous canopies (Verhoef, 1984; 1985) and the semi-empirical forest model FLIM (Rosema et al., 1992). In *INFORM* (and in opposition to *FLIM*), crown transmittance in observation and sun direction, crown reflectance at infinite crown depth and the background reflectance are computed using the *SAILH+PROSPECT* models.

*SLC* is an integrated model consisting of a modified Hapke (1981) soil BRDF model, a robust version of *PROSPECT*, and a modernised canopy model *4SAIL2* (a hybrid two-layer version of *SAILH* which contains elements from *FLIM* (crown clumping), *GeoSAIL* (Verhoef and Bach, 2003; vertical leaf color gradient) and *SAIL++* (Verhoef, 2002; numerical robustness)). In contrast to *INFORM*, *SLC* applies a clumping modulation to all (in total: 11) optical properties of the canopy layer.

*FRT* is a forest stand model built on an early forest reflectance model by Nilson & Peterson (1991). It incorporates *PROSPECT*, the radiative transfer model 6S and the two-layer understory reflectance model *MCRM2* (Kuusk, 2001). Crown shapes are modelled as rotation ellipsoids or as cones, optionally with a cylinder in the lower part. Leaves and branches are uniformly distributed in the crown and spherically oriented. Several tree classes of different size and/or species are possible. The soil reflectance is modelled by Price' vectors (Price, 1990).

### 2.2 Satellite data and field measurements

Chris/PROBA images were acquired at Idarwald test site (Germany) on 5 September 2005 in mode 1 (411-1004 nm) at five observation angles (-44°, -33°, -5°, +28°, and +44°). The sun zenith angle during the sensor overpass was 44° and the relative azimuth angle between sun angle and observation angle

\* Corresponding author: schlerf@itc.nl



was 50° (Figure 1). All five images were geocoded to the local reference system using image-to-image registration and resampled to the nominal ground resolution at nadir view (34 m). The images were radiometrically corrected to top-of-canopy reflectance assuming standard atmospheric parameters.

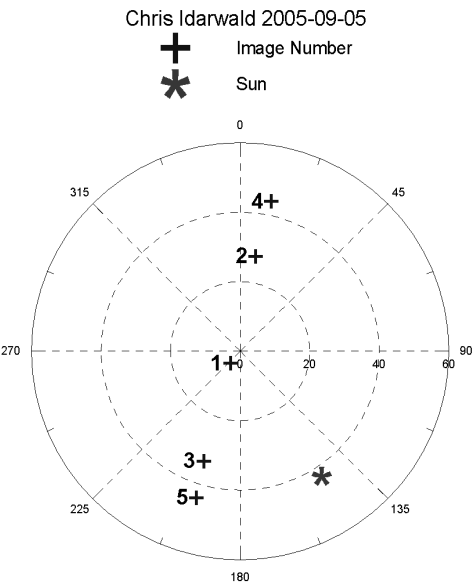


Figure 1: Observation and sun geometry of Chris/PROBA images acquired over Idarwald test site on 05/09 2005

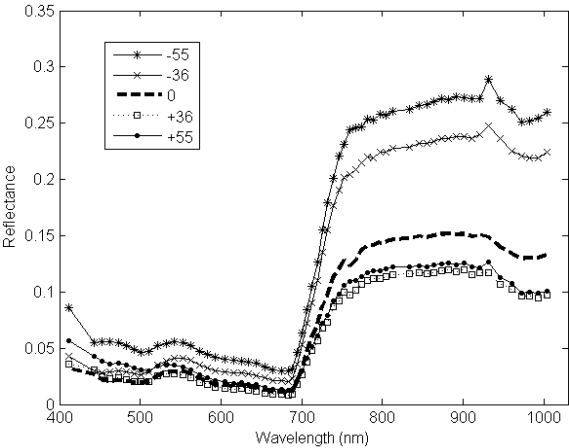


Figure 2: Bi-directional Chris/PROBA spectral reflectances of spruce stands after image radiometric correction. Each curve corresponds to the average signature of 15 stands (60 pixels in total). Beech stands exhibit similar directionality.

Two weeks after the image acquisition, an extensive field campaign was conducted and the canopy structure of altogether 28 forest stands (15 plots of Norway spruce (*Picea abies* L. Karst.) and 13 plots of Beech (*Fagus sylvatica*)) was measured. In each forest stand, a plot of 30x30 m<sup>2</sup> size was established and its central position determined using a hand-held GPS device. Measured attributes include leaf area index (LAI, measured

with Li-Cor LAI-2000), crown diameter (CD), tree density (SD), crown cover (COcr), canopy height (TH), and percent coverage of understorey vegetation (COus).

2.3 Model parameterisation

We identified three typical stands for each species (Table 1): young, medium, and old stands. Young stands (20-30 years; before thinning) typically have small tree crowns, many trees and relatively large canopy LAI, whereas old stands (> 80 years) are usually thinned out and therefore show lower LAI values and larger crowns. At first, for all of the six stands, an average hyperspectral signature was extracted from the four nearest pixels surrounding the GPS-measured plot location in each Chris/PROBA image. The angular variations of the spectral signatures of spruce stands is illustrated in Figure 2.

Type	Age	ID
Spruce	21	83
Spruce	42	109
Spruce	131	301
Beech	40	8
Beech	84	243
Beech	122	245

Table 1: Selected forest stands. Age = stand age in 2005 (years), ID = forest stand identification

ID	CD	TH	SD	LAIc	LAI <sub>s</sub>	COcr	CO <sub>us</sub>
83	1.75	7.9	5000	5.1	7.25	80	30
109	4.30	15.2	689	3.8	6.00	70	70
301	6.60	35.4	211	3.9	7.71	35	40
8	3.03	13.2	3022	6.1	6.59	85	10
243	5.70	24.8	467	3.4	4.80	50	10
245	7.85	25.2	233	4.3	6.29	35	20

Table 2: In situ measured canopy properties. CD = crown diameter (m), TH = tree height (m), SD = stem or tree density (/ha), LAIc = canopy leaf area index (Li-Cor LAI-2000), LAI<sub>s</sub> = single tree leaf area index (LAIc/COcr), COcr = crown cover (%), CO<sub>us</sub> = cover of understorey vegetation (%), visually estimated)

	Spruce	Beech
N	3.0	1.5
Cab	70	50
Cw	0.02	0.02
Cm	0.025	0.015
ala	65	50
hot	0.02	0.04

Table 3: Leaf properties and species specific canopy properties. N = leaf structure parameter, Cab = chlorophyll a+b content (µg/cm<sup>2</sup>), Cw = equivalent water thickness (g/cm<sup>2</sup>), Cm = dry matter content (g/cm<sup>2</sup>), ala = average leaf angle (°), hot = hot spot parameter

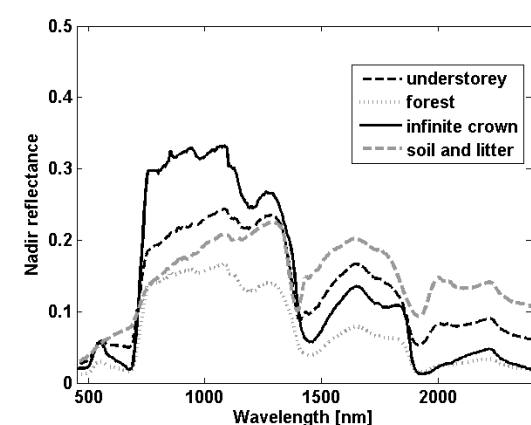


Figure 3: INFORM simulations of a spruce canopy in nadir direction (stand 301).  $R_{\text{soil}}$  (soil and litter) = scaled HyMap spectrum,  $R_{\text{understorey}} = R_{\text{soil}} + \text{understorey vegetation (LAI=0.5)}$ ,  $R_{\text{infinite}} = \text{Tree crown LAI} = 15$ ,  $R_{\text{forest}} = \text{Forest canopy reflectance}$

To allow comparison of modelled and measured reflectance, the models were parameterised to a large extent using the ground truth information that had been measured in the respective forest stands. Ground truth was available for the most important structural canopy parameters (Table 2). Leaf properties and certain canopy properties that have not been measured in the field (Table 3) were fixed to species specific default values or were slightly optimised through comparing INFORM model outputs with Chris reflectances. All models used a similar background spectrum (Figure 3, black dashed line named understorey). Specification of the sun and viewing geometry was matched to the image acquisition (section 2.2). Using the stand type specific canopy attributes and the illumination and viewing geometries of the Chris/PROBA overpass, the canopy reflectance was modelled using the three radiative transfer models.

In FRT, additional input parameters had to be defined. The following input parameters were computed from measured values: crown length (m), trunk diameter (m), total dry leaf weight (DLW, kg/tree), chlorophyll-% of DLW, water-% of DLW, dry matter-% of DLW, among others. For the following input parameters default values were used: shoot shading coefficient, refraction index ratio, shoot length, Markov parameter, among others. Cones (spruce) and ellipses (beech) were assigned to approximate crown shape.

3. RESULTS

Comparison of the directional reflectances simulated by FRT, SLC, and INFORM reveals general agreement but also some differences among the models. In general, the models produce signatures comparable to measured ones for spruce and beech forests of different age and canopy structure. The pronounced bowl shape in the red waveband of the Chris/PROBA data (Figure 4) is not followed by the models; they rather produce a straight line. Possibly, in the atmospheric correction of the satellite data, the value for the aerosol optical thickness should have been higher, yielding lower reflectances in the red, and thus less of a bowl shape.

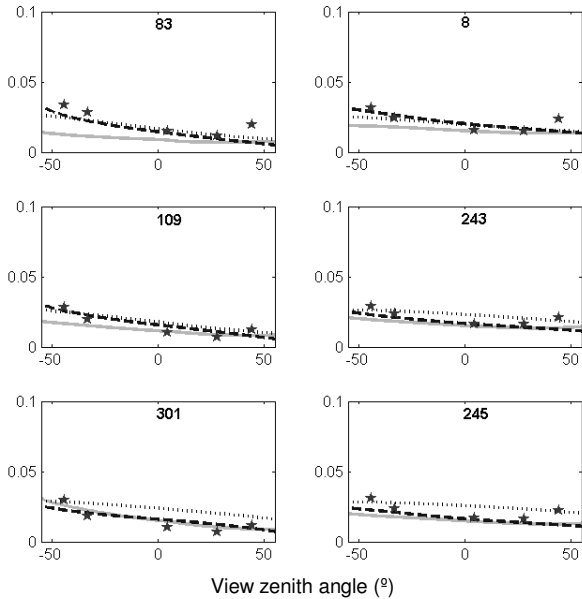


Figure 4: Measured and simulated bi-directional reflectances in the red (670 nm) for spruce forests (left) and beech forests (right) labelled with the respective stand ID. Grey line = FRT, black dashed line = INFORM, black dotted line = SLC, black stars = Chris/PROBA.

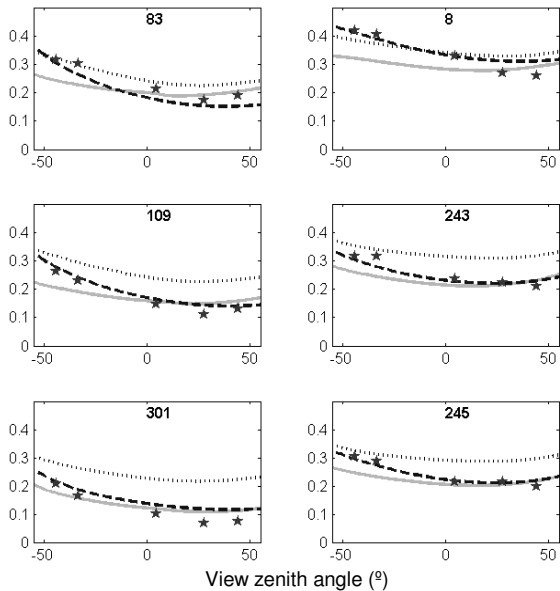


Figure 5: Directional reflectances in the NIR (780 nm) for spruce forest (left) and beech forest (right) labelled with the respective stand ID. Grey line = FRT, black dashed line = INFORM, black dotted line = SLC, black stars = Chris/PROBA.

FRT underestimates red reflectances of young forest stands at large negative viewing angles whereas model outputs of SLC and INFORM are pretty similar to the measured ones.

In the NIR (Fig. 5), differences are more pronounced than in the red. SLC overestimates NIR reflectance for older stands, in particular spruce but also beech. Approximating the Chris/PROBA reflectance curves with SLC for those stands would be possible when a darker background is used or woody material is included. Similar to the red domain, FRT underestimates NIR reflectances at large negative viewing angles. FRT and SLC in general show a relatively low directional variability in the NIR compared to the INFORM model whose outputs better approximate the measured reflectances.

In this study, parameters that were not measured (e.g.  $\alpha$ ,  $C_m$ ) were optimised using INFORM; SLC and FRT had to follow INFORM in those parameter which partly explains why INFORM shows the best results. In the NIR, FRT performs slightly better than SLC as it has additional free parameters that were modified to approximate the satellite measured reflectances.

#### 4. CONCLUSIONS

This is one of the first studies that compare modelled reflectances with satellite-measured reflectances of forest canopies for different wavelengths and view angles. The results are promising, as there is a general agreement between modeled and measured spectra. Most of the differences among the models can be explained by the inherent model structure or by the way the models were parameterized. The results of this research represent an important step towards model development, understanding of radiative transfer in canopies and subsequent model inversion.

#### 5. ACKNOWLEDGEMENTS

The authors would like to thank Bianca Hoersch (European Space Agency, ESA) and Peter Fletcher (Remote Sensing Applications Consultants, RSAC) for acquiring Chris/PROBA data over Idarwald Forest and Andres Kuusk (Tartu Observatory) for providing the FRT model.

#### 6. REFERENCES

ATZBERGER, C. (2000): Development of an invertible forest reflectance model: The INFOR model. In: Buchroithner, M. (Ed.): *Proceedings of the 20th EARSeL Symposium Dresden, Germany, 14-16 June 2000*: 39-44.

BACOUR, C., JACQUEMOUD, S., TOURBIER, Y., DECHAMBRE, M., FRANGI, J.-P. (2002): Design and analysis of numerical experiments to compare four canopy reflectance models. *Remote Sensing of Environment*, 79: 72-83.

BARET, F., FOURTY, T. (1997), Estimation of leaf water content and specific leaf weight from reflectance and transmittance measurements. *Agronomie* 17:455-464.

JACQUEMOUD, S., BACOUR, C., POILVE, H., FRANGI, J.-P. (2000): Comparison of four radiative transfer models to simulate plant canopies reflectance: Direct and inverse mode. *Remote Sensing of Environment*, 74: 471-481.

KUUSK, A., (2001). A two-layer canopy reflectance model. *Journal of Quantitative Spectroscopy & Radiative Transfer* 71: 1-9.

KUUSK, A., NILSON, T. (2000): A directional multispectral forest reflectance model. *Remote Sensing of Environment* 72: 244-252.

NILSON, T., PETERSON, U., (1991). A Forest Reflectance Model and a Test Case. *Remote Sens. Environ.* 37: 131-142.

PINTY B, WIDLOWSKI JL, TABERNER M, ET AL. (2004): Radiation Transfer Model Intercomparison (RAMI) exercise: Results from the second phase. *Journal of Geophysical Research - Atmospheres* 109 (D6).

PRICE, J.C., (1990). On the information content of soil reflectance spectra. *Remote Sens. Environ.* 33: 113-121.

ROSEMA, A., VERHOEF, W., NOORBERGEN, H., & BORGESIU, J. J. (1992). A new forest light interaction model in support of forest monitoring. *Remote Sensing of Environment*, 42, 23- 41.

SCHLERF, M. & ATZBERGER, C. (2006): Inversion of a forest reflectance model to estimate structural vegetation attributes using hyperspectral remote sensing data. *Remote Sensing of Environment*, 100: 281-294.

VERHOEF, W. (1984). Light scattering by leaf layers with application to canopy reflectance modeling: The SAIL model. *Remote Sensing of Environment*, 16, 125- 141.

VERHOEF, W. (1985). Earth observation modeling based on layer scattering matrices. *Remote Sensing of Environment*, 17, 165- 178.

VERHOEF, W. (2002): Improved modeling of multiple scattering in leaf canopies: the model SAIL++. In: Sobrino, J.A. (Ed.), *Proc. 1<sup>st</sup> Int. Symp. on Recent Advances in Quantitative Remote Sensing*, Universitat de Valencia, Spain: 11-20.

VERHOEF, W., BACH, H. (2003): Simulation of hyperspectral and directional radiance images using coupled biophysical and atmospheric radiative transfer models. *Remote Sensing of Environment*, 87: 23/41.

VERHOEF, W. & BACH, H. (2007): Coupled soil-leaf-canopy and atmosphere radiative transfer modeling to simulate hyperspectral multi-angular surface reflectance and TOA radiance data, *Remote Sensing of Environment*, in press.

# SIMULTANEOUS RETRIEVAL OF AEROSOL AND SURFACE OPTICAL PROPERTIES USING MULTI-ANGLE IMAGING SPECTRORADIOMETER (MISR) DATA

J. Keller<sup>a,\*</sup>, S. Bojinski<sup>b</sup>, A. S. H. Prevot<sup>a</sup>

<sup>a</sup> Paul Scherrer Institute, Laboratory of Atmospheric Chemistry (LAC),  
5232 Villigen PSI, Switzerland - [johannes.keller@psi.ch](mailto:johannes.keller@psi.ch)

<sup>b</sup> World Meteorological Organization (WMO), Global Climate Observing System Secretariat (GCOS),  
1211 Geneva 2, Switzerland

**KEY WORDS:** Remote Sensing, Aerosols, Satellite, MISR, Retrieval Algorithm

## ABSTRACT:

The operational aerosol product of the Multi-angle Imaging SpectroRadiometer (MISR) is available only for a grid cell size of 17.6 km. This spatial resolution is too coarse for studies in complex terrains like Switzerland. An algorithm for retrieving simultaneously aerosol and surface optical properties at a resolution of 1.1 km was developed. It uses MISR subregion radiance data of the 9 cameras and 4 spectral bands to generate characteristic functions  $\rho_{\text{surf}} = f_{\lambda, \text{cam}}(\beta_e(550 \text{ nm}))$ , where  $\beta_e(550 \text{ nm})$  and  $\rho_{\text{surf}}$  are the ground level aerosol extinction coefficient at 550 nm and the surface reflectance, respectively. The analysis of the mutual intersections of those functions yield optimum values for  $\beta_e(550 \text{ nm})$ , aerosol optical depth (AOD) at 550 nm and  $\rho_{\text{surf}}$ . MODTRAN 4 v3r1 was used to create radiance look-up tables. The algorithm was tested for MISR paths covering Switzerland and northern Italy. Results of two days (low and high aerosol loads on May 14 and June 17, 2002, respectively) were analyzed and compared with sun photometer measurements. First, ground level aerosol extinction coefficients and optical depth over water were derived. From those data it was possible to retrieve a best-fit aerosol mixture. AOD (550 nm) over water are in satisfactory agreement with both sun photometer data and the operational aerosol product of MISR. Second, the Ross-Li approach for the bidirectional reflectance factor (BRF) supported by MODTRAN 4 was applied to simulate the radiance over vegetation surfaces. In this case the retrieved aerosol extinction coefficients and optical depths over vegetation are significantly lower than the values derived over water. We assume that the incomplete coupling of BRF and radiation in MODTRAN 4 is at least partly responsible for this discrepancy.

## 1. INTRODUCTION AND SCOPE

MISR aboard the Terra satellite observes the earth with 9 cameras (Df to Af: forward, An: nadir, Aa to Da: aftward) in 4 spectral bands (446, 557, 672 and 866 nm) (Figure 1). Numerous operational products are available, in particular georectified radiance (275 and 1100 m resolution, depending on camera and spectral band), optical and microphysical properties of standard aerosol components and mixtures, best fit aerosol optical depth (AOD) and best fit aerosol mixture (Diner *et al.*, 1998; NASA/ASDC, 2002). The MISR aerosol product (17.6 km resolution), however, is too coarse for studies in complex domains such as Switzerland. A novel algorithm is capable of retrieving simultaneously ground level extinction coefficient, AOD, aerosol mixture and surface reflectance on a resolution of 1.1 km. Details are published in Keller *et al.*, 2007.

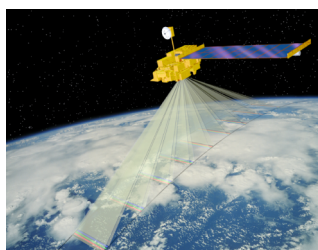


Figure 1: Multi-angle Imaging SpectroRadiometer (MISR)

## 2. SIMULTANEOUS RETRIEVAL (SR) ALGORITHM

Let us assume an idealized atmosphere with given trace gas and aerosol compositions and profiles located at northern mid-latitude. The widely used radiative transfer model (RTM) MODTRAN 4 (Berk *et al.*, 1999; Berk *et al.*, 2003) is designed to simulate the Top of Atmosphere (TOA) spectral radiance for given geometric, atmospheric and surface parameters, in particular the TOA radiance of the spectral band  $\lambda$  for the view geometry of each camera *cam*. The current release is v3r1. Input data may be explicitly specified, e.g. vertical profiles of meteorological parameters and atmospheric constituents, optical properties of aerosols). The basic optical quantity used as a variable input is the extinction coefficient  $\beta_e(550 \text{ nm})$ . Wavelength dependent extinction and absorption coefficients are specified relative to that value. MODTRAN 4 supports the DISORT N-stream option for multiple scattering in inhomogeneous atmospheres. Optical properties of the ground surface may be specified either as lambertian or by Bidirectional Reflectance Distribution Functions (BRDFs). In an inter-comparison workshop in the framework of ACCENT/TROPOSAT 2 (Wagner *et al.*, 2007) 10 RTMs based on different algorithms were tested for various geometries and vertical atmospheric profiles. Since the workshop was focused on Multi-Axes Differential Absorption Spectroscopy (MAXDOAS), only upward-looking view paths were included. The MODTRAN 4 radiances show a close match to the results of the other models. Hence, we are confident that MODTRAN 4

\* Corresponding author.

correctly models scattering and absorption of radiation by gaseous and particulate constituents of the atmosphere. The tropospheric aerosol column density of a given vertical profile is varied by adjusting the aerosol extinction coefficient  $\beta_e$  (550 nm) at ground level.

In the simplest case the ground surface is a lambertian reflector with variable reflectance  $\rho_{surf}$ . Figure 2 shows a typical relationship of the simulated TOA apparent reflectance  $\rho_{app}$  (proportional to the TOA radiance) vs. the scattering angle of the camera Df to Da for  $\beta_e$  (550 nm) = 0.0 (thin solid), 0.2, 0.4 (dotted) and 0.6  $\text{km}^{-1}$  (thick solid), and  $\rho_{surf}$  = 0.0 (left panel) and 0.2 (right panel). It is evident from Figure 2 that in the case of a substantial aerosol load the cameras looking forward at large zenith angles (e.g. Df) observe the same location as an apparently brighter target than the corresponding aftward looking sensors (e.g. Da). At low surface reflectance (e.g.  $\rho_{surf}$  = 0.0) enhanced aerosol loads brighten the target. For bright surfaces (not shown) the observed radiance decreases due to extinction of the reflected radiation.

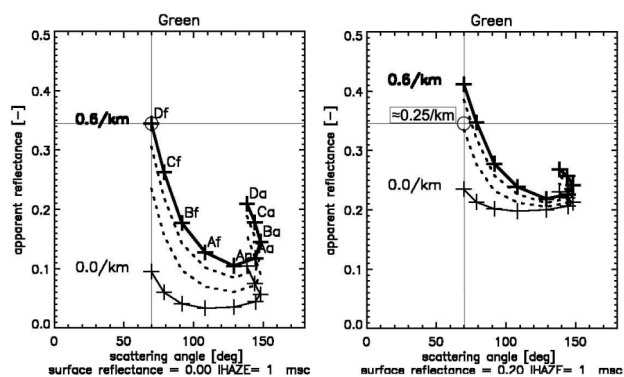


Figure 2: Simulated TOA apparent reflectance  $\rho_{app}$  of the 9 cameras over a lambertian target vs. scattering angle for the green spectral band. Ground level  $\beta_e$  (550 nm) is set to 0 (thin solid), 0.2, 0.4 (dotted, not labelled) and 0.6  $\text{km}^{-1}$  (thick solid).  $\rho_{surf}$  is set to 0 (left) and 0.2 (right). For camera Df and  $\rho_{surf}$  = 0.0,  $\rho_{app}$  = 0.345 is obtained for  $\beta_e$  (550 nm) = 0.6  $\text{km}^{-1}$ . The same  $\rho_{app}$  results for  $\rho_{surf}$  = 0.2 and  $\beta_e$  (550 nm) = 0.25  $\text{km}^{-1}$ .

For  $\beta_e$  (550 nm) = 0.6  $\text{km}^{-1}$  and  $\rho_{surf}$  = 0.0 (left panel of Figure 1), the apparent reflectance observed by camera Df in the green band is about 0.345 (see crosshair). The simulation yields the same radiance, i.e. the same apparent reflectance, also for other data pairs [ $\beta_e$  (550 nm),  $\rho_{surf}$ ], e.g.  $\beta_e$  (550 nm)  $\approx$  0.25  $\text{km}^{-1}$  and  $\rho_{surf}$  = 0.2 (right panel). In other words, over dark targets a small increase of the surface reflectance must be compensated by decreased aerosol scattering to keep the apparent reflectance constant. Hence it is possible to generate characteristic functions  $\rho_{surf} = f_{\lambda, cam}(\beta_e$  (550 nm)). These functions are derived from the camera and wavelength dependent radiance  $L(\lambda, cam)$  for specified reference values  $\beta_{e, ref}$  (550 nm) and  $\rho_{surf, ref}$  (look-up tables, LUT). In Section 3 an example of those functions is given (Figure 4). If all atmospheric and surface properties correspond to reality, the characteristic functions of all cameras should intersect at one single point. Note that in theory the intersection values of  $\beta_e$  (550 nm) are independent of  $\lambda$ , i.e. of the spectral band used for the calculation of the LUT, because  $\beta_e$  (550 nm) controls the radiative transfer model.

In reality, we expect a clustering of the intersections with most probable values  $\beta_{e, \lambda}$  (550 nm) for each spectral band  $\lambda$ . TOA

radiances simulated for the most likely aerosol mixture, for  $\beta_e$  (550 nm) and for  $\rho_{surf, \lambda}$  are supposed to agree best with the MISR radiances of all cameras and spectral bands. In this case the retrieved  $\beta_{e, \lambda}$  (550 nm) of each spectral band  $\lambda$  are expected to scatter least around the best-fit average  $\beta_e$  (550 nm). Finally, most likely vertical AODs are calculated using the best fit  $\beta_e$  (550 nm) as input for the simulation. If we use the LUTs for an unrealistic aerosol mixture, the retrieved values of  $\beta_{e, \lambda}$  (550 nm) depend significantly on the spectral band leading to a larger scatter.

### 3. RESULTS

The SR algorithm was applied to a region of interest that includes Switzerland and parts of the adjacent countries MISR data were analyzed for two overpasses on May 14 (low aerosol loads) and June 17, 2002 (high aerosol loads). Figure 3 shows the RGB MISR radiance image of the nadir looking camera An together with the water target and sun photometer locations used for the analysis.

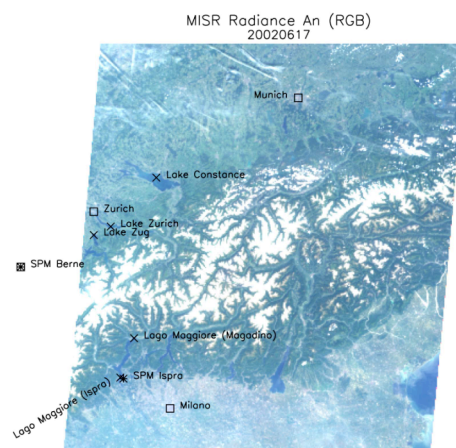
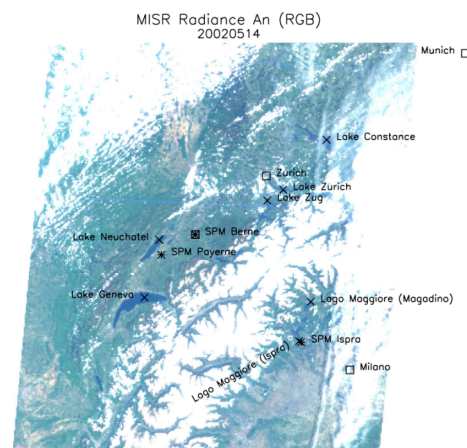


Figure 3: RGB MISR radiance image of the nadir looking camera An. x : water targets; \* : sun photometer (land) targets. Top panel: May 14, 2002 (low aerosol loads), bottom panel: June 17, 2002 (high aerosol loads).

Radiance LUTs were calculated for 7 lake targets shown in Figure 3. A lambertian surface and selected aerosol mixtures of



the MISR aerosol product were specified for the MODTRAN 4 input. The characteristic functions  $\rho_{\text{surf}} = f_{\lambda, \text{cam}}(\beta_e(550 \text{ nm}))$  for each camera and spectral band are depicted in Figure 4. In this example, MISR radiance data of a subregion over Lago Maggiore close to the sun photometer site Ispra was taken to derive those functions. The figure shows the functions for the best fit aerosol mixture 18, which is composed of 75% sulphate-like fine particles and 25% red dust (see Keller *et al.*, 2007 for details). It is evident that for these optimum conditions the intersections of the characteristic functions cluster very well, especially for the green and the red band. Moreover, the retrieved values  $\beta_{e,\lambda}(550 \text{ nm})$  are nearly independent of the MISR spectral band. Finally, the vertical AOD for the assumed vertical atmospheric profile can be calculated from the transmittance LUT and from  $\beta_e(550 \text{ nm})$ . The SR algorithm is capable of retrieving distinct intersections only for clear and hazy conditions. If clouds are present, which have scattering properties different from those specified for aerosols in MODTRAN, the mutual intersections of the intersections do not cluster and no  $\beta_{e,\lambda}(550 \text{ nm})$  can be retrieved. Hence clouds are automatically eliminated by this procedure.

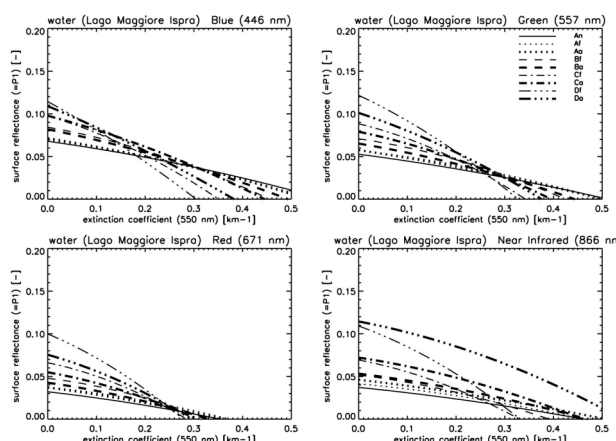


Figure 4: Surface reflectance  $\rho_{\text{surf}}$  vs. ground level aerosol extinction coefficient  $\beta_e(550 \text{ nm})$  for the water target Lago Maggiore close to Ispra. The MISR radiances of the 4 MISR bands for June 17, 2002 and the look-up tables for the optimum mixture 18 were used to derive these functions. A lambertian surface reflectance was assumed.

Table 1 lists the most likely AOD at 550 nm and the associated aerosol mixture for the 7 lake targets taken from the SR algorithm results, from the MISR operational product and from close-by sun photometer measurements. For most water targets, the SR algorithm delivers similar aerosol optical depths and mixtures as the operational product. The Lago Maggiore data agree well with the AERONET sun photometer measurements at Ispra on May 14. For the greater AOD on June 17 the agreement is somewhat worse. Note that the MISR path does not cover Payerne and Bern on June 17.

Over vegetation the lambertian assumption for the surface reflectance is no longer valid. The angular dependence is described by the Bidirectional Reflectance Factor (BRF). There are various options in MODTRAN 4 v3r1 to select BRF models. In this study the Ross-Li approach (Lucht *et al.*, 2000) was chosen and radiance LUT for agriculture and forest were generated (see Keller *et al.*, 2007 for details). The analysis of the SR results for different vegetation and water targets and the

comparison with the MISR product and with the sun photometer at Ispra revealed that  $\beta_e(550 \text{ nm})$  retrieved over vegetation is significantly less than the corresponding values over close-by Lago Maggiore. The difference is about 0.1 and 0.2  $\text{km}^{-1}$  for May 14 (low aerosol concentrations) and June 17 (high aerosol concentrations), respectively. This leads to small AOD values retrieved for the sun photometer sites compared with the measurements and the MISR operational product. For low aerosol concentrations such as those at Payerne and Bern on May 14, the intersection values  $\beta_{e,\lambda}(550 \text{ nm})$  are even negative.

After a careful analysis of the algorithm modules we came to the conclusion that the most likely source relevant for the inconsistencies is the radiation transfer model MODTRAN 4 v3r1. Because realistic AODs are retrieved over water, i.e. for dark, lambertian targets, and the MAXDOAS inter-comparison with other RTMs was successful we suppose that the discrepancies are due to an incomplete coupling of the non-lambertian surface and the radiation streams in the DISORT module of MODTRAN 4. According to information from the developer, the respective improvement announced already at the release of earlier versions is not yet implemented in v3r1. After a preliminary increase of  $\beta_e(550 \text{ nm})$  over land by 0.1 and 0.2  $\text{km}^{-1}$  for May 14 and June 17, respectively, AOD maps were drawn for both days (Figure 5). AOD values north of the Alps are generally lower than in the Po basin on both days. Increased aerosol loads are also found at the valley bottoms. Thin clouds and contrails, which appear as high aerosol concentrations, are detected on June 17 in the north of the scene as well. The algorithm automatically disregards thick clouds. The spatial features are similar to those of the MISR aerosol product (not shown).

#### 4. CONCLUSIONS

A novel algorithm was developed, which is designed to retrieve simultaneously the near surface aerosol extinction coefficient, the aerosol optical depth, the aerosol mixture, and the surface reflectance. This simultaneous retrieval (SR) algorithm has the potential of providing realistic aerosol properties over lambertian water targets on a spatial resolution of 1.1 km., thus enhancing the resolution of the MISR aerosol product (17.6 km). Aerosol optical depths over Lago Maggiore close to the sun photometer site Ispra agree well with measurements. For land targets, however, we found significantly lower aerosol extinction coefficients and optical depths than for close-by water. Differences of 0.1  $\text{km}^{-1}$  and 0.2  $\text{km}^{-1}$  for the green spectral band were estimated for May 14 and June 17, respectively. After an extended analysis of the results, including a RTM inter-comparison in the frame of the European network ACCENT, we believe that the full coupling of BRF and DISORT, which is not yet implemented in the current MODTRAN 4 version, is at least partly responsible for this disagreement. The scope of a new project is the confirmation of this conjecture, the improvement of the relevant modules in MODTRAN 4, and applications of the algorithm for an extended variety of atmospheric conditions and surface targets.

Date / Site	SR algorithm		MISR operational product		SPM
	AOD (550 nm)	Mix	AOD (557 nm)	Mix	AOD (550 nm)
May 14, 2002					
Lake Geneva	0.086±0.002	8	0.067±0.023	8	
Lake Neuchatel	0.082±0.004	5	0.056±0.013	8	
Lake Zug	0.243±0.022	18	n.a.	n.a.	
Lake Zurich	0.260±0.024	9	n.a.	n.a.	
Lake Constance	0.375±0.008	8	n.a.	n.a.	
Lago Maggiore (Magadino)	0.188±0.010	9	n.a.	n.a.	
Lago Maggiore (Ispra)	0.203±0.019	5	0.228±0.044	5	
SPM Payerne	n.a. <sup>1)</sup>	n.a. <sup>1)</sup>	0.076±0.024	10	0.02±0.001
SPM Bern	n.a. <sup>1)</sup>	n.a. <sup>1)</sup>	0.083±0.029	17	0.06±0.003
SPM Ispra	0.127±0.002	5	0.228±0.044	5	0.20±0.002
June 17, 2002					
Lake Geneva	n.a.	n.a.	n.a.	n.a.	
Lake Neuchatel	n.a.	n.a.	n.a.	n.a.	
Lake Zug	0.320±0.010	18	n.a.	n.a.	
Lake Zurich	0.319±0.005	8	n.a.	n.a.	
Lake Constance	0.339±0.007	8	n.a.	n.a.	
Lago Maggiore (Magadino)	0.371±0.006	15	0.747±0.206	5	
Lago Maggiore (Ispra)	0.355±0.011	18	0.386±0.102	18	
SPM Payerne	n.a. <sup>2)</sup>	n.a. <sup>2)</sup>	n.a. <sup>2)</sup>	n.a. <sup>2)</sup>	0.33±0.020
SPM Bern	n.a. <sup>2)</sup>	n.a. <sup>2)</sup>	n.a. <sup>2)</sup>	n.a. <sup>2)</sup>	0.28±0.010
SPM Ispra	0.094±0.003	7	0.386±0.102	18	0.42±0.004

Table 1: Comparison of the best-fit AOD (550 nm) and mixture derived by the simultaneous retrieval (SR) method with the regional mean AOD and mixture of the MISR aerosol product, and with sun photometer AOD. The simultaneous retrieval algorithm assumes the BRF for agriculture when applied to the sun photometer sites.

<sup>1)</sup> May 14, 2002: no SR AOD was calculated because of negative retrievals of the extinction coefficient.

<sup>2)</sup> June 17, 2002: the MISR swath did not cover Lake Geneva, Lake Neuchatel, Berne and Payerne.

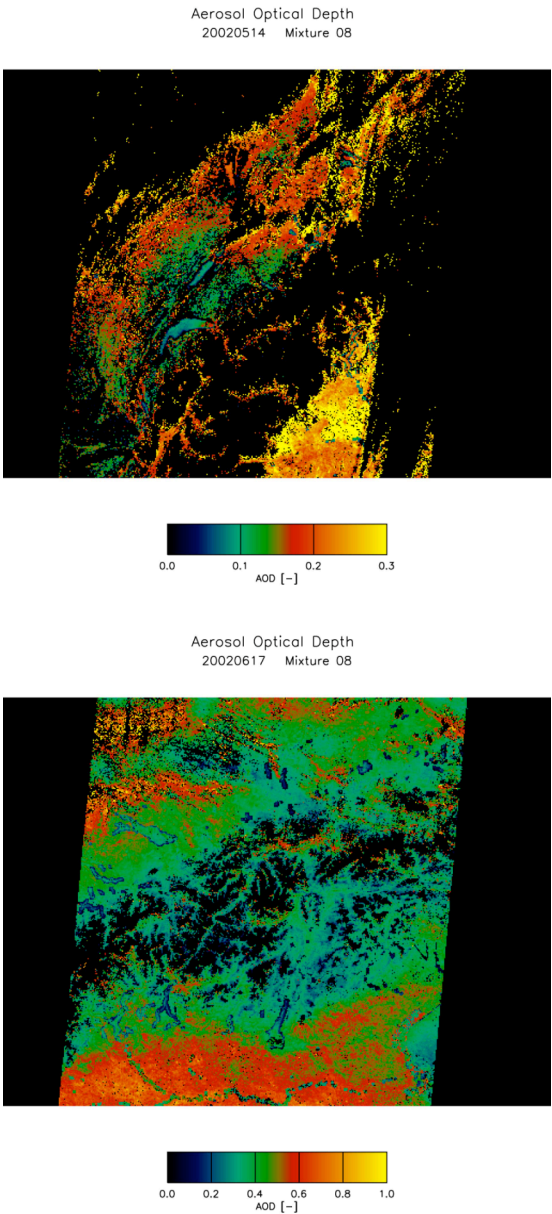


Figure 5: Aerosol optical depth AOD (550 nm) map derived with the simultaneous retrieval method for May 14 (low aerosol concentrations, top) and June 17, 2002 (high aerosol concentrations, bottom). Note the scale difference between those two days. See Figure 3 for related radiance maps.

## 5. REFERENCES

Berk A., Anderson G. P., Acharya P. K., Hoke M. L., Chetwynd J. H., Bernstein L. S., Shettle E. P., Matthew M. W., Adler-Golden S. M., 2003. *MODTRAN4 Version 3 Revision 1 User's Manual*. Air Force Research Laboratory, Space Vehicles Directorate, Air Force Materiel Command, Hanscom AFB, MA 01731-3010, Hanscom.

Berk A., Anderson G. P., Bernstein L. S., Acharya P. K., Dothe H., Matthew M. W., Adler-Golden S. M., Chetwynd J. H. J., Richtsmeier S. C., Pukall B., Allred C. L., Jeong L. S., Hoke M. L. a., 1999. MODTRAN4 Radiative Transfer Modelling for Atmospheric Correction. *SPIE Proceeding on Optical Spectroscopic Techniques and Instrumentation for Atmospheric and Space Research III* 3756, 348-353.

Diner D. J., Beckert J. C., Reilly T. H., Bruegge C. J., Conel J. E., Kahn R., Martonchik J. V., Ackerman T. P., Davies R., Gerstl S. A. W., Gordon H. R., Muller J.-P., Myneni R., Sellers R. J., Pinty B., Verstraete M. M., 1998. Multiangle Imaging SpectroRadiometer (MISR) description and experiment overview. *IEEE Transactions on Geoscience and Remote Sensing* 36, 4, 1072-1087.

Keller J., Bojinski S., Prevot A. S. H., 2007. Simultaneous retrieval of aerosol and surface optical properties using data of the Multi-angle Imaging SpectroRadiometer (MISR). *Remote Sensing of Environment* 107, 1-2, 120-137.

Lucht W., Schaaf C. B., Strahler A. H., 2000. An algorithm for the retrieval of albedo from space using semiempirical BRDF models. *IEEE Transactions on Geoscience and Remote Sensing* 38, 2, 977-998.

NASA/ASDC, 2002. MISR Data and Information.  
<http://eosweb.larc.nasa.gov/PRODOCS/misr/data.html>.

Wagner T., Burrows J., Deutschmann T., Dix B., Hendrick F., von Friedeburg C., Frieß U., Heue K.-P., Irie H., Iwabuchi H., Keller J., McLinden C., Oetjen H., Palazzi E., Petrotoli A., Platt U., Postlyakov O., Pukite J., Richter A., van Roozendael M., Rozanov A., Rozanov V., Sinreich R., Sanghavi S., Wittrock F., 2007. Comparison of box-air-mass-factors and radiances for MAX-DOAS-geometries calculated from different UV/visible radiative transfer models. *Atmospheric Chemistry and Physics* (in press).

## 6. ACKNOWLEDGEMENTS

We wish to thank Ralph Kahn and John Martonchik from the Jet Propulsion Laboratory (JPL) for the fruitful discussions. MISR data were obtained from the NASA Langley Research Center Atmospheric Sciences Data Center. We acknowledge the courtesy of Laurent Vuilleumier and Stephan Nyeki (MeteoSchweiz) for providing the IAP/CHARM sun photometer data, on which MeteoSchweiz hold full copyright. We thank Giuseppe Zibordi (JRC Ispra) for giving access to the sun photometry from the Ispra AERONET site and Lex Berk from Spectral Sciences Inc. for the information exchange and assistance regarding MODTRAN 4 issues.

This project was financially supported by the Federal Office for the Environment, FOEN (Bundesamt fuer Umwelt, BAFU). We also acknowledge the support of the EU network of excellence of atmospheric composition change (ACCENT).

# AN ADVANCED LEAF OPTICAL PROPERTIES MODEL INCLUDING PHOTOSYNTHETIC PIGMENTS

J.-B. Feret <sup>a,c,\*</sup>, G. P. Asner <sup>b</sup>, C. François <sup>c</sup>, R. Martin <sup>b</sup>, S. L. Ustin <sup>d</sup>, S. Jacquemoud <sup>a</sup>

<sup>a</sup> Etudes Spatiales et Planétologie, Institut de Physique du Globe de Paris - Université Paris 7, Paris, France - feret@ipgp.jussieu.fr & jacquemoud@ipgp.jussieu.fr

<sup>b</sup> Department of Global Ecology, Carnegie Institution of Washington, Stanford CA, USA - gpa@stanford.edu & remartin@stanford.edu

<sup>c</sup> Ecologie, Systématique et Evolution, CNRS - Université Paris-Sud, Orsay, France - christophe.francois@ese.u-psud.fr

<sup>d</sup> CSTARs, University of California, Davis CA, USA - slustin@ucdavis.edu

**KEY WORDS:** Remote Sensing, Leaf Optical Properties, Modelling, Hyperspectral Data, Pigments

## ABSTRACT:

PROSPECT, a widely-used leaf directional-hemispherical reflectance and transmittance model, currently treats the behaviour of chlorophylls *a*, *b*, carotenoids, and anthocyanins uniformly, leading to errors. A finer discrimination among these pigments in light-absorbing plant tissues should improve the model. In this paper, a new calibration and validation phase of PROSPECT is performed using two comprehensive databases containing hundreds of leaves collected in temperate latitudes in Angers, France, and in a tropical environment in Hawaii, USA. Leaf biochemical (chlorophylls *a*, *b*, carotenoids, water, and dry matter) and optical properties (directional-hemispherical reflectance and transmittance measured from 400 nm to 2500 nm) were measured and used in the model development steps. The first step consists in providing distinct *in vivo* specific absorption coefficients for the leaf pigments using the Angers database. The model is then inverted to predict the biochemical content of intact leaves from both data sets. The main result of this preliminary study is that the new chlorophyll and carotenoid specific absorption coefficients are in good agreement with available *in vitro* absorption spectra, that the chlorophyll predictions are improved, and that the carotenoids are reasonably retrieved.

## RÉSUMÉ:

PROSPECT, le modèle de réflectance et de transmittance directionnelle-hémisphérique des feuilles aujourd'hui le plus utilisé par la communauté scientifique, suppose que l'absorption de la lumière par les chlorophylles *a*, *b*, caroténoïdes, et anthocyanes est uniquement due aux chlorophylles, ce qui conduit à des erreurs. Une discrimination plus fine de ces pigments dans les tissus végétaux absorbant la lumière devrait permettre d'étendre le domaine d'application du modèle. Cet article présente une nouvelle phase d'étalonnage et de validation de PROSPECT utilisant deux bases de données rassemblant plusieurs centaines de feuilles récoltées dans une région tempérée à Angers, France, et dans une forêt tropicale à Hawaï, USA. La composition biochimique des feuilles (chlorophylles *a*, *b*, caroténoïdes, eau, et matière sèche) et leurs propriétés optiques (réflectance et transmittance directionnelle-hémisphérique mesurées entre 400 nm et 2500 nm) ont été mesurées et ont servi à améliorer le modèle. La première étape consiste à séparer les coefficients spécifiques d'absorption *in vivo* des pigments foliaires en utilisant la base de données d'Angers. Le modèle est alors validé en inversion en déterminant la composition biochimique de feuilles intactes issues des deux jeux de données. Le principal résultat de cette étude préliminaire est que les nouveaux coefficients spécifiques d'absorption des chlorophylles et des caroténoïdes sont en bon accord avec les spectres d'absorption *in vitro*, que les estimations du contenu en chlorophylle sont améliorées, et que les caroténoïdes sont déterminées avec une précision raisonnable.

## 1. INTRODUCTION

Quantification of vegetation canopy physiological status can be achieved by better measurement and knowledge of leaf pigments. Because chlorophyll is directly linked to photosynthetic potential and primary production, the detection and quantification of individual foliar pigments (mostly chlorophylls *a* and *b*, carotenes and xanthophylls, anthocyanins, etc.) by remote sensing techniques is essential to improve our understanding of plant functioning. There are many applications in precision farming (nitrogen management), environmental studies (geobotany), plant physiology (photosynthesis), or ecosystem studies (global change) that would directly benefit from a more detailed knowledge of multiple plant pigments.

The continuing improvement in the spectral resolution of optical sensors could provide new opportunities for large-scale

studies of plants and ecosystems. However, physical, chemical, and biological processes in ecosystems are highly complex, and thus remote sensing approaches require accurate quantitative methods such as radiative transfer models that exploit all types of information in the optical signal. PROSPECT is a widely-used leaf directional-hemispherical reflectance/transmittance model (Jacquemoud and Baret, 1990). To date, its spectral resolution was restricted to 5 nm and only total chlorophyll, water, and dry matter content were incorporated into the model, thus retrievable. Pigment discrimination or solar-induced chlorophyll *a* fluorescence measurement using the next generation of hyperspectral sensors necessitates much finer and more accurate spectral resolutions. The availability of new datasets at 1 nm sampling provides an opportunity to upgrade and refine the model.

\* Corresponding author: Jean-Baptiste Feret

Individually, leaf pigments express specific absorption features that should facilitate analysis based on reflectance and transmittance measurements. This assertion is tempered by two issues: first, *in vitro* absorption spectra are available, but it is a well-known fact that some spectral shifts occur depending on the solvent used to extract them from foliage, and because the membrane-bound protein complex is removed during extraction. Therefore, the *in vivo* configuration of plant pigment absorption coefficients remains uncertain. Second, the overlapping wavelengths of these absorption coefficients make their identification in leaf reflectance or transmittance spectra difficult to predict. In this context, it is particularly challenging to develop a method to estimate the pigment content directly from an intact leaf *via* spectral measurements and modelling.

In this paper, we first refine the core of PROSPECT with the computation of a new refractive index and the setting of a new leaf surface roughness parameter. Then, an analysis of the behaviour of the model is used to develop an optimized calibration stage, the most important improvement of which is the discrimination of relevant specific absorption coefficients for different pigments. Finally, we evaluate inversion methods on independent data sets to predict biochemical concentration from intact leaves by testing the prediction against measured biochemical composition.

2. MATERIAL AND METHOD

2.1 Available datasets

Two databases encompassing hundreds of leaves were used to improve PROSPECT. The first one called ANGERS was collected in 2003 on temperate plants at INRA Angers (France) and the second one called HAWAII was collected in 2007 on tropical Hawaiian plants (USA). Both datasets contain leaf directional-hemispherical reflectance and transmittance spectra measured at 1 nm resolution from 400 nm to 2400 nm using ASD FieldSpec instruments equipped with integrating spheres. Chlorophyll *a* and *b* ( $C_{ab}$ ), total carotenoids ( $C_{cx}$ ), water ( $C_w$  also named equivalent water thickness) and dry matter ( $C_m$  also named leaf mass per area) content are available for each sample. Table 1 summarizes the main characteristics of this database.

	ANGERS 2003	HAWAII 2007
Number of leaf samples	276	41
Number of species	49	41
Mean(Chlorophyll <i>a</i> )	25 $\mu\text{g cm}^{-2}$	37 $\mu\text{g cm}^{-2}$
Mean(Chlorophyll <i>b</i> )	9 $\mu\text{g cm}^{-2}$	13 $\mu\text{g cm}^{-2}$
Mean(Carotenoids)	9 $\mu\text{g cm}^{-2}$	12 $\mu\text{g cm}^{-2}$
Mean(Water)	0.0116 cm	0.0275 cm
Mean(Dry matter)	0.0052 $\text{g cm}^{-2}$	0.0125 $\text{g cm}^{-2}$

Table 1. Characteristics of the databases

In ANGERS, pigments were passively extracted in ethanol 95% in a test tube using fresh material. In HAWAII, frozen leaf discs were ground in 100% acetone with a small amount of quartz sand and  $\text{MgCO}_3$  to prevent acidification in a chilled mortar. Following centrifugation, the absorbance of the supernatant was measured in both experiments using dual beam scanning UV-VIS spectrophotometers. Chlorophyll *a*, *b* and total carotenoid content was determined using a multi-wavelength analysis at 470, 648.6 and 664.2 nm in ANGERS (Lichtenthaler, 1987) and

at 470, 645, 662 and 710 nm in HAWAII (Lichtenthaler and Buschmann, 2001). The relative distribution of pigments in Figure 1 shows that the two datasets are consistent, however with slightly higher distribution of concentrations in HAWAII. The cause of this difference may be explained by:

- A different solvent extraction efficiency which may lead to different amounts of pigments extracted from a leaf according to the protocol carried out.
- Datasets collected in two different ecosystems, under two different climates. This ecological factor may influence the distribution of pigments in vegetation.

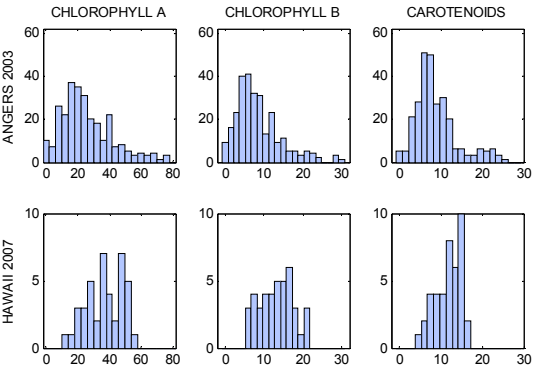


Figure 1. Pigment distribution in the two databases

A preliminary analysis of the data highlights the difficulties to come when trying to discriminate pigment contents. As shown in Figure 2, pigment concentrations are strongly correlated.

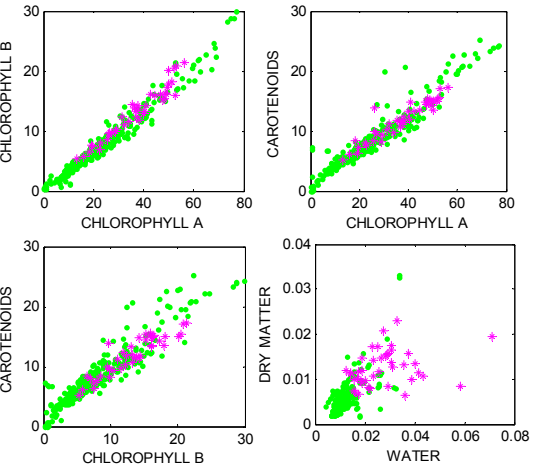


Figure 2. Pigment, water and dry matter correlations (• ANGERS and \* HAWAII)

A particularly interesting point to notice is that the ratios chlorophyll *a* over chlorophyll *b* and total carotenoids over chlorophyll *a* or chlorophyll *b* are similar and particularly stable, although the two datasets have been collected from different ecosystems and different field campaigns. This systematic high correlation of pigments may complicate the calibration. The gathering of new databases including a wider range of pigments and other contents characteristics (by collecting for example leaves in various physiological states) may help us to understand the conditions for stability or variation of these ratios. Since ANGERS is the largest database with a wider range of chlorophyll concentrations, it is used for the calibration stage.



## 2.2 Why an improved version of PROSPECT?

Unlike canopy reflectance models, PROSPECT requires a calibration phase where some physical and optical constants like the leaf surface roughness parameter  $\sigma$ , the refractive index of leaf material  $n(\lambda)$ , and the specific absorption coefficients of the leaf absorbers  $K_{spe}(\lambda)$  must be set up using experimental data. These values are assumed to be invariable from one species to the other, which is true for  $k_{spe}(\lambda)$  but not totally true for  $\sigma$  and  $n(\lambda)$  because of the changing nature of leaf surfaces and wax types (Pfündel et al., 2006). Surprisingly,  $\sigma$  and  $n(\lambda)$  have not been updated since Jacquemoud and Baret (1990). Their accuracy is however crucial to the remaining work and, as PROSPECT is based on physical laws, it is fundamental to develop a model coherent with our knowledge of these constants (le Maire et al., 2004).

**2.2.1 Model's weakness:** Simulations of the reflectance of a compact (leaf structure parameter  $N=1$ ) and totally absorbing (transmission of the elementary layer  $\phi=0$ ) leaf using the former version of PROSPECT demonstrate its inability to reach the lowest experimental values of several datasets, specially in the blue part of the visible region where absorption by pigments is the highest (Figure 3). This disagreement leads to numerical instabilities and underestimation of the specific absorption coefficients in the calibration stage of the model. Moreover, the procedure followed so far, which splits this crucial stage into several steps, raises saturation problems when absorption exceeds a certain level. A new approach which combines updated physical and optical constants and a more efficient algorithm may likely resolve these problems.

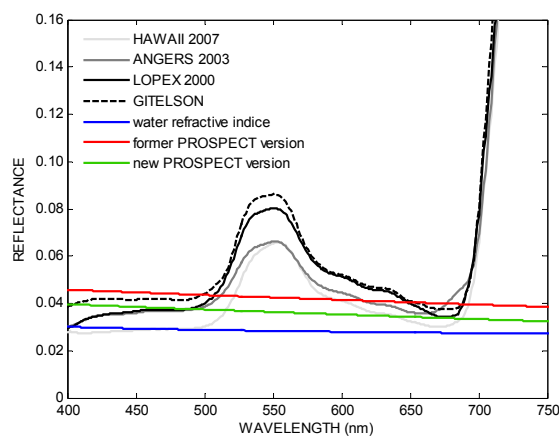


Figure 3. Minimum reflectance of different databases (grey curves) and reflectance of a totally absorbing compact leaf with three indices of refraction (colour curves)

**2.2.2 Reassessment of physical and optical parameters:** In PROSPECT, the incident radiation is assumed to light up a horizontal plane at all angles between  $0^\circ$  and  $\alpha$  to mimic the leaf surface roughness on an intuitive base. Up to now,  $\alpha$  has been set at  $60^\circ$  but this seems to be overestimated. Recent work on leaf BRDF modelling links the probability density function of facet orientations to this angle on a physical base (Bousquet et al., 2005) where  $\alpha$  is the maximum angle between the leaf normal, i.e. the direction of the incident light, and the facet normal. Actual values of the surface roughness parameter  $\sigma < 0.5$  correspond to  $\alpha < 40^\circ$ , which is a more realistic value. Moreover, since the average transmissivity at the interface

varies very slowly between  $0^\circ$  and  $40^\circ$ , the latter value was fixed. This permits a decrease in the minimum reflectance and an improvement in PROSPECT accuracy at high absorption wavelengths.

A new refractive index was determined by inversion of the plate model (Allen et al., 1969) using an albino corn (*Zea mays*) leaf grown under glass. Such a leaf is analogous to a single pigment-free layer: The reflectance and transmittance levels in the near infrared plateau are consistent with a compact (leaf structure parameter  $N=1$ ) and non-absorbing (transmission of the elementary layer  $\phi=1$ ) leaf. The plateau also continues in the visible before falling below 450 nm (Figure 4). The refractive index  $n \approx 1.45$  in the visible and  $n=1.42$  at 800 nm agrees well with the literature (Brown, 1920; Woolley, 1975). The whole spectrum which does not express any particular features due to absorption validates our approach. It was fitted by a third degree polynomial. Figure 5 presents its new spectral variations compared to the refractive index of water (Segelstein, 1981). Although it probably varies somewhat from leaf to leaf,  $n$  is not supposed to change.

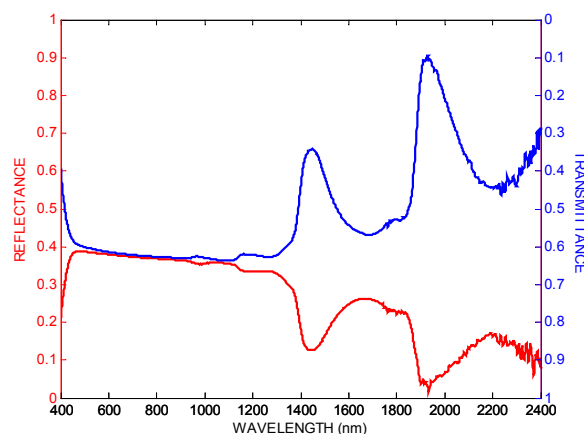


Figure 4. Optical properties of a corn albino leaf

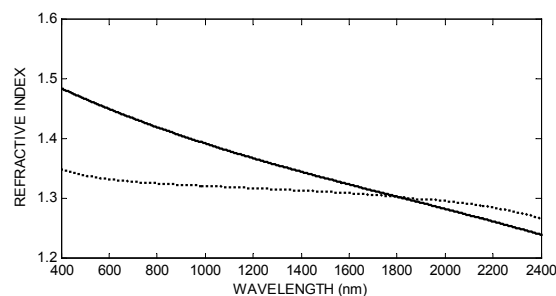


Figure 5. Refractive index of the corn albino leaf (line) and water (dots)

**2.2.3 A new algorithm for calibration:** In addition to the new physical and optical parameters, the algorithm for the calibration phase was simplified to avoid intermediate steps which multiply the sources of errors, leading to inaccuracies. A diagram of this calibration is presented in Figure 6.

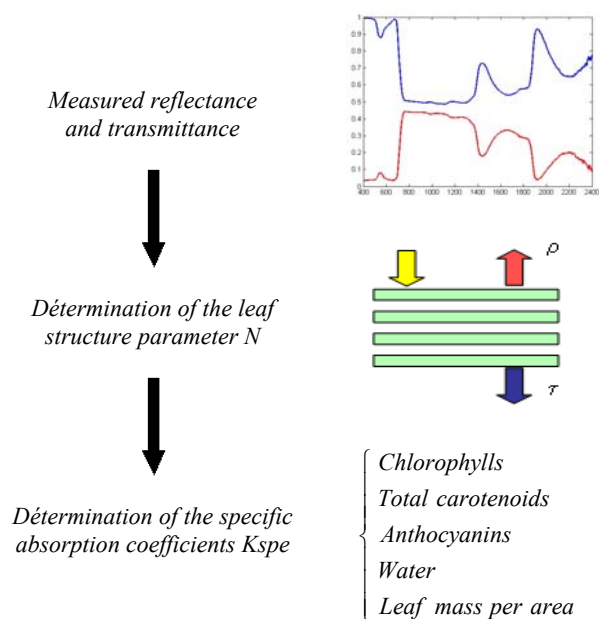


Figure 6. Diagram of the calibration stage of PROSPECT

The structure parameter  $N$  of each leaf, which is assumed to be independent of wavelength, is first determined by inverting PROSPECT on the reflectance and transmittance measured at  $\lambda_1$ ,  $\lambda_2$  and  $\lambda_3$ , the wavelengths of the maximum reflectance and transmittance and minimum absorbance, respectively. For fresh leaves, these three wavelengths are located in the near infrared plateau and may be confounded. The three absorption coefficients are determined at the same time but not used. Second, the specific absorption coefficients of the leaf absorbers are determined by inverting PROSPECT on all the leaves, wavelength by wavelength. The leaf structure parameters fitted in the first step, as well as the pigment, water and dry matter contents measured in the laboratory constrain the inversion.

### 3. RESULTS AND DISCUSSION

In this section, we present the results of the calibration of the model performed with the ANGERS database, and its validation on both the ANGERS and HAWAII databases.

#### 3.1 Computation of the specific absorption coefficients

The most critical stage of this work is the calibration where the *in vivo* specific absorption coefficients are computed. These link the optical and biochemical properties together and are actually known for most pigments but only *in vitro* for purified molecules dissolved in an organic solvent. The main absorption peaks are known nevertheless to shift with the polarity of the solvent so that they cannot be used in PROSPECT. Thus, we must determine these coefficients directly from the experimental data. In the model, the absorption coefficient of a compact layer  $k(\lambda)$  is written as a linear combination of the absorption of each biochemical constituent  $i$ :

$$k(\lambda) = \sum_i K_{spe,i}(\lambda) \times \frac{C_i}{N} \quad (1)$$

with  $\lambda$  the wavelength,  $C_i$  the constituent concentration in the leaf,  $K_{spe,i}$  the corresponding specific absorption coefficient,

and  $N$  the leaf structure parameter, i.e. the number of compact layers. The separation of the  $K_{spe,i}$  in the inversion process is another difficulty to overcome because of overlapping wavelengths of their main absorption peaks and because of the high correlations between their concentrations, as seen earlier.

We first treated the behaviour of all the pigments uniformly, as previously but following the updated method, for computing the specific absorption coefficient of total <sup>2</sup>chlorophyll. We call this version of the model PROSPECT-4. Higher contrasts between non-absorptive (550 nm) and absorptive wavelengths (450 nm and 680 nm), as well as between these two peaks, are noticeable in Figure 7. The new shape, in contrast to the flatness of the former version, is more realistic and corresponds with the literature. The *in vitro* spectrum displayed in Figure 7 is the sum of Gaussian functions calculated after Maier (2000) considering the ratio chlorophyll *a/b* of Figure 2. Furthermore, one can suppose that pigment discrimination will decrease the contrast between the two peaks because of distinct absorption effect of chlorophylls and carotenoids in the blue, which remain unaccounted for.

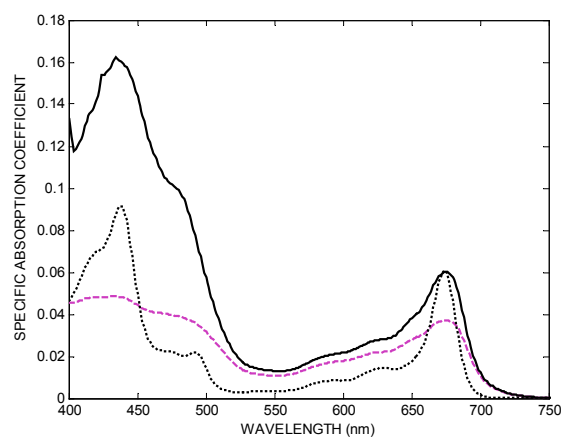


Figure 7. Chlorophyll a and b specific absorption coefficient (expressed in  $\text{cm}^2 \mu\text{g}^{-1}$ ) (line: new version, dashed: former version, dots: *in vitro*)

We now call PROSPECT-5 the version of the model which introduces carotenoids in addition to the chlorophylls. The first attempt to discriminate pigments is presented in Figure 8.

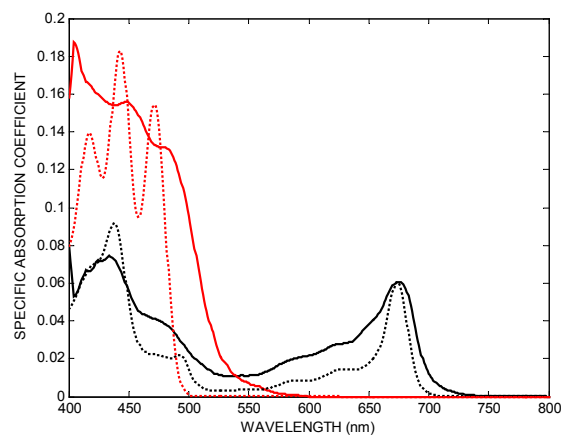


Figure 8. Chlorophylls a and b (black) and total carotenoids (red) specific absorption coefficient (expressed in  $\text{cm}^2 \mu\text{g}^{-1}$ ) (line: new version, dots: *in vitro*)

*In vivo* absorption peak for chlorophyll at 680 nm matches *in vitro* data well, and the shape is globally correct. As expected, the differential between the two main absorption peaks decreases and becomes closer to the observed *in vitro* ratio. The specific absorption coefficient of carotenoids, which contributes to this decrease, is also in good agreement with the literature (Maier, 2000). Slight spectral shifts, a possible effect of *in vivo* absorption, are noticeable for carotenoids, whereas they are less obvious for chlorophylls. Because absorption tends to saturate when pigment content is high, one should mention that it is of major importance to determine accurate absorption coefficients for leaves with low concentrations.

Unfortunately, attempts to separate chlorophyll *a* and *b* with the same method failed, although we surprisingly still obtained good results with carotenoids. A classical numerical algorithm to separate highly correlated data such as leaf photosynthetic pigments is not efficient and may require that we explore new methods, for instance by using leaves with unusual combinations of pigments, or *a priori* constraints, to compute the specific absorption coefficients.

3.2 Biochemical content retrieval

The next step is the retrieval of the leaf biochemical constituents, for each sample, by inversion of PROSPECT both on reflectance and transmittance spectra. Although this paper is focussed on leaf pigments, the near infrared and shortwave infrared are also investigated and the water and dry matter content determined at the same time. In practice, the inversion consists of finding the parameter set symbolized by the vector  $\theta$  which minimizes the following merit function:

$$\chi^2(\theta) = \sum_{\lambda_{\min}}^{\lambda_{\max}} \left( R^*(\lambda) - R_{\text{mod}}(\lambda, \theta) \right)^2 + \left( T^*(\lambda) - T_{\text{mod}}(\lambda, \theta) \right)^2 \tag{2}$$

where  $R^*(\lambda)$  and  $T^*(\lambda)$  are the measured reflectance and transmittance, and  $R_{\text{mod}}$  and  $T_{\text{mod}}$  the modeled ones. The optimization is processed by running a constrained Powell search method for a minimum (Press et al., 1992). Figure 9 confirms the ability of PROSPECT-4 to retrieve the total chlorophyll, water and dry matter contents. As seen in Table 2, the root mean square errors (RMSE) are lower on ANGERS used for the calibration, but still good for HAWAII. As expected, the results obtained with  $C_m$  are not as good as with  $C_w$  because water largely hides the absorption features of dry matter in the shortwave infrared. Unfortunately, the specific absorption coefficient of dry matter could not been re-computed following this new calibration method because only fresh leaves were available in this study. A reassessment of the LOPEX database (Hosgood et al., 1994) which includes such samples will be considered soon.

	PROSPECT-4		PROSPECT-5	
	ANGERS	HAWAII	ANGERS	HAWAII
$C_{ab}$ ( $\mu\text{g cm}^{-2}$ )	6.75	12.38	6.39	12.88
$C_{cx}$ ( $\mu\text{g cm}^{-2}$ )	×	×	4.75	2.94
$C_w$ (cm)	0.00180	0.00571	0.00180	0.00570
$C_m$ ( $\text{g cm}^{-2}$ )	0.00255	0.00530	0.00256	0.00531

Table 2. Root Mean Square Errors (RMSE) calculated on all the retrieved parameters

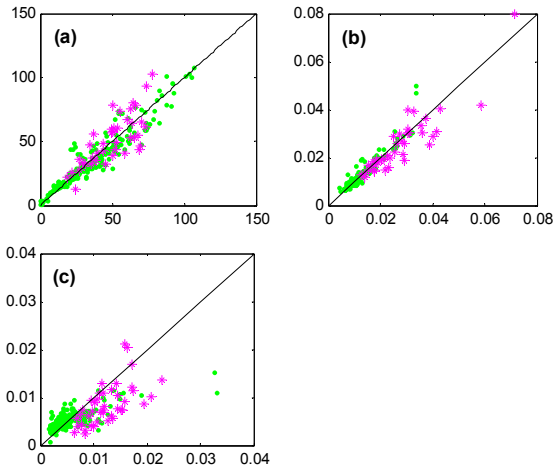


Figure 9. Measured vs. estimated (a) total chlorophyll content, (b) water content, and (c) dry matter content while inverting PROSPECT-4 (• ANGERS and \* HAWAII)

Figure 10 and Table 2 present the results obtained with PROSPECT-5. The comparison between Figures 9 and 10 points out that the retrieved  $C_w$  and  $C_m$  do not vary, which is consistent with the expected result because their influence on leaf optical properties is insignificant in the visible domain. The estimation of  $C_{ab}$  is improved in ANGERS but slightly degraded in HAWAII, for no apparent reason. The main advance is obtained in the determination of carotenoids:  $C_{cx}$  is well retrieved for light-green leaves with low pigment content whereas the accuracy tends to decrease for dark-green leaves with high pigment content. Since the amount of these pigments is almost five times lower than the amount of total chlorophylls, this result is not surprising.

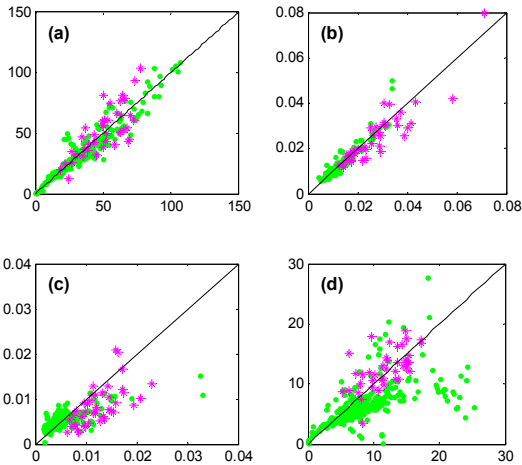


Figure 10. Measured vs. estimated (a) total chlorophyll content, (b) water content, (c) dry matter content while inverting, and (d) total carotenoid content while inverting PROSPECT-5 (• ANGERS and \* HAWAII)

3.3 Optical properties assessment

The reflectance and transmittance of a leaf were computed by PROSPECT-4 (Figure 11a) and PROSPECT-5 (Figure 11b) using the retrieved parameters. It is obvious that chlorophylls by themselves cannot explain some specific absorption features

observed in yellowing or light-green leaves which present low chlorophyll content and high carotenoid content. The introduction of carotenoids into the model partly fixed this problem. This result encourages us to go further into pigment distinction.

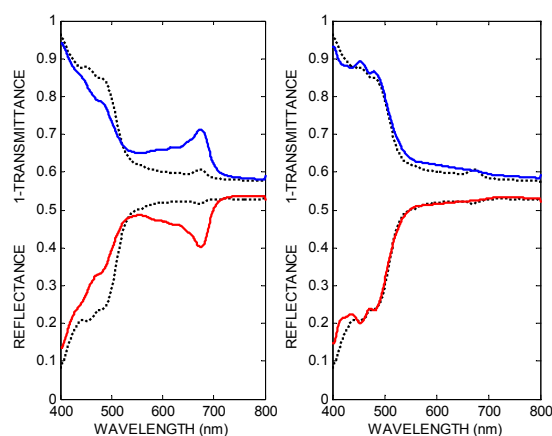


Figure 11. Improvement of the optical properties in the VIS-NIR by assessing carotenoids (dots: measurements, red: modeled reflectance, blue: modeled transmittance)

#### 4. CONCLUSIONS AND FUTURE WORK

PROSPECT is a physically-based model applied to a biological object, the leaf. It consequently appears as a compromise between theoretical physics, applied optics, and biochemical measurements. This paper shows that there is a great potential for further development since the new version of the model provided better simulations of leaf optical properties. Both the optimized calibration stage and the introduction of new pigments improved its accuracy. These results encourage us to continue to refine the calibration method, e.g., to better account for the absorption of dry matter over the whole optical domain. Characterization of *in vivo* specific absorption coefficients for other leaf pigments, e.g. xanthophylls, anthocyanins, and even for chlorophyll *a* and *b* separately could further improve leaf radiative transfer models.

The next critical stage will be to extend the available dataset to the full range of leaf constituents content. A study of unusual leaves (e.g. with unusual ratio between pigments) may help us compute more accurate specific absorption coefficients and thus to resolve the problems due to high correlations between pigments.

PROSPECT is very popular with many current studies on remote sensing of canopies. The model is already included in several applications, which will be able to take advantage of this new version. This modelling work will contribute to develop a more complete understanding of plant pigment function in leaves but also quickly allow an extended field of application for the quantification of photosynthetic processes in ecosystem and remote sensing research by making an advanced use of hyperspectral data.

#### ACKNOWLEDGEMENTS

This study was partly funded by the Programme national de télédétection spatiale (PNTS), by the Centre national d'études spatiales (CNES) through the TOSCA program, and by NASA Terrestrial Ecology Program-Biodiversity grant NNG-06-GI-

87G. We are also very grateful to Dr. Luc Bidet (INRA Montpellier) for the leaf pigment determination in ANGERS and to Dr. Anatoly Gitelson (University of Nebraska-Lincoln) who shared his dataset.

#### REFERENCES

- Allen, W.A., Gausman, H.W., Richardson, A.J., Thomas, J.R., 1969. Interaction of isotropic light with a compact plant leaf, *Journal of the Optical Society of America*, 59, pp. 1376-1379.
- Bousquet, L., Lachérade, S., Jacquemoud, S., Moya, I., 2005. Leaf BRDF measurement and model for specular and diffuse component differentiation. *Remote Sensing of Environment*, 98, pp. 201-211.
- Brown, F.B.H., 1920. The refraction of light in plant tissues, *Bulletin of the Torrey Botanic Club*, 47, pp. 243-260.
- Hosgood, B., Jacquemoud, S., Andreoli, G., Verdebout, J., Pedrini, G., Schmuck, G., 1994. *Leaf Optical Properties Experiment 93 (LOPEX93)*, European Commission - Joint Research Centre, Ispra (Italy), EUR 16095 EN, 20 pp.
- Jacquemoud, S., Baret, F., 1990. PROSPECT: a model of leaf optical properties spectra. *Remote Sensing of Environment*, 34, pp. 75-91.
- Le Maire, G., François, C., Dufrêne, E., 2004. Towards universal deciduous broad leaf chlorophyll indices using PROSPECT simulated database and hyperspectral reflectance measurements. *Remote Sensing of Environment*, 89, pp. 1-28.
- Lichtenthaler, H.K., 1987. Chlorophylls and carotenoids: pigments of photosynthetic biomembranes. *Methods in Enzymology*, 148, pp. 350-382.
- Lichtenthaler, H.K., Buschmann, C., 2001. Chlorophylls and carotenoids: measurement and characterization by UV-VIS spectroscopy. In *Current Protocols in Food Analytical Chemistry*. John Wiley and Sons (New York), pp. F4.3.1-F4.3.8.
- Maier, S.W., 2000. *Modeling the radiative transfer in leaves in the 300 nm to 2.5  $\mu$ m wavelength region taking into consideration chlorophyll fluorescence - The leaf model SLOPE*. PhD Thesis, Technische Universität München, Oberpfaffenhofen (Germany), 110 pp.
- Pfündel, E.E., Agati, G., Cerovic, Z.G., 2006. Optical properties of plant surfaces, in *Biology of the Plant Cuticle* (M. Riederer & C. Müller, eds), Blackwell Publishing, pp. 216-249.
- Press, W.H., Flannery, B.P., Teukolsky, S.A., Vetterling, W.T., 1992. *Numerical Recipes in FORTRAN: The Art of Scientific Computing*. Cambridge University Press, 992 pp.
- Segelstein, D., 1981. *The complex refractive index of water*. M.S. Thesis, University of Missouri-Kansas City.
- Woolley, J.T., 1975. Refractive index of soybean leaf cell walls. *Plant Physiology*, 55, pp. 172-174.

# A METHOD FOR MEASUREING THE PERMITTIVITYOF ARTIFICIAL FROZEN SOIL USING NETWORK ANALYZER

Shaojie Zhao, Lixin Zhang, Liying Li

Research Center for Remote Sensing and GIS, School of Geography, Beijing Normal University, Beijing, 100875, China. — geo\_zhao@126.com

**KEY WORDS:** Frozen Soil, Permittivity, Network Analyzer, Microwave, Remote Sensing

## ABSTRACT:

Frozen soil is best observed by microwave remote sensing due to the big difference of the permittivity comparing with unfrozen soil. The dielectric property of frozen soil has much relation with its microwave radiation. So permittivity is a bridge parameter in monitoring the status of frozen soil and its water content using microwave remote sensing. However, little data of the permittivity of frozen soil has been published. This has restricted the development of permittivity model of frozen soil profoundly. We got soil of different texture from wild field in northern china where seasonal freeze/thaw occurs every year, prepared these soil to frozen soil samples of different temperature. Many problems occurred during the measurement using a network analyzer and a high temperature probe. Among these difficulties the preparing of frozen soil samples, the control of temperature and water content of frozen soil samples and the contact between sample and probe are most significant. These difficulties are finally solved by designing a sample holder. The sample holder ensures the accuracy and repeatability of the measurement of the permittivity of frozen soil. A set of measured data show that the results are credible.

## 1. INTRODUCTION

Frozen soil either permanent or seasonal covers nearly 80% of the total land area in the northern hemisphere. The freezing and thawing process of frozen soil is of great significance for climate and hydrology modeling and further understanding of global change. Microwave remote sensing is a effective technology in monitoring the temporal and spatial distribution of this process. The permittivity of the soil surface is a key parameter in modeling the scattering and emission of microwave signature. And the state of frozen soil is inferred based on the knowledge of the relations between the properties and the permittivity of frozen soil.

Many experiments have been conducted in order to determine the dielectric behavior of soil with different water or saline content in the microwave region (Marti et al., 1985; John 2001; S; Olhoeft, 1977). Data from these experiments are used to support the dielectric model of soil. However, few have measured the permittivity of frozen soil in a wide range of frequency.

Many methods were used to measure the dielectric properties of soil under the room temperature. However, when the soil is frozen, the soil water change into ice and the soil sample becomes hard. These methods can't be applied to measuring frozen soil directly.

The purpose of this paper is to design a feasible method for measuring the permittivity of frozen soil in the laboratory using a microwave network analyzer over a wide range of frequency which covers the mostly used wave bands in microwave remote sensing. In section 2, the measurement system and a sample

holder designed for frozen soil are presented. In section 3, frozen soils of different water content was measured using this method. Permittivity data of these soils are compared with values computed by model.

## 2. MEASUREMENT SYSTEM

### 2.1. The Network Analyzer

A network analyzer is used to carry out the measurement. We use a Agilent vector network analyzer and a 85070E Dielectric Probe Kit which contains a high temperature probe. The high temperature probe withstands a wide  $-40\text{ }^{\circ}\text{C}$  to  $+200\text{ }^{\circ}\text{C}$  temperature range, which allows measurements of frozen soil. This method is called the coaxial probe technique. The material is measured simply by placing the probe on a flat face of a solid or immersing it into a liquid. (Fig.1)

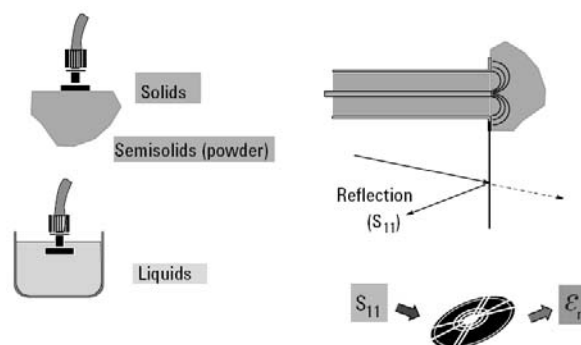


Figure 1. Illustration of coaxial probe



The probe transmits an electromagnetic wave in a range of pre-determined frequencies and captures the reflected part which is not transmitted. Software is then used to compute the permittivity from the coefficient of reflection.

The coaxial probe model which is used to compute permittivity assumes both an infinite ground plane and semi-infinite sample size. However, from a practical point of view, these assumptions are justified if reflections from finite boundaries are not sensed at the probe aperture. The sample requirements of this method is

$$Diameter > 20mm$$

$$Thickness > \left| \frac{20}{\sqrt{\epsilon^*}} \right| mm$$

where  $\epsilon^*$  is the complex permittivity of the sample (Agilent, 2003). In fact, a thickness of 2cm is thick enough for most dielectric.

The error of the analyzer is calibrated before measuring the permittivity of the sample by measuring three standards: 25°C deionized water, air, and a short circuit. In addition, a “refresh calibration” is required to be performed just before each measurement to eliminate the error caused by temperature change and the cable instability. To perform the “refresh calibration” the re-measurement of a single calibration standard is needed.

## 2.2. Soil Samples Preparation

Soil samples were obtained from the Wali region of north Beijing, China. The soil type was silt loam (sand: 32.56%, silt: 62.83%, clay: 4.21%). Soil gathered from the field needs to be grinded and filtrated by a 2-mm sieve to exclude large aggregates and assure the homogeneity of the soil samples. Then they were mixed with calculated quantities of pure water, placed in sealed plastic boxes, and set aside for 48 hour to allow the water content to come to equilibrium. We prepared soil samples with different volumetric moisture content (5%, 10%, 15%, 20%, 25% and 30%). Soil samples that have low water content may need more time to be homogeneous, so it's practical to set them aside for more time before measuring. Make sure that the soil in the box is enough for the whole measurement process.

## 2.3. Sample Holder and Measurement

After the soil samples are homogeneous, we pick some moist soil from these boxes, sealed the soil container, put them into the temperature controller to make frozen soil. Before freezing, a flat surface of the soil sample is needed in order for a perfect contact with the probe when measuring. But the former shaped flat surface becomes uneven because of the freezing and swell of the soil water. In addition, there are frost concentrates at the

surface due to the evaporation-congelation effect during the freezing process. The frost may melt into water when contact the frozen soil sample to the probe which has a room temperature. These difficulties make it impossible to measure the permittivity of frozen soil in the way used in the measurement of unfrozen soil. There are three main difficulties in all:

- (1) The soil sample must be homogeneous and isotropic;
- (2) Make sure that the surface moisture doesn't change during the freezing procedure;
- (3) Ensure that the probe contact well with the surface of the frozen soil sample, so that there is no air between the probe and the frozen soil;
- (4) Make sure that the frozen soil doesn't melt or change temperature when contacted with the probe, it requires that the temperature of the probe and the frozen soil samples are of the same.

A sample holder was designed to solve these problems. The sample holder is made of stainless metal. It has two parts as shown in Figure 2. The left part is has a cylindrical space in the center which is to be filled with soil sample. The space is large enough ( $d=21mm$  which is 1 mm longer than that of the probe) to meet the requirement of being equivalently semi-infinite. It has no bottom, and the end of the wall is shaped like a circular wedge.



Figure 2. The sample holder

This kind of design aim to facilitate the procedure of taking the moist soil out from the boxes in which it becomes homogeneous. During this step one simply needs to press this part of the sample holder vertically into the moist soil and the soil sample filling the space is not disturbed. Then screw the right part of the sample holder to the bottom of the left part. The two parts are joined by the screw. There is cylindrical steel convex at the center bottom of the right part which can not be seen in Figure 2. The soil in the left part of the sample holder can be pushed up by screwing the right part. When the probe was connected to the left part (Figure 3), screwing the left part will squeeze the soil to the probe allowing no interspaces

between them. At the same time this will change the density and the volumetric water content of the soil sample. The volume of the cylindrical soil sample in the sample holder can be calculated according to the position where the left part was screwed to. So the density and the volumetric water content become controllable to some extent.

After the probe and the sample holder are connected tightly, they were frozen together in the temperature controller to an expected temperature. A thermometer was set in the temperature controller to supervise the actual temperature of the frozen soil sample by measuring the soil that has the same properties with the soil measured by the probe. Because the soil in the sample holder was nearly sealed by the sample holder and the probe, there would be little loss of moisture during the whole measurement. When the expected soil temperature was achieved, a measure of permittivity was triggered. Then the real part and the imaginary part of the measured complex permittivity were shown on the screen of the network analyzer respectively.



Figure 3. The probe and the sample holder in temperature controller

The four main difficulties mentioned before are solved during this procedure. However, the refresh calibration can not be performed in the process of measuring frozen soil using the method shown above. To solve this problem, we used a cable the shape of which was always fixed and not easy to change in order to minimize the error. A comparative experiment showed that this disadvantage caused a error less than  $\pm 3\%$  of the measured permittivity over the range of the pre-determined frequencies.

### 3. MEASUREMENT RESULTS

The measured results are shown in Figure 4.

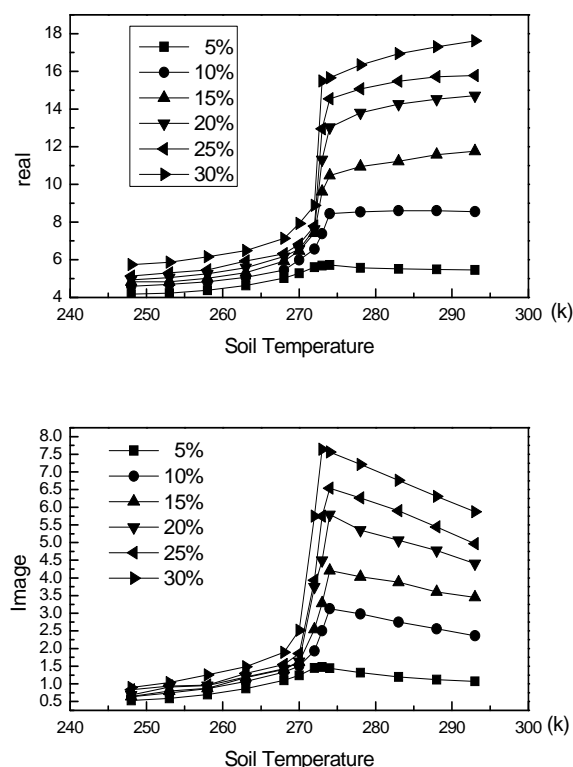


Figure 4. The measured soil permittivity in frequency of 6.89GHz with different water content and temperature

These results are reasonable comparing with the calculation results by Zhang (Zhang et al., 2003). Repeated measurements for the same soil sample were conducted. The relative measurement errors change with water content, temperature and frequency but are less than 5%. These errors are probably due to tiny differences of water content and density of the soil sample.

### 4. CONCLUSION

Measuring frozen soil is different comparing to measuring unfrozen soil using a network analyzer. The sample holder and the method presented in this paper can solve the problems encountered when measuring the frozen soil directly and ensure the accuracy and repeatability of the measure of the permittivity.

### REFERENCES

- Agilent Co., 2003. 85070E Dielectric Probe Kit 200 MHz to 50 GHz. Agilent literature number 5989-0222EN, Agilent Co.
- John O. Curtis, 2001. A durable laboratory apparatus for the measurement of soil dielectric properties. *IEEE Trans. Instrum. Meas.* 50(5), pp. 1364-1369.

Martti T. H. et al., 1985. Microwave dielectric behavior of wet soil - Part I: Empirical models and experimental observations. *IEEE Trans. Geosci. Remote Sensing*, GE-23(1), pp. 25-34.

Olhoeft, 1977. Electrical properties of natural clay permafrost. *Canadian Journal of Earth Science*. 14(1). pp. 16-24,

Zhang, L.X., Shi, J.C., et al, 2003. The estimation of dielectric constant of frozen soil-water mixture at microwave bands. In: IGARSS'03, France.

# SOIL MOISTURE EXPERIMENTS 2005 (SMEX05): PASSIVE MICROWAVE POLARIMETRIC SIGNATURES OF SOIL MOISTURE AND VEGETATION

Jackson, T.<sup>a</sup>, Bindlish, R.<sup>a</sup>, Du, J.<sup>a</sup>, Cosh, M.<sup>a</sup>, Li, L.<sup>b</sup>, Gaiser, P.<sup>b</sup>, Kabela, E.<sup>c</sup>, and Hornbuckle, B.<sup>c</sup>

<sup>a</sup> USDA ARS Hydrology and Remote Sensing Lab, Beltsville, MD

<sup>b</sup> Naval Research Lab, Washington, DC

<sup>c</sup> Iowa State University, Ames, IA

**KEY WORDS:** Microwave Polarimetry, WindSat, APMIR, Soil Moisture, Dew

## ABSTRACT:

Microwave remote sensing provides a direct measurement of soil moisture; however, there have been many challenges in algorithm science and technology that we have faced on the path to providing global measurements. Field experiments, especially those involving both ground and aircraft measurements, provide the linkage between spatial scales necessary for both algorithm development and validation. Soil Moisture Experiments 2005 (SMEX05) was designed to address algorithm development and validation related to several current and scheduled satellite systems that can provide soil moisture. The Airborne Polarimetric Microwave Imaging Radiometer (APMIR), an aircraft simulator of WindSat, was flown on a P3B aircraft over an agricultural domain (corn and soybean) in Iowa, USA. Early morning flights were conducted for several weeks from late June to early July 2005. Efforts in SMEX05 to focus on the early morning time frame offered an opportunity to understand the effect of dew on microwave emissions, which could contribute to improved microwave soil moisture algorithms for satellites with early morning observation times. From the analysis on the preliminary data it was found that 1) the effect of dew on both H and V is small and 2) as dew evaporates the emissivity increases, which suggests a “standing water” effect. Expected differences between forest and crop sites and between polarizations were observed. These preliminary results will be refined following further calibration of the APMIR data.

## 1. INTRODUCTION

Microwave measurement of soil moisture at large scale is crucial for understanding the land-atmosphere interaction, global circulation, and carbon cycling. Major efforts are being made towards the goal of routinely providing accurate satellite-based soil moisture products. Operational moderately low frequency instruments include the Advanced Microwave Scanning Radiometer - EOS (AMSR-E), WindSat radiometer and Conical Scanning Microwave Imager/Sounder (CMIS), and exploratory L-band radiometer, Soil Moisture and Ocean Salinity Mission (SMOS). All of these are capable of retrieving global soil moisture. However, there are still many issues in algorithm science and technology that need to be carefully considered. For example, research is needed to fully exploit the operational satellite instruments, recognizing limitations of these sensors in terms of Radio-Frequency Interference (RFI) mitigation, spatial resolution and vegetation attenuation; and the effects of early morning dew, intercepted rain, and topography also need to be evaluated. Carefully designed field experiments, especially those involving both ground and aircraft measurement, provide the opportunities to study these issues and the datasets necessary for algorithm development and validation.

## 2. SMEX05 DESCRIPTION

Soil Moisture Experiments 2005 and Polarimetry Land Experiment (SMEX05/POLEX) was designed to address algorithm development and validation related to all of the current and scheduled soil moisture satellite systems. Intensive ground sampling concurrent with aircraft and satellite observations were conducted during the experiment. Key objectives of SMEX05 include: 1) exploration of the unique polarimetric information for soil moisture and vegetation, 2)

investigation of the diurnal effects associated with soil, vegetation and atmosphere at the 6 am/6 pm observing times of satellites such as SMOS and WindSat, 3) study the effect of dew on microwave emission, 4) evaluation and mitigation of RFI at low frequencies, and 5) enhancement of WindSat and Aqua AMSR-E soil moisture algorithms.

### 2.1 Experiment Site

In order to satisfy the requirements of the multiple objectives of SMEX05, a regional study area in Iowa and the more intensively measured Walnut Creek watershed were selected to provide a data set for the analysis of polarimetric observations for a range of vegetation structures and water contents. Walnut Creek Watershed is an ideal study site since it has been the focus of research by the USDA ARS National Soil Tilth Lab. It was also the region used in SMEX02.

Nearly 95% of the region and watershed is used for row crop agriculture. Corn and soybean are grown on approximately 95% of the row crop acreage, with greater than 50% in corn, 40-45% in soybean and the remaining 5-10% in forage and grains. The watershed is representative of the Des Moines Lobe, which covers approximately 1/4 of the state of Iowa. The area around central Iowa is considered the pothole region of Iowa because of the undulating terrain. Surface organic matter contents often range from 1-2 % to over 8% in a transect from the pothole areas to the eroded knolls within the same field. These features create a potential condition in the spring and extremely wet summers of a soil surface covered with random water-filled potholes. The climate is humid with an average annual rainfall of 835 mm. The heaviest precipitation months are May and June (about 1/3 of the annual total) Rainfall events in the spring and summer are often thunderstorms, providing brief and intense showers. The topography is characterized by low relief and poor surface drainage. Conventional tillage is most widely

used; however no tillage and ridge tillage have been recently introduced.

2.2 WindSat

WindSat is the first spaceborne polarimetric microwave radiometer developed by the Naval Research Laboratory for the U.S. Navy and the National Polar-orbiting Operational Environmental Satellite System (NPOESS) Integrated Program Office (IPO) (Gaiser et al., 2004). The WindSat radiometer was launched as part of the Coriolis mission in January 2003. WindSat is a conically scanning radiometer providing both fore (1025 km swath) and aft (350 km swath) looking observations. The nominal earth incidence angle is in the range of 50 – 55 degrees. The inclination of the WindSat orbit is 98.7 degrees. It has a sun synchronous polar orbit with an ascending node at 6:00 PM and a descending node at 6:00 AM. The WindSat radiometer has frequencies similar to AMSR-E, but lacks the 89.0 GHz channel. Moreover, it provides fully polarimetric observations at 10.7, 18.7 and 37 GHz. The launch of WindSat has provided an opportunity to study the polarimetric signals of land surface from space. Previous studies of the Taklamakan Desert and Heilongjiang agriculture area in China showed that Windsat could observe systematic variations in the 3rd and 4th Stokes parameters from land surfaces with aligned features (Narvekar et al., 2007).

2.3 Airborne Polarimetric Microwave Imaging Radiometer (APMIR)

The primary aircraft instrument of SMEX05 is the Airborne Polarimetric Microwave Imaging Radiometer (APMIR). APMIR was designed and built by the Naval Research Laboratory as a tool for calibration and validation (cal/val) of the Coriolis WindSat and Defense Meteorological Satellite Program SSMIS satellite microwave radiometer sensors. Additional goals in developing APMIR were to provide data for improving retrieval algorithms and to serve as a cal/val tool for the NPOESS CMIS instrument. APMIR has multiple frequencies and polarizations to match the relevant satellite channels; however, only the C- and X-band channels were operational for SMEX05. X-band is fully polarimetric by way of polarization combining. APMIR can be operated in a non-scanning or conically-scanning mode. For SMEX05 only non-scanning was used. APMIR parameters are listed in Table I. The sub-band design of APMIR shown in Table 1 is especially helpful to detect and mitigate RFI, which has become a serious problem for observations at C-band. In SMEX05, APMIR was flown between 6 am to 10 am local time at a 0.9 km altitude on the Navy P3B.

Table 1 SMX05 APMIR parameters based on 53 degree incidence angle and 0.9 km altitude

Channel (GHz)	Beam width (Deg)	Footprint (km)
6.6, 6.8, 7.2	9.4	0.24 x 0.42
10.7	5.9	0.15 x 0.27

2.4 APMIR Missions

Three different types of APMIR science missions were flown over the Walnut Creek Watershed during the experiment.

2.4.1 Watershed mapping

This mission is intended to provide the critical data base for soil moisture algorithm and polarization effects studies. As shown in Figure 1, a total of eight different lines were flown, seven of which were east-west oriented flightlines that were designed to provide nearly contiguous coverage of the watershed area. The nominal length of these lines was 45 km. Lines were flown east-west with alternating headings. It is important to note that the instrument was rotated 180 degrees in azimuth (with respect to the aircraft) so as to always point in the same compass direction. Measurement differences could occur for different pointing directions as previous experience with aircraft instruments and work in this region indicated. These can be related peculiarities of the installation, RFI, or sun angle.

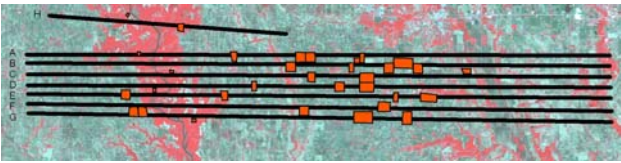


Figure 1. APMIR low altitude mapping.(Black lines are for APMIR flight lines, red rectangles are intensive sampling sites and background image is a Landsat Thematic Mapper false color image of the Walnut Creek Watershed).

2.4.2 Temporal variations

One of the science objectives of SMEX05 concerns the diurnal nature of microwave brightness temperature and its relationship to the characteristics of the atmosphere, vegetation, and soil. Linking the morning and afternoon observations of WindSat and those of AMSR-E requires the study of the changes that occur over the day. One that may be of concern, especially for WindSat, is the presence of dew and low-level atmospheric moisture on the brightness temperature. Very little research has been conducted to address these issues (Jackson and Moy, 1999).

In SMEX05, two east-west lines were flown repeatedly between 0600 LT and 1000 LT on June 30th with supporting ground sampling to characterize the physical variables. Figure 2 shows the flight pattern. The observed brightness temperature changes with time will be used to study the effects of dew on the microwave emission from the land surface.

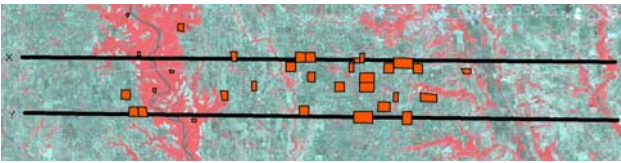


Figure 2. APMIR low altitude temporal variations (Black lines are for APMIR flight lines, red rectangles are intensive sampling sites and background image is a Landsat Thematic Mapper false colour image over the Walnut Creek Watershed).

2.4.3 Azimuthal effects

This mission was designed to examine the azimuthal dependence of brightness temperature for a number of fields by flying over a single point from eight different directions at low altitude in an asterisk pattern. WindSat data analysis (Narvekar et al, 2007) has indicated that such an azimuthal dependence is significant and related to measurement geometries, and thus must be quantified and separated from effects resulting from other geophysical variations. Figure 3 illustrates the general flight pattern of this mission. Each line took about 12 minutes.



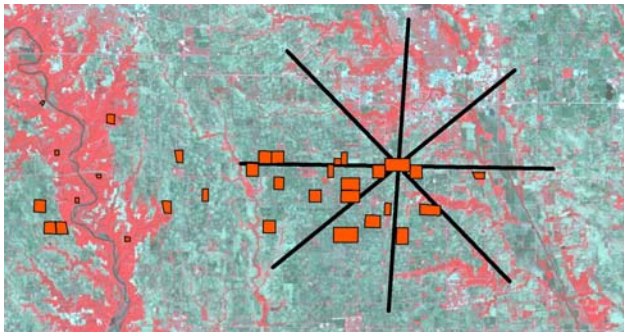


Figure 3. APMIR low altitude azimuthal effects (Black lines are for APMIR flight lines, red rectangles are intensive sampling sites and background image is a Landsat Thematic Mapper false colour image over the Walnut Creek Watershed).

2.5 Field Conditions and Data Collection

SMEX05 was conducted between June 15 and July 3. Soil moisture, soil temperature, soil properties and vegetation measurements were made in 16 corn, 9 soybean, 4 forest and 1 alfalfa field. In addition, dew (leaf wetness) sensors were installed at a number of locations and physical measurements of the amount of dew content were made within corn, soybean and alfalfa sites. During the experiment the vegetation water content of corn increased from 1.35 to 5.68 kg/m2 and soybean increased from 0.52 to 4.17 kg/m2. A significant precipitation event occurred during the study prior to the June 26 APMIR flight.

The satellite and aircraft datasets collected during SMEX05 period are summarized in Table 2. Problems with a geo-referencing system required extensive post-processing of the APMIR data, which has delayed analyses. The calibration of the APMIR channels is currently ongoing. Preliminary data are used here and must be carefully interpreted. Only the H and V data are used here.

Table 2 Aircraft and satellite datasets and precipitation during SMEX05 (\*M - mapping; T - temporal variations; A - azimuthal effects)

Date	APMIR	WindSat	AMSR-E	Precip
June 19	M, A	X	X	-
June 20	M, A	X	-	-
June 21	M, A	X	X	X
June 22	M, A	-	X	-
June 23	-	-	-	-
June 24	-	-	X	-
June 25	-	X	-	-
June 26	M, A	X	X	X (heavy)
June 27	M, A	-	-	-
June 28	-	-	X	X
June 29	-	-	-	-
June 30	T, A	X	X	X
July 1	M, A	X	X	-
July 2	M, A	X	-	-

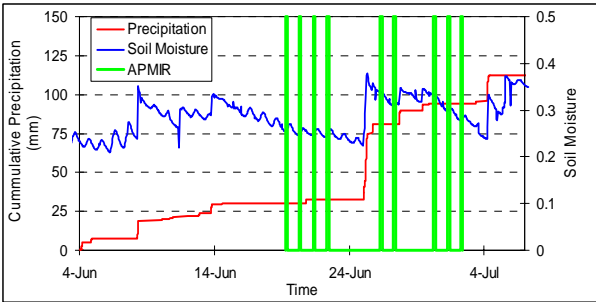


Figure 4. Accumulated precipitation, volumetric soil moisture and APMIR observation time

3. TEMPRAI VARIATION FLIGHTS RESULTS

For both current in-space satellites such as WindSat and the scheduled SMOS, dew effects need to be carefully studied because observations are made during a time of day when dew can occur, early morning. Previous research on this issue have come to different conclusions. In the recent studies, De Jeu et al. (2005) reported that dew noticeably increased L-band microwave emission of grass while Hornbuckle et al. (2006) observed a decrease in L-band brightness temperature for a maize canopy in which dew was present. In SMEX05, the effect of dew on land with varing vegetation cover was studied by combined aircraft and field measurements. C-band and X-band observations were used to study the effect of dew on microwave emissions, which are more likely to be affected by dew than L-band observations.

On June 30 the aircraft flew an ellipse five times between 6:45 am and 9 am (local time) over the same locations. Blocks of corn, soybean, and forest fields along the flight lines were identified (some of these included ground sampling) as shown in Figure 5. During the experiment, dew was measured by two methods, Leaf Wetness Sensor and physical sampling. The Leaf Wetness Sensor employed in SMEX05 is designed to simulate the surface area of a leaf. It is primarily used to determine the percentage of time that a surface (i.e., leaf surface) is wet versus dry. The electrical resistance of the surface is measured and gives an indication of the amount of dew present.

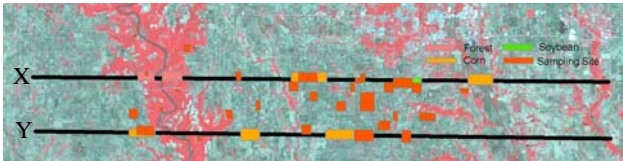


Figure 5. APMIR dew flights and studied feature blocks (Black lines are for APMIR flight lines, rectangles are selected feature blocks and intensive sampling sites and background image is a Landsat Thematic Mapper false color image over the Walnut Creek Watershed)

Physical sampling involves measuring the weight of the water collected by filter paper from sampled leaves. The total amount of dew in a square meter can be calculated by using ancillary vegetation data including row density, row spacing, and leaf count. Figure 6 shows dew measured through physical sampling in two of the corn fields as a function of time. The measured dew was as high as 0.4 kg/m2 at the start of the observation period. At the end of the aircraft microwave observation period (~9 am) the dew had decreased to 0.1 kg/m2. There was no dew left after 10 am on June 30. The amount of dew was a function of the location of the sampling site.

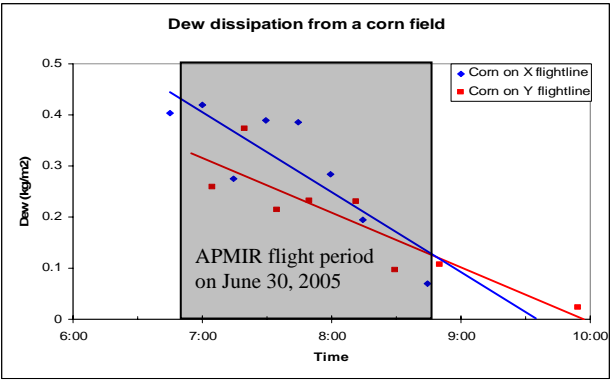


Figure 6. Dew dissipation from corn fields

The brightness temperature for each data block was calculated by averaging the APMIR measurements within the block. We attempted to adjust for temperature changes in the brightness temperature associated with time by computing emissivity using the in-situ surface temperature observations. Data from the C- and X-band H and V channels are plotted as a function of time as shown in Figures 7 to 10. In the figures, feature blocks along with the flight line X or Y are named sequentially from west to east. It can be seen from the plots that forest sites have a higher emissivity and smaller polarization difference than the other sites. At the same time, for both C-band and X-band observations, the V-polarized emissivity for all the feature blocks is always higher than H-polarized emissivity. These behaviors are consistent with theory. The figures also show that the C-band emissivity for forest sites increased by ~0.015 while corn and soybean values increased by ~0.03 during the flight time of about 3.5 hours. The increase in emissivity at X-band is greater than those observed at C-band. This suggests that dew has a greater effect at higher frequencies. As evident from Figure 6, there is a consistent decrease in dew to near zero over study period. This indicates that the presence of dew leads to a slight decrease of the emission from vegetated land observed here.

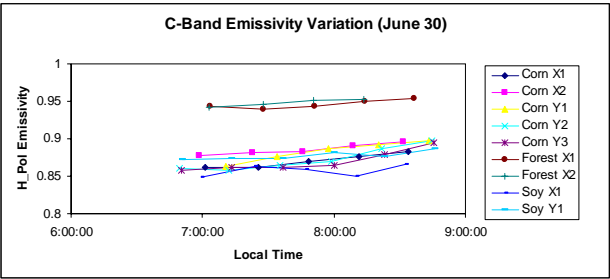


Figure 7. C-band H-Polarized emissivity variation with time

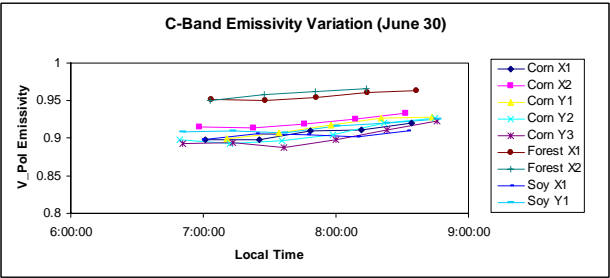


Figure 8. C-band V-Polarized emissivity variation with time

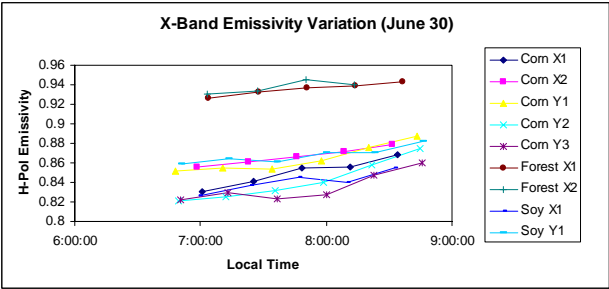


Figure 9. X-band H-Polarized emissivity variation with time

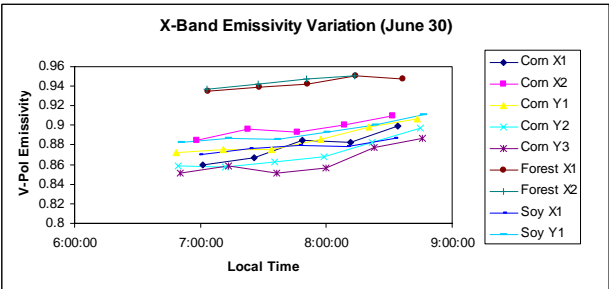


Figure 10. X-band V-Polarized emissivity variation with time

MPDI (Microwave Polarization Difference Index) was computed and is plotted versus time for both C- and X-band (Figures 11 and 12). MPDI is insensitive to surface temperature changes and a small MPDI value has been related to a possible dew event (De Jeu et al., 2005). MPDI is defined as

$$MPDI = \frac{T_{b\_V} - T_{b\_H}}{T_{b\_V} + T_{b\_H}} \tag{1}$$

As expected, forest sites had a lower MPDI than the other sites. However, there is not a clear trend of MPDI change with time. This may related to the MPDI being sensitive to observation errors. Further results will be presented after APMIR data get fully calibrated.

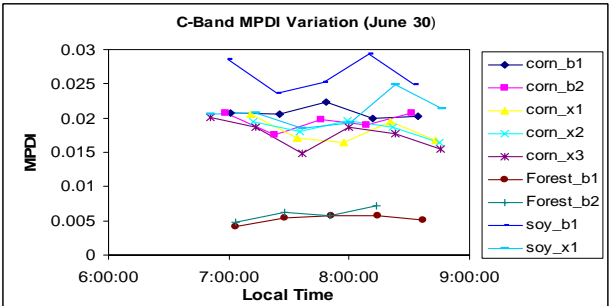


Figure 11. C-band MPDI variation with time

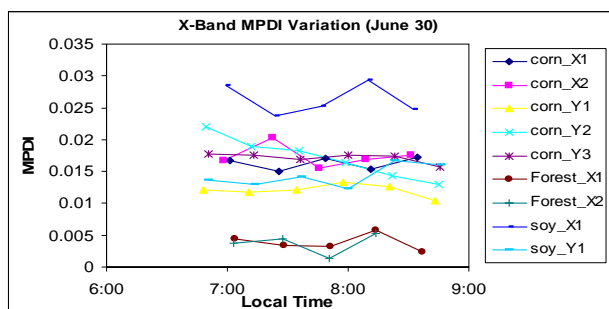


Figure 12. X-band MPDI variation with time

Analysis on the preliminary data suggests that 1) the effect of dew on both H and V is small, 2) as dew evaporates the emissivity increases, which suggests a “standing water” effect and matches the pattern observed at L band by Hornbuckle et al. (2006) and 3) expected differences between forest and crop sites and between polarizations were observed.

#### 4. SUMMARY

SMEX05 had multiple objectives related to polarimetric passive microwave remote sensing of soil moisture. Geo-referencing and calibration issues presented challenges that have resulted in some delays in processing and analysis. Some preliminary results of a sequence of flights designed to observe dew effects were presented. A small effect was observed that was consistent with the limited observations at L band. Upon completion of calibration all SMEX05 objectives will be addressed.

#### Reference

- Gaiser, P.W., K.M. St. Germain, et al., 2004. The WindSat spaceborne polarimetric microwave radiometer: sensor description and early orbit performance. *IEEE Trans. Geosci. Remote Sensing*, 42, pp. 2347-2361, 2004.
- Hornbuckle, B.K., England, A.W., Anderson, M.C., Viner, B.V., 2006. The Effect of Free Water in a Maize Canopy on Microwave Emission at 1.4 GHz. *Agricultural and Forest Meteorology*, 138, pp. 180-191.
- De Jeu, Richard A. M., Holmes, Thomas R. H., Owe, M., 2005. Determination of the effect of dew on passive microwave observations from space. *Remote Sensing for Agriculture, Ecosystems, and Hydrology VII. Edited by Owe, Manfred; D'Urso, Guido. Proceedings of the SPIE*, Volume 5976, pp. 51-59 (2005).
- Jackson, T.J., and Moy, L., 1999. Dew effects on passive microwave observations of land surfaces. *Remote Sensing Environment*, 70, pp. 129-137
- Narvekar, P.S., Jackson, T.J., Bindlish, R., Li, L., Heygster, G., and Gaiser, P.W., 2007. Observations of Land Surface Passive Polarimetry with the WindSat Instrument. *IEEE Trans. Geosci. Remote Sensing*, in press

#### Acknowledgements

This work was partly supported by the NASA Terrestrial Hydrology Program.

# REFERENCE SPECTROMETRY FOR CALIBRATION OF OPTICAL EARTH OBSERVATION SYSTEMS

S. G. R. Salim <sup>a,\*</sup>, N. P. Fox <sup>a</sup>, E. R. Woolliams <sup>a</sup>, R. Winkler <sup>a</sup>, H. M. Pegrum <sup>a</sup>, T. Sun <sup>b</sup>, K. T. V. Grattan <sup>b</sup>

<sup>a</sup> National Physical Laboratory, Hampton road, Teddington, Middlesex, TW11 0LW, UK – (saber.salim, nigel.fox, emma.woolliams, rainer.winkler, heather.pegum)@npl.co.uk

<sup>b</sup> City University, North Hampton Square, London, EC1V 0HB, UK – (T.Sun, K.T.V.Grattan)@city.ac.uk

**KEY WORDS:** Spectrometer, Traceability chain, Blackbody, Thermodynamic temperature

## ABSTRACT:

A small palm-sized, reference spectrometer, mounted on a remote controlled model helicopter is being developed and tested to provide calibrated reference data for optical Earth Observation systems by the National Physical Laboratory (NPL) in conjunction with City University in London. The spectrometer is traceable to NPL's primary standard cryogenic radiometer. The traceability chain includes the use of a novel high temperature fixed-point metal-carbon eutectic blackbody as an ideal source of spectral radiance, whose thermodynamic temperature is measured using absolute radiation thermometry. The spectrometer is a hand held, low weight, photodiode array, which has good stray light capability and wide spectral coverage, from 400 nm to 900 nm, in a single scan. Combining a calibrated small spectrometer with a remote controlled helicopter is a novel solution for providing efficient low cost remote sensing over relatively large or difficult terrains. This technique minimizes potential damage to a site from human observers and can cover much wider areas in shorter timescales. Data obtained will be used to validate satellite measurements of terrestrial targets and determine its spatial homogeneity. This paper describes this vicarious calibration methodology using a eutectic standard and the preliminary results of an evaluation study of the spectrometer characteristics.

## 1. INTRODUCTION

Earth Observation satellites are characterized by their wide spatial coverage and regular and long-term data collection. This has made them the main source of global data about the earth. They are currently able to provide data for a wide range of fields such as topography, oceanography, biological distribution, atmospheric conditions and climate, in which context the accuracy and validity of satellite data is of vital importance. Although a lot of effort has been put into improving the accuracy of satellite sensors before launch, the stress of launch and the harsh environment of space degrades the sensor response and the performance of any on-board calibration equipment. Therefore, it is very important to improve methods for post-launch calibration and validation of data from satellite sensors and encourage their adoption.

Current techniques that are used to calibrate satellite sensors after launch depend on the accurate characterization of a test site before it can be used as a reference or standard source (Dingirard, 1999). Unfortunately, these vicarious calibration techniques are limited by several issues. For example, for the ground-based techniques where small hand held spectrometers are used to characterise the test site, only a small area is physically sampled. Similarly, when more detailed angular information is required, a larger instrument such as the Gonio Radiometric Spectrometer System (GRASS) can be used, but due to its size, there are some restrictions to the measurement location (Pegrum, 2006). Moreover, in many cases the process is time consuming and this in turn increases the uncertainties due to the effect of the changing environment and sun angle particularly. By contrast, the use of airborne techniques can cover wide areas in a relatively small time, but the method is very expensive. This makes it largely unaffordable and restricted to very specific campaigns. In addition, regardless of the technique being used, the accuracy and traceability of the

optical sensors is still a question, and to ensure the highest accuracy, the detectors should be traceable to an internationally accepted primary standard, which is not the general case for such instrumentation.

In order to increase the accuracy of current Earth Observation measurements, a novel ground-based calibration and validation technique that avoids many of the previously mentioned limitations is proposed. This incorporates the development of a small size reference spectrometer, with good stray light performance and wide spectral coverage. The spectrometer will be mounted on a remote-controlled model helicopter to provide a set of reference data in the Visible Near Infra-Red (VNIR) spectral region to calibrate optical Earth Observation systems.

## 2. THE SPECTROMETER

### 2.1 Spectrometer Traceability

The spectrometer will be traceable to NPL's primary standard cryogenic radiometer (Fox, 1995) through a novel high temperature fixed-point Metal-Carbon (M-C) eutectic blackbody. The traceability chain of the spectrometer is shown in Figure 1. A cryogenic radiometer is essentially a detector that compares the heating effect of optical radiation to the heating effect of the electric power. It depends on the electrical substitution principle that has been used in radiometry for more than a century. In 1985 Quine and Martin, at NPL, managed to successfully operate a detector at liquid helium temperature (Martin, 1985). A modified version of Quine-Martin cryogenic radiometer was developed by Fox (Fox, 1995), which is able to measure optical power with an uncertainty approaching  $10^{-5}$  (Martin, 1998).

---

\* Corresponding author.

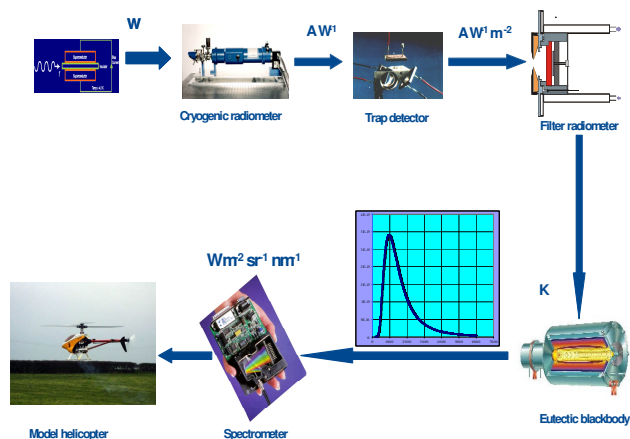


Figure 1: The traceability chain of the spectrometer.

As an absolute detector, the cryogenic radiometer can be used to calibrate the spectral responsivity of a transfer standard detector such as a trap detector (Fox, 1991) by determining the radiant power in high-stabilized laser sources. Due to their high quantum efficiency, low noise to signal ratio, good surface uniformity and predictable relative spectral responsivity, trap detectors are considered ideal transfer standard detectors for spectral radiance.

Using tuneable lasers as light sources, a trap detector- together with a calibrated aperture- can be used to calibrate the spectral response of a narrowband detector that is called filter radiometer. This calibrated filter radiometer is then used to measure the spectral radiance of a reference light source like a blackbody over a narrow spectral range in order to determine its thermodynamic temperature. Then according to Planck's law, the spectral radiance of the blackbody over the whole emitted spectral range can be calculated once the thermodynamic temperature of this blackbody has been determined (Fox, 1991).

## 2.2 Spectrometer Specifications

The calibrated spectrometer or a group of spectrometers, if possible, will be mounted on a remote controlled helicopter together with support equipment such as a viewing camera, a Global Positioning System (GPS), a mini-computer and a laser source. The weight that a remote controlled helicopter can carry is limited (~5 Kg), so a small and lightweight spectrometer is required. One draw back to this, however, is that the smaller the size of the spectrometer, the larger the effect of stray light on it. Although photodiode arrays have the significant advantage in spectrometer design in terms of size and weight, the effect of stray light on them can increase compared to other spectrometer designs.

Stray light can be defined as any undesired signal that is measured simultaneously with the desired signal. There are many sources of stray light, some of which are due to disorder or imperfections in the grating grooves or roughness on the surface of the grating. Other sources may be due to higher order diffraction or attributed to scattered light from the inside surface of the spectrometer walls, the internal input optics or the optical mounts. All of these sources can be avoided or corrected in ordinary mechanical spectrometers. However, the problem in photodiode array spectrometers is that they detect all the light diffracted from the grating at the same time, which, in

turn, causes each pixel both to detect stray light and also re-scatter it, thus increasing the effect of the undesired signal.

Stray light errors arise during the calibration process of the array spectrometer. Often a spectrometer is calibrated against a reference source of spectral radiance/irradiance e.g. a blackbody or an incandescent lamp, where the peak wavelength is usually located in the red or the near infrared spectral region. When the spectrometer is used to measure the spectral radiance/irradiance of a source that has a completely different spectral distribution, the stray light errors coming from the reference source can no longer be assumed to be the same as those of the source under test (Yuqin, 2006).

Two custom-made spectrometers have been chosen for this work, both of which are characterized by their small size, light weight and wide spectral coverage, all of which best suit the requirements of this application. These are discussed below:

- The first spectrometer is a Hamamatsu mini-spectrometer TM series C10083MD with 1024 pixels, where the actual spectral range of the spectrometer is from 250 nm to 1025 nm. The dispersive element is a transmission holographic diffraction grating made of quartz, so a high throughput and low stray light signal is expected. The light is guided into the entrance port of the spectrometer through an optical fibre, a collimating mirror directs the beam onto the grating, and the light transmitted by the grating is focused onto a built-in image sensor by a focusing mirror. Data acquisition is via a USB interface, which also provides the power necessary for circuit operation. This means that no external power supply is needed.
- The second spectrometer is from the Spectroscopic Analytical Company. The spectrometer is attached to a control box that requires an additional power supply, which makes the total weight of the spectrometer relatively high in comparison to the Hamamatsu spectrometer. The spectrometer has 1024 pixels that cover a spectral range from 350 nm to 1150 nm. In order to reduce the stray light signal, modifications have been made to the spectrometer: the internal surface of the spectrometer has been painted with a black coating and a baffle has been added to separate the higher order diffraction.

The spectrometers have been characterized for stray light performance using a set of cut-on filters and an FEL type tungsten halogen 1kw lamp. Assuming a zero transmittance below the cut-on wavelength, the cut-on filter prevents the direct light from the source below the cut-on wavelength from entering the spectrometer. Ideally, the pixels positioned to normally detect this light should give a zero signal, which is not the actual case because of the presence of stray light. Although evaluating the effect of stray light using cut-on filters is not ideal, as the value depends on the source used in the evaluations, it does give an understanding of how much stray light is inside the spectrometer, and it is also a good and fast way in comparing stray light rejection for different spectrometers.

Typical relative spectral stray light values for array spectrometers using a broad-band source is on the order of  $10^{-1}$  to  $10^{-3}$  of the source signal, but this does depend on the quality of the array spectrometer (Yuqin, 2006). The stray light



measurements for the Hamamatsu spectrometer showed that it is reasonably good in comparison to the other array spectrometer as it is well below the 1.0 % of the FEL lamp signal over the spectral range from 400 nm to 900 nm as it is illustrated by Figure 2. However, further evaluation of the stray light performance will be adopted in the future by using monochromatic light, in order to apply a correction before using the spectrometer in the field. A method similar to that described elsewhere will be used (Yuin, 2006).

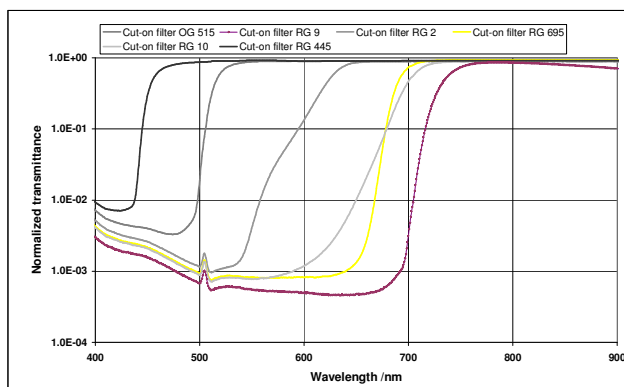


Figure 2: Filter signal to the lamp signal using different cut-on filters for the Hamamatsu spectrometer.

The wavelength accuracy of the spectrometer was determined using spectral lamps, which showed an error in the wavelength of the order of  $\pm 1$  nm. The Full Width at Half Maximum (FWHM) was also checked using the He-Ne laser line and it was found to be around 4.5 nm, which is sufficient for this application.

The long-term and transportation stability of the Hamamatsu spectrometer has been evaluated in another experiment in collaboration with the travel company Expedia. In their “Blue Sky Explorer”, which was designed to determine the “World’s Bluest Sky”, the instrument under went a total of 56 flights, covering 100 000 km in 72 days (Pegrum, 2006). The results showed no significant changes in the wavelength accuracy or the spectrometer readings before and after the series of flights that was undertaken.

### 2.3 Spectrometer calibration

To calibrate the spectrometer, an ideal source of spectral radiance is required. Currently, many National Metrology Institutes (NMIs) use variable high temperature blackbodies to establish their spectral radiance and irradiance scales (Woolliams, 2005). Variable temperature blackbodies can operate at very high temperatures (up to 3500 K), which is an advantage in terms of output power, especially at shorter wavelengths. On the other hand, variable temperature blackbodies are only stable to  $\sim 0.2$  % in the IR and even worse in the UV region. Moreover, the spectral radiance of these blackbodies must be determined using filter radiometers. These filter radiometers are prone to drift which means that they should be recalibrated periodically through a long and relatively expensive calibration chain, which, in turn, adds some restrictions on using variable temperature blackbodies as reference sources.

Fixed-point blackbodies can provide some significant advantages, as they have high temperature uniformity and better

emissivity and stability (Woolliams, 2006). The melting and freezing point of pure metals is an intrinsic property of the metal, which occurs at a fixed thermodynamic temperature. This intrinsic property means that a calibrated filter radiometer need only to be used once to determine the thermodynamic temperature of the blackbody, therefore avoiding costly periodical calibration of the filter radiometers.

Until recently, having a high temperature fixed-point blackbody was a problem, as the crucible that is used to hold the fixed point blackbody inside the furnace, usually made of Carbon, contaminates the pure metal during the heating process. Although Tungsten and Ceramic have high melting points, they are not the ideal substitutions for the Graphite crucible due to their low emissivity, this is why the highest fixed-point on the International Temperature Scale (ITS 90) is the copper point (1357.77 K) (Preston, 1990).

It was not until 1999, when Yamada et al (Yamada, 1999) showed that the contamination problem disappeared if M-C binary eutectic alloys were used instead of pure metals inside the graphite crucible. Since the carbon is an integral part of the eutectic alloys, a graphite crucible could be used safely. Subsequent research has shown the possibility to use a series of M-C and Metal (Carbide)- Carbon (MC-C) eutectics as fixed-points in the range from 1426 K to 3453 K (Woolliams, 2006).

In our application a high temperature M-C eutectic fixed-point blackbody will be adopted as a reference source to calibrate the spectrometer rather than using a variable temperature blackbody. As a preparation for adopting such a source, the thermodynamic temperature of Re-C, Ru-C, Pt-C and Co-C eutectic blackbody cells, which were produced at NPL, were measured by the NPL Absolute Radiation Thermometer (ART) (Salim, 2007) that has been thoroughly investigated and calibrated (Winkler, 2007).

The spectral radiance of a blackbody radiator in vacuum can be determined by Planck’s law as follows:

$$L(\lambda, T) = \frac{c_{1L}}{\lambda^5 (\exp[c_2 / \lambda T] - 1)} \quad (1)$$

Where  $c_{1L}$  is the first radiation constant for spectral radiance and  $c_2$  is the second radiation,  $\lambda$  is the wavelength, and  $T$  is the temperature of the blackbody.

According to Planck’s law, the thermodynamic temperature of the blackbody can be determined if the radiance of this blackbody at a specific wavelength or over a specific wavelength band is measured. Once the thermodynamic temperature has been determined, the spectral radiance of the blackbody over the whole spectral range can be calculated.

As the temperature of the Re-C eutectic cell increases through the heating process, the spectral output increases. This can be monitored over time with a filter radiometer as shown in Figure 3. The plateaus occur at the melting (C) and freezing (E) points of the Re-C cell. The melting point of a eutectic blackbody has been defined in all publications as the minimum of the first differential of the melting process with respect to time (Woolliams, 2006), and the spectrometer will be calibrated at this minimum point.

The spectral changes in the Re-C eutectic over time were simultaneously recorded by the spectrometer at equal time intervals over the melting phase, see Figure 4. As the blackbody reaches the melting point, the rate of change in the optical output decreases and the spectral response curves move closer together. The spectral output starts to increase again after the melt, as the temperature of the blackbody increases.

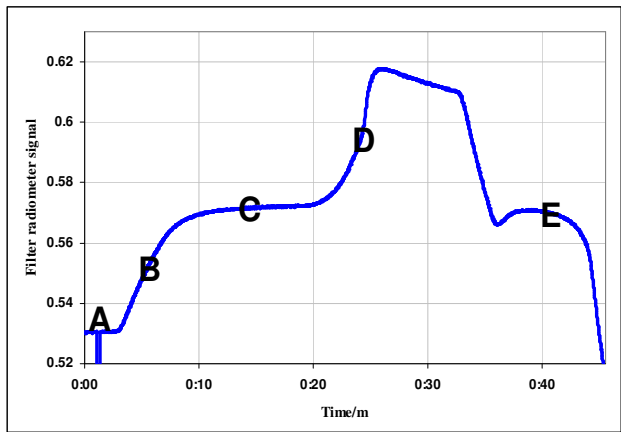


Figure 3: Melt and freeze plateaus of the eutectic cell

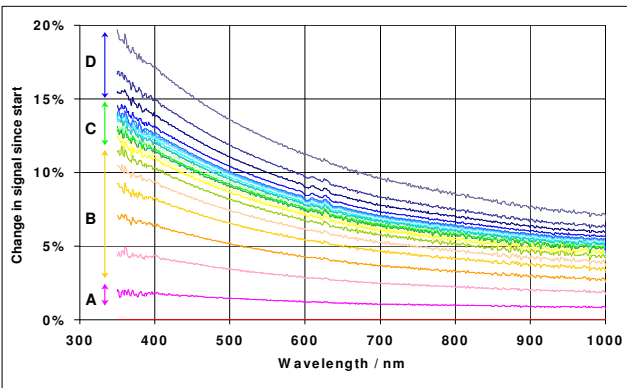


Figure 4: The spectral response of the spectrometer to the Re-C cell with time.

3. THE MODEL HELICOPTER

A remote-controlled model helicopter is an efficient, low cost, remote sensing device for Earth Observation applications. It can fly over relatively large areas and capture data more rapidly than ground-based techniques. When fitted with a spectrometer or group of spectrometers, the helicopter will make relatively large-scale measurements at a number of detection angles in order to determine the surface Bi-directional Reflectance Distribution Function (BRDF) (Nicodemus, 1977).

For this application two model helicopters have been acquired; a small helicopter to learn the handling techniques and a larger one that is able to carry ~ 5 kg of equipment, on which the spectrometer (or group of spectrometers) and the other equipment will be mounted. The helicopter has a controllable flying range of more than 600 m diameter, which allows a spatial coverage of nearly 2.9 x 10<sup>5</sup> m<sup>2</sup>.

4. ADVANTAGES OF THE TECHNIQUE

There are many advantages in combining a calibrated reference spectrometer (with its enhanced traceability) with a remote controlled helicopter as a new technique for Earth Observation measurements and these advantages include:

- Reducing the uncertainty in the current Earth Observation measurements through traceability to an ideal standard source of known spectral radiance, and providing a set of reference data to vicariously calibrate and validate satellite measurements.
- Covering wider areas compared to other ground-based techniques.
- The ability to fly over difficult terrains without any damage to the test site.
- The ability to provide surface measurements at different angles.
- Reducing the time of data collection, which in turn reduces the uncertainties due to the effects of the changing environment.
- A remote control helicopter is not large in size or heavy in weight, and this makes it very easy to transport without incurring restrictions on the measurement location.
- The field-of-view could easily be changed to adapt to the experimental requirements by changing the helicopter's altitude.
- A single person could run the experiment in the field.

It is an accurate, fast, and cheap technique, which has potential applications for use in a variety of measurements.

5. CONCLUSIONS

A new technique that provides accurate Earth Observation measurements is being developed and tested at the National Physical Laboratory (NPL) and in conjunction with City University in London. The optical sensors will be traceable to a new reference source based on high temperature M-C eutectic fixed-point blackbodies that are characterized by their high temperature uniformity, high emissivity, robustness and reproducibility. A remote controlled helicopter, which is an efficient and low cost instrument, will be used to carry the spectrometer. The proposed technique has the potential to provide accurate and low cost surface measurements for large and difficult terrains in a short period of time, the data will be used to calibrate and validate satellite information.

ACKNOWLEDGEMENT

The authors would like to thank Waldgrave School (Twickenham, UK) and the students who helped build the helicopters. One of the authors (Saber Salim) gratefully acknowledges the award of a fellowship from the Cultural Affairs & Missions Sector, Egypt.

This work was supported by the National Measurement System Policy Unit of the UK Department of Trade and Industry.

REFERENCES

Dingirard, M., 1999. Calibration of Space-Multispectral Imaging Sensors: A Review. *Remote Sens. Environ.*, 68(3). pp 194–205.

Fox, N. P., 1991. Trap Detectors and their Properties. *Metrologia*, 28(3). pp 197-202.

Fox, N. P., 1995. A mechanically cooled portable cryogenic radiometer. *Metrologia*, 32(6). pp 581-584.

Fox, N. P., 1991. Absolute spectral radiometric determination of the thermodynamic temperatures of the melting/freezing points of gold, silver and aluminium. *Metrologia*, 28(5). pp 357-374.

Martin, J. E., 1985. A cryogenic radiometer for absolute radiometric measurements. *Metrologia*, 21(3). pp 147-155.

Martin, J. E., 1998. Design considerations for the construction of an absolute radiation detector at the NPL. *Metrologia*, 35(4). pp 229-233.

Nicodemus, F. E., 1977. *Geometrical Considerations and Nomenclature for Reflectance*, National Bureau of Standards, US Department of Commerce, Washington, D.C. pp. 3-7.

Pegrum, H., 2006. "Expedia's Best Blue Sky: Experiments and Results", National Physical Laboratory, UK. <http://www.npl.co.uk/blueskies/> (accessed 10 March 2007).

Pegrum H. , 2006. Design and testing a new instrument to measure the angular reflectance of terrestrial surfaces. *International Geoscience and Remote Sensing Symposium (IGARSS'06)* IEEE. Denver, Colorado.

Preston-Thomas, H., 1990. The International Temperature Scale of 1990 (ITS-90). *Metrologia*, 27(1). pp 3-10.

Woolliams, E. R., 2006. Metal (carbide)–carbon eutectics for thermometry and radiometry: a review of the first seven years. *Metrologia*, 43(6). pp R11-R25.

Yamada, Y., 1999. Radiometric observation of melting and freezing plateaus for a series of metal-carbon eutectic points in the range 1330 °C to 1950 °C. *Metrologia*, 36(3). pp 207-209.

Yuqin, Z., 2006. A Simple Spectral Stray light Correction Method for Array Spectroradiometers. *Applied Optics*, 45(6). pp 1111-1119.

# ESTIMATION OF FOREST STAND PARAMETERS IN DENSITY CLASSES IN ARID AND SEMI-ARID REGIONS USING LANDSAT ETM+ DATA

F. Naseri <sup>a 1</sup>, A. A. Darvishsefat <sup>b</sup>, H. Sobhani <sup>b</sup>, M. Namiranian <sup>b</sup>

<sup>a</sup> International Center of Science, High Technology & Environmental Sciences, Kerman, Iran -  
naseri@icst.ac.ir fmnaseri@yahoo.com

<sup>b</sup> Faculty of Natural Resources, University of Tehran, Karaj, Iran - adarvish@chamran.ut.ac.ir - (hsobhan, mnimir) @nrf.ut.ac.ir

**KEY WORDS:** Landsat, Vegetation, Correlation, Estimation, Model, Parameters, Sampling

## ABSTRACT:

In this investigation the capability of Landsat ETM+ data for estimation of forest stand density and canopy area in National Park of Khabr in Kerman province, Iran in different density classes was evaluated. In a preliminary study, density mapping in the study area was qualitatively implemented and very thin, thin and semi-dense classes were concluded. Measurements made in sample plots in each density class were considered as a reference. Orthorectified satellite data were used to produce different ratios, vegetation indices (VIs), VIs for soil influence decreasing, components of Principal Component Analysis (PCA) and Tasselled Cap transformation features to apply in further analyses together with the original bands. Simple regression between stand parameters and digital values of each synthetic and original band was separately investigated. Ratio3 ((ETM3 – ETM1)/ (ETM3 + ETM1)) showed the highest correlation ( $R = 0.75$  and  $\text{Adj. } R^2 = 0.54$ ) with stand density measurements in sample plots of semi-dense class. Through multiple regression the results of explanation of variability of dependent variables were improved. Utilizing Ratio3 together with Ratio5 ((ETM4 – ETM5)/ (ETM4 + ETM5)) showed the highest ability to model stand density ( $\text{Adj. } R^2 = 0.75$ ) in semi-dense class. Near results achieved from some other bands in this class and the other ones, too. Regression validation showed that the whole models were statistically valid. Higher spatial resolution satellites data such as SPOT5 and IRS are advised to be examined to improve the results.

## 1. INTRODUCTION

In arid and semi-arid regions, vegetation plays an important role in soil conservation, fluid prevention, underground water nutrition and life continuance. Irregular exploiting of forests and rangelands made serious damages during late time and also treated life cycle.

In order to manage vegetation in these areas it is necessary to gather their correct and updated information. In this relation utilizing different possibilities and techniques such as remotely sensed data is advised.

Satellite data were used in estimation of vegetation vital parameters (Ripple *et al.*, 1991; Cohen & Spies, 1992; Chiao, 1996; Xu *et al.*, 2003; Maselli *et al.*, 2005; Sivanpillari *et al.*, 2006).

In this study estimation of crown area and density of forest stands in arid and semi-arid regions was investigated. Such studies have been implemented in different areas (Satterwhite & Henley, 1987; Leprieure *et al.*, 1996; Hurcom & Harrison, 1998).

Various forest trees and shrubs such as *Pistacia atlantica*, *Pistacia khinjuk*, *Acer monspessulanum*, *Amygdalus* spp. and *Juniperus excelsa* exist in the study area and *Pistacia*, *Acer* and *Amygdalus* types were dominant forest types.

In order to meet the study aim, forest species canopy was qualitatively estimated through strip sampling. In this regard 3 density classes consisting very thin (1-5%), thin (6-25%) and semi-dense (26-50%) were recognized. In each density class, crown area and density of forest species in 30 plots were measured.

Landsat ETM+ data dated 19/May/2000 pre-processed and then orthorectified using 14 GCPs based on Toutin model (Ann., 2001). RMS error was less than half a pixel.

Band ratioing (Hurcom & Harrison, 1998, Leprieur *et al.*, 1996), PCA, Tasselled Cap Transformation (Todd & Hoffer, 1998) and band fusion (Darvishsefat, 2002) performed. Based on climatic conditions in the study area, suitable vegetation indices were achieved to reduce soil reflectance (Hurcom & Harrison, 1998; Karteris, 1990). Some of ratios and vegetation indices indicated in table 2 and the whole list is accessible in Naseri, 2002.

Linear and logarithmic regression relations between quantitative values in sample plots and the relevant spectral values in the original and synthetic bands were investigated as the other investigations (Cohen & Spies, 1992, Xu *et al.*, 2003, Maselli *et al.*, 2005; Sivanpillari *et al.*, 2006). Then considering additional sample plots in each density class, regression validation for the models with  $R^2 > 0.5$  in confidence level of 95% was evaluated (Montgomery & Peck, 1992). When control data locate in prediction distance the regression model is statistically valid.

## 2. MATERIALS AND METHODS

This study was implemented in some parts of forest stands (1800 ha) in National Park of Khabr, Kerman, Iran. This area was situated between 28° 46' 00" to 28° 49' 30" northern latitude and 56° 28' 30" to 56° 37' 30" eastern longitude and 2000 to 2600 meters above mean sea level (figure 1).

<sup>1</sup> Corresponding author

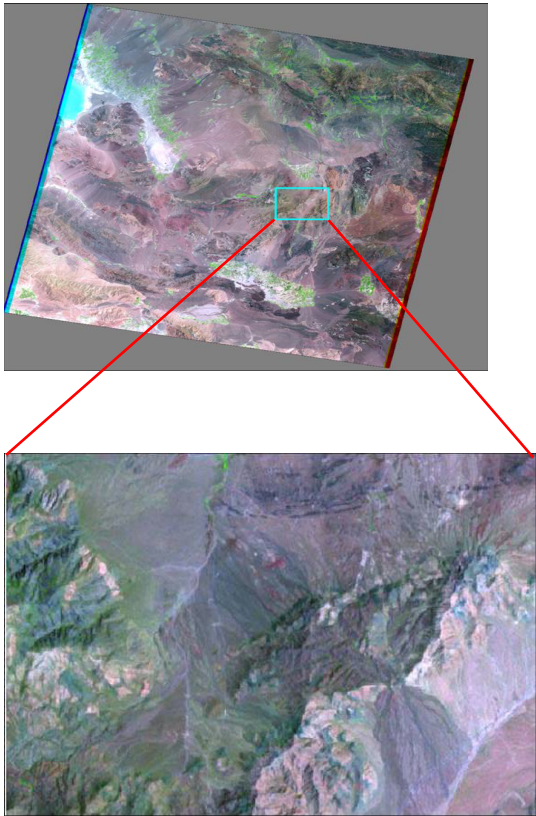


Figure1. Situation of the study area in Iran and in a satellite image frame

3. RESULTS

The best results from simple and multiple regression models possessing the most correlation and determinant coefficients indicated in tables 3 and 4 respectively.

Original / synthetic band	Details
ETM8	ETM+ Pan band
Ratio1	ETM3-ETM2
Ratio2	ETM5/ETM7
Ratio3	(ETM3-ETM1)/ (ETM3+ETM1)
Ratio4	(ETM4-ETM1)/ (ETM4+ETM1)
Ratio5	(ETM4-ETM5)/ (ETM4+ETM5)
SAVI	((ETM4-ETM3) / (ETM4+ETM3+L))(1+L) L = 0, 0.5, 1 for rich, medium and poor vegetation, respectively
PCA1(1,2,3)	First component of PCA for visible bands
PCA1(4,5,7)	First component of PCA for infrared bands
FusionIHS5	Band5 achieved from pan and multispectral bands fusion using Intensity, Hue, Saturation Method
FusionR3	Band3 achieved from pan and multispectral bands fusion using Spectral Response Method

Table2. Synthetic and original bands

Density class	variable	regression model	R	Adj. R <sup>2</sup>	Sig. level
Very thin	NT	NT = -32.225 * LRatio3 + 158.210	0.484	0.207	ns
	CA	CA = - 25.793 * LRatio2 + 149.826	0.072	0.006	ns
Thin	NT	NT = 100.214 * Ratio4- 448.010	0.651	0.403	*
	CA	CA = 224.088 * Ratio4 - 1023.715	0.320	0.070	ns
Semi-dense	NT	NT = - 1.970 * Ratio3 + 255.910	0.748	0.543	**
	CA	CA = 4.535 * Ratio3 - 350.274	0.494	0.217	*

\*, \*\* indicates 1% and 5% significance level, respectively and ns means not significant.

CA= Crown Area (m<sup>2</sup> per plot), NT= Number of Trees and shrubs (density), L= Natural logarithm, R= Correlation Coefficient, Adj. R<sup>2</sup>= Adjusted Determinant Coefficient

Table3. The best simple regression models



Density class	Dependent variable	regression model	Adjusted R <sup>2</sup>	Significance level
Very thin	NT	NT = 0.097128 * FusionIHS5 - 0.31421 * FusionR3 + 43.789 * LETM8 – 182.79	0.7284	*
Thin	NT	NT = - 0.295 * Ratio1 + 1.203 * Ratio3 - 1.061 * Ratio5 + 7.170	0.7316	*
Semi-dense	NT	NT = - 126.46* LPCA1(1.2.3 ) + 137.45 * LPCA1(4.5.7 ) – 184.78 * LSAVI + 796.13	0.7409	**
	LNT	LNT = 4.167 * LRatio3 – 15.082 * LRatio5 + 54.525	0.7504	**

\*, \*\* indicates 1% and 5% significance level, respectively and ns means not significant.  
NT= Number of Trees and shrubs (density), L= Natural logarithm, R<sup>2</sup>= Determinant Coefficient  
Table4. The best multiple regression models

Since determinant coefficients of simple regression models were less than 0.5, except for 1 model, validation was only performed for multiple regression models (table 5).  
Based on the results achieved, the whole regression models were statistically valid.

4. CONCLUSIONS

Based on the results, among crown area and species density, as the two favoured parameters, the best regression models were concluded for the second one. Multiple regression in comparison with simple regression improved the results and the relations between measured parameters in sample plots and their spectral values in ETM+ data were some significant and some highly significant.  
Reflection of forest species is mainly related to trees crown. In this research as in the other ones (Dewulf & Goosens, 1990; xu *et al.*, 2003) when canopy was increased, significant relations were increased too.  
On the other hand, reflection is indirectly related to species density. Hence it is expected that regression models are more significant for crown area rather than for species density. Irregularly, in this research, as in a similar one (Danson, 1987) the opposite result was achieved. In this regard it can be said that in dense forests, only the upper part of trees crowns

observed by sensor. On the other hand, a large number of trees in lower strata not observed. Thus, it is possible that a significant relation between density (no. of trees) and reflection is not obtained.

Density class	Estimated parameter	Control plots no.	Prediction distance for confidence coefficient of 95%	Estimated value	Measured value
Very thin	NT	1	-0.629 : 5.997	2.3903	2
		2	1.199 : 7.891	4.1898	3
		3	1.668 : 8.354	5.0742	7
		4	5.012 : 11.876	8.4335	9
		5	3.435 : 10.080	6.4667	9
Thin	NT	1	-3.483 : 12.929	4.6000	6
		2	-1.679 : 14.225	6.1400	4
		3	10.272 : 33.593	21.8000	20
		4	0.136 : 23.216	11.5600	13
		5	-0.552 : 17.290	8.2450	14
Semi dense	NT	1	-1.091 : 19.481	7.7200	9
		2	5.561 : 25.570	14.2400	16
		3	12.169 : 43.219	25.7600	29
		4	19.487 : 49.342	33.5600	30
		5	23.142 : 46.604	34.0600	32
	LNT	1	1.834 : 2.998	2.3696	2.485
		2	1.646 : 2.821	2.1510	2.302
		3	2.495 : 3.638	2.9635	2.890
		4	2.674 : 3.830	3.1562	3.296
		5	2.843 : 4.109	3.3432	3.466

NT= Number of Trees and shrubs (density) L= Natural logarithm

Table5. Validation results for multiple regression models

In contrast, in areas such as the study area with sparse forests, not only the upper parts of trees but also most of the parts of them are observed by sensor. Therefore, it seems that crown area may not show the whole reflection. Also each of the trees separately is at the field of view of the sensor. So it can be concluded that increasing in species density makes increasing in foliage observed and reflection achieved and consequently significant relations between forest species density and spectral values in satellite data may be deduced.

Based on the results, ETM+ data showed a relative potential for estimating forest species density in the study area. Different similar researches indicated capability of satellite data in estimating vegetation quantitative parameters (Cohen & Spies, 1992; Chiao, 1996; Xu *et al.*, 2003). In This regard, using satellite data with better spatial resolution such as spot5 and IRS is advised.

5. REFERENCES

Anonymous, 2001. Satellite ortho and DEM component, PCI Geomatics, Version 8.2, PCI Geomatics, Canada.  
Chiao, K.M., 1996. Comparisons of three remotely sensed data on forest crown closure and tree volume estimations, In: *The International Archives of photogrammetry and Remote Sensing, 31 (B7)*, pp. 123-130.

- Cohen, W.B. & Spies, T.A., 1992. Estimating structural attributes of Douglas – Fir/Western Hemlock forest stands from Landsat and SPOT imagery, *Remote Sensing Environment*, (41), pp. 1-17.
- Danson, F.M., 1987. Preliminary evaluation of the relationships between SPOT-1 HRV data and forest stand parameters, *International Journal of Remote Sensing*, 6(10), pp. 1571-1573.
- Darvishsefat, A.A., 2002. Data fusion.Proceeding of Geomatic 81 conference, National Cartographic Center of Iran.,Tehran,Iran.
- De Wulf, R.R. & Goossens, R.E. , 1990. Extraction of forest stand parameters from panchromatic and multispectral SPOT-1 data, *International Journal of Remote Sensing*, 11(9), pp. 1571-1588.
- Huang, Ch., Yang, L., Homer, C., Coan, M. , Rykhus, R. Zhang, Z., Wylie, B., Hegge, K., & Zhu, Zh. , 2001. Synergistic use of FIA Plot data and landsat 7 ETM+ images for large area forest mapping, proceeding of the thirty fifth annual Midwest forest mensurationists meeting and the third annual forest inventory and analysis symposium, Traverse City, MI. USA,  
<http://landcover.usgs.gov/pdf/synergistic.pdf>
- Hurcom, S.J. & Harrison, A.R. , 1998. The NDVI and spectral decomposition for semi-arid vegetation abundance estimation, *International Journal of Remote Sensing*, 19(16), pp. 3109-3125.
- Karteris, M.A., 1990. The utility of digital Thematic Mapper data for natural resources classification, *International Journal of Remote Sensing*, 11(9), pp. 1589-1598.
- Leprieur, C., Y.H. Kerr & J.M. Pichon, 1996. Critical assessment of vegetation indices from AVHRR in a semi-arid environment, *International Journal of Remote Sensing*, 17(13), pp. 2549-3798.
- Maselli, F., Chirici, G., Bottai, L., Corona, P & Marchetti, M., 2005. Estimation of Mediterranean forest attributes by the application of K-NN procedures to multitemporal Landsat ETM+ images, *International Journal of Remote Sensing*, 26, pp. 3781-3797.
- Montgomery, D. C., & Peck, E.A. , 1992. Introduction to linear regression analysis, 2<sup>nd</sup> Ed., John Wiley & Sons Inc., New York.
- Naseri, F., 2002. Classification of forest types and estimation of their quantitative parameters in arid and semi-arid regions using satellite data, Ph.D. Thesis, Faculty of Natural Resources, University of Tehran, Iran.
- Ripple, W.J., Wang, S. , Isaacson, D.L. & D.P. Paine, 1991. A Preliminary comparison of Landsat Thematic Mapper and SPOT-1 HRV multispectral data for estimating coniferous forest volume, *International Journal of Remote Sensing*,12(9), pp. 1971-1977.
- Satterwhite, M.B. & Henley, J.P. , 1987. Spectral characteristics of selected soils and vegetation in northern Nevada and their discrimination using band ratio techniques, *Remote Sensing of Environment*, (23), pp. 155-175.
- Sivanpillari, R., Smith, C. T., Srinivasan, R., Messina, M. G., Wu, X. B., 2006. Estimation of managed loboly pine stand age and density with Landsat ETM+ data, *Forest Ecology and management*, 223, pp. 247-255.
- Todd, S.W. & Hoffer, R.M. , 1998. Responses of spectral indices to variation in vegetation cover and soil background, *Photogrammetric Engineering & Remote Sensing (PE & RS)*, 64(9), pp. 915-921.
- Xu, B., Gong, P. & Pu, R., 2003. Crown closure estimation of oak savannah in a dry season with Landsat TM imagery: comparison of various indices through correlation analysis, *International Journal of Remote Sensing*, 24(9), pp. 1811-1822.  
<http://www.cnr.berkeley.edu/~bingxu/pub/closure.pdf>

# THE USE OF SPECTRAL SIGNATURES IN EXTRACTING INFORMATION FROM WATER QUALITY PARAMETERS IN THE LAKE URMIA, IRAN

**Seyd Kazem Alavipanah**

*University of Tehran, Faculty of Geography, Tehran, Iran [salavipa@ut.ac.ir](mailto:salavipa@ut.ac.ir)*

**Reza Amiri**

*Payame Noor University, Department of Geography, Hashtrud, Iran [amiri.reza@Gmail.com](mailto:amiri.reza@Gmail.com)*

**Kamal Khodaei**

*ACECR, Research Institute of Applied Science, Tehran, Iran*

## Abstract

Lake Urmia, the second hyper-saline lake in the world, because of its climatic and economical importance has created a populated region in Iran, and in return its fragile ecosystem has been affected by the presence of this growing population. The economical and social importance of the connection between the population centers in both sides of the lake has encouraged the construction of a causeway; which consequently has been divided the lake into northern and southern parts. Thus, the navigational and hydrological links have been limited to a gap. The aim of this paper is to study the impacts of the division of the lake in water quality parameters such as salinity and sediment concentration and the efficiency of the implemented gap in connecting two parts using remotely sensed data. The multi-temporal Landsat images were used in order to observe the spatial and temporal variations of water quality parameters. The preliminary examinations of the image data have shown that some patterns could be detected through using image composites. To examine the spatial variability of the parameters, certain transects were drawn over reflective and thermal bands and then the spectral signatures were analyzed. Some changes in the spectral behavior of water were studied by the selection of homogenous regions of the lake from both sides of the causeway. The images were closely examined to follow the changes using image processing techniques. The study of spectral signatures of the selected regions of different times revealed a significant difference between two sides of the causeway having increased spatial variability. Thus, it can be concluded that the observed differences of two sections in under-study parameters could be attributed to the blocking effect of the causeway and inefficiency of the gap in preserving the link. The crucial importance of the lake in the region and its endangered ecosystem prompts for continuous study and monitoring of the parameters using remote sensing.

**Key words:** Lake Urmia causeway, Landsat TM, water quality parameters, salinity, sedimentation

## 1. Introduction

The economical and social importance of the connection between the population centers in both sides of Lake Urmia (Fig. 2) encouraged the construction of a road over it. In 1979, one of the country's largest national projects was launched to facilitate road and rail transportation. In order to preserve navigational and hydrological link between the north and south parts of the lake an opening was implemented but may not be successful in maintaining proper linkage. The causeway over the lake has caused changes in its natural conditions. These changes affected the sedimentation pattern inside the lake as well as the spatial pattern of surface temperature in the lake.

The lake has been the subject of several studies focusing mainly on the chemistry, geology, limnology, resource assessment and sedimentology of the lake based on field samplings. Kelts and Shahrabi (1986) examined the sedimentary record of the lake and

projected the evolutionary steps of the lake. They found evidences of historical water-level fluctuations. Comparing the consequences of the causeway in Lake Urmia with those of earthworks in Great Salt Lake in Utah, USA, Nazariha (2002) concluded that the north part of the lake will become more saline. Ahmadi (2002) studied the Physiochemical characteristics of samples of Lake Urmia water from five stations in the north and south of the causeway. The results showed that the electrical conductivity in the north part is greater than south part. Thus, he concluded that the dissolved salt is greater in the north part. He argued that the north part of the Lake nourishes much from saline waters than the south part which nourishes much from opening. Alipour (2006) has done a systematic study of the geochemistry of the lake Based on regular samples from the lake.

Remote sensing by providing a dense grid of information has been used to aid in-situ point observations of hydrologic variables. Remote sensing has been used to monitor spatial extent, organic/inorganic constituents, depth, and temperature of water in rivers, reservoirs, lakes, seas, and oceans (Jensen, 2000). The total radiance recorded by a remote sensor from a water body is a function of electromagnetic energy from four sources (Fig. 1).

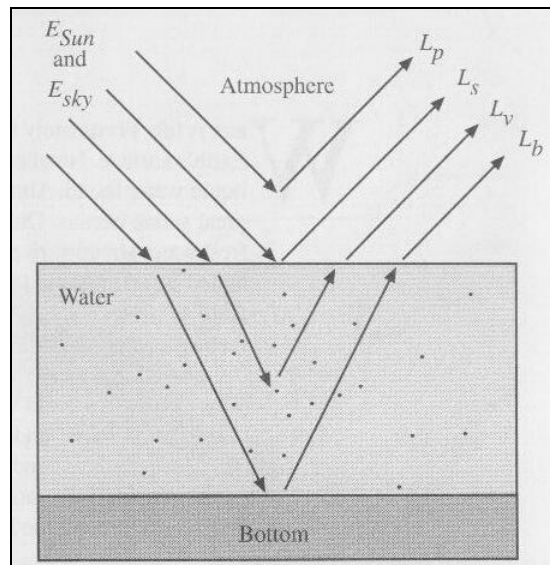


Fig.1. Four sources of electromagnetic energy recorded by remote sensor (After Bukata et al., 1995)

Water bodies receive irradiance from the sun ( $E_{sun}$ ) and atmosphere ( $E_{sky}$ ). The total radiance exiting from a water body towards the remote sensor is a function of the radiance from atmosphere scattering ( $L_p$ ), water-surface radiance ( $L_v$ ), and radiance from the bottom ( $L_b$ ) of the water body (Jensen, 2000).

There has been a significant amount of research to develop methods for quantitative measurement of water quality parameters by means of remote sensing technology. Carpenter and Carpenter (1983) used MSS data to study water quality parameters of fresh-water lakes located on south-east Australia. Khorram and Cheshire (1985) investigated the feasibility of providing water salinity map using MSS data. Bhrgava and Mariam (1992) studied the combined effect of water salinity and solid suspended sediments on the spectral reflection of water in a lab and concluded that the

reflection level is positively correlated with the density of suspended substances and negative correlation with salinity level. Thus, reflection decrease with suspended minerals decrease and salinity increase. Using Landsat TM data and field observations, Serwan (1993) studied water quality parameters like solid suspended substances, salinity, and temperature and modeled the relationship between TM bands and water quality parameters. The model was used to predict and provide map of water quality parameters.

Remote sensing has not been used widely in the study of Lake Urmia. Barzegar and Sadeghian (1991) used MSS, RBV and SPOT image data to investigate the effect of the causeway on the general circulation of the water body between 1972 and 1986. They concluded that the Highway had caused changes in the natural water circulation and hence the process of sedimentation will lead to possible blocking of the gap by deposition of sediments in the opening.

The purpose of this study is to examine the impact of construction of Kalantary highway over Lake Urmia using remote sensing observations and to provide a background for the constant monitoring of the lake's fragile ecosystem by means of this technology

## 2. Study Area

Lake Urmia (a protected biosphere reserve) is the second large hyper-saline lake in the world and the largest inland lake in Iran. This sodium-chloride lake has extended between 37° 40' 0" N and 45° 30' 0" E over an area of about 52000 km<sup>2</sup> in the semi-arid region of the North-West of Iran and has created a natural barrier between two populated provinces of East and West Azerbaijan and their bustling capitals, Tabriz and Urmia. Geologically, the lake is known to be of tectonic origin. The lake receives water from 13 rivers of varied length. The water of the lake has been classified as Na-Mg-SO<sub>4</sub>-CL type (Eugster, 1980). The lake shows an annual fluctuation of about 1 m due to high evaporation during the summer. In the stressed environment of the lake, species are limited to *Artemia Salina* and *Olena*. The hydrologic link between northern and southern parts was maintained by the 15 km wide section which has been narrowed down to a 1.5 km opening.

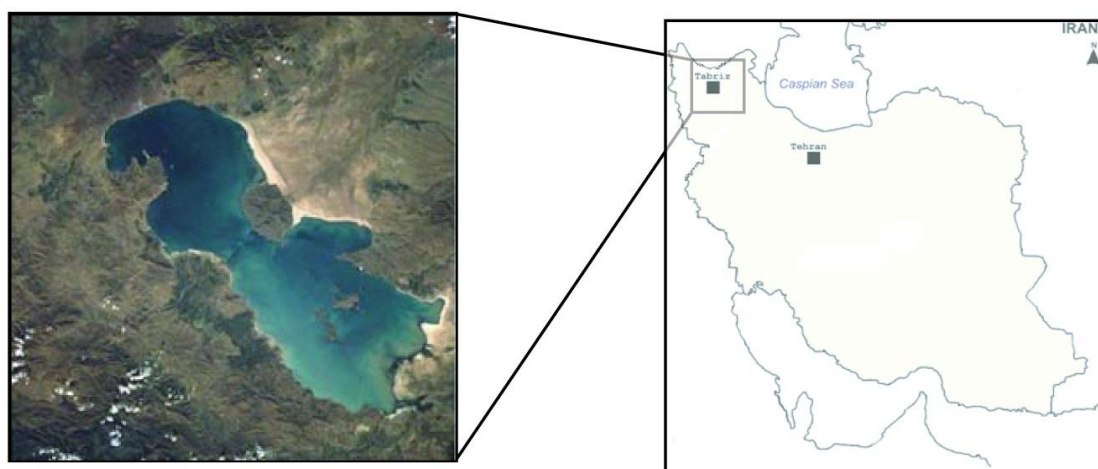


Fig.2. the study area

## 3. Data Set

Multitemporal Landsat TM image data acquired on August 1990 and May 1998 were used in this study. Landsat TM provides multispectral data in 7 spectral bands in



visible, near infrared and thermal regions of electromagnetic spectrum with a resolution of 30 m in VNIR and 120 m in thermal bands.

#### 4. Methods

For investigation of water quality parameters and the impacts of highway construction on the distribution of these parameters, several image processing methods were adopted. False color composites (RGB 3-1-7), contrast stretching, PCA and NDVI were used to detect the suspended load diffusion pattern over the lake. To examine the effect of the causeway in distribution pattern of the suspended substances, spectral profiles were used in the different sections of the Lake. In order to evaluate the information content of different TM spectral bands for recognizing level and distribution of suspended substances and the salinity, some sample image regions from different areas of the lake were taken. These regions were used to extract statistical information in order to compare different bands. Band 3 was selected as the most informative band by calculating the mean value of pixels in each region and as the most sensitive band to the changes in water quality parameters in the lake (Fig. 3). Based on the above results, band 3 was used for determining the proportional salinity distribution and thermal data of band 6 was used to investigate the spatial distribution of the surface temperature in both sides of the causeway by means of spectral profiles.

#### 5. Results and Discussion

*5.1. Spectral behavior of solid suspended substances in water and the impact of the causeway on their distribution patterns.*

Fig. 3a shows FCC (7-1-3) of 1998 Image. It is obvious that considerable amount of suspended materials is transported to the lake by Adji-Chay River and Shahi Island drainage systems from east and Shahar-Chay and Barandoz-Chay Rivers from the west, which may be evidences of a rain prior to satellite imaging.

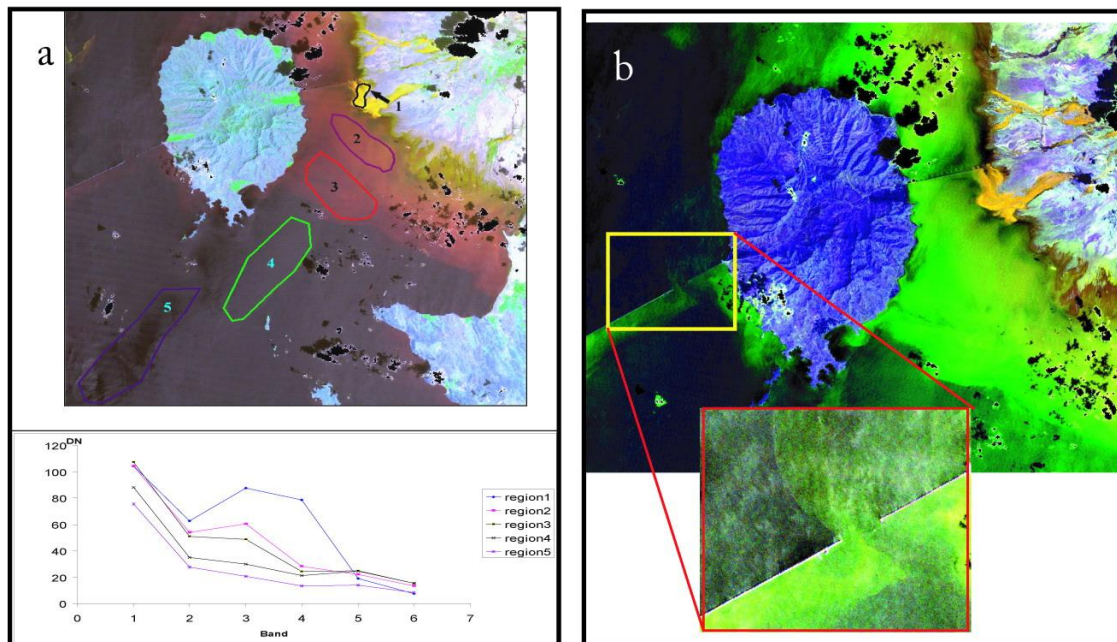


Fig.3. Selected regions for investigating the sensitivity of TM bands to water quality parameters (a), the diffusion of suspended load around the causeway gap (b).

Dense water of the lake prevents solid suspended substances from quick deposition which is useful in recognition of causeway impacts on the natural circulation of the water in the lake. Fig. 3 (b) shows that deposition direction in eastern beach is northward and in western beach is eastward parallel to the causeway. Eastward moving materials have been depositing in the southern side of the western section of the causeway and some find their way through the gap to the northern part of the lake. The causeway seems to have a significant role in creating the above mentioned depositing pattern.

A spectral profile was provided crossing the causeway (Fig. 4a). This profile illustrates a clear reflectional distinction between the south and north parts and depicts that the causeway prevents full connection. Fig. 4b shows the spectral profiles parallel to the Tabriz-Saray road. Because of the northward movement of the load it is possible to distinguish the openings in this part of the road.

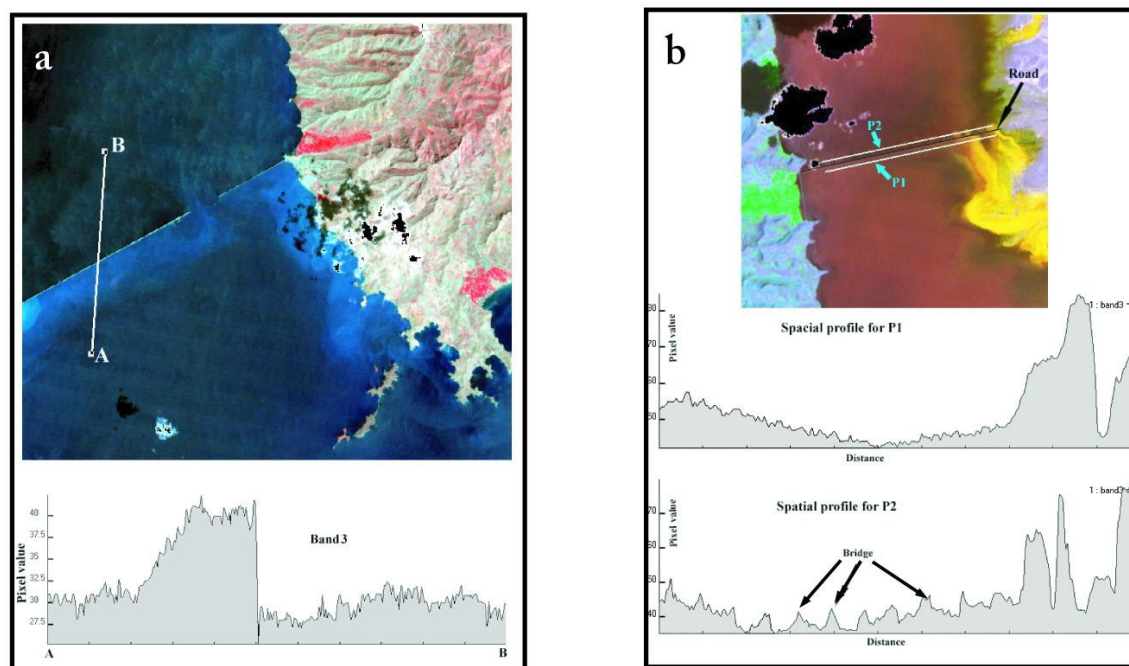


Fig.4. Spectral profile crossing the causeway depicting the different reflection in both sides (a), Spectral profiles along the Tabriz-Saray road from south (P1) and North (P2) parts of the Lake, the number of openings are clear

### 5.2. Causeway impacts on the distribution of salinity.

TM6 thermal infrared and TM3 spectral profiles was provided along the AB transect (Fig. 5a). Band 6 thermal data also shows remarkable differences in both north and south parts which is another clue for causeway impacts on lake's water circulation and for the deficiency of the gap. The profile depicts a gradual reduction in the reflection of the water body in the south-to-north direction, with abrupt fall and anomalies around the causeway. As a result of water-level decrease the salinity level is high and affected the spectral reflection of the 1990 TM. According to Bhargava and Mariam (1992) the spectral reflection has converse relation with water salinity. South-to-north reduction in

the spectral reflection of TM3 can be attributed to the sudden increase in the salinity level which can be due to blocking effect of the causeway. By field sampling from Lake's water and finding relations between TM3 and salinity sample levels, a map of salinity can be provided. However; field sampling is necessary for calibration of satellite data in order to estimate the salinity level and to provide lake's water salinity map.

Fig. 5b shows the provided spectral profile of the bands (5, 4, and 3) along the AB transect. Reflectional difference in the estuary of Adji-Chay River is obvious. The difference of reflected energy from the water body along transect is notable, the low values near the Adji-Chay delta could be related to the shallow water, the reflection from the bottom of the lake and sediment load. As thermal data is different from reflective data in nature (Prakash, 1999), thus; further investigations on both thermal and reflective bands are necessary. Alavipanah (1999a and 1999b) showed that there is a reverse relationship between NDVI values and thermal band data.

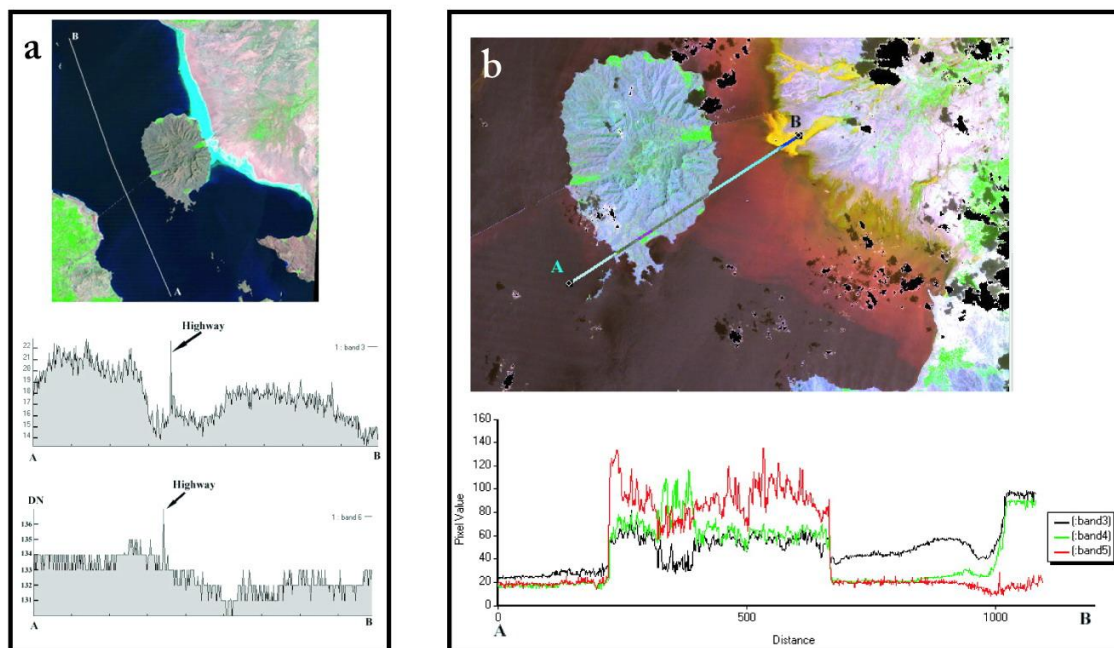


Fig.5. Spectral profile along the AB transect showing the different behavior in the estuary of the Adji-Chay (a), South-to-North spectral profile of TM3 and TM6 showing the difference of the both sides (b)

## 6. Conclusion

- The causeway had restricted hydraulic connections between north and south parts of the lake.
- Landsat TM data is effective for historical study of water quality parameters of the lake. However; field sampling is necessary for calibration data for quantitative applications.
- TM3 and TM6 provide better information for the study of suspended materials, salinity and their distribution.
- Transported suspended load is mostly depositing on the south edge of the western section of the causeway.
- The spectral profiles from both reflective and thermal bands depict south-to-north changes, with abrupt changes near the causeway.

According to the attained results from sediment density and salinity level impacts on spectral reflection and the possible future problems related to the causeway impacts on the changes of the lake system, we suggest that:

- The water quality parameters should be continually controlled.
- The water quality parameters should be studied and the human-induced potential impacts on Urmia Lake's system should be identified and,
- The ecosystems of the lake should be studied through recognizing the interactive impacts among biological, chemical and hydrological characteristics.

### **Acknowledgement**

The authors acknowledge the financial support of the University of Tehran to this research. The authors also would like to acknowledge Iranian Space Agency (ISA) for providing satellite images.

### **References**

- Ahmadi, M. R. (2002). Artemia and the constructed bridge over Lake Urmia. The congress on Lake Urmia causeway and the environment, Tehran.
- Alavi Panah, S. K., Goossens, R. De Dapper, M., (1999a). Study of soil salinity in the Ardakan area, Iran, based upon field observations and remote sensing, G.J.A. Nieuwenhuis, R. A. Vaughan and M. Molenaar (ed.), Operational Remote Sensing for Sustainable Development, Proceeding of 18th EARSeL Symposium, Enschede Netherlands, 11-14 May, 1998, 419-425.
- Alavi Panah, S. K., Goossens, R., (1999b). The role of TM thermal band in describing the state/stress of vegetation in the Iranian Deserts, Proceedings of remote sensing in the 21st Century Economics and Environmental applications, 19th EARSeL Symposium, University of Valladolid, Spain, 31 May – 2 June, 1999, 31-37.
- Barzegar, f. and I. Sadeghian (1991). Study of highway construction effects on sedimentation process in Lake Urmia (NW Iran) on the basis of satellite data. Geocarto International, 3: 63-65
- Bhargava, D.S., and Mariam, D. W., (1992). Cumulative effects of salinity and sediment concentration on reflectance measurements, INT. J. Remote Sensing , 13, 2151-2159.
- Carpenter, D. J., and Carpenter, S. M., (1983). Modelling inland water using Landsat data. Remote Sensing of Environment, 13, 345-352.
- Eugster, P., (1980). Geochemistry & Evaporite Lacustrine Deposits. Ann. Rep. Earth Plant Sci-pp: 33-36.
- Jensen, J. R., (2000). Remote Sensing of the Environment, an earth resources perspectives. Upper Saddle River, N. Y., Prentice Hall, Inc., 544 pp.
- Khorram, S., and Cheshire, H. M., (1985). Remote sensing of water quality in the Mense River estuary, North Carolina, Photogrammetric Engineering and Remote Sensing, 51, 329-341
- Nazariha, M. (2002). The comparison between consequences of construction of causeway in Lake Urmia, Iran and The Great Salt Lake, Utah, USA. The congress on Lake Urmia causeway and the environment, Tehran.
- Prakash, A., (2000). Thermal Remote Sensing Concepts issues and applications, International Archives of Photogrammetry and Remote Sensing, Vol. XXXIII, Part B, Amsterdam 2000.

- Serwan, M. J. Baban, (1993). Detecting water quality parameters in the Norfolk Broads, U. K., using Landsat imagery, INT. J. Remote Sensing, 14, 1247-1267
- Alipour, S. (2006). Hydrogeochemistry of seasonal variation of Urmia Salt Lake, Iran. Saline Systems, 2:9, 1746-1448.
- Kelts K, Shahrabi M. (1986). Holocene sedimentology of hyper saline Lake Urmia, northwestern Iran. Paleogeography, Paleoclimatology and Paleoecology. 54:105-130.



The International Archives of the Photogrammetry, Remote Sensing and Spatial Information Sciences, Vol. 34, Part XXX

## SLIGHT AND MODERATE SALINE AND SODIC SOILS CHARACTERIZATION IN IRRIGATED AGRICULTURAL LAND USING MULTISPECTRAL REMOTE SENSING

A. BANNARI<sup>1</sup>, A.M. GUEDON<sup>1</sup>, A. EL-HARTI<sup>2</sup>, F.Z. CHERKAoui<sup>3</sup>, A. EL-GHMARI<sup>2</sup> AND A. SAQUAQUE<sup>4</sup>

<sup>1</sup> Remote Sensing and Geomatics of Environment Laboratory, Department of Geography, University of Ottawa, Ottawa (Ontario) K1N 6N5 Canada, Phone (613) 562-5800 (Ext. 1042), Fax (613) 562-5145, Email: abannari@uottawa.ca

<sup>2</sup> Laboratoire de Télédétection et des SIG, Faculté des Sciences et Techniques, Béni-Mella, Morocco

<sup>3</sup> Laboratoire de Télédétection et SIG, Office Régional de Mise en Valeur Agricole du Tadla (ORMVAT), Fkih-Ben-Salah, Morocco

<sup>4</sup> Reminex, Managem Groupe Minier de l'ONA, Marrakech, Morocco

### Commission VI, WG VI/4

**KEY WORDS:** Salinity, Sodicty, Electrical conductivity, Remote sensing, Spectral indices, spectroradiometric data, EO-1 ALI sensor.

#### ABSTRACT:

Around the world, especially in semi-arid regions, millions of hectares of irrigated agricultural land are abandoned each year because of the adverse effects of irrigation, mainly secondary salinity and sodicity. Accurate information about the extent, magnitude, and spatial distribution of salinity and sodicity will help create sustainable development of agricultural resources. In Morocco, south of the Mediterranean region, the growth of the vegetation and potential yield are limited by the joint influence of high temperatures and water deficit. Consequently, the over use of surface and ground water, coupled with agricultural intensification, generates secondary soils salinity and sodicity. This research focuses on the potential and limits of the Advance Land Imaging (EO-1 ALI) sensor spectral bands for the discrimination of slight and moderate soils salinity and sodicity in the Tadla's irrigated agricultural perimeter, Morocco. In order to detect affected soils, empirical relationships (second order regression analysis) were calculated between the electrical conductivity (EC) and different spectral salinity indices. To achieve our goal, spectroradiometric measurements (350 to 2500 nm), field observation, and laboratory analysis (EC of a solution extracted from a water-saturated soil, and soil reaction (pH)) were used. The spectroradiometric data were acquired using the ASD (*Analytical Spectral Device*) above 28 bare soil samples with various degrees of soils salinity and sodicity, as well as non-affected soils. All of the spectroradiometric data were resampled and convolved in the solar-reflective spectral bands of EO-1 ALI sensor. The results show that the SWIR region is a good indicator of, and are more sensitive to, different degrees of slight and moderate soil salinity and sodicity. In general, relatively high salinity soils show higher spectral signatures than do sodic soils and non-affected soils. Also, strongly sodic soils present higher spectral responses than moderately sodic soils. However, in spite of the improvement of EO-1 ALI spectral bands by comparison to Landsat-ETM+, this research shows the weakness of multi-spectral systems for the discrimination of slight and moderate soils salinity and sodicity. Although remote sensing offers a good potential for mapping strongly saline soils (dry surface crust), slight and moderately saline and sodic soils are not easily identified, because the optical properties of the soil surfaces (color, brightness, roughness, etc.) could mask the salinity and sodicity effects. Consequently, their spatial distribution will probably be underestimated. According to the laboratory results, the proposed Soils Salinity and Sodicty Indices (SSSI) using EO-1 ALI 9 and 10 spectral bands offers the most significant correlation (52.91 %) with the ground reference (EC). They could help to predict different spatial distribution classes of slight and moderate saline and sodic soils using EO-1 ALI imagery data.

#### 1. INTRODUCTION

The increased use of ground and surface water coupled with the agricultural intensification in the Tadla's irrigated perimeter, Morocco, are the major cause of soil degradation through secondary soil salinity and sodicity. It is common that both saline and sodic conditions occur together.

Sodicty represents the amount of exchangeable sodium (Na+) in water and in soil. Sodicty in soils has a strong influence on the soil structure. Dispersion occurs when the clay particles swell strongly and separate from each other on wetting. On drying, the soil becomes dense, cloddy and without structure (Charters, 1993; Ford *et al.*, 1993; Sumner *et al.*, 1998). Sodic soils have a pH > 8.2 and a preponderance of carbonate and sodium bicarbonate (Richards, 1954).

Salinity refers to the amount of soluble salt in soil, such as sulphates (SO<sub>4</sub>), carbonates (CO<sub>3</sub>) and chlorides (Cl). Strongly saline soils often exhibit a whitish surface crust when dry. The solubility of calcium sulphate, also called gypsum (CaSO<sub>4</sub>), is used as the standard for comparing salinity levels. Unlike sodicty, water movements influence salinity. It occurs in areas where saline ground waters are very close to or at the ground surface, and evaporation exceeds precipitation (Dehaan and Taylor, 2002). In irrigated lands, salinity occurs when salts are concentrated in soils by the evaporation of freestanding irrigation water. The major causes are a combination of poor land management and crude irrigation practices. These practices cause changes in soil and vegetation cover and ultimately loss of vegetation and agricultural productivity. Soil salinity is measured by ground-based geophysics, measurements of soil electrical conductivity (EC) using soil pastes, and water ex-

The International Archives of the Photogrammetry, Remote Sensing and Spatial Information Sciences, Vol. 34, Part XXX

tracts. Saline soils have an  $EC > 4 \text{ dS m}^{-1}$  at  $25^\circ\text{C}$  and a  $pH < 8.2$  (Richards, 1954).

Knowing when, where and how salinity and sodicity may occur is very important to the sustainable development of any irrigated production system (Al-Khaier, 2003). Remedial actions require reliable information to help set priorities and to choose the type of action that is most appropriate in each situation (Metternicht and Zinck, 2003). Ground-based electromagnetic measurements of soil EC are generally accepted as the most effective method for quantification of soil salinity (Norman *et al.*, 1989; cited in Dehaan and Taylor, 2002). Unfortunately, these methods are expensive, time consuming, and need considerable human resources for land surveying. Moreover, the dynamic nature of soil salinity and sodicity in space and time makes it more difficult to use conventional methods for comparisons over large areas (IDNP, 2002). A major challenge of remote sensing, as a potential alternative technique, is to detect different levels of soil salinity and sodicity (Fraser and Joseph, 1998; Taylor *et al.*, 1994). In fact, a large variety of remote sensing techniques have been used for identifying and monitoring salt-affected zones, including aerial photos, spectroradiometric measurements, multispectral, hyperspectral, passive and active microwave images (Chaturvedi *et al.*, 1983; Singh and Srivastav, 1990; Hick and Russel, 1990; Taylor *et al.*, 1996; Metternicht, 1998; Dehaan and Taylor, 2002; Metternicht and Zinck, 2003).

The objective of this research is to analyze, for the first time, the potential and limits of the Advance Land Imaging (EO-1 ALI) sensor spectral bands for the discrimination of slight and moderate secondary soil salinity and sodicity in the Tadla's irrigated agricultural perimeter, Morocco. Empirical relationships (second order regression analysis) were calculated between the EC and different spectral salinity indices to detect slight or moderate soil salinity and sodicity. In order to achieve our goal, spectroradiometric measurements (350 and 2500 nm), field observations, and laboratory analysis (EC of a solution extracted from a water-saturated soil, and soil reaction (pH)) were used. The spectroradiometric data were acquired during the summer season using the ASD (*Analytical Spectral Device*) above 28 bare soil samples with various levels of salinity and sodicity, as well as non-affected soils. All of the spectroradiometric data were resampled and convolved to match the solar-reflective spectral bands of the EO-1 ALI sensor using the updated Herman transfer radiative code, H5S (Teillet and Santer, 1991).

## 2. MATERIAL AND METHOD

### 2.1. Study site

The irrigated agricultural land of the Tadla region is one of the most important in Morocco. It is situated 30 km from the city of Béni-Mellal, at foot of the middle Atlas Mountains, and about 200 km south-east of Casablanca ( $32^\circ 21' \text{ N}$ ,  $6^\circ 21' \text{ W}$ ; Figure 1). The primary crops are grains, legumes and sugar beets. Covering an area of  $3600 \text{ km}^2$  and being at an average altitude of 400 m, the Tadla plain is bordered to the north by the phosphate plateau, to the south by the middle Atlas Mountains of Béni-Mellal, and to the east it narrows as it follows the Oum-El-Rbia river. The river divides the irrigated perimeter into two sub-perimeters with different hydrological and hydrogeologic characteristics: Béni-Amir and Béni-Moussa (Hammani *et al.*, 2004; Bellouti *et al.*, 2002). The sub-perimeter of Béni-Moussa has been irrigated since 1954 with good quality water from Bin-El-Ouidane dam ( $0.3 \text{ g l}^{-1}$  of calcite, halite and gypsum).

Béni-Amir has been irrigated since 1938 by water from Oum-El-Rbia river, and show a salinity level of  $2 \text{ g l}^{-1}$  (mostly calcite and halite). Historically, the Tadla's irrigated perimeter has gone through two periods in the evolution of its water resources. The first period, from 1938 to 1980, was characterized by an abundance of surface water. The second period started in 1981 with a persistent drought that continues to the present day, and is defined by a large water shortage (Hammani *et al.*, 2004). Indeed, because of the impact of climate change (higher temperatures and water deficit), with its average annual rainfall under 350 mm and an average annual evapotranspiration of 1800 mm, the region has become semi-arid. It shows the characteristics of vulnerable Mediterranean landscapes with respect to the processes of soil impoverishment and environmental degradation. Consequently, recourse to underground water resources has become essential, even though the water qualities are poor. Increasing ground water use causes soil salinity and sodicity to become more pronounced in important areas of the Tadla plain (Debbbarh and Badraoui, 2002).

### 2.2. Soils sampling and laboratory analysis

Four different soil classes characterize the Tadla irrigated perimeter. The "iso-humiques" class, which contains medium brown subtropical soils, saline and saline-sodic brown subtropical soils, and medium chestnut soils. This class is the most dominant in the perimeter, representing about 83 % of soils. The class of "calcimagnésique" soils includes brown limestone's (11%), and "rendzini-forme" soils. The class of "feralites" soils with iron sesquioxides and the hydro-morphs soils class are poorly evolved (Bellouti *et al.*, 2002).



Figure 1: Study site, Tadla's irrigated agricultural perimeter (Béni-Mellal, Morocco)

Soils data collection was carried out during the dry season, between August 25 and September 5 2005, in the Tadla's irrigated agricultural perimeter. The soil sampling data consisted of 28 samples which were selected on the basis of the spatial representativeness of the major soil types, and various degrees of salinity and sodicity (Table 1). Samples were taken from the soils upper layer (5 cm depth). Observations and remarks about each sample (color, brightness, texture, etc.) were noted. The location of each point was recorded with a global positioning system (GPS) unit, and photographed using a 35 mm digital camera equipped with a 28 mm lens.

The laboratory analyses consisted of EC extracted from a soil with a water-saturated past, and soil reaction (pH). These elements were analyzed in the laboratory using the current interna-

tional standards methods in soil science (Baize, 1988). Based on the results of our analyses, and according to Metternicht and Zinck (1997), we established three salinity classes using EC (non saline: 0 to 4 dS m<sup>-1</sup>, slight: 4 to 8 dS m<sup>-1</sup>, and moderate: 8 to 16 dS m<sup>-1</sup>), and three sodicity classes using pH (slight: 7 to 8 pH, moderate: 8 to 8.5 pH, and strong: 8.5 to 9 pH). Seven informational classes resulted from the combination of salinity and sodicity classes (Table 1).

Salinity & Sodicity Class	Soil	EC	pH
Moderate salinity & Slight sodicity	4''	8.28	8.0
	7	11.06	7.8
	9	11.19	8.2
	11	10.42	8.0
	18	9.68	8.0
Moderate salinity & Moderate sodicity	17	14.58	8.1
Slight salinity & Moderate sodicity	10	5.83	8.1
	21	6.17	8.0
Slight salinity & Strong sodicity	16	5.87	8.5
	22	4.2	8.68
Non saline & Slight sodicity	3'	0.97	8.0
	5	0.85	8.0
	6	1.72	8.0
	8	3.33	7.8
	12	2.22	8.0
	14	1.76	8.0
	24	0.57	7.94
	25	1.88	7.7
Non saline & Moderate sodicity	27	0.79	7.83
	1	1.8	8.2
	2'	0.66	8.1
	13	2.94	8.4
	19	2.44	8.1
	23	0.69	8.21
Non saline & Strong sodicity	26	0.86	8.25
	28	1.45	8.01
	15	0.77	8.51
	20	1.52	8.5

Table 1: Informational classes resulted from the combination of salinity and sodicity classes

2.3. Spectroradiometric measurements

After the soil sampling and before the laboratory analysis, spectroradiometric measurements were acquired above the 28 bare soil samples using the ASD spectroradiometer (ASD Inc, 1999). This instrument is equipped with three detectors operating in the visible, NIR and SWIR, between 350 and 2500 nm. It allows a continuous spectral signature with 1.4 nm sampling step in the areas from 350 to 1000 nm and 2 nm in the areas of 1000 to 2500 nm. The system resamples the measurements with a 1 nm step, which allows the acquisition of 2151 contiguous bands per spectrum. The sensor is characterized by the programming capacity of the integration time, which allows an excellent performance of the signal-to-noise ratio, as well as a great stability. Measurements were taken at the laboratory using two halogen lamps of 500 W each, equipped with an electrical current regulator. The data were acquired at nadir with a FOV (Field of View) of 25° and an illumination angle approximately 5° from the vertical. The spectroradiometer was installed on a tripod at

a height of approximately 30 cm from the target, which made it possible to observe a surface area of 177 cm<sup>2</sup>. A laser beam was used to locate the center of the ASD FOV compared to the center of each sample. The reflectance factor of each soil sample was calculated in accordance with the method described by Jackson *et al.* (1980) by rationing target radiance to the radiance obtained from a calibrated 25-cm by 25-cm white Spectralon panel (Labsphere, 2001). Corrections were made for the wavelength dependence and non-Lambertian behavior of the panel. The Spectralon radiance was acquired immediately prior to the target radiance. The average of 25 spectra was convolved in the solar-reflective spectral bands of EO-1 ALI sensor using the updated Herman transfer radiative code, H5S (Teillet and Santer, 1991).

2.4 ALI sensor

Launched in November 2000, the Advance Land Imaging (ALI) is the first Earth-Observing (EO-1) sensor to be flown under NASA's New Millennium Program. This sensor was designed as a technology validation instrument for the next generation of Landsat-like instruments. It is a push-broom sensor that employs linear array technology, which is geometrically more stable than the cross-track scanning of MSS, TM and ETM+ systems (Ungar, 2001). This stability allows a simpler, less time-dependent geometric modeling approach but brings with it new challenges associated with the increased focal plane complexity (Storey *et al.*, 2004). Indeed, ALI employs novel wide-angle optics and highly integrated multispectral and panchromatic spectrometers. It uses a triplet telescope with visible, near infrared and shortwave infrared focal planes. The instrument focal plane is partially populated with four sensor chip assemblies (SCA) and each covers 3° by 1.625° (NASA, 2006). Each of the four SCAs contains 320 detectors (i.e. pixels) in the cross-track direction. For the panchromatic band, each SCA contains 960 detectors in the cross-track direction. There is an overlapping coverage of approximately 10 detectors between each adjacent pair of SCAs for the multispectral bands. For the panchromatic band, there is a coverage overlap of approximately 30 detectors between each adjacent pair of SCAs (NASA, 2006). Operating at an orbit of 705 km, the EO-1 ALI across-track ground swath width is 37 km and the along-track length is normally 42 km. The pixel size is very similar to Landsat-7 ETM+, except for the higher-resolution (10 meters) in the panchromatic (band 1) for ALI, and 30 meters in all other bands, 2 to 10 (NASA, 2006). Five bands mimic the ETM+ bands 1, 2, 3, 5, and 7. ETM+ band 4 is split into two bands covering 775 - 805 nm and 845 - 890 nm. In addition, there are two new additional bands labeled 2 and 8 at 433 - 453 nm and 1200 - 1300 nm, respectively, with 30 m pixel size (Bicknell *et al.*, 1999). Table 2 presents the spectral bands of the EO-1 ALI sensor and their respective wavelengths.

Band	Wavelength (nm)	Band	Wavelength (nm)
1*	480 – 690	6	775 – 805
2	433 – 453	7	845 – 890
3	450 – 515	8	1200 – 1300
4	525 – 605	9	1550 – 1750
5	630 – 690	10	2080 – 2350

\* Panchromatic band

Table 2: Spectral bands of EO-1 ALI sensor

2.5. Salinity indices

In the literature, different spectral salinity indices are proposed for salt mineral detection and identification, at least when they are the dominant soil constituent. To retrieve information on the salt-affected areas from the LISS-II sensor of the IRS-1B satellite, Khan *et al.* (2001) proposed three spectral salinity indices: the Brightness index (BI), Normalized Difference Salinity Index (NDSI) and Salinity Index (SI). Among these indices, they found that NDSI provided satisfactory results retrieving different salt classes. According to Al-Khaier (2003), the ASTER salinity index (ASTER-SI), which uses bands 4 and 5, accurately detects overall salinity in bare agricultural soils. A methodology was proposed by the Indo-Dutch Network Project (IDNP, 2002) for identification of soil salinity conditions using remote sensing Landsat-TM system and GIS. Amongst several remote sensing techniques, this project proposes three different salinity indices: SI-1, SI-2 and SI-3. The last is similar to the ASTER-SI index. In this research, all these indices were considered, calculated in EO-1 ALI spectral bands, and tested for the detection of slight and moderate soil salinity and sodicity effects.

$$BI = \sqrt{ALI5^2 + ALI6^2} \tag{1}$$
$$NDSI = (ALI5 + ALI7)/(ALI5 + ALI7) \tag{2}$$
$$SI = \sqrt{ALI3 * ALI5} \tag{3}$$
$$ASTER-SI = (ALI9 - ALI10)/(ALI9 + ALI10) \tag{4}$$
$$SI-1 = (ALI9)/(ALI10) \tag{5}$$
$$SI-2 = (ALI6 - ALI9)/(ALI6 + ALI9) \tag{6}$$
$$SI-3 = (ALI9 - ALI10)/(ALI9 + ALI10) \tag{7}$$

3. RESULTS AND DISCUSSION

Soil spectral signatures can provide information on the soil properties and quality. Indeed, there is a high correlation between soil reflectance and soil properties such as organic matter content, moisture content, mineral composition, iron oxide content, color, brightness, roughness, size and shape of the soil aggregate, and the salt and sodium content. Figure 2 illustrates the spectral signature of the soils measured for this study. In general, this figure illustrates that moderately saline soils show higher spectral signature than do sodic and non-affected soils. Strongly sodic soils show higher spectral response than do moderately sodic soils. Non-affected soils, which have good structure and high organic matter, show very low spectra. Indeed, moderately saline soils are relatively smoother than soils with good structure, and cause high reflectance in the visible and near infrared bands, especially when soil is dry. These observations are very clear when we resample the data in the EO-1 ALI sensor spectral bands and we compare various degrees of soil salinity and sodicity and vegetation cover (Figure 3). This figure also shows that the spectral properties of the soils salinity and sodicity are detectable in the visible and near infrared, but are most evident in the SWIR region. However, in spite of this capability, the color, brightness and the roughness of the soil surfaces have a strong impact on the spectral signature (Figure 4). For instance, after irrigation the fine soil surfaces become dry, smooth and change the optical properties. As well, the spatial distribution of particles size, the roughness and the texture of the soil surfaces change. Consequently, the spectral signature of soil increases automatically, and masks moderate or slight salinity and sodicity effects (Figures 2 and 4). Even if

the spectral reflectance in the near infrared and SWIR wavelengths provides a rapid and expressive means of characterizing strongly saline and sodic soils, it is probable that spectral confusion occurs between moderate or slightly saline and sodic soils, and non-affected soils with bright and clear color. For instance, soils 3' and 6 show the same level of salinity and sodicity, but their spectral signature are different because of the difference of their optical proprieties (Figure 4 and Table 1). Although soil 6 is non-saline with slight sodicity (good structure with organic matter) its signature is similar to that of soil 11, which is moderately saline. The spectral signature of soils 7 and 16 are alike but not their degrees of salinity and sodicity, or their color. These observations are in agreement with other research using field or laboratory analysis, or testing other satellite sensors (Chapman *et al.*, 1989; Hick and Russel, 1990; Crowley, 1991; De Jong, 1992; Mougenot *et al.*, 1993; Rao *et al.*, 1995; Metternicht and Zinck, 1997; Goldshleger *et al.*, 2001). Furthermore, even if the saline soil can be characterized by having different absorption features, Figure 2 shows that it is not possible to characterize, or to distinguish between, slight or moderate saline and sodic soils by their absorption features. This was not expected because the salt and sodium content status was not very strong in the soil samples and, consequently, these absorption features are absent.

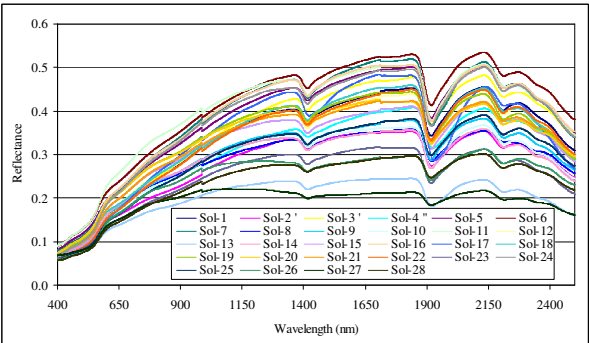


Figure 2: Spectral signatures of the considered soils.

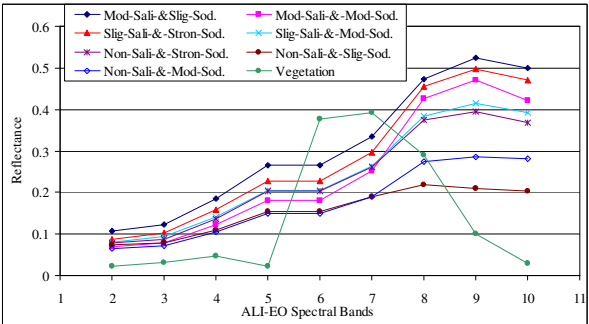


Figure 3: Resampled and convolved spectra in EO-1 ALI spectral bands for vegetation, non-affected soil, slight and moderate saline soils, and sodic soil.

To detect slight and/or moderate saline and sodic affected soils, empirical relationships (second order regression analysis) were undertaken between the EC (ground reference) and different spectral salinity indices. Table 2 presents the resulting correlation coefficients. Among the indices proposed in the literature, only the ASTER-SI (similar to SI-3) provides the highest corre-



lation (46.9 %) especially when we consider just the saline and sodic soils. However, this correlation is not significant enough to retrieve accurate information. Khan *et al.* (2001) found that NDSI provides satisfactory results retrieving different salt classes (dry surface crust), but the research here shows that this index offers a very low correlation coefficient of 22.82% (especially when we consider all soils). If we take into account only the affected soils, this coefficient increases to 42.69 %. The other indices show their limitation and a very low potential discrimination between slight and moderate soil salinity and sodicity effects, and non-affected soils.

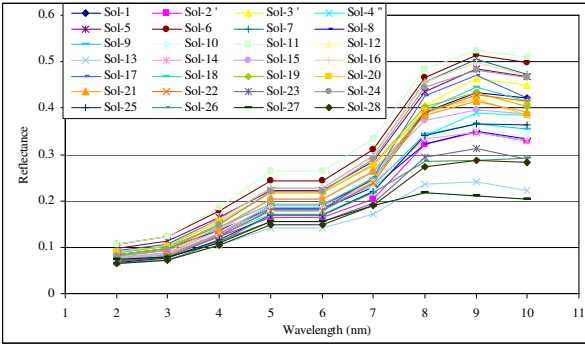


Figure 4: Resampled and convolved spectra in EO-1 ALI spectral bands

Salinity Index	Correlation coefficient (%)	
	All soils	Only saline and sodic soils
SI	4.53	5.65
BI	6.63	2.21
SI-1	18.86	46.70
SI-2	12.88	36.07
SI-3	18.59	46.90
ASTER-SI	18.6	46.90
NDSI	22.82	42.69
SSSI-1	34.00	52.00
SSSI-2	34.21	52.91

Table 2: Correlation coefficient between EC and spectral soil salinity indices

Furthermore, when we correlate EC with the reflectances in each of the EO-1 ALI spectral bands, bands 9 and 10 provide the highest correlation. Using these two SWIR spectral bands, we devised soil salinity and sodicity indices (SSSI). SSSI-1 uses a simple difference between spectral bands 9 and 10, whereas SSSI-2 uses a normalized difference ratio. These empirical relationships are more useful than individual spectral bands or the other indices. They offer a correlation coefficient of 52.91% with the EC using a second order regression analysis. This correlation is not so high, but it's the most significant one compared to the other indices (Table 2). According to these laboratory results, we note that in spite of this correlation, which is at the acceptable limit, the SSSI-1 and SSSI-2 could enhance the slight and moderate saline and sodic zones, and differentiate them from non-affected soils using EO-1 ALI imagery data.

SSSI-1 = (ALI9 - ALI10) (8)

SSSI-2 = (ALI9 \* ALI10 - ALI10 \* ALI10) / ALI9 (9)

4. CONCLUSIONS

This research focused on the potential and limits of the Advance Land Imaging (EO-1 ALI) sensor spectral bands for the discrimination of slight and moderate soil salinity and sodicity in the Tadla's irrigated agricultural perimeter, Morocco. The results show that the SWIR region is a good indicator, being more sensitive to different degrees of slight and moderate soil salinity and sodicity. In general, relatively high salinity soils show higher spectral signatures than do sodic soils and non-affected soils. Also, strongly sodic soils present higher spectral responses than moderately sodic soils. However, in spite of the improvement of EO-1 ALI sensor spectral bands characteristics in comparison to Landsat-ETM+, this research shows the limitation of multi-spectral systems for slight and moderate soil salinity and sodicity discrimination. Although remote sensing offers a good potential for mapping strongly saline soils (dry surface crust), slight and moderate saline and sodic soils are not easily identified, because the optical proprieties of the soils surfaces (color, brightness, roughness, etc.) could mask the salinity and sodicity effects. Consequently, their spatial distribution will probably be under-estimated. To detect slight and moderate soil salinity and sodicity effects, the Soils Salinity and Sodicity Indices (SSSI) using ALI spectral bands 9 and 10, offer the most significant correlation (52.91%) with the ground reference (EC). Even if this correlation is not so high, they could help to predict different spatial distribution classes of slight and moderate saline and sodic soils using EO-1 ALI imagery data.

ACKNOWLEDGMENTS

The authors would like to thank the NATO, AUF, Natural Sciences and Engineering Research Council (NSERC) and the University of Ottawa for their financial support. We would like to thank Mr Hammou El-Khamar head of the ORMVAT for his support and for the laboratory analysis. We are grateful for the Faculty of Science and Technology (FST) of Béni-Mellal, and Mr. M. Farhi and Mr. R. Amediaz from the ORMVAT for their support and assistance in the field work.

REFERENCES

Al-Khaier, F., 2003. Soil Salinity Detection Using Satellite Remotes Sensing. Master's thesis, International institute for Geo-information science and earth observation, Enschede, The Netherlands. 61 pages.

Analytical Spectral Devices, ASD Inc., 1999. <http://www.asdi.com/products-spectroradiometers.asp>

Baize, D., 1988. Guide des analyses courantes en pédologie: choix expression, presentation et interpretation. INRA, Paris, France.

Bellouti, A., Cherkaoui, F., Benhida, M., Debbarh, A., Soudi, B. et Badraoui, M., 2002. Mise en place d'un système de suivi et de surveillance de la qualité des eaux souterraines et des sols dans le périmètre irrigué du Tadla au Maroc. In Marlet, S. et Ruelle, P. (éditeurs): Vers une maîtrise des impacts environnementaux de l'irrigation. Actes de l'atelier du PCSI, Montpellier, France. 11 pages.

Bicknell, W.E., Digenis, C.J., Forman, S.E. and Lencioni, D.E., 1999. EO-1 advanced land imager. *Proceedings of SPIE*, Vol. 3750, pp. 80 - 88.



## The International Archives of the Photogrammetry, Remote Sensing and Spatial Information Sciences, Vol. 34, Part XXX

- Chapman, J.E., Rothery, D.A., Francis, P.W. and Pontual, A., 1989. Remote sensing of vaporite mineral zonation in salt flats (salars). *International Journal of Remote Sensing*, 10, pp. 245 - 255.
- Chartres, C.J., 1993. Sodic soils: an introduction to their formation and distribution in Australia. *Australian Journal of Soil Research*, 31, pp. 751 - 760.
- Chaturvedi, L., Carver, K., Clifford Harlan, J., Hancock, G., Small, F. and Dalstead, K., 1983. Multispectral remote sensing of saline seeps. *IEEE Transactions on Geoscience and Remote Sensing*, 21, pp. 231 - 239.
- Crowley, J.K., 1991. Visible and near-infrared (0.4-2.5  $\mu\text{m}$ ) reflectance spectra of playa evaporite minerals. *Journal of Geophysical Research*, 96(16), pp. 231- 240.
- Debbarh, A. and Badraoui, M. 2002. Irrigation et environnement au Maroc : situation actuelle et perspectives. In Marlet, S. et Ruelle, P. (éditeurs): Vers une maîtrise des impacts environnementaux de l'irrigation. *Actes de l'atelier du PCSI*, Montpellier, France. 14 pages. <http://doc.abhatoo.net.ma/doc/IMG/pdf/irrig.pdf>
- De Jong, S. (1992) The analysis of spectroscopical data to map soil types and soil crusts of Mediterranean eroded soils. *Soil Technology*, 5, pp. 199 - 211.
- Dehaan, R.L. and Taylor, G.R., 2002. Field-derived spectra of salinized soils and vegetation as indicators of irrigation-induced soil salinization. *International Journal of Remote Sensing*, 80, pp. 406 - 417.
- Drake, N. A., 1995. Reflectance spectra of evaporate minerals (400-2500 nm): applications for remote sensing. *International Journal of Remote Sensing*, 16, pp. 2555 - 2571.
- Ford, G.W., Martin, J.J., Rengasamy, P., Boucher, S.C. and Ellington, A., 1993. Soil sodicity in Victoria. *Australian Journal of Soil Research*, 31, pp. 869 - 909.
- Fraser, D. and Joseph, S., 1998. Mapping soil salinity in the Murray Valley (NSW) using satellite imagery. *Proceedings of the 9<sup>th</sup> Australasian Remote Sensing and Photogrammetry Conference*, Sydney, Australia. Paper published on CD.
- Goldshleger, N., Ben-Dor, E., Benyamini, Y., Agassi, M. and Blumber, D., 2001. Characterization of soil's structural crust by spectral reflectance in the SWIR region (1.2 – 2.5  $\mu\text{m}$ ). *Terra Nova*, 13, pp. 12 - 17.
- Hammani, A., Kuper, M., Debbarh, A., Bouarfa, S., Badraoui, M. et Bellouti, A., 2004. Evolution de l'exploitation des eaux souterraines dans le périmètre irrigué du Tadla. *Actes du séminaire sur la modernisation de l'agriculture irriguée*, Rabat, Maroc. 8 pages.
- Hick, P.T. and Russel, W.G.R., 1990. Some spectral considerations for remote sensing of soil salinity. *Australian Journal of Soil Research*, 28, pp. 417-431.
- IDNP, 2003. Indo-Dutch Network Project: A Methodology for Identification of Waterlogging and Soil Salinity Conditions Using Remote Sensing. Central Soil Salinity Research Institute, Karnal, India, 78 pages.
- Jackson, R.D. Pinter, P.J., Paul, J., Reginato, R.J., Robert, J. and Idso, S.B., 1980. Hand-held Radiometry. U.S. Department of Agriculture Science and Education Administration, Agricultural Reviews and Manuals, ARM-W-19, Phoenix, Arizona, U.S.A.
- Khan, N.M., Rastoskuev, V.V., Shalina, E.V. and Sato, Y., 2001. Mapping Salt-Affected Soils using remote sensing Indicators – A simple approach with the use of GIS IDRISI. *Proceedings of the 22<sup>nd</sup> Asian Conference on Remote Sensing*, 5-9 November, Singapore. Center for Remote Imaging, sensing and Processing (CRISP), National University of Singapore; Singapore Institute of Surveyors and Valuers; Asian association on remote sensing.
- Labsphere, 2001. A guide to reflectance coatings and materials. North Sutton, NH., [http://www.labsphere.com/tech\\_info/docs/Coating\\_&\\_Material\\_Guide.pdf](http://www.labsphere.com/tech_info/docs/Coating_&_Material_Guide.pdf).
- Metternicht, G. I., 1998. Fuzzy classification of JERS-1 SAR data: an evaluation of its performance for soil salinity mapping. *Ecological Modelling*, 111, pp. 61 - 74.
- Metternicht, G.I. and Zinck, J.A., 2003. Remote sensing of soil salinity: potentials and constraints. *Remote sensing of the environment*, 85, pp. 1 - 20.
- Metternicht, G. I. and Zinck, J. A., 1997. Spatial discrimination of salt- and sodium-affected soil surfaces. *International Journal of Remote Sensing*, 18, pp. 2571 - 2586.
- Mougenot, B., 1993. Effets des sels sur la réflectance et télédétection des sols salés. *Cahiers ORSTOM, Série Pédologie*, 28, pp. 45 - 54.
- NASA, 2006. Earth Observing 1 (EO-1) User's Guide. <http://eo1.usgs.gov/userGuide/index.html>.
- Norman, C.P., Lyle, C.W., Heuperman, A.F. and Poulton, D., 1989. Tragowel Plains – Challenge of the Plains. In: Tragowel Plains Salinity Management Plan, Soil Salinity Survey, Tragowel Plains Subregional working group, pp. 49-89. Melbourne: Victorian, Department of Agriculture.
- Rao, B., Sankar, T., Dwivedi, R., Thammappa, S., Venkataratnam, L., Sharma, R. and Das, S., 1995. Spectral behaviour of salt-affected soils. *International Journal of Remote Sensing*, 16, pp. 2125 - 2136.
- Richards, L.A., 1954. Diagnosis and improvements of saline and alkali soils. U.S. Salinity Laboratory DA, US Department of Agriculture Hbk 60, 160 pages.
- Singh, R. P. and Srivastav, S. K., 1990. Mapping of waterlogged and saltaffected soils using microwave radiometers. *International Journal of Remote Sensing*, 11, pp. 1879 - 1887.
- Storey, J.C., Choate, M.J. and Meyer, D.J., 2004. A Geometric Performance Assessment of the EO-1 Advanced Land Imager. *IEEE Transaction on Geosciences and Remote Sensing*, 42(3), pp. 602 - 607.
- Sumner, M.E., Miller, W.P., Kookana, R.S. and Hazelton, P., 1998. Sodicity, dispersion, and environmental quality. In Sumner, M.E. and Naidu, R. (eds) "Sodic Soils - Distribution, Properties, Management and Environmental Consequences". Oxford University Press, New York, pp. 149 - 172.
- Szabolcs, I., 1987. The global problems of salt-affected soils. *Acta Agronomica Hungarica*, 36, pp. 159 - 172.
- Taylor, G. R., Mah, A. H., Kruse, F. A., Kierein-Young, K. S., Hewson, R. D. and Bennett, B. A., 1996. Characterization of saline soils using airborne radar imagery. *Remote Sensing of Environment*, 57, pp. 127 - 142.
- Taylor, G.R., Bennett, B.A., Mah, A.H. and Hewson, R.D., 1994. Spectral properties of salinised land and implications for interpretation of 24 channel imaging spectrometry. *Proceedings of the first international remote sensing conference and exhibition*, Strasbourg, France, Vol. 3, pp. 504 - 513.
- Teillet, P.M. and Santer, R.P. (1991) Terrain Elevation and Sensor Altitude Dependence in a Semi-Analytical Atmospheric Code. *Canadian Journal of Remote Sensing*, Vol. 17, No. 1, pp. 36-44.
- Ungar, S.G., 2001. Overview of EO-1: the first 120 days. *Proceedings of IGARSS*, Vol. 1, pp. 43 - 45.

# QUANTITATIVE ASSESSMENT OF SOIL PARAMETERS IN WESTERN TAJIKISTAN USING A SOIL SPECTRAL LIBRARY APPROACH

Bruno Seiler<sup>a\*</sup>, Mathias Kneubühler<sup>a</sup>, Bettina Wolfgramm<sup>b</sup>, Klaus I. Itten<sup>a</sup>

<sup>a</sup> Remote Sensing Laboratories (RSL), Department of Geography, University of Zürich  
Winterthurerstrasse 190, 8057 Zürich, Switzerland, E-mail: bseiler@geo.unizh.ch

<sup>b</sup> Centre for Development and Environment, Institute of Geography,  
University of Berne, Steigerhubelstrasse 3, 3008 Berne, Switzerland

**KEY WORDS:** Soil, Sampling, Hyper spectral, Statistics, Correlation, Modelling, Prediction

## ABSTRACT:

Soil degradation is a major problem in the agriculturally dominated country of Tajikistan, which makes it necessary to determine and monitor the state of soils. For this purpose a soil spectral library was established as it enables the determination of soil properties with relatively low costs and effort. A total of 1465 soil samples were collected from three 10x10 km test sites in western Tajikistan. The diffuse reflectance of the samples was measured with a FieldSpec PRO FR from ASD in the spectral range from 380 to 2500 nm in laboratory. 166 samples were finally selected based on their spectral information and analysed on total C and N, organic C, pH, CaCO<sub>3</sub>, extractable P, exchangeable Ca, Mg and K, and the fractions clay, silt and sand. Multiple linear regression was used to set up the models. Two third of the chemically analysed samples were used to calibrate the models, one third was used for hold-out validation. Very good prediction accuracy was obtained for *total C* ( $R^2 = 0.76$ , RMSEP = 4.36 g kg<sup>-1</sup>), *total N* ( $R^2 = 0.83$ , RMSEP = 0.30 g kg<sup>-1</sup>) and *organic C* ( $R^2 = 0.81$ , RMSEP = 3.30 g kg<sup>-1</sup>), good accuracy for *pH* ( $R^2 = 0.61$ , RMSEP = 0.157) and *CaCO<sub>3</sub>* ( $R^2 = 0.72$ , RMSEP = 4.63 %). No models could be developed for *extractable P*, *exchangeable Ca*, *Mg* and *K*, and the fractions *clay*, *silt* and *sand*. It can be concluded that the spectral library approach has a high potential to substitute standard laboratory methods where rapid and inexpensive analysis is required.

## 1. INTRODUCTION

Soil degradation is a major problem in the agriculturally dominated country of Tajikistan. In the 1990s, increasing poverty triggered by the civil war and the transformation of the economy led to widespread cultivation of steep slopes, formerly used as grazing land. In these areas water erosion is considered to be the fastest and most widespread soil degradation process, also having a highly negative impact on soil fertility (Wolfgramm, 2007). It is therefore necessary to determine and monitor the state of soils. The soil spectral library approach is highly suitable for this task as it enables the determination of soil properties for a big number of soil samples with relatively low costs and effort. The objectives of the present work were:

- to model several soil properties based on the spectral information of the soil samples with satisfying accuracy.
- to evaluate the predictive ability of three approaches *multiple linear regression with continuum removed spectra*, *principal component regression* and *regression tree with first derivatives of spectra*.

## 2. MATERIALS AND METHODS

A total of 1465 soil samples were collected from three 10 to 10 km test areas in the vicinity of the Tajik capital city Dushanbe using a random sampling scheme (Wolfgramm, 2007).

The soil samples were air-dried. 50 g of each soil sample were weighed to be further prepared for the spectrometer measurements and chemical analysis. Further preparation included grinding and sieving through a 2 mm sieve to minimize differences in grain size.

The spectral readings were conducted with an ASD spectrometer, a FieldSpec Pro FR. The instrument has the ability to detect light in the spectral range from 350 to 2500 nm. This includes the spectral regions VIS (350-700 nm), NIR (700-1400nm) and a large part of SWIR (1400-3000 nm). For the purpose of standardization a special lamp was used to illuminate the samples, a Muglight from ASD (ASD, 2007b). Its design minimizes measurement errors associated with stray light and specular reflected components as the sample is illuminated and the reflected radiance is measured from below through a small window. For the white reference measurement a Spectralon from Labsphere was used. The fore-optic field of view of the spectrometer was set to 8 degrees, the scans to be averaged for white reference to 10 and for dark current to 25. A 1 nm sampling resolution was used for the measurements. The soil samples were measured twice with an approximate 90 degree turning in between and the two measurements were averaged. Spectral bands with a signal to noise ratio lower than 90 were removed from the data set. This affected the wavelengths from 350 to 430 and 2440 to 2500 nm. The spectral data was resampled to a 10 nm resolution by keeping every tenth nanometer value to reduce the amount of data. Scattering differences due to different grain size distributions were removed using two methods: *continuum removal* (ENVI, 2007) and *first*

---

\* Corresponding author

derivative with a Savitzky-Golay filter with 20 nm window. Visual observation showed that continuum removal was more effective in removing the scattering effect. Figure 1 shows a typical continuum removed spectrum of a Tajik soil sample. The spectrum shows strong absorption bands of O-H (water) at 1414 and 1914 nm and a band related with CH absorption at 2208 nm (Cozzolino, 2003).

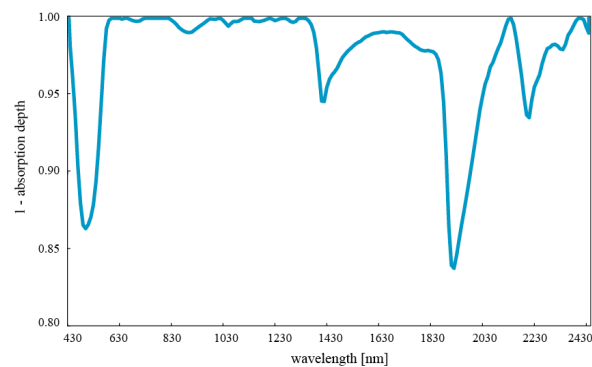


Figure 1: Continuum removed spectrum of Tajik soil sample

Soil color is strongly correlated to certain soil properties as for example  $\text{CaCO}_3$  (Ben-Dor & Banin, 1994; Jarmer et al., 2000). Therefore, the soil color was extracted from the spectra using the CIE color system (Wiszecky & Stiles, 2001) resulting in the three color variables X (red), Y (green), Z (blue). They were used as additional input variables. As at this point of work no information on the chemical composition was available the selection of the calibration and validation samples had to be made based on the spectra of the soil samples. Principal Component Analysis was used to select evenly distributed samples regarding the first and second Principal Components, all in all 252 samples were selected. The chemical analysis of the selected soil samples was carried out in the ICRAF laboratory in Kenya due to reasons of costs and accuracy. The soil samples were analysed for total C, organic C, total N, pH,  $\text{CaCO}_3$ , extractable phosphorus, exchangeable calcium, magnesium and potassium, and the fractions clay, silt and sand. Table 1 shows the applied methods of soil analysis.

Table 1: Methods of soil analysis.

Soil Property	Method
Total C	Dry combustion method
Soil organic C	Dry combustion method on decarbonised samples
Total N	Dry combustion method
pH	pH-meter
$\text{CaCO}_3$	Weight loss method, $\text{CaCO}_3$ was removed using 10% HCl
Extractable phosphorus	Modified Olsen Extractant
Exchangeable calcium	KCl extractant
Exchangeable magnesium	KCl extractant
Exchangeable potassium	Modified Olsen Extractant
Clay (<0.002 mm) Silt (0.002 to 0.05 mm) Sand (>0.05 mm)	Hydrometer method, after penetration with $\text{H}_2\text{O}_2$ to remove organic matter and 10 % HCl to remove the soluble salts.

In the study area high heterogeneity of soils was observed. Thus a homogeneous dataset of brown carbonate soils was determined (166 samples) using a CART classification tree. This resulted in higher prediction accuracy of MLR models. Three approaches were evaluated for their ability to build models for predicting soil properties based on spectral information:

- Multiple linear regression with a stepwise procedure (MLR) with continuum removed data
  - Principal component regression (PCR) with first derivative data
  - Regression tree (CART, 2007) with first derivative data
- 2/3 of the brown carbonate soil samples were used to calibrate the models, 1/3 randomly chosen samples were used for validation. Table 2 shows the  $R^2$  and RMSEP (Root Mean Squared Error of Prediction) for the different methods. Despite of the good results PCR was considered to be not suitable for this application, as new data can not be predicted with the developed models. This is connected to the calculation of the principal components where the calculation of one sample is influenced by all other samples in the data set. As the combination of continuum removed spectra and MLR was performing better than the combination of spectra transformed to first derivatives and CART, it was chosen as method for this work.

Table 2: Comparison of MLR, PCR and CART models at the example of predicting total C and total N. (cr: continuum removed spectra. 1.deriv: 1. derivative of spectra).

	Approach	R <sup>2</sup>	RMSEP
Total C	MLR (cr)	0.72	0.486
	PCR (1.deriv)	0.76	0.436
	CART (1.deriv)	0.63	0.559
Total N	MLR (cr)	0.83	0.030
	PCR (1.deriv)	0.78	0.033
	CART (1.deriv)	0.80	0.035

3. RESULTS AND DISCUSSION

The following correlations could be observed between the soil properties:

- Correlation between total N and SOC:  $R^2 = 0.76$ . Total N is for the largest part bounded in organic matter, which explains the high correlation (Gisi, 1997).
- Correlation between total C and  $\text{CaCO}_3$ :  $R^2 = 0.53$ . Total C is made up of inorganic C (mainly  $\text{CaCO}_3$  in these soils) and organic C content. The analysed Tajik soils show high concentrations of  $\text{CaCO}_3$  and low SOC contents, which explains the high correlation between total C and  $\text{CaCO}_3$ .

It was not possible to set up models for all measured soil properties. No models with satisfying accuracy could be built for extractable P, exchangeable Ca, Mg and K, and for the fractions clay, silt and sand. Poor calibrations for extractable soil properties have also been reported by Udelhoven et al. (2003), whereas the findings of Shepherd and Walsh (2002) are contradictory: they modelled exchangeable Ca and Mg with good accuracy. Successful modelling of the fractions clay, silt and sand was obtained in other studies (Chang, 2001; Cozzolino, 2003). It can be assumed that non-linear methods are more suitable

for the determination of the particle size fractions and the extractable and exchangeable soil properties. Table 3 shows descriptive statistics for the soil properties for which adequate models could be built. The accuracy measures for the MLR models are given in Table 4. All models use between 3 and 6 components. The  $R^2$  values lie between 0.72 and 0.83 for all but the pH model. As the range of the pH values is very low, i.e. between 7.01 and 8.66, modelling of pH in these soils is difficult. The range of  $\text{CaCO}_3$  is very high with 3.7 to 414 g per kg soil.

Table 3: Descriptive statistics for the soil properties

	Unit	Min	Max	Mean	Standard Deviation
Total C	$\text{g kg}^{-1}$	2.5	57.7	29.4	10.8
Organic C	$\text{g kg}^{-1}$	0.2	46	10.9	7.1
Total N	$\text{g kg}^{-1}$	0.2	3.8	1.3	0.6
pH	log H	7.01	8.66	8.05	0.25
$\text{CaCO}_3$	$\text{g kg}^{-1}$	3.7	414	194	93.7

Table 4: Accuracy measures for the calibration models. ( $R^2$  C:  $R^2$  Calibration,  $R^2$  P:  $R^2$  Prediction).

	$R^2$ C	RMSEC	$R^2$ P	RMSEP
Total C	0.85	3.48	0.76	4.36
Org. C	0.74	3.54	0.81	3.30
Total N	0.72	0.30	0.83	0.30
PH	0.61	0.13	0.61	0.16
$\text{CaCO}_3$	0.62	58.7	0.72	46.3

The resulting calibration equations for the different soil properties are given in Table 5. Some of the spectral bands that were selected by the MLR models in this study are consistent with other studies:

- 1860 nm and 2180 nm are absorption bands of carbonates (Jarmer et al., 2000; Hunt&Salisbury, 1971)
- 2320 nm, 2340 nm, 2380 nm are strong absorption bands of carbonates (Jarmer et al., 2000). Figure 2 shows the absorption band at 2340 nm at the example of four soil samples with 15 to 359  $\text{g kg}^{-1}$   $\text{CaCO}_3$ .
- 1530 nm is an absorption of N-H stretch first overtone (ASD, 2007a).

Table 5: Resulting MLR calibration equations ( $X$ denotes red color in the CIE color system, selected wavelengths [nm] are in *italic*).

Total C [ $\text{g kg}^{-1}$ ]	$= -4161.8 + 86.2(X) + 1851.2(2180) - 1097.7(1490) - 1319.5(2320) + 940.8(1860) + 3831.7(1300)$
Org. C [ $\text{g kg}^{-1}$ ]	$= -1426.6 + 1681.5(1870) - 1050.7(1530) + 879.6(2180)$
Total N [ $\text{g kg}^{-1}$ ]	$= -62.94 + 127(1870) - 88.3(1530) + 29.1(900)$
pH	$= 17.8 - 52.3(1860) - 24.4(X) + 36.1(1700) + 18.0(720)$
$\text{CaCO}_3$ [ $\text{g kg}^{-1}$ ]	$= -7956.5 + 1121.9(X) - 5440.7(2340) + 13230.9(2380)$

The appearance of the color variable ‘X’ is not surprising, as the brightness of soil color is strongly correlated to the  $\text{CaCO}_3$  content, and as total C is strongly correlated to  $\text{CaCO}_3$ . The models for organic C and total N both use the

wavelengths 1870 nm and 1530 nm. This is due to the high correlation between the two soil properties.

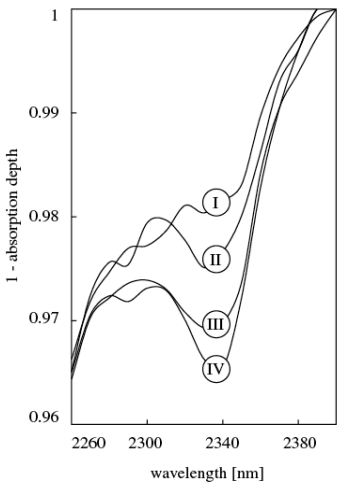


Figure 2: Absorption band of  $\text{CaCO}_3$  at 2340 nm, shown at the example of four soil samples with 15 (I), 110 (II), 288 (III) and 359  $\text{g kg}^{-1}$  (IV) of  $\text{CaCO}_3$ .

Figures 3, 4, 5, 6, 7 illustrate the accuracy of the model predictions for *total C*, *organic C*, *total N*, *pH* and  *$\text{CaCO}_3$*  using plots of the chemical reference data versus the predicted chemical values for the validation data set. The more closely the points approximate the 1:1 line, the more accurate is the predictive model. The models for *total C*, *organic C* and *total N* are very accurate, whereas the models for *pH* and  *$\text{CaCO}_3$*  show rather low accuracies.

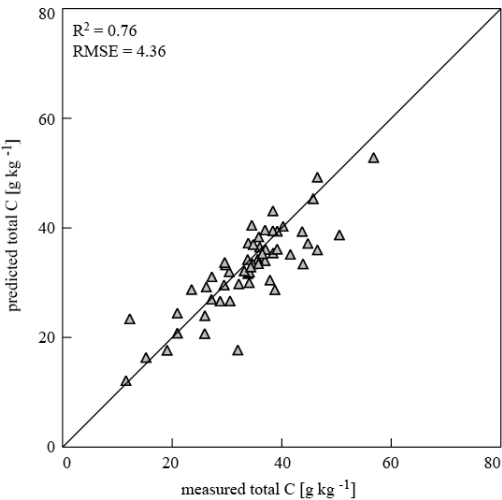


Figure 3: Chemical reference data versus predicted values for the validation data set of the total C model.

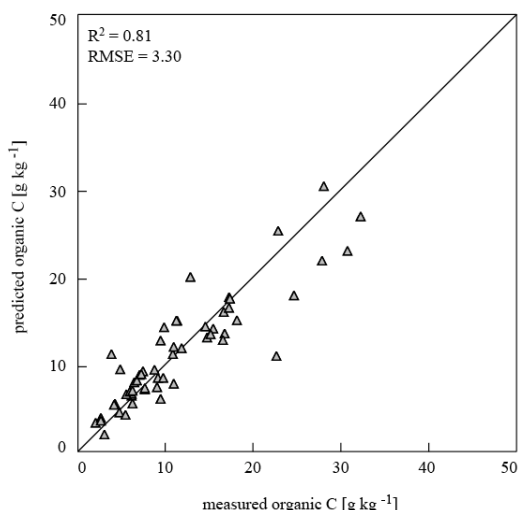


Figure 4: Chemical reference data versus predicted values for the validation data set of the organic C model.

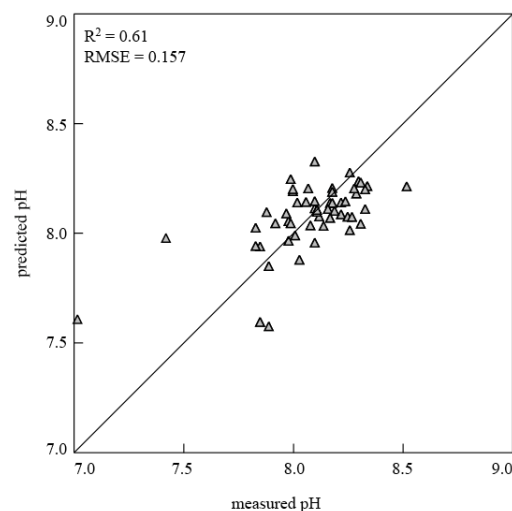


Figure 6: Chemical reference data versus predicted values for the validation data set of the pH model.

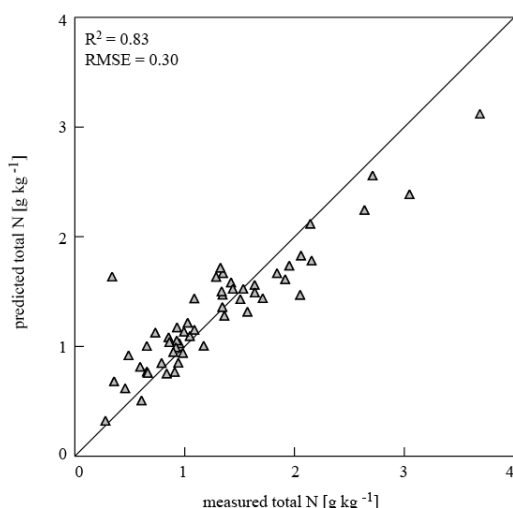


Figure 5: Chemical reference data versus predicted values for the validation data set of the total N model.

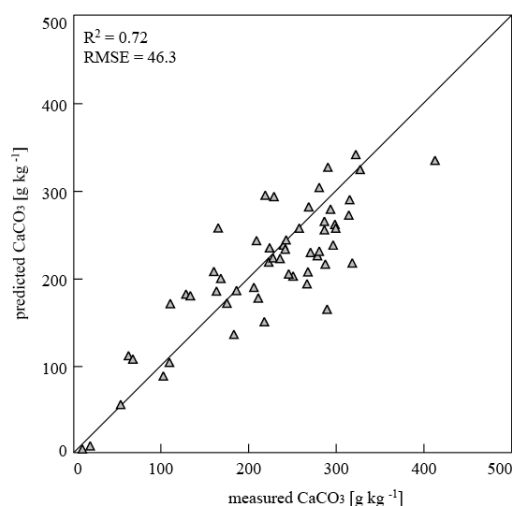


Figure 7: Chemical reference data versus predicted values for the validation data set of the CaCO<sub>3</sub> model.

#### 4. CONCLUSIONS

Modelling soil properties using VIS-NIR-SWIR spectroscopy is a powerful tool to determine chemical and physical soil properties more rapidly and inexpensively than standard soil characterization techniques. Further research is necessary, especially in the field of statistical methods. The results indicate that the pre-processing method is crucial. Further, the potential of the many different statistical methods used in this and other studies should be evaluated further, especially with regard to sample sets with highly heterogeneous soils. This work shows that the classical method of MLR with continuum removed data has the advantage to simplify comparisons among different studies as it uses physically defined absorption bands, whereas some more complex methods - for example multivariate adaptive regression splines (MARS, 2007) - seem to have the ability to model more soil properties. For modelling of key properties in soil fertility (e.g. organic and inorganic C) for homogeneous soils, the MLR method seems

appropriate. For heterogeneous soils and other soil properties such as extractable and exchangeable soil parameters or soil fractions more complex methods must be used. The developed models bear the potential to be applied to future hyperspectral imaging data for regional and rapid assessment of soil state in the area.

#### 5. REFERENCES

- ASD, 2007a. Analytical Spectral Devices. Introduction to NIR Technology. [http://www.asdi.com/ASD-600510\\_NIR-Introduction.pdf](http://www.asdi.com/ASD-600510_NIR-Introduction.pdf) (accessed March 20, 2007).
- ASD, 2007b. Analytical Spectral Devices. Muglight. <http://www.asdi.com/products-accessories-hisp.asp> (accessed March 20, 2007).



Ben-Dor, E., Banin, A., 1994. Visible and Near-Infrared (0.4-1.1  $\mu\text{m}$ ) Analysis of Arid and Semiarid Soils. *Remote Sensing of Environment*, 48, pp. 261-274.

CART, 2007. Classification and Regression Trees. Software by Salford Systems. <http://www.salford-systems.com> (accessed March 20, 2007).

Chang, C.-W., et al., 2001. Near-Infrared Reflectance Spectroscopy - Principal Component Regression Analysis of Soil Properties. *Soil Science Society of America Journal*, 65, pp. 480-490.

Cozzolino, D., Morón, A., 2003. The Potential of Near-Infrared Reflectance Spectroscopy to Analyse Soil Chemical and Physical Characteristics. *Journal of Agricultural Science*, 140, pp. 65-71.

ENVI, 2007. Software by ITT Visual Information Solutions. <http://www.itvis.com> (accessed March 20, 2007).

Gisi, U., 1997. *Bodenökologie*. 2nd edition. Georg Thieme Verlag, Stuttgart, New York.

Hunt, G.R., Salisbury, J.W., 1971. Visible and Near-Infrared Spectra of Minerals and Rocks: II. In: *Modern Geology*, Nr. 2, pp. 23-30.

Jarmer, T., et al., 2000. Spectral Detection of Inorganic Carbon Content along a Semi-Arid to Hyper-Arid Climatic Gradient in the Judean Desert (Israel). *Second EARSeL Workshop on Imaging Spectroscopy*, Enschede, 2000, CD-ROM.

MARS, 2006. Multivariate Adaptive Regression Splines. Software by Salford Systems. <http://www.salford-systems.com> (accessed March 20, 2007).

Shepherd, K.D., Walsh, M.G., 2002. Development of Reflectance Spectral Libraries for Characterization of Soil Properties. *Soil Science Society of America Journal*, 66, pp. 988-998.

Udelhoven, T., Emmerling, C., Jarmer, T., 2003. Quantitative Analysis of Soil Chemical Properties with Diffuse Reflectance Spectrometry and Partial Least-square Regression: A Feasibility Study. *Plant and soil*, 251, pp. 319-329.

Wiszecky, G., Stiles, W.S., 2001. *Color Science: Concepts and Methods, Quantitative Data and Formulae*. Wiley, New York.

Wolfgramm, B., Seiler, B., Kneubühler, M., Liniger, H.-P., 2007. Spatial assessment of erosion and its impact on soil fertility in the Tajik foothills. *EARSeL eProceedings*, 6 (1), pp. 12-25.

# LEAF AREA INDEX ESTIMATES OBTAINED FOR MIXED FOREST USING HEMISPHERICAL PHOTOGRAPHY AND HYMAP DATA

Anja Visscher von Arx\*, Silvia Huber, Mathias Kneubühler and Klaus Itten

Remote Sensing Laboratories (RSL), University of Zurich, Winterthurerstrasse 190, 8057 Zurich, Switzerland -  
avissche@geo.unizh.ch

**KEY WORDS:** Hemisfer, Camera Exposure, Hyperspectral Data, Vegetation Indices, HyMap

## ABSTRACT:

The Leaf Area Index (LAI) is an important measure in many ecological applications because vegetation-atmosphere processes of the canopy, such as photosynthesis are controlled by the foliage and play an essential role in the carbon cycle. Therefore accurate determination of LAI is of great interest. Forest LAI is difficult to estimate due to the complex structure of the canopy and its high variability. Previous studies have shown that hemispherical photography is a useful technique to determine LAI by involving different gap fraction models but exposure seems to affect LAI estimates. Hemispherical photography and LAI-2000 plant canopy analyzer ground measurements were taken to capture the LAI at selected plots in the study site. The photographs were captured with two different exposure settings, namely manual and automatic, to examine the effects on LAI. Subsequently, we analyzed the photographs with the Software Hemisfer that allows the calculation of LAI with five different mathematical methods. Hemisfer was developed by the Swiss Federal Research Institute WSL. In order to obtain an LAI map of the study area, data of the airborne imaging spectrometer HyMap were used, acquired in summer 2004. Three images were recorded approximately at the same time, whereas two of them were North-South oriented and the third perpendicular to them. All HyMap data were preprocessed and across-track illumination variations were corrected. Six two-band Vegetation indices (eg. PVI, SAVI2) were exploited by developing regression models between ground-based LAI and VI's. The VI with the best performance was then applied on HyMap data. The objectives of this study were (1) the evaluation of different mathematical methods to calculate LAI from hemispherical photographs, (2) the investigation of camera exposure influencing LAI estimates and (3) the examination of illumination effects on LAI when applying VI's on HyMap data. The evaluation of the five different LAI calculation methods from hemispherical photographs showed that the coefficients of variation ranged from 10.69 % to 15.43 %. LAI derived with manual camera exposure settings correlated better ( $R^2=0.97$ ) with LAI-2000 values than LAI from automatically exposed photographs ( $R^2=0.85$ ). A comparison of the VI's showed that good results were achieved with SAVI2 as well as with PVI. Investigating illumination effects on LAI indicated that although a correction has been performed, influences on LAI can still be observed.

## 1. INTRODUCTION

In forest ecosystems physical and biogeochemical processes take place. These processes are influenced by the microclimate within and outside of the canopy as well as by other factors. Biogeochemical processes such as photosynthesis, respiration or transpiration are controlled by the plants' foliage. In most studies canopy foliage is measured with the variable Leaf Area Index (LAI) (Chen and Cihlar, 1995; van Gardingen et al., 1999; Zhang et al., 2005). Leaf area index (LAI) is a dimensionless parameter and defined as the one-sided leaf area per ground surface area (Chen and Black, 1992). Since LAI plays a key role in ecological applications accurate determination of LAI is of great interest.

Forest LAI is difficult to estimate due to the complex structure of the canopy and its high variability. LAI can be estimated either directly or indirectly. Since direct methods, which involve destructive sampling or litterfall collection, are time consuming and limited to small areas, indirect techniques were developed. Indirect techniques include optical instruments, such as hemispherical photography or LAI-2000 Plant Canopy Analyzer that allow a non-destructive, quick and low-cost estimation of LAI over large areas (Chen et al., 1997). Previous studies have shown that digital hemispherical photography is a useful technique to determine LAI by

involving different gap fraction models. However, camera exposure settings influence the estimation of light transmission on LAI and are therefore a major cause of measurement errors (Zhang et al., 2005).

Since field estimations over large areas are problematic, remote sensing techniques have been used to measure LAI on a landscape scale (Gong et al., 2003). The most commonly used method to derive LAI of remote sensing data is the application of vegetation indices (VI's) by establishing empirical relationships between the ground-based LAI and the VI values.

The objectives of this study were (1) to evaluate five different mathematical methods to derive LAI from hemispherical photographs, (2) to investigate the effect of camera exposure on LAI and (3) to examine the illumination effects in HyMap images on LAI.

## 2. DATA ACQUISITION AND METHODS

### 2.1 Study Area and Sampling Design

Measurements were conducted in a mixed forest stand located in the Swiss Plateau close to the village of Vordemwald (47°16' N, 7°53' E). It covers about 60 km<sup>2</sup> at an altitude ranging from around 450 to 600 m above sea level. At the study area 15 subplots were determined, dominated mainly by European beech

---

\* Corresponding author.

(*Fagus sylvatica* L.), European ash (*Fraxinus excelsior* L.), black alder (*Alnus glutinosa*), silver fir (*Abies alba*) and Norway spruce (*Picea abies* L.).

The sampling design for each subplot was chosen according to the elementary sampling units of the VALERI project (Baret et al., 2006). For each subplot nine field measurements were collected on the basis of a 3 x 3 grid covering an area of 10 m by 10 m to average out errors in the levelling of the camera (Leblanc et al., 2005). Each subplot was located using GPS and marked for repeatable measurements. Data collections were carried out during the summer months of the years 2005 and 2006. In 2005, measurements were conducted at nine subplots under overcast weather conditions, whereas in 2006 data were acquired at five subplots under cloud free conditions. At four subplots measurements were carried out in both years.

## 2.2 Field LAI Data and Analysis

Field LAI were obtained with hemispherical photography and a Li-Cor LAI-2000 plant canopy analyzer (LI-COR, 1992). These two indirect optical methods allow a fast, inexpensive and non-destructive sampling. Both instruments retrieve LAI from gap fraction analysis. Chen and Black (1992) described LAI estimates derived with optical instruments as effective LAI. This term implies that also non-photosynthetically active plant elements are considered. However, in this study we use the term LAI.

Hemispherical photographs were collected using a Nikon CoolPix 4500 digital camera with a FC-E8 fish-eye lens (Nikon Inc., 2002). The photographs were taken looking upward by keeping the lens horizontal. An advantage of photographs compared to other methods is that they serve as a permanent record of the geometry and canopy openings (Rich, 1990). In order to understand how camera exposure settings affect LAI estimates, two different settings were used: first, the camera was set to automatic exposure and secondly, the aperture was fixed at F5.3 and only shutter speed was adjusted manually by considering the integrated photometer. Finally, at each subplot nine photographs which were either automatically or manually exposed were collected. We used the highest image quality (2272x1704 pixels) for all measurements and saved them in JPEG format. Photographs in this format have three image channels in the red, green and blue part of the electromagnetic spectrum.

All photographs were analyzed with the software Hemisfer, developed at the Swiss Federal Institute for Forest, Snow and Landscape Research (WSL) (Schleppi et al., 2006). Hemisfer derives LAI from the distribution of the gap fraction which was estimated using an overlay of five concentric rings covering the hemispherical photograph (van Gardingen et al., 1999). The gap fractions were determined by setting an automatic threshold which recognizes edges on the picture (Nobis and Hunziker, 2005). The five rings according to the LAI calculation were used together to calculate the threshold for each picture. By applying this brightness threshold Hemisfer classifies each photograph in either white (sky) or black (vegetation) pixels before estimating the LAI. For hemispherical photographs the proportion of white pixels to the total pixel number corresponds to the gap fraction. The next step was to calculate the average number of times, called the contact number, that a light ray would touch the canopy when travelling a distance equal to the thickness of the canopy

(Hemisfer, 2005). These values are finally integrated over the rings to calculate the LAI, but this step differs among methods (Hemisfer Help). Hemisfer permits the calculation of LAI with five different mathematical methods:

- 1) method by Miller (1967)
- 2) method by Miller (1967) as implemented in the LAI-2000
- 3) method by Lang (1987),
- 4) method by Norman and Campbell (1989)
- 5) weighted ellipsoidal method (developed for Hemisfer).

The ellipsoidal method is similar to Norman & Campbell (1989) but it optimizes the LAI itself rather than the light transmission. LAI was calculated by using all five methods in order to evaluate them. Finally, all LAI-estimates were corrected for clumping based on the method of Chen and Cihlar (1995) that is also implemented into Hemisfer. Only the blue band of the photographs was used in the analysis to minimize the interference of multiple scattering in the canopy (Zhang et al., 2005) and corresponding to the LAI-2000 instrument.

The second instrument used to determine LAI was an LAI-2000 plant canopy analyzer. It measures simultaneously diffuse radiation by means of a fish-eye light sensor in five distinct angular bands, with central zenith angle of 7, 23, 38, 53 and 68°. Only the incoming radiation of less than 490 nm is measured to minimize the radiation scattered by the canopy (LI-COR, 1992). LAI-2000 requires measurements below and above the canopy. The latter samples were measured at the same time in a non-wooded clearing. The ratio of the two values gives the transmittance for each sky sector (Jonckheere et al., 2004). From this ratio the gap fraction can be estimated from which the LAI calculations based on Miller's method (1967) are automatically derived (LI-COR, 1992).

## 2.3 HyMap Data Acquisition and Preprocessing

Airborne imaging spectrometer data were acquired on July 29, 2004, with HyVista's Hyperspectral Mapping Imaging Spectrometer (HyMap) (Cocks et al., 1998). The HyMap sensor measures radiance from the ground in 126 contiguous wavebands from 450 to 2500 nm with spectral bandwidths of 10–20 nm and a field of view of 61.3°. A total of three 2.5x12 km images were obtained under cloud free conditions at a flight altitude of 3000 m that resulted in a spatial resolution of 5 m (Huber et al., 2007). Two images were orientated North-South and the third was acquired perpendicular to them while the solar azimuth was at ~127.2° and the zenith was at ~38.2°.

The preprocessing of the HyMap data was performed as described by Huber et al. (2007). The geometric correction based on the parametric geocoding procedure PARGE (Schläpfer and Richter, 2002) and radiometric correction was performed with the ATCOR4 software (Richter and Schläpfer, 2002). Additionally, illumination effects were corrected due to the sensors large field of view. As can be seen from Figure 1, a clear trend of decreasing DN values from the left to the right edge of the image was observable before the across-track-illumination correction. The illumination variations were corrected by applying a procedure implemented in the software package ENVI 4.3. The ENVI routine computed along-track mean brightness values for each across-track pixel and displayed these as a series of curves, one for each band of data in the image. Following this, a second-order polynomial function was fitted to each curve, which is used to remove the across-track variation (Taylor, 2001). View angle compensation was conducted by a

multiplicative technique that is also part of the ENVI routine (Research Systems, 2004).

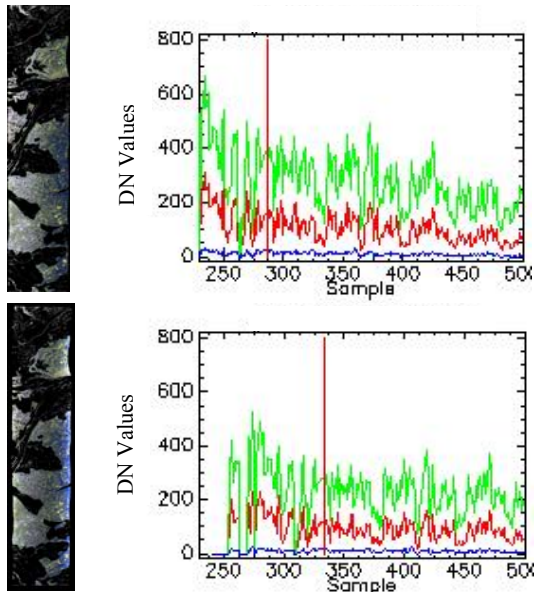


Figure 1. Horizontal reflectance profile before (above) and after (below) the across-track-illumination correction.

2.4 Vegetation indices applied on HyMap Data

Vegetation indices are the main method used to enhance the reflectance signal of vegetation. VI's are originally constructed as functions of red and NIR wavebands. In a recent study, it has been shown that hyperspectral bands in the SWIR region and some in the NIR region have a great potential in forming indices for LAI estimations (Gong et al., 2003; Schlerf et al., 2005). In the SWIR region the liquid water absorption for vegetation is characteristic. Analogously to the study of Hunt (1991), it was hypothesized that the VI's are correlated to the LAI through the summation of the individual leaf equivalent water thicknesses for each leaf layer to obtain a total canopy equivalent water thickness, which can be considered as the depth of water in the foliage (Hunt, 1991).

In this study all three spectral regions (red, NIR, SWIR) were used to calculate VI's. Criteria for selecting the VI's were their performances in forest canopies in previous studies. Table 1 presents the chosen VI's.

Group	Name	Formula	References
Ratio VI	Simple ratio	$SR = \rho_{\lambda 1} / \rho_{\lambda 2}$	(Pearson and Miller, 1972)
Ratio VI	Normalized difference vegetation index	$NDVI = (\rho_{\lambda 1} - \rho_{\lambda 2}) / (\rho_{\lambda 1} + \rho_{\lambda 2})$	(Rouse et al., 1974)
Ratio VI	Non-linear vegetation index	$NLI = (\rho_{\lambda 1}^2 \cdot \rho_{\lambda 2}) / (\rho_{\lambda 1}^2 + \rho_{\lambda 2})$	(Gong et al., 2003)
Orthogonal VI	Perpendicular vegetation index	$PVI = (1/\sqrt{(a^2+1)}) * (\rho_{\lambda 1} - a*\rho_{\lambda 2}-b)$	(Richardson and Wiegand, 1977)

Hybrid VI	Soil adjusted vegetation index	$SAVI = ((\rho_{\lambda 1} - \rho_{\lambda 2}) * (1 + L)) / (\rho_{\lambda 1} + \rho_{\lambda 2} + L)$	(Huete, 1988)
Hybrid VI	Second soil-adjusted vegetation index	$SAVI2 = \rho_{\lambda 1} / (\rho_{\lambda 2} + b/a)$	(Major et al., 1990)

Table 1. Vegetation indices used in this study. ρ stands for reflectance, λ1 and λ2 are wavelengths and a and b represent the soil line coefficients.

Generally, the VI's can be grouped into: 1) ratio indices, 2) orthogonal indices and 3) hybrid indices. Ratio indices are based on the calculation of quotients of two reflectance values of the spectrum. They are computed independently of soil reflectance properties. Orthogonal indices, in contrast, take soil reflectance properties into account. They assume that the reflectance in the NIR and red varies with increasing vegetation density (such as leaf area index) and that these variations are parallel to the soil baseline. The soil line is representing the relationship between red and NIR soil reflectances and the perpendicular distance from the baseline in a NIR-red plot determines the vegetation density. To define the soil line coefficients of our images a tasselled cap was performed which resulted in a slope of 0.9 and an intercept of 0.1. Hybrid indices can be considered as a mixture between the ratio and the orthogonal indices (Broge and Leblanc, 2000). Hybrid indices were developed to account for changes of the optical properties of the background (Broge and Leblanc, 2000). They include the coefficients of the soil line or a soil-adjustment factor (L) to minimize soil-brightness influences. In this study an adjusted factor of L = 0.5 was used which was defined for intermediate vegetation amounts (Huete, 1988).

Before applying equations between field-measured LAI and VI's, we had to extract spectral reflectances from the HyMap data, corresponding to our subplots. To extract the mean spectra of eight subplots from the HyMap images the ENVI Region of Interest Tool was used. Afterwards, HyMap bands were selected from literature to use for the VI's. Only for the Simple Ratio we tried to define our own wavebands. This was done by using all combinations of two wavelengths involving the 126 HyMap bands and correlating them to the LAI obtained from hemispherical photographs acquired with manual exposure. We calculated a correlation matrix for the mean, maximum, minimum and median values of the LAI. In case that measurements of the year 2005 were available these LAI values were used, otherwise we reverted to the LAI values of the year 2006. The results for the mean LAI, which achieved highest R<sup>2</sup> values in this correlation analysis, are presented in Figure 2.

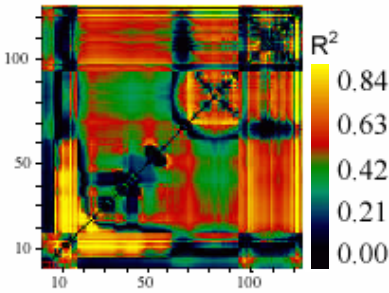


Figure 2. 2D correlation matrix that shows the coefficient of determination (R<sup>2</sup>) between LAI obtained from hemispherical photography and narrow band SR.

The hyperspectral bands for the other VI's were chosen based on their performance in previous studies for forest ecosystems. Table 2 presents the wavebands used in our study. Compared to the ones of the publications referenced the wavebands are slightly modified according to the utilized HyMap data.

Index	$\lambda_1$ (nm)	$\lambda_2$ (nm)	Adjusted $R^2$	References
SR	1113	1007	0.46	(Gong et al., 2003)
SR	786	635	0.40	Own calculation
NDVI	1038	831	0.67	(Gong et al., 2003)
NLI	1558	844	0.37	(Gong et al., 2003)
PVI	1148	1088	0.78	(Baret and Guyot, 1991; Broge and Leblanc, 2001; Schlerf et al., 2005)
SAVI	1038	831	0.59	(Elvidge and Chen, 1995; Huete, 1988)
SAVI2	725	1953	0.73	(Broge and Leblanc, 2000; Darvishzadeh et al., 2006)

Table 2. The wavelength positions used for calculating VI's. Apart from the second Index Simple Ratio, all positions were taken from the publications referenced.

To find out which Index is most promising for our study area, regression models between LAI, obtained from hemispherical photographs, and the VI's were developed. For comparison of the performance of the regression models, the adjusted  $R^2$  was used. With the best VI's LAI maps for the study area were calculated in order to evaluate illumination effects on LAI when using indices derived from HyMap data.

2.5 Statistical analysis

As a first step, the variance homogeneity of LAI calculation methods was evaluated by applying the F-test ( $p<0.05$ ) on LAI estimates. This test was computed to determine differences of the variance between the methods. The hypotheses of the F-test are a) there is no difference between the variances and b) the difference between the variances are significantly different. As a next step, the coefficient of variation was calculated. It is a relative measure for comparing the degree of variation from one dataset to another, even if the means are different from each other. The coefficient of variation is defined as the ratio of the standard deviation to the mean multiplied by 100. Statistical evaluations for this study were performed using the R statistical package, a free software environment for statistical computing and graphics (R Development Core Team, 2005) under the GNU public license.

3. RESULTS

In total, 364 hemispherical photographs were processed with Hemisfer, which were taken on five different dates in 2005 and on one date in 2006. Simultaneously, LAI-2000 measurements were collected at one date in both years for direct comparison of the instruments at four subplots. At one subplot LAI-2000 measurements were carried out in both years. Since not all different kinds of measurements were carried out at each subplot and each date, only the according results were used for this analysis.

3.1 LAI calculation methods

Five different mathematical LAI calculation methods were evaluated, which are implemented in the Hemisfer software. The minimum (1.91; manual exposure) and maximum (4.93;

automatic exposure) LAI were found with the method after Norman and Campbell. The F-test revealed that the weighted ellipsoidal method as well as the method according to Norman and Campbell significantly differed to the other three methods (Licor LAI-2000, Lang, Miller). This result was found for both exposure settings. The lowest coefficient of variation was obtained for LAI estimates calculated after Lang (manual: 10.99 %; automatic: 10.67 %) for both exposure settings. The coefficients of variation of the other methods ranged from 11.53 % to 15.43 % for manual exposure and from 10.69 % to 14.26 % for automatic exposure. The boxplots in Figure 3 illustrate these findings. Additionally, it can be seen from Figure 3 that LAI values of 2006 are lower than those in the other years. Considering only the subplots of 2006, the mean LAI estimates were about 10 % lower.

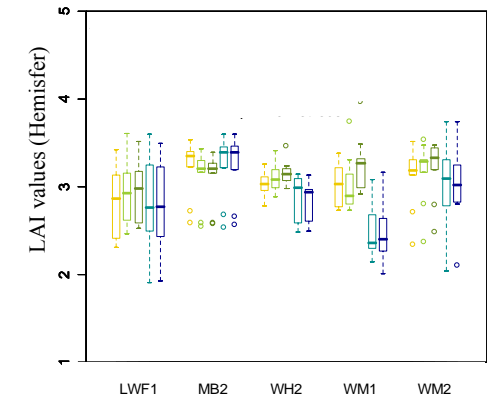


Figure 3. LAI estimates obtained from manually exposed photographs taken at five subplots. LAI were calculated with five different mathematical methods: — LAI-2000 method, — Method Lang, — Method Miller, — Method Norman and Campbell, — weighted ellipsoidal method.

3.2 The influence of camera exposure settings on LAI

In order to investigate the effects of camera light exposure settings on LAI estimates, the hemispherical photographs (only data of 2005 and 2006 and results of the Lang method were taken into account) at each subplot with the two different settings were included in the analysis. A visual comparison of pictures taken with two different settings showed that tree crowns appeared brighter in automatically exposed photographs and with varying green colours than in manually exposed images (Fig. 4).

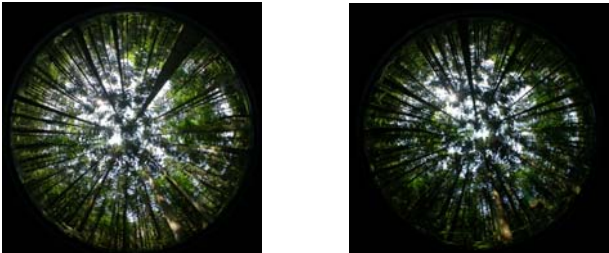


Figure 4. Hemispherical photographs automatically (left) and manually exposed (right).



LAI estimates of photographs obtained with automatic and manual exposure ranged from 2.00 to 4.93 and from 1.91 to 4.49, respectively. The mean LAI of all methods were compared to determine the influence of exposure on LAI estimates. These results illustrate that hemispherical photographs acquired with automatic exposure underestimate the LAI by 10 %.

LAI estimates obtained from manually exposed pictures exhibited a larger variability than those obtained from automatically exposed photographs for all calculation methods (Fig. 4).

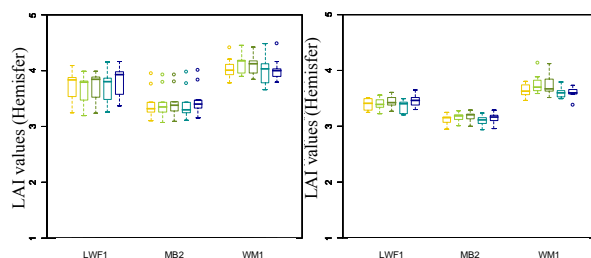


Figure 5. LAI based on photographs of July 15, 2005 for manual exposure (left) and automatic exposure setting (right) for three subplots (— Li-Cor LAI-2000 method, — Method according to Lang, — Method according to Miller, — Method according to Norman and Campbell, — weighted ellipsoidal method).

Further analysis included to test which exposure setting is the most favourable for LAI estimation. LAI derived from hemispherical photographs of the years 2005 and 2006 (only results according to Licor LAI-2000 method) were compared to LAI-2000 measurements taken at the same subplots. The LAI-2000 measurements ranged from 2.93 to 4.19. LAI estimates obtained from hemispherical photographs with automatic exposure correlated not as good with LAI-2000 measurements ( $R^2 = 0.85$ ,  $RMSE = 0.16$ ) as LAI estimates based on manual exposure ( $R^2 = 0.97$ ,  $RMSE = 0.10$ ).

### 3.3 Evaluation of illumination effects on LAI estimates

The evaluation of illumination effects on LAI estimates derived with VI from HyMap data were based on the analysis of continuous LAI estimates. To assess spatial LAI estimates, linear regression models between ground-based LAI and each VI were evaluated. LAI calculated after Lang from manually exposed hemispherical photographs for calibration were used. The formulas in Table 1 were used to compute the VI values. For the SR, the correlation matrix shows mainly high  $R^2$  values for two bands in the Red and NIR region (for example band 14 (635 nm) and 24 (786 nm)), but also in the SWIR region good correlations were found (for example band 104 (2119 nm) and 121 (2404 nm)).

The best linear relationship was achieved for PVI ( $R^2 = 0.78$ ,  $RMSE = 0.16$ ). Thus, we applied the equation based on PVI on all HyMap images to obtain spatial LAI maps. On the HyMap image that was West-East oriented, the mean LAI of the upper and lower edge were compared to determine the illumination effects on LAI estimates. LAI values of the upper

edge of the image showed 8 % higher values than those of the lower edge. Further comparisons indicated that LAI obtained of the West-East image agreed better with the LAI obtained with hemispherical photography than those obtained with the North-South oriented image.

## 4. DISCUSSION AND CONCLUSIONS

This project was undertaken 1) to evaluate five different LAI calculation methods, 2) to investigate the influence of camera exposure settings on LAI estimates and 3) to examine illumination effects on LAI when using VI's applied on HyMap data.

The comparison of five different LAI calculation methods exposed differences among the methods on a subplot level. However, if mean values of several subplots were compared, these differences were reduced. The observed decrease for the year 2006 compared to the other years could be attributed to different weather conditions and therefore also to diverse illumination conditions. This decrease was found for all subplots. Previous studies have mentioned the importance of illumination condition at acquisition time and recommended diffuse conditions as the most advantageous. However, field campaigns cannot always be conducted under ideal conditions. Because the conditions were not identical at the different sampling dates, results have to be interpreted with care. On the question of the most robust LAI calculation method, the findings of this study indicated that the method by Lang is the most robust method what is consistent with Schleppi et al. (2007).

The second objective was the investigation of exposure influencing LAI estimates. Increased exposure, as used with automatic light exposure, resulted in decreasing shutter speeds and increasing image brightness (Zhang et al., 2005). Canopy gaps in photographs acquired with automatic light exposure are visually larger than those in the counterpart, thus resulting in an overestimation of gap fraction and an underestimation of LAI estimations (Zhang et al., 2005). Comparison of the LAI-2000 values and the LAI estimates obtained from manually exposed photographs correlated better than automatically exposed photographs. Hence, it seems that the manual exposure is the better choice for retrieving LAI with hemispherical photography. However, these data must be interpreted with caution because of the small sample size. The relevance of accurate exposure is clearly supported by our findings and they are in agreement with the study of Zhang et al. (2005) who determined the optimum exposure.

Finally, we examined the influence of illumination effects in HyMap data on LAI when using VI's. Although an illumination correction was performed before applying VI's, a visible examination of the images showed strong effects at the edges of all three images. In the HyMap scene flown from West to East, higher LAI values at the upper edge of the image were obtained. A possible explanation for this might be that the whiskbroom sensor with a large field of view ( $61.3^\circ$ ) resulted in higher reflectances due to strong backward scattering of the vegetation.

## References

- Baret, F. and Guyot, G., 1991. Potentials and Limits of Vegetation Indexes for LAI and ARA Assessment. *Remote Sensing of Environment*, 35(2-3), pp. 161-173.
- Baret, F. et al., 2006. VALERI: A network of sites and a methodology for the validation of medium spatial

- resolution satellite products. *Remote Sensing of Environment*, Submitted for publication, pp.
- Broge, N.H. and Leblanc, E., 2000. Comparing prediction power and stability of broadband and hyperspectral vegetation indices for estimation of green leaf area index and canopy chlorophyll density. *Remote Sensing of Environment*, 76(2), pp. 156-172.
- Broge, N.H. and Leblanc, E., 2001. Comparing prediction power and stability of broadband and hyperspectral vegetation indices for estimation of green leaf area index and canopy chlorophyll density. *Remote Sensing of Environment*, 76(2), pp. 156-172.
- Chen, J.M. and Black, T.A., 1992. Defining Leaf-Area Index for Non-Flat Leaves. *Plant Cell and Environment*, 15(4), pp. 421-429.
- Chen, J.M. and Cihlar, J., 1995. Quantifying the Effect of Canopy Architecture on Optical Measurements of Leaf-Area Index Using 2 Gap Size Analysis-Methods. *Ieee Transactions on Geoscience and Remote Sensing*, 33(3), pp. 777-787.
- Cocks, T. et al., 1998. The HyMap™ airborne hyperspectral sensor: the system, calibration and performance. In: *1st EARSeL Workshop on Imaging Spectroscopy*. EARSeL, Zurich.
- Darvishzadeh, R. et al., 2006. Hyperspectral vegetation indices for estimation of leaf area index. In: *ISPRS Commission VII Mid-term Symposium 8-11 May 2006*, Enschede, the Netherlands.
- Elvidge, C.D. and Chen, Z.K., 1995. Comparison of Broad-Band and Narrow-Band Red and near-Infrared Vegetation Indexes. *Remote Sensing of Environment*, 54(1), pp. 38-48.
- Gong, P. et al., 2003. Estimation of forest leaf area index using vegetation indices derived from Hyperion hyperspectral data. *Ieee Transactions on Geoscience and Remote Sensing*, 41(6), pp. 1355-1362.
- Hemisfer, 2005. Hemisfer 1.3 Online Help.
- Huber, S. et al., 2007. Estimating Biochemistry in Mixed Forests from HyMap Data using Band-Depth Analyses and Subset Regression Algorithms. In Preparation, pp.
- Huete, a.R., 1988. A Soil-Adjusted Vegetation Index (Savi). *Remote Sensing of Environment*, 25(3), pp. 295-309.
- Hunt, E.R., 1991. Airborne Remote-Sensing of Canopy Water Thickness Scaled from Leaf Spectrometer Data. *International Journal of Remote Sensing*, 12(3), pp. 643-649.
- Jonckheere, I. et al., 2004. Review of methods for in situ leaf area index determination - Part I. Theories, sensors and hemispherical photography. *Agricultural and Forest Meteorology*, 121(1-2), pp. 19-35.
- Leblanc, S.G. et al., 2005. Methodology comparison for canopy structure parameters extraction from digital hemispherical photography in boreal forests. *Agricultural and Forest Meteorology*, 129(3-4), pp. 187-207.
- LI-COR, 1992. LAI-2000 Plant Canopy Analyser. Instruction manual. LICOR, Lincoln, NE, USA.
- Major, D.J. et al., 1990. A Ratio Vegetation Index Adjusted for Soil Brightness. *International Journal of Remote Sensing*, 11(5), pp. 727-740.
- Miller, J.B., 1967. A Formula for Average Foliage Density. *Australian Journal of Botany*, 15(1), pp. 141-&.
- Nikon Inc., 2002. CoolPix 4500. <http://www.nikonusa.com/template.php?cat=1&grp=2&productNr=25503> (assessed 15 March 2007).
- Nobis, M. and Hunziker, U., 2005. Automatic thresholding for hemispherical canopy-photographs based on edge detection. *Agricultural and Forest Meteorology*, 128(3-4), pp. 243-250.
- Pearson, R.L. and Miller, L.D., 1972. Remote Mapping of standing crop biomass for estimation of the productivity of the short-grass prairie, Pawnee National Grasslands, Colorado. In: *8th International Symposium on Remote Sensing of Environment*. ERIM International, Ann Arbor, Mich.
- R Development Core Team, 2005. R: A language and environment for statistical computing. R Foundation for Statistical Computing., Vienna, Austria.
- Research Systems, 2004. ENVI User's Guide. Research Systems Inc.
- Rich, P.M., 1990. Characterizing Plant Canopies with Hemispherical Photographs. *Remote Sensing Reviews*, 5(1), pp. 13-29.
- Richardson, a.J. and Wiegand, C.L., 1977. Distinguishing Vegetation from Soil Background Information. *Photogrammetric Engineering and Remote Sensing*, 43(12), pp. 1541-1552.
- Richter, R. and Schlaepfer, D., 2002. Geo-atmospheric processing of airborne imaging spectrometry data. Part 2: atmospheric/topographic correction. *International Journal of Remote Sensing*, 23(13), pp. 2631-2649.
- Rouse, J.W. et al., 1974. Monitoring the vernal advancement of retrogradation of natural vegetation. In: *NASA/GSFC, type III, final report (pp. 1-371)*, Greenbelt, MD, USA.
- Schleppi, P. et al., 2006. Correcting non-linearity and slope effects in the estimation of the leaf area index of forests from hemispherical photographs. *Agricultural and Forest Meteorology*, Submitted, pp.
- Schlerf, M. et al., 2005. Remote sensing of forest biophysical variables using HyMap imaging spectrometer data. *Remote Sensing of Environment*, In Press, Corrected Proof, pp.
- Schläpfer, D. and Richter, R., 2002. Geo-atmospheric processing of airborne imaging spectrometry data. Part 1: parametric orthorectification. *International Journal of Remote Sensing*, 23(13), pp. 2609-2630.
- Taylor, G., 2001. Strategies for Overcoming Problems when Mosaicking Airborne Scanner Images. *Earth Observation Magazine*, 10(8), pp.
- van Gardingen, P.R. et al., 1999. Leaf area index estimates obtained for clumped canopies using hemispherical photography. *Agricultural and Forest Meteorology*, 94(3-4), pp. 243.
- Zhang, Y. et al., 2005. Determining digital hemispherical photograph exposure for leaf area index estimation. *Agricultural and Forest Meteorology*, 133(1-4), pp. 166.

# ESTIMATING NITROGEN CONCENTRATION FROM DIRECTIONAL CHRIS/PROBA DATA

S. Huber<sup>a,\*</sup>, M. Kneubühler<sup>a</sup>, B. Koetz<sup>a</sup>, J.T. Schopfer<sup>a</sup>, N. E. Zimmermann<sup>b</sup> and K. I. Itten<sup>a</sup>

<sup>a</sup> RSL, Dept. of Geography, University of Zurich, Winterthurerstrasse 190, 8057 Zurich, Switzerland - (shuber, kneub, bkoetz, jschopf, itten)@geo.unizh.ch

<sup>b</sup> Swiss Federal Research Institute WSL, Land Use Dynamics, Zürcherstrasse 111, 8903 Birmensdorf, Switzerland – niklaus.zimmermann@wsl.ch

**KEY WORDS:** Biochemistry Retrieval, Subset Selection Algorithm, Multiangular, Continuum Removal, Mixed Forest

## ABSTRACT:

Sun and sensor geometry cause directional effects in remotely sensed reflectance data which can influence the estimation of biophysical and biochemical variables. Previous studies have indicated that bidirectional measurements contain added information with which the accuracy of derived plant structural parameters can be increased. Because accurate biochemistry mapping is linked to vegetation structure, nitrogen concentration ( $C_N$ ) estimates might be indirectly improved with multiangular information. We analyzed data of the spaceborne ESA-mission CHRIS on-board PROBA-1, which provides hyperspectral and multiangular data. The images were acquired in July 2006 over a forest study site in Switzerland and were subsequently preprocessed. From each of the five CHRIS images (five different viewing zenith angles) we extracted 60 crown spectra, which correspond to field-sampled trees. Then we developed four-term models by regressing lab-measured  $C_N$  on four datasets either consisting of original reflectance values (SPEC) or continuum-removed data. The wavebands used in the regression models were determined with a subset selection algorithm. For the data of all view angle combinations particular models were generated, in total 31 equations were evaluated per spectral dataset by comparing the coefficients of determination ( $R^2$ ) and cross-validated root mean square errors. The results of this study indicate that added information contained in multiangular data improved regression models for  $C_N$  estimation and lowered RMS errors. Considerable contribution can be achieved with data of a second and third viewing zenith angle. Models based on combinations of off-nadir data performed best. These findings support the potential of multiangular Earth observations for ecological monitoring and modeling studies.

## 1. INTRODUCTION

Sun and sensor geometry cause directional effects in remotely sensed reflectance data which can influence the estimation of biophysical and biochemical variables. The anisotropic reflectance behavior for instance of plant canopies implies that remotely sensed data can vary without a change in the physical or chemical properties of the material observed. This makes it difficult to interpret remotely sensed data of the same geographic location collected with different instruments, spatial scales or times (Asner, 2004). The bidirectional variability is often considered as noise and its impact on the estimation of plant biochemical and structural variables remains unknown in many cases. However, numerous studies have shown that bidirectional measurements contain added information about vegetation structure (Asner et al., 1998; Barnsley et al., 1997; Meyer et al., 1995), such as leaf area index (Diner et al., 1999), gap fraction and leaf orientation (Chen et al., 2003; Ustin et al., 2004).

The complex vertical and horizontal structure of vegetation communities limits the ability to accurately derive biochemical estimates from remotely sensed data without accounting for canopy structure (Ustin et al., 2004). It has been shown that leaf area index (LAI) and leaf orientation have a strong effect on the expression of leaf optical properties, and thus the biochemistry of foliar material, at canopy scales (Asner, 1998). For canopies with small LAI foliar biochemistry is generally underrepresented. In particular the NIR region, which exhibits the strongest multiple-scattering in green foliage canopies has

the best potential for enhancement of the leaf-level signal (Asner, 1998). So far, there has been little discussion about using directional information to assess biochemical properties such as nitrogen concentration.

The objective of this study was to investigate the influence of anisotropic reflectance effects on the estimation of  $C_N$  by evaluating regression models generated on various combinations of CHRIS view angles. We investigated a) if the added information in remotely sensed multiangular data can improve  $C_N$  estimates, b) if this information is still present after continuum removal and normalization have been applied to reflectance values and c) if certain sensor view angles or combinations thereof emerge to be beneficial for estimating  $C_N$ .

## 2. DATA AND METHODS

### 2.1 Study Site

The study site is a mixed forest located in the Swiss Plateau (7°53' E, 47°16' N) at an altitude of about 400–600 meters above sea level. The forest canopy is composed of a mixture of needle-leaf and broadleaf species, dominated by European beech (*Fagus sylvatica* L.), European ash (*Fraxinus excelsior* L.), black alder (*Alnus glutinosa*), silver fir (*Abies alba*) and Norway spruce (*Picea abies* L.). In total nine different species were sampled belonging to two plant functional groups (needle-leaf (evergreen) and broadleaf (deciduous) species).

\* Corresponding author.

At the study site we determined 15 subplots where field sampling took place. We selected the subplots according to their species composition to allow the collection of a broad variety of species. At each subplot 3–10 tree crowns were chosen for foliar sampling. The trees selected for leaf collection were chosen regarding crown dimension and species, in order to minimize soil background effects and to gain a broad range of  $C_N$ . The species were sampled more or less according to their proportion in the forest.

## 2.2 Field Data

We collected field data during a two-week field-campaign in July 2004. Foliar material was sampled from the top of tree canopies to determine biochemistry in the laboratory and additional structural and positional tree properties were measured. At the subplots of the study site, a tree climber excised leaf samples of three different upper sunlit canopy branches from a total of 60 trees, whereof 33 were conifers and 27 broadleaves. To obtain representative samples, we collected 15 leaves from all selected deciduous trees and 50–60 needles from the first three needle years from all needle-leaf trees. For each sampled tree the collected leaf material was pooled, sealed in bags and stored in cool environment for transportation. Tree crown dimensions were assessed with a Hypsometer (Haglöf, Sweden). The mean radius of a broadleaf and a needle-leaf tree crown were found to be 5.1 m and 3.2 m, respectively (Huber et al., 2006a). Leaf area index (LAI) was determined with hemispherical photography and ranged from 2.7 to 4.7 m.

In order to geo-locate the sampled tree crowns later in remotely sensed images, the trunk position of each tree was measured during the field campaign with a Trimble GeoXT GPS receiver, which corrects for multipath biases. We improved the positional accuracy by recording 20 to 40 GPS measurements per trunk and applying a post processing differential correction using the Pathfinder Office software (Trimble, 2005). The GPS horizontal precision among all trees ranged from 1.4 to 5.0 m with a mean value of 2.5 m. CHRIS data acquisition took place three years after field data collection but during the same phenological period (July). We assumed a stable  $C_N$  level during July (Martin and Aber, 1997) and only small inter-annual variability (Grassi et al., 2005) due to similar climatic conditions in the years of data sampling.

## 2.3 Laboratory Analyses

In the laboratory, the leaf area, the fresh and dry weight, and the biochemical composition for all 60 collected leaf samples were determined. We used an LI-3100 Area Meter (LI-COR, 1987) to obtain the single-sided leaf area of the samples. Fresh and dry mass were determined by weighing the samples before and after being oven dried at 85° C until a constant weight was achieved. From the difference between the fresh and dry masses divided by the area we calculated water content per cm<sup>2</sup>. For C:N analyses the samples were dried at 65 °C until a constant weight was achieved, then ground to powder and finally injected into an elemental analyzer (NA 2500; CE Instruments, Milan, Italy). Each sample was analyzed twice and checked for within-sample variation. None of the samples exceeded the threshold of 3 % variation of the mean between the two measurements. The measured  $C_N$  ranged from 1.00 to 2.97 with a mean of 1.68 and a standard deviation of 0.58 percent by dry weight (Huber et al., 2006b).

## 2.4 CHRIS Data Acquisition and Processing

In this study we used the data of the spaceborne ESA-mission CHRIS (Compact High Resolution Imaging Spectrometer) on-board PROBA-1 (Barnsley et al., 2004), which provides in mode 5 multiangular data in the range from 447 nm to 1035 nm in 37 bands with a spatial resolution of 18 m. CHRIS supplies five view angles with the nominal fly-by zenith angles (FZA's) at  $\pm 36^\circ$ ,  $\pm 55^\circ$  and  $0^\circ$  (nadir). The images covered an area of 6.5x13 km and were acquired in July 2006 over the study site Vordemwald.

The FZA's of CHRIS data acquisitions do rarely represent the actual viewing geometry for the date under investigation. The actual view angle for the nadir image was for instance  $-7.3^\circ$  in the backward scattering viewing direction (Figure 1).

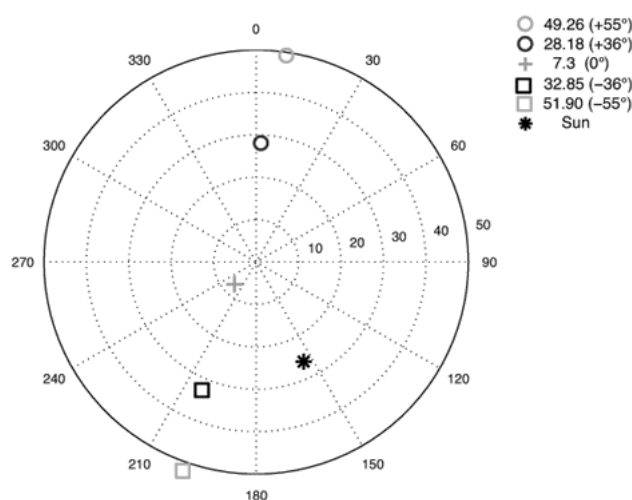


Figure 1. Acquisition geometries and illumination angles for the five CHRIS images acquired on July 1, 2006. The nominal fly-by zenith angles are listed in brackets.

The five CHRIS images were orthorectified and radiometrically corrected (Huber et al., 2006a). Geometric correction was based on a 3D physical model (Toutin, 2004), which is implemented in the commercially available image processing software PCI/OrthoEngine (PCI Geomatics, 2006). High positional accuracy of the respective multiangular products after geometric correction was a prerequisite for a reliable extraction of spectral information from the five images. To achieve a high geometric accuracy, georegistration based on a digital surface model (DSM) (Schläpfer et al., 2003). The resulting RMS errors derived from GCP's were at 0.46–0.79 pixel along track and 0.39–0.73 pixel across track. Subsequent atmospheric correction of the CHRIS radiance data was performed using ATCOR-3 (Richter, 1998), which is based on MODTRAN-4. ATCOR-3 enables the processing of data from tilted sensors by accounting for varying path lengths through the atmosphere, varying transmittance and for terrain effects by incorporating digital terrain models (DTM) data and their derivatives such as slope and aspect, sky view factor and cast shadow. For the atmospheric processing a laser-based DTM with 2 m spatial resolution was resampled to 18 m using bilinear interpolation (Schläpfer et al., 2007).



2.5 Tree Crowns Spectra Extraction and Processing

After geometric and atmospheric correction, tree spectra of the 60 field-sampled crowns were extracted from each of the five CHRIS images. We used the geographical trunk positions (vector data) of the sampled trees to locate the crown pixels in the images (Gorodetzky, 2005) and extracted spectral data with the Region of Interest (ROI) Tool in the ENVI image processing package (Research Systems, 2004). Figure 2 illustrates the different spectral signatures of a Norway spruce obtained from five CHRIS view angles.

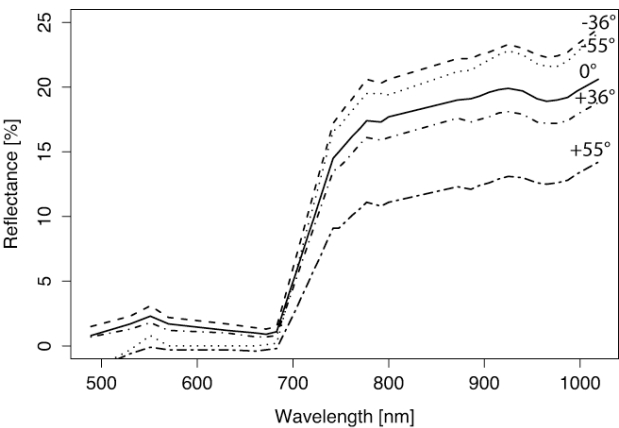


Figure 2. Spectral signatures of Norway spruce from processed CHRIS data of the nominal viewing zenith angles at  $\pm 36^\circ$ ,  $\pm 55^\circ$  and  $0^\circ$ . Negative viewing zenith angles correspond to backward scattering, positive viewing zenith angles represent forward scattering.

For further analyses, four datasets were generated. They either consisted of original reflectance or of continuum-removed data of the five FZA's. The datasets were termed as follows: SPEC included original reflectance values; BNC included band depths normalized to the waveband at the center of the absorption feature, as proposed by Kokaly and Clark (1999); CRDR included continuum-removed derivative reflectance and NBDI included normalized band depth index values, as proposed by Mutanga et al. (2004). Table 1 shows the equations used for the calculation of the datasets.

Continuum removal is a normalization technique and was developed to enhance the spectral features of interest and to minimize extraneous factors, such as atmospheric absorptions, anisotropic effects or soil background effects (Kokaly and Clark, 1999). The observed spectral continuum is considered as an estimate of the other absorptions present in the spectrum, not including the one of interest (Clark and Roush, 1984). To approximate the continuum lines, straight-line segments were used that connect local spectra maxima between 550 and 750 nm. The continuum-removed reflectance ( $R'$ ) is the ratio of the original reflectance values ( $R$ ) and the corresponding values of the continuum line ( $R_c$ ) (Kokaly and Clark, 1999). From the continuum-removed reflectance, the band depth (BD) of each point in the absorption feature was computed by subtracting the continuum-removed reflectance ( $R'$ ) from 1.

We applied continuum removal for  $C_N$  to the absorption feature located between 550 and 750 nm where the leaf water effect is minimal. Studies have shown a strong nitrogen-pigment relationship because the chlorophyll content in foliage is highly

correlated with total protein and, hence, total nitrogen content (Evans, 1989; Field and Mooney, 1986; Johnson and Billow, 1996; Yoder and Pettigrew-Crosby, 1995). The reason for this is that proteins are the major nitrogen bearing leaf constituents, typically holding 70–80% of all nitrogen. An additional 5–10% of nitrogen is allocated to chlorophyll and lipoproteins (Chapin and Kedrowski, 1983).

Dataset	Equation	Reference
SPEC	$R$	-
BNC	$BD/D_c$	(Kokaly and Clark, 1999)
CRDR	$(R'_{(j+1)} - R'_{(j)}) / \Delta_\lambda$	(Mutanga et al., 2004; Tsai and Philpot, 1998)
NBDI	$BD - D_c / BD + D_c$	(Mutanga et al., 2004)

where  $D_c$  is the maximum band depth,  $R'_{(j)}$  is the continuum-removed reflectance at waveband  $j$ ,  $R'_{(j+1)}$  is the continuum-removed reflectance at waveband  $j + 1$ , and  $\Delta_\lambda$  is the difference in wavelengths between  $j$  and  $j + 1$ .

Table 1. Equations used for the calculations of spectral datasets and corresponding references.

2.6 Statistical Analyses

Multiple linear regression analysis was applied to fit models between  $C_N$  (dependent variable) and all possible view angle combinations of the four spectral datasets (SPEC, BNC, CRDR, NBDI). To limit the number of spectral wavebands used in the regression models, this study employed a statistical variable selection method, namely an enumerative branch-and-bound (B&B) search procedure (Miller, 2002). Branch-and-bound algorithms are efficient because they avoid exhaustive enumeration by rejecting suboptimal subsets without direct evaluation (Narendra and Fukunaga, 1977). As a result, a number of wavelengths were selected that best explained  $C_N$ . We limited the number of selected wavebands to four to avoid overfitting of the models. All models were tested for significance with the F-test at the 5 % significance level.

An objective of this experiment was to determine whether assessing canopy  $C_N$  could be improved with additional directional information. Therefore, we started fitting models on data extracted from one view angle (e.g., nadir). Next, we developed models for all possible combinations of two view angles (e.g., nadir &  $-36^\circ$ ) and continued the analysis with three and four view angles to finally introduce all view angles as independent variables. In total, 31 view angle combinations were evaluated for each dataset. The findings were evaluated by comparing the mean  $R^2$  for each dataset yielded from models with the same number of view angles involved. The contribution of individual angles was evaluated by considering  $R^2$  values for the correlations between  $C_N$  and the spectral data for all angular combinations.

In order to assess the predictive capability of the SPEC based models, cross-validated mean RMS (CV-RMSE) and percentage relative errors (% error) were calculated for each model. We used 10-fold cross-validation with random splitting order of the data (Hastie et al., 2001; Huber et al., 2006b).

We implemented all analyses within the R statistical package, a free software environment for statistical computing and graphics



(R Development Core Team, 2005) under the GNU public license.

3. RESULTS

3.1 Contribution of Angular Information

The contribution of angular information to regression models for estimating  $C_N$  is apparent from Figure 3. The coefficient of determination ( $R^2$ ) increased and CV-RMSEs decreased with additional angular information for all four datasets (SPEC, BNC, CRDR, NBDI). Adding the data of a second angle as independent variables to the regression analyses is contributing most to  $R^2$ , thereafter as more directional information is added as smaller becomes the increase of  $R^2$ . For instance  $R^2$  augmented for the dataset SPEC by 15 %, 8 % and 5 % by adding data of a second, third and fourth view angle, respectively.

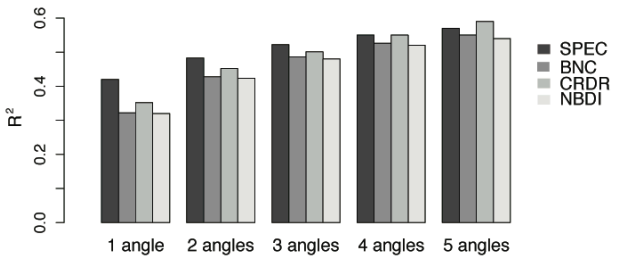


Figure 3. The coefficient of determination ( $R^2$ ) augmented as more CHRIS view angles were involved in regression analyses. All models consisted of four independent variables.

Evaluating the contribution of directional information by spectral datasets (SPEC, BNC, CRDR, NBDI) revealed interesting differences. Models generated from untransformed reflectance values (SPEC) performed best in terms of  $R^2$ . Only with data of all angles CRDR models performed better ( $R^2 = 0.59$ ).

3.2 View Angle Combinations

$R^2$  values, CV-RMSEs and percentage relative errors from models developed on data of all possible view angle combinations ( $n = 31$ ) were compared to discover which view angle combinations are promising to improve  $C_N$  estimates. This was done for all four datasets. We start reporting the results of monodirectional and continue then with multiangular models.

Best results were achieved with single-angle models based on data of the nominal  $-36^\circ$  angle for all datasets except for CRDR, where the  $-55^\circ$  angle performed best. Apart from SPEC, models developed on  $+36^\circ$  data resulted in the lowest  $R^2$  values (Figure 4). For multi-angle models the combination of off-nadir angles yielded the highest training  $R^2$  values. We obtained maximum  $R^2$  values with data of two viewing zenith angles ( $-/+36^\circ$ ) for BNC (training  $R^2 = 0.55$ ) and NBDI (0.54), whereas SPEC (0.57) and CRDR (0.59) needed data of three viewing zenith angles. The three angles for SPEC were at  $-/+36^\circ$  and  $+55^\circ$  and for CRDR at  $+36^\circ$  and  $-/+55^\circ$ . Adding data of more than three angles as independent variables to subset selection did not augment the coefficients of variation any further. Thus, the

subset selection algorithm selected the same CHRIS wavebands as for the two or three-angle models.

We used four different reflectance datasets (SPEC, BNC, CRDR and NBDI) to assess whether bidirectional effects are still present after continuum removal. In all continuum-removed datasets  $R^2$  varied considerably for one-angle models. In Figure 4 the variation can be seen for BNC. Additionally, we observed that SPEC performed particularly well for models developed on data of one and two view angles compared to the transformed datasets.

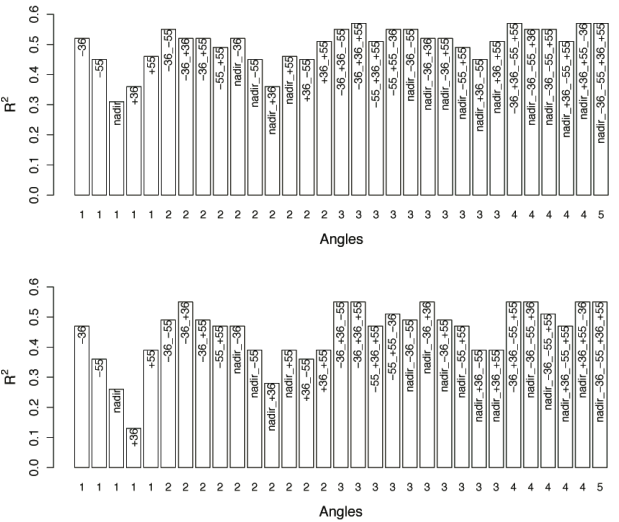
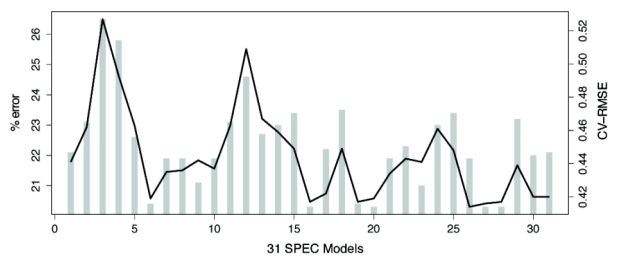


Figure 4. Coefficients of determination  $R^2$  values of  $C_N$  regressed on 31 view angle combinations of SPEC (upper) and BNC (lower figure). On the x-axis is the number of view angles provided as independent variables to the regression analyses listed.

Cross-validation revealed that CV-RMSEs and percentage relative errors tend to be smaller with increasing number of view angles involved (Figure 5). For the dataset SPEC, CV-RMSEs ranged from 0.414 to 0.527 % dry weight  $C_N$  and relative errors varied between 20.3 and 26.5 %. If we consider both cross-validated measures (CV-RMSE and relative errors) the models based on the angles at  $-36^\circ$  and  $-55^\circ$  performed best.



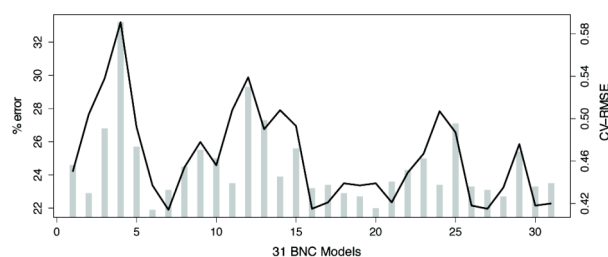


Figure 5. Bars show percentage relative errors (% error) of cross-validated four-term models based on SPEC (upper) and BNC (lower). Root mean square errors (CV-RMSE) are plotted as lines. The x-axis indicates the evaluated 31 models, as higher the number as more view angles were used for regressions.

The CV-RMSE is around 20 % lower compared to the monodirectional nadir model. However, for transformed datasets (BNC, CRDR, NBDI) the combination of backward and forward scattering viewing directions achieved lowest RMSEs. For BNC and NBDI the combination of  $\pm 36^\circ$  data (CV-RMSE 0.414–0.419) was most promising, for CRDR the combination of  $\pm 55^\circ$  and  $\pm 36^\circ$  data (0.404). We observed larger range of CV-RMSEs for transformed datasets than for SPEC. For all datasets CV-RMSEs of the best model dropped more than 20 % compared to the nadir model.

#### 4. DISCUSSION AND CONCLUSIONS

The study showed that multiangular data improved  $C_N$  estimates;  $R^2$  values of regression models increased, for instance from 0.18 (nadir) to 0.57 (three angles) for SPEC, and CV-RMSEs decreased with directional information. In general, CV-RMSEs dropped more than 20 % compared to monodirectional nadir models. This demonstrates that not only the assessment of structural vegetation parameters profit from added information contained in directional reflectance data but also biochemical constituents. These findings support the potential of multiangular Earth observations for ecological monitoring and modeling studies. Further, it points out that biochemistry estimation with wide field of view or sensors with off-nadir viewing capabilities should be interpreted with care.

With four different reflectance datasets (SPEC, BNC, CRDR and NBDI) we assessed whether bidirectional effects are still present after continuum removal. For one-angle models  $R^2$  values varied considerably between view angles for all datasets, indicating that the normalization procedure did not remove all extraneous effects. However, we observed that SPEC performed particularly well for models developed on data of one and two viewing zenith angles. This indicates that untransformed spectral data contains more additional information, for instance about tree structure that possibly improved the regression models. Only starting from four view angles, models developed on continuum-removed datasets improved due to contributing information from additional view angles so that they yielded finally higher  $R^2$  values than SPEC.

In general, monodirectional models trained on data of the  $-36^\circ$  viewing zenith angle achieved higher  $R^2$  values than these developed on data of the forward scattering direction. The finding that most information is contained in backward scattering viewing direction reflectance is consistent with other research which found in boreal forests an increase in

bidirectional reflectance in the backward scattering direction but lower reflectance in forward scattering direction, due to a combination of gap and backshadow effects (Deering et al., 1999; Sandmeier et al., 1998). These effects are more pronounced at large source zenith angles and are emphasized in highly absorbing spectral ranges such as the red band due to the lack of multiple scattering in this wavelength range (Deering et al., 1999). It was also shown that the canopy hotspot effect has rich information content for vegetation characterization, especially indications of canopy structure (i.e., a shadow is not visible) (Gerstl, 1999). The viewing zenith angle of  $-36^\circ$  is located closest to the images hotspot. The minimum reflectance corresponds to the forward scatter direction because the sensor views the unilluminated, shadowed leaf surfaces (Sandmeier et al., 1998).

For SPEC the model which is solely based on the two angles in the backward scattering direction ( $-36^\circ$ – $55^\circ$ ) yielded an  $R^2$  (0.55) close to the maximum of 0.57 obtained with at least three view angles and was characterized by low CV-RMSE and % error. On the other hand, two-angle models developed on continuum-removed datasets reached best results by combining reflectance of the forward and backward scattering directions. With three view angles involved no such distinction was observed among datasets. Nadir view direction played a minor role possibly owing to shaded background that is strongest for viewing zenith angles close to nadir (Ni et al., 1999). The large portion of gaps observed in this direction decreases the portion of leaf material seen from the sensor and thus the reflectance values.

This study has investigated the contribution of directional CHRIS data to the estimation of nitrogen concentration by assessing  $R^2$  values and cross-validated RMSEs of regression models fit between the chemical constituent and 31 angular combinations of four spectral datasets. The results of this research show that (1) added information contained in multiangular data improved regression models for  $C_N$  estimation and lowered RMS errors ( $\sim 20\%$ ), (2) considerable contribution to  $R^2$  values can be achieved with a second and third viewing zenith angle and (3) models based on combinations of off-nadir data performed best.

#### ACKNOWLEDGMENT

The authors would like to thank the Swiss National Science Foundation (SNF: project no. 200020-101517) for funding this project. The continuing effort and support of ESA and SIRA to provide CHRIS/PROBA data is gratefully acknowledged. We are very grateful to the Swiss Federal Research WSL and the many individuals who have helped with data collection and processing.

#### REFERENCES

- Asner, G.P., 2004. Biophysical Remote Sensing Signatures of Arid and Semiarid Ecosystems. In: *Remote sensing for natural resource management and environmental monitoring*. John Wiley & Sons, Hoboken, NJ, pp. 53–109.
- Asner, G.P. et al., 1998. Ecological Research Needs from Multiangle Remote Sensing Data. *Remote Sensing of Environment*, 63(2), pp. 155–165.

- Barnsley, M.J. et al., 1997. On the information content of multiple view angle (MVA) images. *International Journal of Remote Sensing*, 18(9), pp. 1937-1960.
- Barnsley, M.J. et al., 2004. The PROBA/CHRIS mission: a low-cost smallsat for hyperspectral multiangle observations of the Earth surface and atmosphere. *Geoscience and Remote Sensing, IEEE Transactions on*, 42(7), pp. 1512-1520.
- Chapin, F.S. and Kedrowski, R.A., 1983. Seasonal Changes in Nitrogen and Phosphorus Fractions and Autumn Retranslocation in Evergreen and Deciduous Taiga Trees. *Ecology*, 64(2), pp. 376-391.
- Chen, J.M. et al., 2003. Multi-angular optical remote sensing for assessing vegetation structure and carbon absorption. *Remote Sensing of Environment*, 84(4), pp. 516-525.
- Clark, R.N. and Roush, T.L., 1984. Reflectance Spectroscopy: Quantitative Analysis Techniques for Remote Sensing Applications. *Journal of Geophysical Research*, 89(B7), pp. 6329-6340.
- Deering, D.W. et al., 1999. Characterization of the Reflectance Anisotropy of Three Boreal Forest Canopies in Spring-Summer. *Remote Sensing of Environment*, 67(2), pp. 205-229.
- Diner, D.J. et al., 1999. New directions in earth observing: Scientific applications of multiangle remote sensing. *Bulletin of the American Meteorological Society*, 80(11), pp. 2209-2228.
- Evans, J.R., 1989. Photosynthesis and Nitrogen Relationships in Leaves of C<sub>3</sub> Plants. *Oecologia*, 78(1), pp. 9-19.
- Field, C. and Mooney, H.A., 1986. The photosynthesis-nitrogen relationship in wild plants. In: *On the economy of plant form and function: proceedings of the Sixth Maria Moors Cabot Symposium, Evolutionary Constraints on Primary Productivity, Adaptive Patterns of Energy Capture in Plants, Harvard Forest*. Cambridge University Press, Cambridge [Cambridgeshire]; New York.
- Gerstl, S.A.W., 1999. Building a global hotspot ecology with Triana data. In: *Remote Sensing for Earth Science, Ocean, and Sea Ice Applications*. SPIE, Florence, Italy.
- Gorodetzky, D., 2005. Function: `evf_to_rois.sav`, <http://www.itvis.com/codebank/search.asp?FID=93> (assessed 13 Feb. 2007).
- Grassi, G. et al., 2005. Seasonal and interannual variability of photosynthetic capacity in relation to leaf nitrogen in a deciduous forest plantation in northern Italy. *Tree Physiology*, 25(3), pp. 349-360.
- Haglöf (Sweden), <http://www.haglofsweden.com> (accessed 16 Jan. 2007). pp.
- Hastie, T. et al., 2001. *The elements of statistical learning: data mining, inference, and prediction*. Springer, New York, pp. Pages.
- Huber, S. et al., 2006a. Canopy Biochemistry Estimation using Spectrodirectional Information of CHRIS Data. In: *2nd International Symposium on Recent Advances in Quantitative Remote Sensing (RAQRS)*, Torrent (Valencia), Spain.
- Huber, S. et al., 2006b. Estimating Biochemistry in Mixed Forests from HyMap Data using Band-Depth Analyses and Subset Regression Algorithms. In Preparation, pp.
- Johnson, L.F. and Billow, C.R., 1996. Spectrometric estimation of total nitrogen concentration in Douglas-fir foliage. *International Journal of Remote Sensing*, 17(3), pp. 489-500.
- Kokaly, R.F. and Clark, R.N., 1999. Spectroscopic determination of leaf biochemistry using band-depth analysis of absorption features and stepwise multiple linear regression. *Remote Sensing of Environment*, 67(3), pp. 267-287.
- Martin, M.E. and Aber, J.D., 1997. High spectral resolution remote sensing of forest canopy lignin, nitrogen, and ecosystem processes. *Ecological Applications*, 7(2), pp. 431-443.
- Meyer, D. et al., 1995. The effect of surface anisotropy and viewing geometry on the estimation of NDVI from AVHRR. *Remote Sensing Reviews*, 12(1), pp. 3-27.
- Miller, A.J., 2002. *Subset selection in regression*. Chapman & Hall/CRC, Boca Raton, pp. Pages.
- Mutanga, O. et al., 2004. Predicting in situ pasture quality in the Kruger National Park, South Africa, using continuum-removed absorption features. *Remote Sensing of Environment*, 89(3), pp. 393-408.
- Narendra, P.M. and Fukunaga, K., 1977. Branch and Bound Algorithm for Feature Subset Selection. *IEEE Transactions on Computers*, 26(9), pp. 917-922.
- Ni, W. et al., 1999. Variance in Bidirectional Reflectance over Discontinuous Plant Canopies. *Remote Sensing of Environment*, 69(1), pp. 1-15.
- PCI Geomatics, 2006. OrthoEngine, User's Guide Version 10.0.
- R Development Core Team, 2005. R: A language and environment for statistical computing. R Foundation for Statistical Computing., Vienna, Austria.
- Research Systems, 2004. ENVI User's Guide. Research Systems Inc.
- Richter, R., 1998. Correction of satellite images over mountainous terrain. *Applied Optics*, 37, pp. 4004-4015.
- Sandmeier, S. et al., 1998. Physical Mechanisms in Hyperspectral BRDF Data of Grass and Watercress. *Remote Sensing of Environment*, 66(2), pp. 222-233.
- Schläpfer, D. et al., 2003. The influence of DEM characteristics on preprocessing of DAIS/ROSIS data in high altitude alpine terrain. In: *3rd EARSeL Workshop on Imaging Spectroscopy*. EARSeL and DLR, Herrsching, Germany.
- Schläpfer, D. et al., 2007. Spatial PSF Non-Uniformity Effects In Airborne Pushbroom Imaging Spectrometry Data. *IEEE Transactions on Geoscience and Remote Sensing*, accepted., pp. 458-468.
- Toutin, T., 2004. Review article: Geometric processing of remote sensing images: models, algorithms and methods. *International Journal of Remote Sensing*, 25(10), pp. 1893-1924.
- Trimble, 2005. GPS Pathfinder Office Software. Trimble.
- Tsai, F. and Philpot, W., 1998. Derivative Analysis of Hyperspectral Data. *Remote Sensing of Environment*, 66(1), pp. 41-51.
- Ustin, S.L. et al., 2004. Remote Sensing of the Environment: State of the Science and New Directions. In: *Remote sensing for natural resource management and environmental monitoring*. John Wiley & Sons, Hoboken, NJ, pp. 679-729.
- Yoder, B.J. and Pettigrew-Crosby, R.E., 1995. Predicting Nitrogen and Chlorophyll Content and Concentrations from Reflectance Spectra (400-2500nm) at Leaf and Canopy Scales. *Remote Sensing of Environment*, 53, pp. 199-211.

# AIRBORNE HYPERSPECTRAL SCANNER (AHS) MAPPING CAPACITY SIMULATION FOR THE DOÑANA BIOLOGICAL RESERVE SCRUBLANDS

M. Jiménez<sup>a</sup>, R. Díaz-Delgado<sup>b</sup>, P. Vaughan<sup>a</sup>, A. De Santis<sup>c</sup>, A. Fernández-Renau<sup>a</sup>, E. Prado<sup>a</sup>, O. Gutiérrez de la Cámara<sup>a</sup>

<sup>a</sup> Remote Sensing Laboratory. INTA. Carretera de Ajalvir Km 4. Torrejón de Ardoz. 28850. Spain

<sup>b</sup> Doñana Biological Station. CSIC. Avda. Maria Luisa s/n. Sevilla 41013, Spain

<sup>c</sup> Department of Geography, University of Alcalá. Alcalá de Henares, Spain  
jimenezmm@inta.es

**KEYWORDS:** AHS; Hyperspectral; Vegetation mapping; Scrub species discrimination; Doñana National Park; Field spectrometry

## ABSTRACT

Spatial patterns of vegetation species abundance is required for flora conservation strategies of natural areas. Hyperspectral imagery is an increasingly relevant tool for vegetation mapping although results obtained are very dependent on species spectral differences and sensor characteristics. Throughout the Stabilized Sands of Doñana Biological Reserve, (Doñana National Park, SW Spain), three scrubland communities are distributed according to groundwater level variations which are determined by dune topography. The Airborne Hyperspectral Scanner (AHS) is a VIS to TIR 80 band line-scanner that is going to be applied for mapping the shrub species pattern of this eolian ecosystem. The spectral similarity among species and broad reflectance ranges due to intra-species variations of Leaf Area Index (LAI) are important drawbacks encountered for the mapping effort. In this work the AHS capacity to discriminate these two factors is assessed using field spectrometry and Plant Area Index (PAI) measurements. An analysis of the field reflectance spectra of all species presented showed low spectral separability at intra-community level, and for the most representative species (*Erica scoparia*, *Halimium halimifolium*, *Rosmarinus officinalis*, *Ulex australis* and *Stauracanthus genistoides*) the last two species show the minimum reflectance variability due to PAI ranges. Both drawbacks were analysed in terms of Noise Equivalent Difference Radiance (NEDL) of an AHS flight line, and the conclusion is that AHS discrimination values for scrub species at a specific flight conditions consider, show a high mapping capacity among communities but medium capacity for intra-community level

## 1. INTRODUCTION

Vegetation mapping, at species level, is demanded on natural areas, to improve the knowledge of the effects that perturbation and ecological processes have on the spatial distribution of the flora (Magurran, 2004). Doñana National Park (SW, Spain) is one of the most important wetlands in Europe (Muñoz-Reinoso et al, 2000), its marshlands, dunes and stabilized dunes largely dependent on groundwater supply. Within stabilized dunes, scrubland communities play an important ecological role as a habitat, which require cartography to assess the influences of continuous disturbances such as: groundwater level drops and scrublands uprooting (Cobo Garcia et al, 2002).

Airborne hyperspectral imagery is a growing tool for mapping vegetation species. It serves as research for future space missions, and also, in an operational way, as a useful cartography method for inaccessible areas at regional scale (Lewis, 2002), like this very closed scrubland of Doñana. From a remote sensing approach, two of the main drawbacks in vegetation species cartography are: low spectral separability among species with similar ecological adaptations (Lewis, 2002), and on the contrary, high within species spectral variability response, due to the variation ranges in plant constituents (Asner, 1998). Vegetation cartography uncertainties, are very depend on the type of vegetation involved and sensor characteristics. For scrublands several authors have obtained considerable results using CASI Lewis (2002), and AVIRIS Roberts (1998) imagery.

Spanish National Institute for Aerospace Technology (INTA) owns and operates the Airborne Hyperspectral Scanner (AHS). INTA has the objective to apply AHS for Doñana's scrublands cartography. AHS is an imaging spectrometer with complete spectral coverage (VIS to TIR), having bandwidth of 15 nm in the SWIR region, but 30 nm in the VIS/NIR (Fernandez et al,

2005). VIS/NIR region is important for vegetation studies, so prior to the mapping effort, a study for AHS mapping capacity is necessary. This work focuses on the evaluation of AHS spectral and radiometric power resolve for Doñana's scrub species.

In order to evaluate this mapping capacity, a realistic simulation of the at-sensor radiances has to be achieved (Verhoef, 2003). The simulation was carried out taking into account the characteristics of an AHS flight line acquired over Doñana National Park on 28<sup>th</sup> September 2005. The material used for the simulation was plant canopy field reflectance measured with Analytical Spectral Devices (ASD) FieldSpec-3. In the case of scrub species, the variation of the spectral response, at canopy level, are primarily due to changes in Leaf Area Index (LAI), standing litter and soil (Asner, 1998). Furthermore in Doñana's stabilized dunes, groundwater level variations, determined by the dune topography, enhance the ranges of intra-species LAI presented. For this reason, field measurements were planned to assess the importance of LAI parameter over reflectance response.

## 2. STUDY AREA: DOÑANA STABILIZED SANDS

Doñana National Park is located in the southwestern Spanish coast. Doñana has a Mediterranean type climate, with a mean annual precipitations of 560 mm, concentrating the 80% of the rainfall from October to March. This work was carried out in Doñana Biological Reserve (DBR), which is 6794 ha core area that includes the three most important ecosystems: inland marshes, mobile dunes and stabilized dunes.

Stabilized dunes exhibit a rolling topography due to the old dune morphology colonized by vegetation. This ecosystem represents the transition between the recharge and discharge area of the Almonte-Marisma aquifer. The present vegetation is



remnant of the original sabinars (*Juniperus phoenicea subs turbinata*), umbrella pine plantations (*Pinus pinea*), some grasslands, but mostly a mosaic of three scrubland communities, composed of species described in table 1. Spatial distribution of scrubland is determined, at all scales, by the rolling topography that modulate the groundwater level (Muñoz-Reinoso et al, 2002). At regional scale highest zones, 40 - 50m above sea level, are dominated by sclerophyll xerophytic scrub (named locally “Monte Blanco”), for deeper zones, 0-20 m, hygrophytic scrub (named locally “Monte Negro”) is strongly developed. Transitions zones are colonized of a mixture community (named locally “Monte Intermedio”) composed of more adaptable species to a variable conditions of water stress.

Scrub community	Species
"Monte Negro" Hygrophytic scrub	<i>Erica scoparia</i> (Es), <i>Calluna vulgaris</i> (Cv), <i>Ulex minor</i> (Um), <i>Erica ciliaris</i> (Ec)
"Monte Intermedio" Mixed scrub	<i>Halimium halimifolium</i> (Hh), <i>Ulex australis</i> (Ua), <i>Stauracanthus genistoides</i> (Sg)
"Monte Blanco" Xerophytic scrub	<i>Cistus libanotis</i> (Cl), <i>Rosmarinus officinalis</i> (Ro), <i>Halimium commutatum</i> (Hc), <i>Lavandula stoechas</i> (Ls)

Table 1: Representative scrub species in Doñana's stabilized dunes communities. Key to abbreviations.

3. MATERIAL

3.1 Airborne Hyperspectral Scanner (AHS)

The AHS is an airborne line-scanner imaging spectrometer manufactured by ArgonST (formerly Sensytech Inc.). AHS Collets 80 bands form 0.45 to 12.8 microns inside atmospheric windows. It is installed onboard the INTA’s aircraft (CASA C-212) and is integrated with INS/GPS Applanix POS-AV 414. The main characteristics of AHS could see in the table 2.

FOV / IFOV : 90° / 2.5 mrad Scan rates: 12.5, 18.75, 25, 35 r.p.s., (pixel 7 to 2 meters). Digitization precision: 12 bits to sample the analog signal, with gain level from x0.25 to x10. Two controllable thermal black bodies within the field of view.			
PORT	spectral coverage(μm)	n° of bands / FWHM (nm)	λ/Δλ (minimum)
Port 1	0.43 > 1.03	20 / 28 nm	16
Port 2A	1.55 > 1.75	1 / 200 nm	8
Port 2	2.0 > 2.54	42 / 13 nm	150
Port 3	3.3 > 5.4	7 / 300 nm	11
Port 4	8.2 > 12.7	10 / 400 nm	20

Table 2: AHS characteristics.

3.1.1 AHS data simulation conditions

The flight line which is gone be simulated was acquired on 28<sup>th</sup> September 2005 at noon. The altitude was 1839 m above sea level and with scan rate of 18.5 rps which corresponds with a pixel of 4,5 m. The solar azimuth was 133 degrees and solar zenith 50 degrees.

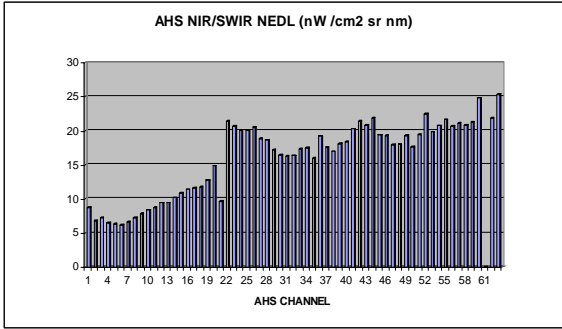


Figure 1: NIR/SWIR NEDL for the AHS flight-line simulated conditions.

3.2 Field spectroscopy campaigns

Scrub reflectance spectra were measured during 2005 and 2006 dry seasons, when the phenological state (no floration) were similar for all species. Analytical Spectral Devices FiledSpec-3 ([www.asdi.com](http://www.asdi.com)) was used to record the reflectance of plants. ASD FieldSpec-3 is a portable spectroradiometer estimates target reflectance between 0.4 to 2.5 μm, using fiber optic (adaptable fore-optic devices). Two kind of measurements at canopy level were record with two different objectives:

Type 1) with the aim to analyze species separability, a total of 200 spectra corresponding with 13 species, were collected. Three different zones in altitude over RBD were sampled, selecting plants with similar aspect in height, diameter and LAI within species. 15 spectra per specie were recorded, and for each plant 5 measures, the fiber optic of the spectrometer was held 1m (GIFOV=44 cm) above canopy in a nadir position.

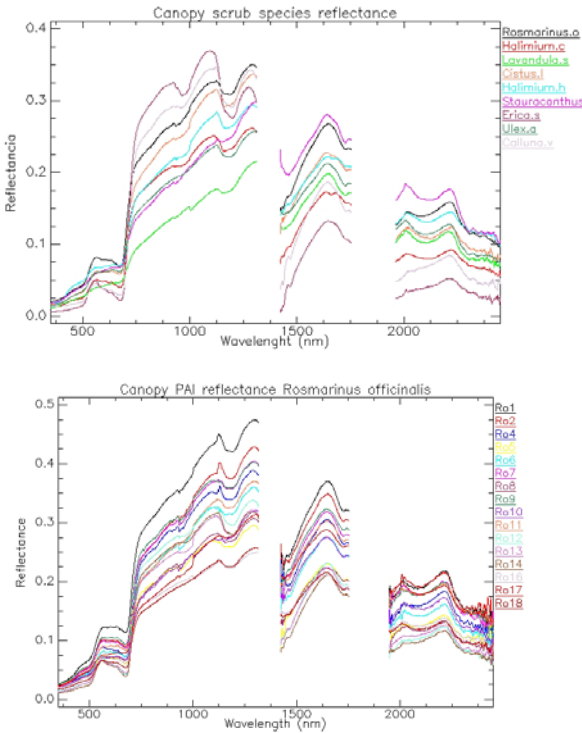


Figure 2: Upper: Averaged spectrum for canopy ASD scrub measurements. Bottom: *Rosmarinus officinalis* spectrum grouped for plant PAI variation.



Type 2) to assess within species reflectance variability due to LAI variations, canopy plant measurement were carried out over dominant species of stabilized dunes (*Erica scoparia*, *Halimium halimifolium*, *Ulex australis*, *Rosmarinus officinalis* and *Stauracanthus genistoides*). Here also 15 plants per specie were collected, in this case selecting individuals of low and high degrees of LAI. For each plant 5 measurements were recorded, the fiber optic of the spectrometer was held 1m (GIFOV=44 cm) above canopy in a nadir position.

In parallel, for each plant measured, hemispherical canopy photography was taken from beneath upwards. To get this 180 degree field of view a NIKON FC-E8 fisheye lens was adapted to a Nikon 4000 Coolpix digital camera. Following protocols for field acquisition photographs were gathered at nearly sunset (Chen at al, 1997).

4. METHODOLOGY

4.1 Plant spectra analysis

The entire set of plant spectra measured was pre-processed applying: bad spectra elimination, convolution smoothed, averaged and standard deviation. Plant spectra average was extracted to a specie level file where, again, the average and standard deviation were calculated. These files were ENVI spectral library formatted (ITT Industries, Inc)

4.1.1 Spectra separability

Using measurement type 1 spectra, the separabilty between all species was assessed in terms of the index Spectral Similarity Value (SSV) (Sweet, 2003). This index, equation 1, estimates the separation between spectra, taking into account shape aspects by correlation, and separation by euclidean distance. The SSV values range from 0 for a completely similarity to 1.4.

SSV = \sqrt{D^2 + (1 - R^2)} \tag{1}

Where:  
D = euclidean distance  
R = correlation coefficient

4.1.2 PAI reflectance variability

Using spectra of field measurement type 2, the reflectance variability due to LAI increments was assessed for the most abundant species of each community. Considering scrub vegetation, canopy LAI variation has strong influence on his reflectance signatures, however woody stem is also very important (Asner, 1998). In this work, due to operative reasons, overall Plant Area Index (PAI) was obtained instead. PAI was calculated processing their corresponding hemispherical canopy photo with Hemiview 2.1 (Delta-T Devices, Ltd). This software estimates gap fraction over the entire photo and calculates the PAI. Only relative increments of PAI were the scope, so no absolute value was manage. All non-destructive field methods underestimate LAI canopy due to clumping effect (Asner 1998), in the case of hemispherical photo methodology, it has a good correlation with the LAI values obtained with Licor 2000 in a work realized by University of Valencia evaluating several crop types for ESA Sen2flex 2005 project (www.uv.es/leo/sen2flex).

Scrub specie	Min PAI	Max PAI	rP NIR	Cv NIR(%)
<i>Erica scoparia</i> (Es)	1.03	2.87	0.63	11
<i>Halimium halimifolium</i> (Hh)	1.1	3.8	0.56	18
<i>Ulex australis</i> (Ua)	1.5	2.5	0.45	12
<i>Rosmarinus officinalis</i> (Ro)	0.8	2.5	0.64	20
<i>Stauracanthus genistoides</i> (Sg)	0.9	2	0.2	6

Table 3: Scrub PAI values obtained with hemispherical photo and some PAI spectra parameters for shrub species.

Two parameters were estimated to evaluate the relation between spectral reflectance and PAI at species level: correlation (r Peason) and coefficient of variation (Cv). The parameters were calculated along wavelength but NIR region is the more related with quantity of leaf. Table 3 shows range values of PAI measured with hemispherical photo, and correlation and coefficient of variation for NIR region .

For the dominant species consider, one standard deviation about the mean reflectance, was used as the criterion to determine species characteristic increment due to PAI ranges. This increment represents the signal level to be evaluated against AHS radiometric and spectral performance.

4.2 AHS mapping capacity simulation

Species reflectance average and PAI increments characteristic was propagated to at-sensor radiance, at illumination and atmospheric conditions of the AHS flight line consider. AHS discrimination capacity for species discrimination and PAI increments, was assessed with their at-sensor radiances analyzing the spectral an radiometric power resolve. In this approach no consideration about spatial aspect was tucked into account, we assume a pixel cover entirely of the specie consider.

4.2.1 At-sensor radiance

Plant reflectance was fed into a standard radiative transfer code, converting surface data into at-sensor radiances with the correspondence atmospheric and illumination conditions of the september AHS flight line. MODTRAN4 (Berk et al 2000) was used to calculate the at-sensor radiances from 400 to 2500 nm, we assumed no adjacency effect and also isotropic radiation.

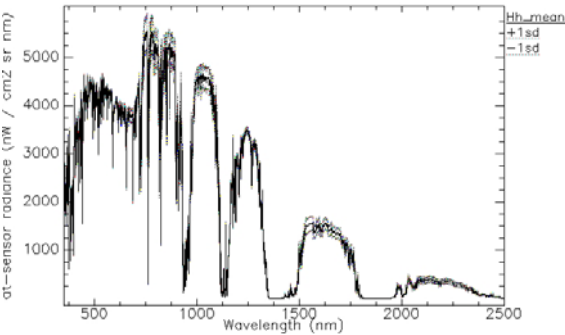


Figure 3: *Halimium halimifolium* (Mean ± 1SD) at- sensor radiance for AHS flight line conditions

Figure 3 shows the *Halimium halimifolium* average at-sensor radiance, plus  $\pm 1$  standard deviation, propagated with MODTRAN4 for the AHS illumination and atmospheric flight line conditions. Clearly it can be seen the water opaque bands (null transmittance), and the high spectral resolution of the MODTRAN output.

4.2.2 AHS radiometric resolve

AHS resolve the incoming signal with 12 bits of dynamic range, having independently channel programmable gain. The gain is set up depending on brightness conditions of ground surfaces, increasing the gain (see point 3.1) maximize the radiometric resolution, but reduce the saturation value.

The radiometric resolution applied is not the final discriminate radiometric capacity because of the noise. Noise is the un-information part of the signal and has multiple sources into and out of the sensor (atmosphere for example). A measurement that estimates the entire noise and the minimum signal discernible of the sensor is the Noise Equivalent Difference Radiance (NEDL), which is the signal with a signal-to-noise ratio of 1. Because of AHS is a mechanical scanner, AHS NEDL is function of the scan speed which image was gathered. The better spatial resolution the faster scan speed, then more NEDL is presented in the image. NEDL is also function of wavelength, in figure 1 the AHS NEDL for the flight-line for simulation is showed, calculated as the standard deviation of the BlackBody radiance registered in each line.

4.2.3 AHS spectral resolve

At-sensor radiance mean spectra and PAI species characteristic increments, of each dominant scrub specie was resampled, weighting by the AHS channel spectral response function. These response functions are band characterize by a wavelength center and a bandwidth or Full Width Half Maximum (FWHM). The response functions were measured at INTA facility using a monochomator with 0.2 nm resolution.

With the aim to evaluate the AHS spectral capacity for the discrimination of scrub species, the at-sensor radiances spectra were also resampled with the spectral configuration of the imaging spectrometer HyMap manufactured by Integrated Spectronics Pty, Ltd (www.intspec.com). HyMap is a reference sensor for vegetation mapping, and acquires images from 0.4 to 2.500 microns having 128 bands with a mean of 15 nm of FWHM. In this cases spectral resampling was realized using the bandcenter and FWHM assuming gaussian function response.

5. RESULTS AND DISCUSSION

Figure 4 shows the values retrieved with SSV algorithm among scrub species of the three communities, including as a reference the separability values of sand dune and *Pinus Pinea*. Very low separability values within community, show that spectral response between species of the same community are very similar in shape and distance. Species are well adapted to environmental conditions, so this behaviour is expected (Lewis, 2002). Furthermore, separability values between species of "Monte blanco" and "Monte Intermedio" are also very low (SSV nearly 0.3), indicating again similar adaptations of these two communities.

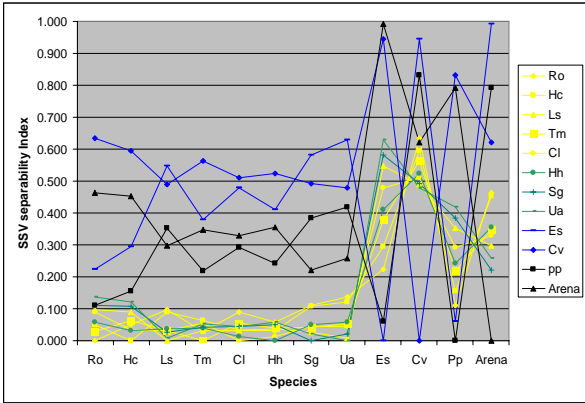


Figure 4: SSV values for spectra shrub species of Doñana's communities.

In order to evaluate if AHS can resolve the little radiometric differences between low separability species, on figure 5, the minimum and maximum separation found in at-sensor radiances values was plotted against AHS NEDL. The minimum was found between *Ulex australis* and *Stauracanthus genistoides*, and comparing with the NEDL of the AHS flight line, the difference is solved with enough capacity except for atmospheric absorptions regions in the VIS/NIR and in the final region of the SWIR. We have to had in mind that in the SWIR region an important factor for the spectral response of scrub is the presence of and litter and soil.

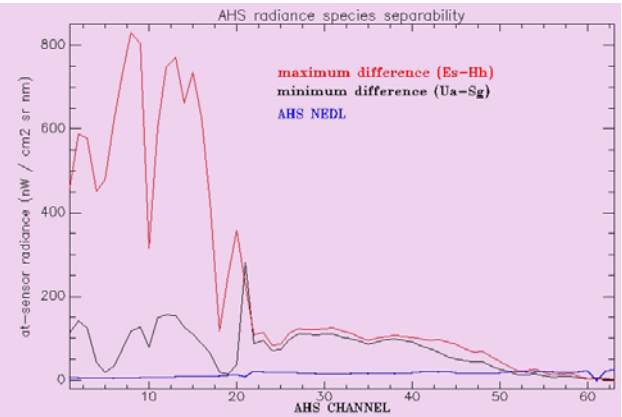


Figure 5: Maximum and minimum spectral differences against AHS NEDL .

As It can be seen in table 3, the relative PAI values, calculated with hemispherical photo, for the most abundant scrub species, has good correlation with the NIR reflectance ( $p < 0.05$ ). This part of the spectrum is more related with foliar presence (Asner, 1998). The worst correlate species in the NIR was *Stauracanthus genistoides* and *Ulex australis*, both species has the ecological adaptation to accumulate non-photosynthetic biomass in the canopy. In the SWIR region, an elevated negative correlation was found due to the influence of litter and soil, see figure 2, in scrub canopy spectra.

To evaluate if the AHS can resolve the variability in the canopy scrub response related with PAI variations, species increments characteristic in compared with the AHS NEDL. In figure 6 it can be seen that *Stauracanthus genistoides* and *Ulex australis* are again the species with the less increment, and it is difficult to discernable by AHS in the SWIR region due to the rise of the NEDL.

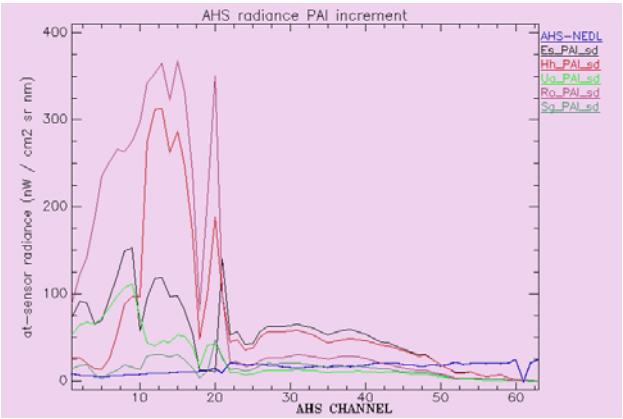


Figure 6: Scrub species PAI increments against AHS NEDL

Spectral resolution is more related with separability between species, specie characteristic features could be determined by proper spectral configuration. As the number, spectral interval and FWHM increase, the spectral response explication is better. In the SWIR part of the spectrum AHS has very good spectral resolution as HyMap, but in the VIS-NIR part is where AHS has half spectral than HyMap. For this reason we plot, in figure 7, the VIS/NIR scrub at-sensor spectra resampled with both spectral configuration. Just the two absorption atmospheric bands in 750 and 840 nm are not detected by AHS, but for the rest the spectrums are very similar.

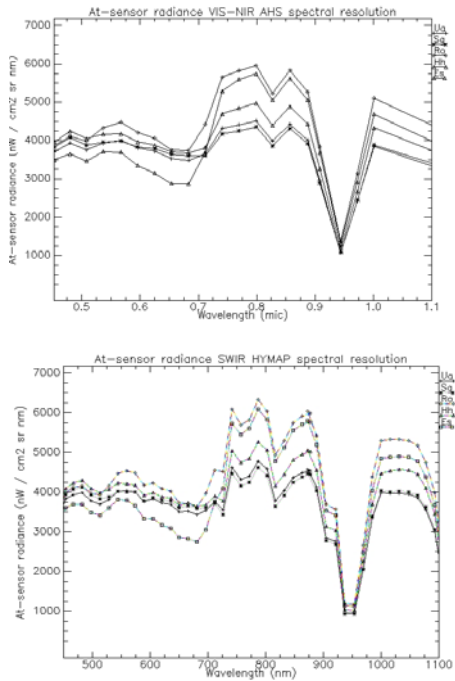


Figure 7: Scrub species VIS/NIR at-sensor radiance resampled to AHS channel (upper) and HyMap (bottom).

6. CONCLUSIONS

The spectral separability of Doñana’s scrub species is high on an inter-community level, but very low on an intra-community level. For AHS flight line conditions consider the NEDL is sufficient to discriminate the minimum separability except for the end part of the SWIR.

The effect of PAI variability over the NIR spectral response is higher on *Rosmarinus officinalis* and *Halimium halimifolium* than on *Ulex australis* and *Stauracanthus genistoides*, and medium level for *Erica scparia*. For AHS flight conditions the species characteristic PAI increments have higher radiance values than the NEDL, except for *Stauracanthus genistoides* over the entire spectrum and *Ulex australis* and *Rosmarinus officinalis* in the SWIR.

The spectral resolution of AHS in the VNIR, is enough to explain the features of the scrub spectrum in the comparison realized with HyMap.

The AHS discrimination values for scrub species at a specific flight condition, shows a high mapping capacity among communities but medium capacity for intra-community level.

7. REFERENCES

Asner, G.P. 1998. Biophysical and Biochemical Sources of Variability in Canopy Reflectance. *Remote. Sens. Env.* 64, pp. 234-253.

Cobo García, D., Sanchez Gullon, E., García Murillo, P. 2002. *Flora y Vegetación. Parque Nacional de Doñana*. Esfagnos. pp. 110-174.

Fernandez-Renau, A. Gómez, J.A. and De Miguel, E. (2005). The INTA AHS system. Proceedings. *SPIE Int. Soc.Opt. Eng.* 5978, 59781 L.

Lewis, M. 2002. Spectral characterization of Australian arid zone plants. *Can.J.Remote Sensing*, 28(2), pp. 219-230.

Magurram, A.E. 2004. *Measuring biological diversity*. Blackwell. pp 44-45.

Muñoz-Reinoso, J.C., Garcia Novo, F. 2000. Vegetation patterns on the stabilized sands of Doñana Biological Reserv. *Proceedings IAVS Symposium*, pp. 162-165.

Roberts, D.A., et al. 1998. Mapping Chaparral in the Santa Monica Mountains using Multiple Endmember. *Remote Sens Env* 65, 267-279.

Schaepman, M.E., Schläpfer, and Muller, A. 2001. Performance Requirements for Airborne Imaging Spectrometers. Final Report Phase B APEX. pp 45-47.

Chen, J.M., P.M. Rich, S.T. Gower, J.M. Norman, and S. Plummer. 1997. Leaf area index of boreal forests: theory, techniques, and measurements. *Journal of Geophysical Research*, BOREAS Special Issue 102(D24):29429-29444.

Verhoef, W., Bach, H. 2003. Simulation of hyperspectral and directional radiance images using coupled biophysical and atmospheric radiative transfer models . *Remote. Sens. Env.* 87, pp. 23-41.

8. ACKNOWLEDGEMENTS

The authors want to acknowledge to the staff of Doñana Biological Reserve for helpful and facilitate on the field spectroscopy campaigns.

# ELUCIDATING PHYSIOLOGY OF PLANT MEDIATED EXCHANGE PROCESSES USING AIRBORNE HYPERSPECTRAL REFLECTANCE MEASUREMENTS IN SYNOPSIS WITH EDDY COVARIANCE DATA

Michael Eiden<sup>1</sup>, Sebastian van der Linden<sup>2</sup>, Jan H. Schween<sup>3</sup>, Christoph Gerbig<sup>4</sup>, Bruno Neininger<sup>5</sup>, Yves Brunet<sup>6</sup>,  
Nathalie Jarosz<sup>6</sup>, Olivier Traullé<sup>7</sup>, Heiner Geiss<sup>8</sup> and Uwe Rascher<sup>1\*</sup>

<sup>1</sup> Institute of Chemistry and Dynamics of the Geosphere, Institute III: Phytosphere, 52425 Jülich / Germany

<sup>2</sup> Geomatics Department, Humboldt-Universität zu Berlin, 10099 Berlin / Germany

<sup>3</sup> Institute of Geophysics and Meteorology, Cologne University, 50937, Cologne / Germany

<sup>4</sup> Max Planck Institute for Biogeochemistry, 07745 Jena / Germany

<sup>5</sup> Metair AG, 8915 Hausen am Albis / Switzerland

<sup>6</sup> INRA Domaine de la Grande-Ferrade BP 81 33883, Villenave-d'Ornon Cedex / France

<sup>7</sup> Météo France, Centre National de Recherches Météorologiques, 31057 Cedex 1 Toulouse / France

<sup>8</sup> Institute of Chemistry and Dynamics of the Geosphere, Institute II: Troposphere, 52425 Jülich / Germany

**KEY WORDS:** *Remote Sensing, CERES, vegetation, photosynthesis, eddy covariance, hyperspectral reflectance, chlorophyll fluorescence, canopy photosynthesis*

## ABSTRACT:

The Carbo Europe Regional Experiment Strategy (CERES), conducted between May and June 2005, aims to determine a spatially resolved regional balance of carbon dioxide fluxes using different methodological approaches bundled within an international framework. In this study we elucidated several meteorological and physiological parameters determining plant mediated exchange processes using airborne hyperspectral reflectance measurements in synopsis with meteorological information like eddy flux covariance data. We used an airborne hyperspectral system to record spatial and temporal transects of vegetated areas surrounding flux tower sites in the Bordeaux / Landes Region (France). Alongside hyperspectral measurements a comprehensive range of meteorological and surface flux parameters were measured at a flux tower site within the same time frame.

Unsupervised data analysis using cluster analysis was performed on predefined spectral wavelength windows. Additionally multiblock principal component analysis was used as explanatory data driven tool to reveal underlying data structures and to elucidate potential interdependencies between airborne hyperspectral reflectance data and meteorological ground measurements.

In detail temporal, physiological changes in relevant ground information like temperature, humidity, vegetation mediated CO<sub>2</sub> flux, latent heat flux or photosynthetic light use efficiency on the one hand and selected regions of the hyperspectral signatures, such as reflectance in the region of 531nm, which determines variations in the photochemical reflectance index (PRI) or in the spectral regions of chlorophyll fluorescence were examined.

Unsupervised cluster analysis revealed coupled dependencies between changes in the derivative spectra in the range of 720 to 740 nm with gross photosynthetic uptake rate, global radiation and time of day. Multiblock principal component analysis revealed that first derivative reflectance in wavelengths from 500 to 540 nm and between 680 and 750 nm had higher loading values in respect to observed ground variables global radiation and gross photosynthetic uptake rate respectively. The significance of these findings is discussed.

## 1. INTRODUCTION

Roughly 90% of the gas exchange between the atmosphere and the bio-geosphere is mediated by plants through stomata and photosynthesis regulation (Ozanne et al. 2003). Photosynthetic apparatus dynamically adapts to environmental constraints and efficiency of photosynthesis depends on the properties and local environment of individual leaves and is difficult to model on the ecosystem level. This causes substantial uncertainties in global carbon models (Running et al. 2000). Variations in light use efficiency (LUE) arise from diverse contributions of plant genetic, morphological and architectural components to core ecosystem functions such as carbon and water vapor fluxes, energy transfer, responses to changing environment, stress and nutrients. On the ground eddy covariance measurements (Baldocchi 2003) are an accepted approach to quantify

photosynthetic carbon uptake, but until now no reliable remote sensing approach exists to quantify the actual physiological status of photosynthesis.

Recent developments in sensor technology and remote sensing sciences may provide direct information to quantify photosynthetic efficiency directly. The photochemical reflectance index (PRI), which can be derived from hyperspectral reflectance measurements, was developed to serve as an estimate of photosynthetic efficiency (Gamon et al. 1993; 1997; Peñuelas et al. 1995). This normalized difference reflectance index uses two wavebands: 531 nm, which is affected by the conversion of two pigments that dynamically adapt to physiological changes in photosynthesis, and 570 nm, which serves as a reference (Gamon et al. 1992). PRI has been successfully used to detect changes in photosynthetic efficiency from the leaf to the ecosystem level (for an overview see

\* Contact: u.rascher@fz-juelich.de



literature cited in Nichol et al. 2006; Rascher et al., 2007). However, effort is still needed to accurately scale these results to canopies, as absolute PRI values are greatly affected species properties (Guo & Trotter 2004) by structural properties, such as leaf angle distribution and seasonal changes in canopy structure (Barton & North 2000; Filella et al. 2004).

As a second promising approach to quantify physiology of photosynthesis is the detection of the fluorescence signal from chlorophyll a of the photosystems that is emitted with two specific maxima at 690 and 740 nm. Even though fluorescence is only 2-5 percent of the reflected light of green vegetation it still may be detectable using high performance hyperspectral sensors. The approach to use the sun-induced fluorescence signal as a measure of photosynthetic efficiency was recently highlighted by ESA's selection of the FLuorescence EXplorer (FLEX) mission to detect canopy fluorescence in the oxygen absorption bands from space (Carter et al., 1990, 1996; Cecchi et al., 1994; Moya et al. 2004)

In this communication we evaluated the potential to detect dynamic changes in canopy reflectance that is correlated to changes in photosynthesis. According to our knowledge this is the first publication combining airborne reflectance data from a natural canopies measured from different heights (100 - 2500 m), different times of the growing season, and different times of the day on the one hand, and ground measured data of photosynthesis on the other hand that was quantified by eddy covariance. In respect to the dynamic nature of photosynthesis, we also applied multiblock principal component analysis to our measurements. This method was originally developed in the field of chemometrics and is routinely used in the process monitoring approaches. Up to our knowledge this is the first time that multiblock principal component analysis is applied in the field of remote sensing with respect to plant physiology.

## 2. MATERIALS AND METHODS

### 2.1 Study site

The campaign was carried out in a 300 x 300 km large area in the South West of France belonging to the Départements Gironde and Landes. The region is dominated by commercially used pine forests, intensively used agricultural fields like maize and bean fields, as well as vineyards. The study site was chosen from a meteorological background, because of its steady westerly winds originating over the Atlantic Ocean. This allows an unbiased examination of changes in carbon dioxide concentration as air packages are moving eastwards over vegetated areas. Details about the experiment strategy and the study site are found in Dolman et al. 2006.

For this study we selected one field situated at 44°24' N and 0°38'22''W in a farmland site called La Cape Sud. The field approximately extends to 800 m in North-South direction and 500 m in East-West direction respectively in is traversed by to small ways used for farming activities. It is covered homogeneously with Maize plants and watered artificially with use of an automatic irrigation system (Figure 1A).

### 2.2 Study period

Flights were conducted on 9 individual days within two distinct periods ranging from May 24<sup>th</sup> to May 27<sup>th</sup> and June 6<sup>th</sup> to June 17<sup>th</sup>, respectively. For some of the observation days, two separate flights were performed: one before noon and one in the afternoon. The data recorded on May 27<sup>th</sup> was chosen as sample data set, which was used to establish the data pre-processing

routine described in the following chapters. The generated routines were then applied to data of all other flights individually.

Altogether, the data pool generated in context of this study comprises out of more than 270.000 individual spectra and accompanying video images. In general, observations were made at flight altitudes between 100 and approx. 2500 m.



Figure 1:

(A) Intensive study site (maize field at La Cape Sud) with eddy covariance tower (back left) and irrigation system (right). The picture is taken at May 25<sup>th</sup> at the beginning of the measurements, thus showing lowest vegetation cover. (B) Hyperspectral reflectance sensor (FieldSpec Pro) mounted in an underwing pod of the Dimona research aircraft. The fibre optics is NADIR pointing with a synchronized video camera and data acquisition is imbedded in the aircrafts positioning and computer system.

### 2.3 Airborne hyperspectral measurements

The ECO-Dimona research aircraft from Metair AG (Menzingen, Switzerland) was used as platform for the hyperspectral measurements. Alongside an extensive range of meteorological parameters like CO<sub>2</sub>, CO, NO<sub>x</sub>, (Neininger, 2001) were also captured simultaneously during flight. Additionally, for all measurements essential background information like flight altitude, position, and orientation was recorded. For the collection of hyperspectral reflectance data, a portable sensor (FieldSpec Pro, ASD Inc., Boulder, CO, USA) was mounted in the left under-wing pod of the aircraft (Figure 1B). Reflected light was captured in nadir orientation with a fiber optic that was equipped with a 1° lens barrel. Incident light was integrated for 130ms and spectrally analyzed in the range from 350 to 1050 nm, with a spectral resolution (FWHM) of 1.4 nm. The instrument was operated in continuous mode, thus spectra were collected with approximately 2 Hz. Spectral measurements were recorded using radiances and exposure time was adjusted to have best signal to noise ratio and to avoid saturation. In order to improve data quality, three spectra were averaged. A TTL trigger signal, generated by the FieldSpec device, was used (i) to record the time of each hyperspectral measurement and (ii) to capture a video image (640 x 480 pixels, 12-bit, grey values) using an industrial video camera (Flea, Point Grey Research, Vancouver, BC, Canada; with a 25



mm lens, Cosmimar/Pentax). Both camera and hyperspectral sensor share the same viewing orientation, but differ in their field of view (1° for the FieldSpec device and 10.5° for the video camera).

2.4 Eddy flux measurements

Meteorological ground measurements and calculation of turbulent fluxes was performed by Yves Brunet’s Group from INRA (Institut national de la recherche agronomique / Bordeaux). An eddy flux tower was installed and operated continuously in the centre of a maize field belonging to the farming site “La Cape Sud”. Flux measurements are related to friction velocity, energy budget and fluxes of trace species. The two former are measured together with the flux of CO<sub>2</sub>. Considering the surface energy balance expressed as the distribution of net radiation R<sub>n</sub> into sensible heat flux (H), latent heat flux (LE), and ground heat flux (G), consists of a 3D sonic anemometer, an infrared gas analyzer measuring CO<sub>2</sub> and H<sub>2</sub>O concentrations, and several radiation sensors. Friction velocity (u\*), H, LE and CO<sub>2</sub> flux were calculated using the eddy covariance technique, following a standardized protocol for instrument setup and data processing. The following instrumentation was used on the tower.

Parameter	Instrument
CO <sub>2</sub> and H <sub>2</sub> O IRGA	Li-7500 (LICOR, Lincoln, NE, USA)
3D-wind	Sonic Young 8100
Horizontal wind speed	Cup anemometer (Cimel)
Wind direction	Campbell
Air temperature and humidity	Vaisala
Net radiation	NR-Lite
Global radiation	Cimel CE 180
PPFD	Skye
Precipitation / irrigation	Several rain jauges

Table 1: Flux tower instrumentation

3. DATA PRE-PROCESSING

3.1 Hyperspectral data pre-processing

To handle and access data effectively, fusion and organization strategies were developed. Since the location of all objects seen by the sensor is a function of the aircraft's position, altitude and orientation, an exact assignment of these parameters to the spectral measurements is implicitly necessary for accurate data correction and subsequent interpretation tasks. To tackle this challenge, we developed a scalable database like data structure, merging all measured information, synchronized via trigger signals and timestamps. In summary, each record consists of 750 data points, of which 701 are spectral reflectance values. The remaining 49 data points are comprised of background information like time, geometric information as well as of meteorological information measured at coincident time on the aircraft.

**Geometric correction:** To determine the ground “foot print” actually observed by the sensor, we reconstructed the relative

viewing geometries for each measurement using the aircraft’s altitude, GPS position, pitch, roll and azimuth angles as well as a digital elevation model. Furthermore unmeasured effects like updraft dependent wing flex of the aircraft were compensated, by comparing calculated “foot print” positions with corresponding video camera imagery, iteratively. We are very confident to determine the foot print’s center position with an accuracy of approximately 1/2 of its diameter. Also the exterior geometry, describing the photon path from the sun to the target and then to the observing sensor, was determined using the relative orientation in conjunction with astronomical information. Knowledge about the relative azimuth and sun elevation is important for the interpretation of bidirectional surface reflection characteristics. For further analyses we only used those reflectance measurements, which centre position was insured to be within the vegetation of the eddy flux site.

**Radiance to Reflection conversion:** To convert the measured radiance spectra into reflectance spectra, a normalizing approach was conducted. The most homogeneous spectral signature found within the study site was the “Dune de Pyla”, Europe's largest wandering dune, located at the Atlantic coast at 44°35'40.0" North and 1° 12' 40.0" West in vicinity of the town Pyla sur Mer. The dune was recorded on many overpasses at varying altitudes during all flight days, due to the fact, that this area was chosen as a turning point in the flight patterns. Using sand as a reference is useful, because of its nearly “lambertian” reflection properties and its compositional homogeneity. Sand was collected from the dune and absolute reflection properties were determined under distinct laboratory conditions. Flight specific “radiance templates” were inferred using all available overpasses of the “Dune de Pyla”. In order to compensate for varying ancillary conditions, like prevailing atmospheric conditions and sand humidity, radiance templates needed to be determined for each flight individually. In a subsequent step, a conversion template was constructed using the quotient of the flight specific radiance template and the true reflection signature. Once this conversion template was computed, all other radiance spectra within the same time frame were converted to reflection spectra via division.

**Atmospheric correction:** Since the aircraft is moving in three dimensions and thus the photon pathway length is different for each measured spectrum, also atmospheric interactions are varying and needed to be compensated for individually. Atmospheric interactions underlie two fundamental principles: absorption and scattering. Gaseous absorption occurs at well defined spectral bands depending on the molecular concentration of the absorbing gas within the radiation pathway (Schande, 1986). In our measured spectral signal, gaseous absorption is mainly caused from oxygen at 762 nm and water vapour at several broad spectral regions, mostly in the mid-infrared region. Since the focus of our work is dominated by plant interactions in the visible and near-infrared regions and information about the spatial and temporal variability of absorbing gases was not available, we decided to segment the spectral data to a range of 350 to 750 nm. Atmospheric scattering caused by molecules and aerosol particles, however has an additive effect (path radiance) on lower wavelength regions. This effect is dependent on the optical thickness of the atmosphere below the sensor and the prevailing aerosol conditions (Angstrom, 1964). In order to describe and correct the additive scattering effects, we investigated the impact of scattering on the spectral signature of water, measured at different flight altitudes.

Roughly 2000 pure water measurements, originating from an area approximately 2 km west of the “Dune du Pyla” were extracted from the dataset. Similar to the dune measurements, these measurements were recorded at varying altitudes. For each wavelength we then investigated the height dependency and applied a robust regression fit to the minimal values. We chose the robust regression approach, because its liability for outliers is minimized compared to the traditional linear regression approach (Street et al, 1988). The height dependency of atmospheric scattering exhibits a nearly perfect linear relationship. Figure (2) depicts the robust regression fit for the wavelength of 350 nm.

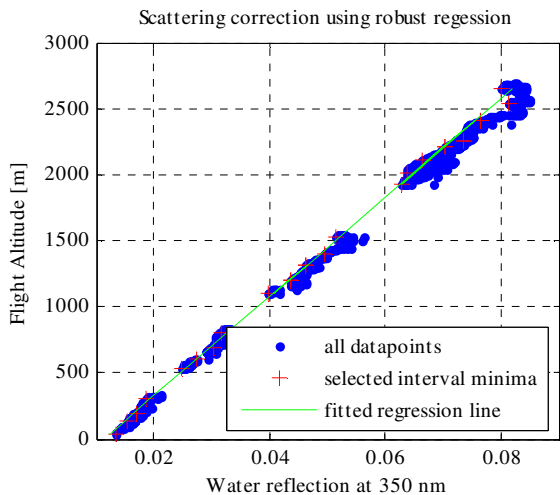


Figure 2:  
Concept of height dependent atmospheric correction of reflectance data using robust regression.

For each wavelength, the robust regression approach determines a correction coefficient and a corresponding offset value. The correction coefficient describes the steepness of the fitted function and therefore characterizes the height dependent scattering effect. The offset value denotes the intersection point of the fitted function with the wavelength axis. It shows that the height dependent influence of scattering decreases in an almost linear way as observed wavelengths increase Figure (3A). Furthermore it shows, that this effect is expanding far into the visual range and thus, might influence single-band based vegetation indices like the photochemical reflectance index (PRI), the cartenoid reflectance index (CRI) and the anthocyanin reflectance index (ARI) and others, if not corrected properly. In our case the minimal regression coefficient is found at 572 nm, showing that, at this wavelength, the slightest height dependent effect can be determined. Coefficients for wavelengths greater than the minimal value show no apparent structure, due to the fact no longer scattering but other processes like gaseous absorption are predominating. Therefore, we decided to restrict the scattering correction to the range of 350 to 572 nm, shown in blue in Figure (Figure 3B).

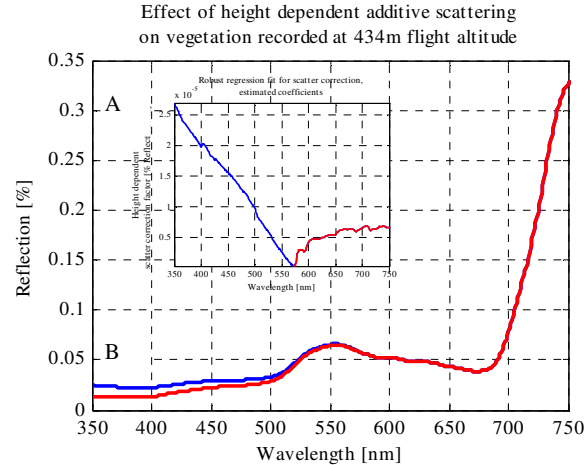


Figure 3.  
Derived correction coefficients (3A) and comparison of uncorrected (blue) and corrected vegetation spectra (3B)

Similar to the conversion from radiance to reflection values, the atmospheric scatter correction was computed for each flight individually. The correction itself was performed by subtracting the product of the determined coefficient with a given height from the original reflection values for wavelengths from 350 to 572 nm.

**Absolute and derivative spectra:** For further analyses we calculated two data sets: one consisting of absolute reflectance data (Figure 4A) and a second one containing the first derivatives of the reflectance data (Figure 4B). Derivative spectra may display narrow waveband features more obvious and are less dependent from changes in intensity of incoming radiation. In order to suppress high frequency noise, we smoothed the derivative spectra using a 15nm Savitzky-Golay smoothing function (Savitzky & Golay, 1965).

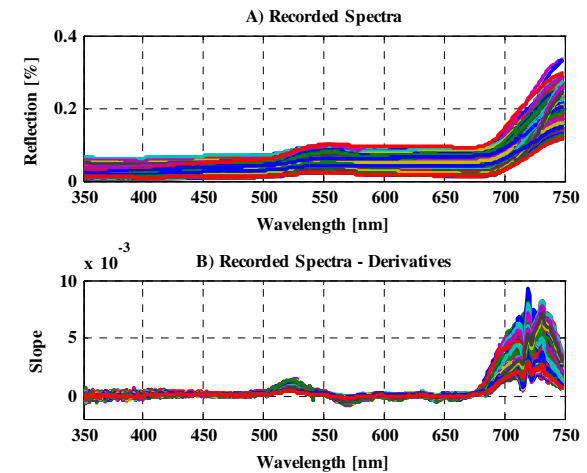


Figure 4.  
Reflectance data that were selected and used for statistical analyses. Altogether roughly 500 spectra were selected after pre-processing (A) original spectra and (B) 1<sup>st</sup> derivative spectra after smoothing with 15nm Savitzky-Golay filter.

### 3.2 Pre-processing of meteorological ground measurements

Similar to the spectral measurements also the meteorological ground measurements required intense data pre-processing procedures described in the following paragraphs.

**Elimination of un reliable fluxes:** The quality of the measured turbulent fluxes is highly dependent on the meteorological conditions. During times with very low wind velocities, turbulence coefficients may be affected by measurement artifacts like flow distortion by the instrument itself, or the influence of small surface inhomogeneities in the direct vicinity of the instrument. Therefore we decided not to use data taken at wind velocities below 2 m/s. Furthermore all data were pre-processed using a 2 hour smoothing filter.

**Eddy flux footprint:** The flux footprint i.e. the surface area where the flux mainly originates from changes its size and location with prevailing wind conditions and thermal stratification of the air. Therefore this footprint is not necessarily identical with the location and direct vicinity of the eddy covariance station itself. In order to ensure, that the inferred fluxes are mediated by fields observed by the airborne sensor we estimated the temporal variability of the flux footprint location and size using the wind direction and velocity. In a subsequent step we only selected those flux measurements, where wind direction ensured a footprint lying within the observed vegetation.

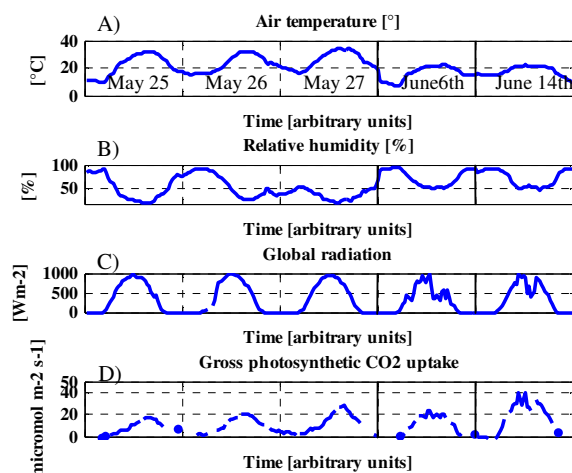


Figure 5.

Environmental factors and photosynthetic CO<sub>2</sub> uptake rate of the studied corn field at the days of overflights. Air-temperature (A), relative humidity (B), and global incoming radiation (C) were measured on the eddy flux tower. Net photosynthetic CO<sub>2</sub> uptake rate (D) were calculated from temperature corrected CO<sub>2</sub> flux data (see text for procedure)

**Inferring gross photosynthetic uptake rate from data:** Since the carbon dioxide exchange rate is comprised of photosynthesis as well as soil respiration the latter part needed to be subtracted in order to achieve gross photosynthetic uptake rate. Therefore an empirical correction scheme was conducted using the nightly carbon dioxide fluxes and soil temperature. As long as water status remains constant, microbial activity in soil and root respiration is mainly temperature dependent. We used all night time CO<sub>2</sub> flux data obtained during the measurement period and plotted those as a function of soil temperature.

Exponential rise of CO<sub>2</sub> fluxes with temperature and a linear correlation in Arrhenius plot supported this approach, the derived Q<sub>10</sub> value was 1.14. From this night time data a temperature corrected estimate of soil respiration was derived and temperature corrected respiration was subtracted from net carbon fluxes yielding photosynthetic CO<sub>2</sub> uptake rates and meteorological and environmental parameters determining plant performance.

## 4. DATA ANALYSIS

Hyperspectral measurements were linked to meteorological information measured on the ground via unique timestamps. After all pre-processing and merging procedures, the dataset consisted out of almost 500 data instances comprising out of two the distinct data blocks.

We treat both airborne hyperspectral and ground based measurements as independent approaches, both characterizing vegetation and its response to changing environmental conditions. Analysis of the data blocks and their interdependencies was conducted using two different approaches.

### 4.1 Forward search for interdependencies between spectral and ground data

We investigated the spectral variability in numerous predefined spectral wavelength windows using an unsupervised data analysis approach.

In detail eight spectral windows (350 – 500 nm, 500 – 600 nm, 600 – 670 nm, 680 – 750 nm, 526 -536 nm, 565 – 575 nm, 680 - 700nm and 720 - 740nm) were analyzed separately.

Absolute and first derivative spectra were partitioned into 5 clusters using Ward's algorithm (Ward, 1963) (5 different colors lower panel of Figure (6) In parallel the histogram distribution of ground measured variables were computed (see upper right panel in Figure (6) for the histogram distribution of photosynthetic CO<sub>2</sub> uptake rate). The interrelation of the two data sets was inspected visually on color coded cluster histograms (upper left panel in Figure (6) shows the cluster partitions and their and their corresponding composition of photosynthetic uptake rate status).

In this example it shows, that cluster 4 and 5, which are related to each other according to the dendrogram plot (data not shown) contain more samples measured at higher photosynthetic uptake rates (i.e. > 27  $\mu\text{mol m}^{-2} \text{s}^{-1}$ ) as clusters 1 to 3, where lower values are dominating. Furthermore Cluster 5 shows no contamination from samples acquired at lower photosynthetic uptake rates.

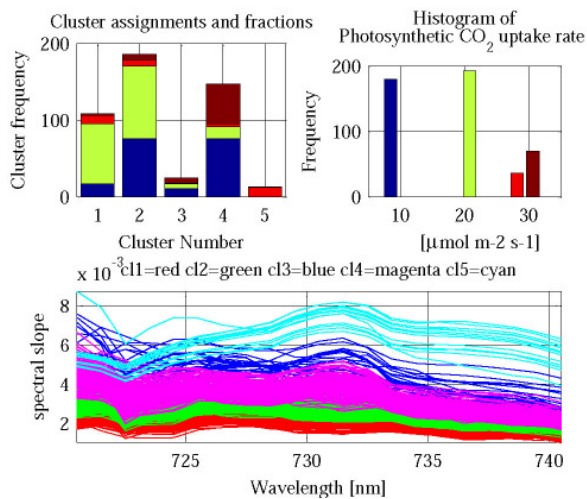


Figure 6

Example output from unsupervised analysis with spectral data colorcoded in cluster assignments (lower panel), cluster distribution and their corresponding combination of selected ground data variable fractions (upper right), histogram distribution of selected ground data variable (upper left).

4.2 Reverse search for interdependencies between spectral and ground data

In this context we performed multiblock-PCA approach to elucidate potential dependencies between the two distinct blocks. The multiblock-PCA approach is an extension of the traditional principal component analysis and was originally developed in field of chemometrics (Westerhuis et al, 1998). It aims at revealing underlying phenomena between predefined data blocks both describing the same object. For example, the blocks can be defined as datasets of two different analytical techniques both investigating the same sample. Firstly the algorithm performs a traditional principal component analysis on each data block separately in order to decompose the dataset into a set of few uncorrelated and independent factors. In a subsequent step the resulting scores and factors for both PCA approaches are then subjected to additional PCA on a so called super level. The multiblock analysis can be used as an explanatory tool and has the advantage it requires no a priori information. One drawback of the multiblock approach is that all data need to be normalized and scaled before projection in order to avoid artefacts due to pre-processing. In the context of this study spectral data was used in a window from 350 up to 750 nm. For the ground data, a set of variables most strongly linked to plant activity was pre-selected. Among them were: gross photosynthetic uptake rate, global radiation, air temperature, relative humidity and latent heat flux.

5. RESULTS

5.1 Forward approach:

According to the visual inspection described in the previous chapter, no obvious dependencies between absolute reflectance data and ground data could be observed. (Table 2) Slight dependencies could also be detected for flight altitude, manifesting in lower wavelength region, which was assumed to be most like due to remaining atmospheric scattering effects. Additionally a possible dependency between derivative

reflectance in the 720 – 740 nm window with photosynthetic uptake rate (Figure 6). , global radiation and time of day could be observed The three parameters: photosynthetic uptake rate, global radiation and time of day are intercorrelated, i.e. global radiation is highest during midday, which also facilitates highest rates of photosynthetic CO<sub>2</sub> uptake. Thus, it's motivating that these three parameters also appear correlated in this analysis.

Original Spectra	350-500nm	500-600nm	600-670nm	680-750nm	526-536nm	565-575nm	680-700nm	720-740nm
First derivate Spectra								
Flight altitude [m]	+	-	-	-	-	-	-	-
Zenith difference [°]	-	-	-	-	-	-	-	-
Azimuth difference [°]	-	-	-	-	-	-	-	-
Time of day	-	-	-	-	-	-	-	-
Absolute time	-	-	-	-	-	-	-	-
Air temperature [°C]	-	-	-	-	-	-	-	-
Wind velocity [m/s]	-	-	-	-	-	-	-	-
Global radiation	-	-	-	-	-	-	-	-
Relative humidity [%]	-	-	-	-	-	-	-	-
Photosynthetic uptake rate [μmol m <sup>-2</sup> s <sup>-1</sup> ]	-	-	-	-	-	-	-	-

Table 2:

Dependencies as identified by the forward cluster analyses. '+' / '++' indicate a weak / apparent dependency between two parameters and '-' indicates no dependency. Dependencies were described by visual inspection of the results.

5.2 Reverse approach:

Since the multiblock analysis is a purely data driven projection method, it provides a more objective view of inherent dependencies of the two independently measured data sets. In this context we used it to reveal common structures inherent in both data sets.

For the “ground data” block it showed, that for Factor 1 the variable “global radiation” indicates the highest loading value (i.e. contribution) compared to gross photosynthetic uptake rate, air temperature, relative humidity, and latent heat flux. In

Factor 2 the variable “photosynthetic uptake rate” is predominating (data not shown).

Since we are primarily interested, which spectral features might be coherent with the observed findings in the ground data block, we examined the super level scores and weights (data not shown) and the corresponding spectral loading plots of those factors found to be most closely linked to the factors determined in the ground data block.

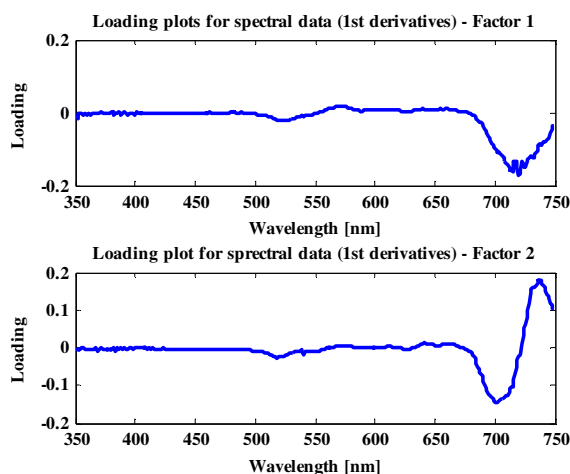


Figure 7:

Spectral loading plots, depicting the contribution of wavelengths to the Factors determined by principal component analysis.

The first Factor computed on derivative spectra was found to be most strongly linked to Factor 1 in the “ground data block” (i.e. dominated by global radiation), whereas the second one was found to be most strongly linked to Factor 2 in the ground data block (i.e. dominated by photosynthetic uptake rate).

The underlying structure of the spectral loading plots revealed, that wavelengths contribute differently to the observed patterns. In spectral data block a contribution of the derivative spectra between 500 and 540 nm and above 680 nm at first factor was clearly observed. Surprisingly at factor 2 a complex 2-peak feature above 670 nm appeared.

## 6. DISCUSSION

With this communication we demonstrate that variations in canopy reflectance that occur in the range of 500-550 nm and 680-750 nm may be associated with changes in canopy photosynthetic carbon fixation measured on the ground. These inter-correlations were detected with two independent statistical methods and only occurred in these wavebands. Whereas the forward analysis approach is highly subjective, the multiblock principal component approach requires no a priori knowledge. The changes could not simply be explained by the increased leaf area index of the vegetation within the whole measuring period. Thus our results point towards dynamic changes in reflectance in these spectral regions during the course of the day and changes that are driven by changing illumination (see Table 2).

During the past years a lot of effort was put in the search for a suitable method to directly measure photosynthetic efficiency to reduce uncertainties in carbon models (Running et al 2000) and

for managing agricultural systems. Up to now two approaches are favored and our results may well contribute in better planning future experiments and to focus on the potentially best spectral regions.

As a first approach hyperspectral reflectance measurements show increasing potential for monitoring function of plant ecosystems. The photosynthetic reflectance index (PRI) positively correlates with photosynthetic efficiency, is negatively correlated with NPQ and has been successfully used to detect changes in photosynthesis on the leaf level (Peñuelas et al., 1995; 1997; Gamon et al., 1997) and small canopy level (Gamon et al., 1992; Stylinski et al., 2002; Trotter et al., 2002; Nichol et al. 2006). However, on the ecosystem high uncertainties arise and only a very few studies are available that could reliably correlate variations of PRI with ecosystem photosynthesis (Nichol et al., 2000; 2002). Other studies explicitly report that they failed to predict photosynthetic efficiency using the PRI (Methy, 2000) or structural changes in the canopy superimposed subtle changes in photosynthetic efficiency.

A second remote sensing approach attempts to directly measure the fluorescence signal of chlorophyll that is closely related to charge separation within the photosystems itself and that can be used to quantify carbon metabolism (Rascher et al 2004). Fluorescence of chlorophyll is emitted as a two peak feature that is related to the physiological status of photosynthesis (see introduction for references). Despite this obvious advantage it still remains a challenge to detect the comparably small variations in fluorescence on the background of reflected and scattered light. Additionally the link between canopy fluorescence and ecosystem carbon exchange still needs to be made.

We acknowledge the uncertainties that still underlie our analyses and we want to point out that the limited data pool and a possible bias in data distribution has to be reevaluated. Thus, our study should be understood as a first promising evaluation of both approaches. Greatly extended measurements will take place in 2007 in the same study site. During these studies additional airborne sensors will be employed, auxiliary ground data will be acquired and care will be taken to avoid bias in the data sets.

But we clearly could demonstrate the potential of the multiblock approach that revealed subtle and unsupervised dependencies between ground measured photosynthesis and airborne and ultimately spaceborne reflectance.

We propose that the fluorescence signal is the superior signature because variations in reflectance at 680-750 nm had a greater contribution to explain variations on the ground (Fig. 7) and the fact that a two-peak feature emerged in this region might point towards the underlying fluorescence that modulate reflectance in this region.

## REFERENCES

- Angstrom, A. (1964), Techniques of determining the turbidity of the atmosphere, *Tellus*, 13, 214, 1
- Baldocchi D.D. (2003) Assessing the eddy covariance technique for evaluating carbon dioxide exchange rates of ecosystems: past, present and future. *Global Change Biology*, 9: 479-492.
- Barton, C.V.M., and P.R.J. North (2000). Remote sensing of canopy light use efficiency using the photochemical reflectance index. *Remote Sensing of Environment*, 78: 264-273.



- Carter, G.A., Jones, J.H. Mitchell R.J., and Brewer C.H. (1996). Detection of solar-excited chlorophyll a fluorescence and leaf photosynthetic capacity using a Fraunhofer line radiometer. *Remote Sensing of Environment*, 55: 89-92.
- Carter G.A. Theisen A.F. Mitchell R.J. (1990) Chlorophyll fluorescence measured using the Fraunhofer line-depth principle and relationship to photosynthetic capacity in the field. *Plant, Cell & Environment* 13, 79-83
- Cecchi, G., Manzocchi, P., Pantani, L., Valentini, R., Tirelli, D., & De Angelis, P. (1994). Remote sensing of chlorophyll a fluorescence of vegetation canopies: 1. Near and far field measurement techniques. *Remote Sensing of Environment*, 47, 18-28
- Dolman A. J. et al. (2006), "CERES, the CarboEurope Regional Experiment Strategy in Les Landes, South West France, May-June 2005". *BAMS Atmospheric Chemistry*, in press.
- Filella I. Peñuelas J. Llorens L. Estiarte M. (2004) Reflectance assessment of seasonal and annual changes in biomass and CO<sub>2</sub> uptake of a Mediterranean shrubland submitted to experimental warming and drought. *Remote Sensing of Environment* 90, 308-318.
- Gamon, J.A., I. Filella, and J. Peñuelas, (1993). The dynamic 531-nm  $\Delta$  reflectance signal: a survey of 20 angiosperm species. Photosynthetic responses to the environment (H.Y. Yamamoto and C.M. Smith, editors), *American Society of Plant Physiologists*, Rockville, MD, pp. 172-177.
- Gamon, J.A., J. Peñuelas, and C.B. Field, (1992). A narrow-waveband spectral index that tracks diurnal changes in photosynthetic efficiency. *Remote Sensing of Environment*, 41: 35-44.
- Gamon, J.A., L. Serrano, and J.S. Surfus, (1997). The photochemical reflectance index: an optical indicator of photosynthetic radiation use efficiency across species, functional types and nutrient levels. *Oecologia*, 112: 492-501.
- Guo J. and Trotter C.M. (2004) Estimating photosynthetic light-use efficiency using the photochemical reflectance index: variations among species. *Functional Plant Biology* 31, 255 - 265.
- Methy, M., 2000. Analysis of photosynthetic activity at the leaf and canopy levels from reflectance measurements: a case study. *Photosynthetica*, 38: 505-512.
- Moya I. Camenen L. Evain S. Goulas Y. Cerovic Z.G. Latouche G. Flexas J. Ounis A. (2004) A new instrument for passive remote sensing: 1. Measurements of sunlight-induced chlorophyll fluorescence. *Remote Sensing of Environment* 91, 186-197.
- Neininger, B. (2001), "A small aircraft for more than just ozone: Metair's 'Dimona' after ten years of evolving development". *Proceedings of the 11th Symposium on Meteorological Observations and Instrumentation*, 81st AMS Annual Meeting, 14-19 January 2001, Albuquerque, NM, USA.
- Nichol, C.J., K.F. Hümmrich, T.A. Black, P.G. Jarvis, C.L. Walthall, J. Grace, and F.G. Hall, 2000. Remote sensing of photosynthetic-light-use efficiency of boreal forest. *Agricultural and Forest Meteorology*, 101: 131-142.
- Nichol, C. J., J. Lloyd, O. Shibistova, A. Arneth, C. Roser, A. Knohl, S. Matsubara, and J. Grace, 2002. Remote sensing of photosynthetic light use efficiency of Siberian boreal forest *Tellus B*, 54: 677-687.
- Nichol C.J., Rascher U., Matsubara S. & Osmond C.B. (2006) Assessing photosynthetic efficiency in an experimental mangrove canopy using remote sensing and chlorophyll fluorescence *Trees – Structure and Function*, 20, 9-15.
- Ozanne CMP, Anhu D, Boulter SL, Keller M, Kitching RL, Meinzer FC, Mitchell AW, Nakashizuka T, Dias PLS, Wright SJ & Yoshimura M (2003) Biodiversity meets the atmosphere: a global view of forest canopies. *Science* 301, 183-186.
- Peñuelas, J., I. Filella, and J.A. Gamon, 1995. Assessment of photosynthetic radiation-use efficiency with spectral reflectance. *New Phytologist*, 131: 291-296.
- Peñuelas, J., J. Llusia, J. Pinol, and I. Filella, 1997. Photochemical reflectance index and leaf radiation-use efficiency assessment in Mediterranean trees. *International Journal of Remote Sensing*, 13: 2863-2868.
- Rascher U., Bobich E.G., Lin G.H., Walter A., Morris T., Naumann M., Nichol C.J., Pierce D., Bil K., Kudayarov V. & Berry J.A. (2004) Functional diversity of photosynthesis during drought in a model tropical rainforest – the contributions of leaf area, photosynthetic electron transport and stomatal conductance to reduction in net ecosystem carbon exchange. *Plant, Cell & Environment*, 27, 1239-1256.
- Rascher U., Nichol C.L., Small C. & Hendricks L. (2007) Monitoring spatio-temporal dynamics of photosynthesis with a portable hyperspectral imaging system. A case-study to quantify photosynthetic efficiency on genetically modified *Arabidopsis thaliana* (L.) Heynh. plants and on leaves of four drought stressed tropical tree species. *Photogrammetric Engineering and Remote Sensing*, 73, 45-56.
- Running SW, Thornton PE, Nemani R & Glassey JM, (2000) Global terrestrial gross and net primary productivity from the earth observing system. In: Sala OE, Jackson RB, Mooney HA & Howarth RW (eds) *Methods in Ecosystem Science* Springer Verlag, New York, pp 44-57.
- Savitzky, A., and Golay Marcel J.E. (1964). Smoothing and Differentiation of Data by Simplified Least Squares Procedures. *Analytical Chemistry*, 36: 1627-1639
- Schande, E., (1988), *Physical Fundamentals of Remote Sensing*, Springer-Verlag, New York, 1986
- Stylinski, C.D., J.A. Gamon, and W.C. Oechel, (2002). Seasonal patterns of reflectance indices, carotenoid pigments and photosynthesis of evergreen chaparral species. *Oecologia*, 131: 366-374.
- Street, J.O. et al, (1988), A Note on Computing Robust Regression Estimates via Iteratively Reweighted Least Squares. *The American Statistician*, 42, p.152-154.
- Trotter, G.M., D. Whitehead, and E.J. Pinkney, (2002). The photochemical reflectance index as a measure of photosynthetic light use efficiency for plants with varying foliar nitrogen content. *International Journal of Remote Sensing*, 23: 1207-1212.

Ward, J., (1963), Hierarchical Grouping to optimize an objective function, *Journal of American Statistical Association*, 58(301)

Westerhuis, J., Kourti, T., Macgregor, J.F., (1998), Analysis of multiblock and hierarchical PCA and PLS models, *Journal of Chemometrics* 12, 301-321

# HYPERSPECTRAL REMOTE SENSING FOR SEASONAL ESTIMATION OF ABOVEGROUND BIOMASS IN GRASSLAND HABITATS

A. Psomas<sup>a,b,\*</sup>, M. Kneubühler<sup>b</sup>, K. Itten<sup>b</sup>, N. E. Zimmermann<sup>a</sup>

<sup>a</sup> Swiss Federal Research Institute WSL, Zuercherstrasse 111, 8903 Birmensdorf, Switzerland – (achilleas.psomas, nez)@wsl.ch;

<sup>b</sup> Remote Sensing Laboratories (RSL), Dept. of Geography, University of Zürich, Winterthurerstrasse 190, 8057 Zürich, Switzerland – (kneub, itten)@geo.unizh.ch

**Working Group VII/1 - Fundamental Physics and Modelling**

**KEY WORDS:** Biomass, Field spectrometer measurements, Hyperion, Species rich grasslands, Subset regression analysis.

## ABSTRACT:

Dry grassland sites are amongst the most species rich habitats of Central Europe. In Switzerland, they are home to a large number of plant and animal species that are classified as endangered or threatened. A key component for designing optimal and effective management schemes ensuring the sustainability of these ecosystems, is knowledge of their biomass production. In this study we explored the potential of hyperspectral remote sensing for mapping above-ground biomass in grassland habitats along a dry-mesic gradient, independent of a specific habitat or a phenological period. We developed statistical models between spectral reflectance collected with a spectrometer but resampled to Hyperion bands, and biomass samples. We then tested to what degree the calibrated biomass models could be scaled to actual Hyperion data collected over the study area. Biomass samples (n = 155) were collected from 11 grassland fields located in the Central part of the Swiss Plateau. To capture normally occurring variation due to canopy growth stage and management factors sampling was performed at 4 time steps during the 2005 growing season. We investigated the relationship between biomass and a.) existing broad and narrow-band vegetation indices, b) narrow band NDVI type indices and c.) multiple linear regression using branch-and-bound variable search algorithms. Best models for estimating and predicting biomass were obtained from the multiple regression and narrow band NDVI type indices contrary to existing vegetation indices. Spectral regions related to plant water content were identified as the best estimators of biomass. Furthermore, results from this study demonstrated the importance of seasonal biomass measurements for building reliable models. Finally, promising results in estimating grassland biomass were not only obtained for the Hyperion resampled field spectrometer data, but also for the actual Hyperion data, showing the potential of up-scaling to the landscape level.

## 1. INTRODUCTION

Dry grassland sites are amongst the most species rich habitats of Central Europe. They originate from centuries of traditional land use and are a characteristic component of the cultural landscape in Europe. In Switzerland, conservation of biodiversity in these habitats is of major ecological importance. Almost 40% of plant and more than 50% of animal species living in these habitats are classified as endangered and are included in red lists (Eggenberg, 2001). Productivity and biomass of these grasslands have strong effects on both species competition and human management schemes, as higher productivity grasslands are more prone to be converted to agricultural areas. Therefore, development of robust and timely biomass estimates is of critical importance for monitoring and designing effective management practices that optimize sustainability of these ecosystems.

Direct measurements of grassland biomass are time consuming and expensive since they require extensive field work. In particular estimation of the spatial and temporal distribution of biomass at the landscape level is difficult to obtain from traditional methods. One of the major sources of information for the study of landscape and for estimating biomass over large areas is remote sensing (Kumar et al., 2001; Wylie, 2002). Attempts to estimate biomass using broadband sensors with spatial resolutions of 30m to 1km have resulted in a wide range of accuracies and precision (Dengsheng, 2006). In most of these

studies, quantity and variability of grassland biomass was estimated with vegetation indices calculated using the red and near-infrared bands of the broadband sensors.

Recently, new remote sensing instruments such as hyperspectral sensors (Van de Meer et al., 2001) that record many individual bands at very high spectral resolution have been developed. Studies using hyperspectral data to retrieve biomass have been carried out under controlled laboratory conditions (Filella, 2004; Mutanga, 2004) or in the field for vegetation types like wheat or corn that show low spatial variability of biomass (Hansen, 2003; Osborne et al., 2002; Xavier et al., 2006). Few studies only exist that have investigated the relationship between hyperspectral remote sensing and biomass production of mixed grassland ecosystems (He, 2006; Mirik et al., 2005; Tarr et al., 2005) and none, to our knowledge, that has extended such analyses over a growing season.

The objective of our study was to develop a method using field spectrometer data for estimating above ground biomass in grassland habitats along a dry-mesic gradient. The method should be independent of specific habitats or phenological period. We further investigated to what degree the calibrated biomass estimation could be scaled to Hyperion hyperspectral data. By this, we aimed at evaluating the potential to scale models calibrated from plot based estimates to larger landscapes as seen from spaceborne sensors.

2. MATERIALS AND METHODS

2.1 Study area

The study was conducted on the Central part of the Swiss Plateau around 8°02' E, 47°25'N near the village of Küttingen. The elevation of the area ranged from 350 to 500 m. Four characteristic grassland types were sampled (Table.1) that were previously mapped in a national mapping campaign (Eggenberg, 2001). The four semi-natural grassland types (AE, AEMB, MBAE, MB) were selected according to their position along a wet-dry gradient. AE is a species-rich Arrhenatherion type managed grassland, that is mesic and nutrient rich. The mesic and species-rich type AEMB includes tall, dense and multi-layered stands composed of many grasses, several herb species, and is still comparably nutrient-rich . In this type, canopy layers close to the ground are relatively damp and cool as a result of the dense growth. The type MBAE stands in-between AEMB and MB with respect of species richness, nutrients and canopy height. Finally, true semi-dry MB grasslands are comparably nutrient-poor and are generally dominated by *Bromus erectus* or *Brachypodium pinnatum* with stems standing well above the surrounding shorter herb vegetation. These stands are generally colourful and rich in herbs and species in general. The main management practice of the grasslands in the study area is for production of hay and only a few are used as pastures.

Type code	Phytosociology	Description
AE	species-rich Arrhenatherion type Transition	Mesic, species rich, nutrient-rich, managed
AEMB	Arrhenatherion to Mesobromion Transition	Moderately-mesic, species-rich
MBAE	Mesobromion to Arrhenatherion	Moderately-dry, species-rich
MB	Mesobromion type	Species-rich, semi-dry grassland

Table 1. Description of the four grassland types sampled

2.2 Biomass sampling

A total of 11 fields belonging to the 4 grassland types were selected from the existing national campaign map. The fields were chosen to have a total area larger than 5 Hyperion pixels and were checked for purity: we only kept grasslands, where the major vegetation type covered at least 75% of the mapped polygon. Sampling was performed at four times during the growing season of 2005 (10<sup>th</sup> June, 23<sup>rd</sup> June, 28<sup>th</sup> July, 10<sup>th</sup> August). We did so to ensure that normally occurring variation due to canopy growth stage and management factors was included in the dataset and the subsequent statistical models. Biomass samples were clipped at ground level using a 32cm radius metal frame. Within each field, 3 randomly selected plots were sampled to account for the spatial variability of the grassland habitats and to assist with the up-scaling of the analysis to the landscape-Hyperion level. A total of 155 biomass samples were collected. The collected material was stored in pre-weighted air-sealed plastic bags and transferred to the laboratory where the total fresh biomass was measured. Then samples were dried in the oven at 65 °C for 72h and weighted again to measure the water content and total dry biomass.

2.3 Field-Satellite Spectral Measurements

Spectral profiles of the grassland types were collected using the Analytical Spectral Devices (ASD) FieldSpec Pro FR spectrometer. This spectrometer has a 350-2500 nm spectral range and 1 nm spectral resolution with a 25° field-of-view. Collected spectra were converted to absolute reflectance by reference measurements over a Spectralon reflectance panel (Labsphere, Inc., North Sutton, N.H.) with known spectral properties. Calibration of the spectrometer was made every 20 measurements to minimize changes in atmospheric condition. Measurements were collected under sunny and cloud free conditions between 10:00 and 16:00 h while walking along 2 diagonal transects across the length of every field. This resulted in 60-100 spectral measurements per field, which ensured that the sampling would cover the spectral variability within each field. Measurements were taken from nadir at a height of ~1.5m above vegetation canopy. Field spectra were then resampled to simulate Hyperion spectral bands. Finally, after removal of erroneous measurements, the mean spectral reflectance of each grassland field was calculated.

Hyperion Level 1R data were acquired over the study area at nadir (overhead) pass on August 10, 2005 at 10:06:49 GMT. The EO-1 satellite has a sun-synchronous orbit at 705 km altitude. Hyperion collects 256 pixels with a size of 30 m on the ground over a 7.65 km swath. Data is acquired in pushbroom mode with two spectrometers. One operates in the VNIR range (70 bands between 356-1058 nm with an average FWHM of 10.90 nm) and the other in the SWIR range (172 bands between 852-2577 nm, with an average FWHM of 10.14 nm). From the 242 Level 1R bands, 44 are set to zero by software (bands 1-7, 58-76, 225-242). Post-Level 1R data processing of the acquired Hyperion scene included correction for striping pixels, smoothing using forward and inverse Minimum Noise Fraction transformation (MNF) (Datt et al., 2003), atmospheric correction using ATCOR-4 (Richter, 2003) and georectification of the scene using 25 ground control points. After removal of Hyperion bands that: were set to zero, were weak and with noisy signal and were strongly affected by atmospheric water, a total of 167 bands were available for further analysis (426 – 2355 nm).

2.4 Statistical analyses

The mean spectral reflectance of the 60-100 spectral measurements and the mean biomass of the 3 samples collected at each grassland field were used in the statistical analysis. Initial analysis revealed a heavily skewed distribution of the biomass data. In order to improve the regression modelling we log-transformed the biomass data so they would approach a normal distribution. Statistical models were calibrated with field spectrometer reflectance data resampled to simulate Hyperion bands.

Firstly we evaluated the relationship between biomass and normalised differences indices (NDVI, SR, RDVI, TVI), red edge indices (GMI, CI, VOG<sub>a</sub>, RESP), three band indices (MCARI, TRVI, MCARI1) and soil line indices (SAVI, MSAVI, SARVI). A detailed description about properties and advantages of these indices can be found in Broge and Leblanc (2000) and in Haboudane et al. (2004).

However, most of the above mentioned indices consider only certain parts of the spectrum, primarily the chlorophyll absorption region (680nm), the NIR reflectance (800nm) and

the green reflectance peak (550nm). Given this limitation and in an attempt to make use of the large number of narrow bands of hyperspectral data we built narrow band NDVI-type ( $nb\_NDVI_{type}$ ) indices as shown in Eq. (1).

$$nb\_NDVI_{type}[\lambda_1, \lambda_2] = \frac{\lambda_1 - \lambda_2}{\lambda_1 + \lambda_2}$$

(1)

All possible two-pair combinations were used in Eq. (1) where  $\lambda_1$  and  $\lambda_2$  were the Hyperion simulated bands from the field reflectance measurements. A total of 27,889 narrow band indices were calculated. These indices were used in linear regression models to determine their relationship with measured biomass.

The disadvantage of existing indices and of the  $nb\_NDVI_{type}$  indices is that they only consider a few of the available hyperspectral bands. Even though much of the information provided by neighbouring bands is often redundant (Thenkabail, 2004) it is still possible that the spectral information is not optimally used by these indices. Therefore, multiple linear regression (MLR) that selects the best combination of linear predictors from the Hyperion simulated bands was used for biomass estimation along the growing season. Branch-and-bound (b&b) (Miller, 2002) variable search algorithms were used to find spectral bands that best explained biomass.

The overall capability of each model in explaining the variability in the biomass was evaluated by the adjusted coefficient of determination ( $adj.R^2$ ). We used the  $adj.R^2$  since it will only increase if the new variable added will improve the model more than would be expected by chance. The model prediction error for estimating biomass was assessed by using a cross-validation (CV) procedure (Diaconis and Efron, 1983). With CV predicted samples are not used to build the model, so the Root Mean Square Error (RMSE) calculated is a good indicator of the model accuracy and predictive power. Cross-validation RMSE (CV-RMSE) was estimated by using all the biomass samples collected during the growing season. Nevertheless, to investigate the effect of seasonal variability we used a 4-fold “Date” CV procedure. By this, we calibrated models using data collected from three dates and then validated their predictions with data collected on the fourth. This process was repeated 4 times until each date was used for validation of model predictions once. Finally, the models with the highest accuracy and predictive power were used on the geometrically and atmospherically corrected Hyperion scene to predict the spatial distribution of biomass over the study area.

3. RESULTS AND DISCUSSION

Before the analysis of the relationship between biomass and remotely sensed data, descriptive biomass statistics were generated and are presented in Table 2 and Figure 1. Highest variability of biomass measurements was observed on the first (10<sup>th</sup> June) and second (23<sup>rd</sup> June) sampling dates. This happened since the grasslands sampled were along a dry-mesic gradient having different availability to water and nutrients and eventually different rates of growth and biomass accumulation. Lower biomass variability observed later on the season could be partly attributed to the management practices (cutting) applied on these fields.

Models using existing indices (e.g., NDVI, SAVI, MCARI, VOG<sub>a</sub>) gave poor  $adj.R^2$  values (Table 3). Marginally better results were obtained for SAVI. This index corrects for the soil background reflectance thus improving the model since many grassland fields did not have complete canopy cover during the season. Models for estimating biomass that used recently developed narrow band indices (e.g., MCARI, TVI, VOG<sub>a</sub>) did not produce higher  $adj.R^2$  (not all results shown here).

	n	Biomass (kg/m <sup>2</sup> )				
		Mean	stdev	Min	Max	Range
Original	50	0.7756	0.5704	0.1785	3.3180	3.1395
Log-transf.	50	-0.4523	0.6186	-1.7230	1.1990	2.9220

Table 2. Summary statistics for original and log-transformed measured biomass at 50 grassland fields over 4 time steps during the 2005 growing season

All possible two band combinations were used to create  $nb\_NDVI_{type}$  indices. Regression coefficients ( $adj.R^2$ ) between biomass and each  $nb\_NDVI_{type}$  index were determined and graphically presented in Figure 3. The  $adj.R^2$  values ranged from 0.007 to 0.72 reflecting a wide variation in the strength of the relationship between  $nb\_NDVI_{type}$  indices and biomass. Compared to existing indices that primarily use the red and NIR parts of the spectrum, our analysis identified regions from the far-NIR and SWIR resulting in much higher  $adj.R^2$  values (Table 3). High  $adj.R^2$  values were found clustered in three spectral regions, namely: 1230nm, 1680nm and 2280nm. These parts of the spectrum are strongly related to plant leaf water content that has a correlation to canopy biomass and LAI (Hunt, 1991) and to cellulose, starch, lignin and nitrogen concentrations (Kumar et al., 2001). Our results, and in particular the  $nb\_NDVI_{type}$  indices formed from bands around 1700 and 1170 nm confirm findings of earlier studies (Cook et al., 1989; Hunt, 1991) that correlate the ratio between NIR and SWIR to productivity and LAI. The use of  $nb\_NDVI_{type}$  indices for estimating biomass did not only improve the  $adj.R^2$ , but also reduced the CV-RMSE thus the overall prediction accuracy of the models.

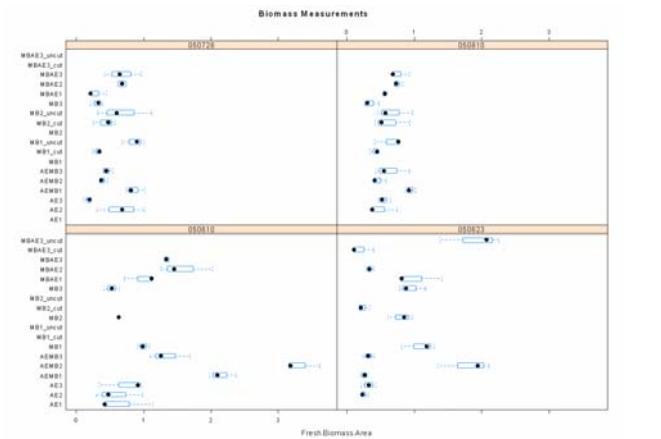


Figure 1. Mean biomass measurements of individual sampled fields during the growing season

Results of the multiple regression models for estimating biomass from spectral reflectance are listed in Table 3. We only built models using up to 4 spectral bands, since accuracies improved only marginally above this number and because we had too few measurements to build models with a high number



of predictors. Although selection of spectral bands was solely based on statistical optimisation of the models, these bands were located at key spectral regions with respect to physical processes of vegetation. The 472, 522 nm bands from the visible region can be correlated with chlorophyll content of vegetation, the 1202 nm from the NIR and the 1716 nm from the SWIR are related to plant leaf water content (Hunt, 1991) and the 2266 nm region to biochemical canopy properties like cellulose, starch and lignin (Elvidge, 1990). Even though models used slightly different bands, these were neighbouring and highly correlated to the ones mentioned above and thus provided the same type of information.

Model	Adj.R2	CV-RMSE
SAVI	0.29	0.53
NDVI	0.28	0.51
VOG <sub>a</sub>	0.22	0.54
nb_NDVI <sub>type</sub> b1715,b1172	0.61	0.39
nb_NDVI <sub>type</sub> b1092,b2266	0.52	0.43
MLR-2 bands b482,b1785	0.77	0.29
MLR-2 bands b472,b1785	0.77	0.31
MLR-3 bands b522,b1695,b1715	0.82	0.27
MLR-3 bands b1192,b1202,b1232	0.82	0.29
MLR-4 bands b522,b1212,b1232,b1715	0.86	0.23
MLR-4 bands b522,b1212,b1232,b1705	0.86	0.25

Table 3. Adjusted regression coefficient (adj.R<sup>2</sup>) and prediction error (CV-RMSE) of the best models for the three approaches (existing indices, nb\_NDVI<sub>type</sub> indices, MLR) for estimating grassland biomass

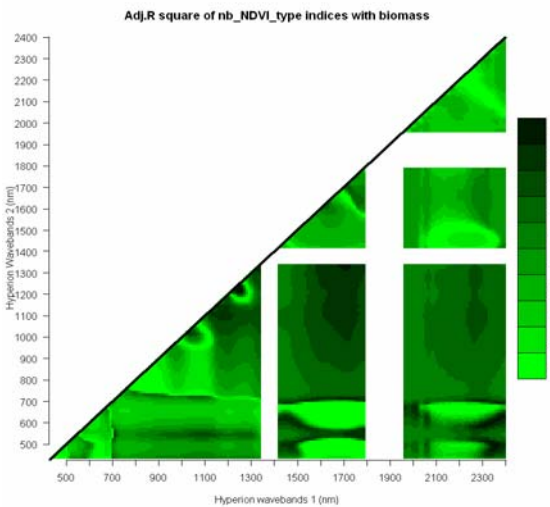


Figure 2. Result of the nb\_NDVI<sub>type</sub> indices analyses. The graph shows the correlations (adj.R<sup>2</sup>) between biomass and nb\_NDVI<sub>type</sub> indices calculated from any band pairs among the simulated Hyperion bands. Darker areas indicate higher adj.R<sup>2</sup>. White gaps are strong water absorption regions that were removed from the analysis

An overall comparison of the strength of the model fit and prediction errors is presented in Figure 4 and 5. Models that used existing indices developed either for broadband or hyperspectral sensors showed comparably poor performance with adj.R<sup>2</sup> ranging from ~0.21 to ~0.29. Development of new nb\_NDVI<sub>type</sub> indices greatly improved the adj.R<sup>2</sup> from 0.29 to 0.61. Relatively similar increase was observed when 2-band MLR models were used for biomass estimation since model

adj.R<sup>2</sup> improved from 0.61 to 0.77. Incorporation of more bands in the MLR models further increased the adj.R<sup>2</sup> moderately (0.7783 for 3-band MLR and 0.8631 for 4-band MLR). Model prediction errors followed a similar pattern. In particular, models using existing indices showed high CV-RMSE (0.5323) that gradually reduced when nb\_NDVI<sub>type</sub> (0.3961) and MLR (0.2935 to 0.2357) models were used for biomass estimation.

Calibration- Validation dates	Exist. indices	nb_ NDVI <sub>type</sub>	RMSE		
			2-band MLR	3-band MLR	4-band MLR
C-2,3,4/V-1	0.67	0.49	0.40	0.34	0.30
C-1,3,4/V-2	0.65	0.50	0.36	0.31	0.34
C-1,2,4/V-3	0.50	0.26	0.21	0.20	0.14
C-1,2,3/V-4	0.44	0.39	0.28	0.25	0.25
Mean-CV	0.56	0.41	0.31	0.27	0.25

Table 4. Prediction errors of best models build with the three approaches. Models were calibrated on three dates and validated on the fourth. C-2,3,4/V-1 means that regression models were calibrated on Dates 2,3,4 and validated on Date 1. Recording dates are, Date-1: 10th June, Date-2: 23rd June, Date-3: 28th July and Date-4: 10th August

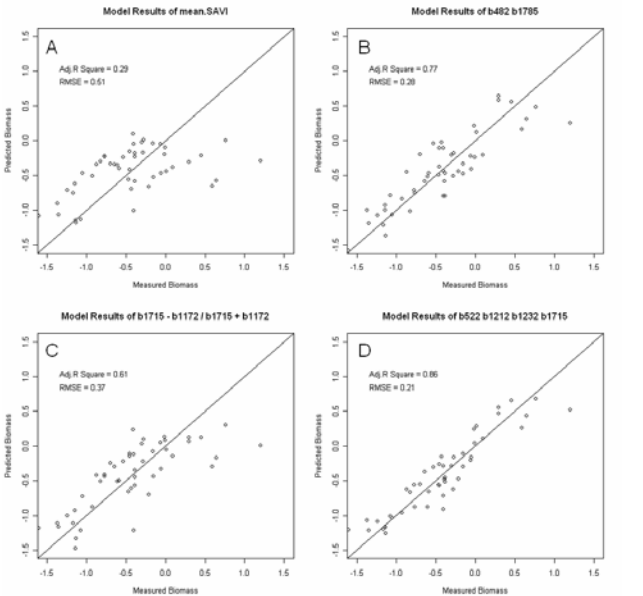


Figure 3. Best measured vs. predicted biomass estimates originating from regression models of A) existing indices, B) 2-band MLR, C) nb\_NDVI<sub>type</sub>, and D) 4-band MLR, optimized with a 4-fold cross-validation using samples from all four sampling dates

The best models of each of the three approaches (existing indices, nb\_NDVI<sub>type</sub> indices, MLR) were used in the 4-fold “Date” CV analyses (Table 4). A clear pattern was observed. Models calibrated from biomass samples collected in the first two sampling dates of the season predicted biomass with lower RMSE. Contrary, models calibrated using samples from only one of these dates gave poorer predictions. For example, the best nb\_NDVI<sub>type</sub> index model for estimating biomass when calibrated with samples from Date 1 and Date 2 yielded RMSE of 0.2669 and 0.3990 that increased to 0.4905 and 0.5022 when samples from only one of these dates were used. This may reflect the high variability of biomass samples collected on Date 1 and Date 2 (Fig. 1). Models calibrated from data from

these dates could account for a much broader range of variability of biomass. Contrary, model calibration with samples from only one of these dates was not sufficient to explain the variability observed on the samples collected on the other date. Thus, when models had to predict these values they produced higher errors.

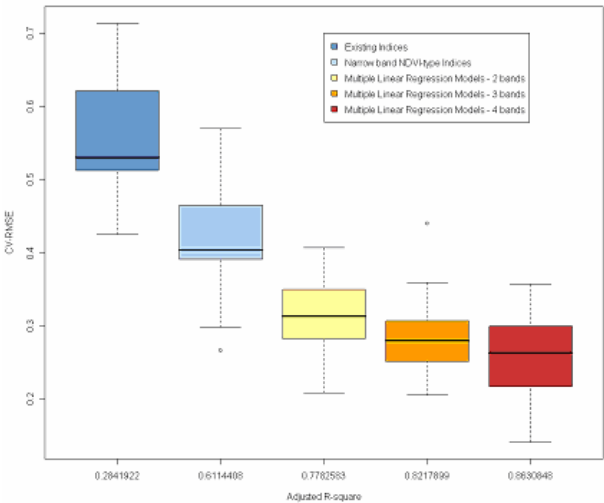


Figure 4. Boxplots of model calibration strength ( $\text{adj.}R^2$ ) against prediction error (CV-RMSE) for the best three performing models of the three modelling approaches

Preliminary results of the spatial distribution of biomass over the study area, from up-scaling the statistical models to the Hyperion scene, are shown in Figure 6. This was done by applying the models calibrated with field spectrometer data resampled to simulate Hyperion bands, to the actual Hyperion scene acquired over the study area. Even though models were calibrated for grassland habitats, forested areas could immediately be observed (dark areas) as high biomass was predicted for these habitats. High variation of predicted biomass values on grassland habitats (areas between dark forest patches) showed the sensitivity of the models in predicting subtle changes of in-field biomass variability. Validation of the model predictions (results not shown here) with field samples collected on the date of the Hyperion acquisition, gave similar prediction errors as obtained from the CV procedure. Cut grasslands with low biomass were correctly predicted and are shown with very light colours. However, over-estimation and higher errors were observed for areas adjacent to forests. This was due to the mixed pixels that affected the spectral signal recorded by the sensor and thus the model prediction.

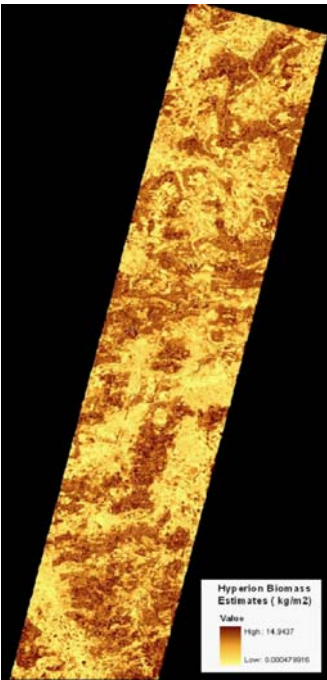


Figure 5. Biomass prediction map ( $\text{Kg/m}^2$ ) created from Hyperion reflectance values, using the  $\text{nb\_NDVI}_{\text{type}}$  index regression model constructed with bands at b1715nm and b1172nm

4. CONCLUSIONS

Results presented in this paper showed the high potential of hyperspectral remote sensing for estimating biomass of grassland habitats along a dry-mesic gradient. Our analyses demonstrated the importance of acquiring biomass measurements along the growing season in order to capture the variability observed and eventually be able to create reliable and more accurate models. This is specifically important in managed grasslands since management activities introduce a high variability in phenological states. Furthermore, we illustrated the necessity of developing new indices since existing vegetation indices using information from the red and near-infrared regions yielded poor biomass estimation results. Rather, spectral regions related with plant leaf water content should be used as they appear to be more suitable for estimating and predicting biomass. Use of multiple linear regression always gave better models for estimation and prediction of biomass. In addition, branch-and-bound (b&b) variable search algorithms proved a powerful statistical approach since bands selected made sense with respect to physical processes of vegetation. Nevertheless, attention should be paid to the number of bands used in the multiple regression models since accuracy does not improve after a certain point and addition of extra bands will only reduce the quality of the models. Finally, preliminary results from up-scaling to Hyperion level showed that we could achieve high accuracies provided that multiple samples covering the in-field variability of biomass have been acquired.

ACKNOWLEDGEMENTS

The authors would like to thank the Swiss Federal Institute for Forest, Snow and Landscape Research (WSL) and the Swiss Agency for the Environment, Forest and Landscape (SAEFL) for funding this research.

## REFERENCES

- Broge, N.H. and Leblanc, E., 2000. Comparing prediction power and stability of broadband and hyperspectral vegetation indices for estimation of green leaf area index and canopy chlorophyll density. *Remote Sensing of Environment*, 76(2): 156-172.
- Cook, E.A., Iverson, L.R. and Graham, R.L., 1989. Estimating forest productivity with Thematic Mapper and biogeographical data. *Remote Sensing of Environment*, 28: 131-141.
- Datt, B., McVicar, T.R., Van Niel, T.G., Jupp, D.L.B. and Pearlman, J.S., 2003. Preprocessing EO-1 Hyperion Hyperspectral Data to Support the Application of Agricultural Indexes. *IEEE TRANSACTIONS ON GEOSCIENCE AND REMOTE SENSING*, 41(2): 1246-1259.
- Dengsheng, L., 2006. The potential and challenge of remote sensing-based biomass estimation. *International Journal Of Remote Sensing*, 27(7-8): 1297-1328.
- Diaconis, P. and Efron, B., 1983. Computer-intensive methods on statistics. *Scientific American*, 248: 96-108.
- Eggenberg, S.D., Thomas; Dipner, Michael & Mayer, Cornelia, 2001. Cartography and evaluation of dry grasslands sites of national importance: Technical report. Environmental Series No. 325, published by Swiss Agency for the Environment, Forests and Landscape (SAEFL), Berne.
- Elvidge, C.D., 1990. Visible and near infrared reflectance characteristics of dry plant materials. *International Journal Of Remote Sensing*, 11(10): 1775-1795.
- Filella, I.P.u., Josep; Llorens, Laura & Estiarte, Marc, 2004. Reflectance assessment of seasonal and annual changes in biomass and CO<sub>2</sub> uptake of a Mediterranean shrubland submitted to experimental warming and drought. *Remote Sensing of Environment*, 90(3): 308-318.
- Haboudane, D., Miller, J.R., Pattey, E., Zarco-Tejada, P.J. and Strachan, I., 2004. Hyperspectral vegetation indices and novel algorithms for predicting green LAI of crop canopies: Modeling and validation in the context of precision agriculture. *Remote Sensing of Environment*, 90(3): 337-352.
- Hansen, P.M.S., J. K., 2003. Reflectance measurement of canopy biomass and nitrogen status in wheat crops using normalized difference vegetation indices and partial least squares regression. *Remote Sensing of Environment*, 86(4): 542-553.
- He, Y.G., Xulin & Wilmschurst, John, 2006. Studying mixed grassland ecosystems I: suitable hyperspectral vegetation indices. *Canadian Journal of Remote Sensing*, 32(2): 98-107.
- Hunt, E.R., 1991. Airborne remote sensing of canopy water thickness scaled from leaf spectrometer data. *International Journal Of Remote Sensing*, 12(3): 643-649.
- Kumar, L., Schmidt, K.S., Dury, S. and Skidmore, A.K., 2001. Imaging spectrometry and vegetation science. In: F.d.J. van de Meer, S.M (Editor), *Imaging Spectrometry. Basic principles and prospective applications*. Kluwer Academic Press, Dordrecht, pp. 111-155.
- Miller, A.J., 2002. Subset selection in regression. Chapman & Hall/CRC, Boca Raton, Florida.
- Mirik, M., Norland, J.E., Crabtree, R.L. and Biondini, M.E., 2005. Hyperspectral one-meter-resolution remote sensing in yellowstone national park, wyoming I. Forage nutritional values. *Rangeland & ecology management*, 58(5): 452-458.
- Mutanga, O.S., Andrew K., 2004. Hyperspectral band depth analysis for a better estimation of grass biomass (*Cenchrus ciliaris*) measured under controlled laboratory conditions. *International Journal of Applied Earth Observation and Geoinformation*, 5(2): 87-96.
- Osborne, S.L., Schepers, J.S., Francis, D.D. and Schlemmer, M.R., 2002. Use of Spectral Radiance to Estimate In-Season Biomass and Grain Yield in Nitrogen- and Water-Stressed Corn. *Crop Science*, 42(1-2): 165-175.
- Richter, R., 2003. Atmospheric / Topographic Correction for Airborne Imagery. ATCOR-4 User Guide, Version 3.0., DLR-IB564-02/03, DLR, pp.66., 66 pp.
- Tarr, A.B., Moore, K.J. and Dixon, P.M., 2005. Spectral reflectance as a covariate for estimating pasture productivity and composition. *Crop Science*, 45(3): 996-1003.
- Thenkabail, P.S.E., Eden A.; Ashton, Mark S. & Van Der Meer, Bauke, 2004. Accuracy assessments of hyperspectral waveband performance for vegetation analysis applications. *Remote Sensing of Environment*, 91(3-4): 354-376.
- Van de Meer, F., de Jong, S.M. and Bakker, W., 2001. Imaging spectrometry for agriculture. In: F.d.J. van de Meer, S.M (Editor), *Imaging Spectrometry. Basic principles and prospective applications*. Kluwer Academic Press, Dordrecht, pp. 157-199.
- Wylie, B.K.M., D.J.; Tieszen, L.L. & Mannel, S., 2002. Satellite mapping of surface biophysical parameters at the biome scale over the North American grasslands A case study. *Remote Sensing of Environment*, 79(2-3): 266-278.
- Xavier, A.C. et al., 2006. Hyperspectral field reflectance measurements to estimate wheat grain yield and plant height. *Scientia Agricola*, 63(2): 130-138.

# DEVELOPMENT OF THE GONIO RADIOMETRIC SPECTROMETER SYSTEM TO CONDUCT MULTI-ANGULAR MEASUREMENTS OF TERRESTRIAL SURFACES

H. M. Pegrum<sup>a,\*</sup>, N. P. Fox<sup>a</sup>, E. J. Milton<sup>b</sup>, M. Chapman<sup>a</sup>.

<sup>a</sup> Optical Technologies and Scientific Computing Team, National Physical Laboratory, Hampton Road, Teddington, TW11 0LW, UK.

(Heather.Pegrum, Nigel.Fox)@npl.co.uk

<sup>b</sup> School of Geography, University of Southampton, Southampton, SO17 1BJ, UK. E.J.Milton@soton.ac.uk

**KEY WORDS:** BRDF, calibration, radiance reflectance.

## ABSTRACT:

The requirement for reliability and confidence in Earth Observation data is being recognised by many international organisations e.g. WMO and CEOS, the latter of which endorsed two recommendations at its 14<sup>th</sup> plenary, which stated that; pre-launch calibration should be performed using equipment and techniques that can be demonstrably traceable to, and consistent with, the SI system of units, and traceability should be maintained throughout the lifetime of the mission, and more recently in a white paper submitted to CEOS plenary 19 summarising CEOS WGCV activities and plans in support of GEOSS. Increasingly, satellites have the capability of measuring surfaces at multiple angles. Due to the variations in slope angle and aspect, there are only a few remotely sensed data sets which are immune to multi-angular effects. To improve the accuracy and traceability of multi-angular field measurements, a new instrument has been designed, in conjunction with the Natural Environmental Research Council (UK) Field Spectroscopy Facility (FSF). The Gonio Radiometric Spectrometer System (GRASS) is being developed at the National Physical Laboratory, in the Optical Technologies and Scientific Computing Team. It is intended to provide quasi-simultaneous, multi-angle, multi-spectral measurements of Earth surface reflected sunlight to support vicarious calibration of satellite sensors operating in the optical region. The GRASS instrument was first deployed in June 2006 as part of an experiment organised by Network for the Calibration and Validation of Earth Observation data (NCAVEO), this paper will summarise the recent developments of the GRASS instrument, and its initial deployment at the NCAVEO Field Experiment.

## 1. INTRODUCTION

The Group on Earth Observation (GEO) is an international partnership leading a worldwide effort to build a Global Earth Observation System of Systems (GEOSS) over the next 10 years. The GEOSS vision, articulated in the 'GEOSS 10 year Implementation Plan' (Mitsos, 2005), reflects a global scientific and political consensus that the assessment of the state of the Earth requires continuous and coordinated observation of our planet at all scales.

With global initiatives such as GEOSS it is an exciting time for metrology within the remote sensing community. The development of techniques for the calibration and validation of remotely sensed data is leading to significant improvements in our understanding of the Sun – Earth system.

Satellite sensors generate large amounts of data, but these only become useful for monitoring global climate change when they are quality controlled and users can have confidence in their accuracy and relevance. Data provided from the multitude of satellites are generally used in models to provide information to policy makers, and thus must provide unequivocal evidence to support national and international legislation. To provide confidence in the data from these sources, the data should be referenced to a traceable and internationally accepted standard (Fox, 1999).

Satellite instruments measure the light reflected from the Earth's atmosphere and surface, but despite detailed pre-launch

calibration campaigns to establish the satellites' performance, post-launch calibration is vital to validate the instruments' performance once in orbit. The validation of satellite instrument performance, (for example, to monitor any degradation of the on-board calibration diffusers or sources), is often achieved by using field instruments, which measure the light reflected from 'calibration sites', that can be viewed by satellite sensors. These techniques are known as vicarious calibration, which is a method that is independent of on-board calibration, (Thome, 1998).

Vicarious calibration provides a suitable method for the validation of the satellite data, however its accuracy is limited by the ground measurements and the validity of the atmospheric radiative transfer models, (Dingirard, 1999). The significant error contribution due to directional reflectance effects and traceability to SI, are of particular interest for this project.

Directional reflectance effects are due to natural targets being non-Lambertian, which means depending on the viewing and illumination angles, a surface can appear brighter or darker – for example a mown lawn or a forest canopy. This interaction with light and matter is of key interest in developing the understanding of the reflectance characteristics in the natural environment.

The Bi-Directional Reflectance Distribution Function (BRDF) is the theoretical function that describes the relationship between the incident flux on a surface and the distribution of

---

\* Corresponding author.

that which is reflected, as defined by Nicodemus in 1977, (Nicodemus, 1977). The BRDF is often used in climate models; therefore an accurate understanding of the BRDF characteristics of different surfaces is required to provide confidence in the climate models.

Currently there are several satellite instruments that have the capability of measuring surfaces at multiple angles. For example the MODerate resolution Imaging Spectroradiometer (MODIS) (Schaaf, 2002), the Multiangle Imaging SpectroRadiometer (MISR) (Bruegge, 2002) and the POLarization and Directionality of the Earth's reflectance (POLDER) multispectral camera (Kaufman, 1997). As the data products from these instruments becomes more readily available for investigations into the BRDF of various terrestrial surfaces, it is vital to validate the satellite data using field instrumentation that can also measure at multiple angles, and to ensure traceability to SI.

### 1.1 Goniometers

There are a few goniometers that are currently used for field measurements, these include the Field Goniometer System (FIGOS) (Sandmeier), the ground-based Portable Apparatus for Rapid Acquisition of Bidirectional Observations of Land and Atmosphere (PARABOLA) (Abdou) and the Automated Spectro-goniometer (ASG) (Painter).

These Goniometers can be used in the field to determine the angular reflectance characteristics of a particular surface. However in the natural environment it is hard to quantify, as the intensity of light in the multiple directions can vary with time. This is due to effects such as the atmosphere and the illumination angle of the Sun, which are constantly changing.

There is also a large contribution to the measured reflectance of a surface due to the diffuse irradiance that is produced from the scattered light. Careful consideration in the field can minimize these errors, but the important factor should be that its contribution should be documented, otherwise the data can be devalued and can become a significant source of error (Milton, 1995).

## 2. THE GONIO RADIOMETRIC SPECTROMETER SYSTEM (GRASS)

The UK Natural Environmental Research Council, Field Spectroscopy Facility (NERC FSF), which is based at the University of Edinburgh, currently has a suite of instruments that can be borrowed by researchers to conduct field or laboratory based experiments. The NERC FSF also provides researchers with calibrated reference reflectance panels that are traceable to the National Physical Laboratory (NPL). This is particularly important for long-term studies, and satellite imagery verification so that measurements can be inter-compared and be traceable to SI. The instruments are predominantly used to make nadir measurements in the field. They are either hand-held or portable (via the use of a backpack) so they can be used in remote locations. The users of the facility have particular requirements for an instrument to be able to measure at multiple angles, which should be lightweight and be able to perform rapid sampling.

### 2.1 GRASS Design

The Gonio Radiometric Spectrometer System (GRASS) is being developed at the National Physical Laboratory, in the Optical Technologies and Scientific Computing Team. It is intended to provide quasi-simultaneous, multi-angle, multi-spectral measurements of Earth surface reflected sunlight to support Remote Sensing based activities.

The instrument is being designed to be easily and quickly assembled in remote situations, be robust and able to be transported by "estate car". GRASS will provide the structure and optics to collect the radiation, which will then integrate to a variety of spectroradiometers (not part of GRASS).

GRASS is being designed to measure the Earth's reflected sunlight over half a hemisphere, at 30-degree intervals i.e. 0°, 30°, 60°, 90°, 120°, 150°, 180°, on a series of seven arms (Figure 1). Six of these arms will have five collecting optics (referred to as a "camera"), and the seventh will have six, to be able to capture the nadir measurement, as well.

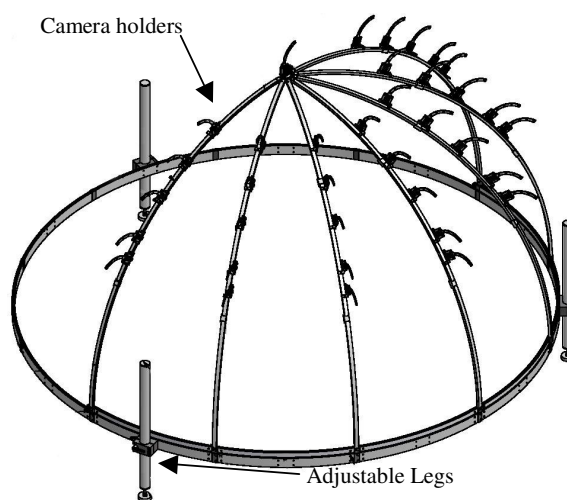


Figure 1. Schematic diagram of the Gonio Radiometric Spectrometer System (GRASS).

This results in 36 cameras / measurement angles, within the half of the hemisphere. Each camera consists of a collimating lens and an optical fiber. The fibers from the entrance optics feed to a series of multiplexers that result in one optical output that can be coupled to a spectrometer. The spectrometers that will be initially considered for integration with the Goniometer are those available from the NERC FSF.

The height of the structure is designed such that the focus of the nadir-viewing camera is 2 m from the centre of the target. The hemispherical structure of GRASS is designed with a series of legs that are adjustable, such that the working height can be altered. The application of this design feature is so that a spectral measurement can be taken of the top of a vegetation canopy, for example.

To be able to take measurements at all chosen geometries, the arms of the Goniometer are being designed so that they can rotate on the circular base of the structure allowing the forward and backward scattered radiation to be measured (Figure 2). The positions of the entrance optics on the arms are also



designed to be moveable so that effectively any five-zenith angles (up to 60°), can be chosen to be captured during each measurement sequence. This allows detailed studies of particular BRDF characteristics, e.g. the specular peak.



Figure 2. Photograph of the GRASS in the Laboratory.

2.2 Diffuse Irradiance

A particular problem in the field is the diffuse radiation that is produced from skylight and scattered light. The light is hard to quantify as it can vary in intensity over the hemisphere and can vary with time due to atmospheric changes. These errors can be reduced if considered carefully, but crucially they should be documented, otherwise the data can be devalued and the diffuse contribution can become a significant source of error.

There are a few methods for calculating it, which include conducting measurements under different conditions e.g. clear skies/hazy skies. By occluding the solar disc, the difference between the direct and diffuse irradiance can be determined, or the complete sky irradiance can be measured.

For these reasons, another design feature of GRASS is that the lenses on the end of each of the fibers can be removed, and replaced with a cosine diffuser, and the orientation of the viewing optic rotated such that the entrance optic can then measure the down-welling irradiance. This means that the instrument can measure both the radiance and irradiance at concurrent angles, (Figure 3).

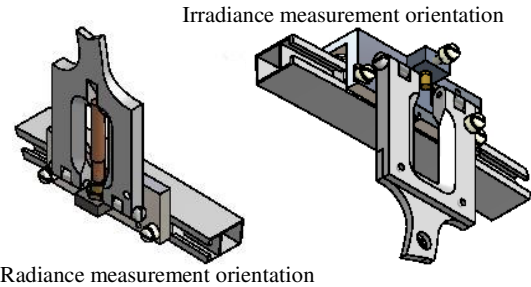


Figure 3. Schematic diagram of the radiance and irradiance orientations of the entrance optic.

3. NCAVEO FIELD EXPERIMENT 2006

3.1 Introduction

The Network for the Calibration and Validation of Earth Observation data (NCAVEO) (Milton, 2006), planned a national field campaign that took place in June 2006. The experiment was a scoping exercise for the establishment of one or more VALERI (*Validation of Land European Remote sensing Instruments*) (Baret, 2006) sites in the UK as well as an opportunity to learn and share best practice amongst NCAVEO partners and the wider earth observation community.

NPL was involved in a couple of aspects of the experiment. To provide traceability to SI, all of the field spectroradiometers used, were compared against the NPL Transfer Standard Absolute Radiance Source (TSARS) (Pegrum, 2004). Secondly, the goniometer was used to perform multi-angular, multi-spectral measurements of the main calibration site used for the experiment that will later be compared with data that was acquired by others during the experiment.

3.2 Traceability

At NPL all optical radiation measurement is traceable to the cryogenic radiometer, as shown in Figure 4. The cryogenic radiometer is used to calibrate solid-state detectors as transfer standards. These detectors, in effect, establish a spectral responsivity scale, forming the top of the calibration chain. Usually the transfer standard calibrated directly against the cryogenic radiometer is a trap detector (Fox, 1991). Trap detectors are used to calibrate filter radiometers and photometers and, from there, provide other scales or services for end-users, within industry and the earth observation community.

For spectral emission scales, the filter radiometers are used to measure the temperature of a high temperature blackbody (up to 3500 K) and this, through Planck's law, provides a known source of spectral radiance. In this way the source emission scales, based on the blackbody, are linked to the more accurate detector scales.

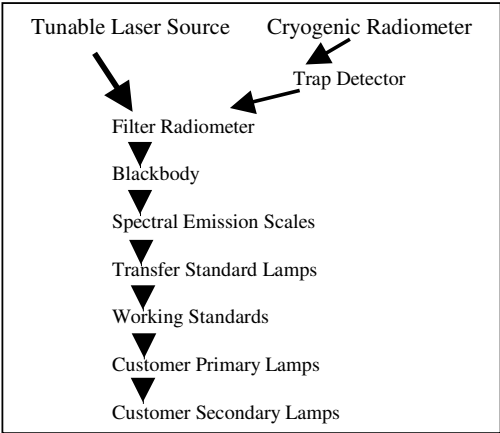


Figure 4. Traceability Chain to the NPL's Primary Standard Cryogenic Radiometer.

The Spectral Radiance and Irradiance Primary Scales (SRIPS) facility (Woolliams, 2005) is used to transfer the scale from the blackbody to lamp and integrating sphere sources through an

intermediate spectrometer (Figure 5). These sources are then used as spectral radiance and irradiance standards for the calibration of customer instruments, for example satellite instruments.

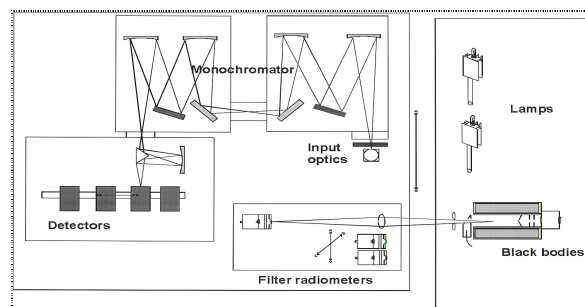


Figure 5. A schematic layout of SRIPS for irradiance measurements

**3.2.1 The Transfer Standard Absolute Radiance Source (TSARS):** has been developed by NPL, to provide customers with a transfer standard that is calibrated on the SRIPS facility, and traceable to the NPL primary standard cryogenic radiometer. The TSARS consists of an integrating sphere that is illuminated by a number of external lamps and has a large area circular exit port. Although this design is common with other such sources, NPL has put significant effort into selecting and positioning sources to improve the uniformity (Hunt, 2001). In addition a set of filter radiometers has been included to allow active stabilisation and monitoring of performance. Versions of this design were used to calibrate the Geostationary Earth Radiation Budget (GERB) (Mossavati, 1998) instrument now flying on Meteosat Second Generation and also at Applied Spectral Research Inc of Canada for calibration of a range of EO instruments. A small compact version was also used in the calibration of the Global Ozone Monitoring Experiment (GOME 2) – FM3 (Pegrum, 2004).

The TSARS was used as calibration source for the spectroradiometers that were used during the NCAVEO field experiment, since the radiance calibration of a spectroradiometer requires a large area, uniform source of known radiance. The TSARS has a uniformity of  $\pm 0.5\%$  across the exit port, and is stable to  $\pm 0.2\%$  over a period of a few hours. The TSARS was calibrated on the SRIPS facility shortly before the Field Experiment. All of the spectroradiometers that were used during the Field Experiment were calibrated against the NPL TSARS, in a laboratory at the Council for the Central Laboratory of the Research Councils (CCLRC) Chilbolton Facility for Atmospheric and Radio Research (CFARR), Hampshire, UK. This ensured that all instrumentation had been calibrated and be traceable to SI.

### 3.3 Multi-angular Measurements

The full GRASS structure was not completed in time for use in the NCAVEO Experiment; however the base structure and three camera holders were ready. These were used (with an ASD FieldSpec Pro, on loan from the FSF), to acquire some multi angular data that will later be compared with data that was acquired by others during the experiment. The three camera positions available were set up as follows: one at the nadir, and two other cameras positioned at a  $50^\circ$  zenith angle, on two arms at  $90^\circ$  to each other. These positions are shown in Figure 6.

The three cameras (lens and fiber) were mounted in a camera holder on the arms, and the fibers were then run back to a multiplexer unit, which was operated by the NPL software. The limited data will later be compared with other data from the experiment.

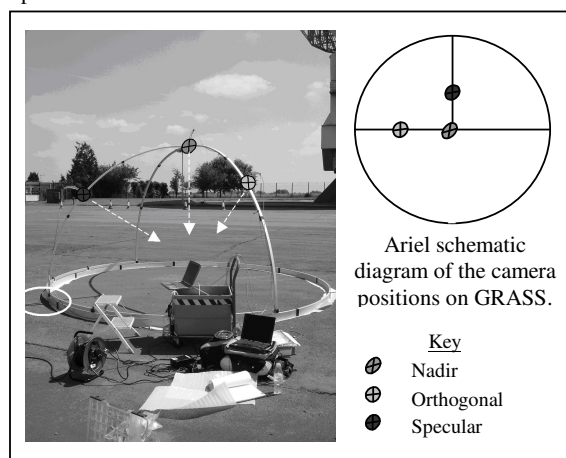


Figure 6. Picture of the GRASS set-up on the calibration site.

## 4. CURRENT STATUS

The full structure of GRASS has now been completed, as shown in Figure 2. Some initial testing of the angular alignment of the instrument showed that the system was flexing, and therefore the angular orientations had significant errors associated with them. Modifications to the instrument have been made, and the instrument is currently being tested in the laboratory, before being utilised in the field.

## 5. CONCLUSIONS

As more satellites have the capability of measuring surfaces at multiple angles, it is vital the field instrumentation can provide in-situ data to validate the satellite measurements. This in-situ data also needs to be made at multiple angles. The design of the Gonio RAdiometric Spectrometer System has led to the provision of quasi-simultaneous measurements of a surface at multiple angles, and through the involvement in the NCAVEO field experiment, it is hoped to provide data for comparison with satellite measurements which will develop an understanding of the anisotropy of natural targets.

## REFERENCES

- Abdou, W. A., Helmlinger, M. C., Conel, J. E., Bruegge, C. J., Pilorz, S. H., Martonchik, J. V. and Gaitley, B. J., 2000. Ground measurements of surface BRF and HDRF using PARABOLA III. *Journal of Geophysical Research-Atmospheres*, 106(D11), pp. 11967-11976
- Baret, F., Weiss, M., Allard, D., Garrigue, S., Leroy, M., Jeanjean, H., Fernandes, R., Myneni, R., Privette, J., Bohbot, J. M. H., Bosseno, R., Dedieu, G., Bella, C. D., Duchemin, B., Espana, M., Gond, V., Gu, X. F., Guyon, D., Lelong, C., Maisongrande, P., Mougou, E., Nilson, T., Veroustraete, F. and Vintilla, R., 2006. VALERI: a network of sites and a methodology for the validation of medium spatial resolution land satellite products. *Remote Sens. Environ.*, Submitted.

Bruegge, C. J., Chrien, N. L., Ando, R. R., Diner, D. J., Abdou, W. A., Helmlinger, M. C., Pilorz, S. H. and Thome, K. J., 2002. Early Validation of the Multi-angle Imaging SpectroRadiometer (MISR) Radiometric scale. *IEEE Transactions on Geoscience and Remote Sensing*, 40(7), pp. 1477-1492

Dingirard, M. and Slater, P., 1999. Calibration of Space-Multispectral Imaging Sensors: A Review. *Remote Sens. Environ*, 68(3), pp. 194-205

Fox, N. P., 1991. Trap detectors and their properties. *Metrologia*, 28(3), pp. 197-202

Fox, N. P., 1999. Improving the accuracy and traceability to SI of space-based radiometric measurements, both pre-flight and post-launch. *Advances in Space Research*, 23(8), pp. 1471-1476

Kaufman, Y. J., Tanré, D., Gordon, H. R., Nakajima, T., Lenoble, J., Frouins, R., Grassl, H., Herman, B. M., King, M. D. and Teillet, P. M., 1997. Passive remote sensing of tropospheric aerosol and atmospheric correction for the aerosol effect. *Journal of Geophysical Research*, 102(D14), pp. 16,815-16,830

Milton, E. J., 2006. Network for the Calibration and Validation of Earth Observation data (NCAVEO). <http://www.ncaveo.ac.uk/>. (accessed 29 Jan 2007).

Mossavati, R., Harries, J. E., S. Kellock, Wrigley, R. T., Mueller, J. and Fox, N. P., 1998. Radiometric calibration of the GERB instrument. *Metrologia*, 35(4), pp. 603-607

Painter, T. H., Paden, B. and Dozier, J., 2003. Automated spectro-goniometer: A spherical robot for the field measurement of the directional reflectance of snow. *Review of Scientific Instruments*, 74(12), pp. 5179-5188

Pegrum, H., Woolliams, E., Fox, N., Riel, L. V., Otter, G. and Kowalewski, M., 2004. Calibration of the NPL Transfer Standard Absolute Radiance Source (TSARS) and its use with GOME 2 – FM3 Spectral Radiance measurements. 11th International Symposium on Remote Sensing, Sensors, Systems, and Next-Generation Satellites VIII, Maspalomas, Spain. *Proc. SPIE*, 5570-72, pp. 503-514.

Sandmeier, S. R. and Itten, K. I., 1999. A field goniometer system (FIGOS) for acquisition of hyperspectral BRDF data. *IEEE Transactions on Geoscience and Remote Sensing*, 37(2), pp. 978-986

Schaaf, C. B., Gao, F., Strahler, A. H., Lucht, W., Li, X., Tsang, T., Strugnell, N. C., Zhang, X., Jin, Y., Muller, J.-P., Lewis, P., Barnsley, M., Hobson, P., Disney, M., Roberts, G., Dunderdale, M., Doll, C., d'Entremont, R. P., Baoxin Hug, Liang, S., Privette, J. L. and h, D. R., 2002. First operational BRDF, albedo nadir reflectance products from MODIS. *Remote Sens. Environ*, 83(1-2), pp. 135-148

Thome, K., Schiller, S., Conel, J., Arai, K. and Tsuchida, S., 1998. Results of the 1996 Earth Observing System vicarious calibration joint campaign at Lunar Lake Playa, Nevada (USA). *Metrologia*, 35(4), pp. 631-638

Woolliams, E. R., M, G., Cox, Fox, N. and P, M., Harris, 2005. Final Report of the CCPR K1-a Key Comparison of Spectral Irradiance 250 nm to 2500 nm. <http://kcdb.bipm.org>. (accessed 19 Mar. 2007).

## ACKNOWLEDGEMENTS

The authors would like to thank NERC and the National Measurement System Directorate of Department of Trade and Industry for financial support of this project. The authors would also like to thank The Tintometer Limited.

# DUAL FIELD-OF-VIEW GONIOMETER SYSTEM FIGOS

J.T. Schopfer\*, S. Dangel, M. Kneubühler, K.I. Itten

Remote Sensing Laboratories (RSL), Departement of Geography, University of Zurich, Winterthurerstrasse 190, 8057 Zurich, Switzerland – (jschopfer, dangel, kneub, itten)@geo.unizh.ch

**KEY WORDS:** Goniometer, FIGOS, Dual Field-of-View, BRDF, Multiangular, Hyperspectral, Spectrodirectional, Incoming Diffuse Radiance

## ABSTRACT:

Almost all natural surfaces exhibit an individual anisotropic reflectance characteristic due to contrasting optical properties of surface elements and background as well as an uneven distribution of illuminated and shadowed areas. The bidirectional reflectance distribution function BRDF is a basic quantity which describes the reflectance characteristic. Many applications, such as BRDF correction of remote sensing data and quantitative retrieval of vegetation parameters require accurate knowledge of the spectrodirectional surface reflectance properties. However, the directly observed quantity in field experiments is affected by atmospheric conditions which need to be accounted for when retrieving the target specific BRDF. The most exact BRDF retrieval from field goniometry measurements can be achieved by considering the diffuse irradiance at angular resolution. However, most goniometer systems are not able to simultaneously collect the reflected and incoming radiances at high spectral and angular resolution.

The dual field-of-view (FOV) goniometer system FIGOS of the Remote Sensing Laboratories (RSL, Switzerland) has this capability and is presented here for the first time along with a full field BRDF retrieval concept proposed by Martonchik et al. (Martonchik, 1994). The dual FOV FIGOS is based on the proven field goniometer system FIGOS extended by two ASD FieldSpec-3, each pointing in opposite directions. Reflected and incoming radiance measurements are performed simultaneously and at the same angular and spectral resolution. The first spectrodirectional dual field-of-view dataset was obtained in summer 2006 in Gilching, Germany. Both a natural and an artificial target were measured. The evaluation showed that the dual field-of-view goniometer system FIGOS substantially supports not only data collection for full field BRDF retrievals but also direct comparisons of field and laboratory measurements. Due to its reliable performance and known characteristics it has the potential to be a reference instrument for extensive field and laboratory experiments.

## 1. INTRODUCTION

In remote sensing research goniometry is widely used to assess spectrodirectional reflectance properties of selected natural or artificial targets. Almost all surfaces exhibit an individual anisotropic reflectance characteristic. This behaviour is due to the contrast between optical properties of surface elements and background as well as the uneven distribution of illuminated and shadowed areas. The concept which describes the reflectance characteristic of a specific target area is called the bidirectional reflectance distribution function (BRDF). Accurate knowledge of the surface BRDF is important for many applications such as BRDF correction of remote sensing data and quantitative retrieval of vegetation (Huber, 2007; Strub, 2002; Weiss, 2000), snow (Painter, 2002) or soil (Gobron, 2000) parameters. Furthermore, BRDF knowledge supports the determination of the surface albedo which is a crucial parameter in modelling the Earth's radiation budget. The surface albedo is defined as the directional integration of reflectance over all sun-view geometries. Practically, an estimate of the albedo is inferred from the measured nadir reflectance since corresponding satellite sensors often operate at only one or a few view angles (Barnsley, 2004; Bruegge, 2002; Kaufman, 1997). Consequently, the surface BRDF often is not considered which may lead to large errors in the retrieved albedo (Maurer, 2002; Schaepman, 2006) and subsequent climate models.

Goniometer systems observe the reflected radiation from a multitude of well-defined angles and can therefore provide a more accurate data basis for model validation as well as for

calibration purposes of air- and spaceborne data. However, in field experiments the incoming radiation is anisotropic and permanently varies due to changing atmospheric conditions and sun zenith angle. Therefore the directly measured quantity in field experiments is affected by atmospheric conditions and called hemispherical conical reflectance factor (HCRF), corresponding to hemispherical illumination and conical observation. The specific target BRDF needs to be reconstructed ("retrieved") from the measured HCRF. The most exact BRDF retrieval from field goniometer measurements can be achieved using an algorithm (Martonchik, 1994) which considers the irradiance at angular resolution. However, few goniometer systems are able to simultaneously collect reflected and incoming radiances at the same angular and at high spectral resolution. Current examples include the known Portable Apparatus for Rapid Acquisition of Bidirectional Observations of Land and Atmosphere (PARABOLA III) and the Gonio Radiometer Spectrometer System (GRASS). Parabola III, which is used for MISR data validation purposes (Abdou, 2000; Bruegge, 2000), is collecting the reflected and incident radiances on a spherical grid of 5° and in 8 spectral channels. GRASS is currently being developed at the National Physical Laboratory (NPL), Teddington, UK (Pegrum, 2006). It shows a promising and novel dual view design, but has not yet reached an operational status.

In order to meet the abovementioned observation criteria for the BRDF retrieval algorithm RSL tested a preliminary dual FOV setup in summer 2005 using the traditional FIGOS setup in conjunction with an upward looking spectroradiometer placed

---

\* Corresponding author.

on a separate tripod which was manually adjusted to the corresponding observation angles. (Schopfer, 2006). The currently final setup consists of two FieldSpec-3 spectroradiometers pointing in opposite directions, mounted onto the goniometer system FIGOS. The dual view capability and the performance of the dual FOV FIGOS were evaluated in summer 2006 during an extensive field campaign in Gilching, Germany. The dual FOV FIGOS is currently the only system in operation which is capable of simultaneous measurements of the reflected and incident radiances at the same high angular and spectral resolution. A characterisation of the system and results from the first dual-view measurements are presented here along with the BRDF retrieval concept proposed by Martonchik et al. (Martonchik, 1994).

## 2. DUAL FIELD-OF-VIEW GONIOMETER FIGOS

### 2.1 Characteristics

The dual FOV goniometer system FIGOS is based on the proven field goniometer system FIGOS (Sandmeier, 1999). It is used either in the field as dual FOV FIGOS or in the laboratory as LAGOS (not dual view). In the field case the reflected and incoming radiances are collected simultaneously at high spectral and at an equal angular resolution. Two wirelessly computer controlled ASD FieldSpec-3 spectroradiometers are used to cover the spectral range from 350nm to 2500nm. Data is sampled at intervals of 1.4nm (350 – 1050nm) and 2nm (1000 – 2500nm) with a spectral resolution of 3nm at 700nm and 10nm at 1400/2100nm, respectively (Analytical Spectral Devices Inc., 1999). Both spectroradiometers are operated with a 3° FOV foreoptic which is connected to the sensor using a 1.4m fibre optic. The idea of having both instruments being moved while taking directional measurements evolved from various considerations. The design of the U-base plate (Fig. 2) supports the attachment of both spectroradiometers as closely as possible to the zenith arc. Therefore, and since the zenith arc is eccentrically positioned, no cast shadow is generated on the target area (except for the dual optic holder at the hotspot direction), even though a large volume is moved along the zenith arc. Additionally, fibre optics of standard length can be used and a sufficient signal to noise ratio (SNR) is obtained. In contrast, having only the optics moved (and the spectroradiometers placed outside the goniometer) would create the need of having very long fibre optics (> 4m) and consequently a lower SNR.

The goniometer itself consists of three major parts: a zenith arc and an azimuth rail, each of 2m radius, and a motorized sled, onto which the two sensors are mounted on a U-base plate. All parts are made of black-coated aluminum in order to minimize adjacency effects. The zenith arc is tightly fixed to four wagons which allow a manual 360° rotation on the azimuth rail. The sled with the two spectroradiometers is driven by a braking motor at a velocity of 2.5°/s. Fully adjustable labels on the zenith arc allow for an automated positioning of the spectroradiometers at desired steps. Currently, measurements are taken at azimuth steps of 30° and zenith steps of 15° (-75° to 75°). A full dual view hemisphere is completed in about 25 minutes. Figure 1 shows the dual FOV goniometer FIGOS being used for data collection over an artificial target.



Figure 1. Dual field-of-view goniometer system FIGOS

To allow measurements in the principal plane the zenith arc is positioned eccentrically on the azimuth arc and only the two optics are moving in the principal plane. By using a dual optic holder both optics are exactly aligned while pointing in opposite directions. Figure 2 shows the U-base plate carrying both spectroradiometers and the dual optic holder. Furthermore, the generated shadow at the hotspot direction is minimized to the optic's size, which is about 1cm in diameter. Since the instantaneous field-of-view is 3° and always pointing to the centre of the hemisphere (downward looking optic), the corresponding ground instant field-of-view (GIFOV) is circular with 10.5cm (diameter) in nadir direction. However, for large off-nadir observation angles the sensor's footprint becomes elliptical with a maximum longitudinal extent of 41cm. It is therefore essential to consider the correct target reference height, especially when measuring a target with limited size.

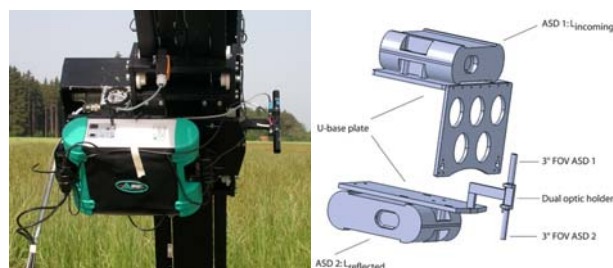


Figure 2. Dual field-of view combination

In order to monitor the pointing accuracy of the downward looking optic, a small laser is integrated into the dual optic holder. The geometric precision of the zenith arc is then referenced while moving the sled over the zenith arc in the principal and in the orthogonal plane. Maximal deviation of the laser spot, representing the centre of the sensor GIFOV, is recorded at a view angle of -75° and is about 4cm (Figure 3). A possible cause for this deviation might be a slight deformation of the respective part of the zenith arc due to extensive usage (assembly/disassembly) over time. However, this is not a limiting factor since the target under observation is usually assumed to be homogeneous and of satisfying spatial extent.



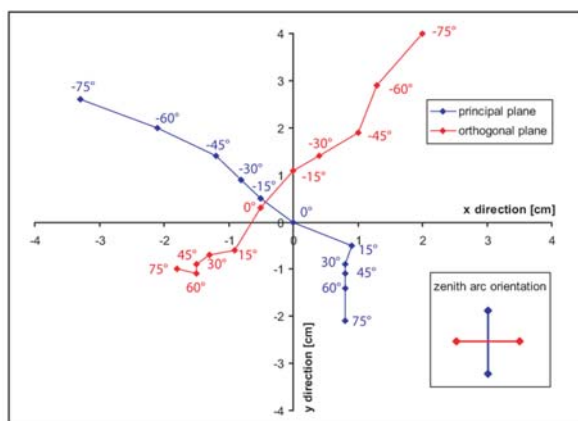


Figure 3. Pointing accuracy over zenith arc. The coordinate system is aligned to the centre of the azimuth circle.

## 2.2 Measurement Setup and Procedure

The two spectroradiometers which are used to simultaneously collect the reflected and incoming diffuse radiances are usually operated in radiance mode. For further processing, the intercalibration coefficients have to be known for both instruments. For this study the intercalibration was performed at the German Aerospace Center (DLR) using an integrating sphere.

Spectrodirectional measurements with the dual FOV FIGOS usually start in the principal plane at a forward scattering direction of 75°. Following a predefined sequence the whole hemisphere is scanned at zenith steps of 15° and azimuth steps of 30°. Spectralon references are collected in the beginning and in the end of each hemisphere as well as at every nadir bypass with the downward looking sensor. This provides a) the potential of calculating reflectances, if wished at a later date, and b) of monitoring atmospheric changes or instrument drifts. In total 140 measurements are taken for one dual view hemisphere (8 reference measurements plus 66 directional measurements for reflected and incoming radiances, respectively). Figure 4 shows the measurement sequence for goniometric measurements with the dual FOV FIGOS.

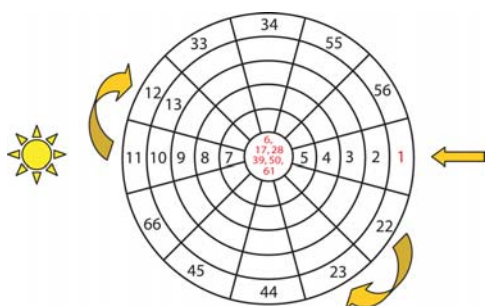


Figure 4. Measurement procedure for dual FOV FIGOS. Red coloured numbers represent reference measurement positions.

Even though shadowing is minimized it might occur anyway when the sun zenith angle equals one of the (downward looking) sensor view angle steps (e.g. at 15°, 30°, 45°, 60°, 75°). If this is the case, the corresponding measurements are either omitted, interpolated, or modelled by fitting to a BRDF model.

Simultaneous sunphotometer measurements are still necessary for a number of reasons: 1) monitoring the state of the atmosphere during the whole measurement time; 2) the direct sun radiance is required as an input parameter to the BRDF retrieval algorithm (refer to Fig. 5). Currently, the dual FOV FIGOS is not yet able to directly measure this quantity, mainly due to the following reasons:

- The upward looking sensor is saturating when directly aligned with the sun view direction. However, this problem might be solved by reducing the integration time of the spectroradiometer.
- Using a 3° FOV accurately pointing at the sun disk is challenging and time consuming. The time for measuring one hemisphere is a critical factor and desired to be as short as possible.

For this study an MFR-7 shadowband sunphotometer has been used which directly records the total and diffuse irradiance in 7 bands (broadband, 415, 500, 615, 673, 870 and 940nm). The direct sun radiance is then calculated as a difference of the two, taking the respective sun zenith angle into account.

## 3. RETRIEVAL CONCEPT

As mentioned above, field goniometer system measurements are affected by changing atmospheric conditions. By retrieving the BRDF from field measurements such influencing factors are corrected. Ideally, the incoming diffuse illumination has to be known at the same angular resolution as the reflected radiation from the target area. The most accurate BRDF retrieval for field measurements can be performed by following the procedure proposed by Martonchik et al. (Martonchik, 1994). It is based on the idea of splitting up the total incident radiance into its direct and diffuse part  $L_{dir}$  and  $L_{diff}$ , respectively. The reflected radiance  $L_{reflected}$  is then calculated as

$$L_{reflected}(-\mu, \mu_0, \varphi - \varphi_0) = \pi^{-1} R(-\mu, \mu_0, \varphi - \varphi_0) * L_{dir}(\mu_0) + L_{diff}(-\mu, \mu_0, \varphi - \varphi_0) \quad (1),$$

where

$-\mu, \mu_0$  = cosines of the view and solar angles  
 $\varphi - \varphi_0$  = is the view azimuthal angle with respect to the solar principal plane and  
 $R$  = bidirectional reflectance factor (BRF) of the target.

$L_{dir}$  is obtained from sunphotometer measurements and the dual FOV FIGOS directly provides spectrodirectional measurements of  $L_{reflected}$  and the incident diffuse radiance  $L_{diff}^{inc}$ .  $L_{diff}$  is the upward diffuse radiance which is calculated as

$$L_{diff}(-\mu, \mu_0, \varphi - \varphi_0) = \pi^{-1} \int_0^1 \int_0^{2\pi} R(-\mu, \mu', \varphi - \varphi') * L_{diff}^{inc}(\mu', \mu_0, \varphi' - \varphi_0) \mu' d\mu' d\varphi' \quad (2).$$

The notation  $-\mu$  and  $\mu$  is used for upwelling and downwelling radiation, respectively. The integral equation (1) is then iteratively solved for  $R$ . As an initial estimate of the BRF,  $R(0)$  is used where the diffuse incident radiance is neglected and atmosphere-surface reflections are ignored ( $L_{reflected}/\pi^{-1} * L_{dir}$ ).

For each iteration, the reflected radiance  $L_{\text{reflected}}$  is calculated on the basis of the current iteration estimate of  $R$ . The iteration is ended when the difference between the calculated and measured reflected radiances,  $L_{\text{reflected}}^{\text{calculated}}$  and  $L_{\text{reflected}}^{\text{measured}}$ , respectively, becomes smaller than a previously defined threshold. Figure 5 shows an overview of the field BRDF retrieval concept. Highlighted boxes represent measured quantities obtained by the sunphotometer and the dual FOV FIGOS.

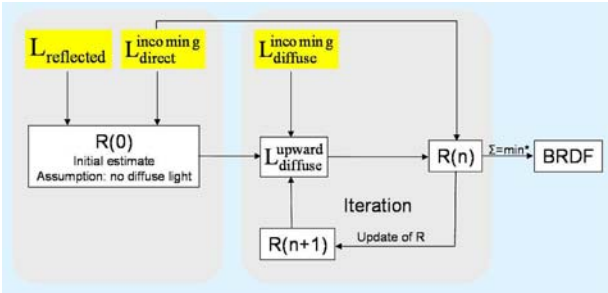


Figure 5. BRDF retrieval concept. Yellow boxes represent measured quantities.

The retrieval accuracy of  $R$  is increased by using multiple datasets of the same target area obtained at different sun zenith angles. For this study, an artificial target was used in order to a) minimize effects due to intrinsic changes of the target, b) guarantee the reproducibility of the measurements and c) to perform validation measurements in the laboratory. The artificial target (80 x 80cm) is made of sanded duralumin and consists of a regular matrix of cubes with known geometrical characteristics. It is well qualified for BRDF investigations, since it exhibits a high angular anisotropy and is inert over time (Govaerts, 1997). This target (Figure 6) has already been extensively used for field-lab comparison measurements (Dangel, 2005) and for various measurements during a dual FOV configuration test setup (Schopfer, 2006).

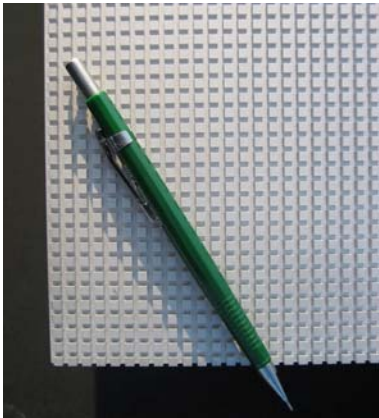


Figure 6. Artificial target

4. EVALUATION RESULTS

During this study the dual FOV goniometer FIGOS was used for the first time in its final configuration. Reflected and incoming diffuse radiances were collected at 20 sun zenith angles ranging from 24.8° to 68° (with respect to nadir) and at varying atmospheric conditions. Due to a sunphotometer malfunction, permanent atmospheric monitoring was only assured for 13 goniometer datasets. Figure 7 reports the ratio of

diffuse to total irradiance for the range of sun zenith angles for which spectrodirectional measurements were performed.

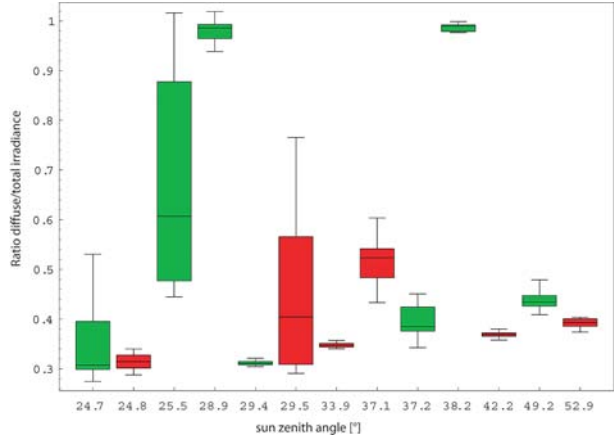


Figure 7. Variability of the ratio of diffuse / total radiation during corresponding goniometer measurements. Data are represented as standard box plots (green for natural target, red for artificial target). The boxes represent 50% of the measurements with the median value and the vertical lines show the total extent of the datasets.

Both the abovementioned artificial target (6 datasets) as well as a natural target (7 datasets) were observed. The natural target consisted of Triticale, a hybrid between rye and wheat, and will not be further analysed in this study. The dual FOV FIGOS showed a stable and reliable performance during the whole measurement campaign. Despite the additional dual FOV combination, measurement times for almost all hemispheres could be kept at about 30 minutes. The slowest part of the goniometer system is the motorized sled which has to be moved between the zenith angle steps, and not the double measurement triggering (for the upward and downward looking spectroradiometers). Table 1 shows the corresponding illumination angles, sun movement and the time period for every hemisphere of the dataset.

Dataset	Start sun zenith	Δ time	Δ sun azimuth	Δ sun zenith
1	29.5°	32 min.	14.3°	3°
2	24.8°	33 min.	17.2°	1.7°
3	37.1°	23 min.	6.3°	3.4°
4	25.5°	26 min.	13.9°	0.8°
5	28.9°	24 min.	9.4°	2.7°
6	38.2°	23 min.	6.1°	3.6°
7	49.2°	23 min.	5.1°	3.8°
8	37.2°	24 min.	7.5°	3.3°
9	29.4°	31 min.	13.9°	2.9°
10	24.7°	25 min.	13.7°	0.3°
11	33.9°	23 min.	7.1°	3.3°
12	42.2°	51 min.	11.5°	8.2°
13	52.9°	27 min.	5.2°	4.5°

Table 1. Total goniometer dataset with corresponding time period and sun movement in azimuth and zenith directions.

As a direct consequence of the rather long measurement time, the illumination direction does not remain constant during the collection of a complete dataset consisting of  $x$  view angles. Typically, larger deviations are obtained in azimuth direction, especially around noon when changes in sun zenith angle are

minimal. However, this effect is partly assessed in the BRDF retrieval process by using the sunphotometer recordings either in a timely resolved manner (corresponding to the single directional measurements) or by using a mean value for the direct incident radiance.

The first analysis of spectrodirectional goniometer measurements were performed for the 4 datasets of the artificial target which are least influenced by atmospheric conditions (dataset 2, 11, 12 and 13). These were obtained at sun zenith angles of 24.8°, 33.9°, 42.2° and 52.9°, respectively. The reflected radiance distribution is dominated by the strong forward scattering characteristic of the target, which increases at large sun zenith angles. The diffuse incident radiance field shows a more or less opposite tendency with increasing values towards the sun view direction. Irregularities are generally more pronounced in the diffuse incident radiance field and possibly occur due to changing atmospheric conditions and sun movement during the measurement time, especially for dataset no. 12 (zenith = 42.2°, measurement time 51 min.). No data were collected at the exact hotspot direction due to instrument saturation (upward looking spectroradiometer) and cast shadowing (downward looking spectroradiometer). Figure 8 shows the incident diffuse and total reflected radiances as directly measured with the dual FOV goniometer system FIGOS.

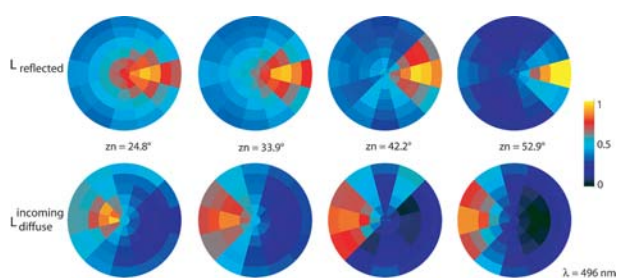


Figure 8. Total reflected and diffuse incoming radiances at various sun zenith angles for 496 nm. The sun position is on the left.

## 5. CONCLUSIONS

The dual FOV goniometer system FIGOS shows a stable and reliable performance for the simultaneous collection of the reflected and incoming diffuse radiances at high angular and spectral resolution. In its present configuration and in conjunction with a sunphotometer the dual FOV FIGOS may be used to provide the necessary dataset for a full field BRDF retrieval of selected targets. Since measurements in both directions are done simultaneously the critical time to measure a whole hemisphere is not affected by having two instruments and is kept at about 20 to 30 minutes. Illumination changes during that time rather depend on atmospheric instability than on the sun movement.

The dual FOV configuration also supports hotspot studies since only the dual fibre optic holder is moving in the solar principal plane and measurements can be made close to the hotspot direction.

The usage of an artificial target provides the advantage of reducing target related measurement errors. Errors due to inherent system inaccuracies persist but are well known for the dual FOV FIGOS. Since the same goniometer can also be used in a laboratory configuration (without dual view option), direct field-laboratory comparisons are supported as well as direct

comparisons to other goniometric systems currently used (Bourgeois, 2006; Painter, 2003; Pegrum, 2006; Peltoniemi, 2005).

Further challenges include the establishment of procedures to reduce sources of uncertainties e.g. intercalibration issues. This can be achieved by collecting all necessary input data for the BRDF retrieval with only one or at least the same type of instruments. However, this requires accurate pointing at the sun disk to collect both the direct irradiance and the diffuse irradiance (shaded sun disk) in the sun view direction. Such pointing accuracy is very time consuming with the existing setup and therefore currently not feasible.

Due to its well known characteristics the dual FOV FIGOS has the potential to be a reference instrument for extensive field and laboratory experiments. The retrieved BRDF of selected targets will be a valuable contribution towards a more accurate validation of air- and spaceborne data as well as BRDF models.

## ACKNOWLEDGMENTS

The authors would like to thank the Swiss National Science Foundation (contract no: 200020 – 101517) and all colleagues who participated at the field experiments. Special thanks go to the Physics Institute of the University of Zurich for its support for the construction of the dual field-of-view configuration.

## REFERENCES

- Abdou, W.A., Helmlinger, M.C. et al., 2000. Ground measurements of surface BRDF and HDRF using PARABOLA III. *Journal of Geophysical Research*, 106 (D11), pp. 11967-11976.
- Analytical Spectral Devices Inc., 1999. Report on "Technical Guide, 4th Ed." Analytical Spectral Devices, Inc., Boulder, Colorado, USA.
- Barnsley, M.J., Settle, J.J. et al., 2004. The PROBA/CHRIS mission: a low-cost smallsat for hyperspectral multiangle observations of the Earth surface and atmosphere. *IEEE Transactions on Geoscience and Remote Sensing*, 42 (7), pp. 1512-1520.
- Bourgeois, C.S., Ohmura, A. et al., 2006. IAC ETH Goniospectrometer: A Tool for Hyperspectral HDRF Measurements. *Journal of Atmosphere and Oceanic Technology*, 23 (4), pp. 573-584.
- Bruegge, C.J., Chrien, N.L. et al., 2002. Early validation of the Multi-angle Imaging SpectroRadiometer (MISR) radiometric scale. *IEEE Transactions on Geoscience and Remote Sensing*, 40 (7), pp. 1477-1492.
- Bruegge, C.J., Helmlinger, M.C. et al., 2000. PARABOLA III: A sphere-scanning radiometer for field determination of surface anisotropic reflectance functions. *Remote Sensing Reviews*, 19, pp. 75-94.
- Dangel, S., Verstraete, M.M. et al., 2005. Towards a Direct Comparison of Field and Laboratory Goniometer Measurements. *IEEE Transactions on Geoscience and Remote Sensing*, 43 (11), pp. 2666-2675.

- Gobron, N., Pinty, B. et al., 2000. Potential of multiangular spectral measurements to characterize land surfaces: Conceptual approach and exploratory application. *Journal of Geophysical Research-Atmospheres*, 105 (D13), pp. 17539-17549.
- Govaerts, Y.M., Verstraete, M.M. et al., 1997. Evaluation of a 3D Radiative Transfer Model against Goniometer Measurements on an Artificial Target. *Journal of Remote Sensing*, 1, pp. 131-136.
- Huber, S., Kneubühler, M. et al., 2007. Estimating Nitrogen Concentration from Directional CHRIS/PROBA Data. *10th International Symposium on Physical Measurements and Signatures in Remote Sensing ISPMSRS*, in print.
- Kaufman, Y.J., Tanre, D. et al., 1997. Passive remote sensing of tropospheric aerosol and atmospheric correction for the aerosol effect. *Journal of Geophysical Research*, 102 (D14), pp. 16815-16830.
- Martonchik, J.V., 1994. Retrieval of Surface Directional Reflectance Properties Using Ground Level Multiangle Measurements. *Remote Sensing of Environment*, 50 (3), pp. 303-316.
- Maurer, J., 2002. Report on "Retrieval of Surface Albedo from Space", University of Colorado, Boulder, USA.
- Painter, T.H., Paden, B. et al., 2003. Automated spectrogoniometer: A spherical robot for the field measurement of the directional reflectance of snow. *Review of Scientific Instruments*, 74 (12), pp. 5179-5188.
- Pegrum, H.M., Fox, N.P. et al., 2006. Design and testing a new instrument to measure the angular reflectance of terrestrial surfaces. *IEEE International Geoscience & Remote Sensing Symposium & 27th Canadian Symposium on Remote Sensing*, CD-ROM.
- Peltoniemi, J.I., Kaasalainen, S. et al., 2005. Measurement of directional and spectral signatures of light reflectance by snow. *IEEE Transactions on Geoscience and Remote Sensing*, 43 (10), pp. 2294-2304.
- Sandmeier, S.R. and Itten, K.I., 1999. A field goniometer system (FIGOS) for acquisition of hyperspectral BRDF data. *IEEE Transactions on Geoscience and Remote Sensing*, 37 (2), pp. 978-986.
- Schaepman, M.E., 2006. Spectrodirectional remote sensing: From pixels to processes. *International Journal of Applied Earth Observation and Geoinformation*, in press.
- Schopfer, J., Dangel, S. et al., 2006. Spectrodirectional assessment of incoming diffuse radiation in field BRDF retrieval. *4th International Workshop on Multiangular Measurements and Models IWMMM-4*, CD-ROM.
- Strub, G., Beisl, U. et al., 2002. Evaluation of diurnal hyperspectral HDRF data acquired with the RSL field goniometer during the DAISEX'99 campaign. *Journal of Photogrammetry and Remote Sensing*, 57 (3), pp. 184-193.
- Weiss, M., Baret, F. et al., 2000. Investigation of a model inversion technique to estimate canopy biophysical variables from spectral and directional reflectance data. *Agronomie*, 20 (1), pp. 3-22.

COMPARISON OF DIFFERENT GROUND TECHNIQUES TO MAP LEAF AREA INDEX OF NORWAY SPRUCE FOREST CANOPY

L. Homolová <sup>a,b,\*</sup>, Z. Malenovský <sup>a</sup>, J. Hanuš <sup>a</sup>, I. Tomášková <sup>a</sup>, M. Dvořáková <sup>a</sup>, R. Pokorný <sup>a</sup>

<sup>a</sup> Institute of Systems Biology and Ecology, Academy of Sciences of the Czech Republic, v.v.i., Poříčí 3b, 60300 Brno, CZ

<sup>b</sup> Department of Applied Geoinformatics and Cartography, Faculty of Science, Charles University in Prague, Albertov 6, 12843 Prague 2, CZ

KEY WORDS: LAI, Sampling strategy, PCA LAI-2000, TRAC, Hemispherical photograph, Norway spruce.

ABSTRACT:

The leaf area index (LAI) of three monocultures of Norway spruce (*Picea abies* (L.) Karst), different in age and structure, was measured by means of two indirect optical techniques of LAI field mapping: 1/ plant canopy analyser LAI-2000, and 2/ digital hemispherical photographs (DHP). The supportive measurements with the TRAC instrument were conducted to produce mainly the element clumping index. The aim of the study was to compare the performances of LAI-2000 and DHP and to evaluate effect of three different sampling strategies on field estimation of leaf area index. One of the suggested sampling designs introduced spatial oversampling around one-point measurement. The oversampling was expected to reveal the importance of sampling point position with respect to surrounding trees. In general, the LAI-2000 instrument produced higher estimates of effective leaf area index than DHP in all experimental stands. On the other hand, the higher "true" estimates of LAI were obtained from DHP. All three sampling strategies produced consistent estimates of effective and "true" LAI in all forest sites. The spatial oversampling of LAI measurement point did not significantly improve the LAI estimate of the canopy subplots.

1. INTRODUCTION

Leaf area index (LAI) of coniferous species is defined as one half the total green leaf/needle area per unit ground surface area (Chen and Black, 1992). It is a dynamic key parameter for interpreting tree or canopy gas, water and energy exchange between photosynthetically active tissue and the atmosphere. It is also important input parameter for eco-physiological models, when up-scaling these canopy fluxes to larger spatial scales.

Many indirect ground measurements techniques have been proposed and tested for mapping of forest LAI (Bréda, 2003; Jonckheere et al., 2004). These techniques are less time consuming and labour-intensive than direct methods of LAI estimations, nevertheless their applicability is still spatially limited. The state-of-art of physically based approaches enable the LAI estimation from optical airborne or satellite remote sensing data at larger scales (Gascon et al., 2004; Wang et al., 2004). The accuracy of these quantitative methods is usually validated by comparison with ground measured LAI. Most frequently used instruments for field LAI mapping are Li-Cor plant canopy analyser LAI-2000 and recently also digital hemispherical photographs.

When working with airborne remote sensing data, their very high spatial resolution (pixel size about 1 meter) needs to be considered. A forest stand appears to be rather heterogeneous at such spatial scale, due to gaps and tree clumping within the canopy. Therefore, a spatial distribution of LAI ground sampling points and their position within a forest stand (especially in a dense young forest canopy) become important aspects for validation of the LAI estimates from RS data of very high spatial resolution.

The objectives of the study are:

- 1. To compare the performances of two indirect LAI ground mapping techniques:
  - digital hemispherical photograph (DHP),
  - Li-Cor plant canopy analyser LAI-2000.
- 2. And to evaluate the effect of three different sampling designs on mapping of leaf area index within three structurally different montane Norway spruce forest stands.

2. METHODS

2.1 Site description

The study site is located at the experimental research site Bily Kriz in the Moravian-Silesian Beskydy Mountains, in the eastern part of the Czech Republic bordering with Slovakia (18.54°E, 49.50°N, altitude of 936 m a.s.l.). The description of the site environmental conditions is given in Kratochvilová et al. (1989). The area is characterized by montane Norway spruce (*Picea abies* (L.) Karst.) forest ecosystems. Three Norway spruce stands of different age and structure (table 1) were selected in the close surroundings of the Bily Kriz experimental site.

Forest stand code	Age	DBH [cm]	Height [m]	trees/ha
YOUNG	28	14	12.5	1436
OLD1	100-110	53	40.1	160
OLD2	75	-	27	420

Table 1. The basic characteristics of three Norway spruce forest stands selected for LAI mapping.

\* Corresponding author. Tel.: +420 543 211 560, e-mail: lucie.homolova@brno.cas.cz.



2.2 Indirect optical techniques of LAI measurements and data processing

All ground measurements of leaf area index were acquired within the frame of the complex field-airborne campaign over the Bily Kriz research site at the turn of August and September 2006.

All optical instruments, used in the study for indirect field estimation of LAI, produced so called effective leaf area index ( $LAI_e$ ). Correction parameters, according to the methods proposed by Chen (1996), were required to convert  $LAI_e$  to the values of "true" leaf area index (eq. 1). The needle-to-shoot area ratio ( $\gamma_e$ ) was obtained from destructive branch analyses conducted at Bily Kriz research site in 2004 (Homolová, 2005). The element clumping index ( $\Omega_e$ ) was produced by the TRAC instrument and from the DHPs analyses. The value of woody correction parameter ( $\alpha$ ) for young Norway spruce trees was derived from destructive sampling conducted by Pokorný (2002). LAI-2000 measurement of totally defoliated mature Norway spruce trees (unpublished) was used to calculate the  $\alpha$  parameter for OLD1 and OLD2 mature Norway spruce forest stands.

where  $\alpha$  = woody-to-total area ratio  
 $\gamma_e$  = needle-to-total area ratio  
 $\Omega_e$  = element clumping index

The leaf area index estimation with Plant Canopy Analyzer PCA LAI-2000 (LI-COR, Inc., Lincoln, NE, USA) is based on measurement of diffuse radiation attenuation caused by canopy in blue part of spectra, which is driven by gap fraction. The measurements with one LAI-2000 unit were taken always under diffuse radiation condition, either in the evening or early morning. A reference measurement to determine above canopy irradiance was taken at meto-towers in the young stand and in canopy openings in case of mature stands. The 45° view cap was used to avoid the influence of the operator and block remaining direct light. The measurements were acquired always above understory, preferably 0.5 m above ground. To avoid multiple scattering effects at larger zenith angles and to reduce the instrument's footprint, the rings 4 and 5 were ignored using C2000 software (Li-Cor, 1992) during the data processing. The view zenith angle of the sensor was thus restricted to 43°.  $LAI_e$  was directly produced by C2000 software. LAI-2000 measurements of  $LAI_e$  were combined with TRAC-derived element clumping index to calculate "true" values of LAI.

$$LAI = (1-\alpha)*LAI_e * \gamma_e / \Omega_e \tag{1}$$

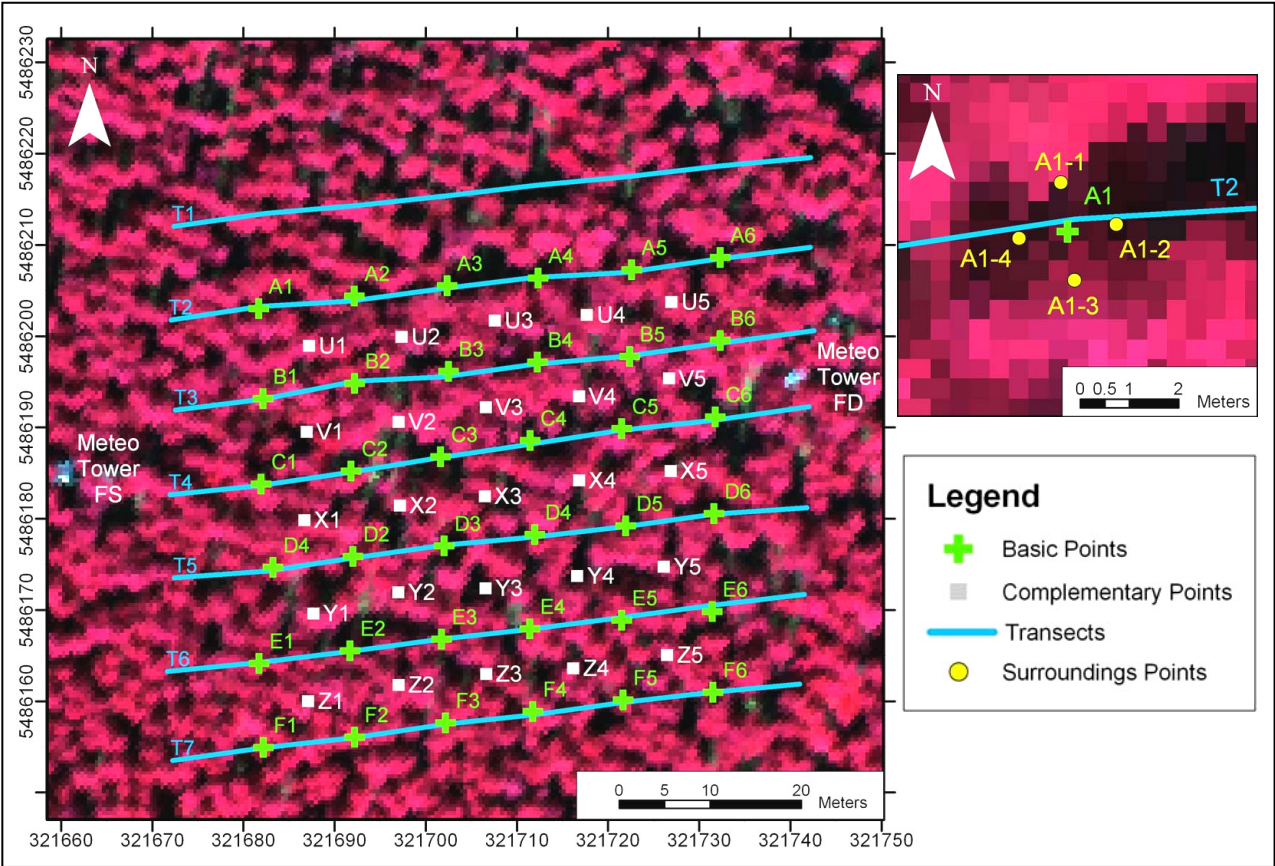


Figure 1. Representation of spatial distribution of basic and complementary LAI sampling points used for DHP and LAI-2000 measurements and TRAC transects in YOUNG forest site. Each basic sampling point was oversampled with another four measurement points as shown in the zoomed image. Background is false RGB colour composite (R859, G653, B551 nm) of AISA Eagle airborne hyperspectral image with pixel size equal to 0.4 m. The AISA image subset is displayed in UTM 34N (WGS-84) coordinate system.

Hemispherical photographs (DHP) were acquired at the same position as LAI-2000 measurements, using digital camera Nikon Coolpix 8700 equipped with Nikon FC-E9 0.2x fisheye converter. The camera was mounted on a tripod in fixed height of 1.5 m above ground. The manual mode to set the camera exposure was used. We kept the fixed lens aperture and adjusted the shutter speed, one or two stops of overexposure relatively to the in-stand automatic exposure (Zhang et al., 2005). The images were processed by the CAN-EYE v5.0 software (Baret and Weiss, 2004). The software produces effective as well as "true" estimates of LAI. In CAN-EYE, the element clumping index is computed using the Lang and Yueqin (1986) logarithm gap fraction averaging methods.

The measurements with the TRAC instrument (3<sup>rd</sup> Wave Engineering, Ottawa, ON, Canada) (Leblanc et al., 2002) require direct solar radiation. It was measured at constant walking pace along several parallel transects, each 70 to 80 m long and oriented preferably in E-W direction. Distance markers were registered each 5 m. The TRAC data record was processed by TracWin software. It calculates effective LAI based on gap fraction and element clumping index  $\Omega_e$  (Chen, 1996) based on the analyses of gap size distribution (Chen and Cihlar, 1995).

2.3 LAI sampling scheme

A regular grid pattern of LAI sampling points combined with several parallel TRAC transects was established at each experimental forest stand. The schema of the sampling design for young Norway spruce forest stand is presented in figure 1. The similar pattern (grid of 3x3 basic sampling points) was established in mature forests. The distance between basic sampling points was driven by mean tree height and view zenith angle of the instruments. The distances were set to be 10 m in young and 20 m in mature forest stand, which corresponded to the zenith view angle of 45°. The sampling scheme was designed in such a way to ensure the spatial comparability between the LAI-2000 measurements and digital hemispherical photographs, acquired per sampling point.

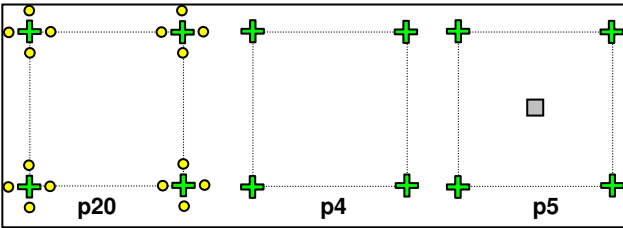


Figure 2. Schematic representation of three different spatial distributions (scenario p20, p4 and p5) of LAI sampling points within a subplot. Crosses represent basic, squares represent complementary and circles represent surroundings (oversampling) LAI sampling points.

Three different scenarios (p20, p4 and p5) of LAI sampling points' distributions were tested within the study (see figure 2). Only four basic point measurements were considered for scenario p4. Each basic LAI sample point was oversampled by four surrounding measurements point in case of scenario p20. Sampling scenario p5 represented five point measurements; four basic sampling points as in the scenario p4, but one more measurement was added to the centre of a subplot (complementary sampling point). In total 20, 4 and 5 measurements, respectively, were processed per subplot in case of p20, p4 and p5 sampling strategy.

In total 21 subplots (one subplot was composed out of 4 basic sampling points) were selected to test the effect of different spatial distributions of LAI sampling points on the estimation of effective and "true" LAI.

3. RESULTS AND DISCUSSION

3.1 Correction parameters: needle-to-shoot area ratio, clumping index and woody-to-total area ratio

Correction of the optical estimates of leaf area index is trade-off between correction for clumping, which causes LAI underestimation, and correction for the woody materials, which causes its overestimation. Thus proportion of woody area and clumping of green elements, especially in coniferous canopies, are important parameters for LAI measurement, however, it is difficult to quantify them properly. The mean values of woody-to-total area ratio ( $\alpha$ ), needle-to-total area ratio ( $\gamma_e$ ) and element clumping index ( $\Omega_e$ ) for each investigated Norway spruce stand are presented in table 2.

In general, the element clumping index derived from TRAC (Chen and Cihlar, 1995) was higher than its estimation from DHPs (Lang and Yueqin, 1986). The largest bias was observed in dense young Norway spruce canopy. Leblanc et al. (2005) reported that the TRAC algorithm produces higher estimates of  $\Omega_e$  than Lang and Yueqin method, though gap fraction measurements performed with TRAC and from DHP were well correlated. The possible explanation of the difference is that in very dense canopies is hard to meet an assumption of the Lang and Yueqin method that analysed segments of DHP contain gaps. Secondly, hemispherical photographs and TRAC are instruments with different field of views representing different parts of forest canopies. The mean correction factor (TRAC-based clumping index combined with woody-to-total area ratio) for young forest was equal to 1.49, which agreed well with the correction factor presented by Pokorný and Marek (2000) for the same canopy. This fact suggests that the canopy element clumping index derived from TRAC would be considered as more reliable estimate.

Forest code	LAI <sub>e</sub>			correction parameters				LAI		
	LAI-2000	DHP CAN-EYE	TRAC	$\alpha$	$\gamma_e$	$\Omega_e$ (TRAC)	$\Omega_e$ (DHP)	LAI-2000 + TRAC	DHP	TRAC
YOUNG	4.94±0.46	3.90±0.77	4.62±0.04	0.133	1.526	0.89±0.04	0.58±0.04	7.42±0.72	8.89±1.17	6.98±0.06
OLD1	2.71±0.05	2.32±0.25	2.58±0.22	0.228	1.422	0.66±0.02	0.57±0.03	4.49±0.05	4.47±0.63	4.18±0.55
OLD2	3.33±0.09	3.10±0.10	3.96±0.13	0.228	1.422	0.67±0.01	0.67±0.01	5.44±0.16	5.10±0.26	6.47±0.01

Table 2. Summary of mean values and standard deviations of forest stand LAI<sub>e</sub>, correction parameters ( $\alpha$  – woody-to-total area ratio,  $\gamma_e$  – needle-to-total area ratio,  $\Omega_e$  – element clumping index) and "true" forest stand LAI observed in three Norway spruce canopies.

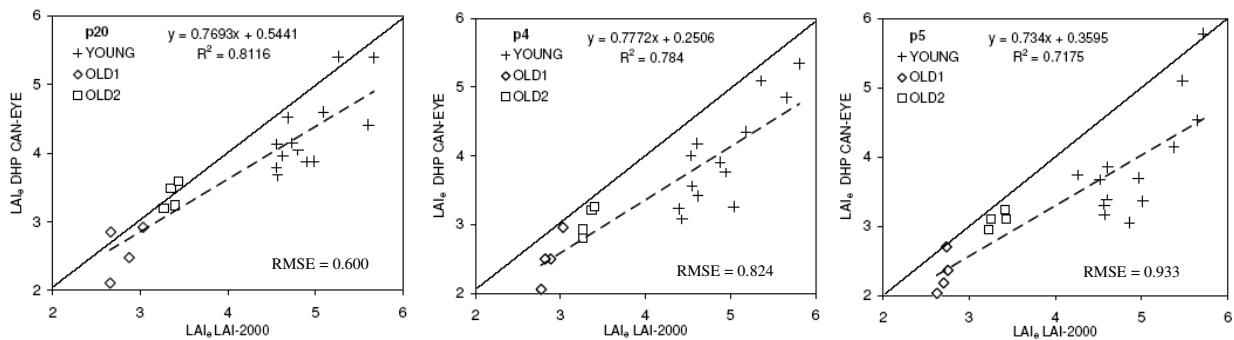


Figure 3. Direct comparison of effective leaf area index values produced by PCA LAI-2000 and hemispherical digital photographs processed in CAN-EYE software, per each investigated Norway spruce forest stands, using three spatial designs (scenarios p20, p4, and p5).

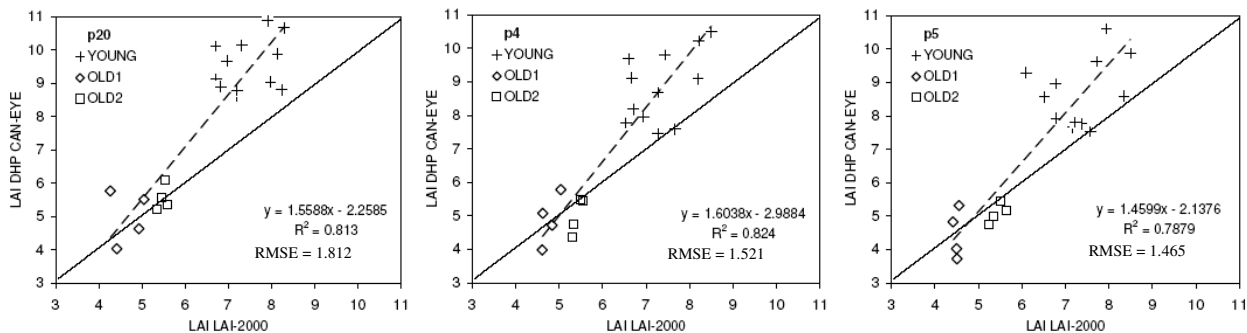


Figure 4. Direct comparison of "true" leaf area index values produced by PCA LAI-2000 and hemispherical digital photographs processed in CAN-EYE software, per each investigated Norway spruce forest stands, using three spatial designs (scenarios p20, p4, and p5).

Digital hemispherical photographs, as a permanent record of canopy structure, can be a suitable tool for quantifying the effect of light blocking woody materials (e.g. trunks, branches). The possible improvement can be the adaptation of a digital camera to acquire images in near infra-red wavelengths (Chapman, 2007), where reflectance of woody materials is higher than reflectance of green biomass.

3.2 Optical indirect estimation of LAI<sub>e</sub> and LAI

Mean stand-level values of effective and "true" leaf area index estimates, for three Norway spruce forest stands different in structure and age, are presented in table 2. The estimates of LAI<sub>e</sub> produced by hemispherical digital photographs were generally lower, in comparison to LAI-2000 estimates, in all investigated forest stands. The largest difference of 21% between LAI-2000 and DHP LAI<sub>e</sub> estimates was observed in dense YOUNG forest stand. These results correspond to Jonckheere et al. (2005a), who reported similar underestimation of DHP effective leaf area index for even-aged forest stand of Scots pine. Also Zhang et al. (2005) observed similar behaviour of LAI<sub>e</sub> estimates from DHP, especially for higher values of LAI. Variability in illumination conditions during DHP acquisition could possibly explain this underestimation, because LAI-2000 measurements were always acquired under more stable diffuse radiation conditions. The sun exposed parts of canopy captured on hemispherical images appeared to be brighter than shaded parts. These sun exposed elements tended to be classified as part of sky and thus caused overestimation of canopy gap fraction. According to (Cescatti, 2007; Jonckheere et al., 2005b), threshold between canopy elements and bright

sky is the most important and at the same time most uncertain aspect in determination of canopy gap fraction from hemispherical photographs. The CAN-EYE software offers only manual thresholding, which is applied over the entire image (or set of images). For instance the automated thresholding system can eliminate a possible bias caused by an operator. The application of different threshold values to separated zenith rings can eliminate the brightness gradients, which were observed within the images with increasing view zenith angle.

Several authors (Leblanc and Chen, 2001; Weiss, 2004) recommended to obtain the gap fraction measurements at view zenith angle of 57.5° (corresponding to the LAI-2000 fourth ring). This gap fraction measurement is supposed to be independent on leaf (needle) angle distribution and allows direct estimation of the effective leaf area index. The above mentioned authors recommended this method as a robust and suitable for canopy LAI<sub>e</sub> estimation.

On the other hand, results of "true" LAI estimates showed opposite trend, i.e. DHP-based estimates were higher than leaf area index obtained from LAI-2000. This can be explained by different methodological approaches of element clumping index determination, discussed in the section 3.1.

3.3 Effect of a sampling strategy on LAI<sub>e</sub> and LAI estimation

One-to-one relationship between LAI-2000 and DHP estimates of canopy leaf area index for three sampling strategies (p20, p4, p5) are presented in figures 3 and 4. The graphs indicate that

there are no important differences between all tested sampling strategies. The spatial oversampling, applied at each basic sample point (see scenario p20), did not improve the LAI estimation. The results revealed that exact position of one-point measurement seems to be less important than the spatial location of whole sampling unit (a subplot) within a forest stand.

Although suitable sampling strategy is an important issue when performing field measurements, very little literature is dedicated to this topic. The LAI sampling design is dependent on the study purpose and canopy characteristics (e.g. canopy height and canopy closure). Main purpose of our LAI measurements was to create ground truth data for validation of LAI maps derived from airborne hyperspectral remote sensing data (spatial resolution of about 1m). Nevertheless, more sampling plots would be needed to validate the satellite based products of medium spatial resolution (pixel size of about 10-30 m). The LAI sampling design developed within the frame of VALERI project (Baret et al., 2007) seems to be an appropriate approach to validate these satellite products.

#### 4. CONCLUSIONS

In general, the plant canopy analyser LAI-2000 produced slightly higher estimates of  $LAI_c$  than obtained from the analyses of DHP in all three age-diverse but structurally homogenous Norway spruce forest stands. On the other hand the "true" estimates of leaf area index obtained from DHP were slightly higher than LAI estimates from PCA LAI-2000. The highest bias between LAI-2000 and DHP based estimates of effective and "true" leaf area index was observed in case of young dense forest stand. It is evident, that both instruments can provide reasonable estimates within an expected range of LAI values. However, there are large uncertainties in estimation of the canopy clumping index, which is an important parameter to correct estimates of  $LAI_c$  obtained from LAI-2000 and DHPs.

The spatial over-sampling, applied at each basic sample point, did not significantly improve values of  $LAI_c$  and LAI measured in all three investigated Norway spruce forests. The results indicated that one-point measurements organized in the regular grid were sufficient enough to properly represent canopy leaf area index.

#### REFERENCES

- Baret, F. and Weiss, M. (2004). Can-Eye: processing digital photographs for canopy structure characterization. INRA, Avignon, France.  
[http://www.avignon.inra.fr/can\\_eye/page2.htm](http://www.avignon.inra.fr/can_eye/page2.htm) (Accessed 21.03.2007).
- Baret, F., Weiss, M., Allard, D., Garrigue, S., Leroy, M., Janjean, H., Fernandes, R., et al., 2007. VALERI: a network of sites and a methodology for the validation of medium spatial resolution land satellite products. *Remote Sensing of Environment*. (submitted)
- Bréda, N.J.J., 2003. Ground-based measurements of leaf area index: a review of methods, instruments and current controversies. *Journal of Experimental Botany*, 54, pp. 2403-2417.
- Cescatti, A., 2007. Indirect estimates of canopy gap fraction based on the linear conversion of hemispherical photographs: Methodology and comparison with standard thresholding techniques. *Agricultural and Forest Meteorology*, 143(1-2), pp. 1-12.
- Gascon, F., Gastellu-Etchegorry, J.-P., Lefevre-Fonollosa, M.-J. and Dufrene, E., 2004. Retrieval of forest biophysical variables by inverting a 3-D radiative transfer model and using high and very high resolution imagery. *International Journal of Remote Sensing*, 25(24), pp. 5601-5616.
- Homolová, L. (2005). *Leaf area index estimation for Norway spruce forest stand by means of radiative transfer modelling and imaging spectroscopy*. Centre for Geo-Information, Wageningen University, Wageningen, pp. 62, (MSc. thesis).
- Chapman, L., 2007. Potential applications of near infra-red hemispherical imagery in forest environments (short communication). *Agricultural and Forest Meteorology*, 143(1-2), pp. 151-156.
- Chen, J.M., 1996. Optically-based methods for measuring seasonal variation of leaf area index in boreal conifer stands. *Agricultural and Forest Meteorology*, 80(2-4), pp. 135-163.
- Chen, J.M. and Black, T.A., 1992. Defining leaf area index for non-flat leaves. *Plant, Cell & Environment*, 15(4), pp. 421-429.
- Chen, J.M. and Cihlar, J., 1995. Quantifying the effect of canopy architecture on optical measurements of leaf area index using two gap size analysis methods. *IEEE Transaction on Geosciences and Remote Sensing*, 33(3), pp. 777-787.
- Jonckheere, I., Fleck, S., Nackaerts, K., Muys, B., Coppin, P., Weiss, M. and Baret, F., 2004. Review of methods for in situ leaf area index determination Part I. Theories, sensors and hemispherical photography. *Agricultural and Forest Meteorology*, 121(1-2), pp. 19-35.
- Jonckheere, I., Muys, B. and Coppin, P., 2005a. Allometry and evaluation of in situ optical LAI determination in Scots pine: a case study in Belgium. *Tree Physiology*, 25(6), pp. 723-732.
- Jonckheere, I., Nackaerts, K., Muys, B. and Coppin, P., 2005b. Assessment of automatic gap fraction estimation of forests from digital hemispherical photography *Agricultural and Forest Meteorology*, 132(1-2), pp. 96-114.
- Kratochvilová, I., Janouš, D., Marek, M., Barták, M. and Říha, L., 1989. Production activity of mountain cultivated Norway spruce stands under the impact of air pollution. *Ekologia*, 8(4), pp. 407-419.
- Lang, A.R.G. and Yueqin, X., 1986. Estimation of leaf area index from transmission of direct sunlight in discontinuous canopies. *Agricultural and Forest Meteorology*, 37(3), pp. 229-243.
- Leblanc, S.G. and Chen, J.M., 2001. A practical scheme for correcting multiple scattering effects on optical LAI measurements. *Agricultural and Forest Meteorology*, 110(2), pp. 125-139.
- Leblanc, S.G., Chen, J.M., Fernandes, R., Deering, D.W. and Conley, A., 2005. Methodology comparison for canopy structure parameters extraction from digital hemispherical



photography in boreal forests. *Agricultural and Forest Meteorology*, 129(3-4), pp. 187-207.

Leblanc, S.G., Chen, J.M. and Kwong, M. (2002). Tracing Radiation and Architecture of Canopies - TRAC manual, version 2.1.3. Natural Resources Canada. <http://www.geog.utoronto.ca/info/facweb/Chen/Chen's%20homepage/PDFfiles/tracmanu.pdf> (Accessed 22.03.2007).

Li-Cor, 1992. LAI-200 Plant Canopy Analyzer; Operating Manual, Li-Cor, Inc., Lincoln, NE.

Pokorný, R. (2002). *Index listové plochy v porostech lesních dřevin (Leaf area index of forest stands)*. Faculty of Forestry and Wood Technology, Mendel University of Agriculture and Forestry, Brno, pp. 135, (PhD. thesis, Czech).

Pokorný, R. and Marek, V.M., 2000. Test of accuracy of LAI estimation by LAI-2000 under artificially changed leaf to wood area proportions. *Biologia Plantarum*, 43(4), pp. 537-544.

Wang, Y., Woodcock, C.E., Buermann, W., Stenberg, P., Voipio, P., Smolander, H., Häme, T., et al., 2004. Evaluation of the MODIS LAI algorithm at a coniferous forest site in Finland. *Remote Sensing of Environment*, 91(1), pp. 114-127.

Weiss, M., 2004. Review of methods for in situ leaf area index (LAI) determination Part II. Estimation of LAI, errors and sampling. *Agricultural and Forest Meteorology*, 121(1-2), pp. 37-53.

Zhang, Y., Chen, J.M. and Miller, J.R., 2005. Determining digital hemispherical photograph exposure for leaf area index estimation. *Agricultural and Forest Meteorology*, 133, pp. 166-181.

#### ACKNOWLEDGEMENTS

This work was supported by the ESA/PECS project No. 98029 and the Research Plan AV0Z60870520 of the Institute of Systems Biology and Ecology, Academy of Sciences of the Czech Republic, v.v.i.



## 2nd GENERATION OF RSL'S SPECTRUM DATABASE "SPECCHIO"

A. Hüni\*, J. Nieke, J. Schopfer, M. Kneubühler and K. I. Itten

Remote Sensing Laboratories, University of Zurich, Winterthurerstrasse 190, 8057 Zurich, Switzerland. -  
(ahueni, nieke, jschopf, kneub, itten)@geo.unizh.ch

**KEY WORDS:** Databases, Data Structures, Metadata, Spectral, Software

### ABSTRACT:

The organised storage of spectral data described by according metadata is important for long term use and data sharing with other scientists. The recently redesigned SPECCHIO system acts as a repository for spectral field campaign and reference signatures. An analysis of metadata space has resulted in a non-redundant relational data model and efficient graphical user interfaces with underlying processing mechanisms minimizing the required user interaction during data capture. Data retrieval is based on imposing restrictions on metadata space dimensions and the resulting dataset can be visualised on screen or exported to files. The system is based on a relational database server with a Java application providing the user interface. This architecture facilitates the operation of the system in a heterogeneous computing environment.

### 1. INTRODUCTION

Ground based hyperspectral signatures are collected for (a) calibration and validation of airborne or spaceborne imagery and its data products, (b) feasibility studies for airborne/spaceborne missions, (c) basic investigation of the relationship between physical or biochemical properties and the electromagnetic reflectance of objects and (d) definition of directional dependence of the reflectance of objects on the illumination and viewing geometry. There are no standardisations of the acquisition process of ground spectral signatures. As a result sharing spectral signature datasets with other scientists is complicated due to differences in data collection techniques and sampling environment conditions (Pfitzner et al., 2006).

Spectral ground sampling campaigns result in significant amounts of data both in number of sampled wavelengths and collected spectra. For efficient research such data need to be documented by metadata and stored in an organized way. This serves three purposes: (a) to ensure the usability of collected data in long-term, (b) to provide other scientists a means of assessing the suitability of a third party dataset for their own research and (c) to enable the retrieval of spectral data based on metadata queries. A relational database seems a natural choice of technology in this respect. However, only two implementations of such systems are currently known: (a) SPECCHIO (Bojinski et al., 2003) and (b) SpectraProc DB (Hueni & Tuohy, 2006).

Experience with the first version of SPECCHIO (Bojinski et al., 2003) has shown that the success of such a system is highly dependant on its utilization by the users. Many researchers were deterred from entering their data into the spectral database due to suboptimal data capturing system interfaces. It has become clear that in order to be successful a spectral database system must (a) provide added value to the user and (b) minimize the manual data input as much as possible by automated metadata generation.

SPECCHIO is used at RSL to (a) store spectral and metadata in a central repository which is accessible to all members of the laboratory, (b) serve as a spectral data source for various

calibration/validation and simulation tasks and (c) provide parameters for APEX level 2/3 processing (Schlaepfer & Nieke, 2007 (in preparation)). Due to shortcomings of the first SPECCHIO version in terms of user friendliness and inconsistencies in the data model a redesign was undertaken with the goal to provide a system for non-redundant, centralised and efficient entry, storage and retrieval of spectral data and associated metadata.

### 2. METHODS

#### 2.1 Spectral, Feature and Metadata Space

A sampled object has a spectral attribute and arbitrary non-spectral attributes, the so called metadata.

The spectral attribute can be interpreted in two principal ways: (a) as a spectral signature in spectral space or (b) as a point in an n-dimensional feature space (Landgrebe, 1997). The sampling process by the spectroradiometer leads to a discretization of the continuous spectral response of the object. Every sampling channel yields a quantitative value which forms a component of the output vector. Spectral signatures represent the spectral response of the sampled object. An object in spectral space is visualized by plotting the spectral response vector against the channel wavelengths. The curve is then again interpreted as a continuous function.

The feature space concept explicitly utilizes the discrete data as produced by the sampling process. Every object is represented by a point in an n-dimensional space, the so called feature space and its position is given by the spectral vector. The dimensionality of the feature space is given by the number of channels of the sensor. The transformation of continuous spectral space into discrete feature space is defined by the spectral response functions of the sensor elements.

Metadata are essentially descriptive data about a resource. In the case of spectral data the resource is the spectral response of an object and the metadata contains further information about the object and the sampling environment at the time of data capture. Metadata spaces are n-dimensional spaces defined by descriptive dimensions. The space is most efficiently described

---

\* Corresponding author.

by orthogonal vectors, i.e. the dimensions are independent of each other (Wason & Wiley, 2000).

In the example of SPECCHIO the metadata vector contains four types of variables: (a) quantitative, (b) categorical (qualitative), (c) alphanumeric string and (d) pictorial.

Quantitative variables are gained from measurements of quantitative features of the sampled object or the surrounding environment, e.g. spatial position, ambient temperature or capturing time.

Categorical variable values are assigned to objects on the basis of a priori knowledge. Examples are: landcover type, species, arbitrary sampling site number or sampling location name.

Alphanumeric strings are used to hold textual descriptions. They do not contain information in a structured way but can help the user in understanding the data. In the context of metadata space alphanumeric string variables neither form clusters nor do they group data in any organised way. Strings dimensions are searchable via full text search or can be crawled and indexed previous to queries.

Pictorial variables can hold supplementary information about the sampled object or its environment in form of images, e.g. photos of sky (hemispherical), sampling setup or target. Pictorial variables have the potential of yielding quantitative or qualitative data if subjected to image analysis or image indexing techniques. This is however not further investigated at this point.

Typically, quantitative variables show a high degree of variability while categorical variables concentrate the data into the available classes. This is illustrated in Figure 1 showing two 2D subspaces of the metadata space.

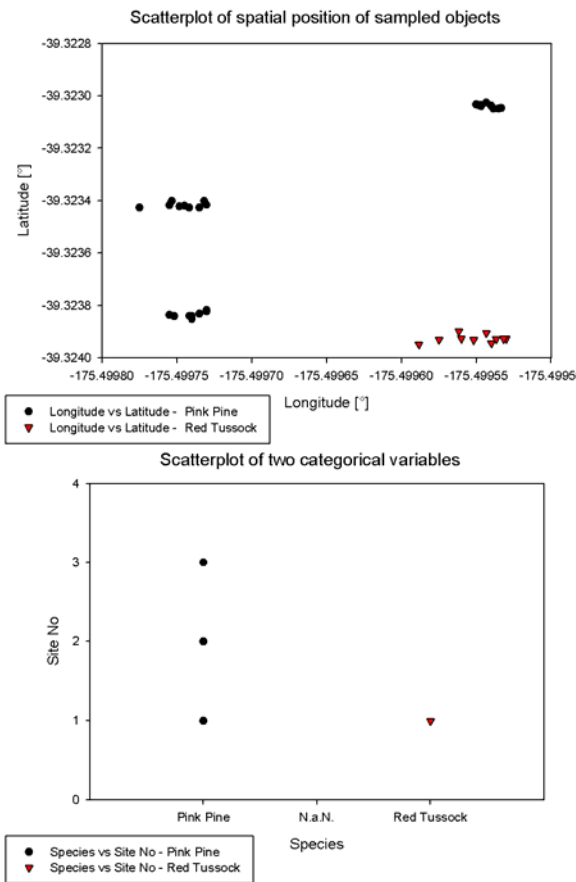


Figure 1: Scatterplots of quantitative (top) and categorical variables (bottom)

The upper plot shows the variability of the spatial position of the samples and the lower plot the grouping function of the categorical variables ‘species’ and ‘site number’. The site number is arbitrarily defined and refers to the spatial region where an object was sampled. For the Pink Pine species there exist three sample sites. In the spatial subspace the sampling positions form clusters that correspond to these sample sites. In the categorical subspace all data points fall into the positions defined by species and site number categories. Two points are worth noting:

(a) Quantitative variables contain individual values per sample. The acquisition of quantitative metadata has the potential of automation by the use of electronic instruments, e.g. GPS or automated weather stations. Setting quantitative variables of a group of samples to the same value (e.g. an average value) is possible if the introduced error is acceptable.

(b) Categorical variables group the data and one value will apply to many samples. Thus the values must not be entered individually per sample but can be set for whole sample groups. Categorical variables lend themselves to data structuring due to the grouping function in categorical subspaces.

Table 1 lists the metadata variables and their data type on spectrum level according to the SPECCHIO data model. The data types are abbreviated as follows: C (Categorical), Q (Quantitative), S (String) and P (Pictorial). The ‘Autom.’ column lists the possibility of automatic retrieval or calculation: SF (Spectral File) and CA (Calculation).

Table 2 lists further metadata that is relevant at campaign level.

Table 1: Metadata on spectrum level

Metadata variable	Type	Autom.
Auto number	C	SF
User comment	S	SF
Capturing date and time	Q	SF
Spectral file name	S	SF
Number of spectra averaged internally by the instrument	Q	SF
Sensor	C	SF
File format	C	SF
Instrument	C	SF
Instrument calibration number	C	SF
Foreoptic	C	SF
Illumination source	C	
Sampling environment	C	
Measurement type (single, directional, temporal)	C	
Measurement unit (Reflectance, DN, radiance, absorbance)	C	SF
Target homogeneity	C	
Spatial position (latitude, longitude, altitude)	Q	SF
Landcover (based on CORINE land cover (European Commission DG XI, 1993))	C	
Cloud cover (in octas)	C	
Ambient temperature	Q	
Air pressure	Q	
Relative humidity	Q	
Wind speed (Qualitative description)	C	

Wind direction (categories in 45 degree steps)	C	
Sensor zenith angle	Q	CA (Goniom.)
Sensor azimuth angle	Q	CA (Goniom.)
Sensor distance	Q	
Illumination zenith angle	Q	CA (Sun pos.)
Illumination azimuth angle	Q	CA (Sun pos.)
Illumination distance	Q	
Spectrum names	C	
Target type	C	
Goniometer model	C	
Pictures	P	
Data structuring information	C	Gleaned from folder structures

Table 2: Metadata on campaign level

Metadata variable	Type
Investigator	C
File path to spectral data on file system	S
Campaign comments/description	S

2.2 Structuring of Spectral Campaign Data

Spectral sampling campaigns yield spectral signatures of objects. Physically, spectroradiometers produce files containing digitized spectral signatures of the sampled objects with usually one file being created per reading. The sheer number of files resulting from sampling campaigns requires an organised method of storage.

Structuring of data is achieved by sorting them according to discriminating metadata attributes. Categorical metadata variables have a grouping feature that is ideally suited for data structuring. Qualitative attributes could also be used for data structuring given that they are transformed into categorical variables first by some classification. In the process of spectral sample data structuring the values of all utilized metadata variables will be implicitly recorded in some form in the resulting structure.

The example introduced in the previous section consists of samples belonging to two different species (Pink Pine and Red Tussock). For the Pink Pine three sample sites exist while Red Tussock has been sampled at only one site. A first level of structuring could use the species variable resulting in a one dimensional hierarchy. By adding the sampling site number as further structuring criterion a two dimensional hierarchy is defined.

These hierarchies can be directly implemented with an according hierarchical folder structure that is subsequently used to store the spectral signatures (cf. Figure 2).

Three points are worth noting:

(a) Data structures implicitly contain metadata information. Metadata can be gleaned from directory structures by the creating agent when the resource is created (Gill et al., 1998). This information can be redundant or complementary in relation to the metadata attributes stored in the database.

(b) The number of dimensions used to structure data can range from zero (flat data structure) to N where N is equal to the number of available categorical metadata variables. Obviously, by the use of a sampling protocol, files can still be tied with their metadata even when using a flat data structure. However, using a folder structure based on metadata parameters to store field data in first place facilitates the data handling at later stages.

(c) Hierarchies are useful to store and retrieve information. Their limitation is the fixed path one has to follow to retrieve

data (Wason & Wiley, 2000). The ordering of the levels usually depends on some logical model the cataloguer has of the data.

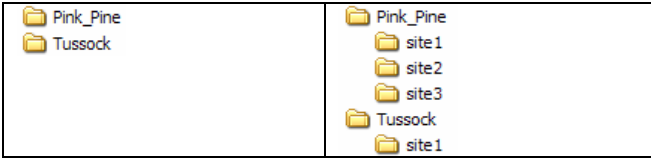


Figure 2: One dimensional hierarchy (left) and two dimensional hierarchy (right)

Data structures always reflect the way the user thinks about the data. Ultimately the structure will depend on the scientific problem to be solved. The data structure is therefore important to the understanding of the data and thus should be stored in the database along with other metadata information. Data structures also facilitate the handling of data and should be utilised in graphical user interface.

2.3 Metadata Generation

The success of a system using metadata relies on the input of such data in first place. If metadata entry involves too much effort users can be deterred from entering their data into the system, thus rendering it useless. The automation must therefore be a prime focus of metadata input.

Many spectroradiometer output files contain a range of parameters that can be directly stored in metadata parameter fields. By conversion to other file formats, e.g. ENVI SLB, some of this information can be lost and subsequently require manual data capture. It is therefore important to support and use native spectroradiometer file formats whenever possible.

While some metadata is available from the input files other data may be generated computationally, e.g. (a) sun geometry and (b) goniometer viewing geometry for the FIGOS and LAGOS goniometers (Schopfer et al., 2007 (in print)).

The importance of automated metadata generation has been pointed out above. Table 1 lists the metadata variables that can be automated. Out of 34 variables, 12 can be read from the input file (for the example of an ASD binary file with a GPS device connected to the field laptop), 1 can be gleaned from the directory structure (data structuring information), 4 can be calculated (illumination geometry and sensor geometry for outdoor sampling and goniometer experiments respectively) and 17 need to be captured manually. Of these remaining 17, three are quantitative variables related to the sampling environment and could be automated using an electronic weather station, 14 are categorical variables and one is pictorial. Categorical variable values apply to groups of spectra in many cases and their data entry can thus be carried out via group operations minimising the needed user interaction.

2.4 Database Model

An optimal data model stores the data in a set of small, stable tables. Complex user views are reduced to such models by the process of database normalisation (McFadden & Hoffer, 1988). The engineering of the database model had three prime goals: (a) removal of data redundancy, (b) minimizing needed data entry by the user and (c) providing high repeatability for categorical parameters. These issues are actually coupled: a non redundant system will implicitly reduce the required data input and store categorical variables in separate tables. The content of categorical parameters should be one entry out of a well defined set of possible values. Repeatability is the ability to have the

same resource described in the same way on two or more occasions (Wason & Wiley, 2000). For categorical variables the repeatability is therefore increased by providing these values in a separate table, thus defining the possible set and restricting the data access to read only for normal users. Data capturing effort is minimized by reducing the action to the selection of one value out of the set.

An example is the cloud cover in octas: the nine possible classes are by definition the only values the cloud parameter can assume. A spectrum will refer to the cloud cover by a foreign key, thus restricting the possible set of values to the predefined ones.

Consider the example of environmental conditions of a sampling site. The parameters involved are: cloud cover, wind speed, wind direction, humidity, air pressure and temperature. If spectra of a sampling site are collected in a short time frame it is unlikely that the environmental variables will change significantly. They thus apply to all collected spectra. Given the normalized data model, these variables are entered only once and all involved spectra are referencing this single entry by foreign keys.

2.5 System Architecture

The core of the SPECCHIO system is a MySQL database (MySQL AB, 2005) hosted on a database server (cf. Figure 3). The SPECCHIO application was implemented as a Java 2 (Sun Microsystems Inc., 2006) application and is therefore operating system independent which is of importance in a heterogeneous computing environment. The application thus runs on any machine with a Java Virtual Machine (VM) installation and connects to the database via TCP/IP on standard port 3306. The application can also be run remotely from a terminal on a server by the use of the X11 protocol. The spatial aspect of the data sets offers the possibility for direct linkage with a GIS system. For the example of ArcGIS (ESRI, 2006) a database connection is established via ODBC (Open Database Connectivity).

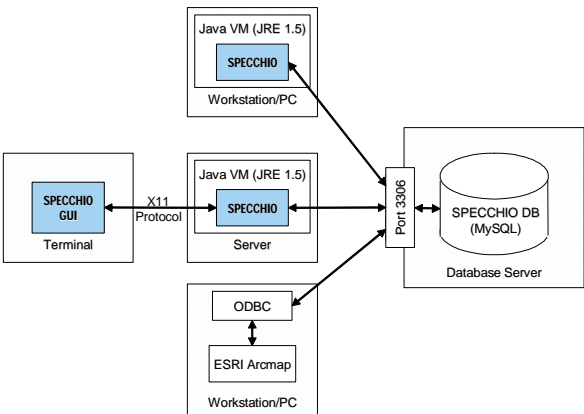


Figure 3: SPECCHIO system architecture

3. RESULTS

The resulting system is documented hereafter by describing the workflow from the loading of a new campaign till the data retrieval.

3.1 Campaign Data Loading

The definition of a new sampling campaign requires only the definition of a campaign name and the specification of the top directory, i.e. the root of the hierarchical structure.

Once a campaign is defined its data is loaded by a single mouse click. The hierarchy of the campaign is automatically parsed. The folder structure is stored in entries in the hierarchy table and spectral files are read and data filled into the appropriate tables.

In the case of new data being added to an existing campaign, the loading process can be started again and will only load the new information into the database.

Supported file formats are: ASD binary (Analytical Spectral Devices Inc.), GER signature (Spectra Vista Co., 2005), ENVI Spectral Library (Research Systems Inc., 2005) and MFR OUT (Yankee Environmental Systems Inc., 2000).

3.2 Metadata Editing

Once data of a campaign have been loaded, their metadata can be edited by using the Metadata Editor (cf. Figure 4). The structure of the campaign is visualized by a tree structure (lower left in Figure 4). Selection of the data to be edited happens via this tree. Three tabs (right side in Figure 4) hold the metadata fields of the campaign, the hierarchy and the spectrum. The content of the fields reflects the current selection in the tree. Multiple updates are possible by selecting multiple hierarchies and/or spectra. A metadata conflict detection is executed for multiple selections and only non-conflicting metadata parameters can be updated, e.g. if every spectrum in a selection already refers to a different spatial position editing will be disabled for the position.

Categorical variable values are selected from combo boxes that are pre-filled from the database. Quantitative variables are entered into fields restricted to numerical values.

Each of the three tabs has associated reset and update buttons which will restore the previous values or commit the changes to the database respectively.

Further functionality includes: highlighting of mandatory fields according to the chosen metadata quality level, indication of missing metadata in the selection tree and overriding of the conflict detection.

3.3 Data Queries and Output

Data is queried by using the Query Builder. Two operational modes are supported: (a) direct selection of records by using a tree structure (browsing) and (b) specification of query conditions (metadata space constraints).

Restriction in several metadata dimensions is achieved by a logical AND of the constraints per dimension.

Figure 5 shows a spectrum report window with a spectral plot on the left side and metadata attributes listed on the right side. Data can be written as CSV (Comma Separated Values) and ENVI Spectral Library files.

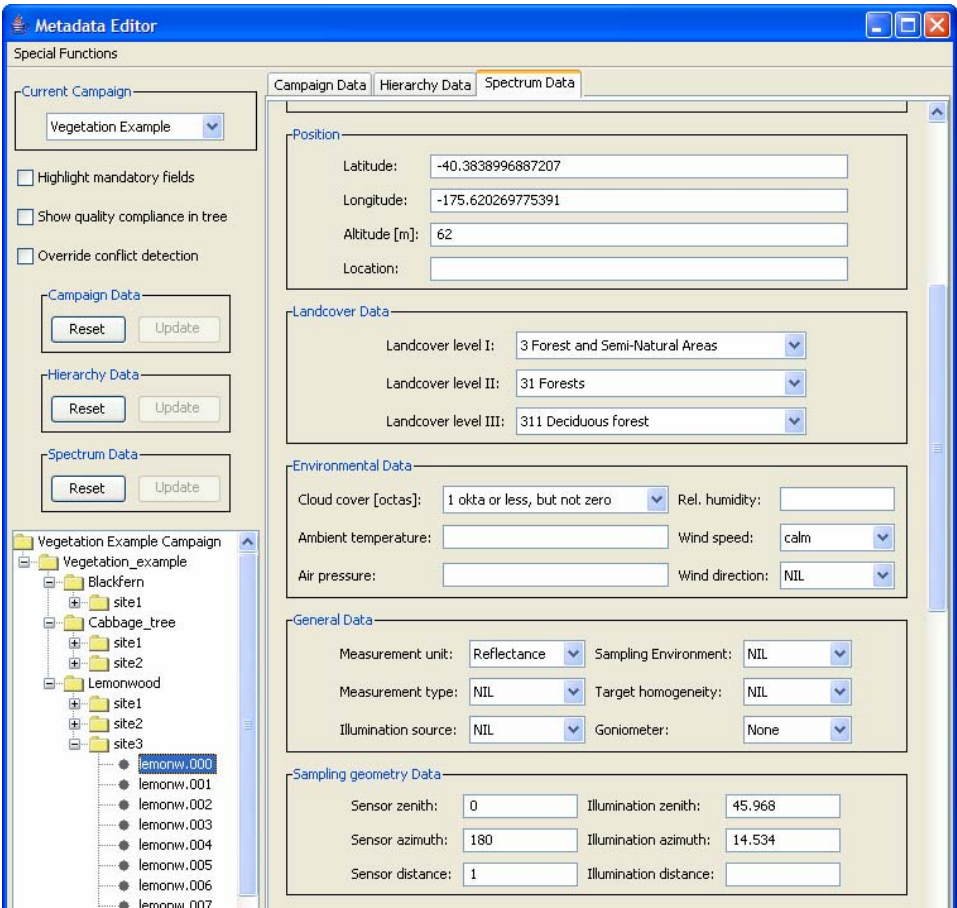


Figure 4: SPECCHIO metadata editor

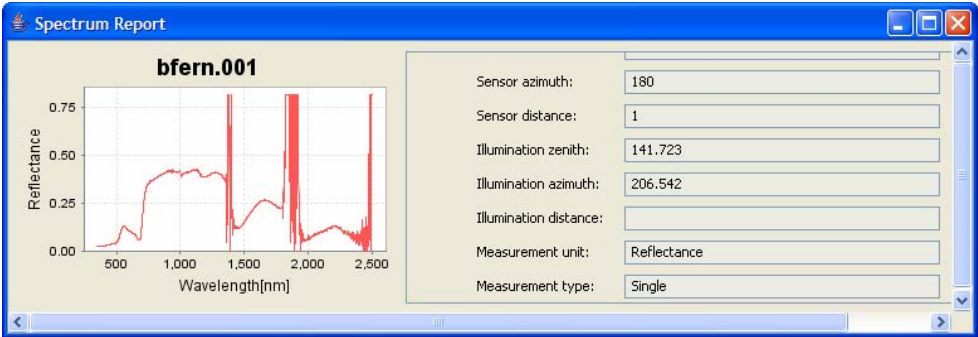


Figure 5: SPECCHIO spectrum report window

4. DISCUSSION

4.1 Spectral Databases

Relational databases are well suited to store spectral data and associated metadata. An issue to consider is the amount of data to be expected. Imaging spectroscopy produces high volumes of data where several hundred gigabytes per campaign may be acquired. SPECCHIO is used to store existing spectral library data and spectral signatures collected during field and laboratory experiments. The number of spectra in commonly available spectral libraries, e.g. USGS spectral library (Clark et al., 1993), is limited by the number of represented materials and the number of spectra per material where the latter is usually one. Field or laboratory campaigns on the other hand can yield several hundred to around thousand spectra per day per sampling instrument. The spectral information, apart from pictorial metadata, requires the most storage space. The

maximum effective table size for MySQL databases is dependent on the operating system and varies between 2GB and 16TB (MySQL AB, 2007). With an average value of 3.5 kilobyte per spectrum storage problems are not expected.

4.2 Data Model

The data model used for SPECCHIO includes metadata already suggested by other authors (Bojinski et al., 2003; Pfitzner et al., 2005). Extensions to the model are expected. Some new requirements might be defined during practical use of the system while others have already been identified such as the documentation of white references. Reference panels show degradations over time. A frequent monitoring of the spectral properties of the panels and checking against national standards is highly recommended. The history of white references should be included in spectral databases and thus should be part of the data model. This would provide (a) basic information for the



assessment of spectral data quality and (b) allow for the correction of spectra based on ratios between used panel and national standard.

### 4.3 Processing Functionality

The processing functionality is currently restricted to metadata operations like sun angle calculation and automated white reference linking.

The main interest of the user is still the spectral data and spectral processing functions are a key factor to the efficient study of hyperspectral data (Hueni & Tuohy, 2006). Possible functions include: waveband filtering (removal of noisy spectral regions), smoothing, sensor convolution, derivatives, feature space transformations (e.g. principal components transformation or MNF), spectral mixing, BRDF (Bidirectional Reflectance Distribution Function) retrieval and statistics. Conceptually different solutions would be possible: (a) adding processing functionality to the SPECCHIO software in form of new Java code, (b) calling external routines, e.g. IDL (Research Systems Inc., 2006) or (c) embedding the SPECCHIO database into a suitable processing package.

## 5. CONCLUSIONS

The second generation of the SPECCHIO system has introduced significant improvements in non-redundant data storage, automated loading of sampling campaigns, documentation of hierarchical campaign structures, extraction of metadata from spectroradiometer files, high repeatability of data entry for categorical variables due to the definition of the possible value sets in the database, efficient metadata entry by group updates and intuitive, flexible and fast data query and output.

The combination of a central database server with the implementation of the user interface and underlying processing functionality in Java allow the utilisation of the system in a heterogeneous computing environment.

Future work includes the validation and possible extension of the data model, the inclusion of spectral processing functionality or embedding of the system in other tools or processing chains and evaluation of methods for the assessment of data quality.

For further information please refer to:

[http://www.geo.unizh.ch/rs/research/SpectroLab/projects/speccchio\\_index.shtml](http://www.geo.unizh.ch/rs/research/SpectroLab/projects/speccchio_index.shtml) (SPECCHIO Website).

## REFERENCES

- Analytical Spectral Devices Inc. Technical Guide. [http://www.asdi.com/tg\\_rev4\\_web.pdf](http://www.asdi.com/tg_rev4_web.pdf) (accessed 20. Mar., 2007)
- Bojinski, S., Schaepman, M., Schlaepfer, D. & Itten, K., 2003. SPECCHIO: a spectrum database for remote sensing applications. *Computers & Geosciences*, 29, 27-38.
- Clark, R. N., Swayze, G. A., Gallagher, A. J., King, T. V. V. & Calvin, W. M., 1993. The U. S. Geological Survey, Digital Spectral Library: Version 1: 0.2 to 3.0 microns, *U.S. Geological Survey Open File Report*, Vol. 93, pp. 1340.
- ESRI. 2006. ArcGIS (V. 9.2). Redlands, CA
- European Commission DG XI. 1993. *CORINE land cover*: European Commission Directorate-General Environment, Nuclear Safety and Civil Protection, Office for Official Publications of the European Communities, Luxembourg.
- Gill, T., Gilliland-Swetland, A. & Baca, M., 1998. *Introduction to Metadata: Pathways to Digital Information*, Getty Research Institute.
- Hueni, A. & Tuohy, M., 2006. Spectroradiometer Data Structuring, Pre-Processing and Analysis - An IT Based Approach. *Journal of Spatial Science*, 51(2), 93-102.
- Landgrebe, D., 1997. On Information Extraction Principles for Hyperspectral Data. West Lafayette, Purdue University.
- McFadden, F. R. & Hoffer, J. A., 1988. *Database Management*. Redwood City, The Benjamin/Cummings Publishing Co.
- MySQL AB. 2005. MySQL, <http://www.mysql.com>
- MySQL AB. 2007. MySQL 5.0 Reference Manual. <http://dev.mysql.com/doc/refman/5.0/en/index.html> (accessed 16. Feb., 2007)
- Pfitzer, K., Bartolo, R. E., Ryan, B. & Bollhöfer, A. 2005. *Issues to consider when designing a spectral library database*. SSC 2005 Spatial Intelligence, Innovation and Praxis: The national biennial Conference of the Spatial Sciences Institute, Melbourne.
- Pfitzer, K., Bollhöfer, A. & Carr, G., 2006. A standard design for collecting vegetation reference spectra: Implementation and implications for data sharing. *Journal of Spatial Science*, 51(2), 79-92.
- Research Systems Inc., 2005. ENVI (V. 4.2). Boulder, CO.
- Research Systems Inc., 2006. IDL (V. 6.3). Boulder, CO.
- Schlaepfer, D. & Nieke, J. 2007 (in preparation), 23-25 April. *Optimizing the Workflow for APEX Level2/3 Processing*. EARSeL Workshop on Imaging Spectroscopy, Bruges, Belgium.
- Schopfer, J., Dangel, S., Kneubühler, M. & Itten, K. 2007 (in print). *Dual Field-of-View Goniometer System FIGOS*. ISPMRS, Davos, Switzerland.
- SPECCHIO Website. [http://www.geo.unizh.ch/rs/research/SpectroLab/projects/speccchio\\_index.shtml](http://www.geo.unizh.ch/rs/research/SpectroLab/projects/speccchio_index.shtml)
- Spectra Vista Co., 2005. *GER 3700 User Manual* (3.2 ed.). New York.
- Sun Microsystems Inc., 2006. Java™ 2 Platform Standard Edition (V. 5.0). Santa Clara, CA
- Wason, T. D. & Wiley, D., 2000. Structured Metadata Spaces. *Journal of Internet Cataloging*, 3(2/3), 263-277.
- Yankee Environmental Systems Inc., 2000. *MFR-7 Rotating Shadowband Radiometer* (2.10 ed.). Turner Falls, MA.

Abstract submission form for the 10<sup>th</sup> ISPMSRS (March 12-14, 2007, Davos, CH)

## **The VENμS mission: Earth Observation with High Spatial and Temporal Resolution Capabilities**

Dedieu G.<sup>1</sup>, Karnieli A.<sup>2</sup>, Hagolle O.<sup>3</sup>, Jeanjean H.<sup>3</sup>, Cabot F.<sup>3</sup>, Ferrier P.<sup>3</sup> and Yaniv Y.<sup>4</sup>

<sup>1</sup>CESBIO, Unité mixte CNES-CNRS-IRD-UPS, 18, avenue Edouard Belin,  
31401 Toulouse Cedex 9, France gerard.dedieu@cesbio.cnes.fr

<sup>2</sup>The Remote Sensing Laboratory, Jacob Blaustein Inst. for Desert Research  
Ben Gurion Univ. of the Negev, Sede Boker Campus 84990, Israel

<sup>3</sup>CNES, 18 avenue Edouard Belin, 31401 TOULOUSE Cedex 9.

<sup>4</sup>MBT Space Division, Israel Aircraft Industries Ltd., P.O.Box 105, Yehud Israel, 56000

gerard.dedieu@cesbio.cnes.fr

### Remote sensing systems

Recent initiative of the Israeli Space Agency (ISA) and the French space agency (CNES) is aimed at developing, manufacturing, and operating a new Earth observing satellite called 'Vegetation and Environment monitoring on a New Micro-Satellite' (VENμS). The satellite is planned to be launched in 2009, and the scientific mission should last at least two years.

The general mission objectives are the provision of data for scientific studies dealing with the monitoring, analysis, and modeling of land surface functioning under the influences of environmental factors as well as human activities. The VENμS scientific mission is also aimed at demonstrating the relevance of superspectral, high spatial resolution observations combined with frequent revisit capabilities in the framework of the European GMES Program.

In order to implement these goals, the mission will acquire frequent, high resolution, multi-spectral images of sites of interest all around the world. The satellite will fly in a near polar sun-synchronous orbit at 720 km height. The whole system will be able to be tilted up to 30 degree along and across track. This configuration will result in a 2-days revisit time, 27 km swath, a camera resolution of 5.3 m, and the capability to observe any site under a constant view angle. The system will cross the equator at around 10:30 AM.

The satellite will carry a super-spectral camera characterized by 12 narrow spectral bands ranging from 415 nm to 910 nm. The band setting was designed to characterize vegetation status, including through red-edge bands, and to estimate the aerosol optical depth and the water vapour content of the atmosphere for accurate atmospheric corrections. The spectral band setting could also prove useful for coastal areas and inland waters studies. The satellite will also carry a Technological Payload – the Israeli Hall Effect Thruster (IHET)- to validate its performance and for orbit keeping.

The data will be acquired over existing or planned experimental sites. All data for a given site will be acquired with the same observation angle in order to minimize directional effects. The baseline product for these selected sites is time composite images of geometrically registered surface reflectances at 10 m resolution. Strong efforts are devoted to provide high quality data, both in term of radiometry (e.g. SNR around 100), geometry (e.g. multitemporal registration better than 3 m), and atmospheric corrections.

## **A generic aerosol retrieval-atmospheric correction algorithm for MODIS**

Lyapustin, Alexei and Wang, Yujie

University of Maryland Baltimore County/NASA GSFC, code 614.4

[alyapust@pop900.gsfc.nasa.gov](mailto:alyapust@pop900.gsfc.nasa.gov)

Theme: Advanced preprocessing and processing of remotely sensed data

If given a consecutive set of images of the same region of the Earth obtained from space, an untrained human will easily solve many of the remote sensing problems, such as selecting clear-skies areas, identifying clouds, distinguishing between clear and hazy conditions, and so on. What, in contrast to our brain's work, is missing in our algorithms, armed with the modern science, that solving these problems becomes difficult and fraught with uncertainties?

One answer is that the contemporary concepts of aerosol and land surface remote sensing from whiskbroom (MODIS-like) sensors are pixel-based and disregard history of previous measurements. In this case, some important invariants of the atmosphere-surface system are overlooked. One example is a spatial structure (or texture) of the land surface at the landscape level, which generally changes at a very slow rate as compared to the frequency of spaceborne observations.

A new MODIS land algorithm was developed, which uses multi-temporal observations and an image-based rather than pixel-based processing. The new algorithm retrieves aerosol optical thickness simultaneously with surface bidirectional reflectance and albedo. It is generic and works over the dark vegetated and bright non-vegetated world regions with the current exception of snow-covered areas. The algorithm has internal water vapor retrievals and a new cloud mask algorithm. An initial validation shows an excellent agreement of retrievals with AERONET water vapor and aerosol measurements.

## ISPMSRS07, March 12-14 – Davos (Switzerland)

# Atmospheric Correction of Airborne POLDER Polarimetric Imagery Using Vectorized 6S

Christoph Borel<sup>1</sup> and Clyde Spencer

Ball Aerospace & Technologies Corp., Systems Engineering Solutions  
2875 Presidential Drive, Fairborn, OH 45324-6269  
cborel@ball.com

Conference theme:

- Advanced preprocessing and processing of remotely sensed data
- Physical modeling in remote sensing
- Radiative transfer based approaches
- Remote sensing applications

### ABSTRACT

We are interested in using wide-field-of-view polarimetric imagers such as airborne POLDER (LOA, University of Lille) and AMPI (NASA) to study polarization signatures of surface targets. The airborne POLDER instrument has a field of view  $\pm 43^\circ$  in along-track and  $\pm 51^\circ$  cross-track. It records imagery through a rotating filter wheel with spectral filters, and in two spectral bands with linear polarization filters orientated at  $0^\circ$ ,  $60^\circ$ , and  $120^\circ$  while flying at 70 m/s, generating images that need to be registered before spectra or the Stokes vectors can be computed. The atmospheric contributions, particularly in the short-wavelength visible bands, are anisotropic due to the scattering from molecules and aerosols, and the contrast is quite low, making automated image registration impossible. Thus, it is necessary to remove the polarized upwelling atmospheric contributions from the at-sensor radiances before the images can be registered, and target-leaving Stokes parameters can be derived. We accomplished the atmospheric correction by using the recently released vectorized version of the Second Simulation of the Satellite Signal in the Solar Spectrum (6Sv) from Eric Vermote *et al.* 1997. We wrote a front-end in IDL to run 6Sv over a range of viewing zenith and azimuth angles. The resulting Stokes parameters are then interpolated to a grid of input viewing coordinates for the sensor. Next, the Stokes hemispherical path radiances are converted to match the data of the airborne POLDER instrument for the linear polarization angles of  $0^\circ$ ,  $60^\circ$ , and  $120^\circ$ . The upwelling atmospheric intensities are subtracted from the respective polarimetric intensity images and the difference is divided by the transmission multiplied with the solar irradiance. This atmospheric correction significantly reduces the low-frequency variations in intensity in the images resulting from atmospheric scattering. The atmospherically corrected intensity images at  $0^\circ$ ,  $60^\circ$ , and  $120^\circ$  are then used to calculate the Stokes parameter images in the usual fashion. From the Stokes parameter images we calculate the degree and azimuth of linear polarization images for the surface.

---

<sup>1</sup> [cborel@ball.com](mailto:cborel@ball.com), phone 1 937 320-7034 ;fax 1 937 429-1687;  
<http://www.ballaerospace.com/>

Abstract submission form for the 10<sup>th</sup> ISPMSRS (March 12-14, 2007, Davos, CH)

## **CYCLOPES prototype V4 LAI, fAPAR and fCover products derived from VEGETATION and AVHRR sensors: description and validation**

F. Baret<sup>1</sup>, M. Weiss<sup>2</sup>, P. Bicheron<sup>3</sup>, R. Lacaze<sup>3</sup>, M. Leroy<sup>3</sup>

<sup>1</sup>INRA-CSE, UMR1114, Avignon, France

<sup>2</sup>Noveltis, Toulouse, France

<sup>3</sup>POSTEL, Toulouse, France

baret@avignon.inra.fr

Inversion of biogeophysical and biogeochemical variables

Validation of remote sensing products

The CYCLOPES project aims at providing high level biophysical products such as LAI, fAPAR, fCover over the globe at 1 km spatial resolution at a 10 days time interval. To provide continuity over long time series, products have to be derived from different sensors while keeping the highest degree of consistency. The products are derived from the fusion of individual products estimated from VEGETATION, AVHRR sensors. The principles used to derive the products are derived from CYCLOPES version 3.1 products. , They mainly consist in radiometric inter-calibration of sensors using, cloud screening, atmospheric correction, BRDF normalization, and biophysical algorithm (for LAI, fAPAR and fCover). All these steps are made in a consistent way between all the sensors to ease the fusion. Emphasis is put on the biophysical algorithm, based on the training of a neural network over a learning data set made of radiative transfer simulations. Improvements have been implemented, based on the definition of the training data base used to calibrate the biophysical algorithm that better account for measurement and model uncertainties as well as prior information on the surface characteristics.

Products are validated against a series of about 60 3x3 km<sup>2</sup> sites where ground measurements are up-scaled to the spatial resolution of the products. The ground measurements are coming from several networks of sites including VALERI, MODLAND, BIGFOOT, CCRS. Products are then inter-compared along years 2000-2003 with MODIS LAI/fPAR products over the BELMANIP network of sites representing a large range of surface types. Statistical distributions of values per vegetation class, scatter-plots between homologue products, as well as temporal smoothness and consistency of products are presented. Results are then discussed.



## **MERIS land surface BRDF/albedo retrieval using data fusion with MODIS BRDF and its validation using contemporaneous EO and in situ data products**

*Jan-Peter Muller<sup>1</sup>, René Preusker<sup>2</sup>, Jürgen Fischer<sup>2</sup>, Marco Zühlke<sup>3</sup>, Carsten Brockmann<sup>3</sup>, Norman Fomferra<sup>3</sup>, Peter Regner<sup>4</sup>*

<sup>1</sup> *Mullard Space Science Laboratory, Department of Space and Climate Physics, University College London, Holmbury St Mary, Dorking, Surrey, RH5 6NT, UK*

<sup>2</sup> *Freie Universität Berlin, Carl-Heinrich-Becker-Weg 6-10, 12165 Berlin, Germany*

<sup>3</sup> *Brockmann Consult, Max-Planck-Str. 2, 21502 Geesthacht, Germany*

<sup>4</sup> *ESA, Via G. Galilei, 00044 Frascati, Italy*

A representative BRDF/albedo is required by ESA<sup>1</sup> for the improved retrieval of atmospheric products, such as water vapour, from the ENVISAT-MERIS instrument. This BRDF/albedo is required at 13 of the 15 spectral channels of MERIS.

An algorithm is described which has been applied to the generation of a global BRDF/albedo for these 13 spectral bands of MERIS over 16-day time periods at a resolution of 0.05° for the whole of 2003 which is currently being applied to the time period from June 2002 to December 2006. Inputs to this algorithm include Spectral surface Directional Reflectances, SDRs (Schröder et al., Preusker et al., 2005<sup>2</sup>).

Owing to the lack of sufficient directional samples for most of the Earth's land surface, even for a monthly time period, direct inversion of BRDF parameters for MERIS are not possible worldwide. Instead the 16-day Collection 4 MODIS BRDFs at 0.05° resolution (derived using either full inversions or magnitude inversions from the MODIS values) were employed in a magnitude inversion scheme for the 4 common MERIS (490±5 [b3], 560±5 [b5], 665±5 [b7], 865±10 [b13]) bands with MODIS (459-479 {b3}, 545-565 {b4}, 620-670 {b1}, 841-8766 {b2}). The impact of applying Terra-only compared to Terra+Aqua-combined are here compared and presented.

Spectral interpolation to the remaining 9 MERIS bands and to 3 broadband regions (0.4-0.7µm, 0.7-3µm, 0.4-3µm) is then performed. As spectral albedo data is required on monthly time-steps for most applications, a simple-minded weighting function based on the fractional time-period of each 16-day time period within a month was adopted for creating monthly products from 16-day products at 10km and 0.1°.

---

<sup>1</sup> work supported under ESA/ESRIN contract 18348/04/I-LG

<sup>2</sup> ESA MERIS workshop 2005, [http://envisat.esa.int/workshops/meris\\_aatsr2005/](http://envisat.esa.int/workshops/meris_aatsr2005/)

Global products on a 16-day time-step have been generated for the whole of 2003 using both Terra-only and, where available, Terra+Aqua-combined Collection 4 MODIS-BRDFs. These EO products have been compared against contemporaneous MODIS spectral albedos (over 16-days) which have been gap-filled for 2003 (Moody et al., 2005). It is planned in the future to compare these against Collection 5 products, as and when these become available. Satellite intercomparisons have also been performed for monthly products of the monthly MERIS spectral albedo products for common bands against MISR level-3 and POLDER level-2 products and the results will be shown. Finally, inter-comparisons are shown of these EO products against ground-based albedometer measurements for a site in Finland<sup>3</sup> and for several worldwide sites available through the CAVE<sup>4</sup>.

---

<sup>3</sup> thanks to Eskelinen Miia (SYKE) and Jouni Pulliainen (FMI) for providing the data for March 2003

<sup>4</sup> <http://www-cave.larc.nasa.gov/cave/cave2.0/Reference.html>

## A Framework of a Remote Sensing Data Assimilation System

Shunlin Liang<sup>1\*</sup>, John Townshend<sup>1</sup> and Robert Dickinson<sup>2</sup>

<sup>1</sup>Department of Geography, University of Maryland, USA

<sup>2</sup>School of Earth and Atmospheric Sciences, Georgia Institute of Technology, USA

Estimating environmental variables from satellite observation is often an ill-posed inversion problem. There are currently multiple satellite sensors available for monitoring land surface environment and people have developed many different algorithms for estimating one particular variable, however, the land surface products provided by the space agencies are usually derived from observations of one satellite using only one algorithm. We are developing a prototype remote sensing data assimilation system. The general idea is to develop a forward, largely radiation transport, model calculation with parameters that are adjusted to optimally reproduce the multispectral and multiangular radiances observed by multiple satellite sensors. Such adjustments are usually made by identifying reasonably close “first guesses” for the model parameters based on the current land products and determining statistically optimum estimates of the parameters by giving appropriate weights to the first guesses versus addition of the error increments needed to get agreement with the observations. The general framework consists of four modules: a knowledge database, radiative transfer modeling, data assimilation algorithm, and sensor characterization. The general methodologies and some preliminary results will be presented.

\*Dr. Shunlin liang

Department of Geography

University of Maryland

College Park, MD 20742, USA

1-301-405-4556 (phone)

1-301-314-9299 (fax)

[sliang@umd.edu](mailto:sliang@umd.edu)

oral presentation

Abstract submission form for the 10<sup>th</sup> ISPMSRS (March 12-14, 2007, Davos, CH)

## **Preparing for the assimilation of remote sensing products by large-scale models with updated land surface process schemes**

Bernard Pinty<sup>(1)</sup>, Thomas Lavergne<sup>(1)</sup>, Michael Vossbeck<sup>(2)</sup>, Thomas Kaminski<sup>(2)</sup>, Ophelie Aussedat<sup>(1)</sup>, Ralf Giering<sup>(2)</sup>, Nadine Gobron<sup>(1)</sup>, Malcolm Taberner<sup>(1)</sup>, Michel M. Verstraete<sup>(1)</sup>, Jean-Luc Widlowski<sup>(1)</sup>

<sup>(1)</sup> Global Environment Monitoring Unit, IES, EC Joint Research Centre,  
TP 440, via E. Fermi, I-21020 Ispra (VA), Italy

<sup>(2)</sup> FastOpt, Schanzenstrasse 36, D-20357 Hamburg, Germany

Bernard.pinty@jrc.it

### **Data assimilation and integration of remote sensing with dynamic process models**

We present a computer efficient inversion software procedure enabling us to retrieve optimally, from operational Terra broadband surface albedo products, a series of key vegetation characteristics such as the Leaf Area Index (LAI), the leaf optical properties and the brightness of the soil underneath the canopy. The approach uses an advanced two-stream radiation transfer model dedicated to climate and carbon flux model applications. This inversion procedure itself implements the adjoint code, generated using automatic differentiation techniques, of a cost function. This cost function balances two main contributions reflecting 1) the a priori knowledge on the model parameter values and, 2) the remotely sensed flux and associated uncertainties together with the requirement to minimize the mismatch between these measurements and the two-stream model simulations. The individual weights of these contributions are specified notably via covariance matrices of the uncertainties in the a priori knowledge on the model parameters and the observations. This package also reports on the probability density functions of the retrieved model parameter values that thus permit the user to evaluate the a posteriori uncertainties on these retrievals.

We will discuss results from applications conducted using MODIS and MISR operational surface albedo products over selected EOS validation sites spanning a range of vegetation type conditions and where ground-based estimates are available. These applications are performed over full phenological vegetation cycles and include snow contaminated conditions. Our results are compared to those available from operational MODIS and MISR algorithms (LAI and Fraction of Absorbed Photosynthetically Active Radiation, among others) and are shown to exhibit much more accurate and consistent temporal patterns.

Abstract submission form for the 10<sup>th</sup> ISPMSRS (March 12-14, 2007, Davos, CH)

## **Approximating photon recollision probability in vegetation canopies**

Möttus, Matti<sup>1</sup>; Rautiainen, Miina<sup>1,2</sup>; Stenberg, Pauline<sup>2</sup>

1 Tartu Observatory, Estonia

2 University of Helsinki, Finland

mottus@ut.ee

Physical modeling in remote sensing

To be applicable to a wide variety of biomes, algorithms for predicting remotely sensed signatures of forests have to rely on physically-based principles. These physically-based models are able to calculate the angular distribution of reflected intensity for any reasonable set of illumination conditions. Recently, parameterizations for physically-based models have been developed to relate canopy absorption and scattering, based on photon recollision probability. Photon recollision probability is the probability that a photon, once scattered, will interact with the canopy again. As a first approximation, it can be considered wavelength-independent and thus connects canopy reflectance at different wavelengths in the visible and near-infrared spectral regions. It is also assumed to remain constant in successive interactions. We present formulas to estimate the first order photon recollision probability as an approximation to the effective recollision probability averaged over all scattering orders.

Using the analytical solution of the two stream equation in vegetation canopies, contributions of different scattering orders were compared. Using these contributions, the influence of the photon recollision probabilities of various scattering orders on the mean recollision probability was studied. The analytical expressions for the recollision probabilities of different scattering orders were derived for a canopy with horizontal leaves. Using a physically-based approach, first-order recollision probability was extended to other leaf inclination angle distributions. This approach was used to estimate the first-order recollision probability in a leaf canopy consisting of discrete crown envelopes. All approximations were compared with Monte Carlo simulations.



## **Circumpolar assessment of the relationship between infrared vegetation indices and leaf area index in forest landscapes**

Fernandes, Richard<sup>1</sup>; Rochdi, N. <sup>1</sup>; Beal, D. <sup>1</sup>; Shahid, K. <sup>1</sup>; Leblanc, S. <sup>1</sup>; Weiss, M. <sup>2</sup>  
Baret, F. <sup>2</sup>; Vierling, L. <sup>3</sup>; Chen, X. <sup>4</sup>; Conley, A. <sup>5</sup>; Deering, D. <sup>5</sup>; Nilson, T.<sup>6</sup>; Stenberg, P. <sup>7</sup>,

<sup>1</sup>Natural Resources Canada, Earth Sciences Sector, Canada Centre for Remote Sensing,  
Programme on Enhancing Resilience to Climate Change

<sup>2</sup>Institute National Recherche Agronomie, France

<sup>3</sup>Institute of Atmospheric Sciences, South Dakota School of  
Mines & Technology

<sup>4</sup>United States Geological Survey

<sup>5</sup>NASA Goddard Spaceflight Centre

<sup>6</sup>Tartu Observatory, Tartu, Estonia

<sup>7</sup>The Finnish Forest Research Institute, Helsinki, Finland

Contact: [Richard.Fernandes@nrcan.gc.ca](mailto:Richard.Fernandes@nrcan.gc.ca)

Leaf area index (LAI) is a key parameter governing atmosphere-vegetation interactions. The Global Climate Observing System (GCOS) has identified LAI as an essential climate variable to be mapped globally at 250m resolution at accuracies on the order of +/-0.5 unit. GCOS also identifies satellite remote sensing as the only current technology that can provide required coverage. However, the GCOS implementation document suggests that passive optical sensors have problems with LAI retrieval due to a) noise in understory variability and b) with saturation in the signal from passive optical sensors at LAI levels commonly found in forest biomes. These conclusions have been based predominantly on empirical and model based studies that attempt to relate LAI to spectral measurements in visible and near infrared wavelengths. Visible wavelengths are also problematic for operational LAI retrieval due to inherent uncertainties in atmospheric correction over low reflectance (e.g. dense forest) targets.

Satellite measurements in infrared wavelengths have reduced sensitivity to the atmosphere and should exhibit lower saturation than the visible due to higher leaf albedo. Little work has been performed to assess the usefulness of infrared vegetation indices for LAI retrieval over northern forests. We first make use of recently developed and validated radiative transfer models (5-Scale and MAC) to explore the theoretical sensitivity of infrared vegetation indices to LAI over discontinuous forest canopies. We then assemble a circumpolar dataset of in-situ LAI measurements from ten different regions in boreal and temperate forest biomes with Canada, Estonia, Finland, Russia, Sweden and the US to examine the relationship between LAI and spectral vegetation indices derived from coincident sensors on Landsat and SPOT platforms. Both modelling and empirical measurements suggest that infrared vegetation indices do not saturate in most northern forest landscapes at 100m resolution. Furthermore, infrared indices tend to reduce sensitivity of LAI algorithms to species or understory variability. Based on these findings we recommend a) the specification of 250m shortwave and near infrared bands on future polar orbiting sensors b) the use of shortwave infrared spectral information in future LAI retrieval algorithms over northern forest landscapes.

Abstract submission form for the 10<sup>th</sup> ISPMSRS (March 12-14, 2007, Davos, CH)

## **Assimilation of MODIS snow data in a detailed model of Alpine snow dynamics and snow hydrology**

Henning Löwe, Tobias Jonas, Michael Lehning  
[loewe@slf.ch](mailto:loewe@slf.ch), [jonas@slf.ch](mailto:jonas@slf.ch), [lehning@slf.ch](mailto:lehning@slf.ch)

WSL Swiss Federal Institute for Snow and Avalanche Research SLF,  
Fluelastrasse 11, CH-7260, Davos Dorf

Conference Theme: Data assimilation and integration of remote sensing with dynamic process models

Snow as a water resource in mountains becomes more and more important as dryer and hotter conditions prevail in many continental areas worldwide. Even maritime or temperate zones such as western and central Europe experience extended hot and dry periods in the summer (e.g. Summer 2003). Therefore, the understanding of the mountains providing fresh water to the low lands needs to be augmented. In this context, the processes dominating the snow cover dynamics and hydrology in mountains are particularly important. In our contribution, we introduce data assimilation to Alpine3D, a very detailed model of Alpine surface processes. Alpine3D consists of modules of snow transport, detailed surface energy balance including terrain effects, vegetation, snow, soil and runoff. The model focuses on snow dynamics and has a very detailed and accurate description of snow – atmosphere interactions and snow mass- and energy fluxes. The presentation discusses the possibilities and limitations of data assimilation in such a detailed model. We focus on the assimilation of MODIS derived snow cover maps with a simple, nudging-like assimilation method. The considerable influence of the assimilation on timing, magnitude and dynamics of runoff is shown.

**Title:**

Inference of impurity radiative forcing in snow from multispectral to hyperspectral imagers

**Authors:**

Thomas H. Painter  
National Snow and Ice Data Center  
[tpainter@nsidc.org](mailto:tpainter@nsidc.org)

Maureen P. Cassidy  
National Snow and Ice Data Center  
[cassidym@nsidc.org](mailto:cassidym@nsidc.org)

**Conference Theme:**

Remote sensing applications to hydrology, carbon cycle, biochemical and –physical cycles, plant ecology, ecosystems, snow, soil moisture, agriculture, natural ecosystems, etc.

**Abstract:**

The inference of the radiative forcing of soot and dust in snow has taken on importance in recent years because of the realization of the climate effects that they have (Hansen and Nazarenko, 2004). To date, there is no operational remote sensing product that allows us to determine the presence of impurities in snow. The change in snow hemispherical-conical reflectance factor due to change in impurity concentration can be small in absolute reflectance but the relative change in absorption is large. However, clean snow with nonspherical grains can appear to have non-zero impurity concentration under the assumption of spherical grains. In this work, we present an analysis of the sensitivity of snow HCRF to snow impurities, snow morphology, and snow texture. We also present a model for impurity concentration from imaging spectrometer and multispectral imager data.

We investigate the sensitivity of snow HCRF with a radiative transfer model that accounts for single scattering of nonspherical particles and external and internal inclusions of dust and soot. From these analyses, we can then understand the uncertainties inherent in remote sensing of snow impurity radiative effects. Springtime desert dust storms regularly deposit radiatively absorbing dust on the snow cover of the San Juan Mountains of southwestern Colorado, USA. With data collected with an Analytical Spectral Devices FieldSpec Spectroradiometer (350-2500 nm with 3-10 nm spectral resolution), the NASA/JPL Airborne Visible/Infrared Imaging Spectrometer (AVIRIS, 400-2500 nanometers with 10 nm spectral resolution and 2 m spatial resolution), and the Moderate Resolution Imaging Spectroradiometer (MODIS – multispectral optical), we investigate the spatial distribution of dust radiative forcing in the mountain snow cover near two energy balance monitoring sites in the alpine and sub alpine of Red Mountain Pass in the San Juan Mountains. The Scaled Integral Dust Index model uses radiative transfer calculations of clean snow directional reflectance for snow of grain size inferred on a pixel by pixel basis from the AVIRIS data themselves. The scaled integral between the AVIRIS spectrum and the radiative transfer spectrum gives the direct measure of the surface shortwave forcing of dust in snow. The model is then applied to MODIS surface reflectance data through incorporation of digital elevation data.

Abstract submission form for the 10<sup>th</sup> ISPMSRS (March 12-14, 2007, Davos, CH)

## **Modeling of small footprint airborne laser scanning returns using ray-tracing and L-systems**

Morsdorf, F.<sup>a</sup>, Frey, O.<sup>a</sup>, Koetz, B.<sup>a</sup>, Meier, E.<sup>a</sup>

<sup>a</sup> Remote Sensing Laboratories (RSL), Dept. of Geography, University of Zurich, Winterthurerstrasse 190, CH-8057 Zurich, Switzerland, Email: morsdorf@geo.unizh.ch

### **Physical modeling in remote sensing**

Airborne Laser Scanning (ALS) has been established as a valuable tool for the estimation of biophysical canopy variables, such as tree height and vegetation density. However, up to now most approaches are built upon empirical stand based methods for linking ALS data with the relevant canopy properties estimated by field work. These empirical methods mostly comprise regression models, where effects of site conditions and sensor configurations are contained in the models. Thus, these models are only valid for a specific study, which renders intercomparison of different approaches difficult. Physically based approaches exist e.g. for the estimation of tree height and tree location, however systematic underestimation depending upon sampling and vegetation type remains an issue. Using a radiative transfer model that builds on the foundation of the Open-Source ray tracer *povray* we are simulating return signals for various ALS system settings (e.g. scan angle, beam divergence) and different canopy types, where the reflectivity and density of canopy elements will be varied. The tree crowns are represented by fractal models (L-systems), which explicitly resolve the position and orientation of single leafs. Of special interest is the distribution and alignment of canopy elements inside the tree crowns and how they affect the ALS return signal and subsequent ALS data products such as tree height and vegetation density estimations (e.g. LAI). A sensitivity study is carried out in order to determine the effect of properties such as beam divergence, canopy reflectance and scan angle on the derived biophysical vegetation products. These forward simulations are a first step in the direction of physically based derivation of biophysical ALS data products and could improve the accuracy of the derived parameters by establishing correction terms.

## 10<sup>th</sup> Intl. Symposium on Physical Measurements and Signatures in Remote Sensing

ISPMSRS07 – March 12-14, 2007 – Davos, Switzerland

### **Normalization of microwave time series observations (1979 – 2005) : application to surface melting analysis over Antarctica and surface temperature over Canada/Alaska.**

Alain Royer (1)\*, Ghislain Picard (2), Michel Fily (2)

(1) Centre d'applications et de recherches en télédétection, Université de Sherbrooke, Sherbrooke Québec, Canada

(2) Laboratoire de glaciologie et géophysique de l'environnement, UMR 5183 CNRS-UJF, Grenoble, France

\* Corresponding author: [Alain.Royer@Usherbrooke.ca](mailto:Alain.Royer@Usherbrooke.ca); Tel.: (1 819) 821 7180; Fax.: (1 819) 821 7944

Polar regions are anticipated to evolve significantly in response to the expected increase in temperature over the next decades. To bypass the lack of meteorological stations in boreal and austral high latitudes, remote sensing observations are the only alternative for characterizing past trends and monitoring the actual evolution. This project deals with the development of two new databases of climatic indicators (melting duration over Antarctica and summer surface temperature over Canada/Alaska) derived from satellite microwave measurements as this type of data presents the strong advantage of being slightly influenced by the atmosphere. Starting with SMMR data, observations are available since 1979 (EASE-Grid NSIDC database). However, the 1979–2005 period includes observations from 4 different sensors (SMMR and SSM/I on board DMSP F8, F11 and F13) whose characteristics vary (mainly calibration and time of acquisition). As a consequence, sensor replacement induces significant artifacts in the derived surface geophysical parameters which, in turn, bias the climatic analysis of the series. We present here two different methods to normalize temperature to overcome calibration variations and changes in data acquisition time (variable overpass time, differences between satellites and satellite drift), as well as to interpolate missing data.

Over Canada, the normalization method uses a diurnal cycle model derived from ERA40 re-analysis (ECMWF 2.5°) dataset which is fitted to the two satellite measurements available per day. The derived parameter is thus a consistent hourly series of temperatures during the summer (without snow). This approach shows that SMM/I F8 data are biased by -2.03°C over the whole Canada/Alaska area, when compared to the ERA40 – SSM/I F11 and F13 differences.

Over Antarctica, we use observations from a constellation of similar sensors observing the surface at various hours of the day since 2002 (SSM/I-F13, -F14, and -F15 and AMSR-E). We combine all these data, first to model the diurnal variations of surface melting and second to correct the time series of melting duration and extent. Results show that the unbiased time series gives a cooling trend over the 1979-199 period with a decreasing rate weaker than previously published uncorrected time series.

Both normalization approaches are discussed and analyzed.



## Title

Space-Time Series of MODIS Snow Cover Products for Hydrologic Scienc

## Authors

Jeff Dozier and James E. Frew

University of California, Santa Barbara

[dozier@bren.ucsb.edu](mailto:dozier@bren.ucsb.edu), [frew@bren.ucsb.edu](mailto:frew@bren.ucsb.edu)

Thomas H. Painter

National Snow and Ice Data Center, University of Colorado

[tpainter@nsidc.org](mailto:tpainter@nsidc.org)

## Conference themes

- Remote sensing applications to hydrology (snow)
- Remote sensing data infrastructures
- Physical modeling in remote sensing
- Advanced methods for time series analysis in remote sensing
- Data assimilation and integration of remote sensing with dynamic process models

## Abstract

The Moderate-Resolution Imaging Spectroradiometer flies on two NASA/EOS satellites, , each imaging most of the Earth every day, Terra in the morning, Aqua in the afternoon. MODIS has 36 spectral bands covering wavelengths from 0.4 to 14.4 $\mu$ m, 2 at 250m spatial resolution, 5 at 500m, and 29 at 1km. Using reflectance values from the 7 “land” bands with 250 or 500m resolution, along with a NASA-identified cloud flag that does not always distinguish cloud from snow, we estimate the fraction of each 500m pixel that snow covers along with the albedo (reflectance) of that snow. The model *MODIS Snow Covered Area, Grain Size, and Albedo (MODSCAG)* is a multiple endmember spectral mixture model coupled with a radiative transfer model of snow directional reflectance. Its products are then used in hydrologic models in several mountainous basins.

The daily products have glitches. Sometimes the sensor cannot view the surface because of cloud cover, and even in the absence of clouds, an off-nadir view in a vegetated area “sees” less ground area than a nadir view. Therefore, we must use the daily time series in an intelligent way to improve the estimate of the measured snow properties for a particular day. We consider two scenarios: one is the “forecast” mode, whereby we use the past, but not the future, to estimate the snow-covered area and albedo on

that day; the other is the “retrospective” mode, whereby in the summer after the snow is gone we reconstruct the history of the snow properties for that water year.

This space-time interpolation presents both scientific and data management challenges. The scientific question is: how do we use our knowledge of viewing geometry, snow accumulation and ablation, along with available ground data, to devise a scheme that is better than generic multidimensional interpolation? The data management involves large three-dimensional objects, identification of erroneous data, and keeping track of the lineage of the way a set of pixel values has been interpreted.

# **A NEW MULTI-TEMPORAL CLASSIFICATION APPROACH FOR LAND COVER MAPPING IN NORTH OF IRAN, BY USING HYPER-SPECTRAL MODIS DATA**

**Abdolreza Ansari Amoli**

**Iranian Space Agency**

**[abdolreza.ansari@gmail.com](mailto:abdolreza.ansari@gmail.com)**

**Abbass Alimohammadi**

**K.N.T. University of Technology**

**[alimoh\\_abb@kntu.ac.ir](mailto:alimoh_abb@kntu.ac.ir)**

- Appropriate Theme: Image classification methods

Satellite data acquired in short time intervals like Terra, NOAA, ... are very suitable in order to map vegetations in the scale of regional. In addition, because of being free of charge, these data are mostly recommended by users in developing and third world countries.

In this research, usefulness of Hyperspectral moderate resolution imaging spectroradiometer (MODIS, 250 m resolution) data installed on Terra satellite for mapping and evaluation of land cover classes in North of Iran has been examined. In this regard, a new classification method has been introduced based upon maximum value composition technique by using multi-temporal and cloud-free data sets of NDVI.

Finally, we established an approach based on the analysis of pattern and shape of the NDVI changes as a function of time, and finally we could separate different land-cover types in Gilan province. The accuracy of classification was changed between %78-%95 for different classes. The maximum accuracy (%95) belongs to rice cultivated farms. This research shows we can reach a high accuracy in image classification even by using medium resolution satellite data specially in conditions of dense vegetations in our region.

**ISPMSRS07, March 12-14 – Davos (Switzerland)****Reflectance Retrieval in Shade using Adjoint Radiosity**

Christoph C. Borel, PhD

Ball Aerospace & Technologies Corp.

2875 Presidential Drive, Suite 180

Fairborn, OH 45324

937-320-7034 Fax: (937) 429-1687

[cborel@ball.com](mailto:cborel@ball.com)

**Conference theme:**

- Advanced preprocessing and processing of remotely sensed data
- Physical modeling in remote sensing
- Radiative transfer based approaches
- Remote sensing applications

**Abstract**

Current reflectance retrieval algorithms assume the target is illuminated only by sun and skylight, and neglect the effect of adjacent 3-D surfaces such as trees and buildings and the impact of non-ideal illumination conditions such as partial cloud cover. We propose to develop new approaches to retrieve the reflectance of objects hidden in shadows for urban environments and under vegetative canopies. The measured sensor radiance of an object facet can be expressed as the convolution of the bi-directional reflectance distribution function of an inclined surface with the hemispherical irradiance field, plus added atmospheric scattering. Using the measured radiance spectrum, it may be possible to retrieve a more realistic reflectance spectrum by estimating the irradiance field and the orientation of the facet. New developments in computer graphics research, adjoint radiosity method, which allows the iterative retrieval of the irradiance field using an image and knowledge of the 3-D structure. We propose to adapt this method for remote sensing purposes.

# **Retrieval of aerosol optical thickness using multi-date and constant viewing angle images from Formosat-2 and VEN $\mu$ S.**

O.Hagolle<sup>1,2</sup>, G.Dedieu<sup>2</sup>, V. Debaecker<sup>2</sup>

*1 CNES, 18 avenue Edouard Belin, 31401 TOULOUSE Cedex 9.  
Olivier.Hagolle@cnes.fr*

*2 CESBIO, Unité mixte CNES-CNRS-IRD-UPS, 18 avenue Edouard Belin, 31401  
Toulouse Cedex 9, France*

**Themes :** Advanced preprocessing and processing of remotely sensed data , Radiative transfer based approaches.

Usually, reflectance time series in the visible and near-infrared domain, such as those provided by SPOT satellites or by wide field of view instruments (VGT, MERIS, MODIS), are degraded by two main geophysical sources of noise : 1) atmospheric effects, mainly because of aerosol scattering, difficult to correct because aerosol optical properties are highly variable and difficult to characterise, and 2) directional effects, since the observed surface reflectances depend on solar and observation angles.

Since 2004, the Formosat-2 satellite, (and in the near future, the VEN $\mu$ S mission, see Dedieu et al, this conference) can provide very frequent high resolution images acquired with constant observation angles in the visible and near infrared. With these features, directional effects are considerably reduced, since only the solar angles vary slowly with time. Furthermore, the quasi absence of surface directional effects allow to improve atmospheric corrections by determining the aerosol properties. For this, we use the following properties:

- aerosol optical properties vary quickly with time but slowly with location.
- reflectances vary quickly with location but slowly with time, when there are no directional effects.

In a few days period, if a variation of the top of atmosphere (TOA) reflectance occurs, it is very likely to be due to variations of aerosol optical properties : it is thus possible to retrieve these properties from TOA reflectance variations. Such a method has been tested using Formosat-2 time series over 3 sites : images are being acquired every third day for two sites in France, every fourth day for a site in Morocco, with constant observation angles. AERONET sun photometers as well as in-situ surface reflectance measurements are available on both sites.

The method is providing quite good results for the optical thickness (standard deviations are below 0.1) and the surface reflectance time series obtained after atmospheric corrections are very smooth.



## **Anomaly detection algorithms for hyperspectral imagery**

**SOOFBAF Seyyed Reza**<sup>1</sup>, **FAHIMNEJAD Hamed**<sup>2</sup>, **VALADAN ZOEJ Mohamad Javad**<sup>3</sup>, **MOJARADI Barat**<sup>4</sup>

Geodesy and Geomatic Faculty, K.N.Toosi University of Technology,  
Vali\_Asr Street, Mirdamad Cross, Tehran, Iran  
Tel: +98 21 8878 6212 , 8877 0218 Fax: +98 21 8878 6213

<sup>1</sup> sr.soofbaf@gmail.com , <sup>2</sup> hamed\_fahimnejad@yahoo.com , <sup>3</sup> valadanzouj@kntu.ac.ir ,  
<sup>4</sup> Mojaradi@yahoo.com

Conference theme: Advanced preprocessing and processing of remotely sensed data

**Keywords :** Hyperspectral , Target detection , Anomaly detection

### **Abstract :**

Nowadays the use of hyperspectral imagery specifically automatic target detection algorithms for these images is a relatively exciting area of research.

An important challenge of hyperspectral target detection is to detect small targets without any prior knowledge, particularly when the interested targets are insignificant with low probabilities of occurrence. The specific characteristic of anomaly detection is that it does not require atmospheric correction and signature libraries. Recently, several useful applications of anomaly detection approaches have been developed in remote sensing.

With this in mind, in this paper some anomaly detectors such as RX-based anomaly detectors (MRX,NRX,CRX,RX-UTD), Combined Fisher Test (CFT) model, as well as adaptive anomaly detectors such Nested Spatial Window-Based approach(NSW), dual window-based eigen separation transform (DWEST) and Gauss Markov Random field model (GMRF) are compared. Finally the most efficient method is proposed for implementation in a planned software system.

Abstract submission form for the 10<sup>th</sup> ISPMSRS (March 12-14, 2007, Davos, CH)

## **Determining the directional response and field of view of two field spectroradiometers**

Mac Arthur, Alasdair,<sup>1</sup> MacLellan, Christopher<sup>1</sup> and Malthus, Timothy.<sup>2</sup>

<sup>1</sup> NERC Field Spectroscopy Facility, School of Geosciences, University of Edinburgh, Grant Institute, Kings Buildings, West Mains Road, Edinburgh EH9 3JW. fsf@nerc.ac.uk;

<sup>2</sup> School of Geosciences, University of Edinburgh, Grant Institute, Kings Buildings, West Mains Road, Edinburgh EH9 3JW.

*Conference theme:* Advanced preprocessing and processing of remotely sensed data

### **Abstract**

Accurately determining the field of view (FOV) has rarely been considered in detail in field spectroscopy where spectroradiometer manufacturers' specifications generally lack clarity or detail. For users, the area of the scene within a FOV is largely an exercise in guess work. This issue can be further compounded with full range systems (0.4 to 2.5 $\mu$ m) which include multiple spectrometers each with their own field of view. In these complex systems the size and alignment of the viewing optics may cause significant spectral non-uniformity across the theoretical measurement area. When recording reflectance spectra from heterogeneous areas such as dwarf shrub (heather) canopies or agricultural crops it is important to have the scene from which the reflectance is being recorded clearly defined. If the actual FOV and its uniformity are unknown, the size of the scene and hence the support cannot be accurately calculated. In order to assess the FOV of field spectroradiometers we choose to adapt the guidelines set out in the CIE Technical Report for assessing the directional response function of photometers. A detailed set of measurements were taken of the Analytical Spectral Devices' Field Spec Pro FR and Spectra Vista Corporation's GER 3700 spectroradiometers. The resulting *directional response functions* were plotted, highlighting a number of areas of concerns.

The FOVs measured were found not to be circular for either system. The GER3700 had a wavelength dependent left/right bias in the 400nm to 1000nm range and an elongated or rectangular FOV for both the infrared spectrometers. The ASD's FOV showed spatial separation by it's individual spectrometers causing highly irregular and sparse coverage of the scene. In addition the measured FOV did not closely match the manufacturer's specified angular FOV.

The use of diagnostic absorption and reflectance features and spectral indices to determine biophysical and biochemical variables of heterogeneous vegetation canopies is dependent on reflectance being recorded from a representative sample of the scene of interest. With a heterogeneous surface, if the responsivity is uneven across the measurement field, if coverage is incomplete and if the shape and area of the measurement field are different from that assumed, then the components considered to be within the scene may not be represented in the *gross reflectance* recorded. The contribution of individual scene components to gross reflectance may be excluded or over emphasised leading to erroneous characterisation of the surface and inaccurate quantification on biophysical and biochemical variables derived from indices. Field campaigns on such targets should include within their methodologies procedures to verify the performance and repeatability of the optical equipment used.

## The effect of noise in AHS thermal bands in the retrieval of pixel temperature

Eduardo de Miguel. Remote Sensing Laboratory - INTA. demiguel@inta.es

Rafael García. Universidad Politécnica de Madrid. Departamento de Ingeniería Cartográfica, Geodesia y Fotogrametría EG. rafael.garcia@upm.es

Alix Fernández-Renau. Remote Sensing Laboratory - INTA. fdezra@inta.es

Conference topic: Advanced preprocessing and processing of remotely sensed data

The AHS is an 80-bands airborne imaging radiometer, operated by INTA in different remote sensing projects. It has 63 bands in the reflective part of the electromagnetic spectrum, 7 bands in the 3 to 5 microns range and 10 bands in the 8 to 13 microns region. The noise in these thermal channels is in a first approach estimated by the standard deviation of values recorded on two thermally controlled blackbodies, a typical value being 0.25 degrees. However, a deeper knowledge of the noise is required for specific projects which require increased radiometric resolution.

In the framework of a project to detect hydric stress in olive trees, we have attempted to measure crown temperature with the maximum resolution and accuracy. Therefore, we have made a complete characterization of the noise, computing different figures to look for spectral, spatial or temporal correlation or systematic patterns that could help in the image restoration. The result of this effort is presented in this work. The main outcome of the study is that spectral averaging using a priori emissivity values could reduce the noise in some extent while preserving spatial and radiometric resolution. In addition, it is discussed if image restoration should account not only for noise but for radiometric artifacts like the subtle ringing caused by the instrument electronics, and also the role of spatial sampling issues.

Abstract submission form for the 10<sup>th</sup> ISPMSRS (March 12-14, 2007, Davos, CH)

## **Hyperspectral image filtering and implications for environmental spectra related to mining contamination: example from the S.Domingos Mine, SE Portugal**

Quental, Lúdia<sup>1</sup>, Sousa, António<sup>2</sup> and Marsh, Stuart<sup>3</sup>

<sup>1</sup> Instituto Nacional de Engenharia, Tecnologia e Inovação

<sup>2</sup> Instituto Superior Técnico

<sup>3</sup> British Geological Survey

[lúdia.quental@ineti.pt](mailto:lúdia.quental@ineti.pt)

Advanced preprocessing and processing of remotely sensed data

The removal of atmospheric components, a key factor that controls all subsequent image processing, is usually dealt through statistical or physical models. However, noise components may not be completely removed from the hyperspectral images, depending on the model(s) used and of the conditions of dataset capture. Part of this noise can be identified through its spatial structure and thus be filtered using geostatistical methods. The objective of this work is the comparison of the spectral response of calibration and noise removal from an airborne hyperspectral image, focusing in significant signatures related to environmental patterns of a contaminated former mining area.

The methodology compares the atmospheric correction using a radiative transfer model and the use of geostatistical tools in radiance dataset. Factorial kriging is the geostatistical method used. The latter is developed following the steps: *i*) A multivariate statistical analysis using a compression algorithm Minimum Noise Fraction (MNF); *ii*) Factorial kriging in the most relevant MNF bands to detect multiple scales of spatial variability and filter the noise, *iii*) An inverse MNF transform of the noise-whitened factors. The resultant synthetic image is cleared off from noise detected spatially in distinct structures. Both synthetic images are then compared focusing on relevant environmental signatures related to Acid Mine Drainage (AMD).

The case study is the former S.Domingos Mine, located in SE Portugal in the Iberian Pyrite Belt. The long term exploitation included pre-roman, roman, and modern time works, with intensive AMD that endures until today. The hyperspectral image was captured in 2000 with HyMap<sup>TM</sup> sensor while field spectra were gathered simultaneously with an ASD spectroradiometer both in radiance and reflectance. The field spectra were collected in waste mining materials. The hyperspectral image was atmospherically corrected using FLAASH as a plug-in to the ENVI software, as well as the multivariate analysis (MNF) and all spectral analysis. Factorial kriging was performed in ANGEODAD.

Each of the resultant synthetic images is analysed with equivalent field spectra, recognised in previous works as the most significant to assess degrees of AMD. The reflectance field spectra is compared with the atmospherically calibrated image using FLAASH software and the radiance field spectra is compared with the noise filtered image using geostatistical methods. The context in which each of the methods is used yields specific results for mining environments also is discussed.

## Preprocessing EO-1 Hyperion hyperspectral data

H. FAHIMNEJAD<sup>1</sup>, S.R. SOOFBAF<sup>2</sup>, A. ALIMOHAMMADI<sup>3</sup>, M. J. VALADAN ZOEJ<sup>4</sup>,

Geodesy and Geomatic Faculty, K.N.Toosi University of Technology, Tehran, Iran

Tel: +989121985407, +982188786212, +982188770218 Fax: +982188786213

<sup>1</sup>hamed\_fahimnejad@yahoo.com, <sup>2</sup>sr.soofbaf@gmail.com,

<sup>3</sup>Alimoh\_abb@yahoo.com, <sup>4</sup>valadanzouj@kntu.ac.ir

### Abstract:

Hyperion hyperspectral imager onboard the Eo-1 platform have 242 spectral bands between 400 and 2500 nm. This image has several errors that we must correct them before use that for analysis. In this paper we examine preprocessing and noise reduction methods that can be applied post-level 1B1 to provide consistent time series of Hyperion data. The noise management strategy includes recognition of "bad" pixels, reducing the effects of vertical striping and compensation for atmospheric effects in data. Preprocessing which includes fixing bad and outlier pixels, local destriping, atmospheric correction, minimum noise fraction smoothing and effort polishing provide improved results.



Abstract submission form for the 10<sup>th</sup> ISPMSRS (March 12-14, 2007, Davos, CH)

## **Operational assimilation of snow depth maps for improved real time runoff nowcasting with spatially distributed hydrological models**

Zappa Massimiliano,  
Swiss Federal Research Institute WSL, Zürcherstrasse 111, CH-8903 Birmensdorf, Switzerland  
massimiliano.zappa@wsl.ch

Morger, Annina  
Swiss Federal Research Institute WSL, Zürcherstrasse 111, CH-8903 Birmensdorf, Switzerland

Jonas, Tobias  
WSL Swiss Federal Institute for Snow and Avalanche Research SLF, Fluelastrasse 11, CH-7260, Davos Dorf

Stoffel, Andreas  
WSL Swiss Federal Institute for Snow and Avalanche Research SLF, Fluelastrasse 11, CH-7260, Davos Dorf, Switzerland

Foppa Nando  
University of Bern, Department of Geography, Hallerstrasse 12, CH-3012 Bern, Switzerland

### **Remote sensing applications to hydrology**

Representative real time information on snow depth and snow water equivalent is needed for several practical purposes, above all avalanche warning and flood forecast and control in spring. This study deals with snow depth and cover maps for updating the snow water equivalent simulated by an operational spatially distributed hydrological model.

An evaluation of operational simulations of snow water equivalent and snow cover distribution for the winter season 2005/2006 will be presented for two Swiss basins. The simulations will be computed by adopting the real-time version of the PREVAH model (Precipitation Runoff EVApotranspiration HRU Model). PREVAH is currently implemented for flood forecast in the Linth basin (central Switzerland).

Model simulations are compared to three sources of snow cover information: a) the operational Swiss wide snow depth map (1x1 km<sup>2</sup> resolution) based on a combination of snow depth ground observations from a dense measurement network and operational NOAA-AVHRR snow cover map. b) a NOAA-AVHRR sub-pixel snow-cover product (1x1 km<sup>2</sup> resolution) with estimation snow cover fraction at sub-pixel scale. c) an interpolated map of snow depth, estimated using information from stations close to the target area.

Evaluations are performed by mean of categorical statistics. Results show, that the hydrological model is well able to provide reliable information on snow cover distribution. The accuracy with respect to the operational snow depth maps is always higher than 90%. The accuracy between the AVHRR snow cover maps and the model simulations is above 90% in the phase of snow accumulation until end of March and sinks below 80% during the ablation period.

We adopted simple assimilation routines, which allow updating the snow cover distribution within the adopted hydrological model. The spatial variability of snow depth and snow cover is obtained from the available maps derived from ground observations and AVHRR. The spatial variability of the simulated snow water equivalent is adjusted to matching the observed variability. The impact of the snow water equivalent update for local estimation of runoff generation and snow ablation will be demonstrated.

The estimation of the final snow ablation days could be improved for almost all stations providing the snow depth measurements. First results indicate that changes in runoff generation for the two basins are rather small. On the other hand the runoff generation from the sub-basins show a stronger reaction to the redistribution of snow within the model domain. Any improvement in the simulation of a catchment internal response represents a step towards better estimations of snowmelt in ungauged basins.

Abstract submission form for the 10<sup>th</sup> ISPMSRS (March 12-14, 2007, Davos, CH)

## **Intercomparison between modelled and satellite-derived snow cover extent within the alpine and subalpine zone of the Swiss Alps**

Foppa, Nando

<sup>a</sup>University of Bern, Department of Geography, Hallerstrasse 12, CH-3012 Bern, Switzerland;  
foppa@giub.unibe.ch (first author)

Zappa, Massimiliano

Swiss Federal Research Institute WSL, Mountain Hydrology and Torrents, Zürcherstrasse 111, CH-8903  
Birmensdorf, Switzerland; massimiliano.zappa@wsl.ch

Stähli, Manfred

Swiss Federal Research Institute WSL, Mountain Hydrology and Torrents, Zürcherstrasse 111, CH-8903  
Birmensdorf, Switzerland; manfred.staehli@wsl.ch

Lehning, Michael

WSL Swiss Federal Institute for Snow and Avalanche Research, Fluelastrasse 11, CH-7260, Davos Dorf,  
Switzerland; lehning@slf.ch

Gustafsson, David

KTH, Department of Land and Water Resources Engineering, SE-100 44, Stockholm, Sweden;  
davidg@kth.se

### **Validation of remote sensing products**

Snow cover represents an important variable with a wide impact on the environmental and socio-economic system within alpine regions such as the Swiss Alps. Snow cover has a relevance within the alpine environment at different spatial scale and is therefore a small to large-scale phenomenon.

This presentation reports on comparisons made between the spatial distribution of snow cover derived from a distributed numerical snowpack heat and mass balance model (ALPINE3D) and an operational snow cover product derived from NOAA AVHRR data. These two methods were applied at the landscape scale represented by the region of Davos in southeastern Switzerland. In area of approximately 630 km<sup>2</sup> we selected data from several days with different snow conditions during the snowmelt season in 2003 and 2004.

The comparative analysis between the model and snow cover product based on earth observation data was performed using a visual pixel-by-pixel comparison and skill score measures based on 2x2 contingency-tables. The comparison includes two different scaling approaches: aggregating the high-resolution model output to the coarser satellite data and disaggregating the AVHRR pixels to the model grid cells. The snow extent simulated by ALPINE3D was reasonably consistent with AVHRR-derived snow cover maps. However, ALPINE3D exhibited a slight underestimation of the snow-covered area compared to the satellite observations. The average agreement between simulated snow-covered grid cells and satellite snow cover determination was 88%. A decrease of the relative spatial accuracy (from 90% to 75%) between model and satellite was observed for the snow-covered area with an advance of the snowmelt period. For forested areas, accuracy decreases below 70% when satellite data estimates less snow than the model. Scaling the data to different spatial resolutions does not have a significant effect on the overall comparison between model and satellite data.

However, discrepancies between the two methods may be attributed to inherent errors associated with either method. For instance, ALPINE3D derived snow cover maps may overestimate snow cover on south exposed slopes and overestimate snow cover on north orientated slopes due to insufficiently modelled topographic effects. Additionally, the AVHRR product shows an underestimation of the snow cover for pixels where forest is present within the subalpine zone.

The results from this intercomparison study represent the initial stage of studies planned in the future to investigate the potential value of assimilating satellite-based snow cover data into ALPINE3D.

## 10<sup>th</sup> Intl. Symposium on Physical Measurements and Signatures in Remote Sensing

ISPMSRS07 – March 12-14, 2007 – Davos, Switzerland

### Modeling microwave brightness temperature in Antarctica.

Ghislain Picard (1) , Ludovic Brucker (1), Michel Fily (1)

(1) Laboratoire de glaciologie et géophysique de l'environnement, CNRS-Université Joseph Fourier, Grenoble, France

\* Corresponding author: Ghislain.Picard@lgge.obs.ujf-grenoble.fr; Tel.: +33 476 82 42 42; Fax.: +33 476 82 42 01

Themes:

Physical modeling in remote sensing

or

Data assimilation and integration of remote sensing with dynamic process models

#### Abstract

The Antarctic climate and its temporal variations are not well known because of the sparsity of meteorological stations. Observations by remote sensing are the only way to bypass this issue and to provide detailed information on the spatial and temporal variability of the Antarctic climate. Our research deals with estimating climatic variables from microwave radiometer observations (SMMR, SSM/I and AMSR-E) as this type of sensors presents strong advantages including: quasi-independence to atmospheric conditions and illumination, availability for nearly 3 decades and strong sensitivity to the variables of interest in climatology, e.g. snow temperature.

Estimating snow surface temperature and/or temperature profile from microwave brightness temperature requires knowing snow emissivity and microwave penetration length within the snow with a high accuracy. Empirical approaches consisting in combining brightness temperatures at various frequencies and polarizations have been inefficient to provide the required accuracy. To tackle this problem, we adopt a complex approach based on physical forward modeling followed by inversion (or data assimilation). This paper presents the forward modeling and the predicted spectral signature (emissivity and penetration length) over Antarctica.

The forward model takes near-surface meteorological data from ERA reanalysis as input and brightness temperatures at 19Ghz and 37Ghz (SSM/I frequencies) and V polarization as output. To achieve this prediction, the model is in fact a thermodynamic snow model that predicts temperature profile within the snow associated with an electromagnetic model that predicts microwave brightness temperatures from temperature profile. Both sub-models are intermediate-complexity so they require parameter calibration prior to prediction. The calibration is performed by a Monte-Carlo method called the Neighborhood Approximation. It provides the optimal parameter set (+pdf) including the emissivities and penetration lengths at selected frequencies for each

100kmx100km pixel in Antarctica. The calibrated model performs well, typical RMSE is 1.5K, except in zone where surface melting occurs.

Maps of emissivities and penetration lengths are interpreted both qualitatively and using a radiative transfer model (DMRT). Results show different facies in Antarctica: melting zones; zones with weak emissivity sensitivity to the frequency, thus revealing fine grains (~0.5mm); zones with strong sensitivity to frequency revealing coarse grains (>0.7mm) and zones with anomalous spectra, i.e. emissivity increasing with frequency.

# Crop model data assimilation with the Ensemble Kalman filter for improving regional crop yield forecasts

A.J.W. de Wit and C.A. van Diepen

A.J.W. de Wit (corresponding author)

Centre for geo-information, Wageningen UR

P.O. Box 47, 6700 AA, Wageningen

The Netherlands

Tel: +31-317-474761

Fax: +31-317-419000

Email: allard.dewit@wur.nl

C.A. van Diepen

Centre for geo-information, Wageningen UR

P.O. Box 47, 6700 AA, Wageningen

The Netherlands

Tel: +31-317-474230

Fax: +31-317-419000

Email: kees.vandiepen@wur.nl



## Abstract

Uncertainty in spatial and temporal distribution of rainfall in regional crop yield simulations comprises a major fraction of the error on crop model simulation results. In this paper we used an Ensemble Kalman filter (EnKF) to assimilate coarse resolution satellite microwave sensor derived soil moisture estimates (SWI) for correcting errors in the water balance of the WOFOST crop model. Crop model simulations with the EnKF for winter-wheat and grain maize were carried out for Spain, France, Italy and Germany for the period 1992-2000. The results were evaluated on the basis of regression with known crop yield statistics at national and regional level. Moreover, the EnKF filter innovations were analysed to see if any systematic trends could be found that could indicate deficiencies in the WOFOST water balance.

Our results demonstrate that the assimilation of SWI has clearly improved the relationship with crop yield statistics for winter-wheat for the majority of regions (66%) where a relationship could be established. For grain maize the improvement is less evident because improved relationships could only be found for 56% of the regions. We suspect that partial crop irrigation could explain the relatively poor results for grain maize, because irrigation is not included in the model.

Analyses of the filter innovations revealed that normalised innovations are not Gaussian and show spatial and temporal patterns correlations, indicating that the EnKF performs suboptimal. Possible solutions to this problem could be that the initialisation period of the crop water balance should be increased, and that the crop parameter values in the current system should be changed in order to make the crop simulation less drought tolerant.

**Conference theme:** Data assimilation and integration of remote sensing in dynamic process models

**Keywords:** crop simulation models, crop yield, regional scale, data assimilation, soil moisture, Ensemble Kalman filter



Abstract submission form for the 10<sup>th</sup> ISPMRS (March 12-14, 2007, Davos, CH)

## **Seasonal comparison of carbon flux estimates from C-TESSEL model and Moderate Resolution Imaging Spectroradiometer (MODIS) over several biomes**

Jia, Li<sup>1</sup>,  
Voogt, M.H.<sup>2</sup>,  
Jacobs, C.M.J.<sup>1</sup>,  
Van den Hurk, B.J.J.M.<sup>2</sup>,  
De Wit, A<sup>1</sup>,  
Moors, E.<sup>1</sup>

1. Alterra, Wageningen University and Research Centre, The Netherlands

2. Royal Netherlands Meteorological Institute, The Netherlands

Li.Jia@wur.nl

### **Conference theme:**

*Remote sensing applications to hydrology, carbon cycle, biochemical and physical cycles, plant ecology, ecosystems, snow, soil moisture, agriculture, natural ecosystems, etc.*

**Or:**

*Data assimilation and integration of remote sensing with dynamic process models*

Text of the abstract (max. 400 words)

Carbon dioxide exchange between vegetation and the atmosphere is determined by absorption of solar radiation by plant leaves and by turbulent transfer in the surface layer. This led to two different streams of methods to estimate carbon flux density: A) models based on parameterizations of aerodynamic resistance, and B) modeling of radiative transfer processes in vegetation canopies. We present here a comparison of one approach of type A (the C-TESSEL model) and one approach of type B (the MODIS gross primary production, i.e. GPP data product). The C-TESSEL model is the extension of the ECMWF land surface scheme TESSEL (Van den Hurk et al., 2000), in which a photosynthesis-based canopy resistance (Jacobs, 1994; Jacobs et al., 1996) and a carbon allocation scheme (Calvet et al., 1998) that represents leaf growth in response to photosynthesis is included. The MODIS GPP is estimated based on the radiation use efficiency logic proposed by Monteith (1972; 1977), which links net primary productivity (NPP) to the absorbed photosynthetically active radiation (APAR). The latter can be obtained by inverting spectro-radiometric data using a radiative transfer model.

To provide an independent reference, the comparison was done for 12 experimental sites equipped with tower-based continuous measurements of CO<sub>2</sub> flux density. Comparison of CO<sub>2</sub> flux densities is complex because of different physical basis of parameterizations used in each case and of the tower based measurements. The latter provide observations of instantaneous CO<sub>2</sub> flux (net ecosystem exchange, i.e. NEE) and a combination of parameterization of ecosystem respiration and integration over time provides estimates of daily GPP (daytime

integral) and NPP (daily integral). The C-TESSEL model provides estimates of CO<sub>2</sub> flux exchange at leaf level and estimations based on parameterizations of GPP and NEE in a half-hour interval over a model grid much larger than the tower footprint. The MODIS data product, at a spatial resolution of 1km, is based on a singular observation of spectral reflectance of vegetation canopies during daytime, from which both daily GPP and NPP are estimated. We have compared the carbon fluxes from the three methods (C-TESSEL, MODIS and tower CO<sub>2</sub> flux) in terms of GPP over several biomes (e.g. grass, crops, coniferous, deciduous and tropical forests). The focuses were paid on the differences of parameterizations of CO<sub>2</sub> flux estimates in the two products. The comparison of the three sets of GPP estimates at 12 sites gave conflicting: the MODIS data product is in good agreement with tower observations most of time, but C-TESSEL performs better in some instance. These results provide insights into the validity of parameterizations, rather than on the accuracy and reliability of a specific data product.



Abstract submission form for the 10th ISPMRS (March 12-14, 2007, Davos, CH)

## Combination of Raman Lidar and Microwave Radiometer Sensed Water Vapour Data

Marc Schneebeli<sup>1</sup>, Ulla Wandinger<sup>2</sup>, Ina Matthis<sup>2</sup>, Emmanuel Brocard<sup>1</sup>, Christian Mätzler<sup>1</sup>

<sup>1</sup>Institute of Applied Physics, University of Bern, Bern, Switzerland

<sup>2</sup>Leibniz Institute for Tropospheric Research, Leipzig, Germany

marc.schneebeli@mw.iap.unibe.ch

Remote sensing systems; Data fusion approaches based on multiplatform or multiple sensor techniques

The international LAUNCH (International Lindenberg campaign for assessment of humidity and cloud profiling systems and its impact on high-resolution modelling) campaign took place in late summer/early fall 2005. One goal of the campaign was the improvement of remote sensing techniques and algorithms for the advancement of meteorological observations. Apart from the main measurement site in Lindenberg, several outposts in and outside of Germany were part of the observational network.

At the Leibniz Institute for Tropospheric Research in Leipzig, our group assembled the multi-channel radiometer system ASMUWARA (All Sky Multi Wavelength Radiometer) (1). This instrument is equipped with nine microwave channels from 17 to 151 GHz, two infrared radiometers measuring in the atmospheric window and a sky camera.

During the campaign, co-located measurements were conducted together with the Temperature-Moisture-Aerosol Raman Lidar (2).

The lidar is able to precisely measure the water vapour mass mixing ratio profile, provided that no clouds are present. In addition, the lidar's height range is reduced during the day because of sunlight contamination in the Raman signal.

The microwave radiometer can measure water vapour density profiles and temperature profiles in almost all weather conditions and during the whole day without reduced data quality, but with the constraint that these water vapor profiles have a coarse height resolution.

We can now combine the two data sets in order to fully benefit from the advantages of the two instruments. We will show the performance of an already existing algorithm based on a Kalman filtering technique (3). This algorithm includes the Integrated Water Vapour (IWV) as the only contribution from the microwave radiometer. As a novelty, we will present a new algorithm based on an optimal estimation technique. This new algorithm includes all channels from the radiometer in order to get more accurate results. We will present results obtained with this data fusion technique and show comparisons with in-situ measurements from a nearby radiosonde station.

(1) Martin, L., Schneebeli, M. and Mätzler, C., 2006. ASMUWARA, a Ground-based Radiometer System for Tropospheric Monitoring. *Meteorologische Zeitschrift*, vol.: 15, no.: 1

(2) Mattis, I., Ansmann, A., Althausen, D., Jänisch, V., Wandinger, U., Müller, D., Arshinov, Y. F., Bobrovnikov, S. M. and Serikov, I. B., 2002. Relative Humidity Profiling in the Troposphere with a Raman Lidar. *Appl. Optics*, 41, 64516462.

(3) Han, Y., Westwater, E. R., Ferrare, R. A., 1997. Applications of Kalman Filtering to Derive Water Vapor Profiles from Raman Lidar and Microwave Radiometers. *Journal of Atmospheric and Oceanic Technology*, vol.: 14, no.: 3

# Abilities of DEMETER Satellite in Observation of Physical Signatures Perturbation of Ionosphere Associated with Seismic Activities

Aida Omani\*, Mohammad R. Saradjian

Center of Excellence in Geomatics Engineering and Disaster Management,  
Department of Surveying and Geomatics Engineering, Engineering Faculty,  
University of Tehran, Tehran, Iran

*Department of Surveying and Geomatics Engineering, Engineering Faculty,  
University of Tehran, North Kargar St., Tehran, Iran*

*Tel: +98-21-8008841*

*Fax: +98-21-8008837*

*{aomani, sarajian}@ut.ac.ir*

## Preferred themes for the presentation:

Physical modeling in remote sensing

Earth System model approaches using remote sensing

## Abstract

Earthquake is one of the most horror natural hazards that cause a lot of damage. So, humans always have been looking for approaches to predict it so that they can reduce its damage. For this purpose, a wide range of researches have been done in a number of fields. Although some researches have been claimed to reach hopeful results in prediction of a few earthquakes, no general and proved methods have offered for it, yet.

On the other hand, applications of remote sensing techniques are being developed because of its advantages (e.g. wide cover, short period of updating, high resolution data and on-time processing methods). In this direction, recently many researches have been trying to use abilities of this technique for earthquake prediction. Earthquake clouds, measurement of temperature anomalies, ground surface displacements and ionospheric perturbations can be enumerated.

Among the above-mentioned earthquake precursors, ionospheric perturbations are so promising. DEMETER (Detection of Electro-Magnetic Emissions Transmitted from Earthquake Regions) satellite was launched on 29 June 2004, in a polar and circular orbit with an altitude 710 km, with the aim of collecting a number of ionospheric parameters to study the relations between their perturbations with seismic

---

\* Corresponding Author

activities. The scientific payload of DEMETER is composed of several instruments which provide a nearly continuous survey plasma, waves and energetic particles:

- *IMSS*, a search-coil magnetometer, measures three field magnetic components in a wide frequency range.
- *ICE*, the electrical field instrument, measures the three components of the electric fields.
- *ISL*, the Langmuir probe instrument is designed to measure the electron density of plasma, electron temperature and the potential of the satellite.
- *IAP*, the thermal ion spectrometer, measures the ion density, compositions, temperature and flow velocity.
- *IDP*, a high energy particle detector, measures high energy electrons and protons.

Data are collected by this satellite in two “Survey” and “Burst” modes to record universe low bit rate and high bit rate data above seismic regions, respectively. The main advantage is covering nearly all the globe’s active seismic regions very quickly.

In this paper, DEMETER satellite and its mission are introduced and abilities in observation of physical signatures of ionosphere associated to seismic activities are considered for some recent Iran’s earthquakes. Results of this research can answer the question that if DEMETER data can be use for any kind of earthquake in all over the world?

Abstract submission form for the 10<sup>th</sup> ISPMSRS (March 12-14, 2007, Davos, CH)

## **Application to MISR land BRFs of the RPV model inversion package to assess environmental patterns**

Thomas Lavergne<sup>(1)</sup>, Thomas Kaminski<sup>(2)</sup>, Bernard Pinty<sup>(1)</sup>, Malcolm Taberner<sup>(1)</sup>, Nadine Gobron<sup>(1)</sup>, Michel Verstraete<sup>(1)</sup>, Michael Vossbeck<sup>(2)</sup>, Jean-Luc Widlowski<sup>(1)</sup>, Ralf Giering<sup>(2)</sup> and Ophélie Aussedat<sup>(1)</sup>

(1) Global Environment Monitoring Unit, IES, EC Joint Research Centre,  
TP 440, via E. Fermi, I-21020 Ispra (VA), Italy.

(2) FastOpt, Schanzenstrasse 36, D-20357 Hamburg, Germany.

Thomas.lavergne@jrc.it

Environmental change detection

The capability of the non-linear Rahman-Pinty-Verstraete (RPV) model to 1) accurately fit a large variety of Bidirectional Reflectance Factor (BRF) fields and 2) return parameter values of interest for land surface applications motivate the development of a computer efficient inversion package. The present paper describes such a package based on the 3 and 4 parameter versions of the RPV model. This software environment implements the adjoint code, generated using automatic differentiation techniques, of the cost function. This cost function itself balances two main contributions reflecting 1) the a priori knowledge on the model parameter values and, 2) BRF uncertainties together with the requirement to minimize the mismatch between the measurements and the RPV simulations. The individual weights of these contributions are specified notably via covariance matrices of the uncertainties in the a priori knowledge on the model parameters and the observations. This package also reports on the probability density functions of the retrieved model parameter values that thus permit the user to evaluate the a posteriori uncertainties on these retrievals. This is achieved by evaluating the Hessian of the cost function at its minimum. Results from a variety of tests are shown in order to document and analyze software performance against complex synthetic BRF fields simulated by radiation transfer models as well as against actual MISR-derived surface BRF products. These RPV parameters are then used to detect a number of surface features and there associated changes.

*Conference theme considered appropriate: "Environmental change detection"*

## **Validation of remote sensing NDVI time series with ground based measurements from the automated climate station network IMIS**

Fabio Fontana<sup>a\*</sup>, Christian Rixen<sup>b</sup>, Tobias Jonas<sup>c</sup> & Stefan Wunderle<sup>a</sup>

<sup>a</sup> Remote Sensing Research Group, Institute of Geography, University of Bern

<sup>b</sup> Swiss Federal Institute for Forest Snow and Landscape Research WSL, Research Unit Ecosystem Boundaries, Team Alpine Ecosystems

<sup>c</sup> Swiss Federal Institute for Forest Snow and Landscape Research WSL, Research Unit Mountain Hydrology and Torrents, Team Snow Hydrology

**Background and data:** Alpine environments are particularly sensitive to climate change such as changes in snow cover. An important instrumentation to detect and monitor snow cover extent and duration as well as vegetation development is satellite-based remote sensing. The unique Advanced Very High Resolution Radiometer (AVHRR) archive of over 25 years provides the opportunity to derive long term data on snow cover and vegetation with high temporal (max. 1 day) and spatial resolution (max. 1x1km<sup>2</sup>). Ground based measurements on snow and vegetation development in the alpine zone of Switzerland can exclusively be provided by the automated climate station network IMIS (Interkantonalessystem).

**Methods:** The aim of this study was to analyze snow cover and vegetation development comparing ground based with remote sensing measurements. At 17 alpine grassland sites, IMIS sensor data was analyzed with respect to Start of Season after snowmelt (SOS), vegetation development, and productivity for the period 1998 to 2005. The same locations and years were investigated using an AVHRR Normalized Difference Vegetation Index (NDVI) time series. Maximum Value Composite (MVC), running mean, and harmonic analysis algorithms were used and tested to derive SOS and maximum NDVI (NDVI<sub>max</sub>) at the grassland sites.

**Results:** The ground based measuring stations showed strong correlations of snow cover characteristics such as snowmelt and plant development, i.e. vegetation phenology and productivity. SOS derived from ground based and from remote sensing data were significantly correlated, however, deviated from each other by +/- 2 weeks.

**Conclusions:** The combination of remote sensing and ground based measurement bears the potential to accurately assess snow and vegetation development in the Alps with high spatial and temporal resolution. Further time series analyses will provide the unique opportunity to estimate vegetation change over the last 25 years.

---

\* corresponding author; email: fontana@giub.unibe.ch

email Rixen: rixen@slf.ch

Jonas: jonas@slf.ch

Wunderle: swun@giub.unibe.ch



## ISPMSRS 2007

10<sup>th</sup> Symposium on Physical Measurements and Signatures in Remote Sensing-  
ISPMSRS07 - March 12-14, 2007 - Davos (Switzerland)

# **A completely automatic spectral rule-based preliminary classification of calibrated Landsat 5 TM and Landsat 7 ETM+ images scalable to ASTER, AVHRR, MODIS, SPOT-4, SPOT-5, and SPOT VEGETATION imagery**

A. Baraldi\*, D. Simonetti\*, V. Puzzolo\*, and S. Natali<sup>#</sup>

\* European Commission Joint Research Centre, Via E. Fermi 1, I-21020 Ispra (Va), Italy,  
Phone: +39 0332 786538, Fax: +39 0332 785154, E-mail: [andrea.baraldi@jrc.it](mailto:andrea.baraldi@jrc.it)

<sup>#</sup> Meteorological and Environmental Earth Observation (MEE0) S.n.c., Strada Luisa, 8 – 44020 S.Giovanni di Ostellato, Ferrara, Italy, E-mail: [info@meeo.it](mailto:info@meeo.it)

### Image classification methods

#### *Abstract*

In recent years the launch of (very) high-resolution (VHR) spaceborne multi-spectral (MS) scanners has made purely supervised remote sensing (RS) image analysis over extended target areas no longer feasible as reference data are difficult, tedious, or expensive to gather.

To overcome limitations of a purely supervised classification approach to RS image classification problems, a two-stage hybrid learning classification scheme can be recommended. In this context, a novel spectral prior knowledge-based preliminary classifier (suitable as a hybrid learning first-stage classifier) is presented hereafter.

The main operational and architectural properties of the proposed rule-based classifier are summarized below.

- o It is input with Landsat 5 TM and Landsat 7 ETM+ images calibrated into planetary reflectance (albedo) and at-satellite temperature.
- o It is fully unsupervised, i.e, it requires:
  - no free parameter to be user-defined and
  - no reference (supervised) data set of examples.
- o It is pixel-based. As a consequence, it is computationally efficient, requiring approximately 15 minutes per Landsat scene (from data calibration to output map generation).
- o It is robust to changes in the input data set, i.e., it is capable of dealing with the inherent fuzziness (variability) of class-specific spectral signatures. As a consequence, unlike traditional (e.g., maximum likelihood) pixel-based classifiers, it

- is not affected by salt-and-pepper classification noise effects.
- o It consists of a dictionary of spectral signatures implemented as a set of fuzzy rules based on prior spectral knowledge. The spectral resolution of these fuzzy rules is assumed to be that of Landsat 5 TM and Landsat 7 ETM+ imagery. As a consequence, these fuzzy rules are scalable to other sensors' spectral properties (e.g., ASTER, AVHRR, MODIS, SPOT-4 and -5, SPOT VEGETATION, etc.)
  - o The fuzzy rule-based pixel classification consists of two processing levels.
    - The first stage matches each pixel-based input data vector with a dictionary of reference spectral signatures modeled as a logical (and, or) combination of inter-band relative relationships (e.g., band 1 greater than band 2) provided with tolerance intervals.
    - The second stage matches each pixel-based input data vector with a dictionary of reference spectral signatures modeled as a logical (and, or) combination of fuzzy sets (e.g., band 1 is high). These fuzzy sets provide a so-called irregular but complete grid-partition of the input feature space.
  - o In its current version, the implemented system detects up to 72 output spectral categories (types, or strata) suitable for the preliminary mapping (baseline map, primal sketch, in the Marr sense) of RS imagery. In particular,
    - Several spectral categories belong to class *Vegetation*.
    - Several spectral categories belong to class *Rangeland*.
    - Several spectral categories belong to class *Bare soil* and *Built-up areas*.
    - Several spectral categories belong to class *Water*.
    - Several spectral categories belong to class *Clouds*.
    - Several spectral categories belong to classes *Snow* and *Ice*.
    - Spectral category *Pit bogs*.
    - Spectral category *Greenhouses*.
    - Spectral category *Unknowns*.
  - o The symbolic meaning of kernel spectral categories (e.g., StrongVegetation) is intermediate between those (low) of clusters and segments and those (high) of land cover classes (e.g., forest). This means that the application domain of kernel spectral strata is by no means alternative to RS data clustering, image segmentation, and land cover classification. Rather, prior knowledge-based kernel spectral categories are naturally suitable for driving stratified application-specific classification, clustering, or segmentation of RS imagery which could involve training and supervision.

The accuracy, robustness, and computational efficiency of the proposed rule-based system, plus its consistency with the CORINE 2000 Land Cover classification scheme (CLC00), are assessed in several operational RS image classification problems.

## SHADOWED FEATURE CLASSIFICATION IN HYPERSPECTRAL IMAGES

**Author:** S.Mohammad.Shahrokhy

**Affiliation :**Remote sensing Dept., Iranian Space Agency

**E-Mail:** S\_M\_Shahrokhy@yahoo.co.uk

**Address:** Iran, Tehran, P.O Box 14395/443

**Theme:** Image classification Methods

In most remotely sensed images, because of earth surface topography and sun zenith and azimuth angles, some of features place in shadow and consequently will not be classified and related to the appropriate class. Traditional unsupervised classification methods such as K-means and ISO-class, which mainly consider spectral proximity of pixels, are not able to integrate the shadowed features with the same illuminated ones in a unique class. Also traditional supervised methods (for example MLC) which generally use statistical properties of class trains such as min, max and mean, have not the potential to integrate same features with different illumination. Some of hyperspectral specific classification methods have the advantage of integration of pixels based on spectral signature similarity instead of absolute value proximity. In this research, all of the above mentioned classification methods are investigated using sample Hyperion hyperspectral image containing relieves and sloped areas that are of different illumination conditions. The results showed that traditional classification approaches are not appropriate for this aim.

A comparison between different specific classification methods has been performed, in addition to a correlation check to find the bands that are more appropriate to detect the affiliation of shadowed and illuminated features. Finally a modified classification method was suggested to best integrate such features and simultaneously prevent heterogeneous features to be classified together.

## Topsoil Mapping Using Hyperspectral Sensing

*Thomas Selige, Urs Schmidhalter, TU München, Lehrstuhl für Pflanzenernährung, Am Hochanger 2, 85354 Freising, Germany, Tel.: +49(0)8161/71-4528, [selige@wzw.tum.de](mailto:selige@wzw.tum.de)*

*Jürgen Böhner, Universität Hamburg, Geographisches Institut, Bundesstraße 55, 20146 Hamburg, Germany, Tel.: +49(0)40/42838-4960, [jboehnel@gwdg.de](mailto:jboehnel@gwdg.de)*

### Abstract

The spatial variability of within field topsoil parameter was studied using airborne hyperspectral imagery of the airborne HyMap scanner. The aim of the study was to develop a method of mapping fine-scale topsoil organic and texture parameters from a combination of field and hyperspectral image data.

The study area is located in East Germany. It is characterized by pronounced soil diversity. It covers three soils, a tertiary plain and the alluvial plain of the river Elbe, both separated by late Pleistocene moraines. The highly diverse soil properties within the fields of the landscapes results in fine-scale pattern of soil texture and organic matter and challenge the future application of modern site specific management practices.

The work investigated the use of both multiple linear regression (MLR) and partial least-square regression (PLSR) to construct the model necessary to estimate the soil physical/chemical variables from the image data. Field data were combined with the image data for the construction of independent models derived using both MLR and PLSR.

Two important topsoil variables for e.g. environmental research or precision farming applications, soil organic matter and soil texture, were found to be correlated with spectral properties of the airborne HyMap scanner. The percentage sand, clay, organic carbon and total nitrogen content could be predicted quantitatively and simultaneously by a multivariate calibration approach using either partial least-square regression (PLSR) or multiple linear regression (MLR). The different topsoil parameters are determined simultaneously from the spectral signature contained in the single hyperspectral image, since the various variables were represented by varying combinations of wavebands across the spectra. The methodology proposed provides a means of simultaneously estimating topsoil organic matter and texture in a rapid and non-destructive manner, whilst avoiding the spatial accuracy problems associated with spatial interpolation. The use of high spatial resolution and hyperspectral remotely sensed data in the manner proposed in this paper can also be used to monitor and better understand the influence of management and land use practices on soil organic matter composition and content. Effect of organic fertilization and crop rotations on organic matter composition could be detected from a geospatial analysis of the achieved soil parameter maps.

### Appropriate Conference themes:

- Inversion of biogeophysical and biogeochemical variables
- Remote sensing applications to hydrology, carbon cycle, biochemical and –physical cycles, plant ecology, ecosystems, snow, soil moisture, agriculture, natural ecosystems, etc.

Abstract submission form for the 10<sup>th</sup> ISPMSRS (March 12-14, 2007, Davos, CH)

## **PAR@METER: a wireless system for fAPAR and LAI continuous monitoring**

F. Baret<sup>1</sup>, G. Billard<sup>2</sup>, O. Marloie<sup>1</sup>, A. Labouret<sup>3</sup>

<sup>1</sup> INRA-CSE, UMR1114, Avignon, France

<sup>2</sup> ARIA, Neung sur Beuvron, France

<sup>3</sup> SOLEMS, Palaiseau, France

baret@avignon.inra.fr

Integration of in situ ('SensorWeb') and remotely sensed data  
Validation of remote sensing products

Ground measurements of photosynthetically active radiation (PAR) balance and leaf area index (LAI) are required for validating, and sometimes calibrating biophysical products derived from satellite observations. Non destructive methods are either based on instantaneous observations of the directional gap fraction from which the fraction of PAR absorbed by the canopy (fAPAR) is approximated by the PAR interception efficiency (fIPAR). LAI can also be derived from gap fraction measurements, leading to estimates of the effective LAI, or to an approximation of the actual LAI under a number of assumptions on leaf clumping and presence of woody elements. Current devices dedicated to gap fraction (and LAI) measurements are generally 'instantaneous': hemispherical photos or light transmittance (LAI2000, TRAC, ACUPAR...) systems operate within one 'shot'. Such systems allow easy replications over several places to account for spatial variability and get better representation of the average value of areas corresponding to a single or few high spatial resolution (5-50m) satellite pixels. However, they are very tedious to operate when describing the seasonality of fAPAR and LAI, which is mandatory for a number of studies. Alternatively, classical PAR balance could be installed at the site level by distributing individual PAR sensors on the ground, which are connected to a data logger. However, this system is relatively tedious to install because of the wires, has limited autonomy (both memory and energy wise) and is relatively costly, limiting thus a large spatial coverage.

The PAR@METER system was developed with the objective to get continuous PAR transmittance measurements with autonomous light sensors communicating with the data logger via a wireless-USB connection. The autonomy of the system is about 6 months, both energy and memory wise. The range of the system is in between 50 to 300 m depending on vegetation density and up to 1000m without obstacles. Individual sensors and data logger are cheap enough to allow larger spatial coverage. The system measures instantaneous PAR transmission every 5 minutes. PAR diffuse fraction is computed from incident PAR measurements. Effective LAI is derived from PAR transmission under several irradiance conditions.

This paper describes the system and its use with more details. Emphasis is put on calibration issues, derivation of the diffuse fraction, uncertainties in fAPAR measurements and LAI estimates. Few experiments are finally presented to illustrate the interest of the PAR@METER system and its connection to remote sensing observations.



## A Study of Surface Directional Reflectance Shapes Using MISR

John V. Martonchik, Michael Bull and Van Thai Dang  
Jet Propulsion Laboratory  
California Institute of Technology  
Pasadena, California 91109 USA

e-mail: [John.V.Martonchik@jpl.nasa.gov](mailto:John.V.Martonchik@jpl.nasa.gov)

Conference theme: Advanced preprocessing and processing of remotely sensed data

MISR (Multiangle Imaging SpectroRadiometer) is an instrument on the EOS Terra platform, which takes data at nine view angles ranging from 70 deg forward to 70 deg aftward in spectral bands centered at 446, 558, 672, and 866 nm. The resulting nearly-simultaneous multiangle, multispectra, radiometrically calibrated imagery has a nominal spatial resolution of 1.1 km and covers the globe in about 9 days. Once the imagery is co-located and co-registered, an aerosol retrieval is performed, followed by an atmospheric correction process which transforms the MISR top-of atmosphere (TOA) multi-angle imagery into spectral land surface hemispherical-directional reflectance factors (HDRFs) and bidirectional reflectance factors (BRFs) as part of MISR's archived surface product.

To facilitate the aerosol retrieval process, it is assumed that the individual multispectral surface HDRF (and BRF) at any given location have the same (or very similar) angular shape. There is some theoretical basis for the justification of this assumption, especially when the multispectral HDRF (or BRF) have similar spectral albedos, but an empirical verification in the context of multiangle remote sensing data needs to be done. This poster presents some results of a study currently in progress to test the HDRF/BRF similarity assumption. It focuses on MISR data, taken at AERONET sites with different surface conditions at the MISR scale of 1.1 km. In contrast to MISR data the AERONET data provide an independent and better constrained determination of the aerosol properties, which then are used to correct the associated MISR TOA imagery for atmospheric effects to produce best estimates (i.e., ground truth) of the AERONET site spectral HDRF and BRF. To understand how the angular shape similarity of the spectral directional reflectance depends on spatial scale, the HDRF and BRF are retrieved at a variety of spatial resolutions, starting at 1.1 km centered at the AERONET site and systematically increasing by pixel averaging around the site to 17.6 km resolution, the spatial scale of the aerosol retrieval. A wide variety of AERONET sites are being analyzed to provide information on how the degree of spectral HDRF/BRF similarity may relate to surface type. Because MISR data has been available since early 2000 to the present, seasonal and secular trends in HDRF/BRF variability also will be investigated.

TO BE PRESENTED AS A POSTER

Abstract submission form for the 10<sup>th</sup> ISPMRS (March 12-14, 2007, Davos, CH)

## **CYCLOPES prototype V4 LAI, fAPAR and fCover products derived from VEGETATION and AVHRR sensors: description and validation**

F. Baret<sup>1</sup>, M. Weiss<sup>2</sup>, P. Bicheron<sup>3</sup>, R. Lacaze<sup>3</sup>, M. Leroy<sup>3</sup>

<sup>1</sup>INRA-CSE, UMR1114, Avignon, France

<sup>2</sup>Noveltis, Toulouse, France

<sup>3</sup>POSTEL, Toulouse, France

baret@avignon.inra.fr

Inversion of biogeophysical and biogeochemical variables

Validation of remote sensing products

The CYCLOPES project aims at providing high level biophysical products such as LAI, fAPAR, fCover over the globe at 1 km spatial resolution at a 10 days time interval. To provide continuity over long time series, products have to be derived from different sensors while keeping the highest degree of consistency. The products are derived from the fusion of individual products estimated from VEGETATION, AVHRR sensors. The principles used to derive the products are derived from CYCLOPES version 3.1 products. , They mainly consist in radiometric inter-calibration of sensors using, cloud screening, atmospheric correction, BRDF normalization, and biophysical algorithm (for LAI, fAPAR and fCover). All these steps are made in a consistent way between all the sensors to ease the fusion. Emphasis is put on the biophysical algorithm, based on the training of a neural network over a learning data set made of radiative transfer simulations. Improvements have been implemented, based on the definition of the training data base used to calibrate the biophysical algorithm that better account for measurement and model uncertainties as well as prior information on the surface characteristics.

Products are validated against a series of about 60 3x3 km<sup>2</sup> sites where ground measurements are up-scaled to the spatial resolution of the products. The ground measurements are coming from several networks of sites including VALERI, MODLAND, BIGFOOT, CCRS. Products are then inter-compared along years 2000-2003 with MODIS LAI/fPAR products over the BELMANIP network of sites representing a large range of surface types. Statistical distributions of values per vegetation class, scatter-plots between homologue products, as well as temporal smoothness and consistency of products are presented. Results are then discussed.

# Large Seasonal Swings in Leaf Area of Amazon Rainforests

Ranga B. Myneni<sup>\*</sup>, Wenze Yang<sup>\*</sup>, Ramakrishna R. Nemani<sup>‡</sup>, Alfredo R. Huete<sup>§</sup>, Robert E. Dickinson<sup>¶</sup>, Yuri Knyazikhin<sup>\*</sup>, Kamel Didan<sup>§</sup>, Rong Fu<sup>¶</sup>, Robinson I. Negrón Juárez<sup>¶</sup>, Sasan S. Saatchi<sup>¶</sup>, Hirofumi Hashimoto<sup>\*\*</sup>, Kazuhito Ichii<sup>††</sup>, Nikolay V. Shabanov<sup>\*</sup>, Bin Tan<sup>\*</sup>, Piyachat Ratana<sup>§</sup>, Jeffrey L. Privette<sup>‡‡</sup>, Jeffrey T. Morisette<sup>§ §</sup>, Eric F. Vermote<sup>¶,‡‡</sup>, David P. Roy<sup>¶</sup>, Robert E. Wolfe<sup>\*\*\*</sup>, Mark A. Friedl<sup>\*</sup>, Steven W. Running<sup>†††</sup>, Petr Votava<sup>\*\*</sup>, Nazmi El-Saleous<sup>‡‡</sup>, Sadashiva Devadiga<sup>‡‡</sup>, Yin Su<sup>\*</sup>, Vincent V. Salomonson<sup>§ § §</sup>

<sup>\*</sup>Department of Geography and Environment, Boston University, 675 Commonwealth Avenue, Boston, MA 02215, USA.

<sup>‡</sup> Ecosystem Science and Technology Branch, NASA Ames Research Center, Mail Stop 242-4, Moffett Field, CA 94035, USA.

<sup>§</sup> Department of Soil, Water and Environmental Science, University of Arizona, Tucson, AZ 85721, USA.

<sup>¶</sup> School of Earth and Atmospheric Sciences, Georgia Institute of Technology, 311 Ferst Drive, Atlanta, GA 30332, USA.

<sup>¶</sup> Jet Propulsion Laboratory, California Institute of Technology, 4800 Oak Grove Drive, Pasadena, CA 91109, USA.

<sup>\*\*</sup> California State University at Monterey Bay and Ecosystem Science and Technology Branch, NASA Ames Research Center, Mail Stop 242-4, Moffett Field, CA 94035, USA.

<sup>††</sup> San Jose State University and Ecosystem Science and Technology Branch, NASA Ames Research Center, Mail Stop 242-4, Moffett Field, CA 94035, USA.

<sup>‡‡</sup> Biospheric Sciences Branch, NASA Goddard Space Flight Center, 8600 Greenbelt Road, Mail Code 614.4, Greenbelt, MD 20771, USA.

<sup>§ §</sup> Terrestrial Information Systems Branch, NASA Goddard Space Flight Center, 8600 Greenbelt Road, Mail Code 614.5, Greenbelt, MD 20771, USA.

<sup>††</sup> Department of Geography, University of Maryland, College Park, MD 20742, USA.

<sup>††</sup> Geographic Information Science Center of Excellence, South Dakota State University, Wecota Hall, Box 506B, Brookings, SD 57007, USA.

<sup>\*\*\*</sup> Raytheon TSC at NASA Goddard Space Flight Center, 8600 Greenbelt Road, Mail Code 614.5, Greenbelt, MD 20771, USA.

<sup>†††</sup> School of Forestry, University of Montana, Missoula, MT 59812, USA.

<sup>†††</sup> Science Systems and Applications Inc., NASA Goddard Space Flight Center, 8600 Greenbelt Road, Mail Code 614.5, Greenbelt, MD 20771, USA.

<sup>§ § §</sup> Senior Scientist (Emeritus) of NASA Goddard Space Flight Center and Research Professor, Department of Geography and Meteorology, University of Utah, Salt Lake City, Utah 84112-0110.

**Conference Theme:**

Inversion of biogeophysical and biogeochemical variables

**Abstract:**

**Despite early speculation to the contrary, all tropical forests studied to date display seasonal variations in the presence of new leaves, flowers and fruits. These past studies were focused on the timing of phenological events and their cues, but not on the accompanying changes in leaf area which regulate vegetation-atmosphere exchanges of energy, momentum and mass. Here we report, from analysis of five years of recent satellite data, seasonal swings in green leaf area of about 25% in a majority of the Amazon rainforests. This seasonal cycle is timed to the seasonality of solar radiation in a manner that is suggestive of anticipatory and opportunistic patterns of net leaf flushing during the light rich dry season and net leaf abscission during the cloudy wet season. These heretofore unknown seasonal swings in leaf area are critical to initiation of the transition from dry to wet season, seasonal carbon balance between photosynthetic gains and respiratory losses, and litterfall nutrient cycling in moist tropical forests.**



### **Plant Biochemical Maps of Forage Quality**

A. Skidmore, J. Ferwerda, O. Mutanga, S. van Wieren, M. Peel, R. Grant, H. Prins

Savanna covers about two-thirds of Africa, with forage quantity and quality being important factors determining the distribution and density of wildlife and domestic stock. Testing hypotheses related to the distribution of herbivores is hampered by the absence of reliable methods for measuring the variability of vegetation quality (e.g., biochemical composition) across the landscape. We demonstrate that hyperspectral remote sensing fills this gap by revealing simultaneously the spatial variation of foliar nitrogen (crude protein) as well as total polyphenols in grasses and trees. For the first time, the pattern of resources important for feeding preference in herbivores (total polyphenol and crude protein) are mapped across an extensive landscape, and the modeled foliar concentrations are shown to fit with ecological knowledge of the area. We explain how estimates of crude protein and condensed tannin may be scaled up and used to understand the variation in forage quality and in the management of savannas, such as farms, communal grazing areas, and conservation areas. This provides a glimpse of the choices herbivores must face in selecting food resources of different quality.

# Physical modelling of Nikon Coolpix camera RGB responses for application in non-destructive leaf chlorophyll imaging

Frank Veroustraete<sup>a,\*</sup>, Willem W. Verstraeten<sup>b</sup>, Koen Hufkens<sup>c</sup>, Bert Gielen<sup>c</sup> and Filip Colson<sup>c</sup>

<sup>a</sup> Flemish institute for Technological Research (VITO), Centre for Remote Sensing and Earth Observation Processes (TAP). Boeretang 200, B-2400 Mol, Belgium – [frank.veroustraete@vito.be](mailto:frank.veroustraete@vito.be)

<sup>b</sup> Laboratory of Soil and Water Management, Katholieke Universiteit Leuven (K.U.Leuven), Celestijnenlaan 200E B-3001 Heverlee, Belgium – [willem.verstraeten@biw.kuleuven.be](mailto:willem.verstraeten@biw.kuleuven.be)

<sup>c</sup> University of Antwerp, Research group Plant- and Vegetation Ecology. Universiteitsplein 1, 2600 Wilrijk, Belgium. - [koen.hufkens@ua.ac.be](mailto:koen.hufkens@ua.ac.be)

## ABSTRACT

Chlorophyll content is an important characteristic of plant leaves and a critical parameter for modelling purposes and the scaling up from leaf to canopy level. Leaf colour is an indicator of chlorophyll content, closely coupled with the nutrient status of a plant more specifically nitrogen content. Therefore leaf colour is an important indicator of processes impacting on leaf chlorophyll and nitrogen metabolism. This typically holds for processes like mutual shading, chlorosis, senescence, viral infections, phenology, species biodiversity and hydrological status (Lillesaeter, 1982). A fast non-destructive imaging method to determine leaf chlorophyll content is therefore interesting for applications related to before mentioned processes.

The use of the leaf colour indicates that the estimation method is based on the visible part of the electromagnetic spectrum ( $\pm 400\text{-}700\text{ nm}$ ). Different research projects have been performed to estimate chlorophyll content of leaves with optical non-destructive methods (Benedict & Swidler, 1961; Inada, 1964; Takano & Tsumoda, 1970; Wallihan, 1973; Hardwick & Baker, 1973; Macnicol *et al.*, 1976, Thomas & Gaussman, 1977) mostly based on Red or NIR reflectance or absorbance. A well accepted method is based on the position of the red edge ( $\lambda_{pg}$ ). This is the inflection point of a leaf reflectance spectral signature, typically between 680 and 740 nm (Barber & Horler, 1981; Ferns *et al.*, 1984; Salisbury *et al.*, 1987; Curran *et al.*, 1991; Miller *et al.*, 1991). Only a small subset of investigators managed to develop a chlorophyll method based on the visible part of the EM spectrum thus enabling the use of commercially available digital RGB camera's as well as building the capacity for chlorophyll imaging. Kawashima & Nakatani (1998) developed a field method for the estimation of leaf chlorophyll content using a video camera and image processing software. Unfortunately, these authors did not perform calibration, nor did they specify the spectral response functions of the video camera used. They neither predicted the transfer function to estimate leaf chlorophyll content applying leaf radiative transfer (RTF) modelling. Hence the repeatability of their method remains questionable.

In the work presented, the PROSPECT-DISORD-RAHMAN-6S (PDRS) RTF modelling environment is used to establish the transfer function for the estimation of chlorophyll content of *Tilia* sp., *Zea* mais L. and *Cornus* sp. using a commercially available RGB camera (Nikon Coolpix). The transfer function is validated with the destructive sampling of leaf chlorophyll content of the leaves of the plant species cited here above. The results of the methodological development will be presented and discussed.

**Keywords:** Leaf optics, non-destructive, chlorophyll content, RGB camera, physical modelling with PDRS.

**Conference Theme:** Physical modelling in the remote sensing of leaf chlorophyll content.

\* Corresponding author

This document was created with Win2PDF available at <http://www.win2pdf.com>.  
The unregistered version of Win2PDF is for evaluation or non-commercial use only.

Abstract submission form for the 10<sup>th</sup> ISPMSRS (March 12-14, 2007, Davos, CH)

## Forest reflectance modeling in the Arctic region: results from a case study in Finland

<sup>1,2</sup>Rautiainen, Miina; <sup>3</sup>Stenberg, Pauline; <sup>4</sup>Manninen, Terhikki; <sup>2</sup>Möttus, Matti; <sup>5</sup>Voipio, Pekka

1 Department of Forest Resources Management, Finland

2 Tartu Observatory, Estonia

3 Department of Forest Ecology, University of Helsinki, Finland

4 Finnish Meteorological Institute, Finland

5 Finnish Forest Research Institute, Finland

[miina.rautiainen@helsinki.fi](mailto:miina.rautiainen@helsinki.fi)

Conference theme: Physical modeling in remote sensing

The Arctic region, defined often as the region north from the polar circle (66° 32' N), is characterized by strong variations in sun light conditions - low intensity insolation with a protracted photoperiod during the summers in contrast to the complete darkness of the winters. The forests growing in the southern part of the region are sparse and have a low productivity. In Fennoscandia, the site type and understory vegetation of these forests ranges from permafrost to infertile, dry lichen heaths and extensive wetlands formed as the result of slow accumulation of organic matter.

In our study, we analyze factors behind the spectral signature of forests growing in the Arctic region of Finland, and apply a physically-based forest reflectance model (PARAS) based on the recollision probability concept to provide a theoretical basis to the analysis. To obtain the empirical input to our study, we collected a ground truth data set on leaf area index (LAI) from approximately 300 forest stands at two study areas, Rovaniemi and Tähtelä, as a part of our VALERI network activities in 2004 and 2006. SPOT HRVIR1 images from summers 2004 and 2006, corresponding to the times of the field campaigns, were used in the analyses to examine the relationship of canopy leaf area index and reflectances for different understory types (lichen heaths, dwarf shrub heaths and wetlands). Results from the study clearly indicate the influence of the various understory types and also provide valuable information on the performance of the reflectance parameterization model.

Abstract submission form for the 10<sup>th</sup> ISPMSRS (March 12-14, 2007, Davos, CH)

## **The Role of Image Properties in Determining Change Detection Accuracy**

Warner, Timothy<sup>1</sup>, Almutairi, Abdullah<sup>2</sup>, Campagna, David<sup>2</sup>, and Nellis, M. Duane<sup>3</sup>

<sup>1</sup>Department of Geology and Geography  
West Virginia University  
Morgantown WV 26508, USA  
Tim.warner@mail.wvu.edu

<sup>2</sup>Geography Department  
Imam Mohammad bin Saud University  
Riyadh, Saudi Arabia

<sup>3</sup>Office of the Provost  
Kansas State University  
Manhattan, KS 66506, USA

Conference theme: Quantitative land use/cover change analysis

There have been a large number of studies comparing land use/cover change detection methods. The results of these studies tend to be contradictory, and consequently no clear consensus on the optimal methods for change detection has emerged. One possible reason for this lack of agreement is that, with a few notable exceptions, change detection studies tend to be anecdotal, using just a single data set for a single site. Thus, the degree to which the results of each study can be generalized may be small. We have therefore studied the relationship between image properties and change detection accuracy in a systematic manner. The image properties examined were class separability, radiometric normalization and image band correlation. The change detection methods used were post-classification comparison, direct classification of multirate imagery, image differencing, principal component analysis (PCA), and change vector analysis (CVA). Simulated data were used to identify general relationships. The potential for using these relationships to guide change detection analysis methodological design was evaluated using real Landsat Thematic Mapper data of three cities in the United States: Las Vegas, Nevada; Phoenix, Arizona, and Atlanta, Georgia.

The simulated data experiments showed that the relative accuracy of the change detection methods varied with changes in image properties, thus confirming the hypothesis that the results of single change detection studies should be generalized with caution. For the class separability experiments, post-classification comparison, direct classification, image differencing, and PCA with a large number of the principal components, were all found to have higher accuracies than CVA and PCA with a small number of the principal components. For classes with very good separability, image differencing produced relatively high accuracies; for classes with poor spectral separability, image differencing was found to have the lowest accuracy. The negative effects of error in radiometric normalization between the image dates varied as a function of class separability and change detection method. For example, image differencing showed the greatest sensitivity to large changes in radiometric error, especially when class separability was weak. Image differencing was also found to be more sensitive to band correlation effects. The change detection analysis using pairs of real Landsat imagery showed that image differencing was relatively consistent in producing good results, and PCA produced satisfactory results. On the other hand, the CVA produced mixed results, depending on whether the classification included the identification of the different unchanged classes.



**Title:**

Contact spectroscopy for determination of stratigraphy of snow optical grain size

**Authors:**

Thomas H. Painter  
National Snow and Ice Data Center  
[tpainter@nsidc.org](mailto:tpainter@nsidc.org)

Noah P. Molotch  
University of California, Santa Barbara  
[molotch@seas.ucla.edu](mailto:molotch@seas.ucla.edu)

Maureen P. Cassidy  
National Snow and Ice Data Center  
[cassidym@nsidc.org](mailto:cassidym@nsidc.org)

Mark Flanner  
University of California, Irvine  
[mflanner@uci.edu](mailto:mflanner@uci.edu)

Konrad Steffen  
University of Colorado at Boulder  
[koni@seaice.colorado.edu](mailto:koni@seaice.colorado.edu)

**Conference Themes:**

- Remote sensing systems (microwave, Lidar, (hyper-)spectral, multiangular, thermal, polarization)
- Remote sensing applications to hydrology, carbon cycle, biochemical and –physical cycles, plant ecology, ecosystems, snow, soil moisture, agriculture, natural ecosystems, etc.

**Abstract:**

We present a technique for *in situ* measurement of the vertical and spatial stratigraphic distribution of snow optical grain size with a coupled contact illumination probe and field spectroradiometer. Accurate measurements of optically equivalent grain size are critical for modeling of radiative properties of snow such as spectral albedo and microwave emission. Here, we refer to grain size inferred from traditional hand lens measurements as TGR (traditional grain radius) and optically equivalent grain radius as OGR (optical grain radius). Given the subjective nature of TGR measurements, it is a poorly defined and as such is not repeatable from observer to observer (S. Colbeck, personal communication). The OGR is well defined as the spherical grain radius required to give the same spectral or spectrally-integrated albedo. OGR may also be represented by the specific surface area (surface area per unit volume ice) for the case of fluxes or albedo for snow or clouds.

Measurements of the spectral reflectance of the snowpit surface are made at 2 cm intervals in the vertical plane under constant illumination and view geometries. We invert the integral of the continuum normalization of the ice absorption feature with maximum at 1.03  $\mu\text{m}$  wavelength for optically equivalent grain size using the validated model of *Nolin and Dozier* (2000) that has accuracy of  $\pm 50$ -100  $\mu\text{m}$  across the grain size range 50 to 900  $\mu\text{m}$ . Results are presented for an alpine site in southwest Colorado across the ablation season and for a Greenland ice sheet site at the onset of snowmelt. These results suggest that only for rounded grains are traditional measurements of grain size from hand lens nearly accurate ( $R^2 = 0.4$ , RMSE = 160  $\mu\text{m}$ ) for estimating optical grain radius, whereas for polycrystals and faceted grains the hand lens approach is strongly inaccurate ( $R^2 = 0.03$  and 0.24, RMSE = 1206 and 1010  $\mu\text{m}$ , respectively). We demonstrate the order of magnitude improvement in modeling of shortwave spectral albedo and net shortwave flux with contact spectroscopy measurements of grain size stratigraphy

over those from hand lens. The observed differences between OGR and TGR as well as the modeled albedo and net shortwave calculations associated with them suggest that the empirical relationships of snow metamorphism and grain growth currently employed in snow models likely require a fundamental revision and re-parameterization if grain size as calculated by the model is to be validated and useful for remote sensing and shortwave radiation calculations.

Abstract submission form for the 10<sup>th</sup> ISPMSRS (March 12-14, 2007, Davos, CH)

## **Estimating Clear-Sky Land Surface Longwave Radiation Budget from MODIS Data**

<sup>1</sup>Wenhui Wang and <sup>1</sup>Shunlin Liang

<sup>1</sup>Department of Geography, University of Maryland, USA

Email: whwang1@umd.edu

Radiative transfer based approaches

### **Abstract**

Surface longwave radiation budget components, including surface upwelling longwave radiation (SULR), surface downwelling longwave radiation (SDLR), and surface net longwave radiation (SNLR), are important parameters in Numerical Weather Prediction (NWP) and hydrological modeling. Today, high resolution NWP and hydrological models (up to 1km) have been widely used in short range forecasting, weather hazards warning, as well as in the next generation operational NWP studies. However, no satellite SLBR products with comparable spatial resolution are available, which limits the accuracy of the high resolution model predictions.

In this study, new statistical models for estimating clear sky SULR, SDLR, and SNLR from the Moderate Resolution Imaging Spectroradiometer (MODIS) data (1km spatial resolution) were developed using more than 1500 high resolution MODIS atmosphere profiles and the Moderate Resolution Transmittance Code Version 4 simulation. Land surface emissivity effect was considered explicitly by incorporating UCSB Emissivity Spectra in the simulation procedures.

Preliminary results show that linear models using MODIS TOA radiances can account for 99% and 98% of variations in SULR and SDLR, with standard errors of 5.2 W/m<sup>2</sup> and 12.7 W/m<sup>2</sup>, respectively. Non-linear (polynomial) model produces better fitting result for SNLR, with correlation coefficient of 74 % and standard error of 7.9 W/m<sup>2</sup>. The models were evaluated using collated ground measurements.

## IMPLEMENTATION OF BIOPHYSICAL FACTORS INTO THE LAND SURFACE AND ATMOSPHERE INTERACTION MODEL

Venkat Lakshmi, University of South Carolina, Columbia SC 29208, [vlakshmi@geol.sc.edu](mailto:vlakshmi@geol.sc.edu)

Bryan Hong, University of South Carolina, Columbia SC 29208, [shong@geol.sc.edu](mailto:shong@geol.sc.edu)

Fei Chen, UCAR, [fei.chen@ucar.edu](mailto:fei.chen@ucar.edu)

Eric Small, University of Colorado, [Eric.Small@colorado.edu](mailto:Eric.Small@colorado.edu)

### Conference Theme Remote sensing applications

We test the NOAA land surface model in the weather research and forecasting model (WRF) by simulating surface skin temperature, vegetation fraction, and evapotranspiration in order to improve the model simulations. This study has two major questions:

- 1) How reliable is the model simulation to real-time land surface observations
- 2) What can be implemented or parameterized into the model simulation as a factor sensitive to the land surface-atmosphere interactions.

The relationship between skin temperature and vegetation fraction impacts the variation of evapotranspiration, which is influenced by moisture availability on the surface and vice versa. The skin surface temperature varies with vegetation amount, land cover types, precipitation, topographical differences, soil types and texture. Complex interactions between them determine the relationship between skin temperature and vegetation fraction and hence the evapotranspiration. Of the factors that influence the land surface-atmosphere interactions, water content in vegetation is investigated to determine the possibility of model improvement. Vegetation water content, which is differently controlled by vegetation type, is parameterized into the model by studying its variation with land cover types as well as with the moisture conditions on the surface. Oklahoma in the central U.S. is selected as the study area because it shows variation of vegetation, from bare soil to fully vegetated, and of surface temperature and soil moisture. The simulated variables are compared to the MODIS remote sensing data and the Mesonet ground-based observation data. With the same spatial resolution of MODIS data, the model simulation is calibrated based on the observations provided by the Oklahoma Mesonet.

## **Spatial variability of the spectral properties of forest structures over the Amazon**

Authors: Liana O. Anderson, Yadvinder Malhi, Luiz Aragão, Yosio Shimabukuro

Email: [lander@ouce.ox.ac.uk](mailto:lander@ouce.ox.ac.uk)

The Amazon forest has been largely studied in terms of biodiversity, carbon cycle, and conservation. All these studies use different strategies and methodologies to capture the local scale findings and to understand the implications of the results in a regional level. However, the number and spatial location of the field inventories is still an issue of concern when we try to understand the Amazon forest variability in a large scale. Just recently the idea that Terra Firme forests might also represent ecologically different forest types was reported in the literature. In this study, we explore the spectral properties of 35 field site plots, located in different forest physiognomies over the Amazon. The main objective is to understand how the spectral properties of the remote sensing data reflect differences in the forest structure. To achieve this objective, we have precisely located all these field plots using Ground Positioning System (GPS) and field information to assure the high quality of the data. Field information was also used (Amazon Forest Inventory Network - RAINFOR project) such as tree inventory: density, species taxonomy and basal area. MODIS MO09GQK daily data product was used due to the high temporal image acquisition frequency permitting a cloud free image of the region of interest and high spectral quality. We have used not only the 7 spectral bands of the MODIS data, but we also generated water indexes based on the short wave infrared bands and fraction images derived from unmixing models. This data were integrated in a Geographical Information System (GIS), to extract the samples. Two statistical approaches are being carried out, the linear regressions and principal component analysis. Our preliminary results on the linear regression analysis have showed two new insights. The first one is in relation of the Band 4 – green channel. It showed significant relationship with the number of species ( $r^2=0.4$ ) and density ( $r^2=0.66$ ) and number of very large trees ( $r^2=0.7$ ) at 95% confidence level. Secondly, we found a significant relationship of shade fraction derived from the MODIS data with the number of species. It indicates that green channel and also shade fraction contain information about forest structure and are being better investigated.



## Estimation of surface shortwave radiation budget from MODIS data

Hye-Yun Kim and Shunlin Liang

Dept. of Geography, University of Maryland

kimhy@umd.edu, sliang@geog.umd.edu

Remote sensing application to surface radiation budget (2<sup>nd</sup> from the bottom)

The surface shortwave radiation budget is a key factor responsible for the redistribution of the available energy in Earth-atmosphere system and its spatial and temporal variation can be estimated from the satellite data. Two components of the surface shortwave radiation balance are considered in the present study: surface shortwave downward radiation (SSDR) and surface shortwave net radiation (SSNR), which are derived from MODIS data using a radiative transfer model.

Accurate and updated calibration of instrument and the calibration of the radiation models with high-quality standard radiative transfer calculation have been issues in shortwave radiation budget estimation from satellite data (Schmetz, 1989; Noia et al., 1993; Pinker et al., 1995). In addition, under- or overestimation of surface albedo in declouding process and narrowband to broadband corrections in atmospheric anisotropy were pointed out as error sources in retrieval techniques (Schmetz, 1989; Noia et al., 1993; Pinker et al., 1995; Perez et al., 2001). In present study, both downward flux (SSDR) and net flux (SSNR) are estimated from top of atmosphere (TOA) reflectance using linear regressions for each solar zenith angle, viewing zenith angle, and relative azimuth angle that are developed from extensive radiative transfer simulations. The presented method uses MODIS TOA reflectance and surface reflectance data which have 1-km spatial resolution at nadir and does not need the declouding process or surface albedo in estimation, therefore we expect to estimate surface radiation budget with finer resolution compared to previous studies, irrespective of those error sources. The methodology, comparisons with other algorithms, and validation results will be presented.

Abstract submission form for the 10<sup>th</sup> ISPMSRS (March 12-14, 2007, Davos, CH)

**Effect of cultivar specificities on the radiometric response: quantification and consequences for biophysical variables estimation in wheat crops**

Kai MA<sup>1</sup>, F. Baret<sup>1</sup>, G. Jubelin<sup>2</sup>, P. Burger<sup>3</sup>, B. Roux<sup>4</sup>, S. Labbé<sup>2</sup>, J.M. Nolot<sup>3</sup>

<sup>1</sup>INRA-CSE, UMR1114, Avignon, France

<sup>2</sup>CEMAGREF, Maison de la télédétection, Montpellier, France

<sup>3</sup>INRA-ARCHE, UMR1248, Toulouse, France

<sup>4</sup>L'Avion Jaune, Montpellier, France

kai.ma@avignon.inra.fr

Remote sensing applications to agriculture

Evaluation of new agricultural cultivars developed by plant breeders is a long and expansive process. Traditional methods based on field measurements over series of micro-plots are very time-consuming and costly, preventing from access to the dynamic on some variables such as LAI or chlorophyll content which provides key information on crop functioning. Remote sensing observations offer great potential for characterizing specificities of each cultivar within agronomical trials, helping the final screening stage of plant selection. However, differences in canopy structure of leaf optical properties may confound relationships between canopy biophysical variables and radiometric measurements. The present study aims at quantifying differences in radiometric signatures between cultivars, and investigating how these differences may impact the estimation of biophysical variables such as LAI, chlorophyll content or nitrogen content.

The experiment was conducted in Toulouse in 2005 over 5 wheat crops. Each cultivar was sown at several densities, and under a range of nitrogen levels. Biophysical variables of each cultivar and particular treatment were measured at six stages along the growing season. Cameras equipped with several filters (green, red, near infrared) were flown on UAVs concurrently over the trial. The images were processed to provide consistent values within and across images from which vegetation indices (NDVI, SAVI, GNDVI, ...) were computed. When considering the first order effects, mapping residuals allow to evaluate soil/cultural practices heterogeneity that could be exploited to better control the experiment. Variance analyses were then conducted to evaluate differences between cultivars, both for radiometric and biophysical variables. Finally, the relationships between canopy biophysical variables and vegetation indices are investigated with due attention to possible cultivar specificities. Results are presented with emphasis on further development of this technique and application to plant breeding and precision agriculture.

## Classification of Blanket Mire Microhabitats using Field and Imaging Spectroscopy

John S Dowens<sup>1\*</sup>, Tim J Malthus<sup>1†</sup>, and Lisa R Belyea<sup>2</sup>

<sup>1</sup> School of GeoSciences, University of Edinburgh; \* [j.s.dowens@sms.ed.ac.uk](mailto:j.s.dowens@sms.ed.ac.uk);

† [tjm@geo.ed.ac.uk](mailto:tjm@geo.ed.ac.uk).

<sup>2</sup> Dept. of Geography, Queen Mary, University of London; [l.belyea@qmul.ac.uk](mailto:l.belyea@qmul.ac.uk).

Blanket mire is a globally rare peatland type, occurring only in temperate oceanic climates where high levels of rainfall have resulted in a mantle of peat covering large tracts of land. Scotland contains approximately 10,000 km<sup>2</sup> of blanket mire, which includes some of the largest and most undisturbed areas of this habitat in the world, and represents around 10% of the total area. Blanket mire plays an important role in the carbon and hydrological cycles, and many sites are protected due to their high conservation value. Peatland sites are threatened by changes in land use, pollution, and climate change, with impacts observed through shifts in fine-scale surface features and vegetation structure. To accurately monitor blanket mires and the effects of environmental change on them, we must survey them down to the scale of hydromorphological microforms – for example, hummocks dominated by ericaceous shrubs or wet hollows formed by *Sphagnum* moss. Given the extensive and remote nature of many peatland sites, this is too large a task for efficient ground survey. Blanket mire is therefore an ideal target for remote sensing methods.

Emerging sensor technology and classification techniques allow for ever more detailed and higher resolution classifications. By using newly acquired airborne Hyperspectral and LiDAR data, imaging spectroscopy is being combined with field ecology to study blanket mire at the crucial micro-scale for the first time. In a ground-up approach, field spectroscopy is being used to create a spectral library of abundant vegetation and other surface cover types from complementary field locations in Scotland. Preliminary findings from May 2006 show that reflectance peak features at NIR wavelengths (800 – 1300nm) should allow discrimination between key vegetated and unvegetated microform classes, while features at SWIR wavelengths give an indication of surface wetness and water table depth. These results give a strong indication of the potential to process airborne data from May 2006 and summer 2007 (AISA Eagle & Hawk; CASI-2) to generate the required fine scale habitat maps. This paper will also address the innovative approach that has been taken in the methods used to collect and examine ground reference data for the project, applying Monte Carlo simulation to the optimisation ecological mapping procedures. By using a combination of data sources at high spatial and spectral resolutions it is hoped to develop classification procedures that are precise enough to detect and quantify subtle changes in the structure of blanket mire sites, and to achieve a finer scale characterisation of this important habitat than has been previously possible with remote sensing.

### Relevant conference theme:

- Remote sensing applications to hydrology, carbon cycle, biochemical and –physical cycles, plant ecology, ecosystems, snow, soil moisture, agriculture, natural ecosystems, etc.

## The POSTEL Land Surface Thematic Center

Marc Leroy, Patrice Bicheron, Roselyne Lacaze, Fernando Niño  
*POSTEL Service Center, Medias-France, 18, avenue E. Belin, 31401 Toulouse, France*  
*Marc.Leroy@medias.cnes.fr*

Frédéric Baret  
*INRA/CSE, Agroparc, 84 914 Avignon, France*

Jean-Louis Roujean  
*CNRM/MATIS, Météo-France, 42, avenue G. Coriolis, 31057 Toulouse, France*

Olivier Hagolle, Gérard Dedieu  
*CESBIO, 18, avenue E. Belin, 31401 Toulouse, France*

Fabienne Maignan, François-Marie Bréon  
*LSCE/CEA, 91191 Gif-sur-Yvette, France*

Conference theme : Remote sensing data infrastructures

Preference: Oral

Key words : Biogeophysical variables, Processing, Thematic Center

POSTEL (<http://postel.mediasfrance.org>) is a thematic center aiming at associating in a perennial way research laboratories and services in order to produce spatialized biogeophysical products derived from space observations, and distribute them to the scientific community and other users. It is intended to become a service element in the forthcoming GMES environmental monitoring services to be implemented in 2008 and beyond.

POSTEL is structured around 1) research entities, such as INRA CSE, CNRM/Météo-France, CESBIO, LSCE, CNES/SI, which have the role to conceive and validate new remote sensing products, and 2) a Service Centre located at Medias-France, responsible for the development of operational processing lines, and for the production and distribution of biogeophysical products to the users. The latter assures the contact with the users (user needs, product customization, data acquisition and quality status). POSTEL is funded by national institutions, CNES, CNRS, Météo-France, INRA, and IRD, and by European and other funding through the participation to a number of projects, including CNES / POLDER and PARASOL, CNES / VEN $\mu$ S, FP6 / AMMA, FP6 / GEOLAND, FP5 / CYCLOPES, ESA / GLOBCOVER, and FP6 / VGT4AFRICA.

POSTEL distributes free of charge to the scientific community through its Web interface a series of biogeophysical products derived in the framework of the various projects above and characterizing land surfaces at regional to global scale. They concern the description of vegetation (leaf area index, fraction of vegetation cover, burnt areas ...), radiation at surface level (albedo, downwelling radiation, temperature), and water (soil moisture, water bodies, evapotranspiration ..).

The paper describes the POSTEL thematic center and the first products available, and outlines its present status and perspectives of development.





Abstract submission form for the 10<sup>th</sup> ISPMRS (March 12-14, 2007, Davos, CH)

## **HYRESSA: Towards an Improved Access to Hyperspectral Data in Europe**

Reusen, IIs and the HYRESSA team

Flemish Institute for Technological Research (VITO), Remote Sensing and Earth Observation  
Processes, Boeretang 200, BE-2400 Mol, Belgium  
[ils.reusen@vito.be](mailto:ils.reusen@vito.be)

Remote sensing data infrastructures

During 20 years Europe has gained a lot of expertise in hyperspectral remote sensing. The last few years several hyperspectral flight campaigns with different kind of sensors have been performed and next-generation European airborne hyperspectral sensors (APEX and ARES) are under construction. These sensors are operated by different data providers across Europe and as a consequence flight campaign planning, sensor calibration, data processing, ... are strongly variable at the expense of the user. Different calibration, acquisition, processing and in-situ protocols and the relatively large costs of uncoordinated sensor deployment are barriers to exploit the full potential of hyperspectral imagery. HYRESSA (HYperspectral REmote Sensing in Europe – specific Support Actions) is a FP6 project to investigate the Strengths, Weaknesses, Opportunities and Threats of hyperspectral remote sensing in Europe and to investigate the user needs of the European scientific hyperspectral remote sensing community. In the frame of the HYRESSA project a European hyperspectral contact database containing about 700 contacts was built and a SWOT and User Needs workshop was organized on 5-6 July 2006 at DLR (15 mainly EU members states were represented). The outcome of this workshop was used to build a web-based Questionnaire on User Needs which was launched end of 2006 to the European scientific hyperspectral remote sensing community. The main user needs identified during the SWOT and User Needs workshop are: standardization (especially for data processing and calibration), more transparency on calibration processes, European platform for hyperspectral remote sensing (e.g. sensor pool, information about campaigns, data pool, spectral libraries, ...), education and training and the increase of the awareness of the added value of hyperspectral remote sensing. Furthermore, HYRESSA will investigate the refinement of protocols (for e.g. calibration, acquisition, processing, in-situ measurements, ...) in compliance with standards and will explore new strategies on how to build a European hyperspectral remote sensing network and on how to coordinate a European user-oriented hyperspectral remote sensing Research Infrastructure. The HYRESSA outcome is a starting point to prepare for a European user-oriented hyperspectral remote sensing Research Infrastructure including networking activities, transnational access to coordinated European hyperspectral flight campaigns and research for the improvement of the access to the Research Infrastructure and to exploit the full potential of hyperspectral imagery. The HYRESSA project, its objectives and outcome will be presented at the symposium. More information can be found at the HYRESSA website (<http://www.hyressa.net>).

## **Spatial Variability and Altitude effects of passive chlorophyll fluorescence measurements over La Mancha (Spain) fields**

Moya, I.,

LMD-CNRS, Ecole Polytechnique, 91128 Palaiseau - France

ismael.moya@lmd.polytechnique.fr

Daumard, F.,

LMD-CNRS, Ecole Polytechnique, 91128 Palaiseau - France

fabrice.daumard@lmd.polytechnique.fr

Moise, N.,

Force-A, Université de ParisXI, 91405 Orsay, France

nicolae.moise@force-a.fr

Goulas, Y

LMD-CNRS, Ecole Polytechnique, 91128 Palaiseau - France

yves.goulas@lmd.polytechnique.fr

Ounis, A

LMD-CNRS, Ecole Polytechnique, 91128 Palaiseau - France

ounis@lmd.polytechnique.fr

AIRFLEX is an optical sensor based on the Fraunhofer Line Discriminator principle applied in the atmospheric oxygen absorption bands, that measures simultaneously fluorescence at 687 nm and 760 nm. The sensor was adapted on a Cessna C 208B Gran Caravan aircraft, from DLR (German Space Agency). It has a total field of view of 2° which corresponds to a footprint of 20 m at the altitude of 600m. In addition to fluorescence measurements, two other parameters were continuously acquired: the spatial localisation with the aircraft navigation system, and the image of the target thanks to a digital video camera.

The sensor was flown over cultivated land during June and July 2005, often separated by bare fields with equivalent size. Excellent reproducibility of the measurements was achieved by measuring along the same track of 10 km length. The effect of the altitude on the signals was investigated in the range of 300 to 3000 m.

Although the AIRFLEX data are not yet been fully exploited, one may conclude that the feasibility of passive fluorescence measurements using the oxygen absorption bands is operative up to 3000 m of altitude, with only marginal signal degradation when compared to 300 m measurements. This led us to be confident on the possibility to extend the method to the detection from a satellite platform with a modified version of the sensor.

- Conférence theme: Remote sensing systems (microwave, Lidar, (hyper-)spectral, multiangular, thermal, polarization)

Abstract submission form for the 10<sup>th</sup> ISPMSRS (March 12-14, 2007, Davos, CH)

## **The Characterisation of Heather Foliage and Canopies by Hyperspectral Reflectance**

Mac Arthur, A. A. and Malthus, T. J.

*School of GeoSciences, The University of Edinburgh, Grant Institute Edinburgh. EH9 3JW*

[alasdair.macarthur@ed.ac.uk](mailto:alasdair.macarthur@ed.ac.uk)

*Conference theme:* Scaling from leaf, canopy to ecosystem

### **Abstract**

Heather dominated uplands form a significant proportion of Scotland's land area and are of significant economic and aesthetic value, of international importance for biodiversity conservation, a hydrological buffer, and are intimately linked to the global carbon cycle. Current management practices are considered to be causing the decline of these areas and climate change may be contributing. The extent and remoteness of upland moors makes manual survey problematic for monitoring ecological and phenological change. Remote sensing offers a complimentary approach but little is known of the detailed reflectance properties of heather. Greater understanding is required of the effect of variations in key biophysical and biochemical parameters influencing the spectral reflectance of heather canopies. Similarly, little has been done to relate the reflectance properties of heather to ecological community membership or to investigate the influence of phenological changes on its reflectance.

Research plots representing each recognised heather age classes and located in distinctly different ecological communities have been established on an upland moor. High spectral and spatial *in situ* reflectance measurements and measurements of key biophysical and biochemical variables influencing reflectance have been acquired from these sites over a number of growing seasons. Heather canopy samples were selected and removed to a laboratory and reassembled to allow detailed high spectral and spatial resolution measurements. Canopy components were then separated and dried for biomass and water content determination. Shoot and leaf samples were 'stacked' and further reflectance spectra acquired. Finally a proportion of the stacked shoots and leaves were used to determine proximate pigment content by wet chemistry methods.

Large variability has been measured in both biophysical and biochemical variables and significant levels of foliar Anthocyanin noted. Poor correlation was found between published universal pigment indices and measured Chlorophylls and Carotenoids content. Distinct changes in shoot and leaf reflectance related to foliar development and senescence were noted. There was an increase in green reflectance to a point of maximum value in late June then a general reduction through the remainder of the growing season. A marked reduction in foliar Chlorophyll content was found in reflectance spectra coincident with the onset of flower development. No differentiation between the age classes and ecological community memberships of the heather samples could be determined from reflectance measurements performed on shoots and leaves. However, changes in red reflectance observed at the onset of flowering did relate to age class and ecological community membership for some research plots.

Imaging spectroscopy using the NERC ARSF Eagle/Hawk platform is now proposed to determine if reflectance features observed in the laboratory are expressed in hyperspectral images. The paper will present the preliminary results of this research project and discuss the implications for monitoring change in upland ecosystems using spectroscopic methods.

## **Validation of FAPAR products derived from optical sensors: method and results.**

Nadine Gobron, Bernard Pinty, Ophélie Aussedat, Malcolm Taberner, Frédéric Mélin, Thomas Lavergne, Monica Robustelli and Jean-Luc Widlowski

Global Environmental Monitoring Unit, Institute for Environment and Sustainability, European Commission Joint Research Centre, Ispra, Italy.

[nadine.gobron@jrc.it](mailto:nadine.gobron@jrc.it)

### Validation of remote sensing products

In the context of scientific research concerning global change issues, remote sensing products have been demonstrated to be essential tools to monitor the characteristics of both land surfaces and their temporal evolution. The biophysical activities on land surfaces are documented from spectral measurements made in space. Advances in the understanding of radiation transfer and availability of higher performance instruments have lead to the development of a new generation of geophysical products able to provide reliable, accurate information on the state and evolution of terrestrial environments. Specifically, a series of optimized algorithms have been developed to estimate the Fraction of Absorbed Photosynthetically Active Radiation (FAPAR) for various instruments. Such an approach allows the synergistic use of FAPAR products derived from different sensors and the construction of regional and global FAPAR time series independent from the life time of these specific sensors. This presentation will present a comparison strategy against ground-based estimations and results from the exercise conducted with products derived from SeaWiFS, MERIS and MODIS.

Abstract submission form for the 10<sup>th</sup> ISPMRS (March 12-14, 2007, Davos, CH)

## **The NCAVEO 2006 Cal/Val Experiment**

Milton, E.J. and colleagues from the NCAVEO Partnership<sup>1</sup>  
University of Southampton, UK  
ncaveo@soton.ac.uk

Validation of remote sensing products

The paper will describe a cal/val experiment organised in the UK in June 2006 by the Network for Calibration and Validation in Earth Observation (NCAVEO). NCAVEO is a knowledge transfer network comprising 24 partners drawn from academia, industry and government in the UK ([www.ncaveo.ac.uk](http://www.ncaveo.ac.uk)). The aim of the network is to disseminate best practice for the calibration and validation of data from airborne and satellite sensors. The NCAVEO 2006 Field Experiment was based at the Chilbolton Facility for Atmospheric and Radio Research in Hampshire, England, and involved over 50 researchers on the ground, three instrumented aircraft and several satellites, including SPOT, CHRIS/Proba and several from the DMC series. The paper will describe the series of experiments undertaken and present some early results, including some on the use of Teillet's QUASAR methodology to validate the radiometric calibration of CHRIS/Proba as well as validation of one or more land products derived from CASI hyperspectral data. It is not possible to give exact details at this stage as the analysis is still underway, but the data have been delivered and several NCAVEO partners will be attending the Davos meeting to help present the poster.

---

<sup>1</sup> Co-authors to be confirmed.



INDEX BY AUTHORS

Author	No.
Adriaensen, S.	T26
Akay, A.E.	P41
Alavipanah, S.K.	P76
Alimohammadi, A.	P7, P22
Alleaume, S.	P29
Allgöwer, B.	P29, T0
Almutairi, A.	P68
Amiri, R.	P76
Anderson, E.	P37
Anderson, L.O.	P83
Ansari Amoli, A.	P7
Aragão, L.	P83
Armitage, R.P.	P9, P10, T28
Asner, G.P.	P67
Atzberger, C.	P64
Aussedat, O.	P38, P96, T12
Bachmann, M.	P62
Baltsavias, M.	P36
Bannari, A.	P77
Baraldi, A.	P42
Barella-Ortiz, A.	P47
Baret, F.	P2, P45, P48, P52, P86, P88, T7, T13, T18
Barroy, P.	T13
Bartholomeus, H.M.	P27
Beal, D.	T18
Belyea, L.	P87
Ben-Dor, E.	P5
Bianchi, R.	P47
Bicheron, P.	P52, P88, T7
Billard, G.	P48
Bindlish, R.	P72
Böhner, J.	P46
Bojinski, S.	P66
Boldo, D.	P13
Borel, C.C.	P14, T6
Borgniet, L.	P29
Bousquet, L.	T13
Brakenridge, G.R.	P37
Bregt, A.K.	P31
Brenguier, J.-L.	H3
Bréon, F.-M.	P88
Briggs, S.	T1
Briottet, X.	P13

Author	No.
Brocard, E.	P33
Brockmann, C.	T8
Brucker, L.	P26
Brunet, Y.	P82
Buddenbaum, H.	P64
Bull, M.	P50
Burger, P.	P86
Cabot, F.	T4
Campagna, D.	P68
Camps-Valls, G.	P6
Cassidy, M.P.	P69, T21
Chabrillat, S.	T26
Chapman, M.	P90
Chen, F.	P74
Chen, X.	T18
Cherkaoui, F.Z.	P77
Chico, J.	P55
Chudnovski, A.	P5
Clevers, J.G.P.W.	P6, P12, P31, P49, T17
Colson, F.	P56
Conejo, E.	P61
Conley, A.	T18
Cosh, M.	P72
Craig, P.S.	P9
Curt, T.	P29
Damm, A.	P51
Dang, V.T.	P50
Dangel, S.	P91
Danson, F.M.	P9, P10, T28
Darvishsefat, A.A.	P75
Daughtry, C.S.T.	P59
Daumard, F.	P58, P93
Debaecker, V.	P15
Dedieu, G.	P15, P88, T4
Deering, D.	T18
Devadiga, S.	P53
Díaz-Delgado, R.	P81
Dickinson, R.E.	P53, T10
Didan, K.	P53
Diepen, C.A. van	P28
Disney, M.I.	P60, P63, T9, T11, T14, T15
Domenico, B.	P30
Dowens, J.	P87

Author	No.
Dozier, J.	P3
Du, J.	P72
Dvoráková, M.	P95
Eiden, M.	P82
Eisenbeiss, H.	P36
El-Ghmari, A.	P77
El-Harti, A.	P77
El-Saleous, N.	P53
Fahimnejad, H.	P18, P22
Feret, J.-B.	P67
Fernandes, R.	T18
Fernández-Renau, A.	P20, P81
Ferrier, P.	T4
Ferwerda, J.	P54
Fily, M.	P1, P26
Fischer, J.	T8
Flanner, M.	P69
Fomferra, N.	T8
Fontana, F.	P39
Foppa, N.	P24, P25
Fox, N.P.	P73, P90
François, C.	P67
Frangi, J.-P.	P61
Frew, J.	P3
Frey, O.	P23, T29
Friedl, M.A.	P53
Fu, A.	T30
Fu, R.	P53
Gagliano, C.	P43
Gaiser, P.	P72
García, R.	P20
Gastellu-Etchegorry, J.P.	T9, T17
Geiss, H.	P82
Gerbig, C.	P82
Giacosa, C.	T28
Gidudu, A.	P11
Gielen, B.	P56
Giering, R.	P38, T12
Ginzler, C.	P36
Giraudoux, P.	P9
Gobron, N.	P38, T12
Gobron, N.	P96
Gómez, J.A.	P47, P55, T26, H1
Gómez, M.	P47

Author	No.
Gómez-Chova, L.	P6
González, R.	P16
Goulas, Y.	P58, P93
Grant, R.	P54
Grattan, K.T.V.	P73
Greenberg, J.A.	P59
Groeve, T. de	P37
Gruen, A.	P36
Guanter, L.	P47
Guedon, A.M.	P77
Gundogan, R.	P41
Gustafsson, D.	P25
Gutiérrez de la Cámara, O.	P81
Gutman, G.	P40
Guyot, G.	T2paper, T2pres.
Hagolle, O.	P15, P88, T4
Hancock, S.	P60
Hanuš, J.	P95
Hashimoto, H.	P53
Heege, T.	P17
Hees, R. van	P30
Hill, J.	P64
Holzwarth, S.	P62, T26
Homolová, L.	P95, T17
Hong, B.	P74
Hoogerwerf, M.	P30
Hornbuckle, B.	P72
Hostert, P.	P51
Huang, D.	T19
Huber, S.	P45, P79, P80
Huete, A.R.	P53
Hufkens, K.	P56
Hüni, A.	P98
Hurk, B.J.J.M. van den	P32
Ichii, K.	P53
Incerti, F.	P43
Itten, K.I.	P17, P78, P79, P80, P84, P91, P98, T26
Jackson, T.	P72
Jacobs, C.M.J.	P32
Jacquemoud, S.	P61, P67
Jappiot, M.	P29
Jaros, N.	P82
Jeanjean, H.	T4

Author	No.
Jia, L.	P32
Jiménez, M.	P47, P55, P81
Jiménez-Muñoz, J.C.	P55, P47
Jonas, T.	P24, P39, T20
Jubelin, G.	P86
Julien, Y.	P47
Kabela, E.	P72
Kaminski, T.	P38, T12
Karas, I.R.	P41
Karnieli, A.	T4
Kaufmann, H.	T26
Kauwe, M. de	T11
Keller, J.	P66
Khodaei, K.	P76
Kim, H.-Y.	P85
Kneubühler, M.	P17, P45, P78, P79, P80, P84, P91, P98
Knyazikhin, Y.	P53, T14, T19
Koetz, B.	P29, P45, P49, P57, P80, T29
Kooistra, L.	P12, P27, T26
Kuechler, M.	P36
Kugler, Z.	P37
Labbé, S.	P86
Labouret, A.	P48
Lacaze, R.	P52, P88, T7
Lachérade, S.	P13
Lakshmi, V.	P74
Lampin, C.	P29
Lavergne, T.	P38, P96, T9, T12
Lawc, B.	T11
Le Men, H.	P13
Leblanc, S.	T18
Lehning, M.	P25, T20
Leroy, M.	P52, P88, T7
Lewis, P.	P60, P63, T9, T11, T14, T15
Li, L.	P70, P72
Liang, S.	P71, P85, T10
Linden, S. van der	P29, P82
Liu, D.	P57
Löwe, H.	T20
Lyapustin, A.	T5
Ma, K.	P86, T13
Mac Arthur, A.A.	P19, P94

Author	No.
MacLellan, C.	P19
Maignan, F.	P88
Malenovský, Z.	P95, T17, T26
Malhi, Y.	P83
Malthus, T.J.	P2, P19, P87, P94, T26, H2
Manninen, T.	P65
Marloie, O.	P48
Marsh, S.	P21
Marston, C.G.	P9, P10
Martin, E.	T9, T17
Martin, R.	P67
Martínez-Fernández, J.	P16
Martonchik, J.V.	P50
Masek, J.	T30
Maselli, F.	P43
Matthis, I.	P33
Mätzler, C.	P33
Meier, E.	P23, T29
Mélin, F.	P96
Menze, B.H.	P8
Miesch, C.	P13
Miguel, E. de	P20, P47, P55, T26
Milton, E.J.	P90, P97
Moise, N.	P93
Mojaradi, B.	P18
Molotch, N.P.	P69
Moors, E.	P32
Moreno, J.	P47
Morger, A.	P24
Morisette, J.T.	P53
Morsdorf, F.	P23, P29, T29
Möttus, M.	P65, T16, T26
Moya, I.	P58, P93
Müller, A.	P4, P62, T26
Muller, J.-P.	P60, T8
Mutanga, O.	P54
Myneni, R.B.	P53, T19
Namiranian, M.	P75
Naseri, F.	P75
Natale, F. de	P43
Natali, S.	P42
Nativi, S.	P30
Negrón Juárez, R.I.	P53
Neininger, B.	P82

Author	No.
Nellis, M.D.	P68
Nemani, R.R.	P53
Nieke, J.	P17, P98, T26
Nilson, T.	T18
Niño, F.	P88
Nolot, J.M.	P86
North, P.R.J.	T9
Odermatt, D.	P17, P29
Ogunbadewa, E.Y.	P10
Omani, A.	P34
Ong, C.	P4
Ounis, A.	P58, P93
Ozdogan, M.	P40
Painter, T.H.	P3, P35, P69, T21
Pedros, R.	P58
Peel, M.	P54
Pegrum, H.M.	P73, P90
Pellikka, P.	T26
Pérez-Gutiérrez, C.	P16
Pfeifer, M.	P63
Picard, G.	P1, P26
Pinty, B.	P38, P96, T9, T12
Pokorný, R.	P95, T17
Prado, E.	P55, P81
Prado, J.	P16
Preusker, R.	T8
Prevot, A.S.H.	P66
Prins, H.	P54
Privette, J.L.	P53
Psomas, A.	P84
Puzzolo, V.	P42
Quaife, T.	T11, T14
Quental, L.	P21
Ramirez, A.	P9, P10
Ranson, K.J.	P57, T30
Rascher, U.	P82
Rast, M.	T22
Ratana, P.	P53
Rautiainen, M.	P65, T16
Regner, P.	T8
Reusen, I.	P89, T26
Riaza, A.	P4
Rixen, C.	P39
Robles, C.	P55
Robustelli, M.	P96, T9
Rochdi, N.	T18

Author	No.
Rosny, G. de	P61
Roujean, J.-L.	P88
Roux, B.	P86
Roy, D.P.	P53
Royer, A.	P1
Running, S.W.	P53
Russ, A.	P59
Ruther, H.	P11
Saatchi, S.S.	P53
Salim, S.G.R.	P73
Salomonson, V.V.	P53
Sánchez, N.	P16
Sanchez-Prieto, L.	P27
Santis, A. de	P81
Saquaque, A.	P77
Saradjian, M.R.	P34
Schaepman, M.E.	P6, P12, P27, P30, P31, P35, P49, T17, T26
Schaepman-Strub, G.	P35
Schlerf, M.	P64
Schmidhalter, U.	P46
Schmutz, W.	T3
Schneebeli, M.	P33
Schopfer, J.T.	P45, P80, P91, P98
Schull, M.	T14
Schween, J.H.	P82
Seiler, B.	P78
Selige, T.	P46
Shabanov, N.V.	P53, T19
Shahid, K.	T18
Shahrokhy, S.M.	P44
Shimabukuro, Y.	P83
Simonetti, D.	P42
Skidmore, A.	P54, P64
Small, E.	P74
Sobhani, H.	P75
Sobрино, J.A.	P47, P55
Som de Cerff, W.	P30
Soofbaf, S.R.	P18, P22
Sòria, G.	P47
Sousa, A.	P21
Spencer, C.	T6
Stähli, M.	P25
Steffen, K.	P69

Author	No.
Stenberg, P.	P65, T16, T18
Steven, M.D.	P2
Stoffel, A.	P24
Su, B.	P47
Su, Y.	P53
Sun, G.	P57, T30
Sun, T.	P73
Taberner, M.	P38, P96, T9, T12
Tan, B.	P53
Thee, P.	P36
Thompson, R.	T9
Timmermans, W.	P47
Tomášková, I.	P95
Townshend, J.	T10
Traullé, O.	P82
Ur, J.A.	P8
Ustin, S.L.	P59, P67, T23
Valadan Zoej, M.J.	P18, P22
Valorge, C.	P13
Vanderbilt, V.C.	P59
Vaughan, P.	P81
Vegte, J. van der	P30
Verhoef, W.	P64, T27
Vermote, E.F.	P53
Veroustraete, F.	P56
Verrelst, J.	P49
Verstraete, M.M.	P38, T9, T12
Verstraeten, W.W.	P56
Vierling, L.	T18
Visscher von Arx, A.	P79
Voipio, P.	P65
Voogt, M.H.	P32
Vossbeck, M.	P38, T12
Votava, P.	P53
Wandinger, U.	P33
Wang, D.	T30
Wang, W.	P71
Wang, Y.	T5
Warner, T.	P68
Waser, L.	P36
Weiss, B.	H4
Weiss, M.	P52, T7, T18
Wel, F. van der	P30
Widlowski, J.-L.	P38, P96, T9, T12
Wieren, S. van	P54
Wilhelmi, O.	P30

Author	No.
Williams, M.	T11
Winkler, R.	P73
Wit, A.J.W. de	P28
Wolfe, R.E.	P53, T25
Wolfgramm, B.	P78
Woolliams, E.R.	P73
Wu, B.	P31
Wunderle, S.	P39
Yang, W.	P53
Yaniv, Y.	T4
Yebra, M.	P10
Zappa, M.	P24, P25
Zaragova-Ivorra, M.M.	P47
Zeng, Y.	P31
Zhang, L.	P70
Zhao, S.	P70
Zimmermann, N.E.	P80, P84
Zühlke, M.	T8
Zurita-Milla, R.	P6, P49, T17

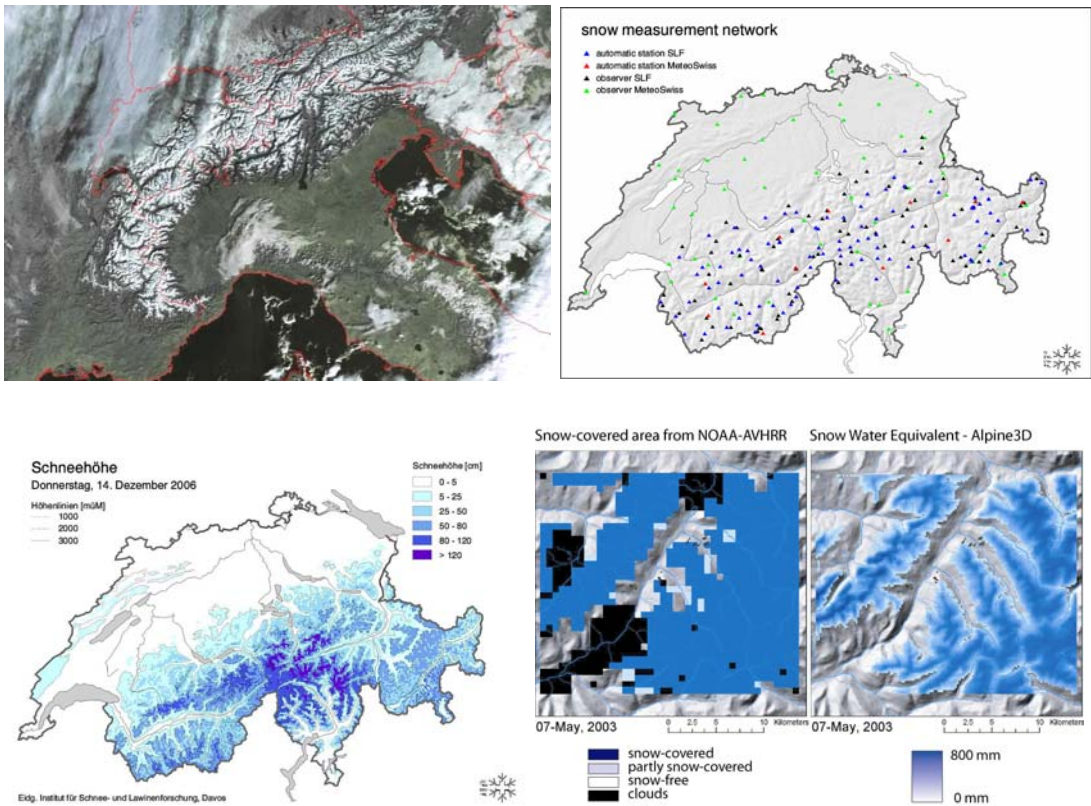


International Society for Photogrammetry and Remote Sensing (ISPRS)

10<sup>th</sup> International Symposium on  
Physical Measurements and Signatures in Remote Sensing

ISPMSRS'07

March 12 – 14, 2007  
Davos, Switzerland



In combination with

HYRESSA Exploratory Workshop  
March 14 – 15, 2007

CEOS/LPV-VALERI Workshop  
March 15, 2007



Snow crystal image courtesy Kenneth G. Libbrecht, <http://www.its.caltech.edu/~atomic/snowcrystals/>

*Snow depth mapping in the Swiss Alps and Alpine 3D snowmelt runoff modelling in the Dischma valley, Davos*

Snow depth in the Alps has a very heterogeneous distribution ranging from small scale to large scale. Area-wide snow depth maps provide important information for avalanche forecasting, hydrological snowmelt runoff modelling and are moreover an important information source for winter tourism. Monitoring snow depth in the Swiss Alps has a long tradition and nation-wide snow depth maps represent a core product of the Institutes snow information system. The Swiss Federal Institute for Snow and Avalanche Research (SLF) in Davos publishes daily information on the web (<http://www.slf.ch/avalanche/avalanche-en.html>) on potential avalanche danger and snow conditions in the Swiss Alps.

Illustrations: © Copyright 2007: NOAA, RSGB, University of Bern and Swiss Federal Institute for Snow and Avalanche Research (SLF, Davos), Kenneth G. Libbrecht (USA)

Content

Introduction ..... 3

Organisation ..... 4

    Programme Committee ..... 4

        Honorary Chair ..... 4

        International Scientific Committee ..... 4

        Local Organising Committee ..... 4

    Organiser ..... 4

General Information ..... 5

    Venue ..... 5

    Davos Congress Center ..... 5

    Registration desk / Symposium secretariat ..... 5

        Information for presenters ..... 5

        Information for poster sessions ..... 5

    Social Programme ..... 6

        Excursion: Physikalisch-Meteorologisches Observatorium Davos / World Radiation Center – PMOD / WRC ..... 6

        Excursion: Swiss Federal Institute for Snow and Avalanche Research (Davos) – SLF ..... 7

        Workshop: RAMI On-line Model Checker (ROMC) ..... 8

        Event: Skiing ..... 8

    Davos Weather ..... 9

Notes Overall Programme ..... 10

Overall Programme ..... 11

    Monday, March 12<sup>th</sup> 2007 ..... 11

    Tuesday, March 13<sup>th</sup> 2007 ..... 11

    Wednesday, March 14<sup>th</sup> 2007 ..... 11

    Thursday, March 15<sup>th</sup> 2007 ..... 11

Notes ..... 12

Detailed Programme ..... 13

    Monday, March 12<sup>th</sup> 2007 ..... 13

    Notes Tuesday, March 13<sup>th</sup> 2007 ..... 14

    Tuesday, March 13<sup>th</sup> 2007 ..... 15

        Interactive Poster Session I ..... 16

            Tuesday, March 13<sup>th</sup> 2007, 20:00 – 21:30 ..... 16

    Wednesday, March 14<sup>th</sup> 2007 ..... 19

        Interactive Poster Session II ..... 20

            Wednesday, March 14<sup>th</sup> 2007, 13:00 – 14:40 ..... 20

    Additional Workshops ..... 23

        Thursday, March 15<sup>th</sup> 2007 – HYRESSA Workshop ..... 23

        Thursday, March 15<sup>th</sup> 2007 – LAI and fAPAR validation under CEOS/LPV-VALERI ..... 25

Notes How to reach Davos ..... 26

How to reach Davos ..... 27

    How to reach Davos by Plane ..... 27

    How to reach Davos by Car ..... 27

    How to reach Davos by Coach ..... 27

    How to reach Davos by Train ..... 27

    Davos – City Map ..... 28

ISPMRSRS'07 Topics ..... 31

ISPMRSRS'07 Follow-up ..... 31



## Introduction

Welcome to the International Symposium on Physical Measurements and Signatures in Remote Sensing (ISPMSRS). This year, it is already the 10<sup>th</sup> occurrence of this meeting, which is much better known as the 'Spectral Signatures' meeting in the scientific user community. Physical measurements and their spectral signatures remain at the forefront of remote sensing research, and the topic has not suffered from attractivity since the first meeting was held back in 1981 (Intl. Colloquium on Spectral Signatures of Objects in Remote Sensing, Avignon, France).

Gradually and over time, the spectral signatures meeting moved from warmer to colder regions (Bordeaux (F), 1983; Les Arcs (F), 1985), finally arriving in well known ski resorts in France (Aussois 1988, 2001; Courchevel 1991, 1997; Val D'Isère, 1994). The 'French period' of the spectral signatures meetings is closely associated with the name of Gérard Guyot, and we are very grateful that he volunteered to serve as honorary chair for this meeting.

In 2005, the ISPRS WG VII/1 organised the meeting in Beijing and attracted many international visitors and raising the idea to have its today's meeting in Davos. You may conclude that the last two locations were selected in the home countries of the ISPRS WG VII/1 chairpersons origin: we conclude that these locations offer both, an excellent opportunity to exchange scientific ideas and enjoy the diversity of nature, culture and society.

However, we are grateful that you have decided to join this meeting. A meeting structure is usually the most difficult to decide on. For this meeting, we have chosen to organize no parallel sessions and offer you plenty of interaction time with both, young scientists and more experienced senior scientists. This interaction will be possible during the oral presentations, the interactive poster presentations and at the various social events. The goal of this workshop is to exchange state-of-the-art results in spectral signatures research. We hope you will share our goal of this workshop by **actively fostering discussion with at least 3 new scientists you have not met previously**, allowing to strengthen all our networks with new contacts!

Appended to the symposium, you will find smaller workshops organized by the HYRESSA team and the CEOS/LPV-VALERI group. We would like to thank Lammert Kooistra and Frédéric Baret extending the Davos event with their contributions.

Our event in the 'Science City Davos' was only made possible with the significant local support of PMOD/WRC (World Radiation Center), RSL (Remote Sensing Laboratories, Univ. Zürich) and SLF (Swiss Federal Institute for Snow and Avalanche Research).

We would like to take the opportunity to thank our generous sponsors for their support, as well as all the helping hands in the background making this event possible.

We wish you all a fascinating conference and fruitful discussions about the continuously emerging topic of spectral signatures in remote sensing!

*Michael Schaepman, Shunlin Liang and Mathias Kneubühler*  
ISPRS WG VII/1 convenors



## Organisation

### *Programme Committee*

#### Honorary Chair

G rard Guyot, *former chair of ISPRS WG VII/1*

#### International Scientific Committee

Michael E. Schaepman, Wageningen University, Wageningen, NL (chair)  
 Fr d ric Baret, INRA, Avignon, F  
 Mike Barnsley, University of Wales Swansea, UK  
 Marvin Bauer, University of Minnesota, USA  
 Jon Atli Benediktsson, University of Iceland, Iceland  
 Peng Gong, University of California at Berkeley, USA  
 David Goodenough, Pacific Forestry Centre, Natural Resources, CDN  
 Klaus I. Itten, RSL, Univ. Zurich, CH  
 Tom Jackson, USDA/ARS at Beltsville, Maryland, USA  
 St phane Jacquemoud, University of Paris 7 / IPGP, F  
 David Jupp, CSIRO Earth Observation Centre, Aus  
 Yann Kerr, CNES/CESBIO, F  
 Marc Leroy, MEDIAS, F  
 Philip Lewis, University College London, UK  
 Xiaowen Li, Beijing Normal University and Institute of Remote Sensing Applications, CN  
 Shunlin Liang, University of Maryland, USA  
 John V. Martonchik, Jet Propulsion Laboratory, USA  
 Ranga Myneni, Boston University, USA  
 Thomas Painter, University of Colorado, Boulder, USA  
 Jeff Privette, NOAA, USA  
 Jon Ranson, NASA/GSFC, USA  
 Mike Rast, GEO, Geneva, CH  
 Gabriela Schaepman-Strub, ESA/KNMI/WUR, NL  
 Werner Schmutz, WRC, Davos, CH  
 Jose Sobrino, University of Valencia, ES  
 Karl Staenz, Canada Centre for Remote Sensing, CDN  
 Alan Strahler, Boston University, USA  
 Frank Veroustraete, VITO, Mol, B  
 Charlie Walthall, USDA/ARS at Beltsville, Maryland, USA  
 Jean-Luc Widlowski, JRC, IES/GEM, Ispra, IT

#### Local Organising Committee

Mathias Kneub hler, RSL, Univ. Zurich, CH  
 Truus van den Hoef, CGI, Wageningen University, NL  
 World Radiation Centre, Davos, CH

#### *Organiser*

Working Group VII.1 on 'Fundamental Physics and Modelling' from the International Society for Photogrammetry and Remote Sensing (ISPRS) Technical Commission VII (on Thematic Processing and Analysis of Remotely Sensed Data).

## General Information

### ***Venue***

The 10<sup>th</sup> ISPMSRS will consist of *oral presentations* discussing state-of-the-art achievements in one of the symposium topics, as well as an extended *poster session* on emerging issues. There will be no parallel sessions and plenty of room for interaction with scientists.

The symposium will take place in Davos, Switzerland (<http://www.davos.ch/>), in its modern congress centre (<http://www.davos.ch/overview-001-020000-en.htm>). The conference will not only be composed of a high quality scientific program, but also on an extended social program, including visits to the World Radiation Centre (<http://www.pmodwrc.ch/>), the Swiss Federal Institute for Snow and Avalanche Research (<http://www.slf.ch/>), the ROMC workshop, the 'Remote Sensors on Skis' event (featuring Gabriela Schaepman-Strub (WUR) and Tom Painter (NSIDC)), and a conference dinner.

### ***Davos Congress Center***

The Congress Centre is located in the heart of Davos. You enter the Congress Centre through the main entrance located adjacent to the main street of Davos, the 'Promenade'. ISPMSRS'07 is mainly located in the Wing C of the Congress Centre, comprised of the 'Sanada' room (seats 200 persons) as well as the 'Foyer C1' (692 m<sup>2</sup> – for poster exhibition and coffee breaks). You will find appropriate signs everywhere. A Public Wireless LAN hotspot is available for Internet connection through swisscom mobile (Credit card, swisscom Value card, or NATEL payment possibilities (CHF 5.00 30 min. / CHF 19.00 4 hrs / CHF 30.00 1 day (24 hrs))).

### **Davos Congress**

Promenade 67

CH-7270 Davos Platz

phone +41 (0)81 415 21 60

fax +41 (0)81 415 21 69

<http://www.davos.ch/wing-c-001-02000103-en.htm>

### ***Registration desk / Symposium secretariat***

The registration desk is located at the main entrance of the Congress Centre. You may register there any time during the conference. Truus van der Hoef (WUR, NL) will be running the registration desk with the support of students from RSL. The symposium secretariat may be able to help you to organize your stay in Davos and assist you with your needs around the symposium.

### **Information for presenters**

We kindly ask presenters to provide their oral presentations as MS PowerPoint or Adobe PDF file prior to the session to the chairperson listed in the programme. We support USB sticks and drives, as well as CD-ROMs for data transfer.

### **Information for poster sessions**

Posters will be on display during the whole conference period. Please make sure that your poster is hanging on the indicated spot in the Foyer C1 corresponding to reference number given in the programme. Posters of the size A0 (Portrait: 841 mm (w) x 1189 mm (h)) are supported. Poster scheduled for the Interactive poster session I should be on display no later than Tuesday, March 13<sup>th</sup> 2007, 19:00, poster for the interactive poster session II no later than Wednesday, March 14<sup>th</sup> 2007, 12:00.

## ***Social Programme***

### **Excursion: Physikalisch-Meteorologisches Observatorium Davos / World Radiation Center – PMOD / WRC**

The "Physikalisch-Meteorologisches Observatorium Davos" (PMOD) was founded in 1907 by Carl Dorno as a privately operated institute with the objective to find out why tuberculosis patients were better cured in Davos than elsewhere. The most obvious climatic difference of a station in the Alps compared to one at lower elevations, as e.g. the Baltic sea shore where Dorno originated from, is obviously the radiation environment: the direct solar radiation is much more intense whereas the sky radiance of the dark-blue sky is of lower intensity. With this in mind, Dorno started 1909 operational measurements of the direct solar irradiance, initiating the world's longest and still continuing time series of this kind. Moreover, he started investigating the biologically active ultra-violet radiation - then called Dorno Radiation, what is today UV-B. With his worldwide famous solar and UV radiation measurements he has set the corner-stones for the PMOD which continued his work as an internationally recognized center for research in radiation measurements and instrumentation. Since 1926 PMOD is embedded in the private foundation "Schweizerisches Forschungsinstitut für Hochgebirgsklima und Medizin" (SFI).

In 1971 the PMOD was designated by the World Meteorological Organization (WMO, Geneva) to serve as a *World Radiation Center*. The operation of the WRC was offered by the Swiss government to World Meteorological Organization (WMO, Geneva) as a contribution of Switzerland to the World Weather Watch Program.

A further service was added in 1996 with the operation of the *World Optical depth Research and Calibration Center* (WORCC), a Swiss contribution to the Global Atmosphere Watch of WMO with the following terms of reference:

- Develop accurate radiometric references for spectral solar radiometry used to determine optical depth (as in the case of the World Radiometric Reference for total solar irradiance radiometry);
- Develop procedures to ensure world-wide homogeneity of optical depth measurements by e.g. providing transfer standards for precision filter radiometry (formerly called sunphotometry);
- Develop and test new instrumentation and methods for the determination of optical depth;
- Implement a trial phase at the GAW GLOBAL OBSERVATORIES with Precision Filter Radiometers (PFR) to test methods for optical depth determination and calibration transfer;
- Develop relevant quality control procedures in cooperation with the GAW Quality Assurance/Science Activity Centers;
- Training of operators of Precision Filter Radiometers.

### **Research Activities**

- Development of instruments and calibration procedures for absolute total and spectral solar and long-wave radiometry;
- Investigation of the solar total irradiance, its spectral distribution and variability for global climate research, solar physics and helioseismology (VIRGO Experiment);
- Investigation of the radiation within the atmosphere and at the ground for the determination of its spectral distribution and variability in the UV, for diagnostics of the atmospheric composition and aerosol content as well as for the determination of the surface radiation budget within the ASRB program.



*Location of the pmod / wrc in Davos*

pmod / wrc  
 Dorfstrasse 33  
 CH – 7260 Davos Dorf  
 Phone +41 81 417 51 11

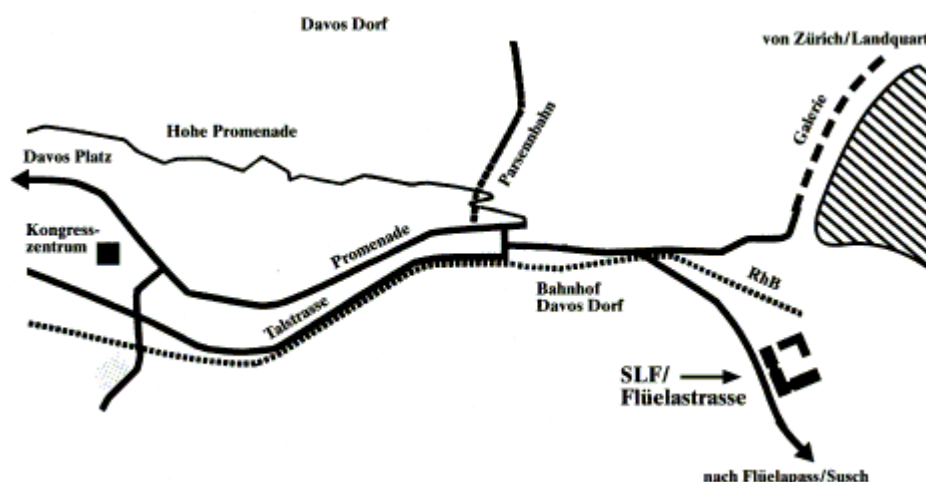
### **Excursion: Swiss Federal Institute for Snow and Avalanche Research (Davos) – SLF**

The Swiss Federal Institute for Forest Snow and Landscape Research (WSL) focuses on the use and protection of landscapes and habitats. Being a part of the ETH domain, the particular function of the research institute is to act as a bridge between pure theoretical science and the practical implementation of scientific findings.

WSL research aims at finding ways to sustainably manage landscapes and forests for maximum benefit to people's quality of life and to handle the natural hazards that typically occur in mountainous countries in the best possible ways for maximum protection at affordable costs. WSL research maintains an international top position and provides the fundamental knowledge for sustainable environmental policies in Switzerland.

In cooperation with partners in the economy, science and society at large, WSL develops strategies to solve problems that are relevant to society. The interdisciplinary and transdisciplinary approach to a research that is problem oriented with a view to practical solutions is a particular strength of WSL. WSL employs around 500 people in Birmensdorf, Davos, Lausanne and Bellinzona and it has a budget of about 65 million Swiss francs.

The SLF is one of the research stations of WSL located in Davos. SLF focuses on research of snow properties and the snowpack as well as avalanche forming and protection.



*Location of the SLF in Davos*

Eidg. Institut für Schnee und Lawinenforschung (SLF)  
 Flüelastrasse 11  
 CH – 7260 Davos Dorf  
 Phone +41 81 4170 111

### **Workshop: RAMI On-line Model Checker (ROMC)**

The RAMI On-line Model Checker (ROMC) is a web-based tool allowing for the autonomous evaluation of canopy reflectance models against a reference data set established during the third phase of RAMI.

The Radiative transfer Model Intercomparison (RAMI) exercise was first launched in 1999, and then again in 2002 and 2005. RAMI aims at evaluating the performance of canopy reflectance models in absence of any absolute reference truth. It does so by comparing models over a large ensemble of test cases under a variety of spectral and illumination conditions. A series of criteria can be applied to select an ensemble of mutually agreeing 3-D Monte Carlo models to provide a surrogate truth against which all other models can then be compared.

The RAMI Online model checker (ROMC) automates this process by allowing both model developers and users to evaluate the performance of their canopy reflectance models a) against previous RAMI test cases (whose results have already been published in the literature), and b) against test cases that are similar to the RAMI cases, but for which no results will be known a priori. As such the ROMC allows models to be "debugged" and/or "validated" autonomously on a limited number of test cases.

ROMC-certified graphics that document a model's performance can be downloaded for future use in scientific presentations and/or publications.

The workshop will take place in the Café Chamonix in the Congress Centre and the instructor is J.-L. Widlowski (JRC, I).

### **Event: Skiing**

The remote sensors on skis event is taking place in the Parsenn skiing area (<http://www.parsenn.ch/?lang=en>) in Davos - on some of the oldest skiing slopes of Switzerland. The cable car starts from Promenade 157, Davos Dorf (see Davos City Map, square M2, No. 157), at 5 min bus riding distance (about 15-20 min walking distance) from the congress centre.

All involved costs (lift ticket, rent of skiing equipment) have to be covered by the participants (self pay). The participation at this event is on your own risk (but we will of course stay on the safe



prepared runs all time and highly recommend following this rule also when you are skiing on your own)!

### *Meeting point and time*

We meet on March 12 at 13.30 in front of the Parsenn railway (in skiing gear), Promenade 157 Davos Dorf, from where we will guide you to the remote sensors on skis contest. You are then free to ski as long as you wish, last possible descent from Weissfluhjoch is at 17.00, the ISPRMSRS'07 reception will start at 19.00 in the Congress Centre. On March 13, we meet at the same time (13.30) in the same place (Parsenn railway (in skiing gear), Promenade 157 Davos Dorf). You are then free to ski as long as you wish, last possible descent from Weissfluhjoch is again at 17.00, the ISPRMSRS conference dinner starts at 18.00.

### *Ticket for lifts*

Afternoon tickets (valid from 1pm) for the Parsenn skiing area (incl. Parsenn railway) are available for 42 SFR (28 Euros). All participants meeting at 13.30 in front of the Parsenn railway (Monday or Tuesday, respectively) will profit from a price reduction on their tickets of 10%.

### *Skiing gear*

Lockers for people bringing their own skis are available at the Congress Centre (you will need a CHF 2.00 coin to operate them).

The skiing equipment needs to be arranged individually, before the meeting time (13.30) in front of the Parsenn railway. The rental services confirmed that they have enough skiing gear and that reservations can directly be done once you arrive in Davos. We provide some addresses for ski rentals located in the proximity of the Parsenn railway:

Ettinger Sport Davos Dorf (just West of the Parsenn railway)

Promenade 153

7260 Davos Dorf

+41 (0)81 410 12 12

[http://www.ettinger.ch/rent\\_en.html](http://www.ettinger.ch/rent_en.html)

Paarsennsport (just East of the Parsenn railway)

Promenade 159

7260 Davos Dorf

+41 (0)81 410 10 10

<http://www.paarsennsport.ch/>

Sportgeschäft Peter Frei (2 minutes walking distance from the Parsenn railway)

Dorfstrasse 5

7260 Davos Dorf

+41 (0)81 416 26 36

Price indications (prices seem to be per day, so you could rent the evening before and have the gear stored in the shop or the Congress Centre. If you are renting 2 consecutive days, you need to indicate this on the first day and will get a lower price for the second day. Indicative (but not binding) prices are approximately:

Skis, incl. poles (Category competition – CHF 50, allrounder – CHF 38, beginner – CHF 28)

Ski shoes CHF 19/pair

Ski clothes - jacket CHF 19, trouser CHF 19

### ***Davos Weather***

Davos is located at an altitude of 1590 m.a.s.l. (46.78 N; 9.85 E). For the month of March, you may expect monthly averaged minimum temperatures of -8.5 deg C, a mean of -3.3 deg C and a max. of 2.5 deg C. The mean humidity is 73.5 % and the precipitation 61 mm (data from 2006). It is advisable to dress warm and you must expect (partly heavy) snowfall at any time.

Notes

## Overall Programme

### *Monday, March 12<sup>th</sup> 2007*

Time	Title	Location
08:00 – 09:00	Registration	Aspen
09:00 – 10:00	Opening and welcome by the organizers	Sanada 1/2
10:00 – 10:30	Plenary Session	Sanada 1/2
10:30 – 11:00	Coffee Break	Foyer C1
11:00 – 12:00	Plenary Session II	Sanada 1/2
12:00 – 14:00	Time for individual lunch	Participants choice
14:00 – 17:00	Social Programme	WRC / SLF / Café Chamonix / Ski slopes
17:00 – 19:00	Time for individual dinner	Participants choice
19:00 – 20:00	Welcome Reception	Foyer C1
20:00 – 21:20	Oral Session	Sanada 1/2

### *Tuesday, March 13<sup>th</sup> 2007*

Time	Title	Location
08:00 – 08:30	Registration	Aspen
08:30 – 10:00	Oral Session	Sanada 1/2
10:00 – 10:30	Coffee Break	Foyer C1
10:30 – 12:20	Oral Session	Sanada 1/2
12:20 – 14:00	Lunch	Participants choice
14:00 – 18:00	Social Programme	WRC / SLF / Café Chamonix / Ski slopes
14:00 – 18:00	Posters on display	Foyer C1
18:00 – 20:00	Conference dinner	Aspen
20:00 – 21:30	Interactive Poster Session I	Foyer C1

### *Wednesday, March 14<sup>th</sup> 2007*

Time	Title	Location
08:00 – 08:30	Registration	Aspen
08:30 – 09:50	Oral Session	Sanada 1/2
09:50 – 10:20	Coffee Break	Foyer C1
10:20 – 12:00	Oral Session (HYRESSA)	Sanada 1/2
12:00 – 13:00	Luncheon and posters	Aspen
13:00 – 14:40	Interactive Poster Session II	Foyer C1
13:00 – 14:40	HYRESSA Round table	Sanada 1/2
14:40 – 15:00	Coffee Break	Foyer C1
15:00 – 16:20	Oral Session	Sanada 1/2
16:20 – 17:00	Closing Session	Sanada 1/2

### *Thursday, March 15<sup>th</sup> 2007*

Time	Title	Location
08:00 – 12:00	<b>HYRESSA Workshop</b>	Central Sporthotel, Davos Vetschstube
12:00 – 13:00	Business Lunch	
13:00 – 17:00	<b>HYRESSA Progress Meeting</b>	
Time	Title	Location
09:00 – 18:00	<b>LAI and fAPAR validation under CEOS/LPV-VALERI Workshop</b>	Morosani Post Hotel, Davos

Notes

## Detailed Programme

### *Monday, March 12<sup>th</sup> 2007*

Time	Title	Speaker	Ref.
08:00 – 09:00	<b>Registration and Opening</b>		
09:00 – 09:15	Opening and welcome by the organizers	Michael Schaepman and Shunlin Liang <i>Chairs ISPRS WG VII/1</i>	
09:15 – 09:30	Welcome by ISPRS	Andrew Skidmore <i>ITC (NL); Vice-President ISPRS Commission VII</i>	
09:30 – 09:45	Welcome by Science City Davos – Cutting edge research in a remote place	Britta Allgöwer <i>Managing Director Science City Davos</i>	
09:45 – 10:00	Organization ISPMSRS'07	Mathias Kneubühler <i>Secretary ISPRS WG VII/1</i>	
<b>Introduction plenary session</b>		Chair: Klaus Itten <i>Univ. Zürich (CH)</i>	
10:00 – 10:30	The Changing Earth	Stephen Briggs <i>ESA/ESRIN (I), Head, Earth Observation Science, Applications and Future Technologies Department</i>	T1
10:30 – 11:00	Coffee Break	Offered	
11:00 – 11:20	Evolution of research orientation in the domain of spectral signatures	Gérard Guyot <i>Founder 'Spectral Signatures Conferences'</i>	T2
11:20 – 11:40	Space experiments of PMOD/WRC to measure the solar constant and the influence of the solar irradiance on the terrestrial climate	Werner Schmutz <i>Director PMOD/WRC (CH)</i>	T3
11:40 – 12:00	The VENuS mission: Earth Observation with High Spatial and Temporal Resolution Capabilities	Gérard Dedieu <i>CNES (F)</i>	T4 605
12:00 – 14:00	Time for individual lunch	Not offered	
14:00 – 18:00	Social Programme	Details see Programme	
18:00 – 19:00	Time for individual dinner	Not offered	
19:00 – 20:00	Welcome Reception	Michael Schaepman, Shunlin Liang	
<b>Surface and atmospheric anisotropy</b>		Chair: Johannes Keller <i>PSI (CH)</i>	
20:00 – 20:20	A generic aerosol-surface reflectance retrieval algorithm for MODIS	Alexei Lyapustin <i>NASA GSFC (USA)</i>	T5 611
20:20 – 20:40	Atmospheric Correction of Airborne POLDER Polarimetric Imagery Using Vectorized 6S	Christoph Borel <i>Ball Aerospace (USA)</i>	T6 712
20:40 – 21:00	CYCLOPES prototype V4 LAI, fAPAR and fCover products derived from VEGETATION and AVHRR sensors: description and validation	Frédéric Baret <i>INRA (F)</i>	T7 702
21:00 – 21:20	MERIS land surface BRDF/albedo retrieval using data fusion with MODIS BRDF and its validation	Jan-Peter Muller <i>Univ. College London (UK)</i>	T8 661



Notes

***Tuesday, March 13<sup>th</sup> 2007***

<b>Time</b>	<b>Title</b>	<b>Speaker</b>	<b>Ref.</b>
08:00 – 08:30	Registration		
	<b>Model Access and Data Assimilation</b>	Chair: Gabriela Schaepman-Strub <i>ESA External Fellow (WUR, KNMI) (NL)</i>	
08:30 – 09:00	The RAMI On-line Model Checker (ROMC)	Jean-Luc Widlowski <i>JRC (I)</i>	T9 628
09:00 – 09:20	A Framework of a Remote Sensing Data Assimilation System	Shunlin Liang <i>Univ. Maryland (USA)</i>	T10 723
09:20 – 09:40	Assimilating reflectance data into a ecosystem model to improve estimates of terrestrial carbon flux.	Tristan Quaife <i>Centre for Terrestrial Carbon Dynamics (UK)</i>	T11 624
09:40 – 10:00	Preparing for the assimilation of remote sensing products by climate models	Bernard Pinty <i>JRC (I)</i>	T12 617
10:00 – 10:30	Coffee Break		
	<b>LOP and Canopy Modelling</b>	Chair: Stéphane Jacquemoud <i>Univ. De Paris 7 (F)</i>	
10:30 – 11:00	A Leaf Optical Properties Model Accounting for Differences between The Two Faces	Kai Ma <i>INRA (F)</i>	T13 708
11:00 – 11:20	Modelling Canopy reflectance with spectral invariants	Philip Lewis <i>Univ. College London (UK)</i>	T14 625
11:20 – 11:40	Approximating photon recollision probability in vegetation canopies	Matti Möttus <i>Tartu Observatory (EST)</i>	T16 527
11:40 – 12:00	Spectral invariant behaviour of a complex 3D forest canopy	Mathias Disney <i>Univ. College London (UK)</i>	T15 630
12:00 – 12:20	Retrieval of Coniferous Canopy Chlorophyll Content from High Spatial Resolution Hyperspectral Data	Zbyněk Malenovský <i>ISBE (Cz)</i>	T17 608
12:20 – 14:00	Lunch	Not offered	
14:00 – 18:00	Social Programme	Details see programme	
14:00 – 18:00	Posters on display	Details see programme	
18:00 – 20:00	Conference dinner	Michael Schaepman, Shunlin Liang	
	<b>Interactive Poster Session I</b>	Chair: Matti Möttus <i>Tartu Observatory (EST)</i>	
20:00 – 21:30	Interactive Poster Session I	Details see programme	P1- P48

***Interactive Poster Session I*****Tuesday, March 13<sup>th</sup> 2007, 20:00 – 21:30**

Topic	Title	Presenter	Poster/ID
<b>Interactive Poster Session I</b>		Chair: Matti Möttöus <i>Tartu Observatory (EST)</i>	
<b>Interactive Poster Session I</b>	Normalization of microwave time series observations (1979 - 2005) : surface melting and temperature analysis	Alain Royer (contact), Ghislain Picard, Michel Fily	P1 / 461
	Intercalibration of Vegetation Indices - an Update	Michael STEVEN (contact), Timothy MALTHUS, Frédéric BARET	P2 / 525
	Space-Time Series of MODIS Snow Cover Products for Hydrologic Science	Jeff Dozier, Thomas Painter (contact), James Frew	P3 / 263
	Pyrite mine wastes monitoring with hyperspectral data as a tool to detect climate change	Asuncion Rianza (contact), Cindy Ong, Andreas Mueller	P4 / 520
	Using Reflectance Spectroscopy for Monitoring Settled Dust in an Indoor Environment	Eyal Ben-Dor (contact), Sandra Chudnovski	P5 / 220
	Multitemporal Unmixing of MERIS FR Data	Raul Zurita-Milla (contact), Luis Gomez-Chova, Jan Clevers, Michael Schaepman, Gustavo Camps-Valls	P6 / 561
	A New Multitemporal Classification Approach for Land Cover Mapping in Iran,by Using Hyperspectral Modis Data	Abdolreza Ansari Amoli (contact), Abbass Alimohammadi	P7 / 636
	Classification of multispectral ASTER imagery in the archaeological survey for settlement sites of the Near Ea	Bjoern Menze (contact), Jason Ur	P8 / 644
	Spatio-temporal modelling of grassland degradation and small mammal distributions using MODIS NDVI time-series	Christopher Marston (contact), Richard Armitage, Mark Danson, Alberto Ramirez, Phillip Craig	P9 / 564
	Web-based model for analysis of time series remotely sensed data	Alberto Ramirez (contact), Richard Armitage, Mark Danson, Christopher Marston, Ebenezer Ogunbadewa, Marta Yebra	P10 / 638
	Comparison of Feature Selection Techniques for SVM Classification	Anthony Gidudu (contact), Heinz Ruther	P11 / 524
	Canopy Water Content Retrieval from Hyperspectral Remote Sensing	Jan Clevers (contact), Lammert Kooistra, Michael Schaepman	P12 / 707
	Development of an inversion code, ICARE, able to extract urban areas ground reflectances	Sophie Lachérade (contact), Christophe Miesch, Didier Boldo, Xavier Briottet, Christophe Valorge, Hervé Le Men	P13 / 341
	Reflectance Retrieval in Shade using Adjoint Radiosity	Christoph Borel (contact)	P14 / 710
	Retrieval of aerosol optical depth using multi-date and constant viewing angle images from Formosat2 and VENμS	Olivier Hagolle (contact), Gérard Dedieu, Vincent Debaecker	P15 / 607
	Estimating vegetation parameters of cereals using an ASTER 1A image	Sánchez Nilda (contact), González Raúl, Martínez-Fernández José, Prado Jesús	P16 / 120
	Mapping chlorophyll-a in Swiss lakes with MERIS data	Daniel Odermatt (contact), Jens Nieke, Mathias Kneubühler, Klaus Itten	P17 / 663
	Anomaly detection algorithms for hyperspectral imagery	Seyyed Reza Soofbaf (contact), Hamed Fahimnejd, Mohamad Javad Valadan Zoej, Barat Mojaradi	P18 / 716

Determining the Directional Response and Field of View of Two Field Spectroradiometers	Alasdair Mac Arthur (contact)	P19 / 482
The effect of noise in AHS thermal bands in the retrieval of pixel temperature	Eduardo de Miguel (contact), Rafael Garcia, Alix Fernandez-Renau	P20 / 521
Hyperspectral image filtering and implications for environmental spectra related to mining contamination: exam	Lidia Quental (contact), António Sousa, Stuart Marsh	P21 / 563
Preprocessing EO-1 Hyperion hyperspectral data	Hamed Fahimnejad (contact), Seyyed Reza soofbaf, Abbas Alimohammadi, Mohammad Javad Valadan zoej	P22 / 602
Tomographic SAR imaging of forested areas by time-domain back-projection processing	Othmar Frey (contact), Felix Morsdorf, Erich Meier	P23 / 760
Assimilation of snow depth maps for improved runoff nowcasting	Massimiliano Zappa (contact), Annina Morger, Tobias Jonas, Andreas Stoffel, Nando Foppa	P24 / 612
Intercomparison between modelled and satellite-derived snow cover extent within the alpine and subalpine zone	Nando Foppa <i>meteo swiss (CH)</i>	P25 / 484
Modeling microwave brightness temperature in Antarctica.	Ghislain Picard (contact), Ludovic Brucker, Michel Fily	P26 / 526
Regional mapping of plant functional types in river floodplain ecosystems using airborne imaging spectroscopy	Lammert Kooistra (contact), Wieger Wamelink, Han Van Dobben, Michael Schaepman	P27 / 603
Crop model data assimilation with the Ensemble Kalman filter for improving regional crop yield forecasts	Allard de Wit (contact), Kees van Diepen	P28 / 662
Fusion of Imaging Spectrometer and LIDAR data using Support Vector Machines for land cover classification	Benjamin Koetz (contact), Felix Morsdorf, Thomas Curt, Sebastian Schiefer, Laurent Borgniet, Daniel Odermatt, Samuel Alleaume, Corinne Lampin, Marielle Jappiot, Britta Allgöwer	P29 / 622
The relevance and use of Atmospheric Data Access for the Geospatial User Community (ADAGUC)	Michael Schaepman (contact), Marc Hoogerwerf, John van der Vegte, Frans van der Wel, Wim Som de Cerff, Richard van Hees, Ben Domenico, Stefano Nativi, Olga Wilhelmi	P30 / 820
Spectral Linear Mixing Model for Endmember Extraction Using High Spatial Resolution and Hyperspectral Data	Yuan Zeng (contact), Michael E. Schaepman, Bingfang Wu, Jan G.P.W. Clevers, Arnold K. Bregt	P31 / 440
Seasonal comparison of carbon flux estimates from C-TESSEL model and Moderate Resolution Imaging Spectroradiometer (MODIS) over several biomes	Li Jia (contact), Voogt, M.H., Jacobs, C.M.J., Van den Hurk, B.J.J.M., De Wit, A., Moors, E.	P32 / 860
Combination of Raman Lidar and Microwave Radiometer Sensed Water Vapour Data	Marc Schneebeli (contact), Ulla Wandinger, Ina Matthis, Emmanuel Brocard, Christian Mätzler	P33 / 533
Abilities of DEMETER Satellite in Observation of Physical Signatures Perturbation of Ionosphere Associated ...	Aida Omani (contact), Mohammad Reza Saradjian	P34 / 404
Albedo Assessment and Evaluation over Arctic Siberian Tundra	Gabriela Schaepman-Strub (contact), Martin Claverie, Thomas Painter, Michael Schaepman	P35 / 720
Environmental change detection in mire ecosystems: Assessing tree growth and shrub encroachment using LiDAR da	Lars Waser (contact), Manos Baltsavias, Henri Eisenbeiss, Armin Gruen, Meinrad Küchler, Patrick Thee	P36 / 560

Towards Near-real Time Global Flood Detection System	Zsafia Kugler (contact), Tom De Groeve), G. Robert Brakenridge, Thierry Benoist	P37 / 402
Application to MISR land BRFs of the RPV model inversion package to assess environmental patterns	Thomas Lavergne (contact), Thomas Kaminski, Bernard Pinty, Malcolm Taberner, Nadine Gobron, Michel Verstraete, Michael Vossbeck, Jean-Luc Widlowski, Ralf Giering, Ophelie Aussedat	P38 / 618
Validation of remote sensing NDVI time series with ground based measurements from the automated climate station network IMIS	Fabio Fontana (contact), Christian Rixen, Tobias Jonas, Stefan Wunderle	P39 / 640
Towards Global Mapping of Irrigated Agriculture	Mutlu Ozdogan, Garik Gutman (contact)	P40 / 140
Classification of Tree and Shrub Species in KSU Research and Application Forest in Kahramanmaras, Turkey	Abdullah Emin Akay (contact), Ismail Rakip Karas, Recep Gundogan	P41 / 480
A completely automatic spectral rule-based preliminary classification of calibrated Landsat TM and ETM+ images	Andrea Baraldi (contact), Dario Simonetti, Virginia Puzzolo, Stefano Natali	P42 / 562
Alternative application of the k-NN method for mapping forest cover type	Caterina Gagliano (contact), Flora De Natale, Francesca Incerti, Fabio Maselli	P43 / 610
Shadowed Feature Classification in Hyperspectral Images	S.Mohammad Shahrokhy (contact)	P44 / 180
Radiative Transfer Model Inversion Based on Multi-temporal CHRIS/PROBA Data for LAI Estimation	Benjamin Koetz (contact), Mathias Kneubühler, Sylvia Huber, Jürg Schopfer, Frédéric Baret	P45 / 621
Topsoil Mapping Using Hyperspectral Sensing	Thomas Selige (contact), Urs Schmidhalter, Jürgen Böhner	P46 / 724
Application of High-Resolution Thermal Infrared Remote Sensing to assess Land Surface Temperature and Emissivi	JOSÉ A. SOBRINO (contact), J. C. JIMENEZ-MUÑOZ, M. GOMEZ, A. BARELLA-ORTIZ, G. SORIA, Y. JULIEN, M.M. ZARAGOZA-IVORRA, J. A. GÓMEZ, E. de MIGUEL, M. JIMENEZ, B. SU, W. TIMMERMANS, J. MORENO, L. GUANTER, R. BIANCHI	P47 / 627
PAR@METER: a Wireless System for fAPAR and LAI Continuous Monitoring	Frédéric Baret (contact), Georges Billard, Olivier Marloie, Anne Labouret	P48 / 701



**Wednesday, March 14<sup>th</sup> 2007**

Time	Title	Speaker	Ref.
08:00 – 08:30	Registration		
	<b>Cold regions and snow</b>	Chair: Petri Pellikka <i>Univ. Helsinki (Fin)</i>	
08:30 – 08:50	Circumpolar assessment of the relationship between infrared vegetation indices and leaf area index in forest	Richard Fernandes <i>Natural Resources (CDN)</i>	T18 643
08:50 – 09:10	Stochastic radiative transfer model for mixture of discontinuous vegetation canopies	Nikolay Shabanov <i>Boston University (USA)</i>	T19
09:10 – 09:30	Assimilation of MODIS snow data in a detailed model of Alpine snow dynamics and snow hydrology	Henning Löwe <i>SLF (CH)</i>	T20 641
09:30 – 09:50	Space-Time Series of MODIS Fractional Snow Cover Products	Thomas Painter <i>NSIDC (USA)</i>	T21 262
09:50 – 10:20	Coffee Break		
	<b>HYRESSA</b>	Chair: Lammert Kooistra <i>Wageningen UR (NL)</i>	
10:20 – 10:40	GEO (Group on Earth Observations) and its Global Earth Observation System of Systems (GEOSS)	Michael Rast <i>GEO Secretariat (CH)</i>	T22 H1
10:40 – 11:00	Plans for the U.S. National Ecological Network:-The contribution of remote sensing	Susan Ustin <i>UC Davis (USA)</i>	T23 H2
11:00 – 11:20	ESA Earth Observation User Services	Stephen Briggs <i>ESA/ESRIN (I)</i>	T24 H3
11:20 – 11:40	Production and distribution of NASA MODIS Remote Sensing Products	Robert Wolfe <i>NASA GSFC (USA)</i>	T25 H4
11:40 – 12:00	User-driven requirements of the European Hyperspectral Remote Sensing Community	Jens Nieke <i>Univ. Zürich (CH)</i>	T26 705
12:00 – 13:00	Luncheon and posters	Offered	
	<b>Interactive Poster Session II</b>	Chair: Zbyněk Malenovský <i>ISBE (Cz)</i>	
13:00 – 14:40	Interactive Poster Session II		P49 – P97
	<b>HYRESSA Round Table</b>	Chair: IIs Reusen <i>VITO (B)</i>	
13:00 – 14:40	HYRESSA Round table	IIs Reusen <i>VITO (B)</i>	
14:40 – 15:00	Coffee Break		
	<b>Advanced Applications and LIDAR</b>	Chair: Jon Ranson <i>NASA/GSFC (USA)</i>	
15:00 – 15:20	A Bayesian optimisation approach for model inversion of hyperspectral-multidirectional observations: the balance with <i>a priori</i> information	Wout Verhoef <i>NLR (NL)</i>	T27 241
15:20 – 15:40	Three-dimensional forest canopy architecture from terrestrial laser scanning	Mark Danson <i>Univ. Salford (UK)</i>	T28 642
15:40 – 16:00	Modeling of small footprint airborne laser scanning returns using ray-tracing and L-systems	Felix Morsdorf <i>Univ. Zurich (CH)</i>	T29 725
16:00 – 16:20	Forest Vertical Structure and Biomass Estimation from GLAS Data	Jon Ranson <i>NASA GSFC (USA)</i>	T30 718
	<b>Closing Session</b>	Chair: Andrew Skidmore <i>ITC (NL)</i>	
16:20 – 17:00	Closing Session	Michael Schaepman, Shunlin Liang <i>Chairs ISPRS WG VII/1</i>	

***Interactive Poster Session II*****Wednesday, March 14<sup>th</sup> 2007, 13:00 – 14:40**

Topic	Title	Presenter	Poster/ID
<b>Interactive Poster Session II</b>		Chair: Zbyněk Malenovský <i>ISBE (Cz)</i>	
<b>Interactive Poster Session II</b>	Angular Unmixing of Photosynthetic and Non-Photosynthetic Vegetation within a Coniferous Forest Using CHRIS-PROBA	Jochem Verrelst (contact), Raul Zurita-Milla, Benjamin Koetz, Michael Schaepman	P49 / 522
	A Study of Surface Directional Shapes Using MISR	John Martonchik (contact), Michael Bull, Van Dang	P50 / 520
	Modelling reflectance of urban chestnut trees: A sensitivity analysis of model inversion for single trees	Alexander Damm (contact), Patrick Hostert	P51 / 523
	CYCLOPES Prototype V4 LAI, fAPAR and fCover Products Derived from VEGETATION and AVHRR Sensors: Description and Validation	Frédéric Baret (contact), Marie Weiss, Patrice Bicheron, Roselyne Lacaze, Marc Leroy	P52 / 702
	Large Seasonal Swings in Leaf Area of Amazon Rainforests	Ranga Myneni <i>Boston Univ. (USA)</i>	P53 / 629
	Plant biochemical maps of forage quality	Andrew Skidmore (contact), Jelle Ferwerda, Onesimo Mutanga, Sipke van Wieren, Mike Peel, Rina Grant, Herbert Prins	P54 / 540
	Airborne Hyperspectral Scanner (AHS) Spectral Emissivity Retrieval in 8-13 $\mu\text{m}$	Marcos Jiménez (contact), Eduardo de Miguel, José A. Gómez, José A. Sobrino, Juan C. Jiménez-Muñoz, Javier Chico, Elena Prado, Cristina Robles	P55 / 613
	Physical modelling of camera RGB responses for application in non-destructive leaf chlorophyll imaging	Frank Veroustraete (contact), Willem W. Verstraeten, Koen Hufkens, Bert Gielen, Filip Colson	P56 / 660
	Simulation studies of the effect of forest spatial structure on InSAR signature	Guoqing Sun, Dawei Liu, Jon Ranson (contact), Benjamin Koetz	P57 / 719
	Correction of Altitude Effects in Measurements of the Depth of A and B Atmospheric Oxygen Absorption Bands.	Fabrice Daumard (contact), Yves Goulas, Abderrahmane Ounis, Roberto Pedros, Ismael Moya	P58 / 722
	Polarization of light from leaves measured from 0.5 - 1.6 $\mu\text{m}$	V.C. Vanderbilt (contact), S.L. Ustin, C.S.T. Daughtry, J.A. Greenberg	P59 / 713
	Using Monte-Carlo ray tracing to investigate the measurement of forest parameters with the Echidna <sub>2</sub> laser scanner	Steven Hancock (contact), Philip Lewis, Jan-Peter Muller, Mathias Disney	P60 / 706
	A biophotonic physiological plants sensor (Field radiometer for canopy remote sensing)	J.P. Frangi, Stephane Jacquemoud, G. de Rosny, Elian Conejo (contact)	P61 / 840
	Influence of Local Incidence Angle Effects on Ground Cover Estimates	Martin Bachmann (contact), Stefanie Holzwarth, Andreas Müller	P62 / 616
	Simulating canopy gap fraction of complex forest scenes	Marion Pfeifer, Mathias Disney (contact), Philip Lewis	P63 / 632
	Comparing three canopy reflectance models with hyperspectral multi-angular satellite data	Martin Schlerf (contact), Wout Verhoef, Joachim Hill, Henning Buddenbaum, Clement Atzberger, Andrew Skidmore	P64 / 340

Forest Reflectance Modeling in the Arctic Region: Results from a Case Study in Finland	Miina Rautiainen (contact), Pauline Stenberg, Terhikki Manninen, Matti Möttöus, Pekka Voipio	P65 / 342
Simultaneous Retrieval of Aerosol and Surface Optical Properties using Multi-angle Imaging SpectroRadiometer	Johannes Keller (contact), Andre Prevot, Stephan Bojinski	P66 / 500
An advanced leaf optical properties model including photosynthetic pigments	Jean-Baptiste FERET (contact), Greg ASNER, Christophe FRANCOIS, Roberta MARTIN, Susan USTIN, Stephane JACQUEMOUD	P67 / 541
The Role of Image Properties in Determining Change Detection Accuracy	Timothy Warner (contact), Abdullah Almutairi, David Campagna, M. Duane Nellis	P68 / 711
Contact spectroscopy for determination of stratigraphy of snow optical grain size	Thomas Painter (contact), Noah Molotch, Maureen Cassidy, Mark Flanner, Konrad Steffen	P69 / 261
A Method for Measuring the Permittivity of Artificial Frozen Soil Using Network Analyzer	Shaojie Zhao (contact), Lixin Zhang, Liying Li	P70 / 531
Estimating Clear-Sky Land Surface Longwave Radiation Budget from MODIS Data	Wenhui Wang (contact), Shunlin Liang	P71 / 680
Soil Moisture Experiments 2005: Passive Microwave Polarimetric Signatures of Soil Moisture and Vegetation	Thomas Jackson (contact)	P72 / 160
Reference Spectrometry for Calibration of Optical Earth Observation Systems	Saber Salim (contact), Nigel Fox, Emma Woolliams, Rainer Winkler, Heather Pegrum, Tong Sun, Ken Grattan	P73 / 300
Implementation of Biophysical Factors into the land surface and atmosphere interaction model	Venkat Lakshmi (contact), Bryan Hong, Fei Chen, Eric Small	P74 / 100
Estimation of forest stand parameters in density classes in arid and semi-arid regions using Landsat ETM+ data	Farzin Naseri (contact), Ali A. Darvishsefat, Hooshang Sobhani, Manuchehr Namiranian	P75 / 240
The Use of Spectral Signatures in Extracting Information from Water Quality Parameters in the Lake Urmia, IRAN	Seyd Kazem Alavipanah, Reza Amiri (contact), Kamal Khodaei	P76 / 260
Characterizing Soil Salinity and Sodicity in Irrigated Agricultural Land Using Ground-Based Reflectance	Abdou Bannari (contact), Anne-Marie Guedon, Abderrazak El-Harti, Mohammed Frahi	P77 / 281
Quantitative Assessment of Soil Parameters in Western Tajikistan using a Soil Spectral Library Approach	Bruno Seiler (contact), Mathias Kneubühler, Bettina Wolfgramm, K.I. Itten	P78 / 528
Leaf Area Index estimates obtained for mixed forest using hemispherical photography and HyMap data	Anja Visscher von Arx (contact), Silvia Huber, Mathias Kneubuehler, Klaus I. Itten	P79 / 600
Estimating Nitrogen Concentration from Directional CHRIS/PROBA Data	Silvia Huber (contact), Mathias Kneubühler, Benjamin Koetz, Jürg T. Schopfer, Niklaus E. Zimmermann, Klaus I. Itten	P80 / 601
Airborne Hyperspectral Scanner (AHS) a priori Mapping Capacity for the Doñana Biological Reserve Shrublands	Marcos Jiménez (contact), Ricardo Díaz-Delgado, Patrick Vaughan, Alix Fernández Renau, Oscar Gutiérrez de la Cámara, Elena Prado	P81 / 614
Elucidating the interaction of plants in the carbon dioxide cycle using airborne hyperspectral reflectance measurements	Michael Eiden (contact), Sebastian Schiefer, Jan Schween, Christoph Gerbig, Bruno Neininger, Olivier Traullé, Heiner Geiss, Uwe Rascher	P82 / 619

Spatial variability of the spectral properties of forest structures over the Amazon	Liana Anderson (contact), Yadvinder Malhi, Luiz Aragao, Yosio Shimabukuro	P83 / 635
Hyperspectral Remote Sensing for Seasonal Estimation of Aboveground Biomass in Swiss Grassland Habitats	Achilleas Psomas (contact), Mathias Kneübhler, Klaus Itten, Niklaus Zimmermann	P84 / 639
Estimation of Surface Shortwave Radiation Budget from MODIS data	Hye-Yun Kim (contact), Shunlin Liang	P85 / 703
Effect of Cultivar Specificities on The Radiometric Response: Quantification and Consequences for Biophysical Variables Estimation in Wheat Crops	Kai MA (contact), Frédéric Baret, Guillaume Jubelin, Philippe Burger, Bruno Roux, Sylvain Labbé, Jean Marie Nolot	P86 / 709
Classification of Blanket Mire Microhabitats using Field and Imaging Spectroscopy	John Dowens (contact), Tim Malthus, Lisa Belyea	P87 / 715
The POSTEL Land Surface Thematic Centre	Marc LEROY (contact), Patrice BICHERON, Roselyne LACAZE, Fernando NINO, Frédéric BARET, Jean-Louis ROUJEAU, Olivier HAGOLLE, Gérard DEDIEU, Fabienne MAIGNAN, François- Marie BREON	P88 / 200
HYRESSA: Towards an Improved Access to Hyperspectral Data in Europe	Ils Reusen (contact)	P89 / 581
Development of the Gonio RAdiometric Spectrometer System to conduct multi-angular measurements of the surface	Heather Pegrum (contact), Nigel Fox, Edward Milton, Magdalena Chapman	P90 / 280
Dual Field-of-View Goniometer System FIGOS	Juerg Schopfer (contact), Stefan Dangel, Mathias Kneubühler, Klaus I. Itten	P91 / 623
The FLuorescence EXplorer (FLEX) Mission - Mission Objectives and derived requirements	Michael Berger (contact), Jose Moreno, and The FLEX Team	P92 / 880
Spatial Variability and Altitude effects of passive chlorophyll fluorescence measurements over La Mancha (Spain) fields	ISMAEL MOYA (contact), FABRICE DAUMARD, NICOLAE MOISE, YVES GOULAS, ABDERRAHMANE OUNIS	P93 / 714
The Characterisation of Heather Foliage and Canopies by Hyperspectral Reflectance	Alasdair Mac Arthur (contact)	P94 / 483
Comparison of different ground techniques to map leaf area index of Norway spruce forest canopy	Lucie Homolova (contact), Zbynek Malenovsky, Jan Hanus, Ivana Tomaskova, Marcela Dvorakova, Radek Pokorny	P95 / 532
Validation of FAPAR products derived from optical sensors: method and results.	Nadine Gobron, Bernard Pinty (contact), Ophelie Ausseidat, Malcolm Taberner, Frederic Melin, Thomas Laverigne, Monica Robustelli, Jean-Luc Widlowski	P96 / 615
The NCAVEO 2006 Cal/Val Experiment	Edward Milton (contact)	P97 / 717

**Additional Workshops****Wednesday, March 14<sup>th</sup> 2007 – HYRESSA dinner**

Time	Title	Speaker	Comment	Ref.
19:00 – open	HYRESSA dinner	Offered, by invitation only	Central Sporthotel, Davos Restaurant Bündnerstübli	

**Thursday, March 15<sup>th</sup> 2007 – HYRESSA Workshop**

Time	Title	Speaker	Comment	Ref.
08:00 – 08:15	Registration		Central Sporthotel, Davos Vetschstube	
08:15 – 08:30	Welcome and Introduction	Lammert Kooistra and Michael Schaepman <i>WUR (NL)</i>		
08:30 – 08:45	The role of protocols and standards in hyperspectral data acquisition	Jose-Antonio Gomez-Sanchez <i>INTA (Sp)</i>		H1
08:45 – 09:30	Discussion	<i>All</i>		
09:30 – 10:00	Coffee Break	<i>Offered</i>		
10:00 – 10:15	Opportunities for the development of a European hyperspectral research infrastructure	Tim Malthus <i>Univ. Edinburgh (UK)</i>		H2
10:15 – 10:30	Trans-national Access at Equal Terms to national research infrastructures in Europe: The case of research aircraft for environmental studies	Jean-Louis Brenguier <i>METEO France (F)</i>		H3
10:30 – 11:15	Discussion	<i>All</i>		
11:15 – 11:45	Research Infrastructures in FP7	Brigitte Weiss <i>Scientific Officer EU Research Infrastructures</i>		H4
11:45 – 12:00	Closing remarks and conclusions	Lammert Kooistra <i>WUR (NL)</i>		H5
12:00 – 13:00	Business Lunch	<i>Offered</i>	Central Sporthotel, Davos Restaurant Bündnerstübli	
13:00 – 15:30	HYRESSA Progress Meeting I	Limited to HYRESSA project participants	Central Sporthotel, Davos Vetschstube	
15:30 – 16:00	Coffee Break	<i>Offered</i>		
16:00 – 17:00	HYRESSA Progress Meeting II	Limited to HYRESSA project participants		



Notes

**Thursday, March 15<sup>th</sup> 2007 – LAI and fAPAR validation under CEOS/LPV-VALERI**

Time	Title	Speaker	Comment	Ref.
			Morosani Post Hotel, Davos <a href="http://www.morosani.ch">http://www.morosani.ch</a>	
09:00 – 9:20	Welcome, Introduction, Objectives of the meeting, Relation to GEO	Frédéric Baret <i>INRA (F)</i>	The objectives of the workshop are to identify the several on going and planned validation activities and discuss methodological and more strategic aspects.	L1
09:20 – 12:00	Ongoing direct validation activities	Participants	To be filled by short contributions (about 5-10 minutes) from Pls of validation sites	L2
12:00 – 12:30	Sample results from direct validation activities	S. Garrigues, F. Baret, R. Lacaze, et al.		L3
12:30 – 14:00	Lunch Break			
14:00 – 15:00	Methodological aspects I	Participants	Ground measurements Comparison of results coming from several devices Devices for continuous monitoring of LAI and fAPAR, and productivity The clumping problem Understory problem Interaction with the flux tower community	L4
15:00 – 16:15	Methodological aspects II	Participants	Transfer functions Sampling scheme and their evaluation Choice of transfer functions depending on available information Accounting for uncertainties Uncertainties associated to local estimates	L5
16:15 – 17:30	Methodological aspects III	Participants	Aggregation at medium resolution Scale and interpolation through time Accounting for PSF Combining high temporal tower measures with moderate and high spatial resolution satellite products Evaluation of uncertainties	L6
17:30 – 18:00	General discussion	Participants	Contribution to GEO/GEOSS task Funding of activities Organization and dissemination of data Other issues	L7
18:00	End of Workshop			

Notes

## How to reach Davos

Davos located in the heart of Graubünden in the Eastern part of Switzerland.



### *How to reach Davos by Plane*

Zürich-Kloten (ZHR) is the most convenient airport to reach Davos in Switzerland. If you are flying Swiss Intl. Airlines, you may request that your luggage be shipped directly to your hotel in Davos (<http://www.zurich-airport.com/>).

Geneva-Cointrin (GVA) over 500 kilometres (310 miles) away is an alternate airport. Since in winter it is not possible to cross the Alps by train or car, you will end up coming along Zürich as well (<http://www.gva.ch>).

Engadin Airport in Samedan (SMV) might be another option, however very few flights are offered on a regular basis to Samedan (<http://www.engadin-airport.ch/>).

### *How to reach Davos by Car*

It will take about 2 hours to get to Davos by car from Zürich (145 km). You will find your way to Davos easily by taking the highway to Landquart (direction Chur).

Depending on road conditions in winter you may need tire chains once you reach Klosters.

<http://www.davos.ch/arrival-by-car-001-040200-en.htm>

### *How to reach Davos by Coach*

There are regular coach services in winter from Zürich to Davos. Tickets can be bought at the airport.

<http://www.davos.ch/arrival-by-coach-001-040206-en.htm>

### *How to reach Davos by Train*

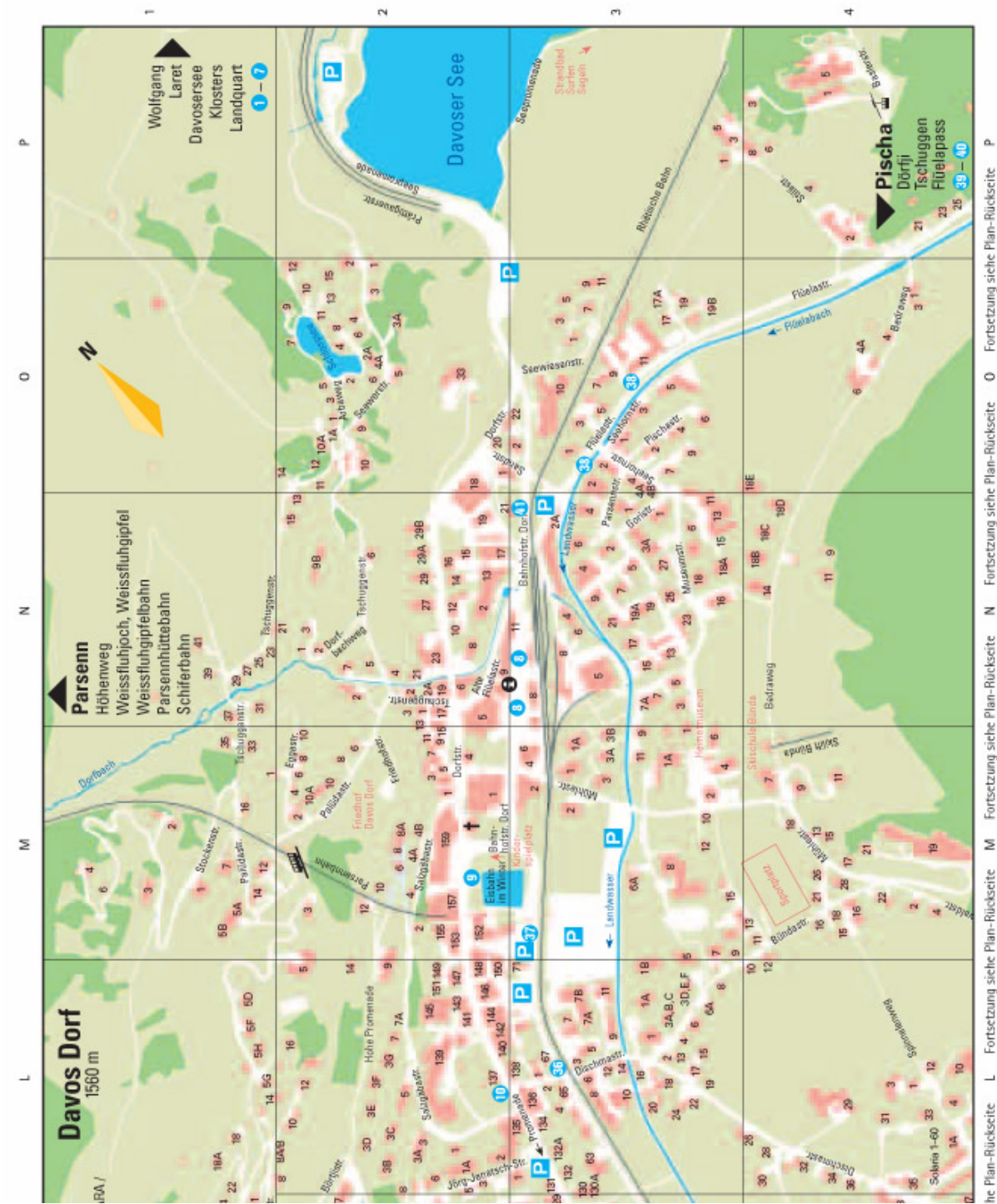
It will take about 2.5 to 3 hours to get to Davos by train from Zürich. From Geneva it will take approx. 5.5 hrs, from Basle 3.4 hrs, depending on connections.

From Zürich airport: In the airport follow the Train icons until you reach the airport train station. Buy your ticket at the counters on the right hand side. Trains bound for Zürich leave about every ten to fifteen minutes. In Zürich, change to an express train bound for Chur. In Landquart (all trains stop there) change to the Rhaetian Railway to Davos. There are two train stations in the city of Davos: Davos Dorf and Davos Platz. Don't get off earlier, e.g. In Davos Wolfgang! Please inform yourself in advance whether Davos Dorf or Davos Platz is closer to your hotel. The Congress Centre is right in between the two. If in doubt, buy your ticket to Davos Platz.

<http://www.davos.ch/arrival-by-train-001-040201-en.htm>

<http://www.sbb.ch/en/index.htm> (Swiss railway)

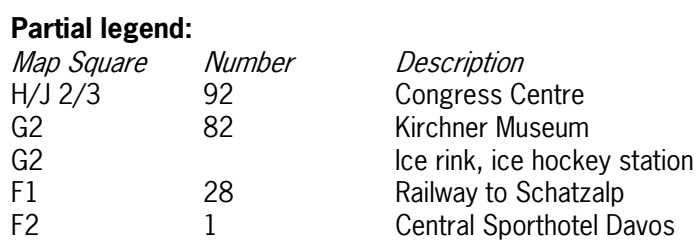
Davos – City Map



Partial legend:

Map Square	Number	Description
M2	157	Railway to Parsenn (ski area)
N3	8	Trainstation Davos Dorf
O2	33	WRC / PMOD
O3	11	SLF









**Partial legend:**

Map Square	Number	Description
D3	4	Trainstation Davos Platz
D3	11	Cable car Jakobshorn (ski area)
E2	42	Morosani Post Hotel

***ISPMSRS'07 Topics***

For ISPMSRS'07, we have solicited the submission of contributions related to physical measurements and signatures in remote sensing in the following categories (but not limited to):

- Remote sensing systems (microwave, Lidar, (hyper-)spectral, multiangular, thermal, polarization)
- Advanced preprocessing and processing of remotely sensed data
- Remote sensing data infrastructures
- Physical modelling in remote sensing
- Inversion of biogeophysical and biogeochemical variables
- Advanced methods for time series analysis in remote sensing
- Image classification methods
- Data assimilation and integration of remote sensing in dynamic process models
- Data fusion approaches based on multi-platform or multiple sensor techniques
- Integration of in situ ('SensorWeb') and remotely sensed data
- Validation of remote sensing products
- Radiative transfer based approaches
- Scaling from leaf to canopies to ecosystems
- Quantitative land use/cover change analysis
- Environmental change detection
- Remote sensing in coupled human-environmental systems
- Remote sensing methods for hydrology, carbon cycle, biochemical and –physical cycles, plant ecology, ecosystems, snow, soil moisture, agriculture, natural ecosystems, etc.
- Earth System model approaches using remote sensing

***ISPMSRS'07 Follow-up***

All submitted full papers for ISPMSRS'07 will be published in the conference proceedings. Please check out the website for submission procedures and deadlines.

ISPMSRS'07 is sponsored by



European Space Agency



HYRESSA (Contract Number 026194):  
Specific Support Action supported by the  
European Commission under the 6th  
Framework Programme



Swiss Academy of Sciences – A network of  
knowledge for the benefit of society.



International Society for Photogrammetry and  
Remote Sensing



IEEE Geoscience and Remote Sensing Society



Centre for Geo-Information, Wageningen  
University (NL)



Remote Sensing Laboratories, University of  
Zurich (CH)

No.	Ti.	Lastname	Firstname	Affiliation	Department	Address1	Address2	ZIP	City	Country	E-mail
1	Mr	Riffler	Michael	University of Bern	Department of Geography	Hallerstrasse 12		3012	Bern	Switzerland	michael.riffler@giub.unibe.ch
2	Mr	Malthus	Tim	University of Edinburgh	School of GeoSciences	Grant Institute, Kings Buildings,	West Mains Road	EH9 3JW	Edinburgh	United Kingdom	tjm@geo.ed.ac.uk
3	Ms	Giacosa	Carolina	University of Salford	School of Environment and Life Sciences	Crescent st		M5 4WT	Salford	United Kingdom	c.giacosa@salford.ac.uk
4	Mr	Schmutz	Werner	PMOD	World Radiation Center	PMOD/WRC	Dorfstrasse 33	CH-7260	Davos Dorf	Switzerland	werner.schmutz@pmodwrc.ch
5	Ms	Schmidt	Anne	Alterra	Centre for Geo-Information	droevendaalsesteeg 3A		6700AA	Wageningen	Netherlands	anne.schmidt@wur.nl
6	Mr	MacLellan	Christopher	University of Edinburgh	NERC Field Spectroscopy Facility Grant Institute	School of Geoscience	West Mains Road	EH9 3JW	Edinburgh	United Kingdom	chris.maclellan@ed.ac.uk
7	Ms	VADON	Hélène	CNES	DCT/PS/TIS	18 abenue edouard belin		31401	Toulouse	France	helene.vadon@cnes.fr
8	Mrs	Darvishzadeh	Roshanak	ITC	NRS	Hengelosestraat 99-	p.o. box 6	7500 AA	Enschede	Netherlands	darvish@itc.nl
9	Ms	Ustin	Susan	University of California, Davis	Department of Land, Air and Water Resources	One Shields Avenue		95616	Davis	United States	slustin@ucdavis.edu
10	Mr	Rast	Michael	GEO - Group on Earth Observations	Secretariat Expert Staff	7 bis, avenue de la Paix		1211	Geneva	Switzerland	mrast@geosec.org
11	Mr	alemu	gonsamo	university of helsinki	geography	PL 64	Gustaf Hällströmin katu 2		14 helsinki	Finland	alemu.gonsamo@helsinki.fi
12	Mr	Wolfe	Robert	NASA	GSFC	Greenbelt Rd.		20771	Greenbelt	United States	rwolfe@pop900.gsfc.nasa.gov
13	Ms	Nydegger	Dania	University of Zurich	Remote Sensing Laboratories	Ahornstr. 22		8051	Zurich	Switzerland	d.nydegger@bluemail.ch
14	Mr	Pisek	Jan	University of Toronto	Department of Geography and Program in Planning	100 St. George Street, Room 5047		M5S 3G3	Toronto	Canada	jan.pisek@utoronto.ca
15	Mr	Jones	Hamlyn	University of Dundee	Division of Applied & Environmental Biology	University of Dundee at SCRI	Invergowrie	DD2 5DA	Dundee	United Kingdom	h.g.jones@dundee.ac.uk
16	Mr	Rossello	Philippe	INRA	Climat, Sol et Environnement	Domaine Saint-Paul	Site Agroparc	84914	Avignon cedex 9	France	rossello@avignon.inra.fr
17	Mr	BUIS	JEAN-PIERRE	CIMEL	RESEARCH	172 RUE DE CHARONNE		75011	PARIS	France	jp-buis@cimel.fr
18	Mr	Marloie	Olivier	INRA	UMR Climat Sol Environnement	Domaine Saint Paul - Site Agroparc		84914	Avignon Cedex 9	France	marloie@avignon.inra.fr
19	Mr	Brenguier	Jean-Louis	METEO France	EUFAR Coordinator	XXX		XXX	XXX	France	jlb@meteo.fr
20	Ms	Jonckheere	Inge	ESF	ESF EUROCORES Programme Coordinator	xxx		xxx	xxx	Belgium	ijonckheere@esf.org
21	Mr	Briggs	Stephen	ESA/ESRIN	EO Science, Applications and Future Technologies	Via Galileo Galilei		44	Frascati	Italy	Stephen.Briggs@esa.int
22	Mr	Guyot	Gerard	INRA	xxx	12, rue Pavilot		84310	Morières-lès-Avignon	France	gerard.guyot@club-internet.fr
23	Mr	Ogunbadewa	Yemi	University of Salford	Centre for Environmental Systems Research	School of Environment and Life Sciences	Peel Building	M5 4WT	Manchester	United Kingdom	e.y.ogunbadewa@pgr.salford.ac.uk
24	Mr	Popp	Christoph	University of Bern	Department of Geography	Hallerstr. 12		3012	Bern	Switzerland	popp@giub.unibe.ch
25	Ms	Guedon	Anne-Marie	Univeristy of Ottawa	Geography	270C Dalehurst Ave.		K2G 4M8	Ottawa	Canada	amguedon@gmail.com
26	Mr	James	Frazier	Divining Technologies	Business Development	Avenue Louise 65, Box 11		1050	Bruxelles	Belgium	james@divining-technologies.com
27	Mr	Berger	Michael	ESA / ESTEC	EOP-SML	Keplerlaan 1		2200 AG	Noorddwijk	Netherlands	Michael.Berger@esa.int
28	Mr	Jonas	Tobias	SLF Swiss Fed. Inst. for Snow and Avalanche Res.	Mountain Hydrology and Torrents	Flüelastr. 11		7260	Davos	Switzerland	jonas@slf.ch
29	Mr	Ranson	Jon	NASA Goddard Space Flight Center	Biospheric Sciences	Code 614.4		20771	Greenbelt	United States	jon.ranson@nasa.gov
30	Mrs	Allgoewer	Britta	Science City Davos	Wissensstadt Davos	Rathaus	Berglistutz 1	7270	Davos Platz	Switzerland	britta.allgoewer@wissensstadt.ch
31	Mrs	Weiss	Brigitte	European Commission	DG RTD, B3	Square de Meeûs 8		1050	Bruxelles	Belgium	brigitte.weiss@ec.europa.eu
32	Mr	Meuleman	Koen	VITO	Remote Sensing and Earth Observation Processes	Boertang 200		2400	Mol	Belgium	koen.meuleman@vito.be
33	Mrs	Van de Hoef	Truus	Wageningen University	Centre for Geo-Information	Droevendaalsesteeg 3		6708 PB	Wageningen	Netherlands	truus.vandehoef@wur.nl
34	Mr	Alavipanh	Seyd Kazem	University of Tehran	Faculty of Geography	University of Tehran		Tehran	Tehran	Iran, Islamic Republic Of	salavipa@ut.ac.ir
35	Mr	Gomez-Sanchez	Jose-Antonio	Instituto Nacional de Tecnica Aeroespacial-INTA	Earth Observation,Remote Sensing&Atmosphere Dept.	Carr.Ajalvir km 4		28850	TORREJON DE ARDOZ (MADRID)	Spain	gomezsj@inta.es
36	Ms	Carrère	Véronique	Univesté de Nantes	Laboratoire de Planétologie et Géodynamique	Faculté des Sciences et des Techniques	2 rue de la Houssinière BP 92208	44322	Nantes	France	Veronique.Carrere@univ-nantes.fr
37	Mr	Schwarz	Jürgen	CREASO GmbH	Technik	Talhofstraße 32a		82205	Gilching	Germany	j.schwarz@creaso.com
38	Mr	Kortmann	Bernhard	CREASO GmbH	CEO	Talhofstraße 32a		82205	Gilching	Germany	
39	Mr	Dye	Daniel	University of Helsinki	Geography	P.O. Box 64		FIN-0001	Helsinki	Finland	daniel.dye@helsinki.fi
40	Mr	Victori	Stéphane	CIMEL ELECTRONIQUE	CIMEL ELECTRONIQUE	172 rue de Charonne		75011	PARIS	France	sales@cimel.fr
41	Mr	Hueni	Andreas	University of Zürich	Remote Sensing Laboratories, RSL	Winterthurerstrasse 190		8057	Zürich	Switzerland	ahueni@geo.unizh.ch
42	Mr	Gutman	Garik	NASA	Headquarters	300 E Street SW		20546	Washington, DC	United States	ggutman@nasa.gov
43	Mr	Schaepman	Michael	Wageningen University	Centre for Geo-Information	Droevendaalsesteeg 3		6708 PG	Wageningen	Netherlands	michael.schaepman@wur.nl
44	Mr	Kooistra	Lammert	Wageningen University	Centre for Geo-information	Droevendaalsesteeg 3		6708 PB	Wageningen	Netherlands	lammert.kooistra@wur.nl
45	Mr	Kneubühler	Mathias	University of Zürich	Dept. of Geography	Winterthurerstrasse 190		8057	Zürich	Switzerland	kneub@geo.unizh.ch
46	Mr	Lakshmi	Venkat	University of South Carolina	Geological Sciences	701 Sumter Street	University of South Carolina	29208	Columbia	United States	viakshmi@geol.sc.edu
47	Mrs	Sánchez	Martin	University of Salamanca	Terrain Engineering	Filiberto Villalobos 119		37007	Salamanca	Spain	nilda@usal.es
48	Mr	Jackson	Thomas	USDA ARS	Hydrology and Remote Sensing Lab	104 B007 BARC-West		MD 20705	Beltsville	United States	tjackson@hydrolab.arsusda.gov
49	Ms	Rautiainen	Miina	Tartu Observatory	--	61602 Toravere, Tartumaa		EE-61602	Toravere	Estonia	miina.rautiainen@helsinki.fi
50	Mr	LEROY	Marc	POSTEL Service Centre	Medias-France	18, avenue E. Belin		31401	Toulouse	France	marc.leroy@medias.cnes.fr
51	Mr	Ben-Dor	Eyal	Tel-Aviv University	Geography	Levanon 1 st.	Ramat Aviv, Tel-Aviv	39040	Tel-Aviv	Israel	bendor@post.tau.ac.il
52	Mr	Verhoef	Wout	National Aerospace laboratory NLR	ASSP	P.O. Box 153		8300 AD	Emmeloord	Netherlands	verhoef@nlr.nl
53	Mr	Painter	Thomas	National Snow and Ice Data Center	University of Colorado	449 UCB		80309	Boulder	United States	tpainter@nsidc.org
54	Mr	SOBRINO	JOSÉ A.	UNIVERSITY OF VALENCIA	Earth Physics and Thermodynamics	C/Dr. MOLINER 50		46100	BURJASSOT	Spain	sobrinov@uv.es
55	Ms	Pegrum	Heather	National Physical Laboratory	Optical Radiation	F4-A1	Hampton Road	TW11 0LW	Teddington	United Kingdom	Heather.Pegrum@npl.co.uk
56	Mr	Salim	Saber	National Physical Lab. & City University	Quality of Life Division, ORM team	Hampton Road, Teddington		TW11 0LW	Middlesex	United Kingdom	saber.salim@npl.co.uk
57	Ms	Lachérade	Sophie	ONERA	DOTA / POS	2 Avenue Edouard Belin - BP 4025	Cedex 04	31055	Toulouse	France	sophie.lacherade@oncert.fr
58	Mr	Simonetti	Dario	Joint Research Centre	GEM	Via Enrico Fermi 1		21020	Ispra (VA)	Italy	dario.simonetti@ext.jrc.it
59	Mr	Schlerf	Martin	ITC	Natural Resource Management	Postbus 6		7500 AA	Enschede	Netherlands	schlerf@itc.nl
60	Mr	Keller	Johannes	Paul Scherrer Institut (PSI)	Laboratory for Atmospheric Chemistry (LAC)	OFLA/012		5232	Villigen PSI	Switzerland	johannes.keller@psi.ch
61	Mr	Mac Arthur	Alasdair	University of Edinburgh	NERC Field Spectroscopy Facility	Grant Institute,	King's Buildings	EH9 3JW	Edinburgh	United Kingdom	alasdair.macarthur@ed.ac.uk
62	Mrs	Kugler	Zsófia	DG Joint Research Center - European Commission	Institute for the Protection & Security of the Cit	Via E. Fermi 1		I-21020	Ispra	Italy	zsafia.kugler@jrc.it
63	Mr	de Miguel	Eduardo	INTA	Remote Sensing Laboratory	Cta Ajalvir s/n		28850	Torrejon de Ardoz	Spain	demiguel@inta.es
64	Mr	Koetz	Benjamin	University of Zürich	RSL	Winterthurerstrasse 190		8057	Zürich	Switzerland	bkoetz@geo.unizh.ch
65	Mr	Martonchik	John	NASA/Jet Propulsion Laboratory	Science Division	4800 Oak Grove Drive	169-237	91109	Pasadena	United States	john.v.martonchik@jpl.nasa.gov
66	Mrs	Zeng	Yuan	Wageningen University and Research Center	Center for Geo-Information	P.O. Box 47		6700 AA	Wageningen	Netherlands	yuan.zeng@wur.nl
67	Mr	Royer	Alain	Universite de Sherbrooke	CARTEL	2500 Bd Universite		J1K 2R1	Sherbrooke	Canada	Alain.Royer@Usherbrooke.ca
68	Mr	Zurita-Milla	Raul	Wageningen University	Centre for Geo-Information	Postbus 47		6700 AA	wageningen	Netherlands	raul.zurita-milla@wur.nl
69	Mr	Akay	Abdullah E	Kahramanmaras Sutcu Imam University	Forest Engineering	KSU Faculty of Forestry	Forest Engineering Department	46100	Kahramanmaras	Turkey	akay@ksu.edu.tr
70	Mr	Jimenez	Marcos	INTA	Remote Sensing Laboratory	Carretera de Ajalvir km 4	Torrejon de Ardoz	28850	Madrid	Spain	jimenezmm@inta.es
71	Mrs	Reusen	Ils	VITO	Remote Sensing and Earth Observation Processes	Boeretang 200		BE-2400	MOL	Belgium	ils.reusen@vito.be
72	Mr	Hagolle	Olivier	CNES	Physics of Optical Measurements Service	BPI 811	18 avenue Edouard Belin	31401	Toulouse	France	olivier.hagolle@cnes.fr
73	Ms	Riaza	Asuncion	Instituto Geologico y Minero de España	Geologia y Geofisica	La Calera 1		28760	Tres Cantos (Madrid)	Spain	a.riaza@igme.es
74	Mr	Verrelst	Jochem	Wageningen University	Centre for Geo-Information, Wageningen University	Droevendaalsesteeg 3,		6708 PB	Wageningen	Netherlands	jochem.verrelst@wur.nl
75	Mr	Schneebeli	Marc	University of Bern	Institute of Applied Physics	Sidlerstrasse 5		3012	Bern	Switzerland	marc.schneebeli@mw.iap.unibe.ch
76	Mr	Damm	Alexander	Humboldt Universität zu Berlin	Geomatics Department	Unter den Linden 6		10099	Berlin	Germany	alexander.damm@geo.hu-berlin.de
77	Mr	Gidudu	Anthony	Makerere University	Surveying	P.O. Box 7062		N/A	Kampala	Uganda	agidudu@tech.mak.ac.ug
78	Mr	STEVEN	Michael	University of Nottingham	School of Geography	University of Nottingham		NG7 2RD	Nottingham	United Kingdom	Michael.steven@nottingham.ac.uk
79	Mr	WIDLOWSKI	Jean-Luc	Joint Research Centre	IES/GEM	Via E. Fermi, 1		21020	Ispra	Italy	jean-luc.widlowski@jrc.it
80	Mrs	Quental	Lidia	INETI	Mineral Resources	Ap.7586		2721-866	Amadora	Portugal	lidia.quental@ineti.pt
81	Mr	picard	ghislain	Universite Joseph Fourier	Laboratoire de Glaciologie	54 rue Molière		F-38400	St Martin d'Hères	France	ghislain.picard@lgge.obs.ujf-grenoble.fr
82	Mr	Möttus	Matti	Tartu Observatory	Remote Sensing of Vegetation	Tõravere		61602	Tartumaa	Estonia	mottus@ut.ee
83	Mr	Seiler	Bruno	University of Zürich	Geography	Schlosshofstrasse 28		8400	Winterthur	Switzerland	bseiler@geo.unizh.ch
84	Mr	zhao	shaojie	Beijing Normal University	School of Geography	Beijing Normal University, Beijing, China		100875	Beijing	China	geo_zhao@126.com
85	Mr	Christopher	Marston	University of Salford	School of Environment and Life Sciences	Peel Building	University of Salford	M5 4WT	Manchester	United Kingdom	c.g.marston@pgr.salford.ac.uk

86	Ms	Homolova	Lucie	Academy of Sciences of the Czech Republic	Institute of Systems Biology and Ecology	Porici 3b		60300 Brno	Czech Republic	lucie.homolova@brno.cas.cz
87	Mr	Skidmore	Andrew	ITC	Department of Natural Resources	PO Box	7500 AA	Enschede	Netherlands	skidmore@itc.nl
88	Mr	FERET	Jean-Baptiste	IPGP, Université Paris 7	Etudes spatiales et planétologie	4, place Jussieu	Tour 14, 4e étage, Aile 14-15	75252 Paris cedex 05	France	feret@ipgp.jussieu.fr
89	Mr	Waser	Lars	Swiss Federal Research Institute WSL	Land Resources Assessment	Zürcherstrasse 111		8903 Birmensdorf	Switzerland	waser@wsl.ch
90	Mr	Muller	Jan-Peter	University College London	Space and Climate Physics	Mullard Space Science Laboratory	Holmbury St Mary	RH5 6NT Dorking	United Kingdom	jpm@mssl.ucl.ac.uk
91	Mrs	Visscher von Arx	Anja	University of Zurich	Dept. of Geography Remote Sensing Laboratories	Winterthurerstrasse 190		8057 Zurich	Switzerland	lake94@freesurf.ch
92	Mr	Löwe	Henning	WSL/SLF	Snow and Permafrost	Flueelastrasse 11		7260 Davos Dorf	Switzerland	loewe@slf.ch
93	Ms	Huber	Silvia	University of Zurich	Dept. of Geography, Remote Sensing Laboratories	Winterthurerstrasse 190		8057 Zurich	Switzerland	shuber@geo.unizh.ch
94	Mr	Dedieu	Gérard	CNES	CESBIO	18 avenue Edouard Belin		31401 Toulouse Cedex 9	France	gerard.dedieu@cesbio.cnes.fr
95	Mr	Malenovsky	Zbynek	Academy of Sciences of the Czech Republic	Institute of Systems Biology and Ecology	Porici 3B		60300 Brno	Czech Republic	zbynek.malenovsky@gmail.com
96	Mrs	Gagliano	Caterina	CRA - ISAFA	Forest and Range Management	Piazza Nicolini, 6		38100 Trento	Italy	caterina.gagliano@entecra.it
97	Mr	Eiden	Michael	Juelich Research Centre	Inst. of Chemistry and Dynamics of the Geosphere	Institute III: Phytosphere	Juelich Research Centre	52425 Juelich	Germany	m.eiden@fz-juelich.de
98	Mr	Lyapustin	Alexei	UMBC GEST/NASA GSFC	Goddard Earth Systems Technology Center	NASA Goddard Space Flight Center	Mail code 614.4	20771 Greenbelt, MD	United States	alyapust@pop900.gsfc.nasa.gov
99	Mr	Pinty	Bernard	JRC	IES- GEM unit	Via E. Fermi		21020 Ispra	Italy	bernard.pinty@jrc.it
100	Mr	Bachmann	Martin	DLR-DFD German Remote Sensing Data Center	Imaging Spectroscopy Workgroup	Münchnerstr. 20		82234 Wessling	Germany	martin.bachmann@dlr.de
101	Mr	Schopfer	Juerg	University of Zurich	Department of Geography, RSL	Winterthurerstrasse 190		8057 Zurich	Switzerland	jschopfer@geo.unizh.ch
102	Mr	Quaife	Tristan	Centre for Terrestrial Carbon Dynamics	Department of Geography	Peason Building	Gower Street	WC1E 6BT London	United Kingdom	tquaife@geog.ucl.ac.uk
103	Mr	Lewis	Philip	University College London and NERC CTCD	Geography	Gower St.,		WC1H 6BT London	United Kingdom	plewis@geog.ucl.ac.uk
104	Mr	Disney	Mathias	University College London	Geography	Gower Street		WC1E 6BT London	United Kingdom	mdisney@geog.ucl.ac.uk
105	Mr	Ramirez	Alberto	Universidad Catolica Nuestra Señora de la Asuncion	Computer Science Department	Gumersindo Sosa 610 y 4 de Julio		1845 Asuncion	Paraguay	A.Ramirez@salford.ac.uk
106	Mr	Menze	Bjoern	University of Heidelberg	Interdisciplinary Center for Scientific Computing	INF 368		69120 Heidelberg	Germany	bjoern.menze@iwr.uni-heidelberg.de
107	Mr	Fontana	Fabio	University of Bern	Remote Sensing Institute of Geography	Hallerstr. 12		3012 Bern	Switzerland	fontana@giub.unibe.ch
108	Mr	Psomas	Achilleas	Swiss Federal Research Institute WSL	Land Use Dynamics	Zürcherstrasse 111		8903 Birmensdorf	Switzerland	achilleas.Psomas@wsl.ch
109	Mr	Danson	Mark	University of Salford	Centre for Environmental Systems Research	School of Environment and Life Sciences	University of Salford	M5 4WT Manchester	United Kingdom	f.m.danson@salford.ac.uk
110	Mr	fernandes	richard	Natural Resources Canada/ Govt. of Canada	Canada Centre for Remote Sensing	588 Booth st		K1A 0Y7 Ottawa	Canada	richard.fernandes@nrcan.gc.ca
111	Mr	Veroustraete	Frank	Flemish Institute for Technological Research	Centre for Remote Sensing and Earth Observation	Boeretang 200		2400 Mol	Belgium	frank.veroustraete@vito.be
112	Mr	de Wit	Allard	Wageningen-UR	Centre for Geo-information	P.O. Box 47		6700 AA Wageningen	Netherlands	allard.dewit@wur.nl
113	Mr	Odermatt	Daniel	University of Zurich	Remote Sensing Laboratories RSL	Winterthurerstrasse 190		8057 Zürich	Switzerland	dodermat@geo.unizh.ch
114	Mrs	Schaepman-Strub	Gabriela	Wageningen UR	Nature Conservation and Plant Ecology	Bornsesteeg 69		6708 PD Wageningen	Netherlands	gabriela.schaepman@wur.nl
115	Ms	Wang	Wenhui	University of Maryland	Department of Geography	Department of Geography, 2181 LeFrak Hall, Univers		20742 College Park, MD	United States	whwang1@umd.edu
116	Mr	Dowens	John	University of Edinburgh	Institute of Geography School of GeoSciences	Drummond Street	Edinburgh	EH8 9XP Edinburgh	United Kingdom	j.s.dowens@sms.ed.ac.uk
117	Mr	Frey	Othmar	University of Zürich	Remote Sensing Laboratories	Winterthurerstrasse 190		CH-8057 Zürich	Switzerland	ofrey@geo.unizh.ch
118	Mr	Baret	Frédéric	INRA	INRA-CSE, UMR1114	Agroparc		8414 Avignon	France	baret@avignon.inra.fr
119	Ms	Kim	Hye-Yun	University of Maryland, USA	Department of Geography	2181 LeFrak Hall	University of Maryland at College Park	MD 20742 College Park	United States	kimhy@umd.edu
120	Mr	Nieke	Jens	Uni Zurich	Department of Geography RSL	Winterthurerstr. 190		8057 ZURICH	Switzerland	nieke@geo.unizh.ch
121	Mr	Hancock	Steven	University College London	Geomatic Engineering and Geography	UCL, Geomatic Engineering,	Gower Street,	WC1E 6BT London	United Kingdom	steveh@ge.ucl.ac.uk
122	Mr	Clevers	Jan	Wageningen University	Centre for Geo-Information	P.O. Box 47		6700 AA Wageningen	Netherlands	jan.clevers@wur.nl
123	Mr	MA	KAI	INRA d'Avignon,France	Unité Climat, Sol et Environnement (CSE)	INRA - CSE,BAT. Climat,Site Agroparc,Domaine Saint		84914 Avignon	France	kai.ma@avignon.inra.fr
124	Mr	Warner	Timothy	West Virginia University	Department of Geology and Geography	425 White Hall		WV 26506 Morgantown	United States	tim.warner@mail.wvu.edu
125	Mr	Borel	Christoph	Christoph Borel	Advanced Geospatial Intelligence group	2875 Presidential Drive	Suite 180	45324 Fairborn	United States	cborel@ball.com
126	Mr	Vanderbilt	Vern	NASA Ames Research Center	Biospherics Branch, Earth Science Division	MS 242-4		94035 Moffett Field, California	United States	vvanderbilt@mail.arc.nasa.gov
127	Mr	MOYA	ISMAEL	CNRS	Laboratoire de Météorologie Dynamique (LMD)	Ecole Polytechnique		91128 PALAISEAU	France	moya@lmd.polytechnique.fr
128	Mr	Milton	Edward	University of Southampton	School of Geography	Highfield Campus		SO17 1BJ Southampton	United Kingdom	e.j.milton@soton.ac.uk
129	Mr	Daumard	Fabrice	LMD - CNRS	Fluorescence and Remote Sening	Ecole Polytechnique		91128 Palaiseau Cedex	France	fabrice.daumard@lmd.polytechnique.fr
130	Mr	Liang	Shunlin	University of Maryland	Department of Geography	2181 LeFrak Hall		20742 College Park, MD	United States	sliang@umd.edu
131	Mr	Selige	Thomas	Technische Universität München	Lehrstuhl für Pflanzenernährung	Am Hochanger 2		85354 Freising	Germany	selige@wzw.tum.de
132	Mr	Morsdorf	Felix	Universität Zürich	Remote Sensing Laboratories	Universität Zürich	Winterthurerstr. 190	8057 Zürich	Switzerland	morsdorf@geo.unizh.ch
133	Ms	Holzwarth	Stefanie	German Aerospace Center (DLR)	German Remote Sensing Data Center (DFD)	Oberpfaffenhofen		82234 Wessling	Germany	stefanie.holzwarth@dlr.de
134	Mr	Pellikka	Petri	University of Helsinki	Department of Geography	PO Box 64		14 Helsinki	Finland	petri.pellikka@helsinki.fi
135	Mr	Itten	Klaus	University of Zurich	Department of Geography	Winterthurerstr. 190		CH-8057 Zurich	Switzerland	itten@geo.unizh.ch
136	Mr	Conejo	Elian	IPGP- Denis Diderot University	Laboratoire de Géomatériaux et Environnement	37 Boulevard Jourdan Fondation Deutsch de la Meurt	75014 Paris	test Paris	France	conejo@ipgp.jussieu.fr
137	Mrs	Jia	Li	Alterra, Wageningen University and Research Centre	Centre for Geo-Information	Droevendaalsesteeg 3		6700AA Wageningen	Netherlands	li.jia@wur.nl
138	Mr	Shabanov	Nikolay	Boston University	Dept. of Geography	675 Commonwealth Avenue		MA 02215 Boston	United States	shabanov@bu.edu
139	Mr	JACQUEMOUD	STEPHANE	University of Paris 7 / IPGP	Space Studies and Planetology	Case 89	4 place Jussieu	75252 Paris Cedex 05	France	jacquemoud@ipgp.jussieu.fr
140	Mrs	Pfeifer	Marion	UCL (UK), Potsdam University (DE)	Department of Geography	Maulbeerallee 2, Potsdam	Jaegerallee 32, Potsdam	14469 Potsdam	Germany	marion.pfeifer@googlemail.com
141	Mr	ATZBERGER	Clement	Geosys SA	Recherche & Methodologie	20 Impasse Rene Couzinet	B.P 65815	31505 Toulouse cedex 5	France	ca@geosys.com